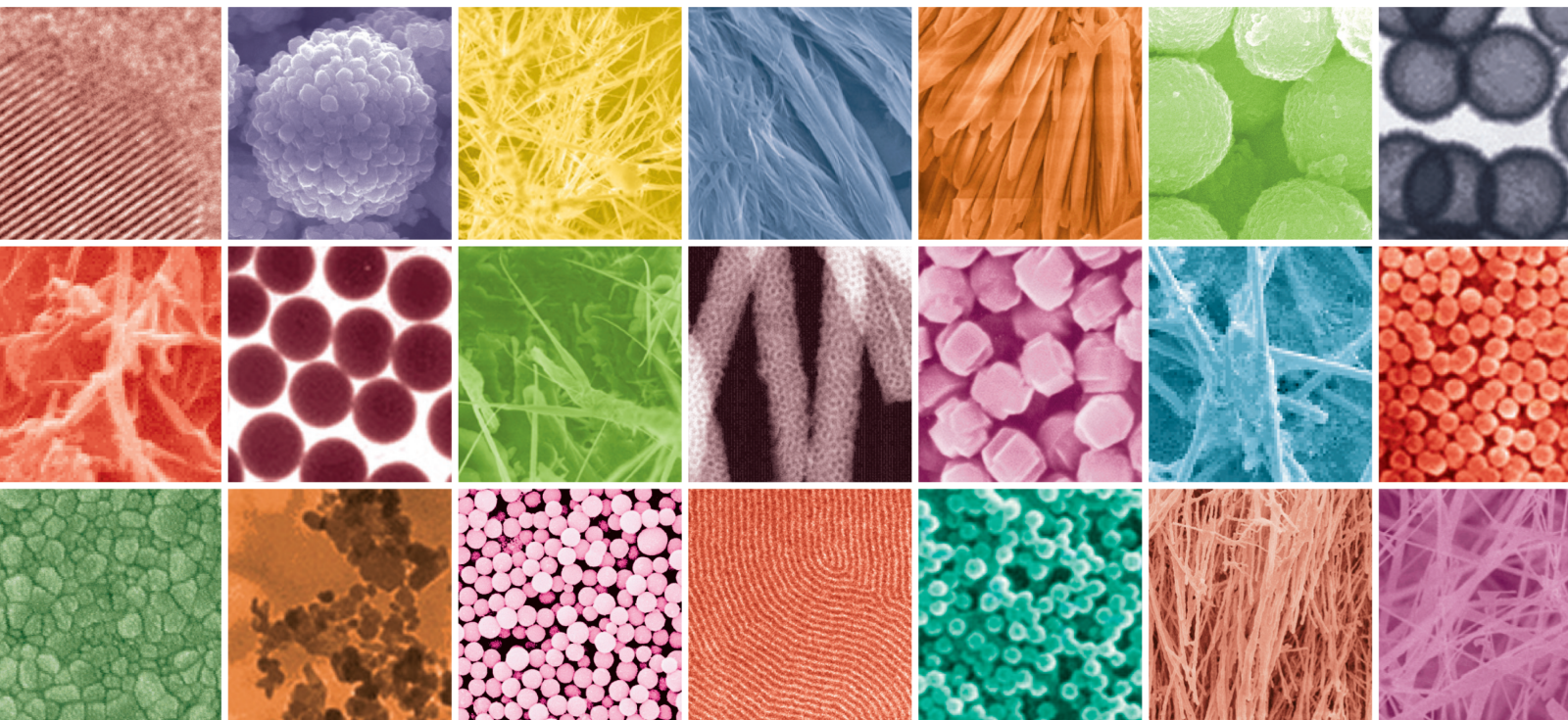


Green Nanometal Oxides for Environmental and Biomedical Applications

Lead Guest Editor: Arpita Roy

Guest Editors: H.C. Ananda Murthy and Hiwa M. Ahmed





Green Nanometal Oxides for Environmental and Biomedical Applications

Journal of Nanomaterials

**Green Nanometal Oxides for
Environmental and Biomedical
Applications**

Lead Guest Editor: Arpita Roy

Guest Editors: H.C. Ananda Murthy and Hiwa M.
Ahmed






Copyright © 2023 Hindawi Limited. All rights reserved.

This is a special issue published in "Journal of Nanomaterials." All articles are open access articles distributed under the Creative Commons Attribution License, which permits unrestricted use, distribution, and reproduction in any medium, provided the original work is properly cited.


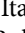

Chief Editor

Stefano Bellucci , Italy

















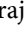
















Associate Editors

Ilaria Armentano, Italy
Stefano Bellucci , Italy
Paulo Cesar Morais , Brazil
William Yu , USA

Academic Editors

Buzuayehu Abebe, Ethiopia
Domenico Acierno , Italy
Sergio-Miguel Acuña-Nelson , Chile
Katerina Aifantis, USA
Omer Alawi , Malaysia
Nageh K. Allam , USA
Muhammad Wahab Amjad , USA
Martin Andersson, Sweden
Hassan Azzazy , Egypt
Ümit Ağbulut , Turkey
Vincenzo Baglio , Italy
Lavinia Balan , France
Nasser Barakat , Egypt
Thierry Baron , France
Carlos Gregorio Barreras-Urbina, Mexico
Andrew R. Barron , USA
Enrico Bergamaschi , Italy
Sergio Bietti , Italy
Raghvendra A. Bohara, India
Mohamed Bououdina , Saudi Arabia
Victor M. Castaño , Mexico
Albano Cavaleiro , Portugal
Kondareddy Cherukula , USA
Shafiul Chowdhury, USA
Yu-Lun Chueh , Taiwan
Elisabetta Comini , Italy
David Cornu, France
Miguel A. Correa-Duarte , Spain
P. Davide Cozzoli , Italy
Anuja Datta , India
Loretta L. Del Mercato, Italy
Yong Ding , USA
Kaliannan Durairaj , Republic of Korea
Ana Espinosa , France
Claude Estournès , France
Giuliana Faggio , Italy
Andrea Falqui , Saudi Arabia





Matteo Ferroni , Italy
Chong Leong Gan , Taiwan
Siddhartha Ghosh, Singapore
Filippo Giubileo , Italy
Iaroslav Gnilitzkiy, Ukraine
Hassanien Gomaa , Egypt
Fabien Grasset , Japan
Jean M. Greneche, France
Kimberly Hamad-Schifferli, USA
Simo-Pekka Hannula, Finland
Michael Harris , USA
Hadi Hashemi Gahruei , Iran
Yasuhiko Hayashi , Japan
Michael Z. Hu , USA
Zhengwei Huang , China
Zafar Iqbal, USA
Balachandran Jeyadevan , Japan
Xin Ju , China
Antonios Kellarakis , United Kingdom
Mohan Kumar Kesarla Kesarla , Mexico
Ali Khorsand Zak , Iran
Avvaru Praveen Kumar , Ethiopia
Prashant Kumar , United Kingdom
Jui-Yang Lai , Taiwan
Saravanan Lakshmanan, India
Meiyong Liao , Japan
Shijun Liao , China
Silvia Licocchia , Italy
Zainovia Lockman, Malaysia
Jim Low , Australia
Rajesh Kumar Manavalan , Russia
Yingji Mao , China
Ivan Marri , Italy
Laura Martinez Maestro , United Kingdom
Sanjay R. Mathur, Germany
Tony McNally, United Kingdom
Pier Gianni Medaglia , Italy
Paul Munroe, Australia
Jae-Min Myoung, Republic of Korea
Rajesh R. Naik, USA
Albert Nasibulin , Russia
Ngoc Thinh Nguyen , Vietnam
Hai Nguyen Tran , Vietnam
Hiromasa Nishikiori , Japan

Sherine Obare , USA
Abdelwahab Omri , Canada
Dillip K. Panda, USA
Sakthivel Pandurengan , India
Dr. Asisa Kumar Panigrahy, India
Mazeyar Parvinzadeh Gashti , Canada
Edward A. Payzant , USA
Alessandro Pegoretti , Italy
Oscar Perales-Pérez, Puerto Rico
Anand Babu Perumal , China
Suresh Perumal , India
Thathan Premkumar , Republic of Korea
Helena Prima-García, Spain
Alexander Pyatenko, Japan
Xiaoliang Qi , China
Haisheng Qian , China
Baskaran Rangasamy , Zambia
Soumyendu Roy , India
Fedlu Kedir Sabir , Ethiopia
Lucien Saviot , France
Shu Seki , Japan
Senthil Kumaran Selvaraj , India
Donglu Shi , USA
Muhammad Hussnain Siddique , Pakistan
Bhanu P. Singh , India
Jagpreet Singh , India
Jagpreet Singh, India
Surinder Singh, USA
Thangjam Ibomcha Singh , Republic of Korea
Korea
Vidya Nand Singh, India
Vladimir Sivakov, Germany
Tushar Sonar, Russia
Pingan Song , Australia
Adolfo Speghini , Italy
Kishore Sridharan , India
Marinella Striccoli , Italy
Andreas Stylianou , Cyprus
Fengqiang Sun , China
Ashok K. Sundramoorthy , India
Bo Tan, Canada
Leander Tapfer , Italy
Dr. T. Sathish Thanikodi , India
Arun Thirumurugan , Chile
Roshan Thotagamuge , Sri Lanka


Valeri P. Tolstoy , Russia
Muhammet S. Toprak , Sweden
Achim Trampert, Germany
Tamer Uyar , USA
Cristian Vacacela Gomez , Ecuador
Luca Valentini, Italy
Viet Van Pham , Vietnam
Antonio Vassallo , Italy
Ester Vazquez , Spain
Ajayan Vinu, Australia
Ruibing Wang , Macau
Magnus Willander , Sweden
Guosong Wu, China
Ping Xiao, United Kingdom
Zhi Li Xiao , USA
Yingchao Yang , USA
Hui Yao , China
Dong Kee Yi , Republic of Korea
Jianbo Yin , China
Hesham MH Zakaly , Russia
Michele Zappalorto , Italy
Mauro Zarrelli , Italy
Osman Ahmed Zeleke, Ethiopia
Wenhui Zeng , USA
Renyun Zhang , Sweden

Contents


Assessment on the Toxic Effects of Chemically Synthesized SPIONs against Model Organisms

Chellapan Justin, Antony V. Samrot , Nagarajan Shobana , Mahendran Sathiyasree, Subramanian Saigeetha, Rajan Renuka Remya , Deenadhayalan Rajalakshmi, and S. Prasath 
Research Article (15 pages), Article ID 4235308, Volume 2023 (2023)


Study of Progress on Nanocrystalline Cellulose and Natural Fiber Reinforcement Biocomposites

T. Aravind, Mohd. Shaikhul Ashraf, Rajesh A. S., N. Ahalya, Mahavir Singh Rawat, B. Uma, Rajneesh Sharma, Ram Subbiah, and SisayKetema Sida 
Review Article (16 pages), Article ID 6519480, Volume 2022 (2022)








Flax- and Graphene-Reinforced Natural Fiber Nanocomposites under Cryogenic Environment for Constructional Applications

Munirah D. Albaqami, N. Krishnamoorthy, S. D. Uma Mageswari, Sarita Santaji Shinde, S. C. V. Ramana Murty Naidu, Neha Munjal, Aboud Ahmed Awadh Bahajjaj, S. H. Mohammed, and Prasath Srinivasan 
Research Article (9 pages), Article ID 4971582, Volume 2022 (2022)


Optimization and Mechanical Characteristics of AA6061/Zirconia Nanocomposites Fabricated by Ultrasonic-Aided Stir Casting Method

Amel Gacem, Moamen S. Refat, H. Elhosiny Ali, S. C. V. Ramana Murty Naidu, B. Beenarani, Pranjali Deole, S. Sandeep Kumar, S. Rama, Amnah Mohammed Alsuhaibani, and Abdi Diriba 
Research Article (15 pages), Article ID 2453412, Volume 2022 (2022)


Optimum Green Synthesis of Silver Nanoparticles with the Highest Antibacterial Activity against *Streptococcus mutans* Biofilm

Azam Chahardoli , Mohsen Safaei , Mohammad Salmani Mobarakeh , Nima Fallahnia , Behnam Fatehi , Mohammad Moslem Imani , and Amin Golshah 
Research Article (7 pages), Article ID 6261006, Volume 2022 (2022)


Investigation of High-Temperature Wear Behaviour of AA 2618-Nano Si₃N₄ Composites Using Statistical Techniques

Santhi M. George, Amel Gacem, A. Kistan, R. Mohammed Ashick, L. Malleswara Rao, Vinod Singh Rajput, N. Nagabooshanam, Moamen S. Refat, Amnah Mohammed Alsuhaibani, and David Christopher 
Research Article (12 pages), Article ID 3449903, Volume 2022 (2022)




Nanotitanium Oxide Particles and Jute-Hemp Fiber Hybrid Composites: Evaluate the Mechanical, Water Absorptions, and Morphological Behaviors

C. R. Mahesha, R. Suprabha, Mahesh S. Harne, Sachin G. Galme, Sandeep G. Thorat, N. Nagabhooshanam, A. H. Seikh, M. H. Siddique, and Mebratu Markos 
Research Article (7 pages), Article ID 3057293, Volume 2022 (2022)

Reconnoitring Wear Resistance and Mechanical Strengths of AA8111/B₄C/ZrO₂ Nanocomposite through Taguchi Route

Sathish Thanakodi, Mohanavel Vinayagam, M. Ravichandran, T. Raja, A. H. Seikh, M. H. Siddique, and Beruk Hailu 
Research Article (10 pages), Article ID 9142336, Volume 2022 (2022)


Electrochemical Detection of H₂O₂ on Graphene Nanoribbons/Cobalt Oxide Nanorods-Modified Electrode

Preethika Murugan, Ashok K. Sundramoorthy , Ramila D. Nagarajan, Raji Atchudan, Rajeshkumar Shanmugam , Dhanraj Ganapathy, Sandeep Arya, Asma A. Alothman , and Mohamed Ouladsmane
Research Article (10 pages), Article ID 9866111, Volume 2022 (2022)


Synthesis of AA8050/B₄C/TiB₂ Hybrid Nanocomposites and Evaluation of Computer-Aided Machining Parameters

T. Sathish, Mohanavel Vinayagam, T. Raja, A. H. Seikh, M. H. Siddique, Ram Subbiah, and Beruk Hailu 
Research Article (13 pages), Article ID 9745418, Volume 2022 (2022)

Tribological Behavior of Al/Nanomagnesium/Aluminum Nitride Composite Synthesized through Liquid Metallurgy Technique

D. Srinivasan, M. Meignanamoorthy, Amel Gacem, Mohanavel Vinayagam, Thanakodi Sathish, M. Ravichandran, Suresh Kumar Srinivasan, Magda H. Abdellattif, and Haiter Lenin Allasi 
Research Article (12 pages), Article ID 7840939, Volume 2022 (2022)





Investigations of Nanoparticles (Al₂O₃-SiO₂) Addition on the Mechanical Properties of Blended Matrix Polymer Composite

K. Logesh, V. M. Vel, A. H. Seikh, Ajit M. Hebbale, Rajesh A S, N. Nagabhooshanam, Ram Subbiah, M. H. Siddique, and S. Praveen Kumar 
Research Article (7 pages), Article ID 4392371, Volume 2022 (2022)






Reduction and Heavy Metal Stabilization of River Sediment by Hydrothermal Treatment

Suyang Sun , Tinggan Fang, Gang Xue , Yueling He, Xiaonuan Wang, Qi Song, Xueke Zang, Yiwei Wang, and Shanshan Zheng
Research Article (13 pages), Article ID 5303955, Volume 2022 (2022)



Biogenic Synthesis of Silver Nanoparticles Using *Rhazya stricta* Extracts and Evaluation of Its Biological Activities

Sami Bawazeer, Abdur Rauf , Talha Bin Emran , Abdullah S. M. Aljohani, Fahad A. Alhumaydhi , Zidan Khan, Laiba Ahmad, Hassan A. Hemeg, Naveed Muhammad, Rohit Sharma , Aneela Maalik, and Ibrahim Khan
Research Article (11 pages), Article ID 7365931, Volume 2022 (2022)

Dynamic Beam Switching by the Highly Sensitive Metasurface Composed of All-Metallic Split-Ring Resonators





Wenrong Si , Chenzhao Fu , Fengyuan Gan , Dun Lan , and Wei Li 
Research Article (6 pages), Article ID 5186069, Volume 2022 (2022)

Study on Optimization of WEDM Process Parameters on Stainless Steel

K. Natarajan, H. Ramakrishnan, Amel Gacem, V. Vijayan , K. Karthiga, H. Elhosiny Ali, B. Prakash, and Addisalem Mekonnen 
Review Article (7 pages), Article ID 6765721, Volume 2022 (2022)




Contents

Recent Breakthrough of Bismuth-Based Nanostructured Materials for Multimodal Theranostic Applications

Dhanraj Ganapathy, Chitra Shivalingam, Rajeshkumar Shanmugam , Ashok K. Sundramoorthy , Karthikeyan Murthykumar, Sivaperumal Pitchiah , Saravanan Sekaran, and Sathish Kumar Ramachandran 


Review Article (7 pages), Article ID 4944320, Volume 2022 (2022)

Nanomaterials: A Potential Hope for Life Sciences from Bench to Bedside

Mahesh Uttamrao Shinde , Mohsina Patwekar , Faheem Patwekar, Majed A. Bajaber, Anuradha Medikeri, Firdous Sayeed Mohammad, Mohammad Mukim, Sanjay Soni, Jewel Mallick , and Talha Jawaid


Review Article (13 pages), Article ID 5968131, Volume 2022 (2022)

Green Synthesis of Gold Nanoparticles Using Extract of *Pistacia chinensis* and Their *In Vitro* and *In Vivo* Biological Activities

Fahad A. Alhumaydhi 







Research Article (11 pages), Article ID 5544475, Volume 2022 (2022)

Evaluation on Powder Metallurgy Process Parameters of Ball-Milled AA8079-B₄C Nanostructured Composites via Taguchi Grey Relational Analysis

M. Meignanamoorthy, Mohanavel Vinayagam, M. Ravichandran, T. Raja, Amel Gacem, Amine Mezni, Mohammed Jameel, and Manikandan Ganesan 








Research Article (12 pages), Article ID 7484053, Volume 2022 (2022)

Fabrication of Silver Nanoparticles from *Ziziphus nummularia* Fruit Extract: Effect on Hair Growth Rate and Activity against Selected Bacterial and Fungal Strains

Muhammad Saqib Khalil, Muhammad Shakeel, Naila Gulfam, Syed Umair Ahmad , Aamir Aziz, Junaid Ahmad, Shabana Bibi , Hitesh Chopra , Fahad A. Alhumaydhi , Abubakr M. Idris , Mayeen Uddin Khandaker, Manal Ewaiss Hassan, and Talha Bin Emran 



Research Article (14 pages), Article ID 3164951, Volume 2022 (2022)

Green Synthesized Calcium Oxide Nanoparticles (CaO NPs) Using Leaves Aqueous Extract of *Moringa oleifera* and Evaluation of Their Antibacterial Activities

Vikram Jadhav , Arun Bhagare , Shadma Wahab , Dnyaneshwar Lokhande , Chandraprabha Vaidya, Akshay Dhayagude , Mohammad Khalid, Jayraj Aher , Amine Mezni, and Mycal Dutta 


Research Article (7 pages), Article ID 9047507, Volume 2022 (2022)

Optimization of Stir Casting Variables for Production of Multiwalled Carbon Nanotubes: AA7149 Composite






Mohamad Reda A. Refaai, Samraj Ravi, S. Prasath , Maridurai Thirupathy, Ram Subbiah, and Abdi Diriba 

Research Article (7 pages), Article ID 2535470, Volume 2022 (2022)


Optimization and Tribological Properties of Hybridized Palm Kernel Shell Ash and Nano Boron Nitride Reinforced Aluminium Matrix Composites

M. Lokeshwari, P. Vidya Sagar, K. Dilip Kumar, D. Thirupathy, Ram Subbiah, P. Ganeshan, A. H. Seikh, S. M. A. K. Mohammed, and David Christopher 
Research Article (9 pages), Article ID 8479012, Volume 2022 (2022)





A Potential Notion on Alzheimer's Disease: Nanotechnology as an Alternative Solution

Sudhir Suryakant Pange, Mohsina Patwekar , Faheem Patwekar, Saad Alghamdi , Ahmad O. Babalghith , Osama Abdulaziz, Talha Jawaid, Mehnaz Kamal , Shahana Tabassum, and Jewel Mallick 
Review Article (8 pages), Article ID 6910811, Volume 2022 (2022)




Optimization and Prediction of Tribological Behaviour of Al-Fe-Si Alloy-Based Nanograin-Refined Composites Using Taguchi with Response Surface Methodology

S. Balaji, P. Maniarasan, S. V. Alagarsamy, Abdullah M. Alswieleh, V. Mohanavel, M. Ravichandran, Byong-Hun Jeon, and Haiter Lenin Allasi 
Research Article (12 pages), Article ID 9733264, Volume 2022 (2022)




Optimization of WEDM Process Parameters in Al2024-Li-Si₃N₄ MMC

K. Raju , M. Balakrishnan , D. V. S. S. V. Prasad, V. Nagalakshmi, Pravin P. Patil, S. Kaliappan, B. Arulmurugan , K. Radhakrishnan, B. Velusamy, Prabhu Paramasivam , and A. El-Denglawey
Research Article (12 pages), Article ID 2903385, Volume 2022 (2022)




An Empirical Analysis of Heat Expulsion and Pressure Drop Attribute in Helical Coil Tube Using Nanomaterials

Salem Algarni, Vineet Tirth , Talal Alqahtani, Pravin R. Kshirsagar , and Worku Abera 
Research Article (8 pages), Article ID 9712065, Volume 2022 (2022)


Anticancer and Antioxidant Activity of *Morinda Citrifolia* Leaf Mediated Selenium Nanoparticles

M. Nagalingam , S. Rajeshkumar , Satheesh Kumar Balu, M. Tharani, and Kalirajan Arunachalam 
Research Article (7 pages), Article ID 2155772, Volume 2022 (2022)

***Azadirachta indica*-Derived Silver Nanoparticle Synthesis and Its Antimicrobial Applications**








Aditya Amrut Pawar, Jyotirmayee Sahoo, Aakash Verma, Abdullah M. Alswieleh , Abhijit Lodh, Rajesh Raut, Jaya Lakkakula , Byong-Hun Jeon, and Md. Rabiul Islam 
Research Article (15 pages), Article ID 4251229, Volume 2022 (2022)

Synthesis and Experimental Investigations of Tribological and Corrosion Performance of AZ61 Magnesium Alloy Hybrid Composites



R. Venkatesh, C. Ramesh Kannan, S. Manivannan, M. Vivekanandan, J. Phani Krishna, Amine Mezni, Saiful Islam, and S. Rajkumar 
Research Article (12 pages), Article ID 6012518, Volume 2022 (2022)

Contents

Fabrication, Characteristics, and Therapeutic Applications of Carbon-Based Nanodots

Zoya Zaidi , Niladri Maiti, Mohammad Irfan Ali , Gunjan Sharma , Sarmad Moin , Harihara Padhy , G. L. Balaji , and Venkatesa Prabhu Sundramurthy 
Review Article (12 pages), Article ID 8031495, Volume 2022 (2022)








Investigation of TiO₂ Nanoparticles Using Leaf Extracts of *Lippia adoensis* (Kusaayee) for Antibacterial Activity

Lamessa Gudata , Abel Saka , Jule Leta Tesfaye , R. Shanmugam , L. Priyanka Dwarampudi, N. Nagaprasad , B. Stalin , and Ramaswamy Krishnaraj 
Research Article (8 pages), Article ID 3881763, Volume 2022 (2022)




Bioinspired Advances in Nanomaterials for Sustainable Agriculture

S. Malini , Kalyan Raj, S. Madhumathy, Khalid Mohamed El-Hady, Saiful Islam, and Mycal Dutta 
Review Article (11 pages), Article ID 8926133, Volume 2022 (2022)



Exclusion of Chromium(VI) Ion in Grueling Activated Carbon Fabricated from *Manilkara zapota* Tree Wood by Adsorption: Optimization by Response Surface Methodology

S. Sujatha , R. Sivarethinamohan , A. Oorkalan , V. Senthilkumar , B. Anuradha , B. Veluchamy, P. Prabhu , Magda H. Abdellattif , and Abdulmohsen Khalaf Dhahi Alsukaibi
Research Article (9 pages), Article ID 8157815, Volume 2022 (2022)









Biogenic Synthesis of Magnetite Nanoparticles Using Leaf Extract of *Thymus schimperi* and Their Application for Monocomponent Removal of Chromium and Mercury Ions from Aqueous Solution

Sintayehu Tamenne Geneti, Gemechis Asfaw Mekonnen, H. C. Ananda Murthy , Endale Tsegaye Mohammed, C. R. Ravikumar, Bedasa Abdisa Gonfa , and Fedlu Kedir Sabir 
Research Article (15 pages), Article ID 5798824, Volume 2022 (2022)




Renewable Polysaccharide and Biomedical Application of Nanomaterials

Rahul Kanaoujiya , Shruti Kumari Saroj, Shekhar Srivastava, and Manoj Kumar Chaudhary 
Review Article (16 pages), Article ID 1050211, Volume 2022 (2022)


Evaluation of Anticancer Potential of Biogenic Copper Oxide Nanoparticles (CuO NPs) against Breast Cancer

Torki A. Zughaihi , Ahmed A. Mirza , Mohd Suhail , Nasimudeen R. Jabir , Syed Kashif Zaidi , Samina Wasi , Ayat Zawawi , and Shams Tabrez 
Research Article (7 pages), Article ID 5326355, Volume 2022 (2022)





Role of *Moringa oleifera* on Green Synthesis of Metal/Metal Oxide Nanomaterials

Vikram Jadhav , Arun Bhagare, Ismat H. Ali , Akshay Dhayagude, Dnyaneshwar Lokhande, Jayraj Aher, Mohammed Jameel, and Mycal Dutta 
Review Article (10 pages), Article ID 2147393, Volume 2022 (2022)

Mechanical and Durability Characteristics of TiO₂ and Al₂O₃ Nanoparticles with Sisal Fibers



R. Rajkumar, R. Nirmala, and V. Vivekananthan 
Research Article (6 pages), Article ID 2813205, Volume 2022 (2022)

Green Synthesis of Gold and Silver Nanoparticles Using *Opuntia dillenii* Aqueous Extracts: Characterization and Their Antimicrobial Assessment

Anees Ahmed, Abdur Rauf , Hassan A. Hemeg, Muhammad Nasimullah Qureshi, Rohit Sharma , Abdullah S. M. Aljohani, Fahad A. Alhumaydhi , Ibrahim Khan, Amir Alam, and Md. Mominur Rahman 



Research Article (17 pages), Article ID 4804116, Volume 2022 (2022)

Experimental Analysis of Heat Transfer by Using Nanofluid and Impact of Thermophysical Properties

L. Karikalan, S. Baskar , N. Poyyamozi , and Kassu Negash 

Research Article (8 pages), Article ID 5119797, Volume 2022 (2022)

Synthesis and Applications of Green Synthesized TiO₂ Nanoparticles for Photocatalytic Dye Degradation and Antibacterial Activity

Annin K. Shimi , Hiwa M. Ahmed , Muhammad Wahab, Snehlata Katheria, Saikh Mohammad Wabaidur, Gaber E. Eldesoky, Md Ataul Islam, and Kantilal Pitamber Rane






Research Article (9 pages), Article ID 7060388, Volume 2022 (2022)

Probe Sonicated Synthesis of Bismuth Oxide (Bi₂O₃): Photocatalytic Application and Electrochemical Sensing of Ascorbic Acid and Lead

K. B. Kusuma , M. Manju , C. R. Ravikumar , V. G. Dileepkumar , A. Naveen Kumar , Mysore Sridhar Santosh , H. C. Ananda Murthy , and K. Gurushantha 




Research Article (13 pages), Article ID 3256611, Volume 2022 (2022)

Effect of Nanoaluminium Nitride Ceramic Particles on Microstructure, Mechanical Wear, and Machining Behavior of Al-Si-Mg Alloy Matrix Composites Produced by Bottom Pouring Type Stir Casting Route

M. Meignanamoorthy, V. Mohanavel , P. Velmurugan , M. Ravichandran , Wadi B. Alonazi , S. Sivakumar, and Atkilt Mulu Gebrekidan 







Research Article (14 pages), Article ID 5013914, Volume 2022 (2022)

Effect of Sodium Selenosulfate Concentration on Microstructural, Morphological, and Luminescence Characteristics of Cadmium Selenide Nanoparticles

Saka Abel , Jule Leta Tesfaye, R. Shanmugam, L. Priyanka Dwarampudi, N. Nagaprasad , Lamessa Gudata, and Ramaswamy Krishnaraj 

Research Article (5 pages), Article ID 2627688, Volume 2022 (2022)



Synthesis of Silver and Gold Nanoparticles: Chemical and Green Synthesis Method and Its Toxicity Evaluation against Pathogenic Bacteria Using the ToxTrak Test

Pankaj Kumar Tyagi , Cristina Quispe, Jesús Herrera-Bravo , Shruti Tyagi , D. Barbhai Mrunal , Manoj Kumar , Anas S. Dabool, Saad Alghamdi , Gaber El-Saber Batiha, Javad Sharifi-Rad , and Seema Ramniwas

Research Article (12 pages), Article ID 3773943, Volume 2021 (2021)

Contents

Anti-inflammatory and Antimicrobial Potential of *Cissus quadrangularis*-Assisted Copper Oxide Nanoparticles

S. Rajeshkumar , Soumya Menon, Venkat Kumar S, M. Ponnaniakajamideen, Daoud Ali, and Kalirajan Arunachalam 

Research Article (11 pages), Article ID 5742981, Volume 2021 (2021)

Research Article

Assessment on the Toxic Effects of Chemically Synthesized SPIONs against Model Organisms

Chellapan Justin,¹ Antony V. Samrot ,² Nagarajan Shobana ,¹ Mahendran Sathiyasree,¹ Subramanian Saigeetha,³ Rajan Renuka Remya ,⁴ Deenadhayalan Rajalakshmi,¹ and S. Prasath ⁵

¹Department of Biotechnology, School of Bio and Chemical Engineering, Sathyabama Institute of Science and Technology, Chennai 600119, Tamil Nadu, India

²School of Bioscience, Faculty of Medicine, Bioscience and Nursing, MAHSA University, Jalan SP2, Bandar Saujana Putra, Jenjarom 42610, Selangor, Malaysia

³Department of Biotechnology, School of Biosciences and Technology, Vellore Institute of Technology, Vellore 632014, Tamil Nadu, India

⁴Centre for Materials Engineering and Regenerative Medicine, Bharath Institute of Higher Education and Research, Chennai 600073, Tamil Nadu, India

⁵Department of Mechanical Engineering, College of Engineering and Technology, Mizan Tepi University, Mizan Teferi, Ethiopia

Correspondence should be addressed to Antony V. Samrot; drantonysamrot@gmail.com and S. Prasath; prasath@mtu.edu.et

Received 17 April 2022; Revised 14 June 2022; Accepted 24 April 2023; Published 19 September 2023

Academic Editor: Hiwa M. Ahmed

Copyright © 2023 Chellapan Justin et al. This is an open access article distributed under the Creative Commons Attribution License, which permits unrestricted use, distribution, and reproduction in any medium, provided the original work is properly cited.

The remarkable physicochemical properties of nanomaterials have attracted researchers due to the numerous applications in the field of chemistry, biology, and physics. Despite the various applications, superparamagnetic iron oxide nanoparticles (SPIONs) are harmful to living organisms and to the environment as they are released without any safety testing. In this study, SPIONs were synthesized and further characterized. The aim of the study was to examine the toxicity of synthesized SPIONs against animal models: Zebrafish—*Danio rerio*, Earthworm—*Eudrilus eugeniae*, and Drosophila—*Drosophila melanogaster* through histology using Hematoxylin–Eosin and Prussian Blue staining. The accumulation of SPIONs was further quantified by using Inductively Coupled Plasma Mass Spectrometry (ICP-MS). Through histology images, it was observed that the SPIONs had caused damages and a lower concentration of 0.001–0.002 $\mu\text{g}/\text{ml}$ of metal accumulation was detected in the ICP-MS analysis.

1. Introduction

New horizons of technical advancement have been opened with the help of nanotechnology [1]. There are some promising applications of nanoparticles in nanomedicine, wastewater treatment, etc. [2–7]. Magnetism is one of the numerous magnificent qualities of nanoparticles that fascinates researchers of both material sciences and biosciences [8–10]. Research is being conducted on the applications of magnetic nanoparticles in many fields [11–14], which include improving cell seeding and distribution in tissue engineering scaffolds, targeted imaging, and therapy [15, 16]; targeted imaging and therapy [17]; improving anticancer drug efficiency by amplifying reactive

oxygen species stress [18]; drug delivery applications [13]; magnetic resonance imaging [19]; magnetically induced local hyperthermia [20–22]; wastewater treatment [23–30], etc. Superparamagnetic Iron Oxide Nanoparticles (SPIONs) act as carriers for drug targets as they obey to an external magnetic field [31]. They can deliver biotherapeutics by targeting the ligands or stimulator-sensitive moieties that are responsive to external stimuli, such as light, ultrasounds, or magnetic fields [32]. They help in the implementation of drugs directly to the target area with lower systemic concentration [33]. SPIONs are also employed in the diagnosis of a variety of diseases. Intravenous injection of folate-tagged SPIONs in an antigen-induced arthritis model improved macrophage

TABLE 1: Dietary ratio provided to *Danio rerio*.

Organism	Feed	Ratio of feed (1)	Ratio of feed (2)	Ratio of feed (3)	Ratio of feed (4)	Control
<i>Danio rerio</i>	NP:NF	1:3	2:2	3:1	4:0	0:4

NPs - Nanoparticles; NF - Normal Feed.

TABLE 2: Dietary ratio provided to *Eudrilus eugeniae*.

Organism	Feed	Ratio of feed (1)	Ratio of feed (2)	Ratio of feed (3)	Ratio of feed (4)	Control
<i>Eudrilus eugeniae</i>	NP:NF	1:3	2:2	3:1	4:0	0:4

NPs - Nanoparticles; NF - Normal Feed.

TABLE 3: Dietary ratio provided to *Drosophila melanogaster*.

Organism	Feed	Ratio of feed (1)	Ratio of feed (2)	Ratio of feed (3)	Ratio of feed (4)	Control	Generation
<i>Drosophila melanogaster</i>	NP:NF	0.002 ml : 50 ml	0.003 ml : 50 ml	0.004 ml : 50 ml	0.005 ml : 50 ml	50 ml of feed without NPs	3

NPs - Nanoparticles; NF - Normal Feed.

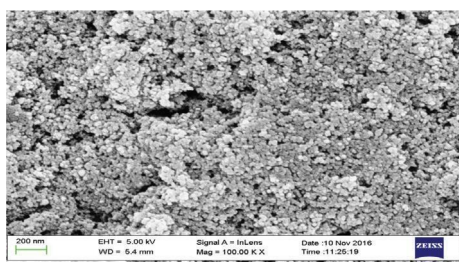


FIGURE 1: SEM analysis of SPIONs.

endocytosis *in vitro* and produced hypointense signals in affected joints; it may also be used in X-ray imaging [34, 35].

Despite the advantages, biocompatibilities and toxicities of iron oxide nanoparticles raise real concerns [36, 37]. When iron oxide nanoparticles were injected into a rat model, it was claimed that they created oxidative stress, lowering the antioxidant capability of the blood cells [38, 39]. It has been reported that nanoparticles induce oxidative stress, which affects cell signaling [40]. SPIONs are reported to cause oxidative stress responses such as inflammation, damage to the membrane, denaturation of protein, mitochondria-mediated apoptosis, lipid peroxidation, genotoxicity, etc. [41, 42]. Low level of oxidative stress activates the genes responsible for transcription defense through transcription factor, leading to the activation of inflammation and apoptosis, and necrosis [43]. The impact of iron oxide nanoparticles on cellular systems, like vascular systems, including blood cells, fibroblast, stromal cells, reproductive cells, lung cells, liver cells, kidney cells, and cerebral cells, have also been reported earlier [44]. Iron oxide nanoparticles induces genotoxicity in intratracheally instilled mouse lungs, and the inflammatory responses lead to oxidative and lipid

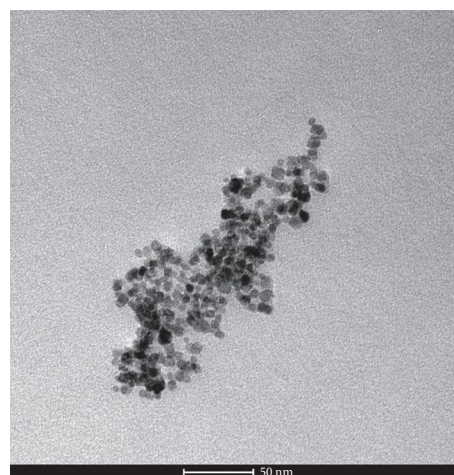


FIGURE 2: TEM analysis of SPIONs.

peroxide-related DNA adduct formations [45–48]. The CCK-8 and lactate dehydrogenase assays can be used to determine cytotoxicity [49], and Comet reaction can be used to determine the genotoxicity in biological tissue [50]. Various functional groups can be added to SPIONs to minimize the adverse biological effects [51]. Mice, *Drosophila* [46], earthworms [52], fishes [53–56], and even its embryos [36, 57] are some of the model organisms previously reported for studying the toxicological effects of iron oxide nanoparticles. The objective of this investigation is to explore the histopathological impact of SPIONs in three different animal models: zebrafish (*Danio rerio*), earthworms (*Eudrilus eugeniae*), and *Drosophila* (*Drosophila melanogaster*). The study aims to assess the harm and accumulation of SPIONs resulting from their administration to these animal models. This research provides insights into the potential applications of SPIONs in fields such as drug delivery and X-ray imaging.

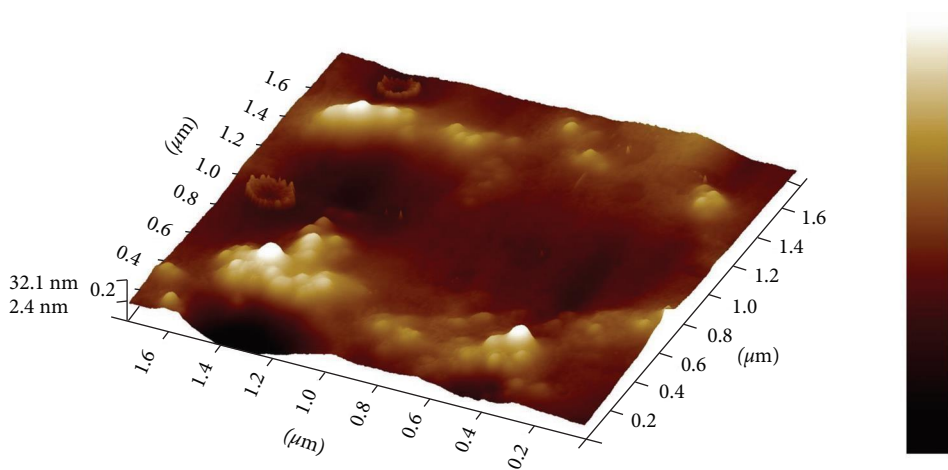


FIGURE 3: AFM analysis of SPIONs.

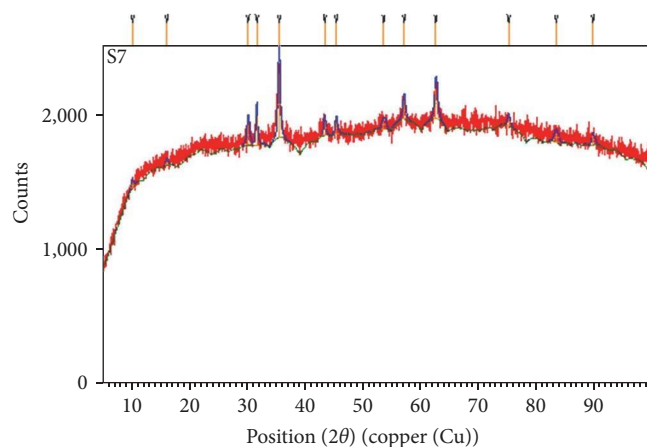


FIGURE 4: XRD analysis of SPIONs.

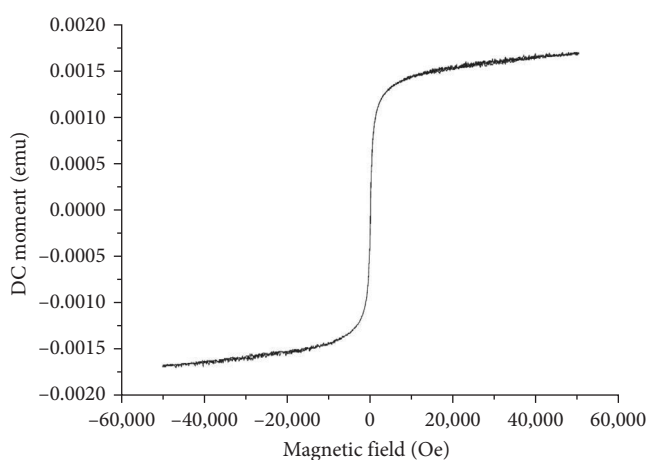


FIGURE 5: VSM analysis of SPIONs.

Previous studies have demonstrated that SPIONs with varying physiochemical properties can exhibit either lower cytotoxicity or toxicity that is dependent on the dosage, particularly at dosages of 100 g/ml or higher [58].

2. Materials and Methods

2.1. Materials Required. Ferrous sulfate heptahydrate ($\text{FeSO}_4 \cdot 7\text{H}_2\text{O}$) was purchased from HiMedia; Ferric chloride hexahydrate ($\text{FeCl}_3 \cdot 6\text{H}_2\text{O}$) from Thomas Baker; Formaldehyde (CH_2O) and tetramethylammonium hydroxide ($\text{C}_4\text{H}_{13}\text{NO}$) from SD Fine-Chem Limited, Mumbai, India, and agar from Micro Fine Chemicals. Semolina was acquired from Vedant Organics (div. of Esteem Pharmaceuticals); jaggery from Cloudtail India. Zebrafish (*D. rerio*) were procured from Aquarium Professionals; earthworms (*E. eugeniae*) from SS Vermicompost and *Drosophila* (*D. melanogaster*) from The Genetics Laboratory of Kristu Jayanti College, Bengaluru, India.

2.2. Synthesis of SPIONs. SPIONs were synthesized using magnetic field-mediated reaction method [35]. Accordingly, 0.1 g of ferric chloride hexahydrate ($\text{FeCl}_3 \cdot 6\text{H}_2\text{O}$) and 0.1 g of

ferrous sulfate heptahydrate ($\text{FeSO}_4 \cdot 7\text{H}_2\text{O}$) were separately dissolved in 1 ml of nitrogenized double distilled water and then mixed together for 5 min. 500 μl of nitrogenized iron salt solution was then added to 500 μl of tetramethylammonium hydroxide ($\text{C}_4\text{H}_{13}\text{NO}$) and kept in vortex for 5 min. The obtained black precipitate was then washed in 1 ml of acetone and dried in hot air oven at 60°C for 30 min. The pellet was then dissolved in 700 μl of formaldehyde solution (CH_2O), and 300 μl of nitrogenized H_2O was added dropwise with simultaneous vortex, which was followed by 500 μl formaldehyde solution. The obtained solution was then kept in the magnetic field for 2 days and was then dispersed in formaldehyde solution. The nanoparticles were then washed four to five times in nitrogen-purged double distilled water prior to toxicological experiments.

2.3. Characterization of SPIONs. Characterization of SPIONs was done to analyze their chemical and structural properties. The SPIONs were subjected to Scanning Electron Microscopy (SEM) (Zeiss Ultra Plus, Oberkochen, Germany), Transmission Electron Microscopy (TEM) (TEECNAI G2 Spirit Biotwin—120 kV), where the size and surface morphology of synthesized SPIONs were checked, Atomic Force Microscopy (AFM)

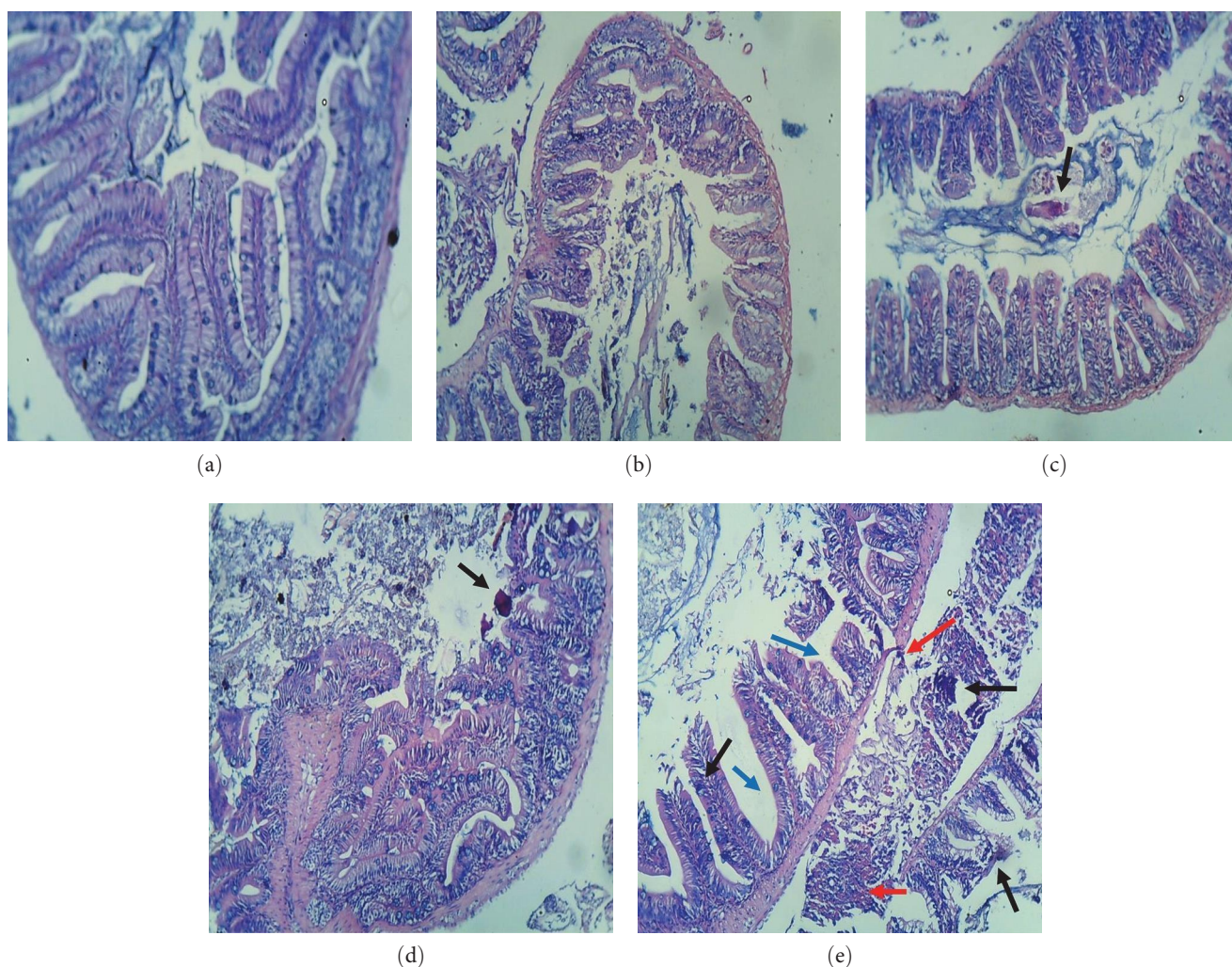


FIGURE 6: Histology images of zebrafish exposed to different concentrations of SPIONs using Hematoxylin–Eosin stain: (a) control; (b) 1 : 3 ratio of SPIONs to feed; (c) 2 : 2 ratio of SPIONs to feed; (d) 3 : 1 ratio of SPIONs to feed; (e) 4 : 0 ratio of SPIONs to feed. Black arrow lipofuscin; red arrow erosion of organ; blue arrow interstitial space.

(Bruker, Dimension icon model, Germany) to examine the confinement of the nanoparticle to the three coordinates as 3D images, X-ray Diffraction (XRD) by Smartlab X-ray Diffractometer (Rigaku Corporation, Japan) to check the crystallinity and Vibrating Sample Magnetometer (VSM) (LakeShore Co. Ltd., Lake Shore 7407, Westerville, Ohio, USA) with a maximum magnetic field of 2.5 T and dynamic moment range of 1×10^{-6} – $10e^3$ emu to check the magnetization property.

2.4. Feed Preparation. Feed was prepared separately for *D. rerio*, *E. eugeniae*, and *D. melanogaster*. Stock solution of 0.010 mg/10 ml of SPIONs were prepared using distilled water and used in this study against earthworm and zebrafish. For study against *Drosophila*, we used different concentrations of SPIONs ranging from 0.002 g/1 ml to 0.005 g/1 ml.

2.4.1. *D. rerio* Feed Preparation. Micro pellet feed was soaked in different concentrations of SPIONs suspension and incubated at room temperature until all the nanoparticles

were absorbed into the feed. It was then dried in a hot air oven at 40°C overnight, after which the nanoabsorbed feed was kept at the room temperature for 15 min to cool and then stored for further use.

2.4.2. *E. eugeniae* Feed Preparation. Dried cow dung was fed to the *E. eugeniae*. The stock SPIONs solution was suspended in the deionized water in different concentrations and were sprayed onto the cow dung and dried, which was then stored for further use.

2.4.3. *D. melanogaster* Feed Preparation. 25 g of jaggery was crushed and boiled in 250 ml of water until it was dissolved completely. 25 g of semolina was added to the previously prepared solution, which was followed by the addition of 10% agar. About 1.9 ml of propionic acid was added to the prepared porridge and thoroughly stirred while it was still hot. The porridge was then transferred to 5 beakers (50 ml each). Stock SPIONs of varied concentrations were added to the heated mixture and thoroughly stirred. 10 ml of each was poured into separate test tubes while the porridge was still

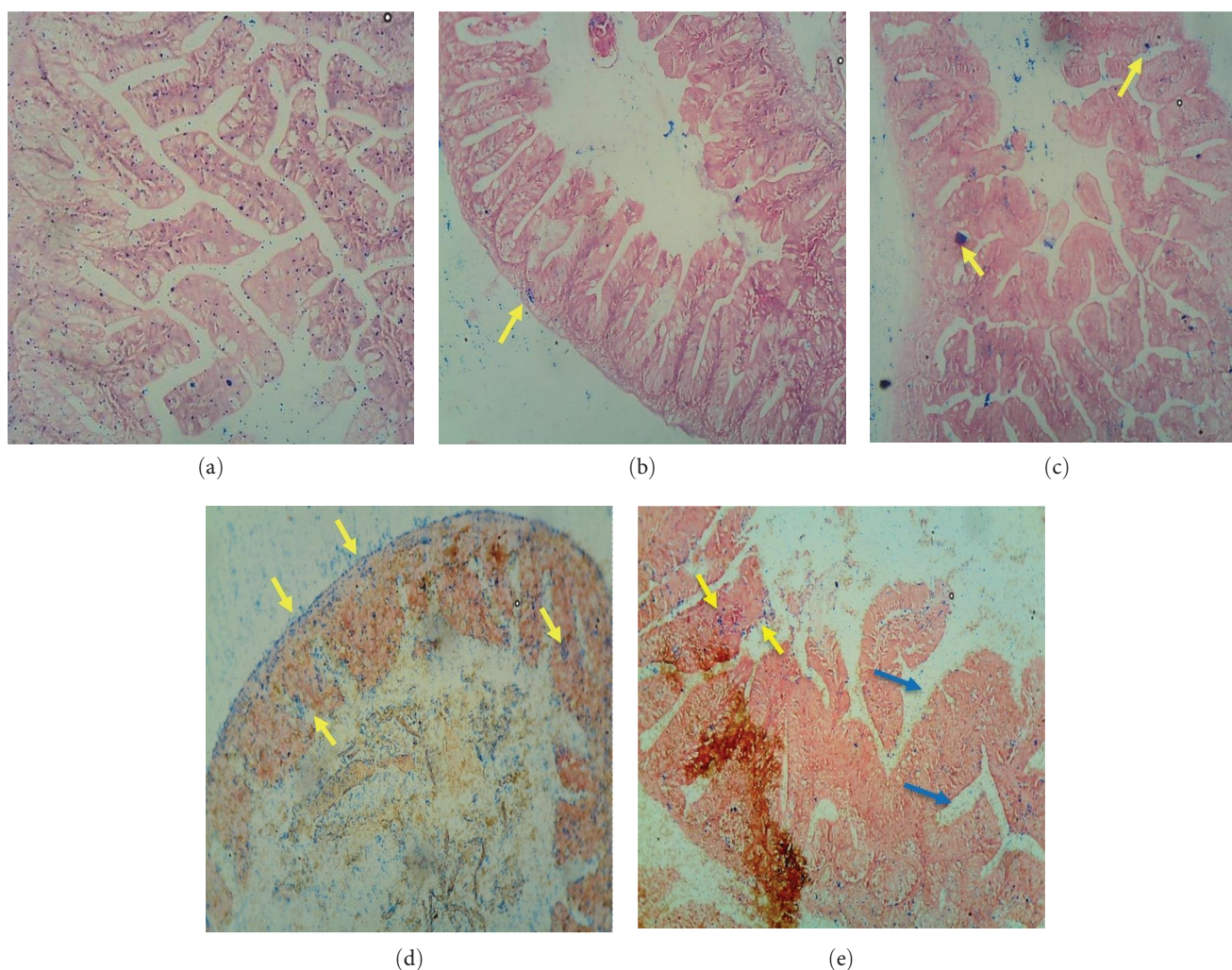


FIGURE 7: Histology images of zebrafish exposed to different concentrations of SPIONs using Prussian Blue stain: (a) control; (b) 1 : 3 ratio of SPIONs to feed; (c) 2 : 2 ratio of SPIONs to feed; (d) 3 : 1 ratio of SPIONs to feed; (e) 4 : 0 ratio of SPIONs to feed. Black arrow lipofuscin; blue arrow interstitial space; yellow arrow denotes iron accumulation.

warm. After 10 min, the moisture content in the test tubes was wiped with cotton and kept overnight for solidification.

2.5. Feeding the Organisms. Four different concentrations of feed were given to *D. rerio*, *E. eugeniae*, and *D. melanogaster*.

2.5.1. Feeding *D. rerio*. After a month-long acclimation, *D. rerio* were bifurcated into five different fish bowls, among which one bowl was considered as control. The administered feed details are given in Table 1.

2.5.2. Feeding *E. eugeniae*. *E. eugeniae* were introduced to the soil containing cow dung in a plastic tub and allowed to acclimate for a week. The earthworms were fed dried cow dung at regular intervals. In order to ensure proper growing circumstances for the earthworms, the moisture conditions in the box were also checked regularly. The administered feed details are given in Table 2.

2.5.3. Feeding *D. melanogaster* Culture. *D. melanogaster* (10 flies each) were inoculated into the prepared test tubes

for feeding and the study for three generations, i.e., larva, pupa, and adult fly, each of which were collected for analysis. The administered feed details are given in Table 3.

2.6. Inductively Coupled Plasma Mass Spectrometry (ICP-MS) and Staining of Organisms. The organisms after the study period, were subjected to histopathological staining, for which they were preserved in 10% formaldehyde solution. Hematoxylin–Eosin (H&E) staining was done to detect changes in the tissue of the organism, according to the procedure followed by Samrot et al. [59] and Cardiff et al. [60]. Prussian Blue staining was also done to examine the iron accumulation inside the tissue [61–63]. Organisms from each concentration were subjected to acid digestion [64] and analyzed using ICP-MS analysis (Agilent Technologies, 7700 series, Santa Clara, CA, USA).

3. Results and Discussion

3.1. Characterization of SPIONs. The topographical view revealed that the size of synthesized SPIONs was in the range

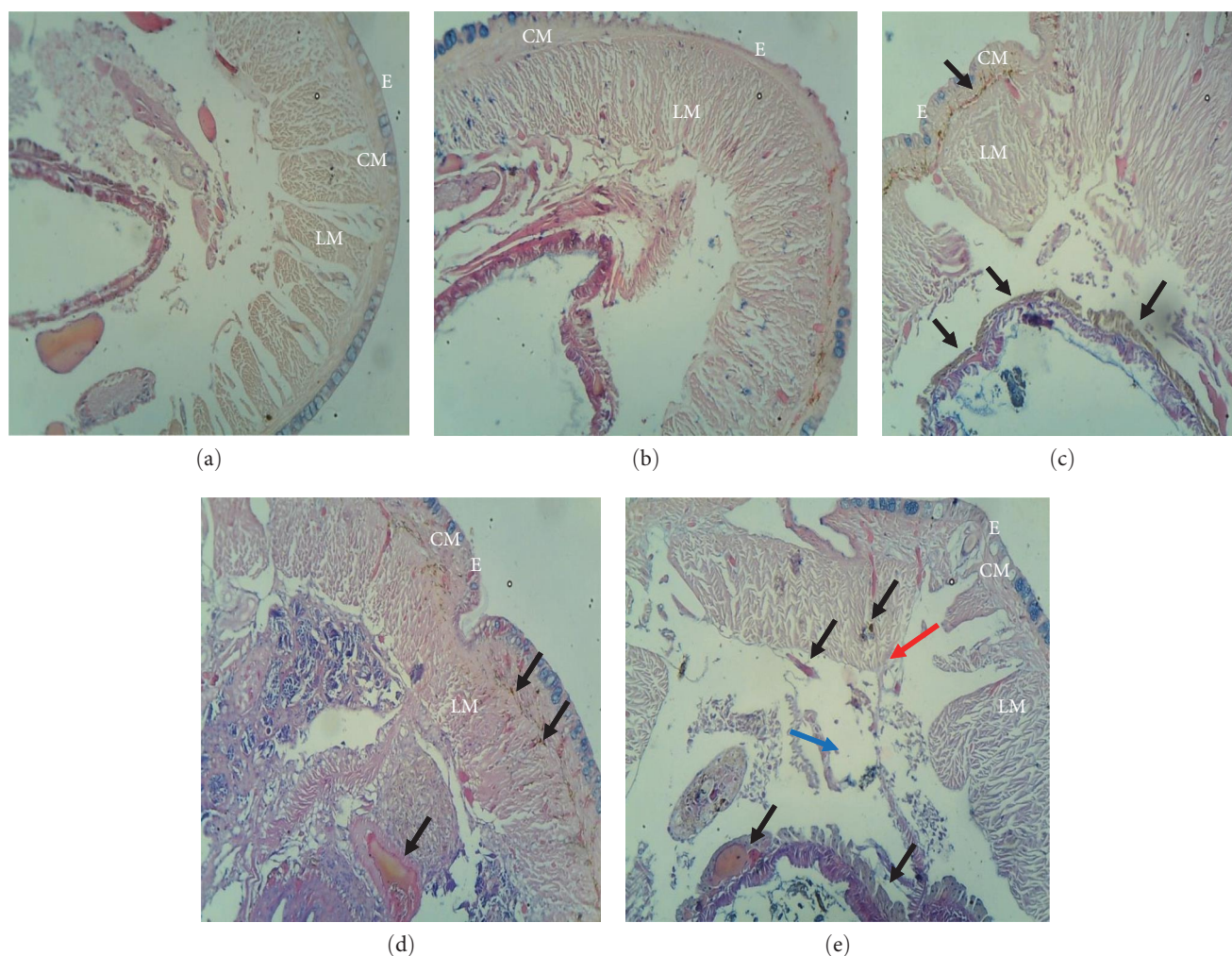


FIGURE 8: Histology images of earthworms exposed to different concentrations of SPIONs using Hematoxylin–Eosin stain: (a) control; (b) 1 : 3 ratio of SPIONs to feed; (c) 2 : 2 ratio of SPIONs to feed; (d) 3 : 1 ratio of SPIONs to feed; (e) 4 : 0 ratio of SPIONs to feed. Black arrow lipofuscin; red arrow erosion of organ; blue arrow interstitial space. E, Epidermis; CM, Circular Muscle; LM, Longitudinal Muscle.

10–25 nm (Figure 1), which was also confirmed by TEM images (Figure 2). Samrot et al. [59] also reported the size of SPIONs to be around 25 nm, synthesized using ammonia as a reducing agent. In earlier reports, Samrot et al. [65] synthesized SPIONs which ranged from 9 to 25 nm. SPIONs synthesized using precursor solutions such as FeCl_3 and FeCl_2 were found to be 40–45 nm in size [66]. In a study by Sathya et al. [67], the size of iron oxide nanoparticles synthesized using a magnetic stirrer and ultrasound method ranged from 20 to 90 nm.

The 3D structure of the synthesized SPIONs was confirmed by AFM analysis (Figure 3). It was confirmed that the particles were spherical and well dispersed. According to the XRD pattern (Figure 4), the synthesized SPIONs were in the inverse spinel structure. Shukla et al. [68] reported that the iron oxide nanoparticles exhibited peaks at 30.1, 35.5, 42.6, 53.6, 57.0, and 62.8 assigned to the diffraction plane of the spinel structured magnetite nanoparticles (220), (311), (400), (422), (511), and (440), respectively. VSM measurements were done to estimate the magnetization and

coercivity of the synthesized SPIONs. The magnetization curves clearly indicated the superparamagnetic behavior of the synthesized SPIONs (Figure 5).

3.2. Histology. H&E stain is usually used for the identification of different kinds of cells and its pattern, shape, and structures, whereas Prussian Blue staining is performed to identify the accumulation of iron as it can form ferric ferrocyanide complex by producing blue color in the tissue [69, 70]. Intestines of *D. rerio* were stained using H&E following exposure to different concentrations of SPIONs (Figure 6). Lower concentrations of SPIONs did not show any significant impact, whereas exposure of higher concentrations caused erosion in the goblet cells in the intestinal area and on the intestinal wall of *D. rerio*. Tissues stained using Prussian Blue (Figure 7) revealed the accumulation of iron oxide nanoparticles inside the tissues. It was accumulated in and around the intestinal walls. Samrot et al. [59] earlier reported that the metal nanoparticles impacted the rate of reproduction.

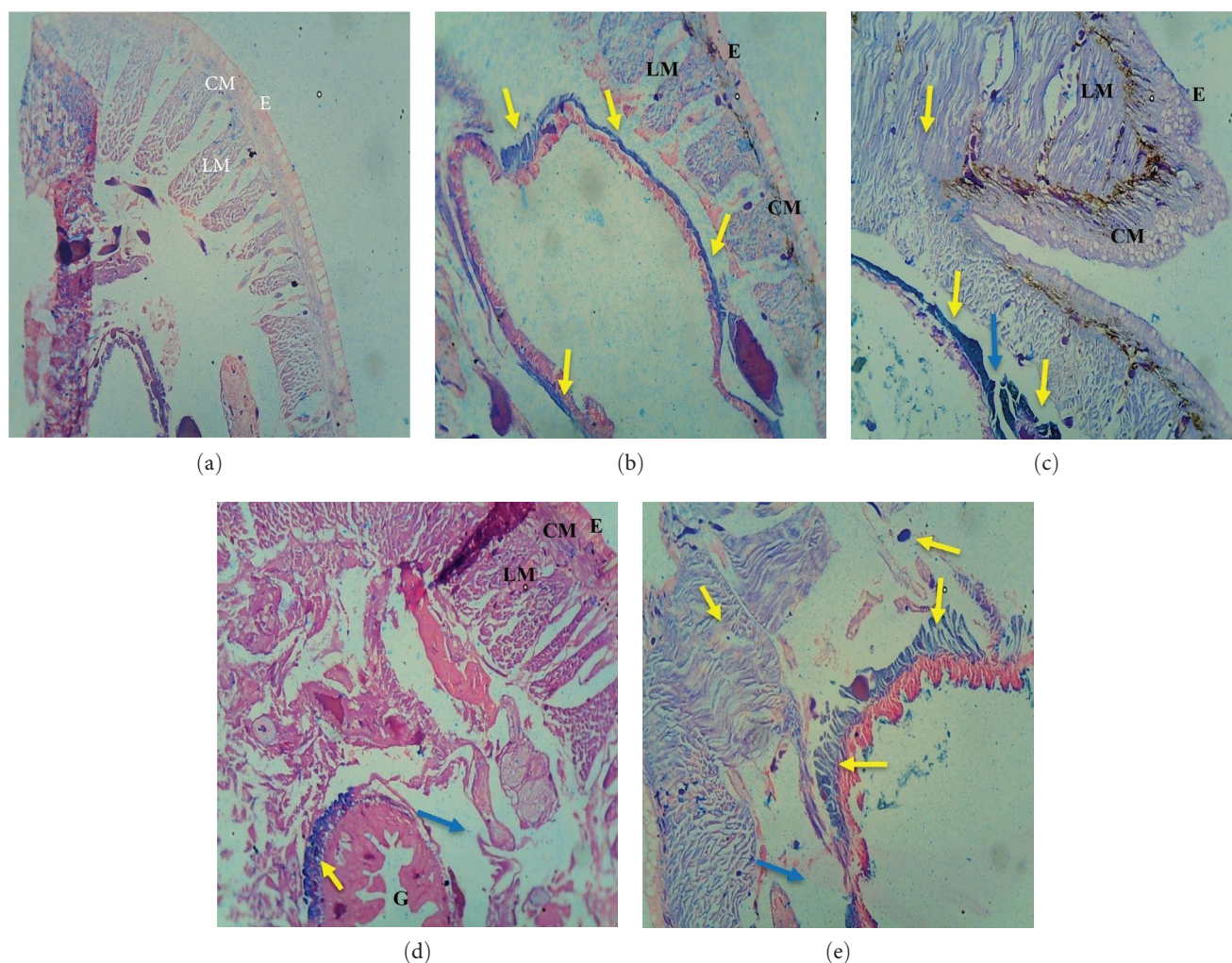


FIGURE 9: Histology images of earthworms exposed to different concentrations of SPIONs using Prussian Blue stain: (a) control; (b) 1 : 3 ratio of SPIONs to feed; (c) 2 : 2 ratio of SPIONs to feed; (d) 3 : 1 ratio of SPIONs to feed; (e) 4 : 0 ratio of SPIONs to feed. Black arrow lipofuscin; blue arrow interstitial space; yellow arrow denotes iron accumulation. G, Gut; E, Epidermis; CM, Circular Muscle; LM, Longitudinal Muscle.

Villacis et al. [71] reported the occurrence of fragmentation of DNA and micronuclei, malondialdehyde generation, and reduction in gene expression.

The exposure of SPIONs had a negative impact on the tissue of *E. eugeniae* as well, which was seen in the histology images. The earthworm's exterior structure was altered significantly. As the concentration of SPIONs increased, the circular and longitudinal muscles were found to be degraded in addition to the gizzard area (Figure 8). *E. eugeniae* treated with different concentrations of SPIONs, and control were also studied using Prussian Blue staining (Figure 9), which showed the accumulation of SPIONs and is believed to be the reason for damaged circular muscle and epidermal erosion. In earlier reports, it has been evidenced that exposure of Fe_2O_3 onto the earthworm, significantly decreased its growth and rate of reproduction [72, 73]. Samrot et al. [52] also reported erosion of epithelium, fibrosis of the circular muscle, and gut disintegration of earthworms on exposure to magnetite nanoparticles.

The histology images of *D. melanogaster* exposed to different concentrations of SPIONs. Figures 10–15 depicted visible distortion in the waxy cuticles of larvae at lower concentrations, whereas degradation at higher concentrations was also noticed (Figure 10). The deposition of iron in the larvae of *D. melanogaster* in Figure 11 is visualized using Prussian Blue staining. The images show the accumulation of SPIONs in the larvae's anterior and in the midguts. The mouth, spiracles, and trachea in the anterior and the ovary and gonads in the posterior of the larvae have been found to be degraded at higher concentrations.

The histology images of the *D. melanogaster* pupa stained with H&E are shown in Figure 12. The images do not show any damages after being exposed to lower concentrations, such as 0.002 g : 50 ml and 0.003 g : 50 ml of SPIONs : feed ratio but higher concentrations, such as 0.004 g : 50 ml and 0.005 g : 50 ml, exhibited erosion of the puparium, anterior, and posterior regions and severe damages in the tracheal region. The Prussian Blue staining of the pupa illustrated the accumulation of the iron

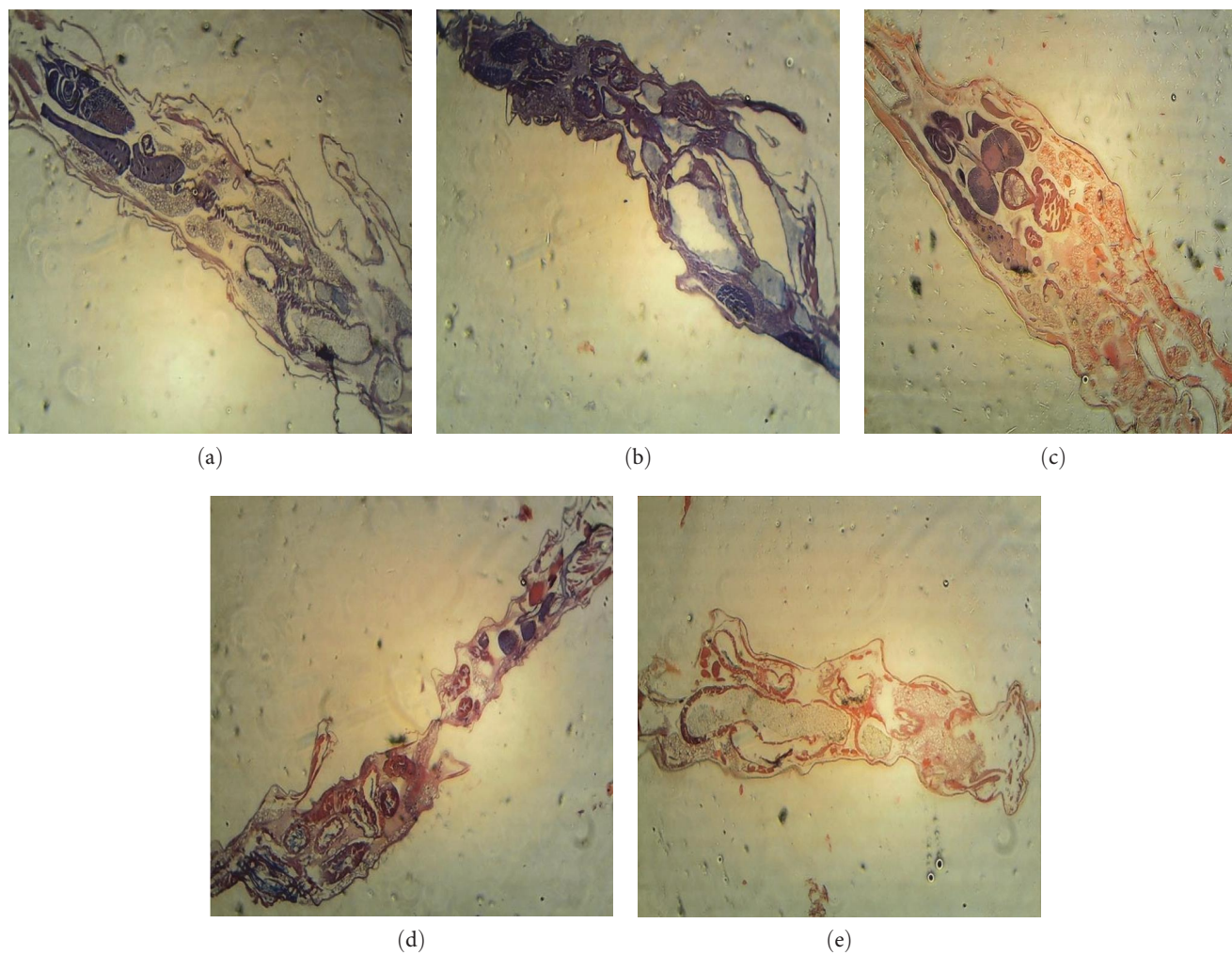


FIGURE 10: Histology images of *Drosophila* larva exposed to different concentrations of SPIONs using Hematoxylin–Eosin stain: (a) Control; (b) 0.002 g:50 ml ratio of SPIONs to feed; (c) 0.003 g:50 ml ratio of SPIONs to feed; (d) 0.004 g:50 ml ratio of SPIONs to feed; (e) 0.005 g:50 ml ratio of SPIONs to feed.

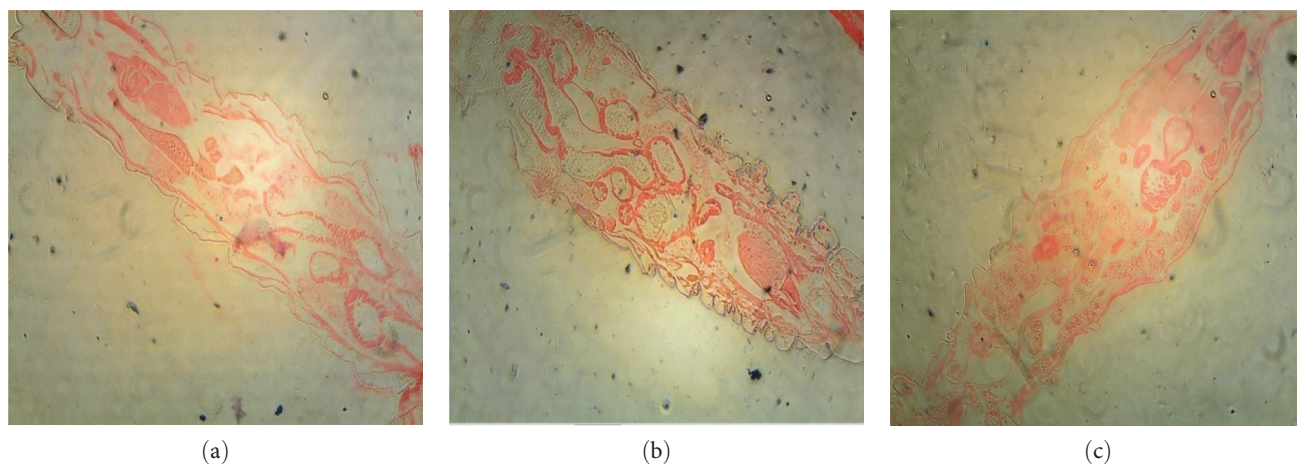


FIGURE 11: Continued.

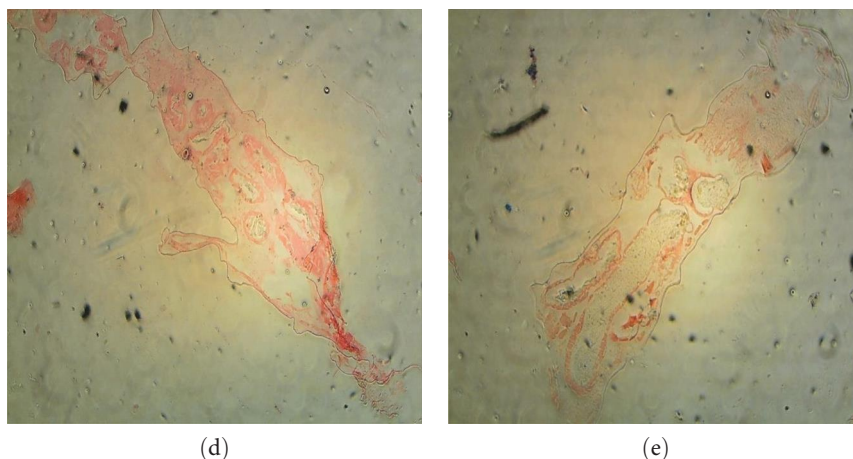


FIGURE 11: Histology images of *Drosophila* larva exposed to different concentrations of SPIONs using Prussian Blue stain: (a) control; (b) 0.002 g:50 ml ratio of SPIONs to feed; (c) 0.003 g:50 ml ratio of SPIONs to feed; (d) 0.004 g:50 ml ratio of SPIONs to feed; (e) 0.005 g:50 ml ratio of SPIONs to feed.

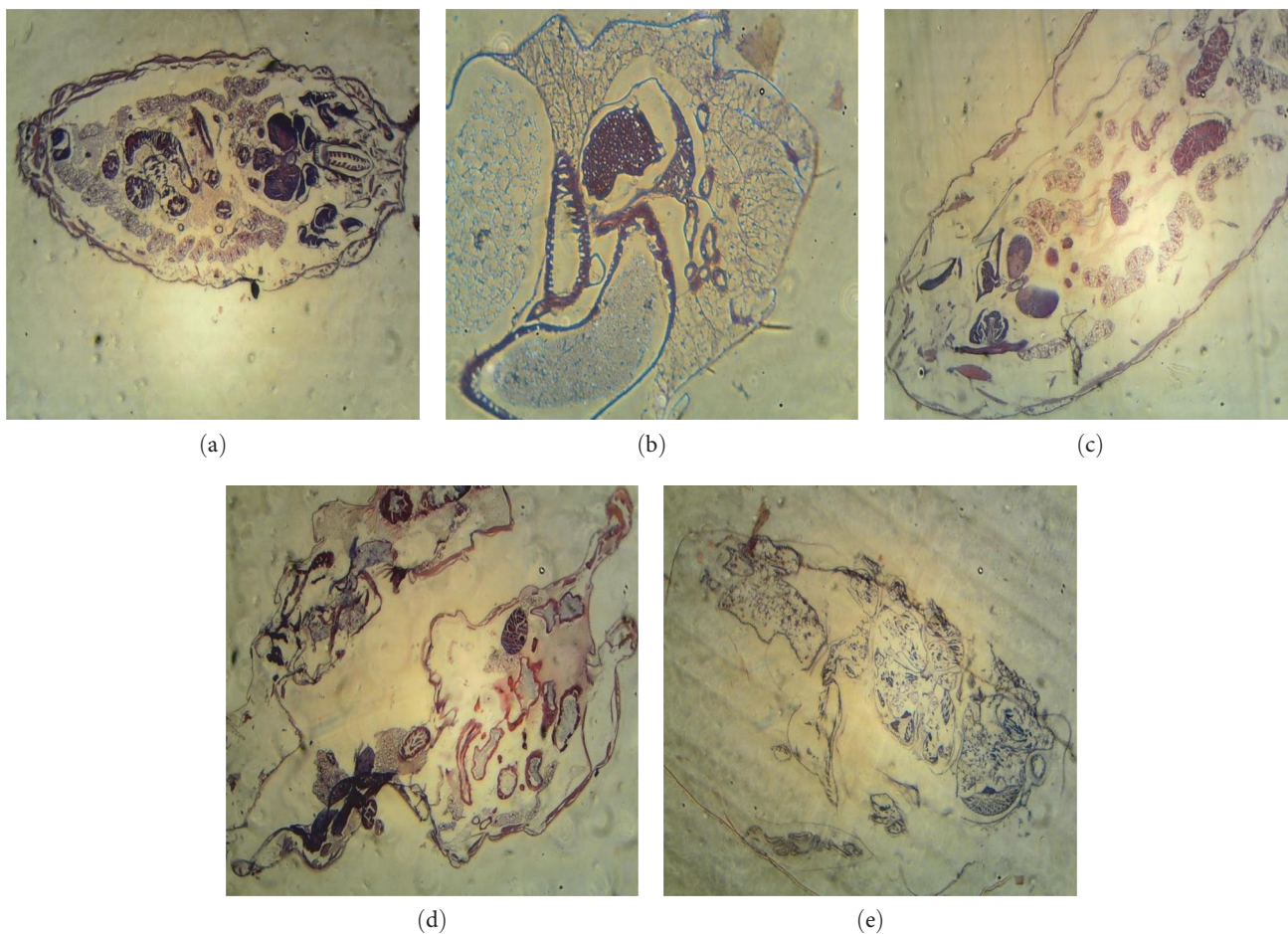


FIGURE 12: Histology images of *Drosophila* pupa exposed to different concentrations of SPIONs using Hematoxylin–Eosin stain: (a) control; (b) 0.002 g:50 ml ratio of SPIONs to feed; (c) 0.003 g:50 ml ratio of SPIONs to feed; (d) 0.004 g:50 ml ratio of SPIONs to feed; (e) 0.005 g:50 ml ratio of SPIONs to feed.

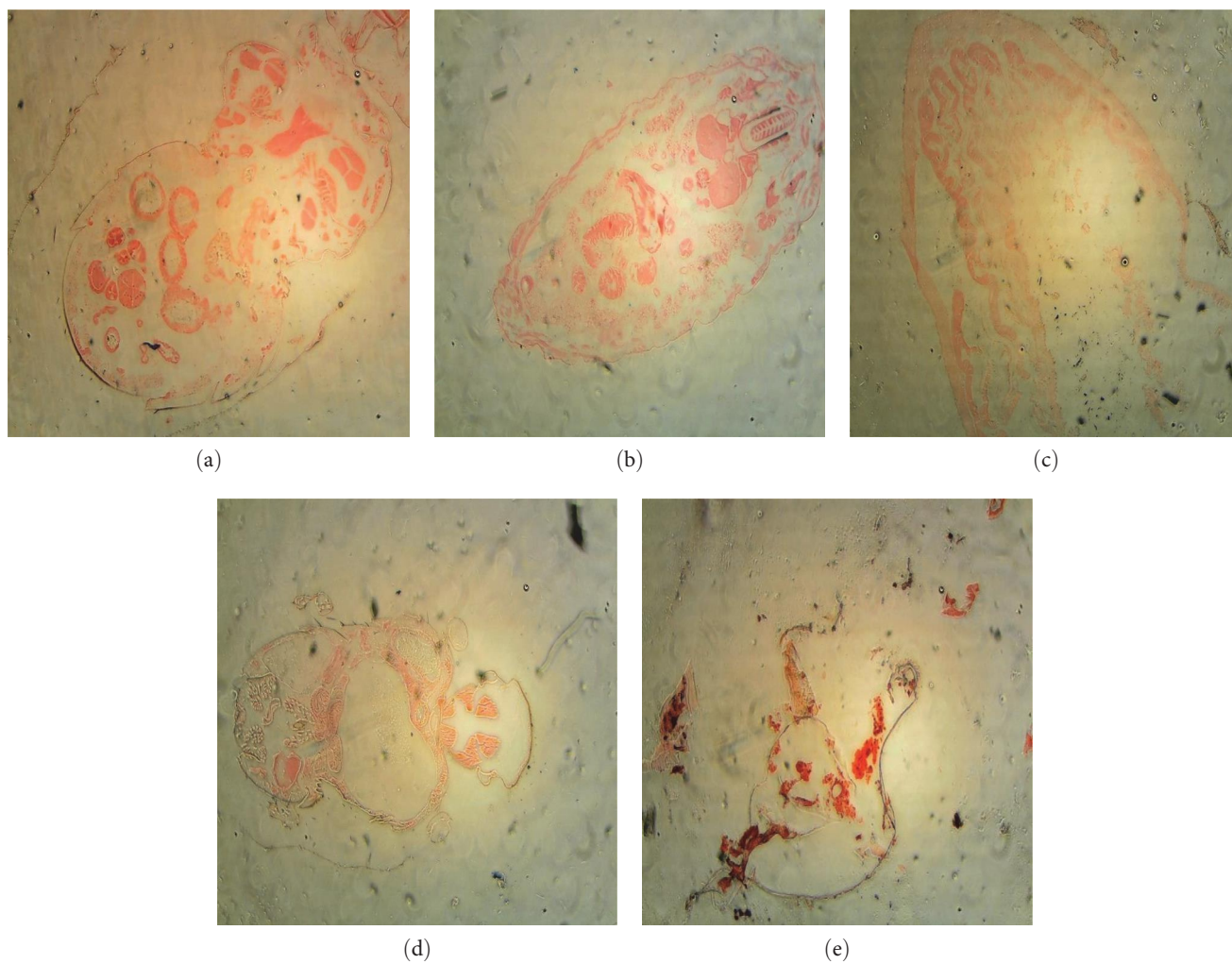


FIGURE 13: Histology images of *Drosophila* pupa exposed to different concentrations of SPIONs using Prussian Blue stain: (a) control; (b) 0.002 g:50 ml ratio of SPIONs to feed; (c) 0.003 g:50 ml ratio of SPIONs to feed; (d) 0.004 g:50 ml ratio of SPIONs to feed; (e) 0.005 g:50 ml ratio of SPIONs to feed.

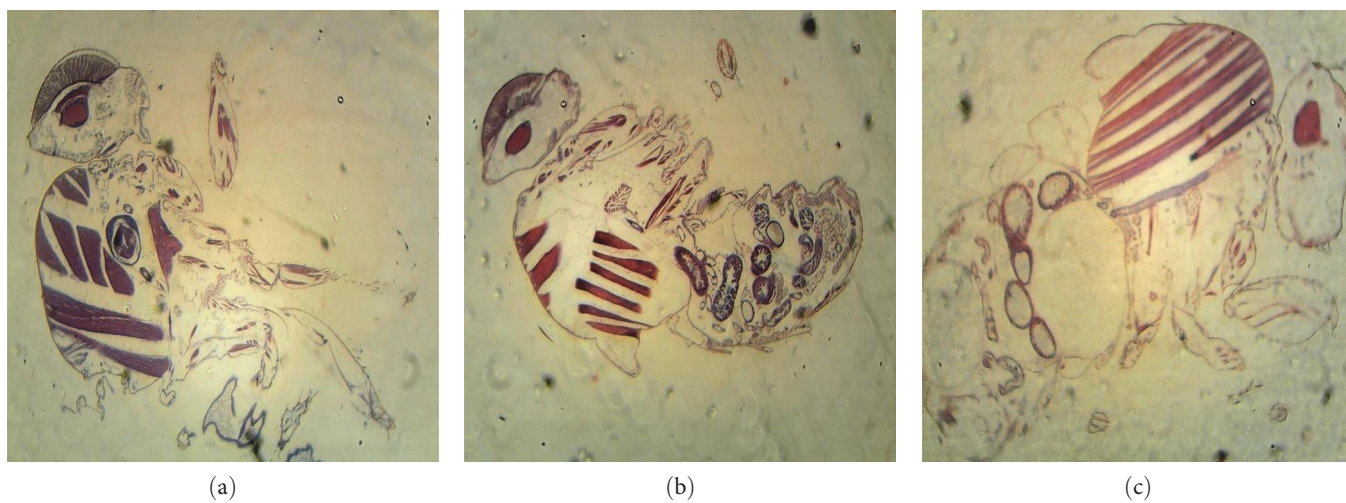


FIGURE 14: Continued.

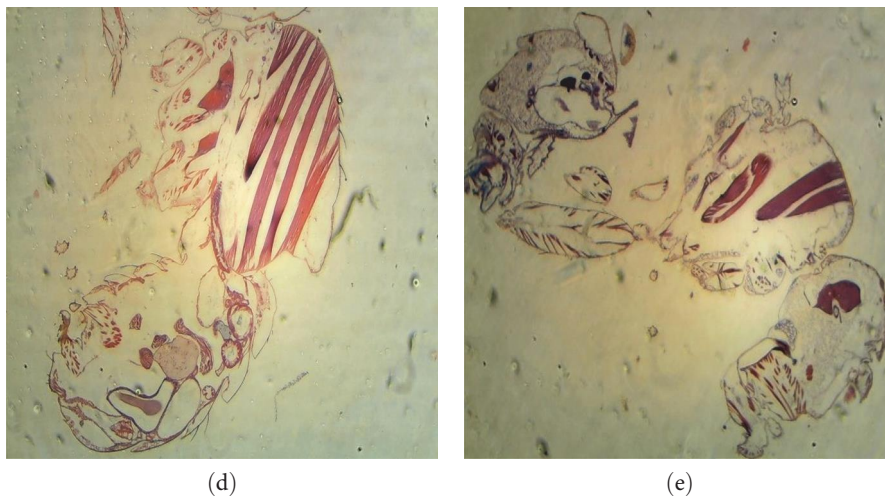


FIGURE 14: Histology images of adult *Drosophila* exposed to different concentrations of SPIONs using Hematoxylin–Eosin stain: (a) control; (b) 0.002 g:50 ml ratio of SPIONs to feed; (c) 0.003 g:50 ml ratio of SPIONs to feed; (d) 0.004 g:50 ml ratio of SPIONs to feed; (e) 0.005 g:50 ml ratio of SPIONs to feed.

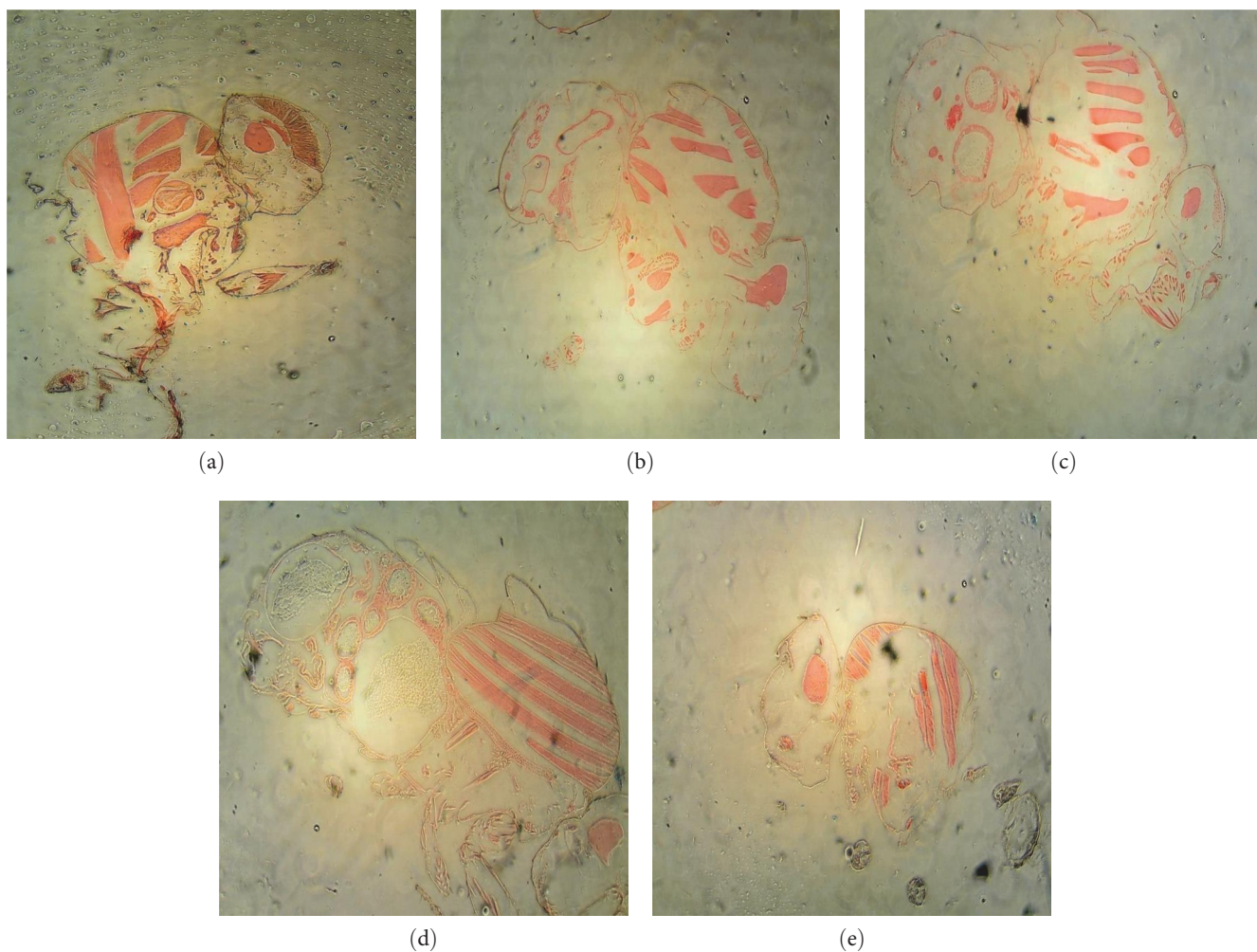


FIGURE 15: Histology images of adult *Drosophila* exposed to different concentrations of SPIONs using Prussian Blue stain: (a) control; (b) 0.002 g:50 ml ratio of SPIONs to feed; (c) 0.003 g:50 ml ratio of SPIONs to feed; (d) 0.004 g:50 ml ratio of SPIONs to feed; (e) 0.005 g:50 ml ratio of SPIONs to feed.

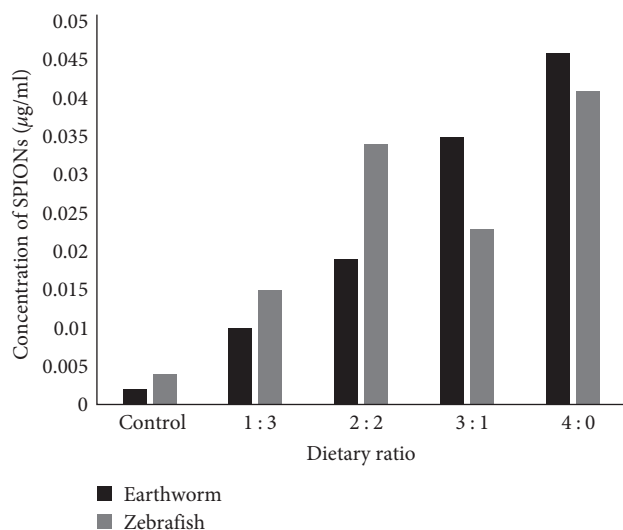


FIGURE 16: ICP-MS analysis for earthworms and zebrafish.

(Figure 13). No visible accumulations were observed at lower concentrations, but at higher concentrations, the posterior region of pupa was accumulated with iron nanoparticles. Raj et al. [74] reported that a high dose of silver nanoparticles at the early stages of development could negatively impact the behavior and metabolism of *D. melanogaster*.

Adult *D. melanogaster* did not show any considerable impact at the lower concentration but revealed the formation of lipofuscin-like granules in the abdominal region. But whereas at higher concentrations, the head, thorax, and abdomen were entirely distorted (Figure 14). The iron accumulation is visible in the histology images (Figure 15) stained by Prussian Blue. Abdominal region of adult *D. melanogaster* also showed lipofuscin-like granules responsible for the erosion in gut area. The thorax and abdomen were entirely degraded at the higher concentrations. Ong [75] revealed that the survival rate of *D. melanogaster* fed with silver nanoparticles decreased significantly when compared to control flies.

3.3. ICP-MS Analysis. The concentration of SPIONs in the aqueous solution of acid-digested organisms from each concentration was studied using ICP-MS analysis [76]. The control samples showed no substantial deposition, albeit a small amount (0.001–0.002 µg/ml) was detected, which can be attributed to the presence of metal in the organism's natural habitat. Figures 16 and 17 shows the metal accumulation inside the bodies of *D. rerio*, *E. eugeniae*, and different stages of *D. melanogaster*, which was supported by histology images as well.

4. Conclusion

SPIONs have been synthesized and characterized using SEM, TEM, AFM, XRD, and VSM in this study. The toxicity studies of SPIONs were carried against *D. rerio*, *E. eugeniae*, and the different stages of *D. melanogaster* and histology studies were carried out by staining the tissues with H&E and Prussian Blue.

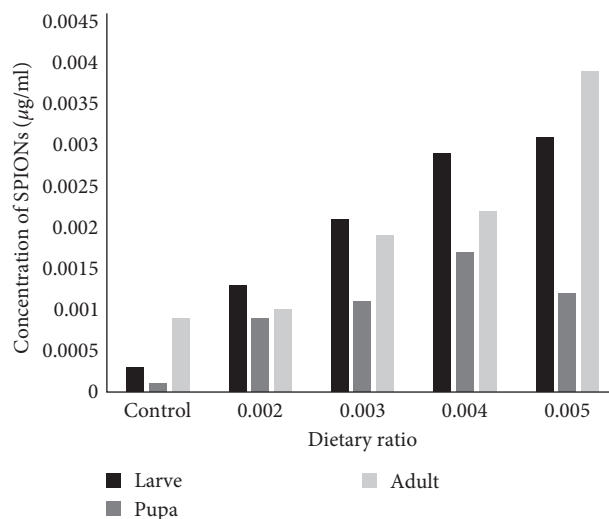


FIGURE 17: ICP-MS analysis for different stages of Drosophila.

The exposure of nanoparticles onto the organisms were depicted through histology studies, and metal accumulation was investigated by ICP-MS analysis. The synthesized SPIONs had considerable damages in the organisms which are suspected to be toxic.

Data Availability

The data used to support the findings of this study are included within the article.

Conflicts of Interest

The authors declare that they have no conflicts of interest.

References

- [1] C. C. Fleischer and C. K. Payne, "Nanoparticle surface charge mediates the cellular receptors used by protein–nanoparticle complexes," *The Journal of Physical Chemistry B*, vol. 116, no. 30, pp. 8901–8907, 2012.
- [2] Y.-M. Chu, U. Nazir, M. Sohail, M. M. Selim, and J.-R. Lee, "Enhancement in thermal energy and solute particles using hybrid nanoparticles by engaging activation energy and chemical reaction over a parabolic surface via finite element approach," *Fractal and Fractional*, vol. 5, no. 3, Article ID 119, 2021.
- [3] Y.-M. Chu, B. M. Shankaralingappa, B. J. Gireesha, F. Alzahrani, M. Ijaz Khan, and S. U. Khan, "Combined impact of Cattaneo-Christov double diffusion and radiative heat flux on bio-convective flow of Maxwell liquid configured by a stretched nano-material surface," *Applied Mathematics and Computation*, vol. 419, Article ID 126883, 2022.
- [4] B. Hayati, N. M. Mahmoodi, and A. Maleki, "Dendrimer–titania nanocomposite: synthesis and dye-removal capacity," *Research on Chemical Intermediates*, vol. 41, pp. 3743–3757, 2015.
- [5] N. M. Mahmoodi, "Synthesis of magnetic carbon nanotube and photocatalytic dye degradation ability," *Environmental Monitoring and Assessment*, vol. 186, pp. 5595–5604, 2014.

- [6] N. M. Mahmoodi, S. Keshavarzi, and M. Ghezlbash, "Synthesis of nanoparticle and modelling of its photocatalytic dye degradation ability from colored wastewater," *Journal of Environmental Chemical Engineering*, vol. 5, no. 4, pp. 3684–3689, 2017.
- [7] N. M. Mahmoodi and M. H. Saffar-Dastgerdi, "Clean Laccase immobilized nanobiocatalysts (graphene oxide–zeolite nanocomposites): from production to detailed biocatalytic degradation of organic pollutant," *Applied Catalysis B: Environmental*, vol. 268, Article ID 118443, 2020.
- [8] S. R. Obireddy and W.-F. Lai, "ROS-generating amine-functionalized magnetic nanoparticles coupled with carboxymethyl chitosan for pH-responsive release of doxorubicin," *International Journal of Nanomedicine*, vol. 17, pp. 589–601, 2022.
- [9] M. Khatami, H. Q. Aljani, B. Fakheri et al., "Super-paramagnetic iron oxide nanoparticles (SPIONs): greener synthesis using *Stevia* plant and evaluation of its antioxidant properties," *Journal of Cleaner Production*, vol. 208, pp. 1171–1177, 2019.
- [10] M. Szekeres, I. Y. Tóth, E. Illés et al., "Chemical and colloidal stability of carboxylated core–shell magnetite nanoparticles designed for biomedical applications," *International Journal of Molecular Sciences*, vol. 14, no. 7, pp. 14550–14574, 2013.
- [11] A. V. Samrot, N. Shobana, P. Durga Sruthi, and C. S. Sahithya, "Utilization of chitosan-coated superparamagnetic iron oxide nanoparticles for chromium removal," *Applied Water Science*, vol. 8, Article ID 192, 2018.
- [12] A. V. Samrot, P. Suresh, D. Rajalakshmi et al., "Super-paramagnetic Iron Oxide Nanoparticles (SPIONs) as antibacterial agent and for Biomedical applications," *Journal of Pharmaceutical Negative Results*, vol. 13, no. 9, pp. 713–718, 2022.
- [13] S. Kayal and R. V. Ramanujan, "Doxorubicin loaded PVA coated iron oxide nanoparticles for targeted drug delivery," *Materials Science and Engineering: C*, vol. 30, no. 3, pp. 484–490, 2010.
- [14] T. Lam, P. K. Avti, P. Pouliot et al., "Fabricating water dispersible superparamagnetic iron oxide nanoparticles for biomedical applications through ligand exchange and direct conjugation," *Nanomaterials*, vol. 6, no. 6, Article ID 100, 2016.
- [15] A. V. Samrot, M. Sathiyasree, S. B. A. Rahim et al., "Scaffold using chitosan, agarose, cellulose, dextran and protein for tissue engineering—a review," *Polymers*, vol. 15, no. 6, Article ID 1525, 2023.
- [16] P. Thevenot, S. Sohaebuddin, N. Poudyal, J. P. Liu, and L. Tang, "Magnetic nanoparticles to enhance cell seeding and distribution in tissue engineering scaffolds," in *2008 8th IEEE Conference on Nanotechnology*, pp. 646–649, IEEE, Arlington, TX, USA, August 2008.
- [17] J. R. McCarthy and R. Weissleder, "Multifunctional magnetic nanoparticles for targeted imaging and therapy," *Advanced Drug Delivery Reviews*, vol. 60, no. 11, pp. 1241–1251, 2008.
- [18] G. Huang, H. Chen, Y. Dong et al., "Superparamagnetic iron oxide nanoparticles: amplifying ROS stress to improve anticancer drug efficacy," *Theranostics*, vol. 3, no. 2, pp. 116–126, 2013.
- [19] N. Schleich, P. Sibret, P. Danhier et al., "Dual anticancer drug/superparamagnetic iron oxide-loaded PLGA-based nanoparticles for cancer therapy and magnetic resonance imaging," *International Journal of Pharmaceutics*, vol. 447, no. 1–2, pp. 94–101, 2013.
- [20] P.-E. Le Renard, R. Lortz, C. Senatore et al., "Magnetic and *in vitro* heating properties of implants formed *in situ* from injectable formulations and containing superparamagnetic iron oxide nanoparticles (SPIONs) embedded in silica microparticles for magnetically induced local hyperthermia," *Journal of Magnetism and Magnetic Materials*, vol. 323, no. 8, pp. 1054–1063, 2011.
- [21] Y.-H. Choi, T. Yi, and D.-K. Kim, "Electron spin resonance (ESR) and microwave absorption studies of superparamagnetic iron oxide nanoparticles (SPIONs) for hyperthermia applications," *Journal of the Korean Ceramic Society*, vol. 48, no. 6, Article ID 577, 2011.
- [22] S. Ruta, R. Chantrell, and O. Hovorka, "Unified model of hyperthermia via hysteresis heating in systems of interacting magnetic nanoparticles," *Scientific Reports*, vol. 5, Article ID 9090, 2015.
- [23] S. R. Mousavi, M. Asghari, and N. M. Mahmoodi, "Chitosan-wrapped multiwalled carbon nanotube as filler within PEBA thin film nanocomposite (TFN) membrane to improve dye removal," *Carbohydrate Polymers*, vol. 237, Article ID 116128, 2020.
- [24] M. Oveisi, M. A. Asli, and N. M. Mahmoodi, "Carbon nanotube based metal–organic framework nanocomposites: synthesis and their photocatalytic activity for decolorization of colored wastewater," *Inorganica Chimica Acta*, vol. 487, pp. 169–176, 2019.
- [25] A. Almasian, M. E. Olya, and N. M. Mahmoodi, "Preparation and adsorption behavior of diethylenetriamine/polyacrylonitrile composite nanofibers for a direct dye removal," *Fibers and Polymers*, vol. 16, pp. 1925–1934, 2015.
- [26] N. M. Mahmoodi, M. Oveisi, M. Bakhtiari et al., "Environmentally friendly ultrasound-assisted synthesis of magnetic zeolitic imidazolate framework–graphene oxide nanocomposites and pollutant removal from water," *Journal of Molecular Liquids*, vol. 282, pp. 115–130, 2019.
- [27] N. M. Mahmoodi, A. Taghizadeh, M. Taghizadeh, and M. A. S. Baglou, "Surface modified montmorillonite with cationic surfactants: preparation, characterization, and dye adsorption from aqueous solution," *Journal of Environmental Chemical Engineering*, vol. 7, no. 4, Article ID 103243, 2019.
- [28] N. M. Mahmoodi, M. Bashiri, and S. J. Moeen, "Synthesis of nickel–zinc ferrite magnetic nanoparticle and dye degradation using photocatalytic ozonation," *Materials Research Bulletin*, vol. 47, no. 12, pp. 4403–4408, 2012.
- [29] A. V. Samrot, R. Sanjay Preeth, P. Prakash et al., "Extraction of fibres from *Cucumis melo* seed coat and its application as biosorbents for the effective removal of various dyes and antibiotic," *Biomass Conversion and Biorefinery*, 2022.
- [30] P. Xu, G. M. Zeng, D. L. Huang et al., "Use of iron oxide nanomaterials in wastewater treatment: a review," *Science of the Total Environment*, vol. 424, pp. 1–10, 2012.
- [31] S. Laurent, A. A. Saei, S. Behzadi, A. Panahifar, and M. Mahmoudi, "Superparamagnetic iron oxide nanoparticles for delivery of therapeutic agents: opportunities and challenges," *Expert Opinion on Drug Delivery*, vol. 11, no. 9, pp. 1449–1470, 2014.
- [32] H. Mok and M. Zhang, "Superparamagnetic iron oxide nanoparticle-based delivery systems for biotherapeutics," *Expert Opinion on Drug Delivery*, vol. 10, no. 1, pp. 73–87, 2013.
- [33] C. Janko, T. Ratschker, K. Nguyen et al., "Functionalized superparamagnetic iron oxide nanoparticles (SPIONs) as platform for the targeted multimodal tumor therapy," *Frontiers in Oncology*, vol. 9, Article ID 59, 2019.
- [34] S. H. Crayton, A. K. Chen, J. F. Liu et al., "3.20 molecular imaging," in *Comprehensive Biomaterials*, vol. 3, pp. 424–466, Elsevier, 2017.

- [35] C. Justin, S. A. Philip, and A. V. Samrot, "Synthesis and characterization of superparamagnetic iron-oxide nanoparticles (SPIONs) and utilization of SPIONs in X-ray imaging," *Applied Nanoscience*, vol. 7, pp. 463–475, 2017.
- [36] A. V. Samrot, N. Shobana, M. Sathiyasree et al., "Toxicity evaluation of SPIONs on *Danio rerio* embryonic development," *Materials Today: Proceedings*, vol. 59, Part 2, pp. 1555–1560, 2022.
- [37] B. Szalay, E. Tátrai, G. Nyírő, T. Vezér, and G. Dura, "Potential toxic effects of iron oxide nanoparticles in *in vivo* and *in vitro* experiments," *Journal of Applied Toxicology*, vol. 32, no. 6, pp. 446–453, 2012.
- [38] A. V. Samrot, S. P. R. Singh, R. Deenadhayalan, V. V. Rajesh, S. Padmanaban, and K. Radhakrishnan, "Nanoparticles, a double-edged sword with oxidant as well as antioxidant properties—a review," *Oxygen*, vol. 2, no. 4, pp. 591–604, 2022.
- [39] U. S. Gaharwar and R. Paulraj, "Iron oxide nanoparticles induced oxidative damage in peripheral blood cells of rat," *Journal of Biomedical Science and Engineering*, vol. 8, no. 4, pp. 274–286, 2015.
- [40] M. Horie and Y. Tabei, "Role of oxidative stress in nanoparticles toxicity," *Free Radical Research*, vol. 55, no. 4, pp. 331–342, 2021.
- [41] N. Shobana, P. Prakash, A. V. Samrot et al., "Evaluation of the toxic effect of *Bauhinia purpurea* mediated synthesized silver nanoparticles against *In-vitro* and *In-vivo* models," *Toxics*, vol. 11, no. 1, Article ID 9, 2023.
- [42] R. Vakili-Ghartavol, A. A. Momtazi-Borojeni, Z. Vakili-Ghartavol et al., "Toxicity assessment of superparamagnetic iron oxide nanoparticles in different tissues," *Artificial Cells, Nanomedicine, and Biotechnology*, vol. 48, no. 1, pp. 443–451, 2020.
- [43] S. Sharifi, S. Behzadi, S. Laurent, M. Laird Forrest, P. Stroeve, and M. Mahmoudi, "Toxicity of nanomaterials," *Chemical Society Reviews*, vol. 41, no. 6, pp. 2323–2343, 2012.
- [44] N. M. Dissanayak, K. M. Current, and S. O. Obare, "Mutagenic effects of iron oxide nanoparticles on biological cells," *International Journal of Molecular Sciences*, vol. 16, no. 10, pp. 23482–23516, 2015.
- [45] Y. Totsuka, K. Ishino, T. Kato et al., "Magnetite nanoparticles induce genotoxicity in the lungs of mice via inflammatory response," *Nanomaterials*, vol. 4, no. 1, pp. 175–188, 2014.
- [46] M. B. Radu, I. M. P. Din, A. Hermenea et al., "Exposure to iron oxide nanoparticles coated with phospholipid-based polymeric micelles induces biochemical and histopathological pulmonary changes in mice," *International Journal of Molecular Sciences*, vol. 16, no. 12, pp. 29417–29435, 2015.
- [47] I. Iavicoli, L. Fontana, V. Leso, and A. Bergamaschi, "The effects of nanomaterials as endocrine disruptors," *International Journal of Molecular Sciences*, vol. 14, no. 8, pp. 16732–16801, 2013.
- [48] A. Awaad, "Histopathological and immunological changes induced by magnetite nanoparticles in the spleen, liver and genital tract of mice following intravaginal instillation," *The Journal of Basic & Applied Zoology*, vol. 71, pp. 32–47, 2015.
- [49] M.-Q. Zhang, B. Chen, J.-P. Zhang, N. Chen, C.-Z. Liu, and C.-Q. Hu, "Liver toxicity of macrolide antibiotics in zebrafish," *Toxicology*, vol. 441, Article ID 152501, 2020.
- [50] S. A. Reinecke and A. J. Reinecke, "The comet assay as biomarker of heavy metal genotoxicity in earthworms," *Archives of Environmental Contamination and Toxicology*, vol. 46, pp. 208–215, 2004.
- [51] W. J. Yang, J. H. Lee, S. C. Hong, J. Lee, J. Lee, and D.-W. Han, "Difference between toxicities of iron oxide magnetic nanoparticles with various surface-functional groups against human normal fibroblasts and fibrosarcoma cells," *Materials*, vol. 6, no. 10, pp. 4689–4706, 2013.
- [52] A. V. Samrot, C. Justin, S. Padmanaban, and U. Burman, "A study on the effect of chemically synthesized magnetite nanoparticles on earthworm: *Eudrilus eugeniae*," *Applied Nanoscience*, vol. 7, pp. 17–23, 2017.
- [53] A. S. Remya, M. Ramesh, M. Saravanan, R. K. Poopal, S. Bharathi, and D. Nataraj, "Iron oxide nanoparticles to an Indian major carp, *Labeo rohita*: impacts on hematology, iono regulation and gill Na⁺/K⁺ ATPase activity," *Journal of King Saud University—Science*, vol. 27, no. 2, pp. 151–160, 2015.
- [54] S. Karthikeyeni, T. Siva Vijayakumar, S. Vasanth, A. Ganesh, M. Manimegalai, and P. Subramanian, "Biosynthesis of iron oxide nanoparticles and its haematological effects on fresh water fish *Oreochromis mossambicus*," *Journal of Academia and Industrial Research*, vol. 1, no. 10, pp. 645–649, 2013.
- [55] M. Saravanan, R. Suganya, M. Ramesh, R. K. Poopal, N. Gopalan, and N. Ponpandian, "Iron oxide nanoparticles induced alterations in haematological, biochemical and ionoregulatory responses of an Indian major carp *Labeo rohita*," *Journal of Nanoparticle Research*, vol. 17, Article ID 274, 2015.
- [56] A. V. Samrot, M. Bavanilatha, S. K. Shree et al., "Evaluation of heavy metal removal of nanoparticles based adsorbent using *Danio rerio* as model," *Toxics*, vol. 10, no. 12, Article ID 742, 2022.
- [57] N. Shobana, P. Prakash, A. V. Samrot et al., "Nanotoxicity studies of *Azadirachta indica* mediated silver nanoparticles against *Eudrilus eugeniae*, *Danio rerio* and its embryos," *Biocatalysis and Agricultural Biotechnology*, vol. 47, Article ID 102561, 2023.
- [58] L. Lei, J. Ling-Ling, Z. Yun, and L. Gang, "Toxicity of superparamagnetic iron oxide nanoparticles: research strategies and implications for nano medicine," *Chinese Physics B*, vol. 22, no. 12, Article ID 127503, 2013.
- [59] A. V. Samrot, C. SaiPriya, J. Lavanya Agnes Angalene et al., "Evaluation of nanotoxicity of *Araucaria heterophylla* gum derived green synthesized silver nanoparticles on *Eudrilus eugeniae* and *Danio rerio*," *Journal of Cluster Science*, vol. 30, pp. 1017–1024, 2019.
- [60] R. D. Cardiff, C. H. Miller, and R. J. Munn, "Manual hematoxylin and eosin staining of mouse tissue sections," *Cold Spring Harbor Protocols*, vol. 2, no. 6, pp. 655–658, 2014.
- [61] D. C. Sheehan and B. B. Hrapchak, *Theory and Practice of Histotechnology*, Battelle Press, Ohio, 2nd edition, 1980.
- [62] L. G. Luna, *Manual of Histologic Staining Methods of the AFIP*, McGraw-Hill, NY, 3rd edition, 1968.
- [63] J. N. Crookham and R. W. Dapson, *Hazardous Chemicals in the Histopathology Laboratory*, ANATECH, 2nd edition, 1991.
- [64] A. V. Samrot, C. S. Sahithya, S. P. Durga et al., "Itraconazole coated super paramagnetic iron oxide nanoparticles for antimicrobial studies," *Biointerface Research in Applied Chemistry*, vol. 10, no. 5, pp. 6218–6225, 2020.
- [65] A. V. Samrot, C. S. Sahithya, J. A. Selvarani, S. Pachiyappan, and S. S. Kumar, "Surface-engineered super-paramagnetic iron oxide nanoparticles for chromium removal," *International Journal of Nanomedicine*, vol. 14, pp. 8105–8119, 2019.
- [66] A. V. Samrot, U. Burman, S. Padmanaban, P. Yamini, and A. M. Rabel, "A study on toxicity of chemically synthesised silver nanoparticle on *Eudrilus eugeniae*," *Toxicology and Environmental Health Sciences*, vol. 10, pp. 162–167, 2018.
- [67] K. Sathya, R. Saravanathamizhan, and G. Baskar, "Ultrasound assisted phytosynthesis of iron oxide nanoparticle," *Ultrasonics Sonochemistry*, vol. 39, pp. 446–451, 2017.
- [68] S. Shukla, A. Jadaun, V. Arora, R. K. Sinha, N. Biyani, and V. K. Jain, "*In vitro* toxicity assessment of chitosan

- oligosaccharide coated iron oxide nanoparticles,” *Toxicology Reports*, vol. 2, pp. 27–39, 2015.
- [69] A. H. Fischer, K. A. Jacobson, J. Rose, and R. Zeller, “Hematoxylin and eosin staining of tissue and cell sections,” *Cold Spring Harbor Protocols*, 2008.
- [70] K. Rowatt, R. E. Burns, S. Frasca Jr., and D. M. Long, “A combination Prussian blue—hematoxylin and eosin staining technique for identification of iron and other histological features,” *Journal of Histotechnology*, vol. 41, no. 1, pp. 29–34, 2018.
- [71] R. A. R. Villacis, J. S. Filho, B. Piña et al., “Integrated assessment of toxic effects of maghemite (γ -Fe₂O₃) nanoparticles in zebrafish,” *Aquatic Toxicology*, vol. 191, pp. 219–225, 2017.
- [72] M. F. Valerio-Rodríguez, L. I. Trejo-Téllez, M. A. Aguilar-González et al., “Effects of ZnO, TiO₂ or Fe₂O₃ nanoparticles on the body mass, reproduction, and survival of *Eisenia fetida*,” *Polish Journal of Environmental Studies*, vol. 29, no. 3, pp. 2383–2394, 2020.
- [73] C. Chakraborty, A. R. Sharma, G. Sharma, and S.-S. Lee, “Zebrafish: a complete animal model to enumerate the nanoparticle toxicity,” *Journal of Nanobiotechnology*, vol. 14, Article ID 65, 2016.
- [74] A. Raj, P. Shah, and N. Agrawal, “Sedentary behavior and altered metabolic activity by AgNPs ingestion in *Drosophila melanogaster*,” *Scientific Reports*, vol. 7, Article ID 15617, 2017.
- [75] C. Ong, L.-Y. Lanry Yung, Y. Cai, B.-H. Bay, and G.-H. Baeg, “*Drosophila melanogaster* as a model organism to study nanotoxicity,” *Nanotoxicology*, vol. 9, no. 3, pp. 396–403, 2015.
- [76] A. V. Samrot, C. SaiPriya, S. A. Jenifer et al., “A study on influence of superparamagnetic iron oxide nanoparticles (SPIONs) on green gram (*Vigna radiata* L.) and earthworm (*Eudrilus eugeniae* L.),” *Materials Research Express*, vol. 7, no. 5, Article ID 055002, 2020.

Review Article

Study of Progress on Nanocrystalline Cellulose and Natural Fiber Reinforcement Biocomposites

T. Aravind,¹ Mohd. Shaikhul Ashraf,² Rajesh A. S.,³ N. Ahalya,⁴ Mahavir Singh Rawat,⁵ B. Uma,⁶ Rajneesh Sharma,⁷ Ram Subbiah,⁸ and SisayKetema Sida⁹

¹Department of Electronics and Communications Engineering, Saveetha Engineering College, Chennai, Tamil Nadu 602105, India

²Department of Botany, HKM Govt. Degree College, Bandipora, Jammu and Kashmir 193502, India

³Department of Mechanical Engineering, JSS Science & Technology University, Mysuru, Karnataka 570006, India

⁴Department of Biotechnology, MS Ramaiah Institute of Technology, Bengaluru, Karnataka 560054, India

⁵Department of Civil Engineering, IFTM University Moradabad, Uttar Pradesh 244102, India

⁶Department of Mathematics, Panimalar Engineering College, Chennai, Tamil Nadu 600123, India

⁷Department of Civil Engineering, Government Engineering College, Jhalawar, Rajasthan 326023, India

⁸Department of Mechanical Engineering, Gokaraju Rangaraju Institute of Engineering and Technology, Hyderabad, Telangana 500090, India

⁹Department of Mechanical Engineering, Kombolcha Institute of Technology, Wollo University, Ethiopia

Correspondence should be addressed to SisayKetema Sida; sisayk@kiot.edu.et

Received 9 April 2022; Revised 7 June 2022; Accepted 27 June 2022; Published 4 October 2022

Academic Editor: Arpita Roy

Copyright © 2022 T. Aravind et al. This is an open access article distributed under the Creative Commons Attribution License, which permits unrestricted use, distribution, and reproduction in any medium, provided the original work is properly cited.

Cellulosic biomass hydrolysis yields a nanoscale substance known as nanocrystalline cellulose (NCC). Gel, liquid, or powder is adaptable to a variety of uses. Nanocrystalline cellulose has unique renewability, biodegradability, and mechanical and physicochemical qualities, and abundance boosts the material's mechanical strength by many orders of magnitude when introduced into the material matrix (polymer, ceramic, or metal). Nanocrystalline cellulose is not related with any serious environmental issues because it is a natural substance. The progress of this biomaterial as a green and renewable biomaterial for the fabrication of lightweight and biodegradable composite materials gives further impetus. The current aim of nanocrystalline cellulose research is to optimise nanocrystalline cellulose characteristics for dispersion in hydrophilic and hydrophilic media. To assess the nanocrystalline cellulose reinforcing, antibacterial, stability, hydrophilicity, and biodegradability, imaging methods and protocols in complicated matrices will need to be developed. This review includes a discussion on nanocrystalline cellulose biocomposites.

1. Introduction about Nanocrystalline Cellulose

Current interest in cellulose-based materials has increased in demand for renewable and environmental considerations [1]. Natural cellulose fibers have exceptional strength and durability benefits, making them unique in various polymer matrices for reinforcement [2]. One of these agricultural wastes is rice straw consisting of three components: cellulose, hemicellulose, and lignin. The organic fiber is cellulose and hemicellulose, whereas the cell wall is lignin. Cellulose constitutes approximately 50% to 1/4 of the plant tissues and is a sig-

nificant component of all plant materials; photosynthesis is continuously supplied [3]. It is environmentally friendly and renewable, has low density, has low surfaces, and contains hydroxyl surface bands that enable strong oxygen bonds in the single or close chains [4]. Cellulose is the world's largest natural biopolymer. Figure 1 shows hierarchical patterns for cellulose microphones, nanofibers and nanocrystals, and transmission electron micrographs of cellulose microphones.

In the natural world, an essential element is the connection of nanocellulose with hydrogen to other polymer matrices, making cells from highly organized structures that hold chains

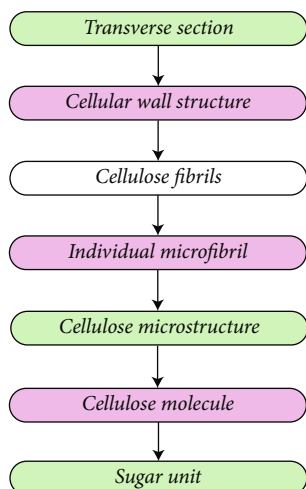


FIGURE 1: Hierarchical structures of cellulose and cellulose microfibrils, nanofibers and nanocrystals, and transmission electron micrographs [5–8].

firmly together and form highly tense microfibrils [9, 10]. Nanocellulose, its unique characteristics, has enhanced mechanical and heat properties such as a layer, mould, and latex [11, 12] by making it an exciting and safe material for polymer strengthening. Various reviews discussed the possible use of composite compounds by cellulose nanocrystals and cellulose nanofibrils [13, 14]. Cellulose has been a typical biomass with a broad spectrum of applications due to sharply growing demands of renewability and sustainability in recent years. During the last decades, particularly, nanocrystalline cellulose has deliberated high surface area, low density, and good mechanical strength, biodegradability, and nontolerable nanostructure characteristics. The nanocrystalline cellulose is now booming in numerous industries and daily applications, including drug excipients, polymers, reinforcement of adherents, and personal care products like hair conditioners and shampoos.

Figure 2 shows the amorphous cellulose chain area removed from cells of a rod structure by acid hydrolysis. Highly intensified scientific research is carried on nanometric cellulose because it is highly available and renovated. They also apply in different fields with their attractive mechanical and chemical characteristics. Both cellulose and nanometric fillers are associated with nanometric cellulose [16]. Nanocellulose is a biological material with the strength of tensile material similar to steel or Kevlar, a high specific surface area of low densities, and good biodegradability. Because of this, nanocellulose is being investigated to be used in some different equipment and sizes, including packaging materials, biomedical equipment, adhesives, electronic, and electroplating [17–25]. In the material sciences, the cellulose-nanofibers attract a considerable number. Due to their magnetic properties (for example, large areas ($100 \text{ m}^2 \text{ g}^{-1}$)), augmented volume-to-volume proportions of 100, and strong crystallinity, it has low density, lightweight mechanical characteristics, and high-porosity arrangement compared with other business fibers [26]. They are also easy to use at cheap rates, as they use less energy during combustion and can be easily recycled [27], in addition to their intrinsic properties and ecologically sodium fibers.

The chemical and mechanical processes are used to extract natural fibers of nanosizes. Hydrolysis chemical is widely used for the extraction of nanocrystalline cellulose. The nanocrystalline celluloses become tremendously interested in material science studies because of its nanometric, high crystallinity, high appearance rates, high mechanical resistance, low density, easy access, and high abundance [28, 29]. The addition of nanocrystalline celluloses has also been reported to decrease starch film permeability by water vapour. It is easy to the morphology of nitric cell fluid, which increases starch-based packaging's slow-down tortuosity and thus improves its suitability for food packing application [30]. The cellulose molecular chains have inter- and intramolecular hydrogen connecting networks as shown in Figure 3.

Students have been highly interested in nanocellulose as a new nanobiomaterial. The nanocrystalline cellulose has a high aspect ratio and a high specific surface area [32]. Furthermore, a highly crystalline area in the single molecular structure makes nanocrystalline celluloses mechanically and accessibly available in food packaging [33]. As a result of its strong hydrogen bonding and its high surface area, the nanocrystalline cellulose is integrated with the organic polymer structures as a packaging material to handle protein defects [34]. Research shows that the alginate film and water barrier [35] are greatly affected by nanocrystalline cellulose.

Cellulose is the primary renewable polymer in the world and is used as nanofiller for PBS. It is often present in plants, tunicates, algae, and bacteria. It consists of a vast molecular polymer composed of multiple β -1,4 glucose units and hydroxyl groups on the side of the chain. Acid hydrolysis is the most common nanocrystalline cellulose extraction technique that breaks down cellulose amorphous areas and crystallises them [36]. Figure 4 shows the structure of the plant cell wall.

In recent years, research has been undertaken intensively on innovative materials filled with nanocellulose [38]. It is because of nanocellulose's exceptional properties. Cellulose is inherently produced from large plant natural sources, such as rice [39, 40] wood, cotton, and biomash [41]. The algae and certain bacteria of cellulose are also synthesized. Marine animal tunics are other exciting sources of cellulose. In many applications, cellulose composites may be used. The adverse effects reduce on polymer composites. For years, it is still known that cellulose has surprised scientists such as automotive, packaging, electronics, and sport [42–44]. The structural structure and cellulose reduction and nonreturn in the planer form are illustrated in Figure 5.

Cellulose is most widely discovered as an important natural material for various applications. Mainly for the production of paper, door panels, seat backs, headliners, packing trays, dashboards, mobile covers, packaging, sports cars or liner, etc., biobased materials are used [46–49].

2. Different Properties of Nanocrystalline Cellulose

The nanocrystalline cellulose meaning covers the strongest and rigid natural market materials [50], such as the resistance of high voltages, high hardness, large surfaces [51],

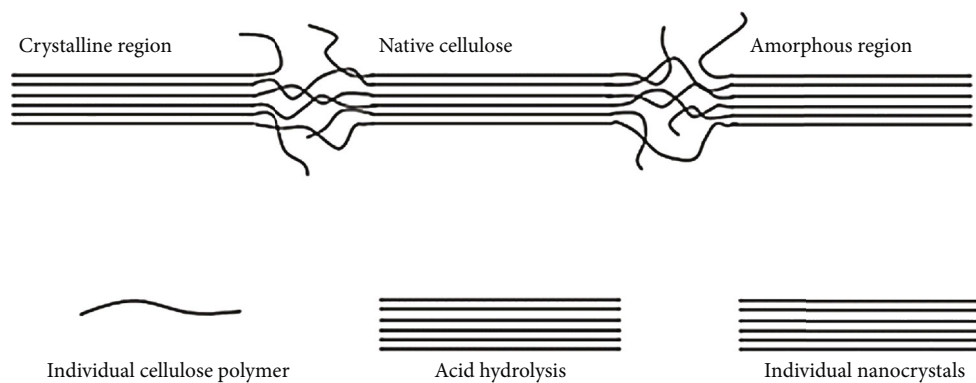


FIGURE 2: Schematic of nanocrystalline cellulose [15].

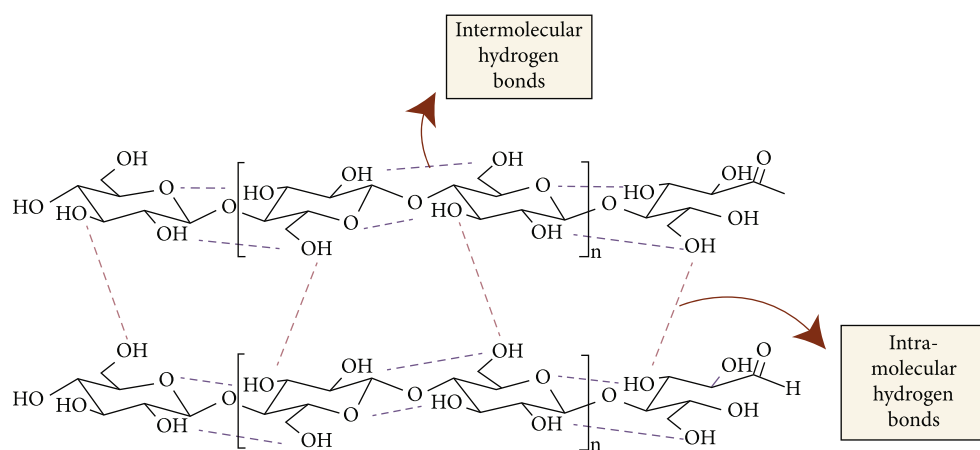


FIGURE 3: Composition of inter- and intramolecular hydrogen bond networks [31].

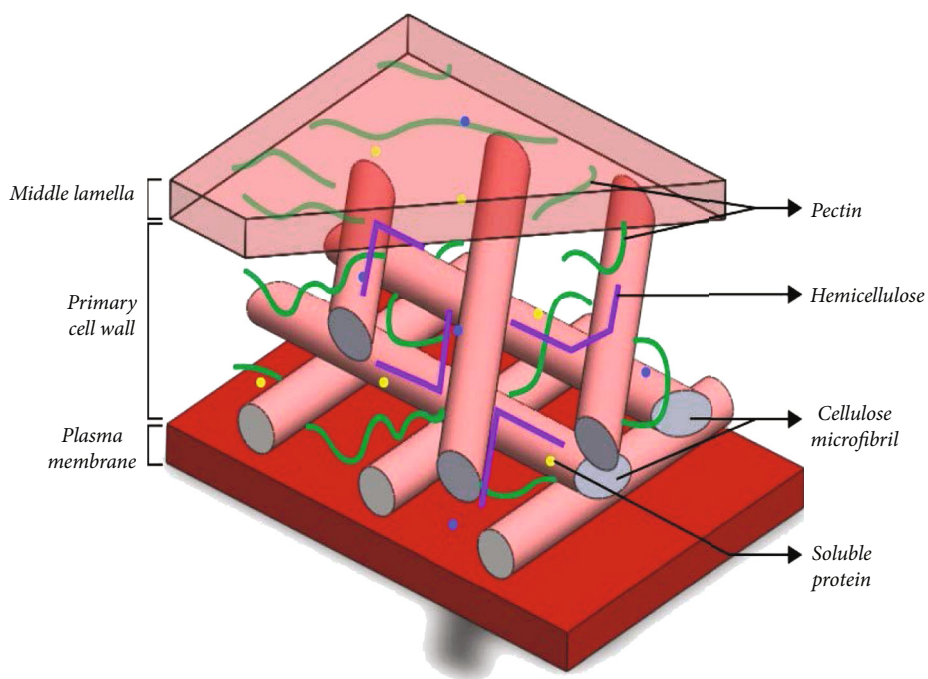


FIGURE 4: A schematic diagram of plant cell wall structure [37].

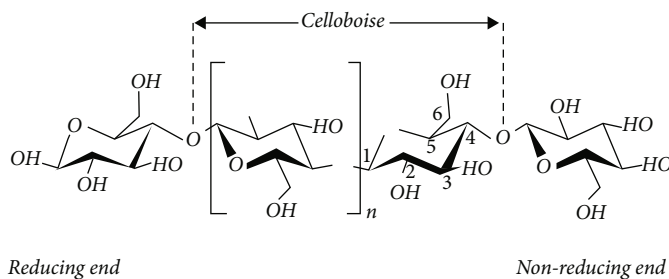


FIGURE 5: Structural organization of cellulose in planner form showing reducing and nonreducing end [45].

low densities, high-load ratio, hydroxyl reactive clusters' variable surface characteristics, and other chemicals, with electrical, mechanical, thermal, and optical characteristics.

2.1. Chemical Properties. Under climatic conditions, age, and degradation process, the natural fiber is structured and chemical. The chemical components spreading across cell walls are the primary and secondary wall layers. Each chemical plant varies from one plant to the next and is presented in Table 1 [52]. Each plant cell wall is primarily charging cellulose. The polymerization of 30-36 β -1 chains and 4 correlated glucose units is a rigid and insoluble crystalline material around cell walls. Hemicelluloses also include plant polymers and acids such as xyloglucans, xylenes, glucomannans, and galactoglucans. Therefore, hydrogen uses to coordinate the cellulose fibrils and gravel them into a matrix of hemicelluloses and lignin's with high molecular weight pectin molecules. In between cellulose and lignin in some walls, the hemicelluloses act as a clamp [53]. Lignin is also a connecting agent that enhances cellulose strength [54].

Cellulose is a biomass-derived biopolymer that is sustainable, abundant, and natural. The cellulose structure is arranged in fibrils with a lignin and hemicellulose matrix surrounding it [56]. It is the classic example for the plant of polymer plants of a renewable and biodegradable fabric polymer [57]. According to researchers, the overall production of the biopolymer is forecast to exceed € 7.5/1010 tonnes per year. However, only about 6 to 109 tonnes are processed in the paper chemical, fabric, material, and chemicals [58]. Figure 6 shows the biodegradable polymer matrices. Table 2 shows the chemical compositions of some natural fibers.

2.2. Thermal Properties. As regards nanocrystalline cellulose, its thermal property is one of the main restrictive factors in the application of nanocrystalline cellulose(NCC) mechanical characteristics at high temperatures [50]; however, the nanocrystalline cellulose is excellent for the treatment of heat thermoplastics ($n200^{\circ}\text{C}$) [61] (NCC degradation, usual at 0 temperature). For example, in the paper industry, paper with extra durability, strength, and flexibility is produced using nanocrystalline cellulose. In addition, nanocrystalline cellulose has unique papers with optical characteristics [62], in some cases.

2.3. Optical Properties. Researchers initially found liquid crystalline nanocrystalline cellulose, which resulted in an

TABLE 1: Chemical composition of standard lignocellulosic fibers [52, 55].

Type of fiber	Source	Composition (wt %)		
		Cellulose	Hemicellulose	Lignin
Wood	Hardwood	31-64	25-40	14-34
	Softwood	30-60	20-30	21-37
Nonwood	Bagasse	32-55.2	16.8	19-25.3
	Coir	32-43.8	0.15-20	40-45
	Corn cobs	26.1	45.9	11.3
	Corn stalks	35	25	35
	Cotton	82.7	5.7	<2
	EFB	43-65	30	19
	Oil palm frond	56.03	27.51	20.48
	Flax	62-72	18.6-20.6	2-5
	Hemp	68-74.4	15-22.4	3.7-10
	Jute	59-71.5	13.6-20.4	11.8-13
	Kenaf	31-72	20.3-21.5	8-19
	Ramie	68.6-85	13-16.7	0.5-0.7
	Sisal	60-78	10-14.2	8-14
	Sunn	80	10	6
	Wheat straw	43.2	34.1	22
	Curua	70.7-73.6	9.9	7.5-11.1
	Abaca	56-63	20-25	7-13
Alfa	45.4	38.5	14.9	
Bamboo	26-65	30	5-31	
Banana	63-67.6	10-19	5	
Coconut	36-43	0.15-0.25	41-45	
Soy hulls	56.4	12.5	18	
Rice husk	25-35	18-21	26-31	
Rice straw	59.1	18.4	5.3	

interesting observation of the nanocrystalline cellulose in 1959, in birefringence suspension. Most of the studies focused on nanocrystalline cellulose observations of this phenomenon. Li et al. produced a solid, cellulose iridescent film with a unique NCC feature to create safety documents such as banknotes, passports, and flat-water supplies [61] concerning the optical qualities of nanocrystalline cellulose.

2.4. Mechanical Properties. Table 3 shows the cellulose nanocrystals and other strengthening materials mechanical



FIGURE 6: Biodegradable polymer matrices [59].

TABLE 2: Chemical compositions of some natural fibers [60].

Fiber	Cellulose (%)	Hemicellulose (%)	Lignin (%)	Waxes (%)
Sugarcane bagasse	45	30	24	1
Bamboo	26-43	30	21-31	—
Flax	71	18.6-20.6	22	1.5
Kenaf	72	20.3	9	—
Jute	61-71	14-20	12-13	0.5
Hemp	68	15	10	0.8
Ramie	68.6-76.2	13-16	0.6-0.7	0.3
Sisal	65	12	9.9	2
Coir	32-43	0.15-0.25	40-45	—
Pineapple leaf fiber	81	—	12.7	—
Curaua	73.6	9.9	7.5	—

properties. Nanocrystalline cellulose characterizations are calculated through atomic force microscopy (atomic force microscope), analysis of radiation diffraction, inelastic radi-

TABLE 3: Cellulose nanocrystals and other strengthening material mechanical properties [10, 64–66, 50].

Material	σ (MPa)	E (GPa)	ρ (g cm ⁻³)
CNC	7500 - 7700	110 - 220	1.6
Glass fiber	4800	86	2.5
302 stainless steels	1280	210	7.8
Softwood kraft pulp	700	20	1.5
Carbon fiber	4100	210	1.8
Boron nanowhiskers	2000 - 8000	250 - 360	—
Aluminum	330	71	2.7
Carbon nanotubes	11000 - 63000	270 - 950	—
Kevlar KM2 fiber	3880	88	1.4

σ = tensile strength; E = elastic modulus in axial direction; ρ = density.

ation dispersion, and Raman effect. It carries theoretical and indirect experimental measures [63].

Nanocrystalline cellulose has been extensively studied in several areas, including polymer electrical electrolytes, packaging, antireflective, and solid iridescent movies for its excellent mechanical properties [67]. Finally, nanocrystalline cellulose natural cellulose characteristics are not only

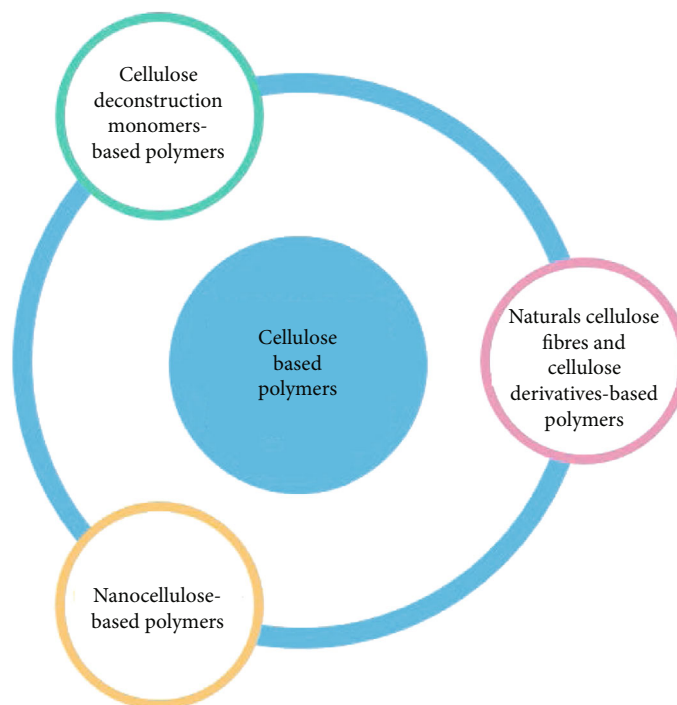


FIGURE 7: Main routes for the production of biopolymeric materials from various forms of cellulose [45].

inherent but have unique features like high crystallinity index (N70 per cent), large surface area ($\sim 150 \text{ m}^2/\text{g}$), and high tensile strength aspect ratios (~ 70) (7500 MPa). NCC has been taken into account in specific sectors in recent years, for example, regenerative medicine, printing, optical applications, and composites [68].

3. Extraction Methods of Nanocrystalline Cellulose

In order to reach nanostructured cellulose molecules of high crystalline and surface areas, the hierarchical structure of natural fibers must be separated. Many extraction methods for glycosidic strips have been reported to break the cellulose nanofibril domain. It includes and combines two or more such techniques and mechanical, chemical, and biological treatment. Furthermore, all such methods lead to the development and disintegration of nanostructured cellulose molecules. Generally, nanofibrillar cellulose, called cellulose nanofiber, is produced by mechanical cellulosic decomposition. Cellulose's nanofibers such as homogenising, cryo-crushing, microfluidisation, grinding, and high-intensity ultrasonic have mechanical approaches available [69]. An essential approach to the alignment process is enzymatic pretreatment for lignocellulosic fiber. We know that pretreatment in mild and chemical processing conditions is economical, energy-free, environmental, productive, and biological [70].

In biological pretreatment, lignin and hemicellulose decay with the help of lignocellulosic materials such as brown, white, and spongy red champagne and bacteria. The natural treatment may include an enzyme from microbes. Brown red and soft fungi attack mainly cellulose,

while white red hits both cellulose and lignin. Compared to other pretreatment procedures, there are also inherent disadvantages, such as long pretreatment times and high rates [71, 72]. Cellulose-nanocrystalline, alkaline pretreatment, acid hydrolysis, oxidants, and ionic fluids are the most promising methods in chemical pretreatment. Acid hydrolysis is the standard method used to prepare nanocrystalline cellulose because of moderate working conditions and excellent suspended stability. The amorphous regions around the cellulose fiber are destroyed in controlled conditions to maintain crystalline areas under acid hydrolysis. Nonetheless, to separate lignin from its cellulose biopolymers must be energetically pretreated. Then, biopolymers formed and required deconstruction, derivation, and nanoparticles. Three main routes are manufactured with cellulose-based polymers. The principal routes for biopolymer production in different forms of cellulose are exhibited in Figure 7.

Natural fillers based on cellulose nanofibrils and cellulose microfibrillated, essential particle size factors affect the stability, durability, and strength of lignocellulose-based biocomposite materials [73–75].

3.1. Plasma Processing Technology. The formation of cellulosic nanomaterials is derived from biomass residues. In the last few years, however, several attempts have been made during production on the bench scale to improve the process' acceptance in an industrial context. In this light, the heterogeneous solid acid catalyst of the cotton linter microcrystalline cellulose with amberlite IR 120 was one step of forming nanocrystalline cellulose in this regard. The first-order kinetics of $42.8 \text{ per } 10^{-2} \text{ min}^{-1}$ and a response rate of $10.1 \text{ per } 10^{-5} \text{ mol/minute}$ were followed in the production method.

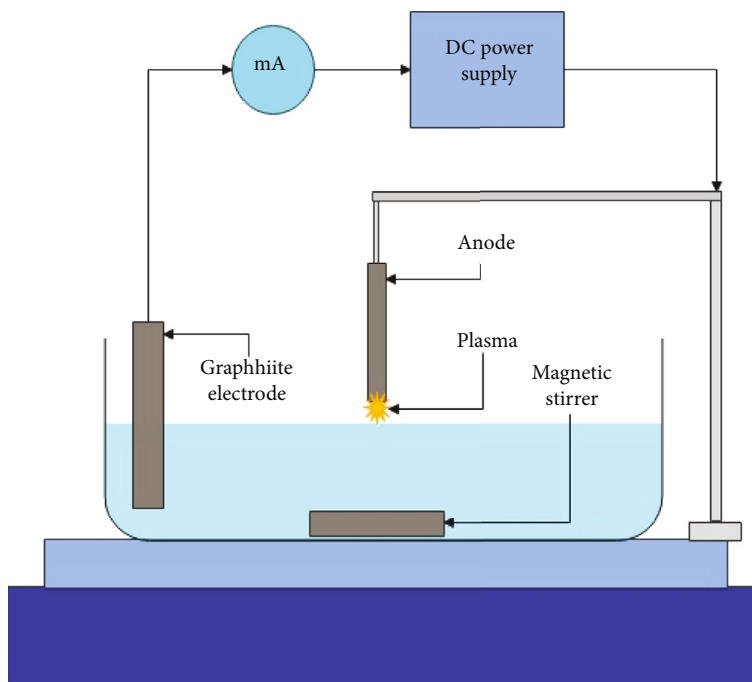


FIGURE 8: Schematic representation of the nanocrystalline cellulose preparation experimental using plasma processing technology [76].

It has shown that in ultrastructural morphological analysis, the average particulate diameter is 36 nm. Furthermore, they investigate four distinct types of lignocelluloses: feedstocks, a rapid and effective grinding method, liquefaction, centrifugation, and washing for nanocrystalline cellulose isolation [77]. Liquefaction of glycol and methane sulfonic acid shows efficacy during isolation. However, in terms of implementation, it takes a lot of time to respond to multistage processes and increases the total cost. In addition, a pot-oxidant method for hydrolysis has been developed as a biomaterial for the manufacture of cellulose tools with plain electroprocess. The mean nanostructure material fiber diameter was 51.6 ± 15.4 nm. In addition to conventional procedure, a 6.5 per cent added to crystallinity for the product acquired with the pot response. A further study used microcrystalline cellulose empty fruits to isolate nanocrystalline cellulose with ultrasound TEMPO oxidation as lignocellulosic feedback. Sonic treatment was observed when the yield increased by about 39 per cent compared to the nonsonic condition, with a significant effect on the insulation process. Structural analysis shows a rod similar to crystalline morphology for extracted nanocrystalline cellulose biomass, with an average length of 122 nm, respectively, and a width of 6 nm [78]. A new plasma solution method helps develop the nanocrystalline cellulose [79], microcrystalline cellulose, and FP as the source material in an electrolytic solution. Figure 8 shows the scheme for the experimental system used in plasma therapy for nanocrystalline cellulose development. The graphic anode placed under atmospheric pressure transmits direct current into the surface area of the electrolytic solution as a cathode. As a consequence, the redox reaction occurs when the glow discharge appears. Cellulose

oxidation causes the hydroxyl surface to occur during the reaction when plasma processing is carried out with distilled water due to subsequent hydrolysis.

3.2. Acid Hydrolysis. Concentrate the desired acid and deionized water in combination with the purified initial product. It is the best technique used to separate cellulose nanocrystals from cellulose fibers [38, 78, 80]. The procedure involves acid-induced deconstruction, including the spread of acid molecules through heterogeneous acid hydrolysis to cellulosic microfibrils. Glycosidic bonds are cleaved into the amorphous cellulose fibrils which cause the hierarchy of fibril bundles to break down into cellulose nanocrystals [39, 81].

There was a selective splitting in the cellulosic chains [20] in the difference in kinetic hydrolysis from paracrystalline to crystalline areas. These acids' most common chemical function consists of the release of a glycosidic cellulosic ion, which causes oxygen elements to spread and amorphous glycosidic bond hydrolytic splits [16] to react to glycosidic bonds between the two oxygen moieties 103, 102, 103, 103, and 102. The acidic therapy hydrolyzes pectin, and hemicellulose residues break polysaccharides into simple sucre. Thanks to their large freedom of motor after the hydrolytic division, these crystallites can grow in size and thus in dimensions greater than the original microfibrils [20]. Cellulose nanocrystals have quickly reduced their polymerization due to acid hydrolysis. Dialysis with deionized water separates and rinses the mixture at the end of the procedure to remove residual acid and neutralised salt as in Figure 9.

Sonic treatment is generally applied [16, 38, 78, 84, 85] to improve and homogeneously disperse cellulose nanocrystals in aqueous media.

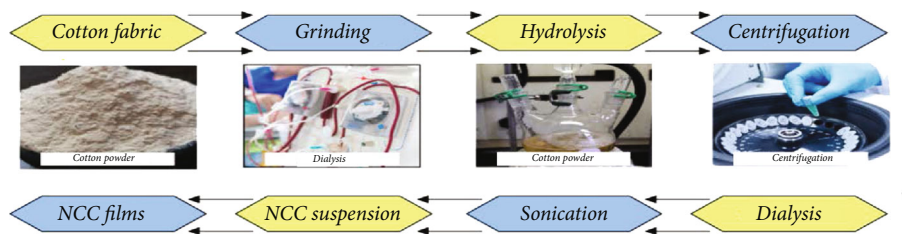


FIGURE 9: Schematic representation of the different steps used to produce CNCs using acid hydrolysis [10, 82, 83].

3.3. Ionic Liquids. Cellulose is a potent solvent ionic liquid. It consists of liquid molten salts and is thus commonly referred to as “green” solvents at environmental temperatures. The first ionic liquid used to isolate NCC from the sugarcane bagasse was 1-butyl-3-methylimidazolium chloride. Studies show that cellulose dissolution in 1-ethyl-3-methylimidazolium acetate results in no substantial 85°C degradations of the polymer cellulose chain. Cellulose dissolving potentially of this sort of ionic liquid is not decided to the same degree by the ionic liquid presence of water [86]. The cellulose has been dissolved and blocked by the homogenizer. Consequently, 100% NCC crystalline structure is one of the effective uses of ionic liquid. Cellulose was dissolved and passed by an ionic fluid without obstruction. Then, by adding water, cellulose was taken in, and by freezing, NCC regenerated. The reaction temperature, microwave power, and weight relationship between cellulose and ionic liquid are soluble in cellulose. The best solubilization found was also demonstrated when the 400 W microwave response temperature was 130°C and 1% ionic liquid ratio [82]. Thus, cellulose insolventy retains 1-ethyl-3-methylimidazolium acetate with just 15-16 wt % of its water content. Some reports describe prepared NCCs, including totally amorphous and partially crystalline NCC, by regenerating lignocellulosic ionic liquid [87]. The crystallinity observed seems to depend on the time of dissolution, cinematic recovery, and solvent-free choice. Therefore, the ionic liquid offers a new route for the disintegration and restoration of lignocellulosic substances.

3.4. Mechanical Treatment. In the process of production with hydrolytic acid, oxidative and enzyme treatment combinations, or directly [14, 88, 89], the mechanical methods of producing nanoscale cellulose particles have also been extensively studied. They include microfluidisation, ultrasound, homogenization at high pressure, and ball milling.

The methods are often used to make cellulose nanofibers with nanometers or decades of nano-thermometers and up to several meters in length [10, 90]. Some researchers have used high energy bead framing (HEBM) [89] to develop a scalable mechanical method in recent years. Applications of commercially available microcrystalline cellulose (MCC) have been isolated from and aqueously dispersed or diluted acid (phosphoric acid) by the authors in the course of a HEBM process. The morphology and the dimension ratio values of acid hydrolysis are very similar to the cellulose nanocrystals. The cellulose nanocrystal output rate was between 57% and 76%. The resulting rod, similar to cellulose nanocrystals, is a high thermal stability crystallinity index

between 85 and 95%, which is used to melt the most common thermoplastics. The isolation of cellulose nanocrystals by ultrasonic use was also mentioned by another mechanical method [61, 89]. Rod-shaped cellulose nanocrystals were made using a purely physical high-intensity ultrasound method from an aqueous dispersion of microcrystalline cellulose. The cellulose nanocrystal was 10-20 nm in diameter and 50-250 nm in length.

However, the output of this method of cellulose nanocrystals does not exceed 10%. The ultrasound effect was not selective, meaning that amorphous cellulose and crystalline cellulose can be eliminated. Water is known to have the ability to hydrolyze polysaccharides [91]. The main features of a prevailing hydrolysis rate are water molecules and the accessibility of H_3O^+ and water species. In sub- and supercritical water, lower and higher species levels are present [92]. Their use for hydrolysis reactions could therefore be efficient. In some studies, water has previously been used to produce lignocellulosic material at high temperatures and pressure. Very few studies on subcritical water hydrolysis method cellulose nanocrystals production have been reported [93]. Not only because of its greener characteristics but also because of the low and cleaner waste, low corrosion, and low reactant costs, it is the sole use of water as a reagent promising. [94] used this procedure for the production of commercial microcrystalline cellulose nanocrystals. The authors reported that optimising reaction conditions certainly means high-quality cellulose nanocrystals [93]. Hydrolyzed cellulose joins with subscriptive water (120°C and 20.3 MPa for 60 minutes). The states of the experiment permit for more water, activity, and ionization diffusion. Partial cellulose hydrolysis with a yield of 21.9% has therefore been achieved. The cellulose nanocrystals obtained showed a high index of crystallinity (79.0 per cent) and rod-like form with the same aspect of cellulose nanocrystal as those reported. Moreover, the thermal firmness of these cellulose nanocrystals was better than the source of cellulosic (approximately 300°C).

4. Modification of Nanocrystalline Cellulose

Table 4 shows the effect of structural modifications on nano-based crystalline cellulose. Change of the nanosurface cellulose is the essential process to ensure homogenous distribution and enhanced polymer matrix compatibility. Some techniques for this purpose have also been registered, including esterification, siltation, polymer grafting, and mediate oxidation of 2,2,6,6-tetramethylpiperidine-1-oxyl (tempo).

TABLE 4: Effect of structural modifications on nanobased crystalline cellulose [95–102].

Methods of modification	Process followed	Key results
Chemical modification	Partial oxidation of cellulose which was immediately followed by interaction of aldehyde groups with amino group of polyglutamic acid	The modified cellulose exhibited enhanced compatibility with hydrophobic polylactic acid when composite materials were prepared
Surfactant-aided modification	Suspension of NCC was mixed with various surfactants of different concentrations using orbital shaker at 200 rpm for 24 hours	The modified NCCs were observed as potent drug carrier for paclitaxel
Surface modification	1% (<i>w/v</i>) of NCC suspension was mixed with TA and DA using 1 and 40 mg/mL of concentrations, respectively. The mixture was stirred for 3 hours at room temperature prior to obtain the final product	The modified NCC obtained from OPEFB was observed with improved curcumin binding efficiency in the ranges of 95–99%
Hexadecyltrimethylammonium bromide- (CTA-) assisted hydrophobic modification	Spin coating technique was used to prepare CTA-based NCC film	Surface plasmon resonance technique revealed the ability of the film to sense copper ions more efficiently
Chemical modification	Alkaline hydrolysis of Eichhornia crassipes using 10% (<i>w/v</i>) of NaOH at 100°C for 3 hours followed by acidic oxidation using peracetic acid (CH ₃ CO ₃ H) at 80°C for 2 hours	NCC obtained from chemical modification of the biomass was observed to remove an anionic dye (reactive blue 21) and basic dye (crystal violet) efficiently
Cationic surfactant cetyltrimethylammonium bromide- (CTAB-) mediated surface modification	100 mL 0.4% (<i>w/w</i>) of NCC suspension prepared from Citrus limetta albedo (by alkali treatment, bleaching, and acid hydrolysis) was added into 100 mL 4 mM of CTAB solution, and the mixture was heated at 60°C for 3 hours	After the modification, NCC was observed with enhanced surface area and also investigated as sustained release drug delivery system for NSAID
Chemical modification	A derivative compound of nanocrystalline cellulose was synthesized, namely, cationic dialdehyde cellulose (CDAC), by sequential oxidative reductive amination process	Nanocrystalline cellulose was observed as promising nanofiller with improved strength and antismearing properties for reinforcing chitosan (CTS) film when 1% of CDAC was well mixed with 1% solution of chitosan
Chemical modification	The surface modification is anticipated in aqueous organic media through aromatic nucleophilic substitution in the presence of an alkaline reagent	The modification explored the chemistry of postmodification for the applications of grafting molecules onto cellulose

4.1. Acetylation. The esterification reaction has become a famous method of hydrophobic cellulose surface treatment. Cellulose pretreatment groups replace the surface cellulose groups with acetic nanoparticles with cellulose function groups (COCH₃). Acetylic anhydride is used in homogeneous and heterogeneous forms with acetylating cellulose nanoparticles in the presence of acetic acid and small amounts of catalysts such as sulfuric acid or perchloric acid. When the partially acetylated molecules are sufficiently soluble during a consistent acetylation process, on the other hand, precipitate isolation is not necessary during the heterogeneous reaction. In homogeneous reaction conditions, a replacement time, temperature, and molar cellulose derivative ratio can be easily managed. Natural polymer degradation is negligible during the response and degrading, and additional routes are available to replace or implement new working groups in full. The state of acetylation plays an essential role in altering the physical properties of cellulose while maintaining the microfiller morphology. Research shows a high degree of transparency and decreased hygroscopicity of acetylated composites and improved thermal resistance to cellulose acetylation and increased natural resistance to acetylated plant fiber/polyester composites [103].

4.2. Silylation. Another efficient mechanism to stabilise the spread of nanocellulose particles into a suspension is the partial nanocellulose situation. On the nanocellulose surface, a random distribution of alkyl molecules such as n-butyl, N-octyle, N-dodecyle, and isopropyl defines its content by surface substitution (DS). Cellulose might disperse with DS value 0.61–1, resulting in a colloiddally stable dispersion, with intact morphological properties, in a solvent that has low polarity (tetrahydrofuran). But since the chains in the centre of crystals are linked with high silylation (DS over 1), crystals are disintegrated and original morphology is lost. After the surfaces were altered by the partial silylation of various alkyl moieties [104], Goussé et al. received a stable suspension of tetrahydrofuran tunicate whiskers (THF).

4.3. Polymer Grafting. An alternative way to improve the fiber-surface hydrophilicity is polymer grafting on the nanocellulose surface. Two main strategies are used for polymer grafting. Connector components are used in the “grafting on” approach to attach the presynthesized polymer chain to the hydroxyl cellulose surface groups. On the other hand, the “graft of” approach-initiated polymerization on location constitutes polymer chains onto the substratum by the immobilized initiator. The first approach to the “grafting

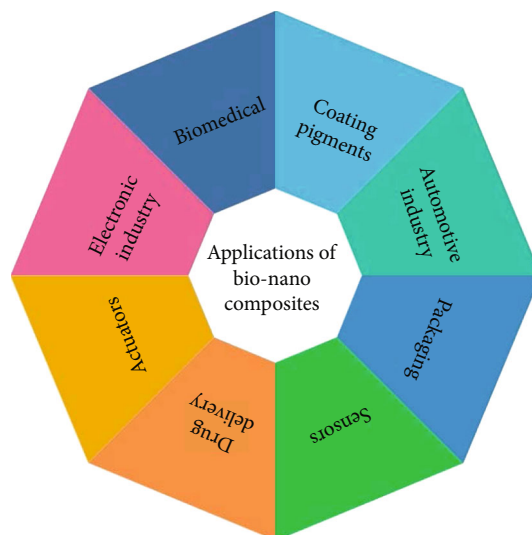


FIGURE 10: Applications of cellulose nanoparticle-reinforced biocomposites in various fields.

on” approach was [105] to take the grafting of DNA oligomers on the cellulose surface [74], while Habibi et al. first reported the “grafting from” approach. This work involved the modification of the area by the grafting of poly (ϵ -caprolactone) using stannous octoate ($\text{Sn}(\text{Oct})_2$) [7] through the ring-opening polymerization.

4.4. Active Agent/Surfactant Surface Area. By interacting with the subfactor and/or active surface agents, the hydrophilic cellulose suspension adhesive can also be increased to a nonpolar hydrophobic polymer matrix. Tensile is generally defined as an agent to lower water surface tension. Thus, the use of cellulose modified by surfactant would alter the dynamic of nanocomposites’ surface tension relative to their interface. The interfacial tensional value generally lies between the two immiscible phases of the surface tension values. Therefore, if two-stage molecules have similar surface tensions, interfacial tension will be zero [106].

For this reason, literature uses stresses such as alkenyl succinic anhydride, isocyanate, polypropylenes malleated, or chlorosilane. Noncovalent surface modification typically takes place by adsorption of the surface of nanocellulose. Surface modification by nanocellulose surfactant made of mono and phosphoric acid diester and alkyl-phenolic tails was introduced by [107]. Cellulose-modified particles have been dispersed in nonpolar solvents. Furthermore, in nanocomposites, [64] reported the polystyrene nanocellulose-coated surfactant. In addition, improve the dispersion of ionic surfactant modification cellulose in poly(lactic acid (PLA) polymer matrix [108].

5. Applications of Cellulose Nanoparticle-Reinforced Biocomposites

The potential for various applications for cellulose nanoparticles is present, and their use in nanocomposites is widely studied. With the integration of biofibers, biofibers, based

on renewable energy resources such as cellulose plastics, starch plastic, polyhydroxyalkanoates, and polylactides, will become green biocomposites soon. Nanocellulose is primarily considered for applications on paper and packaging and construction, automotive and furniture, electronics, pharmaceuticals, and cosmetics as in Figure 10.

For companies producing electro-electro acoustical devices, nanocellulose is used as a high-quality sound membrane. Nanocellulose has been used in various applications, including first-rate electronic paper additives (e-paper), ultrafiltration refining membranes, oils for mineral oil regeneration, and membranes. The high strength, rigidity, and small dimensions of nanocellulose can convey special features to the use of fiber-reinforced composites and may later in different applications, and it is shown in Table 5 [109].

5.1. Biomedical Applications of NCC. Since the toxicity of nanocrystalline cellulose has not been implemented, NCC has been introduced to biomedical applications by several research groups. [116] suggested modified nanocrystalline cellulose, especially chemotherapy agents, for the targeted delivery of medicines [113]. For example, NCC successfully targets and controls the supply of folic acid in the mammalian brain to cancerous tumours. Nanocrystalline cellulose also has numerous biomedical applications, such as the diagnosis and stagnation of NCC (e.g., the use of human elastase enzyme at a damaged site) [117] and also has cardiovascular graft replacements [8], enzyme/protein [118] immobilization, and viral inhibitors (alphaviruses and perhaps also herpes simplex viruses). The fluorescent labelling of nanocrystalline cellulose provides potential applications in biomedical questions such as biosamples, bioassays, and applications in bioimaging [63].

5.2. Other Potential Applications. Tissue engineering, wastewater packaging, structural and efficient characteristics of

TABLE 5: Applications of NCC derivatives in different fields [110–115].

Type of cellulosic derivatives	Field of applications	Key findings
NCC (nanocrystalline cellulose)	Biomedical	3D printable with cartilage regeneration once NCC aerogel structure was crosslinked with polyamide epichlorohydrin
NCC (nanocrystalline cellulose)	Waste water treatment	Starch-based hydrogel nanocomposite reinforced with magnetic functionalized NCCs for the application as a novel nanoadsorbent in the removal of cationic dye from aqueous solution
NCC (nanocrystalline cellulose)	Food packaging	Incorporation of 8% NCC resulted into the improvement in food preservation characteristics both in gelatin and starch-based composite films
MCC (microcrystalline cellulose)	Pharmaceutical	MCC was well observed as an efficient adsorbent for peppermint oil (PO), a multicomponent liquid drug
MCC (microcrystalline cellulose)	Pharmaceutical	MCC-based hydrogels were observed in vitro to load and deliver cephalexin in various simulated body fluids
MCC (microcrystalline cellulose)	Polymer composite	Surface-modified MCC using urea was filled with chitosan for the preparation of polymeric composite materials with improved stability and function
MCC (microcrystalline cellulose)	Adsorption	Pyridonedi acid functionalized (PDA) was synthesized for the removal of lead and cobalt with maximum adsorption capacities of 177.7 and 122.7 mg/g, respectively

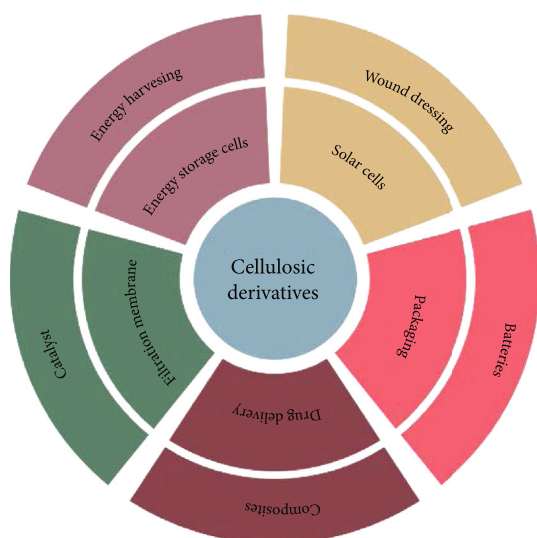


FIGURE 11: Promising applications of cellulosic derivatives.

cellulosic products, and significant applications in the pharmaceutical sectors are also being utilised in several areas: alternative materials, the recognition of metal ions, and the production of electronic goods and parts. In polyvinyl alcohol, nanocrystalline cellulose is widely used and distributed to enhance mechanical properties (PVA). The main ingredient in nanocrystalline cellulose modification as a binding agent was 1-hydroxymethyl-5-dimethylhydantoin with cyanuric chloride (cych) (HDH). The synthesiser NCC cych-HDH-Cl has been discharged into PVA or chitosan for antibacterial film preparation after chlorination. Effects on *Staphylococcus aureus* (ATCC 6538) and *Escherichia coli* O157:H7 (ATCC 43895) [119] were significantly detrimental to the latter. Membranes of cellulose acetate (CA) are also used for food packaging. Nanocrystalline cellulose particles are, however, well integrated with these membranes to enhance their industrial usefulness, using N-halamine pre-

cursors for polymethacrylamide (NCC PMAMs). Thus, for *Staphylococcus aureus* and *Escherichia coli*, the composite membranes had good antibacterial properties within 10 and 5 minutes, respectively [83].

In the recent successful cellulosic derivatives study, Figures 11 and 12 shows a variety of applications. In preparation of biocomposite materials, nanocrystalline cellulose is widely used as possible nanofiller. But poor addition between the matrix and the filler causes nanoparticles to autoaggregate and reduces adhesion of the polymer matrix. Tempo-mediated oxidation was performed for PLA- and PHBV-strengthened polymer composites to overcome these constraints by the nanocrystalline cellulose suspension resulting from OPEFB [120].

The biocomposites are developed to offer full potential as packaging materials through the increased oxygen obstacle and mechanical stability. In addition, nanocrystalline cellulose helps maintain structural integrity in the production of sensors due to its structural description of a high surface area, an important aspect ratio and considerable rigidity. Nanocrystalline cellulose quantum point-assisted tyrosinase [122, 123], an integrated biosensor for aqueous system phenol detection, has been developed.

The NCC was amended during CTAB architecture to improve the conductivity of samples by decreasing the hydrophilicity of the cellulose derivative. In the end, a sensor has urbanized reasonable phenol detection limits with 0.0008 mg/L LODs of 0.5 to 3.8 mg/L. In research, NCC modified by CTAB and GO was produced to permeate the nickel ions selectively. SPR has been used to determine the nanocomposite material's binding affinity constant. A nickel ion of a broad range of 0.01 to 0.1 mg/L is the 1.6/103 binding affinity constant [98]. In addition, for possible use in fuel cells as conducting membrane, a single proton-driving nanocomposite was prepared with NCC imidazole-doped molecule. The maximum electrical conductivity showed at 140 B/C with 1 imidazole per 1.7 units of glucose was 2.7 10⁻² s/m, which is an improvement of 5 times that of non-doping performance [110, 124].

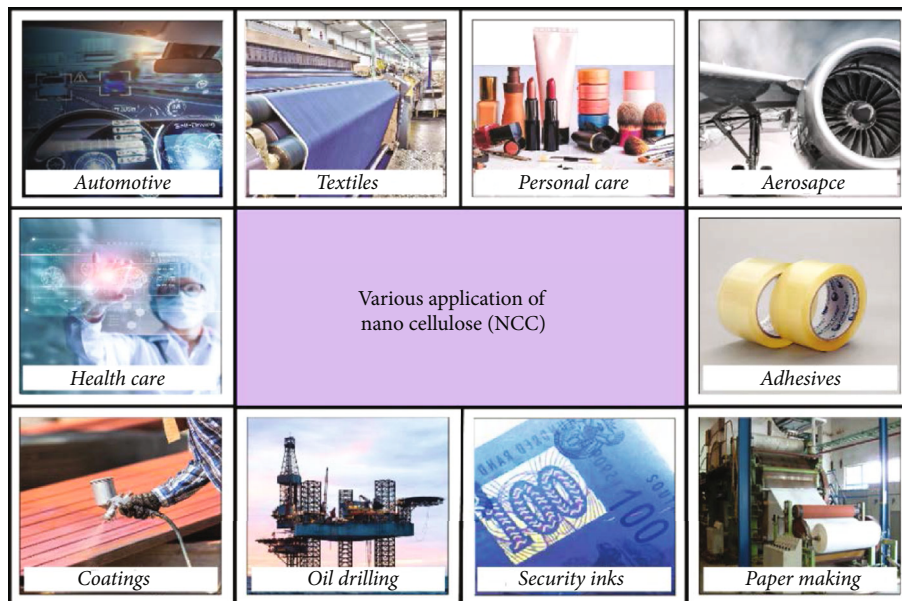


FIGURE 12: Various applications of nanocellulose (NCC) [121].

6. Conclusions

The exploration of new materials for advanced applications has been fascinating for environmentally sound biorenewable materials from various natural resources.

- (i) Among the several renewable resources, cellulose is the most common and significant polymer in nature. Several types of cellulose may be processed, including fiber, cellulose microphones, and nanos
- (ii) Recently, cellulose nanocrystals (CNC), especially for their crystalline structure and crystalline structure, were investigated in several advanced applications. Despite the great advantages of cellulose nanocrystals, their broad application was limited in terms of energy consumption and production costs
- (iii) Thus, the first portion of this study concentrated on cellulose supplies and CNC manufacturing processes. They also spoke about cellulose structural organization and cellulose nanomaterial nomenclature for beginners
- (iv) We consider that the research presented in this paper increases researchers' interest in nanomaterials based on cellulose and a fundamental understanding of nanocrystals from cellulose

Data Availability

The data used to support the findings of this study are included within the article. Further data or information is available from the corresponding author upon request.

Conflicts of Interest

The authors declare that there are no conflicts of interest regarding the publication of this paper.

Acknowledgments

The authors appreciate the support from the Kombolcha Institute of Technology, Wollo University, Ethiopia, for the research and preparation of the manuscript. The author appreciates the assistance from the Saveetha Engineering College, MS Ramaiah Institute of Technology, IFTM University, Government Engineering College, Jhalrapatan, JSS Science & Technology University, for the assistance in doing the work.

References

- [1] A. K. Mohanty, M. Misra, and L. T. Drzal, *Natural Fibers, Biopolymers, and Biocomposites*, CRC press, 2005.
- [2] M. Li, L. Wang, D. Li, Y.-L. Cheng, and B. Adhikari, "Preparation and characterization of cellulose nanofibers from depectinated sugar beet pulp," *Carbohydrate Polymers*, vol. 102, pp. 136–143, 2014.
- [3] N. Johar, I. Ahmad, and A. Dufresne, "Extraction, preparation and characterization of cellulose fibres and nanocrystals from rice husk," *Industrial Crops and Products*, vol. 37, no. 1, pp. 93–99, 2012.
- [4] M. Åkerholm, B. Hinterstoisser, and L. Salmén, "Characterization of the crystalline structure of cellulose using static and dynamic FT-IR spectroscopy," *Carbohydrate Research*, vol. 339, no. 3, pp. 569–578, 2004.
- [5] A. Dufresne, J. Cavaillé, and M. R. Vignon, "Mechanical behavior of sheets prepared from sugar beet cellulose microfibrils," *Journal of Applied Polymer Science*, vol. 64, no. 6, pp. 1185–1194, 1997.

- [6] T. Saito, S. Kimura, Y. Nishiyama, and A. Isogai, "Cellulose nanofibers prepared by TEMPO-mediated oxidation of native cellulose," *Biomacromolecules*, vol. 8, no. 8, pp. 2485–2491, 2007.
- [7] Y. Habibi, A.-L. Goffin, N. Schiltz, E. Duquesne, P. Dubois, and A. Dufresne, "Bionanocomposites based on poly(ϵ -caprolactone)-grafted cellulose nanocrystals by ring-opening polymerization," *Journal of Materials Chemistry*, vol. 18, no. 41, pp. 5002–5010, 2008.
- [8] N. Lin and A. Dufresne, "Nanocellulose in biomedicine: current status and future prospect," *European Polymer Journal*, vol. 59, pp. 302–325, 2014.
- [9] K. Oksman, Y. Aitomäki, A. P. Mathew et al., "Review of the recent developments in cellulose nanocomposite processing," *Composites. Part A, Applied Science and Manufacturing*, vol. 83, pp. 2–18, 2016.
- [10] R. J. Moon, A. Martini, J. Nairn, J. Simonsen, and J. Youngblood, "Cellulose nanomaterials review: structure, properties and nanocomposites," *Chemical Society Reviews*, vol. 40, no. 7, pp. 3941–3994, 2011.
- [11] S. J. Einchhorn, A. Dufresne, M. M. Aranguren et al., "Review: current international research into cellulose nanofibres and nanocomposites," *Journal of Materials Science*, vol. 45, no. 1, pp. 1–33, 2010.
- [12] Y. Habibi, L. A. Lucia, and O. J. Rojas, "Cellulose nanocrystals: chemistry, self-assembly, and applications," *Chemical Reviews*, vol. 110, no. 6, pp. 3479–3500, 2010.
- [13] I. Siró and D. Plackett, "Microfibrillated cellulose and new nanocomposite materials: a review," *Cellulose*, vol. 17, no. 3, pp. 459–494, 2010.
- [14] H. P. S. A. Khalil, A. H. Bhat, and A. F. I. Yusra, "Green composites from sustainable cellulose nanofibrils: a review," *Carbohydrate Polymers*, vol. 87, no. 2, pp. 963–979, 2012.
- [15] R. Li, J. Fei, Y. Cai, Y. Li, J. Feng, and J. Yao, "Cellulose whiskers extracted from mulberry: a novel biomass production," *Carbohydrate Polymers*, vol. 76, no. 1, pp. 94–99, 2009.
- [16] D. Trache, M. H. Hussin, M. K. M. Haafiz, and V. K. Thakur, "Recent progress in cellulose nanocrystals: sources and production," *Nanoscale*, vol. 9, no. 5, pp. 1763–1786, 2017.
- [17] Ø. Eriksen, K. Syverud, and Ø. Gregersen, "The use of microfibrillated cellulose produced from kraft pulp as strength enhancer in TMP paper," *Nordic Pulp & Paper Research Journal*, vol. 23, no. 3, pp. 299–304, 2008.
- [18] A. Chakraborty, M. Sain, and M. Kortschot, *Cellulose Microfibrils: A Novel Method of Preparation Using High Shear Refining and Cryocrushing*, vol. 59, no. 1, 2005 Walter de Gruyter, 2005.
- [19] W. Chen, H. Yu, Y. Liu, Y. Hai, M. Zhang, and P. Chen, "Isolation and characterization of cellulose nanofibers from four plant cellulose fibers using a chemical-ultrasonic process," *Cellulose*, vol. 18, no. 2, pp. 433–442, 2011.
- [20] A. Dufresne, *Nanocellulose: from nature to high performance tailored materials*, Walter de Gruyter GmbH & Co KG, 2017.
- [21] M. Poletto and H. Ornaghi Jr., *Cellulose: Fundamental Aspects and Current Trends*, BoD–Books on Demand, 2015.
- [22] F. Fahma, S. Iwamoto, N. Hori, T. Iwata, and A. Takemura, "Effect of pre-acid-hydrolysis treatment on morphology and properties of cellulose nanowhiskers from coconut husk," *Cellulose*, vol. 18, no. 2, pp. 443–450, 2011.
- [23] X. M. Dong, J.-F. Revol, and D. G. Gray, "Effect of microcrystallite preparation conditions on the formation of colloid crystals of cellulose," *Cellulose*, vol. 5, no. 1, pp. 19–32, 1998.
- [24] M. Henriksson, G. Henriksson, L. A. Berglund, and T. Lindström, "An environmentally friendly method for enzyme-assisted preparation of microfibrillated cellulose (MFC) nanofibers," *European Polymer Journal*, vol. 43, no. 8, pp. 3434–3441, 2007.
- [25] Z. Man, N. Muhammad, A. Sarwono, M. A. Bustam, M. V. Kumar, and S. Rafiq, "Preparation of cellulose nanocrystals using an ionic liquid," *Journal of Polymers and the Environment*, vol. 19, no. 3, pp. 726–731, 2011.
- [26] R. A. Ilyas, S. M. Sapuan, and M. R. Ishak, "Isolation and characterization of nanocrystalline cellulose from sugar palm fibres (*Arenga pinnata*)," *Carbohydrate Polymers*, vol. 181, pp. 1038–1051, 2018.
- [27] A. Kaushik, M. Singh, and G. Verma, "Green nanocomposites based on thermoplastic starch and steam exploded cellulose nanofibrils from wheat straw," *Carbohydrate Polymers*, vol. 82, no. 2, pp. 337–345, 2010.
- [28] R. A. Ilyas, S. M. Sapuan, M. L. Sanyang, and M. R. Ishak, "Nanocrystalline cellulose reinforced starch-based nanocomposite: a review," in *5th Postgraduate seminar on natural fiber composites*, pp. 82–87, Malaysia, 2016.
- [29] R. A. Ilyas, S. M. Sapuan, M. L. Sanyang, M. R. Ishak, and E. S. Zainudin, "Nanocrystalline cellulose as reinforcement for polymeric matrix nanocomposites and its potential applications: a review," *Current Analytical Chemistry*, vol. 14, no. 3, pp. 203–225, 2018.
- [30] N. Follain, S. Belbekhouche, J. Bras, G. Siqueira, S. Marais, and A. Dufresne, "Water transport properties of bio-nanocomposites reinforced by *Luffa cylindrica* cellulose nanocrystals," *Journal of membrane science*, vol. 427, pp. 218–229, 2013.
- [31] Y. Fukaya, A. Sugimoto, and H. Ohno, "Superior solubility of polysaccharides in low viscosity, polar, and halogen-free 1, 3-dialkylimidazolium formates," *Biomacromolecules*, vol. 7, no. 12, pp. 3295–3297, 2006.
- [32] Y. Habibi, "Key advances in the chemical modification of nanocelluloses," *Chemical Society Reviews*, vol. 43, no. 5, pp. 1519–1542, 2014.
- [33] J. Velásquez-Cock, P. Gañán, P. Posada et al., "Influence of combined mechanical treatments on the morphology and structure of cellulose nanofibrils: thermal and mechanical properties of the resulting films," *Industrial Crops and Products*, vol. 85, pp. 1–10, 2016.
- [34] Z. Qazanfarzadeh and M. Kadivar, "Properties of whey protein isolate nanocomposite films reinforced with nanocellulose isolated from oat husk," *International Journal of Biological Macromolecules*, vol. 91, pp. 1134–1140, 2016.
- [35] J. A. Sirviö, A. Kolehmainen, H. Liimatainen, J. Niinimäki, and O. E. O. Hormi, "Biocomposite cellulose-alginate films: promising packaging materials," *Food Chemistry*, vol. 151, pp. 343–351, 2014.
- [36] H. Kargazadeh, M. Ioelovich, I. Ahmad, S. Thomas, and A. Dufresne, "Methods for extraction of nanocellulose from various sources," *Handbook of nanocellulose and cellulose nanocomposites*, vol. 1, pp. 1–51, 2017.
- [37] M. B. Sticklen, "Plant genetic engineering for biofuel production: towards affordable cellulosic ethanol," *Nature Reviews. Genetics*, vol. 9, no. 6, pp. 433–443, 2008.
- [38] M. Jonoobi, R. Oladi, Y. Davoudpour et al., "Different preparation methods and properties of nanostructured cellulose


- from various natural resources and residues: a review," *Cellulose*, vol. 22, no. 2, pp. 935–969, 2015.
- [39] M. Mariano, N. El Kissi, and A. Dufresne, "Cellulose nanocrystals and related nanocomposites: review of some properties and challenges," *Journal of Polymer Science Part B: Polymer Physics*, vol. 52, no. 12, pp. 791–806, 2014.
- [40] J. C. Alcántara, I. González, M. M. Pareta, and F. Vilaseca, "Biocomposites from rice straw nanofibers: morphology, thermal and mechanical properties," *Materials (Basel)*, vol. 13, no. 9, p. 2138, 2020.
- [41] M. Hassan, L. Berglund, R. Abou-Zeid, E. Hassan, W. Abou-Elseoud, and K. Oksman, "Nanocomposite film based on cellulose acetate and lignin-rich rice straw nanofibers," *Materials (Basel)*, vol. 12, no. 4, p. 595, 2019.
- [42] R. Valentim, S. Andrade, M. dos Santos et al., "Composite based on biphasic calcium phosphate (HA/ β -TCP) and nanocellulose from the Açai tegument," *Materials (Basel)*, vol. 11, no. 11, p. 2213, 2018.
- [43] J. Biagiotti, D. Puglia, and J. M. Kenny, "A review on natural fibre-based composites-part I," *Journal of Natural Fibers*, vol. 1, no. 2, pp. 37–68, 2004.
- [44] S. K. Ramamoorthy, M. Skrifvars, and A. Persson, "A review of natural fibers used in biocomposites: plant, animal and regenerated cellulose fibers," *Polymer Reviews*, vol. 55, no. 1, pp. 107–162, 2015.
- [45] A. Pinkert, K. N. Marsh, S. Pang, and M. P. Staiger, "Ionic liquids and their interaction with cellulose," *Chemical Reviews*, vol. 109, no. 12, pp. 6712–6728, 2009.
- [46] G. Di Bella, V. Fiore, G. Galtieri, C. Borsellino, and A. Valenza, "Effects of natural fibres reinforcement in lime plasters (kenaf and sisal vs. polypropylene)," *Construction and Building Materials*, vol. 58, pp. 159–165, 2014.
- [47] K. Majeed, M. Jawaid, A. Hassan et al., "Potential materials for food packaging from nanoclay/natural fibres filled hybrid composites," *Materials and Design*, vol. 46, pp. 391–410, 2013.
- [48] B. NagarajaGanesh and R. Muralikannan, "Physico-chemical, thermal, and flexural characterization of *Cocos nucifera* fibers," *International Journal of Polymer Analysis and Characterization*, vol. 21, no. 3, pp. 244–250, 2016.
- [49] S. H. Osong, S. Norgren, and P. Engstrand, "Processing of wood-based microfibrillated cellulose and nanofibrillated cellulose, and applications relating to papermaking: a review," *Cellulose*, vol. 23, no. 1, pp. 93–123, 2016.
- [50] L. Brinchi, F. Cotana, E. Fortunati, and J. M. Kenny, "Production of nanocrystalline cellulose from lignocellulosic biomass: technology and applications," *Carbohydrate Polymers*, vol. 94, no. 1, pp. 154–169, 2013.
- [51] E. Lam, K. B. Male, J. H. Chong, A. C. W. Leung, and J. H. T. Luong, "Applications of functionalized and nanoparticle-modified nanocrystalline cellulose," *Trends in Biotechnology*, vol. 30, no. 5, pp. 283–290, 2012.
- [52] O. Faruk, A. K. Bledzki, H.-P. Fink, and M. Sain, "Biocomposites reinforced with natural fibers: 2000–2010," *Progress in Polymer Science*, vol. 37, no. 11, pp. 1552–1596, 2012.
- [53] S. Hv and P. Ulvskov, "Hemicelluloses," *Annual Review of Plant Biology*, vol. 61, no. 1, pp. 263–289, 2010.
- [54] A. Stamboulis, C. A. Baillie, and T. Peijs, "Effects of environmental conditions on mechanical and physical properties of flax fibers," *Composites. Part A, Applied Science and Manufacturing*, vol. 32, no. 8, pp. 1105–1115, 2001.
- [55] M. Jawaid and H. P. S. A. Khalil, "Cellulosic/synthetic fibre reinforced polymer hybrid composites: a review," *Carbohydrate Polymers*, vol. 86, no. 1, pp. 1–18, 2011.
- [56] M. F. Rosa, E. S. Medeiros, J. A. Malmonge et al., "Cellulose nanowhiskers from coconut husk fibers: effect of preparation conditions on their thermal and morphological behavior," *Carbohydrate Polymers*, vol. 81, no. 1, pp. 83–92, 2010.
- [57] M. K. M. Haafiz, S. J. Eichhorn, A. Hassan, and M. Jawaid, "Isolation and characterization of microcrystalline cellulose from oil palm biomass residue," *Carbohydrate Polymers*, vol. 93, no. 2, pp. 628–634, 2013.
- [58] N. Lavoine, I. Desloges, A. Dufresne, and J. Bras, "Microfibrillated cellulose - Its barrier properties and applications in cellulosic materials: a review," *Carbohydrate Polymers*, vol. 90, no. 2, pp. 735–764, 2012.
- [59] E. S. Stevens, *Green plastics: an introduction to the new science of biodegradable plastics*, Princeton University Press Princeton, NJ, 2002.
- [60] S. Shinoj, R. Visvanathan, S. Panigrahi, and N. Varadharaju, "Dynamic mechanical properties of oil palm fibre (OPF)-linear low density polyethylene (LLDPE) biocomposites and study of fibre-matrix interactions," *Biosystems Engineering*, vol. 109, no. 2, pp. 99–107, 2011.
- [61] W. Li, J. Yue, and S. Liu, "Preparation of nanocrystalline cellulose via ultrasound and its reinforcement capability for poly(vinyl alcohol) composites," *Ultrasonics Sonochemistry*, vol. 19, no. 3, pp. 479–485, 2012.
- [62] R. Cha, Z. He, and Y. Ni, "Preparation and characterization of thermal/pH-sensitive hydrogel from carboxylated nanocrystalline cellulose," *Carbohydrate Polymers*, vol. 88, no. 2, pp. 713–718, 2012.
- [63] J. George and S. N. Sabapathi, "Cellulose nanocrystals: synthesis, functional properties, and applications," *Nanotechnology, Science and Applications*, vol. 8, p. 45, 2015.
- [64] J.-H. Kim, B. S. Shim, H. S. Kim et al., "Review of nanocellulose for sustainable future materials," *International Journal of Precision Engineering and Manufacturing-Green Technology*, vol. 2, no. 2, pp. 197–213, 2015.
- [65] W. Hamad, "On the development and applications of cellulose nanofibrillar and nanocrystalline materials," *Canadian Journal of Chemical Engineering*, vol. 84, no. 5, pp. 513–519, 2006.
- [66] W. Ding, L. Calabri, X. Chen, K. M. Kohlhaas, and R. S. Ruoff, "Mechanics of crystalline boron nanowires," *Composites Science and Technology*, vol. 66, no. 9, pp. 1112–1124, 2006.
- [67] V. Mohanta, G. Madras, and S. Patil, "Layer-by-layer assembled thin films and microcapsules of nanocrystalline cellulose for hydrophobic drug delivery," *ACS Applied Materials & Interfaces*, vol. 6, no. 22, pp. 20093–20101, 2014.
- [68] Y. Tang, S. Yang, N. Zhang, and J. Zhang, "Preparation and characterization of nanocrystalline cellulose via low-intensity ultrasonic-assisted sulfuric acid hydrolysis," *Cellulose*, vol. 21, no. 1, pp. 335–346, 2014.
- [69] H. P. S. Abdul Khalil, M. R. Nurul Fazita, M. Jawaid, A. H. Bhat, and C. K. Abdullah, "Empty fruit bunches as a reinforcement in laminated bio-composites," *Journal of Composite Materials*, vol. 45, no. 2, pp. 219–236, 2011.
- [70] J. Rojas, M. Bedoya, and Y. Ciro, "Current trends in the production of cellulose nanoparticles and nanocomposites for biomedical applications," *Cellulose: fundamental aspects and current trends*, vol. 2015118–2017121, pp. 193–228, 2015.

- [71] P. Kumar, D. M. Barrett, M. J. Delwiche, and P. Stroeve, "Methods for pretreatment of lignocellulosic biomass for efficient hydrolysis and biofuel production," *Industrial and Engineering Chemistry Research*, vol. 48, no. 8, pp. 3713–3729, 2009.
- [72] B. Yang, Z. Dai, S.-Y. Ding, and C. E. Wyman, "Enzymatic hydrolysis of cellulosic biomass," *Biofuels*, vol. 2, no. 4, pp. 421–449, 2011.
- [73] S. Kamel, "Nanotechnology and its applications in lignocellulosic composites, a mini review," *Express Polymer Letters*, vol. 1, no. 9, pp. 546–575, 2007.
- [74] A. Dufresne, "Processing of polymer nanocomposites reinforced with polysaccharide nanocrystals," *Molecules*, vol. 15, no. 6, pp. 4111–4128, 2010.
- [75] G. Siqueira, J. Bras, and A. Dufresne, "Cellulosic bionanocomposites: a review of preparation, properties and applications," *Polymers (Basel)*, vol. 2, no. 4, pp. 728–765, 2010.
- [76] M. R. Ahmed-Haras, N. Kao, and L. Ward, "Single-step heterogeneous catalysis production of highly monodisperse spherical nanocrystalline cellulose," *International Journal of Biological Macromolecules*, vol. 154, pp. 246–255, 2020.
- [77] M. Kunaver, A. Anžlovar, and E. Žagar, "The fast and effective isolation of nanocellulose from selected cellulosic feedstocks," *Carbohydrate Polymers*, vol. 148, pp. 251–258, 2016.
- [78] D. Klemm, B. Heublein, H. Fink, and A. Bohn, "Cellulose: fascinating biopolymer and sustainable raw material," *Angewandte chemie international edition*, vol. 44, no. 22, pp. 3358–3393, 2005.
- [79] O. V. Surov, M. I. Voronova, N. V. Rubleva et al., "A novel effective approach of nanocrystalline cellulose production: oxidation–hydrolysis strategy," *Cellulose*, vol. 25, no. 9, pp. 5035–5048, 2018.
- [80] S. J. Eichhorn, "Cellulose nanowhiskers: promising materials for advanced applications," *Soft Matter*, vol. 7, no. 2, pp. 303–315, 2011.
- [81] H.-M. Ng, L. T. Sin, T. T. Tee et al., "Extraction of cellulose nanocrystals from plant sources for application as reinforcing agent in polymers," *Composites. Part B, Engineering*, vol. 75, pp. 176–200, 2015.
- [82] E. Csizsar, P. Kalic, A. Kobol, and E. de Paulo Ferreira, "The effect of low frequency ultrasound on the production and properties of nanocrystalline cellulose suspensions and films," *Ultrasonics Sonochemistry*, vol. 31, pp. 473–480, 2016.
- [83] Y. Liu, L. Li, N. Pan et al., "Antibacterial cellulose acetate films incorporated with N halamine, modified nanocrystalline cellulose particles," *Polymers for Advanced Technologies*, vol. 28, no. 4, pp. 463–469, 2017.
- [84] N. F. Vasconcelos, J. P. A. Feitosa, F. M. P. da Gama et al., "Bacterial cellulose nanocrystals produced under different hydrolysis conditions: properties and morphological features," *Carbohydrate Polymers*, vol. 155, pp. 425–431, 2017.
- [85] F. Bettaieb, R. Khiari, A. Dufresne, M. F. Mhenni, and M. N. Belgacem, "Mechanical and thermal properties of Posidonia oceanica cellulose nanocrystal reinforced polymer," *Carbohydrate Polymers*, vol. 123, pp. 99–104, 2015.
- [86] H. Ma, B. Zhou, H.-S. Li, Y.-Q. Li, and S.-Y. Ou, "Green composite films composed of nanocrystalline cellulose and a cellulose matrix regenerated from functionalized ionic liquid solution," *Carbohydrate Polymers*, vol. 84, no. 1, pp. 383–389, 2011.
- [87] H. Li, L. Shen, J. Wang et al., "Design of a nitrogen-doped, carbon-coated $\text{Li}_4\text{Ti}_5\text{O}_{12}$ nanocomposite with a core-shell structure and its application for high-rate lithium-ion batteries," *ChemPlusChem*, vol. 79, no. 1, pp. 128–133, 2014.
- [88] J. K. Pandey, H. T. Lee, H. Takagi, S. H. Ahn, D. R. Saini, and M. Misra, "Dispersion of nanocellulose (NC) in polypropylene (PP) and polyethylene (PE) matrix," in *Handbook of polymer nanocomposites. Processing, performance and application*, pp. 179–189, Springer, 2015.
- [89] K. N. M. Amin, P. K. Annamalai, I. C. Morrow, and D. Martin, "Production of cellulose nanocrystals via a scalable mechanical method," *RSC Advances*, vol. 5, no. 70, pp. 57133–57140, 2015.
- [90] S. Menchaca-Nal, C. L. Londoño-Calderón, P. Cerrutti et al., "Facile synthesis of cobalt ferrite nanotubes using bacterial nanocellulose as template," *Carbohydrate Polymers*, vol. 137, pp. 726–731, 2016.
- [91] M. E. Vallejos, M. D. Zambon, M. C. Area, and A. A. da Silva Curvelo, "Low liquid–solid ratio (LSR) hot water pretreatment of sugarcane bagasse," *Green Chemistry*, vol. 14, no. 7, pp. 1982–1989, 2012.
- [92] A. V. Bandura and S. N. Lvov, "The ionization constant of water over wide ranges of temperature and density," *Journal of Physical and Chemical Reference Data*, vol. 35, no. 1, pp. 15–30, 2006.
- [93] L. P. Novo, J. Bras, A. García, N. Belgacem, and A. A. da Silva Curvelo, "A study of the production of cellulose nanocrystals through subcritical water hydrolysis," *Industrial Crops and Products*, vol. 93, pp. 88–95, 2016.
- [94] L. P. Novo, J. Bras, A. García, N. Belgacem, and A. A. S. Curvelo, "Subcritical water: a method for green production of cellulose nanocrystals," *ACS Sustainable Chemistry & Engineering*, vol. 3, no. 11, pp. 2839–2846, 2015.
- [95] I. V. Averianov, M. A. Stepanova, I. V. Gofman et al., "Chemical modification of nanocrystalline cellulose for improved interfacial compatibility with poly (lactic acid)," *Mendeleev Communications*, vol. 29, no. 2, pp. 220–222, 2019.
- [96] J. N. Putro, S. Ismadji, C. Gunarto et al., "The effect of surfactants modification on nanocrystalline cellulose for paclitaxel loading and release study," *Journal of Molecular Liquids*, vol. 282, pp. 407–414, 2019.
- [97] M. L. Foo, C. R. Tan, P. D. Lim, C. W. Ooi, K. W. Tan, and I. M. L. Chew, "Surface-modified nanocrystalline cellulose from oil palm empty fruit bunch for effective binding of curcumin," *International Journal of Biological Macromolecules*, vol. 138, pp. 1064–1071, 2019.
- [98] W. M. E. M. M. Daniyal, Y. W. Fen, J. Abdullah, A. R. Sadrolhosseini, S. Saleviter, and N. A. S. Omar, "Label-free optical spectroscopy for characterizing binding properties of highly sensitive nanocrystalline cellulose-graphene oxide based nanocomposite towards nickel ion," *Spectrochimica Acta Part A: Molecular and Biomolecular Spectroscopy*, vol. 212, pp. 25–31, 2019.
- [99] A. A. Emam, S. A. A. Faraha, F. H. Kamal, A. M. Gamal, and M. Basseem, "Modification and characterization of nanocellulose crystalline from Eichhornia crassipes using citric acid: an adsorption study," *Carbohydrate Polymers*, vol. 240, article 116202, 2020.
- [100] R. D. Gupta and N. Raghav, "Nano-crystalline cellulose: preparation, modification and usage as sustained release drug delivery excipient for some non-steroidal anti-inflammatory drugs," *International Journal of Biological Macromolecules*, vol. 147, pp. 921–930, 2020.

- [101] X. Tian, D. Yan, Q. Lu, and X. Jiang, "Cationic surface modification of nanocrystalline cellulose as reinforcements for preparation of the chitosan-based nanocomposite films," *Cellulose*, vol. 24, no. 1, pp. 163–174, 2017.
- [102] A. Fatona, R. M. Berry, M. A. Brook, and J. M. Moran-Mirabal, "Versatile surface modification of cellulose fibers and cellulose nanocrystals through modular triazinyl chemistry," *Chemistry of Materials*, vol. 30, no. 7, pp. 2424–2435, 2018.
- [103] V. K. Thakur, *Nanocellulose Polymer Nanocomposites: Fundamentals and Applications*, John Wiley & Sons, 2014.
- [104] C. Goussé, H. Chanzy, G. Excoffier, L. Soubeyrand, and E. Fleury, "Stable suspensions of partially silylated cellulose whiskers dispersed in organic solvents," *Polymer (Guildf)*, vol. 43, no. 9, pp. 2645–2651, 2002.
- [105] A. P. Mangalam, J. Simonsen, and A. S. Benight, "Cellulose/DNA hybrid nanomaterials," *Biomacromolecules*, vol. 10, no. 3, pp. 497–504, 2009.
- [106] K. L. Mittal and R. Jaiswal, *Particle Adhesion and Removal*, John Wiley & Sons, 2015.
- [107] K. J. Saunders, *Organic polymer chemistry: an introduction to the organic chemistry of adhesives, fibres, paints, Plastics and Rubbers*, Springer Science & Business Media, 2012.
- [108] S. Kalia, B. S. Kaith, and I. Kaur, *Cellulose Fibers: Bio-and Nano-Polymer Composites: Green Chemistry and Technology*, Springer Science & Business Media, 2011.
- [109] S. Kalia, A. Dufresne, B. M. Cherian et al., "Cellulose-based bio- and nanocomposites: a review," *International journal of polymer science*, vol. 2011, Article ID 837875, 35 pages, 2011.
- [110] V. C.-F. Li, C. K. Dunn, Z. Zhang, Y. Deng, and H. J. Qi, "Direct ink write (DIW) 3D printed cellulose nanocrystal aerogel structures," *Scientific Reports*, vol. 7, no. 1, pp. 1–8, 2017.
- [111] S. M. Noorbakhsh-Soltani, M. M. Zerfat, and S. Sabbaghi, "A comparative study of gelatin and starch-based nanocomposite films modified by nano-cellulose and chitosan for food packaging applications," *Carbohydrate Polymers*, vol. 189, pp. 48–55, 2018.
- [112] S. T. Keshavarz, M. Imani, and F. Farahmandghavi, "Adsorption and solidification of peppermint oil on microcrystalline cellulose surface: an experimental and DFT study," *Journal of Molecular Structure*, vol. 1205, article 127558, 2020.
- [113] D. Kundu and T. Banerjee, "Development of microcrystalline cellulose based hydrogels for the in vitro delivery of Cephalexin," *Heliyon*, vol. 6, no. 1, article e03027, 2020.
- [114] A. Huang, X. Peng, L. Geng et al., "Electrospun poly (butylene succinate)/cellulose nanocrystals bio-nanocomposite scaffolds for tissue engineering: preparation, characterization and in vitro evaluation," *Polymer Testing*, vol. 71, pp. 101–109, 2018.
- [115] C. Sun, J. Ni, C. Zhao et al., "Preparation of a cellulosic adsorbent by functionalization with pyridone diacid for removal of Pb(II) and Co(II) from aqueous solutions," *Cellulose*, vol. 24, no. 12, pp. 5615–5624, 2017.
- [116] S. Dong, H. J. Cho, Y. W. Lee, and M. Roman, "Synthesis and cellular uptake of folic acid-conjugated cellulose nanocrystals for cancer targeting," *Biomacromolecules*, vol. 15, no. 5, pp. 1560–1567, 2014.
- [117] C. Salas, T. Nypelö, C. Rodriguez-Abreu, C. Carrillo, and O. J. Rojas, "Nanocellulose properties and applications in colloids and interfaces," *Current Opinion in Colloid & Interface Science*, vol. 19, no. 5, pp. 383–396, 2014.
- [118] S. Athar, R. Bushra, and T. Arfin, "Cellulose nanocrystals and PEO/PET hydrogel material in biotechnology and biomedicine: current status and future prospects," *Nanocellulose and nanohydrogel matrices: biotechnological and biomedical applications*, pp. 139–173, 2017.
- [119] Y. Zhang, Y. Liu, R. Li, X. Ren, and T. Huang, "Preparation and characterization of antimicrobial films based on nanocrystalline cellulose," *Journal of Applied Polymer Science*, vol. 136, no. 8, p. 47101, 2019.
- [120] Y. K. Dasan, A. H. Bhat, and F. Ahmad, "Polymer blend of PLA/PHBV based bionanocomposites reinforced with nanocrystalline cellulose for potential application as packaging material," *Carbohydrate Polymers*, vol. 157, pp. 1323–1332, 2017.
- [121] A. H. Bhat, Y. K. Dasan, I. Khan, and M. Jawaid, "Cellulosic biocomposites: potential materials for future," *Green Biocomposites*, pp. 69–100, 2017.
- [122] F. A. Abd Manan, W. W. Hong, J. Abdullah, N. A. Yusof, and I. Ahmad, "Nanocrystalline cellulose decorated quantum dots based tyrosinase biosensor for phenol determination," *Materials Science and Engineering: C*, vol. 99, pp. 37–46, 2019.
- [123] H. Shaghaleh, X. Xu, and S. Wang, "Current progress in production of biopolymeric materials based on cellulose, cellulose nanofibers, and cellulose derivatives," *RSC Advances*, vol. 8, no. 2, pp. 825–842, 2018.
- [124] J. Tritt-Goc, I. Jankowska, K. Pogorzelec-Glaser, R. Pankiewicz, and P. Ławniczak, "Imidazole-doped nanocrystalline cellulose solid proton conductor: synthesis, thermal properties, and conductivity," *Cellulose*, vol. 25, no. 1, pp. 281–291, 2018.

Research Article

Flax- and Graphene-Reinforced Natural Fiber Nanocomposites under Cryogenic Environment for Constructional Applications

Munirah D. Albaqami,¹ N. Krishnamoorthy,² S. D. Uma Mageswari,³ Sarita Santaji Shinde,⁴ S. C. V. Ramana Murty Naidu,⁵ Neha Munjal,⁶ Aboud Ahmed Awadh Bahajjaj,¹ S. H. Mohammed,⁷ and Prasath Srinivasan ⁸

¹Department of Chemistry, Sree Krishna College of Engineering, Vellore, 632101 Tamil Nadu, India

²Department of Physics, Sri Eshwar College of Engineering, Coimbatore, Tamil Nadu 641202, India

³Department of Science and Humanities, R.M.K. Engineering College, Kavaraipettai, Tamil Nadu 601206, India

⁴Department of General Science, Bharati Vidyapeeth's College of Engineering, Kolhapur, Maharashtra 416013, India

⁵Department of Mechanical Engineering, Sri Venkateswara College of Engineering & Technology, Srikakulam, Andhra Pradesh 532410, India

⁶Department of Physics, Lovely Professional University, Phagwara, Punjab 144411, India

⁷Department of Mechanical Engineering, C. Abdul Hakeem College of Engineering & Technology, Melvisharam, 632509 Vellore, Tamil Nadu, India

⁸Department of Mechanical Engineering, College of Engineering and Technology, Mizan Tepi University, Ethiopia

Correspondence should be addressed to Prasath Srinivasan; prasathsrinivasan@mtu.edu.et

Received 11 May 2022; Revised 26 June 2022; Accepted 30 June 2022; Published 3 October 2022

Academic Editor: Arpita Roy

Copyright © 2022 Munirah D. Albaqami et al. This is an open access article distributed under the Creative Commons Attribution License, which permits unrestricted use, distribution, and reproduction in any medium, provided the original work is properly cited.

Mostly at the micro- and nanoscales, efforts were made to produce innovative thermoplastic nanocomposite materials. These composites were reinforced with natural fibres and artificial additives with improved mechanical characteristics. This research entails the creation of a novel nanocomposite material made up of unsaturated polyester resin, graphite at the nanoscale, and flax fibres at the microscale. Flax fibres make up 4, 8, and 12% of the binding matrix's weight, respectively. A constant quantity of nanoparticles equal to 4 wt% of the binding matrix is used. In order to stick the graphene to natural fibres, an appropriate surface alteration approach is needed, and this work will focus on the plasma technique of interface adherence. Fibres were employed as a reinforcement with polyester to create a nanocomposite that improved adherence between the fillers while also retaining the matrix alkalisation. In order to assess interfacial adherence and fibre distribution homogeneity in the matrix system, the composite was made up of hand lay-up technique. The manufactured composite was engrossed into fluid N₂ at -196°C. A SEM was utilized to undertake treated and untreated specimens for spectroscopy analyses. Mechanical possessions like tension and flexural were accomplished. In comparison to previous tested doses, the 5 percent alkali-treated flax incorporating graphite has shown promising outcomes than other samples.

1. Introduction

Awareness of environmental issues and social response is raised, as improved pollution regulations and inefficient oil consumption, prompting consideration of ecofriendly products. Organic fibre is one of the most ecologically

compost resources on the market, exceeding man-made materials in a number of ways. As per a recent industry assessment, the global market for organic fibre-based material is expected to reach \$3.9 billion by 2023. The global trend in the NFPC industry, as per current estimates, will continue to develop fast [1]. A natural fibre-

based polymer composite has become increasingly popular in consumer goods and the rising industrial sectors in recent years. The NFPC industry is expected to increase by 12% worldwide during the next five years (2021–2025), as per forecasts [2, 3]. Natural fibres are nonsynthetic, non-man-made fibres. Animals and plants can both provide them. Natural fibres derived from both sustainable and nonrenewable substances, like groundnut, jute, hemp, and cotton, have gotten a lot of consideration in recent decades. Bast fibres, namely, kenaf, hemp, ramie, flax, and jute as well as all other forms of cellulose fibres, can be classified as “roots and wood.” Fibre-reinforced polymer matrices are extremely lightweight, low cost, and less damaging to processing equipment and have relatively high mechanical properties, so they are used in numerous submissions owing to the better strength and advantages of organic fibres over man-made fibres. It is getting a lot of attention. Flexural strength and tensile strength enhanced surface polish of moulding composites, plentiful recycling, and flexibility at assured individual facilities, renewability, and stumpy interface risks. Plant fibres and particles, both tough and gentle, are added to the polymeric materials [4, 5]. Figure 1 demonstrates the composites with different applications.

Flax appears to be the only major species in the Linaceae class, which has twelve divisions and around 350 names. Flax was still the first fabric produced of grains and subsequently strengthened into mixtures that was recovered in Egyptian burials about 5000 B.C. It is among the most often used biofibres. Flax has been farmed for decades for fabric and lubricants, and it is a main ingredient [6]. Flax is the target of intensive study as well as the incorporation of desired features like herbicide endurance, organic and inorganic antioxidant enzyme activity, and better oils and protein categories. Linseed is a 0.5–2.9 m in height annual herb having branches measuring 11–30 mm [7]. Low density, strong elastic modulus, flexibility, and a high surface to volume ratio characterise such ligno fibres. Flax fibre’s mechanical characteristics are determined by its location in the stems. Enhance the loading level from 2.40% per minute to 8% per minute to raise interfaces shear capacity by few more % with no effect in the composite’s overall strength properties. Even though natural fibre-based composites are not without flaws, they remain a viable option. Since natural fibres have a lower water barrier, they absorb a lot of water and have poor mechanical properties [8]. Figure 2 displays the compensations and drawbacks of dissimilar fibres.

Several additives are contained in the same lattice to produce hybrid composites. By removing the disadvantages of individual aggregates, combination improves the material properties of natural composites [9, 10]. Therefore, the impact of blending fibres in grids has outlived its usefulness in terms of increasing biomechanical qualities. The nanofibres are used to improve the bond between the matrix and reinforcements, significantly increasing the properties. As a result, the use of nanoparticles in thermoplastics is becoming increasingly prevalent. Due to their subatomic scale, nanocrystals have features that can still be utilized to build new items or improve the efficacy of structural members [11].

The nanosized particles have a variety of uses in water purification, energy generation, and contamination detection, and a substantial proportion of research discusses how innovative nanoparticles might be employed to solve key environmental issues. Graphene is a single dioxide film of molecules organised in a hexagon crystalline substance, which is the most recent substance to catch scientists’ interest [12, 13]. The remarkable physicochemical features of graphene, particularly its extremely large surface region, electron and thermal movement, and good mechanical, have piqued curiosity. These remarkable qualities comprise prompted substantial efforts to integrate graphene into a wide range of technological applications, from electronic systems to biomaterials. As well as nanomaterials and polymer composite components have been seen in the identification of innovative activated carbon or photocatalytic activity machinery for economical decontamination, as key components for another water filtration substrate and also as electrocatalyst for particulate traceability or eviction in the area of natural engineering [14–16]. Different chemical treatment procedures can increase the adhesion among unsaturated polyester resin and flax fibre. Thermal comfort may be made from bast fibres such as flax. The elastic modulus of flax fibres was discovered to be influenced by the size and orientation of a tensile strength after evaluating them during loading condition and repetitive packing trials. The formation of coherence interfacial adhesion between both the fibre and matrix improves the fibre-reinforced nanocomposite substance’s effectiveness. Surface modification of the nanocomposites, on the other hand, causes undesired consequences like mechanical deterioration, renegotiation by severe swell, and exterior deterioration [17, 18]. Polymers being used in industrial applications, for instance, would have to be able to endure temperatures of up to 200 degrees Celsius. Microstructural minerals and plastics have the highest rigidity, are much more resilient, and have greater strength and durability. As a result, freezing processing of composites could be a key component of revolutionary goods to increase the quality of organic lignocellulosic fibres [4, 10, 19, 20]. The foremost persistence of this study is to develop and evaluate hybridised organic nanostructures for material characteristics. The graphite and flax fibre fabric hybrids were made by hand. The material properties of the fabricated samples were evaluated following different durations of immersion in aqueous nitrogen at 77 K.

2. Investigational Resources and Methods

2.1. Flax Fiber. Flaxseed that has not been treated is being used in the study. Flaxseed strands have such superior mechanical properties and may be easily extended when damaged. The relative humidity is roughly 11%. The molecular structure seems to have a considerable influence on the properties of the filaments and the properties of the material as a result. Strands were chopped to a 5 mm length in order to be used with textile trimming machinery. The flaxseed strands were supplied by the Ganga fibre factory in Salem, Tamil Nadu, India. Figure 3 illustrates the flax fibre and matrix materials.

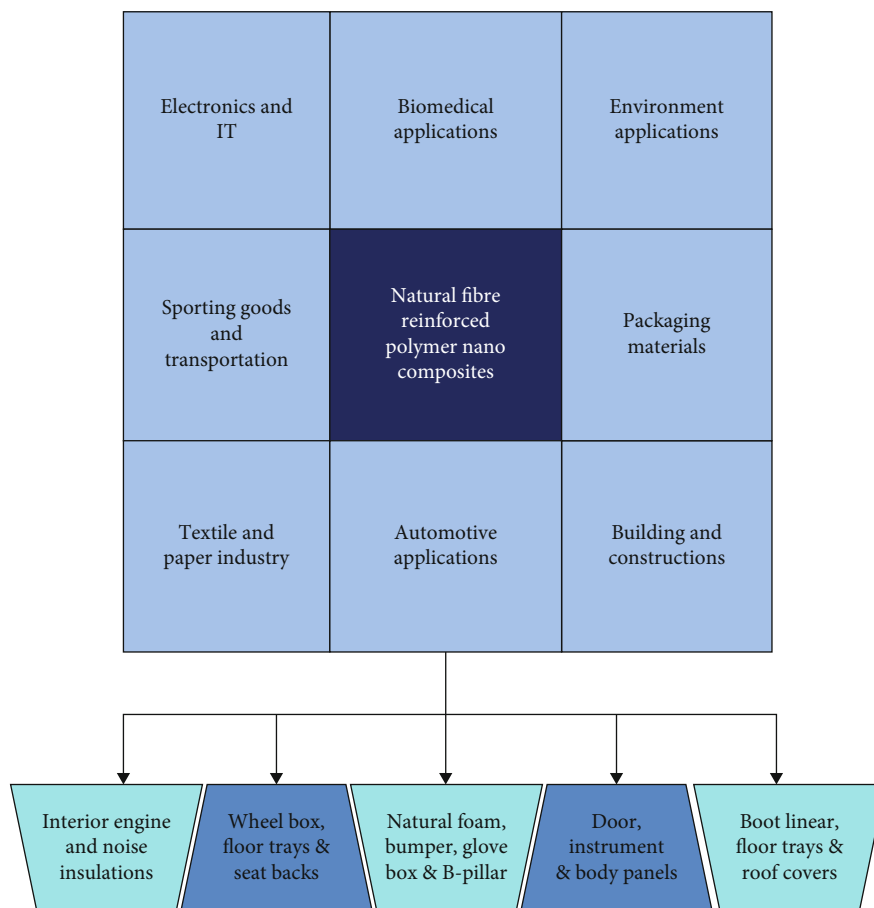


FIGURE 1: The composites with different applications.

		Types of fibers					
		Kenaf	Coir	Flax	Jute	Sisal	Hemp
Advantages		(i) Fast growing. (ii) High fiber yield. (iii) Low cost and easily available.	(i) High abrasion resistance. (ii) Strong and durable. (iii) Good acoustic properties.	(i) Relatively strong. (ii) Used to make clothes.	(i) Low cost. (ii) Widely used in agriculture, textile, woven and non-woven sector.	(i) High specific strength. (ii) Easily available. (iii) Good sound absorption properties.	(i) Very strong and doesn't requires pesticides. (ii) Drought and light frost resistance. (iii) Grows faster than other natural fibres.
Dis-advantages		(i) Brittle fracture. (ii) Handling and processing are hard. (iii) Requires more water for growth.	(i) Has less cellulose than fiber like cotton & flax, thus making it less flexible.	(i) Low elasticity. (ii) Gives off large amount of dust in the early stages of isolation process.	(i) Crease resistance is very low. (ii) Lose of strength when wet.	(i) Restricted maximum processing temperature.	(i) Growth and cultivation are restricted in many countries. (ii) Separation of fiber from bast is labor intensive.

FIGURE 2: The advantages and disadvantages of different materials.

2.2. *Nanofiller*. The graphite employed by the researcher has been of protective coating, with a purity of 90%. To create different nanomaterials, different amounts of 0.1-6 percent

of the polymer matrices were used in sequential increments of 1 percent by weight of the polymer matrices. Figure 4(a) depicts the graphite material used in this experiment. The



FIGURE 3: Photographic images of flax fibre and matrix materials.

graphite used in this study was black in colour with a known quantity of 11.25 g/mol and an iron concentration of ≤ 100 ppm.

2.3. NaOH Dispensation. One of the really common treatments on plant fabrics used for lightweight materials is alkaline hydrolysis. Surface modification disrupts hydrogens on the intermediate scaffolding, resulting in improved load bearing capacity. The quantity of tannins, a lipid that covers the majority of the external skin of flaxseed, is decreased to a considerable extent. Also, it aids in cellulose isomerization and the exposure of lengthier allotropes.

For this type of dehalogenation, fresh flax was obtained and carefully washed. As a consequence, the flaxseed was carefully chopped into lengths ranging from 5 to 8 mm. According to the study, the linseed strand was then soaked in a 10% NaOH solution at maximum strength for four hours. After that, liquid-converted linseed was dampened using methanol until its pH neared 7, as determined by fluorophore. To eliminate any surplus ingredients, the combined material was carefully strained using deionized water. It would bring the acidic process to a close.

2.4. Fabrication of Hybrid Composites. The graphite employed by the researcher has been of protective coating, with a purity of 90%. To create different nanomaterials, different amounts of 0.1-6 percent of the polymer matrices were used in sequential increments of 1 percent by weight of the polymer matrices. The ultrasonic irradiation procedure was applied to distribute graphite with flaxseed in synthetic materials. Furthermore, to distribute the graphite and flax, multiple sheared mixing techniques have been used, as well as continually mixing the mixture. Such motorised mixing is done for a set amount of time till the combination is homogeneous. During motorised churning, gases are maintained but must be removed using a related discipline technique. The mixture is cured for two hours at 650°C , followed by three hours at 1050°C . The resins and cure chemical combinations were poured into a $300\text{ mm} \times 300\text{ mm} \times 3\text{ mm}$ aluminium mould to manufacture biocomposites. Table 1 shows how the nanocomposite manufacturing were made depending also on limitation categories. Following that, the produced specimens were flooded in liquid N_2 at 77 K for cryogenic treatment for various times according

to the specification. The treated plates were detached from the cryogenic compartment and maintained normal temperature.

2.5. Testing of Composite Specimen. As shown in Figure 5, the laminating specimens were extracted to ASTM D 638-03 models for uniaxial tensile testing and ASTM D 790 models for bending testing.

2.6. Scanning Electron Microscope (SEM). SEM was used to do microinspections of fractured lamination testing. To increase the ionic characteristics of the mixes, all materials were laved, dehydrated, and afterwards mechanically coated with nanometres of gold throughout SEM magnification.

3. Result and Discussion

3.1. Tensile Strength. The mean tensile changes of a flax-/graphene-reinforced hybrid composites with fibre weights of 4%, 8%, and 12% were evaluated based on the varied fibre loadings. Figures 6(a) and 6(b) show the bar and area plot of ductile properties. The tensile strength of the composite improves with the addition of flax fibre content till it reaches 8% and then drops to 12%. When compared to a 12 percent fibre-reinforced composites, the inclusion of 3 percent graphene and 8% boosts the tensile strength of the nanocomposites. The poor transfer of stress owing to the maldistribution of fibre all across the matrices is the cause of low durability in 12 percent fibre composites. In the final outcome, the compound formed a polymer high area with weak fibre-to-fibre and fibre-to-graphene contact. The fibres were effortlessly pulled from the resin at loading in current state. It demonstrates that the fibre/graphene hybrid's 12 percent strengthening consequence is inadequate to tolerate the tensile force. The fourth sample (eight percent flax fibre and three percent graphene-reinforced composite) has an extreme ductile value of 48.96 MPa, which really is 10.75 percent greater than the fifth specimen. This is primarily attributable to the establishment of crosslink density between fibre matrices, which occurs as a consequence of the fibres filling in the voids in the composites by admitting extra fibre, thus providing sufficient force distribution across clusters [14, 21].

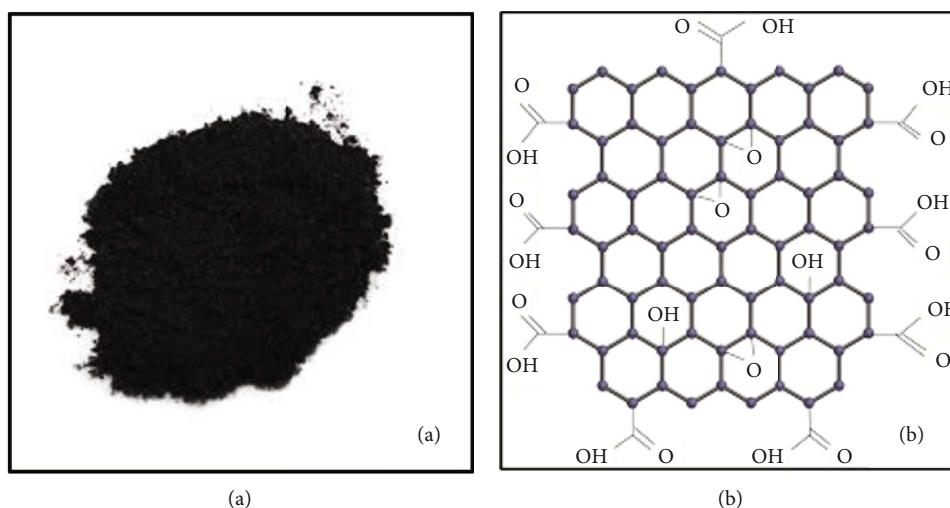


FIGURE 4: (a) Photographic image of graphene powder. (b) Biochemical assembly of filler.

TABLE 1: Combination levels of nanocomposites.

Specimen	Combinations	Treatment
Specimen 1	Polyester+graphene	Untreated
Specimen 2	Polyester+flax	Untreated
Specimen 3	Polyester+4% flax+3% of graphene	3% and 5% of NaOH
Specimen 4	Polyester+8% flax+3% of graphene	3% and 5% of NaOH
Specimen 5	Polyester+12% flax+3% of graphene	3% and 5% of NaOH

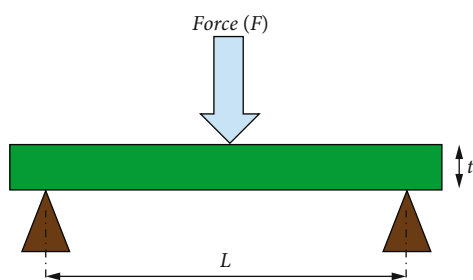


FIGURE 5: Schematic image of flexural testing.

3.2. Flexural Strength. The bending strength of flax/graphene/polyester hybrid composites varied as shown in Figures 7(a) and 7(b). When the fibre content of the hybrids is raised until it reaches 8%, the flexural strength increases until it drops to 12%. When the fibre loading of the composites is increased, the flexural strength value consistently increases. In 8% of the fibre content of the nanocomposite, the highest flexural strength was achieved. The yield of a 4 percent flax with 3 percent graphene sample is 21.78 percent greater than the yield of a 12 percent flax with 3 percent graphene specimen. Furthermore, the percentage of flax with 3 percent graphene is 4.65 percent greater than the percentage of flax with 3 percent graphene specimen in the 12 percent of flax with 3 percent graphene specimen. In all situations, the flexural strength of the fourth specimen is greater than other specimens. Flax fibres are haphazardly put without appropriate orientation, producing unequal fibre distribu-

tion, which is the main source of this disparity. The composite was unable to endure the flexural strength as a result of this. The higher percentage of fibre content could achieve adequate crosslinking density and poor hydrophilicity between fibre and matrix at 12% hybrid, while the needed percent of fibre loading can achieve adequate bonding strength at 8 percent specimen. The 8 percent flax fibre with 3 percent graphene composite exhibits strong bonding, allowing the reinforcement to distribute stress evenly all across the matrices [6, 22].

3.3. Effect of NaOH Treatment. The alkali or NaOH procedure was used to change the morphology of flax fibre's interface. Figures 8(a) and 8(b) show the effect of NaOH treatment on tensile and flexural strength. The impact of NaOH processing on the tensile and flexural characteristics of flax-/graphene-derived nanocomposite is shown in the figure. The mechanical characteristics of the fourth specimen, which contained 8% flax and 3% graphene, were the greatest of the five. The 5 percent NaOH-treated nanocomposite specimens had the best tensile and flexural characteristics when compared to untreated and 3 percent alkali-treated composite specimens. The efficiency of eliminating impurities from the surface of the fibre was not good enough to get through lesser NaOH concentrations, caused by inadequate fibre interaction with matrices. Flax fibres were chemically pretreated for 4 hours with a 5 percent sodium hydroxide (NaOH) solution to remove hydrophilic hydroxyl groups and impurities from cellulose fibre flax. Although

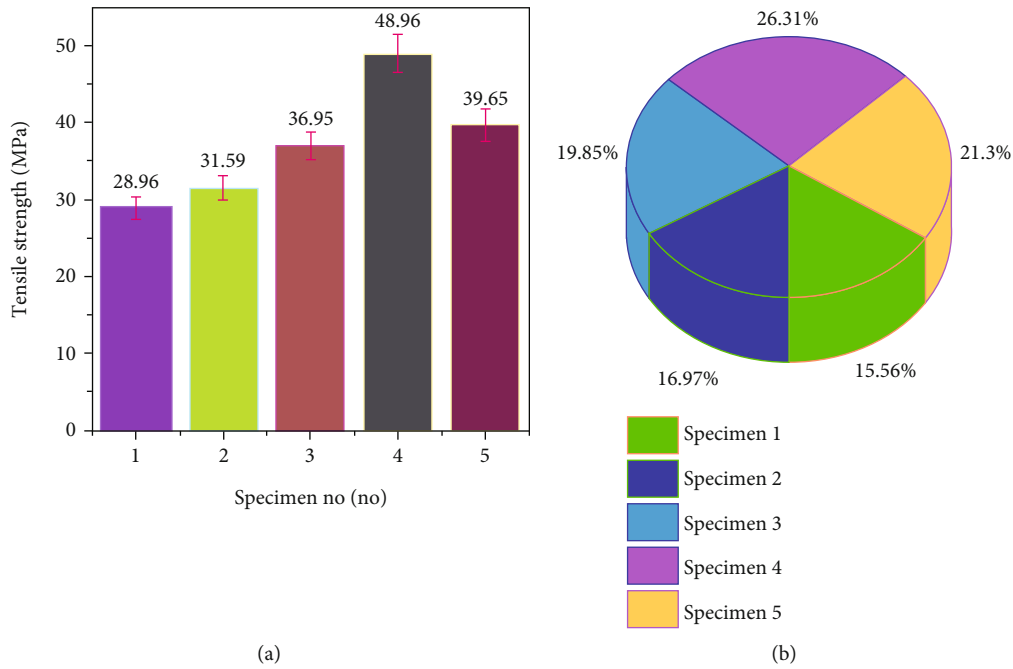


FIGURE 6: (a) Bar chart and (b) surface plot of tensile strength of nanocomposite.

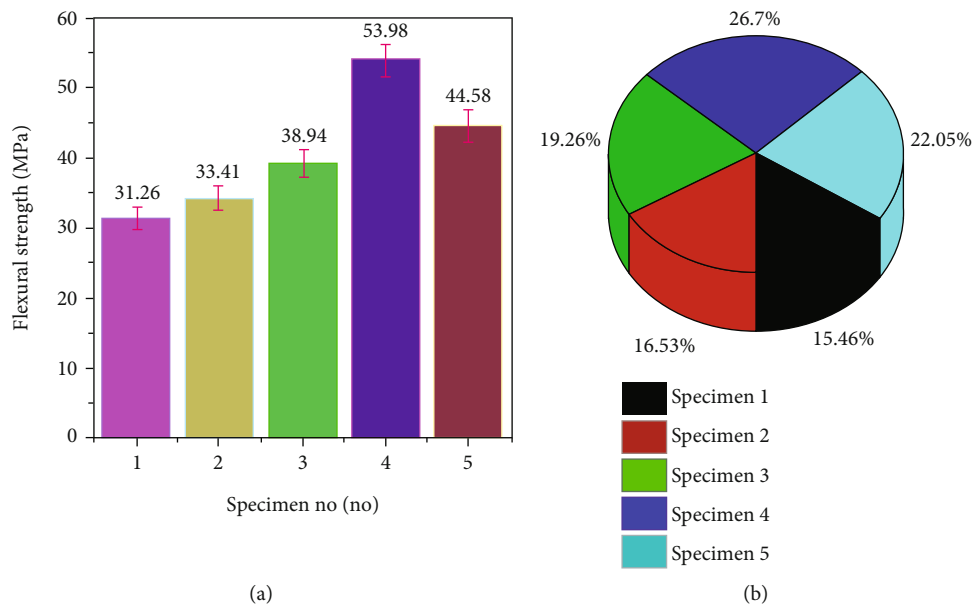


FIGURE 7: (a) Bar chart and (b) surface plot of flexural strength of nanocomposite.

with the polyester matrix and graphene, this will increase fibre adherence and resilience. This improves the mechanical and morphology characterisation by increasing the levels of a polymerization process as well as the degree of crystallinity of fibres [23].

3.4. Effect of Cryogenic Treatment. In cryogenic fabrication, the nanocomposite pieces were subjected to fluid N₂ at -196°C and went through current treatment. Under cold circumstances, the average values of tensile and flexural behav-

our of flax- and graphene-incorporated hybrid materials are revealed in Figure 9. Nanocomposites with 30 minutes cryogenically treated samples had enhanced tensile and flexural strength when compared to untreated samples. It might be owing to the latent stress induced by compression interaction as a consequence of the cold draining of materials. Residual stresses were formed at a low temperature as a result of matrix changes, including fibre contraction. Since fibres have a reduced thermal process of continuous polymeric composites, the resulting stress is compressed as in

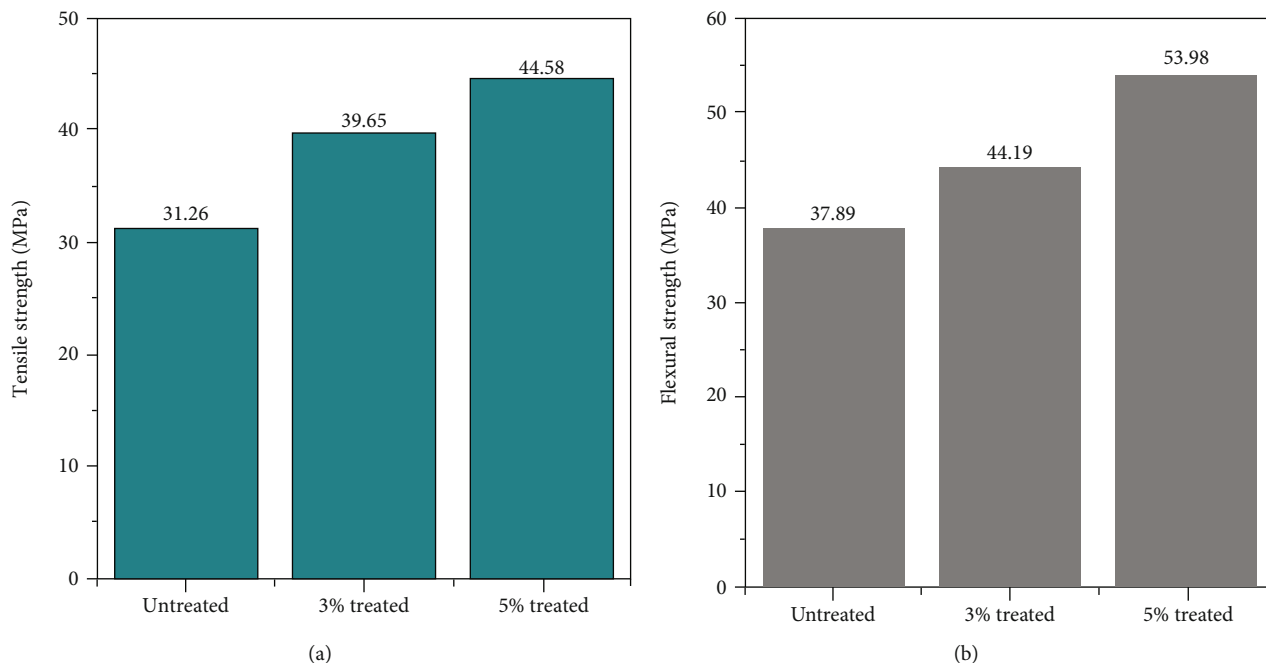


FIGURE 8: Effect of NaOH treatment on (a) tensile strength and (b) flexural strength.

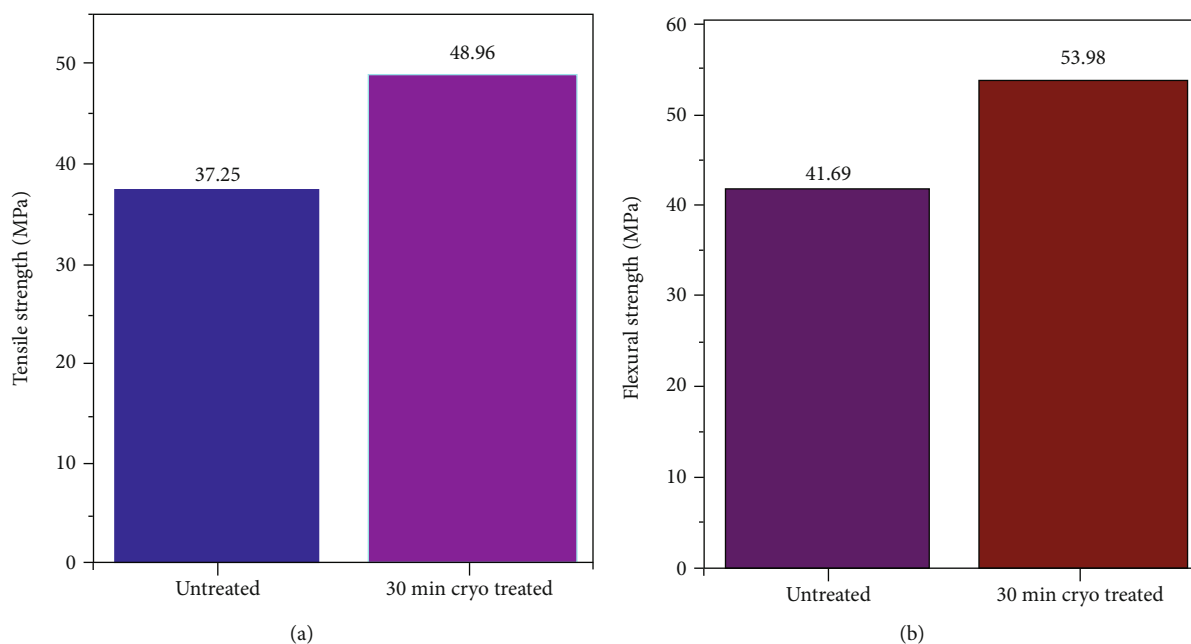


FIGURE 9: Consequence of cryogenic behaviour on (a) tension behaviour and (b) flexural strength.

thread with strain inside the matrix. Such compressing inter-layer pressures help to maintain the fibres and polymers in contact and improve adhesion, which leads to better results. Liquid nitrogen cracking of manufactured composites makes the components more resistant to relatively low temperatures [2, 4, 10]. Figures 9(a) and 9(b) demonstrate the impact of cold working on the physical and mechanical properties of nanomaterials.

3.5. Microstructural Analysis. SEM was employed to investigate the surface morphology of the nanocomposite sample following the transverse tensile test revealed in Figures 10(a)–10(c). The interface of the nanocomposite fails mostly due to inadequate adhesive binding and fibre pull-out for unprocessed flax fibre (Figure 10(a)). Fiber breaking is uneven and happens in the direction of the fibre. The rate of fibre pull-out is reduced, and fibre breaking is

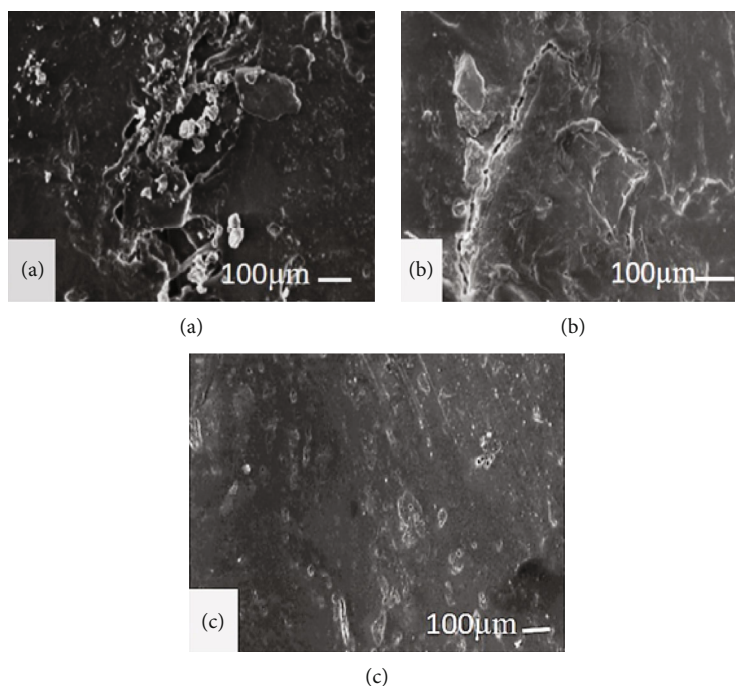


FIGURE 10: Microstructural images of (a) untreated, (b) 3% NaOH-treated, and (c) 5% NaOH-treated nanocomposites.

much more uniform with alkali-treated fibres. This shows that the interfacial adhesion between alkali-treated flax fibre and the polyester matrices has improved. Figure 10(b) illustrates a graphene-based flax fibre composite with a changed fracture surface and good resin-fibre binding. Furthermore, the brittle look of the matrix indicates strong interfacial interaction, which can contribute to improved nanocomposite mechanical characteristics. The permeability of the composite materials is next studied by examining the cross section of alkali- and graphene-treated polymers at greater magnification (Figure 10(c)). The interface permeability (lumen permeability and insemination permeability) in 3 percent alkaline-processed fibre composites is depicted in Figure 10(b). Because of the permeability, the composite may break quickly in the direction perpendicular. Figure 10(c) shows that when alkali-treated flax fibres are exposed to 5% alkali, similar permeability is not observable.

4. Conclusion

From the preceding study that natural fibres can be used more effectively in polymeric materials, the following statements were derived from the experimental part.

- (i) In a tensile test, the 5% surface treatment increased strength by 33 times and load bearing capability by 8 times when compared to a clean polyester specimen. Natural fibres are treated to improve the matrix's toughness
- (ii) We discovered that 3% alkali-processed flax gave more than six times the output of unprocessed flax

in mechanical testing. The strength of the structure decreases when the reinforcement is increased

- (iii) The improper dispersion of flax and the bonding capabilities of flax with polyester might be the reason of the reduced strength of untreated flax. After a certain chemical treatment, fibres grow harder and bonding becomes easier
- (iv) Cellulose depolymerizes, revealing crystallites of short length. As a result, we may conclude that treating flax fibres aids in the attainment of greater strengths
- (v) The nanocomposite that has been cryogenically treated for 30 minutes has the maximum mechanical strength. It might be due to the latent tension created by compression contact as a result of nanocomposites' cryogenic straining
- (vi) In future, chemical treatment effects like bonding, cracks, fracture toughness, and FTIR can be studied

Data Availability

The statistics often used to support the study's conclusions are supplied in the paper. On request, the associated author can provide more data or information.

Conflicts of Interest

The authors state that the publishing of this paper does not include any conflicts of interest.

Acknowledgments

The authors appreciate the supports from the Mizan Tepi University, Ethiopia, for providing help during the research and preparation of the manuscript. The authors thank the Sree Krishna College of Engineering and C. Abdul Hakeem College of Engineering & Technology for providing assistance to this work.

References

- [1] B. Bakri, A. E. E. Putra, A. A. Mochtar, I. Renreng, and H. Arsyad, "Sodium bicarbonate treatment on mechanical and morphological properties of coir fibres," *International Journal of Automotive and Mechanical Engineering*, vol. 15, no. 3, pp. 5562–5572, 2018.
- [2] M. A. Rahuman, S. S. Kumar, R. Prithivirajan, and S. G. Shankar, "Dry sliding wear behavior of glass and jute fiber hybrid reinforced epoxy composites," *International Journal of Engineering Research and Development*, vol. 10, no. 11, pp. 46–50, 2014.
- [3] S. Sanjeevi, V. Shanmugam, S. Kumar et al., "Effects of water absorption on the mechanical properties of hybrid natural fibre/phenol formaldehyde composites," *Scientific Reports*, vol. 11, pp. 1–11, 2021.
- [4] A. Sreenivasulu, K. S. Ashraff Ali, P. Arumugam et al., "Investigation on thermal properties of tamarind shell particles reinforced hybrid polymer matrix composites," *Materials Today: Proceedings*, vol. 59, Part 2, pp. 1305–1311, 2022.
- [5] G. Velmurugan and K. Babu, "Statistical analysis of mechanical properties of wood dust filled jute fiber based hybrid composites under cryogenic atmosphere using Grey-Taguchi method," *Materials Research Express*, vol. 7, no. 6, 2020.
- [6] V. Fiore, T. Scalici, and A. Valenza, "Effect of sodium bicarbonate treatment on mechanical properties of flax-reinforced epoxy composite materials," *Journal of Composite Materials*, vol. 52, no. 8, pp. 1061–1072, 2018.
- [7] N. E. Zafeiropoulos, C. A. Baillie, and J. M. Hodgkinson, "Engineering and characterisation of the interface in flax fibre/polypropylene composite materials. Part II. The effect of surface treatments on the interface," *Composites. Part A, Applied Science and Manufacturing*, vol. 33, no. 9, pp. 1185–1190, 2002.
- [8] M. Evtimova, M. Vlahova, and A. Atanassov, "Flax improvement by biotechnology means," *Journal of Natural Fibers*, vol. 2, no. 2, pp. 17–34, 2005.
- [9] S. Sekar, S. Suresh Kumar, S. Vigneshwaran, and G. Velmurugan, "Evaluation of mechanical and water absorption behavior of natural fiber-reinforced hybrid biocomposites," *Journal of Natural Fibers*, vol. 19, no. 5, pp. 1172–1182, 2022.
- [10] T. Raja, V. Mohanavel, S. Suresh Kumar, S. Rajkumar, M. Ravichandran, and R. Subbiah, "Evaluation of mechanical properties on kenaf fiber reinforced granite nano filler particulates hybrid polymer composite," *Materials Today: Proceedings*, vol. 59, pp. 1345–1348, 2022.
- [11] M. Vovk and M. Šernek, "Aluminium trihydrate-filled poly(methyl methacrylate) (PMMA/ATH) waste powder utilization in wood-plastic composite boards bonded by MUF resin," *BioResources*, vol. 15, no. 2, pp. 3252–3269, 2020.
- [12] V. Ganesan and B. Kaliyamoorthy, "Utilization of Taguchi technique to enhance the interlaminar shear strength of wood dust filled woven jute fiber reinforced polyester composites in cryogenic environment," *Journal of Natural Fibers*, vol. 19, no. 6, pp. 1990–2001, 2022.
- [13] A. Atiqah, M. N. M. Ansari, M. S. S. Kamal, A. Jalar, N. N. Afeefah, and N. Ismail, "Effect of alumina trihydrate as additive on the mechanical properties of kenaf/polyester composite for plastic encapsulated electronic packaging application," *Journal of Materials Research and Technology*, vol. 9, no. 6, pp. 12899–12906, 2020.
- [14] F. Sarker, P. Potluri, S. Afroj, V. Koncherry, K. S. Novoselov, and N. Karim, "Ultrahigh performance of nanoengineered graphene-based natural jute fiber composites," *ACS Applied Materials & Interfaces*, vol. 11, no. 23, pp. 21166–21176, 2019.
- [15] F. Perreault, A. Fonseca De Faria, and M. Elimelech, "Environmental applications of graphene-based nanomaterials," *Chemical Society Reviews*, vol. 44, no. 16, pp. 5861–5896, 2015.
- [16] S. A. Hallad, N. R. Banapurmath, V. Patil et al., "Graphene reinforced natural fiber nanocomposites for structural applications," *IOP Conference Series: Materials Science and Engineering*, vol. 376, no. 1, 2018.
- [17] A. Karthikeyan, K. Balamurugan, and A. Kalpana, "The effect of sodium hydroxide treatment and fiber length on the tensile property of coir fiber-reinforced epoxy composites," *Science and Engineering of Composite Materials*, vol. 21, no. 3, pp. 315–321, 2014.
- [18] V. Ganesan, V. Shanmugam, B. Kaliyamoorthy et al., "Optimisation of mechanical properties in saw-dust/woven-jute fibre/polyester structural composites under liquid nitrogen environment using response surface methodology," *Polymers*, vol. 13, no. 15, p. 2471, 2021.
- [19] G. Velmurugan and K. Babu, "Optimization on mechanical behavior of hemp and coconut shell powder reinforced epoxy composites under cryogenic environment using Grey-Taguchi method," *SSRN Electronic Journal*, vol. 2019, 2019.
- [20] G. Velmurugan, K. Babu, L. I. Flavia, C. S. Stephy, and M. Hariharan, "Utilization of Grey Taguchi method to optimize the mechanical properties of hemp and coconut shell powder hybrid composites under liquid nitrogen conditions," *IOP Conference Series: Materials Science and Engineering*, vol. 923, no. 1, 2020.
- [21] V. S. Srinivasan, S. Rajendra Boopathy, D. Sangeetha, and B. V. Ramnath, "Evaluation of mechanical and thermal properties of banana-flax based natural fibre composite," *Materials and Design*, vol. 60, pp. 620–627, 2014.
- [22] L. Fiore Vincenzo, "Effect of stacking sequence and sodium bicarbonate treatment on quasi-static and dynamic mechanical properties of flax/jute epoxy-based composites," *Materials*, vol. 12, no. 9, p. 1363, 2019.
- [23] S. Kalyana Sundaram, S. Jayabal, N. S. Balaji, and G. Bharathiraja, "Study of chemical and mechanical properties of Dharbai fiber reinforced polyester composites," *Advanced Composite Materials*, vol. 27, pp. 107–117, 2018.

Research Article

Optimization and Mechanical Characteristics of AA6061/Zirconia Nanocomposites Fabricated by Ultrasonic-Aided Stir Casting Method

Amel Gacem,¹ Moamen S. Refat,² H. Elhosiny Ali,^{3,4,5} S. C. V. Ramana Murty Naidu,⁶ B. Beenarani,⁷ Pranjali Deole,⁸ S. Sandeep Kumar,⁹ S. Rama,¹⁰ Amnah Mohammed Alsuhaibani,¹¹ and Abdi Diriba ¹²

¹Department of Physics, Faculty of Sciences, University 20 Août 1955, 26 El Hadaiek, Skikda 21000, Algeria

²Department of Chemistry, College of Science, Taif University, P.O. Box 11099, Taif 21944, Saudi Arabia

³Research Center for Advanced Materials Science (RCAMS), King Khalid University, Abha 61413, P.O. Box 9004, Saudi Arabia

⁴Department of Physics, Faculty of Science, King Khalid University, Abha 61413, Saudi Arabia

⁵Department of Physics, Faculty of Science, Zagazig University, Zagazig, Egypt

⁶Department of Mechanical Engineering, Sri Venkateswara College of Engineering & Technology, Etcherla, Srikakulam, Andhra Pradesh 532410, India

⁷Department of Computer Science Engineering, Saveetha School of Engineering, SIMATS, Chennai, Tamil Nadu 600124, India

⁸Department of Mechanical Engineering, Shri Ramdeobaba College of Engineering and Management, Nagpur, Maharashtra 440013, India

⁹Department of Computer Science Engineering, Koneru Lakshmaiah Education Foundation, Vaddeswaram, Andhra Pradesh 522302, India

¹⁰Department of Mechanical Engineering, Gokaraju Rangaraju Institute of Engineering and Technology, Hyderabad, Telangana 500090, India

¹¹Department of Physical Sport Science, College of Education, Princess Nourah bint Abdulrahman University, P.O. Box 84428, Riyadh 11671, Saudi Arabia

¹²Department of Mechanical Engineering, Mizan Tepi University, Ethiopia

Correspondence should be addressed to Abdi Diriba; abdi@mtu.edu.et

Received 8 May 2022; Revised 16 July 2022; Accepted 19 July 2022; Published 20 September 2022

Academic Editor: Arpita Roy

Copyright © 2022 Amel Gacem et al. This is an open access article distributed under the Creative Commons Attribution License, which permits unrestricted use, distribution, and reproduction in any medium, provided the original work is properly cited.

Using the Taguchi Grey response surface approach, this study investigates the effect of novel ultrasonic-aided stir casting conditions on the production of AA6061/zirconia nanocomposites. A Taguchi L_{16} orthogonal array was utilized to conduct the researches, which included ultrasonic power (1.75-2.5 kW), time (5-20 min), temperature (750-900°C), which can cause premature solidification, stir pressure (100-250 MPa), and reinforcement weight percentage (wt% of reinforcement). Ultrasonic-aided stir casting technique has five adjustable parameters (2-5). The ultimate tensile strength, elongation percentage, hardness, and size of the grain material were some of the metrics used to evaluate the process performance. It was decided to employ the response surface approach to model and optimize the numerous replies into one grey relational analysis. AA6061/zirconia nanocomposites were studied using statistical methods such as 3D surface plots and variance analysis. 2.2537 kW, 16.28 min ultrasonic duration, weight % of reinforcement of 1.9, stirring temperature of 700.73°C, and stirring pressure of 142.63 MPa were found to be the best parameter values.

1. Introduction

In a variety of industries, metal matrix composites play an important role due to their light weight, greater durability, and outstanding resistance to wear as well as corrosion [1]. Lightweight aluminum matrix composites (AMCs) are employed in several technical applications because they have tensile strength, less coefficient of thermal expansion [2], increased mechanical and anticorrosion qualities, and a less coefficient of thermal extension [3, 4]. In contrast, the mechanical characteristics of aluminum matrix composites are strongly reliant on the kind, quantity, and nature of the strengthening properties contained in its matrix [5]. AA6061 is a heating-resistant metal of aluminum and Cu that is a common alloying element [6]. Weight, strength, and corrosion resistance (and high machinability) make them ideal for use in aerospace or automobile engineering. A chemically inert ceramic with outstanding thermomechanical characteristics, zirconia (ZrO_2) is a versatile material [7]. For example, zirconia's density is 3.95 grams per cubic centimeter, its melting point is 2056°C, and its thermal expansion coefficient is $7.4 \mu m/m^\circ C$. Zirconia reinforcements have been found to greatly upgrade the mechanical characteristics of aluminum alloys in previous studies [8, 9]. Furthermore, nano-sized zirconia elements have a significant impact on the mechanics and thermomechanic characteristics of nano-structured owing to their high surface-to-volume proportion [10]. MMCs with near net forms can be produced using the liquid metallurgical process known as stir casting [11]. Since it eliminates porosity and improves surface texture and mechanical qualities while also utilizing a finer microstructure than conventional casting, stir casting is a preferable method [12]. While traditional stir casting may be used to introduce nanoparticles [13] into the metal matrix, it is quite difficult to do so. Excessive churning will result in the matrix being oxidized and clumping together [14]. In these circumstances, ultrasonic therapy (UST) can be employed to efficiently distribute nanosized reinforcements [15]. Grains are refined and degassed using UST in the composite production sectors. When high-intensity ultrasonic waves are used during ultrasonic therapy, the melt is subjected to intense cavitation and acoustic streaming. Because of this, ultrasonic therapy breaks apart nanoparticulate groups and evenly disperses the particles that make up the material melt [16]. It is therefore ineffective to just employ the use of ultrasonic therapy in the production of nanocomposites. To improve nanocomposites' microstructure and mechanical characteristics, the ultrasonic therapy stir casting process is a common production technique [17]. Many recent studies have shown that adjusting the casting process parameters utilizing various optimization tools may improve the mechanical and microstructural characteristics of composites [18]. It was found that 106 MPa, 200°C, and 30 s are the optimal values for stir casting pressure, die heating temperature, and stir duration for the stir casting method of LM₂₄ alloy to increase the UTS and stiffness. Wetting of dispersion issues was resolved by treating AA6061/1 wt% ZrO₂ nano-

TABLE 1: Characteristics of zirconia.

Property	Values
Density	6.15 g/cm ³
Colour	White
Melting point	2973 K
Shape	Spherical

composites with ultrasonic treatment, which caused in a rise in ultimate tensile strength yield of 37% and 81%, correspondingly, as equated to the base alloy [19]. It was found that ultrasonic processing with a 1400 W/cm² power level and a 5% solute concentration resulted in the best grain refinement in a study by [20]. With the help of T-GRA and ANOVA, [21] investigated whether process parameters (UTS, stiffness, and % of extension) affected the microstructure and mechanical characteristics of AA6061-ZrO₂ compounds (ANOVA). The optimal values were discovered to be a stirring pressure of 128 MPa, a molten temperature of 848°C, and a weight percentage of SiC [22]. Improve multiple responses processes with the use of the RSM and examination of the desirability approach, two commonly used methodologies. It is possible to determine the best input conditions using these methods. An ANOVA, RSM, and a desirability function-based technique was utilized by [23] to identify the best combinations of manufacturing parameter A413 alloy, which is made by stir casting. It was found that the physical and microstructural characteristics of LM₁₃ alloy were affected by molten metal and die temperatures, as well as stir pressure. Higher stir pressure decreased grain size and enhanced hardness and density, according to the data [24]. However, hardness declined with increasing melt and die temperatures. Microstructure and mechanical characteristics of 6061 alloy AA were examined by [25]. Assuming 700°C and 140 MPa, the average grain size was 80 nm. Pouring temperature had no effect when the stir pressure was more than 70 MPa. To improve the wear characteristics of AA7150-hBN composites, [26] utilize Taguchi L₂₅ orthogonal array-ANOVA. Taguchi's L₁₆ orthogonal array, stirring pressure, pressure holding duration, and die preheating temperature all had a significant impact on composite reactions including stiffness and high strengthening, according to [27, 28] employing an artificial neural network prediction model to investigate how the settings used in stir casting affected the solidification time. It was shown that both the mold and pouring temperatures had significant effects on casting quality and freeze time. For AA2024-SiC nanocomposites, [29] established remarkably low error % artificial neural network models to forecast the density and hardness. Stir casting processing parameters include pouring temperature, pressuring duration, and die temperature which were examined in depth by [30]. Nanocomposites using traditional stir-stir casting have had difficulty achieving acceptable microstructural and mechanical qualities, as has been widely documented in previous investigations [31]. These obstacles can be

TABLE 2: Processing factors and its levels.

Processing factors	Level 1	Level 2	Level 3	Level 4
Ultrasonic therapy power (KW) (A)	1.75	2	2.25	2.5
UST time (min) (B)	5	10	15	20
Pouring temperature ($^{\circ}$ C) (C)	750	800	850	900
Squeezing pressure (MPa) (D)	100	150	200	250
Weight percentage of reinforcement (wt%) (E)	2	3	4	5

solved by employing a technology known as ultrasonication-stir linked stir casting, which has proven effective in the last several years. No one has employed an optimal combination of ultrasonic therapy stir casting parameters, and the literature study clearly shows that there is a considerable need for improving these parameters to fabricate aluminum nanocomposites. According to [32], L_{16} orthogonal array 16 distinct AA6061/zirconia nanocomposites were made utilizing the UST-stir linked stir casting process. There were five variables that could be tweaked in the ultrasonic-aided stir casting process: power (1.75-2.5 kW), duration (5-20 min), pour temperature (750-900 $^{\circ}$ C), stir pressure (100-250 MPa), and wt% ZrO_2 (2-5%). The results were analyzed using these parameters. We selected hardness, elongation percentage, and particle size as the replies. The TGRSM approach was utilized to invent the finest mixture of parameters [33–35]. The best condition was verified by conducting a desire analysis and a confirmation experiment.

2. Methods and Materials

2.1. Matrix and Reinforcement. It was decided to use zirconia alloy 6061 as the matrix composite in this study. The nanopowder of zirconia (ZrO_2) was used as reinforcement. Table 1 lists the characteristics of ZrO_2 .

2.2. Selection of Process Parameters and Responses. For high-quality castings, it is vital to pick the right casting process parameters and operating levels. Selecting control parameters with an inadequately big or narrow operating range, you may end up with a flawed or incomplete solution. Nanoparticle aggregation and matrix material oxidation would occur if the ultrasonic therapy power and the ultrasonic therapy duration were increased [34]. Lower ultrasonic therapy power and duration, on the other hand, are insufficient for dissolving nanoparticle clusters and removing dendrites from microstructures. Due to a delayed cooling rate, dendritic structures emerge when the melt is poured at a higher temperature. Premature solidification might occur if the pouring temperature is too low and the processing parameters are shown in Table 2.

2.3. AA6061/Zirconia Nanocomposite Fabrication. Initial melting was done in mild steel employing an electric resistance furnace with highest heating system of 1200 $^{\circ}$ C. A K-type thermocouple has been used to show the temperature of the furnace and the melt. We used an inert gas shield to

safeguard the melting process. Zirconia nanoparticles were also dried in a muffle furnace by heating them to 300 $^{\circ}$ C for an hour. The composites were manually stirred for two minutes at 500 revolutions per minute utilizing a graphene layered stainless steel stirrer when it reached the appropriate melting temperature. Zirconia nanopowder was added to the melt and agitated for another 5 minutes before being removed [35]. A titanium alloy ultrasonic probe was used to disseminate ultrasonic waves into the slurry after adequate churning. The sonotrode was submerged in the melting space to a deepness of 300 mm during the ultrasonication operation. Power was raised to 2.5 kilowatt and the frequency was set at 20 kHz. Warm steel mold dies (300 mm high by 50 mm wide) were used to bottom-pour the melt before it could harden. It was critical that all of the experiments be conducted with a 1-minute stir period. Accordingly, the process parameters for producing the 16 distinct AA6061/zirconia nanocomposites were adjusted according to the Taguchi L_{16} orthogonal array. A high-precision weighing scale (accurate to 0.00001 g) was used to measure the porosity of the manufactured materials.

2.4. Heat Treatment of Nanocomposites. Precipitation hardening under a T-6 tempering condition hardened the nanocomposites. In solution treatment, the nanocomposites were maintained at 510 $^{\circ}$ C for two hours before being immediately quenched in water. In addition, the aging process was carried out for 14 hours at 165 $^{\circ}$ C. Heat treatment was done in an argon endangered atmosphere employing a high-temperature muffle boiler. In a double disc-polishing machine, abrasive polishing sheets of 400, 600, 1200, and 2000 grit were used to make microstructural study specimens. Particle size was determined using the ASTM E 112-96 linear intercept method.

2.5. Hardness Test. Nanocomposites were tested for microhardness (VHN) using a Vickers hardness tester (Bluestar Vickers hardness tester). Indentation testing was performed on the polished specimens using a 10 kg load as well as a dwell duration of 15 seconds.

2.6. Tensile Test. Tensile tests were conducted to determine how casting factors affected the nanocomposites' ultimate tensile strength and elongation %. Figure 1 indicates the specimen schematic of tensile tests done on an Instron tensile testing equipment with a strain rate of 1 mm/min. A gauge span of 251 mm was used for the tensile test, which

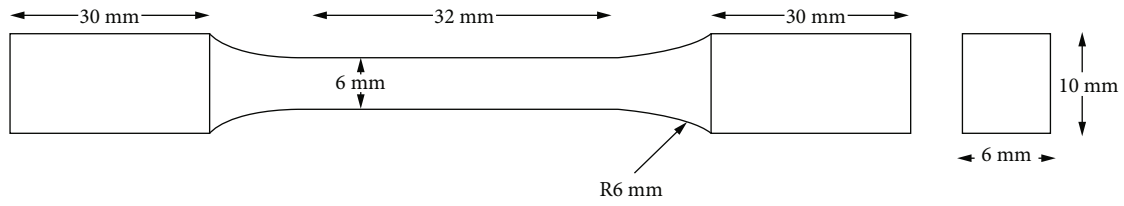


FIGURE 1: Measurement of the tensile test sample.

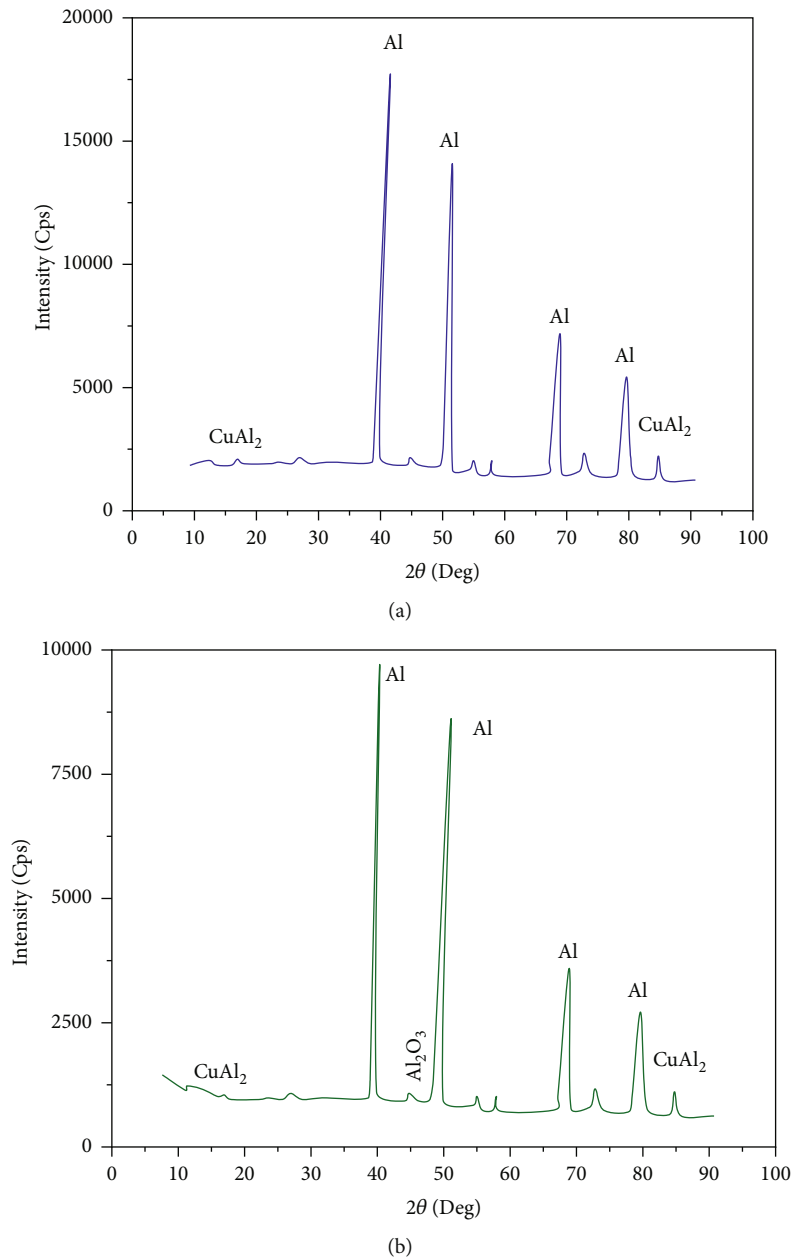


FIGURE 2: XRD forms of materials: (a) AA6061 and (b) zirconia.

TABLE 3: Orthogonal arrangement and experimental outcome on Taguchi L_{16} .

Exp. no.	Processing factors					Hardness (VHN)		Ultimate tensile strength (MPa)		Elongation (%)		Grain size	
	A (watt)	B (min)	C (°C)	D (MPa)	E (wt%)	R1	R2	R1	R2	R1	R2	R1	R2
1	1750	5	750	100	2	124	124	245	226	6.4	6.3	197	197
2	1750	10	800	150	3	126	127	247	268	4.7	6.8	176	174
3	1750	15	850	200	4	127	125	278	274	3.7	6.0	162	166
4	1750	20	900	250	5	122	116	228	234	4.1	3.1	222	208
5	2000	5	800	100	2	128	135	257	274	4.9	4.9	180	176
6	2000	10	850	150	3	137	136	311	291	6.9	6.5	147	139
7	2000	15	900	200	4	134	134	294	304	7.2	6.9	149	150
8	2000	20	750	250	5	128	126	296	272	8.1	10.3	165	169
9	2250	5	800	150	2	138	144	302	331	7.5	7.9	125	127
10	2250	10	850	100	3	132	129	297	301	9.9	9.0	146	142
11	2250	15	900	250	4	144	142	291	305	6.9	6.7	126	128
12	2250	20	750	200	5	138	137	321	314	6.8	7.5	130	130
13	2500	5	850	100	3	146	141	321	334	7.1	9.1	90	90
14	2500	10	800	150	4	140	139	301	273	7.2	7.4	116	112
15	2500	15	900	200	2	143	137	312	337	10.5	11.9	70	64
16	2500	20	750	250	5	149	149	336	340	10.6	10.7	45	41

TABLE 4: Normalized and sound to noise ratio values of trials.

Exp. no.	Sound to noise ratio values				Normalized sound to noise ratio values			
	Hardness (VHN)	Ultimate tensile strength (MPa)	Elongation (%)	Grain size (μm)	Hardness (VHN)	Ultimate tensile strength (MPa)	Elongation (%)	Grain size (μm)
1	42.869	48.409	16.056	45.892	0.188	0.042	0.53	0.946
2	42.043	48.195	15.757	44.872	0.276	0.279	0.394	0.873
3	42.008	48.828	13.976	45.378	0.256	0.472	0.209	0.832
4	42.504	48.278	10.875	46.645	0.000	0.000	0.000	1.000
5	42.368	48.455	13.803	-45.009	0.443	0.357	0.296	0.882
6	42.703	49.556	16.512	-43.110	0.613	0.690	0.564	0.746
7	42.543	49.502	16.954	43.493	0.514	0.674	0.613	0.774
8	42.077	49.043	19.088	44.455	0.293	0.535	0.818	0.843
9	42.979	49.974	17.723	42.008	0.754	0.817	0.686	0.668
10	42.311	49.513	19.478	43.168	0.413	0.677	0.855	0.751
11	43.107	49.477	16.646	42.076	0.819	0.666	0.578	0.672
12	42.768	50.028	17.056	42.279	0.645	0.833	0.623	0.687
13	43.134	50.298	17.972	39.085	0.832	0.915	0.712	0.458
14	42.892	49.127	17.265	41.139	0.709	0.560	0.642	0.605
15	42.913	50.212	20.934	36.530	0.723	0.889	1.000	0.276
16	43.465	50.578	20.548	32.679	1.000	1.000	0.97	0

TABLE 5: GRC and grey relational grade values.

Exp. no.	Hardness (VHN)	Elongation (%)	GRC		Grey relational grade	Rank
			Grain size (μm)	Ultimate tensile strength (MPa)		
1	0.382	0.511	0.902	0.343	0.5337	12
2	0.409	0.453	0.797	0.408	0.5163	14
3	0.403	0.388	0.749	0.486	0.5058	15
4	0.334	0.334	1.000	0.334	0.5000	16
5	0.474	0.416	0.808	0.438	0.5337	13
6	0.564	0.535	0.665	0.618	0.5945	9
7	0.516	0.564	0.688	0.606	0.5933	10
8	0.415	0.733	0.762	0.512	0.6064	8
9	0.668	0.614	0.602	0.733	0.6539	4
10	0.461	0.775	0.668	0.609	0.6272	6
11	0.734	0.543	0.605	0.601	0.6197	7
12	0.585	0.568	0.616	0.751	0.6295	5
13	0.748	0.635	0.481	0.856	0.6792	3
14	0.631	0.583	0.558	0.533	0.5761	11
15	0.642	1.000	0.407	0.819	0.7172	2
16	1.000	0.926	0.334	1.000	0.8148	1

was completed successfully. Hardness and tensile testing were performed on samples.

3. Results and Discussion

3.1. Intermetallic Phase Analysis of Nanocomposites. The XRD patterns of AA6061 and AA6061/2 weight % Zr nanocomposite are shown in Figures 2(a) and 2(b), correspondingly. It can be shown in Figure 2(a) that the natural intermetallic phase generated by Cu and Al atoms reacting in the 6061-aluminum alloy corresponds to the peaks associated with both the phase and the intermetallic CuAl_{12} phase. It may be seen in Figure 2(b).

3.2. Process Optimization Using TGRSM. Taguchi L_{16} orthogonal array was employed to done the testing, with two replications for each trial. Results for each stage of the experiment are summarized in Tables 3 and 4. First, the response values were functional to Grey relational analysis and its GRA output was employed as an input for response surface methodology displaying and optimizing. Every set of normalized sound to noise ratio values of replies is used to determine the GRC values. Grey relational grade was created by averaging the GRC values of different GRCs into a single quality index. All responses and their accompanying grey relational grade are shown in Table 5. When grey relational grade reaches its maximum value on the sixteenth trial, it is close to the optimal parameter level. Variations in grey relational grade values, as seen in Figure 3, illustrate that parameter levels selected have a significant influence on the grey relational grade. RSM was used to analyze the grey relational grade values obtained by RSM. Minitab software was used to determine the model coefficients for the

second-order polynomial equation that expresses the impact of factors on grey relational grade.

3.3. ANOVA on Grey Relational Grade. The ANOVA was chosen to investigate the most critical factors that contribute to the generation of grey relational grade values. Table 6 indicates the ANOVA outcomes for grey relational grade. While the “ p value” showed the importance of the model terms, the “ F value” showed the model’s significance. We identified all of the factors and interactions that were examined in the model (A/B/C/D/E) as the most important variables. Table 7 shows that the polynomial model’s R -squared value was quite near to unity. Using this data, the model is able to forecast future results based on the results of actual experiments.

Figure 4(a) demonstrates the model’s suitability. Polynomial model predictions of grey relational grade agree with those obtained under experimental circumstances; it is discovered. The adjusted R -squared value was quite close to the projected R -squared value. To put this into perspective, the model has an adequate precision of 30.016, as indicated in the tables. Figure 4(b) displays that the studentized residuals follow the normal distribution, as may be demonstrated. This suggests that polynomial models can be used to predict GRG values in the experimental area with reasonable accuracy and precision.

3.4. Grey Relational Grade Surface Plots in 3D. 3D surface plots, as illustrated in Figures 5(a)–5(c), were produced to study the effects of processing factors on grey relational grade. The grey relational grade value is strongly influenced by the ultrasonic therapy power and pouring temperature, as illustrated in Figure 5(a). It has been found that grey relational grade values increase when ultrasonic therapy power

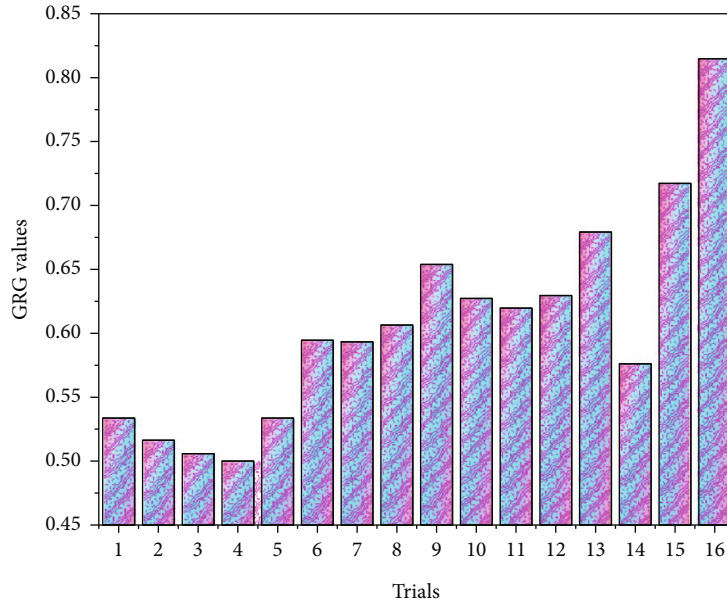


FIGURE 3: Variations in GRG levels among different trials.

TABLE 6: ANOVA on grey relational grade.

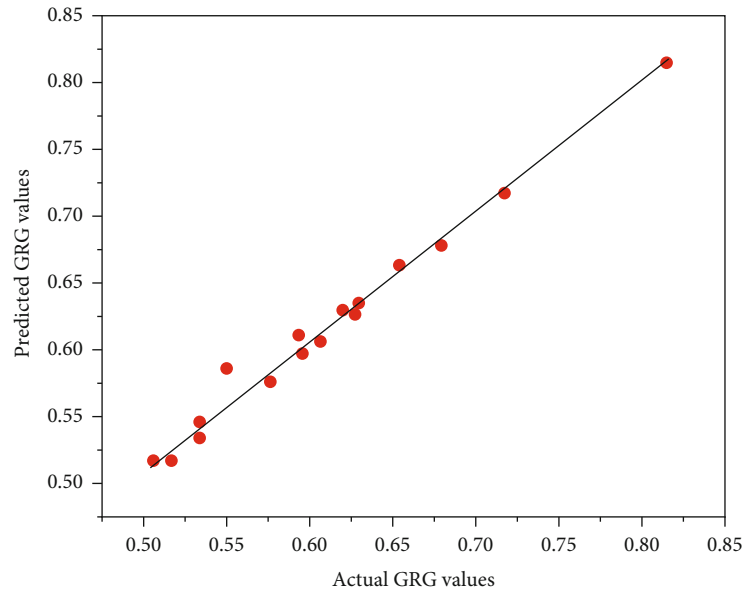
Source	SS	DoF	Mean square	F value	p value
Model	0.1047	8	0.0133	75.23	<0.0002
A	0.01938	1	0.01947	12.32	0.002
B	0.04415	1	0.04415	26.71	0.002
C	0.00222	1	0.00213	13.35	0.011
D	0.00520	1	0.00511	30.76	0.002
E	0.01179	1	0.01179	69.61	0.000
AC	0.00123	1	0.00123	8.14	0.033
BC	0.00446	1	0.00446	26.92	0.002
DE	0.00665	1	0.00665	39.68	0.000
Residual	0.00121	7	0.000182	—	—
Cor. total	0.105	15	—	—	—

TABLE 7: Adequate precision values and model adequacy R-squared.

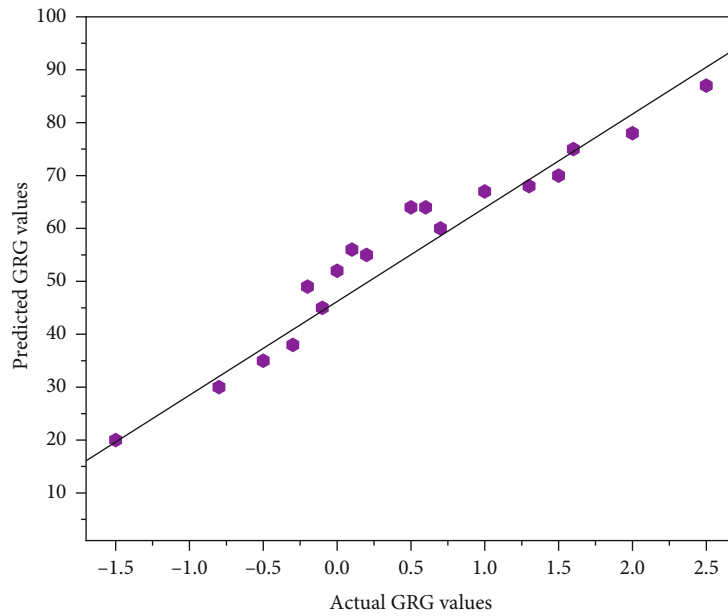
Standard variance	0.0132	R-squared	0.9887
Mean	0.6064	Adjustable R-squared	0.9757
Coefficient of difference	2.1618	Forecast R-squared	0.9049
Forecast residual error SS	0.0064	Adequacy precision	30.0166

increases. Respondent values increased as ultrasonic therapy power increased owing to particle dispersal, grain enhancement, and varied nucleation. Pouring temperatures increase the grey relational grade value. Because the freezing period was prolonged and the number of secondary dendrites increased, there were more secondary dendrite forms. At lower ultrasonic therapy power levels, pouring temperature had little effect. UST time, melt pouring temperature, and other variables, including ultrasonic therapy power (2250

watts), stir pressure (200 MPa), and weight % of reinforcement, are depicted in Figure 5(b) as a function of grey relational grade. The grey relational grade value rises to 0.678 at minimum pouring temperatures and lengthier ultrasonic therapy intervals. Figure 5(b) displays a strong link among the ultrasonic therapy time as well as the pouring temperature. The grey relational grade value fell as the pouring temperature was increased to 900°C. It was found that the grey relational grade was highest when the ultrasonic therapy



(a)



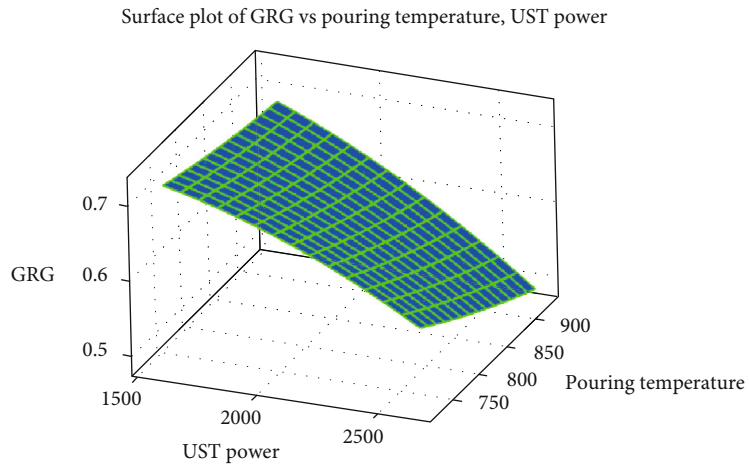
(b)

FIGURE 4: (a) Actual vs. predicted grey relation grade. (b) Studentized residuals vs. normal % probability.

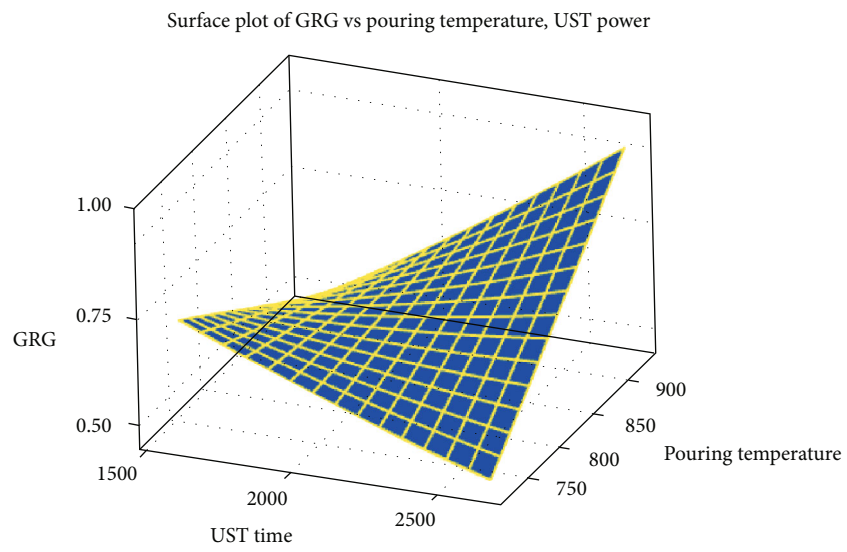
was longer and the pouring temperature was lower. The best strategy to ensure that the product is safe to consume is to increase the ultrasonic therapy duration and lower the pouring temperature as much as feasible. A longer ultrasonic therapy time will reduce the chance of nanoparticle agglomeration. Pouring at a lower temperature speeds up the cooling process, which improves the qualities of the finished product.

Figure 5(c) shows the interaction between stirring pressure and weight percentage. When the ultrasonic therapy power, the ultrasonic therapy duration, and the temperature are all persistent, the grey relational grade values are pro-

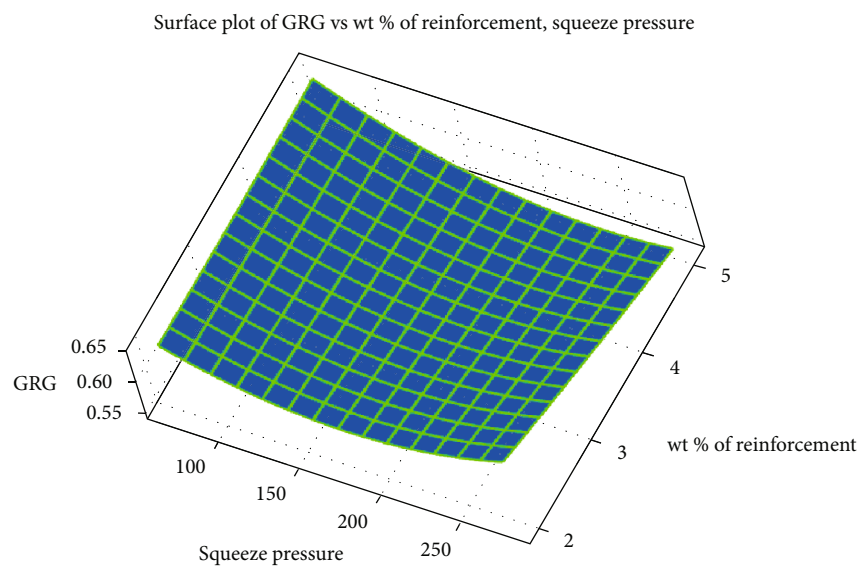
jected over the assortment of stir pressure and particles weight. According to this diagram, a high grey relational grade is produced when the wt% of particles is 6% and the stirring pressure is 250 MPa. Grain refining, elimination of porosity melt, and dendritic fragmentation all contribute to a rise in the grey relational grade value as the stir pressure increases. At first, an increase in nanoparticle weight % increased the multiperformance of AA6061/zirconia nanocomposites cast by ultrasonic-aided stir casting. Reinforcement with a higher wt% results in an increased grey relational grade; this indicates, therefore, an ideal 3 wt% ZrO_2 concentration for enhanced mechanical properties.



(a)



(b)



(c)

FIGURE 5: (a-c) 3D response surface plots of grey relational grade.

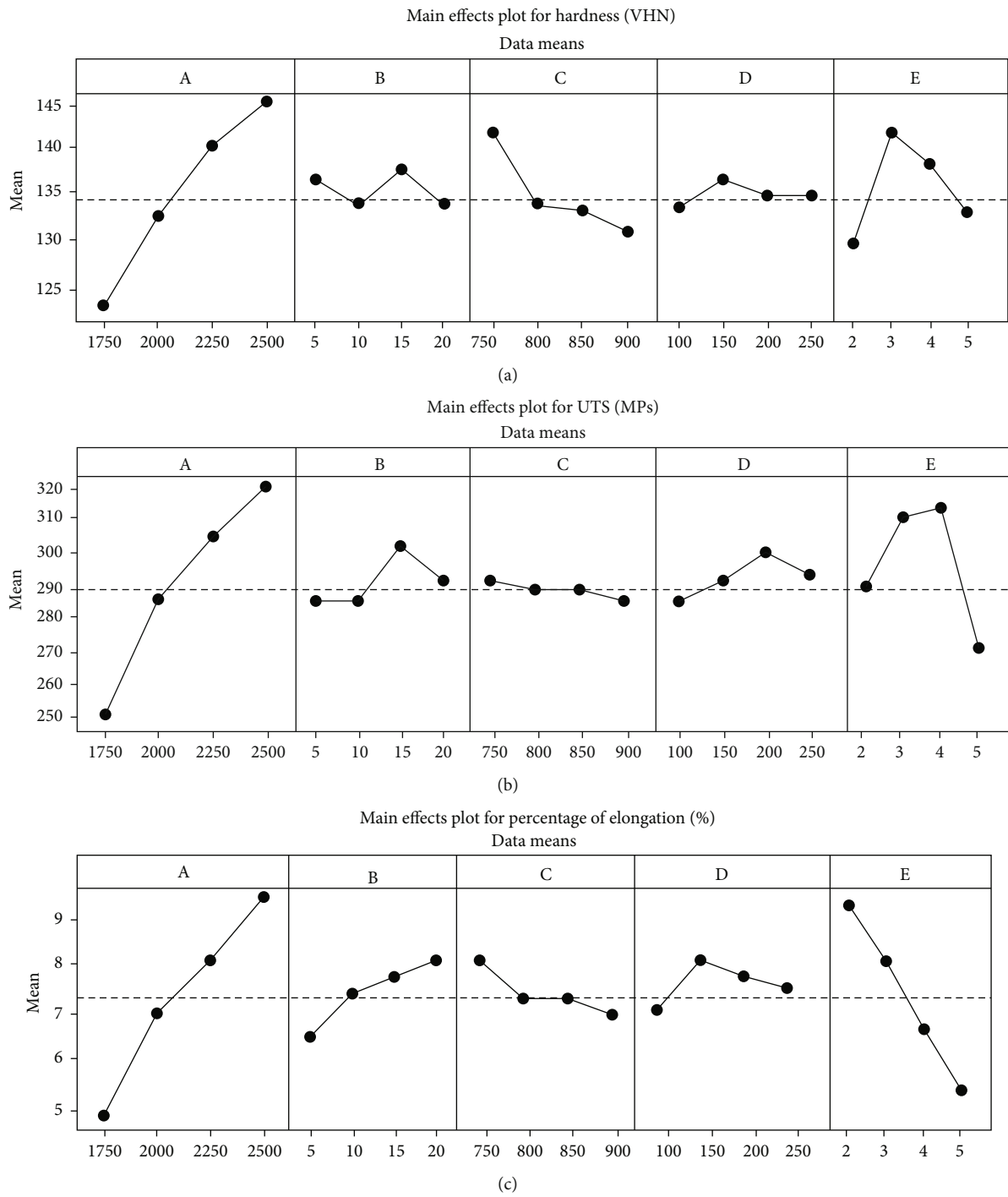


FIGURE 6: Continued.

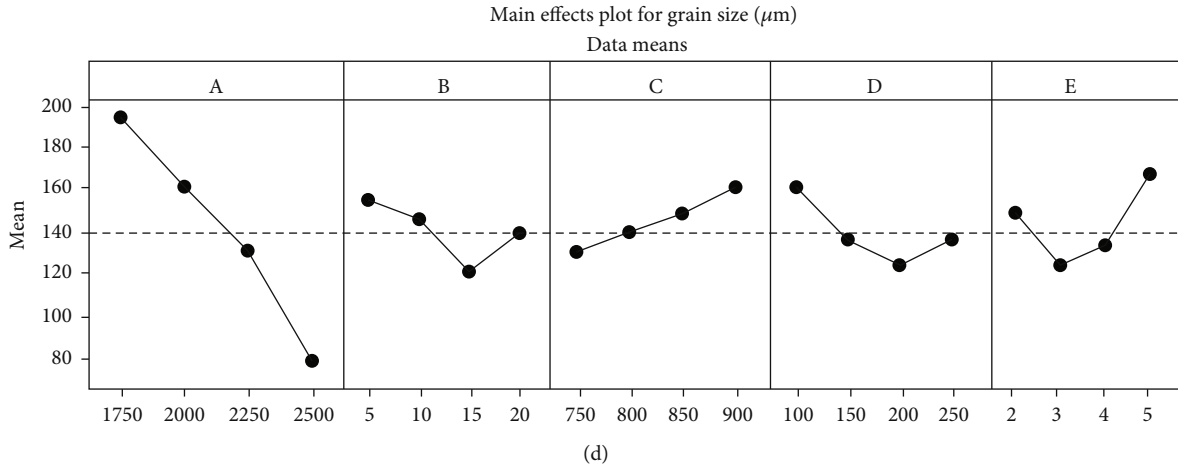


FIGURE 6: Main effects plots: (a) hardness, (b) ultimate tensile strength, (c) elongational %, and (d) size of the grain.

TABLE 8: Results of confirmation trials.

Factor setting	Initial factor	Optimum factors from Taguchi Grey response surface methodology	
		Trial values	Enhancement in response value
Level	$A_3B_3C_1D_2E_4$	Ultrasonic therapy power = 2.25367 kW Ultrasonic therapy time = 16.28 min Pouring temperature = 700.73°C Squeezing pressure = 142.63 MPa Weight % of reinforcement = 1.9	
Grey relational grade	0.6199	0.8208	0.203
Hardness (VHN)	144.75	152	7.250
Ultimate tensile strength (MPa)	298.73	339.58	40.850
% of elongation (%)	6.98	10.6	3.620
Grain size (μm)	128.56	43	85.560

3.5. Influence of Factors on the Response. By means of main effect plots, it is possible to demonstrate the influence of numerous factors on the results. Plots of the principal effects for a range of responses are shown in Figures 6(a)–6(d). On the graphs, it appears that ultrasonic therapy power (A) is the most important factor in determining the correct responses. In addition to improving hardness, ultimate tensile strength, and % of elongation, increasing the UST power also reduced grain size. Intense ultrasonication at a greater ultrasonic therapy power helped disperse the nanoparticles evenly throughout the matrix. At this moment, the nanoparticles were strapped into the intergranular regions of the previously produced grains. Due to the grain's inability to spread any more as a result of this technique, an even finer grain structure was created.

With regard to ultrasonic therapy time (B), it is clear that an increase in this value enhances the replies up to a certain point in time. The ultimate tensile strength, % elongation, and particle size all improved pointedly after a 15-minute UST time. The nanoparticles were evenly disseminated throughout the matrix because of the ultrasonication procedure. As the ultrasonic therapy time increased to 20 min, the hardness, ultimate tensile strength, and elongational percentage all dropped, but the grain size improved. Due to nanoparticle aggregation, the maximum UST duration had

less of an impact on the reactions of the subjects. Because of this, it is possible that an optimal ultrasonic therapy duration at midvalues is all that is needed to distribute nanoparticles effectively.

Plots of the main impacts show how answers vary depending on the weighted percentage of reinforcement used (E). Up to 3% of nanoparticles in the solution increased the reactivity. This was possible because of the uniform dispersion of nanoparticles throughout the system. Amounts of nanoparticles in excess of 3 wt% reduced the responses. It is common for nanoparticles to agglomerate in the matrix at higher percentages of the total weight. In addition to acting as stress concentration locations, the agglomerated particles also reduced mechanical responses. As a result, increasing the weight % of reinforcement reduced ultimate tensile strength and % of elongation. Table 8 shows the confirmation trials results.

Stress and strain graphs of materials manufactured under different processing conditions are shown in Figure 7. Increased ultrasonic therapy power was clearly associated with an increase in strain rate. Using high-powered sonication, a uniform dispersion of nanoparticles and fine grain refinement is achieved. Increases in nanoparticle weight % diminish elongation at various ultrasonic therapy powers, according to stress-strain curves. For example, at increased ultrasonic

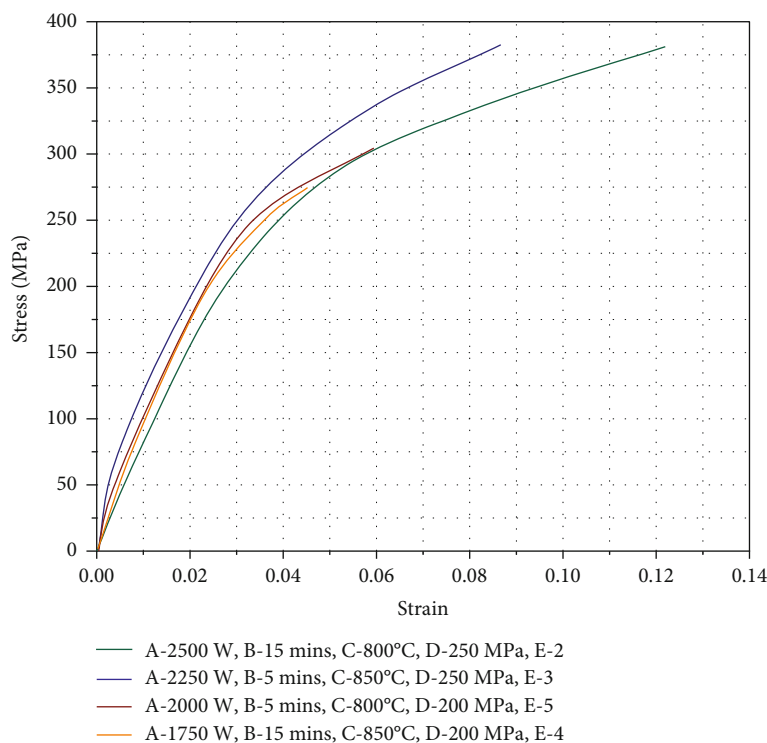


FIGURE 7: Tensile stress-strain curve.

therapy power, the grain fineness was greater and the dispersion of nanoparticles was more homogenous at 1.5 and 6 wt%. Consequently, the ductility improved greatly. In contrast, low-power sonication was unable to achieve uniform dispersion at high levels of reinforcement. To compensate for the loss of ductility, the material was coated with nanoparticles.

4. Conclusion

TGRSM was utilized to optimize ultrasonic therapy power, duration, pouring temperature, and the stir pressure. The investigation's findings are as follows.

- (i) This study demonstrated that grain refinement, homogeneous dispersion, and nanoparticle clustering were all impacted by distinct processing factors. Zirconia particles were shown to be nonreactive with AA6061 according to XRD measurements
- (ii) Multiobjective problems were transformed into similar single-objective problems using GRA. Using a model with a coefficient of determination of 0.9886, we were able to accurately predict the experimental response values. In the sixteenth trial, $A_4B_4C_1D_3E_2$ produced the greatest GRG value
- (iii) As a result of these and other factors, the final results were significantly affected by the UST power and time as well as the temperature, stir pressure, and the weight percentage of reinforcement. It was

found that AC, BC, and DE had significant ANOVA interactions

- (iv) Response surface plots were used to describe the impacts of factors on grey relational grade, and the role of specific parameters was explored. Grain size dropped as UST power rose, yet hardness, ultimate tensile strength, and elongation % increased. Higher pouring temperatures resulted in a decreased solidification cooling rate, which resulted in better composite manufacturing outputs. At a stir pressure of 142 MPa, better responses were obtained and additional increases in pressure had very minimal effects on responses
- (v) Using the TGRSM method, the following was found to be the best set of parameters: pouring temperature was 700.73°C, stir pressure was 142.63, and reinforcement was 1.9 wt%. Hardness of 151.62 VHN, ultimate tensile strength of 346.89 MPa, elongational % of 10.82, and particle size of 48.73 micrometer were found to be the optimal response parameters. Grey relational grade improved by a factor of 0.203 in the confirmation test

Data Availability

The data used to support the findings of this study are included within the article. Further data or information is available from the corresponding author upon request.

Conflicts of Interest

The authors declare that there is no conflict of interest regarding the publication of this article.

Acknowledgments

The authors extend their appreciation to the Research Center for Advanced Materials Science, King Khalid University, Saudi Arabia, for funding this work under grant number KCU/RCAMS/G011-21. Taif University Researchers Supporting Project number (TURSP-2020/01), Taif University, Taif, Saudi Arabia.







References

- [1] E. M. Parsons and S. Z. Shaik, "Additive manufacturing of aluminum metal matrix composites: mechanical alloying of composite powders and single track consolidation with laser powder bed fusion," *Additive Manufacturing*, vol. 50, p. 102450, 2022.
- [2] S. Banerjee, S. Poria, G. Sutradhar, and P. Sahoo, "Nano-indentation and corrosion characteristics of ultrasonic vibration assisted stir-cast AZ31–WC–graphite nano-composites," *International Journal of Metalcasting*, vol. 15, no. 3, pp. 1058–1072, 2021.
- [3] S. Kolappan, T. Arunkumar, V. Mohanavel et al., "Experimental investigation on stir casted hybrid composite AA7068 with SiC and coconut shell fly ash," *Materials Today: Proceedings*, vol. 62, Part 8, pp. 5540–5545, 2022.
- [4] A. Khandelwal, K. Mani, N. Srivastava, R. Gupta, and G. P. Chaudhari, "Mechanical behavior of AZ31/Al₂O₃ magnesium alloy nanocomposites prepared using ultrasound assisted stir casting," *Composites. Part B, Engineering*, vol. 123, pp. 64–73, 2017.
- [5] J. Huang, W. Li, Y. He et al., "Temperature dependent ultimate tensile strength model for short fiber reinforced metal matrix composites," *Composite Structures*, vol. 267, p. 113890, 2021.
- [6] H. Choi, W. Cho, and X. C. Li, "Semi-solid mixing for fabrication of A206/Al₂O₃ master nanocomposites," *AFS Transactions*, vol. 121, pp. 159–164, 2013.
- [7] Y. Sun, H. Choi, and X. C. Li, "Composition optimization for A206/Al₂O₃ nanocomposite," *AFS Transactions*, vol. 121, pp. 205–215, 2013.
- [8] S.-B. Bin, S.-M. Xing, L.-M. Tian, N. Zhao, and L. Li, "Influence of technical parameters on strength and ductility of AlSi9Cu3 alloys in squeeze casting," *Transactions of Nonferrous Metals Society of China*, vol. 23, no. 4, pp. 977–982, 2013.
- [9] P. Loganathan, A. Gnanavelbabu, and K. Rajkumar, "Influence of ZrB₂/hBN particles on the wear behaviour of AA7075 composites fabricated through stir followed by squeeze cast technique," *Proceedings of the Institution of Mechanical Engineers, Part J: Journal of Engineering Tribology*, vol. 235, no. 1, pp. 149–160, 2021.
- [10] R. Ahmad, D. T. Gethin, and R. W. Lewis, "Design element concept of squeeze casting process," *Applied Mathematical Modelling*, vol. 36, no. 10, pp. 4760–4788, 2012.
- [11] T. Lu, W. Chen, B. Li et al., "Influence mechanisms of Zr and Fe particle additions on the microstructure and mechanical behavior of squeeze-cast 7075Al hybrid composites," *Journal of Alloys and Compounds*, vol. 798, pp. 587–596, 2019.
- [12] S. Suresh Kumar and V. Mohanavel, "An overview assessment on magnesium metal matrix composites," *Materials Today: Proceedings*, vol. 59, pp. 1357–1361, 2022.
- [13] D. Yuan, X. Yang, S. Wu, S. Lü, and K. Hu, "Development of high strength and toughness nano-SiCp/A356 composites with ultrasonic vibration and squeeze casting," *Journal of Materials Processing Technology*, vol. 269, pp. 1–9, 2019.
- [14] A. H. Idrisi and A.-H. I. Mourad, "Conventional stir casting versus ultrasonic assisted stir casting process: mechanical and physical characteristics of AMCs," *Journal of Alloys and Compounds*, vol. 805, pp. 502–508, 2019.
- [15] C. Allen and Q. Han, "Grain refinement of pure aluminum using ultrasonics," *International Journal of Metalcasting*, vol. 5, no. 1, pp. 69–70, 2011.
- [16] X. Liu, S. Jia, and L. Nastac, "Ultrasonic cavitation-assisted molten metal processing of cast a356-nanocomposites," *International Journal of Metalcasting*, vol. 8, no. 3, pp. 51–58, 2014.
- [17] A. Gnanavelbabu, K. T. S. Surendran, P. Loganathan, and E. Vinothkumar, "Effect of ageing temperature on the corrosion behaviour of UHTC particulates reinforced magnesium composites fabricated through ultrasonic assisted squeeze casting process," *Journal of Alloys and Compounds*, vol. 856, p. 158173, 2021.
- [18] D. Gao, Z. Li, Q. Han, and Q. Zhai, "Effect of ultrasonic power on microstructure and mechanical properties of AZ91 alloy," *Materials Science and Engineering A*, vol. 502, no. 1–2, pp. 2–5, 2009.
- [19] S. H. Mousavi Anijdan and M. Sabzi, "The effect of pouring temperature and surface angle of vortex casting on microstructural changes and mechanical properties of 7050Al-3 wt% SiC composite," *Materials Science and Engineering A*, vol. 737, pp. 230–235, 2018.
- [20] B. M. Pasha and K. Mohamed, "Taguchi approach to influence of processing parameters on erosive wear behaviour of Al7034-T6 composites," *Transactions of Nonferrous Metals Society of China*, vol. 27, no. 10, pp. 2163–2171, 2017.
- [21] W. Khalifa, Y. Tsunekawa, and M. Okumiya, "Ultrasonic grain refining effects in A356 Al-Si cast alloy," *AFS Transactions*, vol. 118, pp. 91–98, 2010.
- [22] G. Chen, M. Yang, Y. Jin et al., "Ultrasonic assisted squeeze casting of a wrought aluminum alloy," *Journal of Materials Processing Technology*, vol. 266, pp. 19–25, 2019.
- [23] G. Talla, D. K. Sahoo, S. Gangopadhyay, and C. K. Biswas, "Modeling and multi-objective optimization of powder mixed electric discharge machining process of aluminum/alumina metal matrix composite," *Engineering Science and Technology, an International Journal*, vol. 18, no. 3, pp. 369–373, 2015.
- [24] P. Vijian and V. P. Arunachalam, "Optimization of squeeze casting process parameters using Taguchi analysis," *International Journal of Advanced Manufacturing Technology*, vol. 33, no. 11–12, pp. 1122–1127, 2007.
- [25] X. Li, Y. Yang, and D. Weiss, "Ultrasonic cavitation based dispersion of nanoparticles in aluminum melts for solidification processing of bulk aluminum matrix nanocomposite: theoretical study, fabrication and characterization," *AFS Transactions*, vol. 2, pp. 1–12, 2007.
- [26] P. C. Lynch, R. C. Voigt, J. C. Furness Jr., and D. Paulsen, "The effects of non-contact acoustic stimulation on the solidification behavior and microstructure of aluminum alloy A356," *AFS Transactions*, vol. 118, pp. 57–68, 2010.

- [27] S. Wetzel, "Nano's frontier-if you think tiny particles making metals super strong sounds like sci-fi, think again," *Modern Casting*, vol. 100, p. 27, 2010.
- [28] X. Jian, C. Xu, T. Meek, and Q. Han, "Effect of ultrasonic vibration on the solidification structure of A356 alloy," *AFS Transactions*, vol. 113, pp. 131–138, 2005.
- [29] N. Srivastava, G. P. Chaudhari, and M. Qian, "Grain refinement of binary Al-Si, Al-Cu and Al-Ni alloys by ultrasonication," *Journal of Materials Processing Technology*, vol. 249, pp. 367–378, 2017.
- [30] U. Aybarc, H. Yavuz, D. Dispinar, and M. O. Seydibeyoglu, "The use of stirring methods for the production of SiC-reinforced aluminum matrix composite and validation via simulation studies," *International Journal of Metalcasting*, vol. 13, no. 1, pp. 190–200, 2019.
- [31] M. H. Sarfraz, M. Jahanzaib, W. Ahmed, and S. Hussain, "Multi-response parametric optimization of squeeze casting process for fabricating Al 6061-SiC composite," *International Journal of Advanced Manufacturing Technology*, vol. 102, no. 1–4, pp. 759–773, 2019.
- [32] R. Soundararajan, A. Ramesh, N. Mohanraj, and N. Parthasarathi, "An investigation of material removal rate and surface roughness of squeeze casted A413 alloy on WEDM by multi response optimization using RSM," *Journal of Alloys and Compounds*, vol. 685, pp. 533–545, 2016.
- [33] P. Madhukar, N. Selvaraj, C. S. P. Rao, and G. B. Veeresh Kumar, "Tribological behavior of ultrasonic assisted double stir casted novel nano-composite material (AA7150-hBN) using Taguchi technique," *Composites Part B: Engineering*, vol. 175, p. 107136, 2019.
- [34] P. Senthil and K. S. Amirthagadeswaran, "Optimization of squeeze casting parameters for non symmetrical AC2A aluminium alloy castings through Taguchi method," *Journal of Mechanical Science and Technology*, vol. 26, no. 4, pp. 1141–1147, 2012.
- [35] N. Lokesh, J. Sudheerreddy, N. G. Siddeshkumar, and K. Kotresh, "Characterization and evaluation of microstructure and mechanical properties of ZrO₂ reinforced Al6061 metal matrix composite using stir casting process," *Advances in Materials and Processing Technologies*, pp. 1–14, 2022.

Research Article

Optimum Green Synthesis of Silver Nanoparticles with the Highest Antibacterial Activity against *Streptococcus mutans* Biofilm

Azam Chahardoli ¹, Mohsen Safaei ^{2,3}, Mohammad Salmani Mobarakeh ²,
Nima Fallahnia ⁴, Behnam Fatehi ⁴, Mohammad Moslem Imani ⁵,
and Amin Golshah ⁵

¹Department of Biology, Faculty of Science, Razi University, Kermanshah, Iran

²Advanced Dental Sciences Research Center, School of Dentistry, Kermanshah University of Medical Sciences, Kermanshah, Iran

³Division of Dental Biomaterials, School of Dentistry, Kermanshah University of Medical Sciences, Kermanshah, Iran

⁴Students Research Committee, Kermanshah University of Medical Sciences, Kermanshah, Iran

⁵Department of Orthodontics, School of Dentistry, Kermanshah University of Medical Sciences, Kermanshah, Iran

Correspondence should be addressed to Mohsen Safaei; mohsen_safaei@yahoo.com

Received 14 April 2022; Accepted 29 August 2022; Published 19 September 2022

Academic Editor: H C Ananda Murthy

Copyright © 2022 Azam Chahardoli et al. This is an open access article distributed under the Creative Commons Attribution License, which permits unrestricted use, distribution, and reproduction in any medium, provided the original work is properly cited.

Nowadays, resistance to antibiotics has developed in bacterial microorganisms related to dental and oral infections, leading to major problems in public health. Using nanoparticles, particularly silver nanoparticles (AgNPs) may offer a new strategy for the prevention and treatment of dental infections. In the current study, AgNPs were synthesized using *Halomonas elongata* at different conditions according to nine experiments designed by the Taguchi method, and their antibacterial effects were investigated on a *Streptococcus mutans* biofilm. The effects of three factors, including silver nitrate (AgNO₃) concentration, incubation time, and temperature at three different levels, were studied to optimize the synthesis of AgNPs under the designed experiments. Then, the antibacterial effects of these NPs on the *S. mutans* biofilm were examined by the colony-forming unit (CFU) method. According to the results, green-synthesized AgNPs under optimal conditions properly inhibit the formation and growth of the *S. mutans* biofilm. Furthermore, different analyses were applied to investigate the formation, structural, and morphological properties of the green-synthesized AgNPs under optimum conditions. The obtained results of this study indicated that the green-synthesized AgNPs could be a promising antimicrobial agent in the dental and medicinal industry.

1. Introduction

Despite significant therapeutic advances in recent decades, no effective treatment has been found for autoimmune diseases, cancer, and microbial infections [1–3]. The emergence of drug-resistant bacteria has become a main global health concern because it is hard to control these pathogenic strains using commonly available antibiotics [4, 5]. According to a report from the World Health Organization (WHO), resistance to antibiotics has also developed in bacterial microorganisms

related to dental and oral infections [6]. For example, in a study on antibiotic-resistant bacteria, such as oral *Streptococci* from active dental infections, it was shown that 45.9% of *S. mutans* were resistant to clindamycin and moxifloxacin [7]. There are several microorganisms in the oral cavity that may cause oral diseases including caries, periodontitis, and other dental disorders [8]. The majority of dental diseases are caused by the formation of plaque biofilms by a community of bacteria or fungi that protects pathogenic microorganisms from foreign drugs and allows them to escape the host's defenses [9].

Therefore, there is an urgent need to develop and produce new antibacterial agents to control bacterial infections [10]. Due to their large surface area and high charge density, nanoparticles (NPs) may offer a new strategy for the prevention and treatment of dental infections. This is because they interact more with the negatively charged surface of bacterial cells, thereby increasing their antimicrobial activity [8–11].

Among NPs, silver nanoparticles (AgNPs) were introduced as a strong antimicrobial and antibiofilm agent against pathogenic microorganisms, including viruses, bacteria, and eukaryotic microorganisms [4]. Various expensive and environmentally hazardous physical and chemical methods can be used to synthesize AgNPs [12]. Recently, the biological synthesis of NPs using renewable materials (microorganisms and plants), as a safe alternative method, has received huge attention [13]. Green-synthesized NPs have received more attention due to reducing the usage of chemicals, the advantage of ecological friendliness, easy and cost-effective synthesis, energy-efficient approach, etc. [14, 15]. Microorganisms possess the capability to synthesize NPs [16]. Bacteria (the most commonly used microorganisms) have an extraordinary ability to reduce heavy metal ions and are hence considered one of the best candidates for the synthesis of NPs [17]. In recent research, different bacteria such as *Escherichia coli*, *Bacillus subtilis*, *Lactobacillus rhamnosus*, and *Leucas aspera* have been applied to the synthesis of AgNPs [18–21]. Therefore, the present study is aimed at the green synthesis of AgNPs using *Halomonas elongata* as a nonpathogenic Gram-negative proteobacterium at optimum conditions. In addition to the synthesis and characterization of NPs, their highest antibacterial activity against the *S. mutans* biofilm as the main cause of dental caries was investigated in this study.

2. Materials and Methods

2.1. Synthesis of AgNPs using *H. elongata*. Prior to the synthesis of NPs, the bacterial source of *H. elongata* (IBRC-M 10433; Iranian biological resource center) was obtained from the bacterial archive. The obtained strain was cultured in an appropriate sterilized medium, containing glucose (0.2 g), NaCl (3 g), K_2HPO_4 (0.028 g), and $FeSO_4$ (0.0001 g) in an Erlenmeyer flask, and then was incubated at 37°C for 48 h. After the incubation time, the bacteria solution was isolated from the culture medium by centrifugation at 5000 rpm for 10 min. The supernatant was stored for the synthesis of AgNPs, which was optimized using the Taguchi method. According to this method, nine experiments were designed based on different factors, including silver nitrate ($AgNO_3$) concentrations (0.3, 0.6, and 0.9 mg/mL), incubation times (48, 72, and 96 h), and incubation temperatures (27, 32, and 37°C). The synthesis process was started by adding 0.5 mL of the bacterial supernatant to the $AgNO_3$ solution at different concentrations. Then, the reaction solutions were shaken (120 rpm) in an incubator shaker under different temperatures and incubation times. A control sample without bacteria was placed under the same conditions. After the reaction was completed, the formed AgNPs were separated by centrifugation for 15 min at 5000 rpm.

2.2. Antibacterial Effects. The antimicrobial effects of the green-synthesized AgNPs against *S. mutans* were evaluated using colony-forming unit (CFU) methods. From the bacterial archive of the Iranian biological resource center, a strain of *S. mutans* (ATCC 35668) was obtained. *S. mutans* was cultured on brain heart infusion agar (BHIA) medium for 24 h to prepare a new colony. After that, a bacterial suspension (0.5 McFarland) was prepared from the produced colony.

S. mutans was cultured overnight in a BHI broth medium at 37°C to form a bacterial biofilm. Then, the bacterial suspension was inoculated to a 96-well plate and incubated at 37°C for 72 h. Daily, the culture medium was replaced with a fresh BHI broth containing 2% sucrose and 1% mannose. After biofilm formation, it was washed three times with PBS to remove planktonic *S. mutans*. The synthesized AgNPs were then added to each well according to nine experiments designed by the Taguchi method, and the prepared plates were incubated for 24 h. To measure the viable cells in the biofilms, the unattached cells were removed from the wells after incubation at 37°C for 24 h. The adhering cells on the wells were washed (three times), and the resulting suspension was then homogenized using vortex in PBS buffer for 2 min. To test the CFU, the bacterial suspensions were diluted 10 times with BHI broth as a serial dilution. Then, each dilution was cultured on BHIA plates and incubated at 37°C for 24 h. After the incubation time, the number of colonies was counted for nine experiments. All tests were repeated three times.

2.3. Characterization. The characterization of green-synthesized AgNPs was performed using different analysis techniques, including UV-vis (ultraviolet-visible spectrophotometry), FTIR (Fourier transform infrared spectroscopy), XRD (X-ray powder diffraction), FE-SEM (field emission scanning electron microscopy), EDX (energy dispersive X-ray spectroscopy), and TEM (transmission electron microscopy). UV-vis analysis was used to track the bioreduction of silver ions to AgNPs in the wavelength range of 200–800 nm (Thermo Fisher Scientific Company, Wilmington, USA). FTIR spectroscopy between 400 and 4000 cm^{-1} was used to determine the role of functional groups in the synthesis of AgNPs (Thermo Fisher Scientific Company, Wilmington, USA). To determine the crystalline structure of the green-synthesized NPs, an XRD analysis (PHILIPS's PW1730) was performed in the range of 20–80°. The morphology and size of the formed NPs were determined by a field emission scanning electron microscope (FESEM) (TESCAN Company, MIRA III model, Brno, Czech Republic) and TEM (CM120, Philips Company, Eindhoven, Netherlands) analyses. The elemental composition of the synthesized NPs was determined using the EDX analysis.

3. Results and Discussion

3.1. Antibacterial Analysis. To optimize the synthesis of AgNPs with the most potent antibacterial properties, nine Taguchi experiments were designed. Table 1 summarizes the effects of green-synthesized AgNPs under various conditions on the growth inhibition of *S. mutans* biofilms. According to

TABLE 1: Taguchi design of experiments and bacterial growth inhibition rate of green-synthesized AgNPs.

Experiment	AgNO ₃ concentration (mg/mL)			Incubation temperature (°C)			Incubation time (h)			Bacterial viability rate (Log10 CFU/mL)
	0.3	0.6	0.9	27	32	37	48	72	96	
1		0.3			27			48		2.91
2		0.3			32			72		0.94
3		0.3			37			96		1.31
4		0.6			27			72		2.17
5		0.6			32			96		0.61
6		0.6			37			48		2.34
7		0.9			27			96		1.44
8		0.9			32			48		1.12
9		0.9			37			72		1.26

TABLE 2: The main effects of different levels of AgNO₃ concentration, incubation temperature, and incubation time on growth inhibition of *S. mutans* biofilm.

Factors	Level 1	Level 2	Level 3
AgNO ₃ concentration (mg/mL)	1.72	1.71	1.27
Incubation temperature (°C)	2.17	0.89	1.64
Incubation time (h)	2.12	1.46	1.12

TABLE 3: The interaction effects of studied factors on growth inhibiting of *S. mutans* biofilm.

Interacting factor pairs	Column	Severity index (%)	Optimum conditions
AgNO ₃ concentration × incubation time	3 × 1	39.13	[3, 2]
Incubation time × incubation temperature	3 × 2	12.17	[3, 2]
Incubation temperature × AgNO ₃ concentration	2 × 1	8.91	[2, 2]

TABLE 4: The analysis of variance of factors affecting the growth inhibition of *S. mutans* biofilm.

Factors	DOF	Sum of squares	Variance	F ratio (F)	Pure sum	Percent (%)
AgNO ₃ concentration	2	0.39	0.19	69.14	0.38	8.58
Incubation temperature	2	2.49	1.25	444.77	2.49	55.88
Incubation time	2	1.56	0.78	279.17	1.56	35.03

DOF: degree of freedom.

the results, green-synthesized AgNPs in experiment 5 (0.6 mg/mL of AgNO₃, incubation temperature 32°C, and incubation time 96 h) showed the highest antibacterial effects against *S. mutans*. Log CFUs of AgNPs in experiment 5 were the lowest values among the other groups.

Table 2 presents the effect of AgNO₃ concentrations, incubation temperatures, and incubation times on the growth inhibition of the *S. mutans* biofilm. The outcomes showed that the factors of the AgNO₃ concentration and incubation time at level 3 and incubation temperature at level 2 had the greatest impact on the growth inhibition of the *S. mutans* biofilm.

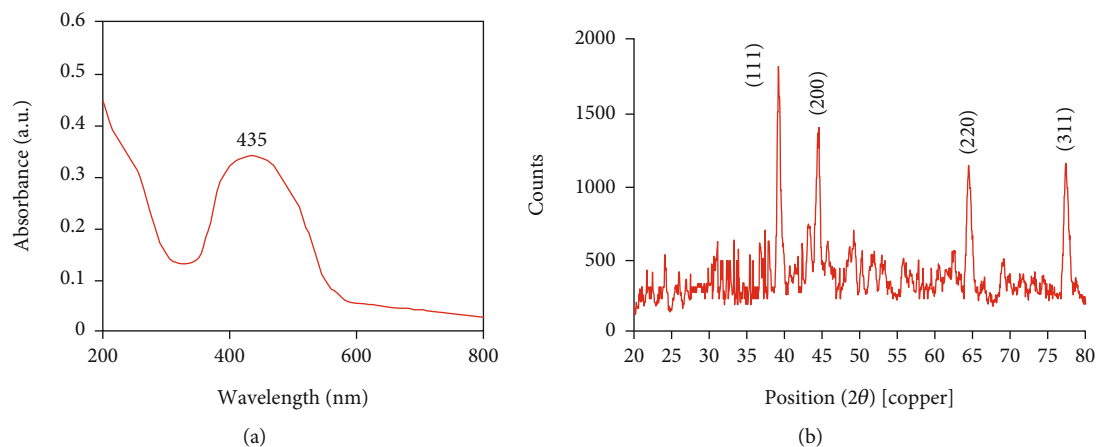
Table 3 presents the interaction between various factors and the inhibition of *S. mutans* biofilm growth. The interac-

tion between AgNO₃ concentration at level 2 and incubation time at level 3 had the greatest effect on the growth inhibition of *S. mutans* biofilm (39.13%). With an intensity index of 12.17%, the interaction between incubation temperature at level 2 and incubation time at level 3 significantly inhibited the growth of *S. mutans* biofilm. The lowest interaction intensity index (8.91%) belonged to the AgNO₃ concentration and incubation temperature at level 2.

Table 4 reveals the analysis of variance for various factors influencing the growth inhibition of *S. mutans* biofilm. The incubation temperature, incubation time, and AgNO₃ concentration with 55.88%, 35.03%, and 8.58% inhibition rates, respectively, showed the greatest effect on the growth inhibition of the *S. mutans* biofilm.

TABLE 5: The optimum conditions for the synthesis of AgNPs with the highest antibiofilm activity.

Factors	Level	Contribution
AgNO ₃ concentration	3	0.29
Incubation temperature	2	0.68
Incubation time	3	0.45
Total contribution from all factors		1.42
Current grand average of performance		1.57
Bacterial growth inhibition at optimum condition		0.15

FIGURE 1: (a) UV-vis spectra and (b) XRD pattern of green-synthesized AgNPs by *H. elongate*.

The optimum conditions for the green synthesis of AgNPs with the maximum antibacterial effects were estimated by analyzing the obtained data from all experiments and investigating the effect of each factor and their interaction (Table 5). Accordingly, the incubation temperature and AgNO₃ concentration showed the highest and the lowest contributions, respectively, to the growth inhibition of the *S. mutans* biofilm. As shown in Table 5, the effect of incubation time on the growth inhibition of the *S. mutans* biofilm is in the middle of the two mentioned factors and is closer to the incubation temperature. It was determined that the third level was ideal for AgNO₃ concentration and incubation time, while the second level was best for incubation temperature. According to the results, it was assessed that the green synthesis of AgNPs under optimal conditions well prevented bacterial activity, which is the closest value to the results of experiment 5 with the lowest Log₁₀ CFU/mL.

The findings of our research are in line with those of Yin et al., who indicated a good antimicrobial effect of green-synthesized spherical AgNPs using epigallocatechin gallate with a diameter of 17 ± 7 nm against the *S. mutans* biofilm [22]. Tavaf et al. showed the antibiofilm activity of green-synthesized AgNPs using *E. coli* (with an average size of 56.1 nm) against *S. mutans* [23].

As reported previously, *S. mutans* is the main oral pathogen causing dental caries and is connected with other systemic diseases, including bacteremia and infective endocarditis. The adhesion of this stain on tooth surfaces

is the main reason for their high cariogenicity [24]. Therefore, green-synthesized AgNPs in the present study with good antibiofilm activity can be an effective agent in the treatment of oral infections or dental caries as well as an alternative way to overcome multi-drug-resistant bacterial infections. The size, ion release capacity, the presence of capping agents, and other physicochemical properties can play a vital role in the antimicrobial activity of AgNPs against various microorganisms such as *S. mutans* [19, 20].

3.2. Physicochemical Characterization of Green-Synthesized AgNPs. In the current study, the bioreduction of Ag⁺ ions to AgNPs using *H. elongata* occurred by changing the color of reaction solutions to brown. The physicochemical properties of green-synthesized AgNPs were analyzed by different techniques such as UV-vis, FTIR, XRD, EDX, FE-SEM, and TEM. Figure 1(a) shows the UV-vis spectrum of AgNPs. The characteristic surface plasmon resonance (SPR) peak for the green-synthesized AgNPs was examined by observing the color change and then by analyzing the maximum absorbance in the range of 400–450 nm, which is evidence of the presence of AgNPs SPR [13]. The maximum absorbance peak of the green-synthesized AgNPs was recorded at 435 nm, which confirmed the production of AgNPs using *H. elongate* strain. The XRD pattern of green-synthesized AgNPs is shown in Figure 1(b). The diffraction peaks at 2θ values of 39.12°, 44.46°, 64.51°, and 77.41° corresponding to reflection peaks of (111), (200), (220), and (311) planes, respectively, revealed

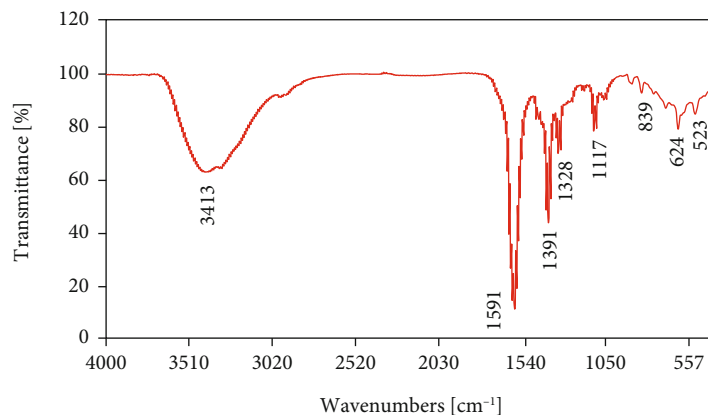


FIGURE 2: FTIR spectrum of green-synthesized AgNPs by *H. elongate*.

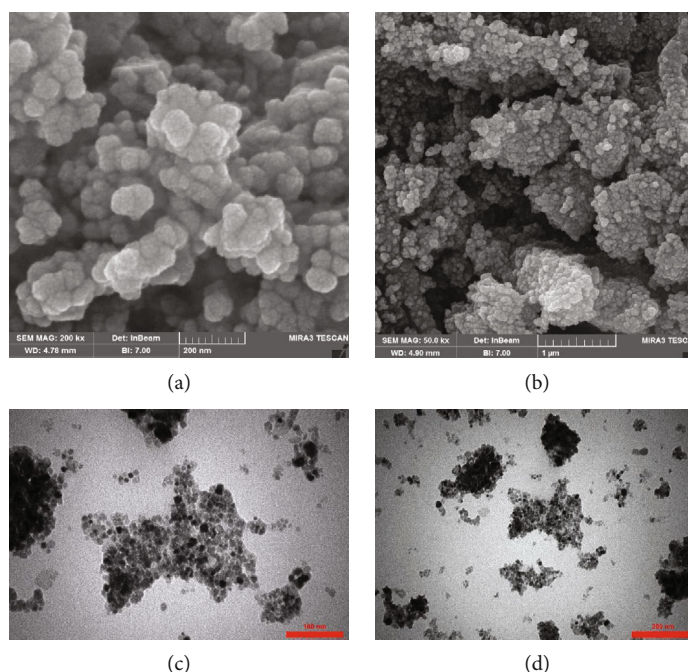


FIGURE 3: The FESEM (a and b) and TEM images (c and d) of green-synthesized AgNPs by *H. elongate*.

the crystalline nature of these AgNPs with a face-centered cubic (fcc) structure. All peaks match with the JCPDS database card No. 04-0783. As shown in Figure 1(b), no additional peaks were observed in the XRD pattern, which confirms the purity of the green-synthesized AgNPs. The highest was found corresponding to the plane (111); thus, this will be the preferred orientation of the cubic structure.

The FTIR spectra of the green-synthesized AgNPs in the range of 400–4000 cm^{-1} are shown in Figure 2. The peaks observed at 3413 and 1591 cm^{-1} correspond to OH and C=O groups, which may be related to bacterial proteins. The peak at 624 cm^{-1} indicates the -CH bond of amino acids in the proteins. The FTIR analysis provides evidence of protein coating on the surface of green-synthesized AgNPs. This means that the proteins in the bacterial extract have more

affinity to bind with Ag^+ ions and act as capping and stabilizing agents, thus reducing the aggregation of produced AgNPs [25, 26]. The peaks in the range of 1380–1410 cm^{-1} belong to strong S=O stretching for sulfonyl chloride [27]. In addition, a band at 1117 cm^{-1} is due to the C–N stretch of aliphatic amines. The peak at 523 cm^{-1} may be due to the presence of Ag–O or pure AgNPs [28].

The morphological and structural features of the green-synthesized AgNPs from *H. elongate*, studied by the FESEM images (Figures 3(a) and 3(b)), showed a high density of green-synthesized AgNPs. According to this analysis, the green-synthesized AgNPs with crystalline nature represented nearly spherical morphology with some aggregates. Images showed that the size of AgNPs ranged between 10 and 80 nm. Furthermore, the TEM images (Figures 3(c)

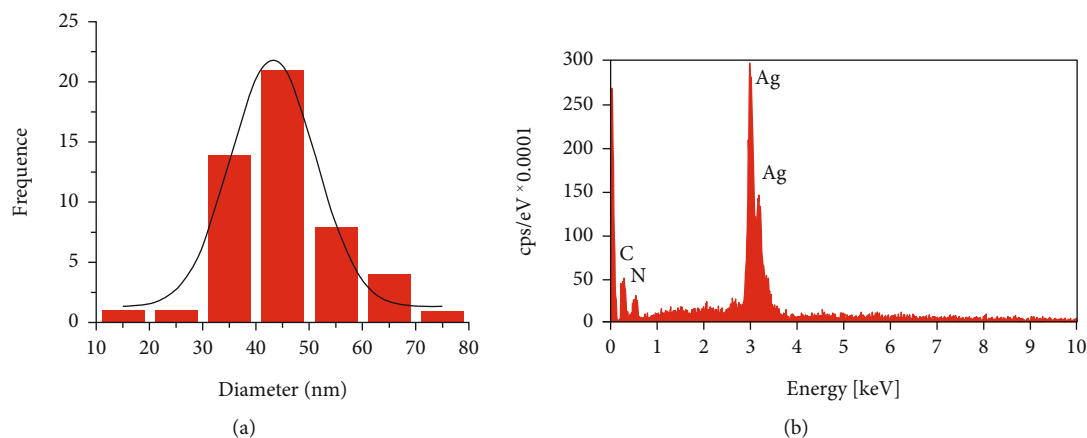


FIGURE 4: (a) Histogram of particle size distribution curve and (b) EDX spectrums of green-synthesized AgNPs by *H. elongate*.

and 3(d)) confirmed the spherical (mostly) and cubic morphologies of the prepared AgNPs. Larger particles are observed from the aggregation of small particles, which may be due to small amounts of observed biological agents or proteins on the surface of AgNPs. Based on the microscopic analyses and the size distribution histogram of green-synthesized AgNPs (Figure 4(a)), the average diameter of nanoparticles was 45 nm. The EDX analysis (Figure 4(b)) revealed the presence of the constituent elements and the purity of the AgNPs produced by green synthesis. These elements included a high amount of silver (80.62%w) and low amounts of carbon (14.75%w) and nitrogen (4.64%w).

4. Conclusion

In the current study, the Taguchi method was applied to optimize the green synthesis process of AgNPs using *H. elongate* as a nonpathogenic bacterial material. At optimal conditions, various techniques (UV-vis, XRD, FTIR, FESEM, and TEM) were used to characterize these NPs. The antibacterial effects of green-synthesized AgNPs were also evaluated against the *S. mutans* biofilm as the famous pathogen of dental caries based on the CFU. The average diameter of these NPs with the most spherical shape measured 45 nm. According to the results of this study, green-synthesized AgNPs in optimal conditions showed higher antibacterial effects. The result confirmed the effective function of these NPs as antibacterial or antibiofilm agents. Therefore, these NPs can be used in dentistry, especially in the treatment of oral infections or dental caries.

Data Availability

The data used to support the findings of this study are included within the article.

Conflicts of Interest

The authors declare that they have no conflicts of interest.

Acknowledgments

The authors gratefully acknowledge the Research Council of Kermanshah University of Medical Sciences (Grant number 990309) for the financial support.


References

- [1] H. R. Mozaffari, E. Zavattaro, A. Abdollahnejad et al., "Serum and salivary IgA, IgG, and IgM levels in oral lichen planus: a systematic review and meta-analysis of case-control studies," *Medicina*, vol. 54, no. 6, p. 99, 2018.
- [2] H. R. Mozaffari, M. Payandeh, M. Ramezani, M. Sadeghi, M. Mahmoudiahmadabadi, and R. Sharifi, "Efficacy of palifermin on oral mucositis and acute GVHD after hematopoietic stem cell transplantation (HSCT) in hematology malignancy patients: a meta-analysis of trials," *Współczesna Onkologia*, vol. 21, no. 4, pp. 299–305, 2017.
- [3] M. Safaei, M. Taran, M. M. Imani et al., "Application of Taguchi method in the optimization of synthesis of cellulose-MgO bionanocomposite as antibacterial agent," *Polish Journal of Chemical Technology*, vol. 21, no. 4, pp. 116–122, 2019.
- [4] M. Huq, "Green synthesis of silver nanoparticles using *Pseudoduganella eburnea* MAHUQ-39 and their antimicrobial mechanisms investigation against drug resistant human pathogens," *International Journal of Molecular Sciences*, vol. 21, no. 4, p. 1510, 2020.
- [5] M. Safaei, M. Taran, L. Jamshidy et al., "Optimum synthesis of polyhydroxybutyrate-Co₃O₄ bionanocomposite with the highest antibacterial activity against multidrug resistant bacteria," *International Journal of Biological Macromolecules*, vol. 158, pp. 477–485, 2020.
- [6] A. Meinen, A. Reuss, N. Willrich et al., "Antimicrobial resistance and the spectrum of pathogens in dental and oral-maxillofacial infections in hospitals and dental practices in Germany," *Frontiers in Microbiology*, vol. 12, p. 1418, 2021.
- [7] J. P. Loyola-Rodriguez, M. E. Ponce-Diaz, A. Loyola-Leyva et al., "Determination and identification of antibiotic-resistant oral streptococci isolated from active dental infections in adults," *Acta Odontologica Scandinavica*, vol. 76, no. 4, pp. 229–235, 2018.
- [8] W. Song and S. Ge, "Application of antimicrobial nanoparticles in dentistry," *Molecules*, vol. 24, no. 6, p. 1033, 2019.

- [9] E. T. Enan, A. A. Ashour, S. Basha, N. H. Felemban, and S. M. F. Gad El-Rab, "Antimicrobial activity of biosynthesized silver nanoparticles, amoxicillin, and glass-ionomer cement against *Streptococcus mutans* and *Staphylococcus aureus*," *Nanotechnology*, vol. 32, no. 21, article 215101, 2021.
- [10] H. Moradpoor, M. Safaei, F. Rezaei et al., "Optimisation of cobalt oxide nanoparticles synthesis as bactericidal agents," *Open access Macedonian journal of medical sciences*, vol. 7, no. 17, pp. 2757–2762, 2019.
- [11] H. Moradpoor, M. Safaei, H. R. Mozaffari et al., "An overview of recent progress in dental applications of zinc oxide nanoparticles," *RSC Advances*, vol. 11, no. 34, pp. 21189–21206, 2021.
- [12] A. Lateef, I. A. Adelere, E. B. Gueguim-Kana, T. B. Asafa, and L. S. Beukes, "Green synthesis of silver nanoparticles using keratinase obtained from a strain of *Bacillus safensis* LAU 13," *International Nano Letters*, vol. 5, no. 1, pp. 29–35, 2015.
- [13] A. Chahardoli, N. Karimi, and A. Fattahi, "Nigella arvensis leaf extract mediated green synthesis of silver nanoparticles: their characteristic properties and biological efficacy," *Advanced Powder Technology*, vol. 29, no. 1, pp. 202–210, 2018.
- [14] B. S. Surendra, C. Mallikarjunaswamy, S. Pramila, and N. D. Rekha, "Bio-mediated synthesis of ZnO nanoparticles using *Lantana camara* flower extract: its characterizations, photocatalytic, electrochemical and anti-inflammatory applications," *Environmental Nanotechnology, Monitoring & Management*, vol. 15, article 100442, 2021.
- [15] B. S. Surendra, T. Kiran, M. V. Chethana, H. S. Savitha, and M. S. Paramesh, "Cost-effective Aegle marmelos extract-assisted synthesis of ZnFe₂O₄: Cu²⁺ NPs: photocatalytic and electrochemical sensor applications," *Journal of Materials Science: Materials in Electronics*, vol. 32, no. 20, pp. 25234–25246, 2021.
- [16] C. Wang, Y. J. Kim, P. Singh, R. Mathiyalagan, Y. Jin, and D. C. Yang, "Green synthesis of silver nanoparticles by *Bacillus methylotrophicus*, and their antimicrobial activity," *Artificial Cells, Nanomedicine, and Biotechnology*, vol. 44, no. 4, pp. 1–6, 2016.
- [17] T. Mustapha, N. Misni, N. R. Ithnin, A. M. Daskum, and N. Z. Unyah, "A review on plants and microorganisms mediated synthesis of silver nanoparticles, role of plants metabolites and applications," *International Journal of Environmental Research and Public Health*, vol. 19, no. 2, p. 674, 2022.
- [18] K. Divya, L. C. Kurian, S. Vijayan, and J. Manakulam Shaikmoideen, "Green synthesis of silver nanoparticles by *Escherichia coli*: analysis of antibacterial activity," *Journal of Water and Environmental Nanotechnology*, vol. 1, no. 1, pp. 63–74, 2016.
- [19] K. I. Alsamhary, "Eco-friendly synthesis of silver nanoparticles by *Bacillus subtilis* and their antibacterial activity," *Saudi Journal of Biological Sciences*, vol. 27, no. 8, pp. 2185–2191, 2020.
- [20] S. M. Aziz Mousavi, S. A. Mirhosseini, M. Rastegar Shariat Panahi, and H. Mahmoodzadeh Hosseini, "Characterization of biosynthesized silver nanoparticles using *Lactobacillus rhamnosus* gg and its in vitro assessment against colorectal cancer cells," *Probiotics and Antimicrobial Proteins*, vol. 12, no. 2, pp. 740–746, 2020.
- [21] H. Zhang, T. Li, W. Luo, G. X. Peng, and J. Xiong, "Green synthesis of Ag nanoparticles from *Leucos aspera* and its application in anticancer activity against alveolar cancer," *Journal of Experimental Nanoscience*, vol. 17, no. 1, pp. 47–60, 2022.
- [22] I. X. Yin, O. Y. Yu, I. S. Zhao et al., "Developing biocompatible silver nanoparticles using epigallocatechin gallate for dental use," *Archives of Oral Biology*, vol. 102, pp. 106–112, 2019.
- [23] Z. Tavaf, M. Tabatabaei, A. Khalafi-Nezhad, and F. Panahi, "Evaluation of antibacterial, antibiofilm and antioxidant activities of synthesized silver nanoparticles (AgNPs) and casein peptide fragments against *Streptococcus mutans*," *European Journal of Integrative Medicine*, vol. 12, pp. 163–171, 2017.
- [24] Á. Martínez-Robles, J. Loyola-Rodríguez, N. Zavala-Alonso et al., "Antimicrobial properties of biofunctionalized silver nanoparticles on clinical isolates of *Streptococcus mutans* and its serotypes," *Nanomaterials*, vol. 6, no. 7, p. 136, 2016.
- [25] F. Jalilian, A. Chahardoli, K. Sadrajavadi, A. Fattahi, and Y. Shokoohinia, "Green synthesized silver nanoparticle from *Allium ampeloprasum* aqueous extract: characterization, antioxidant activities, antibacterial and cytotoxicity effects," *Advanced Powder Technology*, vol. 31, no. 3, pp. 1323–1332, 2020.
- [26] M. Saravanan, S. K. Barik, D. Mubarak Ali, P. Prakash, and A. Pugazhendhi, "Synthesis of silver nanoparticles from *Bacillus brevis* (NCIM 2533) and their antibacterial activity against pathogenic bacteria," *Microbial Pathogenesis*, vol. 116, pp. 221–226, 2018.
- [27] M. M. Al-Ansari, N. D. Al-Dahmash, and A. J. A. Ranjitsingh, "Synthesis of silver nanoparticles using gum Arabic: evaluation of its inhibitory action on *Streptococcus mutans* causing dental caries and endocarditis," *Journal of Infection and Public Health*, vol. 14, no. 3, pp. 324–330, 2021.
- [28] I. A. Wani, "Review—recent advances in biogenic silver nanoparticles and nanocomposite based plasmonic-colorimetric and electrochemical sensors," *ECS Journal of Solid State Science and Technology*, vol. 10, no. 4, article 047003, 2021.

Research Article

Investigation of High-Temperature Wear Behaviour of AA 2618-Nano Si₃N₄ Composites Using Statistical Techniques

Santhi M. George,¹ Amel Gacem,² A. Kistan,³ R. Mohammed Ashick,⁴ L. Malleswara Rao,⁵ Vinod Singh Rajput,⁶ N. Nagabooshanam,⁷ Moamen S. Refat,⁸ Annah Mohammed Alsuhaibani,⁹ and David Christopher ¹⁰

¹Department of Science and Humanities, RMK Engineering College, Thiruvallur, Tamil Nadu 601206, India

²Department of Physics, Faculty of Sciences, University 20 Août 1955, 26 El Hadaiek, Skikda 21000, Algeria

³Department of Chemistry, Panimalar Engineering College, Chennai, Tamil Nadu 600123, India

⁴Department of Civil Engineering, Sri Sairam Engineering College, Chennai, Tamil Nadu 600044, India

⁵Department of Physics, SRI Y N College, Narsapur, West Godavari, Andhra Pradesh 534275, India

⁶Department of Mechanical Engineering, Nowgong Engineering College, Nowgong, Chhatarpur, Madhya Pradesh 471201, India

⁷Department of Mechanical Engineering, Aditya Engineering College, ABD Road, Surampalem, 533437 Andhra Pradesh, India

⁸Department of Chemistry, College of Science, Taif University, P.O. Box 11099, Taif 21944, Saudi Arabia

⁹Department of Physical Sport Science, College of Education, Princess Nourah bint Abdulrahman University, P.O. Box 84428, Riyadh 11671, Saudi Arabia

¹⁰Department of Mechanical Engineering, College of Engineering, Wolaita Sodo University, Ethiopia

Correspondence should be addressed to David Christopher; david.santosh@wsu.edu.et

Received 8 May 2022; Revised 17 July 2022; Accepted 18 July 2022; Published 16 September 2022

Academic Editor: Arpita Roy

Copyright © 2022 Santhi M. George et al. This is an open access article distributed under the Creative Commons Attribution License, which permits unrestricted use, distribution, and reproduction in any medium, provided the original work is properly cited.

The wear behaviour of hot pressed AA 2618 aluminium alloy matrix composites reinforced through nano Si₃N₄ elements (1 percent and 2 percent) has been investigated in this paper. Temperatures of 50°C, 150°C, and 250°C were used to examine the tribological characteristics of the models under a range of loads and pressures. The best wear performance was found in AA 2618/2wt percent Si₃N₄. Under a load of 30 N and temperature of 250°C, it was discovered that Si₃N₄-enriched AA 2618 alloy was 35.7% more wear-resistant than unreinforced AA 2618 alloy. Metal flow and plain delamination were the most common wear mechanisms at higher temperatures. Delamination is the most common wear mechanism at temperatures between 50 and 250 degrees Celsius. In the analysis of variance, the wear rate was influenced by temperature, load, and the presence of Si₃N₄ by 47.2%. In order to predict the wear rate, regression equations (linear and nonlinear) were developed by Taguchi method. Using a high determination coefficient, the nonlinear regression was the preeminent success rate (92.8 percent).

1. Introduction

Lightweight, inexpensive, and energy-efficient alloys are becoming increasingly popular. It is broadly used in the automotive industries for its maximum specific strength, corrosion resistance, and excellent low-temperature properties [1]. Although Al alloys have some drawbacks, the most significant one is their less amount of wear and mechanical properties at higher temperatures [2, 3]. Al metal matrix

composites have been developed to address these shortcomings (AMMCs). Al MMCs are commonly reinforced with a variety of materials, including SiC, Al₂O₃, B₄C, TiC, CNT, GNPs, GO, and Y₂O₃ [4]. Since Si₃N₄ has a high melting point and good thermal conductivity, it was a natural choice for Al MMC reinforcement. Research into MMCs' wear and friction patterns is essential [5–7]. In the event that two surfaces are in close proximity to each other, material loss can occur. Consequently, wear has become a major cause of

failure. MMCs wear more quickly when subjected to varying loads, sliding speeds, temperatures, and reinforcement content [8, 9]. Statistics and the Taguchi method have become increasingly popular in the field of materials science in recent years. The Taguchi method reduces the amount of time and money required to conduct experiments in order to optimise design parameters [10]. Wear rates and friction coefficients can be studied using the analysis of variance method. Wear rate is also predicted using a regression model. The wear behaviour of AA 2618 matrix composites has been studied by researchers. In addition to silicon carbide, aluminium oxide, and carbon nanotubes, a variety of reinforcements were used [11, 12]. While some research has been done on the tribological performance of stir cast AA 2618/Si₃N₄ composite (wt% of 3, 6, and 9 Si₃N₄ content), only a few studies have focused on the properties of 6 percent Si₃N₄. AA 2618/Si₃N₄ (4 wt%) composites were stir casted to investigate the dry sliding wear behaviour [13]. They found that composites have a higher wear resistance than AA 2618 alloy without reinforcement. It has dry sliding tribological properties at elevated temperatures between 30 and 300 degrees Celsius. The fabricated MMCs by stir casting were attributed to the increase in wear resistance [14–16]. The wear performance of AA 2618-SiC-hSi₃N₄ nanocomposites has been improved by the addition of SiC and hSi₃N₄ particles [17–20]. There have been numerous studies on AA 2618/Si₃N₄ composites based on the literature. A liquid metallurgy production method was used in these studies [21]. Additionally, statistical analysis was not used to examine the wear behaviour of the samples. Furthermore, no research has been done on the wear behaviour of monolithic AA 2618/Si₃N₄ composites made by powder metallurgy at elevated temperatures [22–26]. Fuselage structures below tension frequently use AA 2618 alloy because of its high specific strength, good machinability, and high fatigue strength and thermal conductivity [27]. The AA 2618 alloy's tribological performance is known to be poor at high temperatures. Ceramic particles have been added to AA 2618 alloy in order to increase its usefulness in high-temperature applications [28–30]. It is revealed that AA 2618 wear behaviour at elevated temperatures must be studied and improved. An investigation into hot pressing AA 2618/Si₃N₄ composites armoured with Si₃N₄ (1% wt and 2% wt) was primary goal of this research [31]. Different parameters (such as load, Si₃N₄ content, and temperature) were examined for their effects on wear rate using analysis of variance and regression models. It was also used in the search for the best process parameter that had the lowest wear rate [32–34].

2. Experimental Studies

2.1. Production and Materials. AA 2618 alloy powder was used as a matrix material in this research. Because of its ability to work at higher temperatures, AA 2618 is frequently used as pistons and spinning aviation components, as well as in automotive racing. The AA 2618 alloy chemical composition was determined to be 4.7Cu, 1.6Mg, 0.6Zn, 0.5Mn, and 0.2Si and a weight percentage of Al that was bal-

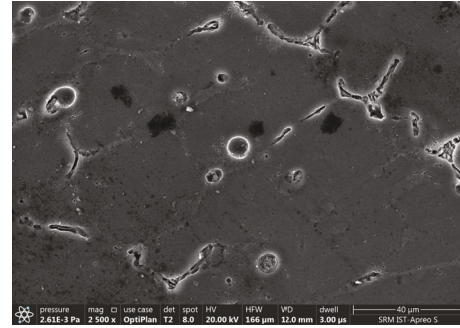


FIGURE 1: SEM image of powder used.

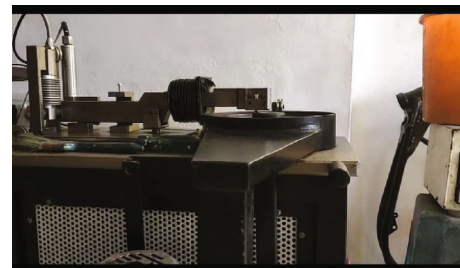


FIGURE 2: Pin on disc wear setup.

TABLE 1: Test parameters for measuring wear.

Levels	Applied load, N	Temperature °C	Wt percent of silicon nitrate
1	15	50	0
2	30	150	1
3	45	250	2

anced. Reinforcement was provided by Si₃N₄ nanoparticles (100 nm). The composites were made using semi-powder metallurgy. To separate the agglomerated particles, Si₃N₄ particles were ultrasonically treated in ethanol for one hour. Next, AA 2618 alloy powder was added to the solution containing Si₃N₄ nanoparticles. In a vacuum distillation system, a magnetic stirrer was used to mix the powders (AA 2618 alloy and Si₃N₄). After three hours, all of the ethanol had been flushed from the system. Previous studies provided a schematic diagram and detailed explanation of semi-powder metallurgy. Si₃N₄ nanoparticles of 0, 1, and 2wt percent were used in the samples. One hour of hot pressing at 525°C under 50 MPa pressure produced the test specimens. The rate of heating was 10°C/min. In an argon atmosphere, all the processes were carried out. Due to the size requirements of this study, the attained samples of 15 mm x 23 mm were maintained. Figure 1 shows SEM image of powder used.

2.2. Mechanical and Wear Tests. A hardness test device was used to take the hardness measurements. It was necessary to

TABLE 2: Specimens' densities and hardness.

Materials	(density) _{theoretical} g/cm ³	(density) _{Experimental} g/cm ³	(density) _{Relative} g/cm ³	Hardness, HV	% of raise in hardness
AA 2618	3.71	3.76	97.1	81.4 ± 3.6	92.4 ± 1.6
AA 2618/1% silicon nitrate	3.82	3.780	98.4	98.1	94.8 ± 1.9
AA 2618/2% silicon nitrate	3.78	3.798	9.4	16.2	10

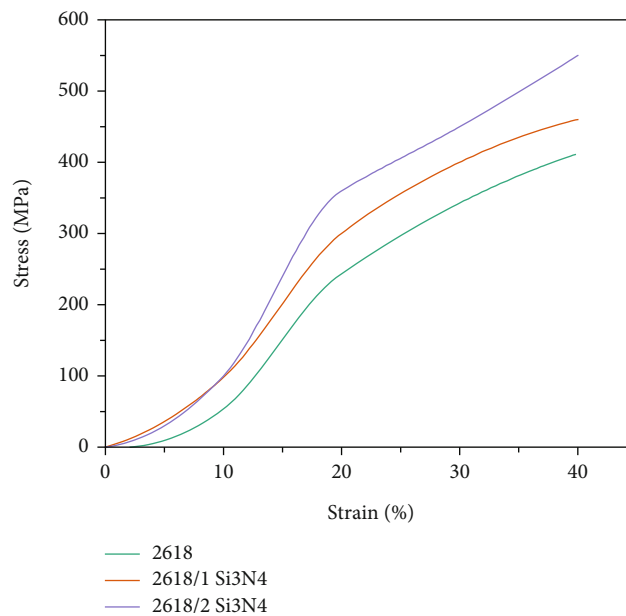


FIGURE 3: Curves of the samples' compression stress and strain.

conduct precise measurements using the metallographic preparation. A 1 kg load and a dwell time of 20 seconds were used to measure hardness. The average of five successful indentations was calculated. A universal testing machine with a 0.5 mm/min test speed was used for the compression tests. A pin-on-disc test device was used to conduct wear tests under dry sliding conditions. Temperatures ranging from 50 to 250 degrees Celsius were used for wear tests at a sliding speed of 120 millimetres per second with loads of 15 to 45 Newtons. The sliding distance was 200 metres. The AISI 52100 steel used for the counterface had a hardness rating of 63 HRC. Figure 2 shows pin on disc wear setup.

2.3. The Experiment Design. The Taguchi method was used with three factors and three levels. Si₃N₄ content, load, and temperature were all factors in the experiment. Table 1 provides the values of the parameters. The Taguchi design used the L27 array.

3. Results and Discussion

Table 2 displays the specimens' densities and hardness of the produced composites.

TABLE 3: Fabricated samples' mechanical properties.

Materials	Grain size,	CYS, Mpa	UCS
AA 2618	20.2	276.2 ± 11.2	516.7 ± 14.2
AA 2618/1% silicon nitrate	19.4	302.6 ± 10.2	591.6 ± 23.4
AA 2618/2% silicon nitrate	15.6	324.6 ± 9.1	665.8 ± 20.1

3.1. Mechanical Properties. According to these results, increasing the amount of Si₃N₄ results in greater compressive yield strength (CYS) and ultimate compressive strength (UCS). Comparing the CYS and UCS of the AA 2618/2Si₃N₄ composite to those of the AA 2618 alloy, 17.2% and 28.9% increases were observed. Figure 3 shows the curves of the samples compression stress and strain. Table 3 summarises the mechanical properties and average grain size for each type of cereal grain. The dislocations are also slowed by the presence of reinforcing particles. Due to the occurrence of reinforcement elements and an increased grain boundary area as a result of grain refinement, dislocation movement

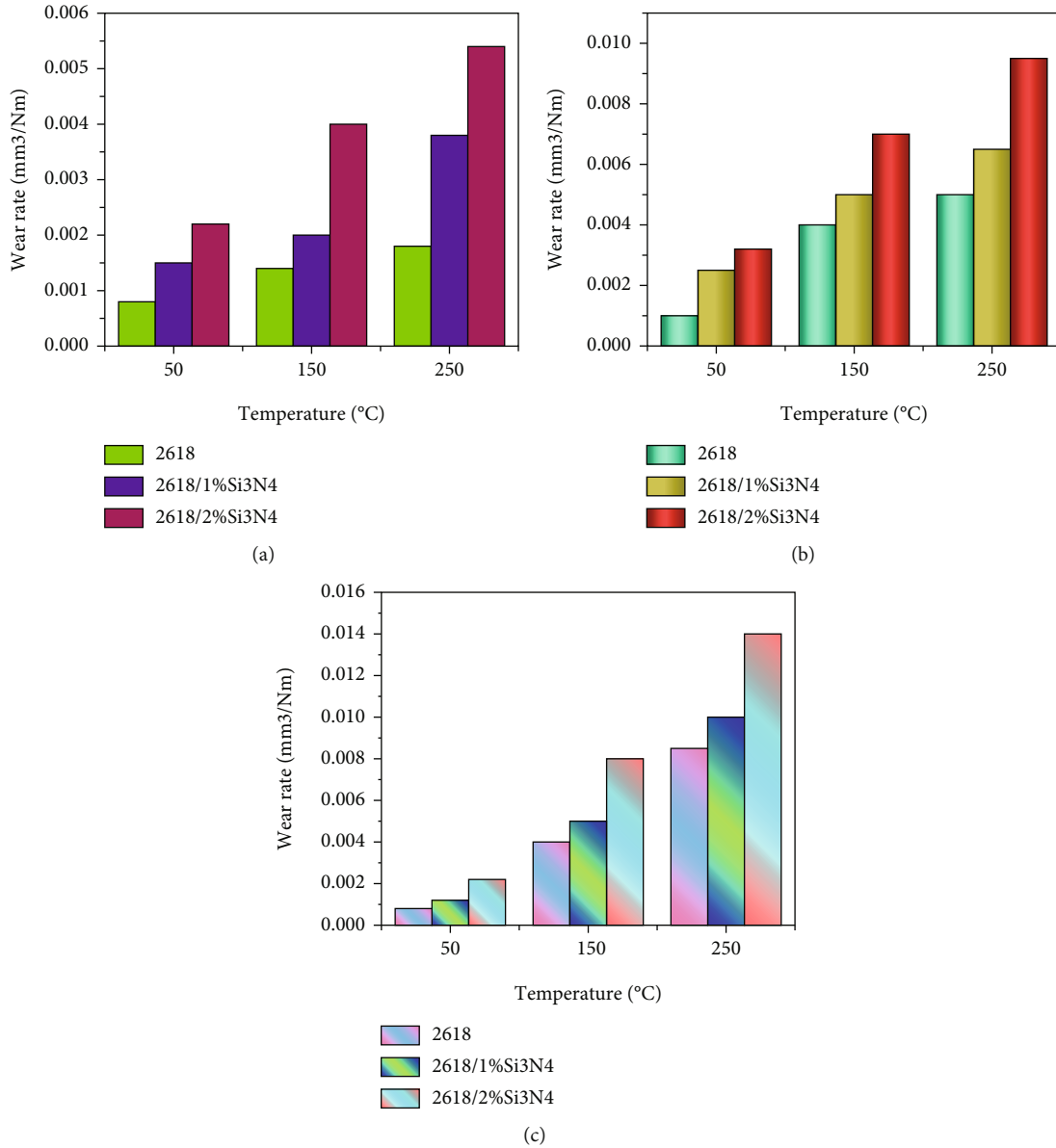


FIGURE 4: Temperature affects the rate of wear on the load: (a) 50°C, (b) 150°C, and (c) 250°C.

is hindered As a result, the strongest material has the smallest grain size. Grain size decreases as the Si₃N₄ content increases. AA 2618/1Si₃N₄ and AA 2618/2Si₃N₄ reduced the grain size by 7.8 percent and 21.9 percent, respectively, when compared to the AA 2618 alloy. Sintering grain refinement may be attributed to the hard Si₃N₄ elements in the structure acting as a wall to grain limit movement. There is also evidence to suggest that nano-reinforcement slows down grain growth by causing pinning at grain boundaries. It is also crucial to have a mechanism for transferring the weight of the load. The transmission of loads from the soft matrix to hard fortification particles has been credited with increasing the strength of composite materials. The interfacial bonding between the matrix material and the reinforcement particles is responsible for the increased strength.

Using Si₃N₄ particles, the researchers were able to transfer loads from a matrix to a reinforcement. Al matrix composites reinforced with nanoparticles can also benefit from the Orowan strengthening mechanism. Nanoparticles are used to form residual dislocation loops in the Orowan strengthening mechanism. The back stress created by the dislocation loops prevents the dislocation from moving forward. Composite materials become stronger as a result.

3.2. Wear Results

3.2.1. *The Effect of Load on the Rate of Wear.* There was a clear correlation between increasing load and increasing wear rate at all temperatures. Aside from that, the AA 2618/2Si₃N₄ composite's wear rate was the lowest. The

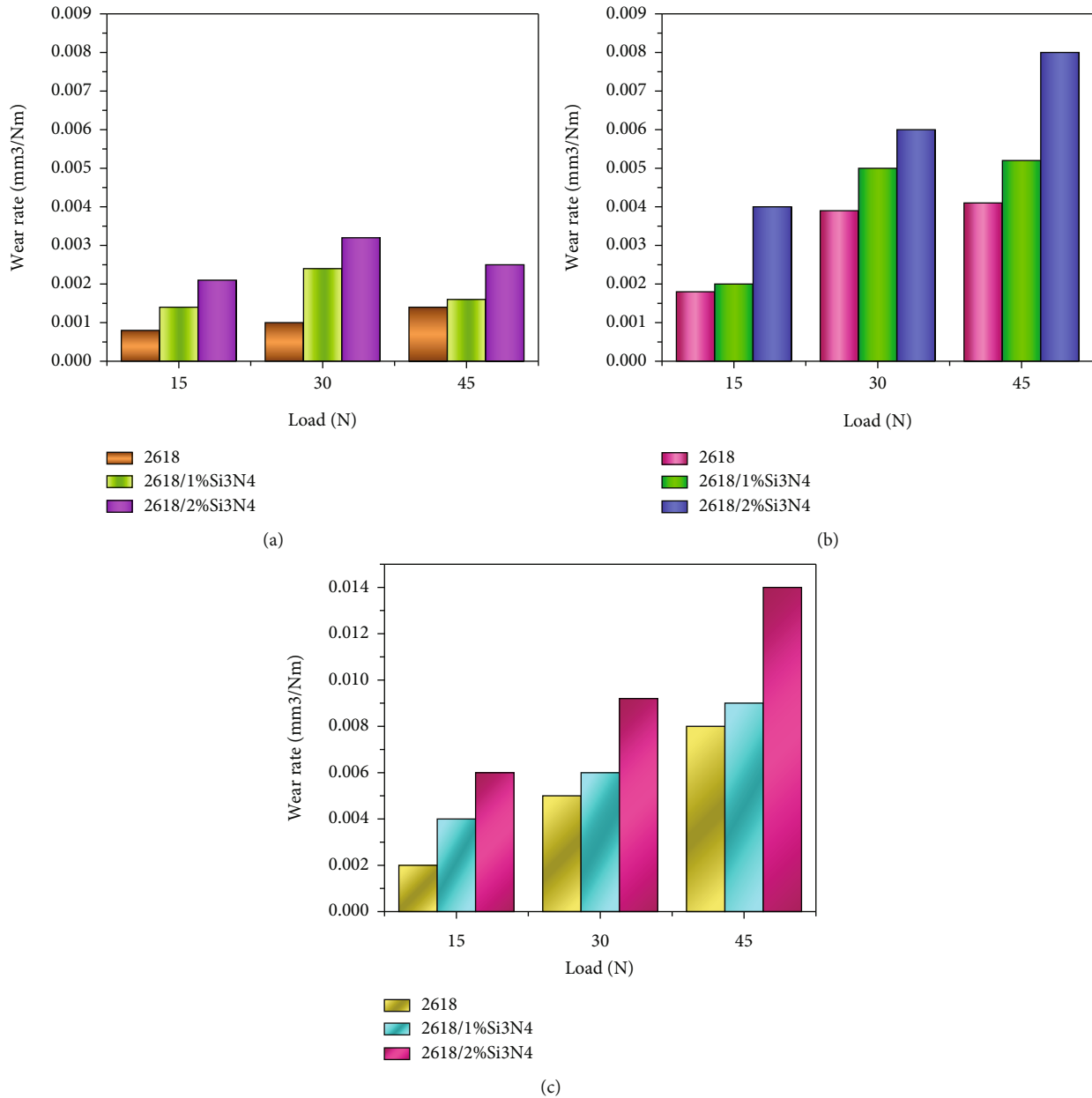


FIGURE 5: Temperature-dependent wear rates under a variety of load conditions: (a) 15 N, (b) 30 N, and (c) 45 N.

lubricating effect of Si₃N₄ particles contributes to the improved wear resistance of composites. Due to the Si₃N₄ particles, composite materials have a lower rate of wear because the metallic contact between sliding surfaces is reduced. A 45 N load on AA 2618/2Si₃N₄ reduces wear rates by 45.8 percent, 42.1 percent, and 35.7 percent compared to an unreinforced alloy at 50°C, 150°C, and 250°C. As the temperature rises, the wear rates of the samples also increase significantly. At temperatures of 50°C, 150°C, and 250°C, AA 2618 has a wear rate of 0.0024 mm⁻³/Nm. for the alloy, according to research.

Dislocation density increases when there is a mismatch in thermal expansion. This has a significant impact on the hardness of composite materials. Grains of AA 2618/Si₃N₄

composites have fewer grain boundaries, resulting in a higher wear resistance. The dislocation movement is hindered by the increased grain boundaries. The improvement in tribological performance was attributed to this. The improved wear performance of AA 2618/Si₃N₄ composites is due to the increased hardness and mechanical properties of the strengthening mechanisms.

3.2.2. Temperature Effect on Wear Rate. With increasing Si₃N₄ content at temperatures between 50 and 250 degrees Celsius, the wear rate of AA 2618/Si₃N₄ composites is reduced. Al matrix thermal stability is said to improve as the amount of Si₃N₄ in the alloy increases. The wear rate of the models also increases the temperature of the test

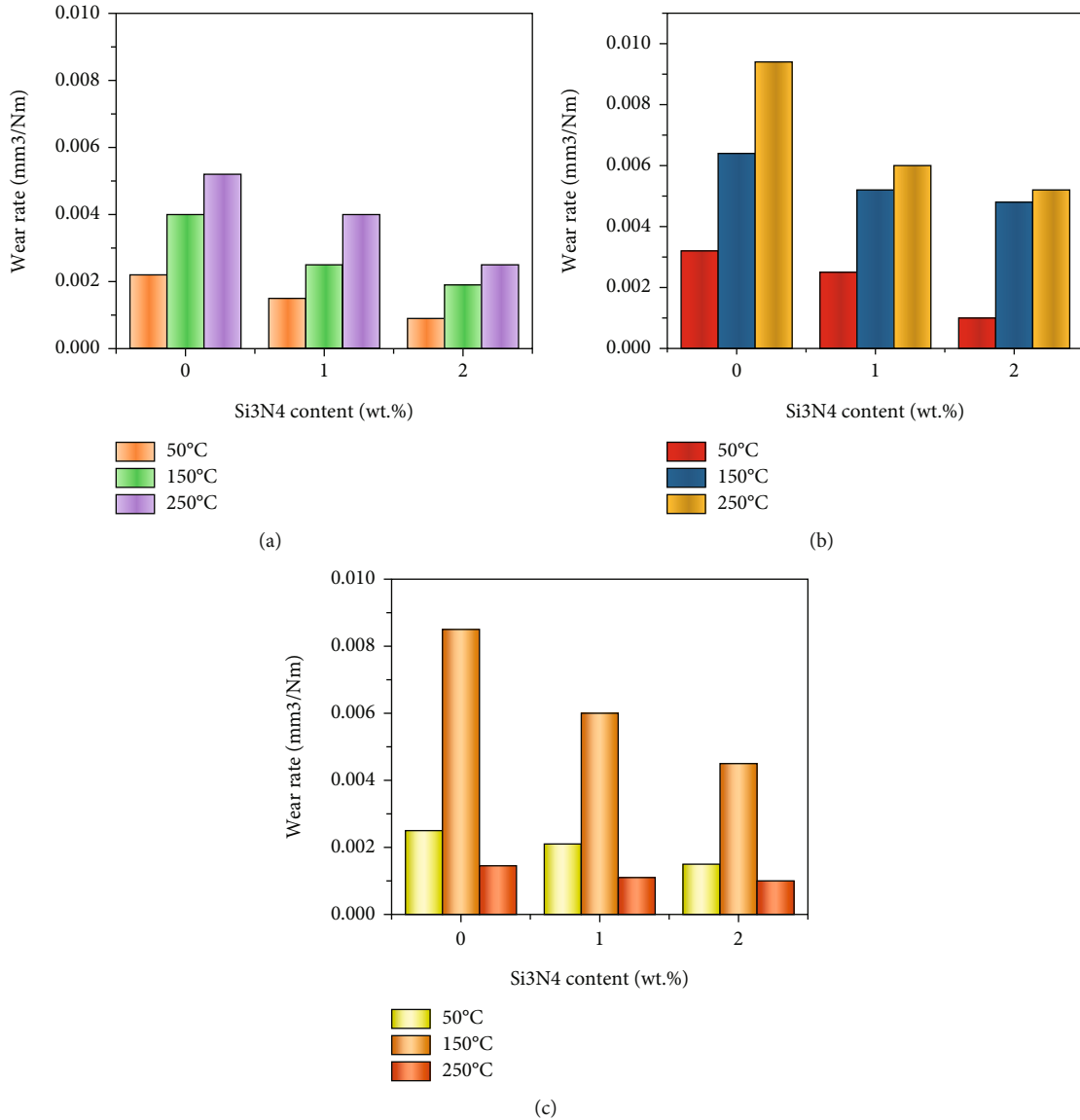


FIGURE 6: Si₃N₄ content's wear rate under various loads: (a) 15 N, (b) 30 N, and (c) 45 N.

increases. As the test temperature rises, the softening trend becomes more pronounced.

3.2.3. Effect of Wear Rate on Silicon Nitride. AA 2618 alloy wear rate is thought to be affected by silicon nitride content below 15 N, 30 N, and 45 N loads at temperatures of 50°C, 150°C, and 250°C. After adding Si₃N₄, the wear performance was noticeably improved in all conditions. Sample and counterface material are subjected to low shear stress because of Si₃N₄ particles in the structure. At a temperature of 250°C and a load of 45 N, the AA 2618 alloy showed severe wear.

3.2.4. Coefficient of Friction. In this graph, friction coefficient (COF) is plotted against load and temperature. Under all wear conditions, it can be seen that friction

coefficient reduces with increasing silicon nitride content. The COF of the samples rises in direct proportion to the increase in load and test temperature. The AA 2618/2Si₃N₄ sample had the lowest COF. This resulted in an average COF value of 0.333 for AA 2618/1Si₃N₄ and 0.210 for the AA 2618/2Si₃N₄ samples tested at a temperature of 50°C. At a temperature of 250 degrees Celsius and a load of 45 Newton, the average COF values of AA 2618/1Si₃N₄ were 0.668, 0.572, and 0.474, respectively, and all are shown in Figures 4 and Figure 5. Composites have low coefficients of friction because of a solid lubricant, Si₃N₄. Furthermore, it was discovered that the presence of hard reinforcement particles reduces the actual contact area between the counterface and the matrix. As a result, composite materials have a lower COF. It is well established that the matrix softens as the temperature rises.

TABLE 4: Taguchi L_{27} orthogonal array results and response value values.

Ex.No	Load	Temp	Si_3N_4 wt%	Wear rate	Ratio of S/N
1	15	50	0	0.0028	54665
2	15	50	1	0.0016	570881
3	15	50	2	0.0009	628482
4	15	150	0	0.0042	492846
5	15	150	1	0.0023	541128
6	15	150	2	0.0018	561086
7	15	250	0	0.0059	462127
8	15	250	1	0.0041	491218
9	15	250	2	0.0026	551342
10	30	50	0	0.0038	489720
11	30	50	1	0.0029	521535
12	30	50	2	0.0019	610012
13	30	150	0	0.0071	450182
14	30	150	1	0.0056	466710
15	30	150	2	0.0049	481312
16	30	250	0	0.0099	413421
17	30	250	1	0.0069	452817
18	30	250	2	0.0059	470816
19	45	50	0	0.0031	530124
20	45	50	1	0.0024	558428
21	45	50	2	0.0024	581868
22	45	150	0	0.0091	421868
23	45	150	1	0.0069	461828
24	45	150	2	0.0054	472858
25	45	250	0	0.0152	381824
26	45	250	1	0.0112	391524
27	45	250	2	0.0096	411015

As the counterface and matrix become more adherent, so does the matrix's adhesion to the counterface material. As a result, the samples' COF rises.

Adding Si_3N_4 particles improves wear performance in this study, according to researchers. The COF is also found to be reduced when Si_3N_4 particles are added. The wear behaviour of Si_3N_4 -reinforced aluminium composites was identified to be similar by several researchers. The Al matrix's wear performance was reported to have improved, and the COF was reported to have decreased and it is shown in Figure 6. Composites with the addition of Si_3N_4 reinforcement were found to be more resistant to wear because of the material's lubricant properties. Due to the matrix strengthening that occurred as dislocation density increased, wear resistance also increased.

Grain refinement and particle dispersion strengthening were both associated with an increase in composite strength and hardness. Composites have grain sizes that are smaller than those of the AA 2618 alloy, as shown in Table 3. Counterface material and matrix are separated by a thin layer of oxide, according to this theory. In this study, the surface was found to be oxidised when heated to high temperatures.

4. Statistical Analysis

4.1. ANOVA Results. Table 4 displays the Taguchi L_{27} orthogonal array results and response value values. The experimental data was analysed using ANOVA. ANOVA can be used to find which variables have greatest impact on the rate at which clothing wears out. The ANOVA studies were conducted with a 95% level of confidence. The ANOVA results are shown in Table 5. Temperature is widely believed to be the most significant factor in the rate of wear (46.21 percent). Load and Si_3N_4 content were found to be responsible for 23.97 percent and 12.92 percent of the total. Interactions appear to have a smaller impact than individual parameters. There is a 13.67 percent correlation between load and temperature, followed by a correlation between temperature and Si_3N_4 (2.43 percent).

Temperature and Si_3N_4 content were independent variables. It was determined that the wear rate was the dependent variable. The wear rate of samples was predicted using a linear and a nonlinear regression model and it is shown in Figures 7 and 8.

TABLE 5: The results of the ANOVA test for each sample.

Source	Degrees of freedom	Seq SS	% of contribution	Adj SS	Adj MS	F value	P value
Load (L)	2	0.000071	23.4	0.000071	0.000038	168.94	0.0000
Temperature (°C)	2	0.000138	46.4	0.000134	0.000069	316.18	0.0000
Si ₃ N ₄ wt%	2	0.000039	11.69	0.000039	0.000021	89.14	0.0000
L x T	4	0.000002	14.24	0.000041	0.000015	17.86	0.0000
L x Si ₃ N ₄	4	0.000009	0.31	0.000001	0.0000	0.79	0.5960
T x Si ₃ N ₄	4	0.000003	3.35	0.000008	0.00003	8.96	0.00070
Error	8	0.000289	0.61	0.000003	0.00000		
Total	26		100				

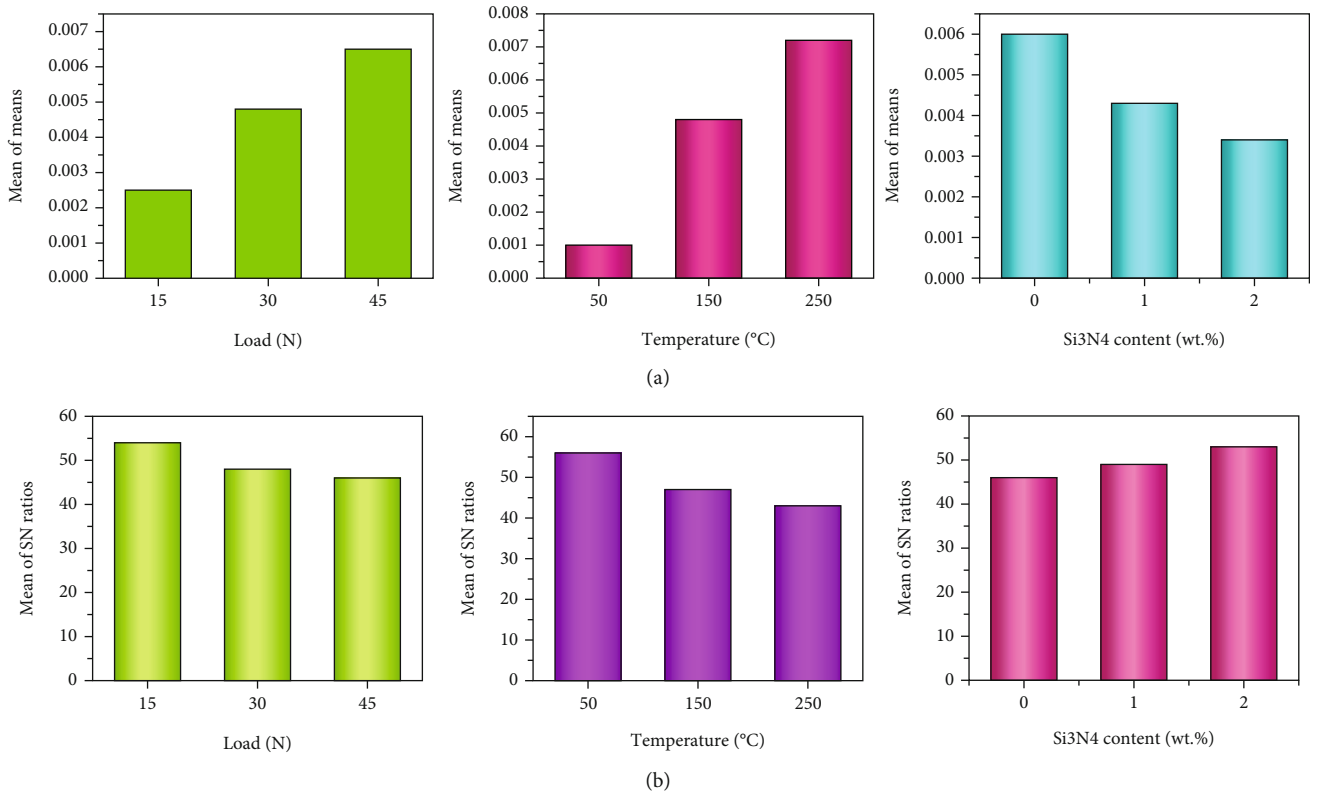


FIGURE 7: (a) Wear rate and (b) S/N ratios for the samples are shown in the main effects plots.

4.2. Analysis of S/N Ratios. This research made use of 27-row, 3-column full-factorial arrays. The constraints, wear rate, and signal-to-noise ratio are listed. Using the S/N ratio “Small is better” characteristic, this study was able to determine the wear rate. Each variable’s impact on output was evaluated using the S/N ratio. Given here is the S/N Ratio (S/N) in equation (1)

$$S/N = -10 \log \frac{1}{n} \left(\sum_{i=1}^n y_i^2 \right). \quad (1)$$

Signal-to-noise ratio (S/N) is the ratio of a signal’s strength to the background noise, and n is how many trials were conducted. This study looked at how different loads,

temperatures, and levels of Si₃N₄ content affected wear rates. Table 6 summarises the relative importance of various wear test parameters and their respective means. The best results are achieved when the S/N ratio of the combination of wear rate-related parameters is the highest. There is a correlation between wear rate and temperature, which is more pronounced than the effects of load and Si₃N₄. The effect of Si₃N₄ content was overshadowed by the effect of load. Plots’ wear rates are the primary goal of the analysis. Alloy AA 2618 must have a low wear rate and high Si₃N₄ content in order to function properly. For the interaction plots, the non-parallelism effect is well-known. If the interaction plot’s lines are not parallel, a finding of low interaction is valid. The wear parameters interact strongly at the intersection of lines. The relationship between load and temperature can

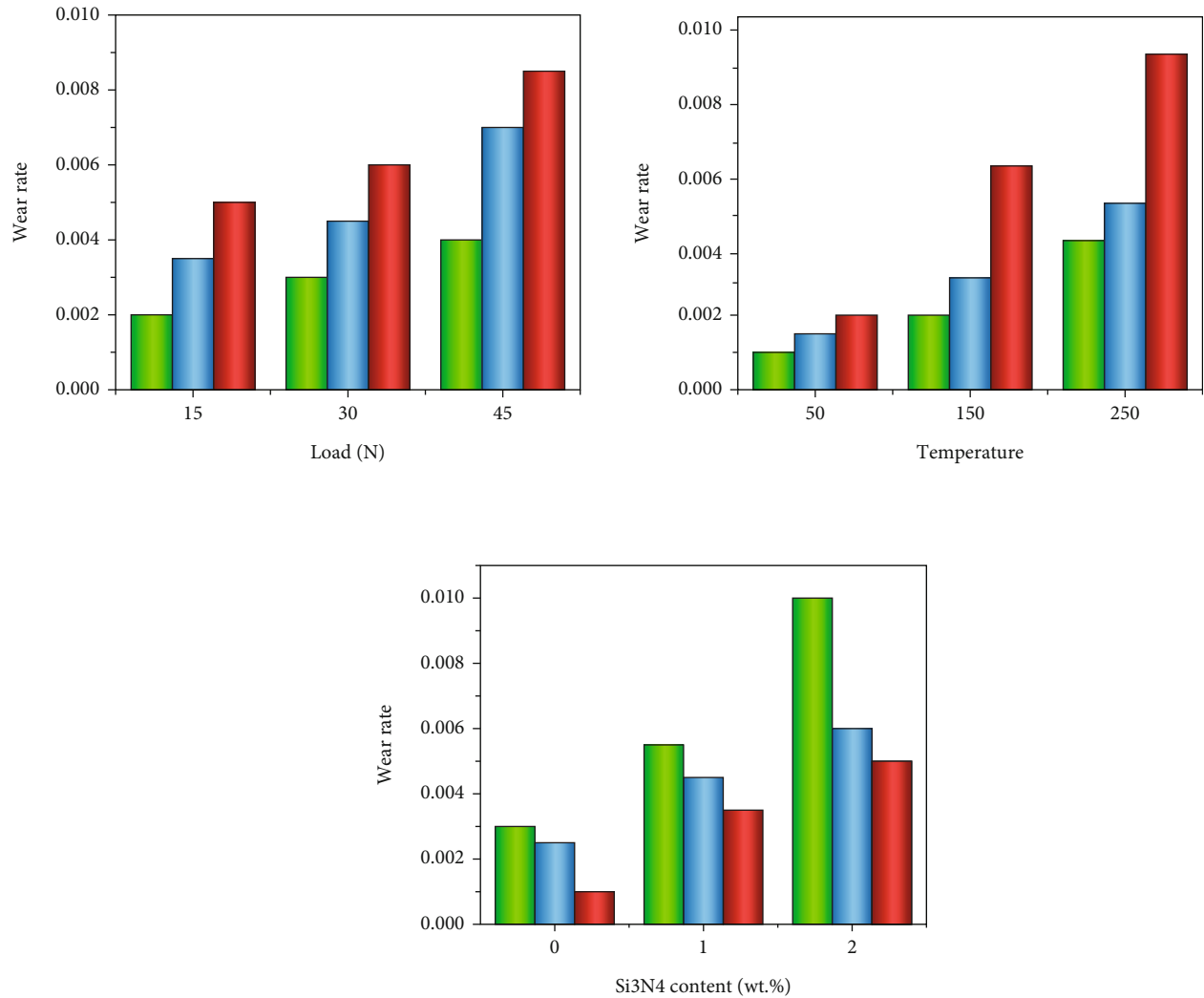


FIGURE 8: Wear rate is plotted as a function of the interaction between wear parameters.

TABLE 6: Responses to the sample S/N ratios.

Levels	Applied load	Temperature of control factors °C	Wt% of Si ₃ N ₄ content
1	54.8	54.8	46.4
2	48.6	48.4	49.8
3	47.1	45.2	53.3
Delta	8.1	13.1	7.4
Rank	2	1	3

be clearly seen. Temperature Si₃N₄ content and load Si₃N₄ content had a low interaction. The signal-to-noise ratio compares the strength of a signal to the background noise.

4.3. Evaluation Parameters. Regression models were assessed against two criteria in this study. R^2 and root mean square error were used to calculate the determination coefficient,

R^2 (RMSE). The following equations were used to calculate the RMSE in equation (2) and R^2 in equation (3).

$$\text{RMSE} = 1 - \left(\frac{1}{n} \sum_{i=1}^n (e_i - p_i)^2 \right)^{1/2}. \quad (2)$$

There are two values: e_i is the actual and p_i is the predicted one, respectively.

$$R^2 = 1 - \left(\frac{\sum_{i=1}^n (e_i - p_i)^2}{\sum_{i=1}^n (e_i - \bar{p}_i)^2} \right)^{1/2}. \quad (3)$$

For the regression models, R^2 is a measure of how well they perform based on the mean of the actual values. High R^2 and low RMSE values are what we are looking for in the model we are building here. Linear and nonlinear regressions have RMSE values of 0.0013 and 0.0009, respectively, for the two methods as in Figures 7 and 8. For linear and nonlinear

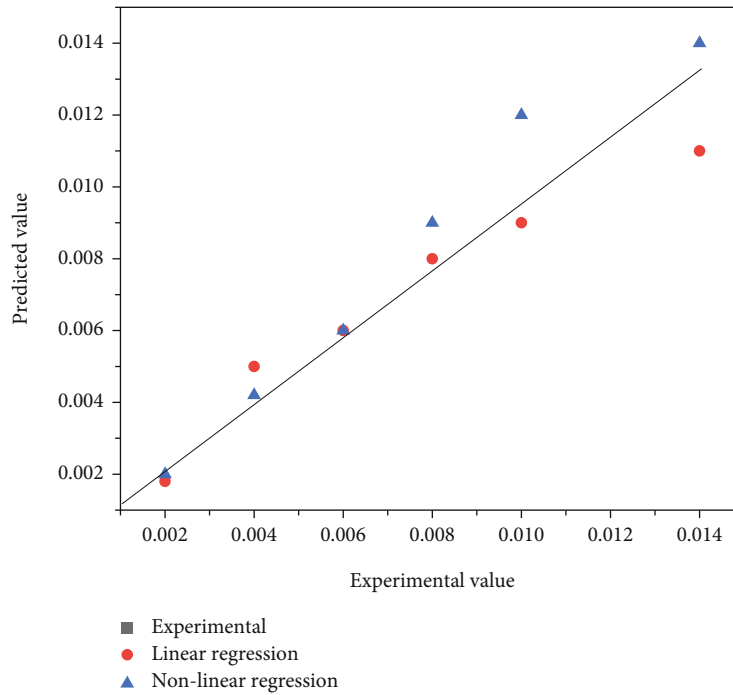


FIGURE 9: The dataset’s regression model results.

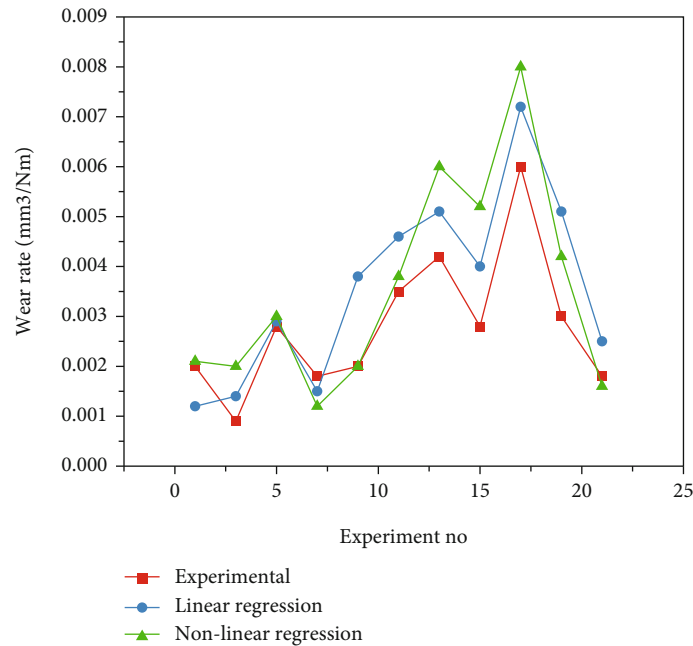


FIGURE 10: Comparison of experiment and predicted values.

regressions, the R^2 (percent) was 84.8 and 91.5, respectively. Regression models with low RMSE values are more likely to be successful. Nonlinear regression models outperformed linear regression models by 1.4 times as in tables.

Prediction accuracy is higher in models that use nonlinear regression than in linear regression models. Lower prediction values were obtained by using a linear regression model. For AA 2618/Si₃N₄ composites, nonlinear regression can be used to accurately predict the wear rate. Tribological

studies can save money and time by using the nonlinear regression model as shown in Figures 9 and 10.

5. Conclusions

This work used experimental and statistical approaches to investigate the wear behaviour of AA 2618/Si₃N₄ (1 and 2wt percent) composites. The following findings were obtained from this investigation. In all test settings, composites

containing AA 2618/2 wt percent Si₃N₄ demonstrated the best wear resistance. Delamination was most noticeable at 50 degrees Celsius, with substantial delamination and metal flow occurring at 250 degrees Celsius.

- (i) There was a 47.32 percent temperature, 24.96 percent load, and 12.51 percent Si₃N₄ content contribution to wear rate, respectively
- (ii) Linear regression had an R^2 of 83.4%, while nonlinear regression had an R^2 of 92.8%. By using nonlinear regression to predict wear rate, examining time and the number of examinations can be reduced
- (iii) Because of their superior elevated temperature tribological performance, AA 2618 with Si₃N₄ composites are the best choice for wear applications at high temperatures

Data Availability

The data used to support the findings of this study are included within the article. Further data or information is available from the corresponding author upon request.

Conflicts of Interest

The authors declare that there are no conflicts of interest regarding the publication of this paper.

Acknowledgments

The authors appreciate the supports from Wolaita Sodo University, Ethiopia, for the research and preparation of the manuscript. The authors thank the RMK Engineering College, and Aditya Engineering College for providing assistance to this work. Taif University Researchers Supporting Project number (TURSP-2020/01), Taif University, Taif, Saudi Arabia.

References

- [1] E. Georgantzia, M. Gkantou, and G. S. Kamaris, "Aluminium alloys as structural material: a review of research," *Engineering Structures*, vol. 227, article 111372, 2021.
- [2] K. Subramani, T. Arunkumar, V. Mohanavel et al., "Investigation on wear characteristics of Al 2219/Si₃N₄/Coal bottom ash MMC," *Materials Today: Proceedings*, vol. 62, no. 8, pp. 5514–5518, 2022.
- [3] M. A. Afifah, O. M. Zaidi, H. Hanizam, S. M. Shukor, and M. I. Fadhilina, "Recent development in graphene-reinforced aluminium matrix composite: a review," *Reviews on Advanced Materials Science*, vol. 60, no. 1, pp. 801–817, 2021.
- [4] P. Ashwath, J. Joel, M. A. Xavier, and H. P. Kumar, "Effect of SiC and Al₂O₃ particles addition to AA 2900 and AA 2024 MMC's synthesized through microwave sintering," *Mater. Today-Proc.*, vol. 5, no. 2, pp. 7329–7336, 2018.
- [5] M. I. Ul Haq and A. Anand, "Dry sliding friction and wear behavior of AA7075-Si₃N₄ composite," *Silicon*, vol. 10, no. 5, pp. 1819–1829, 2018.
- [6] L. Zhang, Z. Wang, Q. Li et al., "Microtopography and mechanical properties of vacuum hot pressing Al/B₄C composites," *Ceramics International*, vol. 44, no. 3, pp. 3048–3055, 2018.
- [7] M. Irfan Ul Haq, A. Raina, A. Anand, S. M. Sharma, and R. Kumar, "Elucidating the effect of MoS₂ on the mechanical and tribological behavior of AA7075/Si₃N₄ composite," *Journal of Materials Engineering and Performance*, vol. 29, no. 11, pp. 7445–7455, 2020.
- [8] V. Mohanavel and M. Ravichandran, "Influence of AlN particles on microstructure, mechanical and tribological behaviour in AA6351 aluminum alloy," *Materials Research Express*, vol. 6, no. 10, article 106557, 2019.
- [9] M. L. Bharathi, S. Adarsh Rag, L. Chitra et al., "Investigation on wear characteristics of AZ91D/nanoalumina composites," *Journal of Nanomaterials*, vol. 2022, Article ID 2158516, 9 pages, 2022.
- [10] M. N. Akhtar, T. Sathish, V. Mohanavel et al., "Optimization of process parameters in CNC turning of aluminum 7075 alloy using L27 array-based Taguchi method," *Materials*, vol. 14, no. 16, p. 4470, 2021.
- [11] M. R. Akbarpour and A. Pouresmaeil, "The influence of CNTs on the microstructure and strength of Al-CNT composites produced by flake powder metallurgy and hot pressing method," *Diamond and Related Materials*, vol. 88, pp. 6–11, 2018.
- [12] E. Ghasali, P. Sangpour, A. Jam, H. Rajaei, K. Shirvanimoghaddam, and T. Ebadzadeh, "Microwave and spark plasma sintering of carbon nanotube and graphene reinforced aluminum matrix composite," *Arch. Civ. Mech. Eng.*, vol. 18, no. 4, pp. 1042–1054, 2018.
- [13] M. E. Turan and F. Aydin, "Improved elevated temperature mechanical properties of graphene-reinforced pure aluminium matrix composites," *Materials Science and Technology*, vol. 36, no. 10, pp. 1092–1103, 2020.
- [14] X. Zeng, J. Teng, J. G. Yu, A. S. Tan, D. F. Fu, and H. Zhang, "Fabrication of homogeneously dispersed graphene/Al composites by solution mixing and powder metallurgy," *Int. J. Min. Met. Mater.*, vol. 25, no. 1, pp. 102–109, 2018.
- [15] J. Su and J. Teng, "Recent Progress in graphene-reinforced aluminum matrix composites," *Frontiers of Materials Science*, vol. 15, no. 1, pp. 79–97, 2021.
- [16] X. Zeng, J. Yu, D. Fu, H. Zhang, and J. Teng, "Wear characteristics of hybrid aluminum-matrix composites reinforced with well-dispersed reduced graphene oxide nanosheets and silicon carbide particulates," *Vacuum*, vol. 155, pp. 364–375, 2018.
- [17] S. K. Selvaraj, M. K. Nagarajan, and L. A. Kumaraswamidhas, "An investigation of abrasive and erosion behaviour of AA 2618 reinforced with Si₃N₄, AlN and ZrB₂ in situ composites by using optimization techniques," *Archiv.Civ.Mech.Eng.*, vol. 17, no. 1, pp. 43–54, 2017.
- [18] K. B. Lee, H. S. Sim, S. W. Heo, H. R. Yoo, S. Y. Cho, and H. Kwon, "Tensile properties and microstructures of Al composite reinforced with BN particles," *Composites. Part A, Applied Science and Manufacturing*, vol. 33, no. 5, pp. 709–715, 2002.
- [19] S. Sardar, S. K. Karmakar, and D. Das, "High stress abrasive wear characteristics of Al 7075 alloy and 7075/Al₂O₃ composite," *Measurement*, vol. 127, pp. 42–62, 2018.
- [20] J. M. Mistry and P. P. Gohil, "Experimental investigations on wear and friction behaviour of Si₃N₄P reinforced heat-

- treated aluminium matrix composites produced using electromagnetic stir casting process,” *Compos. Part. B-Eng.*, vol. 161, pp. 190–204, 2019.
- [21] N. Idusuyi and J. I. Olayinka, “Dry sliding wear characteristics of aluminium metal matrix composites: a brief overview,” *Journal of Materials Research and Technology*, vol. 8, no. 3, pp. 3338–3346, 2019.
- [22] N. Kaushik and S. Singhal, “Wear conduct of aluminum matrix composites: a parametric strategy using Taguchi based GRA integrated with weight method,” *Cogent. Eng.*, vol. 5, no. 1, p. 1467196, 2018.
- [23] A. H. Idrisi and A. H. I. Mourad, “Wear performance analysis of aluminum matrix composites and optimization of process parameters using statistical techniques,” *Metallurgical and Materials Transactions A: Physical Metallurgy and Materials Science*, vol. 50, no. 11, pp. 5395–5409, 2019.
- [24] M. O. Bodunrin, K. K. Alaneme, and L. H. Chown, “Aluminium matrix hybrid composites: a review of reinforcement philosophies; mechanical, corrosion and tribological characteristics,” *Journal of Materials Research and Technology*, vol. 4, no. 4, pp. 434–445, 2015.
- [25] R. A. Khatavkar, A. K. Mandave, D. D. Baviskar, and S. L. Shinde, “Influence of hexagonal boron nitride on tribological properties of AA 2618-HSI3N4 metal matrix composite,” *Int. Res. J. Eng. Technol.*, vol. 5, no. 5, pp. 3792–3798, 2018.
- [26] T. Gangatharan, A. A. Moorthy, and T. Rameshkumar, “Enhancing the tribological properties of composite materials for centrifugal pump applications,” *IRJET*, vol. 3, no. 3, pp. 195–199, 2016.
- [27] H. Chi, L. Jiang, G. Chen, P. Kang, X. Lin, and G. Wu, “Dry sliding friction and wear behavior of (TiB₂ + h-BN)/2024Al composites,” *Materials and Design*, vol. 87, pp. 960–968, 2015.
- [28] P. Paulraj and R. Harichandran, “The tribological behavior of hybrid aluminum alloy nanocomposites at high temperature: role of nanoparticles,” *Journal of Materials Research and Technology*, vol. 9, no. 5, pp. 11517–11530, 2020.
- [29] M. M. Boopathi, K. P. Arulshri, and N. Iyandurai, “Evaluation of mechanical properties of aluminium alloy 2024 reinforced with silicon carbide and fly ash hybrid metal matrix composites,” *American Journal of Applied Sciences*, vol. 10, no. 3, pp. 219–229, 2013.
- [30] M. E. Turan, Y. Sun, F. Aydin, H. Zengin, Y. Turen, and H. Ahlatci, “Effects of carbonaceous reinforcements on microstructure and corrosion properties of magnesium matrix composites,” *Materials Chemistry and Physics*, vol. 218, pp. 182–188, 2018.
- [31] F. Aydin and M. E. Turan, “The effect of boron nitride on tribological behavior of mg matrix composite at room and elevated temperatures,” *Journal of Tribology*, vol. 142, no. 1, pp. 1–7, 2020.
- [32] M. Rahimian, N. Parvin, and N. Ehsani, “The effect of production parameters on microstructure and wear resistance of powder metallurgy Al-Al₂O₃ composite,” *Materials and Design*, vol. 32, no. 2, pp. 1031–1038, 2011.
- [33] F. Aydin and Y. Sun, “Investigation of wear behaviour and microstructure of hot-pressed TiB₂ particulate-reinforced magnesium matrix composites,” *Canadian Metallurgical Quarterly*, vol. 57, no. 4, pp. 455–469, 2018.
- [34] R. Prasad, H. Kumar, P. Kumar, S. P. Tewari, and J. K. Singh, “Microstructural, mechanical and tribological characterization of friction stir welded A7075/ZrB₂ in situ composites,” *Journal of Materials Engineering and Performance*, vol. 30, no. 6, pp. 4194–4205, 2021.

Research Article

Nanotitanium Oxide Particles and Jute-Hemp Fiber Hybrid Composites: Evaluate the Mechanical, Water Absorptions, and Morphological Behaviors

C. R. Mahesha,¹ R. Suprabha,¹ Mahesh S. Harne,² Sachin G. Galme,³ Sandeep G. Thorat,⁴ N. Nagabhooshanam,⁵ A. H. Seikh,⁶ M. H. Siddique,⁷ and Mebratu Markos⁸

¹Department of Industrial Engineering & Management, Dr. Ambedkar Institute of Technology, Bangalore, Karnataka 560056, India

²Department of Mechanical Engineering, Amrutvahini College of Engineering, Sangamner, Maharashtra 422608, India

³Department of Mechanical Engineering, Sandip Institute of Technology and Research Centre, Nashik, Maharashtra 422213, India

⁴Department of Mechanical Engineering, MIT ADT University's MIT School of Engineering, Rajbaug Loni Kalbhor, Pune, Maharashtra 412201, India

⁵Department of Mechanical Engineering, Aditya Engineering College Surampalem, Andhra Pradesh, India

⁶Mechanical Engineering Department, College of Engineering, King Saud University, P.O. Box 800, Al-Riyadh 11421, Saudi Arabia

⁷Intelligent Construction Automation Centre, Kyungpook National University, Daegu, Republic of Korea

⁸Department of Mechanical Engineering, College of Engineering, Wolaita Sodo University, Ethiopia

Correspondence should be addressed to Mebratu Markos; mebratemarkos@wsu.edu.et

Received 11 May 2022; Accepted 26 July 2022; Published 14 September 2022

Academic Editor: Arpita Roy

Copyright © 2022 C. R. Mahesha et al. This is an open access article distributed under the Creative Commons Attribution License, which permits unrestricted use, distribution, and reproduction in any medium, provided the original work is properly cited.

Organic fiber-based biocomposites have gained prominence in a variety of sectors over the last four to five years due to their exceptional mechanical and physical properties. Natural fiber-based composites are increasingly being employed in autos, ships, airplanes, and infrastructure projects. The current study will look at the effect of nanotitanium oxide (TiO_2) fillers on the properties of hybridised jute-hemp-based composites. In this work, TiO_2 -filled biocomposites were created using the hand layup method in hybrid jute-hemp composites containing jute fiber mats, woven hemp mats, and epoxy resin. After nanotitanium oxide fillers were injected in various weight proportions, the mechanical properties of fiber-reinforced polymers were investigated. The mechanical properties of laminated composites were tested using the ASTM standard. Compared to 2 and 4 wt.% of TiO_2 , the 6 wt.% was provided the highest mechanical strength. Among the different types of specimen, the E-type specimen (30 wt.% of hemp, 7 wt.% of jute, 57 wt.% of epoxy, and 6 wt.% of TiO_2) gives their highest contribution, i.e., for tensile 24.21%, for flexural 25.03%, and for impact 24.56%. The scanning electron microscope was utilized to analyse the microstructures of nanocomposites.

1. Introduction

The utilization of composite materials has increased at an astounding rate, and these materials today have a remarkable and wide variety of uses. Minimal weight, strong fatigue tolerance, high corrosion resilience, insulation, and low coefficient of thermal expansion are key benefits of composites over several metallic materials. Polymer matrix composites

(PMCs) offer outstanding physical and thermal qualities, like high specific toughness, as well as high toughness and rust resistance. The researchers emerged as viable alternatives to traditional metals in a wide range of applications, including aeroplanes, warships, housing, vehicles, microelectronics components, and maritime construction [1, 2]. The resources used throughout the airframe of a Boeing 777 contain 50% aluminium and 12% polymers by weightiness. However, in

the completely redesigned Boeing 787 aviation, the proportions by heaviness for aluminium and polymers have altered to 22% and 55%, correspondingly. Fiber-reinforced polymer compounds have a number of appealing qualities, like high stiffness, fracture toughness performance and damage tolerance levels, high thermal stability, nonmagnetic characteristics, oxidation resistance, and low manufacturing energy consumption [3, 4]. Fiber glass-reinforced glass, polypropylene, and graphene are the most prevalent artificial fibers. In polymer matrix composites, harder and tougher fibers can be added to increase the strength and rigidity of the polymers. Because of its outstanding characteristics, such as high specific fracture toughness, adjustable electrical conductivity, temperature resistance, high fatigue barrier properties, and appropriateness for the fabrication of numerous contour substances, fiber-reinforced composites have been widely used. In numerous applications, composite materials have replaced traditional architectural materials like metals, hardwoods, and iron [5, 6]. Car manufacturing, aeroplane production, wind energy plants, yachts, and warships are all examples of composites' uses. The way things are manufactured has altered thanks to filler reinforced structural polymeric or thermoplastic composites. Authors may now be seen not just in air and ground transportation vehicles, sports gear, and electronics but also in bullet barriers, weaponry, percussion equipment, fashion items, and much more. The requirement for materials of good physical qualities, in combination with lighter weight and low price, grows as demand grows [7]. This necessitates a continuous hunt for new ingredients, additions, and production procedures. The standard strategy is to look for a joint that attaches the reinforcement to the matrix and enhances the transfer of load but does not cause considerable matrix fouling at the boundary, permitting crack propagation during dynamic loads [8]. Because of their improved properties, nanostructured membranes made of polymer matrices and nanomaterials/nanofillers have piqued the interest of researchers and industry in their application, leading to high barrier packing for food and gadgets for automobiles and aviation. They offer excellent feature upgrades, including increased thermal and mechanical characteristics, permeability resilience, and flame retardancy at different filler levels, as compared to their typical microscopic and macroscopic or clean equivalents [9, 10]. In the last twenty years, polymer-based nanocomposites have attracted a lot of interest from academia and industry. Different polymer matrixes and nanoparticles have indeed been studied in different configurations. The addition of a small amount of nanofiller has proved to improve the physical characteristics of polymer matrices dramatically. The shape, size, content, and degree of aggregation of the filler, as well as the amount of matrix-filler adherence, have a major impact on the characteristics of a polymeric-filled composite. The use of nanomaterials as fillers creates a bigger dynamic and interactive zone, which might lead to significantly stronger couplings with matrices and a better end product. Nanoparticles can also provide nanocomposite distinctive features like electrical, photonic, magnetism, or transporting capabilities, which opens up endless possibilities for rapid technological use. Synergistic effects from the combining of

separate components contribute to improved properties in polymer-based composites [11, 12]. These gains may be approximated using mixing procedures in ordinary composites, but these begin to fail in nanocomposites since interface connections among constituents become highly important for determining bulk characteristics. Particle polymer composites are made up of microparticles or nanofillers of various types and sizes scattered arbitrarily in matrix materials. Due to tear dulling, fracture deflecting, and fracture anchoring hardening processes, the introduction of titanium oxide and aluminium oxide nanoparticles in epoxy reaches the maximum hardness. The incorporation of nano-SiO₂ increased mechanical characteristics and breakage durability with weight concentration owing to matrix deformations, region buffering, void development, particle-matrix delamination, and localised shearing band hardening mechanisms. Formulation, constituent characteristics, architecture, and interface contact all influence the biomechanical, physical, and chemical characteristics of nanostructured materials, particularly yield strength. If nanoparticles possess an anisometric topology, the direction of the nanoparticles should be considered in estimating material properties. The efficacy of stress transmission among filler and matrix affects the intensity of a particle-filled composite. The TiO₂ nanoparticles are now one of the more intriguing substances [13, 14]. They are gaining popularity not only because of their unusual features but also because of their prospective uses in sectors like paints, perfumes, catalysis, and catalyst support. After ultrasonically processing, the mechanical and absorption properties of polymeric composites containing TiO₂ nanoparticles and epoxy were associated to composite samples containing TiO₂ microscopic particles and epoxy, as well as plain resin. The nanocomposites with proper dispersions of nanoparticles at a loading of 10 wt.% showed a unique mix of attributes, including improvements in impact resistance and elasticity, but also improvements in cyclic loading and swelling tolerance, all while preserving hardness. In comparison to the clean resin, the nanobased composites demonstrated no gain in abrasion confrontation and a reduction in failure to strain [15, 16]. The goal of this study is to see how nanotitanium oxide fillers affect the characteristics of hybrid jute-hemp composites. Hand layup techniques were used to create the composites. The ASTM standard was used to test and analyse mechanical qualities such as tensile, bending, and impact. A scanning electron microscope was used to perform the microstructural study.

2. Experimental

2.1. Materials. To change the epoxy matrices, TiO₂ particles with a size of 30 nm were utilized as caulking substantial. As a reinforcing material, a 350 gsm commercially available jute fiber chop strand mat was employed. As a reinforcing material, a 250 gsm woven hemp mat with an average thickness of 0.65 mm was employed. GVR Fiber Industry, Madurai, Tamil Nadu, India, provided both natural fiber mats. Naga Chemical Ltd. in Chennai, Tamil Nadu, India, provided the TiO₂ filler. Figure 1 reveals the reinforcement materials and TiO₂ fillers.

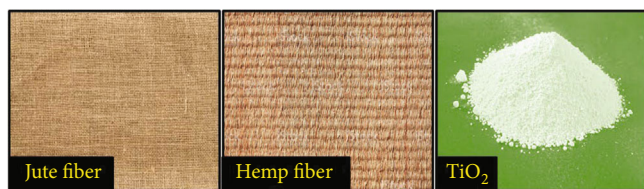


FIGURE 1: Reinforcement and TiO_2 filler materials.

2.2. Alkaline Processing. Alkaline treatment is among the most often utilized chemical methods when natural fibers are combined with polymer to produce a composite. The most notable change generated by alkaline treatment is the breakage of hydrogen bonds in the underlying network, resulting in enhanced surface quality. During alkalization, fibers are immersed in a NaOH solution for a specific period of time. The hemp mat was treated chemically with sodium hydroxide in the current study. For four hours, ordinary hemp and jute were immersed in a container; it contains a 5% NaOH solution. After that, the fiber mats were air dried at ambient temperature [17].

2.3. Fabrication of Hybrid Composites. Depending on the mass of the tiny titanium oxide nanoparticles to an overall weight of the jute, hemp, epoxy resin, and nanotitanium oxide particles, the mass proportions of the nano- TiO_2 filler in the composites were 2 percent, 4 percent, and 6 percent. To make the nano- TiO_2 -mixed epoxy resin, mechanical stirring was used to mix the nano- TiO_2 into the epoxy resin, followed by the addition of the suitable hardener. Hand layup was used to create the hybrid composites, which consisted of three layers of hemp, jute, and hemp. Hemp was used for the bottom and top layers, while jute was used for the middle layer. To make the created hybrid fiber-reinforced plastics easier to remove, a releasing agent was first placed across a flat moulding. A thick coating of nano-scale TiO_2 blended epoxy resin was placed over the release chemical layer. The bottom layer of hemp was then applied to the mould's surfaces. The nanoscale TiO_2 -mixed epoxy resin was then sprayed onto the surface of the hemp that had previously been put in the mould and distributed evenly with a brush. To eliminate any air trapped, a roller was dragged through the bottom layer with little force. A thin coating of nano- TiO_2 epoxy resin was applied once again. The experiment was replicated with the addition of next interfacial layer of jute. Table 1 shows the list of parameters and their constraints of nanocomposites.

2.4. Mechanical Testing. The fabricated composite specimens were cut rendering to ASTM standard of D 638-03 replicas with a dimension of $150 \times 15 \times 3$ mm for tensile testing, ASTM D-790 (width 10 mm, length 125 mm, and thickness 3 mm) for flexural testing, and ASTM D-256 (width 12.7 mm, length 64 mm, and thickness 3 mm) for impact testing as shown in Figure 2.

2.5. Fractographic Study. SEM was employed to conduct fractographic investigations of fractured composite samples. The specimens were laved, dehydrated, and surface coated

TABLE 1: List of parameter and their levels of nanocomposites.

Specimen type	Woven hemp fiber (wt.%)	Woven jute fiber (wt.%)	Epoxy matrix (wt.%)	Titanium oxide (wt.%)
A	0	0	100	0
B	30	7	63	0
C	30	7	61	2
D	30	7	59	4
E	30	7	57	6

with 10 nm of gold earlier SEM clarity to enhance the composites' electric conduction.

3. Result and Discussion

The following session briefly discusses the mechanical goods like flexural, tensile, and impact characteristics of polyester composites based on their input parameters.

3.1. Outcomes of Hybrid Nanocomposites. The mechanical properties like tensile, flexural, and impact behavior of hemp-jute-based titanium oxide filler composites are shown in the figure. This research found that the weight percentage of nanoparticles is directly proportional to the test results. Because the mechanical characterization of hybrid composites increased when the weight percentage of titanium oxide particles was increased in the matrix mixture, the characterization strength of nanocomposites depends on the type of filler materials, adhesion between the matrix mixture and the fibers, and the extent of load shearing capacity. The interfacial stiffness, quality of adherence components, and their static adherence strength played the major roles in determining the composite strength. It helps to transfer the stress and elastic deformation from the matrix to the fiber or fillers and the fiber to the matrix. Figure 3 demonstrates the mechanical properties of hybrid nanocomposites [18, 19].

When compared to microscopic composites, nanomaterials have a higher percentage of interaction. The particles are unable to carry any part of the externally applied if the filler matrix contact is deprived. In this situation, the composite's strength cannot exceed that of the plain matrix material. The elastic modulus of nanoparticle composites could be greater than that of the matrix material if the interaction seen among the filler and the matrices is good enough. Because of the increased high strength nano- TiO_2 filler particles and decreased epoxy in the matrix, the mechanical characteristics of the hybrid composite improve with the inclusion of nanocomposite filler particles [20, 21]. The hybrid composite's enhanced mechanical, flexural, and impact strength indicates that stresses are effectively transmitted over the interaction. The mechanical and physical properties of hybrid jute-hemp hybrid composites are enhanced owing to the cooperative accomplishment of nano- TiO_2 fillers, hemp, jute, and epoxy. Figure 4 shows different specimen contributions in % (a) tensile, (b) bending, and (c) impact strength of hybrid nanocomposites.



FIGURE 2: Setup of impact testing.

With the inclusion of nano-TiO₂ filler particles, the mechanical characteristics of the hybrid composite are greatly enhanced. The tensile strength of the hybrid composites based on 0 wt.% TiO₂ was 58 MPa for the hybrid composites with 0% TiO₂ to 74 MPa for the hybrid composites with 6% TiO₂. Flexural strength improved from 98 MPa at 0% TiO₂ to 143 MPa at 6% TiO₂. The impact strength increased from 49 kg/m² with 0% TiO₂ to 67 kg/m² with 6% TiO₂. The inclusion of nano-TiO₂ filler increases the tensile strength, flexural strength, and impact strength of hybrid composites. Because of fracture-tip dampening, blow refraction, and blow restraining strengthening processes, the inclusion of TiO₂ nanoparticles to fiber-based composites boosted strength. Figures 4(a)–4(c) demonstrate the various sample contribution on mechanical properties. From Figure 4, in tensile, most contributed % is attained in E specimen; in bending and flexural test, most contributed sample is E, respectively.

3.2. Morphological Analysis. Scanning electron microscopy was used to examine the characteristics of tensile surface defects and the fiber-matrix interface. Others have used this approach to determine the stiffness modulus and durability of nanocomposites. Figures 5(a)–5(c) show the SEM micrographs of natural fiber-based nanocomposites after tensile fracture. The TiO₂ dispersion in the epoxy matrix is remarkably constant (Figure 5(a)). At greater loadings, however, the fillers tend to form agglomerates. It is generally recognised that adequate filler dispersion in the matrix is a key aspect in achieving good mechanical characteristics [17, 22, 23]. The use of a greater magnification allows for the observation of a single TiO₂ particle with longitudinal shapes. The aggregation of TiO₂ particles can be seen in Figure 5(b), with the biggest ones being seen using the SEM. It is well known that as filler loading increases, so does the ability to agglomeration.

Polymer discomfort, fiber breaking, and polymer and reinforcement adhesive catastrophe have all been recognised as failure modes for typical fiber-based polymerics in the literature. A weedy border or inadequate contact between fiber and matrix might cause fiber pullout rather than fracture, lowering mechanical properties. In this study, several combinations of these failures were discovered, depending on the nanocomposite's composition. Figure 5(b) depicts a typical SEM micrograph of nanocomposite sample 6 wt.% TiO₂. Fiber pullout and its breakage are shown in the SEM images [24]. As the organic resin content increased, the interaction holes surrounding pull-out fibers grew larger, signifying worse adhesion between the fiber and the biobased matrix. As a consequence, the interface aspects of pull-out failures were examined. The interfacial separation of nanocomposites containing 6 wt.% TiO₂ was the same as that of nanocomposite. This shows that TiO₂ reinforcing has no effect on the fiber-matrix interfacial bonding. Tensile studies support the concept that a weaker interface generates a more spectacular pull-out spectacle, since a drop in mechanical properties was observed as the quantity of organic-based resin material rose as shown in Figure 5(c). The pullout of fiber enables for more oomph to be diffused at the boundaries, which is consistent with the improved impact characteristics and endurance during the chemical type epoxy treatment [16].

4. Water Absorption Behavior

Figure 6 depicts the amounts of moisture content in several composite materials. The rate of water updating for all composite materials was significant at first, but it has since become practically constant and has decreased in the final phase. According to the findings, with longer time durations, all composite materials display a significant moisture absorption rate. Moisture content varied from 12 to 22% after the first day, and it rose to 12–38% for various composites created. Of all the composite materials, the hybrid nanocomposites made with titanium oxide showed the maximum amount of water attraction. This might be owing to the improved hydrophilic behavior of the nanocomposite following fiber mixing and TiO₂ incorporation. The hemp/jute with 6 wt.% TiO₂ (model E) combination had the maximum moisture uptake values when associated to the other amalgams.

This is owing to the large amount of (OH) assemblages current on hemp fiber surfaces. The amount of hydroxyl group and microvoids in the hemp/epoxy composites increased, leading in a considerable rise in moisture fascination. The hybrid wood-hemp combination, on the other hand, absorbed the least amount of water. The hybrid nanocomposite with hydrophilic titanium oxide, on the other hand, absorbed more moisture than the hybrid composite. As compared to 0, 2, and 4, the 6 wt.% of TiO₂-filled hybrid composites exhibits lower moisture absorption. This is owing to the proper spreading of nanoparticles in the resin medium mixture. It helps to reduce the formation of voids, and the fiber pulls out. This may help to increase the moisture absorption characteristics [25].

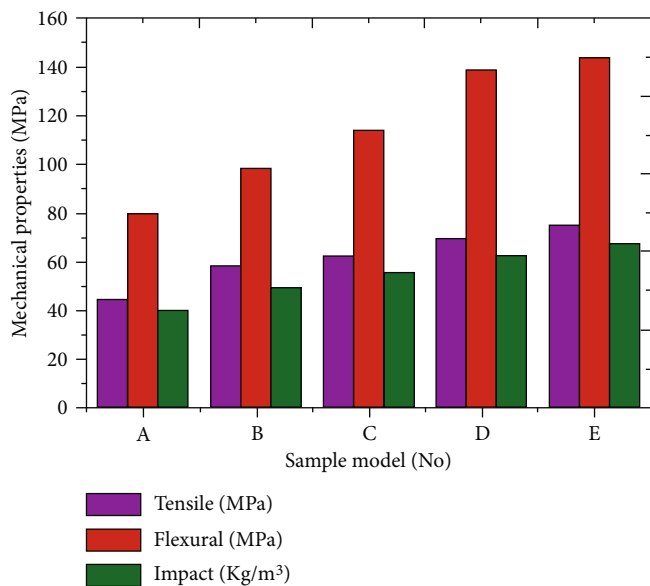


FIGURE 3: Mechanical properties of hemp/jute/nano-TiO₂-based hybrid nanocomposites.

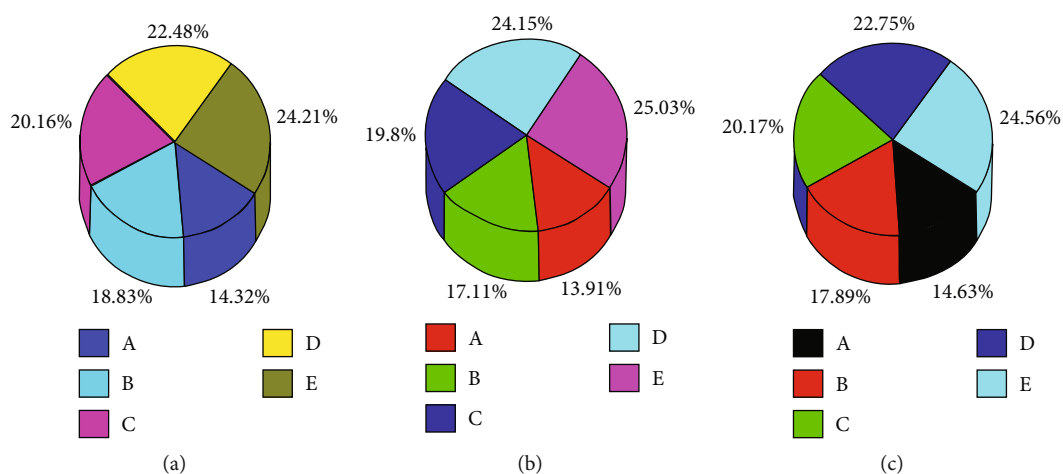


FIGURE 4: Different specimen contribution in % (a) tensile, (b) bending, and (c) impact strength of hybrid nanocomposites.

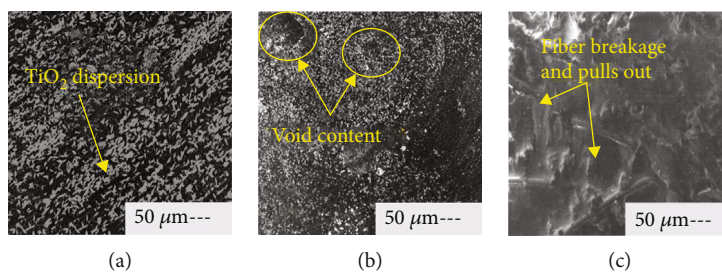


FIGURE 5: Microstructural analysis of TiO₂-filled hemp- and jute-based hybrid composites.

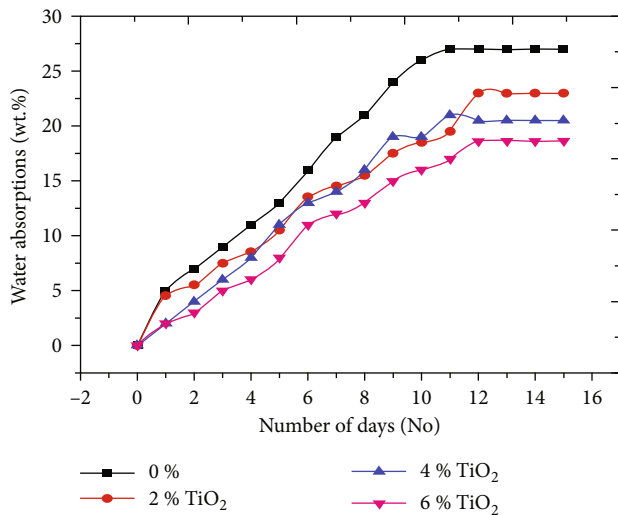


FIGURE 6: Water absorption behavior of TiO₂-filled hybrid nanocomposites.

5. Conclusion

As per the experimental outcomes, the use of nano-TiO₂ filler particles improved the mechanical properties of hybrid composites.

- (i) The 6 wt.% TiO₂ provided the maximum mechanical strength when compared to the 2 and 4 wt.% TiO₂
- (ii) The E-type specimen provides the most to the different types of specimens, with a contribution of 24.21 percent for tensile, 25.03 percent for flexural, and 24.56 percent for impact
- (iii) The creation of TiO₂ particle-hybrid jute-hemp composites indicated that these nanocomposites with excellent mechanical characteristics may be employed in a variety of applications. When compared to the A, B, C, and D types, the E-type specimen has the highest mechanical strength with 6 wt.% TiO₂. The dispersion of nanoparticles in the epoxy mixture was homogeneous in this specimen. SEM pictures corroborated this

Data Availability

The data used to support the findings of this study are included within the article. Further data or information is available from the corresponding author upon request.

Conflicts of Interest

The authors declare that there are no conflicts of interest regarding the publication of this paper.

Acknowledgments

The authors appreciate the supports from Wolaita Sodo University, Ethiopia, for the research and preparation of the manuscript. The authors thank Dr. Ambedkar Institute of Technology, Amrutvahini College of Engineering, and MIT ADT University's MIT School of Engineering for providing assistance to this work. The authors would like to acknowledge the Researchers Supporting Project number (RSP-2021/373), King Saud University, Riyadh, Saudi Arabia.


References

- [1] L. Suárez, J. Castellano, S. Díaz, A. Tcharkhtchi, and Z. Ortega, "Are natural-based composites sustainable," *Polymers*, vol. 13, no. 14, p. 2326, 2021.
- [2] M. S. Chowdary, G. Raghavendra, M. S. R. N. Kumar, S. Ojha, and V. Boggarapu, "Influence of nano-silica on enhancing the mechanical properties of sisal/Kevlar fiber reinforced polyester hybrid composites," *Silicon*, vol. 14, no. 2, pp. 539–546, 2022.
- [3] G. Velmurugan and K. Babu, "Statistical analysis of mechanical properties of wood dust filled jute fiber based hybrid composites under cryogenic atmosphere using Grey-Taguchi method," *Materials Research Express*, vol. 7, no. 6, 2020.
- [4] V. Ganesan and B. Kaliyamoorthy, "Utilization of Taguchi technique to enhance the interlaminar shear strength of wood dust filled woven jute fiber reinforced polyester composites in cryogenic environment," *Journal of Natural Fibers*, vol. 19, no. 6, pp. 1990–2001, 2022.
- [5] V. Mohanavel, S. Suresh Kumar, J. Vairamuthu, P. Ganeshan, and B. Nagaraja Ganesh, "Influence of stacking sequence and fiber content on the mechanical properties of natural and synthetic fibers reinforced Penta-layered hybrid composites," *Journal of Natural Fibers*, pp. 1–13, 2021.
- [6] V. Alagumalai, V. Shanmugam, N. K. Balasubramanian et al., "Impact response and damage tolerance of hybrid glass/Kevlar-fibre epoxy structural composites," *Polymers (Basel)*, vol. 13, no. 16, p. 2591, 2021.
- [7] S. Sanjeevi, V. Shanmugam, S. Kumar et al., "Effects of water absorption on the mechanical properties of hybrid natural fibre/phenol formaldehyde composites," *Scientific Reports*, vol. 11, no. 1, pp. 1–11, 2021.
- [8] K. C. Manikandan Nair, S. Thomas, and G. Groeninckx, "Thermal and dynamic mechanical analysis of polystyrene composites reinforced with short sisal fibres," *Composites Science and Technology*, vol. 61, no. 16, pp. 2519–2529, 2001.
- [9] N. Merah and O. Mohamed, "Nanoclay and water uptake effects on mechanical properties of unsaturated polyester," *Journal of Nanomaterials*, vol. 2019, Article ID 8130419, 11 pages, 2019.
- [10] V. Fiore, T. Scalici, and A. Valenza, "Effect of sodium bicarbonate treatment on mechanical properties of flax-reinforced epoxy composite materials," *Journal of Composite Materials*, vol. 52, no. 8, pp. 1061–1072, 2018.
- [11] R. P. Singh and P. Aggarwal, "Effect of nanosilica on the properties of cement mortar," *CEM International*, vol. 13, pp. 65–70, 2015.
- [12] E. I. Akpan, X. Shen, B. Wetzel, and K. Friedrich, *Design and Synthesis of Polymer Nanocomposites*, Elsevier Inc, 2019.

- [13] G. Raghavendra, S. Ojha, S. K. Acharya, and S. K. Pal, "Influence of micro/nanofiller alumina on the mechanical behavior of novel hybrid epoxy nanocomposites," *High Performance Polymers*, vol. 27, no. 3, pp. 342–351, 2015.
- [14] F. Perreault, A. Fonseca De Faria, and M. Elimelech, "Environmental applications of graphene-based nanomaterials," *Chemical Society Reviews*, vol. 44, no. 16, pp. 5861–5896, 2015.
- [15] J. Datta, P. Kosiorek, and M. Włoch, "Effect of high loading of titanium dioxide particles on the morphology, mechanical and thermo-mechanical properties of the natural rubber-based composites," *Iranian Polymer Journal*, vol. 25, no. 12, pp. 1021–1035, 2016.
- [16] G. Seshanandan, D. Ravindran, and T. Sornakumar, "Mechanical properties of nano titanium oxide particles - hybrid jute-glass FRP composites," *Materials Today: Proceedings*, vol. 3, no. 6, pp. 1383–1388, 2016.
- [17] G. Velmurugan, T. Shaafi, and M. S. Bhagavathi, "Evaluate the tensile, flexural and impact strength of hemp and flax based hybrid composites under cryogenic environment," *Materials Today: Proceedings*, vol. 50, pp. 1326–1332, 2022.
- [18] A. Atiqah, M. N. M. Ansari, M. S. S. Kamal, A. Jalar, N. N. Afeefah, and N. Ismail, "Effect of alumina trihydrate as additive on the mechanical properties of kenaf/polyester composite for plastic encapsulated electronic packaging application," *Journal of Materials Research and Technology*, vol. 9, no. 6, pp. 12899–12906, 2020.
- [19] Z. Yang, H. Peng, W. Wang, and T. Liu, "Crystallization behavior of poly (ϵ -caprolactone)/layered double hydroxide nanocomposites," *Journal of Applied Polymer Science*, vol. 116, pp. 2658–2667, 2010.
- [20] B. Bakri, A. E. E. Putra, A. A. Mochtar, I. Renreng, and H. Arsyad, "Sodium bicarbonate treatment on mechanical and morphological properties of coir fibres," *International Journal of Automotive and Mechanical Engineering*, vol. 15, no. 3, pp. 5562–5572, 2018.
- [21] A. Karthikeyan, K. Balamurugan, and A. Kalpana, "The effect of sodium hydroxide treatment and fiber length on the tensile property of coir fiber-reinforced epoxy composites," *Science and Engineering of Composite Materials*, vol. 21, no. 3, pp. 315–321, 2014.
- [22] G. Velmurugan, M. A. S. Pasha, and V. Arasu, "Woven hemp and glass fiber hybrid composite - a comparative study on flexural and hardness properties with and without NaOH treatment," *International Journal of Pure and Applied Mathematics*, vol. 119, pp. 1973–1978, 2018.
- [23] G. Velmurugan, K. Babu, L. I. Flavia, C. S. Stephy, and M. Hariharan, "Utilization of grey Taguchi method to optimize the mechanical properties of hemp and coconut shell powder hybrid composites under liquid nitrogen conditions," in *IOP Conference Series: Materials Science and Engineering*, vol. 923no. 1, p. 012045, Chennai, India, February 2020.
- [24] M. A. Rahuman, S. S. Kumar, R. Prithivirajan, and S. G. Shankar, "Dry sliding wear behavior of glass and jute fiber hybrid reinforced epoxy composites," *International Journal of Engineering Research and Development*, vol. 10, no. 11, pp. 46–50, 2014.
- [25] N. A. Rahman, A. Hassan, R. Yahya, R. A. Lafia-Araga, and P. R. Hornsby, "Polypropylene/glass fiber/nanoclay hybrid composites: morphological, thermal, dynamic mechanical and impact behaviors," *Journal of Reinforced Plastics and Composites*, vol. 31, no. 18, pp. 1247–1257, 2012.

Research Article

Reconnoitring Wear Resistance and Mechanical Strengths of AA8111/B₄C/ZrO₂ Nanocomposite through Taguchi Route

Sathish Thanakodi,¹ Mohanavel Vinayagam,^{2,3} M. Ravichandran,⁴ T. Raja,⁵ A. H. Seikh,⁶ M. H. Siddique,⁷ and Beruk Hailu ⁸

¹Department of Mechanical Engineering, Saveetha School of Engineering, SIMATS, Chennai, Tamilnadu, India

²Centre for Materials Engineering and Regenerative Medicine, Bharath Institute of Higher Education and Research, Chennai, 600073 Tamil Nadu, India

³Department of Mechanical Engineering, Chandigarh University, Mohali 140413, Punjab, India

⁴Department of Mechanical Engineering, K.Ramakrishnan College of Engineering, Trichy, Tamil Nadu, India

⁵Department of Mechanical Engineering, Vel Tech Rangarajan Dr. Sagunthala R&D Institute of Science and Technology, Chennai, Tamil Nadu, India

⁶Mechanical Engineering Department, College of Engineering, King Saud University, P.O. Box 800, Riyadh 11421, Saudi Arabia

⁷Intelligent Construction Automation Centre, Kyungpook National University, Daegu, Republic of Korea

⁸Faculty of Mechanical Engineering, Haramaya Institute of Technology, Haramaya University, Ethiopia

Correspondence should be addressed to Beruk Hailu; beruk.hailu@haramaya.edu.et

Received 11 May 2022; Accepted 16 July 2022; Published 8 September 2022

Academic Editor: Arpita Roy

Copyright © 2022 Sathish Thanakodi et al. This is an open access article distributed under the Creative Commons Attribution License, which permits unrestricted use, distribution, and reproduction in any medium, provided the original work is properly cited.

Nowadays, the use of aluminium alloys is increasing in all domains of application, including industry, medical, electrical, and household appliances. In general, aluminium alloy is a lightweight material with great strength when compared to other alloys. According to the uses, the aluminium alloy must be strengthened by the inclusion of reinforced particles via the stir casting process. The purpose of this study was to create nanocomposite samples of AA8111/B₄C/ZrO₂ using a stir casting procedure. To prepare nanocomposite samples, the matrix of aluminium alloy AA8111 is supplemented with nanoparticles of boron carbide (B₄C) and zirconium dioxide (ZrO₂) in varied proportions. Optimize the stir casting parameters using a statistical approach such as the Taguchi technique to improve mechanical and wear attributes. The following process parameters were chosen: nanoparticle reinforcement quantity (4% to 10% with the step of 2%), melting temperature (800°C to 950°C with the step of 50°C), stir time (20 min to 35 min with the step of 5 minutes), and stir speed (400 rpm to 550 rpm with the step of 50 rpm). Wear and tensile strength tests are performed; the melting temperature is heavily impacted in the wear test, and the stir speed is heavily influenced in the tensile strength analysis. This experimental effort yielded a minimum wear of 0.085 mm³/m and a maximum ultimate strength of 167.6 N/mm².

1. Introduction

Compared to single material, the combination of different elements presents in the single material possesses extreme strength as well as excellent mechanical properties [1]. Different elements are blended into the base material named as composites materials, more than two materials of mixing called as hybrid composites [2–4]. Composite materials increase its strength while manufacturing the parts. In recent

days, the aluminium alloy material is highly used in the automobile field to satisfy various applications. Making of engine components and the body building of vehicles considered the aluminium alloy vastly due to its light weight and higher strength ratio. Aerodynamic consideration the aluminium alloy is the most wanted material in the aerospace applications; fabrications of wings and body structure are required aluminium alloy [5–7]. Different aluminium alloy series are available, based on the applications the

TABLE 1: AA8111 chemical constituents.

Chemical element	Quantity (%)
Silicon	1.1
Magnesium, mg	0.05
Zinc	0.10
Manganese	0.10
Titanium	0.08
Chromium	0.03
Iron	0.8
Copper	0.10
Aluminium	Remaining.

chosen of aluminium alloy with the main role in the manufacturing process. Household equipment and parts are fabricated by using aluminium alloys at a high rate. Home appliances such as pressure cooker, furniture items, electrical conductors, and packing container in the food processing units highly consumed aluminium alloy [8–10].

Strength of aluminium alloy materials is increased by reinforcing hard particles namely boron carbide, titanium carbide, silicon carbide, zirconium dioxide, aluminium oxide, etc. [11–13]. Reinforced particles boron carbide and zirconium dioxide are blended efficiently to the aluminium alloy which is achieved by powder metallurgy or stir casting process [14]. Using the powder metallurgy technique, the ball milling process was employed in blending the matrix material with reinforcing nanoparticles to obtain the homogeneous mixture. After conducting the ball milling process, the powders are compacted further; the green compact is sintered and extruded for conducting of different mechanical tests [15–17]. Stir casting process is called the liquid metallurgy process; it can be achieved by melting the base material with reinforced particles in the crucible [18, 19]. Stir casting process is improved through the selection of different process parameters. Effective reinforcement is obtained by using the stir casting process; it is a low-cost method for making composite materials [20–22].

In many engineering applications, the quality improvement is attained through statistical approach such as the Taguchi optimization method; it is one of the robust design methods [23, 24]. The Taguchi method is developed by Genichi Taguchi for improving the engineering quality such as the quality of manufacturing goods [25]. Most of the composites are undergone to wear and mechanical properties analysis; these analyses check the reinforcement accumulation and the strength of the composites [26–28]. This experimental work is aimed at fabricating nanocomposite samples of AA8111/B₄C/ZrO₂ through stir casting process and identifying the best performing sample from testing for mechanical strength and wear. Base material and reinforced particles are selected as aluminium alloy (AA8111) and boron carbide/zirconium dioxide, respectively. Taguchi L16 orthogonal array is included to optimize the manufacturing parameter of quantity of reinforcement and process parameters of stir casting process. Responses of this work is considered wear and ultimate tensile stress.

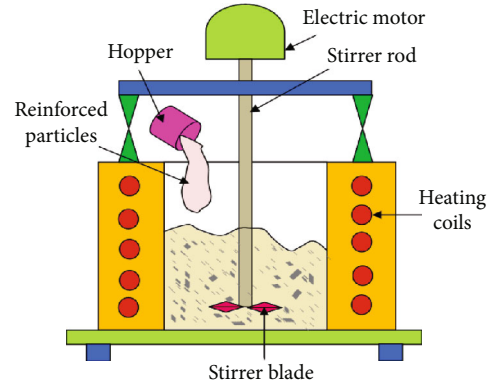


FIGURE 1: Stir casting setup.



FIGURE 2: Wear test specimen.

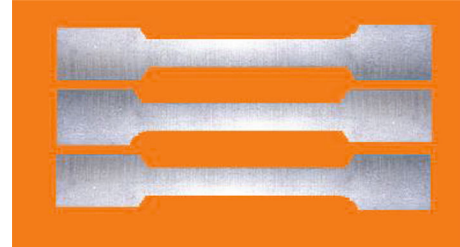


FIGURE 3: Tensile test specimens.

TABLE 2: AA8111/B₄C/ZrO₂ nanocomposite synthesizing variables and levels.

S. No.	Composites and testing parameters	Input levels			
		1	2	3	4
1.	Stir time (min) (ST)	20	25	30	35
2.	Melting temperature (°C) (MT)	800	850	900	950
3.	Stir speed (rpm) (SS)	400	450	500	550
4.	Nanoparticle reinforcement (%) (NPR)	3	6	9	12

2. Materials and Methods

Aluminium alloy AA8111 is the wrought alloy category; it possesses high strength, and hence, the base material was AA8111. The nanoreinforcement particles are zirconium

TABLE 3: Experimental observations' summary of ultimate tensile stress test and wear test.

Exp. runs	Reinforcement (%)	Stir speed (rpm)	Stir time (min)	Melting temperature (°C)	Wear rate (mm ³ /m)	Predicted Wear rate (mm ³ /m)	Ultimate tensile stress (N/mm ²)	Predicted ultimate tensile stress (N/mm ²)
1	4	400	20	800	0.234	0.258	95.2	98.065
2	4	450	25	850	0.303	0.310	112.3	110.815
3	4	500	30	900	0.219	0.362	132.7	123.565
4	4	550	35	950	0.520	0.414	124.2	136.315
5	6	400	25	900	0.085	0.231	78.3	102.870
6	6	450	20	950	0.314	0.164	121.1	96.340
7	6	500	35	800	0.610	0.647	155.8	159.170
8	6	550	30	850	0.544	0.580	163.0	152.640
9	8	400	30	950	0.316	0.282	120.3	115.375
10	8	450	35	900	0.533	0.490	145.7	143.525
11	8	500	20	850	0.655	0.460	124.3	133.115
12	8	550	25	800	0.747	0.668	161.7	161.265
13	10	400	35	850	0.573	0.568	153.2	150.980
14	10	450	30	800	0.686	0.656	167.6	159.850
15	10	500	25	950	0.395	0.433	129.5	137.920
16	10	550	20	900	0.318	0.522	143.7	146.790

TABLE 4: Signal-to-noise ratios for the observations of wear test.

Level	Nanoparticle reinforcement (%)	Stir speed on the melt (rpm)	Time duration of stirring (min)	Melting temperature (°C)
1	10.459	12.231	9.081	5.674
2	10.271	7.289	10.596	6.037
3	5.418	7.301	7.940	12.514
4	6.533	5.861	5.065	8.456
Delta	5.040	6.369	5.531	6.840
Rank	4	2	3	1

dioxide and boron carbide based on their appreciable qualities in improving mechanical and wear strengths [29]. Base material is procured from Sargam Metals Private Limited, Chennai, and reinforced particles are purchased from Ashoka Marketing Agencies, Chennai, with required quantity for conducting of experiments. Table 1 presents the chemical constituents of the AA8111 aluminium alloy and its density is 2.71 g/cc.

The method for synthesizing the samples of the proposed nanocomposite is the stir casting process. The aim this research is to improve the mechanical strengths and wear resistance by hybrid reinforcement of nanoparticles of B₄C and ZrO₂. The objectives of the research are synthesizing nanocomposite samples by varying reinforcement percentage and manufacturing parameters like stirring speed, stir time, and melting time. Statistical approach such as Taguchi methodology is concentrated for this experimental to optimize reinforcement quantity as well as parameters of the stir casting to fabricate best nanocomposite. The main motivation to implement L₁₆ is based on the four-level factors in the selected parameters.

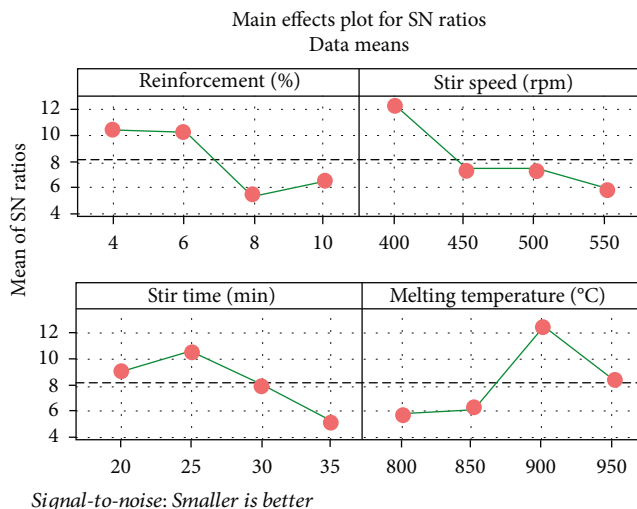


FIGURE 4: Main effects plot for S/N ratio (wear test).

TABLE 5: Analysis of variance (wear test).

Source	DF	Seq SS	Contribution	Adj SS	Adj MS	F value	P value
Regression	4	0.38866	69.51%	0.38866	0.09717	6.27	0.007
Reinforcement of nanoparticles	1	0.09687	17.32%	0.09687	0.09687	6.25	0.030
Stirring speed	1	0.09894	17.69%	0.09894	0.09894	6.38	0.028
Stirring duration	1	0.07103	12.70%	0.07103	0.07103	4.58	0.056
Melting temperature	1	0.12182	21.79%	0.12182	0.12182	7.86	0.017
Error	11	0.17049	30.49%	0.17049	0.01550		
Total	15	0.55915	100.00%				

TABLE 6: Optimization process input (wear test).

Response	Weight	Lower	Upper	Target	Goal	Importance
Rate of wear (mm^3/m)	1		0.7475	0.0847	Minimum	1

TABLE 7: Optimization process results (wear test).

Solution	Reinforcement (%)	Stirring speed	Stirring time	Melting temperature ($^{\circ}\text{C}$)	Wear rate (mm^3/m) fit	Composite desirability
1	4	400	20	950	0.0245325	1

3. Experimental Procedure

The reinforcement nanoparticles are blended at a predefined quantity with the AA8111 powder in a ball mill. Then homogeneous mixture was preheated through furnace separately; heating and melting are achieved by stir casting process. Different elements are melted simply by using the stir casting, and the bottom pouring furnace is considered for this work [30, 31]. The schematic diagram of the stir casting process with key components is furnished as shown in Figure 1.

Initially, the different weight percentages (4% to 10% with the step of increment 2%) of the ZrO_2 and B_4C with equal share were preheated in the furnace. The main advantages of the preheating process are improving the mixture rate and removing the unwanted impurities present in the elements of the reinforced particles. The preheating process is carried out 550°C for 4 hours in the crucible. The base material of the AA8111 is heated at an elevated temperature of 950°C continuously with the aid of bottom pouring furnace. The preheated reinforced molten material is poured into the molten base material; further, the different temperature levels (800°C , 550°C , 900°C , and 950°C) are maintained for melting the blended mixture. Also, the different stir time (20 min to 35 min with the step of increment 5 min) and stir speed (400 rpm, 450 rpm, 500 rpm, and 550 rpm) are considered for achieving homogeneous mixture. Finally, the melted materials are poured into the selected die and received the samples for conducting wear and mechanical tests.

3.1. Wear Test. The standard of ASTM G99 was followed to conduct the wear test. The samples were prepared the dimensions of 12 mm diameter and 35 mm length as shown in Figure 2.

The DUCOM dry sliding wear test apparatus is employed in investigating the wear property. The weight loss is measured by weighing the sample before and after the test. Wear test parameters are as follows: sliding distance of 1500 m, applied load of 40 N, and sliding velocity of 3 m/s were set for testing all specimens.

3.2. Tensile Test. The tensile test is conducted through universal testing machine (UTM) as per the ASTM E8 standard $100 \times 20 \times 5$ mm, and the tensile test specimens' image is illustrated in Figure 3. Specimen is fixed in between the jaws, and load is applied uniformly; at the same time, the strain was measured using an extensometer. Finally, the specimen is broken, and its dimensions are measured. The stir casting parameters and their levels are tabulated in Table 2.

4. Results and Discussion

Table 3 shows the experimental output for the tensile stress test and wear test. The minimum wear was observed at $0.085 \text{ mm}^3/\text{m}$ obtained at the parameter's levels of 900°C of melting temperature, 25 min of stir time, 400 rpm of stir speed, and 4% of nanoparticle reinforcement. In ultimate tensile stress analysis, the maximum ultimate tensile stress occurred at 167.6 N/mm^2 by involving 10% of reinforcement, 450 rpm of stir speed, 800°C molten temperature, 30 min of stir time, and 450 rpm of stir speed.

It was observed in Table 4 that the signal-to-noise ratio for wear test observations, the highly influencing factor, is melting temperature, the next was stir speed, and stir time and percentage of nanoparticle reinforcement are in the ranking order. The high signal was obtained for nanoparticle reinforcement contribution of 4%. In the case of stirring speed level 1400 rpm, the factor of stir time is 25 minutes, and the favourable melting temperature was 900 as shown in Figure 4.

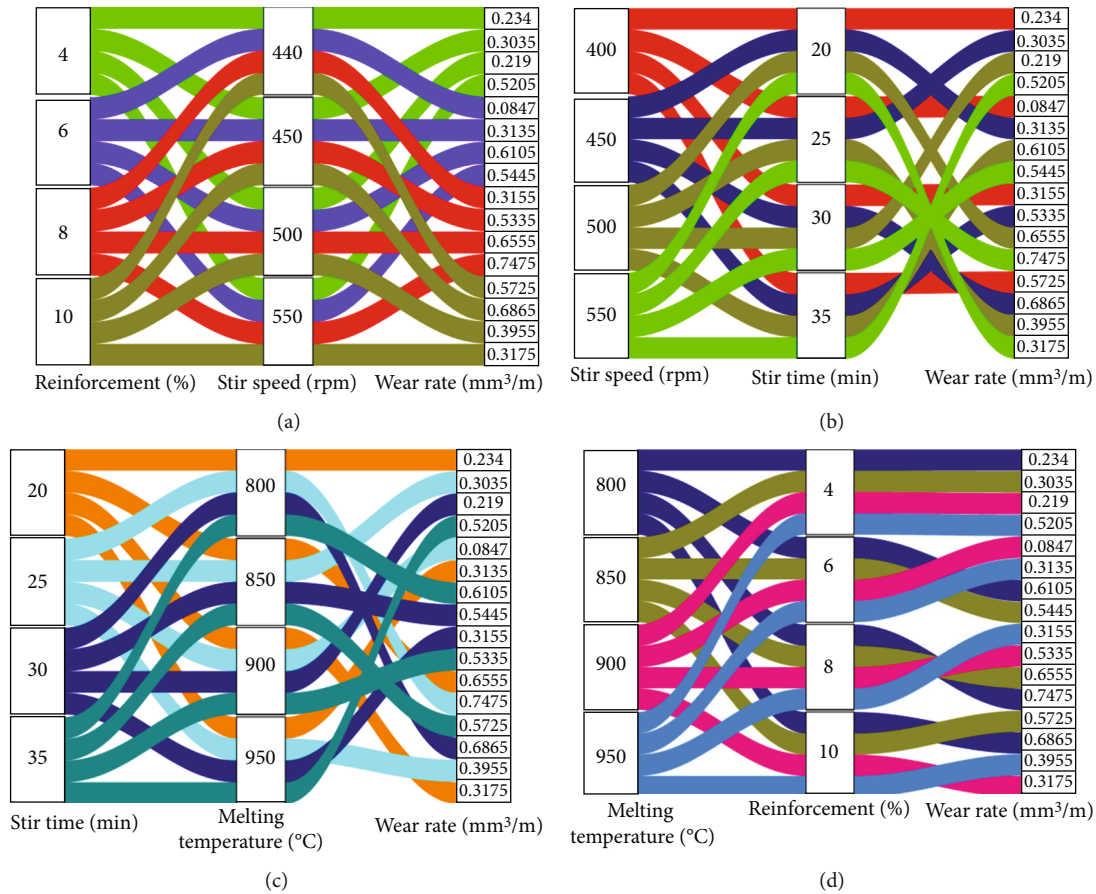


FIGURE 5: Parallel set plots: (a) stirring speed vs. reinforcement nanoparticles (%); (b) stirring time vs. stirring speed; (c) melting temperature vs. stir time; and (d) reinforcement nanoparticles (%) vs. melting temperature.

The minimum reinforcement percentage offered a minimum wear rate, improving the reinforcement percentage that increases the rate of wear of nanocomposite. Similarly, increasing the stir speed increases the wear rate. The minimum wear rate could be achieved at 400 rpm of stir speed offered at minimum. In consideration of the stir time, the 25 min duration resulted in the less rate of wear. Further, increasing the stir time, the wear rate also increases. Increasing the melting temperature decreases the wear rate, and 900°C of melting temperature offered a minimum wear rate.

Table 5 presents the contribution of each parameters in the wear test, and the melting temperature highly contributed as 21.79% compared to the remaining parameters. Stir speed contributed as 17.69%, reinforcement percentage contributed as 17.32%, and stir time contributed as 12.70%. Fisher’s value was estimated with the higher contribution levels.

4.1. Regression Equation.

$$\text{Wear rate (mm}^3/\text{m)} = 0.567 - 0.001561\text{MT} + 0.001407\text{SS} + 0.0348\text{NPR} + 0.01192\text{ST}. \tag{1}$$

Tables 6 and 7 illustrate the input and results of the optimization process; the optimized rate of wear is 0.0245 mm³/

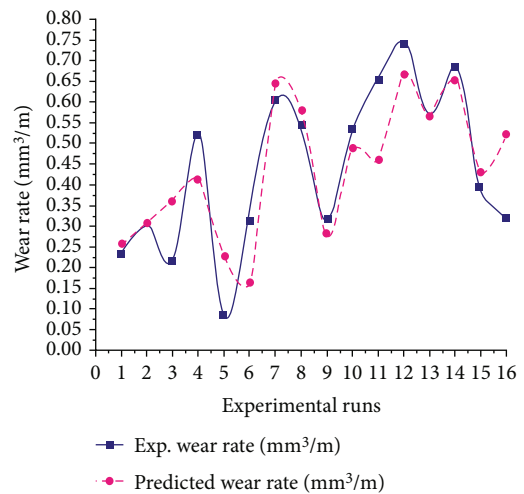


FIGURE 6: Experimental runs vs. wear rate (experimental and predicted).

m at the condition of 950°C of melting temperature by 400 rpm of stir speed, 4% of reinforcement, and 20 min of stir time as shown in Equation (1).

Figure 5 exhibits the correlation between two parameters based on the analysis. The relationship between nanoparticle

TABLE 8: Signal-to-noise ratios results of Taguchi for the observations of ultimate tensile stress.

Level	Reinforcement (%)	Stir speed (rpm)	Stir time (min)	Melting temperature (°C)
1	41.23	40.69	41.57	43.02
2	41.91	42.61	41.33	42.71
3	42.73	42.61	43.20	41.69
4	43.40	43.36	43.18	41.85
Delta	2.17	2.67	1.87	1.33
Rank	2	1	3	4

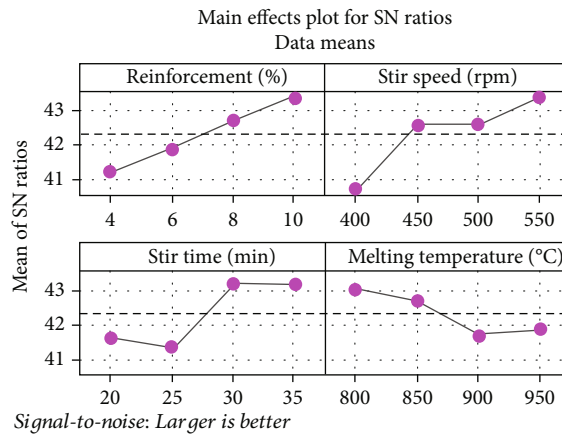


FIGURE 7: Main effects plot for S/N ratio (ultimate tensile stress test).

TABLE 9: Analysis of variance for ultimate tensile stress analysis.

Source	DF	Seq SS	Contribution	Adjusted sum of squares	Adjusted mean square	F value	P value
Regression	4	7614	80.64%	7614	1903.5	11.45	0.001
Reinforcement (%)	1	2232	23.64%	2232	2232.4	13.43	0.004
Stir speed (rpm)	1	2337	24.75%	2337	2337.1	14.06	0.003
Stir time (min)	1	1859	19.68%	1859	1858.6	11.18	0.007
Melting temperature (°C)	1	1186	12.56%	1186	1185.8	7.13	0.022
Error	11	1828	19.36%	1828	166.2		
Total	15	9442	100.00%				

reinforcement (%) and stir speed is shown in Figure 5(a). The minimum wear is observed at the condition of 400 rpm of stir speed and 6% of nanoparticle reinforcement. Figure 5(b) represents that associations among stir time and stir speed, from that 25 min of stirring time duration and 400 rpm of stir speed, offered a minimum wear rate. Figure 5(c) illustrates the connection between stir time and melting temperature, in that the 900°C of melting temperature and 25 min of stirring time duration recorded less rate of wear. Figure 5(d) correlates the melting temperature and reinforcement percentage, 6% of nanoparticle reinforcement, and 900°C of melting temperature registered as the minimum wear rate.

The association among predicted and experimental wear rate is depicted in Figure 6. Many of the observations from

experiment were occupied in between the range of predicted values spread; hence, the preferred model and data points were sufficient for conducting wear test.

From the ultimate tensile stress analysis, the stir speed was extremely involved due to the rank order as presented in Table 8. Further, the reinforcement percentage, stir time, and melting temperature are ranked accordingly based on the influence on the UTS. The higher UTS recorded at the levels of factors are as follows: 550 rpm of stir speed, 800°C of melting temperature, 30 min of stirring time, and 10% of nanoparticle reinforcement.

The highest reinforcement percentage (10%) and stir speed (550 rpm) recorded the maximum ultimate tensile stress as shown in Figure 7. Increasing the stir time from 20 min to 30 min, the ultimate tensile stress was increased.

TABLE 10: Optimization process input (ultimate tensile stress).

Response	Goal	Lower	Target	Upper	Weight	Importance
Ultimate tensile stress (N/mm ²)	Maximum	78.3	167.6		1	1

TABLE 11: Optimization process results (ultimate tensile stress).

Solution	Reinforcement (%)	Stir speed (rpm)	Stir time (min)	Melting temperature (°C)	Ultimate tensile stress (N/mm ²) fit	Composite desirability
1	10	550	35	800	191.11	1

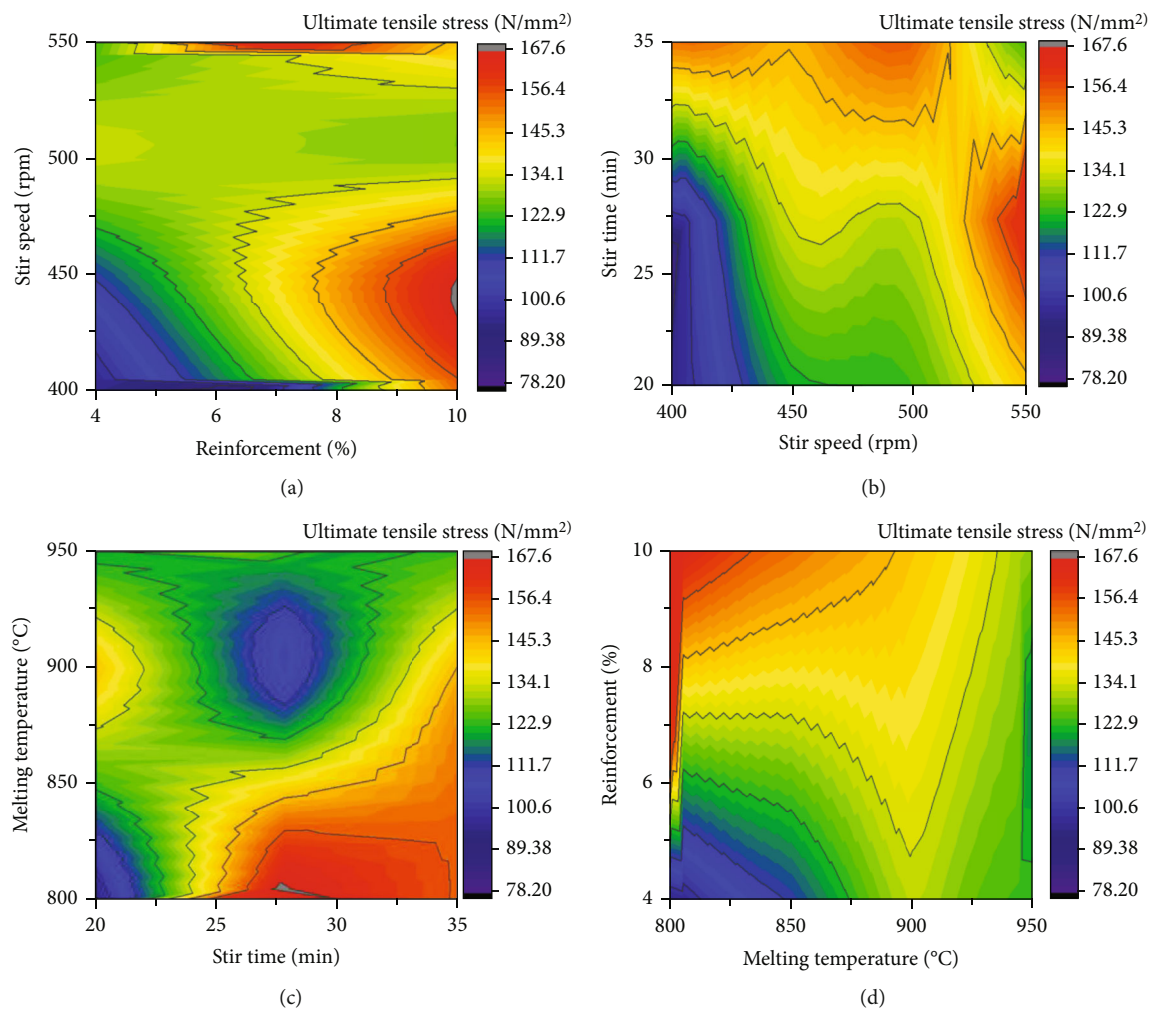


FIGURE 8: Contour plots: (a) stirring speed vs. percentage of nanoparticle reinforcement; (b) stirring duration (time) vs. stirring speed; (c) melting temperature vs. stirring duration (time); (d) percentage of nanoparticle reinforcement vs. melting temperature.

The minimum melting temperature of 800°C recorded the maximum ultimate tensile stress.

Stir speed (24.75%) was highly contributed in the ultimate tensile stress, followed by reinforcement (%) (23.64%), stir time (19.68%), and melting temperature (12.56%). All the contribution was decided by the F value, and a higher F value denoted the higher contribution in the ultimate tensile stress. The contribution of factors on UTS could be obtained from Table 9 based on the F value.

4.2. Regression Equation.

$$\begin{aligned} \text{Ultimate tensile strength (N/mm}^2\text{)} \\ = 75.1 + 1.928\text{ST} - 0.1540\text{MT} + 5.28\text{NPR} + 0.2162\text{SS} \end{aligned} \quad (2)$$

Tables 10 and 11 illustrate the input and results of the optimization process, the optimized ultimate tensile stress

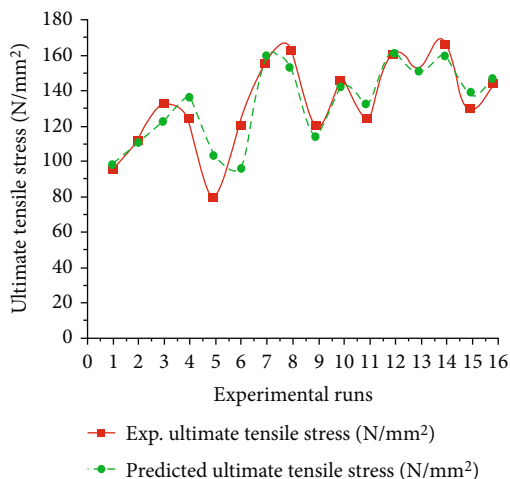


FIGURE 9: Experimental runs vs. ultimate tensile stress.

was registered as $191.110.0245 \text{ N/mm}^2$ by 800°C of melting temperature, 35 min of stir time, 550 rpm of stir speed, and 10% of nanoparticle reinforcement as shown in Equation (2).

The correlation between two parameters for the response of ultimate tensile stress is shown in Figure 8. Figure 8(a) shows the associations between reinforcement (%) and stir speed. The maximum ultimate tensile stress was noticed at the point with the nanoparticle reinforcement of 10% and stirring speed of 450 rpm. Figure 8(b) signifies the correlation between the speed of stirring while synthesizing the nanocomposite and the stirring time duration. Hence, the optimal condition is 30 min of stirring time, and the stirring speed of 550 rpm was recorded the maximum ultimate tensile stress. Figure 8(c) explains the correlation among stirring durations (time) and melting temperature, in that 800°C of melting temperature and stirring time was 30 min of the registered maximum ultimate tensile stress. Figure 8(d) illustrates the melting temperature and reinforcement percentage; hence, 10% of nanoparticle reinforcement with 800°C of melting temperature is the maximum ultimate tensile stress.

Figure 9 shows the relationship between experimental and predicted ultimate tensile stress. From this analysis, many experimental observations were fall within the range of predicted values; hence, the chosen model and data points were adequate for conducting ultimate tensile stress.

5. Conclusion

Using the stir casting process, the aluminium metal matrix (AMMCs) composites ($\text{AA8111} + \text{B}_4\text{C}/\text{ZrO}_2$) were produced successfully, and the stir casting process parameters were optimized. Finally, the minimum wear and maximum ultimate tensile stress was obtained through statistical analysis; the results were concluded as the follows:

- (i) Based on the wear test analysis, the minimum wear was found to be $0.085 \text{ mm}^3/\text{m}$ when 4 percent of nanoparticle reinforcement, 400 rpm stir speed, 25 min stir time, and 900°C melting temperature were all used. In the ultimate tensile stress study,

the maximum ultimate tensile stress was recorded as 167.6 N/mm^2 when 10% reinforcement, 450 rpm stir speed, 30 min stir duration, and 800°C molten temperature were used

- (ii) In the wear test, the best results were obtained with a 4 percent reinforcement, 400 rpm stir speed, 25 minute stir time, and a molten temperature of 900°C . In the same way, the best parameters for ultimate tensile stress analysis were 10% reinforcement, 550 rpm stir speed, 30 min stir time, and 800°C melting temperature
- (iii) From the wear test, the higher contribution was achieved as 21.79% by melting temperature contrast to remaining parameters. Stir speed contributed as 17.69%, reinforcement percentage contributed as 17.32%, and stir time contributed as 12.70%. In the ultimate tensile stress analysis, maximum contribution (24.75%) was reached by stir speed followed by reinforcement (%) (23.64%), stir time (19.68%), and melting temperature (12.56%)
- (iv) In the optimization process analysis, the minimum wear rate was registered as $0.0245 \text{ mm}^3/\text{m}$ at 950°C of melting temperature 400 rpm of stir speed, 4% of reinforcement percentage, and 20 min of stir time. Similarly, the optimized ultimate tensile stress was recorded as 191.11 N/mm^2 by 800°C of melting temperature, 550 rpm of stir speed, 10% of reinforcement percentage, and 35 min of stir time

Data Availability

The data used to support the findings of this study are included within the article. Further data or information is available from the corresponding author upon request.

Conflicts of Interest

The authors declare that there are no conflicts of interest regarding the publication of this paper.

Acknowledgments

The authors appreciate the supports from Haramaya University, Ethiopia, for the research and preparation of the manuscript. The authors thank Saveetha School of Engineering, SIMATS, K.Ramakrishnan College of Engineering, and Chandigarh University, for providing assistance to this work. The authors would like to acknowledge the Researchers Supporting Project Number (RSP-2021/373), King Saud University, Riyadh, Saudi Arabia.

References

- [1] Y. Pazhouhanfar and B. Eghbali, "Microstructural characterization and mechanical properties of TiB_2 reinforced Al6061 matrix composites produced using stir casting process," *Materials Science and Engineering: A*, vol. 710, pp. 172–180, 2018.

- [2] V. Mohanavel and M. Ravichandran, "Optimization of parameters to improve the properties of AA7178/Si3N4 composites employing Taguchi approach," *Silicon*, vol. 14, no. 4, pp. 1381–1394, 2022.
- [3] C. Jia, P. Zhang, X. Wenrui, and W. Wang, "Neutron shielding and mechanical properties of short carbon fiber reinforced aluminium 6061-boron carbide hybrid composite," *Ceramics International*, vol. 47, no. 7, pp. 10193–10196, 2021.
- [4] J. A. Jeffrey, S. S. Kumar, P. Hariharan, M. Kamesh, and A. M. Raj, "Production and assessment of AZ91 reinforced with nano SiC through stir casting process," *Materials Science Forum*, vol. 1048, pp. 9–14, 2022.
- [5] M. Dhanashekar, P. Loganathan, S. Ayyanar, S. R. Mohan, and T. Sathish, "Mechanical and wear behaviour of aa6061/sic composites fabricated by powder metallurgy method," *Materials Today: Proceedings*, vol. 21, pp. 1008–1012, 2020.
- [6] S. Murali, A. Chockalingam, S. Suresh Kumar, and M. Remanan, "Production, characterization and friction stir processing of AA6063-T6/Al3Tip in-situ composites," *International Journal of Mechanical and Production Engineering Research and Development*, vol. 2018, pp. 399–406, 2018.
- [7] N. R. J. Hynes, S. Raja, R. Tharmaraj, C. I. Pruncu, and D. Dispinar, "Mechanical and tribological characteristics of boron carbide reinforcement of AA6061 matrix composite," *Journal of the Brazilian Society of Mechanical Sciences and Engineering*, vol. 42, no. 4, pp. 1–11, 2020.
- [8] J. Zhu, W. Jiang, G. Li, F. Guan, Y. Yang, and Z. Fan, "Microstructure and mechanical properties of SiC_{np}/Al6082 aluminium matrix composites prepared by squeeze casting combined with stir casting," *Journal of Materials Processing Technology*, vol. 283, article 116699, 2020.
- [9] K. Halil, O. İsmail, D. Sibel, and Ç. Ramazan, "Wear and mechanical properties of Al6061/SiC/B₄C hybrid composites produced with powder metallurgy," *Journal of Materials Research and Technology*, vol. 8, no. 6, pp. 5348–5361, 2019.
- [10] A. H. Idrisi and A.-H. I. Mourad, "Conventional stir casting versus ultrasonic assisted stir casting process: mechanical and physical characteristics of AMCs," *Journal of Alloys and Compounds*, vol. 805, pp. 502–508, 2019.
- [11] T. Sathish, V. Mohanavel, K. Ansari et al., "Synthesis and characterization of mechanical properties and wire cut EDM process parameters analysis in AZ61 magnesium alloy+ B4C+ SiC," *Materials*, vol. 14, no. 13, p. 3689, 2021.
- [12] P. Madhukar, N. Selvaraj, R. Gujjala, and C. S. P. Rao, "Production of high performance AA7150-1% SiC nanocomposite by novel fabrication process of ultrasonication assisted stir casting," *Ultrasonics Sonochemistry*, vol. 58, article 104665, 2019.
- [13] N. Faisal and K. Kumar, "Mechanical and tribological behaviour of nano scaled silicon carbide reinforced aluminium composites," *Journal of Experimental Nanoscience*, vol. 13, Supplement 1, pp. S1–S13, 2018.
- [14] H. A. Al-Salihi, A. A. Mahmood, and H. J. Alalkawi, "Mechanical and wear behavior of AA7075 aluminum matrix composites reinforced by Al₂O₃ nanoparticles," *Nano*, vol. 5, no. 3, pp. 67–73, 2019.
- [15] C. A. Chairman, M. Ravichandran, V. Mohanavel et al., "Mechanical and abrasive wear performance of titanium dioxide filled woven glass fibre reinforced polymer composites by using Taguchi and EDAS approach," *Materials*, vol. 14, no. 18, p. 5257, 2021.
- [16] M. A. Taha, R. A. Youness, and M. F. Zawrah, "Review on nanocomposites fabricated by mechanical alloying," *International Journal of Minerals, Metallurgy, and Materials*, vol. 26, no. 9, pp. 1047–1058, 2019.
- [17] M. A. Taha, R. A. Youness, and M. A. Ibrahim, "Evolution of the physical, mechanical and electrical properties of sic-reinforced Al 6061 composites prepared by stir cast method," *Biointerface Research in Applied Chemistry*, vol. 11, pp. 8946–8956, 2020.
- [18] K. Gajalakshmi, N. Senthilkumar, B. Mohan, and G. Anbuezhayan, "An investigation on microstructure and mechanical behaviour of copper-nickel coated carbon fibre reinforced aluminium composites," *Materials Research Express*, vol. 7, no. 11, article 115701, 2020.
- [19] G. Anbuezhayan, B. Mohan, N. Senthilkumar, and R. Pugazhenthii, "Synthesis and characterization of silicon nitride reinforced Al-Mg-Zn alloy composites," *Metals and Materials International*, vol. 27, no. 8, pp. 3058–3069, 2021.
- [20] A. Munimathan, T. Sathish, V. Mohanavel et al., "Investigation on heat transfer enhancement in microchannel using Al₂O₃/water nanofluids," *International Journal of Photoenergy*, vol. 2021, Article ID 6680627, 9 pages, 2021.
- [21] M. Malaki, W. Xu, A. K. Kasar et al., "Advanced metal matrix nanocomposites," *Metals*, vol. 9, no. 3, p. 330, 2019.
- [22] K. Bhoi, H. S. Neeraj, and S. Pratap, "Synthesis and characterization of zinc oxide reinforced aluminum metal matrix composite produced by microwave sintering," *Journal of Composite Materials*, vol. 54, no. 24, pp. 3625–3636, 2020.
- [23] T. Sathish and N. Sabarirajan, "Synthesis and optimization of AA 7175-zirconium carbide composites machining parameters," *Journal of New Materials for Electrochemical Systems*, vol. 24, no. 1, pp. 34–37, 2021.
- [24] P. Mohanty, R. Mahapatra, C. H. Payodhar Padhi, V. V. Ramana, and D. K. Mishra, "Ultrasonic cavitation: an approach to synthesize uniformly dispersed metal matrix nanocomposites—a review," *Nano-Structures & Nano-Objects*, vol. 23, article 100475, 2020.
- [25] S. Thirumalvalavan and N. Senthilkumar, "Experimental investigation and optimization of hvof spray parameters on wear resistance behaviour of Ti-6Al-4V alloy," *Comptes Rendus de l'Academie Bulgare Des Sciences*, vol. 72, no. 5, pp. 665–674, 2019.
- [26] P. R. Jadhav, B. R. Sridhar, M. Nagaral, and J. I. Harti, "Mechanical behavior and fractography of graphite and boron carbide particulates reinforced A356 alloy hybrid metal matrix composites," *Advanced Composites and Hybrid Materials*, vol. 3, no. 1, pp. 114–119, 2020.
- [27] S. Hossain, M. D. Mamunur Rahman, D. Chawla et al., "Fabrication, microstructural and mechanical behavior of Al- Al₂O₃-SiC hybrid metal matrix composites," *Materials Today: Proceedings*, vol. 21, pp. 1458–1461, 2020.
- [28] P. Gurusamy, T. Sathish, V. Mohanavel et al., "Finite Element Analysis of Temperature Distribution and Stress Behavior of Squeeze Pressure Composites," *Advances in Materials Science and Engineering*, vol. 2021, Article ID 8665674, 9 pages, 2021.
- [29] M. Y. Zhou, L. B. Ren, L. L. Fan et al., "Progress in research on hybrid metal matrix composites," *Journal of Alloys and Compounds*, vol. 838, article 155274, 2020.
- [30] M. M. Ravikumar, S. Suresh Kumar, R. Vishnu Kumar, S. Nandakumar, J. Habeeb Rahman, and J. Ashok Raj,

“Evaluation on mechanical behavior of AA2219/SiO₂ composites made by stir casting process,” *AIP Conference Proceedings*, vol. 2405, article 050010, 2022.

- [31] N. K. Bhoi, H. Singh, and S. Pratap, “Developments in the aluminum metal matrix composites reinforced by micro/nano particles—a review,” *Journal of Composite Materials*, vol. 54, no. 6, pp. 813–833, 2020.

Research Article

Electrochemical Detection of H₂O₂ on Graphene Nanoribbons/Cobalt Oxide Nanorods-Modified Electrode

Preethika Murugan,¹ Ashok K. Sundramoorthy ,¹ Ramila D. Nagarajan,² Raji Atchudan,³ Rajeshkumar Shanmugam ,⁴ Dhanraj Ganapathy,¹ Sandeep Arya,⁵ Asma A. Alothman ,⁶ and Mohamed Ouladmane⁶

¹Centre for Nano-Biosensors, Department of Prosthodontics, Saveetha Dental College and Hospitals, Saveetha Institute of Medical and Technical Sciences, Poonamallee High Road, Velappanchavadi, Chennai, 600077 Tamil Nadu, India

²Department of Chemistry, V. V. Vanniaperumal College for Women, Virudhunagar, 626001 Tamil Nadu, India

³School of Chemical Engineering, Yeungnam University, Gyeongsan 38541, Republic of Korea

⁴Centre for Transdisciplinary Research, Department of Pharmacology, Saveetha Dental College, Saveetha Institute of Medical and Technical Sciences, Chennai, India

⁵Department of Physics, University of Jammu, Jammu, Jammu and Kashmir 180006, India

⁶Department of Chemistry, College of Science, King Saud University, Riyadh 11451, Saudi Arabia

Correspondence should be addressed to Ashok K. Sundramoorthy; ashok.sundramoorthy@gmail.com

Received 12 May 2022; Revised 21 July 2022; Accepted 14 August 2022; Published 8 September 2022

Academic Editor: H C Ananda Murthy

Copyright © 2022 Preethika Murugan et al. This is an open access article distributed under the Creative Commons Attribution License, which permits unrestricted use, distribution, and reproduction in any medium, provided the original work is properly cited.

The most important biological changes which have to be monitored is the mechanism of ageing in the human body where the mitochondria play a major role. Hydrogen peroxide (H₂O₂) is one of the important markers for the reactive oxygen species (ROS), which denatures the protein and DNA, that was the main contributory factor of ageing. So, it is very important to monitor H₂O₂ levels in the biological samples. Herein, we reported the preparation of 1D graphene nanoribbon/cobalt oxide nanorod (GNR/Co₃O₄) based nanocomposite-modified electrochemical sensor for H₂O₂. Firstly, GNR was synthesized by oxidative unzipping of multiwalled carbon nanotubes (MWCNTs). Secondly, cobalt oxide nanorods (Co₃O₄) were grown onto GNR by a chemical reduction process. As-prepared nanocomposite was characterized by UV-Visible spectroscopy (UV-Vis) and HR-TEM. Electrochemical properties of GNR/Co₃O₄-coated electrode were studied by cyclic voltammetry (CV) which showed two redox peaks at 0.93 and 0.88 V in phosphate buffer solution. Next, the electrocatalytic activity of GNR/Co₃O₄-coated electrode was studied against H₂O₂ oxidation. The electrochemical studies revealed that GNR/Co₃O₄-coated electrode exhibited high electrocatalytic activity for H₂O₂ oxidation at 0.925 V. This sensor showed a linear response for H₂O₂ oxidation from 10 to 200 μM. The limit of detection (LOD) was calculated to be 1.27 μM. The selectivity of the sensor was also studied with other biomolecules associated in the human body, and the results showed that interference effect is negligible. Thus, the proposed GNR/Co₃O₄-modified electrode can be used for H₂O₂ detection with excellent stability and selectivity.

1. Introduction

Hydrogen peroxide (H₂O₂) is a well-known oxidizing agent. The process of manufacturing of H₂O₂ and its applications in various sectors are well documented [1]. H₂O₂ has been used in different industrial applications such as environmental, textile, clinical, pharmaceutical, and food [2]. Also, the importance of H₂O₂ is reported in many biosynthetic reac-

tions and immune cell activation process [3]. The majority of the biological reactions were catalyzed by different enzymes such as lactate oxidase, cholesterol oxidase, D-amino acid oxidase, glutamate oxidase, and lysine oxidase, which resulted in the formation of H₂O₂ as a by-product. Thereby, it acts as a reactive oxygen species (ROS) that can promote the denaturation of proteins and DNA by oxidative processes [4]. Though it has cytotoxic effects, it plays a vital

role in controlling the physiological process of immune cell activation and vascular remodelling [5]. H_2O_2 involves in enzymatic reactions and acts as an intermediate for the level of glucose, lactose, and cholesterol [6]. Generally, H_2O_2 can enter into our body through consumption of instant coffee, green tea, or black tea that can raise the H_2O_2 concentration level above $100\ \mu\text{M}$ which may enter into the gastrointestinal tract [7]. According to the US National Institute for Occupational Safety and Health, the permitted exposure limit of H_2O_2 is 1 ppm based on time-weighted average, but if it reaches above the level of 75 ppm, that is dangerous to health and may lead to death [8]. The anomalous level of H_2O_2 production in the human body may lead to carcinogenesis and severe complications such as formation of cancer and heart attack [9]. Thus, there is a vital need for monitoring H_2O_2 concentrations in the biological and environmental samples [10]. The analysis of H_2O_2 was generally carried out by traditional analytical methods such as spectrophotometry [11], colorimetry [12], fluorimetry [13], and electrochemical methods [14–17]. Colorimetry and fluorimetry methods are considered to be expensive and may not be suitable for general laboratory use. Electrochemical sensing of H_2O_2 can be performed by enzymatic and nonenzymatic methods [18, 19]. Enzymatic electrochemical sensors are vulnerable to the environmental factors such as temperature, pressure, pH, and biological pathogens [20]. The above-stated problems can be neglected by using nonenzymatic electrochemical sensors [21]. Majumder et al. reported a nonenzymatic electrochemical sensor for H_2O_2 and hydrazine using 3D microsnowflake architectures of $\alpha\text{-Fe}_2\text{O}_3$ [22]. In 2019, Liu et al. prepared an innovative electrochemical sensor for detection of H_2O_2 using the hollow CuO/polyaniline nanohybrid fibers which exhibited a good linear range, lowest LOD, high selectivity, and extended stability [23]. Baghayeri et al. have prepared magnetic graphene oxide functionalized with an amine-terminated material that showed excellent electrochemical activity against H_2O_2 in the linear range of 0.05 to $160\ \mu\text{M}$ with LOD of $0.01\ \mu\text{M}$ [24].

Recently, carbon nanomaterials such as carbon dots (0D), carbon nanotubes (1D) [25, 26], graphene (2D) [27, 28], and graphite (3D) [29, 30] have been exploited as electrode materials for various electrochemical applications [31, 32]. Graphene nanoribbons (GNR) is a narrow strip of graphene with a quasi one-dimensional structure, which holds complementary properties of graphene sheet [33]. From the theoretical analysis, GNR's electrical nature can be tuned by the size and edge formation, and they can differ from metallic to semiconducting nature [34, 35]. The physical properties of the GNR are based on the length, width, and number of layers, which in the sequence depends on their preparation process. There are three methods available for the preparation of GNR: (i) cutting graphene by using different lithographic techniques [36, 37], (ii) bottom-up synthesis from polycyclic molecules [38, 39], and (iii) unzipping of carbon nanotubes [40–42]. Although the bottom-up technique offers a method to definite edge control, the lithographic process can produce GNR with exact location. However, the unzipping process offers the benefit of bulk preparation of GNR on a large scale. GNR prepared by the

unzipping process has been effectively used in many applications such as a catalyst support for lithium-ion batteries [43, 44]. Unzipping of multiwall carbon nanotubes (MWCNTs) are classified into four types: (a) the reductive intercalation-assisted method [45], (b) the oxidative unzipping [46], (c) the electrochemical unzipping [47], and (d) miscellaneous approaches [48]. The first method depends on the familiar capability of alkali compounds to interpolate by the expansion of graphite along the z -axis direction. This process of unzipping of MWCNTs creates lattice expansion tempts high strain within the concentric walls, succeeding in the breaking or opening of longitudinal directions of the tubes [33]. Common intercalants such as lithium and potassium metals have been used [33] which produced GNR with high conductivity, but they persisted multilayered flakes. GNR cannot be separated into single-layer ribbons because of the attraction between the surfaces. The oxidative method comprises treating of MWCNTs in a lower pH environment with a preparation as similar to synthesis of graphene oxide from the natural graphite [49]. Pristine graphene has an inert chemical surface without defects, and they exhibited poor water solubility. On the contrary, as-prepared GNRs are more reactive. The high reactivity of GNRs are linked to the adsorption of analytes via π – π stacking interaction and by electrostatic or hydrogen bonding interactions with functionalities of the target molecules or the oxygen moieties located at the edges of the graphene material [50].

The purpose of using nanomaterials in the fabrication of sensors is to increase the sensitivity, enhance catalytic activity of the process, reduce the over potentials, and increase the electron transfer rate of the reaction [51, 52]. Transitional metals mainly boost the oxidation of several substrates because they can initiate the process of multielectron oxidation [53]. Also, nanoscale compounds can improve diffusion and offers a good active surface for electrocatalytic reactions [54]. Cobalt oxide-based nanomaterials (Co_3O_4) have been used in energy storage, electrochromic thin films, magneto-resistive devices, and heterogeneous catalysis [55]. Additionally, Co_3O_4 remains an attractive catalyst, mainly due to its outstanding electrocatalytic activity against ozone and oxygen.

Herein, a nanocomposite made of 1D GNR/ Co_3O_4 was prepared by the top-down method and then used to fabricate an electrochemical H_2O_2 sensor. Firstly, Co_3O_4 nanorods were synthesized by a chemical reduction process. Secondly, GNR was synthesized by oxidative unzipping of multiwalled carbon nanotubes (MWCNTs). Followed by, GNR/ Co_3O_4 nanocomposite was prepared and characterized by UV-visible (UV-Vis) and HR-TEM. Electrochemical properties of GNR/ Co_3O_4 were studied by cyclic voltammetry (CV) which showed two redox peaks centered at 0.93 and 0.88 V in phosphate buffer solution. Next, electrochemical oxidation of H_2O_2 was performed on GNR/ Co_3O_4 -modified electrode. Further, the electrochemical studies were revealed that the H_2O_2 oxidation occurs at 0.925 V. By using CV, the linear response of the sensor was obtained from 10 to $200\ \mu\text{M}$ H_2O_2 , and LOD was calculated as $1.27\ \mu\text{M}$. The selectivity of the sensor was also studied for H_2O_2 oxidation in the presence of other biomolecules. It was concluded that

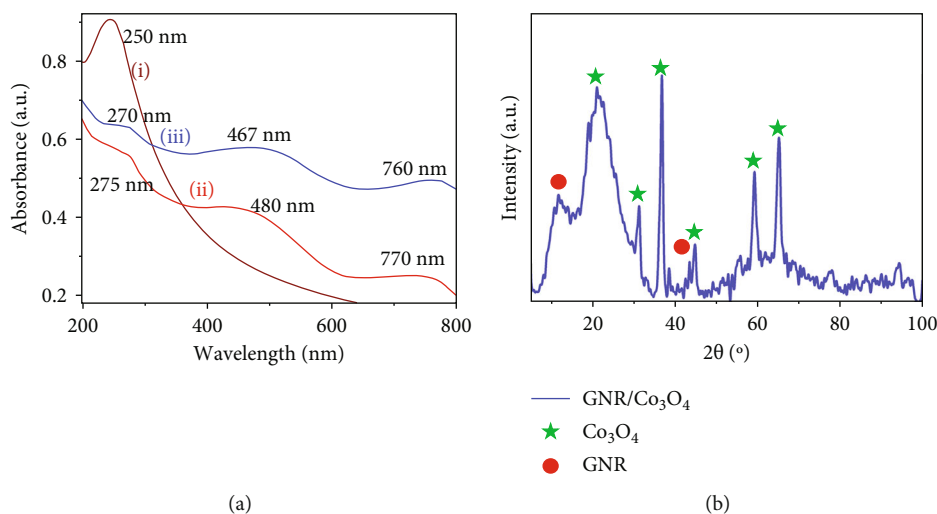


FIGURE 1: (a) UV-Vis spectra of (i) GNR, (ii) Co₃O₄ nanorods, and (iii) GNR/Co₃O₄ dispersions. (b) XRD spectrum of GNR/Co₃O₄ film.

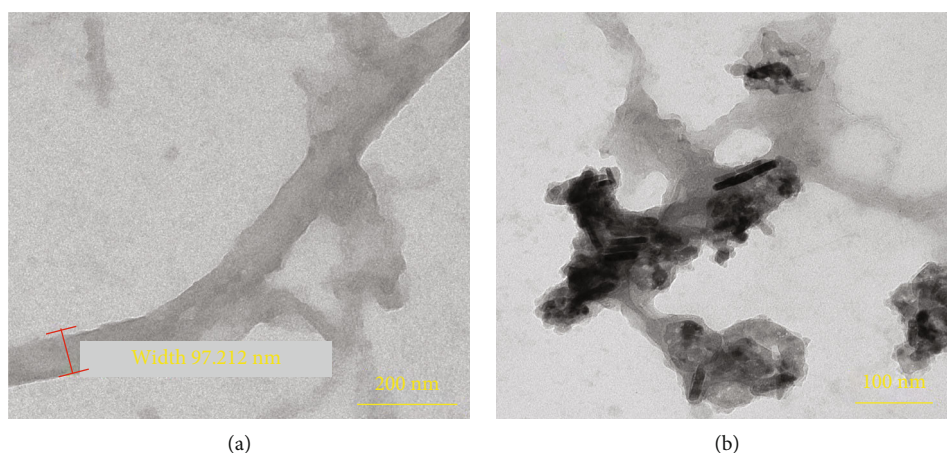


FIGURE 2: HR-TEM images of (a) GNR and (b) GNR/Co₃O₄ nanocomposite dispersions.

the proposed GNR/Co₃O₄-modified electrode could be used for selective detection of H₂O₂.

2. Experimental

2.1. Materials and Methods. Cobalt nitrate hexahydrate, MWCNTs, sodium hydroxide, and ascorbic acid (AA) were obtained from Sigma-Aldrich, India. Sulphuric acid, H₂O₂, uric acid (UA), paracetamol (PA), glucose, lactose, L-isoleucine, L-tyrosine, and potassium permanganate (KMnO₄) purchased from SRL, India. The phosphate buffer electrolyte solution was prepared using NaH₂PO₄ and Na₂HPO₄ (pH = 7.4) for the sensing of H₂O₂. All the chemicals were of analytical grade and used without any further purifications. All the solutions were prepared with the milli-Q-water (18.2 MΩ·cm @ 25 ± 2°C). Electrochemical studies were carried out using a three-electrode system with an electrochemical workstation (Model: CHI-760E, USA). UV-Vis spectra of GNR/Co₃O₄ nanocomposite was recorded using 2000c nanodrop spectrophotometer, Nanodrop Technologies, USA. All the experiments were done at room temperature (25 ± 0.2°C). The surface morphology of GNR/Co₃O₄

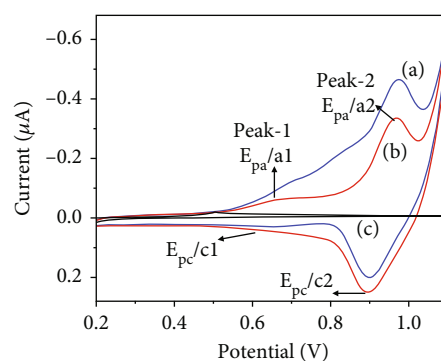


FIGURE 3: CVs of GNR/Co₃O₄/GCE were recorded in the absence (curve b) and presence of 30 μM H₂O₂ (curve a) in 0.1 M PBS (pH 7.4). CVs were also recorded using a bare GCE in 0.1 M PBS (pH 7.4) with 30 μM H₂O₂ (curve c). Scan rate = 50 mV/s.

was examined by high-resolution transmission electron microscope (HR-TEM) (Model: 2100, JEOL, Japan). Samples for HR-TEM were prepared by coating of GNR/Co₃O₄ dispersion on the copper grid and dried in a vacuum oven at room temperature.

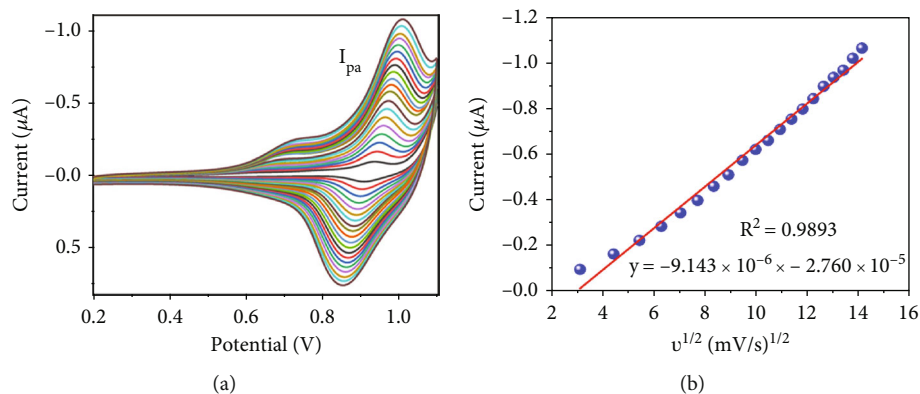


FIGURE 4: (a) CVs were recorded at different scan rates from 10 to 200 mV/s using a GNR/Co₃O₄/GCE in 0.1 M PBS (pH 7.4) containing 30 μM H₂O₂. (b) A linear plot was made between oxidation peak currents of H₂O₂ and square root of scan rates.

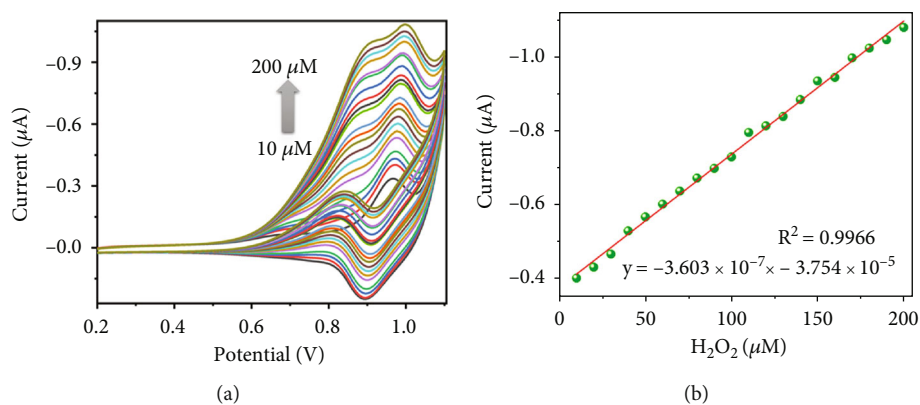


FIGURE 5: (a) CVs of GNR/Co₃O₄/GCE were recorded in 0.1 M PBS (pH 7.4) at a scan rate of 50 mV/s with successive additions of 10 μM of H₂O₂ in the range from 10 to 200 μM. (b) A linear calibration plot was made between I_{pa} vs. [H₂O₂].

2.2. Synthesis of GNR by Unzipping of MWCNTs. 0.025 g of MWCNTs was mixed with 7.5 mL of conc. sulfuric acid and then constantly stirred using a magnetic stirrer for 3 h at room temperature. After that, 0.125 g of potassium permanganate (KMnO₄) was added, and then, solution temperature was maintained at below 10°C using an ice-bath for 2 h. After that, the temperature was increased up to 35°C for 30 min. and then further increased up to 75°C for the next 30 min. Finally, this mixture was added in to 300 mL of ice water containing 10 mL of 30% H₂O₂ and filtered. After that, the reaction mixture washed with distilled water until the solution pH reaches neutral. As-synthesized GNR was filtered and dried in the vacuum oven at 60°C for 10 h [56].

2.3. Synthesis of GNR/Co₃O₄ Nanorods Nanocomposite. Sodium hydroxide (2.0 M, 5.0 mL) solution was added into the cobalt nitrate hexahydrate solution (0.01 M, 50 mL). In this step, the color of the solution turned into pale pink and then dark pinkish brown. 5 mL of GNR (0.1 mg/mL) aqueous dispersion was added into the pinkish-brown solution which turned as a dark black dispersion. After stirring for 0.5 h, AA solution (0.6 M, 5.0 mL) was added drop-wise into the solution. The black color liquid was slowly formed which was stirred for 3 h at 55°C. The precipitate was collected by centrifugation and washed with distilled water to remove the impurities and finally dried in a vacuum oven

at 60°C for 5 h. Additionally, the prepared GNR/Co₃O₄ nanocomposite was calcinated for 2 h at 300°C.

2.4. Preparation of GNR/Co₃O₄/GCE. Initially, GCE was polished on a polishing pad with the sequence of alumina powder (Al₂O₃, sizes with ~1 μm, ~0.3 μm, and ~0.05 μm). Next, the GCE was washed with ultrapure Milli-Q water and left to air-dry at room temperature. After that, 10 μL of homogeneous GNR/Co₃O₄ (1 mg/mL) nanocomposite dispersion was drop casted on the electrode surface and left to dry. To discard the unbounded particles, the GNR/Co₃O₄/GCE was rinsed with distilled water. In the same manner, GNR/GCE and Co₃O₄/GCE were prepared for the control experiments.

3. Results and Discussion

3.1. UV-Visible Spectroscopy. UV-Vis spectra of GNR dispersion showed a strong absorbance band at 250 nm, which denoted the $\pi - \pi^*$ transition of aromatic C=C bonds, that was assigned to the partially oxidized graphene (Figure 1(a), curve i) [57]. Figure 1(a) (curve ii) shows the absorbance bands for Co₃O₄ nanorods at 275 and 480 nm which denoted the charge transfer from (O²⁻ → Co²⁺ and O²⁻ → Co³⁺) [58]. The broad peak found at 770 nm can be assigned to the d-d transition band from ⁴A₂ (F) → ⁴T₁ (p) transition of Co²⁺

TABLE 1: The comparison of the various reported electrochemical H_2O_2 sensors with the proposed method.

S. no.	Electrode modification	Linear range (μM)	LOD (μM)	References
1	GS-PSS/GRCAPS	10-12000	3.3	[63]
2	rGO- Fe_2O_3	50-9000	6	[64]
3	Co_3O_4 -rGO	15-675	2.4	[65]
4	GNR/ Co_3O_4 /GCE	10-200	1.27	This work

G: graphene; PSS: poly(sodium 4-styrenesulfonate); GRCAPS: graphene capsules; rGO: reduced graphene oxide; Fe_2O_3 : iron oxide.

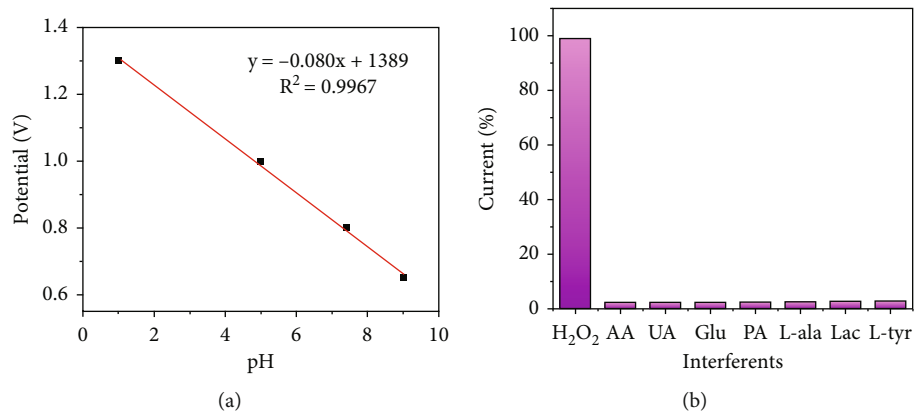


FIGURE 6: (a) A linear plot was made between the pH vs. redox potential of GNR/ Co_3O_4 /GCE. CVs were recorded in different pH (1, 5, 7.4, and 9) buffer solutions using a GNR/ Co_3O_4 /GCE. (b) Bar diagram shows the variations in the obtained current response (%) of $10 \mu M H_2O_2$ after additions of $10 \mu M$ of AA, UA, glucose, PA, L-alanine, lactose, and L-tyrosine.

[58]. Figure 1(a) (curve iii) shows the absorbance spectrum of GNR/ Co_3O_4 nanocomposite, where cobalt charge transfer peaks were blue shifted and observed at 270 and 467 nm. The peak shift was also observed in the d-d transition peak at 760 nm, indicating that composite was formed successfully. Next, the XRD patterns of the GNR/ Co_3O_4 nanocomposite was recorded as shown in Figure 1(b). GNRs exhibited a peak at 2θ of 11.9° , which confirmed the unzipping of MWCNTs, and confirmed the successful formation of GNR sheets [59]. The XRD peaks of MWCNTs were diminished and disappeared at 25.8° and 44° [60]. The other XRD bands were observed at $2\theta = 20.2^\circ$ (111), 30.7° (220), 38.6° (311), 44.8° (400), 58.7° (511), and 65.38° (440), which indicated the presence of Co_3O_4 [61].

3.2. HR-TEM. Figures 2(a) and 2(b) show the HR-TEM images of (a) GNR and (b) GNR/ Co_3O_4 nanocomposite. GNR dispersion showed the unzipped MWCNTs clearly with the breadth of 97.2 nm. The GNR could be observed with few ribbons overlapped with each other as shown in Figure 2(a). Interestingly, for the nanocomposite film, Co_3O_4 nanorods were decorated on the surface of GNRs which can be observed from TEM image of GNR/ Co_3O_4 nanocomposite.

3.3. Electrochemical Oxidation of H_2O_2 . Electrochemical activities of GNR/ Co_3O_4 -modified GCE and bare GCE were performed by cyclic voltammetry (CV). GNR/ Co_3O_4 /GCE exhibited two redox peaks. In the first anodic scan, two oxidation peaks a1 and a2 were observed at 0.68 V and 0.93 V. In the reverse scan, two cathodic peaks (c1 and c2) were observed at 0.65 V and 0.88 V, respectively. The formal

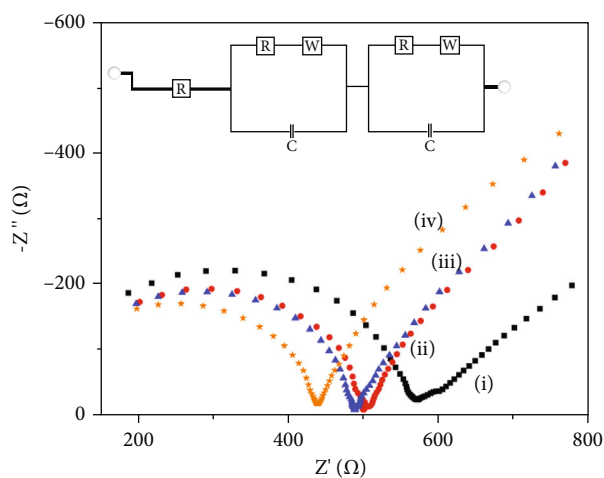


FIGURE 7: The Nyquist plots were recorded using (i) bare GCE, (ii) GNR/GCE, (iii) Co_3O_4 nanorods, and (iv) GNR/ Co_3O_4 /GCE in 0.1 M KCl with 5 mM $[Fe(CN)_6]^{3-/4-}$ by applying an AC voltage with 5 mV amplitude in a frequency range from 100 MHz to 100 kHz.

potential of the two redox peaks were found to be 0.665 V (peak I) and 0.905 V (peak II) (Figure 3 curve b). Cobalt oxide-modified electrode showed two pairs of redox peaks due to the Co(II)/Co(III) transition at the GCE surface as given in Equation (1) [62]. Electrocatalytic activity of the GNR/ Co_3O_4 -modified GCE (Figure 3, curve a) was recorded in 0.1 M phosphate buffer solution (PBS) containing $30 \mu M H_2O_2$. Due to the high electrocatalytic activity of the GNR/ Co_3O_4 /GCE, oxidation peak of Co_3O_4 was enhanced due

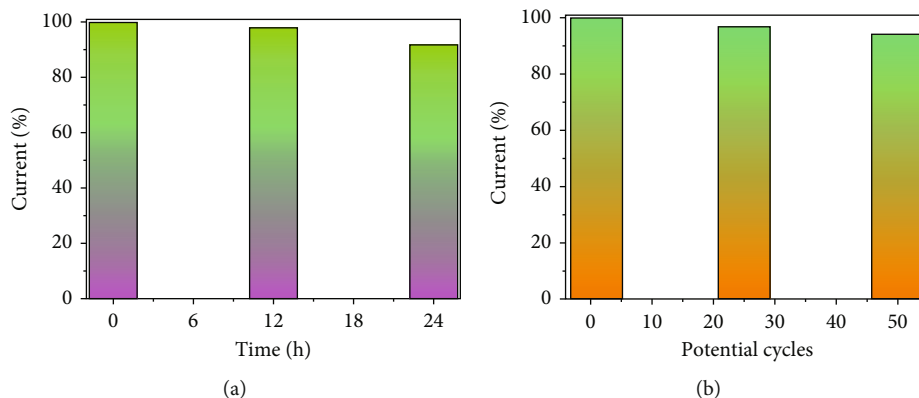
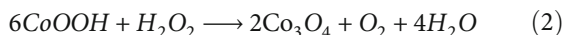
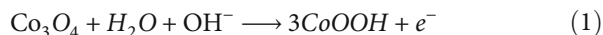


FIGURE 8: (a) The repeatability of GNR/Co₃O₄/GCE tested with 30 μM H₂O₂ after storage for different periods of time. (b) Stability study of GNR/Co₃O₄/GCE in PBS up to 50 CV cycles, scan rate = 50 mV/s.

TABLE 2: Electrochemical analysis of spiked H₂O₂ concentrations in an antiseptic solution using GNR/Co₃O₄/GCE.

S. no.	Samples	Added (μM)	Found (μM)	RSD (%)	Recovery (%)
1	Antiseptic solution with spiked H ₂ O ₂	40	38.7	4.01	96.75
2	Antiseptic solution with spiked H ₂ O ₂	50	49.1	3.61	98.20
3	Antiseptic solution with spiked H ₂ O ₂	60	59.76	3.26	99.60

to H₂O₂ oxidation at 0.925 V (Figure 3 curve a) Equation (2). For comparison, CVs of bare GCE was recorded from 0.2 to 1.1 V at the scan rate of 50 mV/s (Figure 3, curve c). Bare GCE showed only the nonfaradic current, which clearly indicated that GNR/Co₃O₄-modified GCE had more electrocatalytic activity. The surface coverage of the GNR/Co₃O₄-modified electrode was calculated using Equation (3),



$$I_p = \frac{n^2 F^2 \nu A \Gamma}{4RT} \quad (3)$$

where n is the number of electrons ($n = 2$), F is the faraday constant, R is the gas constant, A is the area of the electrode (0.0707 cm²), and T is the temperature [6]. From the slope of the graph between H₂O₂ oxidation current and square roots of scan rate (Figure 4), the surface coverage ($\Gamma_{\text{GNR/Co}_3\text{O}_4}$) of the electrode was calculated as 0.32×10^{-10} mol/cm².

To ascertain about the effects of scan rate, CVs of GNR/Co₃O₄/GCE were recorded in 0.1 M PBS containing 30 μM H₂O₂ with different scan rates (Figure 4(a)). The anodic peak currents of GNR/Co₃O₄/GCE were increased linearly with the increase of the scanning rate from 10 to 200 mV/s. The linear equation was established between H₂O₂ oxidation peak currents and square root of scan rates with a correlation coefficient of (R^2) 0.9893 (Figure 4(b)). It was found that H₂O₂ oxidation on GNR/Co₃O₄/GCE was a diffusion-controlled process [18].

Next, electrocatalytic oxidation of H₂O₂ on the GNR/Co₃O₄/GCE-modified electrode was studied in 0.1 M PBS by varying the concentrations. The oxidation peak of H₂O₂ takes place at the oxidation potential of Co³⁺ (0.925 V) with

each addition of 10 μM of H₂O₂. H₂O₂ oxidation peak currents were increased linearly from 10 to 200 μM (Figure 5(a)). Hence, a calibration plot was made between the concentration of H₂O₂ and the oxidation peak currents, which resulted in a linear equation of $Y = -3.603 \times 10^{-7}x - 3.754 \times 10^{-5}$ and (R^2) of 0.9966 (Figure 5(b)).

This data confirmed that GNR/Co₃O₄ can be used as an appropriate electrocatalyst for the analysis of H₂O₂. The limit of detection (LOD) was estimated as 1.27 μM. The sensitivity of the sensor was calculated as $5.10 \mu\text{A} \mu\text{M}^{-1} \text{cm}^{-2}$. We have also compared the analytical performance of this new sensor with other reported sensors in Table 1. It was clear that this new sensor is more promising than some of the reported H₂O₂ sensors.

3.4. Effect of pH and Interferent Studies on GNR/Co₃O₄/GCE.

GNR/Co₃O₄/GCE was subjected to study the effect of pH. CVs were recorded in different pH electrolyte solutions (from pH 1 to 9). It was found that the redox peak II of GNR/Co₃O₄/GCE was pH dependent which showed that protons are involved in the electron-transfer process. Figure 6(a) shows the linear plot of $E^{\circ'}$ vs. pH which gave a slope value of -80 mV/pH. This indicated that an unequal number of protons and electrons were involved in the electrochemical reactions [66]. For the electrochemical detection of H₂O₂, pH 7.4 was chosen as an appropriate electrolyte because of the physiological condition of the solutions.

The interferents analysis was carried out in the presence of H₂O₂ using the GNR/Co₃O₄/GCE. In this study, various common interfering biomolecules associated with the human body such as AA, PA, UA, glucose, lactose, L-isoleucine, and L-tyrosine were added (10 μM of each compound) with the analysis of 10 μM H₂O₂ (Figure 6(b)) [67]. These interfering molecules did not show any significant response

on the GNR/Co₃O₄/GCE. Therefore, it was suggested that GNR/Co₃O₄/GCE may be used for selective analysis of H₂O₂ by electrochemical oxidation.

3.5. Electrochemical Impedance, Repeatability, and Stability Studies. Electrochemical impedance spectroscopy (EIS) could reveal about the solid–liquid interface process of the modified electrodes. Figure 7 shows Nyquist plots obtained for (i) bare GCE, (ii) GNR/GCE, (iii) Co₃O₄/GCE, and (iv) GNR/Co₃O₄/GCE in 0.1 M KCl containing 5 mM [Fe(CN)₆]^{3−/4−}. The Nyquist impedance spectra obtained for (i) bare GCE (580 Ω), (ii) GNR/GCE (500 Ω), (iii) Co₃O₄/GCE (490 Ω), and (iv) GNR/Co₃O₄/GCE (425 Ω) indicated the charge transfer resistance (R_{ct}) of each electrode by various diameters of semicircles [16]. For bare GCE, a small semicircle was found with the resistance of 580 Ω due to good electron transfer process. However, after modification with GNR/GCE layer, the electron transfer resistance was slightly decreased to 500 Ω, and Co₃O₄/GCE showed R_{ct} of about 490 Ω. Interestingly, as-prepared nanocomposite showed the lowest R_{ct} of about 425 Ω [68, 69], which indicated the high conductivity of GNR in the nanocomposite. As shown in the inset of Figure 7, an equivalent electrical circuit model was prepared and fitted with the EIS data of GNR/Co₃O₄/GCE. In addition, this sensor retained 93% of the electrode response after 24 h of usage (Figure 8(a)) due to good stability of the materials. The repeatability of the GNR/Co₃O₄/GCE sensor was also tested with 30 μM H₂O₂. This new sensor response was only decreased about 5.4% after 50 potential cycles (Figure 8(b)).

3.6. Real Sample Analysis. The real-world sample analysis was carried out using a GNR/Co₃O₄/GCE sensor. In order to measure the concentration of H₂O₂ in a real-world sample, a commercial antiseptic sample was diluted for 10 times in phosphate buffer solution and spiked with 40, 50, and 60 μM of H₂O₂. These samples were analyzed by CV using a GNR/Co₃O₄/GCE sensor. The obtained results are shown in Table 2. The relative standard deviation (RSD) values for the detection of spiked H₂O₂ in three different samples were found to be 4.01%, 3.61%, and 3.26%. Also, the recoveries of spiked H₂O₂ were calculated using the same method, and the values were found in the range of 96.75 to 99.60%. Therefore, the above results indicated that H₂O₂ can be effectively determined in a real-world sample using GNR/Co₃O₄/GCE sensor. We believe that this new method can be adopted for the detection of H₂O₂ in various samples from the environmental and medical fields.

4. Conclusion

In this work, GNR was synthesized by unzipping of MWCNTs, and the Co₃O₄ nanorods were synthesized by AA as a reducing agent in alkaline condition. After that, GNR/Co₃O₄ nanocomposite was successfully prepared and used to modify the surface of GCE. UV-Vis and HR-TEM results showed the successful formation of Co₃O₄ nanorods on the GNR. The electrooxidation of H₂O₂ on the GNR/Co₃O₄-modified electrode taken place at the potential of

0.93 V. Furthermore, GNR/Co₃O₄ nanocomposite-coated GCE was successfully applied for the detection of H₂O₂ with high sensitivity and selectivity. The effect of scan rate on H₂O₂ oxidation at GNR/Co₃O₄ indicated the diffusion-controlled electrochemical process. Using CV, the linear range of H₂O₂ concentration was observed from 10 to 200 μM, and the LOD was estimated as 1.27 μM. The selectivity of the sensor was also studied in the presence of other biomolecules; it was confirmed that GNR/Co₃O₄-modified electrode may be used for selective detection of H₂O₂ with lower LOD.

Data Availability

The research data used to support the findings of this study are included in the article.

Disclosure

This research work was presented as an abstract at the International Conference on Technologies for Smart Green Connected Society, 2021 (SPAST Abstracts, 1(01); <https://spast.org/techrep/article/view/1369>).

Conflicts of Interest

The authors declare that they have no conflicts of interest.

Authors' Contributions

Preethika Murugan, Ashok K. Sundramoorthy, and Raji Atchudan contributed equally to this work.

Acknowledgments

AKS thanks the Science and Engineering Research Board (SERB) for funding through CRG/2021/001517. We thank the Department of Science and Technology (DST) (International Bilateral Cooperation Division), India, for financial support through “INDO-RUSSIA Project (File No. INT/RUS/RFBR/385).” This work was also funded by the Researchers Supporting Project number (RSP-2021/243), King Saud University, Riyadh, Saudi Arabia.

References

- [1] S. C. Perry, D. Pangotra, L. Vieira et al., “Electrochemical synthesis of hydrogen peroxide from water and oxygen,” *Nature Reviews Chemistry*, vol. 3, no. 7, pp. 442–458, 2019.
- [2] S. Chen, R. Yuan, Y. Chai, and F. Hu, “Electrochemical sensing of hydrogen peroxide using metal nanoparticles: a review,” *Microchimica Acta*, vol. 180, no. 1–2, pp. 15–32, 2013.
- [3] S. F. Erttmann and N. O. Gekara, “Hydrogen peroxide release by bacteria suppresses inflammasome-dependent innate immunity,” *Nature Communications*, vol. 10, no. 1, pp. 1–13, 2019.
- [4] S. K. Maji, S. Sreejith, A. K. Mandal, X. Ma, and Y. Zhao, “Immobilizing gold nanoparticles in mesoporous silica covered reduced graphene oxide: a hybrid material for cancer cell detection through hydrogen peroxide sensing,” *ACS Applied Materials & Interfaces*, vol. 6, no. 16, pp. 13648–13656, 2014.

- [5] E. A. Veal, A. M. Day, and B. A. Morgan, "Hydrogen peroxide sensing and signaling," *Molecular Cell*, vol. 26, no. 1, pp. 1–14, 2007.
- [6] R. D. Nagarajan, P. Murugan, K. Palaniyandi, R. Atchudan, and A. K. Sundramoorthy, "Biocompatible MXene (Ti₃C₂T_x) immobilized with flavin adenine dinucleotide as an electrochemical transducer for hydrogen peroxide detection in ovarian cancer cell lines," *Micromachines*, vol. 12, no. 8, p. 862, 2021.
- [7] B. Halliwell, M. V. Clement, and L. H. Long, "Hydrogen peroxide in the human body," *FEBS Letters*, vol. 486, no. 1, pp. 10–13, 2000.
- [8] M. Peng, Y. Zhao, D. Chen, and Y. Tan, "Free-standing 3D electrodes for electrochemical detection of hydrogen peroxide," *ChemCatChem*, vol. 11, no. 17, pp. 4222–4237, 2019.
- [9] B. E. Watt, A. T. Proudfoot, and J. A. Vale, "Hydrogen peroxide poisoning," *Toxicological Reviews*, vol. 23, no. 1, pp. 51–57, 2004.
- [10] C. Lennicke, J. Rahn, R. Lichtenfels, L. A. Wessjohann, and B. Seliger, "Engineering synthetic antibody binders for allosteric inhibition of prolactin receptor signaling," *Signals*, vol. 13, no. 1, pp. 1–19, 2015.
- [11] R. F. P. Nogueira, M. C. Oliveira, and W. C. Paterlini, "Simple and fast spectrophotometric determination of H₂O₂ in photo-Fenton reactions using metavanadate," *Talanta*, vol. 66, no. 1, pp. 86–91, 2005.
- [12] S. Singh, K. Mitra, R. Singh et al., "Colorimetric detection of hydrogen peroxide and glucose using brominated graphene," *Analytical Methods*, vol. 9, no. 47, pp. 6675–6681, 2017.
- [13] R. Tian, B. Zhang, M. Zhao et al., "Fluorometric enhancement of the detection of H₂O₂ using different organic substrates and a peroxidase-mimicking polyoxometalate," *RSC Advances*, vol. 9, no. 22, pp. 12209–12217, 2019.
- [14] J. G. Manjunatha, B. K. Swamy, M. Deraman, and G. P. Mamatha, "Simultaneous determination of ascorbic acid, dopamine and uric acid at poly (aniline blue) modified carbon paste electrode: a cyclic voltammetric study," *International Journal of Pharmacy and Pharmaceutical Sciences*, vol. 5, pp. 355–362, 2013.
- [15] N. Hareesha and J. G. Manjunatha, "Elevated and rapid voltammetric sensing of riboflavin at poly(helianthin dye) blended carbon paste electrode with heterogeneous rate constant elucidation," *Journal of the Iranian Chemical Society*, vol. 17, no. 6, pp. 1507–1519, 2020.
- [16] J. Ju and W. Chen, "In situ growth of surfactant-free gold nanoparticles on nitrogen-doped graphene quantum dots for electrochemical detection of hydrogen peroxide in biological environments," *Analytical Chemistry*, vol. 87, no. 3, pp. 1903–1910, 2015.
- [17] M. Preethika and A. K. Sundramoorthy, "Humic acid/halloysite nanotube/flavin adenine dinucleotide nanocomposite based selective electrochemical biosensor for hydrogen peroxide," *Applied Surface Science*, vol. 488, pp. 503–511, 2019.
- [18] P. Murugan, A. K. Sundramoorthy, D. Ganapathy, R. Atchudan, D. Nallaswamy, and A. Khosla, "Electrochemical detection of H₂O₂ using an activated glassy carbon electrode," *ECS Sensors Plus*, vol. 1, no. 3, article 034401, 2022.
- [19] S. M. M. Raj, R. Atchudan, D. Ganapathy, A. Khosla, and A. K. Sundramoorthy, "Review—recent trends on the synthesis and different characterization tools for MXenes and their emerging applications," *Journal of the Electrochemical Society*, vol. 169, no. 7, article 077501, 2022.
- [20] A. C. Carpenter, I. T. Paulsen, and T. C. Williams, "Blueprints for biosensors: design, limitations, and applications," *Genes*, vol. 9, no. 8, p. 375, 2018.
- [21] G. Jeevanandham, R. Jerome, N. Murugan, M. Preethika, K. VEDIAPPAN, and A. K. Sundramoorthy, "Nickel oxide decorated MoS₂ nanosheet-based non-enzymatic sensor for the selective detection of glucose," *RSC Advances*, vol. 10, no. 2, pp. 643–654, 2020.
- [22] S. Majumder, B. Saha, S. Dey, R. Mondal, S. Kumar, and S. Banerjee, "A highly sensitive non-enzymatic hydrogen peroxide and hydrazine electrochemical sensor based on 3D micro-snowflake architectures of α -Fe₂O₃," *RSC Advances*, vol. 6, no. 65, pp. 59907–59918, 2016.
- [23] T. Liu, Y. Guo, Z. Zhang, Z. Miao, X. Zhang, and Z. Su, "Fabrication of hollow CuO/PANI hybrid nanofibers for non-enzymatic electrochemical detection of H₂O₂ and glucose," *Sensors and Actuators B: Chemical*, vol. 286, pp. 370–376, 2019.
- [24] M. Baghayeri, H. Alinezhad, M. Tarahomi, M. Fayazi, M. Ghanei-Motlagh, and B. Maleki, "A non-enzymatic hydrogen peroxide sensor based on dendrimer functionalized magnetic graphene oxide decorated with palladium nanoparticles," *Applied Surface Science*, vol. 478, pp. 87–93, 2019.
- [25] A. K. Sundramoorthy, S. Mesgari, J. Wang et al., "Scalable and effective enrichment of semiconducting single-walled carbon nanotubes by a dual selective naphthalene-based azo dispersant," *Journal of the American Chemical Society*, vol. 135, no. 15, pp. 5569–5581, 2013.
- [26] G. Tigari and J. G. Manjunatha, "Electrochemical preparation of poly(arginine)-modified carbon nanotube paste electrode and its application for the determination of pyridoxine in the presence of riboflavin: an electroanalytical approach," *Journal of Analysis and Testing*, vol. 3, no. 4, pp. 331–340, 2019.
- [27] C. Raril and J. G. Manjunatha, "Fabrication of novel polymer-modified graphene-based electrochemical sensor for the determination of mercury and lead ions in water and biological samples," *Journal of Analytical Science and Technology*, vol. 11, no. 1, pp. 1–10, 2020.
- [28] J. G. Manjunatha, "A surfactant enhanced graphene paste electrode as an effective electrochemical sensor for the sensitive and simultaneous determination of catechol and resorcinol," *Chemical Data Collections*, vol. 25, article 100331, 2020.
- [29] N. Hareesha and J. G. Manjunatha, "Fast and enhanced electrochemical sensing of dopamine at cost-effective poly(DL-phenylalanine) based graphite electrode," *Journal of Electroanalytical Chemistry*, vol. 878, article 114533, 2020.
- [30] N. G. Yasri, A. K. Sundramoorthy, W.-J. Chang, and S. Gunasekaran, "Highly selective mercury detection at partially oxidized graphene/poly(3,4-ethylenedioxythiophene):poly(styrenesulfonate) nanocomposite film-modified electrode," *Frontiers in Materials*, vol. 1, p. 33, 2014.
- [31] T. H. V. Kumar, S. K. Yadav, and A. K. Sundramoorthy, "Review-electrochemical synthesis of 2D layered materials and their potential application in pesticide detection," *Journal of the Electrochemical Society*, vol. 165, no. 16, pp. B848–B861, 2018.
- [32] T. H. V. Kumar and A. K. Sundramoorthy, "Electrochemical biosensor for methyl parathion based on single-walled carbon nanotube/glutaraldehyde crosslinked acetylcholinesterase-wrapped bovine serum albumin nanocomposites," *Analytica Chimica Acta*, vol. 1074, pp. 131–141, 2019.

- [33] A. M. Dimiev, A. Khannanov, I. Vakhitov, A. Kiiamov, K. Shukhina, and J. M. Tour, "Revisiting the mechanism of oxidative unzipping of multiwall carbon nanotubes to graphene nanoribbons," *ACS Nano*, vol. 12, no. 4, pp. 3985–3993, 2018.
- [34] M. Fujita, K. Wakabayashi, K. Nakada, and K. Kusakabe, "Peculiar localized state at zigzag graphite edge," *Journal of the Physical Society of Japan*, vol. 65, no. 7, pp. 1920–1923, 1996.
- [35] Y.-W. Son, M. L. Cohen, and S. G. Louie, "Half-metallic graphene nanoribbons," *Nature*, vol. 444, no. 7117, pp. 347–349, 2006.
- [36] J. Bai, X. Duan, and Y. Huang, "Rational fabrication of graphene nanoribbons using a nanowire etch mask," *Nano Letters*, vol. 9, no. 5, pp. 2083–2087, 2009.
- [37] V. Abramova, A. S. Slesarev, and J. M. Tour, "Meniscus-mask lithography for fabrication of narrow nanowires," *Nano Letters*, vol. 15, no. 5, pp. 2933–2937, 2015.
- [38] J. Cai, P. Ruffieux, R. Jaafar et al., "Atomically precise bottom-up fabrication of graphene nanoribbons," *Nature*, vol. 466, no. 7305, pp. 470–473, 2010.
- [39] T. H. Vo, M. Shekirev, D. A. Kunkel et al., "Large-scale solution synthesis of narrow graphene nanoribbons," *Nature Communications*, vol. 5, no. 1, pp. 1–8, 2014.
- [40] A. G. Cano-Márquez, F. J. Rodríguez-Macias, J. Campos-Delgado et al., "Ex-MWNTs: graphene sheets and ribbons produced by lithium intercalation and exfoliation of carbon nanotubes," *Nano Letters*, vol. 9, no. 4, pp. 1527–1533, 2009.
- [41] D. V. Kosynkin, W. Lu, A. Sinitskii, G. Pera, Z. Sun, and J. M. Tour, "Highly conductive graphene nanoribbons by longitudinal splitting of carbon nanotubes using potassium vapor," *ACS Nano*, vol. 5, no. 2, pp. 968–974, 2011.
- [42] D. V. Kosynkin, A. L. Higginbotham, A. Sinitskii et al., "Longitudinal unzipping of carbon nanotubes to form graphene nanoribbons," *Nature*, vol. 458, no. 7240, pp. 872–876, 2009.
- [43] Y. Zhu, Z. Sun, Z. Yan, Z. Jin, and J. M. Tour, "Rational design of hybrid graphene films for high-performance transparent electrodes," *ACS Nano*, vol. 5, no. 8, pp. 6472–6479, 2011.
- [44] A.-R. O. Raji, R. Villegas Salvatierra, N. D. Kim et al., "Lithium batteries with nearly maximum metal storage," *ACS Nano*, vol. 11, no. 6, pp. 6362–6369, 2017.
- [45] B. Genorio, W. Lu, A. M. Dimiev et al., "In situ intercalation replacement and selective functionalization of graphene nanoribbon stacks," *ACS Nano*, vol. 6, no. 5, pp. 4231–4240, 2012.
- [46] H. Chen, N. Bucher, S. Hartung et al., "A multi-walled carbon nanotube core with graphene oxide nanoribbon shell as anode material for sodium ion batteries," *Advanced Materials Interfaces*, vol. 3, no. 20, p. 1600357, 2016.
- [47] R. John, D. B. Shinde, L. Liu et al., "Sequential electrochemical unzipping of single-walled carbon nanotubes to graphene ribbons revealed by in situ Raman spectroscopy and imaging," *ACS Nano*, vol. 8, no. 1, pp. 234–242, 2014.
- [48] S. Vadahanambi, J.-H. Jung, R. Kumar, H.-J. Kim, and I.-K. Oh, "An ionic liquid-assisted method for splitting carbon nanotubes to produce graphene nano-ribbons by microwave radiation," *Carbon*, vol. 53, pp. 391–398, 2013.
- [49] F. Cataldo, G. Compagnini, G. Patané et al., "Graphene nanoribbons produced by the oxidative unzipping of single-wall carbon nanotubes," *Carbon*, vol. 48, no. 9, pp. 2596–2602, 2010.
- [50] A. Martín, J. Hernández-Ferrer, M. T. Martínez, and A. Escarpa, "Graphene nanoribbon-based electrochemical sensors on screen-printed platforms," *Electrochimica Acta*, vol. 172, pp. 2–6, 2015.
- [51] L. Zhu, L. Kong, and C. Zhang, "Numerical study on hysteretic behaviour of horizontal-connection and energy-dissipation structures developed for prefabricated shear walls," *Applied Sciences*, vol. 10, no. 4, p. 1240, 2020.
- [52] X. Huang, Y. Zhu, and E. Kianfar, "Nano biosensors: properties, applications and electrochemical techniques," *Journal of Materials Research and Technology*, vol. 12, pp. 1649–1672, 2021.
- [53] W. Jia, M. Guo, Z. Zheng et al., "Electrocatalytic oxidation and reduction of H₂O₂ on vertically aligned Co₃O₄ nanowalls electrode: toward H₂O₂ detection," *Journal of Electroanalytical Chemistry*, vol. 625, no. 1, pp. 27–32, 2009.
- [54] C. L. Bentley, M. Kang, and P. R. Unwin, "Nanoscale surface structure–activity in electrochemistry and electrocatalysis," *Journal of the American Chemical Society*, vol. 141, no. 6, pp. 2179–2193, 2019.
- [55] M. A. Shenashen, D. Hassen, S. A. El-Safty, H. Isago, A. Elmarakbi, and H. Yamaguchi, "Axially oriented tubercle vein and X-crossed sheet of N-Co₃O₄@C hierarchical mesoarchitectures as potential heterogeneous catalysts for methanol oxidation reaction," *Chemical Engineering Journal*, vol. 313, pp. 83–98, 2017.
- [56] Q. Shu, Z. Xia, W. Wei et al., "Controllable unzipping of carbon nanotubes as advanced Pt catalyst supports for oxygen reduction," *ACS Applied Energy Materials*, vol. 2, no. 8, pp. 5446–5455, 2019.
- [57] R. D. Nagarajan and A. K. Sundramoorthy, "One-pot electro-synthesis of silver nanorods/graphene nanocomposite using 4-sulphocalix[4]arene for selective detection of oxalic acid," *Sensors and Actuators B: Chemical*, vol. 301, article 127132, 2019.
- [58] S. Farhadi, M. Javanmard, and G. Nadri, "Characterization of cobalt oxide nanoparticles prepared by the thermal decomposition," *Acta Chimica Slovenica*, vol. 63, no. 2, pp. 335–343, 2016.
- [59] M. Liu, Y. Du, Y.-E. Miao et al., "Anisotropic conductive films based on highly aligned polyimide fibers containing hybrid materials of graphene nanoribbons and carbon nanotubes," *Nanoscale*, vol. 7, no. 3, pp. 1037–1046, 2015.
- [60] V. Sahu, S. Shekhar, R. K. Sharma, and G. Singh, "Ultra-high performance supercapacitor from lacey reduced graphene oxide nanoribbons," *ACS Applied Materials & Interfaces*, vol. 7, no. 5, pp. 3110–3116, 2015.
- [61] B. Sidhureddy, J. S. Dondapati, and A. Chen, "Shape-controlled synthesis of Co₃O₄ for enhanced electrocatalysis of the oxygen evolution reaction," *Chemical Communications*, vol. 55, no. 25, pp. 3626–3629, 2019.
- [62] K. Białas, D. Moschou, F. Marken, and P. Estrela, "Electrochemical sensors based on metal nanoparticles with biocatalytic activity," *Microchimica Acta*, vol. 189, no. 4, p. 172, 2022.
- [63] Z. Fan, Q. Lin, P. Gong, B. Liu, J. Wang, and S. Yang, "A new enzymatic immobilization carrier based on graphene capsule for hydrogen peroxide biosensors," *Electrochimica Acta*, vol. 151, pp. 186–194, 2015.
- [64] M. A. Karimi, F. Banifateme, A. Hatefi-Mehrjardi, H. Tavallali, Z. Eshaghia, and G. Deilamy-Rad, "A novel rapid synthesis of Fe₂O₃/graphene nanocomposite using ferrate(VI) and its application as a new kind of nanocomposite modified

- electrode as electrochemical sensor," *Materials Research Bulletin*, vol. 70, pp. 856–864, 2015.
- [65] L. Kong, Z. Ren, N. Zheng et al., "Interconnected 1D Co₃O₄ nanowires on reduced graphene oxide for enzymeless H₂O₂ detection," *Nano Research*, vol. 8, no. 2, pp. 469–480, 2015.
- [66] A. A. Ensafi, M. Jafari-Asl, and B. Rezaei, "A novel enzyme-free amperometric sensor for hydrogen peroxide based on Nafion/exfoliated graphene oxide- Co₃O₄ nanocomposite," *Talanta*, vol. 103, pp. 322–329, 2013.
- [67] P. Murugan, J. Annamalai, R. Atchudan et al., "Electrochemical sensing of glucose using glucose oxidase/PEDOT: 4-sulfocalix [4] arene/MXene composite modified electrode," *Micromachines*, vol. 13, no. 2, p. 304, 2022.
- [68] B. P. Vinayan and S. Ramaprabhu, "Facile synthesis of SnO₂ nanoparticles dispersed nitrogen doped graphene anode material for ultrahigh capacity lithium ion battery applications," *Journal of Materials Chemistry A*, vol. 1, no. 12, pp. 3865–3871, 2013.
- [69] C. Liu, C. Li, K. Ahmed et al., "High energy and power density Li–O₂ battery cathodes based on amorphous RuO₂ loaded carbon free and binderless nickel nanofoam architectures," *RSC Advances*, vol. 6, no. 85, pp. 81712–81718, 2016.

Research Article

Synthesis of AA8050/B₄C/TiB₂ Hybrid Nanocomposites and Evaluation of Computer-Aided Machining Parameters

T. Sathish,¹ Mohanavel Vinayagam,^{2,3} T. Raja,⁴ A. H. Seikh,⁵ M. H. Siddique,⁶ Ram Subbiah,⁷ and Beruk Hailu⁸

¹Department of Mechanical Engineering, Saveetha School of Engineering, SIMATS, Chennai, 602 105 Tamil Nadu, India

²Centre for Materials Engineering and Regenerative Medicine, Bharath Institute of Higher Education and Research, Chennai, 600073 Tamil Nadu, India

³Department of Mechanical Engineering, Chandigarh University, Mohali-140413, Punjab, India

⁴Department of Mechanical Engineering, Vel Tech Rangarajan Dr. Sagunthala R&D Institute of Science and Technology, Chennai, Tamil Nadu, India

⁵Mechanical Engineering Department, College of Engineering, King Saud University, P.O. Box 800 Al-Riyadh 11421, Saudi Arabia

⁶Intelligent Construction Automation Centre, Kyungpook National University, Daegu, Republic of Korea

⁷Department of Mechanical Engineering, Gokaraju Rangaraju Institute of Engineering & Technology, Hyderabad, Telangana 500090, India

⁸Faculty of Mechanical Engineering, Haramaya Institute of Technology, Haramaya University, Ethiopia

Correspondence should be addressed to Beruk Hailu; beruk.hailu@haramaya.edu.et

Received 8 May 2022; Accepted 1 August 2022; Published 31 August 2022

Academic Editor: Arpita Roy

Copyright © 2022 T. Sathish et al. This is an open access article distributed under the Creative Commons Attribution License, which permits unrestricted use, distribution, and reproduction in any medium, provided the original work is properly cited.

This research focusses on synthesizing the hybrid nanocomposite samples with AA8050 and the reinforcement of B₄C and TiB₂ nanoparticles at 3 different quality grades. To investigate their machinabilities on the prepared composites in the computer-aided machining centre, the objectives are maximizing the material removal rate (MRR) and minimizing the surface roughness for a specific application. Stir casting process was employed in synthesizing the hybrid nanocomposite samples. Utilizing CNC turning centre was employed to investigate machinability performance on hybrid nanocomposite samples. The PVD-coated HSS tool and dry cutting environment were considered. The quality of machining was investigated by observing the surface roughness on the machined surfaces of samples of hybrid nanocomposite. The machining rate was investigated through the response of material removal rate at as per Taguchi design of experiments L27 orthogonal array. The hybrid nanocomposite synthesizing parameter of contribution of nanoparticle reinforcement (8%, 10%, and 12%) and the Turing parameters include spindle speed (800 rpm, 1000 rpm, and 1200 rpm), machining feed (0.05 mm/rev, 0.10 mm/rev, and 0.15 mm/rev) and depth of cut (0.5 mm, 0.75 mm, and 1 mm). The best performing input levels were identified through Taguchi analysis and the involved input variables were analysed and prediction model developed through ANOVA. The maximum material removal rate and the minimum surface roughness were reordered as 1380 mm³/min.

1. Introduction

Hybrid composites presented the high strength of the aluminium alloy for using reinforced particles. In the statistical analysis, the influence of higher cutting speed reduces the cutting force of the tool material. Results between the experimental work and the predicted values of the SiCp/Al nanocomposites, the cutting force is slightly reduced in the

experimental work [1]. Using of carbide cutting tool for turning of E250 steel in the CNC turning process, the material removal rate is increased moderately. Optimum values are attained as 1100 rpm of spindle speed, 0.44 mm of depth of cut, and 0.2 mm/min of feed rate. These optimal output parameters provided better surface finish as well as high MRR [2]. In automobiles, wheel axles are made on hardened alloy steels for giving high strength and absorption of shocks

TABLE 1: Chemical composition of AA8050.

Material	% of composition
Cr	0.05
Cu	0.05
Fe	1.3
Mg	0.05
Mn	0.80
Si	0.03
Zn	0.1
Al	Remaining



FIGURE 1: Schematic view of stir casting process equipment.

and vibrations. Different parameters such as cutting speed, machining feed, depth of cut, relief angle nose radius, and type of insert are involved in machining of hardened alloy steels. The L18 orthogonal array (OA) is suitable to examine the surface roughness and machinability characteristics of the hardened alloy steels. In this study, the influence of optimal parameters is reducing the tool flank wear such as 53.85%; similarly, the surface roughness also reduced by 15.95%. Optimal flank wear was obtained as 0.057 mm, and the optimum surface roughness value was attained as 1.0248 mm [3]. All the industries like as automotive, aerospace, marine, and structural components the 316L stainless steel was highly influenced. In machining of these materials, the tool has to be highly wear and the tool life also reduced increasing of tool life by the way of applying of lubrication with coolant. Using of coolant, the wear has to be approximately 9%. Dry machining increases the wear of the tool comparing to the coolant applied machining process [4]. Machining of titanium alloys is a difficult one; to overcome this, alternative machining techniques were applied. The tool wear was estimated under the working nature such as dry, wet, and cryogenic surroundings. Comparing the wet and dry nature machining, the cryogenic nature offered higher tool life such as 200% to others. Similarly, the surface roughness was reduced 71% by using cryogenic application. Comparing other methods such as wet and dry offered 64% of reduced surface roughness [5]. Aluminium alloy with reinforcement of silicon carbide nanoparticles is prepared

by the stir casting route. Various parameters influencing the CNC turning process decided the surface finish and the MRR. This work concluded the 40 m/min of spindle speed, 0.100 mm/rev of feed rate, 0.3 mm of depth of cut, and 3% SiC, 7% Gr were recorded as optimal parameters [6]. The tungsten carbide inserts are effectively used in the CNC turning process; aluminium alloy (LM6) with silicon carbide particles reinforced composites are machined successfully. They [7] focused to reduce the cutting temperature, vibration, and surface roughness with different optimal parameters. The authors found the poor surface finish was attained due to composite particles sticking to the tool inserts. Many researchers intend to study the aluminium alloy metal matrix composites using coated tool material in the CNC turning process. Only few of the attempts are made on titanium alloy. This work was carried out on titanium metal matrix composites using carbide as well as cubic boron carbide inserts. Machinability study of surface roughness, cylindricity, cutting forces, and tool wear are carried out. In addition, the statistical analysis was included to evaluate the best parameter among the chosen parameters. CBN tool inserts offered good surface finish even in different spindle speeds [8–10]. This article discusses the synthesis of novel aluminium metal matrix composite with composite matrix of AA8050 with equal and hybrid reinforcement of B_4C nanoparticles and TiB_2 nanoparticles at various wt.% and investigates their machinability performance on CNC turning centre. The Taguchi design of experiments and analysis was preferred to optimize the machining parameters for maximizing material removal rate (MRR) and minimizing surface roughness on machined surfaces. With the best of our knowledge, such novel composites were not published or patented so far.

2. Experimental Details

2.1. Materials and Methods. This study conducts the machining process in the CNC turning centre using the material aluminium alloy with reinforcement of boron carbide (B_4C) nanoparticles and titanium diboride (TiB_2) nanoparticles. AA8050 aluminium alloy possesses high strength and excellent mechanical properties; adding of reinforcement nanoparticles, its strength is upgraded in a great level [11–14]. Automotive parts, aerospace components are to be made by using this material. High-strength nanoparticles of boron carbide and titanium diboride nanoparticles are used as reinforcement agent of this study. Boron carbide is a high hard material for antagonism against wear as well as a lightweight material [15]. Titanium diboride is an extreme heat conductivity material and also prevents oxidation, with good stability. The chemical composition of aluminium alloy 8050 is illustrated in Table 1.

Material preparation is conducted through stir casting process; the particles were reinforced at the time of stir casting [16–18]. Stir casted materials are machined through CNC turning using Diamond-Like Carbon- (DLC-) coated tungsten carbide tool [19–21]. CNC turning process is achieved by using different parameters applying L_{27} orthogonal array (Taguchi route). The outcome of this



FIGURE 2: Hybrid nanocomposite machinability investigated at CNC turning centre.

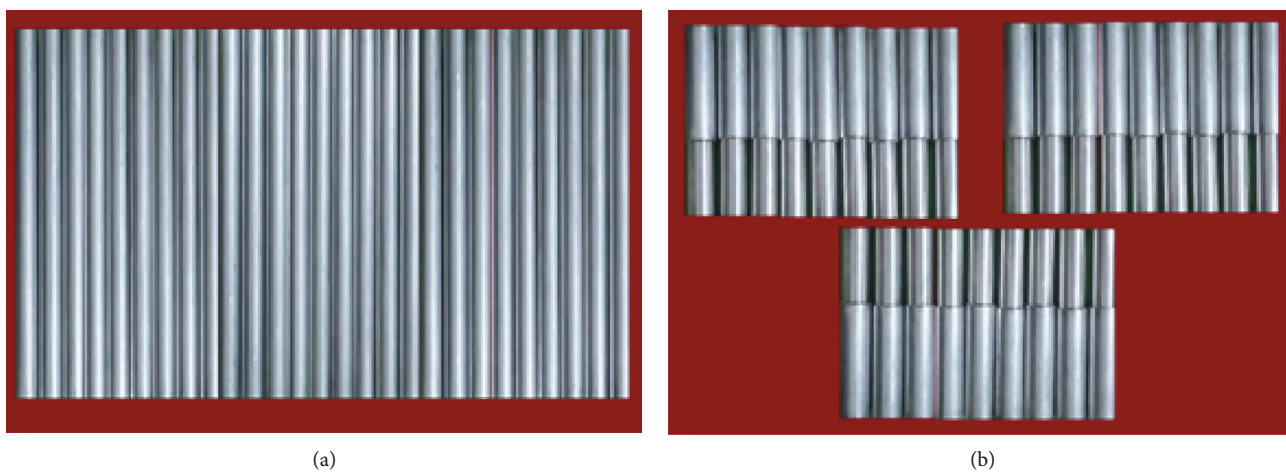


FIGURE 3: Turning specimen: (a) hybrid nanocomposite before turning and (b) after turning.

TABLE 2: Parameters and their levels of MRR.

Level	Nanoparticle reinforcement (NS) (%)	Spindle speed (SS) (rpm)	Machining speed (MS) (mm/rev)	Depth of cut (DC) (mm)
1	8	800	0.05	0.50
2	10	1000	0.10	0.75
3	12	1200	0.15	1.00

experimental work is considered as surface roughness and material removal rate [22–24].

2.2. Experimental Procedure. Stir casting process is employed to this research work to produce the hybrid nanocomposite in the form of round rod. In stir casting process, the base material of aluminium alloy (AA8050) and the reinforced nanoparticles of boron carbide and nanoparticles of tita-

niun diboride are mixed well [25–27]. The reinforced material is added to the base material at different weight percentages such as 8%, 10%, and 12%. Stir casting process is carried out using different parameters for producing the effective hybrid nanocomposite [28–30]. Stirring speed of 650 rpm, stirring time of 30 min, and stirring temperature of 900°C are used as parameters of the stir casting process [31]. The stir casting equipment is model SWAM EQUIP bottom pouring type stir casting as shown in Figure 1.

All the samples are machined using CNC turning machine (brand: Ace Micromatic; model: Super Jobber 500-LM CNC Lathe Machine). This machine was used to turn a maximum of 320 mm diameter and maximum of 500 mm length as shown in Figure 2. Diamond-Like Carbon- (DLC-) coated tungsten carbide tool is used for turning hybrid composite materials [32–34].

In the turning process, the different parameters and levels are used such as spindle speed (800 rpm, 1000 rpm,

TABLE 3: Summary of machining parameters and MRR.

Exp. runs	Nanoparticle reinforcement (%)	Spindle speed (rpm)	Machining feed (mm/rev)	Depth of cut (mm)	MRR (mm ³ /min)
1	8	800	0.05	0.50	360
2	8	800	0.05	0.50	480
3	8	800	0.05	0.50	845
4	8	1000	0.10	0.75	736
5	8	1000	0.10	0.75	1180
6	8	1000	0.10	0.75	638
7	8	1200	0.15	1.00	1315
8	8	1200	0.15	1.00	1289
9	8	1200	0.15	1.00	578
10	10	800	0.10	1.00	481
11	10	800	0.10	1.00	394
12	10	800	0.10	1.00	617
13	10	1000	0.15	0.50	883
14	10	1000	0.15	0.50	1023
15	10	1000	0.15	0.50	1380
16	10	1200	0.05	0.75	1265
17	10	1200	0.05	0.75	595
18	10	1200	0.05	0.75	439
19	12	800	0.15	0.75	762
20	12	800	0.15	0.75	827
21	12	800	0.15	0.75	398
22	12	1000	0.05	1.00	986
23	12	1000	0.05	1.00	1128
24	12	1000	0.05	1.00	1264
25	12	1200	0.10	0.50	1018
26	12	1200	0.10	0.50	912
27	12	1200	0.10	0.50	650

and 1200 rpm), machining feed (0.05 mm/rev, 0.10 mm/rev, and 0.15 mm/rev), and depth of cut (0.5 mm, 0.75 mm, and 1 mm). All these parameters are effectively utilized, and turning operation was successfully carried out; each experimental trial run shows different output results such as MRR and result of surface roughness [35–37]. Figure 3 presents the AA8050/B₄C/TiB₂ of the hybrid nanocomposite material samples before and after machining.

Material removal rate was calculated by the volume of material removal from the specimen with specified time period [38]. The surface roughness was checked using a Mitutoyo tester (model: SJ210 Surface Roughness Tester). Surface roughness was estimated through conducting of three trials for each sample and averaging it [39]. Table 2 presents the parameters and their levels of MRR.

3. Results and Discussion

3.1. MRR. Table 3 represents all parameter correlation and the output result of material removal rate in a detailed manner. Maximum material removal rate of 1380 mm³/min was obtained by 10% of nanoparticle reinforcement, 1000 rpm of

TABLE 4: Response table for means (MRR).

Level	Nanoparticle reinforcement (%)	Spindle speed (rpm)	Machining speed (mm/rev)	Depth of cut (mm)
1	824.6	573.8	818.0	839.0
2	786.3	1024.2	736.2	760.0
3	882.8	895.7	939.4	894.7
Delta	96.4	450.4	203.2	137.4
Rank	4	1	2	3

TABLE 5: Response table for signal to noise ratios (MRR).

Level	Nanoparticle reinforcement (%)	Spindle speed (rpm)	Machining speed (mm/rev)	Depth of cut (mm)
1	56.60	53.99	56.60	57.35
2	56.42	59.67	56.49	56.06
3	58.03	57.39	57.97	57.66
Delta	1.61	5.68	1.48	1.60
Rank	4	1	2	3

spindle speed, 0.15 mm/rev of machining speed, and 0.50 mm of depth of cut [40].

Tables 4 and 5 present the response table for means and response table for S/N ratio, respectively. In these tables, the spindle speed was a higher influence factor of this investigation comparing to others [41]. From the rank order, the factor influence was stated as second rank of machining speed, third rank of depth of cut, and fourth rank is hybrid nanoparticle reinforcement percentage. In the MRR investigation, the optimal factors were obtained as 12% of hybrid nanoparticle reinforcement, 1000 rpm of spindle speed, 0.15 mm/rev, and 1 mm of depth of cut.

Figures 4 and 5 illustrate the main effect plot for means and main effect plot for S/N ratio of material removal rate. Increasing of hybrid nanoparticle reinforcement percentage changes the material removal rate, minimum spindle speed offered low MRR. Moderate level of spindle speed such as 1000 rpm offered higher MRR. Initially, the machining speed 0.05 mm/rev produced good level of MRR, further increasing of feed 0.05 to 0.10 mm/rev the MRR rate was reduced slightly. Feed of 0.15 mm/rev recorded as higher MRR. In depth of cut analysis, 0.75 mm of depth of cut registered as a low level of MRR, and higher MRR was obtained by using of 1.00 mm of depth of cut [42].

From the probability analysis, maximum points lie on the mean line or probability line few points only slightly deviated from the mean line as shown in Figure 6. These points were represented that the chosen parameters, and its correlation was excellent one and also produced better MRR. All the points were scattered homogeneously between the upper and lower limits as shown in Figure 7. Scattered points were positioned within the limits; it has to be enlightened about the relations between the parameters and the accurate results such as MRR.

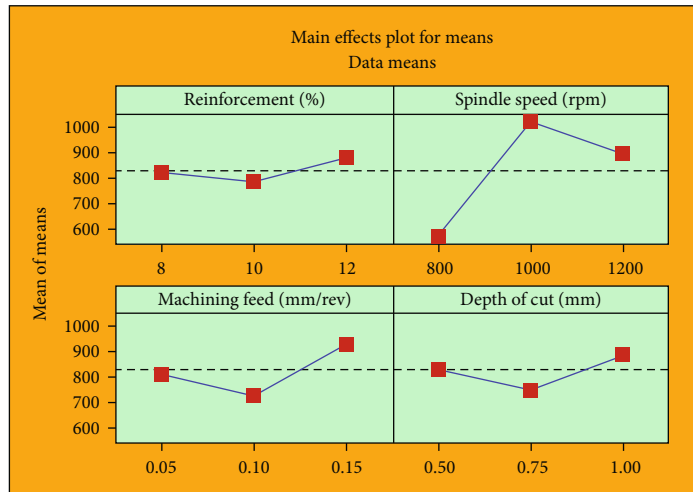


FIGURE 4: Main effect plot for means (MRR).

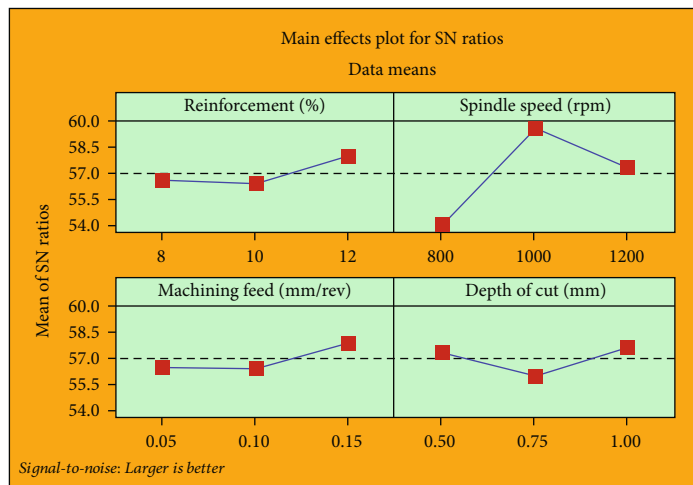


FIGURE 5: Main effect plot for S/N ratio (MRR).

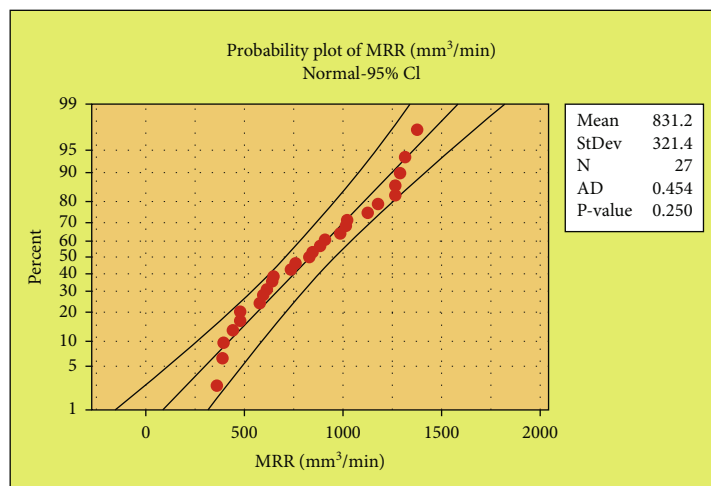


FIGURE 6: Probability plot of material removal rate.

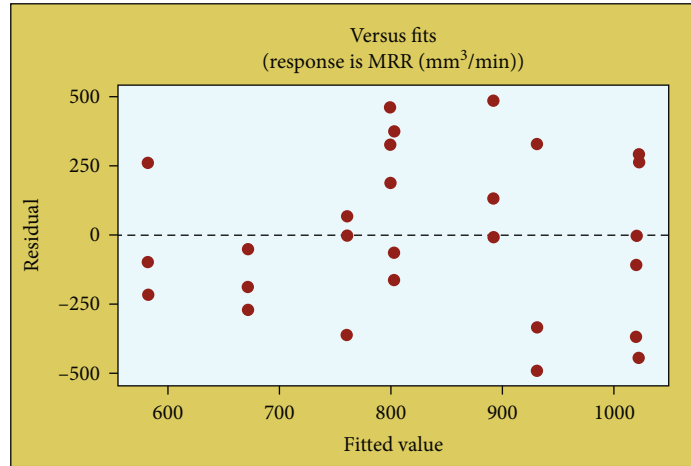


FIGURE 7: Versus fits plot of material removal rate.

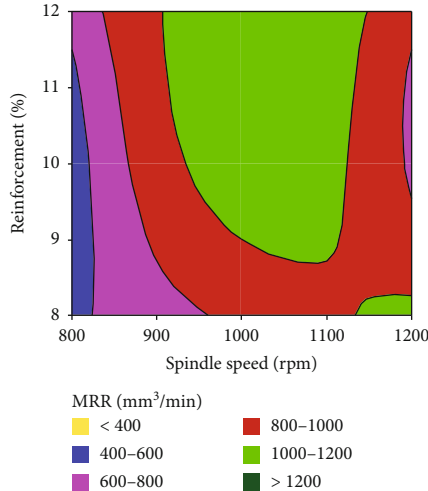
Contour plot of MRR (mm³/min) vs reinforcement (%), spindle speed (rpm)

FIGURE 8: Contour plot: spindle speed vs. reinforcement % for MRR response.

Figure 8 illustrates that the contour plot of spindle speed and percentage of reinforcement of hybrid nanoparticles, the moderate spindle speed and increasing of percentage of reinforcement of hybrid nanoparticles offered excellent MRR. Above 1000 mm³/min of MRR was recorded by influencing 1100 rpm of spindle speed and more than 10% of nanoparticle reinforcement. Figure 9 exemplifies the contour plot of machining feed and spindle speed, higher machining speed such as 0.150 mm/rev and moderate spindle speed provided higher MRR. Figure 10 demonstrates that the contour plot of depth of cut and machining speed, the lower value of depth of cut and higher value of machining speed offered maximum of MRR. Contrary minimum machining feed and higher depth of cut offered excellent MRR. Figure 11 represents the contour plot of reinforcement and depth of cut, moderate reinforcement and low level of depth of cut provided enhanced MRR.

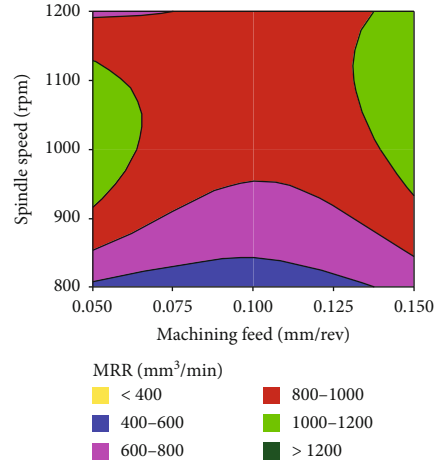
Contour plot of MRR (mm³/min) vs spindle speed (rpm), machining feed (mm/rev)

FIGURE 9: Contour plot: machining feed vs. spindle speed for MRR response.

Figure 12 shows the pie charts of material removal rate (MRR); this plot enlightens the all-parameter contribution and the outcome (MRR) of the research work individually.

The mathematical model developed to predict the MRR with respect to the nanoparticle reinforcement contribution and machining parameters for the specific requirements and shown in

$$\begin{aligned}
 \text{MRR}(\text{mm}^3/\text{min}) &= 831.2 - 6.7 \cdot \text{NS}(\%)_{.8} - 44.9 \cdot \text{NS}(\%)_{.10} \\
 &+ 51.6 \cdot \text{NS}(\%)_{.12} - 257.4 \cdot \text{SS}(\text{rpm})_{.800} \\
 &+ 193.0 \cdot \text{SS}(\text{rpm})_{.1000} + 64.4 \cdot \text{SS}(\text{rpm})_{.1200} \\
 &- 13.2 \cdot \text{MS}(\text{mm/rev})_{.0.05} - 95.0 \cdot \text{MS}(\text{mm/rev})_{.0.10} \\
 &+ 108.2 \cdot \text{MS}(\text{mm/rev})_{.0.15} + 7.8 \text{DC}(\text{mm})_{.0.50} \\
 &- 71.2 \cdot \text{DC}(\text{mm})_{.0.75} + 63.4 \cdot \text{DC}(\text{mm})_{.1.00}.
 \end{aligned} \tag{1}$$

Contour plot of MRR (mm³/min) vs machining feed (mm/rev), depth of cut (mm)

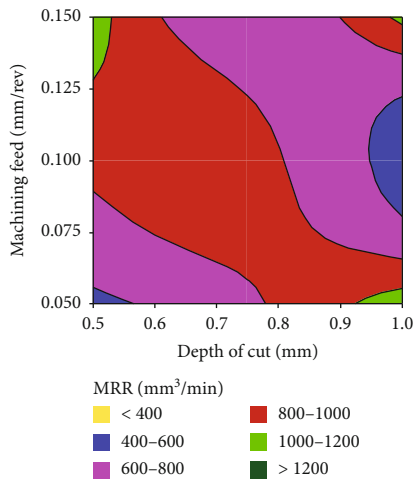


FIGURE 10: Contour plot: depth of cut vs. machining feed for MRR response.

Contour plot of MRR (mm³/min) vs depth of cut (mm), Reinforcement (%)

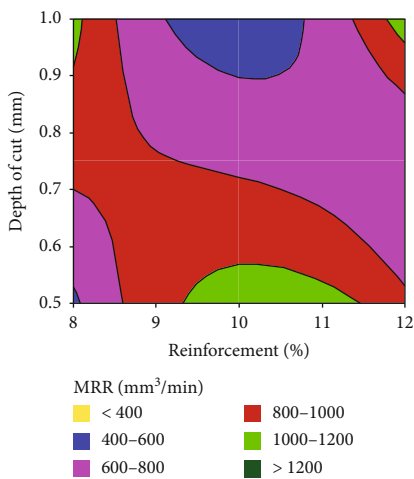


FIGURE 11: Contour plot: reinforcement % vs. depth of cut for MRR response of nanoparticles.

3.2. *Surface Roughness.* Table 6 illustrates each parameter relationship and the yield result of surface roughness in elaborate manner. Minimum surface roughness was found as 0.62 μm in the fourth experimental runs. Reduced surface roughness value was obtained by 8% of hybrid nanoparticle reinforcement, 1000 rpm of spindle speed, 0.10 mm/rev of machining speed, and 0.75 mm of depth of cut.

Tables 7 and 8 offer the response table for means and response table for S/N ratio of surface roughness, respectively. In surface roughness analysis, the machining speed was the major influencing factor compared to remaining factors. From the rank order, the machining feed was first, spindle speed was second, hybrid nanoparticle reinforcement percentage was third, and depth of cut was fourth order. Surface roughness analysis provided optimal parameters such as 12% of hybrid nanoparticle reinforcement, 800 rpm of spindle speed, 0.10 mm/rev, and 0.50 mm of depth of cut.

Pie Chart of MRR (mm³/min)

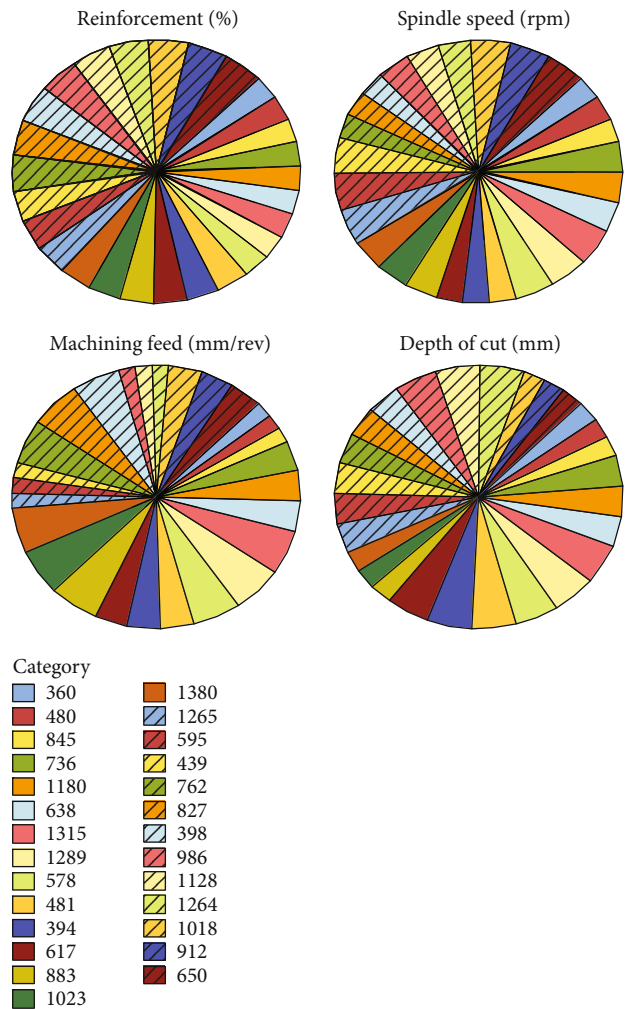


FIGURE 12: Pie chart of MRR.

Figures 13 and 14 show the main effect plot for means and main effect plot for S/N ratio of surface roughness. Higher hybrid nanoparticle reinforcement percentage (12%) offered minimum surface roughness. Minimum spindle speed such as 800 rpm provided better surface roughness, further increasing spindle speed from 800 rpm to 1200 rpm the surface roughness was showed highly on the surfaces of the specimens. Moderate machining speed such as 0.10 mm/rev offered minimum surface roughness, continually increasing the machining speed 0.15 mm/rev maximum surface roughness was observed. From depth of cut analysis, minimum depth of cut (0.50 mm) produced low surface roughness. Increasing of depth of cut increases the surface roughness values.

In the probability investigation, most of the points touch the mean line; few of them deviated from the mean line as shown in Figure 15. All points close and that touch the mean line represented the correlation among chosen parameters. This analysis proved the selected parameters were accurate ones and make a better surface finish. All the experimental runs were converted into scattered plot; the points were

TABLE 6: Summary of machining parameters and surface roughness.

Exp. runs	Nanoparticle reinforcement (%)	Spindle speed (rpm)	Machining feed (mm/rev)	Depth of cut (mm)	Surface roughness (μm)
1	8	800	0.05	0.50	0.89
2	8	800	0.05	0.50	1.56
3	8	800	0.05	0.50	1.97
4	8	1000	0.10	0.75	0.62
5	8	1000	0.10	0.75	1.51
6	8	1000	0.10	0.75	1.76
7	8	1200	0.15	1.00	2.01
8	8	1200	0.15	1.00	1.93
9	8	1200	0.15	1.00	1.28
10	10	800	0.10	1.00	0.93
11	10	800	0.10	1.00	0.74
12	10	800	0.10	1.00	0.73
13	10	1000	0.15	0.50	0.83
14	10	1000	0.15	0.50	1.37
15	10	1000	0.15	0.50	1.65
16	10	1200	0.05	0.75	1.47
17	10	1200	0.05	0.75	2.34
18	10	1200	0.05	0.75	1.94
19	12	800	0.15	0.75	0.78
20	12	800	0.15	0.75	0.62
21	12	800	0.15	0.75	1.36
22	12	1000	0.05	1.00	1.82
23	12	1000	0.05	1.00	1.09
24	12	1000	0.05	1.00	1.72
25	12	1200	0.10	0.50	0.94
26	12	1200	0.10	0.50	0.68
27	12	1200	0.10	0.50	1.59

TABLE 7: Response table for means (surface roughness).

Level	Nanoparticle reinforcement (%)	Spindle speed (rpm)	Machining speed (mm/rev)	Depth of cut (mm)
1	1.503	1.064	1.644	1.276
2	1.333	1.374	1.056	1.378
3	1.178	1.576	1.314	1.361
Delta	0.326	0.511	0.589	0.102
Rank	3	2	1	4

scattered homogeneously among the upper and lower limits as shown in Figure 16. Scattered points informed that the points are positioned in correct manner; hence, the parameter relation has enlightened the surface roughness.

Figure 17 demonstrates that the contour plot of spindle speed and hybrid nanoparticle reinforcement percentage, the minimum spindle speed (800 rpm) increasing hybrid nanoparticle reinforcement percentage offered minimum surface roughness. Higher spindle speed affects the surface roughness. Figure 18 illustrates the contour plot of machining feed and spindle speed, increasing machining speed from 0.050 mm/

TABLE 8: Response table for signal to noise ratios (surface roughness).

Level	Nanoparticle reinforcement (%)	Spindle speed (rpm)	Machining speed (mm/rev)	Depth of cut (mm)
1	-3.8472	-0.5433	-4.4996	-2.4393
2	-2.1262	-0.0840	-0.6880	-2.7994
3	-1.6106	-3.9567	-2.3964	-2.3453
Delta	2.2367	3.4134	3.8116	0.4540
Rank	3	2	1	4

rev and minimum spindle speed presented excellent surface finish. Figure 19 demonstrates the contour plot of depth of cut and machining speed, the higher value of depth of cut and moderate value of machining speed presented minimum surface roughness. Contrary moderate depth of cut and minimum machining feed was increasing the surface roughness. Figure 20 represents the contour plot of hybrid nanoparticle reinforcement percentage and depth of cut, both moderate hybrid nanoparticle reinforcement percentage and depth of cut recorded minimum surface roughness.

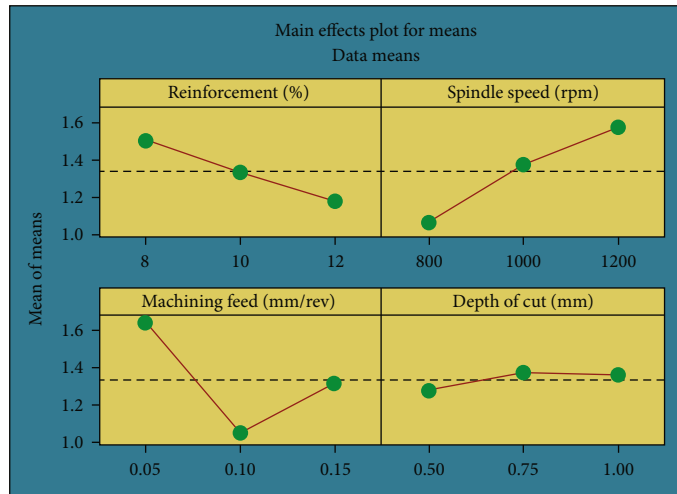


FIGURE 13: Main effect plot for means (surface roughness).

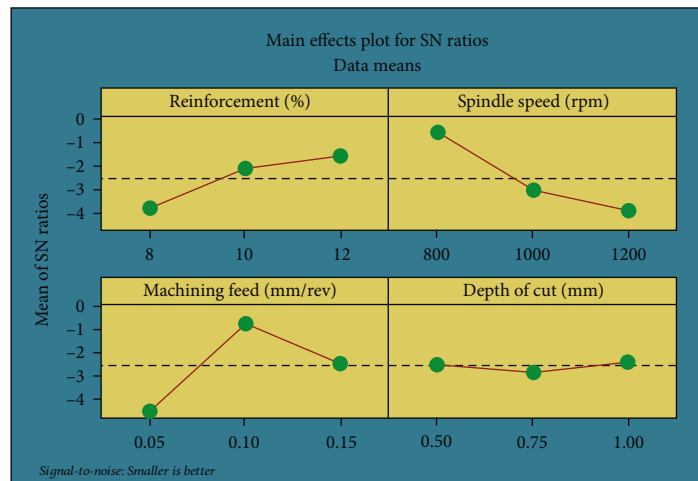


FIGURE 14: Main effect plot for S/N ratio (surface roughness).

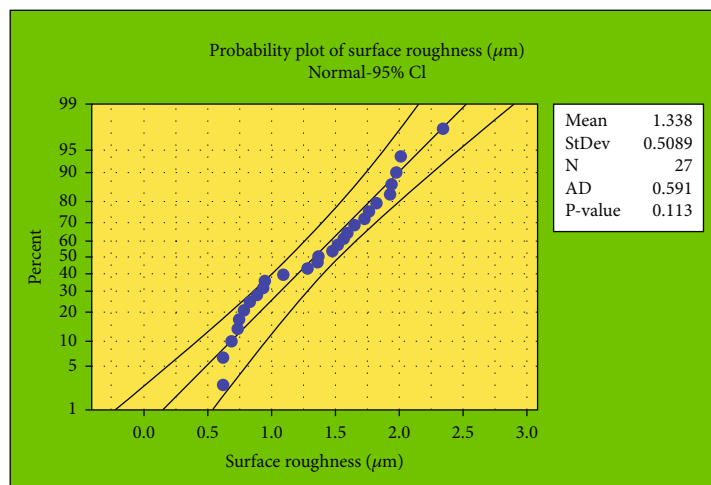


FIGURE 15: Probability plot of surface roughness.

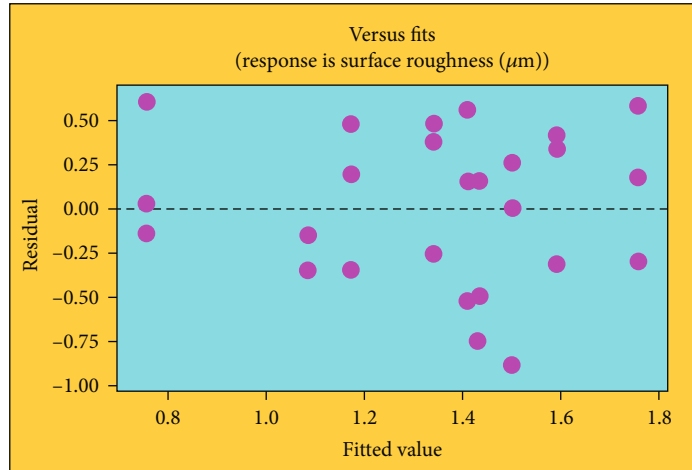


FIGURE 16: Versus fits plot of surface roughness.

Contour plot of surface roughness vs reinforcement (%), spindle speed (rpm)

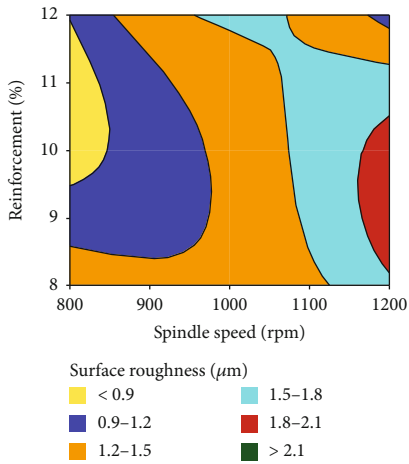


FIGURE 17: Contour plot: spindle speed vs. nanoparticle reinforcement % for surface roughness response.

Contour plot of surface roughness vs machining feed (mm/rev), depth of cut (mm)

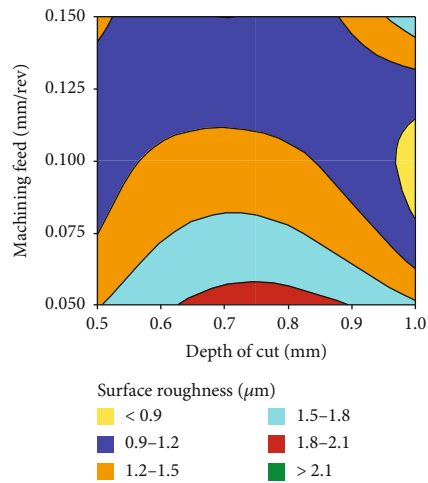


FIGURE 19: Contour plot: depth of cut vs. machining feed for surface roughness response.

Contour plot of surface roughness vs spindle speed (rpm), machining feed (mm/rev)

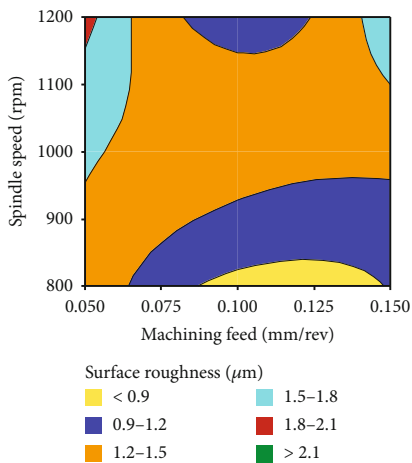


FIGURE 18: Contour plot: machining feed vs. spindle speed for surface roughness response.

Contour plot of surface roughness vs machining feed (mm/rev), reinforcement (%)

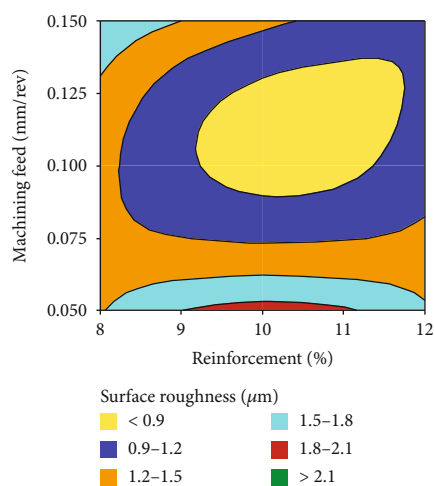


FIGURE 20: Contour plot: machining feed vs. nanomaterial reinforcement for surface roughness response.

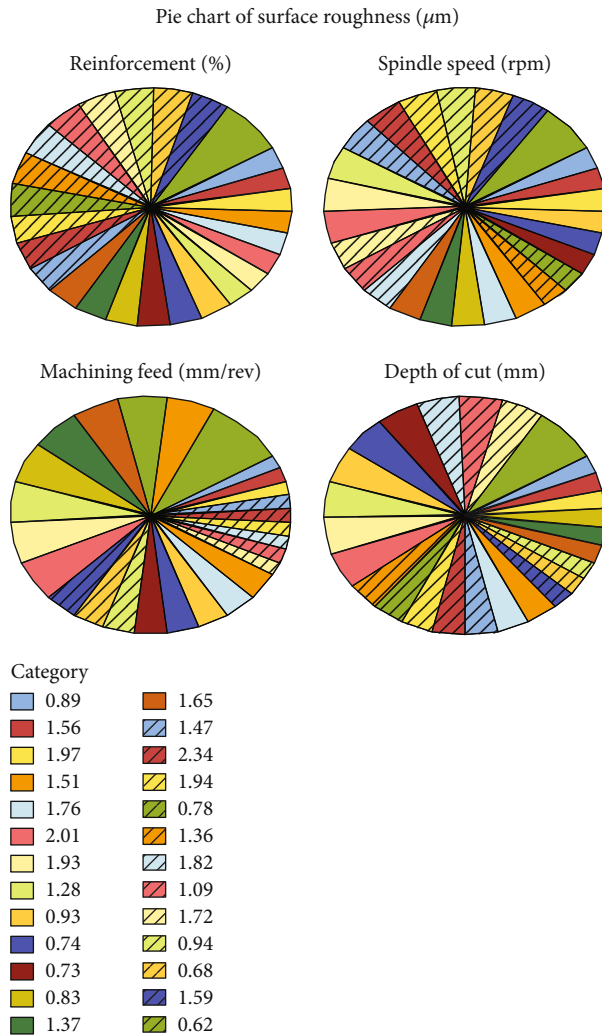


FIGURE 21: Pie chart of surface roughness.

Figure 21 illustrates the pie charts of surface roughness; this plot makes clear all parameter involvement and the result (surface roughness) of the investigation individually. The mathematical model developed and shown below to predict the surface roughness with respect to the hybrid nanoparticle reinforcement percentage and machining parameters for the specific requirements and shown in

$$\begin{aligned}
 \text{Surface roughness}(\mu\text{m}) &= 1.3381 + 0.165\text{NS}(\%)_{.8} - 0.005\text{NS}(\%)_{.10} \\
 &- 0.160\text{NS}(\%)_{.12} - 0.274\text{SS}(\text{rpm})_{.800} \\
 &+ 0.036\text{SS}(\text{rpm})_{.1000} + 0.237\text{SS}(\text{rpm})_{.1200} \\
 &+ 0.306\text{MS}(\text{mm/rev})_{.0.05} \\
 &- 0.283\text{MS}(\text{mm/rev})_{.0.10} \\
 &- +0.024\text{MS}(\text{mm/rev})_{.0.15} - 0.063\text{DC}(\text{mm})_{.0.50} \\
 &+ 0.040\text{DC}(\text{mm})_{.0.75} + 0.023\text{DC}(\text{mm})_{.1.00}.
 \end{aligned} \tag{2}$$

It was observed that machinability condition requirements vary for each grade (based on hybrid nanoparticle

reinforcement percentage) of novel AMMC of AA8050/ $\text{B}_4\text{C}/\text{TiB}_2$. The developed mathematical model will support to make right choice in manufacturing and machining.

4. Conclusion

This research work was carried out for CNC turning with different process parameters that influence to obtain enhanced MRR and surface roughness of hybrid AMMC's (AA8050/ $\text{B}_4\text{C}/\text{TiB}_2$) successfully. Diamond-Like Carbon-(DLC-) coated tungsten carbide tool was used to conduct the turning process with chosen parameters. The results were concluded as follows:

- (i) From the MRR analysis, maximum material removal rate of $1380 \text{ mm}^3/\text{min}$ was obtained by 10% hybrid nanoparticle reinforcement, 1000 rpm of spindle speed, 0.15 mm/rev of machining speed, and 0.50 mm of depth of cut. In the MRR investigation, the optimal factors were registered as 12% hybrid nanoparticle reinforcement, 1000 rpm of spindle speed, 0.15 mm/rev, and 1 mm of depth of cut
- (ii) Moderate level of spindle speed such as 1000 rpm offered higher MRR. Initially, the machining speed 0.05 mm/rev produced good level of MRR, further increasing of feed 0.05 to 0.10 mm/rev the MRR rate was reduced slightly
- (iii) In the surface roughness investigations, minimum surface roughness was found as $0.62 \mu\text{m}$ in the fourth experimental runs. Reduced surface roughness value was obtained by 8% hybrid nanoparticle reinforcement, 1000 rpm of spindle speed, 0.10 mm/rev of machining speed, and 0.75 mm of depth of cut. Surface roughness analysis provided optimal parameters such as 12% hybrid nanoparticle reinforcement, 800 rpm of spindle speed, 0.10 mm/rev, and 0.50 mm of depth of cut
- (iv) From the depth of cut analysis, minimum depth of cut (0.50 mm) formed low surface roughness. Increasing of depth of cut increases the surface roughness values

As aluminium alloys are widely utilized for numerous applications and selection of materials done for the application specific from the range of desired mechanical properties, this novel AMMC type of altering existing mechanical properties like enhanced wear resistance, self-lubrication properties for an automobile spare manufacturing application and this work developed mathematical models for process planning for manufacturing and machining. Hence, this piece of research claims a high social implication.

Data Availability

The data used to support the findings of this study are included within the article. Further data or information is available from the corresponding author upon request.

Conflicts of Interest

The authors declare that there is no conflict of interest regarding the publication of this article.

Acknowledgments

The authors appreciate the supports from Haramaya University, Ethiopia, for providing help during the research and preparation of the manuscript. The authors thank Saveetha School of Engineering, Vel Tech Rangarajan Dr. Sagunthala R&D Institute of Science and Technology, for providing assistance to this work. The authors would like to acknowledge the Researchers Supporting Project number (RSP-2021/373), King Saud University, Riyadh, Saudi Arabia.

References

- [1] R. A. Laghari, J. Li, and M. Mia, "Effects of turning parameters and parametric optimization of the cutting forces in machining SiCp/Al 45 wt% composite," *Metals*, vol. 10, no. 6, p. 840, 2020.
- [2] B. R. Krishnan and M. Ramesh, "Optimization of machining process parameters in CNC turning process of IS2062 E250 Steel using coated carbide cutting tool," *Materials Today: Proceedings*, vol. 21, pp. 346–350, 2020.
- [3] N. Senthilkumar, T. Ganapathy, and T. Tamizharasan, "Optimisation of machining and geometrical parameters in turning process using Taguchi method," *Australian Journal of Mechanical Engineering*, vol. 12, no. 2, pp. 233–246, 2014.
- [4] N. Szczotkarz, R. Mrugalski, R. W. Maruda et al., "Cutting tool wear in turning 316L stainless steel in the conditions of minimized lubrication," *Tribology International*, vol. 156, p. 106813, 2021.
- [5] C. Agrawal, N. Khanna, C. I. Pruncu, A. K. Singla, and M. K. Gupta, "Tool wear progression and its effects on energy consumption and surface roughness in cryogenic assisted turning of Ti-6Al-4V," *The International Journal of Advanced Manufacturing Technology*, vol. 111, no. 5, pp. 1319–1331, 2020.
- [6] A. Kannan, R. Mohan, R. Viswanathan, and N. Sivashankar, "Experimental investigation on surface roughness, tool wear and cutting force in turning of hybrid (Al7075+ SiC+ Gr) metal matrix composites," *Journal of Materials Research and Technology*, vol. 9, no. 6, pp. 16529–16540, 2020.
- [7] K. Balasubramanian, M. Nataraj, and D. Palanisamy, "Machinability analysis and application of response surface approach on CNC turning of LM6/SiCp composites," *Materials and Manufacturing Processes*, vol. 34, no. 12, pp. 1389–1400, 2019.
- [8] S. A. Niknam, S. Kamalizadeh, A. Asgari, and M. Balazinski, "Turning titanium metal matrix composites (MMCs) with carbide and CBN inserts," *The International Journal of Advanced Manufacturing Technology*, vol. 97, no. 1-4, pp. 253–265, 2018.
- [9] M. Kuntoğlu and H. Sağlam, "Investigation of progressive tool wear for determining of optimized machining parameters in turning," *Measurement*, vol. 140, pp. 427–436, 2019.
- [10] J. Allen Jeffrey, S. Suresh Kumar, P. Vaidyaa, A. Nicho, A. Chrish, and J. Joshith, "Effect of turning parameters in cylindricity and circularity for o1 steel using ANN," *Materials Today: Proceedings*, vol. 59, no. 2, pp. 1291–1294, 2022.
- [11] N. Kawin, D. Jagadeesh, G. Saravanan, and K. Periasamy, "Optimization of turning parameters in sugarcane bagasse ash reinforced with Al-Si10-Mg alloy composites by Taguchi method," *Materials Today: Proceedings*, vol. 21, pp. 474–476, 2020.
- [12] M. Mia, P. R. Dey, M. S. Hossain et al., "Taguchi S/N based optimization of machining parameters for surface roughness, tool wear and material removal rate in hard turning under MQL cutting condition," *Measurement*, vol. 122, pp. 380–391, 2018.
- [13] N. G. S. Kumar, G. S. Shiva Shankar, M. N. Ganesh, and L. K. Vibudha, "Experimental investigations to study the cutting force and surface roughness during turning of aluminium metal matrix hybrid composites," *Materials Today: Proceedings*, vol. 4, no. 9, pp. 9371–9374, 2017.
- [14] S. K. Shihab, Z. A. Khan, and A. N. Siddiquee, "RSM based investigations on the effects of cutting parameters on surface integrity during cryogenic hard turning of AISI 52100," *Journal for Manufacturing Science and Production*, vol. 15, no. 3, pp. 309–318, 2015.
- [15] Y. Xiong, W. Wang, R. Jiang, K. Lin, and G. Song, "Surface integrity of milling in-situ TiB2 particle reinforced Al matrix composites," *International Journal of Refractory Metals and Hard Materials*, vol. 54, pp. 407–416, 2016.
- [16] M. M. Ravikumar, S. Suresh Kumar, R. Vishnu Kumar, S. Nandakumar, J. Habeeb Rahman, and J. Ashok Raj, "Evaluation on mechanical behavior of AA2219/SiO₂ composites made by stir casting process," *AIP Conference Proceedings*, vol. 2405, article 50010, 2022.
- [17] Z. Liao, A. Abdelhafeez, H. Li, Y. Yang, O. G. Diaz, and D. Axinte, "State-of-the-art of surface integrity in machining of metal matrix composites," *International Journal of Machine Tools and Manufacture*, vol. 143, pp. 63–91, 2019.
- [18] R. K. Thakur, D. Sharma, and K. K. Singh, "Optimization of surface roughness and delamination factor in end milling of graphene modified GFRP using response surface methodology," *Materials Today: Proceedings*, vol. 19, pp. 133–139, 2019.
- [19] J. Li, X. Yang, C. Ren, G. Chen, and Y. Wang, "Multiobjective optimization of cutting parameters in Ti-6Al-4V milling process using nondominated sorting genetic algorithm-II," *The International Journal of Advanced Manufacturing Technology*, vol. 76, no. 5-8, pp. 941–953, 2015.
- [20] T.-S. Lan, K.-C. Chuang, and Y.-M. Chen, "Optimization of machining parameters using fuzzy Taguchi method for reducing tool wear," *Applied Sciences*, vol. 8, no. 7, p. 1011, 2018.
- [21] V. Parashar and R. Purohit, "Analysis of machining behavior of Al/A206-Al2O₃ metal matrix composite using end milling process," *Materials Today: Proceedings*, vol. 4, no. 2, pp. 2687–2692, 2017.
- [22] R. Sridhar, S. P. Subramaniyan, and S. Ramesh, "Optimization of machining and geometrical parameters to reduce vibration while milling metal matrix composite," *Transactions of the Indian Institute of Metals*, vol. 72, no. 12, pp. 3179–3189, 2019.
- [23] P. S. Bains, S. S. Sidhu, and H. S. Payal, "Fabrication and machining of metal matrix composites: a review," *Materials and Manufacturing Processes*, vol. 31, no. 5, pp. 553–573, 2016.
- [24] A. I. Jumare, K. Abou-El-Hossein, L. N. Abdulkadir, and M. M. Liman, "Predictive modeling and multiobjective

- optimization of diamond turning process of single-crystal silicon using RSM and desirability function approach,” *The International Journal of Advanced Manufacturing Technology*, vol. 103, no. 9, pp. 4205–4220, 2019.
- [25] R. Butola, C. Pratap, A. Shukla, and R. S. Walia, “Effect on the mechanical properties of aluminum-based hybrid metal matrix composite using stir casting method,” *In Materials Science Forum [Trans Tech Publications Ltd]*, vol. 969, pp. 253–259, 2019.
- [26] V. Gaikhe, J. Sahu, and R. Pawade, “Optimization of cutting parameters for cutting force minimization in helical ball end milling of Inconel 718 by using genetic algorithm,” *Procedia CIRP*, vol. 77, pp. 477–480, 2018.
- [27] S. Daniel, R. Ajith Arul, and R. Pugazhenthii, “Multi objective prediction and optimization of control parameters in the milling of aluminium hybrid metal matrix composites using ANN and Taguchi -grey relational analysis,” *Technology*, vol. 15, no. 4, pp. 545–556, 2019.
- [28] H. Tebassi, M. Yaltese, R. Khettabi, S. Belhadi, I. Meddour, and F. Girardin, “Multi-objective optimization of surface roughness, cutting forces, productivity and Power consumption when turning of Inconel 718,” *International Journal of Industrial Engineering Computations*, vol. 7, no. 1, pp. 111–134, 2016.
- [29] M. Nataraj and K. Balasubramanian, “Parametric optimization of CNC turning process for hybrid metal matrix composite,” *The International Journal of Advanced Manufacturing Technology*, vol. 93, no. 1-4, pp. 215–224, 2017.
- [30] R. Butola, S. Kanwar, L. Tyagi, R. M. Singari, and M. Tyagi, “Optimizing the machining variables in CNC turning of aluminum based hybrid metal matrix composites,” *SN Applied Sciences*, vol. 2, no. 8, pp. 1–9, 2020.
- [31] W. Bai, A. Roy, R. Sun, and V. V. Silberschmidt, “Enhanced machinability of SiC-reinforced metal-matrix composite with hybrid turning,” *Journal of Materials Processing Technology*, vol. 268, pp. 149–161, 2019.
- [32] T. Sathish, N. Sabarirajan, and S. Karthick, “Machining parameters optimization of aluminium alloy 6063 with reinforcement of SiC composites,” *Materials Today: Proceedings*, vol. 33, pp. 2559–2563, 2020.
- [33] R. Das, S. S. Mohanty, M. Panigrahi, and S. Mohanty, “Predictive modelling and analysis of surface roughness in CNC milling of green alumina using response surface method and genetic algorithm,” in *1st International Conference on Advanced Engineering Functional Materials (ICAEFM) 21–23 September 2018, GITA [vol. 410, no. 1]*, In IOP Conference Series: Materials Science and Engineering, p. 12022, IOP Publishing, Bhubaneswar, Odisha, India, 2018.
- [34] Ş. Karabulut, U. Gökmen, and H. Çinici, “Optimization of machining conditions for surface quality in milling AA7039-based metal matrix composites,” *Arabian Journal for Science and Engineering*, vol. 43, no. 3, pp. 1071–1082, 2018.
- [35] T. Sathish and N. Sabarirajan, “Synthesis and optimization of AA 7175-zirconium carbide composites machining parameters,” *Journal of New Materials for Electrochemical systems*, vol. 24, pp. 34–3–3417, 2021.
- [36] J. Pfrommer, C. Zimmerling, J. Liu, L. Kärger, F. Henning, and J. Beyerer, “Optimisation of manufacturing process parameters using deep neural networks as surrogate models,” *Procedia CIRP*, vol. 72, pp. 426–431, 2018.
- [37] T. Ding, S. Zhang, Y. Wang, and X. Zhu, “Empirical models and optimal cutting parameters for cutting forces and surface roughness in hard milling of AISI H13 steel,” *The International Journal of Advanced Manufacturing Technology*, vol. 51, no. 1-4, pp. 45–55, 2010.
- [38] A. R. Shinge and U. A. Dabade, “The effect of process parameters on material removal rate and dimensional variation of channel width in micro-milling of aluminium alloy 6063 T6,” *Procedia Manufacturing*, vol. 20, pp. 168–173, 2018.
- [39] P. Gao, Z. Liang, X. Wang, S. Li, and T. Zhou, “Effects of different chamfered cutting edges of micro end mill on cutting performance,” *International Journal of Advanced Manufacturing Technology*, vol. 96, no. 1-4, pp. 1215–1224, 2018.
- [40] B. Das, S. Roy, R. N. Rai, and S. C. Saha, “Application of grey fuzzy logic for the optimization of CNC milling parameters for Al–4.5% Cu–TiC MMCs with multi-performance characteristics,” *Engineering Science and Technology, an International Journal*, vol. 19, no. 2, pp. 857–865, 2016.
- [41] O. Ağuş, Y. Abalı, O. Arslan, and N. O. S. Keskin, “Facile and controlled production of silver borate nanoparticles,” *SN Applied Sciences*, vol. 1, no. 7, pp. 1–8, 2019.
- [42] M. Pul, “The effect of MgO ratio on surface roughness in Al-MgO composites,” *Materials and Manufacturing Processes*, vol. 28, no. 9, pp. 963–968, 2013.

Research Article

Tribological Behavior of Al/Nanomagnesium/Aluminum Nitride Composite Synthesized through Liquid Metallurgy Technique

D. Srinivasan,¹ M. Meignanamoorthy,¹ Amel Gacem,² Mohanavel Vinayagam,^{3,4} Thanakodi Sathish,⁵ M. Ravichandran,^{1,4} Suresh Kumar Srinivasan,⁶ Magda H. Abdellattif,⁷ and Haiter Lenin Allasi⁸ 

¹Department of Mechanical Engineering, K. Ramakrishnan College of Engineering, Trichy, 621112 Tamil Nadu, India

²Department of Physics, Faculty of Sciences, University 20 Août 1955, Skikda, Algeria

³Centre for Materials Engineering and Regenerative Medicine, Bharath Institute of Higher Education and Research, Chennai 600073, Tamilnadu, India

⁴Department of Mechanical Engineering, Chandigarh University, Mohali, Punjab, India

⁵Department of Mechanical Engineering, Saveetha School of Engineering, SIMATS, Chennai, Tamil Nadu, India

⁶Department of General Engineering (MECH), Panimalar Engineering College Chennai City Campus, Chennai, Tamil Nadu, India

⁷Department of Chemistry, College of Science, Taif University, Al Hawiyah, Taif 21944, Saudi Arabia

⁸Department of Mechanical Engineering, Wollo University, Kombolcha Institute of Technology, Kombolcha, Ethiopia

Correspondence should be addressed to Haiter Lenin Allasi; drahlenin@kiot.edu.et

Received 8 May 2022; Revised 9 July 2022; Accepted 11 July 2022; Published 24 August 2022

Academic Editor: Arpita Roy

Copyright © 2022 D. Srinivasan et al. This is an open access article distributed under the Creative Commons Attribution License, which permits unrestricted use, distribution, and reproduction in any medium, provided the original work is properly cited.

Despite its excellent qualities such as hardness, tensile, and yield strength, aluminum alloys are mostly used in aviation fins and car frames. However, wear resistance at maximum load is weak. This effort will now synthesize and investigate the tribological behavior of AA6063- (AlMg0.7Si-) AlN composites. The goal of this experiment is to determine the best wear rate and coefficient of friction for the AA6063-AlN with nanomagnesium composites developed. Weight percent, load (L), sliding velocity (SV), and sliding distance (SD) are the process factors studied, and the output responses are wear rate and friction coefficient. Bottom pouring type stir casting was used to create AA6063-AlN composites with various weight percentages. The various compositions are AA6063, AA6063-4 wt% AlN, AA6063-8 wt% AlN, and AA6063-12 wt% AlN. A pin-on-disc machine inspected the wear rate and friction coefficient of AA6063-AlN composites. Experimentation was done according to L_{16} orthogonal array (OA). Wear rate (WR) and coefficient of friction (COF) examinations were made to identify the optimum parameters to obtain minimum WR and COF for the AA6063-AlN composite via grey relational analysis (GRA). The contour plot analysis clearly displays WR and COF with respect to wt% vs. L, wt% vs. SV and wt% vs. SD. The ANOVA outcomes revealed that wt% is the most vital parameter (85.55%) persuading WR and COF. The optimized parameters to achieve minor WR and COF was found as 12 wt% of AlN, L 20 N, SV 3 m/s, and SD 400 m. The worn surface was analyzed using scanning electron microscope and indicates that addition of AlN particles with matrix reduces the scratches. These articles offer a key for optimum parameters on wear rate and COF of AA6063-AlN composites via Taguchi grey relational analysis.

1. Introduction

The progressions in the production processes alongside the arrangement of adding a scope of reinforcement particles empower the metal matrix composites (MMCs) for enormous fabrication with various usages. MMCs include a

metals or alloys strengthened with ceramic, metallic, or natural mixtures to upgrade the properties like strength, inflexibility, flexible modulus, wear and corrosion opposition, and warm conductivity [1]. Amid the accessible metals, Al has significant utilization in the fabrication of MMCs [2]. MMCs are used majorly in air craft, automobile, construction sec-

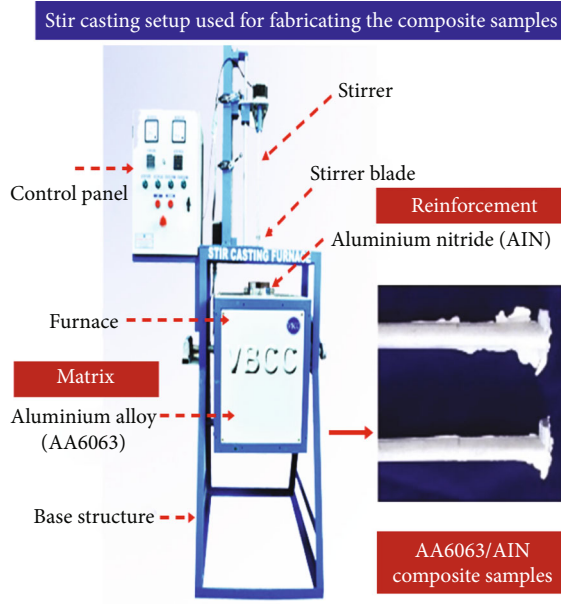


FIGURE 1: Stir casting setup used for the present work.



FIGURE 3: Pin-on-disc wear test apparatus.

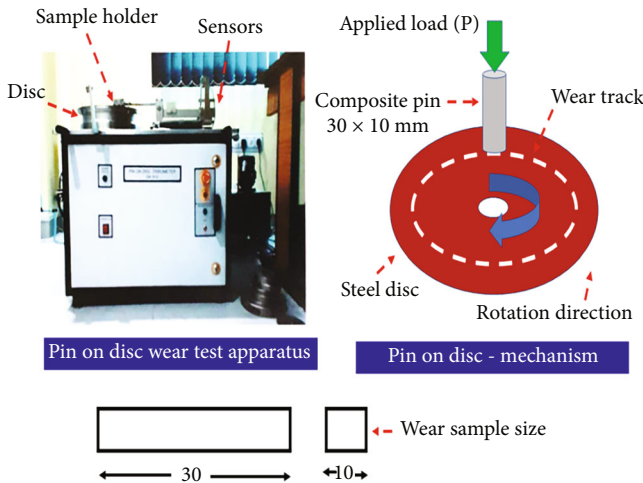


FIGURE 2: Schematic of pin-on-disc wear test apparatus.

tor, electronics stuffing, thermal controlling apparatus's despite of its better strength, superior elastic modulus, precise stiffness, and thermal and electrical conductivity [3]. MMCs strengthened with ceramics exhibit superior properties like wear and corrosion behavior than the customary alloys [4]. MMCs possess sustainable usages in various engineering sector. MMCs are utilized as another material for prevailing alloys in the field of automobile and aerospace sector [5, 6]. In the previous industry development period, aluminum and its alloys were ascertained to be foremost consistent less weight materials; additionally, it was utilized considerably on manufacturing automobile and space vehicle parts [7]. The expanding requests for less weight, excellent strength, superior high-temperature execution, outstanding corrosion opposition, and synthetically latent and energy-convertible materials in the transport, farming,

infrastructure, and production companies have invigorated a consistently developing action to produce explicit composite materials named as aluminum matrix composites (AMCs).

AMCs are less weight and better enactment materials that possess the possibility to substitute traditional materials in numerous progressive usages [8]. AMCs are notable for their better strength to weight proportion, unrivaled tribological behavior, and corrosion opposition properties; because of these reasons, monolithic alloys have been replaced in various fields like automotive, maritime, and aviation sector. Since the most recent thirty years, scientists have given their attention to these materials and are attempting to enhance the property to create them appropriate for usage in difficult territories [9]. Owing to the superior properties, AMCs are used in the manufacturing of aero frame structure, space shuttle component, landing gear, brake disc, knuckle housing, suspension arm, etc. [10]. AMCs have enhanced wear opposition, less weight, and better rigidity, with obvious superiority usages. AMCs can replace traditional materials in automotive and aeronautics sectors [11]. AMCs can be utilized in energy-related application areas like nuclear, renewable, and bioenergy sectors. By using AMCs in energy sectors as well as in oil refining industries, the life time of the component can be enhanced significantly [12, 13]. AlN is a normally necessary strengthening material for AMCs as it gets the compelling mixing of physical, tribological, and mechanical attributes like better hardness, less density, good versatile modulus, and remarkable wear obstruction. Particularly, usage of AlN particles as fortification has consistently upgraded the AMC mechanical properties [14]. AlN reinforced with aluminum is nonreactive; AlN possesses better hardness, better thermal conductivity, and least coefficient of thermal expansion [15].

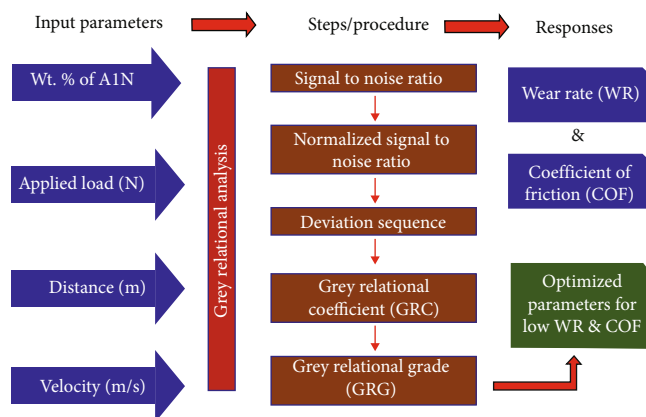


FIGURE 4: Steps followed for the TGRA method.

TABLE 1: Experimental results.

Exp. no.	wt% AlN (A)	L (N) (B)	SV (m/s) (C)	SD (m) (D)	WR (mm ³ /m)	COF
1	0	10	1	400	0.00821	0.374
2	0	20	2	800	0.00884	0.419
3	0	30	3	1200	0.01112	0.392
4	0	40	4	1600	0.00948	0.445
5	4	10	2	1200	0.00556	0.496
6	4	20	1	1600	0.00582	0.501
7	4	30	4	400	0.00565	0.573
8	4	40	3	800	0.00605	0.498
9	8	10	3	1600	0.00469	0.662
10	8	20	4	1200	0.00482	0.598
11	8	30	1	800	0.00503	0.653
12	8	40	2	400	0.00517	0.688
13	12	10	4	800	0.00412	0.462
14	12	20	3	400	0.00407	0.380
15	12	30	2	1600	0.00402	0.411
16	12	40	1	1200	0.00396	0.449

AlN is a hard refractory ceramic and potentially attractive reinforcement. AlN possesses superior mechanical properties, least dielectric constant, enhanced electrical resistivity, good thermal steadiness, and better compatibility with aluminum alloy [16]. Because of the above-mentioned excellent properties, AlN is extensively utilized in electronic pocketing and structural industry uses [17]. Owing to the unique features of stir casting (SC) process, this is a foremost familiar method utilized commercially. Easiness and litness of this method make this as inexpensive process and also suit for extensive production. By using SC method, complicated components can be manufactured via SC route. Nowadays, maximum consideration is given to SC route because homogenous dispersal of reinforcement particles with metal matrix can be attained [18]. SC route that produced MMCs exhibits superior properties despite of its least porosity and least crack creation. Aluminum combination developed MMCs manufactured utilizing SC process possessing enhanced properties [19]. The major

issues experienced in MMC preparing are the dispersal of the reinforcement particles with the matrix amid SC. The above-stated problem can be overcome by selecting proper stirring speed, time, and temperature [20].

They [21] manufactured AlN-Al composite via squeeze casting route and studied the influence of various range cycling treatments on mechanical properties and concluded that broad range cycling treatment was the major valuable in enhancing tensile strength, and modest-range cycling treatment was preferable to improve yield strength and elastic limit. They [22] synthesized A359-AlN composites via stir and squeeze casting methods, and their mechanical properties were studied. It was concluded that adding of AlN particles from 5 to 15 wt% with A359 matrix enhances the hardness, ultimate compressive strength, and yield strength. This work [23] produced AA6061-AlN composites with various weight percentages through stir casting route and investigated the mechanical properties and stated that inclusion of AlN with AA6061 matrix enhances the macro- and microhardness, ultimate tensile strength, and yield strength. Authors [24] produced Al-AlN composites and described that elastic modulus and hardness improved drastically because of grain refinement and interface strengthening mechanism. They [25] manufactured TiB₂-AlN ceramic by hot pressing method and observed their mechanical properties. This work [26] synthesized Al-AlN composites through squeeze casting route, and their tensile strength was investigated. It has been observed that inclusion of AlN particles with Al matrix increases the tensile strength. This work [27] produced Al-AlN composite through in situ fabrication technique, and the results revealed that increasing the AlN particles increases the tensile strength. This work [28] explored the tribological properties of hybrid composites and stated that load was one of the utmost impelling parameters on the wear behavior. They [29] optimized the wear characteristics of aluminum hybrid composites and reported that load is the important parameter to attain least wear rate (WR).

From the in depth literature exploration, it is implicit that scarce research work has been done via AlN as strengthening particle through Al matrix. Therefore, the goal of the paper has been to investigate the tribological properties of AA6063-AlN composites produced via SC process. By

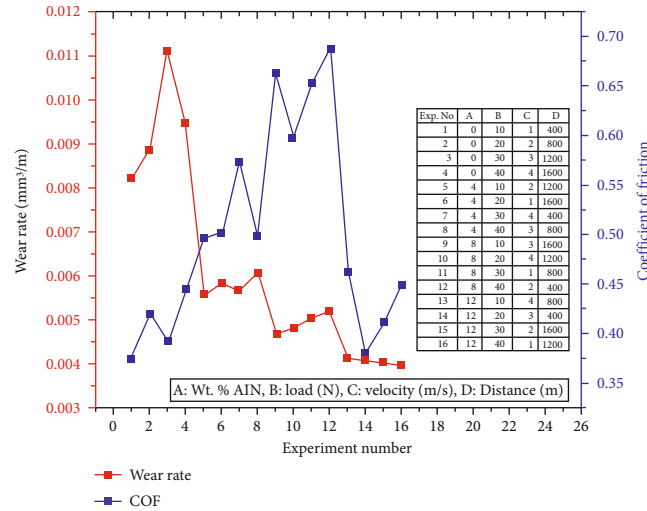


FIGURE 5: Rank plot for WR and COF.

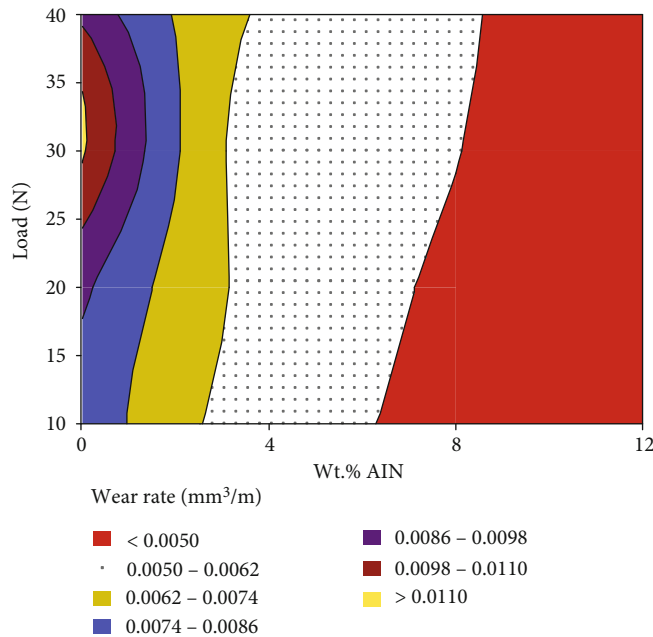


FIGURE 6: Contour plots wt% vs. load.

varying the reinforcing component weight percentage in the matrix composite analyzed and by using Taguchi grey relational analysis, the suitable tribological parameters obtaining optimum wear rate (WR) and coefficient of friction (COF) were identified. Such parameters included load (N), sliding velocity (m/s), and sliding distance (m) which existed in the contact zone analyzed. In this study, four-level four factors were utilized to compose the L_{16} array with prominent techniques of Taguchi.

2. Materials and Methods

2.1. Sample Preparation. AA6063 was employed as base material and AlN as reinforcement. The Chemical composition of AA6063 alloy, Si-0.44 wt%, Mg-0.56 wt%, Cu-

0.02 wt%, Mn-0.03 wt%, Fe-0.46 wt%, Cr-0.03 wt%, Zn-0.66 wt%, Ti-0.02 wt%, Al remaining wt%. The essential quantity of AA6063 and AlN powder was quantified via digital weight instrument. Increasing the wettability, 2 wt% of nanomagnesium particles (45 nm) is included with AlN. Magnesium particles play a vital role in enhancing the bonding with matrix and reinforcement. AA6063 was liquefied using crucible furnace at 825°C temperature. AlN powder was heated at a 400°C temperature. Later, to attain the liquefied range, various wt% of AlN reinforcement particles were included to synthesize numerous combinations AA6063, AA6063-4 wt% AlN, AA6063-8 wt% AlN, and AA6063-12 wt% AlN. The stirring was done at a speed of 500 rpm for 5 min. The stir casting setup utilized for the present study is displayed in Figure 1.

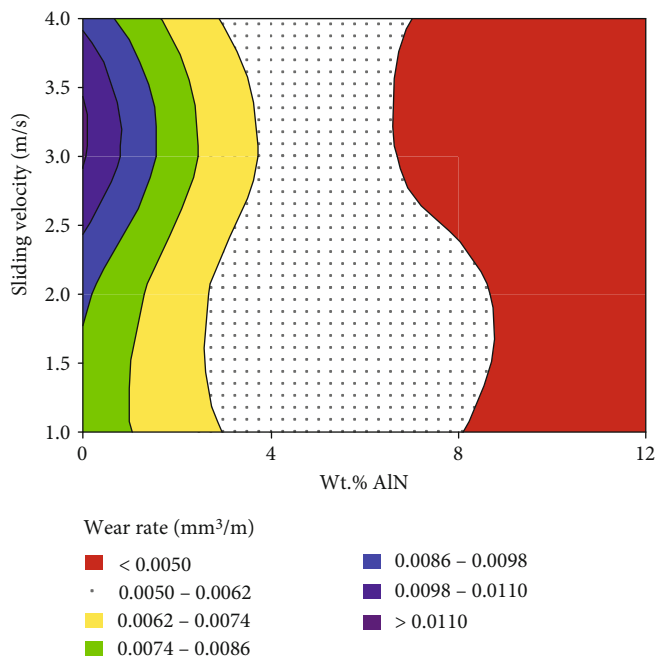


FIGURE 7: Contour plots wt% vs. sliding velocity.

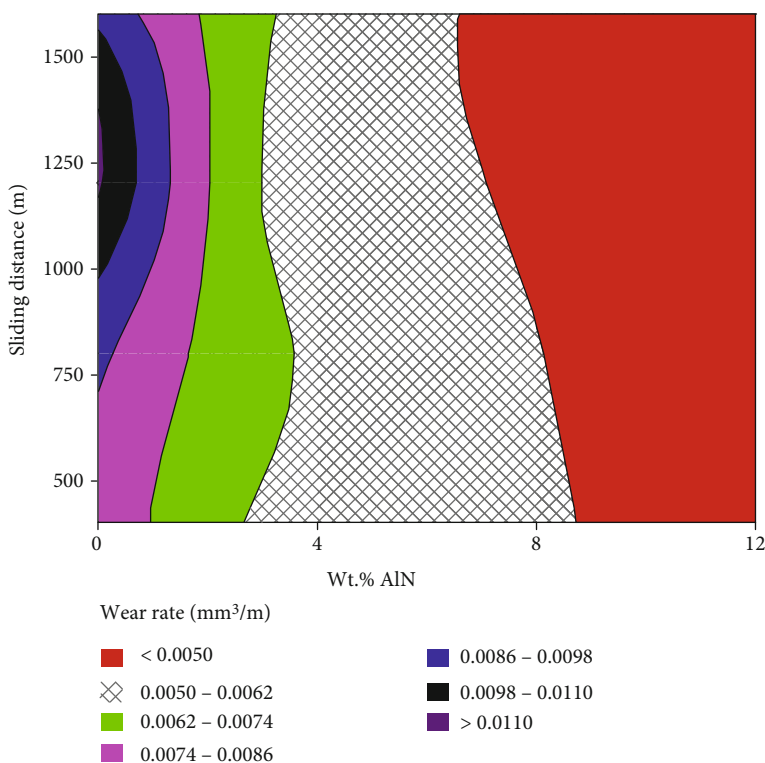


FIGURE 8: Contour plots wt% vs. sliding distance.

2.2. *Tribotester.* Figures 2 and 3 display schematic and actual pin-on-disc apparatus used for tribological analysis.

2.3. *TGRA Method.* Figure 4 displays the steps followed for Taguchi grey relational analysis (TGRA) process. To increase the wettability, magnesium is added in least quan-

tity amid stirring [30]. Immediately, melted metal was distributed into a die to get needed sizes. Scanning electron microscope (SEM) inspection was carried out in the produced specimens. The tribology examination was done via pin-on-disc device DUCOM TR20-LEASTM. The dimension of the pin used was 30 mm length and 10 mm diameter

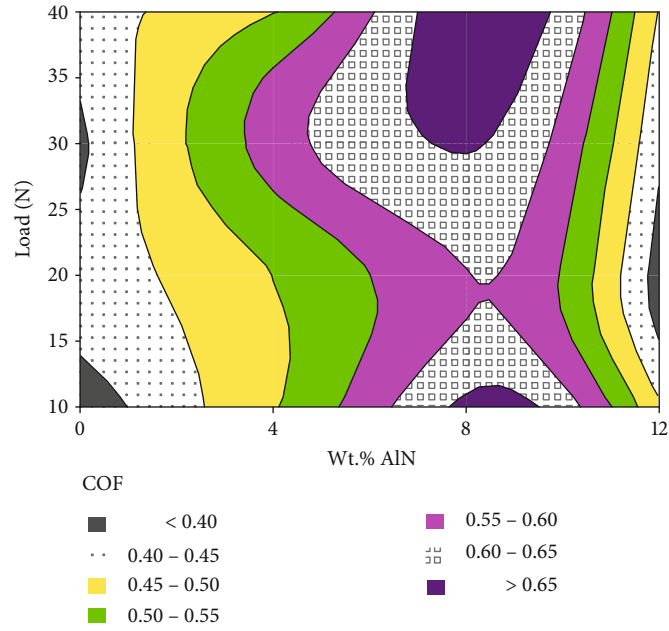


FIGURE 9: Contour plots wt% vs. load.

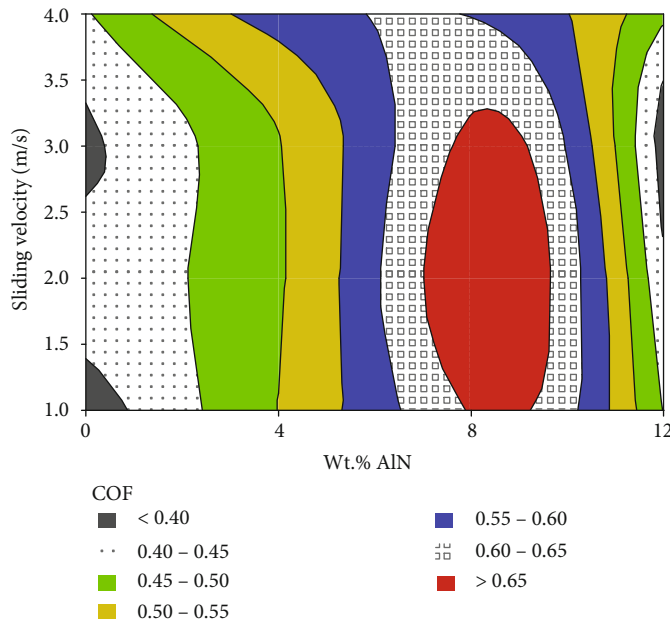


FIGURE 10: Contour plots wt% vs. sliding velocity.

as per ASTM G99-04 standard [31]. EN31 steel was used as disc. The tribological analysis was done at different process parameters load 10, 20, 30, and 40 N; sliding velocity 1, 2, 3, and 4 m/s; and sliding distance 400, 800, 1200, and 1600 m. The initial parameter of the surface roughness of the tested sample is $0.61 \mu\text{m}$.

2.3.1. Multiobjective Valuation. Taguchi process merged with grey is a principal process. By grey approach, the multiobjective valuation can be transformed fair too; just response optimization and obligatory process parameter can be

attained [32]. In this study, GRA was used to identify the optimal level of tribological parameters on the multiobjectives of the responses. The below formulas are used to find the optimum results shown in

$$y_i^*(x) = \frac{\max z_i(y) - z_i(y)}{\max z_i(y) - \text{mix}z_i(y)}, \quad (1)$$

$$\xi_i(k) = \frac{\Delta \text{min} + p\Delta \text{max}}{\Delta x_i(k) + p\Delta \text{max}}, \quad (2)$$

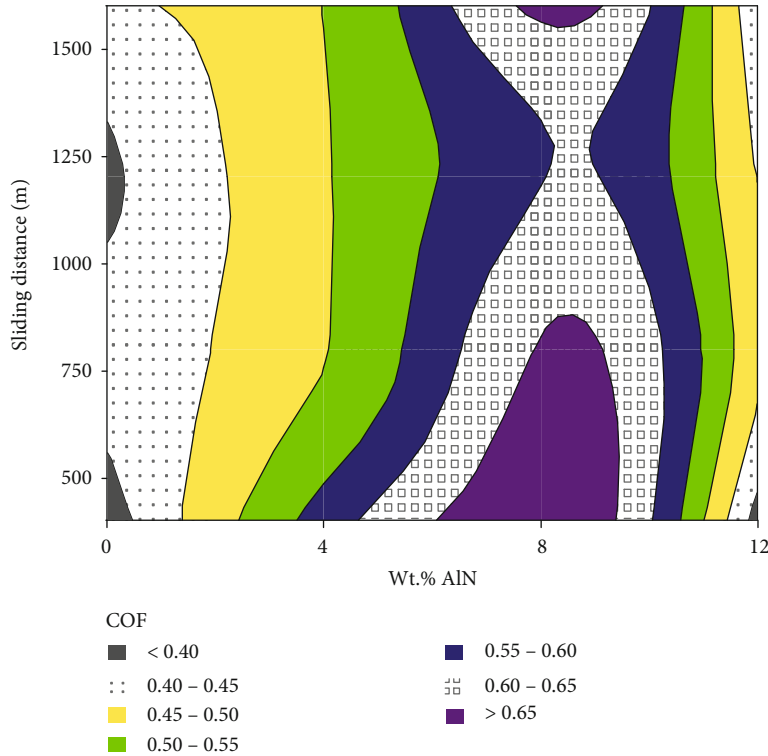


FIGURE 11: Contour plots wt% vs. sliding distance.

TABLE 2: Calculated S/N ratio and normalized S/N ratio values.

Ex. no	S/N ratio		Normalized S/N ratio	
	WR (dB)	COF (dB)	WR (dB)	COF (dB)
1	41.71314	8.54257	0.40642	1.00000
2	41.07095	7.55572	0.31844	0.85669
3	39.0779	8.13428	0.00000	0.94268
4	40.46383	7.03280	0.22905	0.77389
5	45.0985	6.09037	0.77654	0.61146
6	44.70154	6.00325	0.74022	0.59554
7	44.95903	4.83691	0.76397	0.36624
8	44.36489	6.05541	0.70810	0.60510
9	46.57654	3.58284	0.89804	0.08280
10	46.33906	4.46598	0.87989	0.28662
11	45.96864	3.70174	0.85056	0.11146
12	45.73019	3.24823	0.83101	0.00000
13	47.70206	6.70716	0.97765	0.71975
14	47.80811	8.40433	0.98464	0.98089
15	47.91548	7.72316	0.99162	0.88217
16	48.0461	6.95507	1.00000	0.76115

$$\gamma_i = \frac{1}{n} \sum_{k=1}^n \xi_i(k). \quad (3)$$

3. Results and Discussions

3.1. Wear Behavior of AA6063-AlN Composites. Wear rate (WR) and coefficient of friction examinations were made

to identify the optimum parameters to obtain minimum WR and COF for the produced composite via GRA. Experiments were done according to L_{16} OA, and the results were comprehensive in Table 1. Figure 5 displays the rank plot for WR and COF. The rank plot clearly displays the experimental trials with respect to WR and COF. It is clear from the graph COF is less than the WR while increasing the trials.

3.1.1. Effect of Process Parameter on WR. Figures 6–8 display the contour plot for WR (a) wt% vs. L, (b) wt% vs. SV, and (c) wt% vs. SD. It is clear that wear rate rises with the rise in P, V, and D and declines with rise in the wt% of AlN particles. It could be well understood from Figures 5–7 that wt% of AlN particles possesses extreme impact on wear rate as related to another process parameters. Least wear rate is obtained for 12 wt% AlN particles; the major reason is 12 wt% AlN particles tarnished away from the composites creating a tiny film on the counter face at the edge outcomes in enhanced wear resistance. Moreover, the occurrence of AlN particles performs as load behavior element. The wear rate is in the sequence of 12% > 8% > 4% > 0% wt% of AlN. When the wt% of AlN particles increases as well as load and sliding distance rises and wear rate decreases, this could be despite of the reason that with greater loads, the creation of frictional heat lessens the composite hardness which eventually outcome in pull down of the wear resistance [33].

3.1.2. Effect of Process Parameter on COF. Figures 9–11 display the contour plot for COF (a) wt% vs. L, (b) wt% SV, and (c) wt% vs. SD. From Figures 8–10, it is observable that COF declines with the rise in wt% of AlN particles, P, V, and D.

TABLE 3: Calculated deviation sequences, grey relational coefficient, and grade.

Ex. no	Deviation sequence		Grey relational coefficient		Grey relational grade	Rank
	WR	COF	WR	COF		
1	0.59358	0.00000	0.45722	1.00000	0.728608	5
2	0.68156	0.14331	0.42317	0.77723	0.600198	10
3	1.00000	0.05732	0.33333	0.89714	0.615238	7
4	0.77095	0.22611	0.39341	0.68860	0.541002	15
5	0.22346	0.38854	0.69112	0.56272	0.626922	6
6	0.25978	0.40446	0.65809	0.55282	0.605453	9
7	0.23603	0.63376	0.67932	0.44101	0.560164	14
8	0.29190	0.39490	0.63139	0.55872	0.595056	11
9	0.10196	0.91720	0.83063	0.35281	0.591718	12
10	0.12011	0.71338	0.80631	0.41207	0.609190	8
11	0.14944	0.88854	0.76989	0.36009	0.564992	13
12	0.16899	1.00000	0.74739	0.33333	0.540362	16
13	0.02235	0.28025	0.95722	0.64082	0.799018	4
14	0.01536	0.01911	0.97019	0.96319	0.966690	1
15	0.00838	0.11783	0.98352	0.80928	0.896397	2
16	0.00000	0.23885	1.00000	0.67672	0.838362	3

TABLE 4: Response table for GRG.

Level	wt% AlN	L (N)	SV (m/s)	SD (m)
1	0.6213	0.6866	0.6844	0.6990
2	0.5969	0.6954	0.6660	0.6398
3	0.5766	0.6592	0.6922	0.6724
4	0.8751	0.6287	0.6273	0.6586
Delta	0.2986	0.0667	0.0648	0.0591
Rank	1	2	3	4

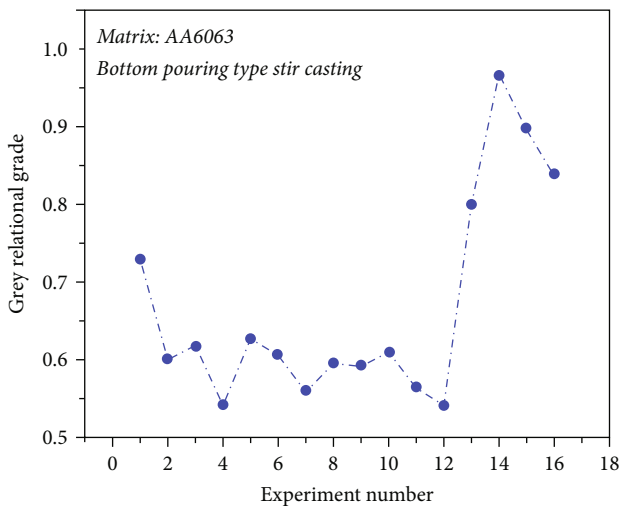


FIGURE 12: Grey relational grade.

The major reason for decreases in COF could be because at the time when the load rises, temperature of the worn surface enhances, which creates the composites to become soft; by this way, the COF declines [34]. As the wt% of AlN rises up to 12 wt%, the COF drops; despite of greater wt% of AlN particles, the distribution of particles is homogenous, which hints to a lesser value as linked to the another composite samples [35].

3.1.3. Grey Relational Analysis

(1) *Multiresponse Examination.* Taguchi technique combined through grey is a dominant technique. By means of grey, the multiresponse examination could be transformed simply to only retort optimization, and needed process parameter can be attained. The procedure intricate in GRA is provided below. The initial procedure is to regularize the restrained values. The fabric made famous by solitary CGF fibres could withstand a light load. As the weight percentage of CG fibres in the composite materials rises, so does the ability to support so much weight. The stress causes failure and has more excellent deformability as the percentage of CG fibre within the layered combination increases. Intended for this situation, Taguchi configuration combined through grey would be utilized for upgraded execution attributes. Table 2 shows the calculated S/N ratio and normalized S/N ratio values for the littler the better as far as WR and COF introduced. Table 3 displays the grey relational coefficient, grey relational grade (GRG), and rank for 16 experimentations. From Table 3, 1st rank shows the upper GRG, which would have the improved multiexecution qualities. As of Table 3, 14th trail has the optimum parameters for many execution attributes as far as WR and COF. Table 4 shows the response table for GRG. From Table 4, it is seen that 0.2986 is the limit of max-min esteem. Thus, it is presumed that wt% of AlN is most affected parameter for WR and COF trailed by L, SV, and SD. The sequence of prompting influences is in the order as enumerated wt% of AlN (0.2986), L (0.0667), SV (0.6648), and SD (0.0591). Figure 12 displays the grey relational grade. Figure 13 displays the main effects plot for GRG.

3.1.4. *Analysis of Variance.* The consequence of the process parameter impelling the numerous superiority features is examined via ANOVA. Table 5 displays the ANOVA for GRG for determining the utmost substantial factors. From Table 5, it can be perceived that the wt% of AlN is the supreme important factor (contributing 85.55%). The wt% of AlN has a foremost impact on the multiperformance characteristics for AA6063-AlN composites trailed by load (contributing 3.97%), sliding velocity (3.66%), and sliding distance (2.71%).

3.1.5. *Confirmation Test.* The optimum level of parameter was utilized to validate the output response qualities for WR of AA6063-AlN composite. The predicted and experimental values of GRG were attained via exploiting

$$\gamma_{\text{pre}} = \gamma_m + \sum_{k=1}^n (\gamma_i - \gamma_m). \quad (4)$$

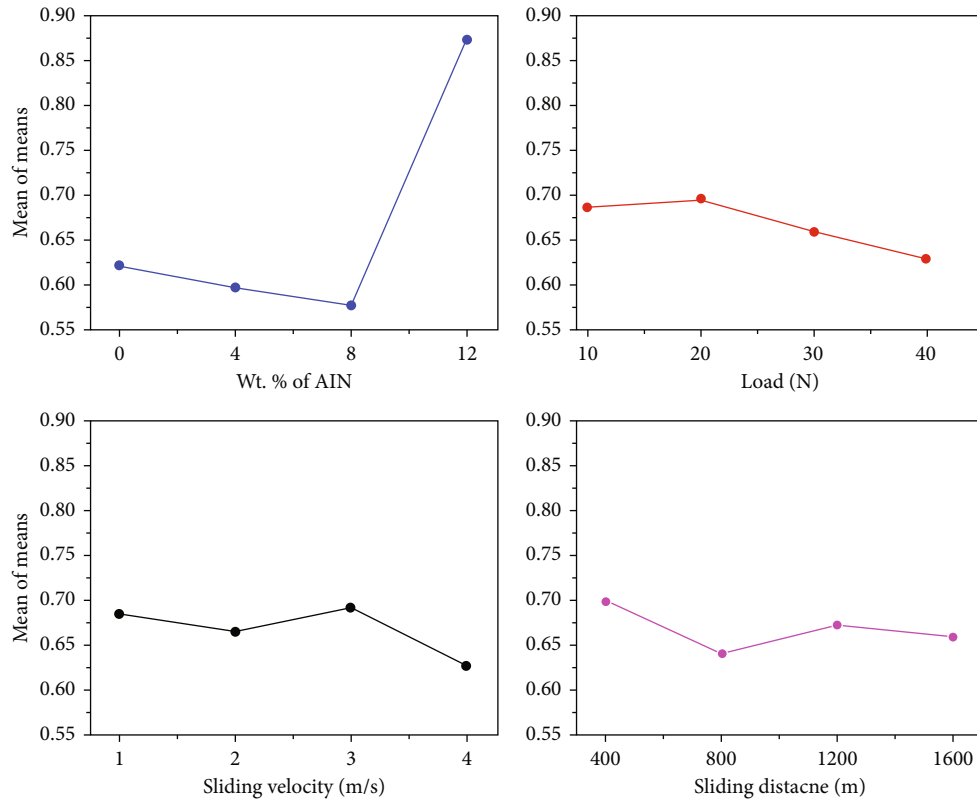


FIGURE 13: Main effect plot for GRG.

TABLE 5: ANOVA for GRG.

Source	DF	Seq SS	Adj SS	Adj MS	F	P	Contribution (%)
wt% AlN - A	3	0.233985	0.233985	0.077995	20.96	0.016	85.55%
L (N) - B	3	0.010863	0.010863	0.003621	0.97	0.509	3.97%
SV (m/s) - C	3	0.010031	0.010031	0.003344	0.90	0.534	3.66%
SD (m) - D	3	0.007434	0.007434	0.002478	0.67	0.627	2.71%
Error	3	0.011163	0.011163	0.003721			4.11%
Total	15	0.273477					100%

$S = 0.0609994$; $R - Sq = 95.92\%$; $R - Sq(\text{adj}) = 79.59\%$.

TABLE 6: Confirmation experimental results.

Responses/level	Predicted value $A_4B_2C_3D_1$	Experimental value $A_4B_2C_3D_1$
WR (mm^3/m)	—	0.00407
COF	—	0.380
GRG	0.959317	0.799018

Table 6 displays the comparison of the predicted and experimental values of the GRG utilizing optimal level parameters, and these values are precise near to one another. The GRG percentage of predicted value is improved by 83.3%.

The normal probability plot of GRG is exposed in Figure 14. It displays that entirely, the errors are originated out to be generally dispersed alongside the straight line at 95% confidence level.

3.2. Worn Surface Analysis. Figures 15(a)–15(d) shows the shallow scratches, sliding direction, microcutting, smeared surfaces, microploughing, wear track, peelers, and delamination of AA6063-AlN composites examined via SEM. Figure 15(a) shows the shallow scratches and sliding direction. Figures 15(b)–15(d) show the worn surface of AA6063-4 wt% AlN, AA6063-8 wt% AlN, and AA6063-12 wt% AlN composites. From Figure 15(b), microcutting and smeared surfaces were observed. From Figure 15(c), microploughing, wear track, and smeared surfaces were witnessed. From Figure 15(d), peelers and delamination were witnessed. From the detailed observation, it could be clearly understood that increase in reinforcement weight percentage results in noticeable wear decline. Minimum scratches were found for composite samples, and presence of reinforcement particles prevents the scratch formation [36].

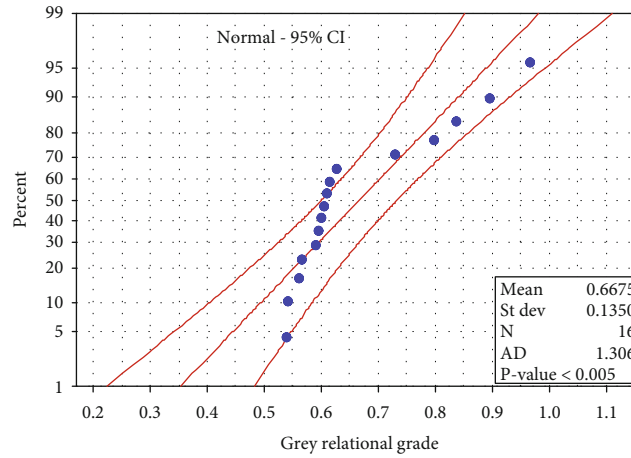


FIGURE 14: Normal probability plot.

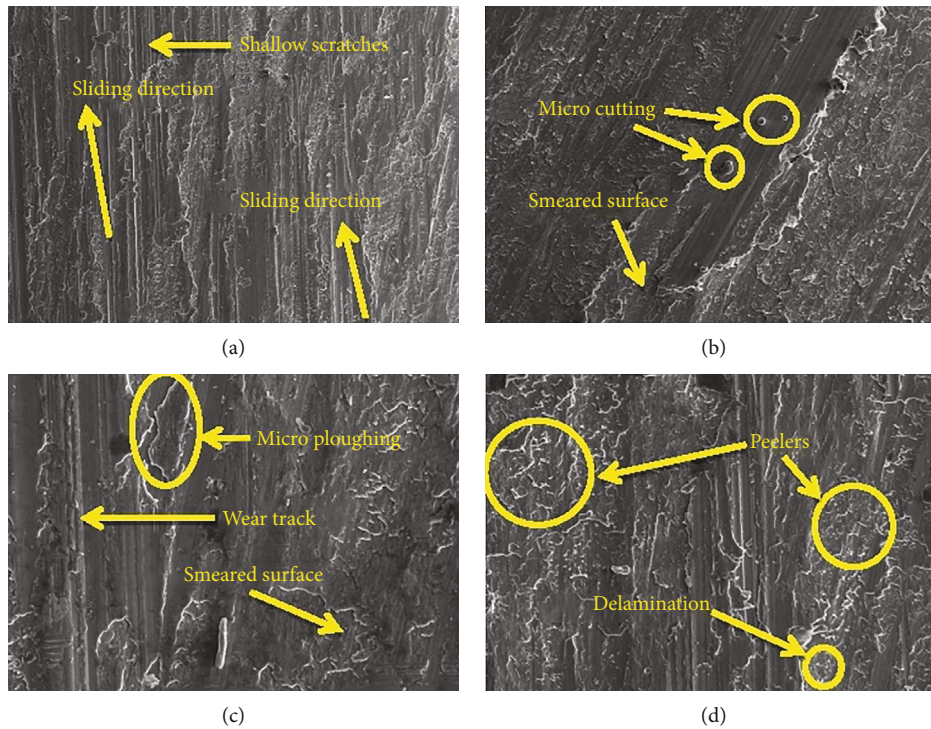


FIGURE 15: Worn surface morphology of (a) AA6063, (b) AA6063-4 wt% AlN, (c) AA6063-8 wt% AlN, and (d) AA6063-12 wt% AlN composites.

4. Conclusions

Stir casting is an appropriate method for producing AMCs with required characteristics for technical applications. Stir casting was used to successfully create AA6063-AlN composites. The influence of AlN on the wear behavior of the AA6063 was examined utilizing a pin-on-disc tribometer.

- (i) GRA is an appropriate method for determining the best process parameters to achieve the lowest WR and COF for AA6063-AlN composites. The tribolog-

ical characteristics of AA6063-AlN composites were examined by GRA, and the best parameters for achieving minimal WR and COF were discovered to be 12 wt% AlN, L 20N, SV 3 m/s, and SD 400 m. ANOVA was used to determine the effect parameters on WR and COF responses. The GRG's estimated value percentage has increased by 83.3 percent

- (ii) SEM was used to examine worn surfaces, and diverse wear mechanisms were observed for all composites
- (iii) The achieved results with the same parameters and output replies were to be studied and compared in

the future utilizing various optimization strategies such as neural network and fuzzy logic system

Data Availability

The data used to support the findings of this study are included within the article. Further data or information is available from the corresponding author upon request.

Conflicts of Interest

The authors declare that there is no conflict of interest regarding the publication of this article.

Acknowledgments

The authors appreciate the support from the Kombolcha Institute of Technology, Ethiopia, for the research and preparation of the manuscript. The authors thank the K. Ramakrishnan College of Engineering, Chandigarh University, University 20 Août 1955, and Taif University, for providing assistance to this work. This study was supported by the Taif University Researchers, supporting project number TURSP-2020/91, Taif University, Saudi Arabia.

References

- [1] P. R. Matli, U. Fareeha, R. A. Shakoore, and A. M. A. Mohamed, "A comparative study of structural and mechanical properties of Al-Cu composites prepared by vacuum and microwave sintering techniques," *Journal of Materials Research and Technology*, vol. 7, no. 2, pp. 165–172, 2017.
- [2] P. Samal, P. R. Vundavilli, A. Meher, and M. M. Mahapatra, "Recent progress in aluminum metal matrix composites: a review on processing, mechanical and wear properties," *Journal of Manufacturing Processes*, vol. 59, pp. 131–152, 2020.
- [3] G. V. Jagadeesh and S. G. Setti, "A review on micromechanical methods for evaluation of mechanical behavior of particulate reinforced metal matrix composites," *Journal of Materials Science*, vol. 55, no. 23, pp. 9848–9882, 2020.
- [4] T. Anandaraj, P. P. Sethusundaram, M. Meignanamoorthy, and M. Ravichandran, "Investigations on properties and tribological behavior of AlMg4.5Mn0.7 (AA5083)-MoO₃ composites prepared by stir casting method," *Surface Topography: Metrology and Properties*, vol. 9, pp. 1–13, 2021.
- [5] J. A. Jeffrey, S. S. Kumar, P. Hariharan, M. Kamesh, and A. M. Raj, "Production and assessment of AZ91 reinforced with nano SiC through stir casting process," *Materials Science Forum*, vol. 1048, pp. 9–14, 2022.
- [6] V. Sivamaran, V. Balasubramanian, M. Gopalakrishnan, V. Viswabaskaran, A. Gourav Rao, and G. Sivakumar, "Mechanical and tribological properties of self-lubricating Al 6061 hybrid nano metal matrix composites reinforced by nSiC and MWCNTs," *Surf. Interfaces*, vol. 21, article 100781, 2020.
- [7] A. E. A. Al-maamari, A. K. M. Asiflqbal, and D. M. Nuruzza-man, "Mechanical and tribological characterization of self-lubricating Mg-SiC-Gr hybrid metal matrix composite (MMC) fabricated via mechanical alloying," *Journal of Science: Advanced Materials and Devices*, vol. 5, pp. 535–544, 2020.
- [8] G. F. Aynalem, "Processing methods and mechanical properties of aluminium matrix composites," *Advances in Materials Science and Engineering*, vol. 2020, 19 pages, 2020.
- [9] D. K. Das, P. C. Mishra, S. Singh, and R. K. Thakur, "Properties of ceramic-reinforced aluminium matrix composites - a review," *International Journal of Mechanical and Materials Engineering*, vol. 9, pp. 1–16, 2014.
- [10] N. K. Bhoi, H. Singh, and S. Pratap, "Developments in the aluminum metal matrix composites reinforced by micro/nano particles - a review," *Journal of Composite Materials*, vol. 54, no. 6, pp. 813–833, 2020.
- [11] V. Mohanavel, S. Prasath, K. Yoganandam, B. G. Tesemma, and S. S. Kumar, "Optimization of wear parameters of aluminium composites (AA7150/10 wt% WC) employing Taguchi approach," *Materials Today: Proceedings*, vol. 33, pp. 4742–4745, 2020.
- [12] A. Jaehyung, A. Mikhaylov, and H. Ulf Richter, "Trade war effects: evidence from sectors of energy and resources in Africa," *Heliyon*, vol. 6, no. 12, article e05693, 2020.
- [13] A. Jaehyung and A. Mikhaylov, "Russian energy projects in South Africa," *Journal of Energy in Southern Africa*, vol. 31, pp. 58–64, 2020.
- [14] V. Mohanavel and M. Ravichandran, "Influence of AlN particles on microstructure, mechanical and tribological behaviour in AA6351 aluminum alloy," *Materials Research Express*, vol. 6, no. 10, article 106557, 2019.
- [15] G. A. Sweet, R. L. Hexemer Jr., I. W. Donaldson, A. Taylor, and D. P. Bishop, "Powder metallurgical processing of a 2xxx series aluminum powder metallurgy metal alloy reinforced with AlN particulate additions," *Materials Science and Engineering A*, vol. 755, pp. 10–17, 2019.
- [16] A. Kareem, J. A. Qudeiri, A. Abdudeen, T. Ahammed, and A. Ziout, "A review on AA 6061 metal matrix composites produced by stir casting," *Maternité*, vol. 14, pp. 1–22, 2021.
- [17] R. Pandiyarajan, P. Maran, S. Marimuthu, and K. C. Ganesh, "Mechanical and tribological behavior of the metal matrix composite AA6061/ZrO₂/C," *Journal of Mechanical Science and Technology*, vol. 31, no. 10, pp. 4711–4717, 2017.
- [18] J. Hashim, L. Looney, and M. S. J. Hashmi, "Metal matrix composites: production by the stir casting method," *Journal of Materials Processing Technology*, vol. 92, pp. 1–7, 1999.
- [19] S. Balasivanandha Prabu, L. Karunamoorthy, S. Kathiresan, and B. Mohan, "Influence of stirring speed and stirring time on distribution of particles in cast metal matrix composite," *Journal of Materials Processing Technology*, vol. 171, no. 2, pp. 268–273, 2006.
- [20] T. Sathish, V. Mohanavel, K. Ansari et al., "Synthesis and characterization of mechanical properties and wire cut EDM process parameters analysis in AZ61 magnesium alloy+B₄C+SiC," *Materials*, vol. 14, no. 13, article 3689, 2021.
- [21] M. Zhao, G. Wu, D. Zhu, J. Jiang, and Z. Dou, "Effects of thermal cycling on mechanical properties of AlNp/Al composite," *Materials Letters*, vol. 58, no. 12–13, pp. 1899–1902, 2004.
- [22] A. M. Essam and A. Y. Churyumova, "Development and characterization of A359/AlN composites for automotive applications," *Journal of Alloys and Compounds*, vol. 727, pp. 540–548, 2017.
- [23] B. Ashok Kumar and N. Murugan, "Metallurgical and mechanical characterization of stir cast AA6061-T6-AlN_p composite," *Materials and Design*, vol. 40, pp. 52–58, 2012.

- [24] Y. Q. Liu, H. T. Conga, W. Wang, C. H. Sun, and H. M. Cheng, "AlN nanoparticle-reinforced nanocrystalline Al matrix composites: fabrication and mechanical properties," *Materials Science and Engineering A*, vol. 505, no. 1-2, pp. 151-156, 2009.
- [25] M. M. Mokhayer, M. G. Kakroudi, S. S. Milani, H. Ghiasi, and N. P. Vafa, "Investigation of AlN addition on the microstructure and mechanical properties of TiB₂ ceramics," *Ceramics International*, vol. 45, no. 13, pp. 16577-16583, 2019.
- [26] Q. Zhang, G. Chen, G. Wu, Z. Xiu, and B. Luan, "Property characteristics of a AlNp/Al composite fabricated by squeeze casting technology," *Materials Letters*, vol. 57, no. 8, pp. 1453-1458, 2003.
- [27] P. Yu, M. Balog, M. Yan, G. B. Schaffer, and M. Qian, "In situ fabrication and mechanical properties of Al-AlN composite by hot extrusion of partially nitrated AA6061 powder," *Journal of Materials Research*, vol. 26, no. 14, pp. 1719-1725, 2011.
- [28] S. Daniel and P. M. Gopal, "Study on tribological behaviour of Al/SiC/MoS₂ hybrid metal matrix composites in high temperature environmental condition," *Silicon*, vol. 10, no. 5, pp. 2129-2139, 2018.
- [29] A. Vaishnavi and G. K. Chandran, "Optimisation of dry sliding wear process parameters for aluminium hybrid metal matrix composites," *Tribology in Industry*, vol. 36, pp. 188-194, 2014.
- [30] L. Poovazhagan, K. Rajkumar, P. Saravanamuthukumar, P. Javed Syed Ibrahim, and S. Santosh, "Effect of magnesium addition on processing the Al-0.8 Mg-0.7 Si/SiCp metal matrix composites," *Applied Mechanics and Materials*, vol. 787, pp. 553-557, 2015.
- [31] C. A. V. Kumar and J. S. Rajadurai, "Influence of rutile (TiO₂) content on wear and microhardness characteristics of aluminium-based hybrid composites synthesized by powder metallurgy," *Transactions of Nonferrous Metals Society of China*, vol. 26, no. 1, pp. 63-73, 2016.
- [32] A. A. Raneen, M. Mozammel, M. K. Aqib, C. Wenliang, K. G. Munish, and I. P. Catalin, "Multi-response optimization of face milling performance considering tool path strategies in machining of Al-2024," *Maternité*, vol. 12, pp. 1-19, 2019.
- [33] S. V. Alagarsamy, M. Ravichandran, P. Raveendran, and B. Stalin, "Evaluation of micro hardness and optimization of dry sliding wear parameters on AA7075 (Al-Zn-Mg-Cu) matrix composites," *Journal of the Balkan Tribological Association*, vol. 25, pp. 730-742, 2019.
- [34] S. Arivukkarasan, V. Dhanalakshmi, B. Stalin, and M. Ravichandran, "Mechanical and tribological behaviour of tungsten carbide reinforced aluminum LM4 matrix composites," *Particulate Science and Technology*, vol. 36, no. 8, pp. 967-973, 2018.
- [35] S. K. Thakur and B. K. Dhindaw, "The influence of interfacial characteristics between SiCp and Mg/Al metal matrix on wear, coefficient of friction and micro hardness," *Wear*, vol. 272, pp. 191-201, 2001.
- [36] Z. Sun, D. Zhang, and G. Li, "Evaluation of dry sliding wear behavior of silicon particles reinforced aluminum matrix composites," *Materials and Design*, vol. 26, pp. 454-458, 2005.

Research Article

Investigations of Nanoparticles (Al_2O_3 - SiO_2) Addition on the Mechanical Properties of Blended Matrix Polymer Composite

K. Logesh,¹ V. M. Vel,² A. H. Seikh,³ Ajit M. Hebbale,⁴ Rajesh A S,⁵ N. Nagabhooshanam,⁶ Ram Subbiah,⁷ M. H. Siddique,⁸ and S. Praveen Kumar ⁹

¹Department of Mechanical Engineering, Vel Tech Rangarajan Dr. Sagunthala R&D Institute of Science and Technology, Chennai, Tamil Nadu, India

²Department of Mechanical Engineering, KLN College of Engineering, Pottapalayam, 630612 Tamil Nadu, India

³Mechanical Engineering Department, College of Engineering, King Saud University, P.O. Box 800, Al-Riyadh 11421, Saudi Arabia

⁴Department of Mechanical Engineering, N.M.A.M Institute of Technology (Affiliated to Nitte Deemed to be University) Nitte, Karnataka 574110, India

⁵Department of Mechanical Engineering, JSS Science & Technology University, Mysuru, Karnataka 570006, India

⁶Department of Mechanical Engineering, Aditya Engineering College, ADB Road, Aditya Nagar, Surampalem 533437, Andhra Pradesh, India

⁷Department of Mechanical Engineering, Gokaraju Rangaraju Institute of Engineering and Technology, Hyderabad, Telangana 500090, India

⁸Department of Mechanical Engineering, Kyungpook University, Republic of Korea

⁹Department of Mechanical Engineering, Arba Minch Institute of Technology (AMIT), Arba Minch University, Ethiopia

Correspondence should be addressed to S. Praveen Kumar; praveen.kumar@amu.edu.et

Received 11 May 2022; Revised 9 July 2022; Accepted 19 July 2022; Published 24 August 2022

Academic Editor: Arpita Roy

Copyright © 2022 K. Logesh et al. This is an open access article distributed under the Creative Commons Attribution License, which permits unrestricted use, distribution, and reproduction in any medium, provided the original work is properly cited.

The manufacture and investigation of the characteristics of nanocomposites with nanoparticles are made by the sol-gel technique. It comprises two substances (aluminium oxide-silicon oxide), as well as the influence of such particles on the mechanical characteristics of a polymeric matrix is described in this study. Tensile, bending, and hardness tests were utilized to assess the mechanical characteristics of the hybrid material. The evaluation results of composite nanoparticles revealed a clear dispersion of chemical components among aluminium oxide and calcium oxide, softness in particulate matter during crystallization at high and low temperatures, the initiation of various nanostructures forms, and distinct stages of an alumina particle. When compared to a polymeric mix without nanoparticle inclusion, mechanical behaviour tests demonstrated a considerable improvement in the mechanical capabilities of the nanocomposites, notably at 2%. Mechanical parameters such as tensile strength are 61.36 MPa, flexural strength is 74.25 MPa, and hardness is 83.27 D at 2.5 wt% at 600°C heat treatment conditions. Under 900°C heat treatment conditions, tensile properties of 54.12 MPa at 1 wt. percent, flexural properties of 79.21 MPa at 2 wt. percent, and shore hardness of 81.21 D at 2.5 wt. percent of nanoparticles were measured.

1. Introduction

Nanotechnology is a large and comprehensive scientific discipline that has exploded in popularity in current decades, and nanoparticles are the foundation of nanotechnologies. Nanostructures are advanced inorganic materials that are gaining professional curiosity due to their remarkable qualities when compared to other types of substances [1]. Nano-

composite particles are made up of two separate materials consolidated into a single hybridized particle, resulting in a multifaceted substance that may be employed in a variety of sectors, such as pharmaceuticals, electronics, and manufacturing, or to improve existing features [2]. As a result, interest in this type of material has grown, as have the tactics employed to make it [3]. Natural fibre may be utilized to make nanostructures, while tapioca plant films could

be employed in a spectrum of uses, including packing and reinforcing materials. Commercial resources could be used to make nanomaterials, with the characteristics of the site of the particles regulated. Nanoparticles can be created using a variety of techniques, including mechanical, physiological, and biochemical methods [4]. Chemical treatments are the most common among the approaches utilized since they produce results quickly and in a short amount of time. Clogging, dispersal, and sol-gel are some of the mechanisms used in biochemical procedures [5]. In comparison to other procedures, the sol-gel technique is a must-have approach since it ensures particle uniformity, cleanliness, and fineness [6]. Basic processes in this approach involve dissolving the raw material (nitro, hydroxides, or salts) in a suitable dissolvent, encouraging particle precipitation to produce the gels, and lastly, using the heating process (dryness and carbonization) to make the powder. Only well-suited substances utilized to make nanostructures are patrolled [7]. The sol-gel technique has the following benefits: (i) improved bonding between both the material and the protective coating; (ii) components can be moulded into complicated geometrical patterns; (iii) high-purity materials can be obtained due to earthenware sulphide precursor chemicals disintegrating inside the alcoholic solution for such sol-gel transition; (iv) low process temperature levels; simple, economical; even with no special or expensive equipment; and (v) a successful mechanism to deliver superior adhesives [8]. The blending of polymers has resulted in the production of a modern trend of polymer materials at low densities, low cost, better resistance to corrosion, and strong performance characteristics while keeping the molecule's original properties. The most notable such polymers are epoxy and polyester, which have been the subject of several studies and are differentiated by a wide range of characteristics that may be used for a variety of technological, manufacturing, and medicinal purposes [9]. Different materials, like granules, fibres, or sheets, can be used to reinforce epoxy and polyester polymer. Nanomaterials are one of the most significant materials used to improve biodegradable polymers as they provide stability, strength, and distinctive and great capabilities to reinforce the polymer structure. Various researches on the fabrication of polymer matrix nanocomposites from organic and inorganic materials have been done. They [10] investigated the mechanical characteristics of polyester-epoxy-treated bamboo fibre mix biocomposites, as well as the influence of nanoclay minerals on those parameters. When the microclay mineral ratio was increased to 10% by weight, all dynamic qualities improved, but after that, the characteristics began to deteriorate. Sugar palm fibre was handled by researchers [11] to produce sugar palm nanocrystals viscose. The researchers created biological nanomaterials in the form of thin films. In comparison to the clean film, it had greater crystalline nature, elastic modulus, mechanical characteristics, thermodynamics, and moisture resistance. The study demonstrated that after being strengthened with sugar palm nanocrystals viscose, the bio-nanocomposites' tensile modulus and deformability rose, and the optimal filler particle level was 0.5 percent. Sugarcane bagasse nanocrystal viscose nanomaterials were developed and employed as a renewable



FIGURE 1: Photographic image of nanoparticles.



FIGURE 2: Setup for tensile testing.

reinforcing phase to enhance the water moisture barrier characteristics of sugarcane bagasse carbohydrate film. [12]. In comparison to sugarcane bagasse and nanomixed sugarcane bagasse bio-nanocomposites, the sugarcane bagasse deteriorated quicker in the bioremediation test. To increase the water resistance qualities of sugarcane bagasse carbohydrate film, nanomaterials are being manufactured and used as disposable reinforcement materials. This work [13] studied the influence of Tungsten Carbide on the epoxy resin, finding the mechanical qualities and fracture toughness. To reinforce the polyester material, [14] employed ferric oxide and blended ferric oxide nanoparticles produced by a chemical decomposition method. When compared to polyester augmented with nanoclusters, the results revealed that the polyester reinforced with f-Fe₂O₃ nanoparticles had better mechanical characteristics. Author [15] investigated the impact of introducing graphene powders to an epoxy-polyester mix as a reinforcing factor. The results demonstrated a significant improvement in mechanical characteristics, particularly at 0.2 percent. Researchers [16] investigated the thermal characteristics of an epoxy-polyester mix with nanoclay as a reinforcing material, finding that increasing the nanoclay content to 5% resulted in enhanced heat breakdown and

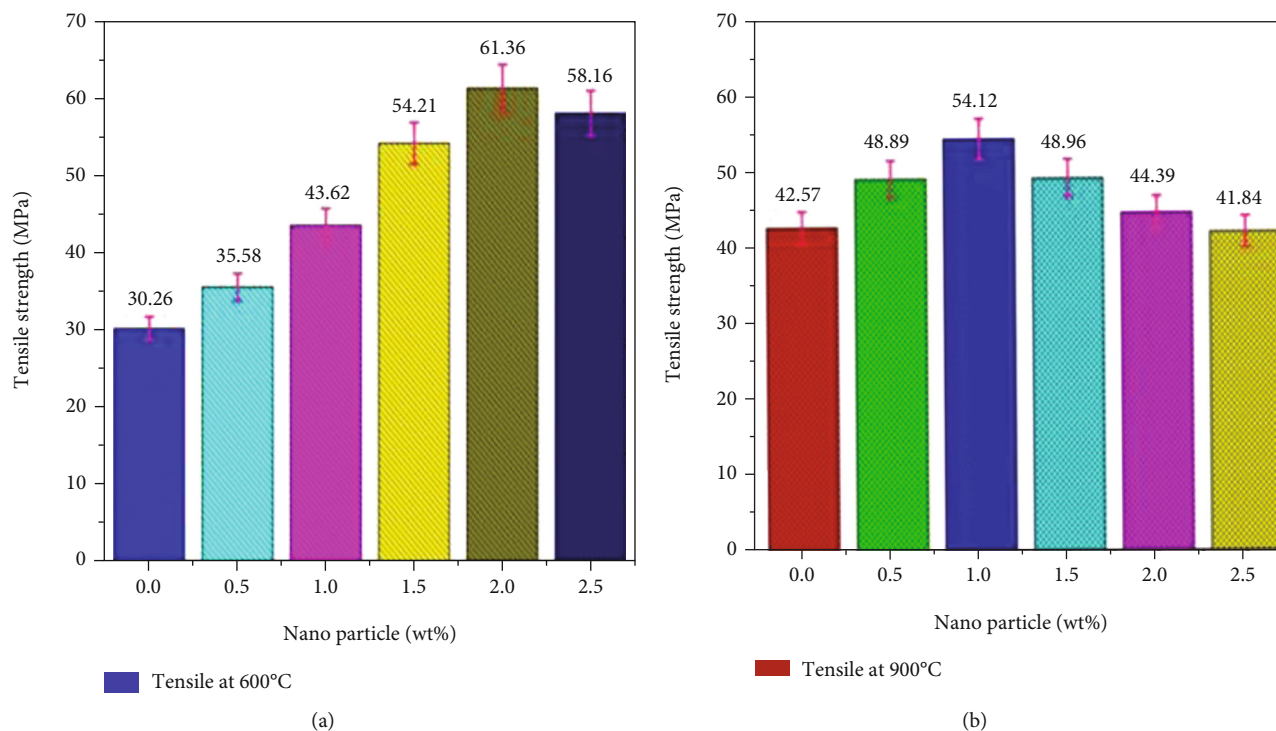


FIGURE 3: Tensile strength of blended polymer-based nanoparticle (Al_2O_3 and Si_2O_3) with heat treatment (a) 600°C and (b) 900°C .

weight loss. Thermal characteristics, on either hand, were enhanced when the glass transition temperature was increased by 4 wt%. It has been discovered in earlier studies that researchers researched the production of nanomaterials from different chemicals. However, researchers did not investigate the production of composite nanostructures and their impacts on the matrix substance's characteristics, particularly the mechanical capabilities. Furthermore, no reference was made to the influence of such nanoparticles on the characteristics of the polymeric mix. As a result, the goal of this research is to complete this assignment using nanomaterials (aluminium oxide and silicon oxide) and describe how they affect the properties of a polymer mixture, and to use a polymeric mixture (4% of epoxy and 96% of polyester) to fabricate the hybridized materials.

2. Experimental Works

2.1. Materials. The GVR chemical plant in Madurai, Tamil Nadu, India, provided the pure epoxy resin and hardeners used in this investigation. The polymer mix is made up of polyester resin, hardener, and accelerators such as methyl ethyl ketone peroxide and cobalt naphthanate, all of which are provided by the same company. The nanocomposite particles were made from aluminium and silicon nitrate nonahydrate from Naga chemicals in Chennai, Tamil Nadu, India, which had a quality of 99 percent. Figure 1 shows the photographic images of aluminium- and silicon-based nanoparticles.

2.2. Nanoparticle and Its Composite Preparation. To make the nano-based particles, both the aluminium nitrate nona-

hydrate and silicon nitrate were disintegrated in 100 ml of distilled water with constant blending on a heating plate mixer at 60°C till the granules disintegrated, then the disintegrated additives for both kinds were taken in a conical flask and mixed up to 3 hours at 60°C . After that, a 2% detergent solution was injected, followed by droplets of ammonia solution incorporated by constant stirring to build stickiness until gel was produced. The prepared solution was then cleaned through strainer material to remove the gels, which had been heated at 80°C for 6 hours. Pasteurization at 600°C and 900°C for 2 hours is the final phase. The polymer blend was then prepared in order to create composite materials. A mechanical mixer was used to combine a specific proportion of each ingredient (4 percent epoxy, 96 percent polyester), as well as bonding agent, catalysts, accelerators, and promoters with ratio of 2:2:2:2. The produced nanoparticles were then placed at 0, 0.5, 1, 1.5, 2, and 2.5 wt percent in the motorized blender and stirred. The slurry was then placed into a mould and cut as per ASTM standards following solidification and curing. To get an appropriate readout, three specimens were produced for every mixture [17].

2.3. Mechanical Testing. The properties of the different nanostructures were evaluated employing tensile and bending tests performed on a universal testing machine as in Figure 2 with a capacity load of 50 kN, with specimens prepared and executed as per ASTM D 638, flexing samples executed as per ASTM D 790, and shore D hardness samples executed as per ASTM D 2240.

2.4. Fractographic Analysis. SEM was utilized to conduct microscopic (Fractographic) investigations into fractured

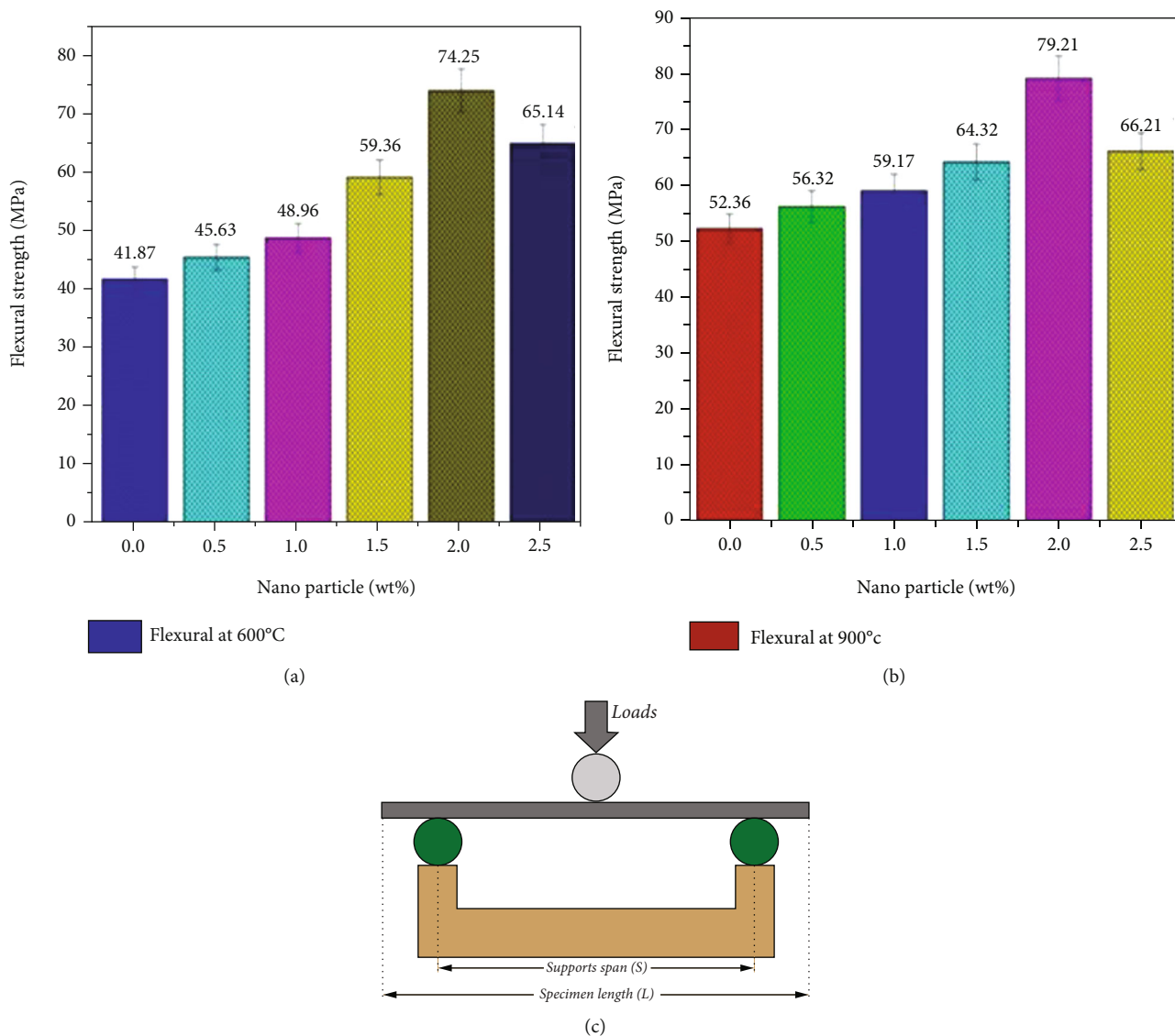


FIGURE 4: Flexural strength of blended polymer-based nanoparticle (Al_2O_3 and Si_2O_3) with heat treatment (a) 600°C and (b) 900°C; (c) flexural strength setup by pictorial view.

composite samples. The specimens were laved, dehydrated, and surface coated with 10 nm of gold before SEM clarity to increase the composites' electrical conductivity.

3. Result and Discussion

3.1. Mechanical Properties of Polymer Blend Matrix

3.1.1. Tensile Behaviour. The most important mechanical test is the tensile test. This test involves applying a slog force to a substance and measuring how it reacts to strain. The tension test assesses the material's strength and its ability to expand in so doing. The tension performance in Figure 3(a) shows the effects of introducing composite nanomaterials (aluminium and silicon oxide) at different rates into a polymeric matrix (4 percent epoxy, 96 percent polyester) after heat treatments at 600°C. The results show that the relationship between elongation behaviour and the quantity

of particle supplied is proportionate. That indicates that when the amount of powder in the nanocomposite increased, the maximum tensile strength increased as well. This means that the nanoscale particle has a greater surface area, which boosts the foundation substance's soaking capacity and offers greater coverage for the nanoparticle's interface, as well as enhances the toughness of the nanoparticle-base materials contact. Figure 3(b) depicts the tensile behaviour of nanoparticles added to a polymer blend (4 percent epoxy and 96% polyester) after thermal treatment at 900°C. The highest stress resistance of the nanocomposite increased as the proportion of powder increased, although not as much as the findings of the nanopowder generated at 600°C. The dispersal efficiency and adhesive intensity of the nanoparticles with the polymer matrices are responsible for the increase in mechanical characteristics [14]. As a result, the mechanical characteristics of the material deteriorate. A decline in characteristics is caused by the diversity

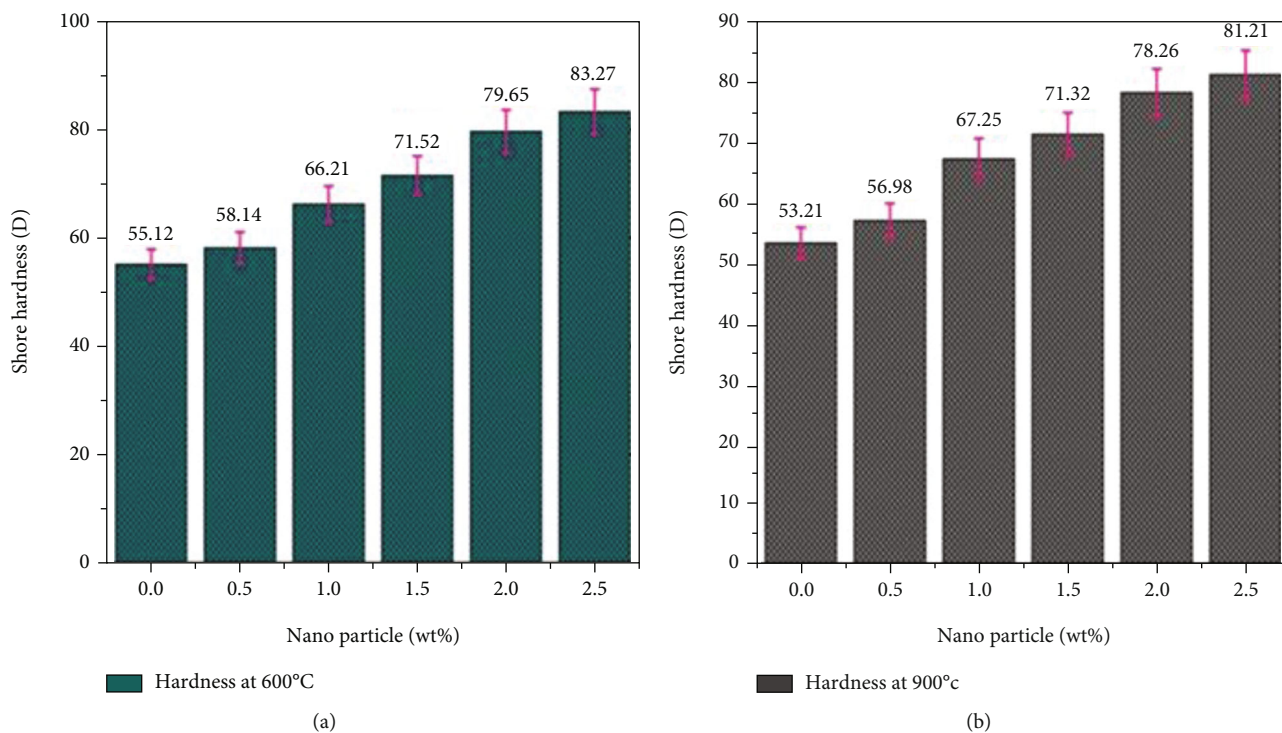


FIGURE 5: Shore hardness of blended polymer-based nanoparticle (Al_2O_3 and Si_2O_3) with heat treatment (a) 600°C and (b) 900°C .

and dispersal of the aggregation of nanoparticles inside the matrix phase.

3.1.2. Flexural Properties. The degree of flexural strength an item can tolerate prior to fracturing or warping is known as flexural strength. The resulting nanopolymerized material, as shown in Figures 4(a) and 4(b), demonstrates that increasing the percentage of nanopowder results in an improvement in flexuralconfrontation levels. It demonstrates that the mixed nanoparticles offer resistance and strength to the polymeric mixtures, as well as making the support material more robust to external loads. SEM further reveals that the smoothness has resulted in a huge surface area. In addition, the irregular form of the composite nanoparticles created at 600°C and 900°C , as seen in SEM, increases the strength of the nanoparticle-base substance contact. The disparity in particle diameter between the nanoscale powders and the aggregation acts as maximum stress centres, which reflect intrinsic faults in the composite material, resulting in a fall in bending resistance values [18]. As a result, we detect a change in resistance. Excessive reinforcement reduces the wet capability of a raw product, resulting in flaws including micro and nanofractures inside the composite, as well as impairment of mechanical qualities [13]. The pictorial representation of flexural strength machine is displayed in Figure 4(c).

3.1.3. Hardness Behaviour. Hardness testing is an important part of many quality control processes. It allows us to evaluate a material's qualities and determine if a substance or material treatment is appropriate and applicable for the task at hand. The hardness testing results after adding nanopow-

der (aluminium and silicon oxide) generated at 600°C and 900°C to the polymer mixture (4 percent epoxy and 96 percent polyester) with varying weight proportions are shown in Figures 5(a) and 5(b). The hardness values of the polymeric matrix have increased. This implies that composite nanomaterials have a high surface area and thus have a good resistance to scratches, which serves to improve the soaking capability of the ground material as well as the toughness of the interaction between both the nanomaterials and the ground plane [6, 19]. The low proportion of imperfections in the nanocomposites, such as microscopic and nanocracks, enhances the mechanical characteristics [17]. The modest discrepancy in hardness values, as seen in, is attributable to the particulate difference in size inside the powders.

4. Fractographic Study

SEM was used to evaluate specimen surface features at very high resolution using a part of an apparatus known as a digital microscope. The beam of electrons concentrates on the sampling site during the SEM test, causing energy to be transferred to the spot and subsequently translated into a result. In this work, the morphology and histologic features of the composite nanopowders created by the sol-gel technique were studied using scanning electron microscopy. Figure 6(a) shows a different magnification image of composite oxide nanoparticles (aluminium and silicon) generated under the same conditions and carbonization at 600°C . As illustrated, particle dispersion and saturation are concentrated in particular sections of nanoparticles, which aids in the cluster formation among big particles. Figure 6(b) depicts a significant magnification resolution of the composite

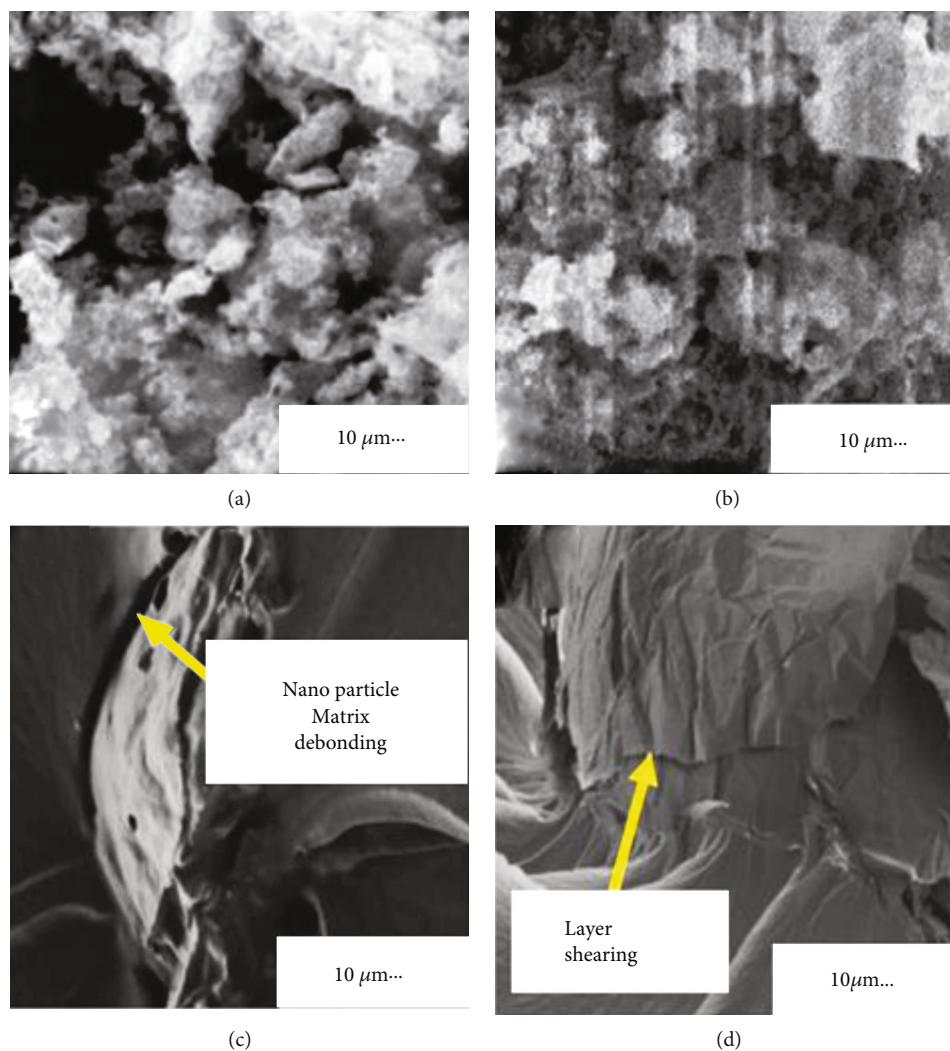


FIGURE 6: SEM image of composite nanoparticle (Al_2O_3 and Si_2O_3) with heat treatment (a) 600°C and (b) 900°C ; (c) failure in tension; (d) failure in flexural.

nanopowder (aluminium and silicon) oxide heated at 80°C for 6 hours and calcined at 900°C for 2 hours. The irregular structure of the nanoparticles aided in the formation of certain particle groupings. Also, due to the various geometric developments of the particles, the resultant particles' shapes are uneven. Figures 6(c) and 6(d) show the nanoparticle matrix failure during mechanical testing. Those figures proved that the brittle failure occurred due to the oxide formation was higher in the particular failed region.

5. Conclusion

- (i) SEM examination of the composite nanoparticles indicated an uneven shape and a homogeneous chemical composition of aluminium oxide and silicon with no impurities. Furthermore, the studies demonstrated that particle smoothness is temperature dependent. Heat treatment at 600 degrees Celsius generated finer and more phases than heat treatment at 900 degrees Celsius. In mechanical tests, the quality of the polymer mix augmented with composite nanoparticles

increased dramatically. According to the mechanical assessment findings, the best qualities were obtained by reinforcing with nanocomposite powder at a concentration of 2 wt%. Mechanical parameters such as tensile strength are 61.36 MPa, flexural strength is 74.25 MPa, and hardness is 83.27 D at 2.5 wt% at 600°C heat treatment conditions

- (ii) Under 900°C heat treatment conditions, tensile properties of 54.12 MPa at 1 wt. percent, flexural properties of 79.21 MPa at 2 wt. percent, and shore hardness of 81.21 D at 2.5 wt. percent of nanoparticles were measured
- (iii) The GRA will be implemented to carry out the optimal parameters to future work

Data Availability

The data used to support the findings of this study are included within the article. Further data or information is available from the corresponding author upon request.

Conflicts of Interest

The authors declare that there are no conflicts of interest regarding the publication of this paper.

Acknowledgments

The authors appreciate the supports from Arba Minch University, Ethiopia, for the research and preparation of the manuscript. The authors thank Vel Tech Rangarajan Dr. Sagunthala R&D Institute of Science and Technology, N.M.A.M Institute of Technology, JSS Science & Technology University, and Rajalakshmi Engineering College for providing assistance to complete this work. The authors would like to acknowledge the Researchers Supporting Project number (RSP-2021/373), King Saud University, Riyadh, Saudi Arabia.

References

- [1] R. Ganesh, P. Anand, and W. D. Mammo, "Experimental investigation on thermal behaviors of nanosilicon carbide/kenaf/polymer composite," *Journal of Nanomaterials*, vol. 2022, Article ID 3906336, 2022.
- [2] S. Sanjeevi, V. Shanmugam, S. Kumar et al., "Effects of water absorption on the mechanical properties of hybrid natural fibre/phenol formaldehyde composites," *Scientific Reports*, vol. 11, no. 1, pp. 13311–13385, 2021.
- [3] P. Khalili, K. Y. Tshai, D. Hui, and I. Kong, "Synergistic of ammonium polyphosphate and alumina trihydrate as fire retardants for natural fiber reinforced epoxy composite," *Composites. Part B, Engineering*, vol. 114, pp. 101–110, 2017.
- [4] M. Vovk and M. Šernek, "Aluminium trihydrate-filled poly(methyl methacrylate) (PMMA/ATH) waste powder utilization in wood-plastic composite boards bonded by MUF resin," *BioResources*, vol. 15, no. 2, pp. 3252–3269, 2020.
- [5] S. A. Hallad, N. R. Banapurmath, V. Patil et al., "Graphene reinforced natural fiber nanocomposites for structural applications," *IOP Conference Series: Materials Science and Engineering*, vol. 376, p. 12072, 2018.
- [6] F. Perreault, A. Fonseca De Faria, and M. Elimelech, "Environmental applications of graphene-based nanomaterials," *Chemical Society Reviews*, vol. 44, no. 16, pp. 5861–5896, 2015.
- [7] G. Seshanandan, D. Ravindran, and T. Sornakumar, "Mechanical properties of nano titanium oxide particles - hybrid jute-glass FRP composites," *Materials Today: Proceedings*, vol. 3, no. 6, pp. 1383–1388, 2016.
- [8] J. Datta, P. Kosiorek, and M. Włoch, "Effect of high loading of titanium dioxide particles on the morphology, mechanical and thermo-mechanical properties of the natural rubber-based composites," *Iranian Polymer Journal*, vol. 25, no. 12, pp. 1021–1035, 2016.
- [9] R. P. Singh and P. Aggarwal, "Effect of nanosilica on the properties of cement mortar," *Cem. Int.*, vol. 13, pp. 65–70, 2015.
- [10] S. Panda and D. Behera, "Effect of red mud on mechanical and chemical properties of unsaturated polyester-epoxy-bamboo fiber composites," *Materials Today: Proceedings*, vol. 4, no. 2, pp. 3325–3333, 2017.
- [11] R. A. Ilyas, S. M. Sapuan, M. R. Ishak, and E. S. Zainudin, "Effect of delignification on the physical, thermal, chemical, and structural properties of sugar palm fibre," *BioResources*, vol. 12, no. 4, pp. 8734–8754, 2017.
- [12] R. A. Ilyas, S. M. Sapuan, M. S. N. Atikah et al., "Effect of hydrolysis time on the morphological, physical, chemical, and thermal behavior of sugar palm nanocrystalline cellulose (*Arenga pinnata* (Wurmb.) Merr)," *Textile Research Journal*, vol. 91, no. 1-2, pp. 152–167, 2021.
- [13] A. Sreenivasulu, S. Rajkumar, S. Sathyanarayana, G. V. Gaurav, and B. D. I. Premkumar, "Impact of nano-filler WC on the fracture strength of epoxy resin," *Materials Today: Proceedings*, vol. 59, no. 2, pp. 1420–1424, 2022.
- [14] G. N. Kumar, Y. V. M. Reddy, and K. H. Reddy, "Synthesis and characterization of iron oxide nanoparticles reinforced polyester/nanocomposites," *International Journal of Scientific and Research Publications*, vol. 52, pp. 39–52, 2015.
- [15] M. T. Le and S. C. Huang, "Thermal and mechanical behavior of hybrid polymer nanocomposite reinforced with graphene nanoplatelets," *Materials (Basel)*, vol. 8, no. 8, pp. 5526–5536, 2015.
- [16] M. A. Kumar, "Thermal analysis of epoxy/polyester blend filled with montmorillonite (MMT) clay–nanocomposite," *Int J Eng Res Ind Appl*, vol. 4, pp. 123–132, 2016.
- [17] H. A. Sallal, A. A. Abdul-Hamead, and F. M. Othman, "Effect of nano powder (Al₂O₃-CaO) addition on the mechanical properties of the polymer blend matrix composite," *Defence Technology*, vol. 16, no. 2, pp. 425–431, 2020.
- [18] A. Atiqah, M. N. M. Ansari, M. S. S. Kamal, A. Jalar, N. N. Afeefah, and N. Ismail, "Effect of alumina trihydrate as additive on the mechanical properties of kenaf/polyester composite for plastic encapsulated electronic packaging application," *Journal of Materials Research and Technology*, vol. 9, no. 6, pp. 12899–12906, 2020.
- [19] F. Sarker, P. Potluri, S. Afroj, V. Koncherry, K. S. Novoselov, and N. Karim, "Ultra-high performance of nanoengineered graphene-based natural jute fiber composites," *ACS Applied Materials & Interfaces*, vol. 11, no. 23, pp. 21166–21176, 2019.

Research Article

Reduction and Heavy Metal Stabilization of River Sediment by Hydrothermal Treatment

Suyang Sun ¹, Tinggan Fang,¹ Gang Xue ¹, Yueling He,¹ Xiaonuan Wang,¹ Qi Song,¹ Xueke Zang,² Yiwei Wang,³ and Shanshan Zheng⁴

¹College of Environmental Science and Engineering, Donghua University, Shanghai 201620, China

²Shanghai Yaxin Urban Construction Co., Ltd., Shanghai 200436, China

³Jing'an District River Water Management Offices, Shanghai 200072, China

⁴Shanghai Triumph Energy Conservation Engineering Co., Ltd., Shanghai 200060, China

Correspondence should be addressed to Gang Xue; xuegang@dhu.edu.cn

Received 7 May 2022; Revised 1 August 2022; Accepted 2 August 2022; Published 22 August 2022

Academic Editor: H C Ananda Murthy

Copyright © 2022 Suyang Sun et al. This is an open access article distributed under the Creative Commons Attribution License, which permits unrestricted use, distribution, and reproduction in any medium, provided the original work is properly cited.

In this paper, hydrothermal treatment was used to treat river sediment. The physicochemical properties, chemical speciation, bioavailability, ecotoxicity, and leaching toxicity of heavy metals (Zn, Cu, Cr, Cd, Ni, Pb) in sediment under different hydrothermal treatment conditions were studied, and stabilization mechanisms of heavy metals were explained. The results showed that hydrothermal temperature and time had a huge impact on sediment reduction and heavy metal stabilization. The best reduction and stabilization of sediments were achieved at a hydrothermal temperature of 260°C and a hydrothermal period of 3 h. The hydrothermal treatment caused the sediment to undergo dehydration, dihydroxylation, decarboxylation, deamination, and aromatization with a gradual decrease in its H/C ratio, O/C ratio, and pH; a gradual increase in porosity and surface area; and a decrease in particle size. This facilitates the dehydration, reduction, and stabilization of the sediment. The bioavailable components of heavy metals in sediment were dramatically reduced following hydrothermal treatment, but the fraction of stable components rose significantly. This resulted in a marked decrease in the environmental bioavailability, ecotoxicity, and leaching toxicity of the heavy metals. Therefore, hydrothermal treatment might be an effective *ex situ* repairment way for reducing, stabilizing, and making river sediment harmless.

1. Introduction

Over the years, large volumes of industrial wastewater, domestic sewage, and agriculture-related sewage have been discharged into rivers [1, 2]. The pollutants in river water will be deposited into the sediment, making the sediment a “breeding ground” for water pollution. Meanwhile, sediments are also the “source” of pollution released to the overlying water [3]. It was reported that the release of nitrogen, phosphorus, and polycyclic aromatic hydrocarbons by river sediment will lead to eutrophication, and the presence of highly biotoxic heavy metals such as Zn, Cu, Cr, Cd, Ni, and Pb in river sediments will pose considerable toxicity threats to the ecosystem and human health when they migrate to water and soil [4, 5]. Therefore, there is an urgent need for the safe disposal of river sediments.

Current methods for the disposal of sediment include sediment dredging, acid washing, and chemical stabilization [6]. Sediment dredging is the most common practice in river sediment treatment, but it needs a very large land area to enable sediment filling. The river sediments are mainly composed of inorganic components with low calorific values that cannot be incinerated, which makes the disposal of the dredged sediment difficult [7]. Acid washing refers to technologies that use various acids to extract and precipitate the metals in the sediment [8]. Due to the complexity of the sediment components, the extract and precipitate reactions will always be complex and hard to regulate. In addition, the resulting secondary leachate is a hazardous waste and should be further disposed of. Chemical stabilization of heavy metals in sediments is primarily achieved by adding immobilizers and stabilizers, but there is still a chance that

the agents may fail and be released into the water column, reducing the stability effect [9].

Hydrothermal methods are chemical reactions carried out in a closed vessel with subcritical water as the solvent at a high temperature and pressure [10]. Hydrothermal heat can promote the dissolution of the dry sludge base, improve the dewatering properties of the sludge, and achieve sludge reduction [11]. In this process, pathogens and parasites can be killed, which will result in stabilization during the hydrothermal process [12]. Hydrothermal treatment can also change the morphology of heavy metals in sludge and promote their transformation from unstable to stable, thereby achieving stabilization and harmlessness of heavy metals in sludge. Many studies on the hydrothermal stabilization of heavy metals have been carried out by researchers. Huang et al. examined the danger of heavy metals in sludge after hydrothermal treatment to the environment, and the findings revealed [13] that the leaching rate of heavy metals in sludge was significantly reduced, as was the ecotoxicity. Shi looked into the movement of heavy metals in sludge after hydrothermal treatment and found [14] that the state of heavy metals such as Ni, Cr, Zn, Cu, Cd, and Pb in sludge changed from weakly bound to stable, and their ecological risk was greatly reduced. Li et al. [15] used subcritical water and supercritical water to gasify sludge and found that the bioavailability and ecotoxicity of heavy metals in the treated sludge were significantly reduced. In particular, the bioavailable content of Cu decreased by nearly 97%. Liu et al. [16] studied the distribution of heavy metals in the hydrothermal carbonization process of sewage sludge and found that hydrothermal treatment reduced the exchangeability/acid solubility and reduced states of heavy metals in the sludge, thus reducing the potential risk of heavy metals in the sludge. Those studies indicate that hydrothermal methods can significantly reduce the ecological risk of sludge land use [17]. At present, the research on hydrothermal technology mainly focuses on excess sludge, etc., and there are few reports of applying it to the treatment of river sediment. They have a great theoretical basis for the treatment of river sediments. The nature of river sediment is different from that of sludge, and it is of interest to further investigate the reducibility of hydrothermally treated river sediments, the stabilizing impact of heavy metals, and the associated mechanisms.

The goal of this research was to reveal the mechanisms of reduction of river sediments by an *ex situ* repairment way which is hydrothermal treatment and evaluate the bioavailability of heavy metals in river sediments after hydrothermal treatment. The effect of hydrothermal treatment on the physicochemical properties of river sediments was studied. Potential ecological risk indicators, environmental risk assessment indicators, and leaching toxicity are identified based on the chemical morphological distribution of heavy metals in the hydrothermal products. Besides, the behavior of heavy metals during hydrothermal treatment, as well as their migration and stabilization mechanisms, was also explored.

2. Materials and Methods

2.1. Experimental Materials. The river sediments utilized in the experiments came from a river in a district of Shanghai.

The dredged river sediment is stirred evenly and screened through 20 mesh screens to remove large stones, gravel, plant debris, and shellfish from the sediment. The sediment was collected in a refrigerator at a temperature of 4°C before being further processed and analyzed. The physicochemical characteristics of the river sediments were analyzed following centrifugation and freeze-drying prior to hydrothermal treatment.

2.2. Hydrothermal Experiment. The following steps were used to conduct hydrothermal experiments in this study: 60 g of river sediment (with around 85% moisture content) was placed into a YZHR 100 ml hydrothermal reaction kettle, and then, the sediment was heated to 180°C, 200°C, 220°C, 240°C, 260°C, and 280°C. After reaching the desired temperature, it was kept at 0.5 h, 1.5 h, 3 h, 4.5 h, 6 h, and 7.5 h. After the hydrothermal kettle cooled naturally to ambient temperature, the reactor was opened, the solid-liquid mixture was withdrawn for extraction, and the filtered solid-liquid combination was collected. The precipitated hydrothermal solid product was heated in an oven at 105°C for 12 hours before being placed in dry glassware for standby. The hydrolysate was put in a refrigerator below 4°C for standby. The original precipitate was denoted by RS, and the filtrate of the original precipitate was denoted by RL. The solid product after hydrothermal treatment was represented by HS, and “HS-Hydrothermal Temperature-Hydrothermal Time” represented the hydrothermal solid product of sediment under different conditions. The hydrolysate was denoted by HL, “HL-Hydrothermal Temperature-Hydrothermal Time,” representing the hydrolysate under different conditions. For instance, HS-180-3 represented the hydrothermal solid product of sediment obtained after hydrothermal treatment at 180°C for 3 h, while HL-180-3 represented the hydrolysate obtained by hydrothermal treatment of sediment at 180°C for 3 h.

2.3. Sample Processing and Analysis. An elemental analyzer (Elementar, Germany) was developed to analyze and determine the elemental (C, H, and N) content of the raw sediment and hydrothermal solid products. The ash content in the raw sediment and sediment hydrothermal solid products was determined by burning the sediment in a muffle furnace at 600°C. The elemental content of O was measured by the difference method [18], namely: $O\% = 100\% - C\% - H\% - N\% - \text{Ash}\%$. The chemical functional groups contained in the hydrothermal solid products of the original sediment and sediment were determined using a Nicolet 550 Fourier transform infrared spectrometer (Nicolet, USA). The specific surface area of the original sediment and the hydrothermal solid products of the sediment could be determined using the Brunauer-Emmett-Teller (BET) method. The surface morphology and structure of raw sediment and the hydrothermal solid products of the sediment were characterized by a scanning electron microscope (Zeiss Gemini SEM 300).

2.4. Determination Method of Organic Reduction Rate. The organic content of the original sediments was calculated as

follows:

$$m_3 = m_1 - m_2, \quad (1)$$

where m_1 is the mass of solid (S1) obtained after suction filtration dehydration and drying at 105°C, m_2 is the mass of solid (S1) burnt at 600°C in a muffle furnace to constant weight, and m_3 is the mass of organics contained in raw sediment.

The mass of organics in the hydrothermal solid product of the sediment was calculated as follows:

$$m_6 = m_4 - m_5, \quad (2)$$

where m_4 is the mass of solid (S2) obtained after suction filtration dehydration and drying at 105°C, m_5 is the mass of solid (S2) burnt at 600°C in a muffle furnace to constant weight, and m_6 is the mass of organics contained in raw sediment.

The organic reduction rate was calculated as follows:

$$\text{Organic reduction rate} = \frac{m_3 - m_6}{m_3} \times 100\%. \quad (3)$$

2.5. Analysis Method of Hydrothermal-Related Parameters. The chemical oxygen demand (COD) in the hydrolysate was determined analytically using the “dichromate method for determination of chemical oxygen demand in water quality” (HJ 828-2017). Inductively coupled plasma mass spectrometry (Thermo Scientific ICAP Q, USA) was used to assess the concentration of heavy metals and salt ions in the hydrolysate after it was filtered through a 0.45 μm membrane.

2.6. Analysis and Evaluation Methods of Heavy Metal

2.6.1. Determination of Total Amount and Form of Heavy Metals. Acid digestion [19] was used to determine the total amount of heavy metals Zn, Cu, Cr, Cd, Ni, and Pb in raw sediment and sediment hydrothermal solid products. The modified BCR four-step extraction method [20] was used to determine the forms of heavy metals Zn, Cu, Cr, Cd, Ni, and Pb in raw sediment and sediment hydrothermal solid products. Several procedures were used to continuously extract heavy metal components by the BCR method: exchangeable or acid-soluble components (T1), reducible components (T2), oxidizable components bound to organics and sulfides (T3), and residual components bound to the lattice (T4). Inductively coupled plasma mass spectrometry was used to determine the heavy metal content in the digestate.

2.6.2. Risk Evaluation Indicator. The environmental risks allied to heavy metals in the raw sediment and sediment hydrothermal solid products were evaluated by means of risk assessment codes (RAC), which are commonly utilized in the evaluation of heavy metal toxicity in the environmental sciences [21]. In this paper, the ratio of heavy metal content in exchangeable or acid soluble components (T1) to total heavy metals in primary sediments and sediment

hydrothermal solid products will be used as an evaluation indicator. The classification of the risk assessment indicator is as follows in Table 1.

2.6.3. Potential Ecological Risk Indicator. Potential ecological risk indicators (RI) [22] on the basis of heavy metal concentrations, toxicity, and sensitivity were utilized to study the potential ecological risk of heavy metal contamination in raw sediments and sediment hydrothermal solid products. The potential ecological risk indicator was calculated according to the following formulas.

$$\begin{aligned} C_f &= \frac{C_m}{C_n}, \\ E_r &= T_r \times C_f, \\ \text{RI} &= \sum E_r, \end{aligned} \quad (4)$$

where C_f is a single heavy metal pollution factor; C_m is the potential flow component of heavy metals (T1, T2, and T3); C_n is the stable component of heavy metals (T4); E_r is the potential ecological risk factor of a single heavy metal; T_r is the toxic reaction factor of a single heavy metal, of which Zn is 1, Cu and Pb are 5, Cr is 2, Cd is 30, and Ni is 6; and RI is the sum of potential ecological risk factors of pollutants.

The relationships between single heavy metal pollution factors, potential ecological risk factors, and potential ecological risk indicators with the degree of contamination are shown in Table 2.

2.6.4. Toxicity Leaching Test. The leaching concentrations of heavy metals in the sediments were measured according to the Toxicity Characteristic Leaching Procedure (TCLP) method of the US Environmental Protection Agency (EPA) [23]. A glacial acetic acid solution (pH = 2.88) was used as the leaching solution for the heavy metals, and a leaching experiment for the toxicity characterization of the raw sediment and sediment hydrothermal solid products was conducted on a leaching solution at a sample mass ratio of 20:1. The raw sediment and sediment hydrothermal solid products were mixed with the leaching solution and placed on an LCD CNC rotary mixer (MX RL Pro, Shanghai Shuangxu Electronics) and shaken at 30 r/min for 18 hours. At the end of the leaching procedure, the supernatant will be obtained by filtration. The content of heavy metals was evaluated using inductively coupled plasma mass spectrometry after passing through a 0.45 μm filter.

2.7. Data Analysis. To ensure the accuracy of the data obtained through the experiment, all data generated during the analysis processes was measured repeatedly three times to avoid random errors, which were plotted with mean and error bars in the graph.

3. Results and Discussion

3.1. Influence of Hydrothermal Treatment on Physicochemical Properties of Sediment. As demonstrated in

TABLE 1: Risk assessment code of heavy metals.

No.	Risk level	RAC = T1/total \times 100 (%)
1	Very high risk	>50
2	High risk	31~50
3	Medium risk	11~30
4	Low risk	1~10
5	No risk	<1

Figure 1(a), as the hydrothermal temperature increased, the rate of organic reduction in the sediment increased as well. The mass of organics in the sediment was reduced by 31.5% when the hydrothermal temperature reached 260°C, compared to prior hydrothermal treatment. This may be due to the fact that the increase in temperature intensified the reaction and destroyed the flocculent structure of the sediment. In the issue, macromolecular organics were released into the liquid phase and hydrolyzed to form small molecules, leading to a decrease in the mass of organics in the sediment. When the hydrothermal temperature was above 260°C, the change in the reduction rate of organic matter levelled off. The optimum hydrothermal temperature was 260°C. After hydrothermal treatment, most of the organics in the sediment would enter the liquid phase. The reduction of organics in sediment could be further confirmed by the change of COD in the hydrothermal solution.

Furthermore, it can be understood from Figure 1(a) that the COD in the hydrothermal solution increased as the temperature of the hydrothermal solution increased, and the trend was generally consistent with the organic matter reduction rate. As seen from Figure 1(b), the reduction ratio of organics in the sediment and the COD of the hydrothermal solution increased continuously as the hydrothermal time was extended. After 3 h of hydrothermal treatment, the mass of organics in the sediment decreased by 31.1% compared with that before hydrothermal treatment, while the COD in the hydrothermal phase of the sediment increased to 3093 mg/L. However, both changes levelled off when the time was further extended. This indicates that the hydrolysis of organics in the sediment has reached an equilibrium state and that the reduction is difficult to increase. Considering the energy consumption and cost, the optimal hydrothermal time was 3 h.

Table 3 shows the physicochemical properties of the sediment hydrothermal solid products obtained on the raw sediment and under different hydrothermal conditions.

As seen from Table 3, the proportions of C, H, ON, O/C, and H/C values in the hydrothermal solid products of the sediments continued to decrease with increasing hydrothermal temperature and time. This may be due to dehydration and decarboxylation during the hydrothermal reaction [24]. It exhibits high aromaticity and strong carbonation [25], which facilitates the dehydration reduction of the sediment.

Furthermore, the ash content in the hydrothermal solid products of the sediments showed an overall increasing trend as the hydrothermal temperature and time increased. This may be due to the hydrothermal heat causing the organic components in the sediment to be released into the

hydrothermal solution. It gave rise to a relative increase in the inorganic component content. Meanwhile, the pH of the sediment hydrothermal solid products decreased as the hydrothermal temperature and time increased [26].

3.2. Functional Group Changes of Raw Sediment and Hydrothermal Solid Products of Sediment. Figure 2 shows the infrared spectra of the raw sediment and sediment hydrothermal solid products under optimal hydrothermal conditions (260°C, 3 h).

In comparison to the raw sediment, the O-H stretching vibration absorption peaks for alcohols and phenols in the sediment hydrothermal solid products are at 3620 cm^{-1} . The N-H stretching vibration absorption peaks of amides and imines are at 3434 cm^{-1} , and the relative intensity of the O-H planar deformation vibration absorption peak for carboxylic acids at 1429 cm^{-1} is reduced. This suggests that the decomposition of carbohydrates (-OH), proteins (-NH), and fatty acids (-COOH) in the sediment is due to hydrothermal-induced material. Simultaneous decomposition of unstable substances in the sediment and dissolution into the liquid phase due to dehydroxylation, decarboxylation, and deamination of other organic substances made the sediment more stable [27].

After hydrothermal treatment, the peak at 2925 cm^{-1} and the relative intensity corresponding with the aliphatic CHn group (C-H stretching vibration) decreased, suggesting that the organic aliphatic structures in the sediment were broken down into gaseous compounds. For example, methane and carbon dioxide are converted into aromatic structures during hydrothermal treatment. The peak at 1635 cm^{-1} corresponds to the aromatic ring stretching (-CONH-) functional group, whose relative intensity decreases after hydrothermal treatment. The C-H out-of-plane deformation vibrational absorption peaks of aromatic hydrocarbons were slightly enhanced at 797 cm^{-1} and 776 cm^{-1} . It indicates that the hydrothermal treatment caused some organic matter (alkanes, cycloalkanes, and so on) in the sediments to undergo aromatization reactions to form aromatic hydrocarbons [28].

3.3. Morphological Characteristics of Raw Sediment and Sediment Hydrothermal Solid Products. Scanning electron micrographs of raw sediment and hydrothermal solid products of sediment under the optimum hydrothermal conditions (260°C, 3 h) are shown in Figure 3.

As shown in Figure 3, the surface structure of the original sediment is flat. After hydrothermal treatment, the sediments showed an increase in the porosity of the hydrothermal solid products and exhibited some degree of fragmentation, resulting in smaller particle sizes.

BET characterization was carried out on raw sediment and hydrothermal solid products of sediment, and the results are shown in Table 4. After hydrothermal treatment, the specific surface areas of sediment increased from 12.648 m^2/g to 32.616 m^2/g , the pore volume increased from 0.075 cc/g to 0.107 cc/g , and the pore diameter decreased from 3.820 nm to 1.936 nm, which is consistent with the observation results of SEM. The increase in pore volume

TABLE 2: The relation between C_f , E_r , RI, and pollution degree.

C_f	E_r	RI
$C_f \leq 1$	No risk	$E_r < 40$
$1 < C_f \leq 3$	Low risk	$40 \leq E_r < 80$
$3 < C_f \leq 6$	Medium risk	$80 \leq E_r < 160$
$6 < C_f \leq 9$	High risk	$160 \leq E_r < 320$
$C_f > 9$	Very high risk	$E_r \geq 320$

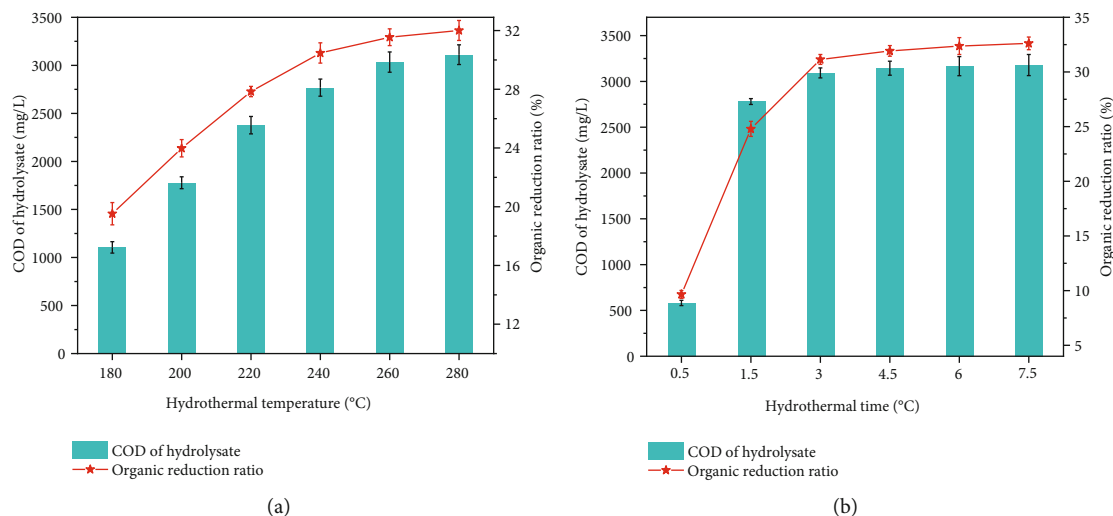


FIGURE 1: Influence of hydrothermal condition on organic reduction and COD of hydrolysate: (a) at 3 h of hydrothermal time, the hydrothermal temperatures were set at 180, 200, 220, 240, 260, and 280 °C; (b) at 260 °C of hydrothermal temperature, the hydrothermal times were set at 0.5, 1.5, 3, 4.5, 6, and 7.5 h.

TABLE 3: Properties of RS and HS.

Parameter	RS	HS-180-3	HS-220-3	HS-260-3	HS-260-0.5	HS-260-6
C%	3.25	2.69	2.37	2.33	3.16	2.32
H%	1.06	0.85	0.74	0.71	1	0.69
N%	0.15	0.08	0.07	0.06	0.12	0.06
O%	2.34	1.65	1.45	1.24	2.02	1.2
Ash%	92.2	93.73	94.37	94.66	92.7	94.73
O/C	0.54	0.46	0.46	0.4	0.48	0.39
H/C	3.91	3.79	3.75	3.66	3.8	3.57
pH	7.25	6.63	6.57	6.39	6.69	6.31

and specific surface area, as well as the decrease in pore diameter, facilitated the release of water from the sediments.

At the same time, the above changes are bound to cause the changes of sediment adsorption performance. Although some studies [29–31] have shown that titanate nanomaterials prepared by hydrothermal method can adsorb heavy metals from water, it remains to be further studied whether the hydrothermal products of the sediment prepared in this study can be used as nanoadsorbent materials.

3.4. Redistribution of Heavy Metals between Solid and Liquid Phases. At present, the traditional environmental risk assess-

ment methods are mainly based on the total concentration of heavy metals and are evaluated from the perspective of total quantity control. This index has always been the most basic basis for controlling the environmental risk of heavy metals [32]. The concentrations of heavy metals in the liquid-solid phase of the sediment before and after hydrothermal treatment are shown in Figure 4.

After hydrothermal treatment, a certain level of heavy metals in the sediment will be liberated or dissolved into the hydrolysate of the sediment, as shown in Figure 4(a). As for the amounts of heavy metals in the liquid phase of the sediment, they should not exceed 1% of the total amount

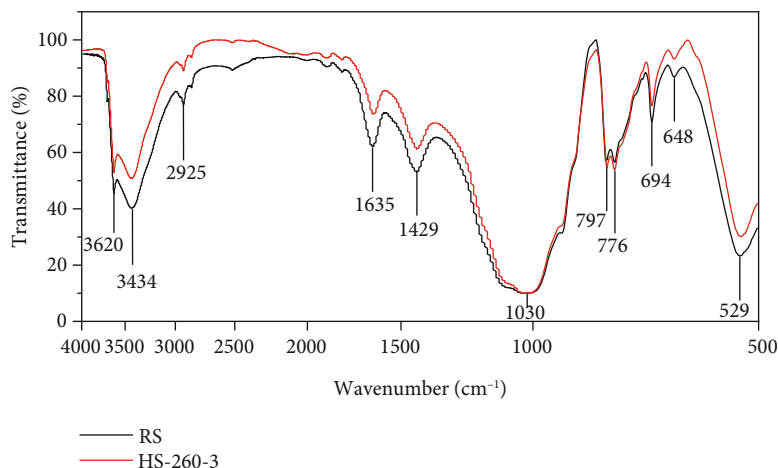


FIGURE 2: Fourier transform infrared (FTIR) spectra of RS and HS-260-3.

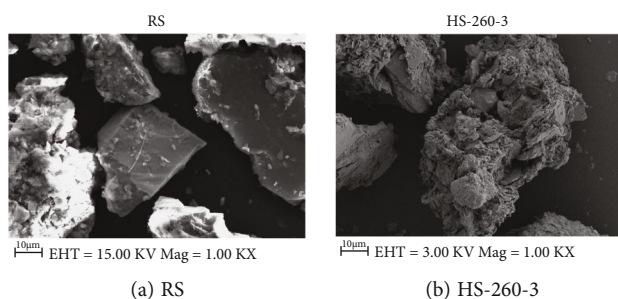


FIGURE 3: Scanning electron micrographs of RS and HS-260-3.

TABLE 4: BET of RS and HS-260-3.

Samples	Specific surface areas (m^2/g)	Pore volume (cc/g)	Pore diameter (nm)
RS	12.648	0.075	3.820
HS-260-3	32.616	0.107	1.936

of each heavy metal. The findings indicate that the hydrothermal treatment has some influence on the dissolving of the heavy metals in the sediment. This may be due to the fact that the hydrothermal treatment decomposes the organics in the sediment, thus releasing the combined heavy metals [33]. Nevertheless, the content of heavy metals entering the liquid phase through solid-liquid separation was very low, indicating that the hydrothermal method was difficult to effectively isolate the heavy metals from the sediment and the vast majority of the heavy metals remained in the solid phase.

As illustrated in Figure 4(b), the concentration of heavy metals in the hydrothermal solid phase of sediment increased as the hydrothermal temperature and time increased. On the one hand, the great majority of the heavy metals remained mainly in the solid phase of the sediment. On the other hand, the hydrolysis of organics during the hydrothermal treatment [21] led to an increase in the relative content of inorganic materials such as heavy metals, showing an enrichment and intensification effect. Nonetheless, whether this enrichment increases the potential risk of

heavy metals in the sediment needs to be further determined by changes in the chemical form of heavy metals.

3.5. Content Changes of Chemical Forms of Heavy Metals during Hydrothermal Treatment. The research results in recent years show that the environmental risk of heavy metals in sludge depends not only on the content of heavy metals in sludge but more importantly on the form of heavy metals in sediment [13, 34, 35]. The BCR extractable chemical form concentration of heavy metals in raw sediment and hydrothermal solid products of the sediment is shown in Figure 5.

As shown in Figure 5, most of the Zn in the sediment is exchangeable (T1: 47% and T2: 21%). After hydrothermal treatment, the proportion of heavy metals in the T1 form of Zn decreased significantly, and the proportion of heavy metals in the T3 and T4 forms increased significantly, reaching 41% and 25%, respectively. In contrast, the proportion of T2 heavy metals remained largely unchanged. This indicates that the morphology of Zn in the sediment changed from a

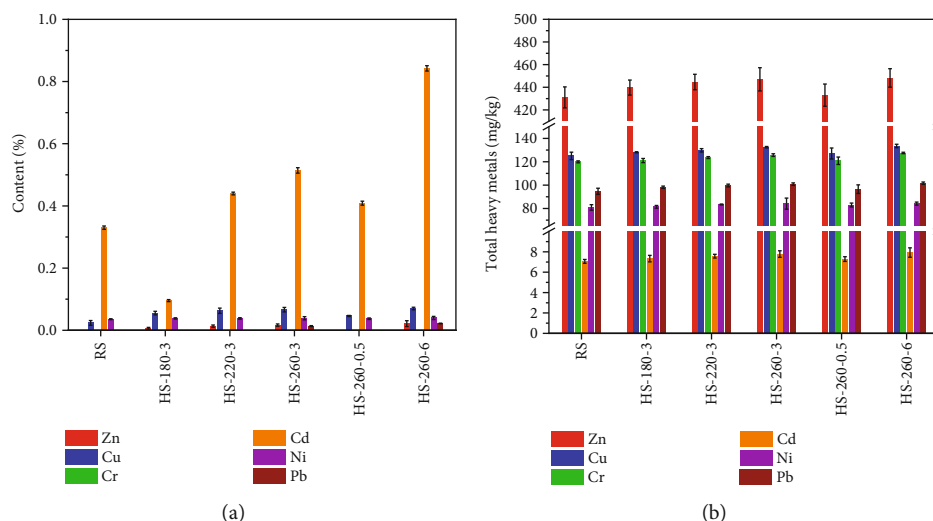


FIGURE 4: The redistribution of heavy metals between liquid phase (a) and solid phase (b) of sediment after hydrothermal treatment.

weakly bound condition to a rather stable state after hydrothermal treatment. The increase in hydrothermal temperature and time promoted the stability of Zn in the generated sediment hydrothermal solid products.

The highest proportion of Cu in the sediment was in the T3 form (47%), followed by T4 (31%). After hydrothermal treatment, Cu was transformed from the T1 form and T2 form into the T3 form and then fixed, with the proportion of heavy metals in T4 remaining largely unchanged. Therefore, as the hydrothermal temperature and duration rose, the fraction of stable components in the sediment grew dramatically, and the findings are consistent with earlier research. That is, Cu may be blind to stronger organic ligands and is contained in minerals with low bioavailability and mobility potential [36].

The proportion of heavy metals in the T1 form of Cr did not change significantly, whereas the proportion of heavy metals in the T3 form decreased somewhat, and the proportion of heavy metals in the T2 and T4 forms increased slightly. Although a rise in the proportion of heavy metals in the T2 form was harmful to the sediment's stability, the proportion of heavy metals in the T4 form increased substantially faster than the T2 form as hydrothermal temperature and duration increased. As a result, Cr is still stabilized by the hydrothermal treatment.

The proportion of heavy metals in the T1 form and T2 form of Cd decreased, so the proportion of heavy metals in the T3 form and T4 form increased significantly. Furthermore, after hydrothermal treatment, the status of Cd transformed from unstable to stable, and the higher the hydrothermal temperature and the longer the hydrothermal time, the more obvious the stabilization trend of Cd.

In terms of heavy metal Pb, the proportion of heavy metal in the T1 form, T2 form, and T3 form decreased significantly, and the proportion of heavy metal in the T4 form increased significantly, reaching about 43%. At the same time, the higher the hydrothermal temperature and the longer the hydrothermal time, the greater the proportion of heavy metals in the T4 state and the greater the stability of

Pb. Evidently, this indicates that hydrothermal heat has a strong stabilizing effect on Pb in sediments and can significantly reduce its bioavailability. These findings support earlier data showing Pb in sediment hydrothermal solid products being very stable and posing little damage to the environment [37].

With regard to the heavy metal Ni, the T1 form with the highest specific gravity did not change significantly before and after hydrothermal treatment. Only a handful of heavy metals in the T1 form were transformed into heavy metals in the T3 form. This indicates that the stabilizing effect of hydrothermal heat on Ni was not significant and that the influence of hydrothermal temperature and time on the morphological changes was limited.

Overall, the hydrothermal treatment led to a marked decrease in the proportion of bioavailable fractions (T1 and T2) and a crucial increase in the stable fraction (T4) of heavy metals in the sediment. The results indicate that the bioavailability of heavy metals decreases significantly after hydrothermal treatment and that heavy metals are more stable in the sediment. The conversion of the unstable heavy metal fractions (T1 and T2) to the reasonably stable fractions (T3) and stable fractions (T4) was significantly influenced by hydrothermal treatment (T4). The higher the temperature or the longer the time, the more pronounced the stabilization.

3.6. Environmental Risk Assessment of Heavy Metals. The environmental risk of heavy metals in sediments can be assessed by the RAC. Since heavy metals in the T1 form are most easily affected by changes in ionic strength and pH value in the environment, the content of this part directly determines the environmental risk of heavy metals [38]. The RAC values of Zn, Cu, Cr, Cd, Ni, and Pb in raw sediment and hydrothermal solid products are shown in Table 5.

Cu and Cr had RAC values of less than 10%, which meant they were at low risk levels and had low environmental toxicity. However, the risk indicator RAC for Zn was as

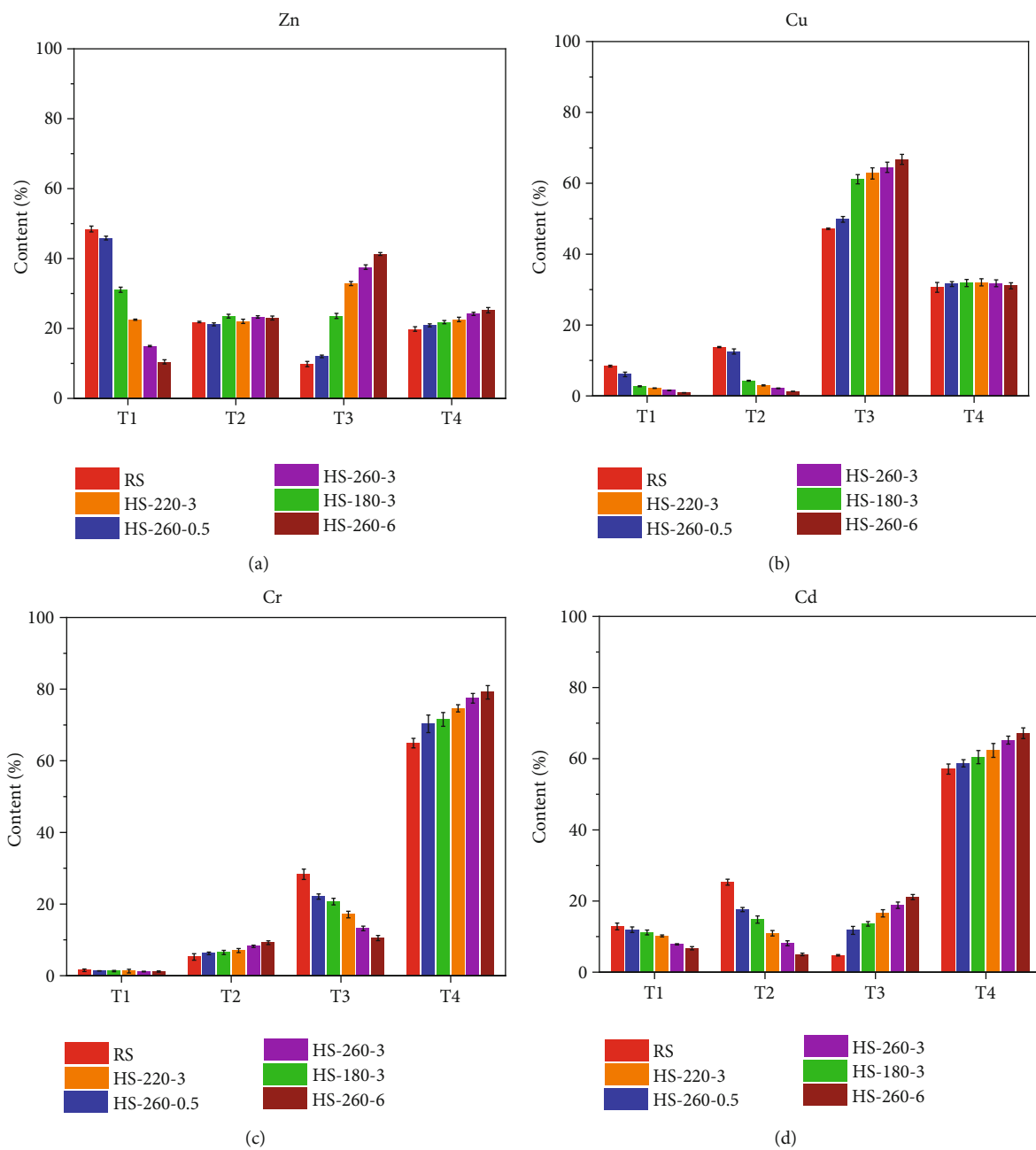


FIGURE 5: Continued.

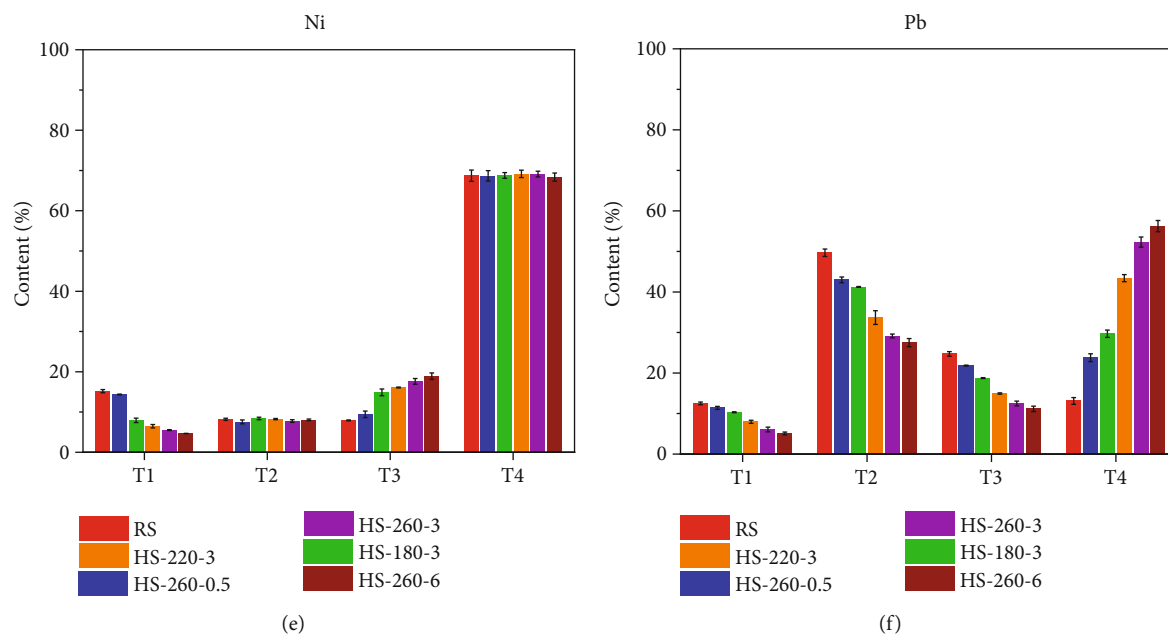


FIGURE 5: The chemical speciation changes of (a) Zn, (b) Cu, (c) Cr, (d) Cd, (e) Ni, and (f) Pb in RS and HS.

TABLE 5: RAC of heavy metals in RS and HS.

Samples	RAC					
	Zn	Cu	Cr	Cd	Ni	Pb
RS	48.45/HR	8.42/LR	1.53/LR	12.88/MR	15.19/MR	12.50/MR
HS-180-3	31.08/HR	2.72/LR	1.28/LR	11.17/MR	7.93/LR	10.32/LR
HS-220-3	22.51/MR	2.20/LR	1.27/LR	10.20/LR	6.48/LR	7.96/LR
HS-260-3	14.98/MR	1.56/LR	1.16/LR	7.83/LR	5.51/LR	6.05/LR
HS-260-0.5	45.87/HR	6.07/LR	1.36/LR	11.94/LR	14.35/MR	11.39/MR
HS-260-6	10.46/LR	0.90/NR	1.15/LR	6.74/LR	4.67/LR	5.10/LR

Note: NR: no risk, representing there is risk free; LR: low risk, representing there is a low risk; MR: medium risk, representing there is a medium risk; HR: high risk, representing there is a high risk.

TABLE 6: Ecological risk assessment of the heavy metals in RS and HS.

Sample	C_f						E_r						RI
	Zn	Cu	Cr	Cd	Ni	Pb	Zn	Cu	Cr	Cd	Ni	Pb	
RS	4.04	2.26	0.54	0.75	0.46	6.63	4.04	11.32	1.08	22.56	2.73	33.14	74.87
HS-180-3	3.59	2.14	0.40	0.65	0.45	2.37	3.59	10.70	0.80	19.61	2.72	11.84	49.26
HS-220-3	3.43	2.12	0.34	0.60	0.45	1.30	3.43	10.60	0.68	18.14	2.67	6.52	42.04
HS-260-3	3.14	2.15	0.29	0.53	0.45	0.91	3.14	10.73	0.58	16.00	2.68	4.56	37.68
HS-260-0.5	3.78	2.17	0.42	0.70	0.46	3.20	3.78	10.84	0.84	21.11	2.74	16.02	55.32
HS-260-6	2.96	2.22	0.26	0.49	0.46	0.78	2.96	11.10	0.53	14.67	2.78	3.89	35.92

high as 48.45%, which was at a high risk level with high environmental risk and ecotoxicity. The risk indicator RACs for Cd, Ni, and Pb were 12.88%, 15.19%, and 12.50%, respectively, which were at a medium risk level and harmful to the environment. After hydrothermal treatment, the RACs of the six heavy metals in the hydrothermal solid products of the sediments all decreased to varying degrees, and the degree of decline increased as the hydrothermal temperature and duration increased. The risk levels of all heavy metals

decreased, except for chromium, which remained at a low level before and after hydrothermal treatment. Zn was reduced from high to low risk after 6 hours of hydrothermal treatment at 260°C. Cu went from being a minimal risk to being completely risk-free. Cd, Ni, and Pb all went from a medium to a low danger level. Meanwhile, the risk indicators for Zn, Cu, Cr, Cd, Ni, and Pb decreased by 78.41%, 89.31%, 24.84%, 47.67%, 69.26%, and 59.20%, respectively, after 6 hours of hydrothermal treatment at 260°C. Combined with

TABLE 7: Leaching toxicity of heavy metals in RS and HS.

Sample	Zn (mg/kg)	Cu (mg/kg)	Cr (mg/kg)	Cd (mg/kg)	Ni (mg/kg)	Pb (mg/kg)
RS	163.72 ± 5.21	3.45 ± 0.07	0.51 ± 0.01	0.44 ± 0.02	9.60 ± 0.05	5.58 ± 0.07
HS-180-3	102.37 ± 1.96	1.40 ± 0.02	0.45 ± 0.01	0.38 ± 0.01	2.34 ± 0.03	2.00 ± 0.06
HS-220-3	72.47 ± 3.23	0.74 ± 0.01	0.42 ± 0.02	0.28 ± 0.01	1.67 ± 0.03	0.91 ± 0.03
HS-260-3	38.69 ± 2.91	0.62 ± 0.01	0.36 ± 0.01	0.20 ± 0.01	1.12 ± 0.02	0.84 ± 0.02
HS-260-0.5	148.30 ± 1.96	2.51 ± 0.03	0.49 ± 0.02	0.40 ± 0.01	8.57 ± 0.04	3.60 ± 0.08
HS-260-6	22.90 ± 1.47	0.55 ± 0.01	0.34 ± 0.01	0.18 ± 0.01	0.87 ± 0.02	0.66 ± 0.01
International permissible leaching limits	25	—	5	0.5	1	5

TABLE 8: Concentration of salt ions in RL and HL.

Sample	NH ₄ ⁺ -N (mg·L ⁻¹)	K ⁺ (mg·L ⁻¹)	Na ⁺ (mg·L ⁻¹)	Ca ²⁺ (mg·L ⁻¹)	Mg ²⁺ (mg·L ⁻¹)
RL	21.12 ± 0.18	9.72 ± 0.19	20.53 ± 0.66	27.22 ± 1.15	3.23 ± 0.13
HL-180-3	88.78 ± 0.73	24.52 ± 0.84	43.35 ± 0.98	38.74 ± 0.54	4.78 ± 0.09
HL-220-3	119.76 ± 0.54	26.27 ± 1.18	59.98 ± 2.11	40.44 ± 0.61	6.45 ± 0.15
HL-260-3	142.57 ± 2.66	28.31 ± 2.21	62.72 ± 2.65	41.20 ± 2.12	9.08 ± 0.10
HL-260-0.5	32.34 ± 0.97	14.43 ± 0.71	23.92 ± 0.38	30.78 ± 0.35	5.69 ± 0.17
HL-260-6	143.82 ± 1.43	29.72 ± 1.63	63.09 ± 2.34	41.61 ± 0.77	9.28 ± 0.28

previous research and findings, the hydrothermal treatment procedure has a practical impact on decreasing the risk levels of heavy metals in sludge [37]. The foregoing findings suggest that hydrothermal treatment can effectively lower the ecotoxicity of heavy metals in sediment, stabilize them, and reduce their risk to the environment and humans.

3.7. Ecological Risk Assessment of Heavy Metals. For single heavy metals in raw sediments and sediment hydrothermal solid products, C_f values for contamination factors, E_r values for potential ecological risk factors, and RI values for the total of potential ecological risk factors are reported in Table 6.

The C_f value of Pb in the raw sediment was 6.63, suggesting a high level of heavy metal contamination. Zn has a C_f value of 4.04, suggesting moderate heavy metal pollution. Cu has a C_f value of 2.26, reflecting a moderate amount of heavy metal pollution. As shown in Table 6 and Table 2, the C_f values for Cr, Cd, and Ni were less than 1, suggesting that they were not contaminated with metals. After hydrothermal treatment, the C_f value of heavy metals in the hydrothermal solid products of the sediment decreased significantly, except for Cu and Ni. Moreover, the higher the hydrothermal temperature and the longer the hydrothermal time, the lower the C_f value. For example, Zn decreased from 4.04 to 2.96, representing a change in risk from moderate to low, and Pb was the most pronounced, decreasing from 6.63 to 0.78, representing a change in risk from high to zero. After hydrothermal treatment, the RI value of river sediment decreased from 74.87 to 35.92. The lower the RI value of hydrothermal solid product sediments, the lower the potential ecological risk level. Further, the potential eco-

logical risk decreases significantly as the hydrothermal temperature and time increase.

3.8. Leaching Toxicity of Heavy Metals. The environmental risks of heavy metals are tightly linked to their leaching characteristics and leaching toxicity. The leaching characteristics are such that leachable heavy metals have direct toxicity to plants and soils during leaching [39]. The leaching concentrations of heavy metals in raw sediment and in the hydrothermal solid products of the sediment are shown in Table 7.

After hydrothermal treatment, the leaching concentrations of all six heavy metals decreased to some extent. At the same time, the higher the hydrothermal temperature or the longer the hydrothermal time, the greater the range of decrease, as shown in Table 6. In particular, the leaching concentration of Zn changed from 163.72 mg/kg to 22.90 mg/kg after 6 hours of hydrothermal treatment at 260°C, which was only 13.99% of the original, below the internationally permitted leaching limit. The leaching concentrations of Cu, Ni, and Pb also decreased to varying degrees and were below the internationally permitted leaching limits. The leaching concentrations of Cr and Cd had reached the internationally permitted leaching limit before hydrothermal treatment and decreased to some extent after hydrothermal treatment. In conclusion, the leaching rates of the various heavy metals did not exceed the internationally permitted leaching limits after the sediment was heated at 260°C for 6 hours. Concurrently, the change in leaching concentration was largely compatible with the change in RI values of heavy metals in the sediment. This is further evidence that hydrothermal treatment can actually lower the environmental risk of heavy metals in sediments by stabilizing them and reducing the risk to the environment and humans.

3.9. Stabilization Mechanism of Heavy Metals. The concentrations of some ions in raw sediment filtrate and the hydrothermal phase of sediment are shown in Table 8.

As the hydrothermal temperature and time increased, the amount of salt ions in the liquid phase increased significantly, as shown in Table 8. This intensified the competition for adsorption sites on the sediment, resulting in some of the weakly bound heavy metals entering the liquid phase after analysis. In addition, the hydrothermal treatment also facilitated the solubilization of heavy metals by facilitating their migration in the sediment, providing an opportunity for them to form more stable minerals in the liquid phase through precipitation and complexation with anions.

According to infrared spectrum analysis (Figure 2), the hydrothermal treatment resulted in the removal of oxygen-containing functional groups (-OH, -COOH) from the sediment, and the ability of the heavy metals to adsorb organic matter via hydroxyl and carboxyl groups was severely disrupted and released into the liquid phase. The heavy metals were then finally immobilized in the minerals by complexation, precipitation, or other means, namely, the transition from the unstable state (T1, T2) to the stable state (T3, T4), and finally, the stabilization of heavy metals in the sediments was achieved [10, 40, 41]. Studies by Huang et al. [13] and Wang et al. [37] also showed that the dehydroxylation and decarboxylation of macromolecules in organics during hydrothermal treatment might play an indispensable role in the reduction of bioavailability or immobilization of heavy metals.

Meanwhile, the C-H out-of-plane deformation vibration absorption peaks of aromatic hydrocarbons were slightly enhanced at 797 cm^{-1} and 776 cm^{-1} after hydrothermal treatment of the sediments. While the peak at $600\text{--}800\text{ cm}^{-1}$ corresponded to aromatic groups and heteroaromatic compounds, aromatic groups have π electrons and high potential energy, which form strong bonds with heavy metal cations [42]. Therefore, another possible reason for the reduction of the bioavailability or stabilization of heavy metals in sediments after hydrothermal treatment is that hydrothermal treatment causes aromatization of some organics (alkanes, cyclic hydrocarbons) in the sediment. The resulting aromatic groups combine with partially dissolved heavy metals or heavy metals in sediments to form strong bond compounds, which are finally fixed in minerals [43].

4. Conclusion

Hydrothermal treatment can significantly improve the dewatering performance of the sediment and remove the organic matter in the sediment to achieve the reduction and stabilization of the sediment. Hydrothermal treatment reduces the bioavailability components of heavy metals in sediments and converts them into more stable components, so that their environmental bioavailability, ecotoxicity, and leaching toxicity are significantly reduced, thereby achieving heavy metal stabilization in sediments. This study provides a new method for the treatment of sediment and provides a certain basis for the subsequent green land use of sediment.

Data Availability

The data used to support the findings of this study are included within the article.

Conflicts of Interest

The authors declare that there is no conflict of interest regarding the publication of this paper.

Acknowledgments

This study was supported by the National Key R&D Program of China (No: 2019YFD1100502) and the Project of Shanghai Science and Technology Commission (No: 19DZ1207903).

References





- [1] K. Y. Kim, M. Ndabambi, S. Choi, and J.-E. Oh, "Legacy and novel perfluoroalkyl and polyfluoroalkyl substances in industrial wastewater and the receiving river water: temporal changes in relative abundances of regulated compounds and alternatives," *Water Research*, vol. 191, article 116830, 2021.
- [2] B. Wijesiri, A. Liu, B. He et al., "Behaviour of metals in an urban river and the pollution of estuarine environment," *Water Research*, vol. 164, article 114911, 2019.
- [3] W. Ouyang, W. Yang, M. Tysklind et al., "Using river sediments to analyze the driving force difference for non-point source pollution dynamics between two scales of watersheds," *Water Research*, vol. 139, pp. 311–320, 2018.
- [4] T. Dalu, R. J. Wasserman, M. L. Magoro, P. W. Froneman, and O. L. F. Weyl, "River nutrient water and sediment measurements inform on nutrient retention, with implications for eutrophication," *Science of the Total Environment*, vol. 684, pp. 296–302, 2019.
- [5] S. Masi, D. Caniani, E. Grieco, D. S. Lioi, and I. M. Mancini, "Assessment of the possible reuse of MSW coming from landfill mining of old open dumpsites," *Waste Management*, vol. 34, no. 3, pp. 702–710, 2014.
- [6] K. Zhang, Q. Wei, S. Jiang et al., "Utilization of dredged river sediment in preparing autoclaved aerated concrete blocks," *Journal of Renewable Materials*, vol. 10, no. 11, pp. 2989–3008, 2022.
- [7] X. Ma, Q. Ren, W. Zhan, K. Zheng, R. Chen, and Y. Wang, "Simultaneous stabilization of Pb, Cd, Cu, Zn and Ni in contaminated sediment using modified biochar," *Journal of Soils and Sediments*, vol. 22, no. 1, pp. 392–402, 2022.
- [8] Y.-J. Shih, S.-Y. Syu, C.-W. Chen, C.-F. Chen, and C.-D. Dong, "Assessment of ex-situ chemical washing of heavy metals from estuarine sediments around an industrial harbor in Southern Taiwan," *Journal of Soils and Sediments*, vol. 19, no. 7, pp. 3108–3122, 2019.
- [9] W. Shin and Y.-K. Kim, "Stabilization of heavy metal contaminated marine sediments with red mud and apatite composite," *Journal of Soils and Sediments*, vol. 16, no. 2, pp. 726–735, 2016.
- [10] L. Wang, Y. Chang, and A. Li, "Hydrothermal carbonization for energy-efficient processing of sewage sludge: a review," *Renewable and Sustainable Energy Reviews*, vol. 108, pp. 423–440, 2019.

- [11] Y. Zhu, Z. Han, X. Liu, J. Li, F. Liu, and S. Feng, "Study on the effect and mechanism of hydrothermal pretreatment of dewatered sewage sludge cake for dewaterability," *Journal of the Air & Waste Management Association*, vol. 63, no. 8, pp. 997–1002, 2013.
- [12] X. Li, J. Wang, J. You et al., "Hazardous waste dewatering and dry mass reduction through hydrophobic modification by a facile one-pot, alkali-assisted hydrothermal reaction," *Water Research*, vol. 155, pp. 225–232, 2019.
- [13] H. Huang, X. Yuan, G. Zeng et al., "Quantitative evaluation of heavy metals' pollution hazards in liquefaction residues of sewage sludge," *Bioresource Technology*, vol. 102, no. 22, pp. 10346–10351, 2011.
- [14] W.-S. Shi, *Migration behavior of heavy metals during hydrothermal treatment of sludge*, China of Geosciences (Beijing), 2015.
- [15] L. Li, Z. R. Xu, C. Zhang, J. Bao, and X. Dai, "Quantitative evaluation of heavy metals in solid residues from sub- and super-critical water gasification of sewage sludge," *Bioresource Technology*, vol. 121, pp. 169–175, 2012.
- [16] T. Liu, Z. Liu, Q. Zheng et al., "Effect of hydrothermal carbonization on migration and environmental risk of heavy metals in sewage sludge during pyrolysis," *Bioresource Technology*, vol. 247, pp. 282–290, 2018.
- [17] J. Shao, X. Yuan, L. Leng et al., "The comparison of the migration and transformation behavior of heavy metals during pyrolysis and liquefaction of municipal sewage sludge, paper mill sludge, and slaughterhouse sludge," *Bioresource Technology*, vol. 198, pp. 16–22, 2015.
- [18] X.-G. Qin, *Study on the hydrothermal liquefaction performance of sludge and its product characteristics*, Chongqing University, 2015.
- [19] S.-X. Fan, *Soil Heavy Metal Pollution and Control*, China Environmental Science Press, Beijing, 2011.
- [20] Y.-Y. Long, L.-F. Hu, C.-R. Fang, Y.-Y. Wu, and D.-S. Shen, "An evaluation of the modified BCR sequential extraction procedure to assess the potential mobility of copper and zinc in MSW," *Microchemical Journal*, vol. 91, no. 1, pp. 1–5, 2009.
- [21] W. Shi, C. Liu, D. Ding et al., "Immobilization of heavy metals in sewage sludge by using subcritical water technology," *Bioresource Technology*, vol. 137, pp. 18–24, 2013.
- [22] L. Håkanson, "Aquatic contamination and ecological risk. An attempt to a conceptual framework," *Water Research*, vol. 18, no. 9, pp. 1107–1118, 1984.
- [23] United States, *Test Methods for Evaluating Solid Waste Physical/Chemical Methods (sw-846) Third Edition*, Solid Waste Management Board EPA publication, 1995, Proposed update III.
- [24] L. Wang and A. Li, "Hydrothermal treatment coupled with mechanical expression at increased temperature for excess sludge dewatering: the dewatering performance and the characteristics of products," *Water Research*, vol. 68, pp. 291–303, 2015.
- [25] T. Chen, Y. Zhang, H. Wang et al., "Influence of pyrolysis temperature on characteristics and heavy metal adsorptive performance of biochar derived from municipal sewage sludge," *Bioresource Technology*, vol. 164, pp. 47–54, 2014.
- [26] Z. Wang, L. Xie, K. Liu et al., "Co-pyrolysis of sewage sludge and cotton stalks," *Waste Management*, vol. 89, pp. 430–438, 2019.
- [27] B. Hu, K. Wang, L. Wu, S.-H. Yu, M. Antonietti, and M.-M. Titirici, "Engineering carbon materials from the hydrothermal carbonization process of biomass," *Advanced Materials*, vol. 22, no. 7, pp. 813–828, 2010.
- [28] C. He, A. Giannis, and J.-Y. Wang, "Conversion of sewage sludge to clean solid fuel using hydrothermal carbonization: hydrochar fuel characteristics and combustion behavior," *Applied Energy*, vol. 111, pp. 257–266, 2013.
- [29] Y.-C. Chen, S.-L. Lo, and J. Kuo, "Pb(II) adsorption capacity and behavior of titanate nanotubes made by microwave hydrothermal method," *Colloids and Surfaces A: Physicochemical and Engineering Aspects*, vol. 361, no. 1-3, pp. 126–131, 2010.
- [30] L. K. Dhandole, S.-G. Kim, H.-S. Bae et al., "Simultaneous and synergistic effect of heavy metal adsorption on the enhanced photocatalytic performance of a visible-light-driven RS-TONR/TNT composite," *Environmental Research*, vol. 180, article 108651, 2020.
- [31] R.-a. Doong and C.-Y. Liao, "Enhanced visible-light-responsive photodegradation of bisphenol A by Cu, N-codoped titanate nanotubes prepared by microwave-assisted hydrothermal method," *Journal of Hazardous Materials*, vol. 322, pp. 254–262, 2017.
- [32] A. A. Zorpas, V. J. Inglezakis, and M. Loizidou, "Heavy metals fractionation before, during and after composting of sewage sludge with natural zeolite," *Waste Management*, vol. 28, no. 11, pp. 2054–2060, 2008.
- [33] L. Appels, J. Degrève, B. Van der Bruggen, J. Van Impe, and R. Dewil, "Influence of low temperature thermal pretreatment on sludge solubilisation, heavy metal release and anaerobic digestion," *Bioresource Technology*, vol. 101, no. 15, pp. 5743–5748, 2010.
- [34] V. Angelova, K. Ivanov, and R. Ivanova, "Effect of chemical forms of lead, cadmium, and zinc in polluted soils on their uptake by tobacco," *Journal of Plant Nutrition*, vol. 27, no. 5, pp. 757–773, 2004.
- [35] X. Xian, "Effect of chemical forms of cadmium, zinc, and lead in polluted soils on their uptake by cabbage plants," *Plant and Soil*, vol. 113, no. 2, pp. 257–264, 1989.
- [36] X. Yuan, H. Huang, G. Zeng et al., "Total concentrations and chemical speciation of heavy metals in liquefaction residues of sewage sludge," *Bioresource Technology*, vol. 102, no. 5, pp. 4104–4110, 2011.
- [37] X. Wang, Q. Chi, X. Liu, and Y. Wang, "Influence of pyrolysis temperature on characteristics and environmental risk of heavy metals in pyrolyzed biochar made from hydrothermally treated sewage sludge," *Chemosphere*, vol. 216, pp. 698–706, 2019.
- [38] M. R. Lasheen and N. S. Ammar, "Assessment of metals speciation in sewage sludge and stabilized sludge from different wastewater treatment plants, Greater Cairo, Egypt," *Journal of Hazardous Materials*, vol. 164, no. 2-3, pp. 740–749, 2009.
- [39] J. Liang, L. Zhang, M. Ye et al., "Evaluation of the dewaterability, heavy metal toxicity and phytotoxicity of sewage sludge in different advanced oxidation processes," *Journal of Cleaner Production*, vol. 265, article 121839, 2020.
- [40] H.-F. Wang, H. Hu, H.-J. Wang, and R. J. Zeng, "Combined use of inorganic coagulants and cationic polyacrylamide for enhancing dewaterability of sewage sludge," *Journal of Cleaner Production*, vol. 211, pp. 387–395, 2019.
- [41] L. Wang, Y. Chang, and Q. Liu, "Fate and distribution of nutrients and heavy metals during hydrothermal carbonization of sewage sludge with implication to land application," *Journal of Cleaner Production*, vol. 225, pp. 972–983, 2019.

- [42] O. R. Harvey, B. E. Herbert, R. D. Rhue, and L.-J. Kuo, "Metal interactions at the biochar-water interface: energetics and structure-sorption relationships elucidated by flow adsorption microcalorimetry," *Environmental Science & Technology*, vol. 45, no. 13, pp. 5550–5556, 2011.
- [43] X. Zhang, J. Zhou, Z. Xu, P. Zhu, and J. Liu, "Characterization of heavy metals in textile sludge with hydrothermal carbonization treatment," *Journal of Hazardous Materials*, vol. 402, article 123635, 2021.

Research Article

Biogenic Synthesis of Silver Nanoparticles Using *Rhazya stricta* Extracts and Evaluation of Its Biological Activities

Sami Bawazeer,¹ Abdur Rauf ,² Talha Bin Emran ,^{3,4} Abdullah S. M. Aljohani,⁵ Fahad A. Alhumaydhi ,⁶ Zidan Khan,⁷ Laiba Ahmad,⁸ Hassan A. Hemeg,⁹ Naveed Muhammad,¹⁰ Rohit Sharma ,¹¹ Aneela Maalik,¹² and Ibrahim Khan¹³

¹Department of Pharmacognosy, Faculty of Pharmacy, Umm Al-Qura University, Makkah, P.O. Box 42, Saudi Arabia

²Department of Chemistry, University of Swabi, Anbar, 23430 Khyber Pakhtunkhwa, Pakistan

³Department of Pharmacy, BGC Trust University Bangladesh, Chittagong 4381, Bangladesh

⁴Department of Pharmacy, Faculty of Allied Health Sciences, Daffodil International University, Dhaka 1207, Bangladesh

⁵Department of Veterinary Medicine, College of Agriculture and Veterinary Medicine, Qassim University, Buraydah, Saudi Arabia

⁶Department of Medical Laboratories, College of Applied Medical Sciences, Qassim University, Buraydah, Saudi Arabia

⁷Department of Pharmacy, International Islamic University Chittagong, Chittagong 4318, Bangladesh

⁸Khyber Medical College Peshawar, Peshawar, KPK, Pakistan

⁹Department of Medical Laboratory Technology, College of Applied Medical Sciences, Taibah University, P.O. Box 344, Al-Madinah Al-Monawra 41411, Saudi Arabia

¹⁰Department of Pharmacy, Abdul Wali Khan University Mardan, KPK, Pakistan

¹¹Department of Rasa Shastra and Bhaishajya Kalpana, Faculty of Ayurveda, Institute of Medical Sciences, Banaras Hindu University, Varanasi, 221005 Uttar Pradesh, India

¹²Department of Chemistry, COMSATS Institute of Information Technology, Abbottabad 22060, Pakistan

¹³Department of Chemistry, GPGC Charsadda, KPK, Pakistan

Correspondence should be addressed to Abdur Rauf; mashaljcs@yahoo.com, Talha Bin Emran; talhabmb@bgctub.ac.bd, and Rohit Sharma; rohitsharma@bhu.ac.in

Received 16 February 2022; Revised 27 April 2022; Accepted 27 June 2022; Published 21 July 2022

Academic Editor: Antonios Kelarakis

Copyright © 2022 Sami Bawazeer et al. This is an open access article distributed under the Creative Commons Attribution License, which permits unrestricted use, distribution, and reproduction in any medium, provided the original work is properly cited.

Rhazya stricta is a well-known medicinal plant and source of numerous potential secondary metabolites including steroids, alkaloids, and tannins. *R. stricta* possesses multimodal applications and used for curing of various diseases such as inflammation, diabetes, sore throat, infectious, helminthiasis, arthritis, and cancer. The current investigation deals with synthesizing AgNPs using aqueous and ethanol extracts of *R. stricta*. The synthesized *R. stricta*-AgNPs were characterized through UV-visible, Fourier transform infrared (FTIR), and atomic force microscopy (AFM) methods. The UV-visible analysis exhibited a characteristic absorption λ_{\max} at 475 nm in *R. stricta* ethanol AgNPs while this peak was absent in *R. stricta* aqueous crude extract. The thermal stability of *R. stricta*-AgNPs demonstrated that by increasing the reduction time and temperature, the absorption of AgNPs also increased, leading to more stable NPs formation. The FTIR spectra showed a broad peak at 450-550 cm^{-1} that confirmed the occurrence of AgNPs of *R. stricta*. The AFM study of the synthesized AgNPs revealed the spherical shape and size ranging from 30 nm to 90 nm. In antioxidant and antibacterial study, the *R. stricta*-AgNPs exhibited good antioxidant activity (87.94% and 88.37%) than the ethanol crude extract (50.00% and 56.81%) at 100 $\mu\text{g}/\text{mL}$ using DPPH assay. Maximum antibacterial activity was recorded against Gram-positive bacteria (*Staphylococcus aureus*), which was 15 and 0 mm, while against Gram-negative bacteria (*Klebsiella pneumoniae*) was found to be 16 and 14 mm, respectively, whereas against *Bacillus subtilis*, a poor activity was recorded as 14 for extract and 0 mm for AgNPs, respectively. In the acetic acid-induced writhing model, the percent effect of extract (100 mg/kg) and AgNPs (15 mg/kg) was 79.98 and 83.23, respectively. The maximum muscle coordination effect of extracts in the inclined plan and traction test was 44% and 38% at

higher doses. A mild sedative effect was also recorded against extract and AgNPs. The significant ($p < 0.05$) effect of extract was noted at 100 mg/kg while AgNPs was more significant ($p < 0.01$) at the tested dose of 15 mg/kg. These findings have concluded that *R. stricta*-AgNPs is an effective bio-reductant of AgNPs synthesis and exhibit several applications in distinctive biomedical and pharmaceutical industries.

1. Introduction

Nanobiotechnology is a promising field of material science leading to the production and development of a variety of nanomaterials. The nanomaterials are being used as bactericidal [1], catalytic, biological labelling, sensor technology [2], electronic, optical devices [3], anticancer therapies, and various other health ailments [4–6]. There are typical routes used for the development of nanoparticles (NPs) such as physical and chemical protocols which are toxic, noneconomic, noneco-friendly, and expensive. Therefore, recently, new biosynthetic methods have been explored for the synthesis of NPs using microorganisms and plants [7]. The study of literature reported that the biosynthesis of NPs with medicinal plant extracts as a source needs to be more thoroughly studied. Most importantly, green synthesis of NPs is a new field of nanotechnology research because of its many advantages, such as how easy it is to work with and how cheap it is. Currently, the development of cost-effective synthetic protocols is the main area of concern for researchers for the production of stable, biocompatible, and reproducible NPs. The world's key threat to mankind is antibiotic resistance. Silver NPs (AgNPs) as nanomedicines in nanobiotechnology play a vital role against drug-resistant bacteria [8, 9]. Oxidative stress is a complexity arising from imbalance between defensive mechanism of antioxidants and generation of free radicals [10]. This noxious phenomenon is responsible for deterioration of protein, lipid, DNA, and other vital elements that forms our body [11]. Oxidative stress may lead to neurological disorders, inflammatory diseases, cardiovascular diseases, and complications in immune system [12–15]. An antioxidant is an agent which can neutralize a free radical by donating an electron and diminish its capability to damage or cause harm to the body [16]. Apart from donation of electron, antioxidant also acts by deactivating the catalyst that initiates the formation of free radicals [17]. Among several antioxidants, the superoxide dismutase acts by initiating disintegration of superoxide anion, forming hydrogen peroxide and oxygen [18, 19] while the glutathione system causes deactivation of hydrogen peroxide which involves more than one chemical cofactors [20]. Ascorbic acid is a potential antioxidant which contingent upon reaction with glutathione to exert its free radical diminishing activity [21]. Medicinal plants shown to have promising stand to be a potential source of antioxidant agent [22–24]. Despite the promising mechanism of antimicrobials to protect the host, the resistance to antimicrobial is becoming a concerning issue nowadays. Inappropriate prescribing and overuse contributes the most in antimicrobial resistance. This demands antibiotic with developed mechanism of action to fight against this modern era crisis [25].

Insomnia is a complication related to lack of sleep due to various factors [26, 27]. The prevalence of insomnia varies

between 10% and 30% of the world populations [28–32]. Anxiety, depression, diabetes, and hypertension can be influenced by insomnia [31]. Sedative shows potential outcome in the treatment of insomnia and depression [33]. Data from a survey report showed that 126.1 million people involved in pain related complications whereas 25.3 million people suffered every day in USA [34]. Yearly global statistics revealed that among every 5-adult people, at least 1 is suffering from pain. On the other hand, 1 in every 10 people is suffering from chronic pain [35]. In the management and treatment of pain analgesic drugs play the vital role which are divided into nonopioid and opioid class [36]. AgNPs are significantly used as antimicrobial agent and were already known for a variety of applications in textiles, antimicrobial, water treatment, paint coatings, HIV prevention, and treatment as well as in medical devices [37]. The plant materials are selected for biosynthesis due to the presence of reducing agents like ascorbic acid and phenolic compounds that may play a vital role in metal NP synthesis [38]. *Rhazya stricta* (family: Apocynaceae) is a traditional medicinal plant commonly found all through Western Asia, India, Afghanistan, and different places of Pakistan [39]. The plant has dense erect branches with smooth stem and overall appears to be glabrous shrub. It is traditionally used as a remedy [38], for fever, rheumatic pain, diabetes, syphilis, sore throat, inflammatory conditions, helminthiasis, and for the treatment of many other diseases [40]. In United Arab Emirates, the plant decoction is used to treat several health ailments, including diabetes mellitus, fever, sore throat, inflammatory conditions, and helminthiasis [41]. The leaves of *R. stricta* are traditionally used as a purported bitter tonic [42, 43] and cure for syphilis [42], chronic rheumatism [42], and associated forms of discomfort [41]. Branches are used as toothbrushes to alleviate toothaches [44]. Compelling evidence suggests that different fraction of this plant is abundant with alkaloids [45–48], which are mostly responsible for its pharmacological effect [40].

The current study aims to synthesize AgNPs from ethanol extract of *R. stricta* and evaluate several biological activities including antioxidant, antimicrobial, analgesic, and muscle relaxation; hence, proposing a potential source of NPs to be a potential medicinal active agent.

2. Materials and Methods

2.1. Plant Collection. Fresh leaves and stem of *R. stricta* were collected from (Khairabad) District Nowshera, Khyber Pakhtunkhwa, Pakistan. The plant identification was carried out by Dr. Barkath Ullah, Department of Botany, University of Peshawar, Peshawar, Pakistan. The voucher specimen Number UOP/Bot609 was kept in the herbarium of mention department.

2.1.1. Extraction. Fresh leaves of *R. stricta* were taken and washed twice with distilled water to make them free from dust and dried in shade at room temperature. The dried leaves (100 g) were ground into powder and soaked in ethanol and (1000 mL) and distilled water, respectively, in separate flasks and kept for three days. The resultant materials were filtered. The aqueous and ethanol (EtOH) filtrates were then concentrated by using low pressure rotary evaporator at 40°C to obtain a paste and were stored at 4°C for further use.

2.1.2. Phytochemical Screening. Phytochemical evaluation plays a major part in the presence of novel compounds and revelation of medications [48]. The presence of secondary metabolites present in aqueous and ethanol extract was carried out by using standard protocols of phytochemical screening [49]. Phytochemical screening of *R. stricta* ethanol extracts demonstrated the presence of tannins, saponins, flavonoids, terpenoids, steroids, coumarins, and emodines which may act as a major source of reducing agents during the AgNP synthesis [50] (Table 1).

2.2. Synthesis of AgNPs

2.2.1. Preparation of Stock Solution and AgNO₃ Salt Solution. Stock solution was prepared by dissolving 1 g of plant crude alcoholic extract in 100 mL distilled water. While 1 mM silver salt solution of silver nitrate (AgNO₃) was prepared (17 mg AgNO₃/100 mL of de-ionized H₂O) for the biosynthesis of metallic NPs of plant extracts [48].

2.2.2. Synthesis of Silver NPs of EtOH Extract. NPs were synthesized by following simple method [51]. Ethanol extract and salt solution were mixed together in various ratios, i.e., 1:1, 1:2, 1:3, and 1:4 by keeping the silver nitrate solution concentration constant. The reaction mixture was first stirred for 1 hour at 70°C, and then, stirring was continued for 4 hours at room temperature. The color of reaction mixture was continuously changing during the stirring, and at last, brown color was developed. The color change indicated the synthesis of NPs by the reduction process. After this, the solution was centrifuged at 5000 rpm for 15 minutes. The pellet obtained after discarding the supernatant was air dried in the incubator. Later on, the abovementioned ratios were then heated to high temperatures (80°C), and UV-visible spectra were recorded for every step to monitor the stability of the synthesized AgNPs. The same procedure was followed with aqueous plant extract of *R. stricta* but no well-defined AgNPs were synthesized.

2.3. Characterization of AgNPs. AgNPs of *R. stricta* were characterized by using UV-visible spectrometer (Hitachi-U-3200, Japan). Atomic force microscopic characterization was done from HEJ, Karachi, where the sample solution was spread on a plate then plate was dried and the image was recorded by AFM Agilent 5500 Japan in dynamic mode.

Fourier transform infrared (FTIR) spectral analysis of *R. stricta* extracts was carried out to find the probable biomolecules which are responsible for reduction as well as capping the bio reduced AgNPs. IR spectrums were recorded on

TABLE 1: Phytochemical screening of ethanol, aqueous, and hexane extracts of *R. stricta*.

Chemical constituents	Ethanol extract	Aqueous extract	n-hexane extract
Anthraquinones	—	—	—
Reducing sugars	—	—	—
Flavonoids	—	—	—
Alkaloids	+	+	—
Steroids	+	—	—
Coumarins	+	+	—
Carbohydrates	—	—	—
Tannins	+	—	—
Anthocyanins and betacyanins	—	—	—
Terpenoids	+	+	+
Glycosides	—	—	—
Cardiac glycosides	—	—	—
Monosaccharides	—	—	—
Phlobatanins	—	—	—
Emodines	—	+	—
Saponins	—	+	—

Here, (+): present, (-): absent.

FTIR (Nicolet 380, Thermo Scientific, Japan) using KBr pellet method.

2.4. Biological Activities of Synthesized AgNPs

2.4.1. Antioxidant Activity. Free radical scavenging activity of *R. stricta* plant extract and their synthesized EtOH-AgNPs were measured by 2,2-diphenyl-1-picrylhydrazyl (DPPH). DPPH solution of 0.1 mM concentration was prepared in ethanol [52]. This solution (1 mL) was added to 5 mL of ethanol crude extract at different concentration (10, 20, 40, 80, 100, 150, and 250 µg/mL) prepared by dilution method. The solutions were mixed by vigorous shaking and then allowed to stand for 30 minutes at room temperature in dark. Later on, by using spectrophotometer at 517 nm, the absorbance was measured. Ascorbic acid was used as a reference standard, and the experiment was repeated thrice. An increase in the antioxidant activity is the measure of the decrease of the DPPH solution absorbance. Antioxidant activity as percent radical scavenging activities (%RSA) by DPPH was calculated as follows.

$$\%DPPH = \left(\frac{OD_{Control} - OD_{Sample}}{OD_{Control}} \right) \times 100, \quad (1)$$

where OD is control and OD sample is the absorbance of samples [49].

2.4.2. Antibacterial Activity. The antibacterial activity of *R. stricta* plant EtOH crude extract as well as their synthesized AgNPs was carried out against different bacterial strains, i.e., *Klebsiella pneumonia* (Gram-negative bacteria), *Bacillus subtilis*,

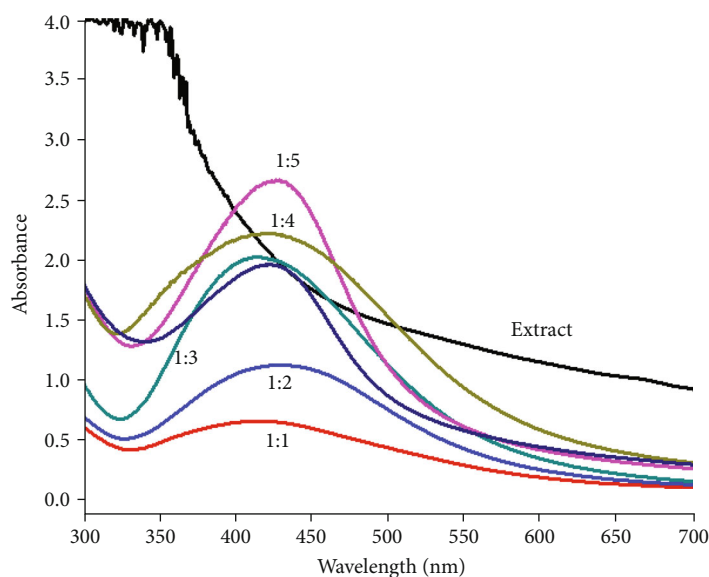


FIGURE 1: Optimization of AgNPs synthesis *R. stricta*.

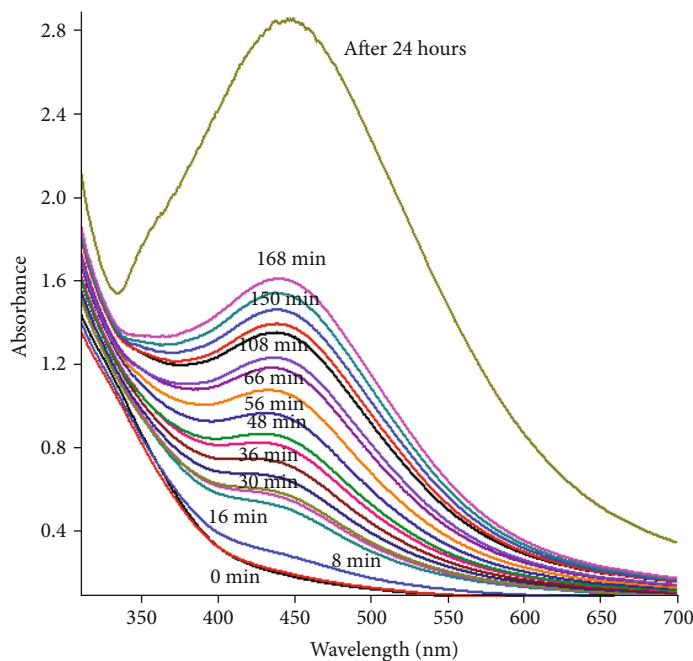


FIGURE 2: Time effect of green synthesized AgNPs of *R. stricta*.

and *Staphylococcus aureus* (Gram-positive bacteria), and to explore their medicinal values by using standard protocol. These bacterial strains were kept in Mueller-Hinton agar at 4°C in the refrigerator [53]. The antibacterial activity was performed by using modified agar well diffusion method where Mueller Hinton agar was used as medium. The culture taken in triplicate was cultivated in petri dish and later on equipped for 24-72 hours at 37°C. The petri dishes were first sterilized; then, 0.6 mL of prepared broth culture was added with the addition of 20 mL sterilized molten MHA to each Petri dish. Wells (size 6 mm) were bored in the agar medium by using sterilized borer and plants; EtOH crude extract at 0.2 mL by volume was poured into each well by the help of a micropipette whereas

2 mg/mL of synthesized AgNPs was used to study its antibacterial potential by using streptomycin (2 mg/mL) as a standard drug. The proper diffusion was carried out by keeping Petri dishes in laminar flow hood for 1 hour followed by the incubation of plates was done for 24 hours at 37°C. The zone of inhibition was measured next day.

Acetic acid induced writhing *in vivo* paradigm was used for assessment of analgesic potential of extract and AgNPs. Animals were classified in different groups ($n = 8$). The negative control group was treated with distilled water (10 mL/kg, i.p.). Positive control group received diclofenac sodium (10 mg/kg, i.p.), and the tested groups were treated with extract (10, 25, 50 and 100 mg/kg, p.o.) and AgNPs (2.5, 5,

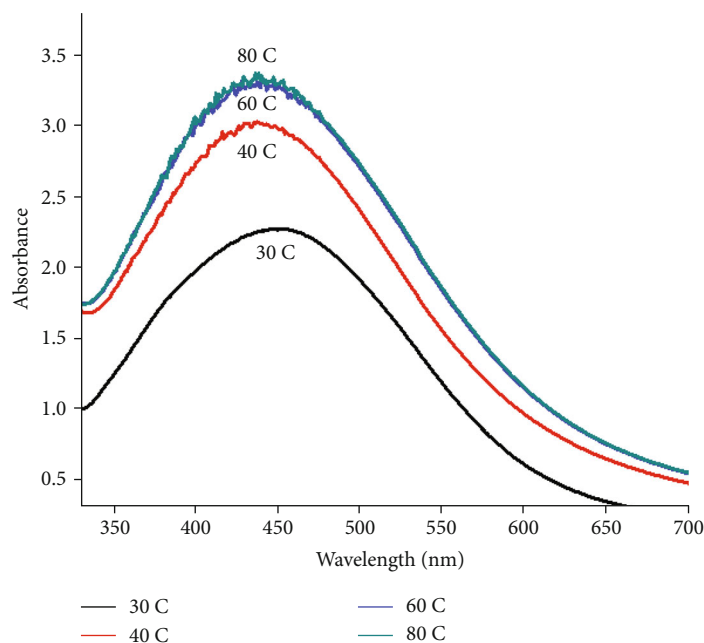


FIGURE 3: Temperature effect of green synthesized AgNPs of *R. stricta*.

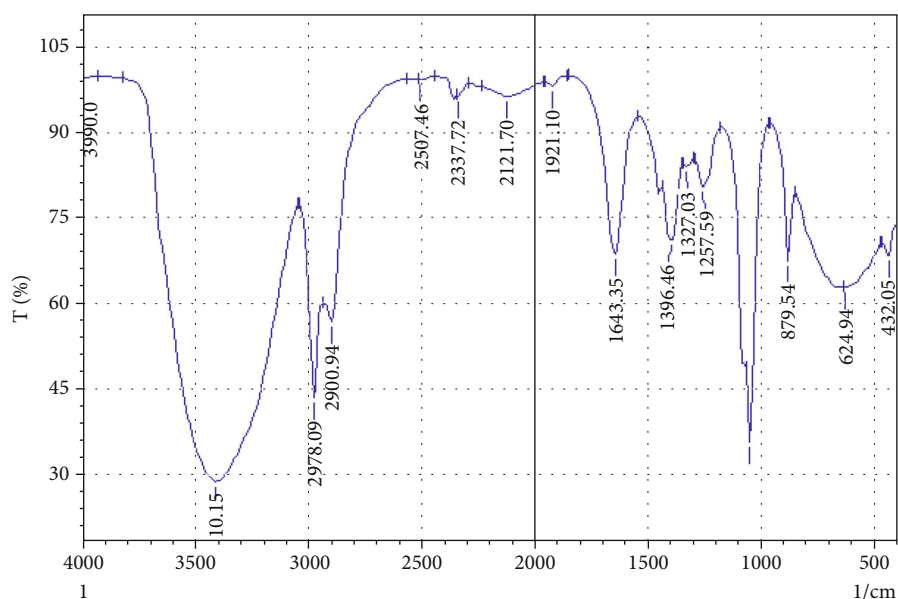


FIGURE 4: FTIR analysis of *R. strict* crude ethanol extract.

10 and 15 mg/kg, p.o.). All the animals were injected with 1% acetic acid solution (i.p.) after 30 min of the above treatments. After 10 min of the acetic acid injection, the number of abdominal contractions (writhing) was counted (for 10 min) for each group ($n = 8$) of animals. The percent effect was quantified using our published method [9].

2.5. Muscle Relaxant Activity

2.5.1. Inclined Plant Test. For the evaluation of fixed oil for muscle coordination effect, a plane of two woods was used in such a way that an angle of 65° was resulted from the connection. Animals after classification in various groups, the

negative group was treated with distilled water (10 mL/kg), the positive group was injected with diazepam (1 mg/kg), and the tested groups were administered extract (10, 25, 50, and 100 mg/kg, p.o.) and AgNPs (2.5, 5, 10, and 15 mg/kg, p.o.). After 30, 60, and 90 min of the above treatment, animals were tested for the muscle coordination effect as, that animal was placed on the upper part of the inclined plane for 30 seconds to hang of fall. This method is the modified form of our published method [38].

2.6. Sedative Activity. For the evaluation of sedative effect of extract and AgNPs, a special box was used. The floor of the box was coated with white sheet (150 cm diameter) and was

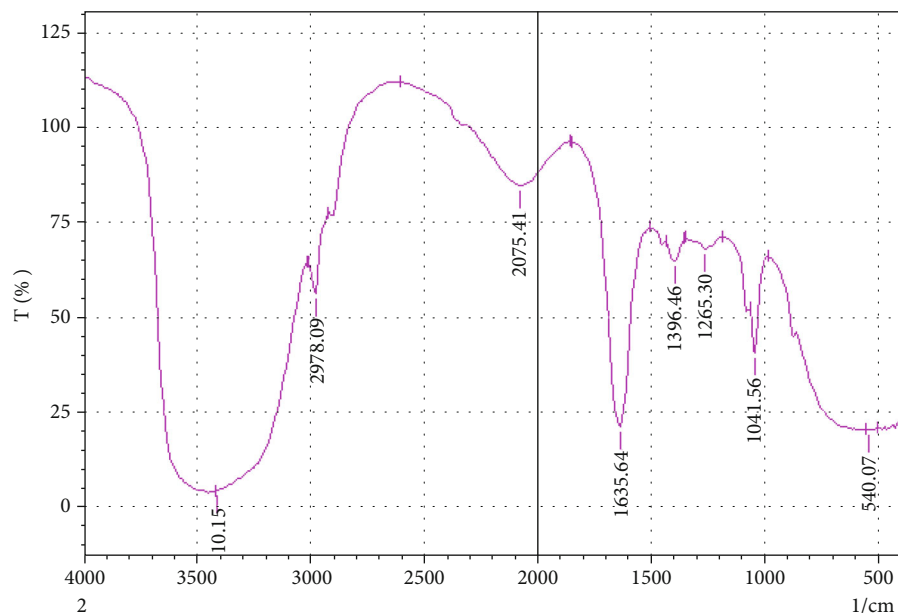


FIGURE 5: FTIR analysis of *R. stricta* AgNPs synthesized from crude ethanol extract.

divided with 20 squares by black lines. This open field box was placed in soundproof experimental room. Animals after classification in various groups, the negative group was treated with distilled water (10 mL/kg), the positive group was injected with diazepam (1 mg/kg), and the tested groups were administered extract (10, 25, 50, and 100 mg/kg, p.o.) and AgNPs (2.5, 5, 10, and 15 mg/kg, p.o.). After post-30 min of the above administration, each animal was tested for sedative effect by keeping in the center of box, and the number of lines crossed by animal was counted. The smaller number of lines crossed was meant for sedative effect.

2.7. Statistical Analysis. The data were expressed as mean \pm standard error of the mean (SEM). Analysis of variance (ANOVA) was followed by Dunnett's test using GraphPad Prism 8.0 (GraphPad Software Inc., San Diego CA, USA).

3. Results

3.1. Optimization of AgNPs. Silver nitrate was used in various ratios to a fixed amount of plant extract, including 1:1, 1:2, 1:3, 1:4, and 1:5. The plant extract was subjected to a reaction flask containing silver nitrate solution and stirred for one hour on high temperature, followed by four hours on low heat. The color of the solution changed from colorless to yellow to brown, and different ratios resulted in different absorbance values, but the optimal ratio was 1:5, which has the highest absorbance and sharpest peak. The sharper the peak, the more AgNPs of uniform size will be produced. The maximum absorption wavelength was between 420 and 440 nm (Figure 1).

3.1.1. Time and Temperature Effect of AgNPs. A UV-visible spectrophotometer was used to monitor the synthesis of AgNPs in order to determine the effect of time. In this study, samples from reaction mixture were drawn at regular interval

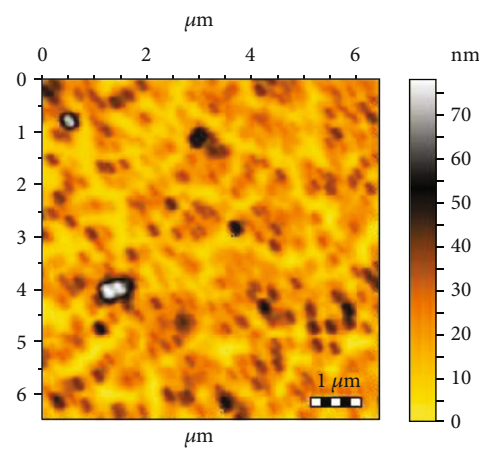


FIGURE 6: AFM image of ethanol AgNPs of *R. stricta*.

TABLE 2: Antioxidant activity of ethanol crude extract and AgNPs of *R. stricta*.

Concentration ($\mu\text{g/mL}$)	Antioxidant activity	
	Ethanol crude extract	AgNPs
40	29.05	80.28
60	29.32	86.32
80	37.23	87.72
100	50.00	87.94
150	56.81	88.37

of time, and UV-visible spectra were noted. It was observed that with the passage of time, the number and uniformity of NPs were increased which was cleared from the increase in the absorbance of the graph (Figure 2).

TABLE 3: Antibacterial activity of crude extract and synthesized AgNPs.

Microorganisms	Zone of inhibition in mm		
	Crude ethanol extract	AgNPs	Streptomycin
<i>Klebsiella pneumonia</i>	16	14	26
<i>Staphylococcus aureus</i>	15	0	28
<i>Bacillus subtilis</i>	14	0	28

TABLE 4: Analgesic effect of extract and AgNPs.

Treatment	Dose (mg/kg)	Percent inhibition of writhing
Normal saline	10 mL/kg	—
Diclofenac sodium	10	85.00 ± 1.00***
	10	40.09 ± 2.09
	25	54.32 ± 1.76
	50	67.09 ± 1.34
Crude extract	100	79.98 ± 1.54
	2.5	43.87 ± 1.09
	5	56.97 ± 1.07
	10	69.23 ± 1.03
AgNPs	15	83.23 ± 1.00

The data collected are denoted as the mean ± for all animals, tolerance to thermal stimuli in sec. The level of significance was identified by ANOVA followed by Dunnett's screening model. Here *** $p < 0.01$.

For the effect of temperature on synthesized NPs, temperature variation was carried out during the synthesis. The NPs were synthesized at different temperature, and UV-visible spectra were obtained (Figure 3).

3.2. FTIR Analysis. FTIR analysis was used to confirm the synthesis of AgNPs in plant crude extract and the presence of different functional groups. FTIR spectra of the plant crude ethanol extract (Figure 4) showed the O-H bond stretching in the region of 3500-3700 cm^{-1} and C-H stretching in the range of 3500-3000 cm^{-1} . The band appeared in between 2500 and 3000 cm^{-1} showed =C-H bond stretching while the stretching for C-H bonds appeared from 1500 to 1700 cm^{-1} , and N-H bond stretching peak appeared from 1400 to 1450 cm^{-1} . The results of FTIR analysis for ethanol AgNPs were shown in Figure 5 where it was noticed that the bands present in the plant crude ethanol extract were found to be absent in the ethanol AgNP spectra. The absence of these bands showed the reduction of Ag^+ ions and the development of silver complexes. The synthesis of ethanol AgNPs was confirmed by the appearance of a broad band in the range of 450-550 cm^{-1} [54].

3.3. AFM Analysis. The shape, morphology, and size of the synthesized AgNPs were studied by atomic force microscopy (AFM). The AFM image (Figure 6) of ethanol AgNPs showed that the NPs possess spherical shape with the calculated sizes 0.1-0.5 μm of AgNPs.

3.4. Biological Activities. *R. stricta* crude extracts and AgNPs of *R. stricta* were subjected to various biological activities to assess and explore their medicinal value.

3.4.1. Antioxidant Effect. The antioxidant activity of ethanol crude extract and AgNPs was determined by their free radical scavenging property against vitamin C (Table 2). The AgNPs displayed a promising effect against DPPH in a fixation subordinate way. The AgNPs showed significant movement of 88.37% and 87.94% at 100 $\mu\text{g}/\text{mL}$ whereas crude ethanol extracts also exhibited excellent activity which was found to be increased from 26.44% to 56.81% along with the increase of concentration from 20 to 150 $\mu\text{g}/\text{mL}$. Generally, the NPs showed good activity than crude ethanol extract.

3.4.2. Antibacterial Activity. The tested samples (extract and AgNPs) against the bacterial strains demonstrated a little antibacterial effect as shown in Table 3. The maximum activity was noted against the Gram-positive bacteria (*Staphylococcus aureus*) was 15 and 0 mm while against Gram-negative bacteria (*Klebsiella pneumonia*) was found to be 16 and 14 mm, respectively, whereas against *Bacillus subtilis*, a poor activity was recorded as 14 and 0 mm, respectively.

3.5. Analgesic Activity. Both the tested samples demonstrated a significant analgesic effect as shown in Table 4. The effect was dose dependent, and a higher attenuation in induced writhing was recorded against higher doses. The percent effect of extract (100 mg/kg) and AgNPs (15 mg/kg) was 79.98 and 83.23, respectively.

3.6. Muscle Relaxant Effect. A dose and time dependent effect was observed against the extract and AgNPs. The muscle coordination effect was not significant in both tested models. However, the maximum muscle coordination effect of extract in inclined plan and traction test was 44 and 38% at higher dose, respectively. A similar muscle relaxant effect was noted against AgNPs as shown in Table 5.

3.7. Sedative Effect. A mild sedative effect was also noted against extract and AgNPs. The significant ($p < 0.05$) effect of extract was noted at 100 mg/kg as shown in Table 6. The effect of AgNPs was more significant ($p < 0.01$) at the tested dose of 15 mg/kg.

4. Discussion

This multiindication, along with safety profile, attracts the researcher for the development and discovery of new, safe, and effective natural products as medicines. It is the confluence of biology and nanotechnology that is known as nanobiotechnology. Recent discoveries revealed novel and interesting biological processes for the production of nano-silver using microorganisms or botanic materials as possible bioreducers and biocappers, as well as new and fascinating biological techniques for the production of nanosilver [55, 56]. The phytochemical study of this plant revealed the accumulation of various constituents of various classes. These chemical constituents are the main biomolecules for the curing of various ailments [57, 58].

TABLE 5: Muscle relaxant activity of extract and AgNPs.

Group	Dose (mg/kg)	Inclined plan test (% activity)			Traction test (% activity)		
		30 min	60 min	90 min	30 min	60 min	90 min
Distilled water	10 mL	0.00 ± 0	0.00 ± 0	0.00 ± 0	0.00 ± 0	0.00 ± 0	0.00 ± 0
Diazepam	1	100 ± 0.00	100 ± 0.00	100 ± 0.00	100 ± 0.0	100 ± 0.00	100 ± 0.00
Crude extract	10	19.22 ± 1.45	25.86 ± 1.72	28.94 ± 1.09	19.34 ± 1.56	20.34 ± 1.45	19.91 ± 1.24
	25	23.77 ± 1.32	29.98 ± 1.83	34.09 ± 1.00	24.97 ± 1.37	25.77 ± 1.56	24.99 ± 1.44
	50	29.34 ± 1.09	34.90 ± 1.22	36.45 ± 1.34	29.44 ± 1.22	30.34 ± 1.60	32.00 ± 1.45
	100	37.28 ± 1.21	43.29 ± 1.45	44.40 ± 1.09	38.39 ± 1.66	38.99 ± 1.23	34.93 ± 1.98
AgNPs	2.5	24.09 ± 1.98	30.44 ± 1.23	31.49 ± 1.66	25.61 ± 1.61	26.32 ± 1.09	24.80 ± 1.98
	5	30.23 ± 1.84	34.51 ± 1.27	35.40 ± 1.89	30.81 ± 1.64	31.83 ± 1.56	30.77 ± 1.45
	10	35.17 ± 1.66	38.19 ± 1.32	43.11 ± 1.94	35.32 ± 1.33	36.82 ± 1.41	35.58 ± 1.09
	15	40.02 ± 1.30	44.43 ± 1.34	46.17 ± 1.33	40.09 ± 1.23	41.98 ± 1.39	40.14 ± 1.23

The data collected are denoted as the mean ± for all animals, tolerance to thermal stimuli in sec. The level of significance we identified by ANOVA followed by Dunnett's screening model.

TABLE 6: Sedative activity of extract and AgNPs in open field screening (locomotive activity).

Treatment	Dose (mg/kg)	No of line crossed in 10 min
Distilled water	10	125.00 ± 1.07
Diazepam	0.5	6.22 ± 1.05***
Crude extract	10	121.02 ± 2.67
	25	109.88 ± 2.44
	50	99.45 ± 2.45
	100	88.09 ± 1.60*
AgNPs	2.5	99.54 ± 1.43
	5	88.32 ± 1.43*
	10	76.09 ± 1.27*
	15	64.32 ± 1.30**

The data collected are denoted as the mean ± for all animals, tolerance to thermal stimuli in sec. The level of significance we identified by ANOVA following by Dunnett's screening model. Here, *** $p < 0.01$ and * $p < 0.05$.

The extract and NPs of *R. stricta* inhibited various pathogenic bacteria which confirm the use of this plant in various infections. The present study showed that AgNPs and crude extract significantly inhibited the Gram-negative and Gram-positive bacteria while higher doses of AgNPs and crude extract exhibited analgesic effect bolstered by inhibition of writhing [59]. Additional experiments also revealed that both of the entities are of muscle relaxant and sedative potential. In most of the cases, infection is associated with fever and pain. Fortunately, this plant is found to have significant analgesic activity. This analgesic effect provides adjuvant to the antibacterial effect. The painkiller potential is always parallel to the antipyretic and anti-inflammatory effect [60, 61]. The reason behind it is the conversion of arachidonic acid into prostaglandins (PGs) which leads to the

analgesic, pyrexia, and inflammatory condition. The current tested plant might be PGs blocker by inhibition of cyclooxygenase (COX) [40, 43, 44, 62]. To confirm the analgesic, antipyretic, and anti-inflammatory, further study is needed to check the COX inhibition by this plant extract/NPs. The mild muscle relaxation effect is also a very good indication along with analgesic property [46, 47, 63]. In most of the painful conditions, muscle relaxation is needed; therefore, if a plant extract is painkiller along with muscle relaxant effect, making it a best option to use as analgesic. The antioxidant effect is also worth mentioning. The free radical scavenging effect is responsible for the blockage of ample of diseases [64, 65].

AgNPs were synthesized from methanol extract of *R. stricta* root with the help of silver nitrate. The AgNPs were found to be 20 nm in size and of spherical shape having potential inhibitory activity against Gram-negative and Gram-positive bacteria [50]. Another study revealed that AgNPs from *R. stricta* are toxic to dengue and malaria containing mosquitos. In addition, it is capable of inhibiting bacteria that are capable to induce fatal diseases to the body [54]. Streptozotocin-induced Swiss albino mice were administered AgNPs from alkaloid extract of *R. stricta*. The dose containing the NPs significantly reduces the glucose in the blood stream as well as the reactive oxygen species to a greater extent [59, 66, 67].

5. Conclusions

To summarize, the biosynthesis of AgNPs using *Rhazya stricta* leaves extract is a simple, eco-friendly, convenient, and cost-effective technique of synthesis. The synthesized AgNPs were spherical in form and ranged in size from 1 to 10 m. The FTIR, UV-vis spectrometer, and AFM characterization techniques revealed that the larger of the NPs was found surrounded by a thin layer of proteins and metabolites such as terpenoids containing functional groups such as ketones, amines, aldehydes, and alcohols. The findings indicate that the form of

the NPs is regulated by the ratio of plant extract to metal ion concentration. Metal ion reduction is crucial in deciding the size of NPs at various concentrations. AgNPs and the crude extract of *Rhazya stricta* exhibited antioxidant, antibacterial, sedative, and analgesic activity. These pharmacological findings corroborate the folklore beliefs about this plant's efficacy in a variety of health ailments.

Data Availability

Available data are presented in the manuscript.

Conflicts of Interest

The authors declare that they have no conflicts of interest.

Authors' Contributions

Sami Bawazeer, Abdur Rauf, and Talha Bin Emran did the conceptualization, investigation, supervision, formal analysis, methodology, validation, writing—original draft, writing—review and editing, and visualization. Ajmal Khan did the investigation, methodology, validation, and writing—review and editing. Abdullah S. M. Aljohani and Fahad A. Alhumaydhi did the project administration, visualization, and writing—review and editing. Zidan Khan and Laiba Ahmad did the formal analysis, validation, and writing—review and editing. Rohit Sharma did the formal analysis, validation, resources, and writing—review and editing. Naveed Muhammad and Aneela Maalik Ibrahim Khan did the data curation, formal analysis, validation, resources, writing—original draft, and editing.

Funding

The authors would like to thank the Deanship of Scientific Research at Umm Al-Qura University for supporting this work by Grant Code: (22UQU4350073DSR05).

References

- [1] M. Rai, A. Yadav, and A. Gade, "Silver nanoparticles as a new generation of antimicrobials," *Biotechnology Advances*, vol. 27, no. 1, pp. 76–83, 2009.
- [2] A. Vaseashta and D. Dimova-Malinovska, "Nanostructured and nanoscale devices, sensors and detectors," *Science and Technology of Advanced Materials*, vol. 6, no. 3-4, pp. 312–318, 2005.
- [3] D. Anderson and M. Moskovits, "A SERS-active system based on silver nanoparticles tethered to a deposited silver film," *The Journal of Physical Chemistry B*, vol. 110, no. 28, pp. 13722–13727, 2006.
- [4] R. Sharma and P. K. Prajapati, "Nanotechnology in medicine: leads from Ayurveda," *Journal of Pharmacy and Bioallied Sciences*, vol. 8, no. 1, pp. 80–81, 2016.
- [5] R. Sharma and P. K. Prajapati, "Liquid media's in Bhavana Samskara: a pharmaceutico-therapeutic prospect," *The Journal of Phytopharmacology*, vol. 4, no. 1, pp. 49–57, 2015.
- [6] V. N. Sonkusare, R. G. Chaudhary, G. S. Bhusari et al., "Mesoporous octahedron-shaped tricobalt tetroxide nanoparticles for photocatalytic degradation of toxic dyes," *ACS Omega*, vol. 5, no. 14, pp. 7823–7835, 2020.
- [7] A. Khalid, P. Ahmad, A. Khan et al., "Effect of Cu Doping on ZnO Nanoparticles as a Photocatalyst for the Removal of Organic Wastewater," *Bioinorganic Chemistry and Applications*, vol. 2022, Article ID 9459886, p. 12, 2022.
- [8] R. Bakry, R. M. Vallant, M. Najam-ul-Haq et al., "Medicinal Applications of Fullerenes," *International Journal of Nano-medicine*, vol. 2, no. 4, pp. 639–649, 2007.
- [9] C. Pandit, A. Roy, S. Ghotekar et al., "Biological agents for synthesis of nanoparticles and their applications," *Journal of King Saud University-Science*, vol. 34, p. 101869, 2022.
- [10] C. L. Rock, R. A. Jacob, and P. E. Bowen, "Update on the biological characteristics of the antioxidant micronutrients: vitamin C, vitamin E, and the carotenoids," *Journal of the American Dietetic Association*, vol. 96, no. 7, pp. 693–702, 1996.
- [11] A. Roy, A. Elzaki, V. Tirth et al., "Biological synthesis of nanocatalysts and their applications," *Catalysts*, vol. 11, no. 8, p. 1494, 2021.
- [12] R. Sharma, K. Kuca, E. Nepovimova, A. Kabra, M. M. Rao, and P. K. Prajapati, "Traditional Ayurvedic and herbal remedies for Alzheimer's disease: from bench to bedside," *Expert Review of Neurotherapeutics*, vol. 19, no. 5, pp. 359–374, 2019.
- [13] M. Rahman, F. Islam, S. Afsana Mim et al., "Multifunctional Therapeutic Approach of Nanomedicines against Inflammation in Cancer and Aging," *Journal of Nanomaterials*, vol. 2022, Article ID 4217529, p. 19, 2022.
- [14] D. Shah, M. Gandhi, A. Kumar, N. Cruz-Martins, R. Sharma, and S. Nair, "Current insights into epigenetics, noncoding RNA interactome and clinical pharmacokinetics of dietary polyphenols in cancer chemoprevention," *Critical Reviews in Food Science and Nutrition*, vol. 26, pp. 1–37, 2021.
- [15] M. P. Mattson, "Apoptosis in neurodegenerative disorders," *Nature Reviews Molecular Cell Biology*, vol. 1, no. 2, pp. 120–130, 2000.
- [16] B. Halliwell, "How to characterize an antioxidant: an update," *Biochemical Society Symposium*, vol. 61, pp. 73–101, 1995.
- [17] N. I. Krinsky, "Mechanism of action of biological antioxidants," *Proceedings of the Society for Experimental Biology and Medicine*, vol. 200, no. 2, pp. 248–254, 1992.
- [18] M. N. Islam, A. Rauf, F. I. Fahad et al., "Superoxide dismutase: an updated review on its health benefits and industrial applications," *Critical Reviews in Food Science and Nutrition*, vol. 2021, pp. 1–19, 2021.
- [19] J. V. Bannister, W. H. Bannister, and G. Rotilio, "Aspects of the structure, function, and applications of superoxide dismutase," *Critical Reviews in Biochemistry*, vol. 22, no. 2, pp. 111–180, 1987.
- [20] H. Chopra, S. Bibi, A. K. Mishra et al., "Nanomaterials: a promising therapeutic approach for cardiovascular diseases," *Journal of Nanomaterials*, vol. 2022, Article ID 4155729, 25 pages, 2022.
- [21] R. Sharma, N. Martins, K. Kuca et al., "Chyawanprash: a traditional Indian bioactive health supplement," *Biomolecules*, vol. 9, no. 5, p. 161, 2019.
- [22] R. Sharma, "Molecular targets of common Ayurvedic herbal antioxidants," *Journal of Ayurvedic and Herbal Medicine*, vol. 3, no. 1, pp. 33–37, 2017.
- [23] T. P. Devasagayam, J. C. Tilak, K. K. Bloor, K. S. Sane, S. S. Ghaskadbi, and R. D. Lele, "Free radicals and antioxidants in

- human health: current status and future prospects,” *Japi*, vol. 52, article 794804, p. 4, 2004.
- [24] W. M. Scheld, “Introduction to microbial disease: host-pathogen interactions,” *Goldman’s Cecil Medicine*, vol. 2, p. 1761, 2012.
- [25] C. L. Ventola, “The antibiotic resistance crisis: part 1: causes and threats,” *Pharmacy and Therapeutics*, vol. 40, no. 4, pp. 277–283, 2015.
- [26] M. S. Khalil, M. Shakeel, N. Gulfam et al., “Fabrication of Silver Nanoparticles from Ziziphus nummularia Fruit Extract: Effect on Hair Growth Rate and Activity against Selected Bacterial and Fungal Strains,” *Journal of Nanomaterials*, vol. 2022, Article ID 3164951, 14 pages, 2022.
- [27] American Academy of Sleep Medicine, *The international classification of sleep disorders: diagnostic & coding manual*, American Academy of Sleep Medicine, Westchester, IL, 2005.
- [28] M. M. Ohayon and C. F. Reynolds, “Epidemiological and clinical relevance of insomnia diagnosis algorithms according to the DSM-IV and the international classification of sleep disorders (ICSD),” *Sleep Medicine*, vol. 10, no. 9, pp. 952–960, 2009.
- [29] T. Roth, C. Coulouvrat, G. Hajak et al., “Prevalence and perceived health associated with insomnia based on DSM-IV-TR; international statistical classification of diseases and related health problems, tenth revision; and research diagnostic criteria/international classification of sleep disorders, second edition criteria: results from the America Insomnia Survey,” *Biological Psychiatry*, vol. 69, no. 6, pp. 592–600, 2011.
- [30] M. M. Ohayon, “Epidemiology of insomnia: what we know and what we still need to learn,” *Sleep Medicine Reviews*, vol. 6, no. 2, pp. 97–111, 2002.
- [31] C. M. Morin, M. LeBlanc, L. Bélanger, H. Ivers, C. Mérette, and J. Savard, “Prevalence of insomnia and its treatment in Canada,” *The Canadian Journal of Psychiatry*, vol. 56, no. 9, pp. 540–548, 2011.
- [32] G. Al Karaki, S. Hallit, D. Malaeb et al., “Prevalence and factors associated with insomnia among a representative sample of the Lebanese population: results of a cross-sectional study,” *Journal of Epidemiology and Global Health*, vol. 10, no. 2, pp. 124–130, 2020.
- [33] F. Islam, J. F. Khadija, R. Islam et al., “Investigating Polyphenol Nanoformulations for Therapeutic Targets against Diabetes Mellitus,” *Evidence-Based Complementary and Alternative Medicine*, vol. 2022, Article ID 5649156, 16 pages, 2022.
- [34] R. L. Nahin, “Estimates of pain prevalence and severity in adults: United States, 2012,” *The Journal of Pain*, vol. 16, no. 8, pp. 769–780, 2015.
- [35] D. S. Goldberg and S. J. McGee, “Pain as a global public health priority,” *BMC Public Health*, vol. 11, no. 1, pp. 1–5, 2011.
- [36] D. A. Queremel Milani and D. D. Davis, *Pain Management Medications*, StatPearls Publishing, Treasure Island (FL), 2020.
- [37] L. Christensen, S. Vivekanandhan, M. Misra, and A. Kumar Mohanty, “Biosynthesis of silver nanoparticles using *murraya koenigii* (curry leaf): an investigation on the effect of broth concentration in reduction mechanism and particle size,” *Advanced Materials Letters*, vol. 2, no. 6, pp. 429–434, 2011.
- [38] F. Islam, S. Shohag, M. J. Uddin et al., “Exploring the Journey of Zinc Oxide Nanoparticles (ZnO-NPs) toward Biomedical Applications,” *Materials*, vol. 15, p. 2160, 2022.
- [39] O. Bahattab, I. Khan, S. Bawazeer et al., “Synthesis and biological activities of alcohol extract of black cumin seeds (*Bunium persicum*)-based gold nanoparticles and their catalytic applications,” *Green Processing and Synthesis*, vol. 10, no. 1, pp. 440–455, 2021.
- [40] N. A. Baeshen, S. A. Lari, H. A. Aldoghaither, and A. I. Elkady, “Biochemical evaluation of the effect of *Rhazya stricta* aqueous leaves extract in liver and kidney functions in rats,” *Natural Science*, vol. 8, no. 4, pp. 136–142, 2010.
- [41] D. MubarakAli, N. Thajuddin, K. Jeganathan, and M. Gunasekaran, “Plant extract mediated synthesis of silver and gold nanoparticles and its antibacterial activity against clinically isolated pathogens,” *Colloids and Surfaces B: Biointerfaces*, vol. 85, no. 2, pp. 360–365, 2011.
- [42] H. Chopra, S. Bibi, I. Singh et al., “Green Metallic Nanoparticles: Biosynthesis to Applications,” *Frontiers in Bioengineering and Biotechnology*, vol. 10, p. 548, 2022.
- [43] B. Ahmad, F. Shireen, A. Rauf et al., “Phyto-fabrication, purification, characterisation, optimisation, and biological competence of nano-silver,” *IET Nanobiotechnology*, vol. 15, no. 1, pp. 1–18, 2021.
- [44] G. M. Saleh, “Green synthesis concept of Nanoparticles from environmental bacteria and their effects on pathogenic bacteria,” *Iraqi Journal of Science*, vol. 61, pp. 1289–1297, 2020.
- [45] M. J. Milner and L. V. Kochian, “Investigating heavy-metal hyperaccumulation using *Thlaspi caerulescens* as a model system,” *Annals of Botany*, vol. 102, no. 1, pp. 3–13, 2008.
- [46] A. Shehzad, M. Qureshi, S. Jabeen et al., “Synthesis, characterization and antibacterial activity of silver nanoparticles using *Rhazya stricta*,” *PeerJ*, vol. 6, article e6086, 2018.
- [47] A. T. Aziz, M. A. Alshehri, N. A. Alanazi et al., “Phytochemical analysis of *Rhazya stricta* extract and its use in fabrication of silver nanoparticles effective against mosquito vectors and microbial pathogens,” *Science of the Total Environment*, vol. 700, article 134443, 2020.
- [48] M. A. Ashehri, “Potential antidiabetic and anti-genotoxic activities of silver nanoparticles of alkaloid extract of *Rhazya stricta* in rat animal model,” *Phyton*, vol. 90, no. 6, pp. 1749–1762, 2021.
- [49] Z. Al Mahmud, T. B. Emran, N. Qais, S. C. Bachar, M. Sarker, and M. M. N. Uddin, “Evaluation of analgesic, anti-inflammatory, thrombolytic and hepatoprotective activities of roots of *Premna esculenta* (Roxb),” *Journal of Basic and Clinical Physiology and Pharmacology*, vol. 27, no. 1, pp. 63–70, 2016.
- [50] I. Khan, S. Bawazeer, A. Rauf et al., “Synthesis, biological investigation and catalytic application using the alcoholic extract of black cumin (*Bunium Persicum*) seeds-based silver nanoparticles,” *Journal of Nanostructure in Chemistry*, vol. 12, no. 1, pp. 59–77, 2022.
- [51] H. M. Ahmed, A. Roy, M. Wahab et al., “Applications of nanomaterials in agrifood and pharmaceutical industry,” *Journal of Nanomaterials*, vol. 2021, Article ID 1472096, 10 pages, 2021.
- [52] L. Leaves and L. Leaves, “Antioxidant activity by DPPH radical scavenging method of *ageratum conyzoides*,” *American Journal of Ethnomedicine*, vol. 1, no. 4, pp. 244–249, 2014.
- [53] G. Kumar, L. Karthik, and K. V. B. Rao, “Antibacterial activity of aqueous extract of *Calotropis gigantea* leaves—an in vitro study,” *International Journal of Pharmaceutical Sciences Review and Research*, vol. 4, no. 2, pp. 141–144, 2010.
- [54] A. K. Potbhare, R. G. Chaudhary, P. B. Chouke et al., “Phyto-synthesis of nearly monodisperse CuO nanospheres using *Phyllanthus reticulatus/Conyza bonariensis* and its

- antioxidant/antibacterial assays,” *Materials Science and Engineering: C*, vol. 99, pp. 783–793, 2019.
- [55] A. Al Gonemi, *Encyclopaedia of the United Arab Emirates Plants Used in Folk Medicine*, United Arab Emirates University Press, Al-Ain, 1992.
- [56] B. Ali, “The effect of treatment with the medicinal plant *Rhazya stricta* Decne on gentamicin nephrotoxicity in rats,” *Phyto-medicine*, vol. 9, no. 5, pp. 385–389, 2002.
- [57] S. A. Gilani, A. Kikuchi, Z. K. Shinwari, Z. I. Khattak, and K. N. Watanabe, “Phytochemical, pharmacological and ethnobotanical studies of *Rhazya stricta* Decne,” *Phytotherapy Research*, vol. 21, no. 4, pp. 301–307, 2007.
- [58] N. Muhammad, M. Saeed, and H. Khan, “Antipyretic, analgesic and anti-inflammatory activity of *Viola betonicifolia* whole plant,” *BMC Complementary and Alternative Medicine*, vol. 12, no. 1, pp. 1–8, 2012.
- [59] M. S. Umekar, G. S. Bhusari, A. K. Potbhare et al., “Bioinspired reduced graphene oxide based nanohybrids for photocatalysis and antibacterial applications,” *Current Pharmaceutical Biotechnology*, vol. 22, no. 13, pp. 1759–1781, 2021.
- [60] R. Rajan, K. Chandran, S. L. Harper, S. I. Yun, and P. T. Kalai-chelvan, “Plant extract synthesized silver nanoparticles: an ongoing source of novel biocompatible materials,” *Industrial Crops and Products*, vol. 70, pp. 356–373, 2015.
- [61] A. Zahoor, S. Sharma, and G. Khuller, “Inhalable alginate nanoparticles as antitubercular drug carriers against experimental tuberculosis,” *International Journal of Antimicrobial Agents*, vol. 26, no. 4, pp. 298–303, 2005.
- [62] A. K. Jha, K. Prasad, and A. Kulkarni, “Synthesis of TiO_2 nanoparticles using microorganisms,” *Colloids and Surfaces B: Biointerfaces*, vol. 71, no. 2, pp. 226–229, 2009.
- [63] M. Markets, “Metalnanoparticless market by metal (platinum, gold, silver, iron, titanium, copper, nickel), end-use industry (pharmaceutical & healthcare, electrical & electronics, catalyst, personal care & cosmetics), and region-global forecast to 2022,” *Marketing Research Report*, vol. 4489142, 2018.
- [64] M. Bilal, T. Rasheed, H. M. N. Iqbal, C. Li, H. Hu, and X. Zhang, “Development of silver nanoparticles loaded chitosan-alginate constructs with biomedical potentialities,” *International Journal of Biological Macromolecules*, vol. 105, Part 1, pp. 393–400, 2017.
- [65] S. Basu, P. Maji, and J. Ganguly, “Rapid green synthesis of silver nanoparticles by aqueous extract of seeds of *Nyctanthes arbor-tristis*,” *Applied Nanoscience*, vol. 6, no. 1, pp. 1–5, 2016.
- [66] M. S. H. Kabir, M. M. Hossain, M. I. Kabir et al., “Phytochemical screening, Antioxidant, Thrombolytic, alpha-amylase inhibition and cytotoxic activities of ethanol extract of *Steudnera colocasiiifolia* K. Koch leaves,” *Journal of Young Pharmacists*, vol. 8, no. 4, p. 391, 2016.
- [67] T. Dutta, A. Paul, M. Majumder, R. A. Sultan, and T. B. Emran, “Pharmacological evidence for the use of *Cissus assamica* as a medicinal plant in the management of pain and pyrexia,” *Biochemistry and Biophysics Reports*, vol. 21, article 100715, 2020.

Research Article

Dynamic Beam Switching by the Highly Sensitive Metasurface Composed of All-Metallic Split-Ring Resonators

Wenrong Si ¹, Chenzhao Fu ¹, Fengyuan Gan ², Dun Lan ², and Wei Li ²

¹State Grid Shanghai Electrical Power Research Institute, Shanghai 200437, China

²State Key Laboratory of Functional Materials for Informatics, Shanghai Institute of Microsystem and Information Technology, CAS, Shanghai 200050, China

Correspondence should be addressed to Wei Li; waylee@mail.sim.ac.cn

Received 1 May 2022; Revised 9 June 2022; Accepted 21 June 2022; Published 14 July 2022

Academic Editor: Hiwa M. Ahmed

Copyright © 2022 Wenrong Si et al. This is an open access article distributed under the Creative Commons Attribution License, which permits unrestricted use, distribution, and reproduction in any medium, provided the original work is properly cited.

The development of metasurfaces capable of arbitrarily manipulating electromagnetic waves has created new opportunities for various applications. However, most tunable metasurface devices via different modulation techniques exhibit large fabrication difficulties or narrow bandwidths. Here, we use the all-metallic split-ring resonator to design a dynamically tunable metasurface that is highly sensitive to the ambient refractive index and capable of broadband beam switching. Different from the previous optical scatters, the split-ring resonator is put on the metal substrate. Due to the existence of metallic substrate and large interaction of corner modes, the proposed resonator has small ohmic loss and high sensitivity to the ambient refractive index. By arraying the all-metallic split-ring resonators with different parameters, dynamic beam switching of anomalous reflection is demonstrated numerically. In particular, the designed metasurface exhibits the dynamic beam switching in a broadband wavelength range of $\Delta\lambda \approx 100$ nm. Such an all-metallic metasurface with high sensitivity can greatly reduce the designing difficulty of the tunable optical devices. The dynamic metadevices may find potential applications in stealth camouflage, information encryption, and data storage.

1. Introduction

Metasurfaces are a two-dimensional array structure composed of artificially designed optical scatterers with subwavelength size. Due to the excellent wavefront controlling capability and spatial resolution [1, 2], functional metadevices hold great promise in next-generation wearable devices and thin optical systems for imaging and sensing. They find important applications in the fields of stealth camouflage [3], virtual/augmented reality [4, 5], biosensing [6], and color display [7]. However, because metasurfaces with discontinuous phase distributions are not sensitive to changes in ambient refractive index, most metadevices are static and have a single function. A dynamically tunable metasurface is more flexible and can further expand the application of metasurface functional devices [8–10].

In recent years, some studies have been conducted on developing dynamic metasurface devices via different modulation techniques. For example, the hydrogenation and

dehydrogenation reactions of magnesium were utilized to design dynamic metasurface holograms, which could be used for optical information processing and encryption [11, 12]. However, the magnesium hydrogenation and dehydrogenation reactions are time-consuming, and hydrogen is highly combustible and dangerous, which is not suitable for widespread application. By stretching the polydimethylsiloxane substrate to change the lattice constant of the Au nanorod array, a metasurface zoom lens of the continuous focal length change from $150 \mu\text{m}$ to $250 \mu\text{m}$ was realized [13]. By utilizing the phase change material, plasmonic metasurfaces for beam switching and bifocal lensing [14] and mid-infrared tunable metasurface capable of broad transmittance spectral shift of 500 nm [15] were successfully demonstrated. However, the metasurfaces in these works are composed of different materials, including elastic material/phase change material and metallic material, which increase the complexity of the structure and the difficulty of fabrication. Based on the nonlinear Kerr effect, a 2D high-Q metalens, which

consisted of Si nanoantennas including the subtle and periodic perturbations, with focal lengths varying from 4 to $6.5\ \mu\text{m}$ was realized [16]. By using the birefringence effect of liquid crystal molecules, dynamic beam switching with an efficiency of 50% is achieved based on the Si nanodisk [17]. However, these two metasurface structures exhibit a narrow-band response due to the resonant effect. Therefore, the realization of broadband and easily manufacturable dynamic metasurface still remains a challenging problem.

In the study, a highly sensitive metasurface is designed based on the all-metallic split-ring resonator, and the dynamically tunable beam switching with a broadband response is demonstrated. Here, the all-metal split-ring resonator can support symmetric and antisymmetric surface plasmon polariton (SPP) modes. Different from the previous optical scatterers placed on dielectric substrates, the powers of two SPP modes are mainly distributed in the external environment ($>95\%$) due to the existence of a metallic substrate and the large interaction of corner modes. As a result, both resonant modes have small ohmic loss and high sensitivity to the ambient refractive index. With the change of the ambient medium from water to a microbubble ($|\Delta n| = 0.333$) by using the laser-induced bubble effect, the shift of reflected spectra of the resonator exceeds 200 nm. Consequently, a dynamic beam switching metasurface is demonstrated numerically by arraying the all-metallic split-ring resonators with different structural parameters. More importantly, the dynamic switching performance exhibits a broadband response (850~950 nm).

2. Principal Analysis

Figure 1(a) shows the proposed unit cell structure, where a split-ring resonator is put on a metallic substrate. Here, the material of the metallic resonator and substrate both are set to gold, and the refractive index of the ambient dielectric of the resonator is $n = 1.333$. The vertical view of the split-ring resonator is shown in the inset in Figure 1(a). The period and width of the resonator are set as $p = 400\ \text{nm}$ and $w = 50\ \text{nm}$, respectively. The opening angle and radius of the resonator are denoted by α and R , respectively. The all-metallic split-ring resonator can support symmetric and antisymmetric SPP modes [18–20]. At 45° polarized light incidence, the symmetric mode in the all-metallic resonator can be excited. The electric field distribution of the symmetric resonant mode is depicted in Figure 1(b). At 135° polarized light incidence, the antisymmetric mode in the all-metallic resonator is excited. The electric field distribution of the antisymmetric resonant mode is depicted in Figure 1(c). As can be seen from the field distribution, due to the existence of a metallic substrate and the large interaction of corner modes, the evanescent fields of the two SPP modes are mainly distributed in the ambient dielectric ($>95\%$). This value is much greater than that of the metal-dielectric and metal-dielectric-metal unit cell structures ($<55\%$) [21–24]. Therefore, the resonance mode of the all-metal split-ring resonator has small ohmic loss and high sensitivity. When the ambient dielectric changes from

water ($n = 1.333$) to a microbubble ($n = 1.0$) via the laser-induced bubble effect [25], the resonant wavelength of the all-metallic resonator shifts significantly ($>200\ \text{nm}$).

At y -polarized light incidence, the symmetric and anti-symmetric resonant modes in the all-metallic resonator are excited simultaneously according to the vector superposition principle. When the phase difference between the two resonant modes is not equal to $m\pi$ (where m is an integer), the reflected beam of the resonator contains the co-polarized (y -axis) component, as well as the cross-polarized (x -axis) component. By changing the opening angle and radius of the all-metallic split-ring resonator, the amplitude and phase of the reflected beam are efficiently modulated. Also, the phase change of the reflected beam with cross-polarization can cover a broad range from 0 to 2π . Thus, the reflected beam with cross-polarization is primarily focused. At the incident wavelength of $\lambda_0 = 850\ \text{nm}$, the calculated amplitudes and phases of the reflected beam with cross-polarization of the all-metallic resonator at different opening angles and radii when the ambient refractive indices are $n = 1.333$ and $n = 1.0$ are displayed in Figure 2. The amplitude reflections at the refractive index of the ambient dielectric of $n = 1.333$ are much larger than those at the ambient refractive index of $n = 1.0$ in the range of $120\ \text{nm} < R < 170\ \text{nm}$ and $\alpha < 270^\circ$. The phase change of the all-metallic resonator at the ambient refractive index of $n = 1.333$ can range from 0 to 2π by changing the structural parameters, while the phase change is difficult to cover the range of $0-2\pi$ at the ambient refractive index of $n = 1.0$. The dynamically tunable property is quite different from the metallic nanostructures placed on the dielectric and dielectric-metal film, which exhibits almost the same varying tendency for the amplitudes and phases under different ambient dielectrics [20]. This phenomenon confirms that the all-metallic split-ring resonator is more sensitive to the ambient dielectric than the previous metallic nanostructures. In addition, when the opening angle and radius of the all-metallic resonator are $\alpha = 100^\circ$ and $R = 150\ \text{nm}$, respectively, the amplitudes of the cross-polarization reflected beam can exceed 0.635 at the ambient refractive index of $n = 1.333$ in the wavelength range from $\lambda_0 = 850\ \text{nm}$ to $\lambda_0 = 950\ \text{nm}$. The polarization conversion efficiencies can reach up to 90%. In contrast, the amplitude of the cross-polarization reflected beam of the resonator is smaller than 0.041 when the ambient refractive index is $n = 1.0$. Therefore, by arraying all-metallic split-ring resonators with different geometry parameters, dynamic broadband metadevices with different functions can be designed based on the laser-induced bubble effect.

Based on the all-metallic split-ring resonator, we design the highly sensitive all-metallic metasurface and demonstrate broadband dynamic beam switching. The amplitude and phase of the cross-polarization reflected beam are efficiently modulated by changing the opening angle and radius of the all-metallic resonator. In consideration of the reflection efficiencies, the radius of the split-ring resonator is set as $R = 150\ \text{nm}$. At the refractive index of the ambient dielectric of $n = 1.333$, the phase change of the reflected beam with cross-polarization can still range from 0 to 2π by changing

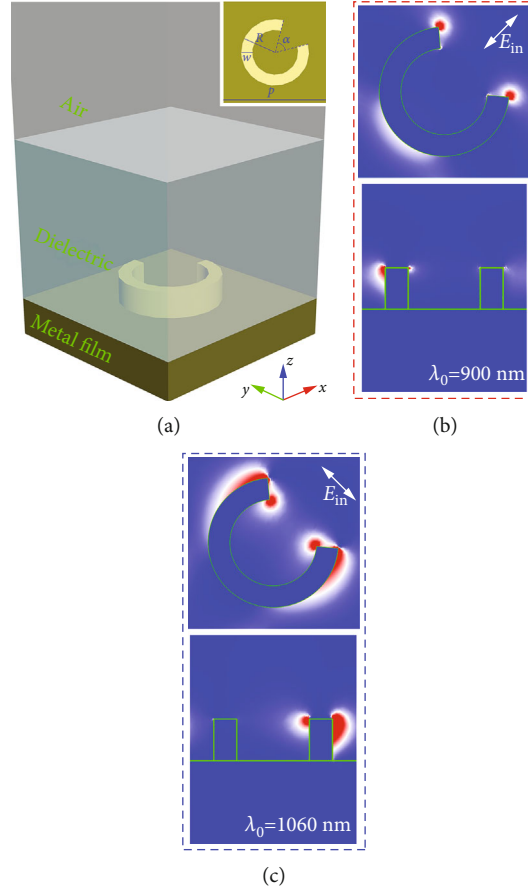


FIGURE 1: Schematic view of the structure of the split-ring resonator and field distribution diagram of the resonant modes: (a) schematic view of the structure; inset: vertical view of the resonator; (b) field distribution diagram of the symmetric resonant mode; and (c) field distribution diagram of the antisymmetric resonant mode.

the opening angle of the resonator, as displayed by the blue dotted line in Figure 3(a). The selected six-unit cells structures are shown in Figure 3(b). The opening angles of the six-unit cells are $\alpha_1 = 33^\circ$, $\alpha_2 = 90^\circ$, $\alpha_3 = 144^\circ$, $\alpha_4 = 195^\circ$, $\alpha_5 = 249^\circ$, and $\alpha_6 = 273^\circ$, respectively. The phase change of the cross-polarization reflected beam of the six-unit cells changed linearly at the ambient refractive index of $n = 1.333$. Comparatively, the phase change is smaller than 0.75π at the ambient refractive index of $n = 1.0$ (the blue solid line in Figure 3(a)). For the amplitude change, the amplitudes of cross-polarization reflected beam are greater than 0.5 at the ambient refractive index of $n = 1.333$ (black dotted line in Figure 3(a)), whereas the amplitudes are smaller than 0.05 at the ambient refractive index of $n = 1.0$ (black solid line in Figure 3(a)). The abovementioned phenomenon also shows that the all-metallic split-ring resonator is highly sensitive to changes in the ambient refractive index.

3. Design and Results

By arranging the six-unit cell structures in a sequence, the gradient metasurface is formed, as displayed in Figure 4(a). When the y -polarized light is incident on the metasurface, the reflected beam includes the normal reflected beam (co-

polarization) and anomalous reflected beam (cross-polarization). For anomalous reflected beam, the phase gradient of the metasurface interface is $d\varphi/dx = \pi/1.2 \text{ rad}/\mu\text{m}$. The reflection angle of the anomalous reflected beam can be calculated according to the following equation:

$$\theta_r = \arcsin \left(\frac{\lambda_0}{2\pi n} \frac{d\varphi}{dx} + \sin \theta_i \right), \quad (1)$$

where θ_i and θ_r represent the incident angle and anomalous reflection angle of the beam, respectively, and n represents the refractive index of the ambient dielectric. By using the finite element method, the optical performance of the gradient metasurface is studied in detail. Under the incident wavelength of $\lambda_0 = 850 \text{ nm}$ and dielectric refractive index of $n = 1.333$, anomalous reflection angle of the metasurface at different incident angles is displayed in Figure 4(b). It can be observed that in the range of $\theta_i = -20^\circ$ to 30° , the anomalous reflection angles obtained by the simulation (black dots in Figure 4(b)) agree well with the calculated results by using Equation (1) (red line in Figure 4(b)). Therefore, the gradient metasurface of anomalous reflection is demonstrated in a wide range of incident angles. At $\theta_i = -$

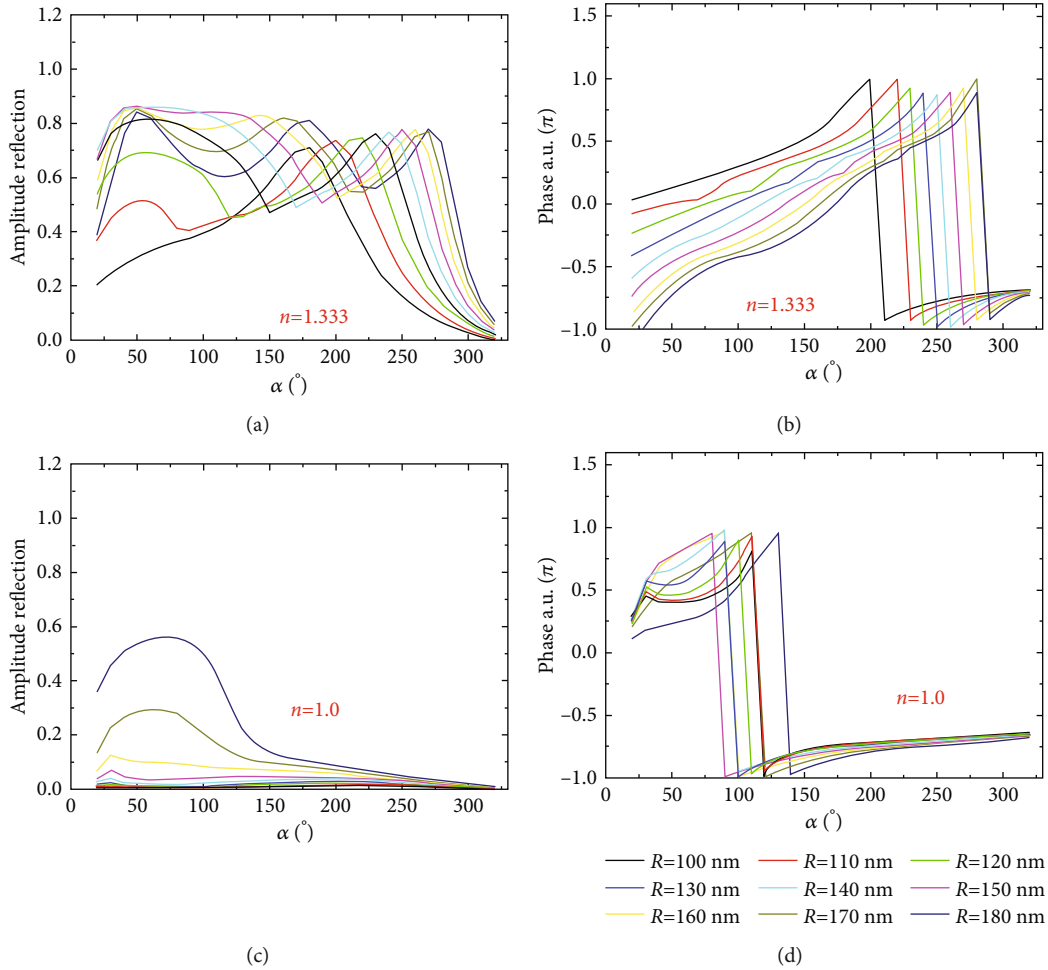


FIGURE 2: Amplitudes and phases of the cross-polarization reflected beam at different structural parameters: (a) amplitudes and (b) phases at the refractive index of the ambient dielectric of $n = 1.333$ and (c) amplitudes and (d) phases at the refractive index of the ambient dielectric of $n = 1.0$.

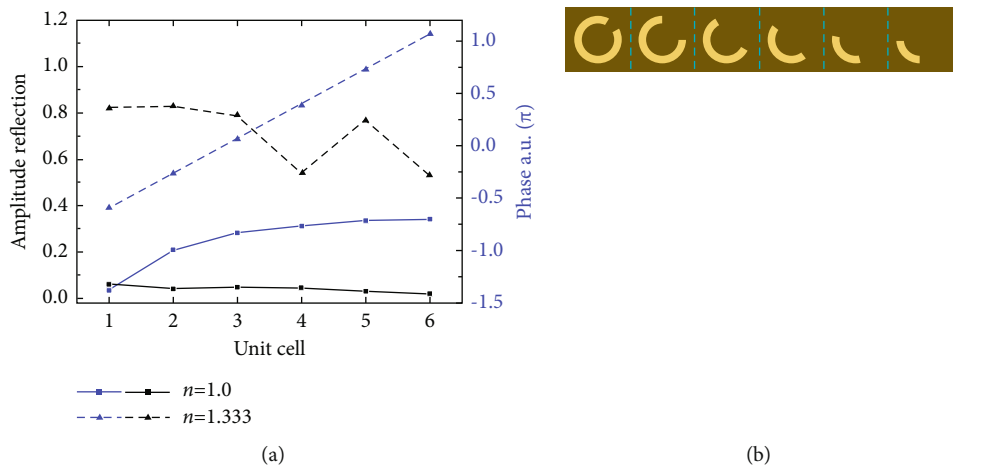


FIGURE 3: Amplitude and phase changes of the cross-polarization reflected beam of the split-ring resonator under different ambient dielectrics: (a) amplitude and phase change of the six-unit cells and (b) schematic view of the six-unit cells structures.

30°, the simulated anomalous reflection angle is different from the calculated angle, which is attributed to the nonlinear phase change of the six-unit cells at large incident angle.

By adding a large field of view phase compensation factor, the field of view of the designed gradient metasurfaces can be further increased.

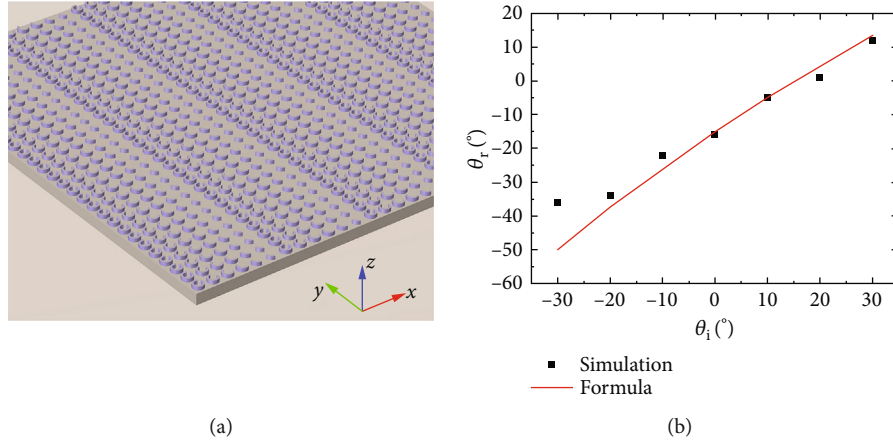


FIGURE 4: Designed dynamic metasurface and anomalous reflection phenomenon of the metasurface: (a) schematic view of the designed metasurface structure and (b) anomalous reflection angles of the metasurface at different incident angles.

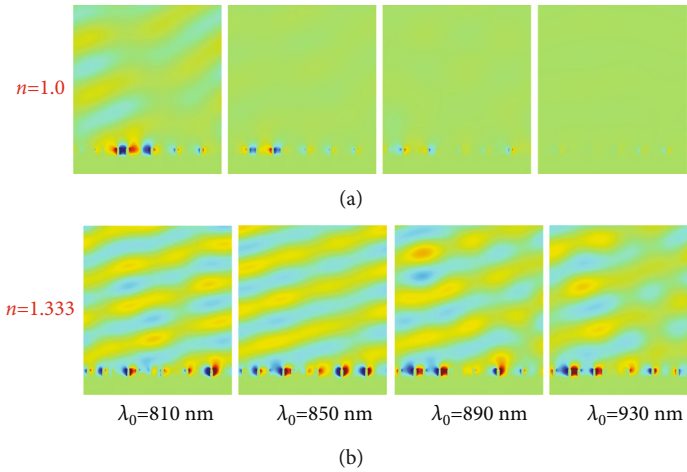


FIGURE 5: Simulation results: (a) scattering field distributions (E_x) at different incident wavelengths when the ambient refractive index is $n = 1.0$ and (b) scattering field distributions (E_x) at different incident wavelengths when the ambient refractive index is $n = 1.333$.

For the incident angle of $\theta_i = 0^\circ$, the scattering field distributions (E_x) of the metasurface at different wavelengths are shown in Figure 5. When the ambient refractive index is $n = 1.0$, the powers of cross-polarization reflected beam of the metasurface are relatively small at the wavelength of $\lambda_0 \geq 850$ nm, which is consistent with the above analysis and calculation results. In contrast, at the refractive index of the ambient dielectric of $n = 1.333$, the anomalous reflections of the cross-polarization beam are observed clearly because of the large reflection amplitude of the cross-polarization component of the resonators. Consequently, the dynamic beam switching metasurface is successfully demonstrated by changing the refractive index of the ambient dielectric. From our previous work, the ambient dielectric of the metasurface could be dynamically modulated between water ($n = 1.333$) and a microbubble ($n = 1.0$) based on the laser-induced bubble effect [25]. Moreover, the dynamic switching properties exhibit a broadband response ($\lambda_0 = 850 \sim 950$ nm), which is greater than that of dielectric metasurfaces in previous work [16, 17]. It should be noted

that the anomalous reflections of the all-metallic metasurface exhibit uneven intensity distributions when the working wavelength deviating from the optimized wavelength. By using particle swarm algorithms, the all-metallic metasurface can be optimized further at multiple working wavelengths to obtain even intensity distributions. Such a dynamic metasurface device with high sensitivity may find potential applications, such as stealth camouflage, information encryption, and data storage. By utilizing the far-field optical microscopy detection system, the beam deflection of the designed dynamic metalens can be investigated experimentally.

4. Conclusion

In summary, by arraying the all-metallic split-ring resonator with different geometry parameters, the highly sensitive gradient metasurface was designed, and dynamic beam switching was demonstrated. Here, the proposed metallic split-ring resonator could support the symmetric and antisymmetric SPP modes. Due to the existence of metallic substrate and

large interaction of corner modes, the two SPP modes exhibited lower ohmic loss and higher sensitivity than the previous optical scatterers placed on the dielectric substrate. At the refractive index of the ambient dielectric of $n = 1.333$, the amplitudes of the reflected beam with cross-polarization of the all-metallic resonator were much larger than that at the ambient refractive index of $n = 1.0$ in the range of $120 \text{ nm} < R < 170 \text{ nm}$ and $\alpha < 270^\circ$. Moreover, the phase change of the reflected beam with cross-polarization could range from 0 to 2π at the ambient refractive index of $n = 1.333$ by changing the structural parameters of the resonator. Therefore, a dynamic beam switching metasurface with a broadband response ($\Delta\lambda \approx 100 \text{ nm}$) was realized numerically by arraying the resonators with different geometry parameters. The proposed all-metallic metasurface with high sensitivity can greatly reduce the designing difficulty of the tunable optical devices. In the future, various dynamic metadevices, such as beam shapers, metasurface hologram, and planar lenses, could be designed based on the all-metallic split-ring resonators with excellent properties. These dynamic metadevices might find potential applications in stealth camouflage, information encryption, and data storage.

Data Availability

The data used to support the findings of this study are included within the article.

Conflicts of Interest

The authors declare that there is no conflict of interest regarding the publication of this paper.

Acknowledgments

This work was supported by Science and Technology Project from State Grid Shanghai Electric Power Company of No. 52094020005J.

References

- [1] N. F. Yu and F. Capasso, "Flat optics with designer metasurfaces," *Nature Materials*, vol. 13, no. 2, pp. 139–150, 2014.
- [2] M. Khorasaninejad, W. T. Chen, R. C. Devlin, J. Oh, A. Y. Zhu, and F. Capasso, "Metalenses at visible wavelengths: diffraction-limited focusing and subwavelength resolution imaging," *Science*, vol. 352, no. 6290, pp. 1190–1194, 2016.
- [3] X. J. Ni, Z. J. Wong, M. Mrejen, Y. Wang, and X. Zhang, "An ultrathin invisibility skin cloak for visible light," *Science*, vol. 349, no. 6254, pp. 1310–1314, 2015.
- [4] G. Y. Lee, J. Y. Hong, S. H. Hwang et al., "Metasurface eyepiece for augmented reality," *Nature Communications*, vol. 9, no. 1, p. 4562, 2018.
- [5] Z. Y. Li, P. Lin, Y. W. Huang et al., "Meta-optics achieves RGB-achromatic focusing for virtual reality," *Science Advances*, vol. 7, no. 5, 2021.
- [6] D. Rodrigo, O. Limaj, D. Janner et al., "Mid-infrared plasmonic biosensing with graphene," *Science*, vol. 349, no. 6244, pp. 165–168, 2015.
- [7] W. J. Joo, J. Kyoung, M. Esfandyarpour et al., "Metasurface-driven OLED displays beyond 10,000 pixels per inch," *Science*, vol. 370, no. 6515, pp. 459–463, 2020.
- [8] H. Gao, X. Fan, W. Xiong, and M. Hong, "Recent advances in optical dynamic meta-holography," *Opto-Electronic Advances*, vol. 4, no. 11, article 210030, 2021.
- [9] C. Meng, P. C. V. Thrane, F. Ding et al., "Dynamic piezoelectric MEMS-based optical metasurfaces," *Science Advances*, vol. 7, no. 26, 2021.
- [10] X. G. Zhang, W. X. Jiang, H. L. Jiang et al., "An optically driven digital metasurface for programming electromagnetic functions," *Nature Electronics*, vol. 3, no. 3, pp. 165–171, 2020.
- [11] J. X. Li, S. Kamin, G. Zheng, F. Neubrech, S. Zhang, and N. Liu, "Addressable metasurfaces for dynamic holography and optical information encryption," *Science Advances*, vol. 4, no. 6, article eaar6768, 2018.
- [12] P. Yu, J. Li, S. Zhang et al., "Dynamic janus metasurfaces in the visible spectral region," *Nano Letters*, vol. 18, no. 7, pp. 4584–4589, 2018.
- [13] H. S. Ee and R. Agarwal, "Tunable metasurface and flat optical zoom lens on a stretchable substrate," *Nano Letters*, vol. 16, no. 4, pp. 2818–2823, 2016.
- [14] X. H. Yin, T. Steinle, L. Huang et al., "Beam switching and bifocal zoom lensing using active plasmonic metasurfaces," *Light: Science & Applications*, vol. 6, no. 7, article e17016, 2017.
- [15] W. L. Dong, Y. Qiu, X. Zhou et al., "Tunable mid-infrared phase-change metasurface," *Advanced Optical Materials*, vol. 6, no. 14, article 1701346, 2018.
- [16] E. Klopfer, M. Lawrence, D. R. Barton, J. Dixon, and J. A. Dionne, "Dynamic focusing with high-quality-factor metalenses," *Nano Letters*, vol. 20, no. 7, pp. 5127–5132, 2020.
- [17] A. Komar, R. Paniagua-Domínguez, A. Miroschnichenko et al., "Dynamic beam switching by liquid crystal tunable dielectric metasurfaces," *ACS Photonics*, vol. 5, no. 5, pp. 1742–1748, 2018.
- [18] L. X. Liu, X. Zhang, M. Kenney et al., "Broadband metasurfaces with simultaneous control of phase and amplitude," *Advanced Materials*, vol. 26, no. 29, pp. 5031–5036, 2014.
- [19] X. Q. Zhang, Z. Tian, W. Yue et al., "Broadband terahertz wave deflection based on C-shape complex metamaterials with phase discontinuities," *Advanced Materials*, vol. 25, no. 33, pp. 4567–4572, 2013.
- [20] F. Y. Gan, X. Yang, Y. Zhou, and W. Li, "Wavelength-multiplexed varifocal and switchable metalens with all-metallic C-shaped antennas," *Optics and Laser Technology*, vol. 147, p. 107630, 2022.
- [21] N. F. Yu, F. Aieta, P. Genevet, M. A. Kats, Z. Gaburro, and F. Capasso, "A broadband, background-free quarter-wave plate based on plasmonic metasurfaces," *Nano Letters*, vol. 12, no. 12, pp. 6328–6333, 2012.
- [22] P. C. Wu, W. Y. Tsai, W. T. Chen et al., "Versatile polarization generation with an aluminum plasmonic metasurface," *Nano Letters*, vol. 17, no. 1, pp. 445–452, 2017.
- [23] F. Ding, Z. Wang, S. He, V. M. Shalaev, and A. V. Kildishev, "Broadband high-efficiency half-wave plate: a supercell-based plasmonic metasurface approach," *ACS Nano*, vol. 9, no. 4, pp. 4111–4119, 2015.
- [24] G. X. Zheng, H. Mühlenbernd, M. Kenney, G. Li, T. Zentgraf, and S. Zhang, "Metasurface holograms reaching 80% efficiency," *Nature Nanotechnology*, vol. 10, no. 4, pp. 308–312, 2015.
- [25] F. Y. Gan, Y. Wang, C. Sun et al., "Widely tuning surface plasmon polaritons with laser-induced bubbles," *Advanced Optical Materials*, vol. 5, no. 4, article 1600545, 2017.

Review Article

Study on Optimization of WEDM Process Parameters on Stainless Steel

**K. Natarajan,¹ H. Ramakrishnan,¹ Amel Gacem,² V. Vijayan ,³ K. Karthiga,⁴
H. Elhosiny Ali,^{5,6,7} B. Prakash,¹ and Addisalem Mekonnen ⁸**

¹Department of Mechanical Engineering, K.Ramakrishnan College of Engineering, Samayapram, Trichy, 621112 Tamil Nadu, India

²Department of Physics, Faculty of Sciences, University 20 Août 1955, BP26, 21000 Skikda, Algeria

³Department of Mechanical Engineering, K.Ramakrishnan College of Technology, Samayapram, Trichy, 621112 Tamil Nadu, India

⁴Department of Mathematics, M.Kumarasamy College of Engineering, Karur, Tamil Nadu, India

⁵Research Center for Advanced Materials Science (RCAMS), King Khalid University, Abha 61413, P.O. Box 9004, Saudi Arabia

⁶Department of Physics, Faculty of Science, King Khalid University, Abha 61413, Saudi Arabia

⁷Department of Physics, Faculty of Science, Zagazig University, Zagazig, Egypt

⁸Department of Mechanical Engineering, Faculty of Manufacturing, Institute of Technology, Hawassa University, Ethiopia

Correspondence should be addressed to Addisalem Mekonnen; addisalemm@hu.edu.et

Received 6 May 2022; Accepted 24 June 2022; Published 11 July 2022

Academic Editor: Arpita Roy

Copyright © 2022 K. Natarajan et al. This is an open access article distributed under the Creative Commons Attribution License, which permits unrestricted use, distribution, and reproduction in any medium, provided the original work is properly cited.

Stainless steel is a material which has high corrosive resistance and oxidation resistance at high temperature with the combination of chromium, nickel, and niobium as a primary constituent. This material which is difficult to machine with complex shape is taken by using wire cut electric discharge machining. Wire electrical discharge machining is a nontraditional process widely taken for cutting and machining for complex shapes. This review paper involves wire cut EDM optimization parameters. Pulse interval, pulse duration, wire feed, voltage, and mean current are the operational parameters. The Taguchi orthogonal array method, analysis of variance (ANOVA), and grey relation analysis (GRA) methods are taken for different kinds of machining various kinds of materials, and different kinds of result with best material removal rate (MRR) and surface roughness (SR) are analyzed. This work suggests the most influencing process parameters and best optimization method for various steel materials.

1. Introduction

The harder materials are preferred for the engineering jobs to increase the service of the components by modifying the surface features to advance the hardness and the abrasion resistance properties. The austenitic stainless steels are preferred for the increasing strength and for higher corrosion resistance but it is very hard to machining in the conventional process. To overcome this problem, the nonconventional machining process is introduced for complex cut processing. Among the nonconventional machining process, the less heat affected zone with more accuracy of machining can be obtained from the WEDM process. This WEDM has widely used to cut hard and complicated to machine. This can be able to machine the high corrosion resistant materials

like super alloys in the application of aerospace, marine, and high temperature application. Sahiti and Reddy [1] and Bharathi [2] have made an analysis for Incoloy 800 alloy and SS304. By using Taguchi's method, the output process parameters like kerf width, MRR, and SR are analyzed. ANOVA is executed to recognizing inputs like wire feed rate, pulse off time, voltage, pulse on time, and the output response parameters like kerf, MRR, and SR [1, 2].

Melting of material is created by electric sparks which is taken as T_{on} and T_{off} is the pulse off time provided for the removal of molten particles from machining one. The spark machining gap is maintained by feed rate of wire (WF), and servo voltage (SV) points out the feeding rate of wire electrode into the zone of machining. The above mentioned parameters are secondary whereas peak current (I_p) and

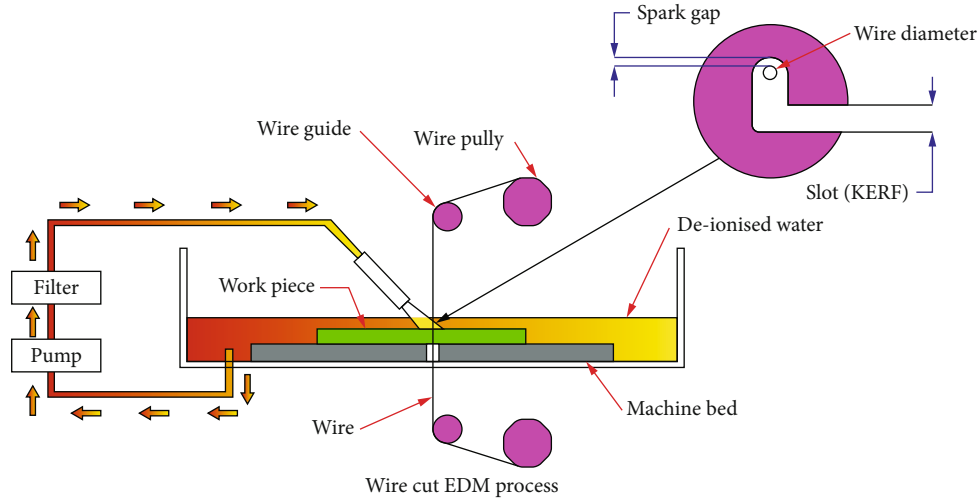


FIGURE 1: Wire cut EDM process.

pulse peak voltage (V_p) are the primary factors which influence the result of WEDM as follows: kerf width, SR, MRR, and recast layer thickness [3, 4]. Among the newest nontraditional manufacturing process machining, difficult-to-machine materials and delicate geometries that traditional machining methods cannot handle can be done by WEDM. The most efficient and cost-effective process is shown in Figure 1.

WEDM uses a wire electrode that moves longitudinally during machining and is directed by two distinct guide wires above and below the work piece [5]. Brass or coated steel wires are common wire electrodes, although tungsten or molybdenum wires are preferred for thin wires with ϕ 0.05–0.3 mm [6]. The work piece is degraded ahead of the wire during the machining process, so there is no direct contact between the work piece and the wire [7]. A mechanical tensioning mechanism is used to keep the wire in place. The melting and vaporization of material from the sample are caused by discharge between electrode and work piece [8]. Each electrical spark's heat believed to be between 15,000 and 21,000 degrees Fahrenheit and erodes a little quantity of material from the sample depicted in Figure 1 [9].

2. Experimental Methods

2.1. Material Selection. For the machining control parameter in the WEDM process, the authors used a variety of materials. The Taguchi method was used to analyse a block of D2 steel with ϕ 0.25 mm (zinc coated) copper wire using the L27 orthogonal array [10]. For SS304 of $100 \times 25 \times 10$ mm size with 0.25 mm diameter diffused brass wire, experimental analysis utilising ANOVA is used [11]. For the examination of SS 15-5 pH martensitic, precipitation hardening stainless steel of $100 \times 40 \times 10$ mm with 0.15 mm zinc-coated brass wire, the Taguchi method of orthogonal array L9 design was used [12]. For SS 316L of $20 \times 10 \times 10$ mm size with ϕ 0.25 mm (zinc coated) copper wire, grey relational analysis using ANOVA was expected [13]. Taguchi orthogonal array design utilised for super alloys

TABLE 1: Input process parameter ranges for WEDM.

Sl. no	Parameters	Units	Range
1	Pulse duration (T_{on})	μs	100-120
2	Pulse interval (T_{off})	μs	30-45
3	Wire feed (WF)	mm/s	4-12
4	Mean current (I)	A	20-50
5	Voltage (V)	V	90-150

of Incoloy types with brass wire diameters of 0.25 mm and wire feed rates of 420 mm/s [14].

2.2. Selection of Process Parameters. The input parameters were chosen to be pulse duration, pulse interval, mean current, voltage in V, and wire feed [15]. Surface texture (Ra), MRR, kerf breadth, straightness, perpendicularity gives output response from several method of studies [16]. It is noted that the following parameters have been changed to find the above results with the various ranges in Table 1.

3. Optimization Methods

There are different types of methods available for conducting the experiments as follows: Taguchi method, ANOVA, and grey relation analysis. Let us see the above methods one by one.

3.1. Taguchi Method. It is the most potent design tool for manipulative quality systems [17]. This provides an effective, simple method for optimising the concert, superiority, and budget [18]. Process parameter adjustment is a vital stage for attaining the excellence without raising costs [19]. Taguchi technique uses a particular design of orthogonal arrays with a minimal number of experiments to solve conventional process parameter design [20].

3.2. ANOVA. The analysis of variance (ANOVA) was used to determine significant and insignificant factors using the S/N and raw data [21]. Plotting the signal-to-noise data

TABLE 2: Experimental analysis of WEDM process with various techniques.

S. no	Material used	Methods conducted	Process parameters	Output	Authors/reference
1	SKD61 alloy	Taguchi method, ANOVA	T_{on} , T_{off} , WFR	SF, MRR	Kumar and Singh [29]
2	DC53 die steel	ANOVA, Taguchi method	V , I , T_{on} , T_{off}	SF, MRR	Kanlayasiri and Boonmum [30]
3	EN34 steel	Taguchi method, ANOVA	T_{on} , T_{off} , WFR	MRR, S/N ratio	Mohammad Taha and Bose [31, 32]
4	SS304	Taguchi method, orthogonal array	T_{on} , T_{off} , V , I	MRR	Ragunath and Vignesh [33]
5	SS316	Taguchi method	T_{on} , T_{off} , I	MRR, SR S/N ratio	Ramesh Babu and Subhair [34]
6	Ti-6Al-4V super alloy	Taguchi L-18 mixed orthogonal array	T_{on} , I , dielectric flushing pressure	MRR, TWR, overcut, and taper	Parmeswara and Sarcar [35]
7	Nimonic 80A	Taguchi method, ANOVA	T_{on} , T_{off} , WFR (wire offset)	MRR, SR	Goswami and Kumar [36]
8	Inconel 625	ANOVA, Taguchi method	T_{off} , WFR, T_{on}	SF, MRR	Goyal [37]
9	HCHCR	Taguchi process and GRA	T_{on} , T_{off} , V , I , WFR	MRR, SF	Patel et al. [38]
10	Inconel 718	Taguchi L-9 orthogonal array	T_{on} , T_{off} , I	MRR, SR, S/N ratio	Ramakrishnan and Karunamoorthy [39]
11	Monel 400	Taguchi method, ANOVA	T_{on} , T_{off} , V , I , WFR	MRR	Rajyalakshmi [40]
12	Nitinol (superelastic shape-memory alloy)	Heat-transfer search algorithm	T_{on} , T_{off} , I	MRR, SF	Chaudhari et al. [41]
13	Ti-6Al-4V (grade 5)	Taguchi orthogonal array	T_{on} , T_{off} , I , wire offset	Overcut in convex and concave profile, corner radius	Muhammad Umar Farooq and Muhammad Asad Ali [42]
14	Shape memory alloy (Ni 55.8 Ti)	NSGA-II, Taguchi	T_{on} , T_{off} , I , wire offset	MRR, SF	Magabe et al. [43]
15	Inconel 718	Discharge experiment design	V , I , dielectric pressure, pulse width, pulse interval, wire speed	MRR, SF	Chen and Zhou [44]
16	Hybrid Al-MMC (AA6061)	Taguchi method, ANOVA	T_{on} , T_{off} , WFR	MRR, SF	Kumar and Grover [45]
17	Composites of aluminium Al-SiC-B4C	RSM	T_{on} , T_{off} , V , I , WFR, B4C content	Kerf width, cutting speed	Suresh Kumar and Erdemir [46]
18	Steel SKD11	NSGA-II, hybrid method of RSM	T_{on} , T_{off} , WFR	SR, MRR, S/N ratio	Zhang et al. [47]
19	Ti50Ni45Co5 shape memory alloys	PCA, GRA technique	T_{on} , T_{off} , V	MRR, SF	Soni et al. [48]
20	EN31 alloys steel	AHP and MOORA	T_{on} , T_{off} , V , I , WFR, dielectric flushing pressure	Kerf width, MRR, SF	Patel and Kalpesh [49]

TABLE 3: Optimal process parameters for various research.

T_{on} (μ s)	T_{off} (μ s)	WF (mm/min)	Voltage (V)	Current (I)	Reference
10	10	6	20	215	Kumar and Singh [29]
125	52	8	15	220	Mohammad Taha and Bose [31]
10	5	10	25	200	Ragunath and Vignesh [33]
9	8	12	22	210	Ramesh Babu and Subhair [34]
118	45	5	30	110	Chen and Zhou [44]
10	4	7	60	205	Ramakrishnan and Karunamoorthy [39]

and raw data for the response curves (primary effect) reveals the parametric impacts on the response characteristics [22]. The ideal values of important process parameters in terms of mean response characteristics were determined by examining the ANOVA table and response curves [23].

3.3. Grey Relational Analysis (GRA). Dr. Deng J.L. et al. introduced the grey theory, which covers grey modelling prediction [24]. Numerous analysis can be done by GRA related to performance [25]. The grey relation analysis transforms the optimization of complex numerous performance variables into the single GRA optimization [26].

3.4. Optimizing the Process Variables. Table 2 depicts many types of research analyses used to conclude the best value for the process parameters of wire EDM. It is challenging to identify the right parameter through a series of experiments [27]. A large number of tests are carried out, and the best combination of machining parameters is chosen for the materials using the Taguchi orthogonal array and the ANOVA table. The analysis is carried out by several authors utilising analytical and statistical approaches. The MRR, kerf width, and surface roughness are S/N ratio-based metrics of process performance [28].

Table 2 shows the various experimental analysis by various researchers.

4. Result and Discussion

It was proposed in this review paper work to investigate various factors like T_{on} , T_{off} , V , I , and WFR dielectric flushing pressure used for wire EDM by various methods of analysis so as to maximise MRR and minimise surface roughness [50]. Signal to Noise ratio is used to craft one of the best feasible parametric sequences for the severe MRR. The reference articles listed in Table 3 conducted several observations.

4.1. Material Removal Rate. Greater energy is delivered by longer pulse on time and results more heat energy generation on that time. As the pulse on time grows, the rate of material removal and wire wear increases, while the surface polish drops [51]. Cutting speed can be increased by reducing pulse off time. The wire advances and retracts are controlled by servo voltage, which functions as a reference voltage. As the SV grows, the gap between the workpiece and the wire expands, limiting the amount of sparks, stabilising the electric discharge, and slowing the cutting rate [52]. The mean gap narrows when the SV is reduced, leading in increase electric sparks and a higher rate of machining

which leads to breakage of wire. In discharge machining, the amount of power used is termed as peak current denoted in amps [53]. Cutting speed can be increased by shortening the duration between pulses. The servo voltage, which also serves as a reference voltage, controls how far the wire advances and retracts. MRR rises in direct proportion to peak current [54].

4.2. Surface Roughness. It is quantified by the deviations in the direction of the normal vector of a real surface from its ideal form. Rough surface makes large variance while smooth one makes minimal [55]. Surface roughness of the machined surfaces was measured using a portable surface roughness over five to six machined surfaces [56].

Kumar and Singh [29] infer that selection of an optimal combination of WEDM parameters for proper machining of Skd 61 alloy will lead to achieve better surface finish. Mohammad Taha and Bose [31] conclude for EN34 steel that with the value of T_{on} 10 μ s, T_{off} 11 μ s, and wire feed ratio 7 mm/min for huge MRR and infer that signal to noise ratio is directionally proportional to MRR.

With the help of the Minitab software, Ramesh Babu and Subhair [34] examined the data by signal to noise ratios and L9 array and concluded that optimal input parameter for the SS316 with greatest MRR with voltage 23 V, T_{on} 9 s, and T_{off} 6 s. Muhammad Umar Farooq and Muhammad Asad Ali [42] present the results of Ti-6Al-4V for minimising undercut and overcut in profile curvature as SV of 80 V, T_{off} of 42 ms, and WS of 7 mm/s are found to be the optimal process parameters, as well as T_{on} of 9 ms and 7 ms for concave and convex profile production.

According to the grey relational analysis, the optimal process parameters for the MRR, kerf width, and surface roughness are T_{on} 13 s and T_{off} 5 s at level 3 and at level 2 servo voltage 59 volts [16]. Supply voltage to be applied to the gap stipulates the size of electric discharge. When voltage gap rises, so does the peak current, resulting in a greater MRR. The dielectric flow rate is the rate at which the dielectric fluid is circulated which makes efficient machining. As the wire feed rate increases, so will the consumption of wire and the expense of machining. Breakage of wire occurs when cutting at a high speed with a low speed of wire. Increasing tension of wire dramatically improves accuracy, cutting speed within a set of parameters. The discharge current was shown to be the most effective on the surface roughness, followed by pulse duration [15]. According to a report on WEDM, the SR increases if T_{on} , V , I and reduces if T_{off} increases [19]. The various L9 and L27 orthogonal arrays

of Taguchi approaches are used on the austenitic stainless steels for finding the best processing inputs and the optimal values for optimization technique like GA [27, 28]. The genetic algorithm is adopted for cutting the SS347 using laser beam machining, and the parametric optimization is adopted to find the best model [57]. The TOPSIS approach was used for the turning process to find the optimum result.

Most research concentrated on a little bit of process components on a single time to design and optimise a variety of responses, according to the literature, which could result in inaccurate results for the taken process due to lot of process parameters. Furthermore, individual response modelling and optimization have been prioritised by the majority of academics. Multiobjective optimization with good results has a lot of potential. The majority of the researchers worked on tungsten carbide, tool steels, and titanium alloys with little concentration on alloys of nickel and alloys of super structure being mentioned. As a result, research on WEDM over nickel-based alloys and stainless steel offers potential [58, 59]. The investigations on nontraditional machining, Taguchi method, and grey relational analysis can be carried out to find the best optimum solutions [60–63].

5. Conclusion

The manufacturing procedures for machining the materials that are tough to machine and complicated geometries are not easily processed in traditional machining methods. WEDM is a highly accurate process that produces great accuracy and a high surface polish. As the pulse on time is increased, more energy is created, resulting in increased wire wear and MRR. Cutting speed can be increased by shortening the duration between pulses. By widening the distance between the workpiece and the wire, the MRR is lowered. The MRR is directly related to the peak current and increases as the peak current increases. As the gap voltage rises, so does the peak current, leading in greater MRR values. Within a specific range, increasing wire tension dramatically improves cutting speed and accuracy. We infer that the input parameters of T_{on} , T_{off} , V , I , WF , WT , and dielectric flushing pressure have a significant impact on the MRR and surface topography based on the review of different authors about the investigation of various materials on WEDM. It is critical to focus on the input parameter in order to achieve good product quality. To simplify the procedure parameter range selection, greater focusing of multiobjective functions and decision-making algorithms is required. Steel, composites, titanium alloys, aluminium alloys, Monel, Inconel materials, and low-grade stainless steels are employed in the majority of studies. In the future, higher-grade austenitic stainless steels, superaustenitic stainless steels, and nickel-based alloys can be researched using various sets of process parameters to identify the best optimal solutions.

Data Availability

The data used to support the findings of this study are included in the article. Should further data or information

be required, these are available from the corresponding author upon request.

Disclosure

This study was performed as a part of the Employment Hawassa University, Ethiopia.

Conflicts of Interest

The authors declare that there are no conflicts of interest regarding the publication of this paper.

Acknowledgments

The authors extend their appreciation to the Research Center for Advanced Materials Science, King Khalid University, Saudi Arabia, for funding this work under grant number KKKU/RCAM/G011/21. The authors appreciate the technical assistance to complete this experimental work from Faculty of Manufacturing, Institute of Technology, Hawassa University, Ethiopia. The authors thank K. Ramakrishnan College of Engineering, Trichy, for the support of draft writing, proof reading, and technical assistance.

References

- [1] M. Sahiti, M. R. Reddy, B. Joshi, J. P. Praveen, and B. N. Rao, "Optimum WEDM process parameters of Incoloy Alloy 800 using Taguchi method," *International Journal of Industrial and Manufacturing Systems Engineering*, vol. 1, no. 3, pp. 64–68, 2016.
- [2] P. Bharathi, "Optimum WEDM process parameters of SS304 using Taguchi method," *International Journal of Industrial and Manufacturing Systems Engineering*, vol. 1, no. 3, pp. 69–72, 2016.
- [3] S. Sarkar, S. Mitra, and B. Bhattacharyya, "Parametric analysis and optimization of wire electrical discharge machining of γ -titanium aluminide alloy," *Journal of Materials Processing Technology*, vol. 159, no. 3, pp. 286–294, 2005.
- [4] A. Ikram, N. A. Mufti, M. Q. Saleem, and A. R. Khan, "Parametric optimization for surface roughness, kerf and MRR in wire electrical discharge machining (WEDM) using Taguchi design of experiment," *Journal of Mechanical Science and Technology*, vol. 27, no. 7, pp. 2133–2141, 2013.
- [5] V. D. Patel and R. V. Vaghmare, "A review of recent work in wire electrical discharge machining (WEDM)," *International Journal of Engineering Research and Applications*, vol. 3, no. 3, pp. 805–816, 2013.
- [6] K. Prasath, R. Prasanna, and D. S. Milton, "Optimization of process parameters in wire cut EDM of mild steel and stainless steel using robust design," *International Journal for Chemical Technology Research*, vol. 11, no. 1, pp. 83–91, 2018.
- [7] K. H. Ho, S. T. Newman, S. Rahimifard, and R. D. Allen, "State of the art in wire electrical discharge machining (WEDM)," *International Journal of Machine Tools and Manufacture*, vol. 44, no. 12–13, pp. 1247–1259, 2004.
- [8] G. Venkateswarlu and P. Devaraj, "Optimization of machining parameters in wire EDM of copper using Taguchi analysis," *International Journal of Advanced Materials Research*, vol. 1, no. 4, 2015.

- [9] H. Singh and A. Singh, "Effect of pulse on/pulse off time on machining of AISI D3 die steel using copper and brass electrode in EDM," *International Journal of Engineering and Science*, vol. 1, pp. 19–22, 2012.
- [10] S. S. Mahapatra and A. Patnaik, "Optimization of wire electrical discharge machining (WEDM) process parameters using Taguchi method," *International Journal of Advanced Manufacturing Technology*, vol. 34, no. 9-10, pp. 911–925, 2007.
- [11] M. Shunmuga Priyan, W. Willbert Swin, V. Anand, P. Kelvin, and V. S. Ai Siva, "Investigation of surface roughness and MRR on stainless steel machined by wire EDM," *International Journal of Engineering Research and Technology*, vol. 5, no. 3, 2016.
- [12] A. M. Kurian, B. C. Yeldose, and E. M. Mathew, "Study on the Influence of Process parameters on surface roughness and MRR of AISI 420 stainless steel Machined by EDM," *International Journal Of Engineering and Innovative Technology*, vol. 15, no. 2, pp. 54–58, 2014.
- [13] M. Saini, R. Sharma, G. S. Abhinav, and P. Mangla, "Optimizations of machining parameter in wire EDM for 316L stainless steel by using Taguchi method, Anova, and Grey analysis," *International Journal of Materials Engineering and Technology*, vol. 7, no. 2, pp. 307–320, 2016.
- [14] K. Manikandana, P. Ranjith Kumarb, D. Raj Kumarb, and K. Palanikumar, "Machinability evaluation and comparison of Incoloy 825, Inconel 603 XL, Monel K400 and Inconel 600 super alloys in wire electrical discharge machining," *Journal of Material Research and Technology*, vol. 9, no. 6, pp. 12260–12272, 2020.
- [15] A. J. Raj, K. Balasubramanian, D. Palanisamy, and A. G. S. Emmanuel, "Experimental investigations on WEDM process for machining high manganese steel," *Materials and Manufacturing Processes*, vol. 35, no. 14, pp. 1612–1621, 2020.
- [16] S. P. BisariaHimanshu, "Experimental investigation on wire electric discharge machining (WEDM) of Nimonic C-263 superalloy," *International Journal of Engineering Research and Technology*, vol. 34, no. 1, pp. 83–92, 2019.
- [17] B. K. Lodhi and S. Agarwal, "Optimization of machining parameters in WEDM of AISI D3 steel using Taguchi technique," *Procedia CIRP*, vol. 14, pp. 194–199, 2014.
- [18] P. Jaganathan, T. Naveen Kumar, and R. Sivasubramanian, "Machining parameters optimization of wire electrical dischargemachining process using Taguchi method," *International Journal of Mechanical and Production Engineering*, vol. 2, no. 12, 2012.
- [19] V. K. Saini, Z. A. Khan, and A. N. Siddiquee, "Optimization of wire electric discharge machining of composite material(Al6061/SiCp) using Taguchi method," *International Journal of Mechanical and Production Engineering*, vol. 2, no. 1, pp. 61–64, 2013.
- [20] S. Y. Martowibowo and A. Wahyudi, "Taguchi method implementation in taper motion wire EDM process optimization," *Journal of the Institution of Engineers (India): Series C*, vol. 93, no. 4, pp. 357–364, 2012.
- [21] R. Venkatesha and V. R. Lenina, "Optimization of machining parameters in wire cut EDM of stainless steel 304 using Taguchi techniques," *Advanced Materials Manufacturing & Characterization*, vol. 8, no. 1, 2018.
- [22] D. R. Unune and H. S. Mali, "Experimental investigation on low-frequency vibration assisted micro-WEDM of Inconel 718," *International Journal of Mechanical and Production Engineering*, vol. 20, no. 1, pp. 222–231, 2017.
- [23] A. Kumar, V. Kumar, and J. Kumar, "Experimental Investigation on Material Transfer Mechanism in WEDM of Pure Titanium (Grade-2)," *Advances in Materials Science and Engineering*, vol. 2013, 20 pages, 2013.
- [24] M. Durairaj, D. Sudharsunb, and N. Swamynathan, "Analysis of Process Parameters in Wire EDM with Stainless Steel Using Single Objective Taguchi Method and Multi Objective Grey Relational Grade," *International Journal of Mechanical and Production Engineering*, vol. 64, pp. 868–877, 2013.
- [25] J. T. Huang and Y. S. Liao, "Optimization of machining parameters of wire-EDM based on grey relational and statistical analyses," *International Journal of Production Research*, vol. 41, pp. 1707–1720, 2003.
- [26] S. Datta and S. Mahapatra, "Modeling, simulation and parametric optimization of wire EDM process using response surface methodology coupled with grey-Taguchi technique," *International Journal of Engineering, Science and Technology*, vol. 2, no. 5, pp. 162–183, 2010.
- [27] H. Ramakrishnan, N. Ganesh, R. Balasundaram, and N. Karthikeyan, "Experimental investigation of cut quality characteristics on SS321 using plasma arc cutting," *Journal of the Brazilian Society of Mechanical Science and Engineering*, vol. 40, no. 2, pp. 1806–3691, 2018.
- [28] H. Ramakrishnan and R. Balasundaram, "Experimental Investigation of Process Parameters for Pack Boronizing of SS410 Using Anova and Machine Learning Approaches," *Surface Topography: Metrology and Properties*, vol. 9, no. 2, p. 025046, 2021.
- [29] A. Kumar and D. K. Singh, "Performance analysis of wire electric discharge machining (W-EDM)," *International Journal of Engineering Research and Technology*, vol. 1, no. 4, pp. 1–9, 2012.
- [30] K. Kanlayasiri and S. Boonmung, "An investigation on effects of wire-EDM machining parameters on surface roughness of newly developed DC53 die steel," *Journal of Materials Processing Technology*, vol. 187, pp. 26–29, 2007.
- [31] S. S. Mahapatra and A. Patnaik, "Optimization of process parameters on EN 34 steel for WEDM operations," *The International Journal of Advanced Manufacturing Technology*, vol. 34, no. 9, pp. 911–925, 2007.
- [32] S. Balasubramanian and S. Ganapathy, "Grey relational analysis to determine optimum process parameters for wire electro discharge machining (WEDM)," *International Journal of Engineering Science and Technology*, vol. 3, no. 1, pp. 95–101, 2011.
- [33] L. Rangunath and D. Vignesh, "Optimization of wire-cut EDM process parameters for SS304 using design of experiment," *International Journal of Mechanical and Production Engineering Research and Development*, vol. 8, no. 2, 2018.
- [34] R. Ramesh Babu and S. Subhair, "Optimization of machining parameters in WEDM for stainless steel 316 by using Taguchi method," *International Journal of Engineering Research and Technology*, vol. 7, no. 9, 2018.
- [35] C. V. S. Parmeswara and M. M. M. Sarcar, "Evaluation of optimal parameters for machining brass with wire cut EDM," *Journal of Scientific and Industrial Research*, vol. 68, pp. 32–35, 2009.
- [36] A. Goswami and J. Kumar, "Trim cut machining and surface integrity analysis of Nimonic 80A alloy using wire cut EDM," *International Journal of Engineering Science and Technology*, vol. 20, no. 1, pp. 175–186, 2017.

- [37] A. Goyal, "Investigation of material removal rate and surface roughness during wire electrical discharge machining (WEDM) of Inconel 625 super alloy by cryogenic treated tool electrode," *Journal of King Saud University-Science*, vol. 29, no. 4, pp. 528–535, 2017.
- [38] V. B. Patel, J. D. Patel, and K. D. Maniya, "Selection of the wire cut electrical discharge machining process parameters using GRA method," *International Journal of Advance Engineering and Research Development*, vol. 1, no. 5, 2014.
- [39] R. Ramakrishnan and L. Karunamoorthy, "Modeling and multi-response optimization of Inconel 718 onmachining of CNC WEDM process," *Journal of Materials Processing Technology*, vol. 2, no. 7, pp. 343–349, 2007.
- [40] G. Rajyalakshmi, "Modelling and multi-objective optimization of WEDM of commercially Monel super alloy considering multiple users preferences," *Journal of Pharmaceutical Sciences and Research*, vol. 8, no. 8, pp. 902–908, 2016.
- [41] R. Chaudhari, J. J. Vora, S. S. Mani Prabu et al., "Multi-response optimization of WEDM process parameters for machining of super elastic Nitinol shape-memory alloy using a heat-transfer search algorithm," *Materials (journal of materials science and engineering)*, vol. 12, no. 8, p. 1277, 2019.
- [42] A. Muhammad Umar Farooq and A. Muhammad Asad Ali, "Curved profiles machining of Ti6Al4V alloy through WEDM: investigations on geometrical errors," *Journal of Material Research and Technology*, vol. 9, no. 6, pp. 16186–16201, 2020.
- [43] R. Magabe, N. Sharma, K. Gupta, and J. Paulo Davim, "Modeling and optimization of wire-EDM parameters for machining of Ni55.8Ti shape memory alloy using hybrid approach of Taguchi and NSGA-II," *International Journal of Advance Engineering and Research Development*, vol. 102, no. 5-8, pp. 1703–1717, 2019.
- [44] Z. Chen, H. Zhou, Z. Yan, F. Han, and H. Yan, "A new high-speed observation system for evaluating the spark location in WEDM of Inconel 718," *Journal of Material Research and Technology*, vol. 13, pp. 184–196, 2021.
- [45] A. Kumar, N. Grover, A. Manna et al., "Investigating the influence of WEDM process parameters in machining of hybrid aluminum composites," *Advanced Composites Letters*, vol. 29, p. 2633366X2096313, 2020.
- [46] S. Suresh Kumar and F. Erdemir, "Investigation of WEDM process parameters of Al-SiC-B₄C composites using response surface methodology," *International Journal of Lightweight Materials and Manufacture*, vol. 3, no. 2, pp. 127–135, 2020.
- [47] G. Zhang, Z. Zhang, W. Ming, J. Guo, Y. Huang, and X. Shao, "The multi-objective optimization of medium-speed WEDM process parameters for machining SKD11 steel by the hybrid method of RSM and NSGA-II," *International Journal of Advance Engineering and Research Development*, vol. 70, no. 9-12, pp. 2097–2109, 2014.
- [48] N. S. HargovindSoni and M. R. Ramesh, "Experimental investigation on effects of wire electro discharge machining of Ti50Ni45Co5 shape memory alloys," *Science*, vol. 10, no. 6, pp. 2483–2490, 2018.
- [49] J. D. Patel and K. D. Maniya, "Application of AHP/MOORA method to select wire cut electrical discharge machining process parameter to cut EN31 alloys steel with brasswire," *Materials Today Proceedings*, vol. 2, no. 4-5, pp. 2496–2503, 2015.
- [50] K. Mouralova, L. Benes, J. Bednar et al., "Using a DoE for a comprehensive analysis of the surface quality and cutting speed in WED-machined hadfield steel," *Journal of Mechanical Science and Technology*, vol. 33, no. 5, pp. 2371–2386, 2019.
- [51] A. Roy and S. Narendranath, "Effect of spark gap voltage and wire electrode feed rate on machined surface morphology during wire EDM process," *Materials Today: Proceedings*, vol. 5, no. 9, pp. 18104–18109, 2018.
- [52] A. Pramanik and A. K. Basak, "Effect of wire electric discharge machining (EDM) parameters on fatigue life of Ti-6Al-4V alloy," *International Journal of Fatigue*, vol. 128, p. 105186, 2019.
- [53] K. Lingadurai, B. Nagasivamuni, M. Muthu Kamatchi, and J. Palavesam, "Selection of wire electrical discharge Machining Process parameters on stainless steel AISI grade-304 using Design of experiments approach," *Journal of The Institution of Engineers India : Series C*, vol. 93, no. 2, pp. 163–170, 2012.
- [54] M. K. Va, S. B. Ab, V. Rc, and R. Md, "Optimization of the WEDM parameters onmachining Incoloy800 superalloy with multiple qualitycharacteristics," *International Journal of Engineering Science and Technology*, vol. 2, no. 6, pp. 1538–1547, 2010.
- [55] A. Kumar, V. Kumar, and J. Kumar, "Multi-response optimizationof process parameters based on response surface methodology forpure titanium using WEDM process," *International Journal of Advance Engineering and Research Development*, vol. 2013, no. 68, pp. 2645–2668, 2013.
- [56] P. Sharma, D. Chakradhar, and S. Narendranath, "Evaluation of WEDM performance characteristics of Inconel 706 for turbine disk application," *Materials and Design*, vol. 88, pp. 558–566, 2015.
- [57] H. Ramakrishnan, N. Ganesh, D. J. D. James, and B. Ashok, "Experimental analysis of cut quality on SS347 material using CO₂ assisted laser beam cutting and parametric optimization using genetic algorithm," *Surface Review and Letters*, vol. 28, no. 10, p. 2150085, 2021.
- [58] H. Ramakrishnan, R. Balasundaram, P. Selvaganapathy, M. Santhakumari, P. Sivasankaran, and P. Vignesh, "Experimental investigation of turning Al 7075 using Al₂O₃ nano-cutting fluid: ANOVA and TOPSIS approach," *SN Applied Science*, vol. 1, no. 12, pp. 1–17, 2019.
- [59] H. Ramakrishnan, "Application of six sigma principles and design-analysis soft wares to increase the pass percentage at the vehicle testing shop," *International Journal of pure and applied Mathematics*, vol. 120, no. 6, pp. 2593–2608, 2018.
- [60] I. Nayak and J. Rana, "Multi-response optimization in wire electrical discharge machining (WEDM) of D2 steel using utility approach," *Manufacturing Review*, vol. 8, p. 16, 2021.
- [61] R. Chaudhari, S. Khanna, J. Vora et al., "Experimental investigations and optimization of MWCNTs-mixed WEDM process parameters of nitinol shape memory alloy," *Journal of Material Research and Technology*, vol. 15, no. 38, pp. 2152–2169, 2021.
- [62] K. Zadafiya, Dinbandhu, S. Kumari, S. Chatterjee, and K. Abhishek, "Recent trends in non-traditional machining of shape memory alloys (SMAs): a review," *CIRP Journal of Manufacturing Science Technology*, vol. 32, pp. 217–227, 2021.
- [63] M. Sheth, K. Gajjar, A. Jain et al., "Multi-objective optimization of Inconel 718 using combined approach of Taguchi grey relational analysis," in *Advances in mechanical engineering*, vol. 35, Springer, Singapore, 2021.

Review Article

Recent Breakthrough of Bismuth-Based Nanostructured Materials for Multimodal Theranostic Applications

**Dhanraj Ganapathy,¹ Chitra Shivalingam,¹ Rajeshkumar Shanmugam^{1,2},
Ashok K. Sundramoorthy¹, Karthikeyan Murthykumar,³ Sivaperumal Pitchiah¹,
Saravanan Sekaran,¹ and Sathish Kumar Ramachandran¹**

¹Department of Prosthodontics, Saveetha Dental College and Hospitals, Saveetha Institute of Medical and Technical Sciences, Chennai, India

²Nanobiomedicine Lab, Department of Pharmacology, Saveetha Dental College and Hospitals, Saveetha Institute of Medical and Technical Sciences, Chennai, India

³Department of Periodontics, Saveetha Dental College and Hospitals, Saveetha Institute of Medical and Technical Sciences, Chennai, India

Correspondence should be addressed to Rajeshkumar Shanmugam; rajeshkumars.sdc@saveetha.com and Ashok K. Sundramoorthy; ashok.sundramoorthy@gmail.com

Received 12 May 2022; Revised 9 June 2022; Accepted 20 June 2022; Published 4 July 2022

Academic Editor: Arpita Roy

Copyright © 2022 Dhanraj Ganapathy et al. This is an open access article distributed under the Creative Commons Attribution License, which permits unrestricted use, distribution, and reproduction in any medium, provided the original work is properly cited.

Cancer is a lethal disease ravaging mankind claiming millions of lives. Most frequent methods of management include surgery, radiotherapy, chemotherapy, or a combination of all the above-mentioned methods. However, there is no specific medication available to cure this condition completely and several compounds and drugs are constantly explored for their therapeutic effects. Recently, photothermal therapy, photodynamic therapy, radiotherapy, targeted drug delivery, and hyperthermia have shown to be of great interest in cancer treatment. In this direction, bismuth oxide (Bi_2O_3) nanoparticles can be a promising option in cancer treatment and diagnosis as well. Bi is a well-known radioactive isotope; this emits high-energy gamma (γ) rays to the affected cells. This technology can pair with existing chemotherapy to enhance the therapeutic efficacy.

1. Introduction

Bismuth (Bi) is one of the significant nanoparticles (NPs) with specific spatial, physical, chemical, and compositional characteristics to integrate diverse attributes, including an affirmatively elevated X-ray attenuation coefficient [1]. This material exhibits outstanding photothermal transition effectiveness and a protracted promulgation half-life, as a non-toxic as well as cost-effective diamagnetic heavy metal [2]. Bismuth-doped nanoparticles (BiNPs) have been found to offer promising properties in the areas of combinational tumor therapy, photothermic and radiation therapeutics, augmentative imaging, theranostics, drug transport, biosensors, and tissue engineering (Figure 1) [3].

Day by day, cancer is becoming more severe as well as a common disease all over the world; 2 million women were affected by breast cancer in the year 2018; similarly, prostate, colorectal, stomach, and lung cancer cases are also drastically increasing. Breast cancer causes leading counts of death among females in over 103 countries [4]. Generally, constipation, dizziness, dermatitis, dry mouth, nausea, headache, insomnia diarrhea, and drowsiness are the common problems by the time of cancer treatment. Hence, upcoming technologies are encouraged to solve this problem with a better cure and lower side effects. Detailed toxicological aspects and the exact mechanism of action in therapeutics and nanoparticle interaction with other cellular/intracellular components and their reaction mechanism are bottlenecks

[5]; to explore the technology, a lot more research is essential to prove the concepts and bring them into practical applications.

2. Current Therapeutics

Currently, nanotechnology is proving a plethora of possibilities for theranostics in terms of a contrast agent for magnetic resonance imaging (MRI), hyperthermia, and targeted drug delivery; in this direction, radioactive isotope of higher atomic number elements is also possessing research breakthroughs towards the cure of tumor because of their improved photoelectric effect. *Z* element's interaction with X-rays is higher than light elements such as O, N, H, and C; therefore, those elements could enhance the energy deposition as well as radiolytic hydrolysis in and around the materials. Iron oxide, germanium nanoparticulates, iodine, lanthanide compounds, Cs_xWO_3 [6], and nuclear targeting gadolinium nanoparticles can act as an adjuvant to stimulate cellular radiation [7]. Generally, the combination of various functional materials hooked on one complex form of nanomaterials for multitasking functions balances several factors to perform relevant applications. However, those materials have severe drawbacks owing to their complex composition, mutual intrusion, and drug leakage. In contrast, one material with several element-like composites in the perfect crystal lattices satisfies all the above-mentioned strategies to employ one material to achieve all the intrinsic properties for multifunctional purposes (multimodal imaging modalities and photothermal therapy). Generally, surgery and chemotherapy followed by radiation therapy are the ongoing common treatment for the cure of cancer. Similarly, immunotherapy, targeted therapy, hormone therapy, bone marrow, and stem cell transplant are also sequentially developing in the field of cancer treatment [8]. In the recent era of cancer treatment, CAR T cell therapy, monoclonal antibodies, immune checkpoint inhibitors, and immune system modulators are emerging to establish better treatments [9].

3. Properties of Bismuth Nanoparticulates

Bismuth nanoparticles are the best among the nanostructured materials due to their incredible properties such as high surface area, excellent stability, high electrical, strong diamagnetic, and magnetoresistance properties in the presence of a magnetic field; it has chemical inertness, catalytic activity, cost effectiveness, low toxicity, adoptable functionalization, radiosensitization, radiostability, and high X-ray attenuation. Bismuth (Bi) is a high *Z* ($Z = 83$) element, and the X-ray attenuation coefficient of this component is larger than that of gold (Au), platinum (Pt), and Iodide (I). Hence, Bi-based nanocomponents such as Bi_2S_3 nanorods, Bi_2S_3 nanodots, and Bi_2Se_3 nanostructures with various morphologies have been recemented as contrast agents (CT) photothermal/radiotherapy sensitizing agents [7]. Remarkably, Bi_2Se_3 nanostructures possibly release vivacious selenium ions for reducing the fatality and occurrence of the prostate, liver, and lung cancers compared with Bi_2S_3 [10] and also stated that two-dimensional materials have remarkable

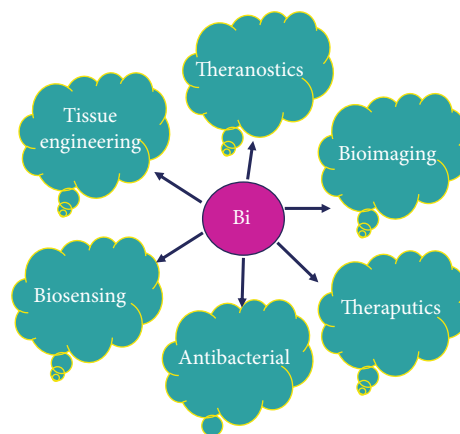


FIGURE 1: Bismuth nanoparticle's potential impact in biomedical applications.

attention in X-ray irradiation and related metabolism to inhibit the growth of tumor [11]. Bi is one of the less-reactive heavy metals in the biological environment with minimal toxicity, and this is more appropriate for *in vivo* applications than other metals like silver [12].

Nanovaccines may show enhanced efficacy in immunotherapy, and they play an impactful role in all the aspects of therapeutics for cancer. Nanoparticles explicate superior inhibition and denaturation of cancer cells with relevant current technologies. However, the major limitations of nanoparticles are toxicological aspects of reactive nanoparticles and researchers need more attention to detailed demonstration to explore these nanoparticles at the next level [13]. Bismuth (Bi) is a diamagnetic semimetal with nominal bandgap, and also, this material exhibits attractive properties like thermal conductivity, magnetoresistance, and dominant anisotropic electronic features; these potential characteristics of bismuth nanoparticles trigger and tune the electronic properties, which may influence the sensitization enhancement ratio (SER) towards the development of cancer treatment [14].

4. Radioactive Properties of Bi_2O_3

Bismuth oxide revealed tremendous radiotherapy effects owing to its optimal physiobiochemical effect. Bi is heavy metal, so it explicates side effects like brain toxicity, renal toxicity, and neurological problems. The toxicological effect of bismuth can be ascribed in terms of the following: Bi binds to enzymes belonging to sulfhydryl groups in the human body; as a result of this, enzymes may denature and the functionality of that is also inhibited. As of now, Bi compound's metabolic as well as toxicological aspects are not clear and thus need to be explored. Hence, investigating biodegradability and interreaction with drug components as well as the human biological system may generate a significant platform for medical society [15]. It was declared that genotoxicity aspects of bismuth with genomic DNA of tumor cells were rapidly higher than the nonexposed tumor cells' DNA; these results suggested that bismuth nanoparticles inhibit the growth of tumor cells in a

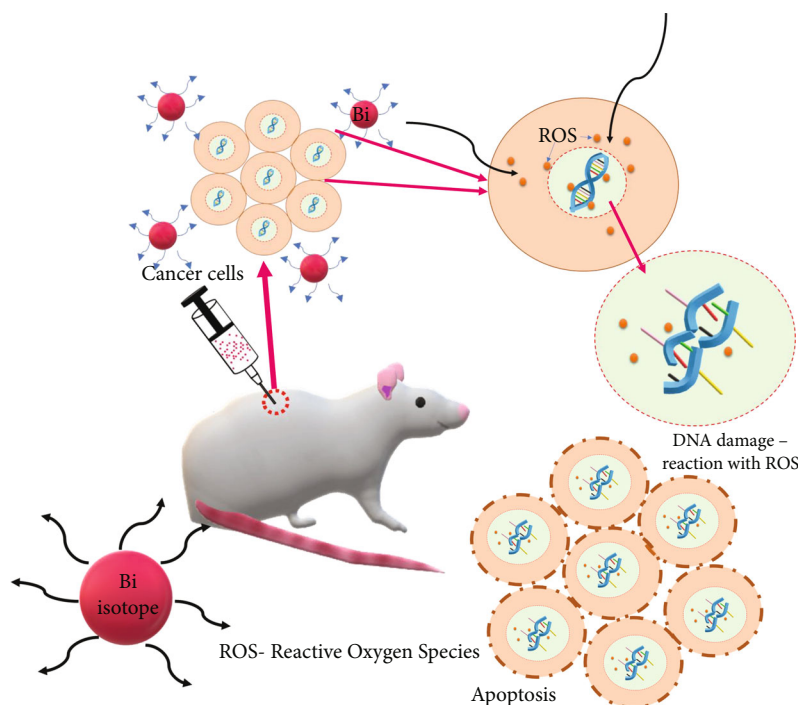


FIGURE 2: Conceptual diagram of Bi radioactive isotope reaction strategies for cancer treatment.

dose-dependent manner [16]. In another recent report, [17] investigated the radiosensitization effect of bismuth oxide nanostructured rods by megavoltage radiotherapy treatment technology; and the authors also quantified the generation of sensitization enhancement ratio (SER) via photon and electron beams with respect to cancer cell death and further summarised that ultrasmall Bi_2O_3 nanoparticulates regulate the efficient radiotherapy [16].

Radiation therapy comprises brachytherapy, and this is suggested as an acceptable palliative curing therapy for cancer patients. Radioactive isotopes percolate internally near the surrounding specific region of cancer and emit high-dose energy of gamma (γ) to the affected cells [18]. This radiotherapy is generally paired with chemotherapy to improvise therapeutic efficiency to cure cancer. Mostly, drugs like doxorubicin, gemcitabine, and cisplatin are collectively enhancing the lethal efficacy of radiation as a radiosensitizer [19, 20]. These are the common treatment currently followed to cure malignant tumors. Recently, research is moving towards the significant radiosensitization effect with high atomic number metallic nanoparticles. High radiation energy damages cancer cells as well as adjacent healthy cells/tissues and also causes several complications. Hence, nanoparticles may possess potential radiosensitization properties; this possibly targets the DNA of cancer cells, so that healthy cells will not rupture. Bismuth nanoparticles were considered promising materials for cancer treatment such as chemoradiotherapy [21], thermochemotherapy [22], radioimmunotherapy [23, 24], and thermoradiotherapy [25, 26], with enhanced inhibition of cancer cells than the existing monotherapies.

Bismuth oxide (BiO) nanoparticles and cisregulatory element combination produce the reactive oxygen species, and

these materials possess a radiosensitization effect under the irradiation of photons and electrons in terms of radiotherapy and high-dose-rate (HDR) brachytherapy. It was reported that BiO nanoparticles with cisregulatory combination with photon/electron effect (brachytherapy) on MCF-7 breast cancer cells exhibited the maximum sensitization enhancement ratio (SER) values [27] (Figure 2).

Brachytherapy is a kind of internal treatment mechanism that uses radionuclides as a source to emit high gamma (γ) ray; this induces radiation surrounding the target sites [18]; this energy contains mainly radium along with cesium-137, iridium-192, gold-198, palladium-103, and iodine-125 [28]. Currently, brachytherapy (radionuclides) is gaining more attention due to the source half-life, flexibility, and gamma- (γ -) energy properties than other external therapies related to photons and electrons. Radiosensitization effect was predicted with various kinds of cancer cells such as human squamous-cell carcinoma (A431) [29], lung cancer cells (A549), cervical cancer cells (HeLa), and prostate cancer cells (DU145) to analyze the morbidity tolerable properties [30].

5. Nanoparticle-Dependent Cancer Therapeutics

In another dimension, photothermal therapy (PTT) is one of the promising therapeutic techniques for tumor ablation due to its low invasion, high efficiency, and remote controllability. Carbon-based quantum dots, magnetic nanoparticulates, gold nanoparticulates, tungsten bronzes, bismuth and copper-based compounds, nano-shell-like structures, and organic polymers are the extensively focussing PTT agents [31]. Bismuth selenium (Bi_2Se_3) has gained enormous

attention in imaging because of its optical, thermoelectric, photoelectric, and chemical properties. Bi is an effective element for contrast agents (X-ray) owing to its high atomic number [31].

Bi has been conventionally following material in the generation of pharmaceutical products for the therapeutic purposes of hypertension, gastrointestinal disorders, and syphilis. On the contrary, the nanoform of bismuth was analyzed in various domains to estimate the active features in X-ray radiotherapy, heavy-metal ion detectors, biosensors, bio-imaging, tissue engineering, microbial inhibition assessments, and cancer therapy [32–35]. The single compound of Bi can be used to fabricate intermediate materials like bismuth-chalcogenides (Bi_2S_3 , Bi_2O_3 , and Bi_2Se_3), bismuth-oxyhalides-BiOX (X-Br/I/Cl), and bismuth selenide (Bi_2Se_3), which may influence and enhance the properties of the material. Nanostructured bismuth-based compounds may possess various crystal growth owing to the nucleation, growth, and saturation, and those properties resemble morphological features such as nanorods, nanowires, nanotubes, nanoneedles, nanoflakes, nanosheets, nanoflowers, nanoplates, and nanooctahedra. In another mode, multicomponent bismuth nanostructures (BiFeO_3 , Bi_2MoO_6 , Bi_2WO_6 , and $(\text{Bi}_2\text{O})_2\text{CO}_3$), BiPO_4 , BiVO_4 , and Bi dimercaptopropanol (BisBAL) are possessing great importance in biomedical applications. Generally, in the case of nanoparticles, morphology-dependent application aspects such as photocatalytic degradation, sensing ability, compatibility properties, and imaging efficiency were analyzed. Besides, there are not many strenuous reports on the morphological importance of cancer treatment that have to be explored by the research community. Various kinds of morphologies and crystal structures are possible to develop via feasible wet chemical approaches, which include solvothermal, hydrothermal, evaporation methods, precipitation methods, sol-gel approaches, chemical reduction, microemulsion techniques, sonochemical synthesis approaches, microwave irradiations, laser-mediated fabrication techniques, and all the possible chemical synthesis routes. Material-dependent properties are essential to analyze the interreactive functions to exactly execute the applications [12, 36].

6. Important Findings of Bi_2O_3 towards Theranostics

Song et al. investigated the bismuth selenide nanosheets for imaging purposes as a targeted theranostic agent and found that Bi_2Se_3 has outstanding tumor targeting ability and also showed the potential radiosensitization efficacy for imaging and radiotherapy and also mentioned the *in vivo* biocompatibility of the material [7]. Similarly, according to Cheng et al., bismuth sulfide-based nanoagents for photothermal therapy damage the DNA of cancer cells due to the enhanced radiation dose and also, as a CT contrast agent, have an influential parameter in multimodal imaging; and they summarised distant metastasis inhibition mechanism they have explained in the tumor model [37]. Yang et al. proposed that 1,2-dilauroyl-sn-glycero-3-phosphocholine (DLPC) membrane-coated Bi NPs revealed significant

photothermal conversion efficiency, CT/PA contrast imaging, biocompatibility, photostability, efficient cellular uptake, and tumor accumulation through EPR effect; this material has a multifunctional theranostic platform to cure cancer [38]. Sisin et al. illustrated that Bi nanoparticles induce ROS in and around the cells and enhance the SER value during brachytherapy and high radiosensitization [4]. Stewart et al. demonstrated that dose enhancement factor (DEF) simulation studies exhibit a lower Sensitisation Enhancement Ratio (SER) found via cell survival experiments; the authors found cell population in simulated DEF compared to experimental SER measurements [32].

7. Management Strategies in Cancer

Despite decades of dedicated research on cancer monotherapy, effective tumor eradication at an incipient stage persists as a significant hurdle. The majority of tumors are not identified until they have grown to a substantial size, increasing the chances of poor treatment response and spread. To address the drawbacks of individual therapies, an alternate option is to combine more than one therapy technique with diagnostic tools [39, 40]. The utilization of imaging modalities and multitherapy at the same time necessitates the development of versatile nanotheranostic agents [41]. BiNPs was advocated in this regard due to their wide range of uses, including CT imaging, phototherapy, and radiotherapy. Bi_2Se_3 nanodots possess steep photothermal translation effectiveness in phototherapy while also functioning as CT imaging-piloted synergistic sensitizers in radiotherapeutics [42].

8. Application of Bismuth Oxide Nanoparticles in Cancer Theranostics

BiNPs' inherent properties have been coupled with different imaging aspects or treatment techniques, in particular, MRI, chemo, and immunotherapeutics, to create unique theranostics. These monodisperse multicomponent nanoagents are very promising as cancer theranostic agents due to their fast cellular uptake, substantial tumor accumulation, good *in vivo* dispensation, minor acute toxicity, and excellent photothermal tumor ablation without recurrence.

Another innovative strategy recently emphasized targeting multitherapeutic cancer ablation is combination phototherapy with immunotherapy employing BiNPs [43]. Song et al. developed immune-adjuvant encased Bi_2Se_3 nanocages in metastatic treatment with enhanced photothermal properties [43]. Through enhanced production of inflammatory cytokines such as TNF α and interferon γ , along with IL-12p40, employing this immunogenic NP effectively ablated the photoexposed cancerous tissues but also elicited significant antineoplastic immunity to prevent the formation of a remote subsidiary tumor. These nanomedicines' potential can be leveraged in future research and development as multifunctional theranostics.

Alyani Nezhad et al. used the intraoperative radiotherapy technique to explore and measure the average dose enhancement component in the proximity of nanoparticles.

A unique hydrothermal approach was used to make bismuth oxide nanoparticles (Bi_2O_3 NPs) as sheets and spherical shapes. As a result, IORT in combination with Bi_2O_3 NPs may be able to minimize treatment duration and normal tissue dosage, as well as deliver localized dose augmentation [44]. Bi_2O_3 NPs may have harmful consequences at the intracellular level, according to Alamer et al., who recommend additional research before using them for medicinal purposes [45].

Researchers attempted to propose multifunctional bismuth gadolinium nanoparticles (BiGdO_3) as a novel theranostic vehicle in irradiation treatment, computed tomography, and magnetic resonance imaging. The biocompatibility of BiGdO_3 nanoparticles was assessed using the CCK-8 test after they were synthesized and surface modified with PEG. They used gel dosimetry, in vitro, and in vivo experiments to study the nanoparticles' dosage amplification characteristics. The findings of their experiments showed that BiGdO_3 -PEG coupled nanoparticles had multimode imaging along with radiosensitizing characteristics. The findings suggest that nanoparticles should be investigated furthermore as a potential novel theranostic agent [46].

Abudayyak et al. intended to evaluate the harmful effects of Bi oxide (Bi_2O_3) nanoparticles in cell cultures of the HepG2 hepatocarcinoma cells, NRK-52E kidney epithelial cells, Caco-2 colorectal adenocarcinoma cells, and A549 lung carcinoma cells. All cells readily absorbed Bi_2O_3 nanoparticles (149.1 nm) and demonstrated cytotoxic and genotoxic impacts. The predominant cell death mechanisms in HepG2 and NRK-52E cells included apoptosis with necrosis in A549 as well as Caco-2 cells treated with Bi_2O_3 nanomaterials, respectively. In these cancer cell lines, the levels of glutathione, malondialdehyde, and 8-hydroxy deoxyguanosine too were dramatically altered, with the exception of the A549 cell [47].

In hominin breast tumor (MCF-7) cells, Ahamed et al. investigated the dosage-dependent cytotoxic effects and apoptotic responses of Bi_2O_3 NPs, as well as probable pathways of the lethality of Bi_2O_3 NPs via oxidative stress. Bi_2O_3 NPs possess a crystalline architecture and spherical form with an average dimension of 97 nm, according to a physicochemical investigation. Bi_2O_3 NPs diminish cell viability but also produce dose-dependent membrane injury within a concentration spectrum of 50–300 g/ml, according to toxicological tests. The cell cycle in MCF-7 cells was likewise disrupted by Bi_2O_3 NPs. They discovered that exposing MCF-7 cell types to Bi_2O_3 NPs caused apoptosis, as seen by poor modulation of the Bcl-2 and Bax, as well as caspase-3-specific genes. Bi_2O_3 NPs promoted lethality in MCF-7 cells via modifying redox balance via Bax/Bcl-2 cascade, according to the researchers [48].

The conjunction of BiONPs and cisplatin has been shown as a potential radiosensitization enhancer that would improve tumor control effectiveness while protecting healthy tissues at a lower dose. Cisplatin and BiONPs are possible radiosensitizers that might increase the efficacy of radiation in eradicating cancer cells. When used in radiotherapy, this combination of such powerful radiosensitizers may have numerous implications [4]. It was demonstrated that BiONPs, cisplatin, and combined brachytherapy had a

synergetic effect that will benefit future chemoradiotherapy approaches in cancer medicine [49].

Bismuth nanorods with ultra-small-size nanoparticles generate an enhanced sensitization enhancement ratio, which supports potential reduction in cancer cells and also explicates effective radiotherapy. Bismuth oxide showed optimal compatibility and effective radiation therapy, and also, it was reported that it has a tendency to bind bimolecular such as proteins and enzymes that may drive the targeted therapies [50]. In this review, we collectively drew the properties of Bi_2O_3 nanoparticle's impact in cancer treatment, existing nanoparticles' potential contribution to cure cancer, and a brief overview discussing the aspects of relevant properties to achieve reaction mechanism towards theranostics. Currently, there are existing therapeutic technologies for cancer as well as challenges faced to attain appropriate applications in terms of imaging, radiotherapy, drug delivery, etc. Overall, the view of Bi as a radioactive isotope and the importance of γ rays have been discussed along with the toxicological aspects of the material. Hence, the pros and cons of Bi_2O_3 and other nanoparticles' impactful role in cancer treatment, as well as expected technologies to fulfill current problems, were briefly discussed.

9. Future Perspectives and Conclusion

Bi_2O_3 is one of the influential isotopes that possess radioactive properties, which is encouraged in radiotherapy to cure cancer. Similarly, optimal biocompatibility was reported by earlier research articles. The simple alteration of these BiNPs' interfaces with biopolymers and proteins potentially optimizes their pharmacokinetics, culminating in greater colloidal stabilization and longer blood circulation but also lower toxicity. The theranostic role of BiNPs can be experimented in cell line studies and animal and human trials for various neoplastic transformations. The key biomedical scientific topics employing BiNPs have created a novel paradigm regarding their promising therapeutic application including potential cancer progression suppression. BiNPs hold great promise to function as both definitive and adjunct.

Data Availability

The review data used to support the findings of this study are included within the article.

Conflicts of Interest

The authors declare that they have no conflicts of interest.

References

- [1] S. Alshahri, M. Alsuhybani, E. Alosime, M. Almurrayshid, A. Alrwais, and S. Alotaibi, "LDPE/bismuth oxide nanocomposite: preparation, characterization and application in X-ray shielding," *Polymers*, vol. 13, no. 18, 2021.
- [2] X. Liu, S. Zhang, S. Guo et al., "Advances of 2D bismuth in energy sciences," *Chemical Society Reviews*, vol. 49, no. 1, pp. 263–285, 2020.

- [3] M. Bartoli, P. Jagdale, and A. Tagliaferro, "A short review on biomedical applications of nanostructured bismuth oxide and related nanomaterials," *Materials*, vol. 13, no. 22, 2020.
- [4] N. N. Talik Sisin, K. Abdul Razak, S. Zainal Abidin et al., "Synergistic influence of bismuth oxide nanoparticles, cisplatin and baicalein-rich fraction on reactive oxygen species generation and radiosensitization effects for clinical radiotherapy beams," *International Journal of Nanomedicine*, vol. 15, no. 15, pp. 7805–7823, 2020.
- [5] J. Jeevanandam, A. Barhoum, Y. S. Chan, A. Dufresne, and M. K. Danquah, "Review on nanoparticles and nanostructured materials: history, sources, toxicity and regulations," *Beilstein Journal of Nanotechnology*, vol. 9, no. 9, pp. 1050–1074, 2018.
- [6] W. Guo, C. Guo, N. Zheng, T. Sun, and S. Liu, "Cs_xWO₃ nanorods coated with polyelectrolyte multilayers as a multifunctional nanomaterial for bimodal imaging-guided photothermal/photodynamic cancer treatment," *Advanced Materials*, vol. 29, no. 4, 2017.
- [7] Z. Song, Y. Chang, H. Xie, X. F. Yu, P. K. Chu, and T. Chen, "Decorated ultrathin bismuth selenide nanosheets as targeted theranostic agents for *in vivo* imaging guided cancer radiation therapy," *NPG Asia Materials*, vol. 9, no. 10, pp. e439–e439, 2017.
- [8] C. Pucci, C. Martinelli, and G. Ciofani, "Innovative approaches for cancer treatment: current perspectives and new challenges," *Ecancermedicalscience*, vol. 13, p. 961, 2019.
- [9] A. N. Miliotou and L. C. Papadopoulou, "CAR T-cell therapy: a new era in cancer immunotherapy," *Current Pharmaceutical Biotechnology*, vol. 19, no. 1, pp. 5–18, 2018.
- [10] X. Cai, C. Wang, W. Yu et al., "Selenium exposure and cancer risk: an updated meta-analysis and meta-regression," *Scientific Reports*, vol. 6, no. 1, p. 19213, 2016.
- [11] X. D. Zhang, J. Chen, Y. Min et al., "Metabolizable Bi₂Se₃ nanoplates: biodistribution, toxicity, and uses for cancer radiation therapy and imaging," *Advanced Functional Materials*, vol. 24, no. 12, pp. 1718–1729, 2014.
- [12] Y. Xuan, X. L. Song, X. Q. Yang et al., "Bismuth particles imbedded degradable nanohydrogel prepared by one-step method for tumor dual-mode imaging and chemophotothermal combined therapy," *Chemical Engineering Journal*, vol. 375, p. 122000, 2019.
- [13] S. Gavas, S. Quazi, and T. M. Karpiński, "Nanoparticles for cancer therapy: current progress and challenges," *Nanoscale Research Letters*, vol. 16, no. 1, p. 173, 2021.
- [14] C. Gomez, G. Hallot, S. Laurent, and M. Port, "Medical applications of metallic bismuth nanoparticles," *Pharmaceutics*, vol. 13, no. 11, 2021.
- [15] J. Huang, Q. Huang, M. Liu, Q. Chen, and K. Ai, "Emerging bismuth chalcogenides based nanodrugs for cancer radiotherapy," *Frontiers in Pharmacology*, vol. 13, no. 13, article 844037, 2022.
- [16] R. Hernandez-Delgadillo, C. M. García-Cuellar, Y. Sánchez-Pérez et al., "In vitro evaluation of the antitumor effect of bismuth lipophilic nanoparticles (BisBAL NPs) on breast cancer cells," *International Journal of Nanomedicine*, vol. 13, pp. 6089–6097, 2018.
- [17] A. Jamil, S. Z. Abidin, K. A. Razak, H. Zin, M. A. Yunus, and W. N. Rahman, "Radiosensitization effects by bismuth oxide nanorods of different sizes in megavoltage external beam radiotherapy," *Reports of Practical Oncology and Radiotherapy*, vol. 26, no. 5, pp. 773–784, 2021.
- [18] W. N. W. Abd Rahman, "Gold nanoparticles: novel radiobiological dose enhancement studies for radiation therapy, synchrotron based microbeam and stereotactic radiotherapy," *MIT University*, 2010.
- [19] B. Kalaghchi, R. Abdi, F. Amouzegar-Hashemi, E. Esmati, and A. Alikhasi, "Concurrent chemoradiation with weekly paclitaxel and cisplatin for locally advanced cervical cancer," *Asian Pacific Journal of Cancer Prevention*, vol. 17, no. sup3, pp. 287–291, 2016.
- [20] S. Chandel and R. Jain, "Evaluation of role of radical radiotherapy and chemotherapy in cervical cancer patients- a preliminary report," *Clin Cancer Investig J*, vol. 5, no. 2, p. 126, 2016.
- [21] M. Ma, Y. Huang, H. Chen et al., "Bi₂S₃-embedded mesoporous silica nanoparticles for efficient drug delivery and interstitial radiotherapy sensitization," *Biomaterials*, vol. 37, pp. 447–455, 2015.
- [22] R. Dou, Z. Du, T. Bao et al., "The polyvinylpyrrolidone functionalized rGO/Bi₂S₃ nanocomposite as a near-infrared light-responsive nanovehicle for chemo-photothermal therapy of cancer," *Nanoscale*, vol. 8, no. 22, pp. 11531–11542, 2016.
- [23] Z. Li, Z. Li, L. Sun et al., "Core-shell Bi₂Se₃@mSiO₂-PEG as a multifunctional drug-delivery nanoplatform for synergistic thermo-chemotherapy with infrared thermal imaging of cancer cells," *Particle and Particle Systems Characterization*, vol. 35, no. 3, p. 1700337, 2018.
- [24] H. Yu, Y. Yang, T. Jiang et al., "Effective radiotherapy in tumor assisted by Ganoderma lucidumpolysaccharide-conjugated bismuth sulfide nanoparticles through radiosensitization and dendritic cell activation," *ACS Applied Materials & Interfaces*, vol. 11, no. 31, pp. 27536–27547, 2019.
- [25] N. Yu, Z. Wang, J. Zhang et al., "Thiol-capped Bi nanoparticles as stable and all-in-one type theranostic nanoagents for tumor imaging and thermoradiotherapy," *Biomaterials*, vol. 161, pp. 279–291, 2018.
- [26] E. Li, X. Cheng, Y. Deng et al., "Fabrication of PEGylated Fe@Bi₂S₃ nanocomposites for dual-mode imaging and synergistic thermoradiotherapy," *Biomaterials science*, vol. 6, no. 7, pp. 1892–1898, 2018.
- [27] D. W. O. Rogers, J. E. Cygler, American Association of Physicists in Medicine Summer School, and American Association of Physicists in Medicine, "Clinical dosimetry measurements in radiotherapy: Proceedings of the American Association of Physicists in Medicine Summer School," Medical Physics Pub, Colorado College, Colorado Springs, Colorado, 2009.
- [28] F. M. Khan and J. P. Gibbons, "Khan's the Physics of Radiation Therapy," Lippincott Williams & Wilkins, 2014.
- [29] W. N. W. Abd Rahman, W. W. Mansor, R. Ab Rashid, and R. Abdullah, "Comparative analysis of HDR intracavitary brachytherapy fractionation: in-vitro study," *Jurnal Sains Nuklear Malaysia*, vol. 31, no. 2, pp. 44–49, 2019.
- [30] E. Shahhoseini, P. Ramachandran, W. Patterson, and M. Geso, "Determination of dose enhancement caused by AuNPs with Xoft^{®} Axxent^{®} electronic (eBx^{™}) and conventional brachytherapy: in vitro study," *International Journal of Nanomedicine*, vol. 13, pp. 5733–5741, 2018.
- [31] J. Li, F. Jiang, B. Yang et al., "Topological insulator bismuth selenide as a theranostic platform for simultaneous cancer imaging and therapy," *Scientific Reports*, vol. 3, no. 1, p. 1998, 2013.
- [32] C. Stewart, K. Konstantinov, S. McKinnon et al., "First proof of bismuth oxide nanoparticles as efficient radiosensitisers on

- highly radioresistant cancer cells,” *Physica Medica*, vol. 32, no. 11, pp. 1444–1452, 2016.
- [33] R. Zhou, H. Wang, Y. Yang et al., “Tumor microenvironment-manipulated radiocatalytic sensitizer based on bismuth heteropolytungstate for radiotherapy enhancement,” *Biomaterials*, vol. 189, pp. 11–22, 2019.
- [34] H. Fan, S. Zhang, P. Ju, H. Su, and S. Ai, “Flower-like Bi_2Se_3 nanostructures: synthesis and their application for the direct electrochemistry of hemoglobin and H_2O_2 detection,” *Electrochimica Acta*, vol. 64, no. 64, pp. 171–176, 2012.
- [35] A. Soli’s, H. Luna, H. I. Pe’rez, N. Manjarrez, R. Sa’nchez, and A. Gutie’rrez, “(S)-Naproxen® as a derivatizing agent to determine enantiomeric excess of cyanohydrins by HPLC,” *Tetrahedron letters*, vol. 38, 1998.
- [36] M. A. Shahbazi, L. Faghfour, M. P. A. Ferreira et al., “The versatile biomedical applications of bismuth-based nanoparticles and composites: therapeutic, diagnostic, biosensing, and regenerative properties,” *Chemical Society Reviews*, vol. 49, no. 4, pp. 1253–1321, 2020.
- [37] X. Cheng, Y. Yong, Y. Dai et al., “Enhanced radiotherapy using bismuth sulfide nanoagents combined with photo-thermal treatment,” *Theranostics*, vol. 7, no. 17, pp. 4087–4098, 2017.
- [38] C. Yang, C. Guo, W. Guo, X. Zhao, S. Liu, and X. Han, “Multifunctional bismuth nanoparticles as theranostic agent for PA/CT imaging and NIR laser-driven photothermal therapy,” *ACS Applied Nano Materials*, vol. 1, no. 2, pp. 820–830, 2018.
- [39] J. A. Barreto, W. O’Malley, M. Kubeil, B. Graham, H. Stephan, and L. Spiccia, “Nanomaterials: applications in cancer imaging and therapy,” *Advanced Materials*, vol. 23, no. 12, pp. H18–H40, 2011.
- [40] A. Jakhmola, N. Anton, and T. F. Vandamme, “Inorganic nanoparticles based contrast agents for X-ray computed tomography,” *Advanced Healthcare Materials*, vol. 1, no. 4, pp. 413–431, 2012.
- [41] M. H. Yao, M. Ma, Y. Chen et al., “Multifunctional Bi_2S_3 /PLGA nanocapsule for combined HIFU/radiation therapy,” *Biomaterials*, vol. 35, no. 28, pp. 8197–8205, 2014.
- [42] F. Mao, L. Wen, C. Sun et al., “Ultras-small biocompatible Bi_2Se_3 nanodots for multimodal imaging-guided synergistic radiophotothermal therapy against cancer,” *ACS Nano*, vol. 10, no. 12, pp. 11145–11155, 2016.
- [43] Y. Song, Y. Wang, S. Wang et al., “Immune-adjuvant loaded Bi_2Se_3 nanocage for photothermal-improved PD-L1 checkpoint blockade immune-tumor metastasis therapy,” *Nano Research*, vol. 12, no. 8, pp. 1770–1780, 2019.
- [44] Z. Alyani Nezhad, G. Geraily, F. Hataminia, W. Parwaie, H. Ghanbari, and S. Gholami, “Bismuth oxide nanoparticles as agents of radiation dose enhancement in intraoperative radiotherapy,” *Medical Physics*, vol. 48, no. 3, pp. 1417–1426, 2021.
- [45] A. Alamer, D. Ali, S. Alarifi et al., “Bismuth oxide nanoparticles induce oxidative stress and apoptosis in human breast cancer cells,” *Environmental Science and Pollution Research International*, vol. 28, no. 6, pp. 7379–7389, 2021.
- [46] A. Rajae, S. Wang, L. Zhao et al., “Multifunction bismuth gadolinium oxide nanoparticles as radiosensitizer in radiation therapy and imaging,” *Physics in Medicine and Biology*, vol. 64, no. 19, article 195007, 2019.
- [47] M. Abudayyak, E. Öztaş, M. Arici, and G. Özhan, “Investigation of the toxicity of bismuth oxide nanoparticles in various cell lines,” *Chemosphere*, vol. 169, pp. 117–123, 2017.
- [48] M. Ahamed, M. J. Akhtar, M. A. M. Khan, S. A. Alrokayan, and H. A. Alhadlaq, “Oxidative stress mediated cytotoxicity and apoptosis response of bismuth oxide (Bi_2O_3) nanoparticles in human breast cancer (MCF-7) cells,” *Chemosphere*, vol. 216, pp. 823–831, 2019.
- [49] N. N. T. Sisin, K. A. Razak, S. Z. Abidin et al., “Radiosensitization effects by bismuth oxide nanoparticles in combination with cisplatin for high dose rate brachytherapy,” *International Journal of Nanomedicine*, vol. 14, no. 14, pp. 9941–9954, 2019.
- [50] D. M. Griffith, H. Li, M. V. Werrett, P. C. Andrews, and H. Sun, “Medicinal chemistry and biomedical applications of bismuth-based compounds and nanoparticles,” *Chemical Society Reviews*, vol. 50, no. 21, pp. 12037–12069, 2021.

Review Article

Nanomaterials: A Potential Hope for Life Sciences from Bench to Bedside

Mahesh Uttamrao Shinde¹, **Mohsina Patwekar**², **Faheem Patwekar**², **Majed A. Bajaber**³, **Anuradha Medikeri**², **Firdous Sayeed Mohammad**⁴, **Mohammad Mukim**⁵, **Sanjay Soni**⁶, **Jewel Mallick**⁷, and **Talha Jawaid**⁸

¹K.T Patil college of Pharmacy, Osmanabad, Maharashtra, India

²Luqman College of Pharmacy, Gulbarga, Karnataka, India

³Chemistry Department, Faculty of Science, King Khalid University, P.O. Box 9004, Abha 61413, Saudi Arabia

⁴Department of Pharmacology, Calcutta Institute of Pharmaceutical Technology and AHS, Uluberia, Howrah, 711316 West Bengal, India

⁵Kota College of Pharmacy, Kota, India

⁶Industrial and Production Engineering Jabalpur Engineering college, Jabalpur, India

⁷Department of Pharmacy, BGC Trust University Bangladesh, Chittagong 4381, Bangladesh

⁸Department of Pharmacology, College of Medicine, Al Imam Mohammad Ibn Saud Islamic University (IMSIU), Riyadh 13317, Saudi Arabia

Correspondence should be addressed to Mahesh Uttamrao Shinde; mahesgnpil@gmail.com, Mohsina Patwekar; mohsina.patwekar@gmail.com, and Jewel Mallick; jewel@bgctub.ac.bd

Received 12 May 2022; Accepted 13 June 2022; Published 30 June 2022

Academic Editor: Arpita Roy

Copyright © 2022 Mahesh Uttamrao Shinde et al. This is an open access article distributed under the Creative Commons Attribution License, which permits unrestricted use, distribution, and reproduction in any medium, provided the original work is properly cited.

In this review we hope to explain regarding nanoparticles (NPs), Nanoparticles are very small materials that range from 1 to 100 nm size. And the subclasses of nanoparticles are mentioned. Nanomaterials are formulated by nanoparticles. Research on nanomaterials is used to improve in material technology and synthesis gained the support. Nanomaterials are gradually becoming popularized and starting to arise as commodities. Nanotechnology refers to a set of scientific disciplines and designing where peculiarities that occur at aspects in the nanometre scale are used in the plan, characterization, formulation and use of materials, structures gadgets and system. Here application of nanomaterial and nanotechnology is explained. The use of nanomaterials in the production of biosensors for detection of pathogens, formulation of nanomaterial-based biosensors for detection of antibiotics, Nanomedicines and the application of nanotechnology in food business Etc were discussed. Hazards and risk of nanomaterials are studied under nanotoxicology. Nanotechnology is an arising science as would be considered normal to have quick areas of strength for improvements. It is anticipated to contribute altogether to financial development and occupation creation in the next few decades.

1. Introduction

The prefix ‘nano’ is alluded to Greek signifying ‘dwarf’ (nanos = dwarf) or ‘every small’ and represents a thousand millionth of a meter (10^{-9}) [1]. Nanomaterials are materials that have, at least, one outer aspect approximate 1 to 100 nm (Figure 1). According to the European commission’s

definition, the molecular size of approximately fifty percent of the particle in the number size distribution should be 100 nm or less. Nanoparticles have an exceptional spot in nanotechnology, not just on account of their specific effects coming about because of their diminished aspects, yet additionally on the grounds that they are promising structure blocks for more perplexing nanostructures [2]. We ought

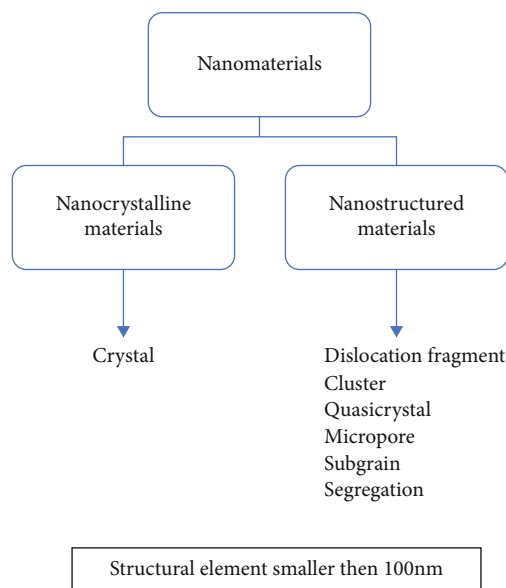


FIGURE 1: Types of Nanoparticles.

to recognize nanoscience, and nanotechnology. Nanoscience is the investigation of designs and particles on the scale of nanometres going somewhere in the range of 1 to 100 nm, and the innovation that uses it in reasonable applications example, gadget and so forth is called nanotechnology [3]. Nanotechnology (NT) is a multidisciplinary field that encompasses nanoscience, nanochemistry, nanophysics, nanomaterials, nanoelectronics, nanometrology, nanobionics, and other fields. Nanotechnology is a relatively recent discipline of science with several applications ranging from energy generation to industrial manufacturing processes to medicinal applications. Nanotechnology is anticipated as an arising designating modernism for the 21st centurial, nevertheless the generally determined areas of data innovation and biotechnology. This is a result of the logical intermingling of physical science, chemistry, biology, materials and designing at nanoscale, and the importance of the management of controversy at nanoscale on practically every alteration. Nanoparticle producing a fundamental part of nanotechnology, the fact that the particular actions are acknowledged at the nanoparticle, nanocrystal or nanolayer level, and gathering of forerunner particles and related structures is the most nonexclusive course to create nanostructured materials [4]. Different types of nanomaterials and their various applications have been mentioned in Figures 1-3.

History: Human imagination and fantasies are frequently the source of new science and technology. Nanotechnology, a twenty-first-century frontier, sprang from such fantasies. Although humans have been exposed to nanoparticles throughout history, it rose considerably during the industrial revolution. He gave a talk titled “There’s Plenty of Room at the Bottom” during the 1959 American Physical Society conference at Caltech, in which he introduced the notion of influencing matter at the atomic level. Norio Taniguchi, a Japanese scientist, was the first to use the term “nanotechnology” to describe semiconductor processes on the order of a nanometer, over 15 years after Feyn-

man’s talk. Kroto, Smalley, and Curl discovered fullerenes in the 1980s, and Eric Drexler of Massachusetts Institute of Technology (MIT) incorporated concepts from Feynman’s “There is Plenty of Room at the Bottom” and Taniguchi’s word nanotechnology in his 1986 book “Engines of Creation: The Coming Era of Nanotechnology.” Drexler introduced the concept of a nanoscale “assembler” capable of creating copies of itself as well as other things of arbitrary complexity. “Molecular nanotechnology” is a term used to describe Drexler’s view of nanotechnology. Another Japanese scientist, Iijima², produced carbon nanotubes, which took nanotechnology much further. The developing areas of nanoscience and nanotechnology sparked significant attention at the turn of the century [5].

2. Classification Of Nanoparticles

Nanoparticles (NPs) are extensively partitioned into different classes relying upon their morphology, size and compound properties. In light of physical and substance attributes, a portion of the notable classes of particles are given as beneath.

- (i) Carbon based NPs
- (ii) Metal NPs
- (iii) Ceramic NPs
- (iv) Semiconductor NPs
- (v) Polymeric NPs
- (vi) Lipid based NPs

2.1. Nanomaterials. Nanomaterials are typically recognized as materials having something like one outside aspect that contain 100 nanometres or underneath or including inner layout estimating 100 nm or lesser. They may be look like

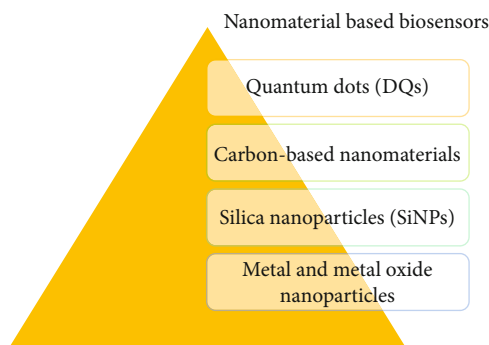


FIGURE 2: Different types of Nanomaterials.

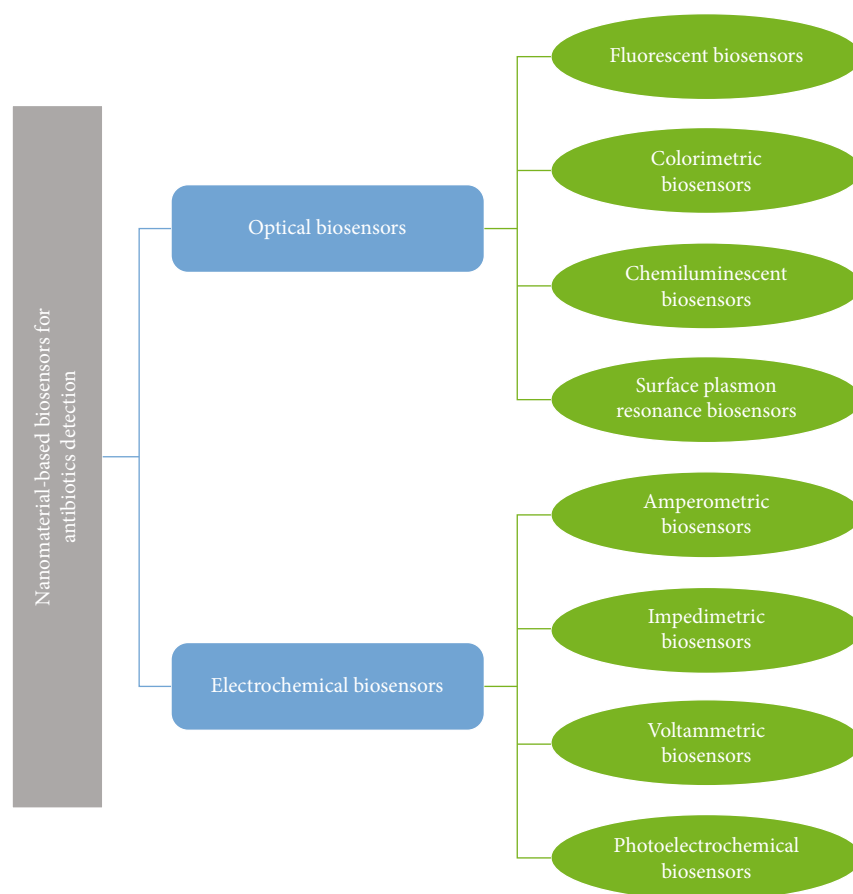


FIGURE 3: Types of Nanomaterial-Based Biosensor for Antibiotic Detection.

particles, bars, filaments or cylinders. The nanomaterials that bear much alike synthesis as realized materials in mass structure might carry different physico – compound properties compared to alike materials in mass structure, and be permitted to act differently assuming they enter body. They may hence present different expected risks. Amassed nanomaterials likewise should be surveyed in this light as they might display properties that are like those of the single nanoparticles, particularly when they have a bizarrely enormous surface region for a given measure of material. The quantity of item delivered by nanotechnology or containing nanomaterials it is expanding to enter the market [6].

2.2. Nanotechnology. Nanotechnology additionally abbreviated to 'Nanotech', is the utilization of issue on a nuclear, sub-atomic and supramolecular scale for modern desire. The primeval, far-reaching portrayal of nanotechnology alluded to the specific mechanical objective of unequivocally controlling particles also atoms with creation of macroscale items, likewise present alluded as sub-atomic nanotechnology. A most summed up depiction of nanotechnology is accordingly settled by the. Nanotechnology is defined as the administration of material with at least one dimeter sized between 1 and 100 nanometres, according to the Public Nanotechnology Initiative. Because quantum mechanical

influences are significant at this scale, the term has evolved from a specific technical goal to a research division that encompasses other forms of experiments and techniques can handle among the peculiar features of material that exist underneath the stated threshold. As a result, the terms 'nanotechnologies' and 'nanoscale technologies' are frequently attributed to a broad number of studies and implementations with a frequent characteristic of size. [7, 8]

Nanotechnology's future ramifications are now being debated among scientists. Scientists are now debating the potential implications of nanotechnology. Nanotechnology has the potential to create a wide range of novel materials and devices with a wide range of applications, including biomaterials, nanomedicine, nanoelectronics, consumer goods and energy generation. However, nanotechnology brings many of the same concerns as any new breakthrough, including concerns about the safety and natural effects of nanomaterials. And their potential implications for global financial elements, as well as hypotheses concerning various judgement day scenarios. These concerns have spurred a debate among supporters and legislators over whether exceptional nanotechnology guidelines are necessary [9].

3. Applications

3.1. NANOMATERIAL BASED BIOSENSORS. Ongoing advancements in nanotechnology along with the chance of composing electrodes for a tiny scope, nanoscale sensors produce conceivable as well as brought about another arrangement of analytic biosensors termed as Nanobiosensors. Nonstop reduction in particle aspect, deriving out of huge scope to little one in the reach somewhere in the range of 1 and 100 nm, does not change biosensor properties however fundamentally works on their pertinence. The surface cooperation of the sensors with analyte turns out to be exceptionally productive because of the very huge surface to volume proportions in Nano-size gadgets [10]. Thusly, nanoscale matters exhibit extraordinary highlights, usefulness, also actions. These days, nanotechnology is centred around end of impediments of actual techniques considering infection identification to limit expenses and tedious. Moreover, the implantation of nanomaterials for the development of biosensors brought about expanding of effectiveness also, responsiveness of these frameworks [11].

By planning the connection between organic component with nanomaterial-based transducer, we may get biosensors supported through broadly utilization beneficial to the location of biomolecules including infection diagnostics. These gadgets are able to identify patient physiological condition aside wellbeing break down the food including ecological examples for pesticides and water contamination rapidly [12]. A few nanomaterials, for example, nanotubes, nanorods, nanowires, slight movies and nanoparticles are investigated for biomedical utilization because of their utilitarian electrical as well as mechanical highlights for biomedical operation. For the manufacturing of pathogenic viral biosensors, we are concentrating on the utilisation of various nanomaterials like quantum dots (QDs), carbon nanotubes, graphene oxide, silica and metal nanoparticles [13].

3.1.1. Quantum Dots. Nanoscale semiconductor crystals having optical and electrical characteristics fluctuating starting with 2 to 10 nm in diameter. As a result of their compact diameter, QDs are extremely versatile [14]. Increasing curiosity in Quantum dot-based sensors enabling chemical and biological analysis has contributed to the growth of many methods for producing QDs, including plasma synthesis, colloidal synthesis, electrochemical assembly, viral assembly, and so on. Quantum dots of the most recent generation are widely utilised in intracellular processes, tumour targeting, in vivo cell trafficking monitoring, diagnostics, and high-resolution cellular imaging. The ability of QDs to emit light is advantageous in a variety of therapeutic marking, scanning, and sensing techniques, including differentiating among healthy and cancerous cells [15], gene therapy investigations [16], proteomics [17], and so on.

3.1.2. Carbon-Based Nanomaterials. Among carbon-based nanomaterials, Graphene oxide (GO) is the ideal choice which acquainted with identifying frameworks because of particular assortment of properties like containing normal origin, biocompatible also financially savvy. The best benefits of carbon-based nanostructure is the capacity of surface treatment to be a decent prisoner for immobilizing of ligands, nanoparticles along with single-strand DNA in aptasensors. Graphene is a notable carbon-based compound and produced from automated peeling of graphite [18]. Graphite oxide can be used to make graphene oxide, which contains carboxylic, phenol hydroxyl, but also epoxide groups. Aside from the materials' unusual electronic, mechanical, and thermal capabilities, certain notable implications in nanodevices and nanomedicine have put them in the spotlight [19]. Carbon nanotubes (CNTs) are assuming a significant part in planning biosensors which can distinguish target atoms in follow sums. This strong part of CNTs is obtained by transduction of physical or chemical intercommunication furthermore large surface area to volume proportion. CNT based frameworks have presented another age of biosensors which brought about high responsiveness and selectivity concurring to their grave surface area [20].

3.1.3. Silica Nanoparticles (SiNPs). Silica nanoparticle, also known as silicon dioxide, are amorphous materials with a spherical shape. They come in wide range of forms and sizes. Silica nanoparticles contain large surface area, steadiness in critical thermic also chemical environment, great similarity like biomolecules, similar to proteins, being green about natural difficulties [21]. Many molecules, such as antigen-antibodies, peptides, and DNA, can be linked to silica nanoparticles, making such nanomaterials unique elements for biological and immunosensors. Some handful outstanding qualities concerning optoelectronic angles, such as visible luminescence behaviour, create these essential in biotechnological study, despite their biocompatibility. Many scientific applications, including cancer and antibacterial therapies, have shown to be profitable with silica nanoparticles [22].

3.1.4. Metal and Metal oxide Nanoparticles

- (i) Silver Nanoparticles (AgNPs): Silver nanoparticles varied in diameter between 1 to 100 nanometres,

this accomplish them suitable for biomedical activities. On diminishing the diameter of AgNPs, the proportion of surface area to volume shockingly increments impressively and that impact to recognizable modification within organic, physical and compound exercises. As of late, AgNPs are tried in novel as well as innovative symptomatic equipment, for example, bio and immunosensors [23].

- (ii) Gold Nanoparticles (AuNPs): Gold nanoparticles are broadly utilized in the dimension of infection discovery inferable from their extraordinary optical or electrical properties [24].
- (iii) Magnetic Nanoparticle (MNPs): Magnetic nanoparticles an extensive assortment of particles along with properties, counting attractive liquids, catalysis action also magnetic resonance imaging which shaped them helpful in the spectrum. [25].
- (iv) Zinc oxide Nanoparticles: Zinc oxide (ZnO) being the most prevalent zinc compound found in nanostructures. ZnO could be used in a variety of applications, including transducers, surface acoustic wave instruments, gas sensors, and photonic instruments. ZnO, which has piezoelectric capabilities, is used in a certain unique detectors known as mechanochemical sensors. [26].
- (v) Aluminium Nanoparticles (Al NPs): From various types of aluminium nanoparticles, nanoporous morphology is the generally well known also appealing for the researchers associated with biosensing. A few significant substance, optical along with actual properties like chemical including thermic steadiness, essentially viable in bio conditions such as human body as a consequence having large surface region compose this nanostructure appropriate to be involved it in insightful techniques [27].
- (vi) Copper Nanoparticles (CuNPs): Copper nanoparticles have gotten a lot of attention because of their enormous capability considering substitution for more overpriced nanoparticles. CuNPs' infectious activity can now be investigated using cutting-edge nanotechnology. The intrinsic susceptibility of these nanoparticles to oxidise in ambient circumstances is a severe disadvantage. Copper nanoparticles, on the other hand, provide well characteristics, therefore various biosensors targeting viral diagnosis are being created based on their use. [28].

3.2. Nanomaterial-based biosensor for Antibiotic Detection

(A) Optical Biosensor

Transmitters in optical discovery might catch signals delivered by the cooperation of the biorecognition component plus the targeted element as well as convert them into optical signs [29]. Optical biosensors were widely used for anti-infection agent identification in recent times due to its

potential advantages such as ease of use, comfort, and responsiveness. The incorporation of nanoparticles into optical biosensors has enabled ultrasensitive and mark-free antimicrobial detection techniques. The nanomaterial-based optical biosensors in antimicrobials detection could generally classified into different categories, according to the optical sign transducing system: fluorescent, colorimetric, chemiluminescent, and surface plasmon reverberation biosensing [30].

- (1) Fluorescent Biosensor: The fluorescent biosensors including fluorogenic tests are enhancing progressively famous because of their innate benefits, like activity comfort, quick hybridization energy, and simplicity of computerization [31]. Such tests normally comprise of a fluorophore also a quencher to frame a Förster Reverberation energy transfer (FRET) match, in whichever the distance-subordinate fluorescence extinguishing is intricately intended considering biomolecular acknowledgment appreciated. Nanomaterials are utilized in the process of original fluorescent biosensing stages based on their remarkable optical and electronic properties. Throughout recent many years, there is a blast of importance in the plan of novel nanoprobos via combining nanomaterials plus biomedicle acknowledgment occasions for touchy recognition of anti-infection agents [32].
- (2) Colorimetric Biosensor: Colorimetric strategies have acquired extraordinary interest as a result of their intrinsic benefits in addition to modest formulation, fast discovery, also no requirement for convoluted mechanical assembly. Colorimetry have generally used considering insightful utilized because it tends to act distinguished along just with bare eyes concluded a color change. Colorimetric biosensors are particularly well with other optical biosensors for antimicrobial location because of these qualities. Colorimetric biosensors based on nanomaterials have two different sorts: colorimetric biosensors depending upon their inherent optical characteristics of nanomaterials like plasmonic AuNPs and colorimetric biosensors based on the reactant capabilities of nanostructures like Fe_3O_4 MNPs. [33].
- (3) Chemiluminescent biosensors: Chemiluminescence (CL) is the discharge of radiant based upon chemical responses. For the most part, chemiluminescent responses are multistep oxidation responses with quick response kinetic [34]. Chemiluminescent recognition technique is widely utilized in various spectrum, particularly at optical biosensing frameworks. It assumes a strong also significant part in insightful procedure because of its benefits including high responsiveness, wide unique reach, minimal expense along with functional effortlessness. Contrasted with the fluorescence, CL have the benefits like no prerequisite as long as an outside radiation source, along with greater life span compared to that of fluorescent [35].

(4) Surface plasmon resonance biosensors: The peculiarity for swaying which arises just at connection point among two substances, that may get inspired from the pair electrons as well as photons, is known as surface plasmon resonance (SPR) [36]. It is extremely touchy for the refraction record of the dielectric that is connected with the metal outer layer. Because the refraction record is the inborn component, everything considered, each dielectric connected to the metal surface can go distinguished. In light of this standard, the SPR biosensors as a rule immobilize different organic mixtures including neutralizer, protein, and nucleic corrosive on the outer layer of metal [37].

(B) Electrochemical biosensors

Electrochemical biosensors are widely recognized also oftentimes utilized biosensors between different kinds of biosensors, because the compound responses might prompt variation in estimation of electrons either particle, that significantly affect electrical boundaries of arrangements. Nanomaterial-based electrochemical biosensors are unmistakable against anti-infection agent location attributable to their favored benefits including high responsiveness, selectivity, minimal expense, and simple activity. In view of the different sort of transducers, electrochemical biosensors may act characterized within voltammetric, impedimetric, amperometric, and photoelectrochemical biosensors [38].

- (1) Amperometric biosensors: Amperometric biosensor operates beneath the rule because sample focus is straight to the transferred electrons [39]. It assesses the sufficiency of a decrease or oxidation stream targeting a particular prospective during a decent time-frame. Numerous nanomaterials are integrated towards amperometric biosensors due to further developed discovery in anti-toxins [40].
- (2) Impedimetric biosensors: Electrochemical impedance spectroscopy (EIS) is a complimentary strategy which is profoundly delicate to variation/collaborations appearing in a surface. It can remove data about electrochemical highlights of the electrochemical framework really, for example, dual layer capacitance, dispersion impedance, charge transport cycles also arrangement opposition [41]. Throughout recent years, EIS plays had a significant influence in biosensing for different anti-microbials because of their high awareness and fast discovery times [42].
- (3) Voltammetric biosensors: Voltammetry is based on the principle of estimating the power flow through the conducting electrode. The functioning electrode is drenched in an answer containing electroactive animal groups that can be examined by changing potential. The capacity to effortlessly distinguish the analyte by its voltammetric top potential makes it incredibly delicate and particular [43].

(4) Photoelectrochemical biosensors: Photoelectrochemical (PEC) biosensor deals with the premise of the mix of the PEC oxidation and explicit biorecognition [44]. It shows more prominent execution than customary optical and electrochemical biosensors on the grounds that it joins the upsides of them. During the beyond couple of years, insightful techniques in light of PEC biosensors have been given a developing consideration because of their huge benefits, for example, basic mechanical assembly, simple scaling down, quick reaction, diminished foundation signal, and ultrahigh precision. As of late, consolidating practical nanomaterials are generally used to improve the exhibition of PEC biosensors for anti-infection agent discovery [45].

3.3. *Nanomedicine.* Nanomedicine is the clinical use of nanotechnology [46]. The utilization of nanotechnology for clinical purposes has been named nanomedicine and is characterized as the utilization of nanomaterials for diagnosis, monitoring, control, prevention and treatment of disease. Nanomaterials can be applied in nanomedicine for clinical purposes in three distinct regions: diagnosis (nanodiagnosis), controlled drug Delivery (nanotherapy), and regenerative medication. Another region which consolidates diagnostics and treatment named the ranostics is arising and is a promising methodology which holds in a similar framework both the finding/imaging specialist and the medication. Nanomedicine is holding promising changes in clinical practice by the presentation of novel drugs for both determination and treatment. Nanomaterials can be designed to have different size, shape, compound arrangement and surface, making them ready to associate with explicit biological targets. An effective biological result must be acquired turning to cautious molecule plan. Accordingly, an extensive information on how the nanomaterials connect with biological frameworks are expected for two primary reasons [47, 48].

The first is connected with the physio-pathological idea of the infections. The organic cycles behind illnesses happen at the nanoscale and can depend, for instance, on changed qualities, misfolded proteins, contamination by infection or microbes. A superior comprehension of the sub-atomic cycles will give the judicious plan on designed nanomaterials to focus on the particular site of activity wanted in the body [49]. The other concern is the communication between nanomaterial surface and the climate in natural liquids. In this specific situation, portrayal of the biomolecules crown is of most extreme significance for understanding the common communication nanoparticle-cell influences the organic reactions. This point of interaction includes dynamic systems including the trade between nanomaterial surfaces and the surfaces of natural parts (proteins, layers, phospholipids, vesicles, and organelles) [50].

3.3.1. *Physicochemical Characterization.* The portrayal of a nanomedicine is important to grasp its way of behaving in the human body, and to give direction to the cycle control and wellbeing evaluation. This portrayal is not consensual in that frame of mind of boundaries expected for a right and complete portrayal. Globally normalized procedures

and the utilization of reference nanomaterials are the way to fit every one of the various feelings about this subject [51]. Preferably, the portrayal of a nanomaterial ought to be completed at various stages all through its life cycle, from the plan to the assessment of its in vitro and in vivo execution. The association with the natural framework or even the example readiness or extraction strategies might alter a few properties and slow down certain estimations. Also, the assurance of the in vivo and in vitro physicochemical properties is significant for the comprehension of the likely gamble of nanomaterials [52].

3.3.2. Drug Delivery. Nanotechnology has given the chance of conveying medications to explicit cells utilizing nanoparticles [53]. The general medication utilization and incidental effects might be brought down fundamentally by keeping the active pharmaceutical agent in the dismal district just and in no higher portion than required. Designated drug conveyance is expected to reduce the symptoms of medications with attendant declines in utilization and treatment costs. Furthermore, designated drug conveyance diminishes the secondary effect moved by rough medication by means of limiting undesired expose to the health cells. Drug conveyance centres around boosting bioavailability both at explicit spots in the body and throughout some undefined time frame. This might possibly be accomplished by sub-atomic focusing by nanoengineered gadgets [54]. An advantage of utilizing nanoscale for clinical advancements is that more modest gadgets are less obtrusive and might potentially be embedded inside the body, in addition to biochemical response times are a lot more limited. These gadgets are quicker and more touchy than ordinary medication delivery. The viability of medication conveyance through nanomedicine is generally founded on [55]:

- (a) productive exemplification of the medications
- (b) effective conveyance of medication to the designated district of the body, and
- (c) fruitful arrival of the medication

Drug conveyance frameworks, lipid-or polymer-based nanoparticles, can be intended to work on the pharmacokinetics and biodistribution of the drug [56]. However, the pharmacokinetics and pharmacodynamics of nanomedicine is exceptionally factor various among patients. When intended to avoid from the body's defence systems, nanoparticles have helpful properties that can be utilized to further develop drug delivery [57]. Complex medication conveyance instruments are being created, including the capacity to help drugs through cell membranes and into cell cytoplasm. Triggered response reaction is one way for drug atoms to productively be utilized more. Drugs are set in the body and just actuate on experiencing a specific sign. For instance, a medication with unfortunate solubility will be substituted by a medication conveyance framework where both hydrophilic and hydrophobic conditions exist, increasing the solubility [58].

Some nanotechnology-based drugs that are industrially accessible or in human clinical trails include:

- (1) *Abraxane*, supported by the U.S. Food and drug Administration (FDA) to treat breast cancer [59], non-small cell lungs cancer (NSCLC) [60] and pancreatic cancer [61], is the nanoparticle albumin bound paclitaxel
- (2) *Rapamune* is a nanocrystal-based drug that was endorsed by the FDA in 2000 to forestall organ dismissal after transplantation. The nanocrystal parts take into account expanded drug solubility and disintegration rate, prompting further developed ingestion and high bioavailability [62].
- (3) Onivyde, liposome encapsulated *irinotecan* to cure metastatic pancreatic cancer, was supported by FDA in October 2015 [63].

Somewhat recently, we have helped to the interpretation of a few utilizations of nanomedicine in the clinical work on, going from clinical devices to nanopharmaceuticals. Nonetheless, there is as yet quite far toward the total guideline of nanomedicines.

3.3.3. Nanotechnology for Covid-19. COVID-19 is presently posing an unparalleled public health risk. The fast spread of illnesses has prompted requests for new virus-fighting strategies. Nanotechnology is gaining traction in the fight against SARS-CoV-2 infection prevention, diagnosis, and therapy. Given the rising demand for pandemic management, a comprehensive assessment that emphasises the role of nanomaterials in the pandemic response is extremely desirable [64].

COVID-19 outbreaks are becoming more common at an alarming rate. Pharmaceutical (vaccines and antiviral medicines) and non-pharmaceutical countermeasures are used in pandemic prevention techniques. In this section, we look at how nanomaterials, such as disinfectants, personal protection devices, and nanocarrier systems, may be used to build vaccines [65]. COVID-19 is inhibited by diagnostics, which limits its transmission by identifying and isolating infected patients. Despite the introduction of a few diagnostic techniques, creating a sensitive and quick COVID-19 diagnostic test remains a challenge. Virus detection today uses a variety of nanomaterials, including carbon nanotubes, quantum dots, polymeric nanoparticles, metallic nanoparticles, and silica nanoparticles (NPs). New medicines are needed to combat the proliferation of new viruses and their heterogeneity. The primary drawbacks of existing antiviral treatments are their lack of specificity, which causes damage in host cells. Nanotechnology opens up new possibilities for antiviral treatment. Nanoparticles are adjustable vectors for particular therapeutic medication delivery and viral targeting due to their flexibility. The use of nanoparticles to combat SARS-CoV-2 may include processes that impact the virus's entrance into the host cell until it is inactivated. Because inhibiting viral surface proteins may result in virus death, targeting nanoparticles that specifically target virus produced proteins may reduce viral internalisation. Nanomaterials' unique qualities, including as their strong optical and electrochemical capabilities, sizes, biocompatibility,

and cost-effectiveness, play a crucial role in a wide range of applications. Applications of nanomaterials Their characteristics may be easily modified and functionalized utilising a variety of substrates, opening up a world of possibilities for practical applications. Despite substantial progress, COVID-19 research is still in its early stages, and numerous hurdles remain [66].

3.4. Nanotechnology in food industry. Recent developments in nanotechnology have changed various logical and modern regions including the food business. Utilizations of nanotechnology have arisen with expanding need of nanoparticle utilizes in different fields of food science and food microbial science, including food handling, food packaging, functional food advancement, food safety, discovery of foodborne microorganisms, and time span of usability augmentation of food or potentially food items (Figure 4). The nanostructured food fixings are being created with the cases that they offer better taste, surface, and consistency. Nanotechnology expanding the timeframe of realistic usability of various types of food materials and furthermore help cut down the degree of wastage of food because of microbial invasion. These days nanocarriers are being used as delivery system to carry food added substances in food items without upsetting their fundamental morphology [67].

Nanotechnology gives a scope of choices to further develop the food quality and furthermore helps in upgrading food taste. Nanoencapsulation methods have been utilized comprehensively to further develop the flavour delivery and maintenance and to convey culinary equilibrium [68]. The utilization of nano-emulsions to convey lipid-solvent bioactive mixtures is much well known since they can be created utilizing regular food fixings utilizing simple creation techniques, and might be intended to improve water-dispersion and bioavailability.

3.4.1. Nutritional Value. A larger part of bioactive mixtures like lipids, proteins, carbs, and nutrients are touchy to high acidic climate and chemical movement of the stomach and duodenum. Embodiment of these bioactive mixtures not just empowers them to oppose such unfriendly circumstances yet additionally permits them to acclimatize promptly in food items, which is very difficult to accomplish in non-encapsulated structure because of low water-solvency of these bioactive mixtures. Nanoparticles-based minuscule eatable cases with the intend to further develop conveyance of meds, nutrients or delicate micronutrients in the day-to-day food varieties are being made to give critical medical advantages [69]. The nanocomposite, nano-emulsification, and nano-structuration are the various procedures which have been applied to exemplify the substances in smaller than expected structures to all the more actually convey supplements like protein and antioxidant p for definitively designated wholesome and medical advantages [70].

3.4.2. Preservation or Shelf-Life. Encapsulation practical parts inside the droplets frequently empowers a stoppage of compound debasement processes by designing the properties of the interfacial layer encompassing them. For

instance, curcumin the most dynamic and less stable bioactive phytochemical of turmeric (*Curcuma longa*) demonstrated decreased cancer prevention agent action and viewed as steady to sanitization and at various ionic strength after capsulation [71].

3.4.3. Food Packaging. Nano-based “smart” and “dynamic” food packaging’s present a few benefits over regular bundling strategies from giving better bundling material superior mechanical strength, barrier protection, antimicrobial films to nanosensing for microbe recognition and making buyers aware of the wellbeing status of food [72].

3.4.4. Pathogen Detection. Nanomaterials for use in the development of biosensors offers the elevated degree of awareness and other novel ascribes. In food microbial science, Nano sensors or Nano biosensors are utilized for the location of microorganisms in handling plants or in food material, evaluation of accessible food constituents, alarming customers and merchants on the wellbeing status of food [73].

3.4.5. Safety Issues. Other than a great deal of benefits of nanotechnology to the food business, security issues related with the nanomaterial cannot be disregarded. Numerous specialists talked about security concerns related with nanomaterial giving accentuation on the chance of nanoparticles move from the bundling material into the food and their effect on customer’s wellbeing [74].

3.5. Nanotoxicology. The study of the toxicity of nanomaterials is known as nanotoxicology [75]. Nanomaterials have new features may interact with their wider companions and have an influence on overall toxicities due to various smaller quantum dimension and larger surface area to volume proportion. Potential consequences include exposure to air, which seems may cause the most worry, as well as a concentration on pneumonic effects such as fibrosis, inflammation, and cancer-causing tendency for particular nanomaterials. Assimilation exposure as well as dermal exposure are indeed concerns [76].

- (1) **Respiratory:** Exposure to the air is the widely recognized course of openness to airborne components within the working environment. The form and size of the nanoparticles or associated agglomerates determine potential placement inside the respiratory route, and they have been kept in the airways to a greater extent compared to larger inhalable particulates. In view of creature research, nanoparticles are able to invade the circulation system driving out of the lungs also transfer to different organs, in addition to the CNS [77]. The inward breath danger is impacted through the dustiness of the components, the inclination of particles to become airborne in light of an improvement. Dust age is impacted by the molecule shape, size, mass thickness, also intrinsic electrostatic powers, and where the nanocomposites would be in the form of a granules, a sludge, or perhaps a liquid suspension [78].

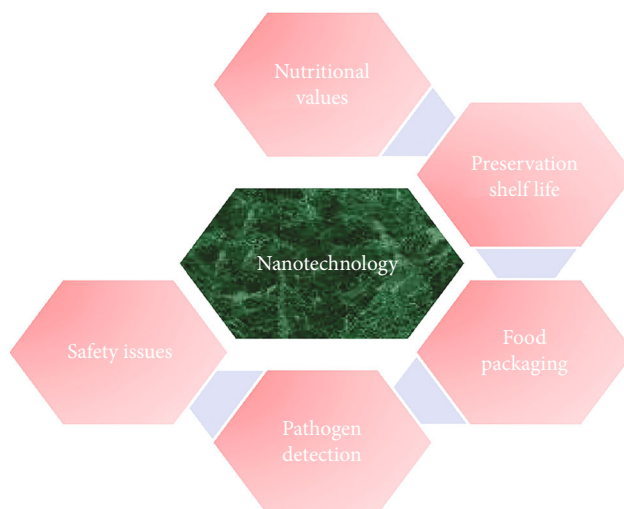


FIGURE 4: Action of Nanotechnology in different section of Food Industry.

- (2) **Dermal:** A few examinations propose that nanomaterials might actually move within the body from flawless skin during word related openness. Research are explained that components with less than $1\ \mu\text{m}$ in measurement might infiltrate within precisely crumpled skin tests, also that nanoparticles alongside fluctuating physicochemical actions had the option to enter the unblemished dermis of pigs. Aspects like size, shape, water solvency, and surface covering straightforwardly influence a nanoparticle's capability to infiltrate the dermis. As of now, it is not entirely realized whether dermal entrance of nanoparticles may bring about antagonistic impacts in creature models, albeit effective utilization of crude SWCNT to naked mice are displayed to cause skin aggravation, and *in vitro* examinations utilizing essential or refined human dermal cells are demonstrated the way a well-known carbon nanotubes are able to infiltrate cells also lead to arrival of supportive of fiery cytokines, oxidative pressure, as well as diminished practicality. It stays hazy, nonetheless, in what way these discoveries might be hypothesized to a likely word related hazard [79, 80]. Moreover, nanoparticles be allowed get in the body by means of injuries, alongside particles moving within the blood also lymph nodes [81].
- (3) **Gastrointestinal:** Ingestion may happen starting with inadvertent hand to mouth move of ingredient; this is established to occur accompanying customary materials, also it is deductively sensible for expect that it likewise be capable of occur in the course of treatment of nanomaterials. Ingestion can likewise go with inward breath openness since fragments that are expelled from the lungs lot by means of the mucociliary escalator might be gulped [82].

Particle toxicology has a subspecialty called nanotoxicology. Nanomaterials appear to have toxicity effects that are unusual and not seen in larger particles, and these

smaller particles may pose a greater threat to the human body due to their ability to move with a much greater degree of freedom, whereas the human body is designed to attack larger particles rather than nanoscale particles. Nanoparticles have substantially higher surface area to unit mass ratios, which might contribute to more pro-inflammatory effects in lung tissue, for example. Furthermore, certain nanoparticles appear to be able to travel from their deposition site to distant locations such as the blood and the brain [83].

3.6. Future Prospects in Nanotechnology. As of now, nanotechnology, along with its related exploration discipline of nanoscience, constitute the total range of exercises spreading over the entire range of actual compound, organic, and numerical sciences. The arising areas of nanoscience and nanotechnology are likewise making the vital exploratory and computational instruments for the plan and manufacture of nano-layered electronic, photonic, natural, and energy move parts, for example, quantum spots, nuclear wires, working on nanoscopic length scales, and so forth. Nanotechnology's numerous uses have changed the globe, ranging from industrial breakthroughs to touching our daily lives. Nanomaterials, particularly those with biological and other health-related features, have given the subject of nanotechnology new dimensions. Various nanotechnological applications are now being deployed to improve the aquaculture sector, which might play an essential part in the industry's future development and sustainability. Nanoscience and nanotechnology ought to significantly affect a few critical logical and mechanical exercises in an imminent future. Developments regarding these matters will have a lot to do on the innovative advances in instruments and apparatuses of manufacture and control in nano scale. Such instruments and apparatuses are the means for live representation and control in a nano world. They are by and by costly, and accordingly, not accessible to numerous agents. Innovative advances are generally followed with decrease of costs, as has been the case with the electronic and correspondence industry items in ongoing many years [84].

The unequivocal and significant driving job of atomic based strategies for the investigation of issue in the areas of nanoscience and nanotechnology is surely known. Any improvement in this field will have an incredible arrangement to do with progresses in these procedures. Progresses in the sub-atomic based investigation of issue in nanoscale will assist with understanding, reenact, anticipate, and plan new materials using the fields of quantum and measurable mechanics, intermolecular connection, sub-atomic recreation, and sub-atomic displaying. We may then have the option to comprehend how to plan new atomic structure blocks, which could permit self-get together or self-replication to propel the granular perspective of creating the vital materials for the progression of nanotechnology. The previous pattern of the commitments of sub-atomic based investigation of issue in naturally visible nanotechnology is very encouraging [85].

4. Conclusion

We concluded in this review article is that nanomaterials are made up of nanoparticles with size ranging, from 1 to 100 nanometers. In past few decades a huge development seen in the field. Because of the unique features that arise at the nanoscale, nanomaterials have piqued researcher's interest. These characteristics include a large surface area for chemical reactions, distinctive surface structures, and various ways to interact with light. Distinct category of nanomaterial-based biosensors like quantum dots, carbon-based nanomaterials, silica nanoparticles along with metal and metal oxide nanoparticles are developed. For detection of antibiotic various nanomaterial-based biosensors are growth is expanded. Nanomedicines and the application of nanotechnology in the food industry was discussed. By designing biological molecules, nanotechnology has begun to uncover promising applications in the field of functional food and Nanomedicine. Nanotechnology have received a lot of attention because of its potential to boost biotechnology and medical research. The major current goal is to concentrate on the design of nanomaterials by engineering and produces, as well as to establish standards for new materials and products in terms of human and environmental safety.

Data Availability

All data used to support the findings of this study are included within the article.

Conflicts of Interest

The authors declare that they have no conflict of interest.

Funding

None.

Acknowledgments

The authors express their appreciation to the Deanship of Scientific Research at King Khalid University, Saudi Arabia, for funding this work through research group program under grant number RGP. 2/196/43.

References

- [1] G. A. Mansoori and T. A. F. Soelaiman, *Nanotechnology—An introduction for the standards community*, ASTM International, 2019.
- [2] A. Roy, "Plant derived silver nanoparticles and their therapeutic applications," *Current Pharmaceutical Biotechnology*, vol. 22, no. 14, pp. 1834–1847, 2021.
- [3] A. Roy, H. A. Murthy, H. M. Ahmed, M. N. Islam, and R. Prasad, "Phylogenetic synthesis of metal/metal oxide nanoparticles for degradation of dyes," *Journal of Renewable Materials*, vol. 10, no. 7, p. 1911, 2021.
- [4] J. A. Schwarz, C. I. Contescu, and K. Putyera, *Dekker encyclopedia of nanoscience and nanotechnology*, vol. 5, CRC Press, 2004.
- [5] J. E. Hulla, S. C. Sahu, and A. W. Hayes, "Nanotechnology," *Human & Experimental Toxicology*, vol. 34, no. 12, pp. 1318–1321, 2015.
- [6] A. Roy, V. Singh, S. Sharma et al., "Antibacterial and Dye Degradation Activity of Green Synthesized Iron Nanoparticles," *Journal of Nanomaterials*, vol. 2022, Article ID 3636481, 6 pages, 2022.
- [7] A. Roy, A. Elzaki, V. Tirth et al., "Biological synthesis of nanocatalysts and their applications," *Catalysts*, vol. 11, no. 12, p. 1494, 2021.
- [8] A. Roy, M. Roy, S. Alghamdi et al., "Role of microbes and nanomaterials in the removal of pesticides from wastewater," *International Journal of Photoenergy*, vol. 2022, 2022.
- [9] C. Buzea, I. I. Pacheco, and K. Robbie, "Nanomaterials and nanoparticles: sources and toxicity," *Biointerphases*, vol. 2, no. 4, pp. MR17–MR71, 2007.
- [10] L. M. Bellan, D. Wu, and R. S. Langer, "Current trends in nanobiosensor technology," *Wiley Interdisciplinary Reviews. Nanomedicine and Nanobiotechnology*, vol. 3, no. 3, pp. 229–246, 2011.
- [11] A. Roy, A. Sharma, S. Yadav, L. T. Jule, and R. Krishnaraj, "Nanomaterials for remediation of environmental pollutants," *Bioinorganic Chemistry and Applications*, vol. 2021, 16 pages, 2021.
- [12] V. P. Kumar, N. Manikandan, N. Nagaprasad, J. LetaTesfaye, and R. Krishnaraj, "Analysis of the performance characteristics of ZnO nanoparticles dispersed polyester oil," *Advances in Materials Science and Engineering*, vol. 2022, Article ID 4844979, 10 pages, 2022.
- [13] A. Perumal, C. Kailasanathan, B. Stalin et al., "Multi response optimization of wire electrical discharge machining parameters for Ti-6Al-2Sn-4Zr-2Mo (α - β) alloy using Taguchi-Grey relational approach," *Advances in Materials Science and Engineering*, vol. 2022, Article ID 6905239, 13 pages, 2022.
- [14] S. Mittal and A. Roy, "Fungus and plant-mediated synthesis of metallic nanoparticles and their application in degradation of dyes," in *Photocatalytic degradation of dyes*, pp. 287–308, Elsevier, 2021.
- [15] X. Liu, G. B. Braun, H. Zhong et al., "Tumor-Targeted Multimodal Optical Imaging with Versatile Cadmium-Free Quantum Dots," *Advanced Functional Materials*, vol. 26, pp. 267–276, 2016.
- [16] D. Shao, J. Li, Y. Pan et al., "Noninvasive theranostic imaging of HSV-TK/GCV suicide gene therapy in liver cancer by folate-targeted quantum dot-based liposomes," *Biomaterials Science*, vol. 3, no. 6, pp. 833–841, 2015.

- [17] C. Pandit, A. Roy, S. Ghotekar et al., "Biological agents for synthesis of nanoparticles and their applications," *Journal of King Saud University-Science*, vol. 34, no. 3, article 101869, 2022.
- [18] M. Hasanzadeh, N. Shadjou, A. Mokhtarzadeh, and M. Ramezani, "Two dimension (2-D) graphene-based nanomaterials as signal amplification elements in electrochemical microfluidic immune-devices: Recent advances," *Materials Science and Engineering: C*, vol. 68, pp. 482–493, 2016.
- [19] K. Yang, S. Zhang, G. Zhang, X. Sun, S.-T. Lee, and Z. Liu, "Graphene in mice: ultrahigh in vivo tumor uptake and efficient photothermal therapy," *Nano Letters*, vol. 10, no. 9, pp. 3318–3323, 2010.
- [20] N. Yang, X. Chen, T. Ren, P. Zhang, and D. Yang, "Carbon nanotube based biosensors," *Sensors and Actuators B: Chemical*, vol. 207, pp. 690–715, 2015.
- [21] D. Tang, R. Yuan, and Y. Chai, "Magnetic control of an electrochemical microfluidic device with an arrayed immunosensor for simultaneous multiple immunoassays," *Clinical Chemistry*, vol. 53, no. 7, pp. 1323–1329, 2007.
- [22] A. G. Cullis, L. T. Canham, and P. D. J. Calcott, "The structural and luminescence properties of porous silicon," *Journal of Applied Physics*, vol. 82, no. 3, pp. 909–965, 1997.
- [23] K. Varner, J. Sanford, A. El-Badawy, D. Feldhake, and R. Venkatapathy, *State of the Science Literature Review: Everything Nanosilver and More*, US Environmental Protection Agency, Washington DC, 2010.
- [24] C. Lee, P. Wang, M. A. Gaston, A. A. Weiss, and P. Zhang, "Plasmonics-Based Detection of Virus Using Sialic Acid Functionalized Gold Nanoparticles," in *Biosensors and Biodetection*, A. Rasooly and B. Prickril, Eds., vol. 1571 of *Methods in Molecular Biology*, pp. 109–116, Humana Press, New York, NY, 2017.
- [25] S. Gul, S. B. Khan, I. U. Rehman, M. A. Khan, and M. I. Khan, "A Comprehensive Review of Magnetic Nanomaterials Modern Day Theranostics," *Frontiers in Materials*, vol. 6, p. 179, 2019.
- [26] U. Ozgur, Y. I. Alivov, C. Liu et al., "A Comprehensive Review of ZnO Materials and Devices," *Journal of Applied Physics*, vol. 98, no. 4, article 041301, 2005.
- [27] T. Kumeria, A. Santos, and D. Losic, "Nanoporous anodic alumina platforms: engineered surface chemistry and structure for optical sensing applications," *Sensors*, vol. 14, no. 7, pp. 11878–11918, 2014.
- [28] S. Magdassi, M. Grouchko, and A. Kamyshny, "Copper Nanoparticles for Printed Electronics: Routes towards achieving oxidation stability," *Materials*, vol. 3, no. 9, pp. 4626–4638, 2010.
- [29] S. M. Yoo and S. Y. Lee, "Optical Biosensors for the Detection of Pathogenic Microorganisms," *Trends in Biotechnology*, vol. 34, no. 1, pp. 7–25, 2016.
- [30] F. Davis and S. Higson, "Label-free immunochemistry approach to detect and identify antibiotics in Milk," *Pediatric Research*, vol. 67, no. 5, pp. 476–480, 2010.
- [31] S. E. Kim, K. Y. Ahn, J. S. Park et al., "Fluorescent Ferritin Nanoparticles and Application to the Aptamer Sensor," *Analytical Chemistry*, vol. 83, no. 15, pp. 5834–5843, 2011.
- [32] E. Hirata and E. Kiyokawa, "Future Perspective of Single-Molecule FRET Biosensors and Intravital FRET Microscopy," *Biophysical Journal*, vol. 111, no. 6, pp. 1103–1111, 2016.
- [33] S. C. Gopinath, T. LakshmiPriya, and K. Awazu, "Colorimetric detection of controlled assembly and disassembly of aptamers on unmodified gold nanoparticles," *Biosensors and Bioelectronics*, vol. 51, pp. 115–123, 2014.
- [34] D. L. Giokas, A. G. Vlessidis, G. Z. Tsogas, and N. P. Evmiridis, "Nanoparticle-assisted chemiluminescence and its applications in analytical chemistry," *TrAC Trends in Analytical Chemistry*, vol. 29, no. 10, pp. 1113–1126, 2010.
- [35] N. Li, D. Liu, and H. Cui, "Metal-nanoparticle-involved chemiluminescence and its applications in bioassays," *Analytical and Bioanalytical Chemistry*, vol. 406, no. 23, pp. 5561–5571, 2014.
- [36] C. Situ, M. H. Mooney, C. T. Elliott, and J. Buijs, "Advances in surface plasmon resonance biosensor technology towards high-throughput, food-safety analysis," *TrAC Trends in Analytical Chemistry*, vol. 29, no. 11, pp. 1305–1315, 2010.
- [37] S. Chand and B. D. Gupta, "Surface plasmon resonance based fiber-optic sensor for the detection of pesticide," *Sensors and Actuators B: Chemical*, vol. 123, no. 2, pp. 661–666, 2007.
- [38] S. Wang, X. Li-Ping, and X. Zhang, "Ultrasensitive electrochemical biosensor based on noble metal nanomaterials," *Science of Advanced Materials*, vol. 7, no. 10, pp. 2084–2102, 2015.
- [39] M. Tomassetti, M. Serone, R. Angeloni, L. Campanella, and E. Mazzone, "Amperometric Enzyme Sensor to Check the Total Antioxidant Capacity of Several Mixed Berries. Comparison with Two Other Spectrophotometric and Fluorimetric Methods," *Sensors*, vol. 15, no. 2, pp. 3435–3452, 2015.
- [40] A. Hayat, G. Catanante, and J. L. Marty, "Current Trends in Nanomaterial-Based Amperometric Biosensors," *Sensors*, vol. 14, no. 12, pp. 23439–23461, 2014.
- [41] O. N. Oliveira, F. J. Pavinatto, C. J. L. Constantino, F. V. Pavlovich, and M. C. F. de Oliveira, "Information visualization to enhance sensitivity and selectivity in biosensing," *Biointerphases*, vol. 7, no. 1-4, p. 53, 2012.
- [42] F. Conzuelo, M. Gamella, S. Campuzano et al., "Integrated Amperometric Affinity Biosensors Using Co²⁺-Tetradentate Nitrilotriacetic Acid Modified Disposable Carbon Electrodes: Application to the Determination of β -Lactam Antibiotics," *Analytical Chemistry*, vol. 85, no. 6, pp. 3246–3254, 2013.
- [43] D. Kamysbayev, B. Serikbayev, G. Arbutz, G. Badavamova, and K. Tasibekov, "Synthesis and electrochemical behavior of the Molybdenum-Modified electrode based on Rice husk," *Eurasian Chemico-Technological Journal*, vol. 19, no. 4, pp. 315–321, 2017.
- [44] H. Shi, J. Zhao, Y. Wang, and G. Zhao, "A highly selective and picomolar level photoelectrochemical sensor for PCB 101 detection in environmental water samples," *Biosensors and Bioelectronics*, vol. 81, pp. 503–509, 2016.
- [45] Y. Li, S. Zhang, H. Dai, Z. Hong, and Y. Lin, "An enzyme-free photoelectrochemical sensing of concanavalin a based on graphene-supported TiO₂ mesocrystal," *Sensors and Actuators B: Chemical*, vol. 232, pp. 226–233, 2016.
- [46] R. A. Freitas, *Nanomedicine: Basic Capabilities*, Landes Bioscience, Austin, TX, 1999.
- [47] E. A. Bleeker, W. H. de Jong, R. E. Geertsma et al., "Considerations on the EU definition of a nanomaterial: science to support policy making," *Regulatory Toxicology and Pharmacology*, vol. 65, no. 1, pp. 119–125, 2013.
- [48] V. S. Chan, "Nanomedicine: an unresolved regulatory issue," *Regulatory Toxicology and Pharmacology*, vol. 46, no. 3, pp. 218–224, 2006.
- [49] B. Y. Kim, J. T. Rutka, and W. C. Chan, "Nanomedicine," *The New England Journal of Medicine*, vol. 363, no. 25, pp. 2434–2443, 2010.
- [50] A. E. Nel, L. Mädler, D. Velegol et al., "Understanding biophysical interactions at the nano-bio interface," *Nature Materials*, vol. 8, no. 7, pp. 543–557, 2009.

- [51] P. C. Lin, S. Lin, P. C. Wang, and R. Sridharb, "Techniques for physicochemical characterization of nanomaterials," *Biotechnology Advances*, vol. 32, no. 4, pp. 711–726, 2014.
- [52] S. Abel, J. L. Tesfaye, L. Gudata et al., "Investigating the Influence of Bath Temperature on the Chemical Bath Deposition of Nano Synthesized Lead Selenide Thin Films for Photo Voltaic Application," *Journal of Nanomaterials*, vol. 2022, Article ID 3108506, 6 pages, 2022.
- [53] R. Ranganathan, S. Madanmohan, A. Kesavan et al., "Nanomedicine: towards development of patient-friendly drug-delivery systems for oncological applications," *International Journal of Nanomedicine*, vol. 7, pp. 1043–1060, 2012.
- [54] D. A. LaVan, T. McGuire, and R. Langer, "Small-scale systems for *in vivo* drug delivery," *Nature Biotechnology*, vol. 21, no. 10, pp. 1184–1191, 2003.
- [55] A. Saka, J. L. Tesfaye, L. Gudata et al., "Synthesis, characterization, and antibacterial activity of ZnO nanoparticles from fresh leaf extracts of Apocynaceae, *Carissa spinarum* L. (Hagamsa)," *Journal of Nanomaterials*, vol. 2022, Article ID 6230298, 6 pages, 2022.
- [56] T. M. Allen and P. R. Cullis, "Drug delivery systems: entering the mainstream," *Science*, vol. 303, no. 5665, pp. 1818–1822, 2004.
- [57] N. Bertrand and J. C. Leroux, "The journey of a drug-carrier in the body: an anatomo-physiological perspective," *Journal of Controlled Release*, vol. 161, no. 2, pp. 152–163, 2012.
- [58] Z. K. Nagy, A. Balogh, B. Vajna et al., "Comparison of electrospun and extruded Soluplus®-based solid dosage forms of improved dissolution," *Journal of Pharmaceutical Sciences*, vol. 101, no. 1, pp. 322–332, 2012.
- [59] US Food and Drug Administration, *Highlights of Prescribing Information, Abraxane for Injectable Suspension*, Food and Drug Administration, 2012.
- [60] Paclitaxel (Abraxane), U.S. Food and Drug Administration, 2012, <https://www.nytimes.com/2013/09/07/business/fda-approves-drug-for-late-stage-pancreatic-cancer.html#:~:text=The%20Food%20and%20Drug%20Administration,than%20two%20months%20on%20average>.
- [61] US Food and Drug Administration, *FDA approves Abraxane for late-stage pancreatic cancer*, US Food and Drug Administration, 2013.
- [62] L. Gao, G. Liu, J. Ma et al., "Application of drug nanocrystal technologies on oral drug delivery of poorly soluble drugs," *Pharmaceutical Research*, vol. 30, no. 2, pp. 307–324, 2013.
- [63] "FDA approves new treatment for advanced pancreatic cancer," vol. 22, 2015 [https://www.webmd.com/cancer/pancreatic-cancer/news/20191231/fda-approves-drug-for-pancreatic-cancer-treatment#:~:text=Dec.,the%20drug%20olaparib%20\(Lynparza\)](https://www.webmd.com/cancer/pancreatic-cancer/news/20191231/fda-approves-drug-for-pancreatic-cancer-treatment#:~:text=Dec.,the%20drug%20olaparib%20(Lynparza)).
- [64] Y. Rasmi, K. S. Saloua, M. Nemati, and J. R. Choi, "Recent Progress in nanotechnology for COVID-19 prevention, diagnostics and treatment," *Nanomaterials (Basel)*, vol. 11, no. 7, p. 1788, 2021.
- [65] M. Hassanpour, J. Rezaie, M. Nouri, and Y. Panahi, "The role of extracellular vesicles in COVID-19 virus infection," *Infection, Genetics and Evolution*, vol. 85, article 104422, 2020.
- [66] Z. Zhao, H. Cui, W. Song, X. Ru, W. Zhou, and X. Yu, *A simple magnetic nanoparticles-based viral RNA extraction method for efficient detection of SARS-CoV-2*, BioRxiv, 2020.
- [67] H. M. Ahmed, A. Roy, M. Wahab et al., "Applications of nanomaterials in Agrifood and pharmaceutical industry," *Journal of Nanomaterials*, vol. 2021, Article ID 1472096, 10 pages, 2021.
- [68] T. P. Sari, B. Mann, R. Kumar et al., "Preparation and characterization of nanoemulsion encapsulating curcumin," *Food Hydrocolloids*, vol. 43, pp. 540–546, 2015.
- [69] A. B. Ozturk, S. Argin, M. Ozilgen, and D. J. McClements, "Formation and stabilization of nanoemulsion-based vitamin E delivery systems using natural biopolymers: Whey protein isolate and gum arabic," *Food Chemistry*, vol. 188, pp. 256–263, 2015.
- [70] S. S. Yan and J. M. Gilbert, "Antimicrobial drug delivery in food animals and microbial food safety concerns: an overview of *in vitro* and *in vivo* factors potentially affecting the animal gut microflora," *Advanced Drug Delivery Reviews*, vol. 56, no. 10, pp. 1497–1521, 2004.
- [71] R. Langer and N. A. Peppas, "Advances in biomaterials, drug delivery, and bionanotechnology," *AIChE Journal*, vol. 49, no. 12, pp. 2990–3006, 2003.
- [72] U. Chadha, P. Bhardwaj, S. K. Selvaraj et al., "Current trends and future perspectives of nanomaterials in food packaging application," *Food Hydrocolloids*, vol. 2022, Article ID 2745416, p. 32, 2022.
- [73] S. D. F. Mihindukulasuriya and L. T. Lim, "Nanotechnology development in food packaging: a review," *Trends in Food Science and Technology*, vol. 40, no. 2, pp. 149–167, 2014.
- [74] Q. Cheng, C. Li, V. Pavlinek, P. Saha, and H. Wang, "Surface-modified antibacterial TiO₂/Ag⁺ nanoparticles: Preparation and properties," *Applied Surface Science*, vol. 252, no. 12, pp. 4154–4160, 2006.
- [75] E. L. Bradley, L. Castle, and Q. Chaudhry, "Applications of nanomaterials in food packaging with a consideration of opportunities for developing countries," *Trends in Food Science and Technology*, vol. 22, no. 11, pp. 604–610, 2011.
- [76] N. van Zandwijk and A. L. Frank, "Awareness: potential toxicities of carbon nanotubes," *Translational Lung Cancer Research*, vol. 8, no. Suppl 4, p. S471, 2019.
- [77] V. E. Orel, O. Dasyukevich, O. Rykhalskyi, V. B. Orel, A. Burlaka, and S. Virko, "Magneto-mechanical effects of magnetite nanoparticles on Walker-256 carcinosarcoma heterogeneity, redox state and growth modulated by an inhomogeneous stationary magnetic field168314," *Journal of Magnetism and Magnetic Materials*, vol. 538, 2021.
- [78] L. Hodson, M. Methner, and R. D. Zumwalde, *Approaches to Safe Nanotechnology: Managing the Health and Safety Concerns Associated with Engineered Nanomaterials*, US National Institute for Occupational Safety and Health, 2009.
- [79] C. Beaucham and L. Hodson, *General Safe Practices for Working with Engineered Nanomaterials in Research Laboratories*, US National Institute for Occupational Safety and Health, 2012.
- [80] J. Howard, *Current Intelligence Bulletin 65: Occupational Exposure to Carbon Nanotubes and Nanofibers*, DHHS (NIOSH) Publication, 2013.
- [81] US National Institute for Occupational Safety and Health, *Current Intelligence Bulletin 63: Occupational Exposure to Titanium Dioxide*, DHHS (NIOSH) Publication, 2011.
- [82] S. W. Dean, G. A. Mansoori, and T. A. F. Soelaiman, "Nanotechnology — An Introduction for the Standards Community," *Journal of ASTM International*, vol. 2, no. 6, p. 13110, 2005.
- [83] A. Sukhanova, S. Bozrova, P. Sokolov, M. Berestovoy, A. Karaulov, and I. Nabiev, "Dependence of Nanoparticle Toxicity on Their Physical and Chemical Properties," *Nanoscale Research Letters*, vol. 13, pp. 1–21, 2018.

- [84] G. A. Mansoori, "An Introduction to Nanoscience & Nanotechnology," in *Nanoscience and Plant–Soil Systems*, M. Ghorbanpour, K. Manika, and A. Varma, Eds., vol. 48 of *Soil Biology*, pp. 3–20, Springer, Cham, 2017.
- [85] G. A. Mansoori and T. A. F. Soelaiman, "Nanotechnology — An Introduction for the Standards Community," *Journal of ASTM International*, vol. 2, pp. 1–21, 2005.

Research Article

Green Synthesis of Gold Nanoparticles Using Extract of *Pistacia chinensis* and Their *In Vitro* and *In Vivo* Biological Activities

Fahad A. Alhumaydhi 

Department of Medical Laboratories, College of Applied Medical Sciences, Qassim University, Buraydah, Saudi Arabia

Correspondence should be addressed to Fahad A. Alhumaydhi; f.alhumaydhi@qu.edu.sa

Received 14 April 2022; Revised 6 June 2022; Accepted 7 June 2022; Published 30 June 2022

Academic Editor: H C Ananda Murthy

Copyright © 2022 Fahad A. Alhumaydhi. This is an open access article distributed under the Creative Commons Attribution License, which permits unrestricted use, distribution, and reproduction in any medium, provided the original work is properly cited.

The synthesis of metal nanoparticles by using plant extracts is previously explored in phytomedicines. Nanobiotechnology has many applications, including cosmetic, packing, coating, biomedicine, and enhanced biological activity. Keeping in view the importance of *Pistacia chinensis*, its gold nanoparticles (AuNPs) have been synthesized by the eco-friendly and cost-effective method. In this study, the synthesized nanoparticles were characterized by advanced techniques such as UV-visible spectroscopy, Fourier transform infrared (FT-IR), and atomic force microscope (AFM) analysis. The biological activities of these synthesized nanoparticles were examined *in vitro* by measuring the enzymatic inhibition potential on urease and carbonic anhydrase and *in vivo* by determining the analgesic and sedative activities. The UV spectrum indicated various peaks at the range of 530–550 nm, showing nanoparticles formation. The FT-IR spectroscopy of the extracts and AuNPs indicated the presence of NH, C=N, and N=O in the extract involved in the nanoparticles synthesis. The size of nanoparticles was determined by AFM analysis. The AFM showed that the nanoparticles range from 10 to 100 nm and are almost spherical in shape. The synthesized AuNPs exhibited significant urease inhibition potential with an IC_{50} value of 44.98. Similarly, the nanoparticles exhibited good carbonic anhydrase inhibition with an IC_{50} value of 53.54 against acetazolamide having IC_{50} 0.13. *Pistacia chinensis* extract and its AuNPs exhibited excellent attenuation $p < 0.01$ in acetic acid-induced writhing model at a dose of 15 mg/kg. The synthesized nanoparticles showed a significant sedative effect $p < 0.001$ compared to the standard drug. This research work has developed a green method to synthesize nanoparticles by using *Pistacia chinensis* extract and directed the researcher to purify active phytochemicals from *Pistacia chinensis* involved in nanoparticles synthesized.

1. Introduction

Application of nanotechnology has found to be of significant importance in different fields such as imaging, sensing, and biomedical sciences [1–4]. It has also a broad-spectrum usage in several areas including cosmetics, energy, electronics, food, agriculture, and biomedicine [5–7]. Nanotechnology has attained attention in medical sciences because of its role in plant, animal, and human health which led to many applications in the field of medicine [1, 8]. Examples of these include controlled delivery of drugs, electroluminescent, imaging, detection, destruction of tumor, cancer diagnosis, and tissue engineering [9–15].

Nanoparticles (NPs) are a novel technique used in the field of medical sciences which has been shown to have

promising results [16]. Extensive researches have revealed the importance of NPs in medicine owing to their role in catalytic degradation [17], antiviral [18], antibacterial [19], anticancer [20], antidiabetic [21], and wound healing [22].

Different physical, chemical, and biological approaches are used to synthesize NPs [16]. The most commonly used metals to synthesize NPs are platinum, palladium, silver, and gold [23]. Among these common metals, gold is possessing a high ionic conductivity, and synthesized gold nanoparticles (AuNPs) can be adjusted based on their surface state, shape, and size [18, 21, 23–27].

Biological derived NPs are shown to be sustainable, effective, safe, and cost-efficient [28–30]. Metals are used for the synthesis of NPs [26, 31, 32] from different resources such as bacteria, algae, fungi, and plant extracts [33–38].

Among these resources, metallic NPs prepared from natural plant materials have different biological activities, owing to their altered features such as small particle size, enhanced surface area, and varied shape [30, 33, 34, 39, 40].

Pistacia chinensis Bunge, also known as Chinese pistache, is a well-known member of the family Anacardiaceae [41]. It is distributed in many places such as Pakistan, India, China, the Philippines, North America, and Taiwan [42]. It is a deciduous tree having characteristics of a rounded crown [43]. Foliage comprises of compound, dark green leaves, which are aromatic when bruised [44]. *Pistacia* genus consists of 11 species. It has previously been showed that *Pistacia chinensis* can be used to treat various diseases such as asthma, fever, cough, and respiratory disease [44, 45]. In various countries, its seeds are used as an oil material [46]. Various secondary metabolites such as flavonoids and phenolic compounds have been reported from various parts of *Pistacia chinensis* [46]. Two 4-arylcomarin moieties (neoflavone) dimers have been reported from *Pistacia chinensis* with excellent estrogen-like properties [47]. Various phenolic compounds such as digallic acid, gallic acid, quercetin, quercetin-3-O(6''-galloyl)- β -D-glucosides, and 6-O-galloyl arbutin-quercitrin have been documented from the leaves of *Pistacia chinensis* [48]. Tender burgeons of *Pistacia chinensis* also reported the presence of a new pyrrolidone derivative [46]. *Pistacia chinensis* plant has been reported for excellent anti-inflammatory potency [49]. The compounds isolated from aerial parts of *Pistacia chinensis* have been reported for promising anti-HCV activity [50]. The chemical, which is isolated from the leaves of *Pistacia chinensis*, also possesses excellent antimicrobial potency [51].

Thus, keeping in view the significance of NPs in drug delivery and medicinal importance of *Pistacia chinensis*, the present work was aimed for the development, characterization, and evaluation of the biological efficiency of *Pistacia chinensis*-based gold nanoparticles (AuNPs). Purposely, both *in vitro* (enzyme inhibitory activities) and *in vivo* (sedative and antinociceptive properties) investigations were conducted in this study to determine the biological effectiveness of prepared *Pistacia chinensis* extract and its AuNPs.

2. Material and Method

2.1. Plant Collection. *Pistacia chinensis* Bunge seeds was kindly gifted from Dr. Abdur Rauf, Department of Chemistry, University of Swabi, KP, Pakistan. These plant seeds were collected from the ground of Hostel 2, University of Peshawar, KPK, Pakistan. The plant specimens were recognized by Dr. Muhammad Ilyas at Department of Botany, University of Swabi, KP, Pakistan. The voucher specimens were stored in Department of Botany, University of Swabi, KP, Pakistan.

2.2. Preparation of Extract. The obtained seed was dried in the shade for 20 days and was with water to remove the dust. After that, the dried seed was subjected to the grinder to obtain a powder. The powder plant material (1 kg) was soaked in methanol for 10 days to obtain a maximum number of polar secondary metabolites. The extract obtained was

concentrated at low temperature and pressure with the help of a rotary evaporator, which afforded 18.9 g extract.

2.3. Synthesis of Nanoparticles. To synthesize gold nanoparticles, 2 mg of extract was transferred to 100 mL distilled water and dissolved to prepare stock solution of extract. Similarly, 1 mM stock solution of gold salt (HAuCl_4) was prepared for synthesizing nanoparticles of *Pistacia chinensis* seed extract. To reduce Au⁺³ into Au⁰, the extract solution was combined with a syringe to the salt solution in various ratios. The gold salt solution (HAuCl_4) was kept constant, and the extract concentration was changed (1:1; 1:2; 1:3; 1:4; 1:6; 1:8; 1:10; 1:12, etc.) and then stirred for 30 minutes at 40°C. Then, the solution was kept for stirring continuously for a period of 5 hours to optimize condition for formation on nanoparticles. The change in color indicates the formation of gold nanoparticles.

2.4. Characterization of Gold Nanoparticles. The synthesis of nanoparticles by reaction gold solution (1 mM) and *Pistacia chinensis* extracts at various concentrations was characterized by ultraviolet visible spectrophotometer spectroscopy (SP-3000 Plus, Japan), Fourier transform infrared (FT-IR), Prestige-21 (Shimadzu, Japan), atomic force microscope (AFM) (Agilent technology, USA), and clear change in color. Changes in the ration of plant extracts and gold salt intensity of the peaks changed to the visible region.

2.5. Animals. BALB/c mice were used in this study for *in vivo* screening with range of weight from 20 to 26 g. The mice were obtained from animal house facility of King Saud University, Saudi Arabia. After transferring the mice, they were reserved at room temperature in standard laboratory conditions at the College of Applied Medical Sciences, Qassim University, Saudi Arabia. They were served with standard food and water ad libitum. All the experiments were performed in this study following the guidelines of the National Research Council (US) Guide for the Care and Use of Laboratory Animals after being reviewed and approved by the Committee of Research Ethics, Deanship of Scientific Research, Qassim University, Saudi Arabia (Ethical Approval No. 21-09-07).

2.6. Enzyme Inhibitory Screening. *Pistacia chinensis* extract and its AuNPs were assessed for urease and carbonic anhydrase inhibitory by following the recently published method [52–57]. For urease inhibitory activities, the ammonia production after treating the samples with urea was measured via indophenol method. Thiourea was used in the urease inhibitory evaluation as a standard inhibitor. Concentration of *Pistacia chinensis* extract, gold nanoparticles of *Pistacia chinensis*, and standard inhibitor used in this experiment was 0.2 μg . Data were recorded after 50 minutes of incubation, and the formula used to determine the percent inhibition was the following:

$$\% \text{Inhibition} = 100 - (\text{OD test well} / \text{OD control}) \times 100 \quad (1)$$

Pistacia chinensis extract and synthesized AuNPs of *Pistacia chinensis* were tested also for carbonic anhydrase

inhibitory potential. A yellow-colored compound (4-nitrophenol) was produced during the test. The assay was done at room temperature, and acetazolamide was used in this experiment as a standard inhibitor. Concentration of *Pistacia chinensis* extract, gold nanoparticles of *Pistacia chinensis*, and standard inhibitor used in this experiment was 0.2 mM.

2.7. Analgesic Activity. *Pistacia chinensis* extract and its AuNPs was screened for analgesic activity by following the recently published procedure using a standard method [58–60]. Mice were divided into different groups in this study, and each group comprised six mice ($n = 6$). The weight of the mice ranged from 20 to 26 gram. One of the mice groups was treated with a standard drug called diclofenac as a dose of 10 mg/kg, i.p. Another group of the mice was administrated with normal saline at concentration (10 mL/kg i.p.), while the other groups of mice in this study received *Pistacia chinensis* extract at different doses (25, 50, and 100 mg/kg (i.p.)) and gold nanoparticles at different doses (5, 10, and 15 mg/kg (i.p.)). After the completion of treatment (40 minutes), acetic acid (0.9%) (v/v, 0.1 mL/10 g body weight) was used to induce the pain in the mice by intraperitoneal injection (i.p.). The muscle contraction was noted for every mouse in this experiment for a period of 10 minutes after injection of acetic acid.

2.8. Sedative Activity. *Pistacia chinensis* extract and its AuNPs were screened for sedative activity by following the recently published procedure [58, 59, 61]. The sedative activities of the extract were investigated in this study by using an open-field screening technique which was performed in a room with light and sound attenuated. All mice groups in the study were adapted and familiarized with the red light (40 W red bulb) with also water and food accessible ad libitum for 2 weeks before starting of the experiment. Normal saline was used as a negative control, and diazepam was used as a reference drug. One of the mice groups was treated with the plant extract at different doses (25, 50, and 100 mg/kg (i.p.)), and another mice group was treated with gold nanoparticles at doses of 5, 10, and 15 mg/kg i.p. After that, each mouse in the current experiment was kept in the white wood arena in the center, and then, the number of lines crossed was counted for every mouse in each group of mice.

2.9. Statistical Analysis. Outcomes of the current research were presented as mean \pm SEM (standard error of the mean). The level of significant differences ($p \leq 0.05$) between all the groups in this study was evaluated using one-way analysis of variance (ANOVA). Dunnett's multiple comparison test was performed for comparison purpose.

3. Results

3.1. Characterization of Gold Nanoparticles

3.1.1. UV-Spectroscopy. The results of UV-visible spectra indicate that gold nanosized nanoparticles were prepared successfully at various ratios by recording peaks in the definite region for gold nanoparticles. Figure 1 indicates various peaks at the range from 530 to 550 nanometer showing dif-

ferent absorbance as a result of the different sizes of the synthesized AuNPs. In addition, the sharpness of the peak indicated the uniformity of AuNPs, and based on this information, it was observed that the peak for AuNPs (1:4) showed the highest absorbance by considering the peak height from the baseline of the spectrum. This was the indication to the presence of greater concentration of AuNPs in the solution, while other peaks presented also in Figure 1 showed lower peak height (measured from the baseline of spectrum) and broadness which can reveal the presence of a greater number of nonuniform AuNPs in the solution. Thus, the ratio (1:4) was used in the current study for the preparation of the bulk solutions for further investigations.

3.1.2. Kinetic Study of AuNPs. Results for the kinetic study of the synthesis of AuNPs are indicated in Figure 2. It was observed that the number and uniformity of nanoparticles increased with the passage of time.

3.1.3. Stability towards pH. The pH of AuNP solution was adjusted in the current study between 1 and 14 to evaluate the effect of varied pH on the stability of AuNPs as shown in Figure 3. The solution was kept at room temperature for 24 hours, and its affect was determined by recording UV-visible spectrum. Results of the stability towards pH showed that AuNPs were more stable in pH between 3 and 12, while less stability was observed in pH between the range from 1 to 2 and from 13 to 14 indicating lower stability of the AuNP solution in acidic and basic conditions. Maximum stability was detected in this experiment at alkaline pH range of 8–10, while moderate stability of the AuNPs was noticed at pH range of 3 to 4 as in this range, the gold nanoparticles showed peak broadening. However, the removal of plant extract, considered as the stabilizer, from the gold surface to destabilize the nanoparticles can be the reason for the instability of AuNPs found at lower and higher pH. In addition, very low pH may cause the reoxidation of neutral AuNPs.

3.1.4. Stability towards NaCl. The effects of salt (NaCl) on AuNPs of *Pistacia chinensis* were examined in this current study by using varying concentration of the salt from 0.1 to 0.5 M on synthesized AuNPs. During the assay, the AuNPs (2 mL) were mixed with NaCl solution (1 mL) which have concentrations ranging from 0.1 to 0.5 M in order to find the salt effect. The UV-vis spectra were recorded after keeping the intermixed solution of salt and AuNPs for 24 hours. Results showed that the AuNPs start precipitating by increasing the salt concentration, and the solution becomes colorless at a high concentration of the salt as shown in Figure 4.

3.1.5. FT-IR Spectral Analysis. In the FT-IR spectrum (Figure 5) of *Pistacia chinensis*, multiple peaks were observed between 563 cm^{-1} and 3417 cm^{-1} . Furthermore, the green synthesis of AuNPs was confirmed by Fourier transform infrared (FT-IR) spectroscopy analysis in Figure 6, which exhibited different secondary metabolites present in extracts involved in the synthesis of gold nanoparticles (AuNPs). The FT-IR spectrum of extract and

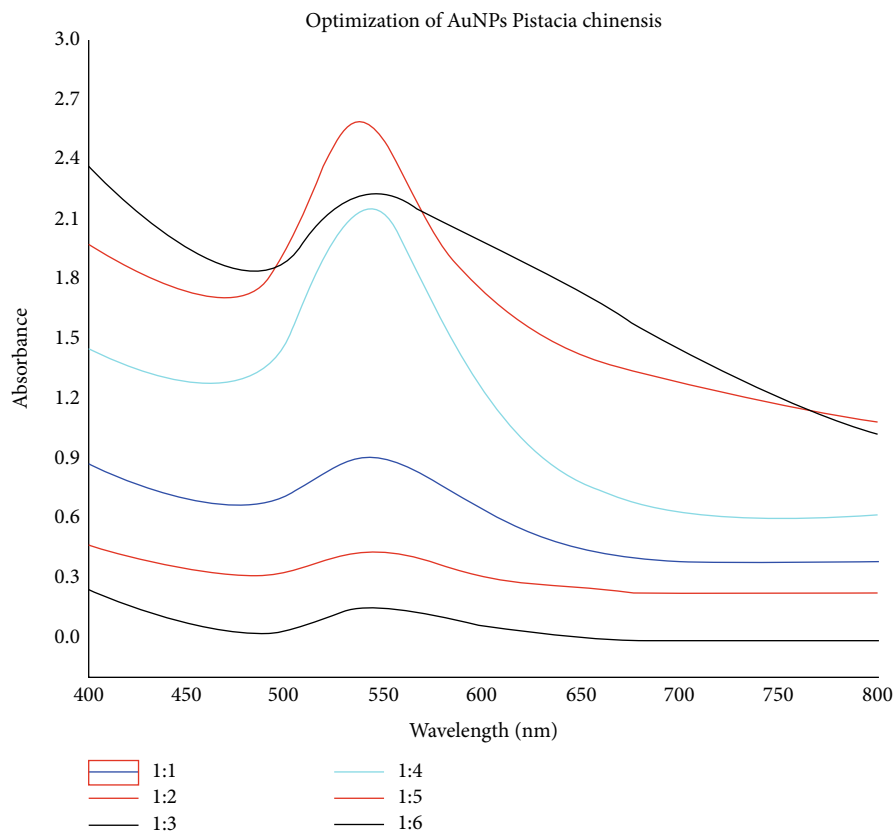


FIGURE 1: UV-visible spectra of gold nanoparticles prepared from *Pistacia chinensis* extract.

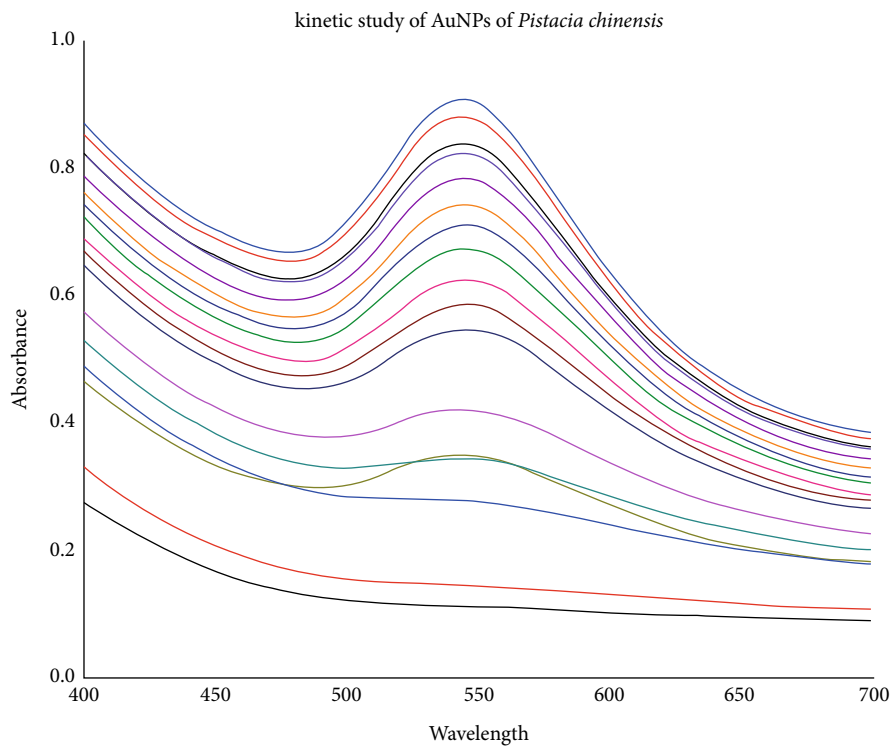


FIGURE 2: UV-visible data of kinetic study of AuNPs of *Pistacia chinensis*.

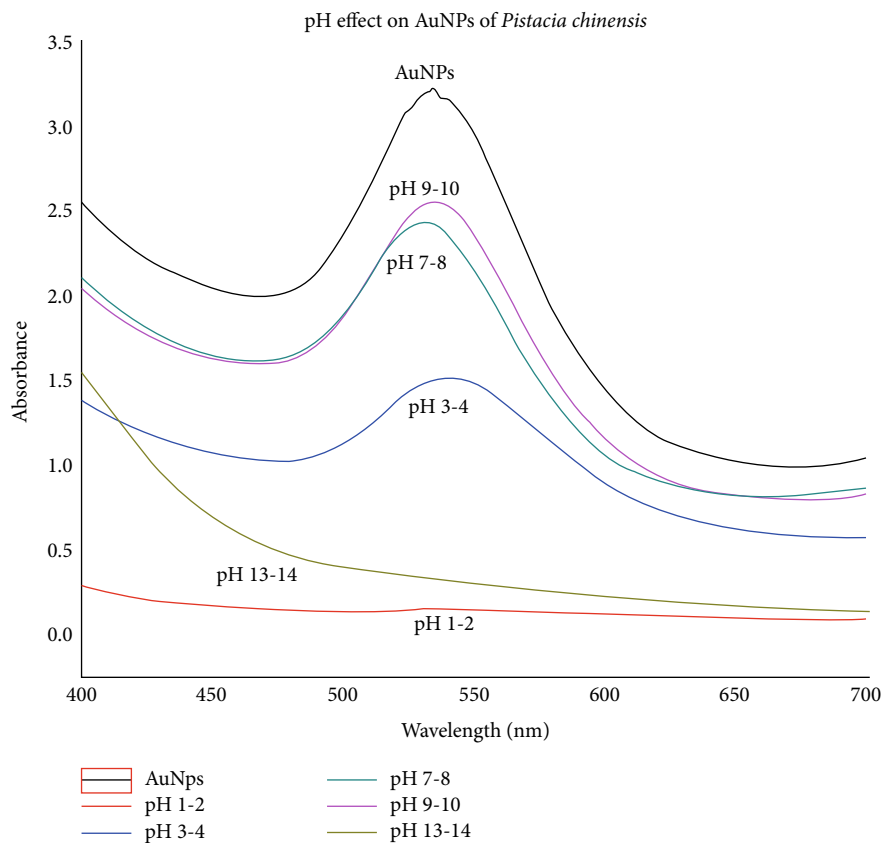


FIGURE 3: UV-visible data of pH effect on AuNPs of *Pistacia chinensis*.

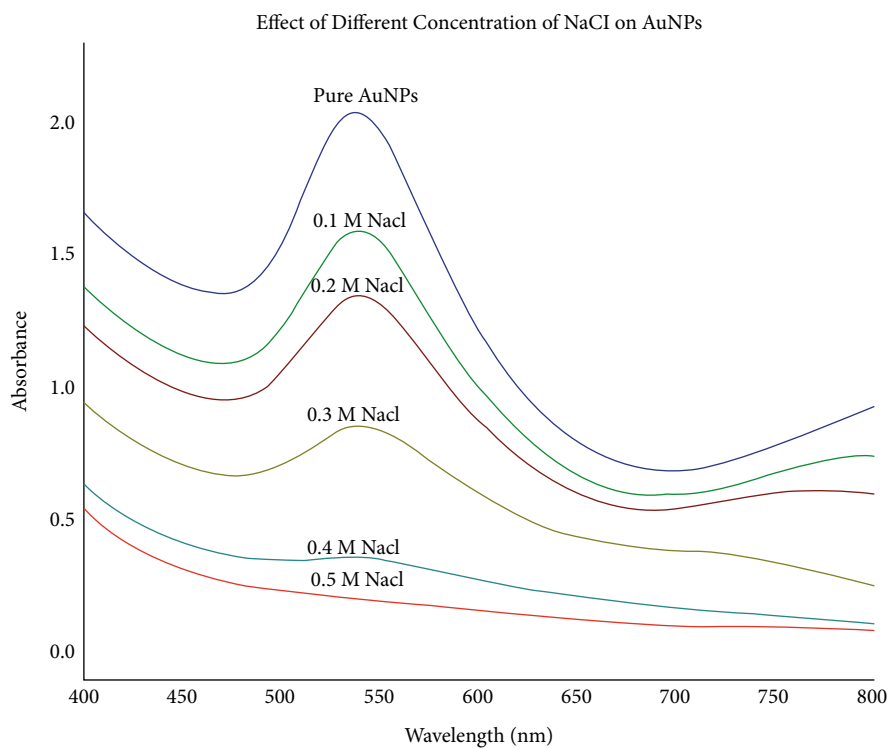


FIGURE 4: UV-visible data of effect of NaCl on *Pistacia chinensis* AuNPs.

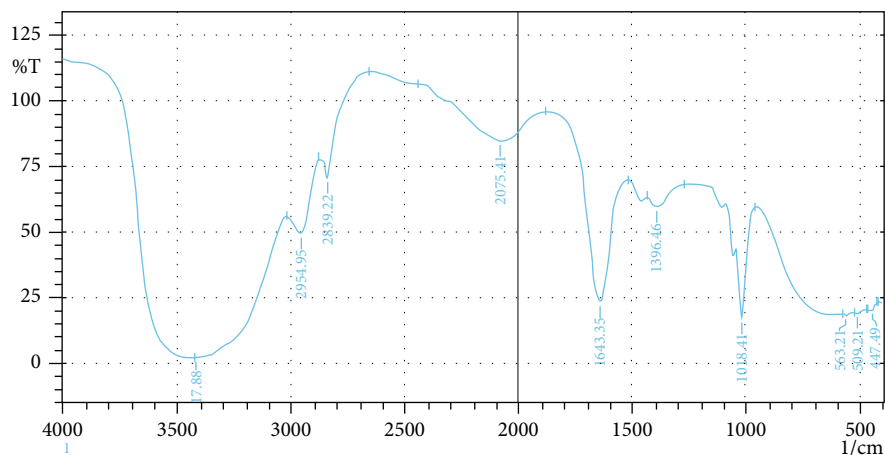


FIGURE 5: FT-IR spectral analysis of crude extract of *Pistacia chinensis*.

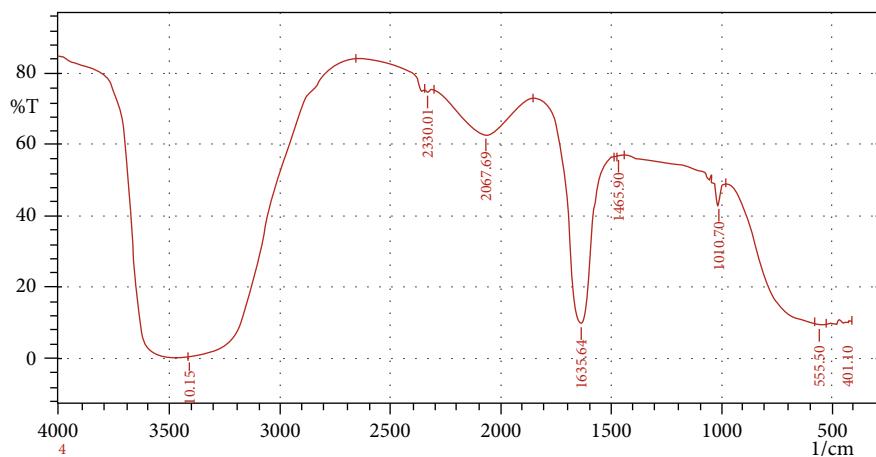


FIGURE 6: FT-IR spectroscopy of synthesized AuNPs of *Pistacia chinensis*.

synthesized nanoparticles exhibited a broad peak at 3417, 1643, 1386, and 1018 cm^{-1} , which indicated the presence of NH, C=N, and N=O in the extract. In AuNPs, these peaks change toward higher frequency, showing that these functional group are involved in the synthesis of nanoparticles.

3.1.6. Atomic Force Microscope (AFM) Imaging. Atomic force microscope (AFM) indicated the synthesized nanoparticles' morphology and size. The size range of gold nanoparticles of *Pistacia chinensis* ranges from 10 to 100 nm and is almost spherical in shape as shown in Figure 7.

3.2. Enzyme Inhibitory Potential. The results of urease and carbonic anhydrase enzyme inhibitory potential of *Pistacia chinensis* extract and its AuNPs are given in Tables 1 and 2. The synthesized AuNPs exhibited significant urease inhibition potential with an IC_{50} value of 44.98 $\mu\text{g}/\text{mL}$ and activity 92% as shown in Table 1.

Also, the extract and AuNPs exhibited moderate carbonic anhydrase enzyme inhibitory potential as compared to standard (acetazolamide). The nanoparticles exhibited carbonic anhydrase inhibition with an IC_{50} value 53.54 $\mu\text{g}/$

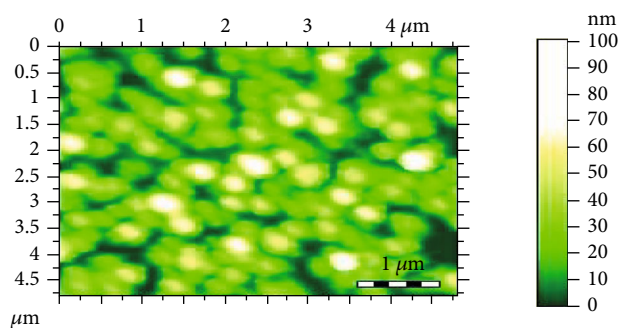


FIGURE 7: AFM image of AuNPs of *Pistacia chinensis* extract.

TABLE 1: Urease inhibitory activity of extract and AuNPs of *Pistacia chinensis*.

Tested samples	Concentration	% activity	IC_{50} ($\mu\text{g}/\text{mL}$)
<i>P. chinensis</i> extract	0.2 μg	47.65 \pm 1.40	—
Gold nanoparticles (AuNPs)	0.2 μg	92.09 \pm 1.54	44.98 \pm 1.02
Thiourea	0.2 μg	97.87 \pm 1.21	21.54 \pm 0.12

TABLE 2: Carbonic anhydrase activity of extract and AuNPs of *Pistacia chinensis*.

Tested samples	Concentration	% activity	IC ₅₀ ($\mu\text{g/mL}$)
<i>P. chinensis</i> extract	0.2 mM	26.98 \pm 1.32	—
Gold nanoparticles (AuNPs)	0.2 mM	76.43 \pm 1.09	53.54 \pm 0.32
Acetazolamide	0.2 mM	89.76 \pm 1.00	0.13 \pm 0.32

TABLE 3: Analgesic effect of *Pistacia chinensis* extract and its AuNPs.

Treatment	Dose (mg/kg)	No. of writhing in 10 mints
Saline	10 ml/kg	146.98 \pm 3.09
Diclofenac sodium	10	83.00 \pm 0.51***
	25	25.32 \pm 1.98
<i>P. chinensis</i> extract	50	34.23 \pm 2.09
	100	45.76 \pm 1.76**
Gold nanoparticles (AuNPs)	5	58.09 \pm 1.30**
	10	69.65 \pm 1.08***
	15	78.09 \pm 1.00***

TABLE 4: Sedative effect of *Pistacia chinensis* extract and its AuNPs.

Treatment	Dose (mg/kg)	No. of lines crossed in 10 mints
Saline	10 mL/kg	125.23 \pm 1.09
Diazepam	0.5	5.23 \pm 0.03***
	25	60.98 \pm 2.66
<i>P. chinensis</i> extract	50	51.92 \pm 2.34
	100	42.03 \pm 2.98**
	5	56.65 \pm 1.87**
Gold nanoparticles (AuNPs)	10	44.32 \pm 1.34***
	15	35.54 \pm 1.05***

mL, while the standard drug acetazolamide showed to have IC₅₀ value 0.13 $\mu\text{g/mL}$ (Table 2).

3.3. Analgesic Activity. The analgesic effect results of *Pistacia chinensis* extract and its AuNPs are given in Table 3. The AuNPs exhibited excellent attenuation ($p < 0.01$) in the acetic acid-induced writhing model at dose of 15 mg/kg. The extract also exhibited excellent effect ($p < 0.001$) at a higher dose as compared to standard drug (diclofenac sodium).

3.4. Sedative Activity. The results of the sedative effect for the different doses of *Pistacia chinensis* extract and its AuNPs are presented in Table 4. The synthesized nanoparticle showed a significant sedative effect ($p < 0.001$) compared to the standard drug (diazepam).

4. Discussion

Synthesized nanoparticles have multiapplication in cosmetics, packing, coating, biomedicine, etc. [3, 62]. These applications depend on prepared nanoparticles having uniform composition, size, shape, and stability [24, 63–65]. Medicinal plant-prepared nanoparticles gain key importance throughout the globe due to its eco-friendly and simplicity [8, 66, 67]. The plant contains bioactive compounds which have a strong capacity to reduce heavy metals [66, 68]. Many plants, including *Salix alba*, *Allium cepa*, *Crocus sativus*, and *Tropaeolum majus*, have been documented to synthesize metal nanoparticles [25, 64, 69–71]. In the present investigation, it is proved that the extracts of the title plant contain various classes of compounds that possess the capacity to reduce gold ion and produce stable nanoparticles.

The plant extract is acting as both reducing and stabilizing agents during the synthesis of nanoparticles and mixed with solutions of the metal precursor at different reaction conditions. The phytochemicals present in plants are responsible for bioreduction of nanoparticles. Sugars in plant extract can be responsible for the formation of metallic nanoparticles. Proteins found in plant extract with functionalized amino groups ($-\text{NH}_2$) can participate in the reduction of metal ions. The capping ligands play important role to stabilize the nanoparticles and prevent uncontrolled growth and agglomeration [72].

The synthesis of nanoparticles when the gold ion is exposed to extracts of title plant could be observed by changing color, followed by UV-visible spectroscopy. UV-visible spectroscopy is the preliminary technique to determine the formation and stability of NPs in an aqueous solution [8, 24, 27, 64]. The results of UV-visible spectra indicated that gold nanosized nanoparticles were prepared successfully at various ration by recording peaks in the definite region for gold nanoparticles. The UV spectrum indicated various peaks ranging from 530 to 550 nanometer showing different absorbances, which designated different size of synthesized AuNPs. The sharpness of the peak exhibited the uniformity of AuNPs. It was reported that UV-vis spectra for the AuNPs of alcoholic seed extract of black pepper exhibited many peaks at the range of 530 to 550 nanometer [24]. In addition, UV-vis spectra of saffron stigma-based AuNPs showed broad peaks and lower intensities at the wavelength of 540 nanometer [64].

Kinetic study of the synthesized nanoparticles showed that the number and uniformity of nanoparticles increased with the passage of time. This result is consistent with other data obtained from a recent study performed using AuNPs prepared from *Opuntia dillenii* aqueous extracts [8]. Furthermore, the prepared nanoparticles were more stable between the range of pH from 3 to 12, whereas lower stability of these prepared nanoparticles was noticed more in acidic and basic conditions, for example, in pH 1-2 and pH 13-14. The instability of AuNPs found at lower pH and higher pH in the current study can be attributed to the removal of stabilizer (extract) from the gold surface to destabilize the prepared NPs. Previous study showed that AuNPs had maximum stability at pH 10 using the extract of

Momordica charantia [73]. Salt effect on prepared nanoparticles showed that by increasing the concentration of salt, the stability of nanoparticles decreased. Similarly, Alhumaydhi et al. identified similar effects of salt stress on synthesized AuNPs prepared from saffron stigma [64]. Bawazeer et al. have also described similar stability findings of black pepper-based AuNPs in different concentrations of NaCl [24].

The FT-IR spectroscopy of the extracts and AuNPs indicated the involvement of the various functional group in the reduction of gold ions and formation of stable nanoparticles. FT-IR spectra of the extracts showed the presence of NH, C=N, and N=O in extract that are completely or partially involved in reducing gold ion and preparation of nanoparticles [74, 75]. The size AFM analysis showed that the nanoparticles range from 10 to 100 nm and are almost spherical in shape. Similar to this study, Uz-Zaman et al. described uniform distribution of AuNPs prepared using the *Trillium govianum* Wall. Ex. Royle crude extract, reporting the spherical shape of NPs having a particle size between 6.5 and 65.5 nanometer [76]. Similarly, Sadeghi et al. revealed that the size of synthesized stevia leaf extract-based AuNPs was between 21 and 45 nanometer and was spherical in shape [77].

Pistacia chinensis extract and synthesized nanoparticles showed excellent urease and carbonic anhydrase enzyme potential. The synthesized AuNPs exhibited significant urease inhibition potential with an IC₅₀ value of 44.98. Similarly, the nanoparticles exhibited good carbonic anhydrase inhibition with an IC₅₀ value 53.54 against acetazolamide having IC₅₀ 0.13. Many previous studies have reported different enzyme inhibition activities of different plant extracts and their AuNPs as compared to the standard [66, 69].

Pistacia chinensis extract and its AuNPs exhibited excellent attenuation ($p < 0.01$) in acetic acid-induced writhing model at dose of 15 mg/kg. The synthesized nanoparticle showed a significant sedative effect ($p < 0.001$) compared to the standard drug. Findings of the current work are in accordance with the outcomes of other recently published findings showing promising *in vivo* activities for different plant extract-based AuNPs [24, 64].

5. Conclusion

Synthesized NPs from natural products has gained significant importance in the field of nanotechnology because of their ecofriendly, safe, and efficient nature. The current study has developed a rapid and green methods to synthesize nanoparticles by using *Pistacia chinensis* extract and evaluated the effectiveness of these biosynthesized AuNPs by conducting different *in vitro* and *in vivo* experiments. The size of prepared nanoparticles was from 10 to 100 nm and almost spherical in shape. The synthesized AuNPs exhibited significant urease and carbonic anhydrase inhibition potential with an IC₅₀ values of 44.98 and 53.54, respectively. In addition, outcomes of this work concluded that biosynthesized AuNPs from *Pistacia chinensis* extract exhibited excellent attenuation $p < 0.01$ in acetic acid-induced writhing model at a dose of 15 mg/kg and also showed a significant sedative

effect $p < 0.001$ compared to the standard drug. This research work directed the researcher to purify active phytochemicals from *Pistacia chinensis* involved in nanoparticles synthesized. More investigations should be performed to study and understand the probable mechanism of action associated with these activities.

Data Availability

The data produced has been included all in the main text of this paper.

Conflicts of Interest

The author declares no potential conflict of interest.

Acknowledgments

The researcher would like to thank the Deanship of Scientific Research, Qassim University, for funding the publication of this project.

References

- [1] C. Pandit, A. Roy, S. Ghotekar et al., "Biological agents for synthesis of nanoparticles and their applications," *Journal of King Saud University-Science*, vol. 34, no. 3, article 101869, 2022.
- [2] S. Ghotekar, S. Pansambal, M. Bilal, S. S. Pingale, and R. Oza, "Environmentally friendly synthesis of Cr₂O₃ nanoparticles: characterization, applications and future perspective – a review," *Case Studies in Chemical and Environmental Engineering*, vol. 3, article 100089, 2021.
- [3] H. Chopra, S. Bibi, F. Islam et al., "Emerging trends in the delivery of resveratrol by nanostructures: applications of nanotechnology in life sciences," *Journal of Nanomaterials*, vol. 2022, Article ID 3083728, 17 pages, 2022.
- [4] M. Hafeez, S. Afyaz, A. Khalid et al., "Synthesis of cobalt and Sulphur doped titanium dioxide photocatalysts for environmental applications," *Journal of King Saud University-Science*, vol. 34, no. 4, article 102028, 2022.
- [5] S. Wong and B. Karn, "Ensuring sustainability with green nanotechnology," *Nanotechnology*, vol. 23, article 290201, 2012.
- [6] M. C. Roco, C. A. Mirkin, and M. C. Hersam, "Nanotechnology research directions for societal needs in 2020: summary of international study," *Journal of Nanoparticle Research*, vol. 13, no. 3, pp. 897–919, 2011.
- [7] J. Kasthuri, K. Kathiravan, and N. Rajendiran, "Phyllanthin-assisted biosynthesis of silver and gold nanoparticles: a novel biological approach," *Journal of Nanoparticle Research*, vol. 11, no. 5, pp. 1075–1085, 2009.
- [8] A. Ahmed, A. Rauf, H. A. Hemeg et al., "Green synthesis of gold and silver nanoparticles using *Opuntia dillenii* aqueous extracts: characterization and their antimicrobial assessment," *Journal of Nanomaterials*, vol. 2022, Article ID 4804116, 17 pages, 2022.
- [9] C. Rivière, F. P. Boudghène, F. Gazeau et al., "Iron oxide nanoparticle-labeled rat smooth muscle cells: cardiac MR imaging for cell graft monitoring and quantitation," *Radiology*, vol. 235, no. 3, pp. 959–967, 2005.

- [10] J. Panyam and V. Labhasetwar, "Biodegradable nanoparticles for drug and gene delivery to cells and tissue," *Advanced Drug Delivery Reviews*, vol. 55, no. 3, pp. 329–347, 2003.
- [11] J. Ma, H. Wong, L. B. Kong, and K. W. Peng, "Biomimetic processing of Nanocrystallite bioactive apatite coating on titanium," *Nanotechnology*, vol. 14, no. 6, pp. 619–623, 2003.
- [12] K. B. Narayanan and N. Sakthivel, "Heterogeneous catalytic reduction of anthropogenic pollutant, 4-nitrophenol by silver-bionanocomposite using *Cylindrocodium floridanum*," *Bioresource Technology*, vol. 102, no. 22, pp. 10737–10740, 2011.
- [13] D. P. O'Neal, L. R. Hirsch, N. J. Halas, J. D. Payne, and J. L. West, "Photo-thermal tumor ablation in mice using near infrared-absorbing nanoparticles," *Cancer Letters*, vol. 209, no. 2, pp. 171–176, 2004.
- [14] W. Zhong, "Nanomaterials in fluorescence-based biosensing," *Analytical and Bioanalytical Chemistry*, vol. 394, no. 1, pp. 47–59, 2009.
- [15] K. Aslan and V. H. Pérez-Luna, "Quenched emission of fluorescence by ligand functionalized gold nanoparticles," *Journal of Fluorescence*, vol. 14, no. 4, pp. 401–405, 2004.
- [16] Y. Kashid, S. Ghotekar, M. Bilal et al., "Bio-inspired sustainable synthesis of silver chloride nanoparticles and their prominent applications," *Journal of the Indian Chemical Society*, vol. 99, no. 5, article 100335, 2022.
- [17] A. A. Menazea and A. M. Mostafa, "Ag doped CuO thin film prepared via pulsed laser deposition for 4-nitrophenol degradation," *Journal of Environmental Chemical Engineering*, vol. 8, no. 5, article 104104, 2020.
- [18] V. Raji, K. Pal, T. Zaheer et al., "Gold nanoparticles against respiratory diseases: oncogenic and viral pathogens review," *Therapeutic Delivery*, vol. 11, no. 8, pp. 521–534, 2020.
- [19] A. A. Menazea and N. S. Awwad, "Antibacterial activity of TiO₂ doped ZnO composite synthesized via laser ablation route for antimicrobial application," *Journal of Materials Research and Technology*, vol. 9, no. 4, pp. 9434–9441, 2020.
- [20] V. Krishnan, G. Bupesh, E. Manikandan et al., "Green synthesis of silver nanoparticles using piper Nigrum concoction and its anticancer activity against MCF-7 and Hep-2 cell lines," *Journal of Antimicrobial Agents*, vol. 2, pp. 1212–2472, 2016.
- [21] A. A. Aljabali, B. Al-Trad, L. Al Gazo et al., "Gold nanoparticles ameliorate diabetic cardiomyopathy in streptozotocin-induced diabetic rats," *Journal of Molecular Structure*, vol. 1231, article 130009, 2021.
- [22] M. K. Ahmed, S. F. Mansour, R. Al-Wafi, and A. A. Menazea, "Composition and design of nanofibrous scaffolds of Mg/Se-hydroxyapatite/graphene oxide @ ϵ -polycaprolactone for wound healing applications," *Journal of Materials Research and Technology*, vol. 9, no. 4, pp. 7472–7485, 2020.
- [23] S. I. Asiya, K. Pal, S. Kralj, G. S. El-Sayyad, F. G. de Souza, and T. Narayanan, "Sustainable preparation of gold nanoparticles via green chemistry approach for biogenic applications," *Materials Today Chemistry*, vol. 17, article 100327, 2020.
- [24] S. Bawazeer, I. Khan, A. Rauf et al., "Black pepper (piper Nigrum) fruit-based gold nanoparticles (BP-AuNPs): synthesis, characterization, biological activities, and catalytic applications—a green approach," *Green Processing and Synthesis*, vol. 11, no. 1, pp. 11–28, 2022.
- [25] B. Ahmad, N. Hafeez, S. Bashir, A. Rauf, and Mujeeb-ur-Rehman, "Phytofabricated gold nanoparticles and their biomedical applications," *Biomedicine & Pharmacotherapy*, vol. 89, pp. 414–425, 2017.
- [26] J. Huang, Q. Li, D. Sun et al., "Biosynthesis of silver and gold nanoparticles by novel sundried *Cinnamomum camphora* leaf," *Nanotechnology*, vol. 18, no. 10, article 105104, 2007.
- [27] J. Kasthuri, S. Veerapandian, and N. Rajendiran, "Biological synthesis of silver and gold nanoparticles using apiin as reducing agent," *Colloids and Surfaces B: Biointerfaces*, vol. 68, no. 1, pp. 55–60, 2009.
- [28] I. Pastoriza-Santos and L. M. Liz-Marzán, "Formation of PVP-protected metal nanoparticles in DMF," *Langmuir*, vol. 18, no. 7, pp. 2888–2894, 2002.
- [29] A. Taleb, C. Petit, and M. P. Pileni, "Synthesis of highly monodisperse silver nanoparticles from AOT reverse micelles: a way to 2D and 3D self-organization," *Chemistry of Materials*, vol. 9, no. 4, pp. 950–959, 1997.
- [30] D. Andreescu, C. Eastman, K. Balantrapu, and D. Goia, "A simple route for manufacturing highly dispersed silver nanoparticles," *Journal of Materials Research*, vol. 22, no. 9, pp. 2488–2496, 2007.
- [31] A. Zahoor, S. Sharma, and G. Khuller, "Inhalable alginate nanoparticles as antitubercular drug carriers against experimental tuberculosis," *International Journal of Antimicrobial Agents*, vol. 26, no. 4, pp. 298–303, 2005.
- [32] A. K. Jha, K. Prasad, and A. R. Kulkarni, "Synthesis of TiO₂ nanoparticles using microorganisms," *Colloids and Surfaces B: Biointerfaces*, vol. 71, no. 2, pp. 226–229, 2009.
- [33] H.-J. Bai, B.-S. Yang, C.-J. Chai, G.-E. Yang, W.-L. Jia, and Z.-B. Yi, "Green synthesis of silver nanoparticles using *Rhodobacter sphaeroides*," *World Journal of Microbiology and Biotechnology*, vol. 27, no. 11, pp. 2723–2728, 2011.
- [34] D. D. Merin, S. Prakash, and B. V. Bhimba, "Antibacterial screening of silver nanoparticles synthesized by marine microalgae," *Asian Pacific Journal of Tropical Medicine*, vol. 3, no. 10, pp. 797–799, 2010.
- [35] A. Bankar, B. Joshi, A. R. Kumar, and S. Zinjarde, "Banana peel extract mediated novel route for the synthesis of silver nanoparticles," *Colloids and Surfaces A: Physicochemical and Engineering Aspects*, vol. 368, no. 1-3, pp. 58–63, 2010.
- [36] T. Santhoshkumar, A. A. Rahuman, G. Rajakumar et al., "Synthesis of silver nanoparticles using *Nelumbo nucifera* leaf extract and its larvicidal activity against malaria and filariasis vectors," *Parasitology Research*, vol. 108, no. 3, pp. 693–702, 2011.
- [37] S. P. Dubey, M. Lahtinen, and M. Sillanpää, "Green synthesis and characterizations of silver and gold nanoparticles using leaf extract of *Rosa rugosa*," *Colloids and Surfaces A: Physicochemical and Engineering Aspects*, vol. 364, no. 1-3, pp. 34–41, 2010.
- [38] C. Krishnaraj, E. G. Jagan, S. Rajasekar, P. Selvakumar, P. T. Kalaichelvan, and N. Mohan, "Synthesis of silver nanoparticles using *Acalypha indica* leaf extracts and its antibacterial activity against water borne pathogens," *Colloids and Surfaces B: Biointerfaces*, vol. 76, no. 1, pp. 50–56, 2010.
- [39] J. Y. Song and B. S. Kim, "Rapid biological synthesis of silver nanoparticles using plant leaf extracts," *Bioprocess and Biosystems Engineering*, vol. 32, no. 1, pp. 79–84, 2009.
- [40] D. Mubarak Ali, N. Thajuddin, K. Jeganathan, and M. Gunasekaran, "Plant extract mediated synthesis of silver and gold nanoparticles and its antibacterial activity against

- clinically isolated pathogens," *Colloids and Surfaces B: Biointerfaces*, vol. 85, no. 2, pp. 360–365, 2011.
- [41] H. L. Li, Z. X. Zhang, S. Z. Lin, and X. X. Li, "Research advances in the study of *Pistacia chinensis* Bunge, a superior tree species for biomass energy," *Forestry Studies in China*, vol. 9, no. 2, pp. 164–168, 2007.
- [42] J. T. Lu, Y. H. Qiu, and J. B. Lu, "Effects of Landscape fragmentation on genetic diversity of male-biased dioecious plant *Pistacia chinensis* Bunge populations," *Forests*, vol. 10, p. 792, 2019.
- [43] B. Zhu, Q. Wang, E. F. Roge, P. Nan, Z. Liu, and Y. Zhong, "Chemical variation in leaf oils of *Pistacia chinensis* from five locations in China," *Chemistry of Natural Compounds*, vol. 42, no. 4, pp. 422–425, 2006.
- [44] K. Naz, M. R. Khan, N. A. Shah, S. Sattar, F. Noureen, and M. L. Awan, "*Pistacia chinensis*: a potent ameliorator of CCl₄ induced lung and thyroid toxicity in rat model," *BioMed Research International*, vol. 2014, Article ID 192906, 13 pages, 2014.
- [45] J. Y. Park, M. Hong, Q. Jia et al., "*Pistacia chinensis* methanolic extract attenuated MAPK and Akt phosphorylations in ADP stimulated rat platelets In Vitro," *Evidence-based Complementary and Alternative Medicine*, vol. 2012, Article ID 895729, 7 pages, 2012.
- [46] J. J. Liu, C. A. Geng, and X. K. Liu, "A new pyrrolidone derivative from *Pistacia chinensis*," *Chinese Chemical Letters*, vol. 19, no. 1, pp. 65–67, 2008.
- [47] S. Nishimuta, M. Taki, S. Takaishi, Y. Iijima, and T. Akiyama, "Structures of 4-aryl-coumarin (neoflavone) dimers isolated from *Pistacia chinensis* Bunge and their estrogen-like activity," *Chemical and Pharmaceutical Bulletin*, vol. 48, no. 4, pp. 505–508, 2000.
- [48] Q. Shi and C. Zuo, "Chemical components of the leaves of *Pistacia chinensis* Bge," *China Journal of Chinese Materia Medica*, vol. 17, no. 7, pp. 422–423, 1992.
- [49] T. Yayeh, M. Hong, Q. Jia et al., "*Pistacia chinensis* inhibits NO production and upregulates HO-1 induction via PI-3K/Akt pathway in LPS stimulated macrophage cells," *The American Journal of Chinese Medicine*, vol. 40, no. 5, pp. 1085–1097, 2012.
- [50] K. Rashed, G. Deloison, Y. Rouill , and S.  . Karin, "In-vitro antiviral activity of *Pistacia chinensis* flavonoids against hepatitis C virus (HCV)," *Journal of Applied Pharmacy*, vol. 6, pp. 8–18, 2014.
- [51] K. Rashed, A. Said, A. Abdo, and S. Selim, "Antimicrobial activity and chemical composition of *Pistacia chinensis* Bunge leaves," *International Food Research Journal*, vol. 23, p. 316, 2016.
- [52] A. Rauf, F. A. Alhumaydhi, U. Rashid et al., "Naphthoquinones from *Diospyros lotus* as potential urease inhibitors: In vitro and in silico studies," *South African Journal of Botany*, vol. 143, pp. 301–305, 2021.
- [53] A. Rauf, Y. S. Al-Awthan, O. Bahattab et al., "Potent urease inhibition and in silico docking study of four secondary metabolites isolated from *Heterophragma adenophyllum* Seem," *South African Journal of Botany*, vol. 142, pp. 201–205, 2021.
- [54] A. Rauf, M. Raza, M. Saleem et al., "Carbonic anhydrase and urease inhibitory potential of various plant phenolics using in vitro and in silico methods," *Chemistry & Biodiversity*, vol. 14, no. 6, article e1700024, 2017.
- [55] A. Rauf, S. Bawazeer, M. Naseer et al., "In vitro α -glycosidase and urease enzyme inhibition profile of some selected medicinal plants of Pakistan," *Natural Product Research*, vol. 35, no. 23, pp. 5434–5439, 2021.
- [56] A. Rauf, A. S. M. Aljohani, F. A. Alhumaydhi, and S. Naz, "A novel compound from the bark of *Diospyros lotus* and their urease inhibitory activity," *Chemistry of Natural Compounds*, vol. 56, no. 6, pp. 1005–1007, 2020.
- [57] F. A. Alhumaydhi, "Urease, alpha-glucosidase inhibitory potential of various extracts of *Chenopodium botrys* L," *Zeitschrift fuer Arznei-und Gewuerzpflanzen*, vol. 25, pp. 52–54, 2020.
- [58] F. A. Alhumaydhi, "In vivo analgesic, muscle relaxant, sedative and toxicological studies of *Senna bicapsularis* (L.) Roxb," *Journal of Taibah University for Science*, vol. 15, no. 1, pp. 340–346, 2021.
- [59] A. Rauf, T. Abu-Izneid, F. A. Alhumaydhi et al., "in vivo analgesic, anti-inflammatory, and sedative activity and a molecular docking study of Dinaphthodiospyrol G isolated from *Diospyros lotus*," *BMC Complementary Medicine and Therapies*, vol. 20, no. 1, p. 237, 2020.
- [60] A. SM Aljohani, T. Abu-Izneid, Z. Ali Shah et al., "Density functional theory, molecular docking and in vivo muscle relaxant, sedative, and analgesic studies of indanone derivatives isolated from *Heterophragma adenophyllum*," *Journal of Molecular Structure and Dynamics*, vol. 39, no. 17, pp. 6488–6499, 2021.
- [61] F. A. Alhumaydhi, A. S. M. Aljohani, U. Rashid et al., "In Vivo Antinociceptive, muscle relaxant, sedative, and molecular docking studies of Peshawaraquinone isolated from *Fernandoa adenophylla* (Wall. Ex G. Don) Steenis," *ACS Omega*, vol. 6, no. 1, pp. 996–1002, 2021.
- [62] S. Ghotekar, H. Dabhane, P. Tambade, and V. Medhane, "Plant-based green synthesis and applications of cuprous oxide nanoparticles," *Handbook of Greener Synthesis of Nanomaterials and Compounds*, vol. 2, pp. 201–208, 2021.
- [63] M.-C. Daniel and D. Astruc, "Gold nanoparticles: assembly, supramolecular chemistry, quantum-size-related properties, and applications toward biology, catalysis, and nanotechnology," *Chemical Reviews*, vol. 104, no. 1, pp. 293–346, 2004.
- [64] F. A. Alhumaydhi, I. Khan, A. Rauf et al., "Synthesis, characterization, biological activities, and catalytic applications of alcoholic extract of saffron (*Crocus sativus*) flower stigma-based gold nanoparticles," *Green Processing and Synthesis*, vol. 10, no. 1, pp. 230–245, 2021.
- [65] H. Dabhane, S. Ghotekar, P. Tambade et al., "A review on environmentally benevolent synthesis of CdS nanoparticle and their applications," *Environmental Chemistry and Ecotoxicology*, vol. 3, pp. 209–219, 2021.
- [66] N. U. Islam, K. Jalil, M. Shahid, N. Muhammad, and A. Rauf, "*Pistacia integerrima* gall extract mediated green synthesis of gold nanoparticles and their biological activities," *Arabian Journal of Chemistry*, vol. 12, no. 8, pp. 2310–2319, 2019.
- [67] H. N. Cuong, S. Pansambal, S. Ghotekar et al., "New Frontiers in the plant extract mediated biosynthesis of copper oxide (CuO) nanoparticles and their potential applications: a review," *Environmental Research*, vol. 203, article 111858, 2022.
- [68] S. Mitra, A. J. Chakraborty, A. M. Tareq et al., "Impact of heavy metals on the environment and human health: novel therapeutic insights to counter the toxicity," *Journal of King Saud University-Science*, vol. 34, no. 3, article 101865, 2022.

- [69] N. U. Islam, K. Jalil, M. Shahid et al., "Green synthesis and biological activities of gold nanoparticles functionalized with *Salix alba*," *Arabian Journal of Chemistry*, vol. 12, no. 8, pp. 2914–2925, 2019.
- [70] S. Bawazeer, A. Rauf, S. U. A. Shah et al., "Green synthesis of silver nanoparticles using *Tropaeolum majus*: phytochemical screening and antibacterial studies," *Green Processing and Synthesis*, vol. 10, no. 1, pp. 85–94, 2021.
- [71] H. C. Ananda Murthy, T. D. Zeleke, K. B. Tan et al., "Enhanced multifunctionality of CuO nanoparticles synthesized using aqueous leaf extract of *Vernonia amygdalina* plant," *Results in Chemistry*, vol. 3, article 100141, 2021.
- [72] J. Singh, T. Dutta, K.-H. Kim, M. Rawat, P. Samddar, and P. Kumar, "Green synthesis of metals and their oxide nanoparticles: applications for environmental remediation," *Journal of Nanobiotechnology*, vol. 16, p. 84, 2018.
- [73] S. Pandey, G. Oza, A. Mewada, and M. Sharon, "Green synthesis of highly stable gold nanoparticles using *Momordica charantia* as nano fabricator," *Archives of Applied Science Research*, vol. 4, pp. 1135–1141, 2012.
- [74] A. K. Mittal, Y. Chisti, and U. C. Banerjee, "Synthesis of metallic nanoparticles using plant extracts," *Biotechnology Advances*, vol. 31, no. 2, pp. 346–356, 2013.
- [75] S. Iravani, "Green synthesis of metal nanoparticles using plants," *Green Chemistry*, vol. 13, no. 10, pp. 2638–2650, 2011.
- [76] K. Uz-Zaman, J. Bakht, B. K. Malikovna et al., "Trillium govanianum Wall. Ex. Royle rhizomes extract-medicated silver nanoparticles and their antimicrobial activity," *Green Processing and Synthesis*, vol. 9, no. 1, pp. 503–514, 2020.
- [77] B. Sadeghi, M. Mohammadzadeh, and B. Babakhani, "Green synthesis of gold nanoparticles using *Stevia rebaudiana* leaf extracts: characterization and their stability," *Journal of Photochemistry and Photobiology B: Biology*, vol. 148, pp. 101–106, 2015.

Research Article

Evaluation on Powder Metallurgy Process Parameters of Ball-Milled AA8079-B₄C Nanostructured Composites via Taguchi Grey Relational Analysis

M. Meignanamoorthy,¹ Mohanavel Vinayagam,² M. Ravichandran,^{1,3} T. Raja,⁴ Amel Gacem,⁵ Amine Mezni,⁶ Mohammed Jameel,⁷ and Manikandan Ganesan ⁸

¹Department of Mechanical Engineering, K. Ramakrishnan College of Engineering, Trichy 621112, Tamil Nadu, India

²Centre for Materials Engineering and Regenerative Medicine, Bharath Institute of Higher Education and Research, Chennai 600073, Tamil Nadu, India

³Department of Mechanical Engineering and University Centre for Research & Development, Chandigarh University, Mohali 140413, Punjab, India

⁴Department of Mechanical Engineering, Vel Tech Rangarajan Dr. Sagunthala R&D Institute of Science and Technology, Chennai, 600062 Tamil Nadu, India

⁵Department of Physics, Faculty of Sciences, University 20 Août 1955, Skikda, Algeria

⁶Department of Chemistry, College of Science, Taif University, P.O. Box 11099, Taif 261944, Saudi Arabia

⁷Department of Civil Engineering, College of Engineering, King Khalid University, Abha, Saudi Arabia

⁸Department of Electromechanical Engineering, Faculty of Manufacturing, Institute of Technology, Hawassa University, Ethiopia

Correspondence should be addressed to Manikandan Ganesan; mani301090@hu.edu.et

Received 17 February 2022; Revised 22 April 2022; Accepted 9 June 2022; Published 24 June 2022

Academic Editor: Arpita Roy

Copyright © 2022 M. Meignanamoorthy et al. This is an open access article distributed under the Creative Commons Attribution License, which permits unrestricted use, distribution, and reproduction in any medium, provided the original work is properly cited.

This work made an attempt to optimize the powder metallurgy (PM) process parameters of ball-milled AA8079-B₄C composites via Taguchi grey relational analysis to attain better mechanical properties. The process parameters are reinforcement weight percentage, compaction pressure, sintering temperature, and sintering time, and the output responses are micro Vickers hardness and compressive strength. The different reinforcement weight percentages are AA8079-x wt.%B₄C (X = 5, 10, and 15 wt.%). The nanograin-refined green compacts were made at various compaction pressure 200 MPa, 300 MPa, and 400 MPa. The various sintering temperatures are 375°C, 475°C, and 575°C at different sintering times 1 h, 2 h, and 3 h. Taguchi L₂₇ orthogonal array was utilized to examine the powder metallurgy process parameters. It could be understood from the results that higher reinforcement weight percentage, compaction pressure, and sintering temperature were determined as appropriate parameters to obtain maximum hardness and compressive strength.

1. Introduction

Metal matrix composite (MMC) offers a symbiotic blend of properties; this could not be obtained in traditional materials. The MMCs can be attained by combining particulates B₄C, SiC, Al₂O₃, AlN, and Ash into less weight alloys are the preferred to substitute traditional materials in numerous usages defence, structural, automobile, aero-

space, marine, and mining industries [1–3]. Owing to the less density, better specific strength and better thermal conductivity aluminium alloys are extensively utilized [4]. To fulfill the necessities such as better mechanical properties and wear resistance of aluminium matrix composites (AMCs), AMCs are reinforced with outstanding structural, and physical properties are significantly required [5, 6]. Amid the different reinforcements, boron carbide (B₄C)

possesses extreme hardness subsequent to diamond and cubic boron nitride. Moreover, B_4C has lesser specific gravity (2.51 g/cm^3), and this is lower than Al (2.7 g/cm^3). B_4C possesses extreme wear and impact resistance, better resistance to chemical agents, and high melting point [7, 8]. Despite of extreme mechanical properties, the utilization of B_4C reinforcement has been improved extremely [9, 10].

Powder metallurgy (PM) production method includes various steps, namely, blending of powders, compaction, sintering, and secondary finishing method to manufacture parts with reliable net-shape. Metal components produced through PM can be utilized in automobile, aerospace, defence, and electronic industry because of its superior physical and mechanical properties. Near net shape components can be fabricated via PM method; furthermore, material wastage can be eliminated. Uniform distribution of reinforcement particle with matrix can be attained [11, 12]. Precision metal components can be fabricated through PM route so this technique has been acknowledged as extremely established technique. In the course of the most recent seven eras, the innovation has developed from fabricating bearings for autos to difficult transferor gear set in vehicle transposal and engines connecting rods [13]. Figure 1 shows the process sequence for fabrication of MMC using PM. Nowadays, many of the researchers focused to study the powder metallurgy process parameters such as reinforcement weight percentage, compaction pressure, and sinterability [14–18]. Zakir Hussain et al. [19] examined the powder metallurgy process parameters of diamond–copper composites in terms of compaction pressure, sintering temperature, and holding time and reported that compaction pressure 525 MPa, sintering temperature 900°C , and holding time 2 h are the most influencing parameters. Pravin et al. [20] utilized Taguchi system to optimize the process parameters of Al-10% Cu composites, and the process parameters are compaction load, lubricant, sintering atmosphere, and dwell time and stated that lubricant is a major influencing parameter. Ravichandran and Anandakrishnan [21] examined the PM parameters to obtain higher strength coefficient in aluminium matrix composite via Taguchi method and described that compaction pressure and sintering temperature are major substantial parameters.

From the detailed literature study, it has been clearly evidenced that many of the researchers investigated the powder metallurgy process parameters as in Figure 1 using different matrix materials and reinforcement particles but none of the work has been carried out in AA8079- B_4C composites. Due to that, an attempt has been taken to optimize powder metallurgy process parameters on the mechanical properties. In general, a material should possess excellent hardness and compressive strength properties then only it can be used for desired application; according to that, this two mechanical properties have been studied by grey Taguchi method.

2. Experimental Details

In this investigation, AA8079 powder was produced by mingling the elemental powders Cu, Fe, Si, and Zn with Al pow-

der. Purity of Al, Cu, Fe, Si, and Zn powders is 99.5%, and mesh size as $10\ \mu\text{m}$ as AA8079 possesses less weight with high strength. B_4C was selected as reinforcement particle with 99.5% purity and mesh size as $10\ \mu\text{m}$ as it has excellent hardness; in addition, it has less density, and it is the third hardest reinforcement next to diamond and cubic nitride. The chemical composition of the pure elemental powders is essential to synthesis AA8079 0.05Cu, 1.3Fe, 0.3Si, 0.15Zn, and Al remaining (each one in wt %). The SEM image of the produced AA8079 and as received B_4C is displayed in Figures 2(a) and 2(b).

Figure 3 shows the details of fabrication of ball milled aluminium alloy and its composites. The needed amount of elemental powders was exactly weighted by utilizing an electronic weight balance machine to produce the composition, AA8079, AA8079-5% B_4C , AA8079-10% B_4C , and AA8079-15% B_4C and ball milled via high energy ball mill for 10 h [22]. The drum speed maintained was 100 rpm [23]. The diameter of the steel ball utilized here was 10 mm, and ball to powder ratio was 10:1 [24].

The ball milled powders were compressed into cylindrical billets (Dia $24 \times 10\text{ mm}$). A computerized universal testing machine capacity of 10 ton has been used to acquire a green compact. Figure 4 shows the compaction press used and other testing process conducted for the present work. The green compacts were compacted at three different compaction pressure 200 MPa, 300 MPa, and 400 MPa. Then, the green compacts were sintered at three different sintering temperatures 375°C , 475°C , and 575°C at three different sintering times 1 h, 2 h, and 3 h. As per ASTM, E384-08 Vickers hardness test was performed at a load of 0.3 kg and a dwell time of 10 s on the samples [25], and as per ASTM, E9-89a compression strength test was done via computerized universal testing machine [26]. In this investigation, trials were carried out with four parameters, and three level have been selected. Hence, L27 orthogonal array was selected like reinforcement wt. %, compaction pressure, sintering temperature, and sintering time. Table 1 displays the process parameters and their levels, and the details of the experimental plan by means of L27 OA are enumerated in Table 2. Figure 5 shows the procedure followed for Taguchi grey relational analysis in this work.

3. Results and Discussions

3.1. S/N Ratio Analysis. Taguchi technique is a dominant utensil in value optimization for fabrication routes. Taguchi technique creates use of an unusual design of OA to inspect the worth characteristics over a nominal amount of experiments [27]. Word “signal” indicates the necessary value for the output characteristic, and “noise” indicates the horrible value for the output characteristic. The S/N ratios could be deliberate using Equations (1) and (2)

$$\frac{S}{N} \text{ ratio} = -10 \log (\text{MSD}). \quad (1)$$

MSD is mean square deviation.

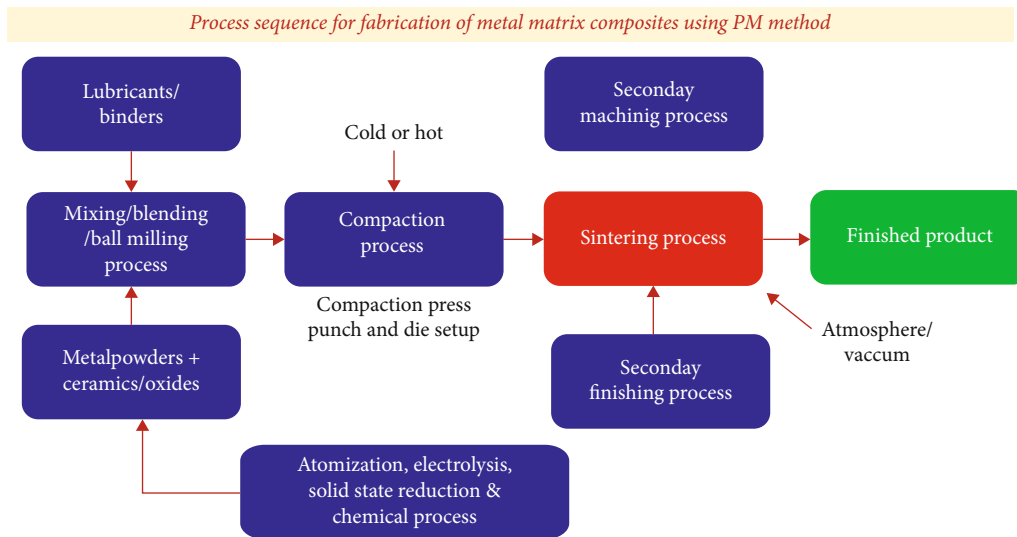


FIGURE 1: Process sequence for fabrication of MMC using PM.

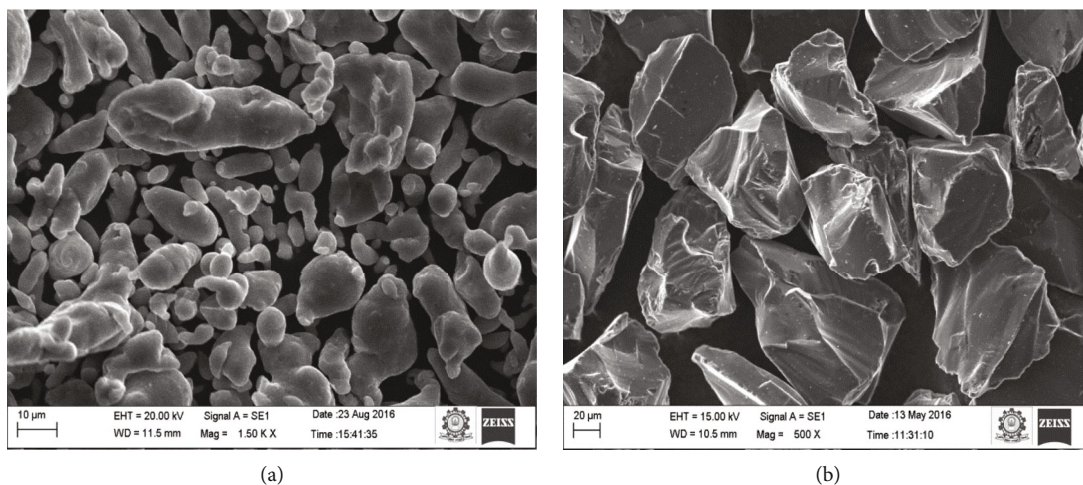


FIGURE 2: (a) SEM images of 10 h ball milled AA8079 powders; (b) as received B₄C.



FIGURE 3: Fabrication of ball milled aluminium alloy and its composites.

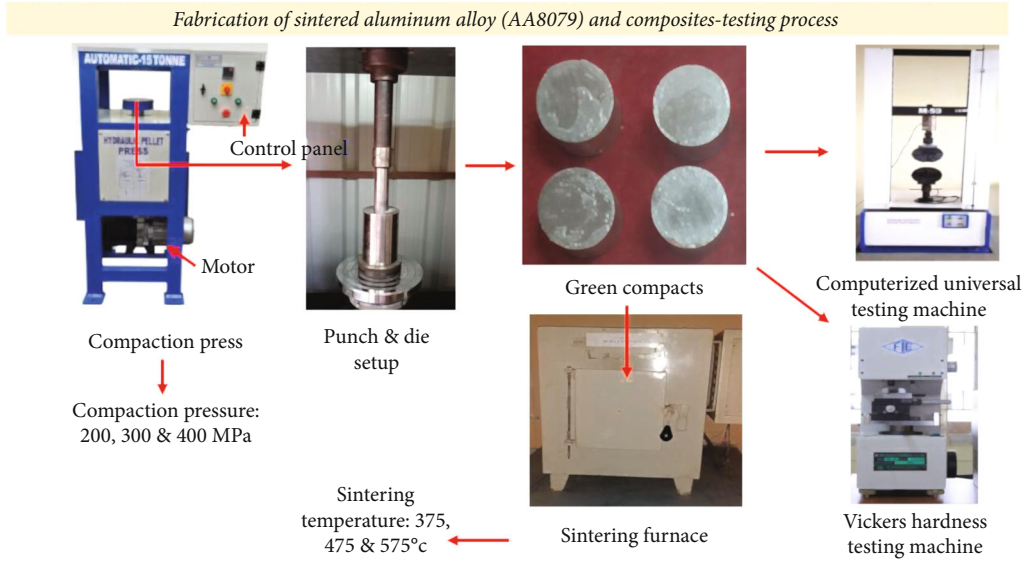


FIGURE 4: Powder metallurgy process to produce alloy and composite samples.

TABLE 1: Process parameters and their levels.

Symbols	Parameters	Unit	Level 1	Level 2	Level 3
A	Reinforcement wt. %	%	5	10	15
B	Compaction pressure	MPa	200	300	400
C	Sintering temperature	°C	375	475	575
D	Sintering time	hr	1	2	3

The MSD for the higher the better quality characteristic is expressed as

$$MSD = \frac{1}{n} \sum_{i=1}^n \frac{1}{T_i^2}. \quad (2)$$

An entire degree of factor was six to four factors. The tests would permanently be carried out extra in numbers than that of designated DOF. Therefore, L27 OA was chosen based as per Taguchi's design of experiments [28].

3.2. Interaction Effects of Factors. S/N response table for the microhardness and compressive strength is displayed in Table 3, and S/N response graph is shown in Figure 6, drawn via the results provided in Table 3. The microhardness and compressive strength increase with increasing the reinforcement wt %, compaction pressure, and sintering temperature [29, 30]. Here, the reinforcement wt % has been found to be the supreme active parameter and compaction pressure; sintering temperature and sintering time have been identified to be a slight consequence on mechanical properties founded on S/N ratio. From the Figure 6, it is clearly witnessed that reinforcement wt % is the major noteworthy factor on the response. It is detected that the interaction of reinforcement wt % with compaction pressure is minor at low sintering temperature and noteworthy at higher sintering temperature, the foremost cause is improper bind amid the particles

at low compaction pressure and low sintering temperature; and repeatedly, it decreases the microhardness and compressive strength value of the composites. Interaction of compaction pressure with sintering temperature is minor at low pressure and important at higher pressure. The maximum microhardness and compressive strength are attained when the compaction pressure is higher at sintering temperature [31–35]. The interaction of sintering temperature with sintering time is major at maximum temperature and minor at least temperature for the microhardness, because diffusion of atoms takes place at maximum temperature [36]. They [37] reported that increase in reinforcement wt % and sintering temperature increases the microhardness of the composites. This work [38] reported that rise in compaction pressure and sintering temperature increases the compressive strength.

3.3. Grey Relational Analysis. It is one of the easiest and simplest tools to provide exact results. The values of grey relation coefficient, grey relation grade, and its rank of each experiments are arranged in Table 4. The author [39] reported maximum the grey relational grade; the superior would be the multirecital characteristics. Figure 7 displays interaction plot for grey relational grade. Figure 8 displays grey relational response for parameters for instance microhardness and compressive strength. The optimal parameter is acquired from trial 27. Table 5 displays response table of

TABLE 2: Experimental results as per L27 OA.

Expt. no	Reinforcement (wt%)	Compaction pressure (MPa)	Sintering temperature (°C)	Sintering time (hr)	Compressive strength	Hardness
1	5	200	375	1	125.49	141.59
2	5	200	475	2	133.74	145.27
3	5	200	575	3	140.05	120.09
4	5	300	375	2	131.48	147.92
5	5	300	475	3	149	149.73
6	5	300	575	1	142	167.3
7	5	400	375	3	105.33	151.25
8	5	400	475	1	156.03	114.89
9	5	400	575	2	157.11	112.62
10	10	200	375	1	108.09	138.97
11	10	200	475	2	110.81	164.85
12	10	200	575	3	151.24	136.06
13	10	300	375	2	112.79	120.45
14	10	300	475	3	145.98	128.53
15	10	300	575	1	154.77	154.7
16	10	400	375	3	116.22	122.02
17	10	400	475	1	141.06	152.38
18	10	400	575	2	148	132.41
19	15	200	375	1	139.09	161.56
20	15	200	475	2	120	126.42
21	15	200	575	3	122.12	165.98
22	15	300	375	2	147.19	145.69
23	15	300	475	3	150.06	184.41
24	15	300	575	1	156.88	159.14
25	15	400	375	3	145.02	151.77
26	15	400	475	1	164.33	174.2
27	15	400	575	2	171	158.03

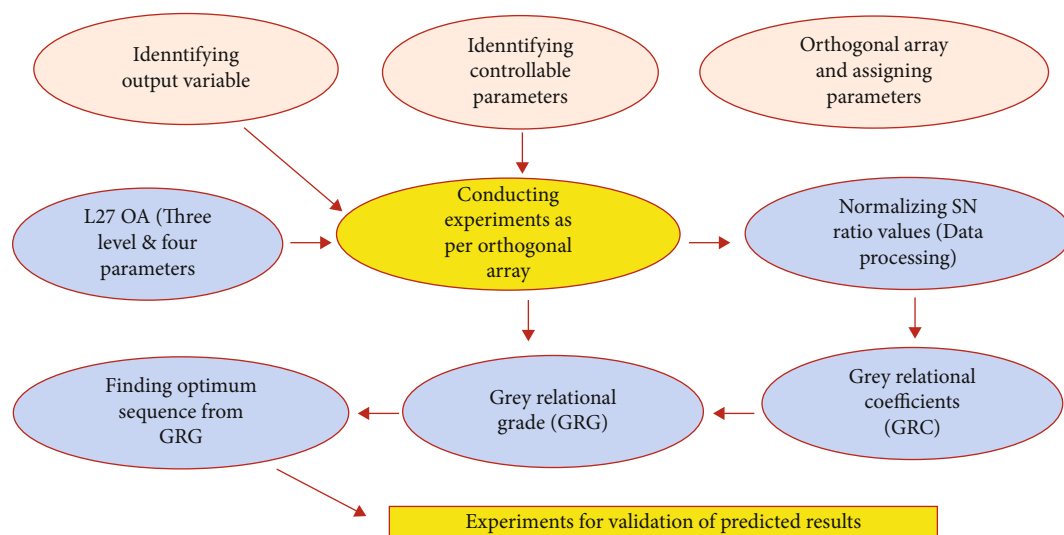


FIGURE 5: Procedure for Taguchi grey relational analysis.

TABLE 3: Response table normalized SN ratios.

Expt. no	Normalized S/N ratios	
	Microhardness	Compressive strength
1	0.403538	0.306989
2	0.454799	0.432618
3	0.104053	0.528704
4	0.491712	0.398203
5	0.516924	0.664992
6	0.761666	0.558398
7	0.538097	0
8	0.03162	0.772042
9	0	0.788488
10	0.367043	0.042028
11	0.727539	0.083448
12	0.326508	0.699102
13	0.109068	0.113598
14	0.221619	0.619004
15	0.586154	0.752855
16	0.130937	0.165829
17	0.553838	0.544084
18	0.275665	0.649764
19	0.681711	0.514086
20	0.192227	0.22339
21	0.743279	0.255672
22	0.460649	0.63743
23	1	0.681133
24	0.648001	0.784986
25	0.545341	0.604386
26	0.85778	0.898432
27	0.632539	1

the average grey relational grade for every level of the parameters. According to these stages, average grey relational grade has been identified; (i) grey relational grades have been combined via factor equal for every column in the orthogonal array and (ii) average obtained [40]. The abovementioned step has been repeated to determine the normal grey relational grade values for every level of the parameters. They [41] reported that average grey relational grade indicates the level of correlation amid reference sequence and the comparability sequence, the superior the value of the grey relational grade, the stronger the correlation to the reference sequence.

The optimal process parameter combination is achieved from Table 5. The optimal reinforcement weight percent level 3; optimal compaction pressure level 2; optimal sintering temperature, level 3 and duration, level 1; and the best combination of process parameters, $A_3 B_2 C_3 D_1$. The optimal process parameters values are reinforcement content 15 wt %, compaction pressure 400 MPa, sintering temperature 575°C, and sintering time 1 h. It could be understood from the Table 6 the maximum value is 0.1479, and the equivalent control factor, i.e., the reinforcement wt % has

the strongest effect on multiperformance characteristics. The order of consequence of the process parameter is factor A (reinforcement wt %), B (sintering temperature), C (compaction pressure), and D (sintering time), i.e., $0.1479 > 0.1179 > 0.0907 > 0.0620$. Factor A is utmost important influence in the process for the multiperformance characteristics.

3.4. ANOVA. From ANOVA in Table 7, it is detected that the reinforcement weight %, sintering temperature, and compaction pressure are vital parameters from the F values. The sintering temperature is the most second influential parameter. The compaction pressure has been considered as third dominant part on the responses. Reinforcement weight % is notable as utmost serious factor with highest contribution percentage as shown in Figure 9. The compaction pressure, sintering temperature, and sintering time are subsidized fair with contributions. Figure 9 shows the contribution plot for all the parameters drawn from ANOVA table.

Sintering normal for Al_2O_3 -reinforced 2xxx series Al composite powders was explored to acquire improved densification. The dissemination of the fluid stage was speedier in the composite powder sintered example than in the mixed powder sintered example. The outcomes demonstrate that a more prominent measure of fluid stage is expected to improve the sinterability of 2xxx series Al composite materials [42]. From Tables 3–6, the ideal parameters for the compressive strength and hardness can be anticipated as the reinforcement weight 15%, compaction pressure 400 MPa, the sintering temperature 575°C, and the sintering time 1 h. This result is near the S/N and ANOVA comes about.

3.5. Confirmation Test. Five examples were finished with $A_3B_2C_3D_1$ parameters, and their normal quality coefficient was found. Table 8 reveals the relationship of the predicted quality coefficient and real quality coefficient of this composite preforms. A low rate blunder of 2.2% is gotten amid anticipated; what is more, trial esteem is demonstrating a decent relationship as appeared in Table 8.

3.6. Microstructure Analysis of the Composites Produced by Anticipated Parameters. SEM analysis had been conducted for the samples fabricated from the predicted parameters ($A_3B_2C_3D_1$), and the images are shown in Figures 10(a) and 10(b). From the SEM images, the occurrence of weight percentage of B_4C particles in the AA8079 matrix was attained. The foremost factors manipulating the microstructure of PM components are compaction pressure along with sintering temperature as per the results obtained from the present study. It is observed from Figures 10(a) and 10(b) that the higher compaction pressure and sintering temperature enhance proper bonding amid B_4C particles and AA8079 matrix. This creates denser structure owing to greater diffusion rates results in fine microstructure. The uniform distribution of B_4C particles in Figure 10(b) is evident in the proper identification PM parameters from the TGRA. This proper microstructure of the composite sample enhanced the properties such as CS and hardness.

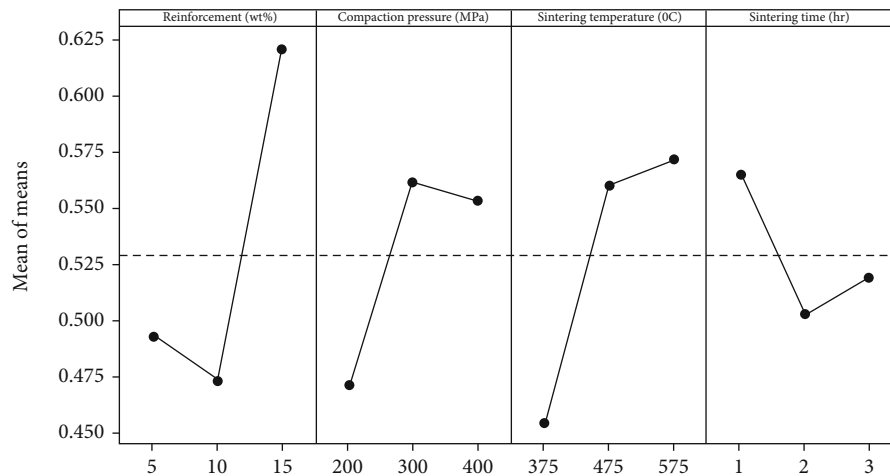


FIGURE 6: S/N ratio response graph for microhardness and compressive strength.

TABLE 4: Grey relational coefficient.

Expt. no.	Grey relation coefficient		Grey relational grade	Rank
	Microhardness	Compressive strength		
1	0.456012	0.419108	0.43756	22
2	0.478377	0.468436	0.473406	19
3	0.35818	0.514776	0.436478	21
4	0.49589	0.453804	0.474847	18
5	0.508608	0.598796	0.553702	8
6	0.6772	0.53101	0.604105	6
7	0.519803	0.333333	0.426568	23
8	0.340511	0.686853	0.513682	15
9	0.333333	0.702729	0.518031	14
10	0.441323	0.342942	0.392133	24
11	0.647282	0.35297	0.500126	16
12	0.426079	0.624299	0.525189	13
13	0.359471	0.360646	0.360059	27
14	0.39112	0.56754	0.47933	17
15	0.547138	0.669214	0.608176	5
16	0.365213	0.374765	0.369989	26
17	0.52845	0.523059	0.525755	12
18	0.408385	0.588072	0.498229	16
19	0.611031	0.507143	0.559087	7
20	0.382329	0.391662	0.386996	25
21	0.660746	0.401823	0.531284	10
22	0.481069	0.579663	0.530366	11
23	1	0.6106	0.8053	1
24	0.586855	0.699287	0.643071	4
25	0.523747	0.558276	0.541011	9
26	0.778549	0.831161	0.804855	2
27	0.576395	1	0.788198	3

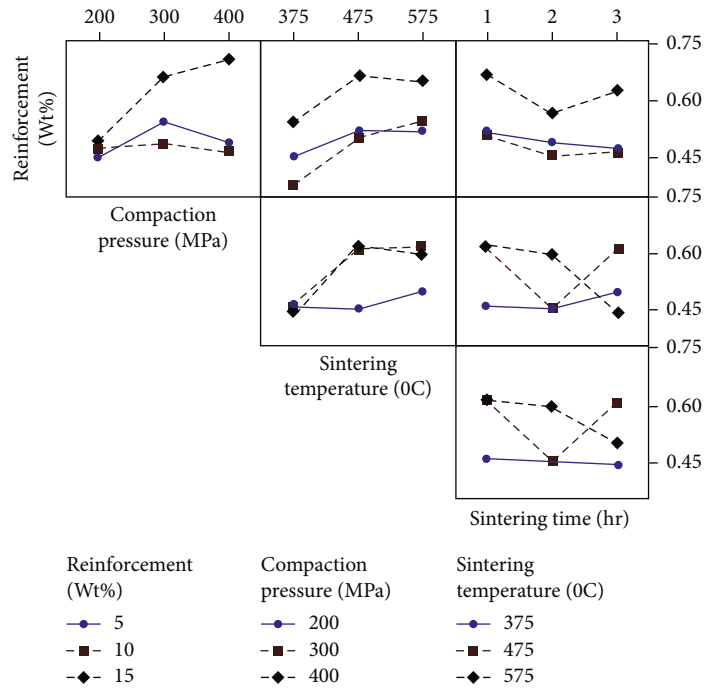


FIGURE 7: Interaction plot for grey relational grade.

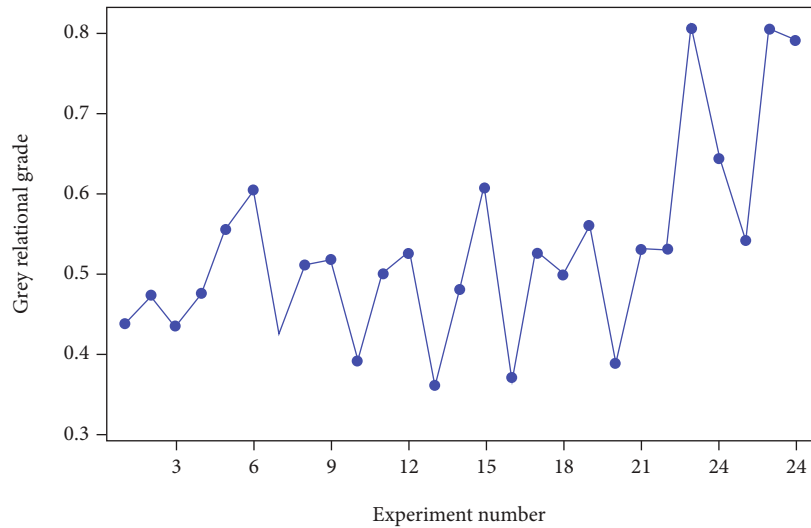


FIGURE 8: GRGs for response parameters (MH, CS).

TABLE 5: Grey relational grade for each level of parameters.

Factor	Parameters	Level 1	Level 2	Level 3	Delta	Rank
A	Reinforcement wt. %	-6.195	-6.622	-4.367	2.255	1
B	Compaction pressure	-6.601	-5.198	-5.384	1.403	3
C	Sintering temperature	-6.954	-5.269	-4.961	1.992	2
D	Sintering time	-5.128	-6.160	-5.896	1.032	4

TABLE 6: Response table for means.

Factor	Parameters	Level 1	Level 2	Level 3	Delta	Rank
A	Reinforcement wt. %	0.4932	0.4732	0.6211	0.1479	1
B	Compaction pressure	0.4714	0.5621	0.5540	0.0907	3
C	Sintering temperature	0.4546	0.5604	0.5725	0.1179	2
D	Sintering time	0.5654	0.5034	0.5188	0.0620	4

TABLE 7: Analysis of variance for grey relational grade, using adjusted SS for tests.

Source	DF	Adj SS	Adj MS	F value	P value
Reinforcement wt. %	2	0.115957	0.057979	8.61	0.002
Compaction pressure	2	0.045403	0.022702	3.37	0.057
Sintering temperature	2	0.075683	0.037842	5.62	0.013
Sintering time	2	0.018770	0.009385	1.39	0.274
Error	18	0.121183	0.006732		
Total	26				

S = 0.0820511; R - Sq = 67.86%; R - Sq(adj) = 53.57%.

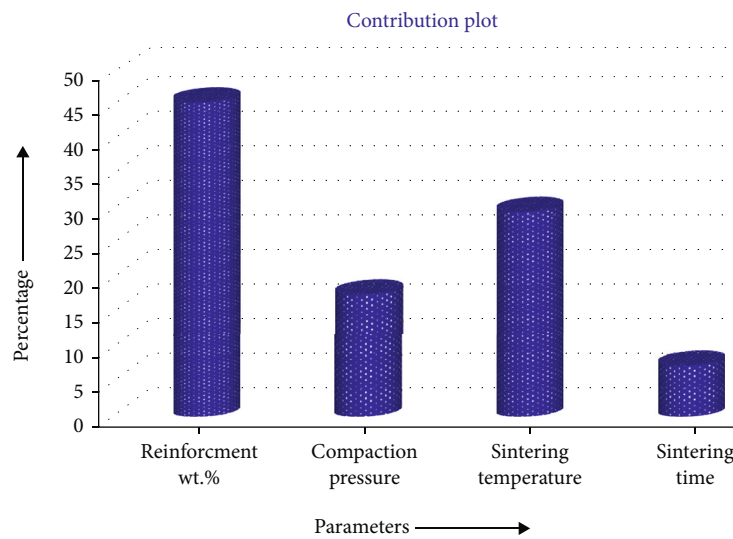


FIGURE 9: Contribution plot from ANOVA.

TABLE 8: Confirmation results.

Parameter	Optimal process parameters	
	Predicted	Experiment
Microhardness	$A_3B_2C_3D_1$	190 VHN
Compressive strength		177 MPa

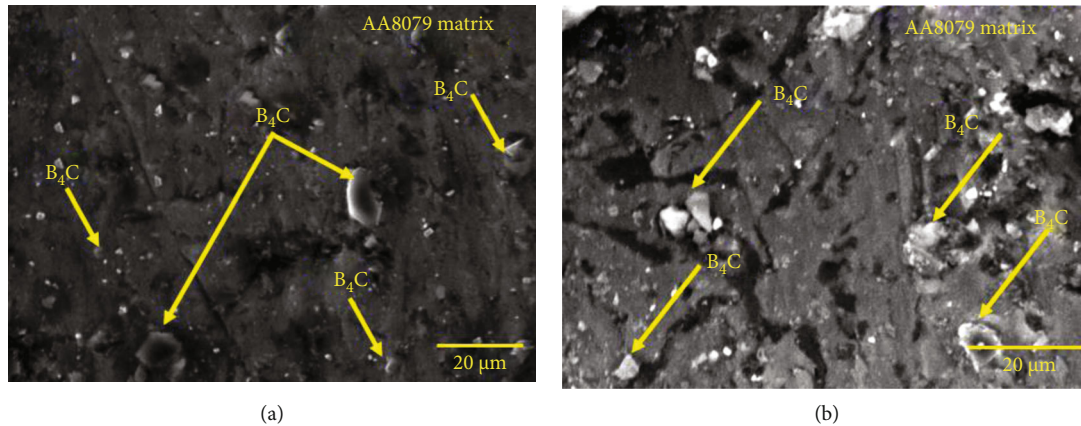


FIGURE 10: (a, b) SEM image of the AA8079-15%B₄C composites fabricated as per the optimized PM parameters.

4. Conclusions

The subsequent conclusions have been strained from the investigations conducted on the AA8079-B₄C composites under various process parameters.

The AA8079-B₄C composites were fabricated via powder metallurgy manufacturing method.

The influence of powder metallurgy process parameters on AA8079-B₄C composites was studied.

The important parameters reinforcement weight percentage, compaction pressure, sintering temperature, and sintering time were analysed by using Taguchi grey analysis on the responses such as hardness and compressive strength of AA8079-B₄C samples.

Amid the parameters, reinforcement weight percentage 15%, sintering temperature 575°C, compaction pressure 400 MPa, and sintering time 1 h shows a positive consequence on the mechanical properties.

SEM examination on the AA8079-B₄C sintered composites fabricated by the optimized parameters shows the homogenous dispersal of the reinforcement with the matrix and good bonding between the matrix and reinforcement.

In future, the same results were optimized by using some other optimization tools like genetic algorithm and neural network.

Data Availability

The data used to support the findings of this study are included within the article. Further data or information is available from the corresponding author upon request.

Conflicts of Interest

The authors declare that there are no conflicts of interest regarding the publication of this paper.

Acknowledgments

The authors appreciate the supports from Hawassa University, Ethiopia, for the research and preparation of the manuscript. This study was funded by Taif University Researchers Sup-

porting Project number (TURSP-2020/28), Taif University, Taif, Saudi Arabia.

References







- [1] V. Mohanavel, K. Rajan, and M. Ravichandran, "Synthesis, characterization and properties of stir cast AA6351-aluminium nitride (AlN) composites," *Journal of Materials Research*, vol. 31, no. 24, pp. 3824–3831, 2016.
- [2] M. L. Bharathi, S. Adarsh Rag, L. Chitra et al., "Investigation on wear characteristics of AZ91D/nanoalumina composites," *Journal of Nanomaterials*, vol. 2022, Article ID 2158516, 9 pages, 2022.
- [3] M. Meignanamoorthy and M. Ravichandran, "Synthesis, properties and microstructure of sintered and hot extruded boron carbide reinforced AA8079 (Al-Cu-Fe-Si-Zn) matrix composites," *Materials Research Express*, vol. 5, no. 11, p. 116508, 2018.
- [4] R. Guan, Y. Wang, S. Zheng et al., "Fabrication of aluminum matrix composites reinforced with Ni-coated graphene nanosheets," *Materials Science and Engineering A*, vol. 754, pp. 437–446, 2019.
- [5] B. Chen, J. Shen, X. Ye et al., "Length effect of carbon nanotubes on the strengthening mechanisms in metal matrix composites," *Acta Materialia*, vol. 140, pp. 317–325, 2017.
- [6] M. Ravichandran, V. Mohanavel, T. Sathish, P. Ganeshan, S. S. Kumar, and R. Subbiah, "Mechanical properties of AlN and molybdenum disulfide reinforced aluminium alloy matrix composites," *Journal of Physics: Conference Series*, vol. 2027, p. 012010, 2021.
- [7] A. Alizadeh and M. J. Abdollahi Aand Radfar, "Processing, characterization, room temperature mechanical properties and fracture behavior of hot extruded multi-scale B₄C reinforced 5083 aluminum alloy based composites," *Transactions of Nonferrous Metals Society of China*, vol. 27, no. 6, pp. 1233–1247, 2017.
- [8] A. Sivkov, I. Rakhmatullin, I. Shanenkov, and Y. Shanenkova, "Boron carbide B₄C ceramics with enhanced physico-mechanical properties sintered from multimodal powder of plasma dynamic synthesis," *International Journal of Refractory Metals and Hard Materials*, vol. 78, pp. 85–91, 2019.
- [9] Y. H. Celik and K. Secilmis, "Investigation of wear behaviours of Al matrix composites reinforced with different B₄C rate

- produced by powder metallurgy method,” *Advanced Powder Technology*, vol. 28, no. 9, pp. 1–7, 2017.
- [10] J. A. Jeffrey, S. S. Kumar, V. A. Roseline, A. L. Mary, and D. Santhosh, “Contriving and assessment of magnesium alloy composites augmented with boron carbide VIA liquid metallurgy route,” *Materials Science Forum*, vol. 1048, pp. 3–8, 2022.
- [11] A. Gokce, F. Findik, and A. O. Kurt, “Microstructural examination and properties of premixed Al-Cu-Mg powder metallurgy alloy,” *Materials Characterization*, vol. 62, no. 7, pp. 730–735, 2011.
- [12] M. Meignanamoorthy and M. Ravichandran, “Synthesis of metal matrix composites via powder metallurgy route: a review,” *Mechanics and Mechanical Engineering*, vol. 22, no. 1, pp. 65–76, 2018.
- [13] R. Narayanasamy, T. Ramesh, and K. S. Pandey, “Workability studies on cold upsetting of Al- Al₂O₃ composite material,” *Materials & Design*, vol. 27, no. 7, pp. 566–575, 2006.
- [14] M. Delavari, A. Salarvand, A. Rahi, and F. Shahri, “The effect of powder metallurgy process parameters on mechanical properties of micro and nano-iron powder,” *International Journal of Engineering, Science and Technology*, vol. 3, no. 9, pp. 86–94, 2011.
- [15] R. U. Din, Q. A. Shafqat, Z. G. H. ZahidAsghara et al., “Microstructural evolution, powder characteristics, compaction behavior and sinterability of Al 6061–B4C composites as a function of reinforcement content and milling times,” *Russian Journal of Non-Ferrous Metals*, vol. 59, no. 2, pp. 207–222, 2018.
- [16] N. Showaiter and M. Youseffi, “Compaction, sintering and mechanical properties of elemental 6061 Al powder with and without sintering aids,” *Materials & Design*, vol. 29, no. 4, pp. 752–762, 2008.
- [17] O. Joo Won, S. K. Ryu, W. S. Lee, and S. J. Park, “Analysis of compaction and sintering behavior of 316L stainless steel nano/micro bimodal powder,” *Powder Technology*, vol. 322, pp. 1–8, 2017.
- [18] V. V. Vani and S. K. Chak, “The effect of process parameters in aluminum metal matrix composites with powder metallurgy,” *Manufacturing Review*, vol. 5, pp. 1–13, 2018.
- [19] M. D. Zakir Hussain, S. Khan, and P. Sarmah, “Optimization of powder metallurgy processing parameters of Al₂O₃/Cu composite through Taguchi method with grey relational analysis,” *Journal of King Saud University - Engineering Sciences*, vol. 31, pp. 1–13, 2019.
- [20] T. Pravin, M. Sadhasivam, and S. Raghuraman, “Optimization of process parameters of Al-10% Cu compacts through powder metallurgy,” *Applied Mechanics and Materials*, vol. 813-814, pp. 603–607, 2010.
- [21] M. Ravichandran and V. Anandkrishnan, “Optimization of powder metallurgy parameters to attain maximum strength coefficient in Al-10 wt% MoO₃composite,” *Journal of Materials Research*, vol. 30, no. 15, pp. 2380–2387, 2015.
- [22] M. Ravichandran, A. Naveen Sait, and V. Anandkrishnan, “Workability studies on Al+2.5%TiO₂+Gr powder metallurgy composites during cold upsetting,” *Materials Research*, vol. 17, no. 6, pp. 1–13, 2014.
- [23] H. T. Son, T. S. Kim, C. Suryanarayana, and B. S. Chun, “Homogeneous dispersion of graphite in a 6061 aluminum alloy by ball milling,” *Materials Science and Engineering A*, vol. 348, no. 1-2, pp. 163–169, 2003.
- [24] D. Jeyasimman, S. Sivasankaran, K. Sivaprasad, R. Narayanasamy, and R. S. Kambali, “An investigation of the synthesis, consolidation and mechanical behaviour of Al 6061 nanocomposites reinforced by TiC via mechanical alloying,” *Materials & Design*, vol. 57, pp. 394–404, 2014.
- [25] S. J. Hong and P. W. Kao, “SiC-reinforced aluminium composite made by resistance sintering of mechanically alloyed powders,” *Materials Science and Engineering A*, vol. 119, pp. 153–159, 1989.
- [26] D. Srinivasan, M. Meignanamoorthy, and M. Ravichandran, “Optimization of process parameters of boron carbide filled aluminium matrix composites using grey Taguchi method,” *Materials Research Express*, vol. 6, no. 7, article 076504, 2019.
- [27] S. Marichamy, M. Saravanan, M. Ravichandran, and G. Veerappan, “Parametric optimization of electrical discharge machining process on α - β brass using grey relational analysis,” *Journal of Materials Research*, vol. 31, no. 16, pp. 2531–2537, 2016.
- [28] V. Umasankar, M. Anthony Xavier, and S. Karthikeyan, “Experimental evaluation of the influence of processing parameters on the mechanical properties of SiC particle reinforced AA6061 aluminium alloy matrix composite by powder processing,” *Journal of Alloys and Compounds*, vol. 582, pp. 380–386, 2014.
- [29] M. Dewidar, M. B. G. T. Abdel-Jaber, and H. Badry, “Effect of processing parameters and amount of additives on the mechanical properties and wear resistance of copper-based composite,” *International Journal of Mechanical & Mechatronics Engineering*, vol. 10, no. 3, pp. 20–26, 2010.
- [30] M. Rahimian, N. Ehsani, N. Parvin, and H. R. Baharvandi, “The effect of sintering temperature and the amount of reinforcement on the properties of Al-Al₂O₃ composite,” *Materials & Design*, vol. 30, no. 8, pp. 3333–3337, 2009.
- [31] Z. Hussain and L. C. Kit, “Properties and spot welding behaviour of copper-alumina composites through ball milling and mechanical alloying,” *Materials & Design*, vol. 29, no. 7, pp. 1311–1315, 2008.
- [32] G. K. Meenashisundaram, S. Seetharaman, and M. Gupta, “Enhancing overall tensile and compressive response of pure Mg using nano- TiB₂ particulates,” *Materials Characterization*, vol. 94, pp. 178–188, 2014.
- [33] O. El-Kady and A. Fathy, “Effect of SiC particle size on the physical and mechanical properties of extruded Al matrix nanocomposites,” *Materials & Design*, vol. 54, pp. 348–353, 2014.
- [34] C. Li, R. Qiu, B. Luan, and Z. Li, “Effect of carbon nanotubes and high temperature extrusion on the microstructure evolution of Al-Cu alloy,” *Materials Science and Engineering A*, vol. 704, pp. 38–44, 2017.
- [35] C.-A. Wang and L. F. Hu, “Effect of sintering temperature on compressive strength of porous yttria-stabilized zirconia composites,” *Ceramics International*, vol. 36, no. 5, pp. 1697–1701, 2010.
- [36] A. Wagih, A. Fathy, and T. A. Sebaey, “Experimental investigation on the compressibility of Al/Al₂O₃ nanocomposites,” *International Journal of Materials and Product Technology*, vol. 52, no. 3/4, pp. 312–332, 2016.
- [37] M. Rahimian, N. Ehsani, N. Parvin, H. r. Baharvandi, and H. R. Baharvandi, “The effect of particle size, sintering temperature and sintering time on the properties of Al-Al₂O₃ composites, made by powder metallurgy,” *Journal of Materials Processing Technology*, vol. 209, no. 14, pp. 5387–5393, 2009.

- [38] P. Balamurugan and M. Uthayakumar, "Influence of process parameters on Cu-Fly ash composite by powder metallurgy technique," *Materials and Manufacturing Processes*, vol. 30, no. 3, pp. 313–319, 2015.
- [39] C. C. Tsao, "Grey-Taguchi method to optimize the milling parameters of aluminum alloy," *International Journal of Advanced Manufacturing Technology*, vol. 40, no. 1-2, pp. 41–48, 2009.
- [40] H. Siddhi Jailani, A. Rajadurai, B. Mohan, A. Senthil Kumar, and T. Sornakumar, "Multi-response optimisation of sintering parameters of Al-Si alloy/fly ash composite using Taguchi method and grey relational analysis," *The International Journal of Advanced Manufacturing Technology*, vol. 45, no. 3-4, pp. 362–369, 2009.
- [41] N. Tosun, "Determination of optimum parameters for multi-performance characteristics in drilling by using grey relational analysis," *The International Journal of Advanced Manufacturing Technology*, vol. 28, no. 5-6, pp. 450–455, 2006.
- [42] M. K. Ho, K. S. Pil, K. Dae-Gun, and K. Y. Do, "Sintering characteristic of Al₂O₃-reinforced 2xxx series Al composite powders," *Journal of Alloys and Compounds*, vol. 400, no. 1-2, pp. 150–153, 2005.

Research Article

Fabrication of Silver Nanoparticles from *Ziziphus nummularia* Fruit Extract: Effect on Hair Growth Rate and Activity against Selected Bacterial and Fungal Strains

Muhammad Saqib Khalil,¹ Muhammad Shakeel,² Naila Gulfam,³ Syed Umair Ahmad ⁴,
Aamir Aziz,¹ Junaid Ahmad,⁵ Shabana Bibi ^{6,7} Hitesh Chopra ⁸,
Fahad A. Alhumaydhi ⁹, Abubakr M. Idris ^{10,11} Mayeen Uddin Khandaker,¹²
Manal Ewaiss Hassan,^{13,14} and Talha Bin Emran ^{15,16}

¹Institute of Biological Sciences, Sarhad University of Science and Information Technology, Peshawar, Khyber Pakhtunkhwa, Pakistan

²Department of Biotechnology, Bacha Khan University, Charsada, Khyber Pakhtunkhwa, Pakistan

³Jinnah College for Women, University of Peshawar, Peshawar, Khyber Pakhtunkhwa, Pakistan

⁴Department of Bioinformatics, Hazara University, Mansehra, Pakistan

⁵Department of Microbiology, Hazara University Mansehra, KPK, Pakistan

⁶Department of Biosciences, Shifa Tameer-e-Millat University, Islamabad, Pakistan

⁷Yunnan Herbal Laboratory, College of Ecology and Environmental Sciences, Yunnan University, Kunming, 650091 Yunnan, China

⁸Chitkara College of Pharmacy, Chitkara University, Punjab 140401, India

⁹Department of Medical Laboratories, College of Applied Medical Sciences, Qassim University, Buraydah 52571, Saudi Arabia

¹⁰Department of Chemistry, College of Science, King Khalid University, Abha 62529, Saudi Arabia

¹¹Research Center for Advanced Materials Science (RCAMS), King Khalid University, Abha 62529, Saudi Arabia

¹²Centre for Applied Physics and Radiation Technologies, School of Engineering and Technology, Sunway University, 47500 Bandar Sunway, Selangor, Malaysia

¹³Department of Pathology, Medical College, Jouf University, Al-Jawf 72388, Saudi Arabia

¹⁴Department of Biochemistry and Molecular Biology, Faculty of Medicine, Beni-Suef University, Beni-Suef 62521, Egypt

¹⁵Department of Pharmacy, BGC Trust University Bangladesh, Chittagong 4381, Bangladesh

¹⁶Department of Pharmacy, Faculty of Allied Health Sciences, Daffodil International University, Dhaka 1207, Bangladesh

Correspondence should be addressed to Shabana Bibi; shabana_bibi@ynu.edu.cn, Abubakr M. Idris; abubakridris@hotmail.com, and Talha Bin Emran; talhabmb@bgctub.ac.bd

Received 26 February 2022; Revised 24 April 2022; Accepted 6 June 2022; Published 25 June 2022

Academic Editor: Dong Kee Yi

Copyright © 2022 Muhammad Saqib Khalil et al. This is an open access article distributed under the Creative Commons Attribution License, which permits unrestricted use, distribution, and reproduction in any medium, provided the original work is properly cited.

Nanoparticles are extensively used in biomedical and biotechnological research. Their large surface area, excellent physical properties, high permeability, and retention effect make them ideal for biomedical applications including diagnosis and treatment. Silver nanoparticles proved to be the safest for therapeutic uses. In the present study, silver nanoparticles (AgNPs) were prepared using various ratios of *Ziziphus nummularia* fruit extract and silver nitrate solution. The nanoparticles were investigated for hair growth and antibacterial and antifungal activities. Characterization of AgNPs was done by using UV-spectrophotometer, scanning electron microscope (SEM), X-ray diffractometer (XRD), thermogravimeter (TG), energy dispersive X-ray (EDX), Fourier transform infrared spectroscopy (FTIR), and master sizer. UV-spectrophotometer results showed the best ratio 10:10 of *Z. nummularia* fruit aqueous extract to silver solution for nanoparticle production at 400 to 430 nm wavelength. The size of AgNPs was 40 nm as measured by SEM. Characterization of AgNPs through EDX resulted in a silver peak at 3 keV. In contrast, differential scanning calorimetry (DSC) spectra show that the AgNPs are stable up to 160°C.

The XED spectra gave 12 nm size of crystallite at 2 theta degree angle. FTIR bands for the metal oxides were recorded at 665 cm^{-1} . Weight loss of the prepared nanoparticles was observed due to moisture loss when subjected to TGA, whereas particle size distribution $0.1\text{ }\mu\text{m}$ to $0.17\text{ }\mu\text{m}$ was recorded by the master seizer. The *Z. nummularia* fruit aqueous extract-mediated AgNPs were noted highly effective against Gram-positive bacteria compared to ethanolic, methanolic, chloroform, and ethyl acetate extracts of *Z. nummularia* fruit. The Gram-negative bacteria fungal species showed less sensitivity to AgNPs. The hair growth activity was observed to be higher for AgNPs followed by minoxidil than ethanolic and methanolic extracts of *Z. nummularia* fruit. These findings have concluded that *Z. nummularia*-AgNPs have an effective hair growth activity and exhibit several applications in distinctive biomedical and pharmaceutical industries.

1. Introduction

Nanotechnology has induced a great scientific advancement in research and technology. It deals with science and technology to control matter at the molecular level. On the nanoscale level, the properties of matter are considerably different from their properties in bulk. It refers to the ability to design, characterize, produce, and apply structures, devices, and systems by controlling shape and size at the nanometer gage. Nanotechnology is the study and application of small objects which can be used across all fields such as chemistry, biology, biotechnology, physics, material science, and engineering [1].

The preparation of metallic nanoparticles has attracted attention due to their unique biotic and physicochemical characteristic related to their macroscaled counterparts. Gold, silver, zinc, iron, and copper stable dispersions of nanoparticles are very useful in microbiology, photography, catalysis, biological labeling, photonics, and optoelectronics. Silver nanoparticles are of prime importance because of their wide applications in medical devices and pharmaceutical products [2], antimicrobial properties, and low toxic effects on animal and human cells. For such applications, small particle size can enhance the antimicrobial effect. So the reactants used to prepare nanoparticles should be nontoxic or nonirritant. Therefore, a method is known as green synthesis favor well these purposes. The nanoparticles prepared through "green synthesis" are eco-friendly, nontoxic, and safe reagents [3]. Several methods are available for the fabrication of silver nanoparticles, including a reduction in solutions, chemical and photochemical reactions in reverse micelles, thermal decomposition of silver compounds, radiation assisted, electrochemical, sono-chemical, microwave-assisted process, and recently via green chemistry route [4]. The use of environmentally friendly materials such as plant extract, microorganisms (bacteria, fungi), and enzymes for the preparation of silver nanoparticles has many advantages of eco-friendliness, compatibility for pharmaceuticals, and other biomedical applications as they do not contain toxic material for the fabrication protocol. Chemical synthesis methods for the preparation of nanoparticles lead to the presence of some harmful material absorbed on the surface that may cause adverse effects in treating various ailments. Green synthesis has advantages over chemical and physical methods; for example, it is cost-effective, eco-friendly, and easy preparation for large scale synthesis. Moreover, there is no need to utilize high pressure, energy, temperature, and toxic chemicals [5].

The role of hairs is of great importance in mammals, especially in the padding of heat and community patterns.

Comparatively, the human body consists of fewer hairs than other mammals. The presence of hairs on the human body has cosmetic importance rather than the existence of life. Hair loss in humans is a skin disorder. It has remained an issue for many years due to disturbance in metabolism, genetic factor, irregular secretion of hormones, and use of different drugs like immunosuppressant and antineoplastic agents. The FDA approved synthetic drugs for hair growth such as minoxidil and finasteride have been discouraged due to side effects. Therefore, searching for new sources from natural product of plant origin can play a significant role in overcoming these problems [6]. *Z. nummularia*, commonly known as Malla or Jher berry, belong to Rhamnaceae. The fruit of *Z. nummularia* has a cooling and astringent effect and can be used as an appetizer, stomachic, to treat mucous and enhance biliousness effect [7]. Different parts of *Z. nummularia* have been reported for the traditional treatment of various types of diseases [8]. however, no published data are available regarding the preparation of silver nanoparticles from its fruits. The roots, leaves, bark, and seeds of *Z. nummularia* have been focused on in all the research work up till now, and fruits have been neglected so far as a possible subject of study and analysis [9, 10].

In this study, silver nanoparticles (AgNPs) were formed by blending different amounts of fruit extract from *Z. nummularia* and silver nitrate solution. The nanoparticles were studied for their effect on hair growth and activity against pathogenic bacterial and fungal strains.

2. Materials and Methods

2.1. Fruit Collection and Preparation. Healthy and fully ripened fruits of *Z. nummularia* were collected from plants during the fruiting season and washed thoroughly with deionized water. The fruits were cut into pieces and kept in a sterile shady environment for drying. After drying, the samples were ground into the powdered form using mortar and pestle and transferred into polythene bags. Extraction from the dried plant material was done in five different solvents, i.e., water, chloroform, ethanol, methanol, and acetone. In 100 mL of each solvent, 25 g of the dried powder sample was taken in a beaker and kept on a shaker for 48 h. The solutions were then filtered using Whatman No.1 filter paper (pore size $25\text{ }\mu\text{m}$) into conical flasks, and the filtrates were kept for drying in a shady sterile environment. Under reduced pressure, solvents were allowed to be evaporated, and the dried extracts were stored at 25°C for analysis.

2.2. Preparation of Silver Nanoparticles. Silver nanoparticles (AgNPs) were prepared via the standard method described by Turkevich et al. [9]. Aqueous extract of *Z. nummularia* fruit was used as a bioreductant to synthesize silver nanoparticles. A 0.085 g of silver nitrate was thoroughly dissolved in 100 mL of distilled water to get a 1 mM solution of AgNO₃. Then, silver nitrate solution was mixed with aqueous extract of *Ziziphus* fruit in the ratios of 6:1, 8:1, 10:1, 12:1, and 14:1. The mixture was kept on a shaker for about 4 h. The change of color from colorless to yellowish-brown was observed, indicating silver nanoparticles' formation.

2.3. Characterization of Silver Nanoparticle. Characterization of AgNPs was carried out by UV-Vis spectral analysis through UV-Vis spectrophotometer UV-2450 (Shimadzu). Infrared spectra were obtained using a Fourier transform infrared spectrometer (I.R. Prestige Fourier transform infrared spectrophotometer, SHIMADZO, Japan) ranging 4000-600 cm⁻¹. XRD analysis was performed using Joel X-ray diffractometer JDX-3532 with coat JCPDS no. 003-1018 and Ni filter, using monochromatic CuK α radiation of wavelength 1.5418 Å. The X-ray generator was operated at 40 kV and 30 mA. The scanning range 2 θ / θ was selected. The scanning speed of 10 min⁻¹ was employed for precise determination. Hitachi S-4500 SEM machine was used for scanning electron microscopic (SEM) analysis. EDX Sight Oxford instrument was used for EDX analysis. The thermal gravimetric analysis used the Diamond Series TG, PerkinElmer, USA, analyzer using Al₂O₃ as reference. The particle size analyzer gives an order about the size of the synthesized silver nanoparticles formed by the leaf extract of *Ziziphus nummularia*.

2.4. Antibacterial Assay. *S. aureus* (ATCC 6538), *E. coli* (ATCC 35218), *Streptococcus pyogenes* (ATCC 19615), *Pseudomonas aeruginosa* (ATCC 125668), *S. pneumoniae* (ATCC 6303), *Streptococcus faecalis* (ATCC 9790), *Proteus vulgaris* (ATCC 6380), and *Proteus mirabilis* (ATCC 14153) were obtained from Sarhad University microbiology lab. The agar well-diffusion was followed to determine antibacterial activity. Nutrient agar (N.A.) plates were swabbed (sterile cotton swabs) with 8 h old-broth culture of respective bacteria. A sterile cork borer was used for making wells of about 10 mm diameter and about 2 cm apart in each of these plates. A stock solution of each plant extract was prepared at a 1 mg/mL concentration in different plant extracts, viz., methanol, ethanol, petroleum ether, and water. Around 100 μ L of various plant solvent extracts was syringed into the wells and left to diffuse for 2 h at room temperature. Control experimentations, including inoculums without plant extract, were carried out. The incubation of plates was carried out for bacterial pathogens at 37°C for 18-24 h. The activity index was also calculated, and the diameter of the inhibition zone (mm) was also measured. The experiment was repeated three times for maintaining triplicates. The readings were taken in three different fixed directions for each replicate, and the average values were noted [11].

2.5. Antifungal Assay. *Candida albicans* (ATCC 60193), *Cryptococcus neoformans* (ATCC 14115), and *Aspergillus*

niger (ATCC 6275) were obtained from Sarhad University microbiology lab. A well-diffusion method was followed to determine the antifungal activity. Potato dextrose agar (PDA) plates were swabbed (sterile cotton swabs) with 8 h old-broth culture of respective fungi. Wells (10 mm diameter and about 2 cm apart) were made in each plate using a sterile cork borer. A stock solution of each plant extract was prepared at a 1 mg/mL concentration in different plant extracts, viz., methanol, ethanol, petroleum ether, and water. About 100 μ L of different concentrations of plant solvent extracts was added sterile syringe into the wells and allowed to diffuse at room temperature for 2 h. Control experimentations, including inoculums without plant extract, were carried out. The incubation of plates was carried out for bacterial pathogens at 37°C for 18-24 h. The activity index was also calculated, and the diameter of the inhibition zone (mm) was also measured. The experiment was repeated three times for maintaining triplicates. The readings were taken in three different fixed directions for each replicate, and the average values were noted [12].

2.6. Determination of Minimum Inhibitory Concentration (MIC). The extracts of *Z. nummularia* were very effective as antimicrobial agents. Later on, the MIC and MBC values were also determined for each strain by applying tests. The extracts were diluted to give the final concentrations of 75, 37.5, 18.8, 9.4, 4.7, 2.4, 1.2, 0.6, 0.3, and 0.15 mg/mL. 100 μ L of 10⁵ CFU/mL of the microbial strains was inoculated in tubes with an equal volume of nutrient broth and plant extracts. The tubes were incubated aerobically for 24-48 h at 37°C. Three control tubes were maintained for each strain (organism control, extract control, and media control). The least concentration of the extract (highest dilution) that did not produce visible growth (no turbidity) in the initial 24 h as compared to the control tubes was considered as preliminary "MIC." The dilutions that showed no turbidity were further incubated for 24 h at 37°C. The lowest concentration that did not show any visual turbidity after the overall incubation period of 48 h was considered the final "MIC."

2.7. Determination of Minimum Bactericidal Concentration (MBC). The value of MBC was found out by subculturing the test dilution (which did not show any visual turbidity) on newly prepared nutrient agar media. Further incubation of plates was carried out for 18-42 h at 37°C. The highest dilution that yielded no single bacterial colony on the nutrient agar plates was taken as MBC [13].

2.8. Minimum Fungicidal Concentration (MFC). The MFC determination was carried out initially by choosing those tubes that did not show any growth during "MIC" determination. An inoculating loop full from each tube was subcultured onto agar plates free from the extract and incubated at 37°C for further 24 h. That minimum concentration, at which there was no growth observation, was considered the "MFC" [14].

2.9. Hair Grow Activity. Four rabbits of almost the same weight were taken and kept in the animal house for one week. All the rabbits were offered the same diet. After one

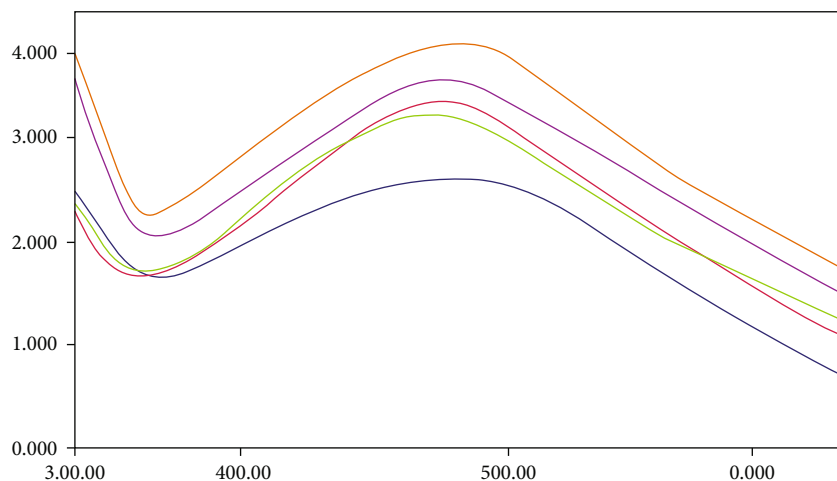


FIGURE 1: UV-spectrophotometer spectra of silver nanoparticles of different ratios of *Ziziphus nummularia* fruit.

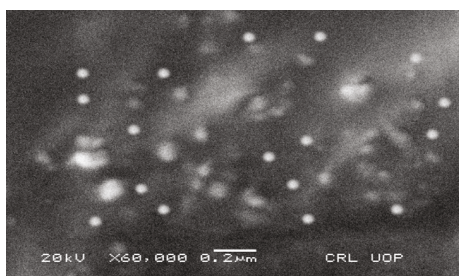


FIGURE 2: SEM image of silver nanoparticles of *Ziziphus nummularia* fruit extract at 60,000 magnification level.

week, the right limb of rabbits was shaved with a razor in a dimension of 1×3 inch. Then, the shaved area was massaged with minoxidil, ethanolic, and methanolic extracts of *Z. nummularia* and silver nanoparticles three times a day throughout the experimental periods. The size length of hairs was measured by the scale and noted in photographs [15]. All rabbits throughout the experimental study provided the same diet and environmental conditions.

3. Results and Discussion

Z. nummularia aqueous fruit extract was used as a reducing agent to synthesize silver nanoparticles and characterized using various sophisticated instruments. The prepared silver NPs were analyzed by UV-spectrophotometer, SEM, XRD, TGA, DSC, EDX, and particle size analyzer. Further, the prepared AgNPs were evaluated for antimicrobial and hair growth activities.

3.1. Analysis of Silver Nanoparticles by UV-Spectrophotometer. Figure 1 shows peaks of different sizes and shapes of silver nanoparticles confirmed at a region of 460 to 485 nm. The silver nanoparticle formations depend on the concentration of silver and plant extracts. The maximum absorbance of silver nanoparticles depends on Ag concentration concerning plant extract [16, 17]. The maximum absorbance was noted with a ratio of 1:12 of plant extract

and silver nitrate solution indicated by the uppermost orange line, which is the optimum ratio peak, while the other lines show minimum absorbance specified for nanoparticles larger in size than the orange line. Namratha and Monica [18] studied that variation in the absorption peaks of the synthesized silver nanoparticles might be the difference in the morphology of the nanoparticle. Analysis of silver nanoparticles by scanning electron microscopy white patches as shown in Figure 2 indicates silver nanoparticles' formation using *Z. nummularia* fruit extract. The silver nanoparticles formed are round; however, some white large dull patches can also be seen that represents an accumulation of the particles. The round and uniform silver nanoparticles have been noted with a diameter of 40 nm. The SEM results indicated that *Z. nummularia* fruit extract acts as a strong reducing agent, resulting in spherical and uniform Ag nanoparticles. However, the large white spot may be an aggregation of the nanoparticles. Our results showed particle size contrast [13], where the observed particle sizes ranged between 4 nm and 6.5 nm.

3.2. Analysis of Silver Nanoparticles by EDX. EDX spectroscopy is used for elemental analysis, as depicted in Figure 3. The EDX spectra show the high intensive silver peak, which represents the formation of silver nanoparticles. The spectra indicated the silver nanoparticles peak at 34 keV, whereas carbon and oxygen peaks are also present, representing the mixed precipitation in the plant extract. It has been reported that oxygen and carbon peaks are due to the presence of biomolecules attached to the surface of the silver nanoparticles [19, 20]. Priya et al. [21] also studied plant-mediated silver nanoparticles. They reported the presence of silver, carbon, and oxygen peaks when analyzed through EDX. Jiang et al. [22] suggested that Ag is only the major element present in the NPs under study. Our results are also in concordance with the study of [14], which observed silver, carbon, and oxygen peaks in *Z. nummularia* fruit aqueous extract-mediated silver nanoparticles characterized by EDX.

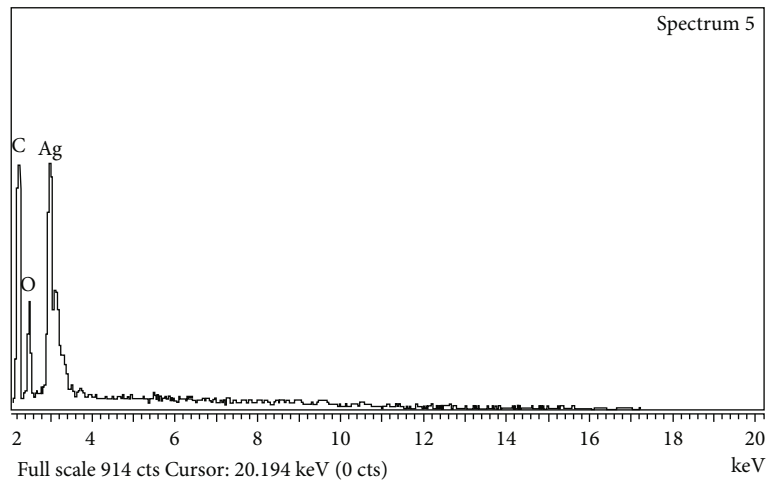


FIGURE 3: EDX spectra of silver nanoparticle of *Ziziphus nummularia* fruit.

Sample: Nano particles (water)
 Size: 5.260 g
 Method: Ramp
 Comment: Thermal properties

Instrument: DSC Q100

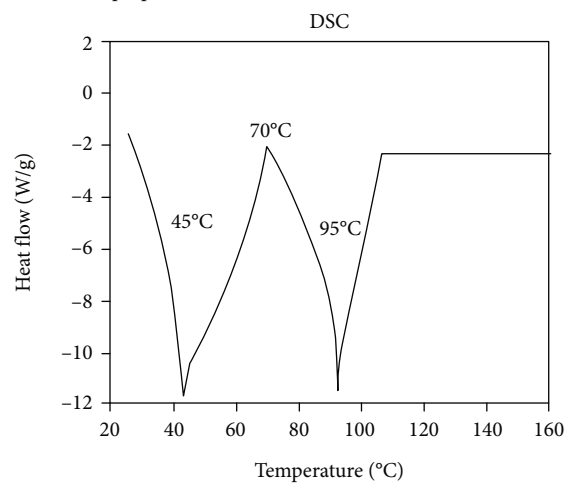


FIGURE 4: DSC pattern of silver nanoparticles of *Ziziphus nummularia* fruit.

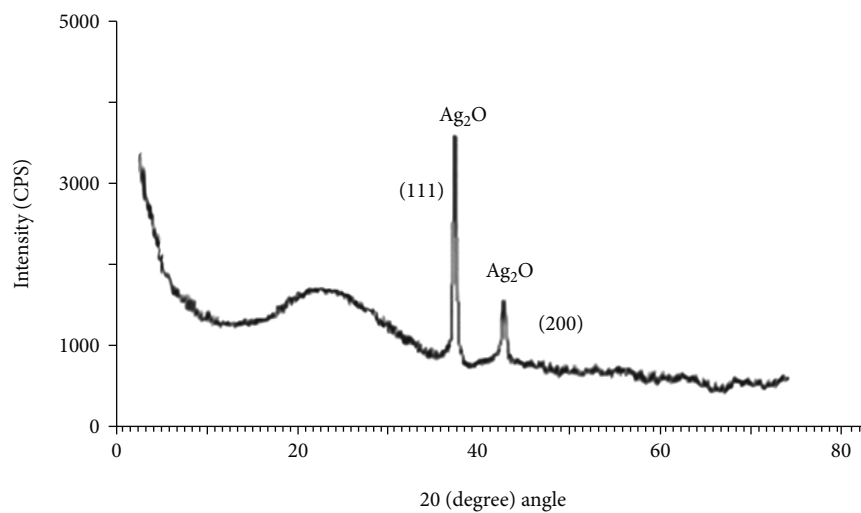


FIGURE 5: XRD spectra of silver nanoparticle of *Ziziphus nummularia* fruit.

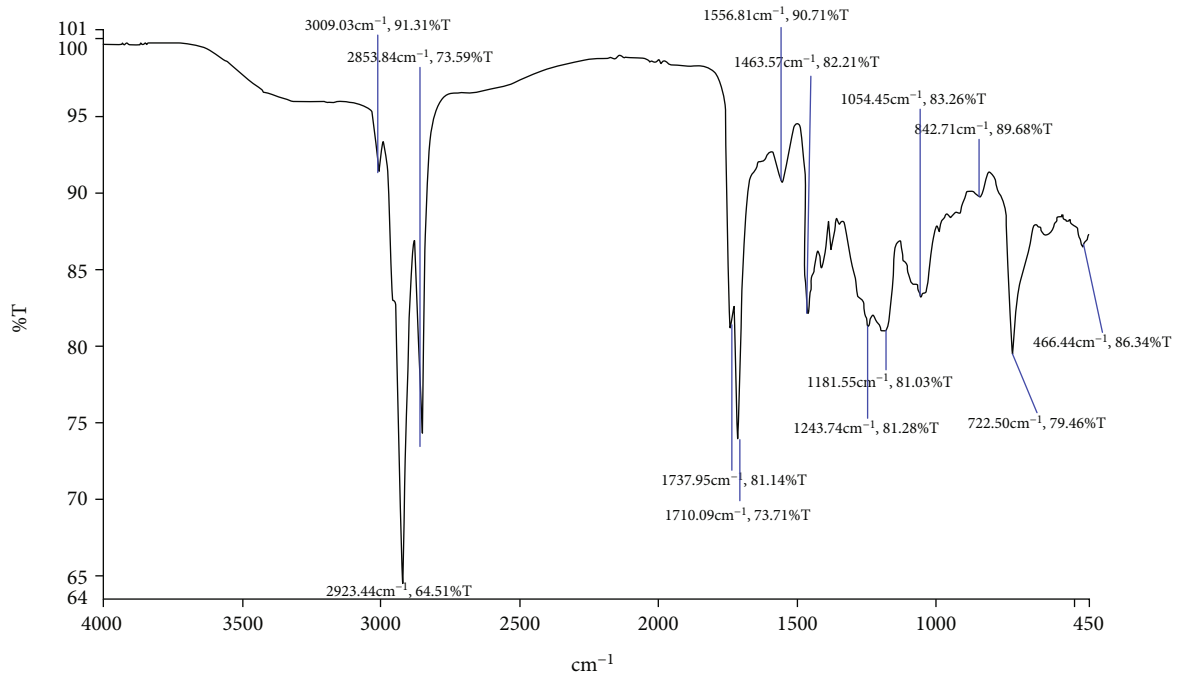


FIGURE 6: FTIR spectra of silver nanoparticle of *Ziziphus nummularia* fruit.

Sample: Nano particles (water)
 Size: 8.4160 mg
 Method: Ramp
 Comment: Thermal properties

Instrument: TGA Q100

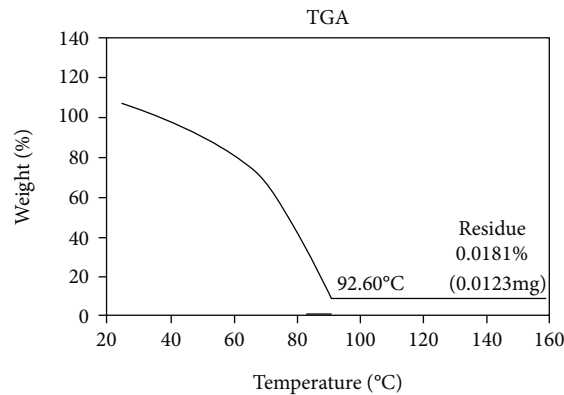


FIGURE 7: TGA peak pattern of silver nanoparticle of *Ziziphus nummularia* fruit.

3.3. Analysis of Silver Nanoparticles by DSC. DSC has been used to study the isothermal behaviour of silver nanoparticles. Figure 4 shows the DSC spectra of silver nanoparticles with temperatures ranging from 20°C to 160°C. The DSC spectra clearly show various exothermic peaks at 45, 70, 95, and 99°C. These peaks indicated that the gradual loss of water started at a temperature of 45°C and ended at 99°C, whereas above 99°C, the silver nanoparticles were found stable up to 160°C. Our results are nearly in agreement with Farhat et al. [16], where AgNPs of *Z. nummularia* leaf extract were stable up to 93°C.

3.4. Analysis of Silver Nanoparticles by XRD. The XRD spectra of silver nanoparticles at 2θ (degree) angle are shown in

Figure 5. The diffraction peaks at 37 and 43 represent the correspondence indices 111 and 200, respectively. The correspondence peaks indicated the typical face-centered cubic structure of silver nanoparticles. Sulochana et al. [23] investigated the XRD technique of *Andrographis paniculata* leaf extract's silver nanoparticles. The diffraction peaks of silver nanoparticles at 37 and 44 confirmed the indices 111 and 200, respectively. The particle size of the prepared silver nanoparticles was noted at 15 nm by using the Deby Scherer equation as listed below.

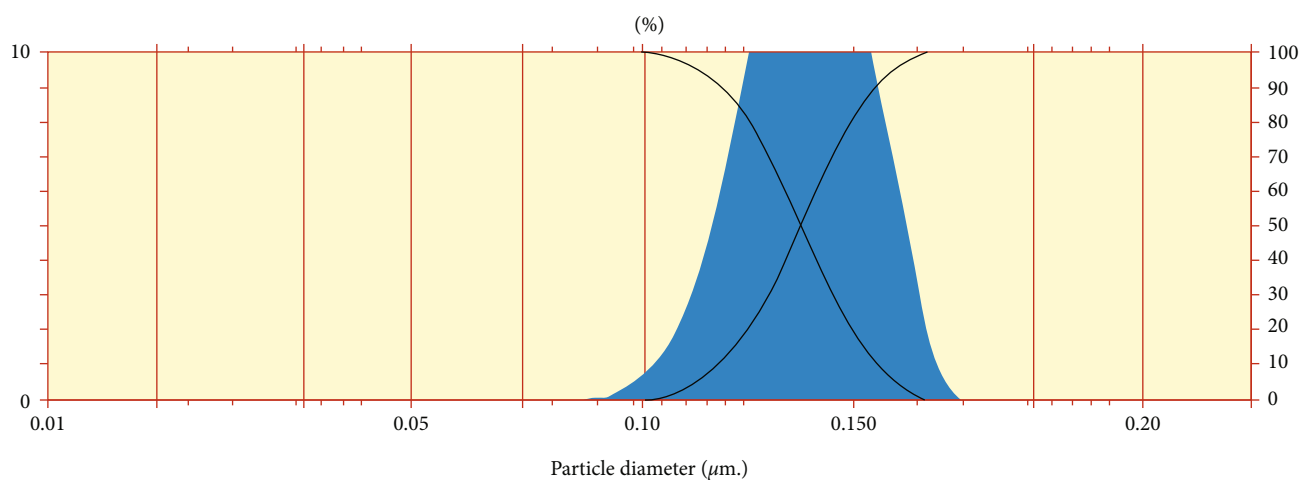
$$D = \frac{K\lambda}{\beta \cos\theta}, \quad (1)$$

Zone of inhibition (mm) \pm standard deviation

Sample details			
Sample ID: SC-1	Run number: 1		
Sample file: SC-1			
Sample path: MASTER~1\MS-2014	Result source: Analysed		
Sample notes: A			
Stir/pump: 2960r. Receiving date: 04-11-2014			
Water/sodium hexametaphosphate	Ultrasonic: Outside 10 min.		
Operator	Checked by		

Sample details			
Range lens: 300RF mm	Beam length: 2.40 mm	Sampler: MS14	Obscuration: 37.45%
Presentation: 3THD [particle R.I. = (2.5935, 0.1000); Dispersant R.I. = 1.3300]			Residual: 0.123%
Analysis model: Polydisperse			
Modifications: None			

Result statistics			
Distribution type: Volume	Concentration: 0.0628 % Vol	Density: 1.2g/cub. cm	Specific S.A. = 0.009
Mean diameters:	D (v, 0.1) = 0.036 μ m	D (v, 0.5) = 0.139 μ m	D (v, 0.9) = 0.053 μ m
D [4, 3] = 0.149 μ m	D [3, 2] = 0.139 μ m	Span = 9.811E-01	Uniformity = 3.044E-01

FIGURE 8: MSA pictogram of silver nanoparticle of *Ziziphus nummularia* fruit.TABLE 1: The antibacterial activity of different extract of *Ziziphus nummularia* fruit and silver nanoparticle against Gram-positive bacteria.

	Aqueous	Methanol	Ethanol	Chloroform	Ethyl acetate	Ag nanoparticles
<i>S. aureus</i> (ATCC 6538)	11.66 \pm 1.52	13.66 \pm 1.52	13.33 \pm 2.51	06.33 \pm 0.57	06.66 \pm 1.15	16.66 \pm 1.52
<i>S. pyogenes</i> (ATCC 19615)	13.00 \pm 2.00	16.13 \pm 1.15	15.66 \pm 2.08	10.66 \pm 0.57	06.25 \pm 0.57	20.00 \pm 1.00
<i>S. pneumonia</i> (ATCC 6303)	06.33 \pm 1.15	09.63 \pm 1.15	08.66 \pm 2.00	04.10 \pm 0.57	04.33 \pm 1.52	12.00 \pm 1.00
<i>S. faecalis</i> (ATCC 9790)	12.54 \pm 1.52	13.00 \pm 2.64	10.38 \pm 0.57	05.00 \pm 1.00	05.66 \pm 1.52	17.00 \pm 2.00

TABLE 2: The antibacterial (Gram negative) activity of different extract of *Ziziphus nummularia* fruit and silver nanoparticle (mean \pm SD).

Gram-negative bacteria	Zone of inhibition (mm) \pm standard deviation					Ag Nanoparticles
	Aqueous	Methanol	Ethanol	Chloroform	Ethyl acetate	
<i>E. coli</i> (ATCC 35218)	06.24 \pm 1.00	08.73 \pm 0.57	07.39 \pm 0.57	04.00 \pm 1.00	03.66 \pm 0.57	18.66 \pm 1.15
<i>P. aeruginosa</i> (ATCC 125668)	06.51 \pm 0.21	07.15 \pm 0.57	06.54 \pm 1.15	03.78 \pm 1.00	02.99 \pm 1.00	13.00 \pm 1.00
<i>P. mirabilis</i> (ATCC 14153)	07.33 \pm 1.52	07.07 \pm 1.00	06.00 \pm 1.00	03.71 \pm 1.15	02.68 \pm 0.57	14.00 \pm 1.00
<i>P. vulgaris</i> (ATCC 6380)	06.87 \pm 1.54	06.61 \pm 0.57	07.08 \pm 0.32	03.43 \pm 0.57	03.19 \pm 1.15	10.00 \pm 1.00

TABLE 3: The antifungal activity of different extract of *Ziziphus nummularia* fruit and silver nanoparticle (mean \pm SD).

Fungi	Zone of inhibition (mm) \pm standard deviation					
	Aqueous	Methanol	Ethanol	Chloroform	Ethyl acetate	Ag nanoparticles
<i>C. albicans</i> (ATCC 60193)	13.00 \pm 1.73	14.33 \pm 1.53	12.12 \pm 1.53	03.00 \pm 1.73	08.74 \pm 1.15	14.67 \pm 1.53
<i>C. neoformans</i> (ATCC 14115)	11.31 \pm 1.15	15.54 \pm 2.08	13.00 \pm 1.73	07.33 \pm 0.58	03.67 \pm 1.53	23.67 \pm 1.53
<i>A. niger</i> (ATCC 6275)	05.60 \pm 1.15	10.11 \pm 2.08	11.41 \pm 0.58	06.67 \pm 0.58	03.57 \pm 0.58	21.00 \pm 1.73

TABLE 4: MIC and MBC of ethanolic and methanolic extracts of *Ziziphus nummularia* and silver nanoparticles ($\mu\text{g/mL}$).

Gram-positive bacteria	Ethanolic extract ($\mu\text{g/mL}$)		Methanolic extract ($\mu\text{g/mL}$)		Silver nanoparticles ($\mu\text{g/mL}$)	
	MIC	MBC	MIC	MBC	MIC	MBC
<i>S. aureus</i> (ATCC 6538)	250	500	230	475	100	200
<i>S. pyogenes</i> (ATCC 19615)	200	500	210	425	100	150
<i>S. pneumonia</i> (ATCC 6303)	300	550	275	510	150	250
<i>S. faecalis</i> (ATCC 9790)	300	600	280	525	100	300

TABLE 5: MIC and MBC of ethanolic and methanolic extracts of *Ziziphus nummularia* and silver nanoparticles ($\mu\text{g/mL}$).

Gram-negative bacteria	Ethanolic extract ($\mu\text{g/mL}$)		Methanolic extract ($\mu\text{g/mL}$)		Silver nanoparticles ($\mu\text{g/mL}$)	
	MIC	MBC	MIC	MBC	MIC	MBC
<i>E. coli</i> (ATCC 35218)	300	600	310	630	200	375
<i>P. aeruginosa</i> (ATCC 6303)	250	500	280	540	200	350
<i>P. mirabilis</i> (ATCC 14153)	250	450	290	510	150	300
<i>P. vulgaris</i> (ATCC 6380)	300	500	280	490	250	400

TABLE 6: MIC and MFC of ethanolic and methanolic extracts of *Ziziphus nummularia* and silver nanoparticles ($\mu\text{g/mL}$).

Fungi	Ethanolic extract		Methanolic extract		Silver nanoparticles	
	MIC	MBC	MIC	MBC	MIC	MBC
<i>C. albicans</i> (ATCC 60193)	350	600	325	570	200	400
<i>C. neoformans</i> (ATCC 14115)	300	600	270	550	150	250
<i>Aspergillus niger</i> (ATCC 6275)	300	550	250	510	200	300

where D is the mean size, K is the constant (0.94) proportionality, λ is the wavelength (1.54060 Å) of X-ray, β is the excess line broadening, and θ is the Bragg angle.

$$B = B - b, \quad (2)$$

where B stands for line width (radian) and b is instrument line broadening (radian). The crystallite sizes were found to be 20-60 nm using the above formula. Geethalakshmi et al. [24] reported that *Trianthema decandra* extract mediated silver nanoparticles and was characterized by XRD at 2 theta, ranging from 10 to 80. According to the study, the average size of prepared silver nanoparticles was 15 nm, ranging from 10 to 50 nm. The diffraction pattern corresponds to no impurities present; this proves that

pure silver nanoparticles were prepared. Similar XRD pattern reports were observed in the *Eclipta prostrate*, *Tribulus terrestris*, and *Prosopis juliflora* extracts for synthesized AgNPs [23].

3.5. Analysis of Silver Nanoparticles by FTIR. Fourier transform infrared spectroscopy of AgNPs is shown in Figure 6. An infrared study was carried out to ascertain the nature and purity of the Ag nanoparticles. The infrared spectrum consists of two regions, i.e., fingerprint and functional group regions. The absorption band for organic compounds is observed in the functional group region. At the same time, metals normally show absorption spectra in the fingerprint region, resulting from the atomic vibration of the molecules. The peak detected at 3443.22 cm^{-1} show the O-H group,

TABLE 7: Correlations among antibacterial (Gram positive) activity of *Ziziphus nummularia* fruit extract in different solvents and in combination with silver nanoparticles. The symbols * and ** show the significance of a correlation.

	Aqueous	Methanol	Ethanol	Chloroform	Ethyl acetate	Silver nanoparticles
Aqueous	1.00					
Methanol	0.89**	1.00				
Ethanol	0.63	0.91**	1.00			
Chloroform	0.60	0.89**	0.95**	1.00		
Ethyl acetate	0.86**	0.86*	0.79	0.62	1.00	
Silver nanoparticles	0.94**	0.99**	0.83*	0.84*	0.83*	1.00

TABLE 8: Correlations among antibacterial (Gram negative) activity of *Ziziphus nummularia* fruit extract in different solvents and in combination with silver nanoparticles. The symbols * and ** show the significance of a correlation.

	Aqueous	Methanol	Ethanol	Chloroform	Ethyl acetate	Silver nanoparticles
Aqueous	1.00					
Methanol	-0.57	1.00				
Ethanol	-0.85*	0.50	1.00			
Chloroform	0.20	0.42	0.24	1.00		
Ethyl acetate	-0.15	0.00	0.64	0.63	1.00	
Silver nanoparticles	0.63	-0.39	-0.95**	-0.47	-0.85*	1.00

TABLE 9: Correlations among antifungal activity of *Ziziphus nummularia* fruit extract in different solvents and in combination with silver nanoparticles. The symbols “*” and “***” show the significance of a correlation.

	Aqueous	Methanol	Ethanol	Chloroform	Ethyl acetate	Silver nanoparticles
Aqueous	1					
Methanol	0.91**	1.00				
Ethanol	0.84*	0.99**	1.00			
Chloroform	-0.52	-0.12	0.03	1.00		
Ethyl acetate	0.64	0.26	0.11	-0.99**	1.00	
Silver nanoparticles	-0.39	0.03	0.18	0.99**	-0.96**	1.00

which result from the stretching and deformation of water molecules adsorbed to the surface of the metal. Similarly, the peaks were observed at 1646 cm^{-1} , 1458 cm^{-1} , 1140 cm^{-1} , 1056 cm^{-1} , and 7787.6 cm^{-1} , representing other functional groups present in the synthesized particle. FTIR stretching vibrations showed that the biomolecules such as alkaloids, flavonoids, and phenols in bark extract were responsible for reducing, capping, and stabilizing silver nanoparticles. A similar trend was also observed in the synthesis of AgNPs using *Artocarpus heterophyllus* Lam [25] and *Abelmoschus esculentus* [26, 27] seed extracts.

3.6. Analysis of Silver Nanoparticles by TGA. By increasing the temperature and employing the thermal gravimetric analysis, % weight loss of AgNPs was detected, as shown in Figure 7. The experimental conditions for gravimetric analysis were set at a temperature range of 200°C to 1600°C to determine the decomposition of the prepared silver nanoparticles. It was found that the decomposition started at 25°C . At the same time, the size of the particles was noted

to have been decreased up to 92.60°C . The initial sample size was 8.416 mg which gradually decreased to 0.0123 mg due to extensive loss of moisture contents at a temperature of 92.60°C . Kasthuri et al. [28] analyzed the TGA of the phyllanthin extract loaded with gold and silver NPs when heated from 35 to 800°C . The initial weight loss observed at 150°C was attributed to the water molecules present. In our study, no further weight loss occurs beyond 92.60°C as proposed by Farhat et al. [16] for *Z. nummularia* fruit extract-mediated silver nanoparticles.

3.7. Analysis of Silver Nanoparticles by MSA. Master sizer is mainly used to measure the particle size in the nanometer range. The synthesized silver nanoparticles of *Z. nummularia* fruit extracts are shown in Figure 8. Further analysis of the synthesized particle confirmed their size range from $0.10\text{ }\mu\text{m}$ to $0.17\text{ }\mu\text{m}$. On the mass medium diameter analysis, 50% of the particles were small in their size and diameter of 0.9 micrometres . Jeyanthi et al. [29] prepared *Dracaena mahatma* leaf extract-mediated silver nanoparticles and

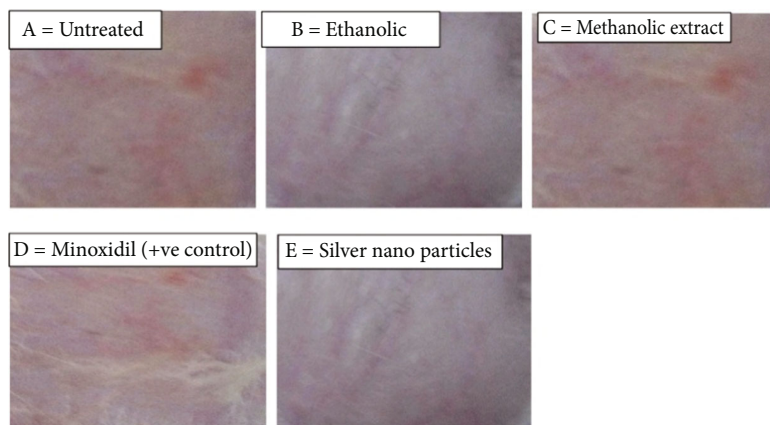


FIGURE 9: Shaved areas of rabbit skin.

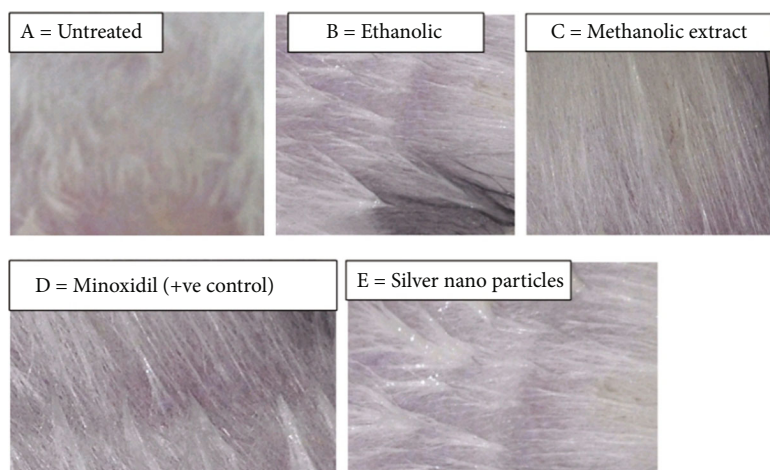


FIGURE 10: Air growth on the shaved area of rabbits in response to various extracts on the 7th day.

confirmed that average particle size obtained 0.87 micrometres through master size analyzer. In contrast, the average particle size of the synthesized nanoparticle 108 nm was reported by Tugçe et al. [30].

3.8. Antimicrobial Activities. Nowadays, multiresistant bacterial strains have been developed, resulting in increased morbidity and mortality. Due to the high cost and unwanted effects of commercially available antibiotics, searching low-cost and potentially active compounds is needed that can act as new antimicrobial agents. Therefore, new antibiotics from other sources, especially plant origin with known antimicrobial activity, are required [30–33]. Table 1 shows that the zone of inhibition 11.66 mm was produced against *S. aureus* (ATCC 6538) by aqueous extract followed by 13.66 mm and 13.33 mm by methanolic and ethanolic extracts, respectively. Chloroform and ethyl acetate extract was noted less effective, having 6.33 mm and 3.66 mm zone of inhibition, respectively.

In contrast, a silver nanoparticle of *Z. nummularia* fruit extract was noted highly effective with a 16.66 mm zone of inhibition. *Streptococcus pyogenes* (ATCC 19615) showed high resistance against ethyl acetate extract, having a

6.25 mm zone of inhibition; however, methanolic extract was found highly effective, having a 16.13 mm zone of inhibition against *Streptococcus pyogenes* followed by a 20.00 mm zone of inhibition produced by *Z. nummularia* fruit extract AgNPs. *Streptococcus pyogenes* (ATCC 19615) showed high resistance against chloroform and ethyl acetate extract with 4.10 mm and 4.33 mm zone of inhibition, respectively. The same bacteria showed less resistance against *Z. nummularia* fruit extract AgNPs having a 12.00 mm zone of inhibition. In the case of *Streptococcus faecalis*, the methanolic extract was found effective, having a 13.00 mm zone of inhibition; however, the silver nanoparticle of *Z. nummularia* fruit extract was noted highly effective with a 17.00 mm zone of inhibition.

Table 2 reveals that ethyl acetate extract of *Z. nummularia* fruit extract was less effective with a 3.66 mm zone of inhibition against *E. coli*, followed by a 4.00 mm zone of inhibition produced by chloroform extract. AgNPs of *Z. nummularia* fruit extract had the maximum zone of inhibition of 18.66 mm. *Pseudomonas aeruginosa* (ATCC 125668) was noted to be highly resistant to chloroform and ethyl acetate extract with 3.78 and 2.99 mm zone of inhibition. Aqueous and ethanolic extracts showed nearly the same activity of

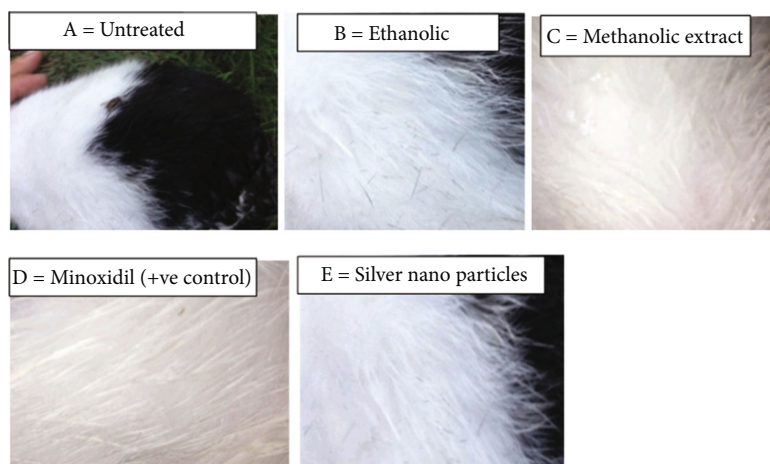


FIGURE 11: Investigation of hair growth on the shaved area of rabbits in response to various extracts on the 14th day.

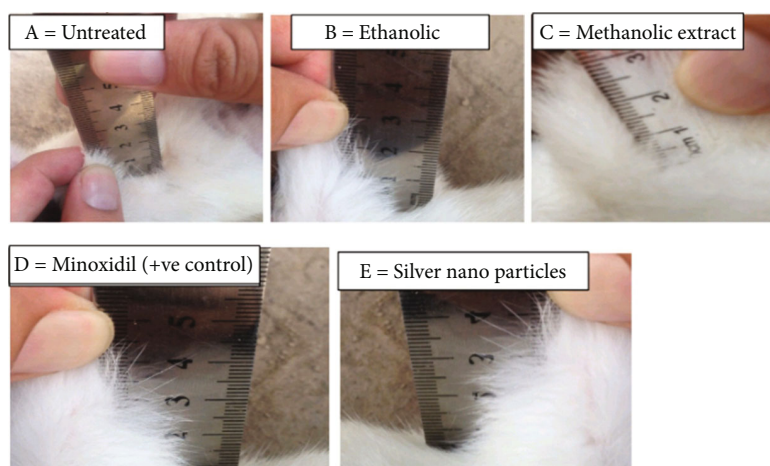


FIGURE 12: Analysis of hair growth in response to various extracts on the 21st day.

TABLE 10: Measurement of newly grown hairs of rabbits in response to different solvent extracts and *Ziziphus nummularia* fruit-mediated silver nanoparticles.

Time period	Length of hair measurement in centimeter (cm)				
	Untreated	Ethanolic extract	Methanolic extract	Minoxidil (positive control)	Silver nanoparticles
Day 0	0	0	0	0	0
Day 7	0.6	0.7	0.7	0.9	0.9
Day 14	1.4	1.9	1.8	2.8	3.1
Day 21	2.4	3.3	3.5	4.5	4.8

6.51 and 6.54 mm zone of inhibition against the same bacteria. The prepared silver NPs were found highly effective with 13.00 mm zone of inhibition. The highest zone of inhibition, 14 mm, was recorded against *Proteus mirabilis* (ATCC 14153) by silver NPs, while the zone of inhibition of all the extracts was in the range of 2.68 to 7.33 mm. The least zone of inhibition, 3.19 mm of ethyl acetate, was recorded against *Proteus vulgaris* (ATCC 6380) whereas the highest zone of inhibition, 10.00 mm of silver NPs, was measured against *Proteus vulgaris* (ATCC 6380). Taking together, the *Z. nummularia* fruit-mediated silver nanoparticles were found

highly effective against various types of tested bacteria and possessed maximum antibacterial activity. Previous studies conducted to examine plant-mediated silver nanoparticles [23] also report the maximum antimicrobial potential of silver nanoparticles.

Table 3 represents the antifungal activity of different extracts of *Z. nummularia* fruit and the silver NPs of *Z. nummularia* fruit extract. It shows that the methanolic extract and AgNPs were found highly effective against *Candida albicans* (ATCC 60193) having 14.33 and 14.67 mm zone of inhibition followed by 13.00, 12.12, 8.74, and

3.00 mm zone of inhibition of aqueous, ethanolic, ethyl acetate, and chloroform extracts, respectively. Methanolic and ethanolic extracts of *Z. nummularia* fruit were effective with 15.54 and 13.00 mm zone of inhibition against *Cryptococcus neoformans* (ATCC 14115). However, the highest zone of inhibition was 23.67 mm of AgNPs against the same fungi. In the case of *Aspergillus niger* (ATCC 6275), the methanolic and ethanolic extracts of *Z. nummularia* fruit produced a nearly same zone of inhibition (10.11 and 11.41 mm). In contrast, the highest zone of inhibition, 21.00 mm of AgNPs, was recorded against *Aspergillus niger* (ATCC 6275). The values of the zone of inhibition of other extracts of *Z. nummularia* fruit were in the range of 3.57 to 6.67 mm. Our results showed that silver nanoparticles were highly effective against various tested fungal species. Tugçe et al. [30] reported that silver nanoparticles possess an effective antifungal property against *C. albicans*, *C. kefyr*, and *A. niger*. The present study emphasizes using the medical plant to synthesize silver nanoparticles with an antifungal effect.

Table 4 shows the MIC and MBC values of ethanolic and methanolic extracts of *Z. nummularia* fruit and silver nanoparticles of the respective plant fruit extract. According to this data, the MIC value 250 $\mu\text{g}/\text{mL}$ of ethanolic extract was noted against *Staphylococcus aureus* (ATCC 6538), whereas the MBC value 500 $\mu\text{g}/\text{mL}$ was recorded against the same bacteria. The methanolic extract was found more effective than ethanolic extract having 230 $\mu\text{g}/\text{mL}$ and 475 $\mu\text{g}/\text{mL}$ MIC and MBC values. However, the AgNPs were highly effective with 100 $\mu\text{g}/\text{mL}$ MIC value and 200 $\mu\text{g}/\text{mL}$ MBC value. The MIC and MBC values 200 $\mu\text{g}/\text{mL}$ and 500 $\mu\text{g}/\text{mL}$ of the ethanolic extract were recorded against *Streptococcus pyogenes* (ATCC 19615). The prepared silver nanoparticles were found highly effective than ethanolic and methanolic extracts having MIC value 100 $\mu\text{g}/\text{mL}$ and MBC value 150 $\mu\text{g}/\text{mL}$. In the case of *Streptococcus pneumoniae* (ATCC 6303) and *Streptococcus faecalis* (ATCC 9790), methanolic extract was more effective than ethanolic extract; however, both the bacteria showed less resistance against silver nanoparticles.

Table 5 reveals that silver nanoparticle was highly effective against *E. coli* (ATCC 35218) having 200 $\mu\text{g}/\text{mL}$ and 400 $\mu\text{g}/\text{mL}$ MIC and MBC values, respectively. *Pseudomonas aeruginosa* (ATCC 125668) showed more resistance against ethanolic and methanolic extracts and less resistance against the AgNPs with 200 $\mu\text{g}/\text{mL}$ MIC and 250 $\mu\text{g}/\text{mL}$ MBC values. The MIC and MBC values of methanolic extract were noted higher than ethanolic extract; however, the prepared nanoparticle was found highly effective against *Proteus mirabilis* (ATCC 14153) than ethanolic and methanolic extracts. The ethanolic and methanolic extracts were less effective against *Proteus vulgaris* (ATCC 6380). In contrast, the prepared nanoparticle was more effective than ethanolic and methanolic extracts with 250 $\mu\text{g}/\text{mL}$ MIC and 400 $\mu\text{g}/\text{mL}$ MBC values.

The MIC and MFC values 350 $\mu\text{g}/\text{mL}$ and 600 $\mu\text{g}/\text{mL}$ of the ethanolic extract were measured against *Candida albicans*, whereas the MIC and MFC values of methanolic extracts were recorded 325 $\mu\text{g}/\text{mL}$ and 570 $\mu\text{g}/\text{mL}$ (Table 6). *Cryptococcus neoformans* (ATCC 14115) showed

less resistance against the prepared AgNPs than ethanolic and methanolic extracts. The MIC and MFC values of ethanolic extract were measured higher than methanolic extract against *Aspergillus niger* (ATCC 6275); however, the prepared nanoparticle was more effective with 200 $\mu\text{g}/\text{mL}$ and 300, respectively, against *Aspergillus niger* (ATCC 6275).

3.9. Correlation among Antimicrobial Activities of Solvents. Correlations calculated for antimicrobial activity of *Z. nummularia* fruit extract in different solvents (aqueous, methanol, ethanol, chloroform, and ethyl acetate) and an aqueous solution of silver nanoparticles were informative (Table 7). The antimicrobial activity of methanolic extract of *Z. nummularia* fruit demonstrated a significant positive correlation with the other solvents and the aqueous solution of silver nanoparticles. A mixture of silver nanoparticles and *Z. nummularia* fruit extract showed significantly positive correlations with the fruit extracts in different solvents such as aqueous, methanol, ethanol, chloroform, and ethyl acetate. The highest significant positive correlation ($R^2 = 0.94$) was found between methanolic extract and silver nanoparticles.

In combination with silver nanoparticles and an aqueous solution, fruit extracts demonstrated negative correlations (Table 8) with the antimicrobial activities of the *Z. nummularia* fruit extracts in the other solvents. *Z. nummularia* fruit extracts in ethanolic solution showed strong negative correlations with the fruit extract in aqueous solution ($R^2 = -0.85$) and the aqueous mixture of silver nanoparticles and the fruit extract ($R^2 = -0.95$). A highly significant positive correlation ($R^2 = 0.99$) was observed (Table 9) between chloroform and silver nanoparticles, while strong negative correlations were noted for ethyl acetate with chloroform ($R^2 = -0.99$) and silver nanoparticles.

3.10. Hair Growth Activity. Hair growth activity of minoxidil, methanolic extract, ethanolic of *Z. nummularia* fruit, and silver nanoparticle is shown in Figures 9–12. The photographs taken after one week indicated that the shaved area of rabbits massaged by silver nanoparticles gave good results compared to ethanolic and methanolic extracts. The length of newly grown hairs in the area massaged by minoxidil and silver nanoparticles was found maximum than that of ethanolic and methanolic extracts of *Z. nummularia* fruit (Figures 9–12). The hair growth activity of *Z. nummularia* leaf extract and its respective silver nanoparticles have also been studied by Kaya et al. [14]. All the results for hair growth activity were presented in photographs. As shown in Table 10, maximum hair growth was recorded on the 21st day in groups D and E, which were treated with minoxidil and silver nanoparticles, respectively. However, groups B and C treated with ethanolic and methanolic extracts were found less effective as full hair growth did not occur there. The hair growth values in untreated group A (negative control) were less than all treated groups. A similar study was conducted by Deepa et al. [31] using different groups of rabbits treated with Amla, methi, and Neem hair oil in different concentrations. It was reported that each hair oil (Amla, methi, and Neem) in 7.5% concentration was highly effective

than 3.5 and 4.5% concentration in combination to achieve the full hair growth.

4. Conclusions

Z. nummularia aqueous fruit extract-mediated silver nanoparticles were prepared and confirmed through UV-spectrophotometer and FTIR. The size of the particles was measured at 40 nm through SEM, whereas XRD confirmed the crystalline nature of the particles. The prepared nanoparticles were found stable from 90°C to 160°C when analyzed by DSC, and EDX confirmed the intense sharp peak of the silver. In conclusion, the size silver nanoparticles of 40 nm were noted to be highly effective against both Gram-positive and Gram-negative bacteria and different tested species of fungi compared to other extracts of *Z. nummularia* fruit. Moreover, the prepared silver nanoparticles exhibited the highest hair growth activity, followed by minoxidil. However, the toxicological study of the prepared silver nanoparticles is highly recommended before their use on a commercial level. Furthermore, clinical trials are required to determine its therapeutic effect on various bacteria.

Data Availability

The data used to support the findings of this study are included within the article.

Conflicts of Interest

We wish to confirm that there are no known conflicts of interest associated with this publication.

Acknowledgments

The authors express their gratitude to the Research Center of Advanced Materials, King Khalid University, Saudi Arabia, for support (award number KKU/RCAMS/22).

References

- [1] P. P. Shanmuga, V. S. Vasantha, J. Jeyasundari, and B. Brightson, "Synthesis of plant-mediated silver nanoparticles using *Ficus microcarpa* leaf extract and evaluation of their antibacterial activities," *European Chemical Bulletin*, vol. 4, no. 3, pp. 117–120, 2015.
- [2] A. Roy, A. Elzaki, V. Tirth et al., "Biological synthesis of nanocatalysts and their applications," *Catalysts*, vol. 11, no. 12, p. 1494, 2021.
- [3] D. V. Goia and E. Matijevec, "Preparation of monodispersed metal particles," *New Journal of Chemistry*, vol. 22, no. 11, pp. 1203–1215, 1998.
- [4] N. A. Begum, S. Mondal, S. Basu, and D. Laskar, "Biogenic synthesis of Au and Ag nanoparticles using aqueous solutions of Black Tea leaf extracts," *Biointerfaces*, vol. 71, no. 1, pp. 113–118, 2009.
- [5] K. Anal and P. Kamal, "Green synthesis and antimicrobial activity of silver nanoparticles on cotton fabric: an amenable option for textile industries," *Advance Materials Letters*, vol. 7, no. 1, pp. 42–46, 2016.
- [6] R. Suraj, G. Rejitha, J. S. J. Anbu, K. Sunilson, and P. P. Anandarajagopal, "In vivo hair growth activity of *Prunus dulcis* seeds in rats," *Biology and Medicine*, vol. 1, no. 4, pp. 34–38, 2009.
- [7] M. Rathore, "Evaluation of the physico-chemical characteristics, minerals and heavy metals in wild and cultivated variety of AEGLE MARMELOS (L) CORREA," *Journal of Horticulture and Forestry*, vol. 1, no. 7, pp. 103–108, 2009.
- [8] A. K. Singh, A. S. Raghubanshi, and J. S. Singh, "Medical ethnobotany of the tribals of Sonaghati of Sonbhadra district, Uttar Pradesh, India," *Journal of Ethnopharmacology*, vol. 81, no. 1, pp. 31–41, 2002.
- [9] D. David, J. Evanoff, and C. George, "Synthesis and optical properties of silver nanoparticles and arrays," *ChemPhysChem*, vol. 6, no. 7, pp. 1221–1231, 2005.
- [10] A. Mohamed Azharudeen, T. Suriyakala, M. Rajarajan, and A. Suganthi, "An improved sensitive and selective non-enzymatic glucose biosensor based on PEG assisted CuO nanocomposites," *Egyptian Journal of Chemistry*, vol. 62, no. 3, pp. 487–500, 2019.
- [11] A. M. Azharudeen, A. Roy, R. Karthiga et al., "Ultrasensitive and selective electrochemical detection of dopamine based on CuO/PVA nanocomposite-modified GC electrode," *International Journal of Photoenergy*, vol. 2022, Article ID 8755464, 9 pages, 2022.
- [12] K. P. Vijay, S. Pammi, P. Kollu, K. Satyanarayana, and U. Shameem, "Green synthesis of silver nanoparticles: a review," *Industrial Crops and Products*, vol. 52, pp. 562–566, 2014.
- [13] B. Mahesh and S. Satish, "Antimicrobial activity of some important medicinal plant against plant and human pathogens," *World Journal of Agriculture and Soil Sciens*, vol. 4, pp. 839–843, 2008.
- [14] O. Kaya, F. Akcam, and G. Yayl, "Investigation of the in-vitro activities of various antibiotics against *Brucella melitensis* strains," *Turkish Journal of Medical Sciences*, vol. 42, pp. 145–148, 2012.
- [15] R. Irkin and M. Korukluoglu, "Control of *Aspergillus niger* with garlic, onion and leek extracts," *African Journal of Biotechnology*, vol. 6, pp. 384–387, 2007.
- [16] A. K. Farhat, Z. Muhammad, J. Abdul, and R. Aziz, "Green synthesis of silver nanoparticles by using *Z. nummularia* leaves aqueous extract and their biological activities," *Journal of Nanomaterials*, vol. 2016, Article ID 8026843, 8 pages, 2016.
- [17] V. K. Shukla, S. Pandey, and A. C. Pandey, "Green synthesis of silver nanoparticles using neem leaf *Azadirachta indica* extract," *AIP Conference Proceedings*, vol. 1276, no. 1, pp. 43–49, 2010.
- [18] N. Namratha and P. V. Monica, "Synthesis of silver nanoparticles using *Azadirachta indica* (Neem) extract and usage in water purification," *Asian Journal of Pharmacy and Technology*, vol. 3, no. 4, pp. 170–174, 2013.
- [19] H. M. Ahmed, A. Roy, M. Wahab et al., "Applications of nanomaterials in agrifood and pharmaceutical industry," *Journal of Nanomaterials*, vol. 2021, Article ID 1472096, 10 pages, 2021.
- [20] K. M. A. El-Nour, A. A. Eftaiha, A. Al-Warthanb, and R. A. Ammar, "Synthesis and applications of silver nanoparticles," *Arabian Journal of Chemistry*, vol. 3, no. 3, pp. 135–140, 2010.
- [21] B. Priya, S. Mantosh, M. Aniruddha, and D. Papita, "Leaf extract mediated green synthesis of silver nanoparticles from widely available Indian plants: synthesis, characterization,

- antimicrobial property and toxicity analysis,” *Bioresources and Bioprocessing*, vol. 1, no. 1, pp. 1–3, 2014.
- [22] X. Jiang, D. Sun, G. Zhang et al., “Investigation of active biomolecules involved in the nucleation and growth of gold nanoparticles by *Artocarpus heterophyllus* Lam leaf extract,” *Journal of Nanoparticle Research*, vol. 15, no. 6, pp. 1741–1751, 2013.
- [23] S. Sulochana, P. Krishnamoorthy, and K. Sivaranjani, “Synthesis of silver nanoparticles using leaf extract of *Andrographis paniculata*,” *Journal of Pharmacology and Toxicology*, vol. 7, no. 5, pp. 251–258, 2012.
- [24] R. Geethalakshmi and D. V. L. Sarada, “Synthesis of plant-mediated silver nanoparticles using *Trianthemadecandra* extract and evaluation of their anti microbialactivities,” *International Journal of Engineering Science and Technology*, vol. 2, no. 5, pp. 970–975, 2010.
- [25] C. Pandit, A. Roy, S. Ghotekar et al., “Biological agents for synthesis of nanoparticles and their applications,” *Journal of King Saud University-Science*, vol. 34, no. 3, article 101869, 2022.
- [26] D. Raghunandan, B. Ravishankar, G. Sharanbasava et al., “Anti-cancer studies of noble metal nanoparticles synthesized using different plant extracts,” *Cancer Nanotechnology*, vol. 2, no. 1-6, pp. 57–65, 2011.
- [27] B. Ankamwar, C. Damle, A. Ahmad, M. Sastry, and J. Nanosci, “Biosynthesis of gold and silver nanoparticles using *Emblica officinalis* fruit extract, their phase transfer and transmetallation in an organic solution,” *Journal of Nanoscience and Nanotechnology*, vol. 5, no. 10, pp. 1665–1671, 2005.
- [28] J. Kasthuri, K. Kathiravan, and N. Rajendran, “Phyllanthin-assisted biosynthesis of silver and gold nanoparticles: a novel biological approach,” *Journal of Nanoparticle Research*, vol. 11, no. 5, pp. 1075–1085, 2009.
- [29] P. Jeyanthi, K. M. Merin, S. Anushree, N. Ashwini, and C. Ramalingam, “Green synthesis of silver nanoparticles from *Dracaena mahatma* leaf extract and its antimicrobial activity,” *Journal of Pharmaceutical Sciences and Research*, vol. 7, no. 9, pp. 690–695, 2015.
- [30] E. Tugçe, F. Y. Fethiye, K. Bijen, and O. Mine, “Green synthesis of silver nanoparticles using *Arbutus andrachne* leaf extract and its antimicrobial activity,” *Tropical Journal of Pharmaceutical Research*, vol. 15, no. 6, pp. 1129–1136, 2016.
- [31] H. Chopra, S. Bibi, A. K. Mishra et al., “Nanomaterials: a promising therapeutic approach for cardiovascular diseases,” *Journal of Nanomaterials*, vol. 2022, Article ID 4155729, 25 pages, 2022.
- [32] Y. Rout, S. Behera, A. K. Ojha, and P. L. Nayak, “Green synthesis of silver nanoparticles using *Ocimum sanctum* (Tulashi) and study of their antibacterial and antifungal activities,” *Journal of Microbiology and Antimicrobials*, vol. 4, no. 6, pp. 103–109, 2012.

Research Article

Green Synthesized Calcium Oxide Nanoparticles (CaO NPs) Using Leaves Aqueous Extract of *Moringa oleifera* and Evaluation of Their Antibacterial Activities

Vikram Jadhav ^{1,2}, Arun Bhagare ¹, Shadma Wahab ³, Dnyaneshwar Lokhande ⁴, Chandraprabha Vaidya,⁵ Akshay Dhayagude ¹, Mohammad Khalid,⁶ Jayraj Aher ⁴, Amine Mezni,⁷ and Mycal Dutta ⁸

¹Department of Chemistry, M.V.P. Samaj's K.K. Wagh Arts, Science, And Commerce College, Pimpalgaon (B.), Nashik, 422 209 Maharashtra, India

²Post Graduate Department of Chemistry, K.R.T. Arts, B.H. Commerce, And A.M. Science College, Nashik, 422002 Maharashtra, India

³Department of Pharmacognosy, College of Pharmacy, King Khalid University, Abha 61421, Saudi Arabia

⁴Department of Chemistry, M.V.P. Samaj's K.P.G. Arts, Science, And Commerce College, Igatpuri, Nashik, 422 403 Maharashtra, India

⁵Biochemistry Division, Department of Chemistry, Savitribai Phule Pune University, Ganeshkhind Road, India

⁶Department of Pharmacognosy, College of Pharmacy, Prince Sattam Bin Abdulaziz University, P.O. Box 173, Al-Kharj 11942, Saudi Arabia

⁷Department of Chemistry, College of Science, Taif University, P.O. Box 11099, Taif 21944, Saudi Arabia

⁸Department of Pharmacy, BGC Trust University Bangladesh, Chittagong 4381, Bangladesh

Correspondence should be addressed to Jayraj Aher; js_aher@rediffmail.com and Mycal Dutta; mycal@bgctub.ac.bd

Received 10 May 2022; Revised 18 May 2022; Accepted 21 May 2022; Published 24 June 2022

Academic Editor: Arpita Roy

Copyright © 2022 Vikram Jadhav et al. This is an open access article distributed under the Creative Commons Attribution License, which permits unrestricted use, distribution, and reproduction in any medium, provided the original work is properly cited.

Calcium oxide nanoparticles (CaO NPs) have unique catalytic and biological properties; their activities are highly influenced by their morphology; as a result, these characteristics are most needed for various applications in several fields, including material science, environmental science, and medicinal science. The primary motivation for synthesizing CaO NPs using a biological method is to suppress the usage of hazardous chemicals used in making its process, which will be more cost-effective and ecologically profitable. However, due to the complexity of the biological extracts employed in chemical processes, large-scale manufacturing of nanoparticles via the green synthesis approach remains a significant problem. As a result, the production of CaO NPs utilizing *Moringa oleifera* plant leaves aqueous extract as an alternative biological agent for capping, stabilizing, and reducing agents due to rich phytochemical parameters in synthesis was investigated in this study. The structural characterization of the CaO NPs obtained by using UV-Vis, FTIR, XRD, and SEM-EDS indicates the presence of purity and primarily aggregated spherical nanosized material with an average size of 32.08 nm observed. The XRD study revealed that heat annealing increased the size of the crystallites, favoring monocrystalline. Finally, these findings, together with the cheap cost of synthesizing the plant-mediated CaO NPs produced, show good antimicrobial (gram-positive) activities.

1. Introduction

Technology must be miniaturized to nanoscale size materials to function in the twentieth century. Nanostructures are a

scientific discipline that involves manipulating materials on a nanoscale level. Nanomaterials act like atoms because they have a larger surface area, enormous surface potential, and unique surface properties [1]. These nanosized materials



FIGURE 1: *Moringa oleifera* plant.

exhibit high surface by volume ratios compared to bulk materials. The physical characteristics of larger particles are stable, have less surface volume ratio, and limit their applicability in many disciplines. Because of their size, shape, and morphology, bulk materials exhibit improved and unique characteristics when manipulated at the nanoscale level [2]. As an individual, they are helpful in various disciplines, including material science [3], photochemistry, medicine [4], and solar energy [5]. Calcium oxide (CaO) finds wide use in cosmetics, medicine, waste remediation, destructive adsorbent, and catalyst [1]. Chemical precipitation, hydrothermal, microemulsion, sol-gel, gas phase, microwave synthesis, and electrochemical methods have been described for CaO NPs synthesized and for other nanomaterials such as NiO, FeO, ZnO, Ag, and Au. Green method is significant for cost-effective, harmless, and eco-friendly than any other methods like chemical and physical [6, 7]. According to the literature, some of the phytoremediation notions found in the plant extract may be related to nanomaterial production's chemical mechanism [8, 9]. Metal/metal oxide nanoparticles (NPs) are considered the best way for future generations to use everywhere within clinical care, consumer items, and other industrial applications [6, 10]. The adsorption of CO₂, biomedical applications, gas sensing, and photocatalytic activity of CaO NPs have also gotten much attention [11].

Moringa oleifera plant, as shown in Figure 1, is a drumstick evergreen or deciduous tree of a single genus in the *Moringaceae* family; because of its numerous nutritional, medicinal, and industrial benefits [12, 13], it is regarded as a "wonder tree." It is a tiny, fast-growing ornamental tree found throughout Africa and Asia's tropical areas. It is primarily appreciated for its edible parts as fruits, leaves oil, leaves, and flowers, and it is widely utilized in traditional medicine [14]. According to a literature survey, the leaves have a high nutritional content, including vitamins, minerals, and amino acids used as an alternate source for dietary supplements [15] and growth boosters [16, 17]. Because of their high coagulation properties, the *M. oleifera* seeds pow-

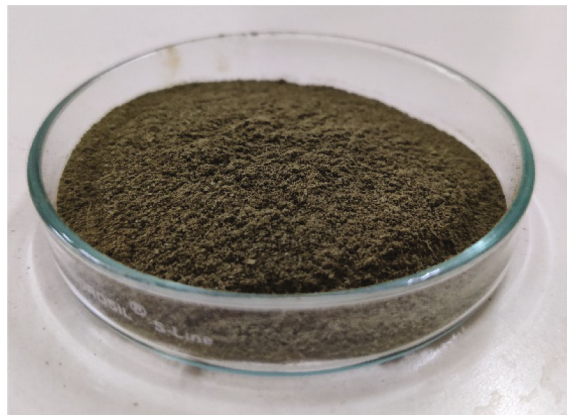
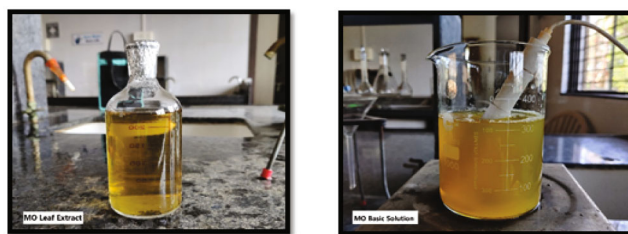
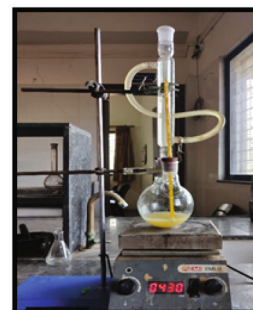


FIGURE 2: *Moringa oleifera* leaf powder.



(a)



(b)

FIGURE 3: (a) *Moringa oleifera* leaves powder extract and its basic solution. (b) Yellow-colored precipitate of MO-CaO NPs.

der has traditionally been used for purification of water in many rural regions [18]; in coagulation studies, a slight reduction in the total bacterial count of the filtered water was found, with antibacterial and antioxidant effects, indicating that the seeds may contain antibiotic compounds [19]. *Moringa* is said to offer a variety of therapeutic properties [12, 14]. Thus, the *M. oleifera* tree parts are used in traditional medicine to cure diarrhea, hypertension, and folk medicines. As a result, herbal plants used in medicine, also known as phytomedicine, are still reliable [12]. Plant components function as cardiac stimulants and anticancer [20], antilucer, antipyretic, and anti-inflammatory [15]. The *M. oleifera* Plant also has anticancer, antimicrobial, antidiabetic, antibiotic, antihypertensive, antioxidant, hepatoprotective, and cholesterol-lowering effects [14, 21, 22].

Due to the more effective and environmentally friendly approach to the biosynthesis of CaO NPs, the utilization of

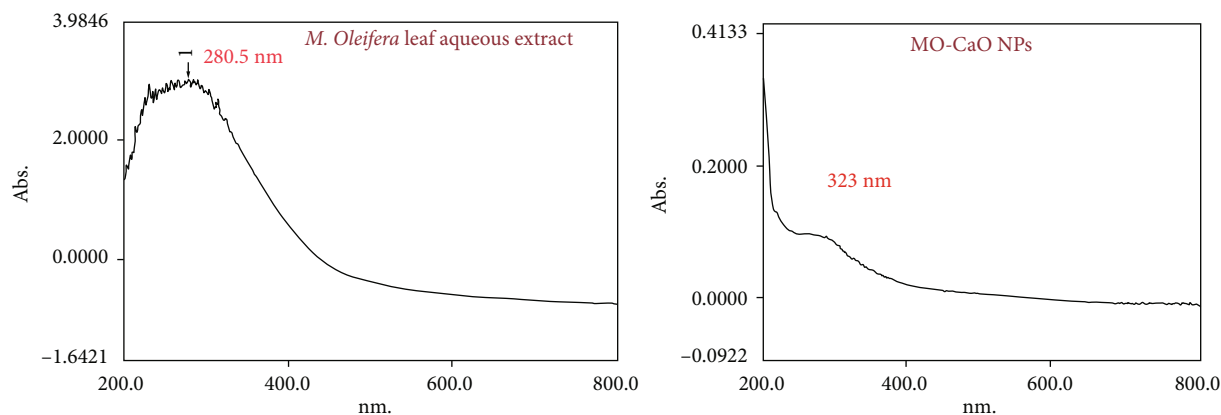
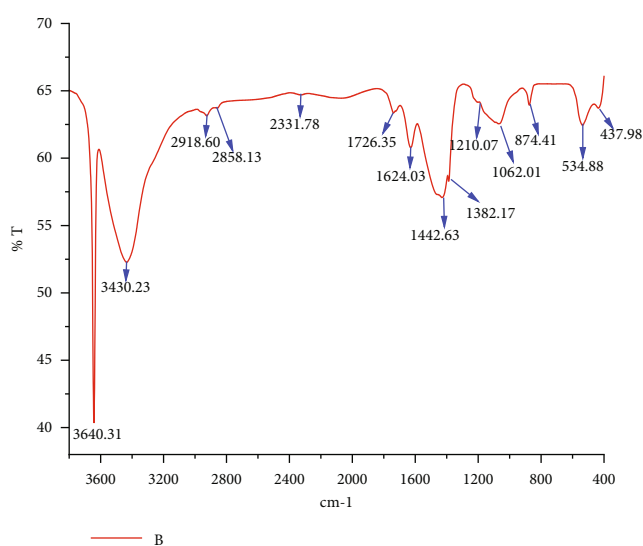
FIGURE 4: UV spectra of *M. oleifera* leaf aqueous extract and MO-CaO NPs.

FIGURE 5: FTIR spectrum of MO-CaO NPs.

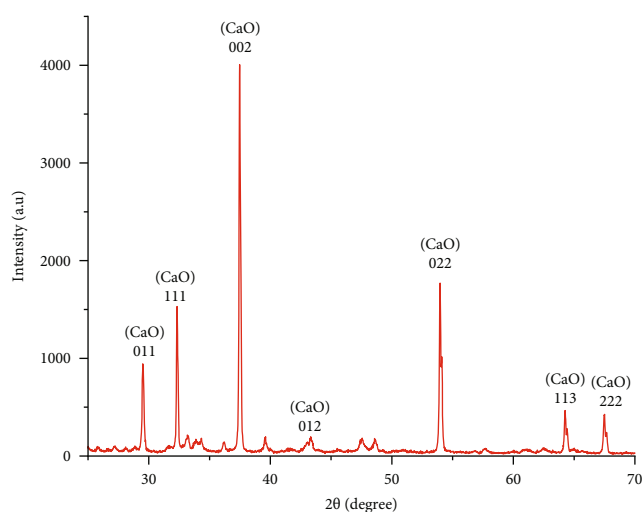


FIGURE 6: XRD pattern of MO-CaO NPs.

TABLE 1: XRD data.

No.	2θ	Θ	d-Spacing (Å°)	Intensity (a.u)	(hkl)
1	29.596	14.798	3.015	921.858	011
2	32.216	16.108	2.775	1302.459	111
3	37.348	18.674	2.405	3171.038	002
4	42.812	21.406	2.109	436.0656	012
5	53.829	26.914	1.701	1424.864	022
6	64.091	32.045	1.451	432.2400	113
7	67.335	33.667	1.388	416.9390	222

plant leaves aqueous extracts will be a worthy scientific challenge [4, 23, 24]. It is long been recognized that phytochemicals present in a plant material can function as a biological reduction on metal and metal oxide production [25, 26], with flavonoid compounds being one of the most influential families of secondary metabolites in plant tissues for metal ion reduction [27]. Depending on the kind of plant, most flavonoid compounds include ascorbic acid, phenolics, and carotenoids [16, 22]. "*M. oleifera* leaf has been reported to

be a rich source of beta-carotene, protein, vitamin C, carotenoids, polyphenols, phenolic acids, flavonoids, alkaloids, glucosinolates, isothiocyanates, tannins, saponins, calcium, and potassium, as well as a good source of natural antioxidants, and thus improve the shelf life of fat-containing foods due to various antioxidant compounds such as ascorbic acid, flavonoids, phenolics, and carotenoids" [12, 28]. In recent research, *Moringa* leaf powder aqueous extracts have been used to make nanoparticles [16]. This is the first time a shrub has been used for green nanoparticle deposition. We perform work for the biosynthesis of CaO nanoparticles with the employment of *Moringa oleifera* leaves aqueous extract secondary metabolite compounds and its study regarding antibacterial activity because there is still a lack of scientific reports on using the extract of *Moringa oleifera* (MO) leaves as a biologically reductive and capping agent on the biosynthesis of MO-CaO nanoparticles [16]. Furthermore, the antibacterial activity outline of nanomaterial was investigated in contrast to bacterial fears, with the final result revealing that Gram-positive (G+) bacteria (*Escherichia coli*) are more vulnerable than Gram-negative (G-) bacteria at various concentrations.

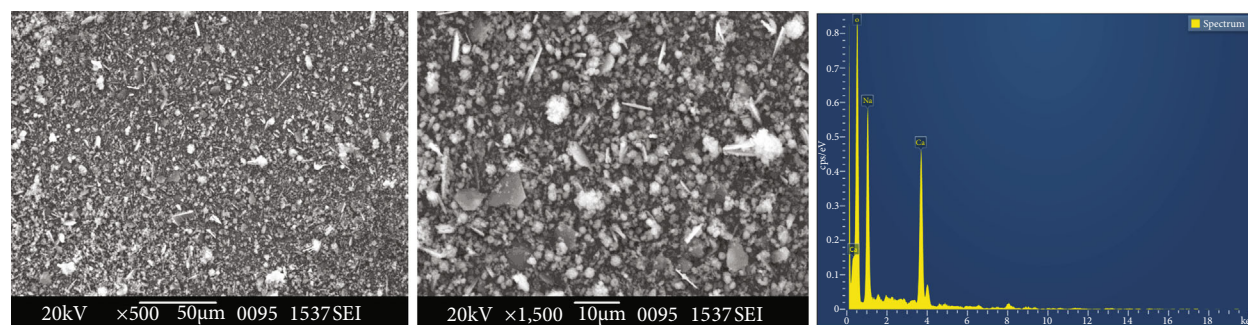


FIGURE 7: SEM images and EDS of MO-CaO NPs.

TABLE 2: Ca and O elements composition in the synthesized CaO nanoparticles.

Element	Line type	Wt%	Atomic %
O	K series	59.81	72.22
Na	K series	23.45	19.71
Ca	K series	16.74	8.07
Total:		100	100

2. Materials and Methods

2.1. Materials. Analytical grades with 98% of purity of calcium nitrate $\text{Ca}(\text{NO}_3)_2 \cdot 6\text{H}_2\text{O}$ and sodium hydroxide (NaOH) and deionized water grade-I (Extra pure) Charco Chemicals. *M. oleifera* leaves are collected through the local farm in Nashik, Pimpalgaon (B), Maharashtra, India.

2.2. Preparation of Moringa oleifera Plant Leaves Powder. Fresh mature *Moringa* leaves were collected during the daytime from the local farm, removed the leaves and discarded the stems and stalks, and then thoroughly were washed with distilled water and followed with deionized water to remove the various impurities such as mud, dust particles, and unwanted material. The MO leaves were allowed to dry in the oven at 80°C for 2 hrs after drying and made powder using mortar and pestle, and leaves powder, as shown in Figure 2, was taken for MO-CaO NPs synthesis purposes.

2.3. Synthesis of Calcium Oxide Nanoparticles Using *M. oleifera* Leaves (MO-CaO NPs). The 2 g MO leaves powder was boiled in deionized water for 25 min at 60°C . A light brown colored solution in Figure 3 was formed during the boiling and cooled at room temperature (RT). After that, the brown-colored aqueous extract was filtered (Whatman No. 1), and the filtrate (stock solution) was stored in the refrigerator (2°C to 4°C) for further work. 20 mL MO plant aqueous extract was boiled at 50°C to 60°C using a magnetic stirrer. The temperature of the solution was reached at 50°C to 60°C ; 2 g of calcium nitrate ($\text{Ca}(\text{NO}_3)_2 \cdot \text{H}_2\text{O}$) was added to maintain the basic nature of the aqueous extract solution by using a few drops of sodium hydroxide (2 M NaOH) solution [29] as shown in Figure 3(a). Then the mixture was boiled until it became a yellow-colored paste (Figure 3(b)) and filtered through filter paper, and the precipitate was transferred to a crucible and heated in a muffle furnace up

to 400°C for 3 hrs to obtain the white powder; it is the MO-CaO NPs which were identified by the characterizations and used for various applications.

3. Results and Discussion

3.1. UV-Vis Absorption Spectroscopy Analysis. The absorption spectra of *M. oleifera* leaf aqueous extract and MO-CaO NPs with an absorption peak of about 280.5 nm and 323 nm, respectively, are shown in Figure 4. The leaf extracts bump at 250 nm to 300 nm; it could be the presence of polyphenolic bioactive compounds responsible for reducing calcium ions to CaO NPs [30]. The UV-Vis spectra of MO-CaO were taken in the solid-state, with the substantial excitation binding energy at 25°C ; MO-CaO NPs show exciton absorption at 323 nm. Demonstrating UV-Vis of MO-CaO NPs, it can be seen that the nanomaterial has a good absorption capacity in the visible region [11].

3.1.1. Vibrational Properties. The aqueous extract of MO contains a lot of phytochemicals such as alkaloids, glycosides, phenols, tannins, saponins, glucosinolate, and flavonoids. These major bioactive components will act as capping and stabilizing agents and can be reduced from calcium metal salt (Ca^{2+}) precursors to CaO NPs. To further affirm the formation of the CaO NPs crystal structure, FT-IR spectroscopy is shown in Figure 5. The strong IR band located at 534 cm^{-1} attributed to fundamental vibrations of CaO, confirming the formation of CaO NPs. The broad peak observed at 1062 cm^{-1} corresponds to the C-O stretching frequency of phytochemicals in the *Moringa oleifera* aqueous leaves extract. The peaks around 1382 cm^{-1} correspond to the O-H bend of flavonoids and polyphenols, confirming the presence of an aromatic group. The absorption peak appearing around 1442 and 3430 cm^{-1} could be correlated to adsorbed water's bending and stretching vibrations bands and the residual -OH group. The bioactive/biomolecules in leaf extract of *Moringa oleifera* are responsible for the capping, reducing, and stabilizing CaO NPs. To identify the nature of the MO extract, which was responsible for the reduction of calcium ions to form the CaO NPs, the aqueous extract of MO were investigated [30]; the major bioactive compounds, as shown in Scheme 1 in *Moringa oleifera* leaf aqueous extract, may be responsible for capping and reducing the nature of the CaO NPs [30].

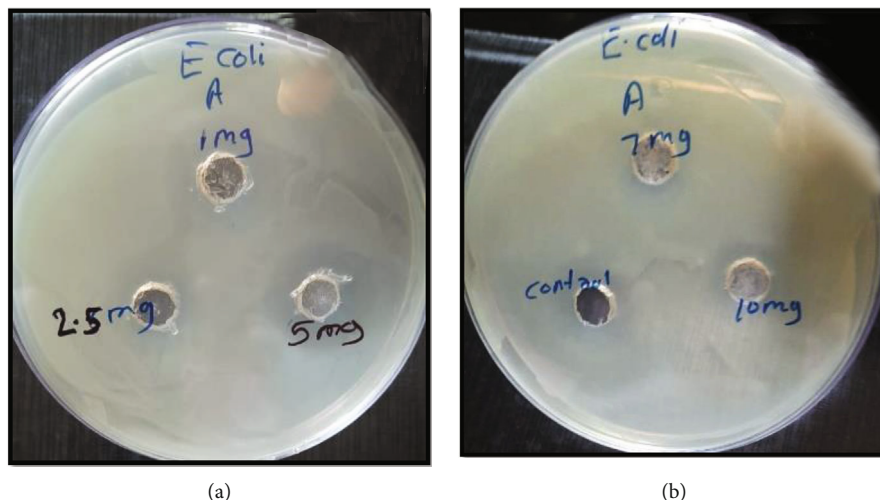


FIGURE 8: The antibacterial activity of plant-mediated CaO NPs (a) and (b) *Escherichia coli* at various concentrations.

3.2. FT-IR Analysis. For the MO-CaO NPs and *M. oleifera* leaf aqueous extract, IR measurements were performed at room temperature using the KBr technique in the wavenumber range (400 to 4000 cm^{-1}). The CaO bond bending vibration appears as a peak in the low energy area at 437.98 cm^{-1} . Ca-oxygen is responsible for the zone between (400 and 600) cm^{-1} . The stretching vibration of the -OH group is responsible for the prominent peak in the higher energy area at 3600–3450 cm^{-1} . At roughly 2933–2915 cm^{-1} , the -CH stretching vibration band appears, indicating the existence of an alkanes group. The amide I and amide III sections of proteins/enzymes are responsible for the peaks around 1620–1655 and 1150–1390 cm^{-1} . The presence of functional groups of alcohols, and a carboxylic acid, may be seen in the influential bands detected at 1120–1065 cm^{-1} C–O stretching vibration. The absorption bands at 3430, 2918, 1624, 1442, and 1062 cm^{-1} in the FT-IR spectra indicate the structure of *M. oleifera* in which high phytochemicals parameters caused these peaks, as shown in Figure 5. As a result, water-soluble phenolic acid and flavonoid components are essential in the bioreduction process. The interactions between reducing phenolic acids such as ascorbic, cardiac glycoside, gallic acid, and calcium ions can lead to MO-CaO NPs. The mechanism of CaO NPs stabilization by *M. oleifera* leaf extract ascorbic acids and green production of CaO NPs might entail the reduction of calcium nitrate ions, which can form intermediate complexes with phenolic -OH groups found in hydrolyzable tannins, which are then oxidized to quinone forms, resulting in calcium reduction to CaO NPs. However, the process is yet unknown and has to be investigated further.

3.3. X-Ray Diffraction Microscopy (XRD). The XRD patterns show perceptible peaks of CaO NPs at 29.59°, 32.22°, 37.35°, 42.81°, 53.83°, 64.09°, and 67.34°, corresponding to (011), (111), (002), (012), (022), (113), and (222) planes of cubic system CaO NPs as shown in Table 1. The plane values of XRD patterns agree with CaO (lime, syn, JCPDS card No. 00-004-0777) with cubic crystal system and lattice parameters ($a = 4.8152 \text{ \AA}$). All recorded peak intensities were char-

acteristics of the cubic structure; the relatively high intensity of the (002) peak indicates anisotropic growth and implies a preferred orientation of the crystallites, as shown in Figure 6. The stiff and narrow diffraction peaks suggest that the product is excellent crystalline. There is no shift in the diffraction peaks, and other crystalline impurities are not observable.

3.3.1. Calculation of d-Spacing between Calcium Oxide Nanoparticles. It can be calculated by using Bragg's equation:

$$n\lambda = 2d \sin \theta \quad (1)$$

where $\lambda = 1.54 \text{ \AA}$ wavelength of X-rays, n is the order of diffraction ($n = 1$), d is the distance between adjacent CaO layers, and θ is the diffraction angle.

d-Spacing is calculated by using above equation:

$$d = \frac{n\lambda}{2x \sin \theta} \quad (2)$$

Crystal planes for the cubic system:

$$d_{hkl} = \frac{a}{\sqrt{h^2 + k^2 + l^2}} \quad (3)$$

$$a = b = c = 4.8152 \text{ \AA}$$

According to the Scherrer equation,

$$D = \frac{K\lambda}{\beta \cos \theta} \quad (D \leq 200 \text{ nm}) \quad (4)$$

where D is the average crystallite size/diameter (particle size); K is the Scherrer constant, 0.68 to 2.08, 0.94 for spherical crystallites with cubic symmetry; $\beta = \beta' \pi / 180$, broadening at FWHM in radians; β' is the full width at half maximum; λ is the X-rays wavelength ($\text{CuK}\alpha = 1.5408 \text{ \AA}$); and θ is the Glancing angle in degrees half of 2θ .

Using the above Scherrer equation, the mean or average particle size of the plant-mediated CaO NPs is 32.08 nm.

TABLE 3: Concentration dependence of the antibacterial activity of MO-CaO NPs against *Escherichia coli* and *Staphylococcus aureus* (ND: not detected).

Compound	Concentration	Gram (+)	Gram (-) bacteria
		<i>Escherichia coli</i>	<i>Staphylococcus aureus</i>
MO-CaO NPs	1.0 mg/ml	19 mm	ND
	2.5 mg/ml	20 mm	ND
	5.0 mg/ml	22 mm	ND
	7.5 mg/ml	23 mm	9 mm
	10.0 mg/ml	24 mm	11 mm

3.4. Scanning Electron Microscopy and Energy Dispersive X-Ray Analysis (SEM-EDS). The sample's SEM studies in Figure 7 show the synthesized MO-CaO NPs. The images depicted both individual CaO NPs and the number of aggregates. The picture shows that the particles are round, granular, and nanosized. The size and form of the MO-CaO NPs are visible in the SEM images. NPs were spherical with a group of aggregated particles; according to XRD analysis, the average particle sizes are within 30–40 nm, as shown in Figure 6. To confirm the purity of the MO-CaO, the energy dispersive X-ray analysis was done. EDS spectrum clearly shows that the synthesized material is highly pure, which shows peaks due to Ca, O, and Na elements as shown in Figure 7 and Table 2, and the presence of Na may be due to the basic solution of MO plant leaves aqueous extract. The FTIR analysis shows that Ca and O atoms produce weak and strong bonding peaks due to macromolecules such as alcoholic or phenolic compounds; weak peaks are detected from the elements S, K, C, Na, Ca, and O [5].

3.4.1. Antibacterial Activity. According to the minimal inhibitory concentration (MIC) method, *Escherichia coli* and *Staphylococcus aureus* were used as microorganisms in this study. Stock solutions of synthesized compounds were prepared in DMSO. Cultures were incubated in nutrient broth for 24 hrs at 37°C at 160 rpm. The turbidity of bacterial suspension was adjusted at a concentration of approximately 10⁶ cells/ml. The microorganisms grown were spread on the nutrient agar medium plate, and then a well was prepared with the help of a good borer. Then 100 µl of a synthesized compound of various concentrations was added to each well, as shown in Figure 8. After that, all plates were incubated at 37°C for 24 hrs in the incubator. The minimum inhibitor concentration was taken as the MIC value, at which no growth was observed.

4. Conclusion

Leaf powder extracts of the *Moringa oleifera* plant act as capping and reducing agents due to phytochemical parameters used to make CaO nanoparticles for this study. Still, the reaction mechanism and specific bioactive groups are unknown and must be investigated further. The use of nanoparticles made from leaf extracts is a promising alternative to the more conservative chemical method. Ultraviolet visible

(UV-Vis), Fourier transform infrared resonance (FTIR), X-ray diffraction (XRD), and scanning electron microscopy-energy dispersive X-ray analysis (SEM-EDS) were used to examine the plant-mediated CaO NPs. Furthermore, using the minimal inhibitory concentration (MIC) method approach, this work investigated the antibacterial activities of the produced CaO nanoparticles in contrast to scientific and traditional concerns. Finally, CaO nanoparticles synthesized from *M. oleifera* leaf powder aqueous extract exhibited promising results in Gram-positive bacterial strains, as shown in Table 3 with severe inhibition areas of 19 mm, 20 mm, 22 mm, 23 mm, and 24 mm at various concentrations when employing a consistent quantity of CaO NPs.

Data Availability

All data used to support the findings of this study are included within the article.

Conflicts of Interest

The authors declare that they have no conflict of interest.

Acknowledgments

The authors extend their appreciation to the Deanship of Scientific Research at King Khalid University for funding this work through Large Groups Project under grant number RGP.2/58/43 and Taif University Researchers Supporting Project number TURSP-2020/28, Taif University, Taif, Saudi Arabia.

References

- [1] A. Roy, V. Singh, S. Sharma et al., "Antibacterial and dye degradation activity of green synthesized iron nanoparticles," *Journal of Nanomaterials*, vol. 2022, 6 pages, 2022.
- [2] S. Kaur and A. Roy, "Bioremediation of heavy metals from wastewater using nanomaterials," *Environment, Development and Sustainability*, vol. 23, no. 7, pp. 9617–9640, 2021.
- [3] A. Roy, "Biofertilizers for Agricultural Sustainability: Current Status and Future Challenges," in *In Current Trends in Microbial Biotechnology for Sustainable Agriculture*, pp. 525–553, Springer, Singapore, 2021.
- [4] A. Roy, A. Elzaki, V. Tirth et al., "Biological synthesis of nanocatalysts and their applications," *Catalysts*, vol. 11, no. 12, p. 1494, 2021.
- [5] S. Pal, S. Mondal, J. Maity, and R. Mukherjee, "Synthesis and characterization of ZnO nanoparticles using *Moringa oleifera* leaf extract: investigation of photocatalytic and antibacterial activity," *International Journal of Nanoscience and Nanotechnology*, vol. 14, no. 2, pp. 111–119, 2018.
- [6] A. Roy, A. Sharma, S. Yadav, L. T. Jule, and R. Krishnaraj, "Nanomaterials for remediation of environmental pollutants," *Bioinorganic Chemistry and Applications*, vol. 2021, 16 pages, 2021.
- [7] A. Kamboj, M. Amjad, W. Ahmad, and A. Singh, "A general survey on green synthesis and application of calcium oxide nanoparticles," *Int. J. Health Clin. Res.*, vol. 3, pp. 41–48, 2020.
- [8] N. Narayan, A. Meiyazhagan, and R. Vajtai, "Metal nanoparticles as green catalysts," *Materials*, vol. 12, no. 21, p. 3602, 2019.

- [9] C. Pandit, A. Roy, S. Ghotekar et al., "Biological agents for synthesis of nanoparticles and their applications," *Journal of King Saud University-Science*, vol. 34, no. 3, article 101869, 2022.
- [10] V. L. Gurav, R. A. Samant, S. B. Manjare, U. K. Patil, S. R. Solkar, and S. S. Moghe, "Biosynthesis of calcium oxide nanoparticles using *Ocimum sanctum* (Tulsi) leaf extracts and screening its antimicrobial activity," *Asian Journal of Nanosciences and Materials*, vol. 3, no. 2, pp. 115–120, 2020.
- [11] T. H. Moghaddas, S. Sadat, S. S. Moosavi, and R. K. Oskuee, "Green synthesis of calcium oxide nanoparticles in *Linum usitatissimum* extract and investigation of their photocatalytic and cytotoxicity effects," *Biomass Conversion and Biorefinery*, pp. 1–10, 2022.
- [12] A. K. Dhakad, M. Ikram, S. Sharma, S. Khan, V. V. Pandey, and A. Singh, "Biological, nutritional, and therapeutic significance of *Moringa oleifera* Lam.," *Phytotherapy Research*, vol. 33, no. 11, pp. 2870–2903, 2019.
- [13] B. K. Sujatha and P. Patel, "Moringa oleifera–nature's gold," *Imperial Journal of Interdisciplinary Research*, vol. 3, no. 5, pp. 1175–1179, 2017.
- [14] H. M. Ahmed, A. Roy, M. Wahab et al., "Applications of nanomaterials in agrifood and pharmaceutical industry," *Journal of Nanomaterials*, vol. 2021, 10 pages, 2021.
- [15] D. Meireles, J. Gomes, L. Lopes, M. Hinzmann, and J. Machado, "A review of properties, nutritional and pharmaceutical applications of *Moringa oleifera*: integrative approach on conventional and traditional Asian medicine," *Advances in Traditional Medicine*, vol. 20, no. 4, pp. 495–515, 2020.
- [16] V. Jadhav, A. Bhagare, I. H. Ali et al., "Role of *Moringa oleifera* on green synthesis of metal/metal oxide nanomaterials," *Journal of Nanomaterials*, vol. 2022, 10 pages, 2022.
- [17] B. Moyo, P. J. Masika, A. Hugo, and V. Muchenje, "Nutritional characterization of *Moringa* (*Moringa oleifera* Lam.) leaves," *African Journal of Biotechnology*, vol. 10, no. 60, pp. 12925–12933, 2011.
- [18] A. Ndagengesere, K. S. Narasiah, and B. G. Talbot, "Active agents and mechanism of coagulation of turbid waters using *Moringa oleifera*," *Water Research*, vol. 29, no. 2, pp. 703–710, 1995.
- [19] N. Matinise, X. G. Fuku, K. Kaviyarasu, N. Mayedwa, and M. J. A. S. S. Maaza, "ZnO nanoparticles via *Moringa oleifera* green synthesis: physical properties & mechanism of formation," *Applied Surface Science*, vol. 406, pp. 339–347, 2017.
- [20] A. Roy, N. Jauhari, and N. Bharadvaja, "Medicinal plants as a potential source of chemopreventive agents," in *In Anticancer Plants: Natural Products and Biotechnological Implements*, pp. 109–139, Springer, Singapore, 2018.
- [21] A. A. Ezhilarasi, J. J. Vijaya, K. Kaviyarasu, M. Maaza, A. Ayeshamariam, and L. J. Kennedy, "Green synthesis of NiO nanoparticles using *Moringa oleifera* extract and their biomedical applications: cytotoxicity effect of nanoparticles against HT-29 cancer cells," *Journal of Photochemistry and Photobiology B: Biology*, vol. 164, pp. 352–360, 2016.
- [22] U. Eilert, B. Wolters, and A. Nahrstedt, "The antibiotic principle of seeds of *Moringa oleifera* and *Moringa stenopetala*," *Planta Medica*, vol. 42, no. 5, pp. 55–61, 1981.
- [23] W. Ahmad, A. Kamboj, I. Banerjee, and K. K. Jaiswal, "Pomegranate peels mediated synthesis of calcium oxide (CaO) nanoparticles, characterization, and antimicrobial applications," *Inorganic and Nano-Metal Chemistry*, pp. 1–8, 2022.
- [24] S. Bano and S. Pillai, "Green synthesis of calcium oxide nanoparticles at different calcination temperatures," *World Journal of Science, Technology and Sustainable Development*, vol. 17, no. 3, pp. 283–295, 2020.
- [25] S. G. Nair and V. R. Jadhav, "Biosynthesis of silver nanoparticles and comparing its antifungal property with ethanolic extract of *Ixora coccinea* plant," *Asian Journal of Research in Chemistry*, vol. 13, no. 3, pp. 198–202, 2020.
- [26] P. Nagore, S. Ghotekar, K. Mane, A. Ghoti, M. Bilal, and A. Roy, "Structural properties and antimicrobial activities of polyalthia longifolia leaf extract-mediated CuO nanoparticles," *Bio Nano Science*, vol. 11, no. 2, pp. 579–589, 2021.
- [27] A. Roy, A. Khan, I. Ahmad et al., "Flavonoids a Bioactive Compound from Medicinal Plants and Its Therapeutic Applications," *BioMed Research International*, vol. 2022, Article ID 5445291, pp. 1–9, 2022.
- [28] J. Shindano and C. Kasase, *Moringa (Moringa Oleifera): A Source of Food and Nutrition, Medicine and Industrial Products*, 2010.
- [29] V. R. Jadhav, "Mathematical treatment to understanding the concentration terms," *International Journal of Research & Review*, vol. 6, no. 1, 2019 <https://www.ijrrjournal.com>.
- [30] C. Tiloke, K. Anand, R. M. Gengan, and A. A. Chuturgoon, "*Moringa oleifera* and their phytonanoparticles: potential antiproliferative agents against cancer," *Biomedicine & Pharmacotherapy*, vol. 108, pp. 457–466, 2018.

Research Article

Optimization of Stir Casting Variables for Production of Multiwalled Carbon Nanotubes: AA7149 Composite

Mohamad Reda A. Refaai,¹ Samraj Ravi,² S. Prasath ,³ Maridurai Thirupathy,⁴ Ram Subbiah,⁵ and Abdi Diriba ³

¹Department of Mechanical Engineering, College of Engineering, Prince Sattam Bin Abdulaziz University, Saudi Arabia Alkharj 16273

²Department of Mechanical Engineering, Chennai Institute of Technology, Chennai, Tamil Nadu, India

³Department of Mechanical Engineering, Mizan Tepi University, Ethiopia

⁴Department of Mechanical Engineering, Saveetha School of Engineering, SIMATS, Chennai, Tamil Nadu, India

⁵Department of Mechanical Engineering, Gokaraju Rangaraju Institute of Engineering and Technology, Hyderabad, 500090 Telangana, India

Correspondence should be addressed to Abdi Diriba; abdi@mtu.edu.et

Received 17 February 2022; Accepted 16 April 2022; Published 23 June 2022

Academic Editor: Hiwa M. Ahmed

Copyright © 2022 Mohamad Reda A. Refaai et al. This is an open access article distributed under the Creative Commons Attribution License, which permits unrestricted use, distribution, and reproduction in any medium, provided the original work is properly cited.

Combining liquefied metals with multiwalled carbon nanotube-aluminium alloy 7149 composites enables the creation of intricate designs and mass production was manufactured using mechanical stir casting, thixoforming, and T6 heat treatment. Taguchi with two factorial levels was chosen to investigate the optimum parameter and affect variables such as carbon nanotube concentration, magnesium wettability, and ring mechanical stir duration were used in addition to a robust design of experiments. The response variables were the S/N ratio, hardness, and ultimate tensile strength. The fourth DOE run resulted in an optimised nanocomposite with 107.8 HV hardness and 278.1 MPa tensile strength that contained 0.75 wt.% magnesium and 1% multiwalled carbon nanotube and stirred time of 10 minutes. The as-forged AA7149 alloy had a lower hardness value (76.3%) but a higher ultimate tensile strength value (108.4%). It was demonstrated that combining thixoforming and heat treatment improves the mechanical properties of multiwalled carbon nanotube produced under mechanical stir casting conditions.

1. Introduction

Multiwalled carbon nanotubes have been employed in a number of investigations on composites. Load transmission, strengthening, and thermal expansion strengthening are just a few of the factors that go into making multiwalled carbon nanotubes so strong [1, 2]. The key obstacles in metal matrix composites manufacture are often achieving homogeneous distribution and adequate wetting qualities, as well as interfacial phases between reinforced particles and matrix [3]. Rather than relying on more traditional approaches, the powder metallurgy industry has opted to tackle these problems instead. Processing powder metallurgy, on the other hand, is prohibitively expensive and can only be used for simple, not elaborate,

parts [4, 5]. It is possible to use liquid metallurgy processing, a cheaper option [6], for complex designs and large-scale manufacturing. It is, however, difficult to overcome the large density difference between multiwalled carbon nanotube and aluminium alloy. Composite reinforcement requires consideration of a variety of factors, including the purification and activation of reinforced materials, the mixing of those materials, the amount of wetting agent, and other variables (sintering, extrusion, compaction, thixoforming, and heat treatment).

Taguchi is a great technique for optimising parameters for composite development conferring to [7, 8] have shown that a number of variables, including the quantity of strengthened material, processing temperatures, wettability agents, and stirring method, have an effect on the physical

TABLE 1: Chemical composition of AA 7149 by weight percentage.

Silicon	Copper	Magnesium	Manganese	Zinc	Nickel	Iron	Lead	Titanium	Aluminium
6.5	0.2	0.2	0.3	0.1	0.1	0.5	0.1	0.2	Balance

TABLE 2: Layout of L8 orthogonal array.

Ex. no	Multiwalled carbon nanotubes (wt%)	Magnesium (wt%)	Stirring time (minutes)
1	1.0	0.50	5
2	1.0	0.50	10
3	1.0	0.75	5
4	1.0	0.75	10
5	1.5	0.50	5
6	1.5	0.50	10
7	1.5	0.75	5
8	1.5	0.75	10

and mechanical characteristics of stir cast aluminium alloys. There have been numerous investigations on the mechanical characteristics of metal composites incorporating carbon nanotubes, which have been published [9, 10]. By mixing mechanically in the liquid state with a carbon nanotubes weight fraction ranging from 0.5–1.0 weight %, the hardness of the AA7149 alloy with carbon nanotubes was enhanced to 2.5 wt.%. Though the rise in compressive strength was drastically reduced in the alloy having additional than 1.0 wt% carbon nanotubes [11–13]. Addition of 4.5% carbon nanotubes to pure aluminium powder in solid-state mixing by ball milling resulted in rise in the composite’s hardness and tensile strength, respectively, from 60 HV and 123 MPa to 130 HV and 420 MPa.

With 6.0 wt% carbon nanotubes [14, 15] achieved the highest hardness of 140 HV, however, the value declined as the amount of carbon nanotubes. Two phases of rolling and melting were performed on an AA7149 alloy containing 0.5 weight % carbon nanotubes by [16]. It was shown that when carbon nanotube content was increased to more than 2% by volume, accumulation and flexible flow in the metal matrix decreased the composite’s hardness [17]. Wettability between carbon nanotubes and metal matrix was the focus of this study in order to achieve an effective interfacial area and load transmission. Surface tensions among dissimilar materials include carbon nanotubes (100–200 mN/m) and liquid aluminium (865 mN/m) and may be wetted and broken with relative ease. An indicator of this is wettability, which is the ability to soak up water [18]. Coatings, ceramic treatment, and alloying elements can all be utilised to enhance the wettability of a material, according to [19, 20]. To increase the wettability of the AMC using strengthened materials, Mg is one of the most commonly employed materials [21], for example, increased melt wettability by adding 0.75 weight % Mg. For both carbon nanotubes and other reinforcing materials, the effects of stirring have been extensively studied.

At 500 revolutions per minute, [22] mixed SiC in a pure aluminium matrix in their study. The interfacial reaction

was made stronger and more resistant to cracking thanks to the stirring process. To ensure an even dispersion of Al₂O₃ in the AA7149 matrix alloy, [23, 24] used stirring times of 10 and 15 minutes, respectively. Induction stir casting for multiwalled carbon nanotubes and pure Al composites improved hardness and ultimate tensile strength by 45% and 52%, respectively, according to [25, 26]. Making a multiwalled carbon nanotube, aluminium alloy is therefore viable and has drawn substantial interest from the MMC community. Mechanical stirring, wetting agent, and an optimised multiwalled carbon nanotube concentration have all been tested, but their effects on the composite are still unknown. Multiwalled carbon nanotube and AA7149 aluminium alloy were synthesised utilising mechanical stir casting, thixoforming, and T6 heat treatment in this study [27]. There were two factorial levels of Taguchi technique employed to optimise 3 variables, like carbon nanotubes, magnesium, and mechanical stirring duration, while all other components remained fixed. When it comes to mechanical qualities like as hardness and the ultimate tensile strength, bigger S/N values were shown to be more advantageous. On the other hand, we also talked about how the microstructures have evolved. These factors and their impact on a multiwalled carbon nanotube-strengthened alloy matrix composites were shown in detail in this study.

2. Experimental Procedures

Mechanical stir casting was used to fabricate multiwalled carbon nanotube/AA7149 alloy composites in this investigation. Table 1 shows the chemical composition of AA 7149 by weight percentage. The experiment also made use of the dependable Taguchi method and the Minitab software. AA7149 aluminium alloy and multiwalled carbon nanotube of industrial quality (Sigma-Aldrich, purity > 88 %; outside 20–40 nanometer, within 5 to 10 nanometer, with an overall length of 10–30 nanometers) were utilised as the AMC and the strengthened particles, correspondingly. A wettability ingredient was added to the mixture in the form of preweighed 1 mm magnesium pellets as it increases solid solution strengthening and adds strength to composites. Mechanical stirring time and multiwalled carbon nanotube/Mg weight percentage were both studied to see what effect they had on the results. There were two response functions: Vickers hardness (HV) and ultimate tensile strength. Taguchi balanced orthogonal arrays focus on ensuring all stages of all factors are considered fairly. At random, eight tests with two levels of primary factors and the Taguchi method L8 orthogonal array were conducted as in Table 2.

Analysis of response S/N ratios (bigger is better) was used to determine the degree of variation in the data. Table 2 shows the percentages of multiwalled carbon

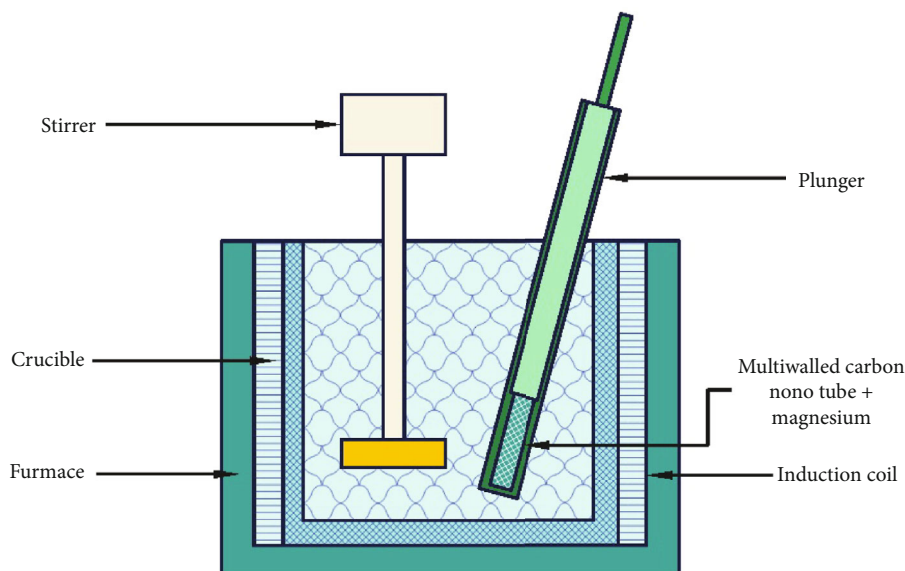


FIGURE 1: Mixing process schematic diagram.

TABLE 3: Parameters of T6 heat treatment.

Quenching	Treatment solution	Artificial ageing
27°C at room temperature	540°C for 1 hour	180°C for 2 hour

nanotube, and Mg used to make the composites, which were then wrapped in aluminium foil. The alloy was molten in an induction furnace at a temperature of 650 degrees celsius after being melted at temperatures as high as 700 degrees celsius (400 was completely consumed). It was wrapped in foil, placed in the crucible, and mechanically churned at 200 revolutions per minute using a three-blade propeller for specific periods of time (Table 2). To create new metal alloys in the semisolid state, thixoforming is a novel process. Thixoforming techniques rely on customised casting process. The thixo feedstock billet was formed by immediately pouring the mixed composite into a mould. Use of T30-80 KHz thixoforming machine was used as in Figure 1. It was heated to 580°C (semisolid temperature) with the aid of pneumatic ram and then smashed into hot work tool steel mould with a forging load of 5 tonnes at a speed of 1 m/s inside induction coils. After being removed from the mould, the billet was allowed to cool to ambient temperature.

The MT6 heat treatment process was sped up. The samples were heated to 540°C and cooled to room temperature before being quenched with water. In the Nabertherm furnace, the specimens were aged at 180°C for one hour at 30–3000°C. Following treatment for 5 minutes by [28] and it is represented in Table 3, particles will developed and hardness comparable to ASTM B917 can be attained after 20 minutes, according to this study. Because the samples had previously undergone thixoforming prior to MT6, a quicker treatment time was chosen.

The samples were sectioned, ground (400, 600, 800, and 1200 grits), polished (6 μ , 3 μ , and 1 μ with diamond solution), and etched with Keller's solution before and after thix-

forming/heat treatment. To establish the mechanical qualities, we used the VH testing machine (with a load of 1 kgf and a dwell time of 10s) and the universal testing machine (with tensile tests). According to ASTM E8, the tensile test samples were machined and shown in schematic as Figure 2. Calculated on the basis of experiment results, a follow-up experiment was conducted. Reliable findings could only be achieved by conducting tests on at least three samples per step.

3. Result and Discussion

3.1. Mechanical Responses. It is seen in Table 4 that the average hardness (HV) and ultimate tensile strength of the runs are summarised. In run 4, hardness and ultimate tensile strength were optimised using 1 weight % multiwalled carbon nanotube, 0.75 weight % Mg, and ten minutes of mechanical stirring. The hardness HV and tensile strength of the AA7149 cast ingot arrived in the laboratory at 59.5 HV and 132.9 MPa, correspondingly. A hardness of 104.2 HV and a tensile strength of 271.5 MPa were measured in the confirmation studies.

The S/N response graphs were created using minitab software as in Figures 3(a) and 3(b). The number of carbon nanotubes was found to be the second most important determinant of hardness, after mechanical stirring. When it came to composite hardness, magnesium content had the least impact. Although carbon nanotubes and magnesium were present, mechanical stirring time had the greatest impact on the composite's strength. Comparing run 4 to as-cast AA7149 alloy, the hardness and hardness of the composite improved by 76.3% and by 108.4%, respectively. In the following subchapter, we will go into more detail about this topic. It was shown that when the rheocast alloy was compared to the gravity cast aluminium alloy AA7149, the ultimate tensile strength was 73.5% greater after a 50% decrease in compaction. After thixoforming and T6 heat

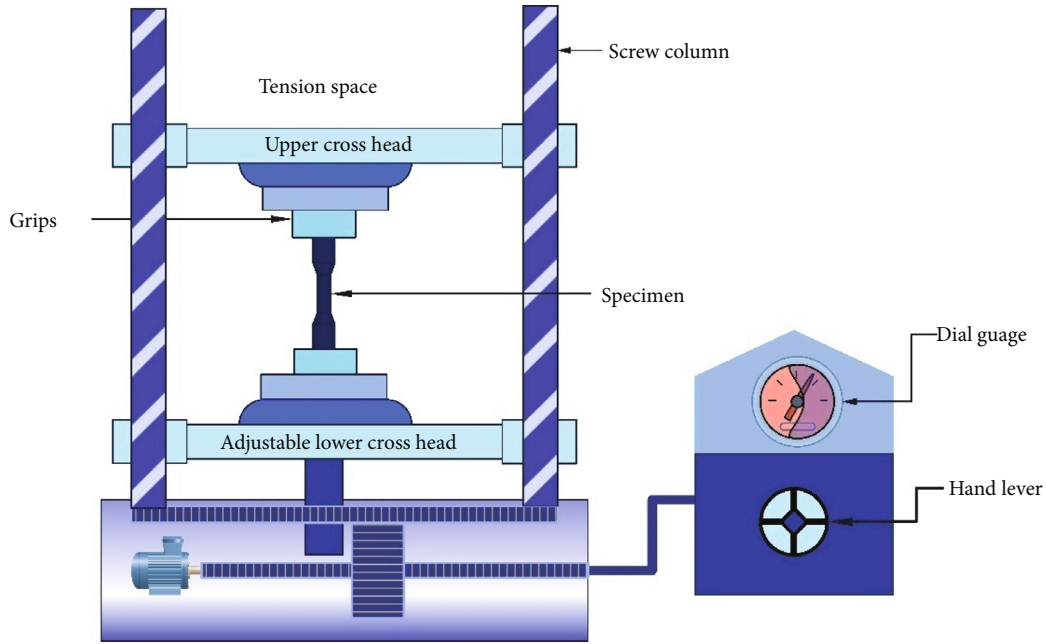


FIGURE 2: Shows schematic view of universal testing machine.

TABLE 4: Results for hardness and ultimate tensile strength.

Run	Hardness	Ultimate tensile strength
1	103.5	180.5
2	105.2	263.6
3	99.6	164.8
4	107.8	278.1
5	105.6	196.7
6	101.2	232.4
7	102.9	208.5
8	104.7	244.3

treatment, the ultimate tensile strength of an AA7149 alloy containing 6% copper was determined to be 361 MPa by [29, 30]. When silicon particles in the AA7149 alloy, [31] found that solution treatment decreased ultimate tensile strength somewhat.

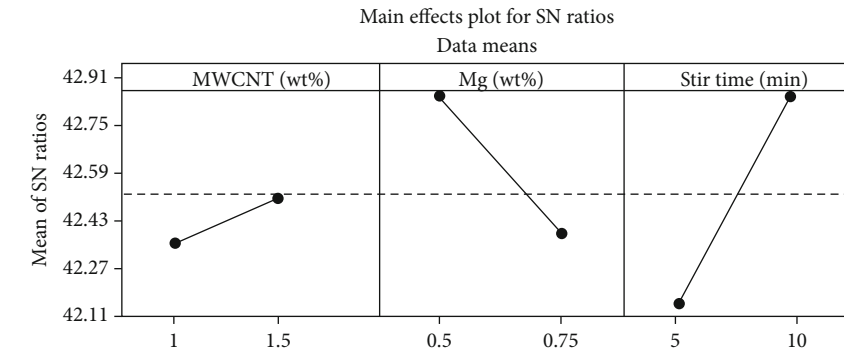
3.2. Homogeneity and Wettability of Multiwalled Carbon Nanotubes. A study of the fracture surfaces of tensile specimens exposed that the recommended manufacturing method produced fracture surfaces that were uniformly wettable. The matrix's multiwalled carbon nanotubes structure also showed no signs of heat deterioration. They found that wet shake mixing and cold compaction/hot extrusion achieved similar results for 1% multiwalled carbon nanotubes and 1.5% carbon nanotubes in pure aluminium matrix, respectively.

In spite of the lack of interfacial phases, such as Al_4C_3 , which could be attributed to technical limitations, there were discovered to be favourable conditions for the nanotubes to spread and bridge across the grains, indicating adequate wet-

ting. Reinforced strengthening may also be a factor in the increased ultimate tensile strength characteristics of base and composite alloys. There was also evidence of multi-walled carbon nanotubes clumping in the sample from run 5. There was a correlation between the composite's mechanical properties and the reinforcing amount.

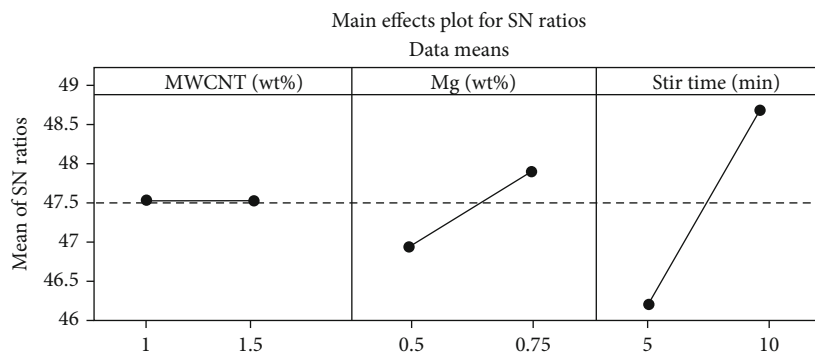
3.3. Effect of Mechanical Stirring. As multiwalled carbon nanotube particles were injected into the melt, the matrix's density and surface tension caused some of the particles to float and aggregate immediately. However, when mechanical stirring was introduced, the particles began to dissipate and were incorporated into the melt. A layer of multiwalled carbon nanotube particles had formed on the surface after 5 minutes of agitation, and this layer was gradually eroding in size. It is possible that the stir ring helped disseminate the particles and avoided density segregation in the molten matrix, which has been observed before. Disruption in viscoplastic behaviour was made possible by the shearing action of whirling blades that deagglomerated and homogenised molten alloy components. As observed by [19], a vortex is created when metal is vigorously stirred during liquid metallurgy processing, aiding in the transfer of nanoparticles and keeping them suspended.

The composite's hardness and ultimate tensile strength decreased as a result of the stirring process, which created voids and porosities. Therefore, thixoforming and heat treatment were required as secondary operations in order to minimise these effects. As the temperature rose, so did the grain boundaries, until they were unbroken. These operations had a direct impact on the matrix alloy. Both of the highest-response samples showed a similar significant reduction in porosity in all samples. It is assumed that a low porosity results in increased hardness.



Signal-to-Noise: Larger is better

(a)



Signal-to-Noise: Larger is better

(b)

FIGURE 3: Main effects of S/N ratio for (a) hardness and (b) ultimate tensile stress responses.

3.4. Effect of Carbon Nanotubes and Magnesium Contents. It was found that carbon nanotube content had a greater impact on hardness than tensile characteristics, according to the DOE data. By utilising carbon nanotubes with a lower content of 1%, hardness and tensile strength were both improved. When the entire metal matrix density is greater than 0.5 weight %, low porosity and high-density dislocations might arise. Additionally, stirring aided to enhance the grain's microstructures. It is because of the inclusion of an agglomerated reinforcing material, the carbon nanotube content had a smaller impact on ultimate tensile strength than on hardness in this investigation.

Compared to 0.5 wt.% of Mg in the matrix, 0.75 wt.% contributed to greater and more consistent hardness and ultimate tensile strength values. Carbon nanotubes can penetrate the grain boundaries of the molten matrix thanks to the wettability of pure Mg, which functions as a lubricant. Even though the additional 0.75 weight % of Mg in the AA7149 alloy may have altered the composition, it was still within the alloy's maximum Mg range given that 0.2 weight % of Mg had been added to it. Multiwalled carbon nanotubes and magnesium concentrations in the metal matrices could not be determined with any precision. Reinforced particles are still difficult to quantify, despite earlier research on varied percentages of these particles in their matrix.

4. Conclusions

Hardness and ultimate tensile strength of the multiwalled carbon nanotubes—AA7149 composite was studied in this analysis. The manufacturing parameters were optimised using Taguchi's robust L8 orthogonal array with two layers of major factors. Using the S/N ratio responses, we were able to determine how much the hardness and ultimate tensile strength varied from one response to the next. As a result of the uniform distribution and pullouts of multiwalled carbon nanotubes across grain boundaries, it was possible to produce a multiwalled carbon nanotubes—AA7149 composite via processing. Despite this, a small number of multiwalled carbon nanotube particles clumped together in the MWCNT sample (1.0 wt%). It was subjected to a modified short-solution treatment after thixoforming and heat treatment (MT6). Using a mixture comprising 1 weight % multiwalled carbon nanotubes, 0.5 weight % magnesium, and mechanical stirring for 10 minutes, we were able to attain T6 conditions.

A 76.3% increase in the composite's hardness compared to the AA7149 alloy resulted in an increase in its ultimate tensile strength (108.4%). According to Taguchi analysis, mechanical stirring duration was the most critical factor in increasing the mechanical properties of the composite.

There was a greater correlation between the amount of multiwalled carbon nanotubes and the material's hardness and its ultimate tensile strength. The amount of magnesium in the composite had the least impact on its two attributes. The current findings have shown nanoparticles are distributed and suspended throughout the matrix as a result of vortex activity during stirring, which breaks surface tension. The increased wettability was partially attributed to the magnesium level as well, but this contribution was small. After thixoforming and MT6, the size of Al remained constant and grew. Porosity reduced by 11% after MT6, leading to an increase of hardness and ultimate tensile strength. Thixoforming and heat treatments can improve the composite's mechanical characteristics even further.

Data Availability

The data used to support the findings of this study are included within the article. Further data or information is available from the corresponding author upon request.

Conflicts of Interest

The authors declare that there are no conflicts of interest regarding the publication of this paper.

Acknowledgments

The authors appreciate the supports from Mizan Tepi University, Ethiopia, for the research and preparation of the manuscript. The author thank the support from Prince Sattam bin Abdulaziz University, Rajalakshmi Institute of Technology, for the assistance in completing the work.

References

- [1] M. Das, T. K. Pani, and B. Sundaray, "Electrical properties of solution cast films of polystyrene/polyaniline- multiwalled carbon nanotube nanocomposites," *Composites Part C: Open Access*, vol. 2, article 100025, 2020.
- [2] M. Mansoor and M. Shahid, "Carbon nanotube-reinforced aluminum composite produced by induction melting," *Journal of Applied Research and Technology*, vol. 14, no. 4, pp. 215–224, 2016.
- [3] J. A. Jeffrey, S. S. Kumar, P. Hariharan, M. Kamesh, and A. M. Raj, "Production and assessment of AZ91 reinforced with nano SiC through stir casting process," *Materials Science Forum*, vol. 1048, pp. 9–14, 2022.
- [4] M. S. Salleh and M. Z. Omar, "Influence of Cu content on microstructure and mechanical properties of thixoformed Al-Si-Cu-Mg alloys," *Transactions of the Nonferrous Metals Society of China*, vol. 25, no. 11, pp. 3523–3538, 2015.
- [5] M. S. Salleh, M. Z. Omar, J. Syarif, K. S. Alhawari, and M. N. Mohammed, "Microstructure and mechanical properties of thixoformed A319 aluminium alloy," *Materials and Design*, vol. 64, pp. 142–152, 2014.
- [6] V. Mohanavel, K. Rajan, and M. Ravichandran, "Synthesis, characterization and properties of stir cast AA6351-aluminium nitride (AlN) composites," *Journal of Materials Research*, vol. 31, no. 24, pp. 3824–3831, 2016.
- [7] M. L. Bharathi, S. A. Rag, L. Chitra et al., "Investigation on wear characteristics of AZ91D/manaolunina composites," *Journal of Nanomaterials*, vol. 2022, Article ID 2158516, 9 pages, 2022.
- [8] V. Mohanavel, S. Prasath, and K. Yoganandam, "Optimization of wear parameters of aluminium composites (AA7150/10 wt% WC) employing Taguchi approach," *Materials Today: Proceedings*, vol. 33, pp. 4742–4745, 2020.
- [9] T. Peng and I. Chang, "Uniformly dispersion of carbon nanotube in aluminum powders by wet shake- mixing approach," *Powder Technology*, vol. 284, pp. 32–39, 2015.
- [10] B. Chen, J. Shen, X. Ye et al., "Solid-state interfacial reaction and load transfer efficiency in carbon nanotubes (CNTs)-reinforced aluminum matrix composites," *Carbon*, vol. 114, pp. 198–208, 2017.
- [11] A. B. Elshalakany, T. A. Osman, A. Khattab, B. Azzam, and M. Zaki, "Microstructure and mechanical properties of MWCNTs reinforced A356 aluminum alloys cast nanocomposites fabricated by using a combination of rheocasting and squeeze casting techniques," *Journal of Nanomaterials*, vol. 2014, 14 pages, 2014.
- [12] B. Abbasipour, B. Niroumand, and S. M. M. Vaghefi, "Compo-casting of A356-CNT composite," *Transactions of the Nonferrous Metals Society of China*, vol. 20, no. 9, pp. 1561–1566, 2010.
- [13] S. C. Tjong, "Recent progress in the development and properties of novel metal matrix nanocomposites reinforced with carbon nanotubes and graphene nanosheets," *Materials Science and Engineering: R: Reports*, vol. 74, no. 10, pp. 281–350, 2013.
- [14] J.-Y. Lim, S.-I. Oh, Y.-C. Kim, K.-K. Jee, Y.-M. Sung, and J. H. Han, "Effects of CNF dispersion on mechanical properties of CNF reinforced A7xxx nanocomposites," *Materials Science and Engineering A*, vol. 556, pp. 337–342, 2012.
- [15] M. S. Chang, "Use of Taguchi method to develop a robust design for the magnesium alloy die casting process," *Materials Science and Engineering A*, vol. 379, no. 1–2, pp. 366–371, 2004.
- [16] İ. Gürkan and H. Cebeci, "An approach to identify complex CNT reinforcement effect on the interlaminar shear strength of prepreg composites by Taguchi method," *Composite Structures*, vol. 141, pp. 172–178, 2016.
- [17] S. Tahamtan, M. A. Golozar, F. Karimzadeh, and B. Niroumand, "Microstructure and tensile properties of thixoformed A356 alloy," *Materials Characterization*, vol. 59, no. 3, pp. 223–228, 2008.
- [18] C. Chen, L. Guo, J. Luo, J. Hao, Z. Guo, and A. A. Volinsky, "Aluminum powder size and microstructure effects on properties of boron nitride reinforced aluminum matrix composites fabricated by semi-solid powder metallurgy," *Materials Science and Engineering A*, vol. 646, pp. 306–314, 2015.
- [19] Y. Yang, C. Ramirez, X. Wang et al., "Impact of carbon nanotube defects on fracture mechanisms in ceramic nanocomposites," *Carbon*, vol. 115, pp. 402–408, 2017.
- [20] H. Abou Bakr, A. Khattab, T. A. Osman, B. Azzam, and M. Zaki, "A novel technique for dispersion of MWCNTs in aluminum alloys," *Minia Journal of Engineering Technology*, vol. 33, no. 1, pp. 1–14, 2014.
- [21] L. Ceschini, A. Dahle, M. Gupta et al., *Aluminum and Magnesium Metal Matrix Nanocomposites*, Springer, Berlin, Germany, 2017.
- [22] X. Yang, T. Zou, C. Shi, E. Liu, C. He, and N. Zhao, "Effect of carbon nanotube (CNT) content on the properties of in-situ

- synthesis CNT reinforced Al composites," *Materials Science and Engineering A*, vol. 660, pp. 11–18, 2016.
- [23] S. Simões, F. Viana, M. A. L. Reis, and M. F. Vieira, "Microstructural characterization of aluminum-carbon nanotube nanocomposites produced using different dispersion methods," *Microscopy and Microanalysis*, vol. 22, no. 3, pp. 725–732, 2016.
- [24] M. Shayan and B. Niroumand, "Synthesis of A356-MWCNT nanocomposites through a novel two stage casting process," *Materials Science and Engineering A*, vol. 582, pp. 262–269, 2013.
- [25] H. H. Kim, J. S. S. Babu, and C. G. Kang, "Fabrication of A356 aluminum alloy matrix composite with CNTs/Al₂O₃ hybrid reinforcements," *Materials Science and Engineering A*, vol. 573, pp. 92–99, 2013.
- [26] H. Hanizam, M. S. Salleh, M. Z. Omar, and A. B. Sulong, "Optimisation of mechanical stir casting parameters for fabrication of carbon nanotubes-aluminium alloy composite through Taguchi method," *Journal of Materials Research and Technology*, vol. 8, no. 2, pp. 2223–2231, 2019.
- [27] S. Dong, J. Zhou, D. Hui, Y. Wang, and S. Zhang, "Size dependent strengthening mechanisms in carbon nanotube reinforced metal matrix composites," *Composites. Part A, Applied Science and Manufacturing*, vol. 68, pp. 356–364, 2015.
- [28] S. Menargues, E. Martín, M. T. Baile, and J. A. Picas, "New short T6 heat treatments for aluminium silicon alloys obtained by semisolid forming," *Materials Science and Engineering A*, vol. 621, pp. 236–242, 2015.
- [29] J. Singh and A. Chauhan, "Characterization of hybrid aluminium matrix composites for advanced applications - a review," *Journal of Materials Research and Technology*, vol. 5, no. 2, pp. 159–169, 2016.
- [30] M. T. Sijo and K. R. Jayadevan, "Analysis of stir cast aluminium silicon carbide metal matrix composite: a comprehensive review," *Procedia Technology*, vol. 24, pp. 379–385, 2016.
- [31] J. Hashim, L. Looney, and M. S. J. Hashmi, "The wettability of SiC particles by molten aluminium alloy," *Journal of Materials Processing Technology*, vol. 119, no. 1–3, pp. 324–328, 2001.

Research Article

Optimization and Tribological Properties of Hybridized Palm Kernel Shell Ash and Nano Boron Nitride Reinforced Aluminium Matrix Composites

M. Lokeshwari,¹ P. Vidya Sagar,² K. Dilip Kumar,³ D. Thirupathy,⁴ Ram Subbiah,⁵ P. Ganeshan,⁶ A. H. Seikh,⁷ S. M. A. K. Mohammed,⁸ and David Christopher ⁹

¹Department of Civil Engineering, RV College of Engineering, Bengaluru, Karnataka 560059, India

²Department of Computer Science & Engineering, Koneru Lakshmaiah Education Foundation, Vaddeswaram, Andhra Pradesh 522502, India

³Department of Mechanical Engineering, Lakireddy Bali Reddy College of Engineering, Mylavaram, Andhra Pradesh 521230, India

⁴Department of Mechanical Engineering, Saveetha School of Engineering, SIMATS, Chennai 602105, India

⁵Department of Mechanical Engineering, Gokaraju Rangaraju Institute of Engineering and Technology, Hyderabad, Telangana 500090, India

⁶Department of Mechanical Engineering, Sri Eshwar College of Engineering, Coimbatore, 641202 Tamil Nadu, India

⁷Mechanical Engineering Department, College of Engineering, King Saud University, P.O. Box 800, Al-Riyadh 11421, Saudi Arabia

⁸Department of Mechanical and Industrial Engineering, Ryerson University, Toronto, Ontario, Canada M5B 2K3

⁹Department of Mechanical Engineering, College of Engineering, Wolaita Sodo University, Ethiopia

Correspondence should be addressed to David Christopher; david.santosh@wsu.edu.et

Received 17 February 2022; Accepted 15 April 2022; Published 22 June 2022

Academic Editor: Hiwa M. Ahmed

Copyright © 2022 M. Lokeshwari et al. This is an open access article distributed under the Creative Commons Attribution License, which permits unrestricted use, distribution, and reproduction in any medium, provided the original work is properly cited.

The tribological properties of hybridized reinforced aluminium matrix composites were optimized using Taguchi and Grey Relational Analysis in conjunction with an L16 orthogonal array. The combination of palm kernel shell ash (PKSA) (0–5 wt. %) along with nano BN reinforcements was taken in interest. Loads and speeds (500, 750, 1000, and 1250 rpm) were employed as control parameters for the experiment. Using a Taber type abrasion machine, the wear samples were made, and the wear experiments were carried out. Speed and load were more important than the percentage of reinforcements in composites when it came to evaluating wear index and loss of volume. With respect to wear index and volume loss, Taguchi-relational Grey's analysis identified A3B1C1 (reinforcement = 5 wt. %; load = 500 g; speed = 500 rpm) as the optimal process parameter combination, with a reinforcement of 3 wt. %, load = 500 g, and speed = 500 rpm being the second-best option. Validation tests have revealed that the anticipated and experiment values at the optimal situations are both within the acceptable range. Performance is influenced more by speed than by load, which is influenced more by the weight percentage of composites, as demonstrated by the application of the Taguchi and Grey Relational Analysis methods.

1. Introduction

Metal matrix composites have been widespread use in advanced material development because of the improved properties of the base metals as a result of various reinforcement inclusions [1]. Metal matrix composites can be found in numerous industries, including automotive, sports and recreation, aviation, and maritime [2]. The outline of rein-

forcing elements into the metal matrix could enhance the mechanical and tribological characteristics of metal matrix composites. Metal matrix composites have been made using both monolithic and hybrid reinforcements. As a result, a wide range of metal matrix composites with various mechanical and tribological characteristics have been created. Metal matrix composites from Al6061 were produced by [3] using a hybrid reinforcement of boron nitride and

boron carbide. Inorganic and organic ingredients can be combined in a variety of ways to create hybrid materials that have a wide range of applications. Aluminium metal matrix composites were investigated for their wear and mechanical properties without optimizing the procedures. This study examined the hardness and wear behavior of hybridized reinforcement composites using LM25 alloy ingots embedded with activated carbon and mica ingots [4]. All of the relevant physical factors were taken into account. As a result of this flaw, it appears that optimization strategies for Al6063 composite materials are underutilized.

Taguchi and response surface methodology have been studied extensively. They are helpful in giving data on the numerous criteria that go into ranking them. Composites produced by [5] employed an artificial neural network to increase their tribological qualities (ANN). We employed the sliding block-on-disc tribometer for the tribological experiments. The L27 orthogonal array was employed to optimize 3 variables: speed and load (40, 80, and 120 N), sliding distance (0.3, 0.6, and 1.2 m/s), and load (60, 90, and 120 N) [6, 7]. The optimization took into account all three variables (2400 m). Using a 95% confidence level ANOVA, the wear rate and coefficient of friction were examined. Hybridized mixtures containing 3% graphite have lower wear and friction values. To estimate the wear rate and the COF, ANN produced a regression coefficient of 0.98905 [8].

The wear of an Al 7050 alloy reinforced with boron nitride was studied using Taguchi's method. Data was gathered and analyzed using a L9 orthogonal array in the DOE. Reinforcement percentage level of 0, 4, and 6%; sliding velocity of 1, 2, and 3 m/s; and distance of 1000 to 14000 metres were used in this investigation. The sliding distance was found to have the greatest impact on the output characteristics. Fuzzy and Grey's relational analysis utilized by [9] to improve tribological characteristics of Al composites. In the Al6061 base metal, tungsten carbide and graphite were employed as reinforcement. In order to determine the COF (coefficient of friction) and to test different degrees of load, sliding distance, and sliding velocity, an experimental run of 30 runs was conducted at 9% and three different levels of water content [10, 11]. The wear rate and the COF were also calculated. Because COF and wear rate are closely related, FGRA was used to find optimal control variable values that would reduce both of these. The experimental results validated the appropriate tribological conditions, which were confirmed in the study [12, 13]. Powder metallurgy was used to produce MMCs with a monolithic boron nitride reinforcement in Al6082. By employing Grey-method Taguchi's of optimization, the tribological performance of synthetic MMCs was improved. A pin-on-disc tester was used to assess volume loss and frictional force using an L27 orthogonal array. When applying the Grey Relational Analysis, the ideal SWR and COF values were obtained [14, 15]. Friction and wear behavior were shown to be strongly influenced by % volume, the most important of the four variables. Taguchi's concept was adopted to enhance the tribological characteristics of Al hybrid composites incorporating A356 alloy, 10% boron nitride, and graphite [16]. Using compo-casting,

hybrid composites were created. When it came to the wear tests utilizing the block-on-disc method, the sliding speed was 0.25, 0.50, and 1.25 m/s, as well as 10 and 30 N loads, and the graphite weight % ranged from 0, 3, and 5%. The SWR was analyzed using Taguchi's method to find the most effective settings [17, 18]. The study found that the SWR was influenced primarily by the percentage of load applied. Al hybrid metal composites were optimized using Gray-approach Taguchi's by [19] in another work. Molybdenum disulfide (varying from 2 to 4% of the total weight) was combined with 5% alumina and stir cast to make metal matrix composites. Once it came to testing for wear, we employed a pin-on-disc tribometer [20]. Calculating SWR and COF, volume loss and frictional force were considered. The experiment was constructed using Taguchi-Grey Relational Analysis, which was used to identify the ideal SWR and COF values as different factors can really be optimized concurrently in the Taguchi technique, allowing for the extraction of many more quantitative information from fewer experimentations, while the GRA is being used to identify the optimum condition for multiple input variables in order to obtain the best quality characteristics [21]. The control parameters have an impact on the tribological performance. It is well known that Taguchi-Grey Relational Analysis approach is used in improving wear properties of mixed reinforced composites, particularly by [22, 23] and others. Hybrid Al6063/palm kernel shell ash reinforcement with 2% BN is not clear how it can increase its tribological qualities. The PKSA concentration varies from 0% to 6%, with a 2% weight percentage gap between each percentage point. In an orthogonal array experimental design of L16, the Taguchi and Grey Relational Analysis methods were used to optimize dry sliding performance by modifying control factors. Analysis of variance is used to analyze tribological performance of the composite under examination and determine the relative relevance of the various factors and their interactions [24–26].

2. Taguchi and Grey Relational Analysis

Taguchi is amongst the best effective strategies for manufacturing high-quality orthogonal array trials. As long as process control settings are optimized, using an orthogonal array can assist decrease measurement variation. Designing for performance, cost, and quality in an integrated manner is a common practice in the industry. Taguchi differentiates out from other experimental methodologies because it focuses on the impact of variance on processing quality assessments moderately than mean. The Taguchi method uses a limited number of orthogonal array experiments to study the whole design space in order to control factors impact and their relations with all other factors. Since the optimal design parameters can be predicted, it is easier to minimize the objective function while still ensuring that constraints are maintained.

To help with the optimization process, Taguchi goes into great detail in Taguchi to describe the sequence in which Taguchi's technique is implemented. Reaction S/N ratio relies on the product or process that is being optimized for quality. Using three various forms of S/N ratios, Taguchi's

TABLE 1: Chemical constituents of (a) Al6063 and (b) palm kernel shell ash (PKSA).

Constituents (a)	Si	Fe	Mn	Mg	Cu	Ti	Zn	Cr	Sn	Al	
%	0.45	0.18	0.04	0.49	0.01	0.03	0.01	0.01	0.01	Bal.	
Constituents (b)	Na2O	MgO	Al2O3	SiO2	P2O5	K2O	CaO	TiO2	Fe2O3	MnO	LOI
%	0.18	3.15	6.45	65.80	3.76	5.21	5.48	0.54	5.68	0.08	2.56

method makes use of HB, HB, and the nominal-is-best (NB). As AMC quality decreases, the better their tribological features become. This is why AMCs should be used to their fullest. In order to find statistically significant experimental variables, the analysis of variance is frequently performed. Thus, S/N ratios and analysis of variance analyses may be utilized to discover the optimal process parameters. Confirmation experiments are often carried out to confirm that the optimal process variables have been established. It is therefore necessary to introduce Grey Relational Analysis. Tribological characteristics such as wear rate and volume loss can be reduced by optimizing the tribological parameters in this study. In this case, the multiresponse optimization technique is being utilized. Grey Relational Analysis is a useful method for analyzing numerous answers, in which the target functions are first normalized between 0 and 1 before the analysis begins. Grey's connection score and the overall Grey relationship grade are then calculated. According to a number of performance metrics, the highest GRG value serves as an indicator of optimal process parameters. Analysis of variance is widely used to determine the relative relevance of numerous features and their relations on the tribological characteristics.

3. Materials and Method

These ashes are generated as a byproduct of palm oil mills, as it possesses pozzolanic activity and contributes significantly to the performance and toughness of mixed materials. The PKS had been sorted, cleaned, and dried. PKS ash extraction at 900 degrees Celsius [13]. The base alloy for the AMCs was Al6063, as aluminum 6063 is being used to achieve an appealing finish for architectural and building application fields that are visually appealing, which had the composition shown in Table 1. Boron nitride and PKSA with the chemical constituents listed in Table 1 were used as hybrid reinforcements. The BN and PKSA particle reinforcements have typical diameters of 30 m and 40 m. Many writers have described the two-stir casting procedure which was hired in the production process.

3.1. Hybrid Composite Synthesis. Stir casting, a well-known liquid metallurgy technology, was used to create the composites. The composites were made via dual stir casting. Between 0% and 10% reinforcement combinations can be generated with (40-60 μ m) PKSA, 50 nm BN (1%), and Al6063. Strengthening particles of BN and PKSA were heated to 250°C in order to remove humidity and boost its ability to adhere to the base metal. The billets of Al6063 alloy were heated to 750°C in a gas-fired crucible furnace. In order to complete the cooling process, the partially formed metal

was removed and put in a 600°F oven. When the Al6063 alloy was melted, the warmed reinforcements of PKSA and nano BN were applied. The slurry was ready for use after a 10-minute hand-stirring session. To achieve a temperature range between 780°C and 30°C, the semisolid composites were heated mechanically at 400 rpm for around 10 minutes. Mechanical stirring was used to break down particle agglomerates by enhancing particulate distribution in the molten metal matrix. It was then necessary to use an already prepared mould in order to harden the liquid composites. Figure 1 shows the schematic view of double stir casting process.

3.2. Tribological Characteristics. The ASTM D4060-16-compliant composites' wear resistance was tested using a Taber Type Abrasion Tester. Measurements of diameter and thickness were made for each test sample (5 mm). Taber abrasion machine turntable platform was used for the sample's surface to be scratched. Continual pressure was applied to the sample's surface using two abrasive wheels that had been lowered and secured in place. There were four different weights (masses) applied to each sample, and four different speeds (rpms) applied to each sample: 500, 750, 1000, and 1250 g and 1000 rpm, respectively. The sample was rubbed against itself by the machine's abrasive wheels, resulting in loose composite debris. After 15 minutes of abrasion testing, the starting and end weights were recorded.

Equations (2) and (3) were used to compute the wear characteristics of the composites. The mass (g) and volume (mm^3) lost were calculated by means of

$$\text{Mass loss} = \text{Initial mass } (m_i) - \text{Final mass } (m_f), \quad (1)$$

$$\text{Volume loss} = \frac{\text{mass loss}}{\rho}. \quad (2)$$

The Taber wear rate index was attained by the relation as shown as follows::

$$\text{Taber Wear Index, } I = \frac{m_i - m_f}{T} \times 1000. \quad (3)$$

3.3. Design of Experiment. These parameters are reinforced, load, and speed, with four levels of each element selected for consideration in this study. Reinforcement is available in levels 3, 5, 7, and 9 weight %, while load is available in a range of 500 to 1250 grammes, while speed is available in a range of 500 to 1250 revolutions per minute (RPM). Taguchi's technique was used to optimize the wear index and loss of volume for synthesized AMCs. On the basis of four main processing factors, the L16 orthogonal array was selected. S/

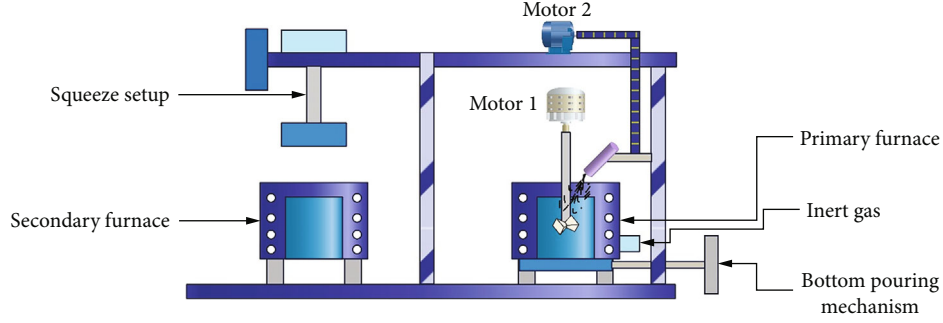


FIGURE 1: Schematic view of double stir casting.

N ratios are frequently employed in Taguchi's approach to express goal function values. In order to minimize the wear index and loss of volume, Equation (1) was employed to calculate the S/N ratio since the less the value, the better in

$$S/N = -10 \log \left(\frac{1}{n} \sum_{i=1}^n y_i^2 \right). \quad (4)$$

3.4. ANOVA. As a consequence of ANOVA, the relative importance of various process parameters in achieving the desired outcome was determined. Minitab 14 (statistics software) was used for the Taguchi and ANOVA analyses in this research.

3.5. Confirmation Test. In order to verify the Taguchi-based optimal conditions for wear rate (WR_{opt}) and volume loss (VL_{opt}), a confirmation test was carried out. For the purpose of estimating the optimal answers, we used the following:

$$WR_{opt} = m_W + (A_3 - m_W) + (B_1 - m_W) + (C_1 - m_W), \quad (5)$$

$$VL_{opt} = m_V + (A_1 - m_V) + (B_1 - m_V) + (C_1 - m_V). \quad (6)$$

There are two ideal levels of wear rate and volume loss: A3B1C1 and A1B1C1. The WR_{opt} and VL_{opt} averages from the study are m_W and m_V , respectively. In order to determine if the projected optimal responses are in agreement with the experimental results, in order to calculate individual response CIs, we used

$$CI = \sqrt{F_{\alpha,1,fe} V_e \left[\frac{1}{n_{eff}} + \frac{1}{R} \right]}, \quad (7)$$

$$n_{eff} = \frac{N}{1 + T_{dof}}. \quad (8)$$

3.6. Grey Relational Analysis (GRA). The first step in the GRA process is to normalize the investigational data to a value between 0 and 1. It was decided to use equation to evaluate the performance of each response based on the

principle of the smaller, the better in

$$\text{The smaller - the - better, } y_i(s) = \frac{\max x_i(s) - x_i(s)}{\max x_i(s) - \min x_i(s)}. \quad (9)$$

After the experimental findings have been standardised using Equations (10) and (11), the grey relational coefficient (GRC) is commonly determined in (11).

$$\varepsilon_i(s) = \frac{\Delta_{\min} + \phi \Delta_{\max}}{\Delta_{oi}(s) + \phi \Delta_{\max}}, \quad (10)$$

where $\Delta_{oi}(s)$ is the deviation sequence estimated by employing

$$\Delta_{oi}(s) = |x_0(s) - x_i(s)|. \quad (11)$$

For instance, the comparability sequence consists of the terms $x(s)$, $\min(s)$, and $\max(s)$. The term $x_0(s)$ is the referential order, and the term ϕ is the coefficient of identification. The value can be anywhere from 0 to 1.

4. Results and Discussion

4.1. S/N Ratio Analysis of the Responses. Displayed in Table 2, the processing parameters' response characteristics and S/N ratios are analyzed. The results of the experiments varied from run to run. Subsequent sections go into greater depth on the outcomes and the analysis that will be done on them.

4.2. Analysis of a Response (Wear Index). Process parameters were ranked according to the wear index value, with the mean S/N ratio being the most important. The wear index of the synthetic aluminium metal composites is depicted in Figure 2, which reveals the substantial effect of each parameter. As a means of identifying, the best processing parameter variations, the best S/N ratios will help. A set of method settings was developed that resulted in the highest possible wear index. The applied load was 500 g, and the sliding speed was 500 rpm at the moment, with a reinforcement percentage of 5%. At a sliding speed of 500 revolutions per minute and a weight of 500 gm, the ideal wear index for Al6063 may be attained with the addition of 2% BN and

TABLE 2: Process parameters, responses, and S/N ratios.

Exp no.	Process parameters			Responses (target functions)		S/N ratio for various responses	
	Reinforcement (wt.%)	Load (g)	Speed (rpm)	Wear index (g/min)	Loss of volume (mm ³)	Wear index	Volume loss
1	3	500	500	0.00301	15.183	51.469	-23.621
2	3	750	750	0.00362	20.012	49.812	-26.015
3	3	1000	1000	0.01824	96.842	36.354	-40.528
4	3	1250	1250	0.07569	418.42	23.612	-53.412
5	5	500	500	0.00512	29.455	47.128	-30.182
6	5	750	750	0.00491	27.528	47.583	-29.512
7	5	1000	1000	0.06614	382.84	24.126	-52.654
8	5	1250	1250	0.02965	164.21	31.245	-45.349
9	7	500	750	0.00118	58.24	60.124	-36.345
10	7	750	1250	0.001785	97.415	36.354	-40.824
11	7	1000	500	0.006428	37.965	44.135	-32.168
12	7	1250	750	0.01884	104.24	35.012	-41.345
13	9	500	1250	0.01562	88.48	36.512	-39.934
14	9	750	1000	0.01247	70.18	39.754	-37.912
15	9	1000	750	0.01364	73.86	39.0963	-38.248
16	9	1250	500	0.00854	50.02	42.621	-34.812

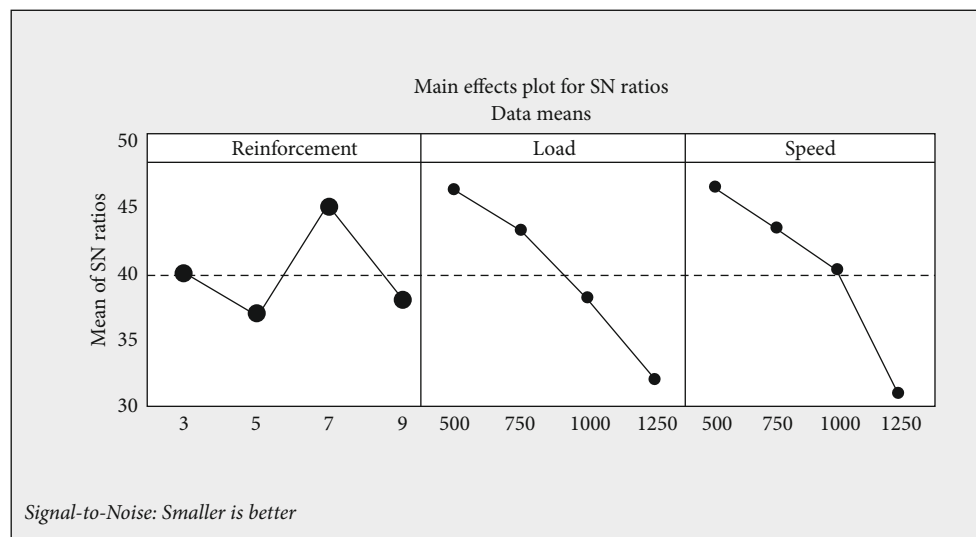


FIGURE 2: Analysis of the S/N ratio of each parameter's effect on wear index.

5% PKSA as hybrid reinforcements ($A_3B_1C_1$). As a result, this indicates that the wear index is in good shape. Optimal value was most strongly influenced by sliding speed and load, with reinforcing percentage weight having the least impact, according to the ranking.

4.3. Analysis of Volume Loss Target Functions. Mean SNR ratio and ranking order of reinforcement, load, and speed were used to calculate volume loss value. As each process parameter changes, so does the volume loss, as seen in Figure 3. The most significant effect on volume loss was found to be associated with the sliding speed. Furthermore, the reinforcing impact was considered as the least important. It is important to have 3% reinforcement in the AMCs to get

the optimum volume loss value at 500 g applied load and 500 revolution per minute sliding speed, as can be shown in Figure 3.

4.4. ANOVA of the Responses

4.4.1. Wear Index. ANOVA has been recommended by [6] for verifying the statistical consistency of Taguchi analysis outcomes. The % of each AMC factor's impact on the wear index was calculated. It is shown in Table 3 that the ANOVA results for wear index of AMC samples reveal the percentage influence of each process parameter. In the ANOVA investigation, the applied load was demonstrated to be the most important component, accounting for 42.83%. Only 6.97%

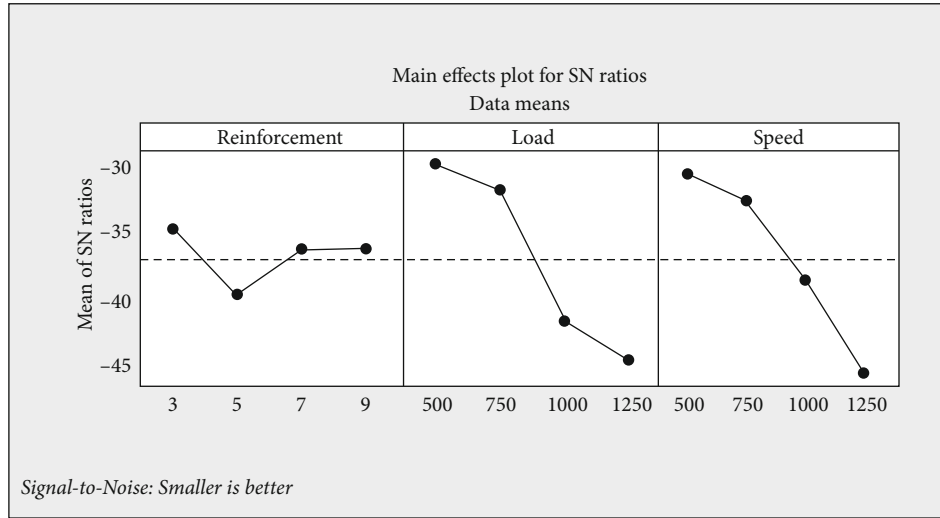


FIGURE 3: Analysis of the S/N ratio of each parameter's effect on volume loss.

TABLE 3: Analysis of variance for wear index.

Source	DF	Seq SS	Adj SS	Adj MS	F value	p value	Contribution (%)	R-sq
Reinforcement	3	98.46	100.4	34.16	1.48	0.342	6.85	0.915
Load	3	612.13	612.12	204.18	10.16	0.018	43.18	
Speed	3	582.62	581.45	194.15	9.42	0.016	40.45	
Error	6	135.54	135.62	24.45			9.52	
Total	15	1428.75						

of the total was accounted for by reinforcing weight, which had a 40.74% share. However, the main effect plots and ANOVA results of Taguchi's approach were ordered differently. An ANOVA test, however, indicated that speed and load were in that order, despite a Taguchi test indicating the opposite. As a result, the wear index is most strongly influenced by load and speed, whereas reinforcement has the least. Researchers [25] back up the findings of this investigation. When compared to the weights and sliding speeds they were tested against, the graphite addition to composites had no influence on their performance. With increasing applied load and speed, raising the AMC wear index is significantly impacted. According to [4], as the applied force increases, tribological characteristics such as wear rate and COF can rise. As the load increases, the plastic deformation increases as well. Each process parameter's p value revealed which ones have a significant impact on the wear index. There is no correlation between the wear index value and the reinforcing process parameter because the p value is much above the 0.05 level of confidence. The composites' wear index values are strongly influenced by the loads and speeds applied.

4.4.2. Volume Loss. Table 4 indicates the outcomes of the ANOVA as well as the volume loss contribution proportion of the three variables. After doing an analysis of process parameters using ANOVA, which indicated that speed had a 60.16% effect, followed by applied load (34.35%) and reinforcement (11.64%), reinforcement's percentage contribu-

tion to volume loss is negligible as compared to speed and load. Like the ANOVA findings, we can see how the process parameters affect volume loss. Strengthening ($p = 0.467$) was not significant, but speed ($p = 0.0001$) and load ($p = 0.002$) were highly significant in terms of volume loss ($p = 0.002$). Variables like load and speed have an effect on responsiveness when the p value is less than 0.05. The findings of the experiments showed that the composites' volume loss increased without reference to the reinforcing weight percentage as load and speed increased. As observed in the study from [14], sample volume loss increased correspondingly as speed and load increased. Following speed, applied load, and % reinforcement weight, Taguchi and ANOVA analysis indicated that % reinforcement weight was the least influential factor. If the findings from [24] are correct, then the use of optimization techniques is confirmed to be accurate, as indicated by [23].

4.4.3. Confirmation Test. These tribological properties underwent a confirmation test in order to ascertain their exact optimum values. As expected, the experimental results were within the CI computed using Equations (7) and (8). For this purpose, the following values were substituted into Equations (7) and (8). As shown in Table 5, the anticipated and experimentally optimal CI values for each of the goal functions are all within acceptable ranges.

4.5. Grey Relational Analysis (GRA). Multiple performance characteristics were the consequence of combining GRA's

TABLE 4: Impact of processing parameter loss of volume.

Source	Degrees of freedom	Seq SS	Adj SS	Adj MS	F value	p value	Contribution (%)	R-sq
Reinforcement	3	17.9	19.3	7.034	0.98	0.671	2.06	0.945
Load	3	348.46	348.64	116.84	19.64	0.003	34.46	
Speed	3	609.84	610.81	203.912	33.48	0.0001	59.00	
Error	6	38.6	38.3	6.348			3.72	
Total	15	1015.5					100	

TABLE 5: Predicted and actual results for each reaction at optimal conditions.

Response	Condition at optimum level	Predicted	Experiment
Wear index (g/min)	A ₃ B ₁ C ₁ (reinforcement = 5 wt.%; load = 500 g; speed = 500 rpm)	0.00132	0.00267
Loss of volume (mm ³)	A ₁ B ₁ C ₁ (reinforcement = 3 wt.%; load = 500 g; speed = 500 rpm)	14.915	15.016

TABLE 6: Optimized results for the Grey Relational Analysis.

S. no	Normalized		GRCs		GRG	Rank
	Wear index	Loss of volume	Wear index	Loss of volume		
1	0.96842	1.0134	0.9456	1.000	0.9834	2
2	0.9742	0.9976	0.9461	0.9842	0.9664	1
3	0.7914	0.8016	0.7052	0.7231	0.7161	16
4	0	0	0.3341	0.3342	0.3433	12
5	0.9541	0.9745	0.9125	0.9468	0.9287	3
6	0.9585	0.9812	0.9182	0.9543	0.9351	4
7	0.1283	0.0961	0.3743	0.3661	0.3712	14
8	0.6342	0.6419	0.2812	0.5758	0.5842	15
9	1.0124	0.9041	1.0146	0.8349	0.9114	5
10	0.7965	0.8074	0.7142	0.7124	0.7124	6
11	0.9347	0.9546	0.8832	0.9128	0.8972	11
12	0.7830	0.7816	0.6950	0.7042	0.6910	10
13	0.8124	0.8168	0.7346	0.7456	0.9398	13
14	0.8614	0.8342	0.7789	0.7954	0.7785	9
15	0.8431	0.8643	0.7632	0.7869	0.7769	7
16	0.9012	0.9243	0.8434	0.8661	0.8534	8

two primary goals (MPC). The key objectives are the wear index and loss of volume. As shown in Table 6, the GRC, the GRG, and the rankings generated by applying Equations (9)–(11) to the grey's relational grade are all shown. For the best MPC, a research with the maximum GRG in all of its runs will yield the most accurate results. On the basis of GRG's responses, the order of each process parameter's rating was determined. Speed is listed first, followed by load, and then reinforcement. Reinforcement comes in at a distant third place, with rotational speed taking precedence. The results from experiment 1 were the most impressive.

Figure 2 shows the most important impact of each processing parameter on a typical wear specimen. A3B1C1 is the best answer for a wide range of questions. When evaluating A3B1C1's ideal values, it is important to take into account the weight of 6%, the loads applied of 500 gms, and the speed of 500 revolutions per minute (rpm). Using

ANOVA, the GRG findings were analyzed, and the % contribution of each constraints was evaluated. 47.38% and 23.9%, respectively, of the MPC's impact are due to speed and load. According to the GRG response's ranking order, this is also true in Table 6. This characteristic, speed, outperforms both loads and reinforcement in terms of significance due to its *p* value being less than or equal to 0.05. Using the wear index and loss of volume and the S/N ratio as a proxy, Table 5 compares reinforcement, load, and speed. A correct response will be based heavily on these factors.

5. Conclusions

Aluminum metal composites were improved by combining Taguchi and Grey's Relational Analysis approaches. We found that reinforcing percentage weight, load, and speed all had an impact on wear index and volume loss. The experiment's outcomes were analyzed and verified using ANOVA. We can finally conclude the following:

- (i) Reinforcement percentages of 5% and 3% were used to optimize wear indexes and volume loss at A3B1C1, while volume loss was optimized at the same location
- (ii) Speed is the most important component in determining wear index and volume loss, according to Taguchi and GRA
- (iii) A 95% confidence interval confirmation test was used to check that anticipated and investigational findings were within permitted range
- (iv) The tribological characteristics of a material were improved using both of the methods utilized in this investigation

Data Availability

The data used to support the findings of this study are included within the article. Further data or information is available from the corresponding author upon request.

Conflicts of Interest

The authors declare that there are no conflicts of interest regarding the publication of this paper.

Acknowledgments

The authors appreciate the supports from Wolaita Sodo University, Ethiopia, for the research and preparation of the manuscript. The authors appreciate the support from RV College of Engineering, Lakireddy Bali Reddy College of Engineering, Sri Eshwar College of Engineering, and Ryerson University, for the assistance in doing the work. This project was supported by the Researchers Supporting Project number (RSP-2021/373), King Saud University, Riyadh, Saudi Arabia.

References






- [1] V. Mohanavel, K. S. Ashraff Ali, S. Prasath, T. Sathish, and M. Ravichandran, "Microstructural and tribological characteristics of AA6351/Si3N4 composites manufactured by stir casting," *Journal of Materials Research and Technology*, vol. 9, no. 6, pp. 14662–14672, 2020.
- [2] K. K. Alaneme, M. O. Bodunrin, and A. A. Awe, "Microstructure, mechanical and fracture properties of groundnut shell ash and silicon carbide dispersion strengthened aluminium matrix composites," *Journal of King Saud University-Engineering Sciences*, vol. 30, no. 1, pp. 96–103, 2018.
- [3] M. L. Bharathi, S. Adarsh Rag, L. Chitra et al., "Investigation on wear characteristics of AZ91D/nanoalumina composites," *Journal of Nanomaterials*, vol. 2022, Article ID 2158516, 9 pages, 2022.
- [4] B. P. Kumar and A. K. Birru, "Tribological behavior of aluminium metal matrix composite with addition of bamboo leaf ash by GRA-Taguchi method," *Tribology in Industry*, vol. 40, no. 2, pp. 311–325, 2018.
- [5] T. A. Orhadahwe, O. O. Ajide, A. A. Adeleke, and P. P. Ikubanni, "A review on primary synthesis and secondary treatment of aluminium matrix composites," *Arab Journal of Basic and Applied Sciences*, vol. 27, no. 1, pp. 389–405, 2020.
- [6] M. Sarikaya and A. Güllü, "Taguchi design and response surface methodology based analysis of machining parameters in CNC turning under MQL," *Journal of Cleaner Production*, vol. 65, pp. 604–616, 2014.
- [7] B. Stojanović and L. Ivanović, "Application of aluminium hybrid composites in automotive industry," *Tehnički vjesnik*, vol. 22, no. 1, pp. 247–251, 2015.
- [8] A. S. Canbolat, A. H. Bademlioglu, N. Arslanoglu, and O. Kaynakli, "Performance optimization of absorption refrigeration systems using Taguchi, ANOVA and Grey Relational Analysis methods," *Journal of Cleaner Production*, vol. 229, pp. 874–885, 2019.
- [9] K. K. Alaneme, M. H. Adegun, A. G. Archibong, and E. A. Okotete, "Mechanical and wear behaviour of aluminium hybrid composites reinforced with varied aggregates of alumina and quarry dust," *Journal of Chemical Technology & Metallurgy*, vol. 54, no. 6, 2019.
- [10] S. Chamoli, P. Yu, and A. Kumar, "Multi-response optimization of geometric and flow parameters in a heat exchanger tube with perforated disk inserts by Taguchi grey relational analysis," *Applied Thermal Engineering*, vol. 103, pp. 1339–1350, 2016.
- [11] K. Halil, O. İsmail, D. Sibel, and Ç. Ramazan, "Wear and mechanical properties of Al6061/SiC/B4C hybrid composites produced with powder metallurgy," *Journal of Materials Research and Technology*, vol. 8, no. 6, pp. 5348–5361, 2019.
- [12] B. N. Sarada, P. L. S. Murthy, and G. Ugrasen, "Hardness and wear characteristics of hybrid aluminium metal matrix composites produced by stir casting technique," *Materials Today: Proceedings*, vol. 2, no. 4–5, pp. 2878–2885, 2015.
- [13] P. P. Ikubanni, M. Oki, A. A. Adeleke, A. A. Adediran, and O. S. Adesina, "Influence of temperature on the chemical compositions and microstructural changes of ash formed from palm kernel shell," *Results in Engineering*, vol. 8, article 100173, 2020.
- [14] A. Acir, M. E. Canli, İ. Ata, and R. Çakıroğlu, "Parametric optimization of energy and exergy analyses of a novel solar air heater with grey relational analysis," *Applied Thermal Engineering*, vol. 122, pp. 330–338, 2017.
- [15] M. Thangaraj, R. Annamalai, K. Moiduddin, M. Alkindi, S. Ramalingam, and O. Alghamdi, "Enhancing the surface quality of micro titanium alloy specimen in WEDM process by adopting TGRA-based optimization," *Materials (Basel)*, vol. 13, no. 6, p. 1440, 2020.
- [16] V. R. Rao, N. Ramanaiah, and M. M. M. Sarcar, "Dry sliding wear behavior of TiC-AA7075 metal matrix composites," *International Journal of Applied Science and Engineering*, vol. 14, no. 1, pp. 27–37, 2016.
- [17] N. H. Naquiddin, L. H. Saw, M. C. Yew et al., "Numerical investigation for optimizing segmented micro-channel heat sink by Taguchi-Grey method," *Applied Energy*, vol. 222, pp. 437–450, 2018.
- [18] P. J. Unnikrishna, S. Ikshita, S. T. M. Manikandakumar, and G. Moshe, "Optimisation of multiple response characteristics on end milling of aluminium alloy using Taguchi-Grey relational approach," *Measurement*, vol. 124, pp. 291–298, 2018.
- [19] B. Stojanović, A. Vencl, I. Bobić, S. Miladinović, and J. Škerlić, "Experimental optimisation of the tribological behaviour of Al/SiC/Gr hybrid composites based on Taguchi's method and artificial neural network," *Journal of the Brazilian Society of Mechanical Sciences and Engineering*, vol. 40, no. 6, pp. 1–14, 2018.
- [20] N. Mandal, B. Doloi, B. Mondal, and R. Das, "Optimization of flank wear using zirconia toughened alumina (ZTA) cutting tool: Taguchi method and regression analysis," *Measurement*, vol. 44, no. 10, pp. 2149–2155, 2011.
- [21] S. S. Hiremath, N. S. Shanmugam, and B. R. R. Babu, *Advances in Manufacturing Technology: Select Proceedings of ICAMT 2018*, Springer, 2019.
- [22] V. Dharanikota, "Optimization of tribological properties of Al-6082/BN metal matrix composite by Grey-Taguchi's method," *International Journal of Scientific and Engineering Research*, vol. 5, p. 629, 2014.
- [23] K. K. Alaneme, A. V. Fajemisin, and N. B. Maledi, "Development of aluminium-based composites reinforced with steel and graphite particles: structural, mechanical and wear characterization," *Journal of Materials Research and Technology*, vol. 8, no. 1, pp. 670–682, 2019.
- [24] V. Mohanavel, M. Ravichandran, S. S. Kumar, M. M. Sridhar, S. Dineshkumar, and M. M. Pavithra, "Microstructural and tribological characterization of Al/egg shell ash composites

prepared by liquid metallurgy process," *Journal of the Balkan Tribological Association*, vol. 26, no. 2, pp. 319–326, 2020.

- [25] S. Veličković, B. Stojanović, M. Babić, and I. Bobić, "Optimization of tribological properties of aluminum hybrid composites using Taguchi design," *Journal of Composite Materials*, vol. 51, no. 17, pp. 2505–2515, 2017.
- [26] S. Dharmalingam, R. Subramanian, K. Somasundara Vinoth, and B. Anandavel, "Optimization of tribological properties in aluminum hybrid metal matrix composites using gray-Taguchi method," *Journal of Materials Engineering and Performance*, vol. 20, no. 8, pp. 1457–1466, 2011.

Review Article

A Potential Notion on Alzheimer's Disease: Nanotechnology as an Alternative Solution

Sudhir Suryakant Pange,¹ Mohsina Patwekar²,, Faheem Patwekar,² Saad Alghamdi³,, Ahmad O. Babalghith⁴,, Osama Abdulaziz,⁵ Talha Jawaid,⁶ Mehnaz Kamal⁷,, Shahana Tabassum,² and Jewel Mallick⁸

¹ASPM's K. T. Patil College of Pharmacy, Osmanabad, India

²Luqman College of Pharmacy, Gulbarga, Karnataka, India

³Laboratory Medicine Department, Faculty of Applied Medical Sciences, Umm Al-Qura University, Makkah, Saudi Arabia

⁴Medical Genetics Department College of Medicine, Umm Al-Qura University, Makkah, Saudi Arabia

⁵Clinical Laboratory Sciences Department, College of Applied Medical Sciences, Taif University, Taif Province, Saudi Arabia

⁶Department of Pharmacology, College of Medicine, Al Imam Mohammad Ibn Saud Islamic University (IMSIU), Riyadh 13317, Saudi Arabia

⁷Department of Pharmaceutical Chemistry, College of Pharmacy, Prince Sattam Bin Abdulaziz University, Al-Kharj 11942, Saudi Arabia

⁸Department of Pharmacy, BGC Trust University Bangladesh, Chittagong 4381, Bangladesh

Correspondence should be addressed to Mohsina Patwekar; mohsina.patwekar@gmail.com and Jewel Mallick; jewel@bgctub.ac.bd

Received 13 May 2022; Accepted 3 June 2022; Published 17 June 2022

Academic Editor: Hiwa M. Ahmed

Copyright © 2022 Sudhir Suryakant Pange et al. This is an open access article distributed under the Creative Commons Attribution License, which permits unrestricted use, distribution, and reproduction in any medium, provided the original work is properly cited.

Alzheimer's disease is an eventually destroying disease of the overaged people featured by the dynamic and gradual brain erosion because of construction of extracellular plaques in the hippocampus. It is an undertreated and underrecognized disease that is becoming a major public health concern. From the study, it is known that production of plaques takes place twenty years back, before the commencement of clinical syndromes. As per report, in 2019, above 50 million people got into Alzheimer's disease. Recent developments include improved clinical diagnostic guidelines and improved treatment of both cognitive disturbance and behavioral problems. Treatment majorly focus on cholinergic therapy has been clinically evaluated by different studies including randomized, double-blind, placebo-controlled, parallel-group studies measuring performance-based tests of cognitive function, activities of daily living, and behavior. The presence of extracellular plaques of insoluble β -amyloid peptide ($A\beta$) and neurofibrillary tangles (NFT) containing hyperphosphorylated tau protein (P-tau) in the neuronal cytoplasm is a remarkable pathophysiological cause in patients' brains. The graph of increasing patients, suffering from Alzheimer's disease, is being ascended. The outcome of this turn into fatal, deadly situation. So, there is a possibility of breaking down world economics and human strength. There is a different kind of organic as well as inorganic nanocomponent group, those have been pursued with satisfaction. By studying and researching over pathogenesis specifically, diagnosis of this AD as per its symptoms is possibly done. Treatment of this neurodisease is under processing. The experts are playing an extremely appreciable role for displacing this disease completely. The present review summarizes the pathophysiology and role of the nanoparticle in the diagnosis and treatment of AD.

1. Introduction

Alzheimer's disease, a neurodegenerative disorder, generates memory and learning scarcity. It is not a reversible disorder.

People, who are above 65, mostly suffer from this disease. Though the pathophysiology of Alzheimer's disease is very distinct to us, the procedure of treatment is not of clear perspective at all. It only gives a very less satisfaction to

minimize enhancement of symptoms of the disease and to regulate the phenomenon of disease. It stands fifth as reason of death of over 65 aged people. The approved drugs used for this treatment of Alzheimer's disease are relied on neurotransmitter or modulation of enzymes like acetylcholinesterase inhibitors. Again, it is not found as a successful treatment. It cannot pass because of less solubility, low bio-availability, and incapability of overthrowing barriers resides along with drug transportation routes as well, especially while transcending blood brain barrier. As we know, the blood-brain barrier is the most specific, made up of tightly connected endothelial cells and irregular stratum of pericytes [1]. Here, paracellular or transcellular transport is possible. Here, drugs are being enhanced and improved for targeting $A\beta$ attestation and tau phosphorylation. There are more than 100 drugs, which are in phase II and III clinical trials and are not so effective as per depressed outcomes. In the early step of AD, AMPA dysfunction is instigated by soluble Ab as well as dendritic changes. Solanezumab is a monoclonal antibody that targets AB, basically improved to restrict cognitive deficits, and was not successful to develop cognition or sectional capability in patients with Alzheimer's disease in clinical trial. Leuco-methylthioninium bis might prevent tau accumulation, but adequate trial is required to assure the potential. In these circumstances, it is highly required to have a new, innovative device for treatment of this Alzheimer's disease [2].

2. Pathogenesis of Alzheimer's Disease

Alzheimer's disease is a persistent neurodegenerative disease distinguished by the disablement of evocation and coherent obligation (Figure 1). It is one of the usual neurodegenerative diseases in the world. Mostly, people, who are aged above sixty-five, are mainly affected with this specific disease [3].

2.1. Pathophysiology. In the area of brain, deprivation of synapse widely and neuronal expiry takes place. As a result, analytical functions stop over there. Apoptosis of the neuron inside the brain comes out because of existence of accumulated amyloid plaques (amyloid beta peptide) and neurofibrillary tangles (tau protein filaments). These accumulations create diminished constraints. As per pathology, there are two types of postulations. One is based on amyloid cascade neurodegeneration and another one related to the disablement of cholinergic process (Figure 1). The initiation of Alzheimer's disease happens through the proteolytic splitting of the amyloid pioneer proteins (by disarranging of homeostatic mechanism) that effects in the excess abundance of amyloid-beta and production of amyloid plaques. There are some conditions like age, ecological, and hereditary which accelerates in shifting metabolically that can hold esteem in the system of amyloid protein pioneer. Here, two enzymes, beta-secretase and gamma-secretase (constituents of the presenilin compounds), helps to split amyloid-beta peptides (Figure 2). The outcome of mutation in the amyloid pioneer protein with a presenilin

compound is enhancement of amyloid-beta accumulation in patients with Alzheimer's disease [4].

2.2. Characteristics of Nanomaterials and their Appliance in Nanomedicine. Nanomaterials play a significant role in developing drug durability and therapeutic efficiency. These possess a wide embarked surface area, which helps in lading huge amounts of drug and conserving drugs from enzymatic deterioration. These materials show specific physicochemical features because of their surface yield, quantum dimension outcomes, and macroquantum effects. Nanomedicines are very advantageous and potent as per its appliance [5]. So, choosing and designing of nanotransporters for transporting and carrying are under tough conditions. One must be very careful and responsible at the time of selection of nanomaterials. Evaluation of toxic level and safety measurement is one of the beneficial steps. For making the transport successful and increasing the efficiency of treatment, it must be focused on size, shapes, surface impose, and surface functionalization. Uptaking and transporting nanoparticles are size dependent. Size of nano-materials must be relevant because of specific route of administration, carrier procedure, fluid-chemistry. As per previous data, nanoparticles sized less than 200 nm are capable of intense brain permeation and wide space circulation as compared to bigger particle sized materials. Nanoparticles, which have diameter less than 5 nm (Figure 3), have been constructed to be impregnable to fast renal removal added to restricted dealing capacity and rapid drug deliverance dynamics that put them insufficient transport fluids. The surface charge of upgraded nanomaterials leads an important disposition regarding revival and cellular toxicity of enhanced technicality for brain transportation. Here, positively charged mediums are desired for transportation of siRNA9 (negatively charged), and earlier data revealed that nanotransporters containing positive charges produce the toxic effect to BBB (Figure 4). So, to get efficiency, transporters with a neutral to negative charge have been more generally pursued as a carrier. The surface charge of nanoporters is affected through protein adsorption. By utilizing in vitro and in vivo pattern, interrelation between nanoparticles and serum substituents are being evaluated. Apart from that surface charge also impacts over cellular intake, dispensation, and efficiency of nanodrug particles relying on route of administration, cell target, and functions [6].

2.3. Dendrimers. Dendrimers are the polymers, which are suprabranched. The structure is 3-D arranged with excess regulated mass. Size, shape, magnitude, volumes, and surface chemistry carry beneficial features for treatment and diagnosis of particular disease. These particles are framed with a basic core, surrounded by linked functional groups along the peripheral region. By affixing of subsequent strata with every generation, diameter of dendrimer maximizes by 1 nm. Dendrimers are used for transportation of drugs. These are able to maintain drug levels at therapeutic levels, maximize the circulation half-life of active components, and raise drug transport and durability. Biomolecules conjugate to the surface of dendrimers, and an excess drug

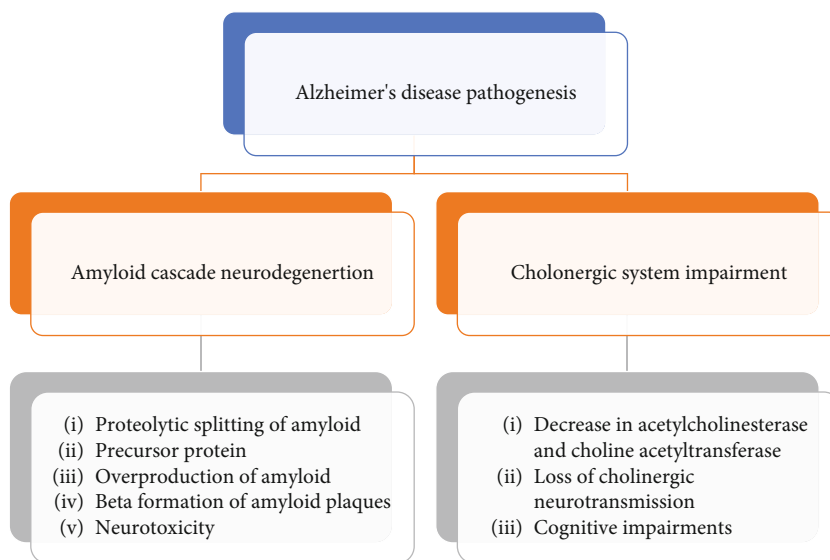


FIGURE 1: Chart Pathogenesis of Alzheimer's disease.

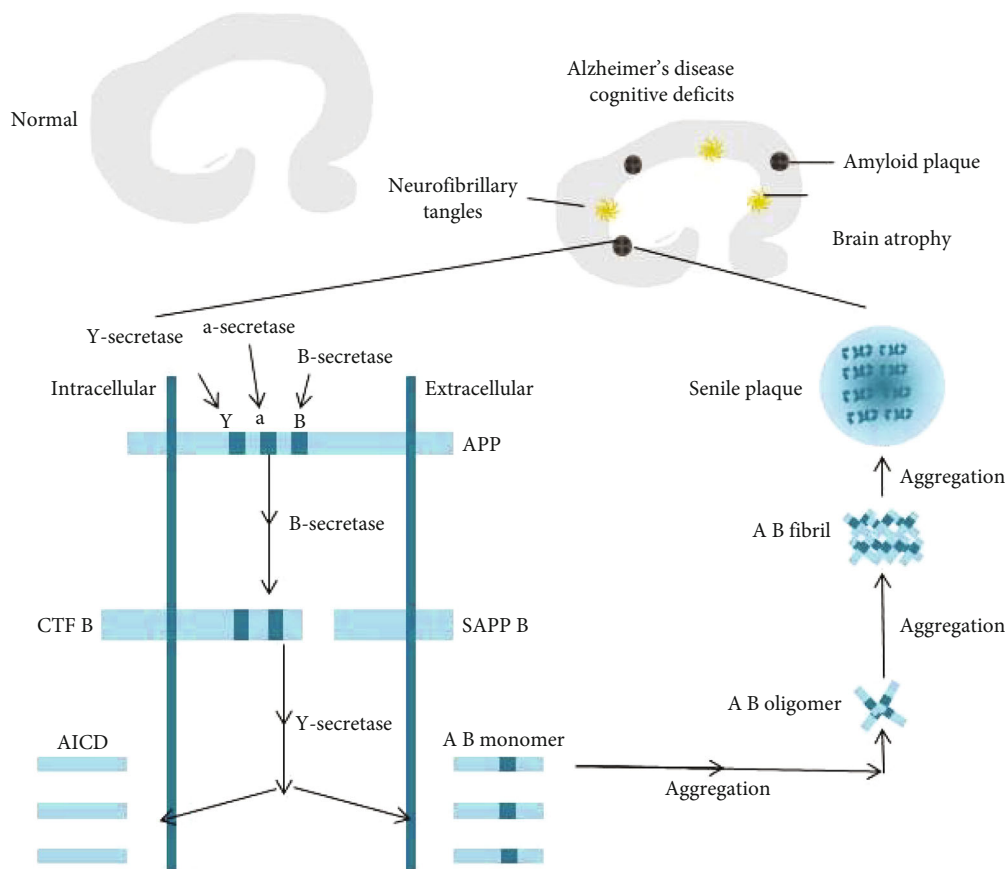


FIGURE 2: The major pathological characteristics of Alzheimer's disease. Accumulation of amyloid beta, neurofibrillary tangles persuaded by hyper phosphorylated tau protein and neuronal apoptosis. Amyloid beta is produced from amyloid beta precursor protein splitted by beta secretase and gamma secretase. AB monomer accumulates to produce oligomers of various molecular weight and then fibriller AB. These forms plaques in the brains of AD patients. Excessive accumulation, tau hyperphosphorylation, and neuronal apoptosis initiate series of pathological alterations including cognitive deficits and brain atrophy.

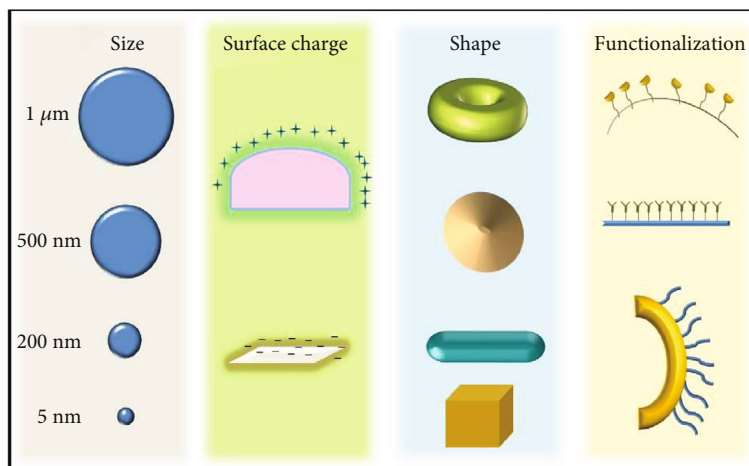


FIGURE 3: Key physicochemical characteristics for the development of nanomaterial technologies to cross the blood–brain barrier for Alzheimer’s disease treatment. Size, shape, surface charge, and functionalization greatly influence the nanocarrier efficacy for drug delivery to the brain. Nanoparticles between 5 and 200 nm have been shown to penetrate the brain more efficiently than larger particles, in addition to being efficaciously internalized by macrophages for cell-mediated delivery across the blood–brain barrier. The surface charge of the nanotechnologies used for brain delivery must be carefully controlled to minimize the potential toxicity of each platform. Furthermore, nanoparticle shape can significantly enhance the circulation and uptake of nanomedicines. Finally, surface functionalization of the nanocarrier offers an extensive range of possibilities to improve brain penetration and target specific cell receptors with the use of small molecules, antibodies, or peptides.

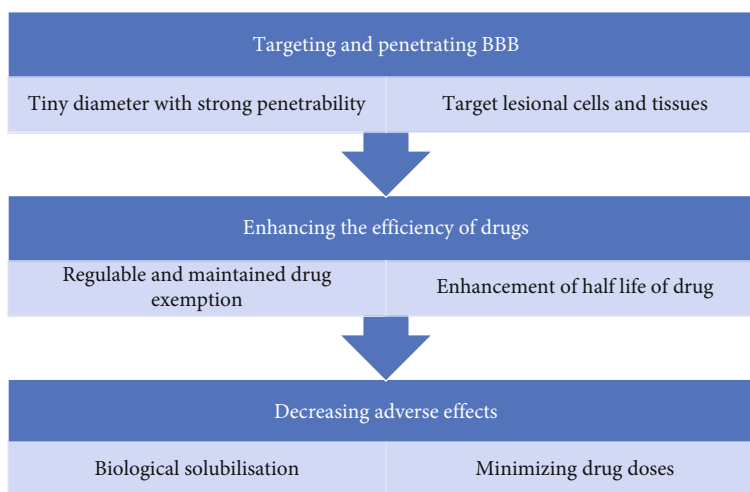


FIGURE 4: Characteristics of nanomaterials are shown in the chart. Modified nanomaterials can target lesional cells and tissues. Nanomaterials modified with specific molecules have small diameters with high efficient penetrability that make them focus and penetrate the blood-brain barrier with perpetuated drug release, developed bioavailability, and enhanced drug half-life, therefore minimizing drug doses, enlarging drug efficacy, and reducing adverse effects.

burdening capacity inside inner perforation is shown. These molecules are keen of proteins, peptides, lipids, ligands, and nucleic acid highly. Some dendrimers are wide in a variety like poly(aminoamine) (PAMAM), polyether hydroxylamine (PEHAM), and poly-(propyleneimine) (PPI) dendrimers. The PAMAM dendrimer has comprehensive chemical features. This polycationic PAMAM consists of te primary amine group at its surface area. Another half-generation PAMAM dendrimer is polyanionic, which contains carboxylic acid groups on surface. It helps in efficient appliance of these transporters. Dendrimers are utilized as

antiamyloidogenic components. For example, fourth-generation PPI maltose (PPI-G4-Mal) and fifth-generation PPI maltose (PPI-G5-Mal) glycodendrimers have shown the efficiency of shattering the amyloid-beta peptide, especially A beta (1-40) fibrilization. Every individual process has various procedures to hinder AB fibrilization. Whereas PPI-G4-Mal produces grove fibrils at down side of dendrimers-peptide ratios as well as amorphous accumulates at elevated ratios, the fifth-generation dendrimers prevent fibril organization by producing granulated nonfibrillar amorphous assemblies. From this information,

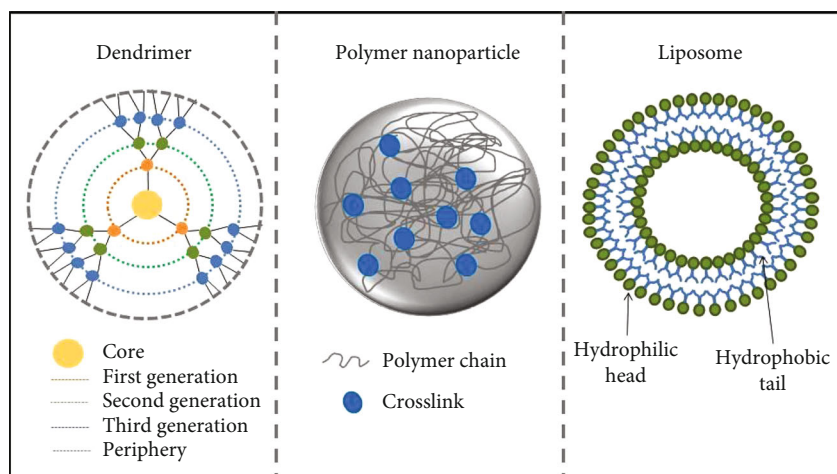


FIGURE 5: Anatomy of nanocarriers used for Alzheimer's disease drug delivery across the blood–brain barrier. Dendrimers, polymeric nanoparticles, and liposomes are examples of nanocarriers that have been used to deliver therapeutic agents across the blood–brain barrier for the treatment of Alzheimer's disease. To cross the blood–brain barrier, studies have shown optimal particle diameters ranging from 5 to 200 nm.

we came to know that protecting fibril clumping may be utilized as an efficient access in identifying the upgradation of Alzheimer's disease. CPDs (generation 3 and 4) have anti-inflammatory features through blocking acetylcholine hydrolysis as well as occupying antioxidant characteristics (Figure 5) [7, 8].

2.4. Polymeric Nanoparticles. The size of polymeric nanomaterials are approximately 1 to 1000 nm as well as multipurpose and harmonious process. In comparison with other materials, polymers have singular combined form of features possessing those components to be utilized for different drug transportation appliances (Figure 5) [9, 10]. Additionally, nanocomponents can be synthesized both naturally and artificially from polymers. Polysaccharides, poly(ethylenimines), poly(alkyl cyanoacrylates), poly(methylidene malonates), and polyesters are examples of polymers utilized for transportation. Polybutylcyanoacrylate (PBCA) is the earliest polymer-dependent nanocomponents used to transport therapeutic materials to the CNS. These were formed through emulsion polymerization of polyalkylcyanoacrylates. As per this information, an opioid peptide named dalargin burdened PBCA nanomolecules were wrapped with polysorbate 80 (Tween80) and transported intravenously. The ultimate object of that was to get therapeutic steps of dalargin, residing in CNS, marking drug passes through BBB. Polysorbate 80 accelerates the power of penetrating of polymeric nanomolecules through the BBB. Nanocomponents, which stream through blood, are rapidly caught by reticuloendothelial process through opsonization. Inside the process of circulation, to increase the duration time of residing, there should be minimization of particle size/absorption of surfactants (polysorbate 80) on the surface that is operative, particularly, surfactant polysorbate 80.

2.5. Liposome. Liposomes are globules, with composition of one lipid bilayer, encompassed with an inward aqueous chamber (Figure 5) [11]. Liposomes incorporate with phos-

pholipids, and thus, unilamellar and multilamellar formations take place. There are some phenomenons, by which liposomes can be prepared like sonication, extrusion, reverse-phase evaporation, or high-pressure homogenization. The method of synthesis of liposome is simple. These have property of intense bioavailability, biocompatibility, and less poisonous. Additionally, these globules are capable of transporting such kind of drugs, which are hydrophilic, hydrophobic, and lipophilic in nature. The usage of liposome in the transportation process exhibits suitable features because of their rapid elevation by reticuloendothelial process. For increasing time of circulating, the globule size is reduced to tiny extent as well as surfaces are rectified by utilizing PEG. Liposomes trigger on $\alpha\beta$ peptides to hinder the synthesis of senile plaques. Even if, PEG-covered liposomes were active by utilizing anti $\alpha\beta$ monoclonal antibodies. Though the proper mechanism of penetrating peptide is unknown, yet, this establishment of these peptides raised penetrative power through the blood–brain barrier.

3. Diagnosis

The nanomaterial is also accepting growing focus for the treatment of AD. Nanomaterial are the nanostructural material that carries therapeutically active substance cross the BBB and have powerful target affinity and likely high effectiveness Therefore, he nanomaterial coupled to therapeutically active substance may be useful for monogenic disease like AD [12].

3.1. Nanotechnology in Diagnosis of AD. The recent focus in producing NPs for imaging and molecular tackling of biomarkers is the promise of accurate diagnosis of Alzheimer's disease. Nanotechnology allows for highly powerful signal transduction, which might aid in the early detection of Alzheimer's disease. The physical (magnetic, optical, or electrical), chemical, and/or biological quality of cleverly structured nanomolecules is the foundation for this possible application

of nanotechnology in imaging/diagnostic. Traditionally, the soluble biomarkers of Alzheimer's disease may be discovered using one of two methods. The first is relied on assessing the total amount of tau protein or $A\beta$ concentration in CSF or plasma. Because of the overlapping of such biological markers in general and disturbed people, this technique has produced some dubious results. Only hypothesized pathogenic biomarkers, such as phosphorylated tau protein, splitter tau protein, or $A\beta$ -derived diffusible ligands, are targeted in the second strategy (ADDL). Though this method yields more conclusive results, such pathogenic markers cannot be reliably assessed with traditional ELISA or western blotting tests because their quantities in CSF are extremely less in the previous stages of Alzheimer's disease [12, 13].

Nanodiagnostics for AD in in vitro is as follows:

- (1) Nanoparticle conjugates: DNA-NP clusters may detect protein biomarkers at extremely small molar concentrations, even as low as 10–18 moles per liter. This approach has demonstrated to be effective in detecting ADDL in CSF for in vitro AD diagnosis [14]
- (2) Localized surface plasmon resonance-based nanosensor (LSPR): when incoming light irradiates a solid material, the surface plasmon resonance (SPR) is a condition of resonant and collective oscillation of valence electrons. In all directions, photon absorption and emission occur with a same frequency. SPR events in several inorganic NPs make them useful for imaging and researchers can better applications in a variety of illnesses, including Alzheimer's disease. Many metallic NPs-based ultrasensitive and cost-effective approaches for detecting AD biomarkers such as ADDL have recently been developed based on the SPR effect [15]

Nanodiagnostics for AD in in vivo is as follows:

- (1) Magnetic resonance imaging (MRI): in recent decades, iron oxide nanoparticles (IONPs) as well as magnetic nanoparticles (MNPs) were extensively studied as MRI contrast agents. Monocrystalline IONPs with ultrasmall SIONPs have been studied as MRI probes by two different sets of scientists. The researchers used in vivo studies of $A\beta$ plaques in the brains of mice with Alzheimer's disease. Intravenously administered MRI enhancing agents (NPs) were deemed minimally intrusive [16]
- (2) Optical imaging (OI): optical imaging (OI) with a particular near-infrared (NIR) fluorescent dye is a new method being researched with in vivo studies of molecular biomarkers in many diseases, including Alzheimer's disease. The capacity of an imaging probe to penetrate the BBB and specificity to targeting AD linked biomarkers are two of the most prevalent requirements for an AD diagnostic inquiry. NIAD-4, a fluorescent dye that works in the NIR region, was proposed for in vivo molecular detection

of A. Because of its unusual structure and low molecular weight, it may quickly pass-through BBB [17]

3.2. *Treatment.* A nanomaterial is also accepting growing focus for the treatment of AD. The nanomaterial is a nanostructural material that carries therapeutically active substance across the BBB and has powerful target affinity and likely high effectiveness. Therefore, nanomaterial coupled to therapeutically active substance may be useful for monogenic disease like AD [18].

3.2.1. *Nanomaterial as Drug Carriers in AD.* The blood-brain barrier adjusts the access of polymer into the brain to ensure the CNS. These also hinder the movement of the drug inside the brain for possessing small diameter as well as elevated perceptibility; surface-modified nanostructures can be utilized as a conveyer for effectively bringing drugs to CNS. Nanodrug bringing procedures can naturalize the perception of drug molecules into the CNS and better their bioavailability in a particular brain region. This numerous nanocarriers have been altering to upgrade therapeutic with delayed extrication property and better efficiency, such as by generating polymers, emulsions, lipocarriers, carbon nanotubes, and metal-based carriers. Recyclable oxidized perforated silicon was used as a transporter to load. The nerve growth factor into the brain lowers cholinergic neuronal loss in AD. The liberation of NGF was delayed for over a month and its uninterrupted liberation. Inhibited AB-included cytotoxicity in differentiated PC12 cells. NGF-PSIO2 may therefore be potent carriers NGF that permit its continuity and sustain redemption while reserving bioactivity. Moreover, PSIO2 chips inserted above the dura mater for eight weeks do not show swelling or adverse effect, and biolistic bringing of PSIO2 microparticle enter the brain and reach to depth of 150 μm in the brain, purposing that recyclable PSIO2 transporters were a usable bringing process for NGF inside the brain [19, 20]. It combines with TiO_2 -nanowired cerebrolysin along with neprilysin and P-tau antibodies effectively augmented neuroconservancy in rat ideal of Alzheimer's disease. This shows better significant activity than cerebrolysin, neprilysin, and P-tau antibody (administrated merely). A surface-enhanced Raman scattering- (SERS-) relied sandwich assay by utilizing a combined form of monoclonal anti-tau-functionalized hybrid magnetic NPs and polyclonal anti-tau-immobilized gold NPs was particular for tau (collection through a simple magnet). The interrelation between tau concentration (25 fM to 500 nM) found as linear. In terms of susceptibility and tackling extent for tau protein identification, Gold NPS functionalized with tau-specific monoclonal antibodies and an oligonucleotide template for immuno-polymerase chain reaction (Nano-iPCR) seemed as auspicious. A cholinesterase inhibitor, donepezil (implicated with polylactide-co-glycolide (PLGA)) exhibits more brain accumulation than donepezil unaccompanied.

3.2.2. *Nanomaterial Targetting $\alpha\beta$ Accumulation.* The parnormal congestion of $\alpha\beta$ inside brain is nothing but a significant stamp for AD, and it influences alterations of AD

neuropathologically. So, it is a very necessary condition to search out drug, which can hinder $\alpha\beta$ congestion and minimize $\alpha\beta$ toxicology. Au-NPs wrapped with PAA (Au PAA) have been expressed to impact $\alpha\beta$ fibril accumulation in mice. If it is covered by insulin, there is hapazar situation in fibril arrangements shown. The duplex action PEG-PLA-NPs toned down with TGN and QSH specially aimed amyloid plaques with less neurotoxicity. For eradicating accumulated $\alpha\beta$ through the immune process, immune therapy utilizing nanotechnical is drawing deliberation. Zinc-filled nanomolecules are used to hinder synaptic minimization and prevent neuronal inflammation.

3.2.3. Nanomaterials Targeting Tau for AD Treatment. From the present research, it is known that tau channel belongs to a very potent therapeutic trigger because it is compactly assorted with clinical upliftment of AD impediments. An $\alpha\beta$ inhibitor (LK7) coupled and PEG-stagnant black phosphorus (BP) nanoprocess exhibit nice permanency and importantly increased preventive capacity with respect to $\alpha\beta$ 42 fibrillogenesis.

3.3. Future Perspective. The appliance of nanotechnology in Alzheimer's disease therapy is very much worthful. Though most of the research is still in preclinical level of study, it is expected that it could turn towards upgraded therapeutics and theragnostic results. There are so many advancing modernness simultaneously with nanotechnology-dependent procedures showing prospective in drug or bioparticles or transport of any agents across the BBB deliberate for Alzheimer's disease action. There are some technical proficiencies that accelerates the enhancement of nanoparticle mediated CNS transportation smoothly [21, 22].

3.4. Ultrasound-Mediated BBB Disruption. Focused ultrasound (FUS) enhances the penetrability of drugs and drug transporters across the BBB and thus nanoparticles intended in the brain. From the past several years, as per biomedical research in that specific field, brain cancer and Alzheimer's disease are being emphasized MRI influenced FUS individually for BBB disruption. Focused ultrasound blood-brain barrier disarrangement is majorly influenced by ultrasound context including amplitude of applied pressure, prevalence, duty circle, number of cycles per pulse, dose, and magnitude of microbubble [23]. Regulation of such measurements is not so easy because of disrupting of endothelium next to sonication regarding in vivo data. Enhancement of vascular penetrability across the tissue next to sonication space takes place because of interrelation of sonication and vasculature. Application of FUS shows better result in brain cancer treatment than Alzheimer's disease treatment. Hence, damage of BBB creates complications inward streaming of circulating components into the CNS would be neuronoxious, carrier malfunction, modified protein articulation, inflammatory action, oxidative force, and neuronal disruption. Here, it is distinct evidence that disrupted BBB turns into intensified Alzheimer's disease [24].

4. Direct Convection Therapy in Alzheimer's Disease

Convection-enhanced delivery (CED) is a system to transfer the various diagnostic/therapeutic substance straightly inside the brain along with BBB. Parenteral administration of different therapeutic components into the brain has been relied on diffusion hypothesis and relies on concentration gradient to get the better of prevention because of biological obstructions. The outcome of it is restricted transportation of delivered components, and drug permeates stay enclosed to several millimeters from the location of administration. Here, CED uses a fluid pressure gradient at the infusion catheter tip and bulk stream to circulate the components within extracellular fluid place. Nowadays, CED is being evaluated clinically in the eras of neurodegenerative diseases and neurooncology due to excess drug congregation over widened regions of aimed tissues in comparison to general injection manner of administration [25].

5. Conclusion

As there is swift progression of nanotechnology, nanocomponents display extreme efficiency in biomedicine because of their extraordinary biophysical characteristics. The combined form of nanotechnology as well as biomedicines supply new eras for the diagnosis and treatment procedure. From the research and various suitable information, we came to know that nanomolecules are capable of slowing the enhancement of Alzheimer's disease through different types of systems like functioning as drug transportation vehicles, preventing $\alpha\beta$ accumulation, raising $\alpha\beta$ demote, putting down tau accumulation, minimizing tau phosphorylation, and unburdening the oxidative pressure provoked $\alpha\beta$ accumulation [26]. Overall, the toxic nature of nanomolecules varies upon several factors such as materialistic neatness, molecular size, chemical construction, dose, accumulated state, and time of exposing. To increase focus efficiency, surface modifications and other procedures can be utilized. Such that contraindications can be minimized to civilize their appliances. Again, research, concentration, development, and investigations are highly required for looking at the new horizon of success in diagnosing as well as treatment of Alzheimer's disease. To reduce, to regulate, and to eradicate advance levelled research upon nanoparticles are needed abundantly.

Data Availability

All data used to support the findings of this study are included within the article.

Conflicts of Interest

The authors declare that they have no conflict of interest.

References

- [1] L. G. Apostolova, "Alzheimer disease," *Continuum: Lifelong Learning in Neurology*, vol. 22, no. 2 Dementia, pp. 419–434, 2016.
- [2] R. Mayeux and Y. Stern, "Epidemiology of Alzheimer disease," *Cold Spring Harbor Perspectives in Medicine*, vol. 2, no. 8, p. a006239, 2012.
- [3] A. Akter, F. Islam, S. Bepary et al., "CNS depressant activities of Averrhoa carambola leaves extract in thiopental-sodium model of Swiss albino mice: implication for neuro-modulatory properties," *Biologia*, vol. 77, no. 5, pp. 1337–1346, 2022.
- [4] A. Kumar, A. Singh, and Ekavali, "A review on Alzheimer's disease pathophysiology and its management: an update," *Pharmacological Reports*, vol. 67, no. 2, pp. 195–203, 2015.
- [5] H. Skaff and T. Emrick, *Nanoparticles: Building Blocks for Nanotechnology*, V. Rotello, Ed., Springer Science & Business Media, 2004.
- [6] K. K. Jain, "Nanomedicine: application of nanobiotechnology in medical practice," *Medical Principles and Practice*, vol. 17, no. 2, pp. 89–101, 2008.
- [7] M. Fischer and F. Vögtle, "Dendrimers: from design to application—a progress report," *Angewandte Chemie International Edition*, vol. 38, no. 7, pp. 884–905, 1999.
- [8] F. Islam, S. Mitra, M. H. Nafady et al., "Neuropharmacological and antidiabetic potential of *Lannea coromandelica* (Houtt.) Merr. leaves extract: an experimental analysis," *Evidence-Based Complementary and Alternative Medicine*, vol. 2022, 10 pages, 2022.
- [9] C. Vauthier and K. Bouchemal, "Methods for the preparation and manufacture of polymeric nanoparticles," *Pharmaceutical Research*, vol. 26, no. 5, pp. 1025–1058, 2009.
- [10] F. Islam, J. F. Khadija, M. Harun-Or-Rashid et al., "Bioactive compounds and their derivatives: an insight into prospective phytotherapeutic approach against Alzheimer's disease," *Oxidative Medicine and Cellular Longevity*, vol. 2022, 22 pages, 2022.
- [11] Y. Barenholz, "Liposome application: problems and prospects," *Current Opinion in Colloid & Interface Science*, vol. 6, no. 1, pp. 66–77, 2001.
- [12] M. Bilal, M. Barani, F. Sabir, A. Rahdar, and G. Z. Kyzas, "Nanomaterials for the treatment and diagnosis of Alzheimer's disease: an overview," *Nano Impact*, vol. 20, p. 100251, 2020.
- [13] S. Mitra, J. Anjum, M. Muni et al., "Exploring the journey of emodin as a potential neuroprotective agent: novel therapeutic insights with molecular mechanism of action," *Biomedicine & Pharmacotherapy*, vol. 149, p. 112877, 2022.
- [14] N. H. Khan, M. Mir, E. E. Ngowi et al., "Nanomedicine: A Promising way to manage Alzheimer's disease," *Frontiers in Bioengineering and Biotechnology*, vol. 9, p. 630055, 2021.
- [15] F. Islam, A. Akter, A. A. Mimi et al., "Neuropharmacological effects of *Chassalia curviflora* (Rubiaceae) leaves in Swiss albino mice model," *Archives of Razi Institute*, vol. 77, no. 2, pp. 881–890, 2022.
- [16] R. Singh and K. Kostarelos, "Designer adenoviruses for nanomedicine and nanodiagnosics," *Trends in Biotechnology*, vol. 27, no. 4, pp. 220–229, 2009.
- [17] M. Rahman, S. Majumder, F. Akter, F. Islam, M. Shahriar, and J. Alam, "Pre-clinical investigation of analgesic, anti-diarrheal and CNS depressant effect of *Pterocarpus indicus* in Swiss albino mice," *Jordan Journal of Pharmaceutical Sciences*, vol. 14, no. 1, 2021.
- [18] H. Zeng, Y. Qi, Z. Zhang, C. Liu, W. Peng, and Y. Zhang, "Nanomaterials toward the treatment of Alzheimer's disease: recent advances and future trends," *Chinese Chemical Letters*, vol. 32, no. 6, pp. 1857–1868, 2021.
- [19] Z. Yang, Y. Zhang, Y. Yang et al., "Pharmacological and toxicological target organelles and safe use of single-walled carbon nanotubes as drug carriers in treating Alzheimer disease," *Nanomedicine: Nanotechnology, Biology and Medicine*, vol. 6, no. 3, pp. 427–441, 2010.
- [20] J. Hou, X. Sun, Y. Huang et al., "The design and application of nanomaterials as drug carriers in cancer treatment," *Current Medicinal Chemistry*, vol. 27, no. 36, pp. 6112–6135, 2020.
- [21] A. Di Stefano, A. Iannitelli, S. Laserra, and P. Sozio, "Drug delivery strategies for Alzheimer's disease treatment," *Expert Opinion on Drug Delivery*, vol. 8, no. 5, pp. 581–603, 2011.
- [22] B. Wilson, M. K. Samanta, M. S. Muthu, and G. Vinothapooshan, "Design and evaluation of chitosan nanoparticles as novel drug carrier for the delivery of rivastigmine to treat Alzheimer's disease," *Therapeutic Delivery*, vol. 2, no. 5, pp. 599–609, 2011.
- [23] M. M. Rahman, F. Islam, M. A. Anwar Parvez, G. M. Ashraf, M. F. Ullah, and M. Ahmed, "Citrus limon L.(lemon) seed extract shows neuro-modulatory activity in an in vivo thiopental-sodium sleep model by reducing the sleep onset and enhancing the sleep duration," *Journal of Integrative Neuroscience*, vol. 21, no. 1, pp. 42–49, 2022.
- [24] Y. J. Lin, K. T. Chen, C. Y. Huang, and K. C. Wei, "Non-invasive focused ultrasound-based synergistic treatment of brain tumors," *Journal of Cancer Research and Practice*, vol. 3, no. 3, pp. 63–68, 2016.
- [25] S. Mitra, M. S. Lami, T. M. Uddin et al., "Prospective multi-functional roles and pharmacological potential of dietary flavonoid narirutin," *Biomedicine & Pharmacotherapy*, vol. 150, p. 112932, 2022.
- [26] A. Mietelska-Porowska, U. Wasik, M. Goras, A. Filipek, and G. Niewiadomska, "Tau protein modifications and interactions: their role in function and dysfunction," *International Journal of Molecular Sciences*, vol. 15, no. 3, pp. 4671–4713, 2014.

Research Article

Optimization and Prediction of Tribological Behaviour of Al-Fe-Si Alloy-Based Nanograin-Refined Composites Using Taguchi with Response Surface Methodology

S. Balaji,¹ P. Maniarasan,¹ S. V. Alagarsamy,² Abdullah M. Alswieleh,³ V. Mohanavel,^{4,5} M. Ravichandran,^{5,6} Byong-Hun Jeon,⁷ and Haiter Lenin Allasi⁸ 

¹Department of Aeronautical Engineering, Nehru Institute of Engineering and Technology, Coimbatore, 641 105 Tamil Nadu, India

²Department of Mechanical Engineering, Mahath Amma Institute of Engineering and Technology, Pudukkottai, 622 101 Tamil Nadu, India

³Department of Chemistry, College of Science, King Saud University, Riyadh 11451, Saudi Arabia

⁴Centre for Materials Engineering and Regenerative Medicine, Bharath Institute of Higher Education and Research, Selaiyur, Chennai, Tamil Nadu, 600073, India

⁵Department of Mechanical Engineering, Chandigarh University, Mohali, 140 413 Punjab, India

⁶Department of Mechanical Engineering, University Centre for Research & Development, Chandigarh University, Mohali, 140 413 Punjab, India

⁷Department of Earth Resources & Environmental Engineering, Hanyang University, 222-Wangsimni-ro, Seongdong-gu, Seoul 04763, Republic of Korea

⁸Department of Mechanical Engineering, WOLLO University, Kombolcha Institute of Technology, Kombolcha, Ethiopia

Correspondence should be addressed to Haiter Lenin Allasi; drahlenin@kiot.edu.et

Received 17 February 2022; Revised 30 March 2022; Accepted 4 April 2022; Published 25 May 2022

Academic Editor: Hiwa M. Ahmed

Copyright © 2022 S. Balaji et al. This is an open access article distributed under the Creative Commons Attribution License, which permits unrestricted use, distribution, and reproduction in any medium, provided the original work is properly cited.

Aluminium matrix composites (AMCs) are broadly used to change the monolithic materials in aviation, automotive, and defense industries owing to their superior characteristics such as specific strength with light weight, greater hardness, good wear resistance, and better thermal properties. This novel work was aimed at estimating the specific wear rate (SWR) of zirconium dioxide- (ZrO_2 -) filled AA8011 (Al-Fe-Si alloy) matrix composites. A Taguchi method and response surface methodology (RSM) were used to find out the optimum range of control parameters on SWR of proposed composites. The stir casting technique was used to fabricate the composite specimens with varying proportions (5, 10, and 15 wt.%) of ZrO_2 particle addition. The wear tests were performed as per L27 orthogonal design by using a pin-on-disk apparatus under dry conditions. For this test, four control parameters such as wt.% of ZrO_2 , load, disc velocity, and sliding distance each at three levels were selected. Based on the experimental results, 15 wt.% of ZrO_2 , 29.43 N of load, 0.94 m/s of disc velocity, and 1000 m of sliding distance provide the minimum SWR of the developed composite sample. ANOVA result revealed that the load (49.04%) was the primary dominant factor for affecting the SWR, followed by wt.% of ZrO_2 content (29.24%), respectively. Moreover, scanning electron microscopy (SEM) analysis was performed to study the wear mechanism of worn-out surface of the composite test specimens.

1. Introduction

In the past few decades, aluminium and its alloys are essential materials for fabrication of high recital parts in engineering applications like aerospace, automotive, and defense industries due to their excellent characteristics like specific

strength, light weight, high stiffness, good elastic modulus, and better thermal characteristics [1]. Among the many Al series alloys, Al-Fe-Si alloy has emerging material for various engineering structural applications owing to its unique characteristics such as high strength and hardness. However, these alloys have obtained very poor tribological properties.

TABLE 1: Chemical elements of AA8011.

Elements	Fe	Si	Mn	Cu	Zn	Ti	Mg	Cr	Al
Wt.%	1.0	0.9	0.20	0.10	0.10	0.08	0.05	0.05	Remain

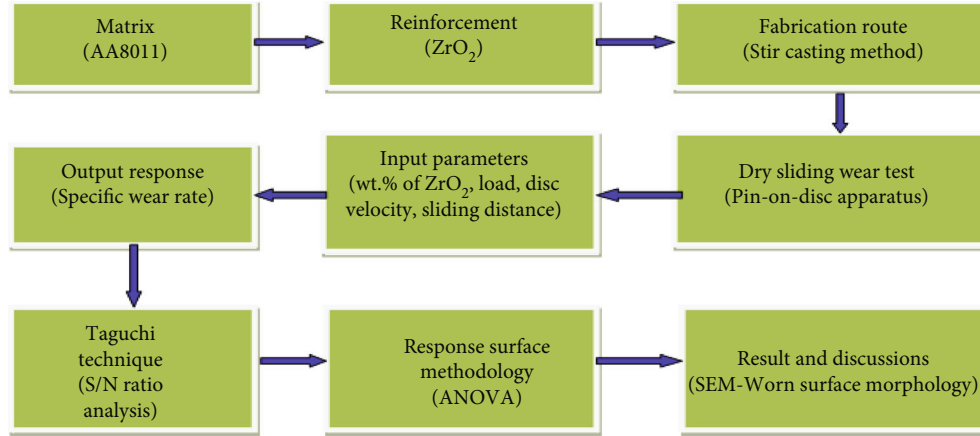


FIGURE 1: The layout of current investigation.

Hence, these alloys are made with self or hard ceramic particulates such as ZrO_2 [2], TiC [3], TiB_2 [4], Al_2O_3 [5], B_4C [6, 7], ZnO [8], Si_3N_4 [9], and Gr [10] to improve the tribological properties. The development of Al-based composites increases widespread in recent days because of it providing more wear resistance. Stir casting, powder metallurgy, infiltration, compo casting, etc., are commonly employed to develop the AMCs [11]. Among them, stir casting technique is most preferable due to their merits like simple and flexible; more economic and mass production can be achieved [12]. The limitation of the stir casting method is to obtain sufficient wetting of reinforcement particles by molten alloy and to get a homogeneous distribution of the particles and also to reduce the porosity. However, these are prohibited by proper utilization of casting process variables. They [13] fabricated AA7075 composites reinforced with TiO_2 particulates by liquid casting technique, and they reported that the properties of the developed AMCs drastically enhanced due to even allocation of reinforcement. They [14] conducted the wear test of Al- ZrO_2 composites under dry conditions and concluded that the wear resistance, improved gradually with an increasing ZrO_2 content. Generally, a variety of factors like load, disc velocity, lubricating medium, and sliding distance are controlling the wear rate of fabricated components. Therefore, selection of optimal parameters is more essential during the wear test. Optimization techniques like the Taguchi method and response surface method are most suitable for prediction of optimum wear control parameter level. The Taguchi method is one of the primary statistical technique which is applied in various areas such as design optimization, parameter selection, and prediction of output responses. It provides a simple, efficient, and systematic approach to optimize the wear control parameters. They [15] optimized the wear parameters of AMCs (356/ B_4C) using Taguchi technique. They observed that load was a predomi-

TABLE 2: Control parameters and its level.

Symbol	Control parameters	Unit	Level		
			1	2	3
A	% of ZrO_2	wt.%	5	10	15
B	Load	N	9.81	19.62	29.43
C	Disc velocity	m/s	0.94	1.88	3.76
D	Sliding distance	m	1000	1500	2000

nant factor trailed by sliding distance with contributions of 35% and 25%, respectively. This work [16] conducted the wear test for AA6062 using a pin-on-disk apparatus under dry conditions. The optimum level of parameters was determined by RSM coupled with desirability analysis. The SEM image of the worn surface reveals that abrasive wear mechanism was occurring. This work [17] optimized the wear control factors such as wt.% of reinforcement, load, sliding distance, and speed on wear resistance of AA7150- TiO_2 nanocomposites by employing the Taguchi method. They [18] presented the wear performance of SiC-Gr-filled AMCs, and they reported that a raise in load rises the wear of the fabricated composites. The author [19] considered the wear rate of nanosize of SiC particle-filled AMCs proposed by two-step stir casting route and reported that the dispersion of SiC_n (60.15%) content was the strongest impact factor, trailed by sliding distance (35.33%), respectively. The worn surface analysis shows that the formation of the oxide layers resists the metal removal from the pin surface, thus resulting in decreasing the wear. They [20] analyzed the tribological performances of ZrO_2 -reinforced Al7068 MMCs produced through liquid metallurgy route. They stated that 12 wt.% ZrO_2 composition addition drastically improves the tribological performances of the matrix alloy. They [21] explored the wear behavior of in situ AA8011- ZrB_2 MMCs using Taguchi-Grey analysis, and they

TABLE 3: L27 orthogonal array experimental layout.

Ex. no.	ZrO ₂ (wt.%)	Load (N)	Disc velocity (m/s)	Sliding distance (m)	SWR (mm ³ × 10 ⁻⁴ /Nm)	S/N ratio (dB)
1	5	9.81	0.94	1000	4.495	-13.055
2	5	9.81	1.88	1500	5.250	-14.403
3	5	9.81	3.76	2000	5.902	-15.420
4	5	19.62	0.94	1500	2.431	-7.716
5	5	19.62	1.88	2000	2.808	-8.968
6	5	19.62	3.76	1000	3.374	-10.563
7	5	29.43	0.94	2000	2.620	-8.366
8	5	29.43	1.88	1000	2.433	-7.723
9	5	29.43	3.76	1500	2.372	-7.502
10	10	9.81	0.94	1500	4.067	-12.185
11	10	9.81	1.88	2000	4.730	-13.497
12	10	9.81	3.76	1000	3.884	-11.786
13	10	19.62	0.94	2000	2.503	-7.969
14	10	19.62	1.88	1000	2.411	-7.644
15	10	19.62	3.76	1500	2.217	-6.915
16	10	29.43	0.94	1000	1.770	-4.959
17	10	29.43	1.88	1500	1.852	-5.353
18	10	29.43	3.76	2000	1.944	-5.774
19	15	9.81	0.94	2000	2.742	-8.761
20	15	9.81	1.88	1000	2.192	-6.817
21	15	9.81	3.76	1500	2.559	-8.161
22	15	19.62	0.94	1000	1.646	-4.329
23	15	19.62	1.88	1500	1.830	-5.249
24	15	19.62	3.76	2000	2.059	-6.273
25	15	29.43	0.94	1500	1.709	-4.655
26	15	29.43	1.88	2000	1.831	-5.254
27	15	29.43	3.76	1000	1.464	-3.311

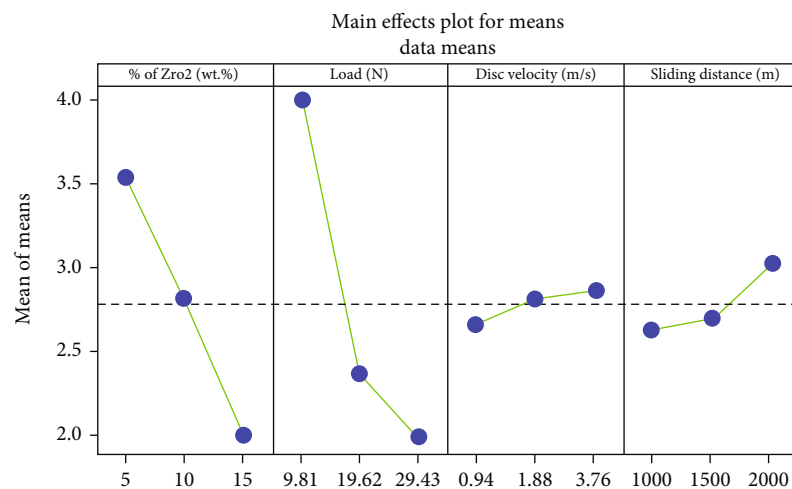


FIGURE 2: Main effect plot for means of SWR.

found that the load and sliding velocity are the most decisive factors among the others. This work [22] predicted the SWR of Al7075 composites incorporated with B₄C (8wt.%) and fly ash (2wt.%). The RSM was accomplished to create an

empirical model of SWR in terms of various input factors. The worn-out surface shows that the deep plowing grooves and fine debris exist which ensure the presence of plowing mechanism. They [23] studied the wear behavior of LM25

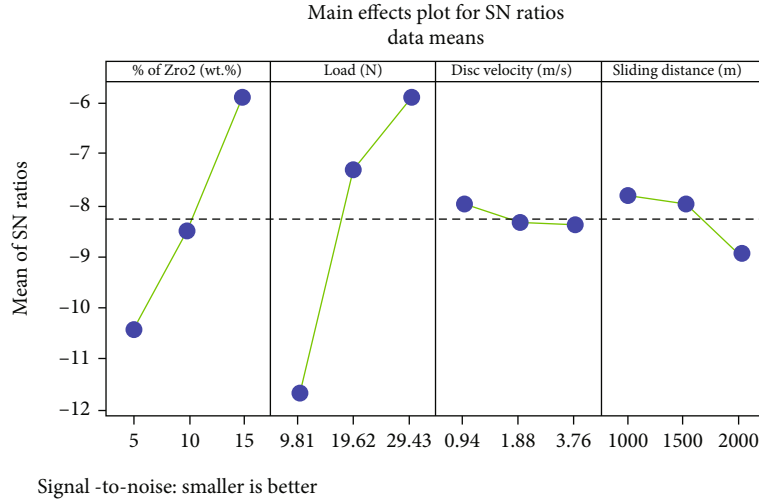


FIGURE 3: Main effect plot for S/N ratios of SWR.

matrix composites reinforced with varying proportions (3, 6, 9, 12, and 15 wt.%) of ZrO_2 particles. They reported that the WR decreases with an increase in the wt.% of ZrO_2 content.

From the detailed literatures, we had observed that the most research work has been studied on AA8011 with different reinforcements such as B_4C , Al_2O_3 , SiC, TiC, TiB_2 , Si_3N_4 , and graphite, but none of them attempted for AA8011 with ZrO_2 as reinforcement via stir casting route. Hence, the present work was aimed at analyzing the SWR of ZrO_2 -filled AA8011 matrix composites developed through stir casting route. An optimization technique such as the Taguchi method and RSM has been applied to find out the optimum conditions of factors on SWR of the fabricated composites.

2. Materials and Methods

In the current study, the matrix constituent was chosen as AA8011 (Al-Fe-Si alloy) received from Coimbatore Metal Mart, Coimbatore, India. Recently, AA8011-containing Al-Fe-Si alloy has emerging material in modern engineering applications such as aerospace, automotive, and defense industries where enhanced strength, hardness, and good wear resistance materials are enormously required. Table 1 provided the weight fraction of chemical elements present in the matrix alloy. Similarly, the reinforcement was used as zirconia (ZrO_2) particulates with a particle size of $10 \mu m$ received from LOBA Chemie, Mumbai, India. It has a density of $5.68 g/cm^3$, hardness of $1350 kg/mm^2$, Young's modulus of 250 GPa, and thermal conductivity of $2.7 W/m.K$, respectively. The stir casting technique adopted the production of AA8011 matrix composites by adding different weight fractions (5 wt.%, 10 wt.%, and 15 wt.%) of ZrO_2 particles. The layout of current investigation is illustrated in Figure 1.

Primarily, the required amount of AA8011 rod was stored into the crucible, and it was placed in the electric furnace. The furnace temperature was maintained at $750^\circ C$, till the entire alloy was melted. At the same time, the different weight percentages such as 5 wt.%, 10 wt.%, and 15 wt.% of

TABLE 4: Means table for SWR.

Level	A	B	C	D
1	3.521	3.980	2.665	2.630
2	2.820	2.364	2.815	2.699
3	2.004	1.999	2.864	3.015
Delta	1.517	1.981	0.199	0.386
Rank	2	1	4	3

TABLE 5: S/N ratios table for SWR.

Level	A	B	C	D
1	-10.413	-11.565	-7.999*	-7.798*
2	-8.454	-7.292	-8.323	-8.016
3	-5.868*	-5.877*	-8.412	-8.920
Delta	4.545	5.688	0.412	1.122
Rank	2	1	4	3

*Optimum level.

ZrO_2 particles were preheated at $300^\circ C$ [12] to promote the dry condition and proper wettability with the molten metal. After that, the ZrO_2 particles were slowly fed into the slurry of molten alloy. Meanwhile, the composite slurry was stirred at a speed of 300 rpm about 10 min [13]. Then, the slurry was poured into the mould, and it was permitted to solidify at normal air temperature. After solidification, the composites were taken out from the mould, and the required test specimens were prepared.

After getting the composite specimen, the wear test was executed according to ASTM G-99 standard by TR-20 DUCOM pin-on-disk tribometer. The wear test pins' size of $10 mm \times 10 mm \times 30 mm$ was prepared by wire cut EDM. During the wear test, the test pins were pushed on the EN-31 steel counter disc with 60 HR_C hardness. To achieve the clean surface, the test specimen and the counter disc were polished using fine emery sheet and also cleaned by the

TABLE 6: ANOVA table for SWR.

Source	Adj SS	Dof	Adj MS	F-value	P value
Model	34.84	14	2.49	21.27	<0.0001
A-% of ZrO ₂	10.60	1	10.60	90.62	<0.0001
B-load	17.78	1	17.78	151.97	<0.0001
C-disc velocity	0.1784	1	0.1784	1.52	0.2405
D-sliding distance	0.6495	1	0.6495	5.55	0.0363
AB	2.68	1	2.68	22.94	0.0004
AC	0.2506	1	0.2506	2.14	0.1690
AD	0.0227	1	0.0227	0.1937	0.6677
BC	0.1555	1	0.1555	1.33	0.2714
BD	0.2591	1	0.2591	2.21	0.1625
CD	0.0012	1	0.0012	0.0099	0.9223
A ²	0.0200	1	0.0200	0.1709	0.6866
B ²	2.35	1	2.35	20.06	0.0008
C ²	0.0409	1	0.0409	0.3496	0.5653
D ²	0.0924	1	0.0924	0.7900	0.3916
Residual	1.40	12	0.1170		
Cor total	36.25	26		R ²	0.9613
Std. Dev.	0.3420			Adjusted R ²	0.9161
Mean	2.78			Predicted R ²	0.7769
C.V. %	12.30			Adeq precision	17.6566

acetone solution. Usually, there are many control parameters involved to conduct the wear test. Based on the earlier studies [13], we have considered four parameters with three levels such as wt.% of ZrO₂ (A), load (B), disc velocity (C), and sliding distance (D), respectively. Based on the parameters and its levels (Table 2), Taguchi L₂₇ orthogonal design was formulated to perform the wear tests. After the tests, the SWR of tested composite specimens is determined by using

$$\text{SWR}(\text{mm}^3/\text{Nm}) = \frac{\Delta m/\rho}{L \times D}, \quad (1)$$

where Δm is the mass loss of test pin (g), ρ is the density of the fabricated composite (g/mm³), L is the load (N), and D is the sliding distance (m). The estimated SWR for each experiment is provided in Table 3.

3. Optimization Methodologies

3.1. Taguchi Method. The Taguchi method is a reliable statistical approach which can be employed to find out the permissible range of parameter conditions with minimum experimental trials performed. The intend of this method is used to make high-quality product with minimum cost [24]. For applying this method, suitable orthogonal array design is formulated based on the quantity of input factors and its levels concerned. Notably, three arithmetic S/N ratio equations can be used to determine the response such as smaller is better, nominal is best, and larger is better, respectively [25]. Here, the objective of this study is to identify the

optimal control factors on SWR while dry sliding process of AA8011-ZrO₂ composites. To compute the S/N ratio for the SWR, smaller the better arithmetic S/N ratio equation can be used and it was provided in

$$\text{S/Nratio} = -10 \log_{10}(1/n) \sum_{k=1}^n Y_{ij}^2, \quad (2)$$

where n is the no. of trials and Y_{ij} is the response, where $i = 1, 2, 3 \dots n$ and $j = 1, 2, 3 \dots k$. The calculated S/N ratios for the SWR are given in Table 3.

3.2. Response Surface Method. RSM is a powerful and advanced mathematical tool. The main goal of this method is to determine the impact of independent factors on the dependent responses clearly represented by theoretically developed model [26]. In this study, we had employed to predict the SWR and how it is dominated by the independent control factors including wt.% ZrO₂ (A), load (B), disc velocity (C), and sliding distance (D), respectively, by using the “design expert version 12” software, to create an empirical model of SWR in terms of control parameters. To explicate the mathematical appropriate relation between the input factors and SWR, the second-order polynomial regression equation was proposed.

$$Y = \beta_0 + \sum_{i=1}^k \beta_i X_i + \sum_{i=1}^k \beta_{ii} X_i^2 + \sum_{i<j}^k \beta_{ij} X_i X_j + \varepsilon. \quad (3)$$

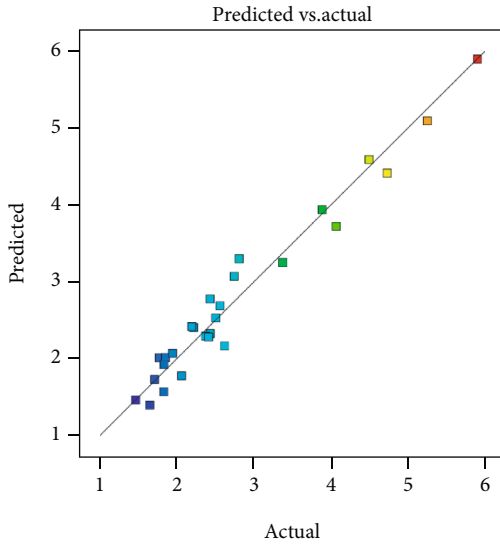


FIGURE 4: Predicted vs. actual plot for SWR.

Here, β_0 is constant, β_i is the linear terms, β_{ii} is the quadratic terms, β_{ij} is the interaction terms, and X_i and X_j are the levels of input parameters, respectively.

4. Results and Discussion

4.1. S/N Ratio Analysis. Figures 2 and 3 reveals the main effect plots for mean and S/N ratio on the SWR with each level of control parameters, namely, wt.% of ZrO_2 , load, disc velocity, and sliding distance. In Figure 2, it is seen that the SWR is gradually decreased with an increasing trend of ZrO_2 content. The reason is that the inclusion of ceramic (ZrO_2) particulates improved the hardness of the fabricated composites, which result in reduced the SWR. From Figure 3, it can be proved that the higher S/N ratio is nearer to the optimum conditions. Hence, the less SWR is produced at the optimum level parameters $A_3B_3C_1D_1$, represented as wt.% of ZrO_2 at 15 wt.%, load at 29.43 N, disc velocity of 0.94 m/s, and sliding distance at 1000 m. Tables 4 and 5 depicted the response table for means and S/N ratio of SWR. It was revealed that the order of impact parameters on response is represented as rank 1, 2, ..., etc. Normally, the rank 1 is assigned as most significant parameter followed by others. Based on Tables 4 and 5, it can be understood that the load has been identified as rank 1 which is more influencing parameter on SWR, subsequently by wt.% of ZrO_2 , sliding distance, and disc velocity, respectively. The SWR is directly proportional to the load applied, which is obeyed by Archard's law. Hence, the SWR increases with increasing applied load due to more contact pressure between the surfaces. The similar observations were previously reported [27].

4.2. Analysis of Variance (ANOVA). ANOVA is a collection of statistical approach used to decide the noteworthy parameters on the responses under the group of process parameters [28]. The purpose of the current investigation is to

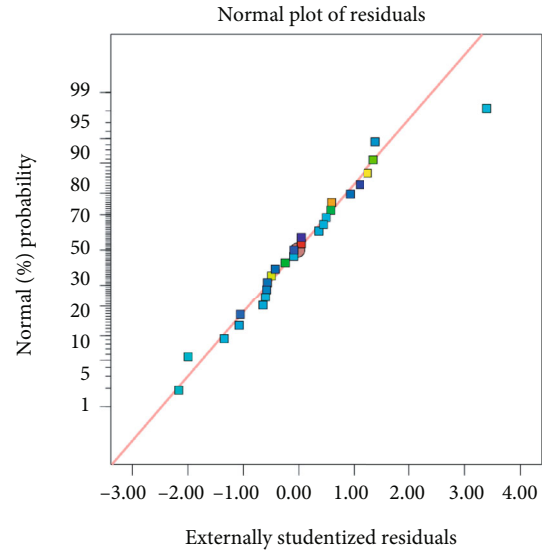


FIGURE 5: Normal probability plot for SWR.

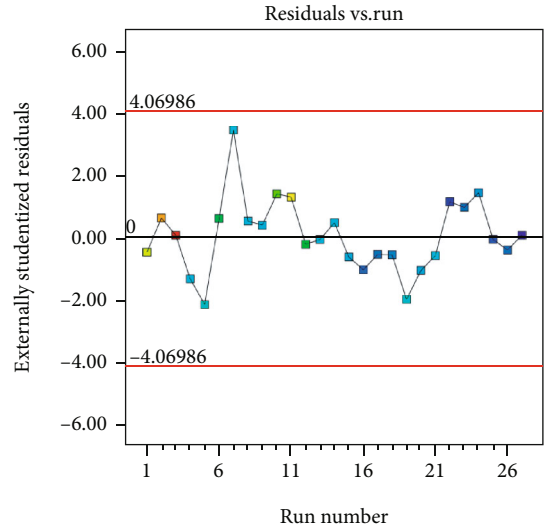


FIGURE 6: Residual vs. run plot for SWR.

identify the impact of control parameters including wt.% ZrO_2 (A), load (B), disc velocity (C), and sliding distance (D) on SWR during dry sliding wear test. ANOVA result of SWR is presented in Table 6. In order to find the noteworthy effect of parameters on SWR, the F -ratio and P value (Table 6) are considered at 95% CI and 5% significant level. The F -value of 21.27 indicates that the developed empirical model is significant, as seen in Table 5. Similarly, the developed model terms are significant which ensured by the P value (<0.0001). It has also been found that the terms A, B, D, AB, and B^2 are considered as the important (most dominant) factors on the SWR. Usually, the R^2 is used to determine the fitness of the empirical model. For current analysis, R^2 value is 0.9613 and adjusted R^2 value is 0.9161 which shows the greater significance of the model. Hence, there is also a well concurrence between the predicted and the adjusted R^2 value.

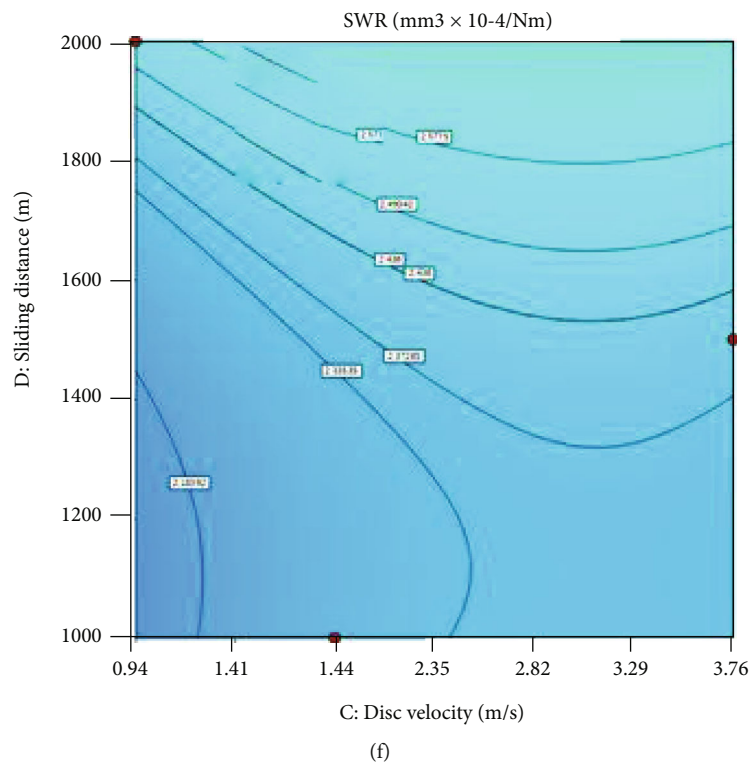
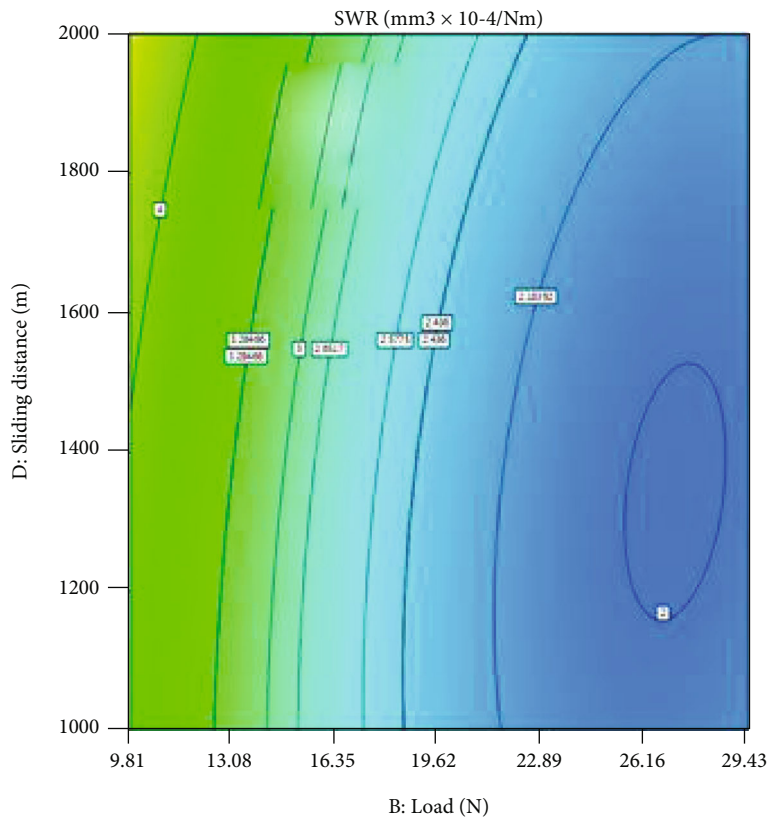


FIGURE 7: (a-f) Contour plots for SWR with respect to control parameters.

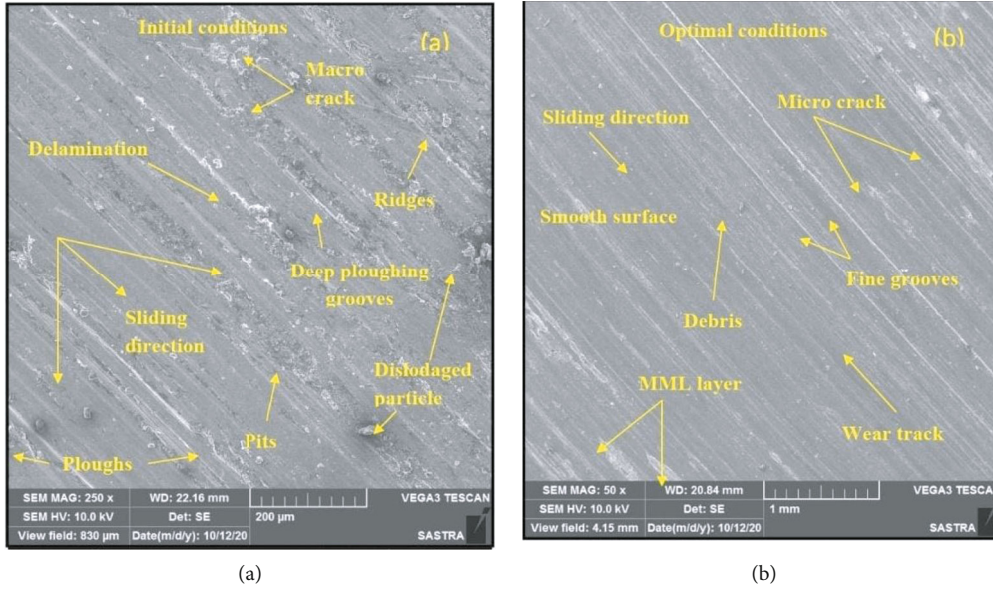


FIGURE 8: SEM images of the worn-out surface (a) at initial conditions and (b) at optimal conditions.

The mathematical relations for the SWR in terms of coded and actual factors are given in

$$\begin{aligned} \text{SWR} = & +2.40 - 0.7745A - 1.00B + 0.0996C + 0.1917D \\ & + 0.4794AB - 0.1438AC + 0.0441AD - 0.1133BC \\ & - 0.1489BD - 0.0098CD - 0.0577A^2 + 0.6254B^2 \\ & + 0.0946C^2 + 0.1241D^2, \end{aligned} \quad (4)$$

$$\begin{aligned} \text{SWR} = & +8.718 - 0.2789A - 0.3901B + 0.6798C \\ & - 0.0006D + 0.0097AB + 0.0204AC \\ & + 0.000018AD - 0.008192BC - 0.000030BD \\ & - 0.000014CD - 0.002309A^2 + 0.006499B^2 \\ & - 0.047575C^2 + 4.964E^{-7}D^2. \end{aligned} \quad (5)$$

Figure 4 displays the predicted and actual values of SWR. It clearly understood that the predicted values are reasonably closer to the experimental values. Figure 5 shows the probability vs. externally studentized residual plot of the SWR. It can be ensured that the residuals are evenly located along a straight line, which confirms that the developed model is fitted. The externally studentized residual with experiment order is shown in Figure 6. From the plot, the experiment number 7 provided the high residual value among the others.

4.3. Interaction Effect of Parameters on SWR. Figure 7 illustrates the 2D surface plots for SWR with related to the control parameters. The main purpose of surface plot is used to reveal the interaction effect of parameters on the response. Figures 7(a)–7(c) illustrate the interaction of reinforcement on SWR of developed composites with respect to other parameters like load (B), disc velocity (C), and sliding distance (D). It can be revealed that the SWR gradually increases with increasing the weight.% of ZrO₂ particles.

By considering the load (B), SWR is less for AA8011-15 wt.% of ZrO₂ composite with maximum load condition. The middle level of disc velocity (C) produces low SWR for 15 wt.% of ZrO₂ composite. By considering the sliding distance (D), the higher SWR is produced at higher levels of sliding distance (2000 m) with low weight.% of ZrO₂ content. Figures 7(d) and 7(e) show the interaction of load (B) with disc velocity (C) and sliding distance (D) on SWR. SWR increases with an increasing trend of disc velocity at low level of load (9.81 N). However, the low SWR of $2 \text{ mm}^3 \times 10^{-4} / \text{Nm}$ is obtained at 29.43 N of load with the middle level of disc velocity. From Figure 7(e), it can be observed that the high SWR of $4 \text{ mm}^3 \times 10^{-4} / \text{Nm}$ is produced at a maximum sliding distance of 2000 m with initial load of 9.81 N. The effects of disc velocity (C) and sliding distance (D) on SWR is shown in Figure 7 (f). It can be clearly revealed that the SWR steadily increases with an increase in the sliding distance at middle level of disc velocity 1.88 m/s. But, the less SWR $2.18 \text{ mm}^3 \times 10^{-4} / \text{Nm}$ is attained at 0.94 m/s disc velocity and 1000 m sliding distance, respectively.

4.4. Worn Surface Morphology. The SEM morphology of the worn-out surface of developed AA8011-ZrO₂ composite specimens tested at various conditions of control parameters is illustrated in Figures 8(a) and 8(b). From the figure, the presence of mechanisms in the worn surfaces was exactly noticed.

Figure 8(a) depicts the worn-out surface of the initial test conditions including 5 wt.% of ZrO₂-filled composite at a load of 9.81 N, disc velocity of 0.94 m/s, and sliding distance of 1000 m, respectively. It shows the presence of deep ploughing grooves, delamination, some pits, and macrocrack on the worn-out surface. The asperities of the counter disc generated deep ploughing grooves while sliding, resulting in the formation of ridges. The dislodged particles existence in some region due to the repetitive sliding action and also

some debris removed from the ridges. Due to the removal of reinforcement (ZrO_2) particles, some pits are formed in the worn-out surface. This causes the abrasive mechanism involved. The worn-out surface of the optimal test conditions of 15 wt.% of ZrO_2 -dispersed composite at a load of 29.43 N, disc velocity of 0.94 m/s, and sliding distance of 1000 m is shown in Figure 8(b). It obviously revealed the presence of the smooth surface as well as fine grooves on the worn-out surface. The reason is behind that is that the dispersion of higher amount of ZrO_2 (15 wt.%) particles improves the surface hardness among the other composites, thus will reduce the SWR. Due to higher load (29.43 N) conditions, the microcrack exists in a few regions on the surface. However, the mechanical mixed layer (MML) is formed due to transfer of materials between the counterpart and pin surface which causes reduced the SWR.

5. Conclusions

This work investigated the effects of control parameters on SWR of zirconia- (ZrO_2 -) filled AA8011 composites under dry sliding conditions. The given observations were obtained in this study:

- (i) The various weight fractions (5, 10, and 15 wt.%) of ZrO_2 particle were incorporated with AA8011 matrix composites through stir casting route. A pin-on-disk machine was used to conduct the wear tests under dry conditions
- (ii) A Taguchi technique was applied to identify the optimal control parameters on SWR of proposed composites. Based on the main effect plot, the less SWR is obtained at 15 wt.% of ZrO_2 , 29.43 N of load, 0.94 m/s of disc velocity, and 1000 m of sliding distance
- (iii) RSM-based ANOVA result revealed that the load has been considered as the more influencing parameter on SWR, followed by wt.% of ZrO_2 content with percentage contributions of 49% and 29.24%, respectively
- (iv) SWR drastically minimizes when there is an increasing trend of ZrO_2 particles within the matrix alloy. The reason is behind that is that the inclusions of ceramic content improved the hardness, thus reducing the SWR of the developed composite
- (v) The SEM micrograph of the worn-out surface reveals the presence of deep grooves, plugs, and cracks on the surface of the initial parametric conditions. However, at optimal parametric conditions, the fine grooves and smooth surface are formed due to higher amount (15 wt.%) of ZrO_2 addition that creates the MML layer, thus reducing the SWR
- (vi) In the future, other optimization techniques such as fuzzy logic and artificial neural network and machine learning approaches can be used to predict the SWR of the developed composites

Data Availability

The data used to support the findings of this study are included within the article. Further data or information is available from the corresponding author upon request.

Conflicts of Interest

The authors declare that there are no conflicts of interest regarding the publication of this paper.

Acknowledgments

The authors appreciate the support from the Wollo University, Kombolcha Institute of Technology, Ethiopia, for the research and preparation of the manuscript. The authors would like to acknowledge the Researchers Supporting Project number (RSP-2021/238), King Saud University, Riyadh, Saudi Arabia.





References

- [1] V. Mohanavel, K. Rajan, and M. Ravichandran, "Synthesis, characterization and properties of stir cast AA6351-aluminium nitride (AlN) composites," *Journal of Materials Research*, vol. 31, no. 24, pp. 3824–3831, 2016.
- [2] H. Ghandvar, S. Farahany, M. H. Idris, and M. Daroonparvar, "Dry sliding wear behavior of A356-ZrO₂ metal matrix composite," *Advanced Materials Research*, vol. 1125, pp. 116–120, 2015.
- [3] S. Baskaran, V. Anandkrishnan, and M. Duraiselvam, "Investigations on dry sliding wear behavior of in situ casted AA7075-TiC metal matrix composites by using Taguchi technique," *Materials and Design*, vol. 60, pp. 184–192, 2014.
- [4] V. Mohanavel, "Mechanical and microstructural characterization of AA7178-TiB₂ composites," *Materials Testing*, vol. 62, no. 2, pp. 146–150, 2020.
- [5] S. Sakthivelu, P. P. Sethusundaram, M. Ravichandran, and M. Meignanamoorthy, "Experimental investigation and analysis of properties and dry sliding wear behavior of Al-Fe-Si alloy matrix composites," *Silicon*, vol. 13, pp. 1285–1294, 2021.
- [6] J. A. Jeffrey, S. S. Kumar, V. A. Roseline, A. L. Mary, and D. Santhosh, "Contriving and assessment of magnesium alloy composites augmented with boron carbide VIA liquid metallurgy route," *Materials Science Forum*, vol. 1048, pp. 3–8, 2022.
- [7] R. Suresh, "Comparative study on dry sliding wear behavior of mono (Al₂₂₁₉/B₄C) and hybrid (Al₂₂₁₉/B₄C/Gr) metal matrix composites using statistical technique," *Journal of the Mechanical Behavior of Materials*, vol. 29, no. 1, pp. 57–68, 2020.
- [8] M. I. U. Haq and A. Anand, "Dry sliding friction and wear behavior of AA7075-Si₃N₄ composite," *Silicon*, vol. 10, pp. 1819–1829, 2018.
- [9] S. V. Alagarsamy, R. Balasundaram, M. Ravichandran, V. Mohanavel, A. Karthick, and S. S. Devi, "Taguchi approach and decision tree algorithm for prediction of wear rate in zinc oxide-filled AA7075 matrix composites," *Surface Topography*, vol. 9, pp. 1–15, 2021.
- [10] N. Radhika, R. Subramanian, S. V. Prasat, and B. Anandavel, "Dry sliding wear behaviour of aluminium/alumina/graphite

- hybrid metal matrix composites," *Industrial Lubrication and Tribology*, vol. 64, pp. 356–366, 2021.
- [11] B. S. Yigezu, P. K. Jha, and M. M. Mahapatra, "The key attributes of synthesizing ceramic particulate reinforced Al-based matrix composites through stir casting process: a review," *Materials and Manufacturing Processes*, vol. 28, pp. 969–979, 2013.
- [12] S. Balaji, P. Maniarasan, S. V. Alagarsamy, and P. Raveendran, "Dry sliding wear behaviour of aluminium metal matrix composite using response surface methodology," *Materials Today: Proceedings*, vol. 2021, 2021.
- [13] S. V. Alagarsamy and M. Ravichandran, "Parametric studies on dry sliding wear behaviour of Al-7075 alloy matrix composite using S/N ratio and ANOVA analysis," *Materials Research Express*, vol. 7, pp. 1–17, 2020.
- [14] M. Ramachandra, A. Abhishek, P. Siddeshwar, and V. Bharathi, "Hardness and wear resistance of ZrO₂ nano particle reinforced Al nano composites produced by powder metallurgy," *Procedia Materials Science*, vol. 10, pp. 212–219, 2015.
- [15] J. Udaya Prakash, S. Jebarose Juliyana, M. Saleem, and T. V. Moorthy, "Optimization of dry sliding wear parameters of aluminium matrix composites (356/B₄C) using Taguchi technique," *International Journal of Ambient Energy*, vol. 42, no. 2, pp. 140–142, 2018.
- [16] K. Gajalakshmi, N. Senthilkumar, and B. Prabu, "Multi-response optimization of dry sliding wear parameters of AA6026 using hybrid gray relational analysis coupled with response surface method," *Measurement and Control*, vol. 52, no. 5–6, pp. 540–553, 2019.
- [17] P. Madhukar, N. Selvaraj, V. Mishra, and C. S. P. Rao, "Optimization of wear parameters of AA7150-TiC nanocomposites by Taguchi technique," *Numerical Optimization in Engineering and Sciences*, vol. 979, pp. 543–550, 2020.
- [18] A. G. Joshi, M. Manjaiah, S. Basavarajappa, and R. Suresh, "Wear performance optimization of SiC-Gr reinforced Al hybrid metal matrix composites using integrated regression-antlion algorithm," *Silicon*, vol. 13, no. 11, pp. 3941–3951, 2020.
- [19] M. T. Alam, S. Arif, A. H. Ansari, and M. N. Alam, "Optimization of wear behaviour using Taguchi and ANN of fabricated aluminium matrix nanocomposites by two-step stir casting," *Materials Research Express*, vol. 6, no. 6, pp. 1–10, 2019.
- [20] M. Madhusudhan and K. Mahesha, "Taguchi based validation of wear prediction for Zirconium dioxide particulate reinforced aluminium 7068 composites," *International Journal of Metallurgy and Alloys*, vol. 4, no. 1, pp. 37–50, 2018.
- [21] B. M. MuthamizhSelvan, V. Anandkrishnan, M. Duraiselvam, R. Venkatraman, and S. Sathish, "Multi objective optimization of wear behaviour of in situ AA8011-ZrB₂ metal matrix composites by using Taguchi-grey analysis," *Materials Science Forum*, vol. 928, pp. 162–167, 2018.
- [22] M. K. Sahu and R. K. Sahu, "Experimental investigation, modeling, and optimization of wear parameters of B₄C and Fly-ash reinforced aluminum hybrid composite," *Frontiers of Physics*, vol. 8, p. 219, 2020.
- [23] G. Karthikeyan and G. Jinu, "Dry sliding wear behaviour of stir cast LM25/ZrO₂ metal matrix composites," *Transactions of Famena*, vol. 4, pp. 89–98, 2015.
- [24] C. Chanakyan, S. Sivasankar, M. Meignanamoorthy, and S. V. Alagarsamy, "Parametric optimization of mechanical properties via FSW on AA5052 using Taguchi based grey relational analysis," *Incas Bulletin*, vol. 13, no. 2, pp. 21–30, 2021.
- [25] P. Raveendran, S. V. Alagarsamy, M. Ravichandran, and M. Meignanamoorthy, "Effect of machining parameters on surface roughness for aluminium matrix composite by using Taguchi method with decision tree algorithm," *Surface Review and Letters*, vol. 28, no. 4, article 2150021, 2021.
- [26] S. V. Alagarsamy, M. Ravichandran, and H. Saravanan, "Development of mathematical model for predicting the electric erosion behaviour of TiO₂ filled Al-Zn-Mg-Cu (AA7075) alloy composite using RSM-DFA method," *Journal of Advanced Manufacturing Systems*, vol. 20, no. 1, pp. 1–26, 2021.
- [27] S. V. Alagarsamy and M. Ravichandran, "Investigations on tribological behaviour of AA7075-TiO₂ composites under dry sliding conditions," *Industrial Lubrication and Tribology*, vol. 71, pp. 1064–1071, 2019.
- [28] V. Mohanavel, S. Prasath, K. Yoganandam, B. G. Tesemma, and S. S. Kumar, "Optimization of wear parameters of aluminium composites (AA7150/10 wt%WC) employing Taguchi approach," *Materials Today: Proceedings*, vol. 33, pp. 4742–4745, 2020.

Research Article

Optimization of WEDM Process Parameters in Al2024-Li-Si₃N₄ MMC

K. Raju ¹, **M. Balakrishnan** ¹, **D. V. S. S. V. Prasad**,² **V. Nagalakshmi**,³ **Pravin P. Patil**,⁴ **S. Kaliappan**,⁵ **B. Arulmurugan** ⁶, **K. Radhakrishnan**,⁷ **B. Velusamy**,⁸ **Prabhu Paramasivam** ⁹, and **A. El-Denglawey**¹⁰

¹M. Kumarasamy College of Engineering, Karur, Tamilnadu, India

²Department of Mechanical Engineering, Aditya College of Engineering, Surampalem, Andhra Pradesh 533437, India

³Department of Chemistry, Ch.S.D. St. Theresa's College for Women (A), West Godavari district, Eluru, Andhra Pradesh 534003, India

⁴Department of Mechanical Engineering, Graphic Era Deemed to be University, Dehradun, Uttarakhand 248002, India

⁵Department of Mechanical Engineering, Velammal Institute of Technology, Chennai, 601204 Tamil Nadu, India

⁶Department of Mechanical Engineering, KPR Institute of Engineering and Technology, Coimbatore, Tamilnadu, India

⁷Department of Mechanical Engineering, K. Ramakrishnan College of Technology, Samayapuram, Trichy, India

⁸Department of Mechanical Engineering, K. Ramakrishnan College of Engineering, Samayapuram, Trichy, India

⁹Department of Mechanical Engineering, College of Engineering and Technology, Mettu University, Metu, Ethiopia

¹⁰Department of Physics, College of University College at Turabah, Taif University, P.O. Box 11099 Taif 21944, Saudi Arabia

Correspondence should be addressed to Prabhu Paramasivam; drprabhu@meu.edu.et

Received 28 February 2022; Revised 8 April 2022; Accepted 11 April 2022; Published 21 May 2022

Academic Editor: Arpita Roy

Copyright © 2022 K. Raju et al. This is an open access article distributed under the Creative Commons Attribution License, which permits unrestricted use, distribution, and reproduction in any medium, provided the original work is properly cited.

The present study focuses on optimization of operating parameters in wire electric discharge machining of AA2024 aluminium alloy reinforced with lithium and silicon nitride particles. Aluminium composite was produced through the two-step stir casting route with the combination of 2% lithium and 10% silicon nitride reinforcements. Experiments were performed using the Taguchi design of experiments to optimize the selected input parameters such as pulse on time, pulse off time, current and wire feed for the response parameter, material removal rate, and surface roughness. An ANOVA-based regression equation with genetic algorithm was used to optimize the input variables. The gray relational grade was also performed to optimize multiple performance characteristics. Taguchi-based optimization analysis results in wire feed as the domination factor for material removal rate and surface roughness. Increased wire feed increases the material removal rate with good surface finish as confirmed from gray relational grade analysis. Regression equation generated results with minimum error (<2%) proving the accuracy of the investigation. A genetic algorithm-based study also confirms the analysis of Taguchi and gray relational grade. The wire feed rate at 3 m/min and pulse on time of 120 microseconds were found to be similar for material removal rate and surface finish. Current at 50 A increases the material removal rate and current at 30 A results in good surface finish.

1. Introduction

Advanced composite materials with high strength, high hardness, and light weight finds applications in defense, space craft, and engineering industries [1]. Aluminium composites with SiO₂, SiC, B₄C, and TiB₂ reinforcements has shown remarkable improvements in terms of microstructural, mechanical,

and thermal properties. Silica added composite reveals good fluidity with lower stiffness values. Increased heat transfer and wear resistance with better mechanical properties were noticed for the addition of silicon with the aluminium matrix [2, 3]. Machining of such composite materials is difficult in conventional machines and need focus on nonconventional techniques for good surface finish with accuracy. Wire



FIGURE 1: Prepared specimens for wire electrical discharge machining.



FIGURE 2: Photograph of Electronica sprint cut CNC wire-cut electrical discharge machine.

electrical discharge machining (WEDM) has shown effective machining methods for composite materials [1, 4]. This machining needs input parameters which are classified as electrical and nonelectrical. The major electrical inputs are current (A), voltage (V), pulse on time (Ton), and pulse off time (Toff). The wire material, wire size, wire feed rate, and dielectric medium are used as nonelectrical input parameters. The major output parameters for optimization are the material removal rate (MRR) and surface roughness (R_a) [5, 6]. The response surface methodology- (RSM-) based Box-Behnken design was used to analyze the output response for surface roughness of aluminium-reinforced silicon carbide (SiC) particles machining using WEDM [7]. Investigation on machining of SiC-reinforced aluminium alloy 2024 composite was carried out and reports suggested that surface roughness is increased for increased pulse on time, and MRR is increased when increasing the pulse on time and peak current [8]. Machining of aluminium 7178 reinforced with 10 wt% ZrB₂ composite was made using the Taguchi-based gray rational analysis (GRA) technique. The L16 orthogonal array was used to optimize MRR and R_a with four parameters at four levels. The result showed that the peak current and pulse on time are the influencing parameters for higher MRR and better [9]. The Box-Behnken design with RSM was used to analyze the machining parameters where the increase in pulse on time decreases the surface roughness [10]. In WEDM of Al 6063

TABLE 1: Selected input parameters and its levels.

Factors	Symbol	Unit	Parameter levels		
			Level 1	Level 2	Level 3
Current	I	A	30	40	50
Wire feed	Wf	m/min	1	2	3
Pulse on time	Ton	μ s	110	120	130

TABLE 2: Response values as per L9 design matrix.

Exp.no	Input parameters			Output parameters		Standard deviation	
	I	Wf	Ton	MRR	R_a	MRR	R_a
1	30	1	110	0.09	3.217	0.02	1.13
2	30	2	120	0.11	2.924	0.01	1.12
3	30	3	130	0.12	2.668	0.02	1.11
4	40	1	120	0.11	3.425	0.02	1.12
5	40	2	130	0.11	3.182	0.01	1.12
6	40	3	110	0.13	2.781	0.01	1.11
7	50	1	130	0.12	3.544	0.02	1.13
8	50	2	110	0.13	3.256	0.02	1.11
9	50	3	120	0.15	2.814	0.01	1.11

with zirconium silicate reinforcement, analysis of variance (ANOVA) concluded that the influencing parameters are peak current and pulse on time [11]. Taguchi's GRA was used to optimize the MRR and surface finish. The results showed that the combined effect of pulse on time, pulse off time, wire tension, and flush rate are essential for a good surface finish with greater MRR [12, 13]. The Taguchi design of experiment (DOE) technique was used to perform experimentation on ballistic grade aluminium alloy using the RSM model [14]. Machining of Al 5083 alloy in WEDM concluded that pulse off time and wire tension does not have any control over surface roughness [15]. An adaptive neuro fuzzy system was used to correlate the relationship between output and input parameters in WEDM of aluminium and SiC composites. The dielectric medium was changed from liquid to gas. Brass wire with oxygen medium was found to have higher cutting velocity [16, 17].

Aluminium alloy 6061 reinforced with SiC was used to optimize the MRR. It was reported that the increase in percentage volume of SiC particle decreases MRR by their study considering L9 orthogonal array [18]. Considering R_a in the WEDM process of Al6061 alloy reinforced with varied 5 to 10 percentage of boron carbide particle, increment in current decreases the surface quality and higher gap voltage increases the surface finish [19]. Machining of maraging steel SS350 was optimized using Taguchi ANOVA-based DOE. In that study, pulse on time, pulse off time, spark gap voltage, and peak current was selected as input parameters. The output parameter selected was MRR and surface roughness. The results clearly indicated that increase in pulse on time and peak current increases the MRR and R_a . It was also observed that the peak current was the most influencing parameter for both MRR and R_a [20]. It was

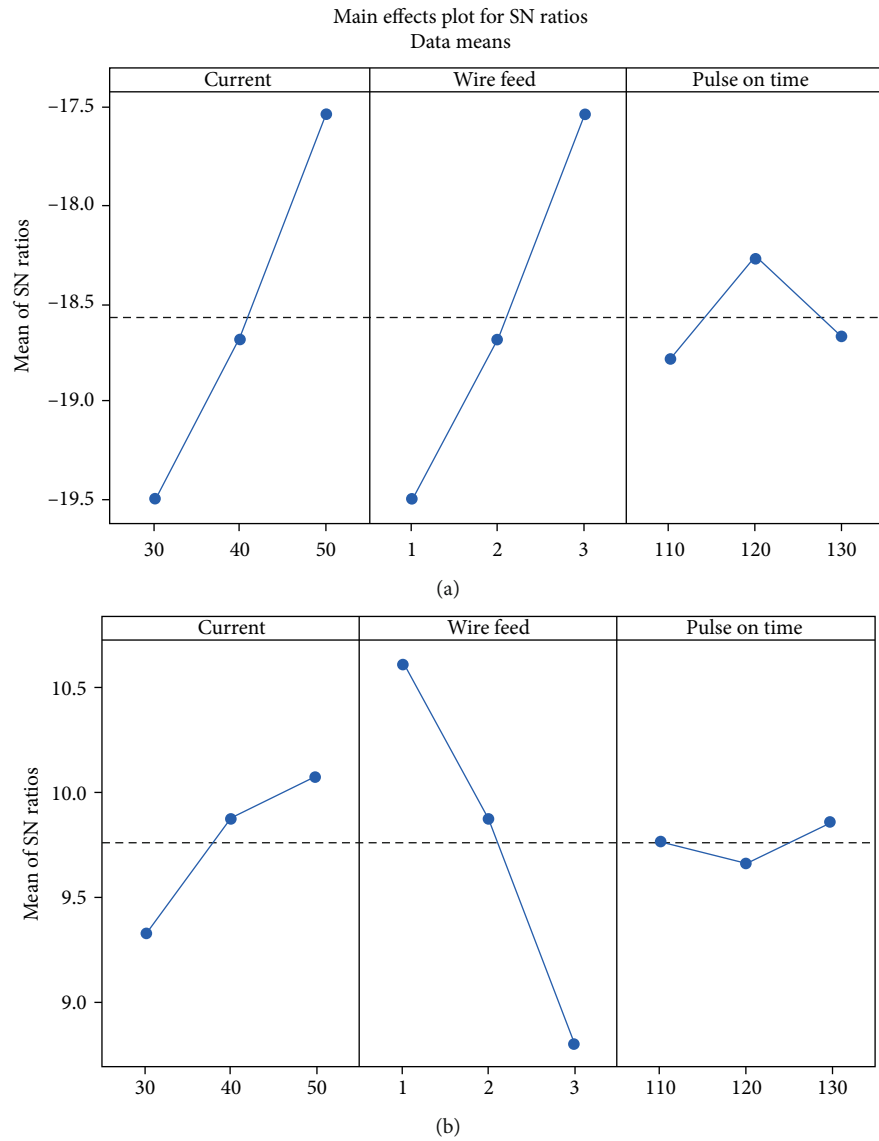


FIGURE 3: Mean effect plot of (a) MRR for S/N ratio and (b) R_a for S/N ratio.

TABLE 3: Analysis of variance for MRR.

Source	DF	Adj SS	Adj MS	F value	P value
Regression	3	0.002133	0.000711	22.86	0.002
Current	1	0.001067	0.001067	34.29	0.002
Wire feed	1	0.001067	0.001067	34.29	0.002
Pulse on time	1	0.000000	0.000000	0.00	1.000
Error	5	0.000156	0.000031		
Total	8	0.002289			

concluded that MRR is influenced by the wire feed rate and R_a is influenced by pulse on time for the selected input response as pulse on time, pulse off time, and wire feed in machining of SS304 [21]. The Taguchi L18 orthogonal array design was applied for machining Al6061 alloy with the pulse on time, pulse off time, feed rate, and wire tension as input parameters. The output parameter selected for analysis

was surface roughness. Results concluded that surface roughness is highly influenced by pulse on time [22]. The Taguchi L9 array type DOE was used for WEDM of AA6082-T6 alloy. Molybdenum was selected as the wire material for the analysis of surface roughness. Results revealed that pulse on time ranked first as the most influencing parameter for minimum surface roughness among pulse off time and current [23]. The Box-Behnken design with the L27 array model was used for machining Al 6061 composite reinforced with graphite and SiC particles. Pulse on time, pulse off time, current, and control speed were taken as input parameters for analysis of cutting speed. From the results, pulse off time was identified as a major influencing parameter on cutting speed followed by the peak current [24]. Pulse on time and current plays a major role towards R_a and kerf width in machining of hybrid Al 7075 composite reinforced with aluminium oxide and silicon carbide particulates using Taguchi GRA analysis [25]. RSM-based Taguchi

TABLE 4: Analysis of variance for R_a .

Source	DF	Adj SS	Adj MS	F value	P value
Regression	3	0.727592	0.242531	60.05	0.000
Current	1	0.108004	0.108004	26.74	0.004
Wire feed	1	0.616321	0.616321	152.60	0.000
Pulse on time	1	0.003267	0.003267	0.81	0.410
Error	5	0.020195	0.004039		
Total	8	0.747787			

DOE was found to be easy and accurate in the optimization of MRR and R_a as output responses for pulse on time, pulse off time, gap voltage, and peak current as input parameters [26]. Aluminium hybrid composite with fly ash and boron carbide using the Taguchi L9 orthogonal array on the WEDM process was investigated. Four input parameters as pulse on time, pulse off time, wire feed, and gap voltage with three levels was used for the investigation. From the analysis, it was found that gap voltage acts as a dominating parameter towards MRR and pulse off time was significant factor in analyzing R_a [27]. WEDM characteristics on Al 6063 and SiC composites were investigated using the L9 orthogonal array. Pulse on time, pulse off time, wire feed, and gap voltage were taken as input responses and MRR along with R_a as the output response. The result showed that MRR and R_a are highly influenced by pulse on time followed by the wire feed rate [28]. Wire electrical discharge machining of Al/AlCoCr-FeNiMo0.5 metal matrix composite produced by powder metallurgical route indicates that the response parameter MRR and R_a are highly influenced by pulse on time rather than pulse off time and wire feed taken as the input parameter [29]. Increased wear rate was identified for agglomerated silicon carbide and fly ash content within the composite [30]. In electrical discharge machining of aluminium-based metal matrix composite, both current and pulse on time were found to be significant parameter with voltage having no significance [31]. Corrosion studies on Al 7005 alloy reinforced with industrial waste based fly ash and glass fibre showed increased corrosion resistance for composite containing fly ash particles [32]. In machining Al6061/SiC(12%)/Gr(5%) composite using EDM, MRR was found to be increased rapidly for increased current and pulse duration. Copper electrode showed higher MRR compared to brass electrode [33]. Studies on predicting the effect of fly ash on concrete's mechanical properties by the artificial neural network indicated that the mechanical properties of concrete was influenced with fly ash and SiO₂ as reinforcements [34]. From the available literature, it is understood that there has been many results supported in the optimization of machining parameters of aluminium MMC. In this study, an aluminium composite with increased strength and decreased density was aimed for defense, aerospace, structural, and engineering applications. Thus, an attempt was made to machine the aluminium alloy 2024 composite reinforced with lithium (Li) and silicon nitride (Si₃N₄) using WEDM. Taguchi DOE was applied for the optimization of

process parameters as it gives the entire study of parameters with low number of experiments. The gray relational grade (GRG) and genetic algorithm (GA) analysis were also conducted and compared with the results of Taguchi optimization.

2. Materials and Methods

2.1. Composite Fabrication. Aluminium alloy 2024 reinforced with Si₃N₄ and Li with weight percentage of aluminium alloy matrix 88%, Li 2% of particle size 50 μ m, and Si₃N₄ 10% of particle size 70 μ m was fabricated through the stir casting route. Direct chilled two-step stir casting under argon atmosphere was selected for manufacturing of composite due to its added advantage in terms of cost and easy processing. Aluminium alloy 2024 was melted in the furnace to a temperature of 760°C temperature. Si₃N₄ reinforcement was added to the melt and uniform mixing was done by continuous stirring for 10 min at 300 rpm. The melt was then transformed to the crucible containing Li and stirred and then transformed to the mould surrounded by cooling water in order to avoid defects in casting. Oxidation of the melt with atmospheric air is controlled by surrounding the melt with argon gas. Thus, a defect free casting was prepared and machined to identify the optimized WEDM process parameters. Figure 1 shows the photograph of prepared specimens for wire electrical discharge machining process.

WEDM selected for machining the synthesized composite is best suited to machine hard and complex shapes at faster rate with good accuracy. The experiments were performed on Electronica sprint cut CNC wire-cut EDM as per the design matrix. Brass wire of 0.25 mm diameter was considered the wire material for machining the synthesized composite. MRR is determined by taking the difference in weight of the specimen before and after machining divided by the time taken for the process to complete. R_a is measured directly from the display of surface roughness tester. Three trials of surface roughness values are taken, and the average of the trials is taken as final surface roughness value. Figure 2 shows the photograph of Electronica sprint cut CNC wire-cut EDM used for this study.

2.2. Design of Experiment. Taguchi-based DOE is the best suited optimization technique in minimizing time and cost of experiment with fewer experiments using an orthogonal array design. MRR was calculated by taking the difference between the weight of specimen before machining and after machining with a 0.001 g accurate weighing balance. Performance characteristics are found using the categories larger the better for MRR and smaller the better for R_a . Analysis of variance (ANOVA) is done to confirm the optimum values of input parameters towards better MRR and R_a . The L9 orthogonal array design was selected with 3 factors at three levels [9]. Table 1 shows the selected input parameters and its levels.

2.3. Gray Relational Analysis. GRA is a tool used for optimizing multiple characteristics with huge experimental runs. This method gives a single best optimized response for

TABLE 5: Regression equation for selected response variable.

Response	Regression equation
MRR	$0.11889 - 0.01222 \text{ Current}_{.30} - 0.00222 \text{ Current}_{.40} + 0.01444 \text{ Current}_{.50} - 0.01222 \text{ wire feed}_{.1} - 0.00222 \text{ wire feed}_{.2} + 0.01444 \text{ wire feed}_{.3} - 0.00222 \text{ pulse ON time}_{.120} - 0.00222 \text{ pulse ON time}_{.130}$
R_a	$3.0901 - 0.11538 \text{ Current}_{.30} + 0.0392 \text{ Current}_{.40} + 0.1146 \text{ Current}_{.50} + 0.3052 \text{ wire feed}_{.1} + 0.0306 \text{ wire feed}_{.2} - 0.3358 \text{ wire feed}_{.3} - 0.0054 \text{ pulse ON time}_{.110} - 0.0358 \text{ pulse ON time}_{.120} + 0.0412 \text{ pulse ON time}_{.130}$

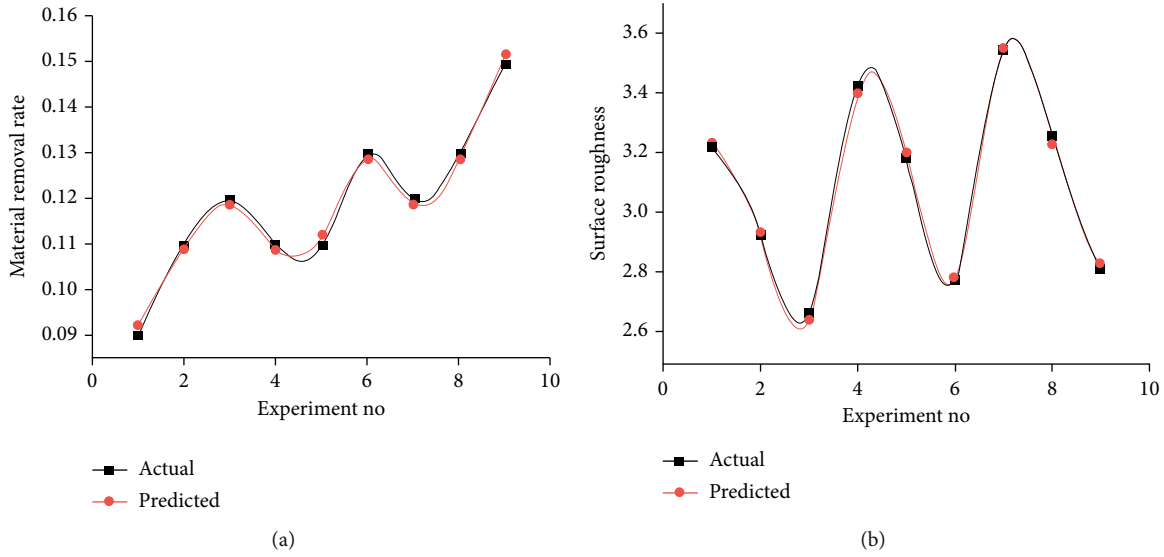


FIGURE 4: Relationship between observed value and predicted value for (a) MRR and (b) R_a .

TABLE 6: The gray relational grade for the selected response variables.

Exp. no	MRR		R_a		GRG
	Normalized	GRC	Normalized	GRC	
1	0	0.333333	0.373288	0.443769	0.388551
2	0.333333	0.428571	0.707763	0.631124	0.529848
3	0.5	0.5	1	1	0.75
4	0.333333	0.428571	0.135845	0.366527	0.397549
5	0.333333	0.428571	0.413242	0.460084	0.444328
6	0.666667	0.6	0.871005	0.794918	0.697459
7	0.5	0.5	0	0.333333	0.416667
8	0.666667	0.6	0.328767	0.426901	0.51345
9	1	1	0.833333	0.75	0.875

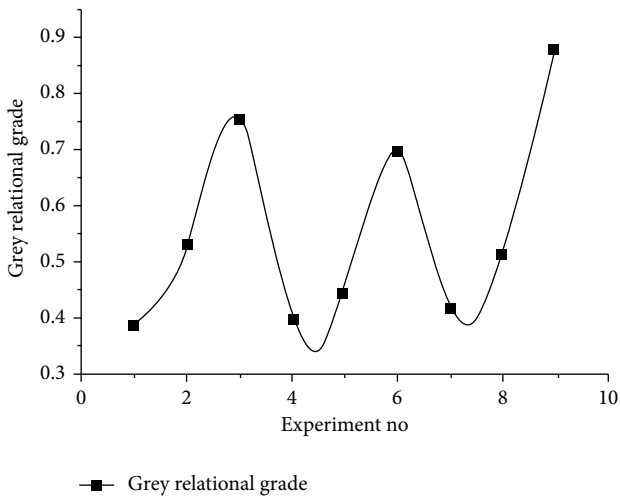


FIGURE 5: Gray relational grade values for response variable MRR and R_a .

TABLE 7: Confirmation test results.

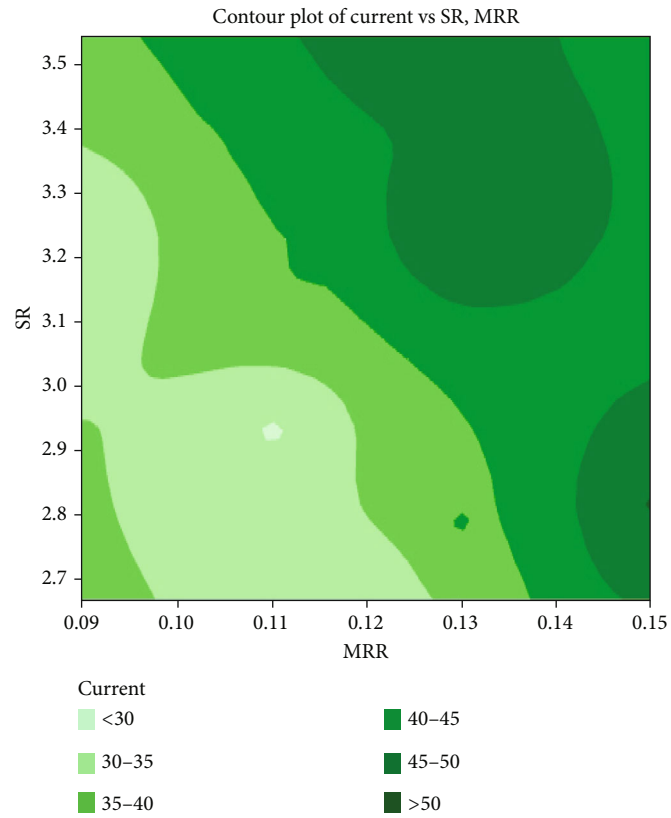
S.no	Input parameters			Output parameters		Standard deviation	
	I	W_f	T_{on}	MRR	R_a	MRR	R_a
1	50	3	120	0.15	2.810	0.01	1.11
2	30	3	120	0.12	2.620	0.01	1.11

multiple experimental runs. Here, larger the better is considered for calculating MRR and smaller the better is considered for calculating R_a .

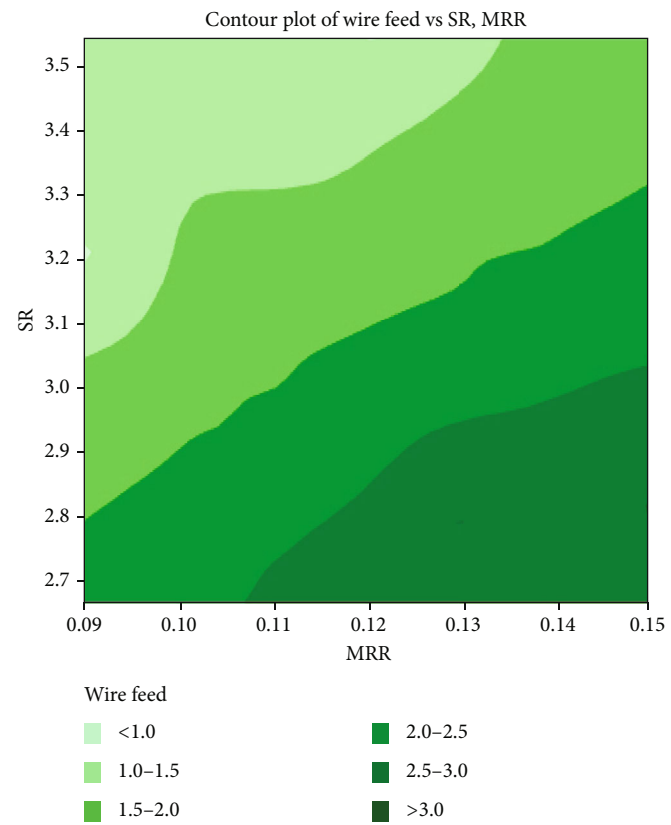
Normalization of MRR and R_a to the range of 0 and 1 is based on following equations:

$$N_i(x) = \frac{g_i(x) - \min g_i(x)}{\max g_i(x) - \min g_i(x)} \tag{1}$$

Equation (1) gives the gray relational generation for



(a)



(b)

FIGURE 6: Continued.

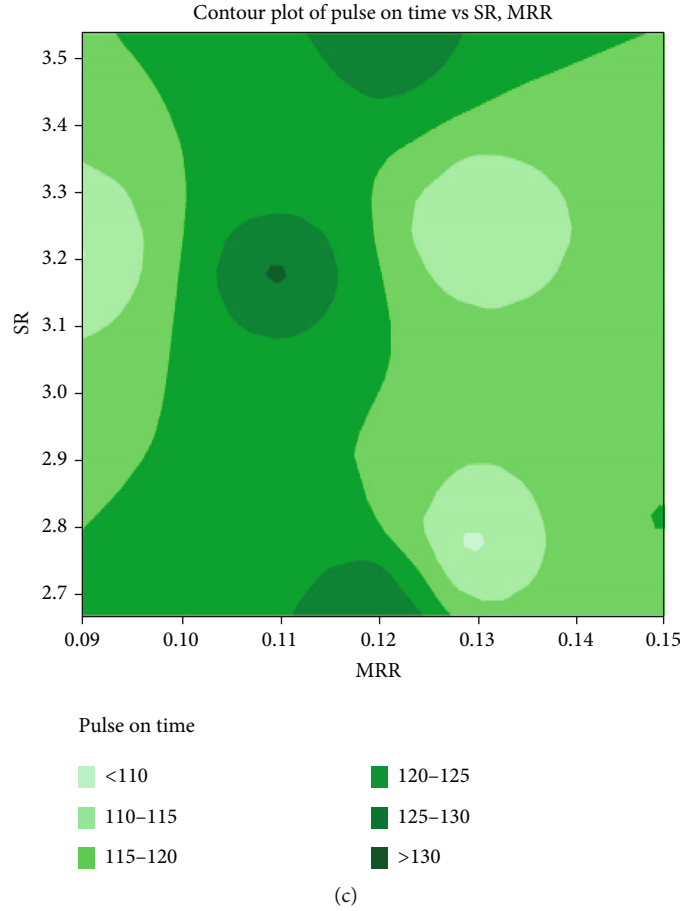


FIGURE 6: Contour plot of (a) current with MRR and R_a , (b) wire feed with MRR and R_a , and (c) pulse on time with MRR and R_a .

larger the better response.

$$N_i(x) = \frac{\max g_i(x) - g_i(x)}{\max g_i(x) - \min g_i(x)}. \quad (2)$$

Equation (2) gives the gray relational generation for smaller the better response, where $N_i(x)$ = Normalised value of grey relational generation, $g_i(x)$ = Value of particular attribute for xth response, $\max g_i(x)$ = Largest value of $g_i(x)$ for xth response, and $\min g_i(x)$ = Smallest value of $g_i(x)$ for xth response.

The gray relational coefficient calculated from normalized values is shown in Equation (3) for the weighing factor of 0.5. This shows how closer the variables are for different sequences.

$$\Delta_i(x) = \frac{\Delta_{\min} + \xi \Delta_{\max}}{\Delta_{oi}(x) + \xi \Delta_{\max}}. \quad (3)$$

where $\Delta_{oi}(x) = |N_o(x) - N_i(x)|$, Δ_{\max} = Maximum value of $\Delta_{oi}(x)$, and Δ_{\min} = Minimum value of $\Delta_{oi}(x)$.

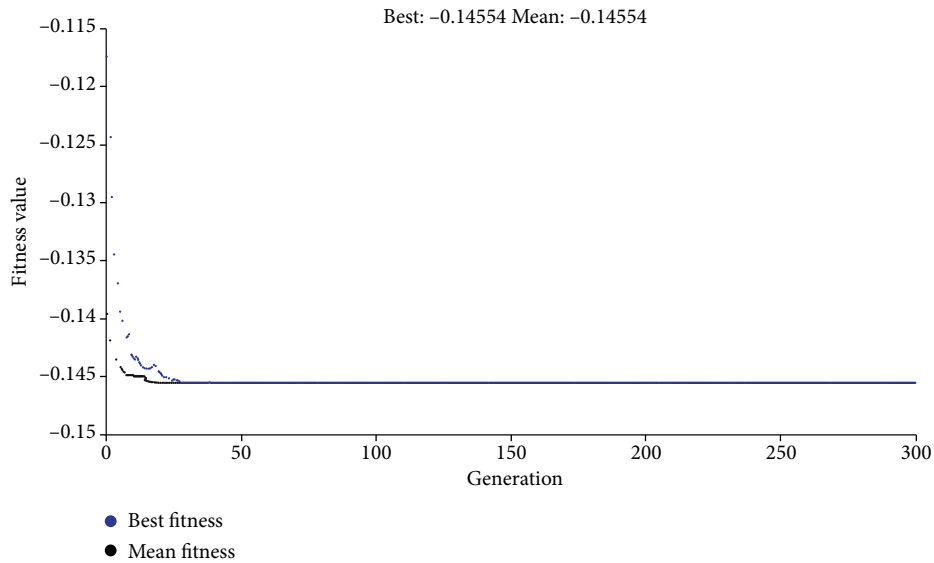
The gray relation grade from the gray relational coefficient is calculated using Equation (4).

$$R_i = \frac{1}{n} \sum_{x=1}^n \Delta_i(x), \quad (4)$$

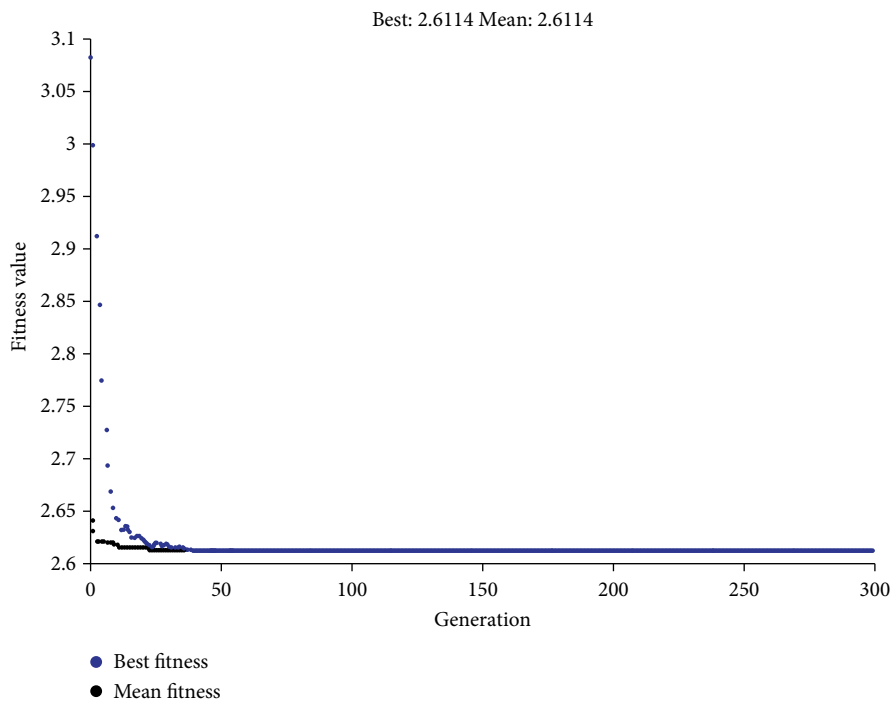
where n is the number of process response.

The set of input parameter levels corresponding to the highest value of the gray relational grade is considered the optimized input parameters for both MRR and R_a . The sequence of optimized levels of input parameters are ranked from highest value to lowest value of the obtained grade relational grade.

2.4. Genetic Algorithm. GA is an optimization technique used to solve lifetime problems with the fastest and easiest method. It is also referred as a search-based techniques to obtain optimal results of difficult problems. Research optimization and machine learning finds these applications to solve complex and difficult problems using natural selections. This process takes a set of input parameters and processes it with required generations to deliver the best optimal results using the fitness equation derived from the regression equations. GA are randomized in nature to solve problems having large search space with more number of



(a)



(b)

FIGURE 7: Best fitness value of (a) MRR and (b) R_a .

parameters. Discrete and continuous function optimization with multiobjective problems can use this method to obtain good solution with optimum results.

3. Results

The obtained values of MRR (grams per minute) and R_a (microns) during experimentation are presented in Table 2. Input parameters corresponding for higher value of MRR is considered the optimum parameter for this study since the performance characteristics taken is larger the better. Simi-

larly, the input parameters corresponding for lower value of R_a is considered the optimum parameter for this study since the performance characteristics taken is smaller the better.

4. Discussion

Response table for S/N ratio along with delta ranking showed current and wire feed as the most influencing parameter for MRR followed by pulse on time. While considering surface roughness, wire feed ranks as the most influencing parameter followed by current and pulse on

time. From the delta rank, it is clearly understood that wire feed and current are the factors to be considered for good accuracy in machining of synthesized composite.

Mean effect plot for S/N ratio of MRR and R_a is indicated in Figures 3(a) and 3(b). From Figure 3(a), current at 50 A, wire feed at 3 m/min, and 120 μ s pulse on time is identified as optimized values for better MRR as the performance characteristics of signal to noise ratio is considered as larger the better.

From Figure 3(b), current at 30 A, wire feed at 3 m/min, and 120 μ s pulse on time is identified as optimized values for better R_a as the performance characteristics of signal to noise ratio is considered the smaller the better.

Tables 3 and 4 show the ANOVA table for MRR and R_a . The most influencing factor is selected based on P value closer to zero and F value greater than unity.

The results of ANOVA clearly indicate that wire feed and current are closely associated towards MRR, whereas wire feed influences highly for surface finish than all other parameters. Therefore, ANOVA results shows wire feed is the most influencing parameter towards MRR and R_a in machining aluminium composite reinforced with Li and Si_3N_4 .

The response variation in percentage is mentioned as R^2 in the model. A better model is selected for higher values of R^2 . An adjusted R^2 value displays the accurate model by adding more predictors. The closer the values of R^2 and adjusted R^2 indicate that the registered predictors are correct and accurate. Predicted R^2 indicates the response for new observation with assumptions. Lower values of predicted R^2 compared to R^2 value indicates that the model is with unimportant predictions. The model summary result indicates response variation of 99.03% for MRR and 99.56% for R_a . The adjusted R^2 for MRR and R_a is 96.12% and 98.23% with predicted R^2 value of MRR (80.34%) and R_a (91.04%). Thus, the selected model best suits the experimentation and can be further used for other predictions.

To predict the response values with the actual measured values, regression equations are used. Table 5 shows the regression equation for response variable MRR and R_a . Figures 4(a) and 4(b) displays the correlation between observed value and predicted value of MRR and R_a showing a close relationship tracing the valley and peak of both curves. The minimal error (<2%) proves the accuracy of experiment conducted is accurate and is a generalized form considering all factors.

The gray relational generation is the initial step in which the normalization of values are made to have the output values between zero and one. Table 6 displays the values of GRG for the selected response variables.

Figure 5 represents the grey relational grade values for different experimental runs of MRR and R_a . The highest peak is found on 9th experimental run which represents the optimal levels of input parameter for the selected responses followed by experimental run 3 and 6. Therefore, aluminium composite material with Si_3N_4 and Li are found to have good machining characteristics at pulse on time of 120 μ s, wire feed of 3 m/min, and current of 50 A as the opti-

mized parameter for the selected response MRR and R_a . Thus, the gray relational grade optimization and ANOVA results represents the similar set of input parameters and thus proving the accuracy of the investigation.

Confirmatory test conducted for the optimized input parameters shows a close relationship with the obtained experimental values using the Taguchi design matrix. The values obtained in Table 7 confirm the accuracy of the investigation carried out.

Figure 6(a) shows the contour plot of input parameter current for the responses MRR and R_a . Increase in current increases MRR and decrease in current increases the values of R_a . Higher MRR and lower R_a is noted for higher current of 50 A. Figure 6(b) displays the contour plot of input parameter wire feed for the responses MRR and R_a . Increased wire feed rate increases MRR and lowers the value of R_a leading to good surface finish. Wire feed of 3 m/min shows good surface finish with higher MRR. Figure 6(c) shows the contour plot of input parameter pulse on time for the responses MRR and R_a . Increased pulse on time showed lower MRR with good surface finish. Higher MRR and lower R_a is seen for the pulse on time ranging from 120 to 125 μ s. Thus, from the contour plots of current, wire feed, and pulse ON time, good surface finish with better MRR is noticed for a current of 50 A, wire feed rate of 3 m/min, and pulse on time ranging from 120 μ s to 125 μ s. Experimental results of ANOVA, GRG, and contour plots results with the similar set of optimized input parameters confirming the accuracy of studies made on Al-Li- Si_3N_4 MMC.

GA-based trial runs were generated for the fitness function derived from the regression equation using MATLAB R2014 software. The best fitness value for MRR and R_a were identified as 0.14554 grams per minute and 2.6114 microns generated for 300 iterations as shown in Figures 7(a) and 7(b). The values obtained are confirming the experimental results of Taguchi and GRG analysis.

5. Conclusions

From the investigation of aluminium metal matrix composite reinforced with Li and Si_3N_4 , the following conclusions were derived:

- (1) Aluminium metal matrix composite without defects was fabricated using stir casting technique
- (2) Machining parameters for the composite in WEDM was optimized using Taguchi-based DOE using the L9 orthogonal array
- (3) Regression equation with gray relational grade and GA was analyzed for the obtained experimental values
- (4) Wire feed was found to be the dominating parameter followed by current and pulse on time for MRR and R_a
- (5) Higher MRR were identified for the wire feed at 3 m/min, current at 50 A, and pulse on time of 120 μ s

- (6) Good surface finish is obtained for wire feed at 3 m/min, current at 30 A, and pulse on time of 120 μ s
- (7) GA-based study also confirms the analysis of Taguchi and gray relational grade. The regression model shows identical values suggesting that the experiment is with minimal error (<2%) in terms of MRR and R_a

Thus, from the obtained conclusions, correlation of Taguchi, gray relational grade, and GA analysis confirms the accuracy of the experimental values obtained in this investigation.

Data Availability

The data used to support the findings of this study are included in the article. Should further data or information be required, these are available from the corresponding author upon request.

Disclosure

It was performed as a part of the Mettu University, Metu, Ethiopia.

Conflicts of Interest

The authors of this article declare that we have no conflict of Interests.

Acknowledgments

The authors wish to extend their sincere thanks to Covai wire EDM centre for conducting the machining study and the Department of Mechanical Engineering, Saranathan College of Engineering, for providing surface roughness testing facility. Special thanks to M. Kumarasamy College of Engineering, for giving stir casting facility to carry out this research. Taif University Researcher Supporting Project number TURSP-2020/45, Taif University, Taif, Saudi Arabia, supported this study.

References

- [1] D. VijayPraveen, D. RangaRaju, and M. V. JagannadhaRaju, "Optimization of machining parameters of wire-cut EDM on ceramic particles reinforced Al-metal matrix composites - a review," *Materials Today: Proceedings*, vol. 23, no. 3, pp. 495–498, 2020.
- [2] C. Kumar, R. Ramesh, M. RaviRaja, and V. JaiGanesh, "Role of sic on mechanical, tribological and thermal expansion characteristics of B4C/Talc-reinforced al-6061 hybrid composite," *SILICON*, vol. 12, no. 6, pp. 1491–1500, 2020.
- [3] M. Karthigairajan, P. K. Nagarajan, M. R. Raviraja et al., "Effect of silane treated rice husk derived biosilica on visco-elastic, thermal conductivity and hydrophobicity behavior of epoxy biocomposite coating for air-duct application," *SILICON*, vol. 13, no. 12, pp. 4421–4430, 2021.
- [4] V. K. Saini, Z. A. Khan, and A. N. Siddiquee, "Optimization of wire electric discharge machining of composite material (Al6061/SiCp) using Taguchi method," *International Journal of Mechanical and Production Engineering*, vol. 2, no. 1, pp. 61–64, 2013.
- [5] S. A. Sonawane and M. L. Kulkarni, "Optimization of machining parameters of WEDM for nimonic-75 alloy using principal component analysis integrated with Taguchi method," *Journal of king saud university-Engineering sciences*, vol. 30, no. 3, pp. 250–258, 2018.
- [6] N. Sharma, R. Khanna, and R. D. Gupta, "WEDM process variables investigation for HSLA by response surface methodology and genetic algorithm," *Engineering science and technology, an international journal*, vol. 18, no. 2, pp. 171–177, 2015.
- [7] H. Kumar, A. Manna, and R. Kumar, "Modeling of process parameters for surface roughness and analysis of machined surface in WEDM of Al/SiC-MMC," *Trans. In. Inst. Met*, vol. 71, no. 1, pp. 231–244, 2018.
- [8] A. R. Srivastava and S. Dixit, "A 11-year-old boy with oral sub-mucous fibrosis: a rare case report," *Int. J. Adv. Res. Innov*, vol. 4, no. 4, pp. 511–515, 2014.
- [9] S. Dinesh Kumar and M. Ravichandran, "Synthesis, characterization and wire electric erosion behaviour of AA7178-10 wt.% ZrB2 composite," *SILICON*, vol. 10, no. 6, pp. 2653–2662, 2018.
- [10] V. R. R. Dey, K. M. P. Bandi, and K. M. Pandey, "Wire electrical discharge machining characteristics of AA6061/cenosphere aluminium matrix composites using RSM," *Mater. Today. Proc*, vol. 5, no. 1, pp. 1278–1285, 2018.
- [11] M. P. Garg and A. Sharma, "Examination of accuracy aspect in machining of ZrSiO₄/6063 aluminium MMC using CNC wire electrical discharge machining," *Compo. Commun*, vol. 6, pp. 6–10, 2017.
- [12] C. V. Reddy, N. Deepthi, and N. Jayakrishna, "Multiple response optimization of wire EDM on aluminium HE30 by using grey relational analysis," *Mater. Today. Proc*, vol. 2, no. 4-5, pp. 2548–2554, 2015.
- [13] N. B. Raju, M. Raja Roy, S. Rajesh, and K. Ramji, "Optimization of machining parameters for cutting AMMC's on wire cut EDM using RSM," *International Journal of Engineering Trends and Technology (IJETT)*, vol. 23, no. 2, pp. 82–89, 2015.
- [14] R. Bobbili, V. Madhu, and A. K. Gogia, "Multi response optimization of wire-EDM process parameters of ballistic grade aluminium alloy," *Eng. Sci. Technol. Int. J*, vol. 18, no. 4, pp. 720–726, 2015.
- [15] G. Selvakumar, G. Sornalatha, S. Sarkar, and S. Mitra, "Experimental investigation and multi-objective optimization of wire electrical discharge machining (WEDM) of 5083 aluminum alloy," *Transactions of the Nonferrous Metals Society of China*, vol. 24, no. 2, pp. 373–379, 2014.
- [16] R. B. Azhiri, R. Teimouri, M. G. Baboly, and Z. Leseman, "Application of Taguchi, ANFIS and grey relational analysis for studying, modeling and optimization of wire EDM process while using gaseous media," *International Journal of Advanced Manufacturing Technology*, vol. 71, no. 1-4, pp. 279–295, 2014.
- [17] A. S. Gore and N. G. Patil, "Wire electro discharge machining of metal matrix composites: a review," *Proc. Manuf*, vol. 20, pp. 41–52, 2018.
- [18] S. Prashantha, R. B. Veerasha, S. M. Shashidhara, U. S. Mallikarjun, and A. G. Shivasiddaramaiah, "A study on machining characteristics of Al6061-SiC metal matrix composite through wire - cut electro discharge machining," *Mater. Today. Proc*, vol. 4, no. 10, pp. 10779–10785, 2017.

- [19] Ş. Karabulut, H. Karakoç, and R. Çitak, "Effect of the B4C reinforcement ratio on surface roughness of Al6061 based metal matrix composite in wire-EDM machining," in *8th International Conference on Mechanical and Aerospace Engineering*, pp. 812–815, Prague, Czech Republic, 2017.
- [20] K. Dayakar, K. V. M. K. Raju, and C. R. B. Raju, "Prediction and optimization of surface roughness and MRR in wire EDM of maraging steel 350," *Mater. Today. Proc.*, vol. 18, pp. 2123–2131, 2019.
- [21] S. Gijoy, S. S. Abhilash, and S. J. Hari Krishnan, "Optimization of wire electrical discharge machining process parameters using Taguchi method," *J. Current. Eng. Scientific. Res.*, vol. 4, no. 7, pp. 76–85, 2017.
- [22] J. Johnson, K. T. Bibin, and A. Sankar, "Optimization of wire electric discharge machining parameters on Al 6061," *Int. J. Eng. Sci. Res. Technol.*, vol. 7, no. 4, pp. 447–455, 2018.
- [23] M. F. Mohamed and K. Lenin, "Optimization of wire EDM process parameters using Taguchi technique," *Mater. Today. Proc.*, vol. 21, no. 1, pp. 527–530, 2020.
- [24] G. M. Muniappan, V. Shaqib, G. B. Jayakumar, R. S. Raja, and R. Soloman, "Experimental investigation of WEDM process parameters for cutting speed using response surface methodology," *Materials Science and Engineering*, vol. 402, pp. 1–9, 2018.
- [25] S. Lal, S. Kumar, Z. A. Khan, and A. N. Siddiquee, "Multi-response optimization of wire electrical discharge machining process parameters for Al7075/Al2O3/SiC hybrid composite using Taguchi-based grey relational analysis," *Proc. IMech. E. Part. B: J. Eng. Manuf.*, vol. 229, no. 2, pp. 229–237, 2015.
- [26] H. Singh and R. Khanna, "Parametric optimization of cryogenic-treated D-3 for cutting rate in wire electrical discharge machining," *Journal of Engineering Technology*, vol. 1, no. 2, pp. 59–64, 2011.
- [27] J. U. Prakash, J. M. Peter, and T. V. Moorthy, "Optimization of wire EDM process parameters of aluminium alloy/flyash/boron carbide hybrid composites," *Int. Rev. Mech. Eng.*, vol. 6, no. 3, pp. 449–455, 2012.
- [28] D. Satishkumar, M. Kanthababu, V. Vajjiravelu, R. Anburaj, N. T. Sundarajan, and H. Arul, "Investigation of wire electrical discharge machining characteristics of Al6063/SiCp composites," *International Journal of Advanced Manufacturing Technology*, vol. 56, no. 9-12, pp. 975–986, 2011.
- [29] S. Karthik, K. Soorya Prakash, P. M. Gopal, and J. Sathiskumar, "Influence of materials and machining parameters on WEDM of Al/AlCoCrFeNiMo0.5 MMC," *Materials and Manufacturing Processes*, vol. 34, no. 7, pp. 759–768, 2019.
- [30] N. A. Patil, S. R. Pedapati, O. B. Mamat, and A. M. H. S. Lubis, "Effect of SiC/Fly ash reinforcement on surface properties of aluminum 7075 hybrid composites," *Coatings*, vol. 10, no. 6, pp. 541–562, 2020.
- [31] M. Singh and S. Maharana, "Investigating the EDM parameter effects on aluminium based metal matrix composite for high MRR," *Materials Today: Proceedings*, vol. 33, 2021.
- [32] P. K. Swamy, S. Mylraiah, M. P. G. Chandrashekarappa et al., "Corrosion behaviour of high-strength Al 7005 alloy and its composites reinforced with industrial waste-based fly ash and glass fibre: comparison of stir cast and extrusion conditions," *Materials*, vol. 14, no. 14, pp. 3929–3946, 2021.
- [33] M. Singh, H. K. Garg, S. Maharana et al., "An experimental investigation on the material removal rate and surface roughness of a hybrid aluminum metal matrix composite (Al6061/SiC/Gr)," *Metals*, vol. 11, no. 9, pp. 1449–1461, 2021.
- [34] M. M. Roshani, S. H. Kargar, V. Farhangi, and M. Karakouzian, "Predicting the effect of fly ash on concrete's mechanical properties by ANN," *Sustainability*, vol. 13, no. 3, pp. 1469–1485, 2021.

Research Article

An Empirical Analysis of Heat Expulsion and Pressure Drop Attribute in Helical Coil Tube Using Nanomaterials

Salem Algarni,¹ Vineet Tirth ,¹ Talal Alqahtani,¹ Pravin R. Kshirsagar ,² and Worku Abera ³

¹Mechanical Engineering Department, College of Engineering, King Khalid University, Abha, 61421 Asir, Saudi Arabia

²Department of Artificial Intelligence, G.H. Rasoni College of Engineering, Nagpur, India

³Department of Food Process Engineering, College of Engineering and Technology, Wolkite University, Wolkite, Ethiopia

Correspondence should be addressed to Vineet Tirth; vtirth@kku.edu.sa and Worku Abera; worku.abera@wku.edu.et

Received 1 March 2022; Accepted 5 April 2022; Published 16 May 2022

Academic Editor: Hiwa M. Ahmed

Copyright © 2022 Salem Algarni et al. This is an open access article distributed under the Creative Commons Attribution License, which permits unrestricted use, distribution, and reproduction in any medium, provided the original work is properly cited.

Water nanofluids were examined in a horizontal helical coil tube with constant temperature limitations for Dean values between 1000 and 10,000 to determine the rate of thermal radiation transmission and pressure drop characteristics. When conducting the tests, a variety of Al₂O₃ water nanofluid requirements were used, including varying mass flows, heat exchange rates for various nanoparticle volume concentrations, and changes in coil-side drop in pressure versus coil-side Dean number. Since nanoparticles have enhanced heat capacity, nanoparticles are developing as a transitional beginning of heat transfer fluids with significant potential in thermal management applications. Many applications require nanofluids to be used as heat transfer fluids; thus, scientists are concentrating their efforts on these fluids. The Reynolds values on the coil and shell were in the 1000 to 7000 range on either side of the wire. This paper discusses the impact of particle volume density on shell-side flow temperatures, heat expulsion rate, and thermal conduction. The result shows that the average heat transfer rises by 13% and 17% when nanoparticle volume fraction percentage density is 0.1%, 0.2%, and 0.3 percent. The results demonstrate that reducing the mass flow by an increase in particle volume density, pipe diameter, and coil radius improves heat exchanger performance. The efficiency of the model is enhanced by increasing the diameter of the tube while simultaneously decreasing the diameter of the coil.

1. Introduction

There is a significant difference in the thermal properties between water nanofluid and their underneath fluid counterparts. Heat transfer coefficients grow in conjunction with nanofluid thermal conductivity. This enhanced heat transfer velocity may be useful in resolving the primary problem of constructing a compact heat exchanger [1]. Helically coiled tubes are superior heat transfer apparatuses because of their stiffness and better heat transfer efficiency than those of sharp tube heat exchangers [2]. Shell and helical coil tubes, which have a single heat exchanger canal, are prevalent. There are two types of fluids in a cold/hot fluid system: flowing out of the shell through the helical coil tube, one travels towards the center, and another travels through the helix coil

tube. Additional heat transfer in helical tubes is more reliable because of secondary flow. In the modern world, helically coiled pipes for heat transfer have gained great attention due to the numerous applications for which they may be used. Food and dairy production plants as well as chemical plants and natural gas processing facilities, as well as power plants, all use them heavily [3, 4], as do a wide range of other sectors as well. Another passive way to improve heat transmission is to introduce nanoparticles into the base fluid to generate nanofluid with high specific heat capacity than the base fluid [5].

The use of nanofluid in heat transfer activities has increased considerably in the last decade. For the most part, these experiments called for the use of water as a basic fluid. Nanofluids based on water show Newtonian behavior. The

chemical and food industries all employ non-Newtonian fluids, as do the healthcare and biopharmaceutical industries as well as the polymer and oil industries. Methods for improving performance can be classified as passive or active [2, 3]. The active methodology makes use of surface vibration signals and fluid vibrations, whereas the passive approach employs various inserts and pitch adjustments. Active methods are harder to employ than passive ones due to their complexity [4]. Pitch variation aids heat transfer, but it also reduces shell-side heat transfer rate and causes a considerable pressure decrease. In terms of improving heat transfer without pressure decreases, we used Al_2O_3 nanofluids to increase the pressure loss heat transfer characteristics [3, 5].

2. Objective

The coiled tube heat exchangers are recommended based on the results of the analysis, and the paper's major objective is to improve heat transmission by utilizing nanofluids. To determine how much nanofluid is being used, these relationships are used. Then, that information is plotted against the amount of nanofluid used to show the shell and tube heat thermal resistance.

3. Literature Survey

Wang et al. [1] discussed how well a new helically tube test device transfers heat and how much water it moves. The helical tube shape of the coil was modified to increase its thermal efficiency. A 20 percent increase in heat transfer rates was reported when reversed loops were used as a design change. In addition, the increase in heat transmission and pressure drop was increased by reducing the reversed loop's size.

Ardekani et al. [2] examined the fluid flow and heat transmission in a circular tube of water nanofluids with constant heat limits. Different coil designs across a range of particle volume fractions and Reynolds numbers between 8,900 and 11,970 were examined to see how geometrical variables influenced the results. The researchers discovered that using nanofluids inside helical coils improved the heat transfer coefficient more than using straight tubes [3]. They also provided two correlation experimental results that predicted the Nusselt number and friction factor.

Job et al. [6] discussed that symmetrical wavy trapezoid container, Al_2O_3 -water, and SWCNT-water nanofluids were shown to have unstable magnetohydrodynamics (MHD) free convection flows. The study discovered that for alumina-water nanofluids with low Hartmann numbers, the rate of heat transmission decreased (Ha).

Rakhsha et al. [7] discussed their Nusselt number that improved by around 21.53 percent, but their pressure remained the same. CuO nanofluid flow within helical coils with constant wall average temperature was studied computationally and empirically in steady-state turbulent forced convection.

Ahire et al. [8] demonstrated that many heat transfer activities benefit from the usage of nanofluid, and Al_2O_3 is

a nanoparticle that is combined with a base fluid to produce nanofluids. For estimating the chemical and physical characteristics, there is correlation that is accessible.

Sharma et al. [9] investigated the fluid flow characteristics in straight tubes and helical coils with nanofluid. Both ethylene glycol and propylene glycol/water (EG/W) nanofluids included 0–2.5 vol percent alumina nanoparticles and were mixed in a 60:40 wt ratio. A higher friction factor was reported for nanofluids in both straight and helical coil tubes compared to base fluids.

Bhanvase et al. [10] systematically used a vertical helically coiled tube heat exchanger to comprehensively study the rise in water-based PANI (polyaniline) nanofluid heat transfer. PANI nonmaterial at 0.1 and 0.5 vol percent increased the heat transfer by 10.52 and 69.62 percent, correspondingly, according to the researchers' findings.

4. Application of Nanofluids

A broad range of heat transfer uses, such as transportation, cooling of electronics, energy storage, and mechanical applications have revealed that nanofluids have enhanced heat transfer characteristics and increased energy efficiency than conventional fluids. When it comes to the development of next-generation technology for a wide range of technical and medical applications, nanofluid is critical. The next parts go through a few of these use cases [11].

4.1. Automobile Applications. Standard engine coolants and oils can be improved by adding nanoparticles and nanotubes to produce nanofluids, increasing their thermal conductivity, and increasing heat exchange rates and fuel economy [12]. Use of these advances can reduce cooling system sizes or remove heat from vehicular emission inside the same cooling system, depending on your preference.

4.2. Solar Applications. As a consequence of the disparity in timing between energy supply and demand, it was required to build a storage system. With a concentration on effective use and preservation of heat losses and solar energy, thermal energy storage such as that found in solar thermal systems and buildings has emerged as an essential element of energy conservation [5, 12]. Due to a lack of power generation, solar energy is becoming increasingly important in energy applications. Fossil fuel usage will be restricted in the future based on perceived resource depletion concerns.

4.3. Friction Reduction. Minimizing wear and friction is a major focus of tribological development. Proved challenging may run more efficiently and reliably using improved fluids. Because of their high load-bearing capacity, high resilience to severe pressure, and friction-reducing properties, nanoparticles have recently attracted a lot of study attention [13]. In contrast to water-based Al_2O_3 fluids, the cast iron MQL grinding process included diamond nanofluids. A thick and solid sludge layer develops on the surface during nanofluid MQL grinding, which might improve grinding efficiency, reducing grinding force, better surface roughness, and burn protection of the workpiece due to the usage of nanofluid technology [6]. MQL grinding has the potential

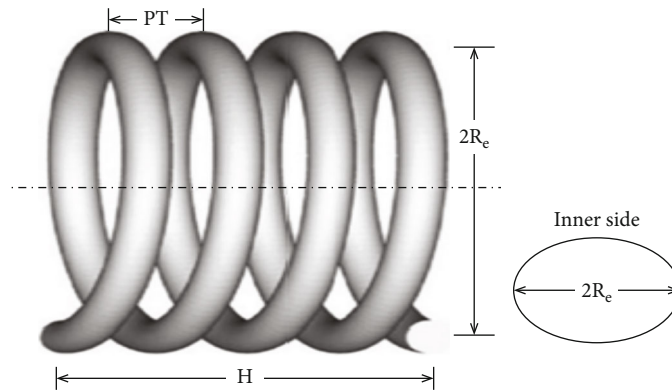


FIGURE 1: A schematic of the helical coil tube.

to considerably lower the grinding temperature when compared to dry grinding.

4.4. Electronics Cooling. Smaller computer chips and micro-electronic elements have much higher power dissipation than larger ones. It is necessary to have superior heat control and cooling fluids with enhanced thermal transfer characteristics to operate safely [11, 13]. Nanofluids have been proposed as heat pipe working fluids for cooling applications because of their low thermal conductivity.

4.5. Magnetic Sealing. Because it is less expensive and has lower friction losses than mechanical seals, magnetic seals are an excellent choice for ecological and dangerous gas sealing in a range of industrial rotating equipment. There are unique nanofluids such as ferromagnetic fluid (ferromagnetic fluid). Magnetite and other tiny magnetic particles are suspended in a stable colloidal solution (Fe_3O_4). Nanoparticle magnetite [6], which is a component of magnetic nanofluids, may be made to have a different magnetic field strength by changing the size and protective coatings. Magnetic nanofluids are dispersed in nonpolar and polar carrier liquids to meet the dispersion requirements that responders verified [7].

5. Material and Methods

5.1. Helical Coil Tube Specifications. A helically shaped tube is seen in Figure 1. The inner diameter of the copper helical coil tube is “ $2r$,” and the coils have a helical shape to prevent tangling. When you see the letters “ d ” and “ D ” in this picture, it means that you are looking at the inner tube diameter and coil diameter, correspondingly [8]. Pitch is a term used to describe the amount of time between two successive rotations. The curvature ratio, represented by the symbol “ d/D ,” is another critical parameter in helical coil tubes (HCT).

This relationship between Reynolds number and Dean value is evident in helical coil tubes (HCTs). The Dean value determines fluid flow in an HCT [14].

$$\text{De} = \text{Re} \sqrt{\frac{r}{R_c}}. \quad (1)$$

There are three variables in this equation: the Reynolds number (Re), the tube inner diameter (r), and the coil radius (R_c).

$$\text{Re} = \frac{2rA\tau}{\mu} \quad (2)$$

Average velocity is represented by “ A ” in this equation, density is represented by τ , and viscosity is represented by μ .

5.2. Proposed System. Figure 2 shows the experimental setup’s flow map. The setup is comprised of two loops, which are designated as shell area loop and helically coiled region loop, respectively. Hot air is handled by the shell side loop, while Al_2O_3 /water nanofluid is handled by the coiled tube loop [8, 14]. Aluminum insulating ropes, thermocouples with LCDs, and condensers for cooling nanofluid are all part of the experimental setup. The test area also includes an air-duct heating chamber and a power meter and rotameter [9].

5.3. Preparation of Nanofluid. Sustainable nanofluid may be made using a variety of methods. In addition, utilizing a stabilizing agent as well as a dispersing agent or an ultrasonic vibrator is an option. Surface treatment is a popular method among them because of its versatility, low cost, and benefits. The nanofluids can only be stabilized for 45 minutes without the use of appropriate chemicals [14]; however, surfactants can significantly improve the stability of nanofluids. Sigma-Aldrich chemicals provided the Al_2O_3 nanofluid (2 mg/ml) and nanoparticles with a diameter of 20-50 nm for the experiment. It was necessary to add the necessary nanoparticle volume proportion and the optimal quantity of the associated surfactant to the measuring jar to distribute the alumina nanoparticles in distilled water [9]. Acoustic pulses were generated for 12 hours using a magnetic stirrer (2000 rpm). This results in homogeneous dispersion and stable suspension. The “thermophysical” characteristics of the generated nanofluids were computed using the following models [12].

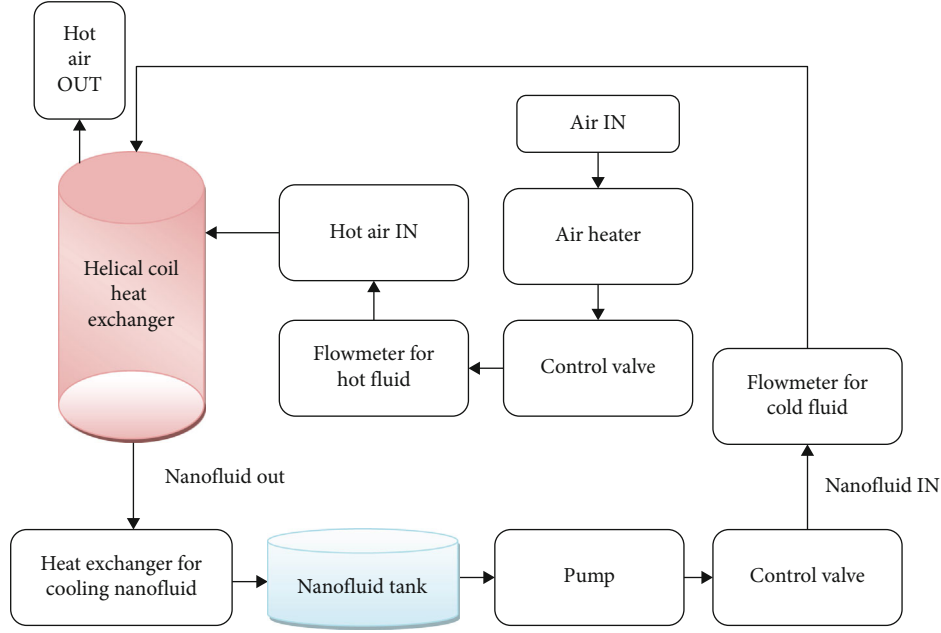


FIGURE 2: Block diagram of the experimental setup.

5.3.1. *Thermal Conductivity.* We compared the KD2 Pro thermal performance analyzer's Al_2O_3 -water nanofluid resistivity results to two well-established formulae's anticipated values. The most often used formula for predicting the thermal conductivity of a solution is as follows [6, 12]:

$$h_{\text{eff}} = \frac{h_b + (n-1)h_g - (n-1)(h_g - h_b)\varphi}{h_b + (n-1)h_g + (h_g - h_b)\varphi}. \quad (3)$$

Here, the heat transfer performance is represented by h_{eff} , and the shape factor n is represented by " $n^{1/4}3\psi$," where ψ "sphericity" is the radius of the curvature. It has values of 1 for spherical particles and 0.5 for cylindrical ones, depending on the form [10]. The quantities h_b and h_g indicate the thermal conductivity of particles and fluids, respectively.

5.3.2. *Viscosity.* It is accurate that the vast majority of the mathematical correlations that have been utilized to predict the viscosity of nanofluids have been derived from the well-known Einstein model [15].

$$\theta_{ng} = \theta_{bg}(1 + 2.5\varphi), \quad (4)$$

where the viscosity of the solvent is represented by θ_{bg} , the viscosity of the base fluid is denoted by θ_{ng} , and φ denotes the volume fraction of the solution.

5.3.3. *Density.* When considering nanofluid density, the volume fraction of solid (nanoparticles) to liquid in the process is directly proportional. There is a direct correlation between nanoparticle concentration in a fluid and its density, with the former being greater when there are more of them present [7, 9]. Nanofluid density has been claimed to

be in line with the mixing theory proposed in the lack of experimental data.

$$\sigma_{\text{nf}} = (1 - \varphi)\sigma_{\text{bf}} + \varphi\sigma_s, \quad (5)$$

where σ_{nf} represents the density of nanofluid, σ_{bf} denotes the density of the base fluid, σ_s represents the density of solid particles, and ϕ is the volume concentration.

5.3.4. *Specific Heat.* As the volume particle size of the nanofluid increases, the heat capacity of the nanofluid decreases continuously [6, 13]. The relationship between them demonstrates excellent correlation with the predictions made using the thermodynamic equilibrium technique; however, the simple mixing model fails to estimate the heat capacity of nanofluid properly. Specific heat is determined in an experiment by using the following formula:

$$T_{\text{pnf}} = \frac{\varphi\rho(T_P)_P + (1 + \varphi)\rho T_{\text{pf}}}{\rho_{\text{nf}}}, \quad (6)$$

The density and specific heat of a particle are represented by $\rho(T_P)_P$, the density and specific heat of fluid are represented by ρT_{pf} , and T_{pnf} indicates the density and specific heat of a nanofluid [16].

To determine the critical Reynolds number in helical coils,

$$\text{Re}_{\text{cr}} = 2300 \left[1 + 8.6 \left(\frac{r}{R_c} \right)^{0.45} \right]. \quad (7)$$

Coil diameter (r) and tube diameter (d) are also important parameters to consider while determining this value (R_c). The coil's curvature ratio was 0.0552, resulting in a

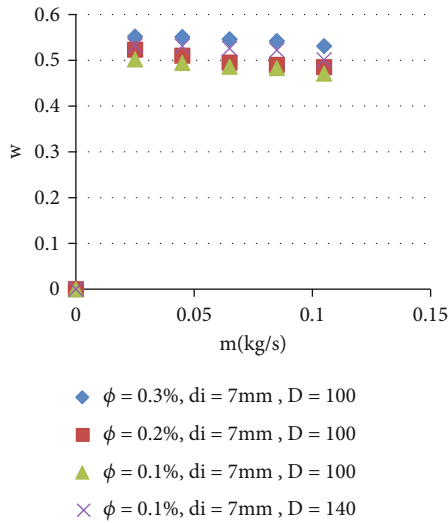


FIGURE 3: Effectiveness varies with mass flow rate due to a variety of factors.

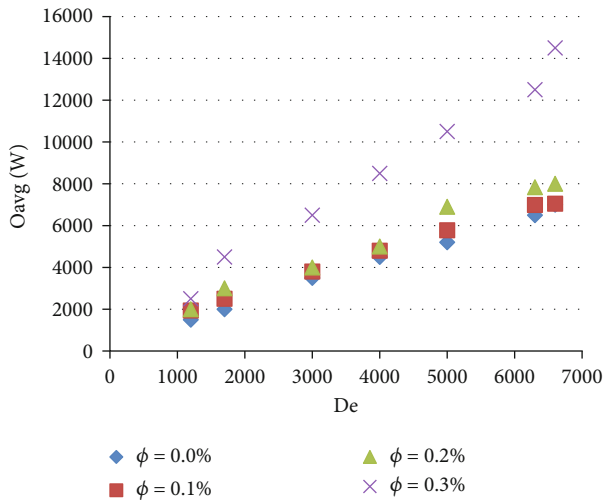


FIGURE 4: The rate of heat transmission for various concentrations of nanoparticles.

critical Reynolds number of 7671 for the system. The Reynolds numbers used in this paper span from 1837 to 6869.

5.4. Experimental Procedure. At different cold fluid flow rates under turbulent circumstances, a test was carried out in a tube heat exchanger with or without circular fins utilizing Reynolds numbers ranging from 1000 to 7000 and stable hot air velocity of 5 meters/seconds [10, 15]. A helical coil in the thermal storage tube bundle circulates cold distilled water, which swaps heat with hot air from the heat exchanger. The system takes 30-35 minutes to stabilize, according to the results of the preliminary tests [17, 18]. Stream temperatures are monitored at the entrance and outlet. To monitor the controlled flow of cold fluid, a rotameter was installed at the test section's inlet [19]. Circular fin designs with and without fins, as well as flow rates varying greatly, were also investigated. Al_2O_3 nanoparticles dispersed in distilled water were studied using the aforemen-

tioned technique in a coil in a shell heat exchanger with and without circular fins at volume concentrations ranging from 0.25 percent to 1 percent [12, 13].

To calculate the errors of dependent items, the following equation is used:

$$\delta D = \left[\sum_{i=1}^N \left(\frac{\partial D}{\partial Y_i} \delta Y_i \right)^2 \right]^{0.5}. \quad (8)$$

Y_i and D are the independent and dependent variables, respectively, in this correlation.

5.5. Data Validation. To validate the reliability of trials, experts had to run accuracy tests with pure water first, then with nanofluids [20]. We provide the equations for laminar flows in helical coils with a constant heat flux as the beginning condition [16].

$$Nu = \left[0.76 + 0.65\sqrt{De} \right] Pr^{0.175}, \quad (9)$$

$$Nu = 0.7Re^{0.43}Pr^{(1/6)} \left(\frac{d}{D} \right)^{0.07}. \quad (10)$$

De indicates Dean value and Pr indicates Prandtl values, respectively, in the above equations. D is the diameter of the coil, whereas d is the inner diameter [17, 18].

Theoretical pressure drop in helically coiled tubes may be calculated with the help of the following formula:

$$\Delta P = g_c \left(\frac{1}{\bar{d}} \right) \left(\frac{\tau U^2}{2} \right). \quad (11)$$

The friction coefficient of the circular tube is represented by g_c in this equation and may be determined using the following correlation [21]:

$$\frac{g_c}{g_s} = 0.47136De^{0.25}. \quad (12)$$

Petukhov equation is used to calculate the friction coefficient in a tube bank.

$$g_s = (0.79 \ln(Re) - 1.64)^{-2}. \quad (13)$$

6. Results and Discussions

6.1. Performance Analysis of the Heat Exchanger. In real-world applications, it is better to have a higher heat transfer rate than to have a worse pressure drop, which necessitates greater pumping power. This means that in coiled tube heat exchangers, investigating and evaluating the opposing impact of increased heat transmission and higher pressure drop are essential. Equation ((14)) is used to determine the heat exchanger's efficiency.

$$\varepsilon = \frac{O_{avg}}{O_{max}}. \quad (14)$$

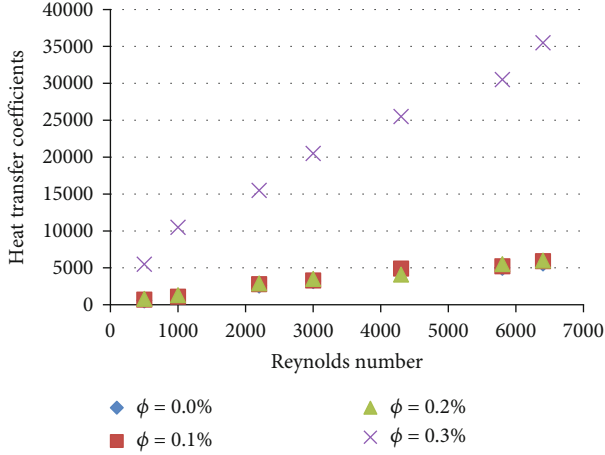


FIGURE 5: Heat transfer coefficient of coil side changes with Reynolds number on the coil side.

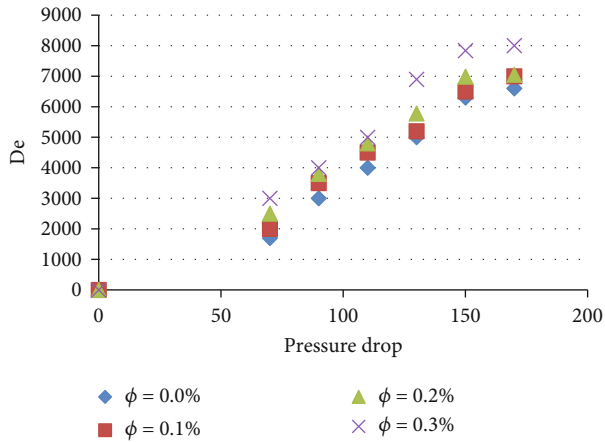


FIGURE 6: Variations of coil-side Dean number vs. coil-side pressure drop.

Equation ((15) is used to compute the heat exchanger's performance index, which measures how well it performs in terms of pressure drop.

$$\theta = \frac{O_{\text{avg}}}{\Delta P_{\text{coil}}}. \quad (15)$$

Figure 3 demonstrates that when the heat transfer rate increases, the efficiency rises with the mass nanoparticle concentration. As the mass flow rate increases, the temperature differential between the inlet and exit narrows, reducing efficiency. As tube and coil diameters increase, the heat transfer field expands, resulting in improved efficiency.

Figure 4 shows that raising the particle volume concentration increases the heat transfer rate. The reason for this is due to the nanofluid's thermophysical characteristics. First, as the volume concentration of nanoparticles increases, so does their thermal conductivity, increasing the rate at which heat is transferred. Second, greater nanofluid viscosity

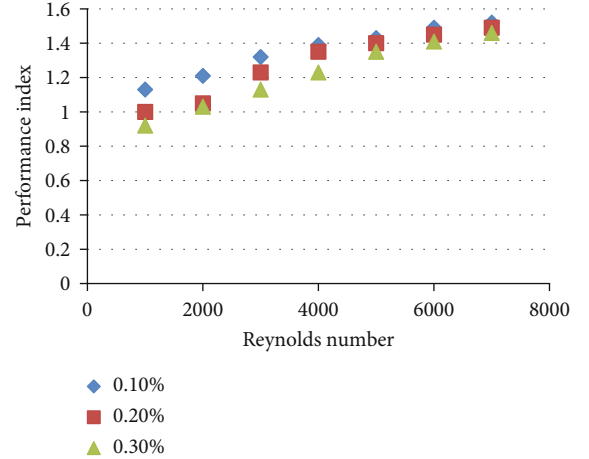


FIGURE 7: Performance index–Reynolds number variations.

increases flow velocity for the same Reynolds number, resulting in higher heat transfer rates.

Figure 5 shows the connection between both the Reynolds number and the change in coil-side heat transfer rate. Heat transmission coefficients grow in direct proportion to the volume fraction of nanoparticles. As the Reynolds number rises, the heat exchanger's instability causes its heat transfer coefficients to rise as well.

For a given particle volume concentration and Dean number, the pressure decrease may be shown in Figure 6. Due to the increased viscosity that results from a rise in particle volume concentration, pressure drops increase as well.

The coefficient of heat transfer and the pressure drop are two unrelated variables that are not linked by an equation. There should be some criteria used to compare the different heat transfer improvement techniques so that they can be compared. To achieve this, the performance index, a PEC (performance evaluation criterion), is used.

$$\eta = \left(\frac{h_{\text{NF}}}{h_{\text{BF}}} \right) \left(\frac{\Delta P_{\text{NF}}}{\Delta P_{\text{BF}}} \right)^{-1}. \quad (16)$$

Nanofluid and base fluid are denoted by the subscripts "NF" and "BF," respectively. When the performance index exceeds unity, it appears that the heat transfer approach favors heat transfer enhancement above pressure drop increase. For nanofluids of various weight concentrations flowing in the louvered channel, Figure 7 illustrates the changes in performance index vs. Reynolds number. For all nanofluids except for 0.2 and 0.3 percent wt nanofluids at the lowest Reynolds number, the performance index is higher than 1. Additionally, the performance index increases dramatically with the Reynolds number, as can be seen in the graph below. Additionally, when the weight percentage of nanoparticles increases, so does the performance index. A maximum performance index of 3.967 is found at Reynolds number 7,200 for nanofluid with 0.10 percent weight concentration.

7. Conclusion

An Al_2O_3 /water nanofluid inside a helical coil tube was analyzed for convective heat transfer using fluid heat transfer in this paper. As the number of particles grows, the nanofluid temperature decreases, while the water temperature rises, along with the amount of heat transferred. The results revealed that when nanoparticle volume concentrations of 0.1 percent, 0.2 percent, and 0.3 percent are present, the average heat transfer rate increases by 13% and 17%. It was found that when nanoparticle volume concentration increased, the thermal performance efficiencies on the coil, shell, and overall improved. When the mass flow rate is the same as water, the thermal transfer rate of nanofluids significantly increases, but the volume particle concentration rises slightly. The results of the analysis revealed that decreasing the mass flow rate while increasing the density of nanoparticles, tube diameter, and coil diameter all resulted in better performance. At Reynolds number 7,200, a nanofluid with a weight concentration of 0.10% has a maximum performance measure of 3.967.

Data Availability

The datasets used and/or analyzed during the current study are available from the corresponding author on reasonable request.

Conflicts of Interest

The authors declare that they have no conflicts of interest.

Acknowledgments

The authors gratefully acknowledge the Deanship of Scientific Research, King Khalid University (KKU), Abha 61421, Asir, Kingdom of Saudi Arabia, for funding this research work under the grant number RGP.2/9/43.

References

- [1] W. Yi, J. L. Alvarado, and W. Terrell Jr., "Thermal and flow characteristics of helical coils with reversed loops," *International Journal of Heat and Mass Transfer*, vol. 126, pp. 670–680, 2018.
- [2] A. Mokhtari Ardekania and V. Kalantara, "Experimental study on heat transfer enhancement of nanofluid flow through helical tubes," *Advanced Powder Technology*, vol. 30, no. 9, pp. 1815–1822, 2019.
- [3] H. Javaniyan Jouybari, S. Saedodin, A. Zamzamian, M. Eshagh Nimvari, and S. Wongwises, "Effects of porous material and nanoparticles on the thermal performance of a flat plate solar collector: an experimental study," *Renew Energy*, vol. 114, no. B, pp. 1407–1418, 2017.
- [4] P. Naphon, "Thermal performance and pressure drop of the helical-coil heat exchangers with and without helically crimped fins," *International Communications in Heat and Mass Transfer*, vol. 34, no. 3, pp. 321–330, 2007.
- [5] S. Aberoumand and A. Jafarimoghaddam, "Mixed convection heat transfer of nanofluids inside curved tubes: An experimental study," *Applied Thermal Engineering*, vol. 108, pp. 967–979, 2016.
- [6] V. M. Job, S. R. Gunakala, B. Rushi Kumar, and R. Sivaraj, "Time-dependent hydromagnetic free convection nanofluid flows within a wavy trapezoidal enclosure," *Applied Thermal Engineering*, vol. 115, pp. 363–377, 2017.
- [7] M. Rakhsha, F. Akbaridoust, A. Abbassi, and S.-A. Majid, "Experimental and numerical investigations of turbulent forced convection flow of nano-fluid in helical coiled tubes at constant surface temperature," *Powder Technology*, vol. 283, pp. 178–189, 2015.
- [8] S. Ahire, B. S. PurushottamShelke, and N. Totala, "Fabrication and analysis of counter flow helical coil heat exchanger," *International Journal of Engineering Trends and Technology (IJETT)-Volume*, vol. 15, no. 5, pp. 229–240, 2014.
- [9] P. Sharma, R. Gupta, and R. K. Wanchoo, "Hydrodynamic studies on glycol based Al_2O_3 nanofluid flowing through straight tubes and coils," *Experimental Thermal and Fluid Science*, vol. 82, pp. 19–31, 2017.
- [10] B. A. Bhanvase, S. D. Sayankar, A. Kapre, P. J. Fule, and S. H. Sonawane, "Experimental investigation on intensified convective heat transfer coefficient of water based PANI nanofluid in vertical helical coiled heat exchanger," *Applied Thermal Engineering*, vol. 128, pp. 134–140, 2018.
- [11] A. M. Fsadni, J. P. M. Whitty, M. A. Stables, and A. A. Adeniyi, "Numerical study on turbulent heat transfer and pressure drop characteristics of a helically coiled hybrid rectangular-circular tube heat exchanger with Al_2O_3 -water nanofluids," *Applied Thermal Engineering*, vol. 114, pp. 466–483, 2017.
- [12] M. Hemmat Esfe, H. Hajmohammad, R. Moradi, and A. A. Abbasian Arani, "Multi-objective optimization of cost and thermal performance of double walled carbon nanotubes/water nanofluids by NSGA-II using response surface method," *Applied Thermal Engineering*, vol. 112, pp. 1648–1657, 2017.
- [13] A. Tahiri and K. Mansouri, "Theoretical investigation of laminar flow convective heat transfer in a circular duct for a non-Newtonian nanofluid," *Applied Thermal Engineering*, vol. 112, pp. 1027–1039, 2017.
- [14] V. Bianco, "Numerical simulation of water/ Al_2O_3 nanofluid turbulent convection," in *Dipartimento di IngegneriaAerospaziale e Meccanica*, SecondaUniversitadegliStudi di Napoli, Via Roma 29, 81031 Aversa, Italy, 2010.
- [15] V. Kumar, A. K. Tiwari, and S. K. Ghosh, "Effect of variable spacing on performance of plate heat exchanger using nanofluids," *Energy*, vol. 114, pp. 1107–1119, 2016.
- [16] B. P. S. Singh and A. Tripathi, "Experimental study of heat transfer of a car radiator with nano fluid- Al_2O_3 water mixture as coolant," *International Journal of Advanced Research in Science, Engineering and Technology*, vol. 2, no. 9, pp. 830–837, 2015.
- [17] R. Boonsri and S. Wongwises, "Mathematical model for predicting the heat transfer characteristics of a helical-coiled, crimped, spiral, finned-tube heat exchanger," *Heat Transfer Engineering*, vol. 36, no. 18, pp. 1495–1503, 2015.
- [18] B. ChinnaAnkanna and B. Sidda Reddy, "Performance analysis of fabricated helical coil heat exchanger," *International Journal of Engineering Research*, vol. 3, no. Special 1, pp. 33–39, 2014.
- [19] K. A. Amid, W. H. Azmi, R. Mamat, and K. V. Sharma, "Experimental investigation on heat transfer performance of TiO_2 nanofluids in water-ethylene glycol mixture," *International*

Communications in Heat and Mass Transfer, vol. 73, pp. 16–24, 2016.

- [20] W. H. Azmi, K. Abdul Hamid, N. A. Usri, R. Mamat, and M. S. Mohamad, “Heat transfer and friction factor of water and ethylene glycol mixture based TiO_2 and Al_2O_3 nanofluids under turbulent flow,” *International Communications in Heat and Mass Transfer*, vol. 76, pp. 24–32, 2016.
- [21] R. N. Singh, P. Rajat, I. Lav, and P. K. Pandey, “Experimental studies of nanofluid TiO_2/CuO in a heat exchanger (double pipe),” *Indian Journal of Science and Technology*, vol. 9, no. 31, 2016.

Research Article

Anticancer and Antioxidant Activity of *Morinda Citrifolia* Leaf Mediated Selenium Nanoparticles

M. Nagalingam ¹, S. Rajeshkumar ², Sathesh Kumar Balu,³ M. Tharani,² and Kalirajan Arunachalam ⁴

¹Department of Biochemistry, Indo American College, Cheyyar 604407, India

²Department of Pharmacology, Saveetha Dental College and Hospital, Saveetha Institute of Medical and Technical Sciences, Saveetha University, Chennai 600077, India

³Department of Oral Pathology, Saveetha Dental College and Hospital, Saveetha Institute of Medical and Technical Sciences, Saveetha University, Chennai 600077, India

⁴Department of Science and Mathematics, School of Science, Engineering and Technology, Mulungushi University, Kabwe 80415, Zambia

Correspondence should be addressed to Kalirajan Arunachalam; akalirajan@mu.edu.zm

Received 12 February 2022; Accepted 26 April 2022; Published 11 May 2022

Academic Editor: Arpita Roy

Copyright © 2022 M. Nagalingam et al. This is an open access article distributed under the Creative Commons Attribution License, which permits unrestricted use, distribution, and reproduction in any medium, provided the original work is properly cited.

The goal of the present work is to fabricate selenium nanoparticles utilising *Morinda citrifolia* leaves extract via green approach. UV-Vis spectroscopy, FT-IR, and TEM were used to characterise the green nanoparticles. The size of generated SeNPs in *Morinda citrifolia* was anticipated to be 12-160 nm based on TEM images. The antioxidant activity of selenium NPs was discovered to be 66.7 to 83.7% of free radical inhibition. When the concentration of nanoparticles rises, the viability of cancer cells decreases. It shows that biosynthesized selenium nanoparticles have anticancer properties that depend on the concentration. The brine shrimp lethality assay revealed that *Morinda citrifolia* mediated selenium nanoparticles have low cytotoxic effects.

1. Introduction

Nanotechnology addresses a progressive way for technological advancement that includes the administration of material at the nanometer scale (one billion times less than a meter) [1]. Nanotechnology implies any innovation on the nanoscale that has various applications in reality. Nanotechnology in a real sense incorporates the fabrication and utilization of chemical, physical, and biological systems at scales ranging from atoms to submicron measurements, and furthermore the combination of these subsequent nanomaterials into larger systems [2, 3].

Selenium (Se) is a fundamental trace component present in our body. Selenium is found in proteins as selenocysteine (Sec), which is referred to as selenoproteins. The presence of selenium in enzymes, which have a critical function in shielding the organism from the effects of oxidative stress,

explains the element's importance in human nutrition [4, 5]. The presence of oxidoreductase in selenoproteins regulates redox equilibrium in the body. Because of the low toxicity of selenium nanoparticles (SeNPs), they have been investigated for variety of oxidative pressure as well as inflammatory diseases. Therefore, SeNPs pave a way to transmit various medications to the site of action (Amit [6]). The current study exposes the fabrication of SeNPs using *Morinda citrifolia* extract.

Fabrication of nanoparticles via green approach using medicinal plants extracts has recently gained popularity. Phytochemicals, in particular, constitute the backbone of plants, may readily produce nanoparticles with lower toxicity. As the benefits of *Morinda citrifolia* L. and its products become more widely known, researchers have begun to take an interest in them [7]. *M. citrifolia* L., belongs to the family Rubiaceae spread all over in tropical Asia and Polynesia. It

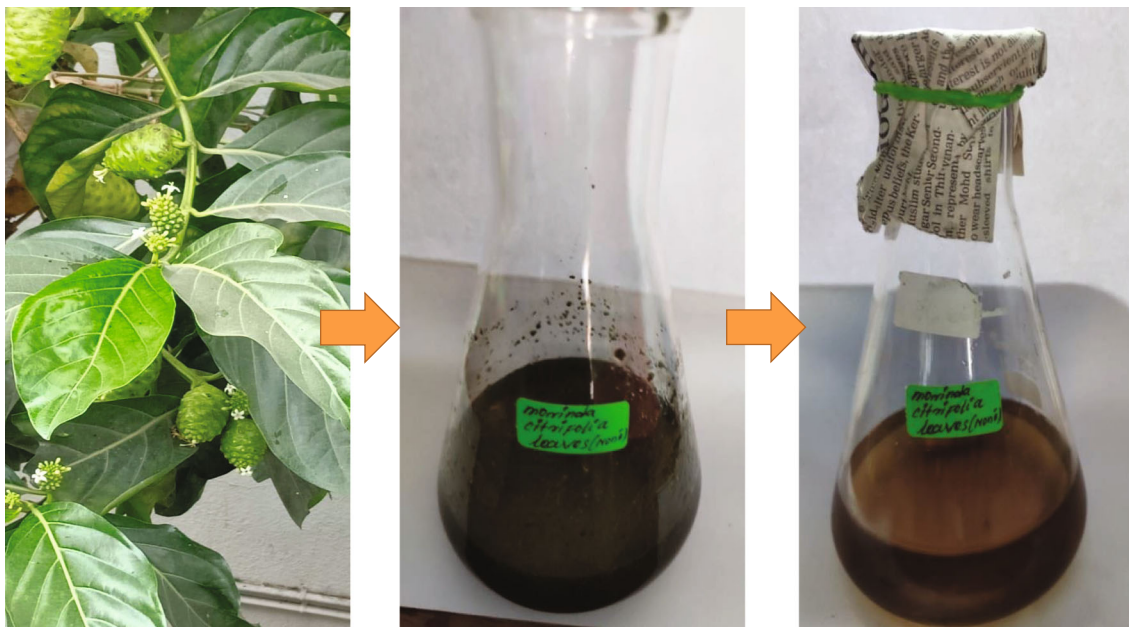


FIGURE 1: Preparation of *Morinda citrifolia* plant extract.

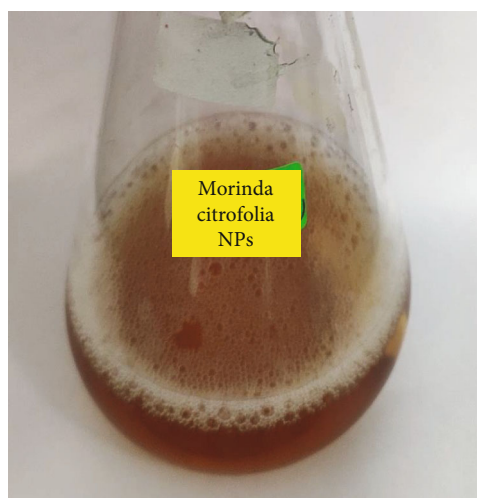


FIGURE 2: Green synthesis of selenium nanoparticles.

appears to have been highly valued therapeutically in the Tropical regions, and the plant is normally produced for its root system, leaves, and organic matter. These plants roots are an excellent source of anthraquinones, which are typically found as aglycones and, to a lesser extent, as glycosides. All components of the tree have been widely used medicinal services for the relief of arthritic as well as other pains, and for their healing properties [8].

2. Materials and Methods

2.1. Preparation of Extract. *Morinda citrifolia* leaves were obtained from Thiruparuthikundaram, Kancheepuram. The collected leaves were thoroughly washed under the tap water. For seven days, the leaves were dried in the shade at room temperature. The leaves of *Morinda citrifolia* sepa-

rately grounded using mixer grinder into fine powder. 1gm of powdered leaves of *Morinda citrifolia* was added to 100 mL of distilled water and heated at a temperature of 60-70°C using a heating mantle. Finally, using Whatmann No. 1 filter paper, the mixture was filtered and the extract was stored for further use (Figure 1).

2.2. Synthesis of Selenium Nanoparticles. Sodium selenite (Na_2SeO_3), 30 mM dissolved in 50 mL of distilled water. To that, 50 mL of *Morinda citrifolia* leaf extract was slowly added. Then the reaction mixture was kept on a magnetic stirrer at 650-700 rpm for 48-72 hours.

2.3. PURIFICATION AND CHARACTERIZATION of NPs USING TEM & FT-IR. The collected NPs were kept for centrifugation at 8000 rpm for 10 min. The pellet obtained dried at 70°C in hot air oven for 12 h. The dried pellet was grinded

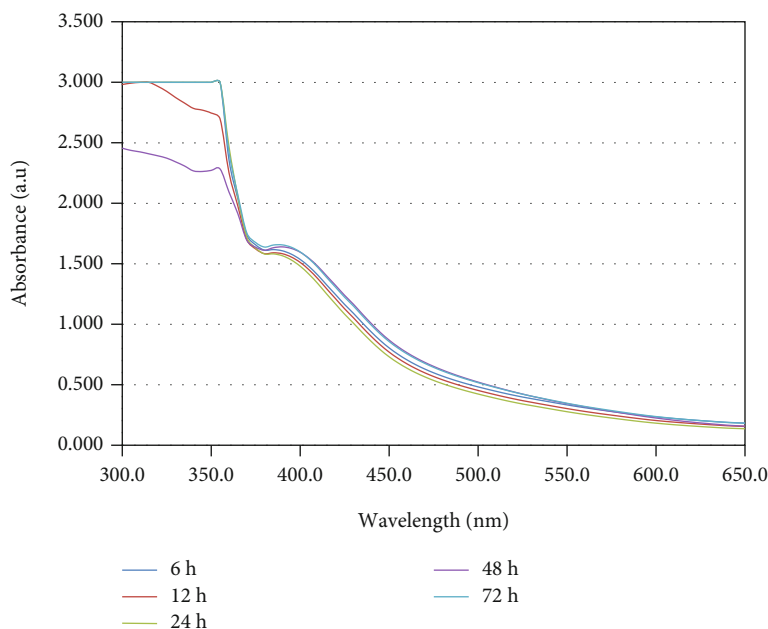


FIGURE 3: UV-Visible spectra of biosynthesized SeNPs.

using mortar and pestle and the powder was stored for further use. The TEM and FT-IR analysis was carried out using the powdered pellet.

2.4. Antioxidant Assay. The DPPH assay of free radical scavenging using *Morinda citrifolia* leaves extract mediated SeNPs was carried out by the procedure reported in (Rajeshkumar et al. [9]). Various concentrations (10, 20, 30, 40 and 50 $\mu\text{g/mL}$) of *Morinda citrifolia* extract synthesized selenium nanoparticles was added to 1 mL of DPPH and 450 μL of TrisHCl buffer was added and kept in incubation for 30 mins. The free radical scavenging was analysed by measuring absorbance at 517 nm. As a control, BHT was used. Ascorbic acid was employed as a reference substance. The inhibition percentage was determined from the following equation,

$$\% \text{inhibition} = \frac{\text{absorbance of control} - \text{absorbance of sample}}{\text{absorbance of control}} \times 100 \quad (1)$$

2.5. Anticancer Activity

2.5.1. MTT Assay. MTT assay is called as (3-(4, 5-dimethyl thiazol-2yl)-2, 5-diphenyl tetrazolium bromide. Mossman proposed the MTT assay for the first time in 1982. MTT is broken in live cells by mitochondrial dehydrogenase, resulting in the quantifiable purple product formazan. The quantity of formazan generated is related to the number of live cells and inversely related to the extent of cytotoxicity. The wells should be washed twice or three times with MEM (w/o) FCS. Add 200 μL of MTT with a concentration of 5 mg/mL, followed by incubation for 6-7 hrs. Following incubation, DMSO (1 ml) was added to the wells and stir with a pipette for 45 seconds. If live cells contain formazan

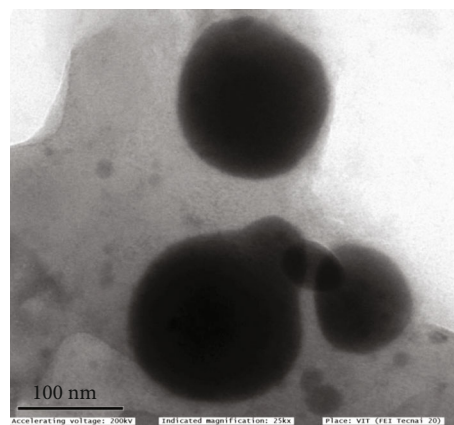


FIGURE 4: Transmission electron microscopic image of SeNPs synthesized using *Morinda citrifolia*.

crystals following the addition of solubilizing reagent (DMSO), the purple colour development occurs. The solution was tested using the UV-visible spectroscopy and the optical density at 595 nm measured using DMSO as control. The percentage of cell viability was calculated using the below equation.

$$\text{Cell viability}(\%) = \frac{\text{Mean OD}}{\text{Control OD}} \times 100 \quad (2)$$

2.6. Cytotoxicity Activity. Weighing and dissolving 2 g of iodine-free salt in 200 mL of purified water. 10-12 ml saline water filled in 6 well ELISA plates. 10 nauplii were added to the wells (5, 10, 15, 20, 25 μL & control). The nanoparticles were then introduced at the desired concentration level and incubated the plates for 24 h.

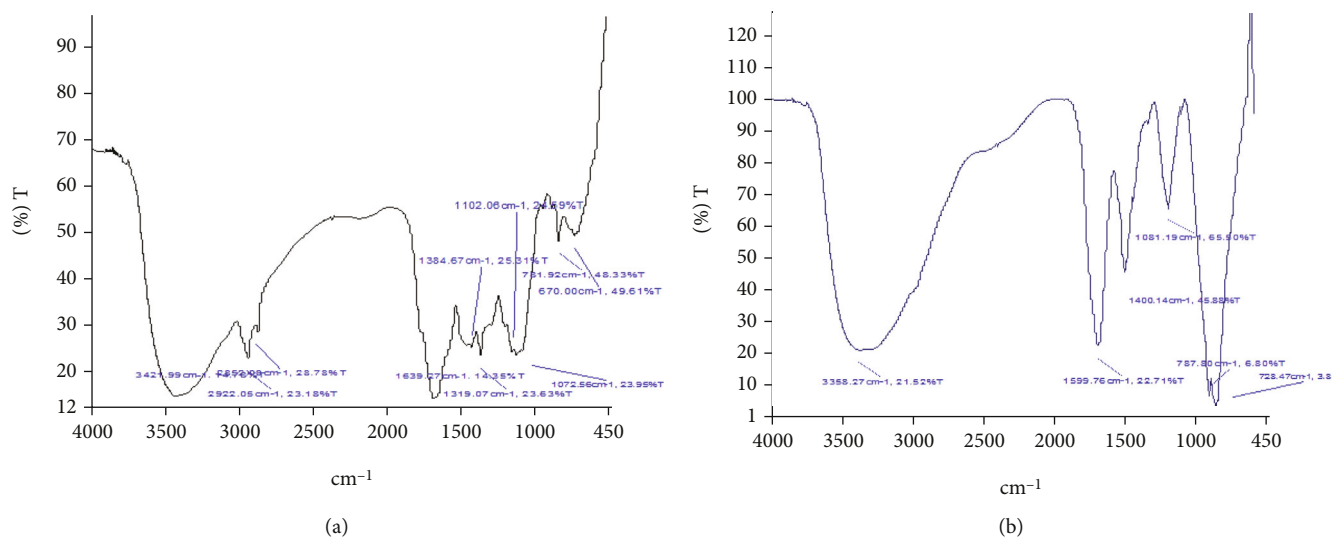


FIGURE 5: Fourier Transform Infra-red spectrum of (a) *Morinda citrifolia* leaves extract (b) *Morinda citrifolia* leaves extract mediated SeNPs.

TABLE 1: Functional groups present in the reducing agent and nanoparticles.

<i>Morinda citrifolia</i>			SeNPs		
Functional group	Peaks	Types of vibration	Functional group	Peaks	Types of vibration
Phenols and alcohols	3427.99	Hydrogen bonded O-H stretch	Phenols and alcohols	3358.27	Hydrogen bonded O-H stretch
Amide group	1639.27	N-H bend	Amines primary	1599.76	N-H bend
Nitro group	1319.09	N=O bend	Nitro groups	1400.16	N=O bend
Nitro group	1384.67	N=O bend	Ethers	1081.19	C-O stretch
Ethers	1102.06	C-O stretch	Esters	787.27	C-O stretch

After incubation, the plates were counted for the presence of live nauplii and the number was estimated using the following formula:

$$\frac{\text{number of dead nauplii}}{\text{number of dead nauplii} + \text{number of live nauplii}} \times 100 \quad (3)$$

3. Results and Discussion

3.1. Visual Observation. The formation of metal nanoparticles upon the addition the plant extract is accompanied by the colour change of the solution. As depicted in Figure 2 the *Morinda citrifolia* mediated selenium nanoparticles gradually changes its colour to light brown after 28 h and pale brown colour after 31 h and finally brownish red colour was obtained after 56 h.

3.2. UV-Visible Spectroscopy Analysis. The formation of SeNPs by using *Morinda citrifolia* leaf extract was preliminarily confirmed by UV-visible spectroscopy (Figure 3). The readings were recorded at specific time intervals such as 6, 12, 24, 48 and 72 h. SeNPs exhibited an absorption peak at 390 nm in its UV spectrum.

3.3. Transmission Electron Microscope. The morphological characteristics of biosynthesized SeNPs observed through

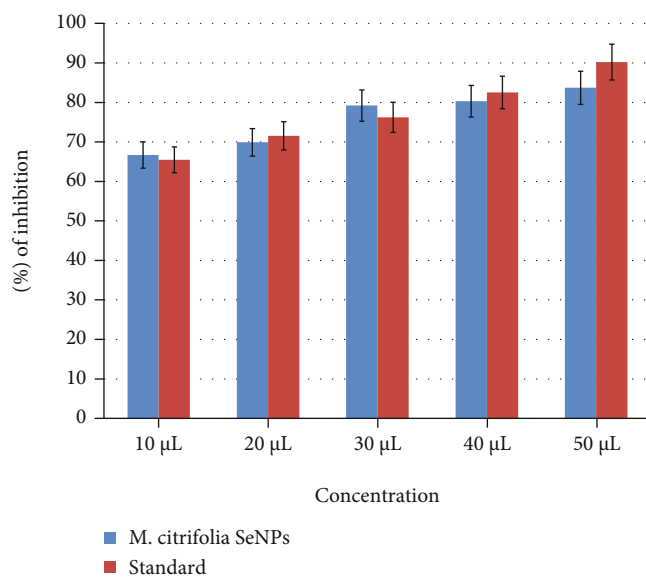


FIGURE 6: Free radical scavenging activity of *Morinda citrifolia* leaves extract mediated SeNPs.

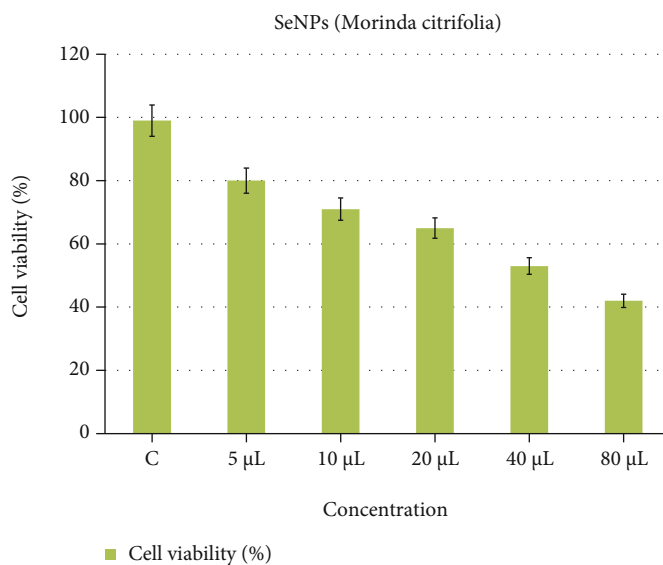


FIGURE 7: Anticancer activity of *Morinda citrifolia* mediated selenium nanoparticles against Hep G2 cell line.

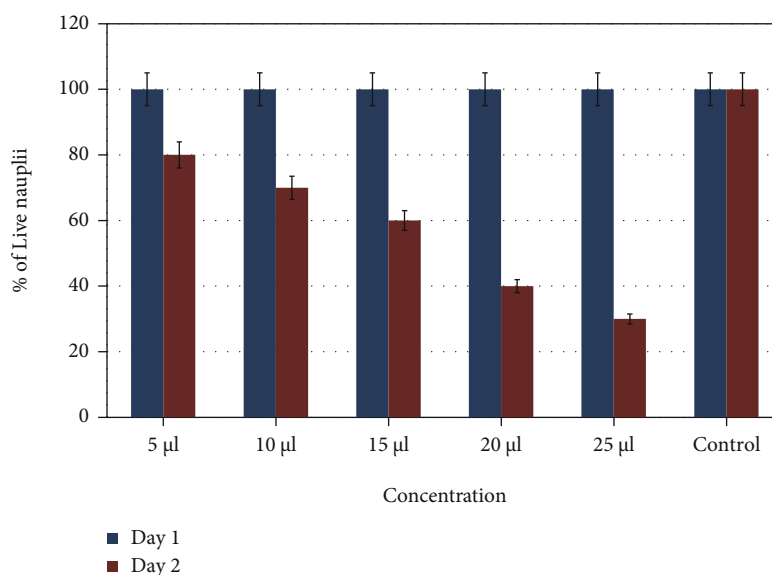


FIGURE 8: Brine shrimp lethality assay of SeNPs synthesized using *Morinda citrifolia*.

Transmission Electron Microscopy (TEM). Figure 4. shows the spherical morphology of SeNPs with the size ranges from 120-160 nm.

3.4. *Ft-IR*. Substance specific vibrations of the molecules led to the specific signals obtained by the FT-IR spectroscopy. Some of the absorption peaks at 3427.99 and 1639.27 cm^{-1} represents stretching Hydrogen bonded O-H phenols, alcohol and N-H bend amide functional groups which was depicted in Figure 5(a) and Table 1. And peaks at 1319.09 and 1384.67 cm^{-1} indicates the N=O bend nitro group. The peaks at 1102.06 cm^{-1} corresponds the stretching C-O ether functional group.

As depicted in Figure 5(b), the FT-IR spectra of green synthesized SeNPs showed peak at 3358.27 cm^{-1} , which indicated the presence of stretching Hydrogen bonded O-H phenols and alcohol groups. The band at 1599.76 cm^{-1} indicated N-H Bend primary amine functional group. The peaks obtained at 1400.16 and 1081.19 cm^{-1} indicated the N=O bend nitro group and C-O stretch ether functional groups. The bands at 787.27 cm^{-1} indicates the C-O stretching of esters.

3.5. *Antioxidant Activity*. Antioxidants acts as a defense mechanism to prevent the body from experiencing alleviating chronic diseases by reducing the cellular oxidative damage caused by the free radicals [10]. The antioxidant

activity of *Morinda citrifolia* mediated selenium nanoparticles was analysed by adopting DPPH method. As shown in Figure 6, the selenium nanoparticles showed significant free radical inhibition higher at 50 μL concentration in dose dependent manner. At 10 μL concentration the selenium nanoparticles showed free radical inhibition around 66.7% and 83.7% was obtained for 50 μL concentration.

3.6. Anticancer Activity. Figure 7 shows the Screening of bio-synthesized SeNPs results in potential anticancer activity against HepG2. Different concentrations of selenium nanoparticles (5, 10, 20, 40, 80 μL) was used in this study. The cytotoxicity analysis of the SeNPs shown a concentration dependent response and higher cytotoxicity increment observed at higher concentration (80 μL).

3.7. Cytotoxic Effect of Brine Shrimp Lethality Assay. The cytotoxicity of green synthesized selenium nanoparticles was tested by adopting brine shrimp lethality assay. At day 2, the percentage of live nauplii at lower concentration (5 μL and 10 μL) was found to be 70% & 80%. As shown in Figure 8, only 30% of nauplii was alive at higher concentration (25 μL). Therefore, the cytotoxic results predicted low toxicity of selenium nanoparticles.

4. Discussion

The microbial synthesis of SeNPs using non-pathogenic bacterium *Zooglea ramigera* obtained trigonal selenium nanorods [11]. In previous research work, broccoli mediated selenium nanoparticles, FT-IR analysis showed peaks at 3235, 1595, 1407, and 1099 cm^{-1} indicates the presence of O-H stretch, N-H bend, C-F stretch and C-O stretch of aliphatic ether, respectively. SeNPs (64 g/mL) exhibited complete inhibitory action against *Streptococcus agalactiae*, *Escherichia fergusonii*, and *Pseudomonas aeruginosa* and could be used in replacement of antibiotics for treating cutaneous infections caused by bacteria [12]. Biosynthesis of SeNPs synthesized using *Clausea dentata* exhibited strong larvicidal activity with increased concentration against the fourth instar larvae stage of *Culex quinquefasciatus*, *Aedes Aegypti*, and *Anopheles stephensi* [13]. SeNPs with doxorubicin combination exhibited excellent anti-cancer effect and it was found that SeNPs induced MCF-7 cell death through apoptosis [14]. The microbial synthesis of SeNPs by using *Bacillus species* against *Candida albicans* and *Aspergillus fumigatus* exhibited good antifungal activity (Mojtaba Shakibaie et al., 2015). SeNPs were biosynthesized using *Azoarcus* sp. which transformed the selenite to Se and generated spherical SeNPs. Dried *Vitis vinifera* (raisin) extract synthesized uniformly shaped and biopolymer (lignin)-capped selenium nanoballs [15]. The biogenic fabrication of SeNPs via the flower extract of *Bougainvillea spectabilis* resulted in stable hollow SeNPs with an average size of 24.24 ± 2.95 nm [16]. The cytotoxic behaviour of SeNPs in combination with X-ray was demonstrated in treating lung cancer cell lines. The participation of SeNPs in caspase-3 activation and its downstream target showed that lung cancer cells undergo apoptosis [17–22]).

5. Conclusion

Using the leaf extract of *Morinda citrifolia*, a simple approach was explored to develop a green, eco-friendly manner to synthesize SeNPs. The production of SeNPs was validated by the brownish red color obtained after adding sodium selenite to *Morinda citrifolia* leaf extract. UV-Vis spectroscopy, FT-IR, and TEM were also used to confirm the SeNPs, which were found to be 120–160 nm in size in *Morinda citrifolia*. In *Morinda citrifolia*, selenium NPs was shown to have an antioxidant activity of 66.7 percent to 83.7 percent of free radicals. The viability of tumour cells lowered, while increasing the concentration of nanoparticles. It proves that selenium nanoparticles mediated *Morinda citrifolia* have anticancer properties. In the brine shrimp lethality assay, selenium nanoparticles produce less harmful findings. The findings of this study imply that selenium nanoparticles mediated by *Morinda citrifolia* can be employed in biomedical applications in the future.

Data Availability

The data used in this study is done by the authors.

Conflicts of Interest

The authors declare, there is no conflict of interest.

Authors' Contributions

SR designed, SR, MN, carried out research, and SR, MN, MT, KA and SB wrote and corrected the manuscript.

Funding

Self-funding.

Acknowledgments

The authors would like to thank Saveetha Dental College and Hospital, SIMATS for providing lab facilities and constant support.




References

- [1] M. Nasrollahzadeh, M. Sajjadi, S. M. Sajadi, and Z. Issaabadi, "Green nanotechnology," in *Interface Science and Technology*, vol. 28, pp. 145–198, Elsevier, 2019.
- [2] C. Binns, *Introduction to Nanoscience and Nanotechnology*, John Wiley & Sons, 2010.
- [3] G. A. Silva, "Introduction to nanotechnology and its applications to medicine," *Surgical Neurology*, vol. 61, no. 3, pp. 216–220, 2004.
- [4] G. Dhanraj and S. Rajeshkumar, "Anticariogenic effect of selenium nanoparticles synthesized using brassica oleracea," *Journal of Nanomaterials*, vol. 2021, Article ID 8115585, pp. 1–9, 2021.
- [5] M. Shakibaie, H. Forootanfar, Y. Golkari, T. Mohammadi-Khorsand, and M. R. Shakibaie, "Anti-biofilm activity of biogenic selenium nanoparticles and selenium dioxide against clinical isolates of *Staphylococcus aureus*, *Pseudomonas*

- aeruginosa_, and _Proteus mirabilis_,” *Journal of Trace Elements in Medicine and Biology*, vol. 29, no. 29, pp. 235–241, 2015.
- [6] A. Khurana, S. Tekula, M. A. Saifi, P. Venkatesh, and C. Godugu, “Therapeutic applications of selenium nanoparticles,” *Biomedicine & Pharmacotherapy*, vol. 111, pp. 802–812, 2019.
- [7] R. Abou Assi, Y. Darwis, I. M. Abdulbaqi, L. Vuanghao, and M. H. Laghari, “Morinda citrifolia_ (Noni): A comprehensive review on its industrial uses, pharmacological activities, and clinical trials,” *Arabian Journal of Chemistry*, vol. 10, no. 5, pp. 691–707, 2017.
- [8] A. D. Pawlus and A. D. Kinghorn, “Review of the ethnobotany, chemistry, biological activity and safety of the botanical dietary supplement Morinda citrifolia (noni),” *Journal of Pharmacy and Pharmacology*, vol. 59, no. 12, pp. 1587–1609, 2007.
- [9] S. Rajeshkumar, J. Santhoshkumar, M. Vanaja et al., “Evaluation of zebrafish toxicology and biomedical potential of aeromonas hydrophila mediated copper sulfide nanoparticles,” *Oxidative Medicine and Cellular Longevity*, vol. 2022, Article ID 7969825, 12 pages, 2022.
- [10] M. Ali, P. Singh, L. Singh, and S. Kumar, *Phytochemical Constituents and Pharmacological Activities, Profile of Morinda Citrifolia: A Review*, 2020.
- [11] N. Srivastava and M. Mukhopadhyay, “Biosynthesis and structural characterization of selenium nanoparticles mediated by Zooglea ramigera,” *Powder Technology*, vol. 244, pp. 26–29, 2013.
- [12] D. Hegerova, K. Cihalova, P. Kopel, V. Adam, and R. Kizek, *Selenium Nanoparticles And Evaluation Of Their Antimicrobial Activity On Bacterial Isolates Obtained From Clinical Specimens*, Nanocon, 2015.
- [13] P. Sowndarya, G. Ramkumar, and M. S. Shivakumar, “Green synthesis of selenium nanoparticles conjugated Clausena dentata plant leaf extract and their insecticidal potential against mosquito vectors,” *Artificial Cells, Nanomedicine, and Biotechnology*, vol. 45, no. 8, pp. 1490–1495, 2017.
- [14] C. H. Ramamurthy, K. S. Sampath, P. Arunkumar et al., “Green synthesis and characterization of selenium nanoparticles and its augmented cytotoxicity with doxorubicin on cancer cells,” *Bioprocess and Biosystems Engineering*, vol. 36, no. 8, pp. 1131–1139, 2013.
- [15] G. Sharma, A. R. Sharma, R. Bhavesh et al., “Biomolecule-mediated synthesis of selenium nanoparticles using dried Vitis vinifera (raisin) extract,” *Molecules*, vol. 19, no. 3, pp. 2761–2770, 2014.
- [16] B. Deepa and V. Ganesan, “Biogenic synthesis and characterization of selenium nanoparticles using the flower of Bougainvillea spectabilis Willd,” *International Journal of Science and Research (IJSR)*, vol. 4, pp. 690–695, 2013.
- [17] L. Y. Cruz, D. Wang, and J. Liu, “Biosynthesis of selenium nanoparticles, characterization and X-ray induced radiotherapy for the treatment of lung cancer with interstitial lung disease,” *Journal of Photochemistry and Photobiology, B: Biology*, vol. 191, no. 191, pp. 123–127, 2019.
- [18] M. Nasrollahzadeh, S. M. Sajadi, M. Sajjadi, and Z. Issaabadi, *An Introduction to Nanotechnology* Elsevier.
- [19] O. Potterat and M. Hamburger, “Morinda citrifolia(Noni) Fruit - Phytochemistry, Pharmacology, Safety,” *Planta Medica*, vol. 73, no. 3, pp. 191–199, 2007.
- [20] N. Srivastava and M. Mukhopadhyay, “Biosynthesis and structural characterization of selenium nanoparticles mediated by _Zooglea ramigera_,” *Powder Technology*, vol. 244, no. 244, pp. 26–29, 2013.
- [21] T. Francis, S. Rajeshkumar, A. Roy, and T. Lakshmi, “Anti-inflammatory and Cytotoxic Effect of Arrow Root Mediated Selenium Nanoparticles,” *Pharmacognosy Journal*, vol. 12, no. 6, pp. 1363–1367, 2020.
- [22] H. Fernández-Llamosas, L. Castro, M. L. Blázquez, E. Díaz, and M. Carmona, “Biosynthesis of selenium nanoparticles by Azoarcus sp. CIB,” *CIB. Microbial cell factories.*, vol. 15, p. 1, 2016.

Research Article

Azadirachta indica-Derived Silver Nanoparticle Synthesis and Its Antimicrobial Applications

Aditya Amrut Pawar,¹ Jyotirmayee Sahoo,¹ Aakash Verma,¹ Abdullah M. Alswieleh ,² Abhijit Lodh,¹ Rajesh Raut,¹ Jaya Lakkakula ,^{1,3} Byong-Hun Jeon,⁴ and Md. Rabiul Islam ⁵

¹Amity Institute of Biotechnology, Amity University Maharashtra, Mumbai-Pune Expressway, Bhatan, Panvel, Mumbai 410206, India

²Department of Chemistry, College of Science, King Saud University, Riyadh 11451, Saudi Arabia

³Centre for Computational Biology and Translational Research, Amity institute of Biotechnology (AIB), Amity University Maharashtra, Mumbai-Pune Expressway, Bhatan, Panvel, Mumbai 410206, India

⁴Department of Earth Resources & Environmental Engineering, Hanyang University, 222-Wangsimni-ro, Seongdong-gu, Seoul 04763, Republic of Korea

⁵Department of Pharmacy, University of Asia Pacific, Dhaka, Bangladesh

Correspondence should be addressed to Jaya Lakkakula; spencerjaya@gmail.com and Md. Rabiul Islam; robi.ayaan@gmail.com

Received 5 April 2022; Accepted 25 April 2022; Published 9 May 2022

Academic Editor: Hiwa M. Ahmed

Copyright © 2022 Aditya Amrut Pawar et al. This is an open access article distributed under the Creative Commons Attribution License, which permits unrestricted use, distribution, and reproduction in any medium, provided the original work is properly cited.

Advancement of biologically driven experimental procedure for the generation of metal nanoparticles is a major aspect in the domain of nanotechnology. Herein, we synthesized one pot silver nanoparticles (AgNPs) using *Azadirachta indica* (Neem plant) via green synthesis method. The alkaloids and flavonoids in the plant extract served as capping and reducing agent to develop silver nanoparticles. The characterization of synthesized AgNPs was performed using analytical techniques such as UV-visible spectroscopy, FTIR, and SEM. The synthesized AgNPs were further impregnated onto a cotton cloth and the antimicrobial studies were performed. The AgNPs embedded in cotton fabric were found to show zone of inhibition against the fungi *Candida albicans*, gram-negative bacteria *Escherichia coli*, and gram-positive bacteria *Staphylococcus aureus*. This experimental study suggests that the AgNPs impregnated on cotton cloth could have great potential for application in smart nanobandages for wound dressing, medical textiles, sports clothing, etc.

1. Introduction

Nanotechnology is the interdisciplinary science which involves chemistry, physics, biology, material sciences, and the wide range of the engineering disciplines. Nanotechnology is the science and engineering of devices and materials on the scale of atoms or small groups of atoms having material size ranged from 0.1 to 100 nm [1]. These nanoscale ranged groups of atom possess various characteristics such as physical strength, magnetism, optical effects, chemical reactivity, and electrical conductance because of its small

size. The change in all the parameters or properties is due to two reasons. Firstly, very large surface area-to-volume ratio, and secondly, quantum mechanics change at nanoscale [2]. Nanotechnology has two approaches, i.e., top-down and bottom-up approach. In top-down approach, the structural size is diminished from larger to smaller, while in bottom-up approach the individual molecules or atoms get changed into nanostructures [3].

Metal nanoparticles such as silver, platinum, gold, and palladium are utilized for many purposes in industry and research. Amongst all these, AgNPs have been extensively

used due to its unique physical and chemical features, which consists of high electrical conductivity and thermal, optical, antimicrobial, and biological properties [4]. Owing to its unique properties, AgNPs are widely used in biomedical applications such as wound dressings [5], antiseptic fabrics [6], topical creams [7], and sprays [8]. AgNPs exhibit biocidal effect against microorganisms through interruption of the membrane followed by disruption of their enzymatic activities [9].

AgNPs are synthesized through three methods, i.e., chemical, physical, and biological. Chemical and physical methods have many disadvantages. Physical methods involve high energy and cost, hence is mostly not preferred method for synthesis [10, 11]. Chemical synthesis involves hazardous chemical which are hazardous to environment [12]. Preferred method for synthesis is by biological method as it is simple, rapid, nontoxic, dependable, and has greener approach [13]. Biological synthesis includes synthesis by microorganisms [14], plant extracts [15], and agricultural wastes [16]. Plant extracts contain biocompounds such as phenolic compounds, alkaloids, terpenoids, sugars, enzymes, and proteins which reduces metallic salts from positive oxidation state to zero oxidation state [17]. When the AgNP synthesis happens in the presence of plant extract, not only the silver salts are reduced but also the plant extracts act as capping agent [18]. The capping of AgNPs avoids the nanoparticle agglomeration, reduces toxicity, and enhances antimicrobial action.

In the current study, we have studied the use *Azadirachta indica* (neem) leaf extract for AgNP synthesis. Neem belongs to the Meliaceae family and is found extensively in India [19]. *Azadirachta indica* leaves are widely available in the subcontinent and also have rapid growth. Neem leaves contain polyphenolic flavonoids named β -sitosterol and quercetin which are known for its antibacterial and antifungal activities [20]. Neem leaves and its components were reported to have anti-inflammatory, immunomodulatory, antiulcer, anti-hyperglycemic, antioxidant, antimutagenic, anticarcinogenic, antimalarial, antifungal, antibacterial, and antiviral properties [21]. The neem leaves were further selected as the reducing agent in the biological synthesis of AgNPs because of its antimicrobial nature, and thus, we tend to enhance its antimicrobial efficacy by developing AgNPs. The neem leaf extract not only has the potential to reduce the silver salts to AgNPs but also stabilizes AgNPs [18].

Hence, in the current study, we examined the antibacterial activity of AgNPs entrapped on greige cotton cloth against gram-positive (*S. aureus*) and gram-negative bacteria (*E. coli*). Additionally, antifungal activity was also checked for *C. albicans*. The silver nanoparticles entrapped cloths were washed for 25 times and each of the successive washed clothes was checked for its antimicrobial activity. Formation of AgNPs was detected using UV-Vis spectroscopy. The size and morphology of AgNPs was confirmed by scanning electron microscopy (SEM) and transmission Electron Microscopy (TEM). Entrapment of AgNPs on cloth and size was confirmed by SEM. Fourier-transform infrared spectroscopy (FTIR) studies were performed for AgNPs entrapped cloth.

2. Materials and Methods

2.1. Materials. Silver Nitrate (AgNO_3), Potato dextrose agar (PDA), Potato dextrose broth (PDB), Nutrient broth (NB), Agar Agar Type-1, and Itraconazole were procured from HIMEDIA Pvt. Ltd., Mumbai, India. Ampicillin and Itraconazole were used as positive control for antibacterial and antifungal studies, respectively. During the experiment, double distilled water was used. The leaves of *Azadirachta indica* were collected from Bhatan village, Mumbai, India. Culture of *Staphylococcus aureus* of strain 6538P and *Escherichia coli* was used for antibacterial test. *Candida albicans* was used for studying antifungal activity of the cloth. Fabric cotton cloth was collected from a local shop in Mumbai, India.

2.2. Extraction of Plant Extract. *Azadirachta indica* leaves harvested locally were washed with tap water and rinsed with double distilled water several times with a view to clear out any dust or unwanted particles that might restrict adhesion of Ag^+ ions during the synthesis process. The washed leaves were dried, accurately weighed, and finely cut for the preparation of leaf extract. The mixture was then boiled for 30 minutes in double distilled water to release intracellular material into the solution. Following it, the mixture was cooled and filtered through Whatman filter paper. The filtrate obtained was thus stored at 4°C and later used for biosynthesis of silver nanoparticles.

2.3. Synthesis of Silver Nanoparticles Using Neem Plant Extract. The filtered suspension obtained was further treated with AgNO_3 solution for AgNP synthesis. The entire process was carried out on a magnetic stirrer at fixed RPM. The bio-reduction of silver ions in the solution was observed at regular time interval by scanning the UV-Vis spectra at a range from 200 to 900 nm. The synthesized AgNPs obtained were further subjected to centrifugation and washing for removal of unreacted Ag^+ ions. Synthesized AgNPs were kept at 4°C for further analysis.

2.4. Impregnation of Silver Nanoparticles on Cotton Cloth. Cloth material was washed at room temperature (RT) with double distilled water, dried, and cut to the dimension of $4\text{ cm} \times 4\text{ cm}$. The cut clothes were immersed in plant extract for 2 h at RT and then dried. These plant extract entrapped clothes were immersed in the AgNO_3 solution for 1 hour at RT and were removed and dried. The clothes were further analyzed by means such as SEM, FTIR, and antibacterial examinations.

2.5. Characterization of Silver Nanoparticles

2.5.1. UV-Vis Spectrophotometer. The progress of AgNP synthesis was observed using UV-Visible spectrophotometer (SHIMADZU UV-1800). The absorption spectrum was recorded in the range of 200-900 nm.

2.5.2. Scanning Electron Microscopy. The surface morphology of AgNPs was characterized by SEM which was performed using VEGA3TESCAN. Different samples including

plain cotton cloth, cotton cloth with Neem extract, and cotton cloth impregnated with AgNPs before and after washing were irradiated with an electron beam at 10 kV. Before analysis, samples were gold coated through sputter deposition due to the fact that gold has higher conductivity and does not interfere with investigation of AgNPs.

2.5.3. FTIR. FTIR was used to recognize the biomolecules of the Neem leaf extract which plays crucial role in capping, reducing, and stabilizing the AgNPs. FTIR spectra were obtained for the plain cloth, cloth impregnated AgNPs, cloth impregnated AgNPs washed with water, cloth impregnated AgNPs washed with mild detergent, and cloth impregnated AgNPs washed with strong detergent by using BRUKER spectrophotometer in the spectral range of 4000-400 cm^{-1} having a resolution of 4 cm^{-1} . The fundamental component of the universal attenuated total reflectance sample holder was a ZnSe/diamond composite. The FTIR analysis was studied to validate the presence of AgNPs before and after washing steps.

2.6. Washing of Impregnated Silver Nanoparticle Clothes. To confirm the leaching of the AgNPs from the impregnated cotton cloth, they were further subjected to 25 cycles of washing process with distilled water and detergents (strong and mild detergent). Upon the first cycle of washing, clothes were dried, ironed, and then again subjected to second cycle of wash and this was repeated till 25 cycles. Later antibacterial and antifungal activities were carried on AgNPs impregnated cloth before and after washing steps.

2.7. Antimicrobial Assay

2.7.1. Antibacterial Activity of Entrapped Silver Nanoparticle on Cloth. Antibacterial activity was performed against two bacterial stains, i.e., gram-positive *Staphylococcus aureus* and gram-negative *Escherichia coli* bacteria. Loop full of both bacterial cultures was taken from stock culture and inoculated for 24 h in nutrient broth at 37°C. Spread plate technique was used to streak the sterile nutrient agar plates for both the fresh cultures. The impregnated AgNPs on cotton cloth of dimension 4 cm × 4 cm were subjected to 25 cycles of distilled water wash and each of these cloth pieces of 1 cm × 1 cm dimension was placed on the streaked nutrient agar plates to check its antibacterial activity. Same procedure was followed for mild detergent washed clothes and strong detergent washed clothes. Later, the petri plates were incubated at 37°C for 24 h followed by observation of zone of inhibition. Positive control used for both the cultures was ampicillin which was entrapped on cotton cloth of dimension 1 cm × 1 cm.

2.7.2. Antifungal Activity of Entrapped Silver Nanoparticle on Cloth. Antifungal activity was performed against *Candida albicans*. Loop full of fungal culture was taken from stock culture and inoculated for 48 h in potato dextrose broth at 37°C. Swabbing was performed on sterile potato dextrose agar plates with the fresh culture. The impregnated AgNPs on cotton cloth of dimension 4 cm × 4 cm were subjected to 25 cycles of distilled water wash and each of these cloth

pieces of 1 cm × 1 cm dimension was placed on the streaked nutrient agar plates to check its antifungal activity. Same procedure was followed for mild detergent washed clothes and strong detergent washed clothes. Later, the plates were incubated at 37°C for 24 to 48 h. The zone of inhibition was also observed. Itraconazole discs were used as positive control for antifungal studies.

3. Results and Discussion

3.1. To Analyze the Formation, Size, and Shape of AgNPs

3.1.1. UV-Vis Spectroscopy. For different aqueous AgNO_3 concentrations, comparative studies were carried out to examine the effect of different amounts of leaf biomass on bioreduction rate of AgNPs. The quantity of leaf extract showed a significant role in size dispersion of AgNPs. The plant extract showed peak at 280 nm but no peak was observed between 400 nm and 500 nm. The reduction of the silver ions into AgNPs in the presence of plant extract can be observed through change in color. The leaf extract solution color changed from yellowish green to brown and became darkish brown gradually with time on addition of Ag^+ ions due to the surface plasmon resonance (SPR). Ag^+ ions reduction occurred rapidly in the presence of neem leaf extract and AgNP synthesis was completed in 1 h. The change in the absorbance was noted down every 10 minutes interval but there was no change in absorbance after 1 h indicating no further formation of nanoparticles as observed in Figure 1. The maximum absorption peak at 420 nm was observed in the UV-Vis spectrophotometer analysis indicating the formation of AgNPs. This broad SPR peak has been well studied for AgNPs with the size ranged from 10 to 100 nm [18].

3.2. To Confirm Impregnation of AgNPs on the Cloth

3.2.1. FTIR Analysis. The FTIR spectra were measured for the plain cloth and impregnated cloth with AgNPs (Figure 2). The spectrum for plain cloth showed bands at 3302.23 cm^{-1} , 3257.11 cm^{-1} , and 3336.32 cm^{-1} which corresponds to carboxylic O-H stretching, alcoholic O-H stretching, and N-H stretching for secondary amine, respectively. The band located at about 1103.43 cm^{-1} and 1023.74 cm^{-1} can be allocated to C-O-C or C-O functional groups. The spectrum for impregnated cloth with AgNPs showed broad intense band at 3335.10 cm^{-1} which can be attributed to the N-H stretching frequency which arises from the peptide linkages available in the proteins of the neem leaf extract and 1635.65 cm^{-1} band for amide I bonds for proteins (carbonyl C=O stretching). The amide I bond in the spectrum might have originated from the proteins available in the leaf extract which act as capping ligands of the synthesized nanoparticles. These proteins contained in leaf extract could be flavanones or terpenoids which help in reducing and stabilizing the synthesized AgNPs, whereas the band around 1600 cm^{-1} was not visible in the spectrum of plain cloth.

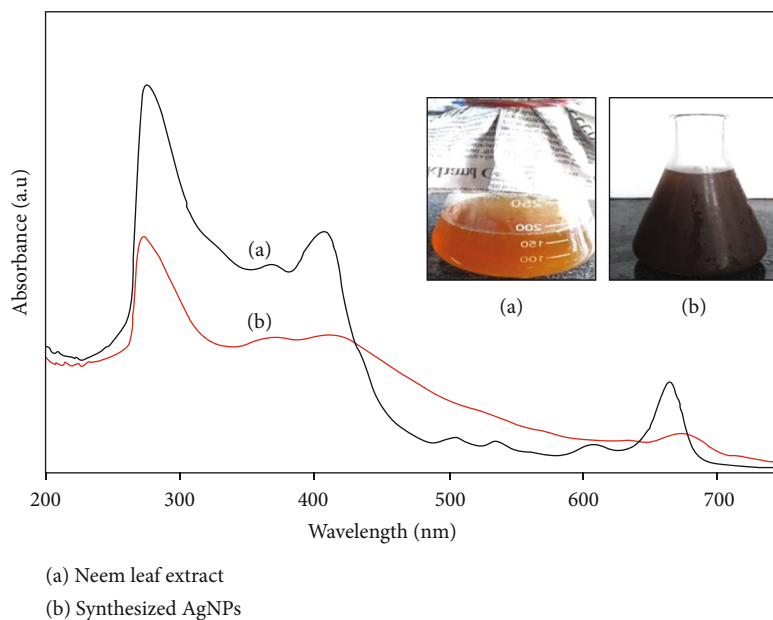


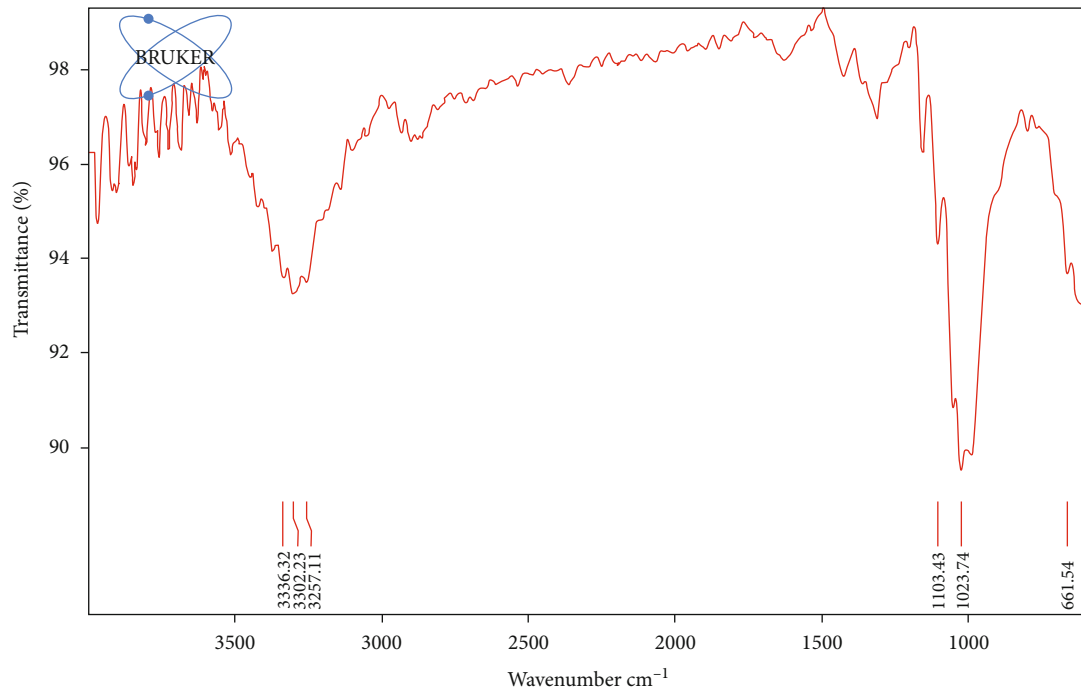
FIGURE 1: UV-Vis spectra of (a) neem leaf extract and (b) synthesized AgNPs.

3.2.2. SEM Analysis. The surface morphology of plain cotton cloth, cotton cloth impregnated with AgNPs, cotton cloth impregnated with AgNPs (after 25 cycles of distilled water wash), cotton cloth impregnated with AgNPs (after 25 cycles of mild detergent wash), and cotton cloth impregnated with AgNPs (after 25 cycles of strong detergent wash) was analyzed using SEM. The micrograph obtained in Figure 3 clearly confirmed the presence of AgNPs from Figures 3(b)–3(e), whereas no AgNPs were observed in Figure 3(a). Thus, we clearly demonstrate the impregnation of AgNPs on cotton cloth and adherence of AgNPs were still observed even after 25th washing with water or detergent. The antibacterial and antifungal results obtained clearly justify the results.

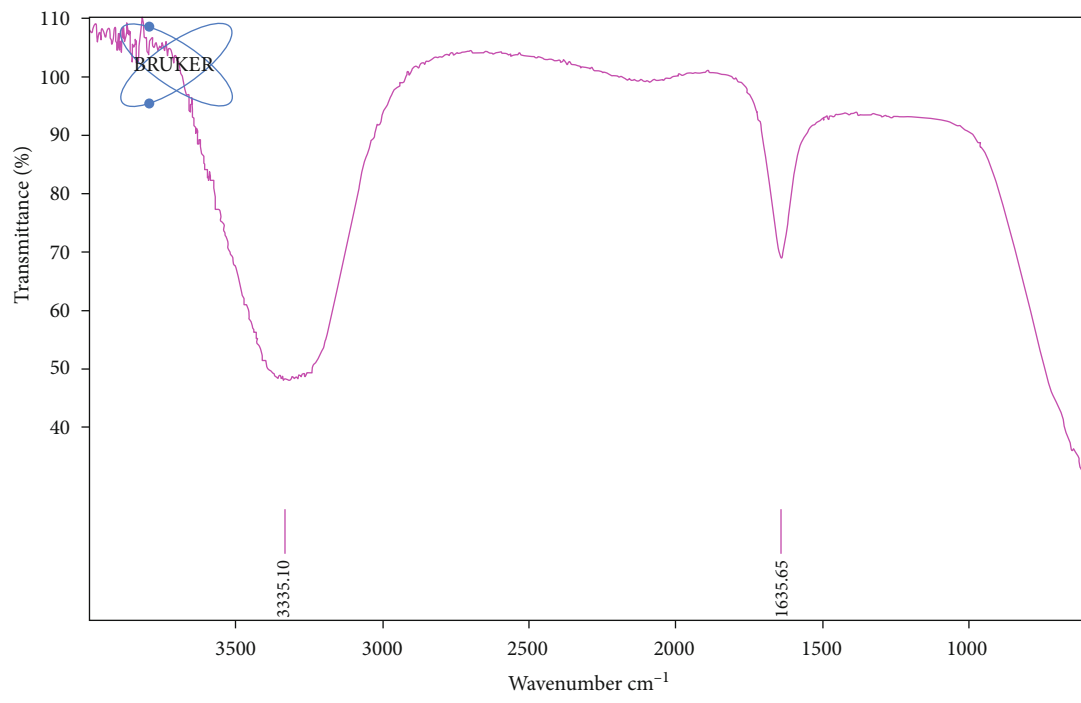
3.3. Antibacterial Activity. The two strains of bacteria *E. coli* (gram-negative) and *S. aureus* (gram-positive) are most commonly associated with infected wounds which were selected for antibacterial studies. Both the strains were exposed to clothes impregnated with AgNPs before and after 25 cycles of washes (mild and strong detergent) to confirm its antibacterial property. The effect of synthesized AgNPs on both gram-positive and gram-negative bacteria could indicate possible mode of action. AgNPs are known to display extensive range of antibacterial effects via different biochemical pathways. The AgNPs entrapped 1 cm × 1 cm cloth were immediately tested for respective antimicrobial activities against gram-negative (*E. coli*) (Figures 4(a) and 4(b)) and gram-positive (*S. aureus*) (Figures 5(a) and 5(b)) bacterial strains showing the respective zone of inhibition. Based on the zone of inhibition produced, it can be confirmed that the AgNPs demonstrated excellent antibacterial activity till 25 washes against both *S. aureus* and *E. coli*. The high surface to

volume ratio and small size of nanoparticles produce a significant bactericidal effect which permits the AgNPs to penetrate the cell wall of the bacteria and trigger the cell death [22, 23]. AgNPs when interact with the bacterial cell membrane having proteins along with sulfur compounds, the silver ion further attacks metabolic chain of bacteria and DNA molecules further causing the cells get damaged and died [24]. Thus, the results show that biologically synthesized AgNPs when embedded on cloth have antibacterial activity against gram-positive and gram-negative bacteria. Due to antimicrobial activity of AgNPs, coated cloth can be used as a potential fabric material for front-line health workers, sportspersons, military people, etc.

3.4. Antifungal Activity. The AgNPs entrapped 1 cm × 1 cm cloth were similarly tested for antifungal activity against *C. albicans* showing the respective zone of inhibition. The AgNPs coated cloth showed excellent antifungal activity even after washing the cloth with strong and mild detergent. Based on inhibition zone produced, it can be assumed that the synthesized AgNPs exhibited antifungal activity till 25 washes against *C. albicans* (Figures 6(a) and 6(b)) and (Figures 7(a) and 7(b)). AgNPs might have got attached and penetrate the cell membrane of the fungi by creating pores or “pits” in the membrane causing the leakage of the intracellular components out and it is also reported that AgNPs get attached to the respiratory sequence causing inhibition cell division and ultimately cell death [25, 26]. Therefore, it is expected that the neem leaf extract synthesized AgNPs coated fabric can be used in medical applications such as uniform for health workers, undergarments, bedding linen, and towels since it has antifungal activity against harmful fungal pathogens.



(a)



(b)

FIGURE 2: FTIR spectra for (a) plain cloth and (b) cloth impregnated with AgNPs.

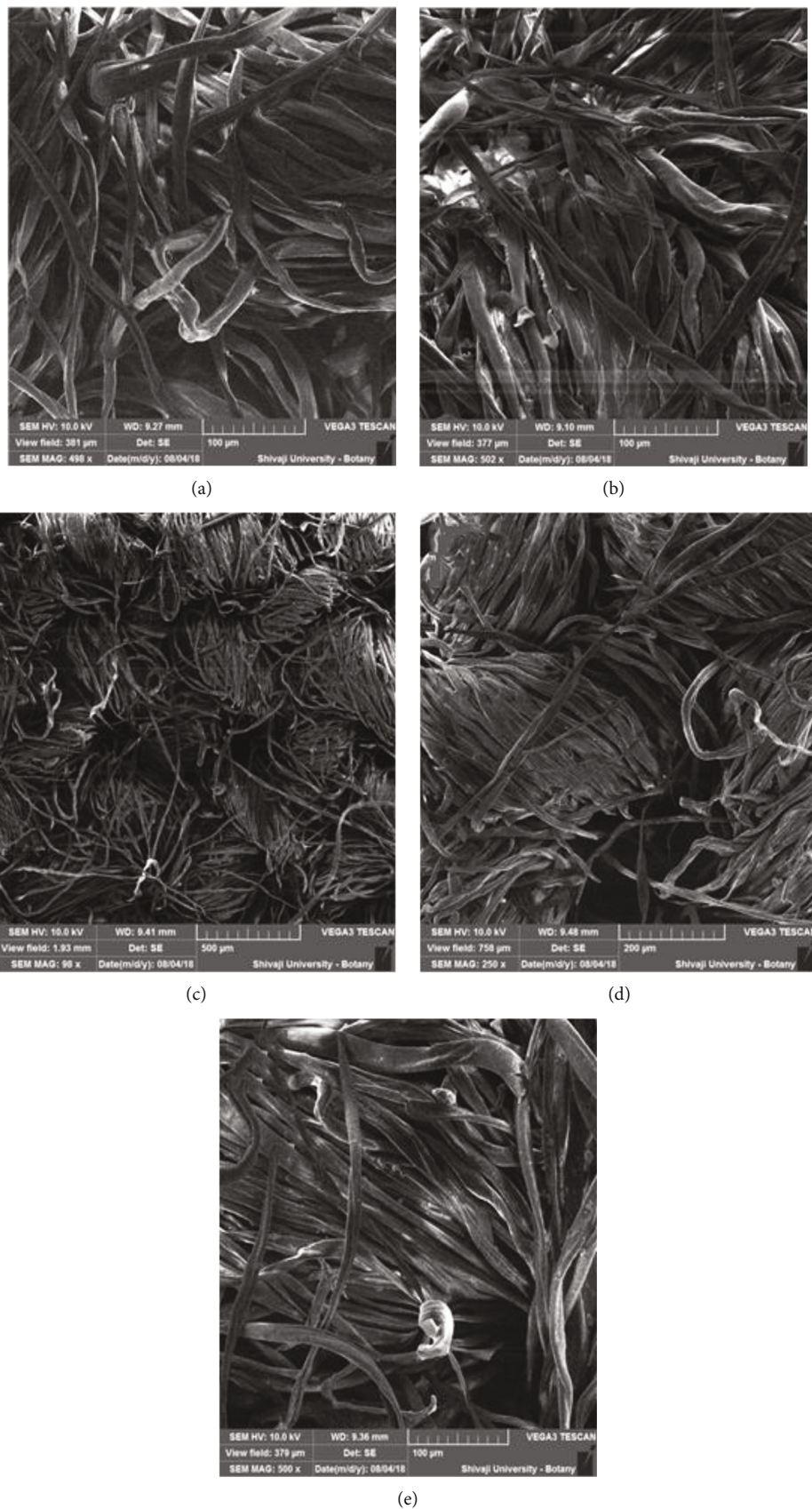
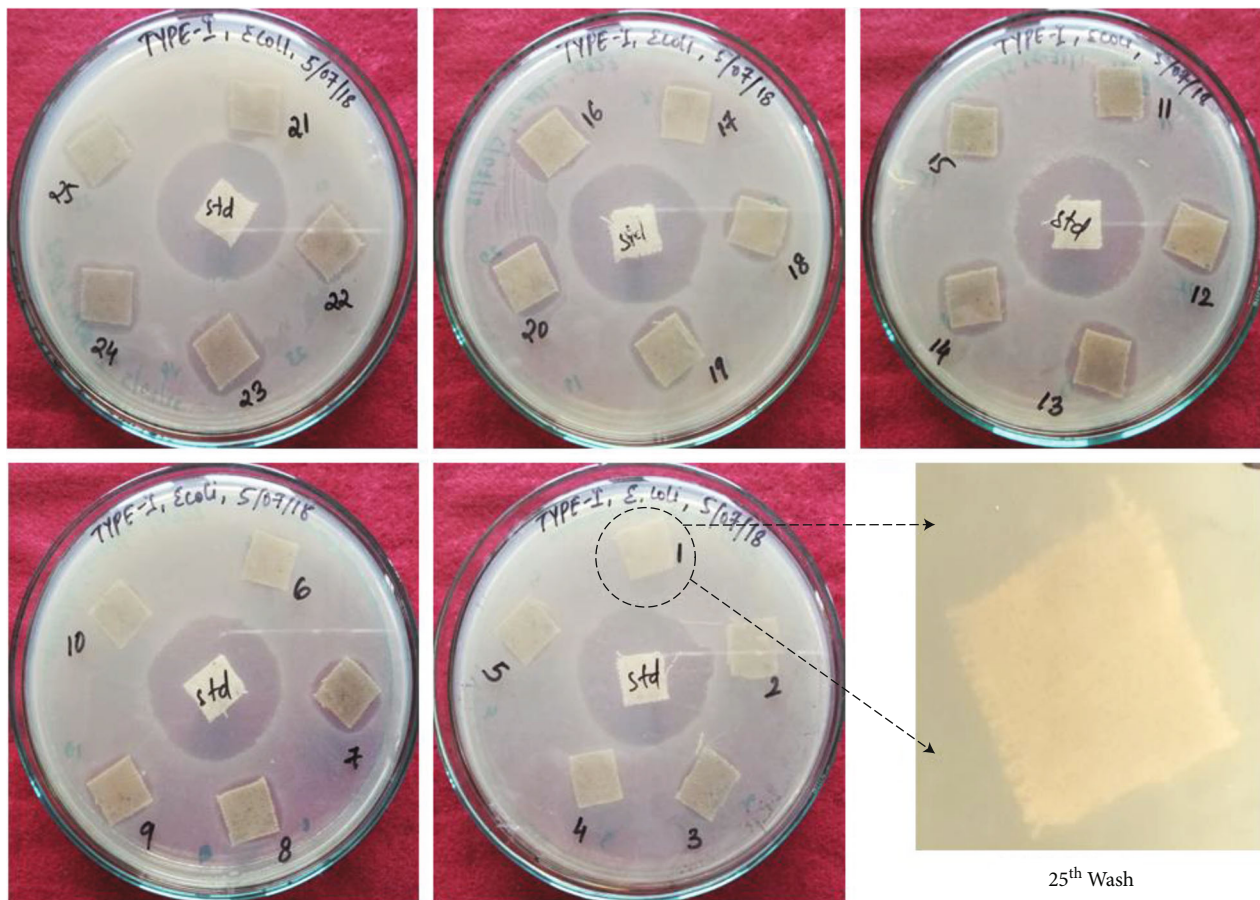


FIGURE 3: SEM image of (a) cotton cloth with plant extract only (top left). (b-e) AgNPs embedded onto the fibers of the cotton cloth.



(a)

FIGURE 4: Continued.

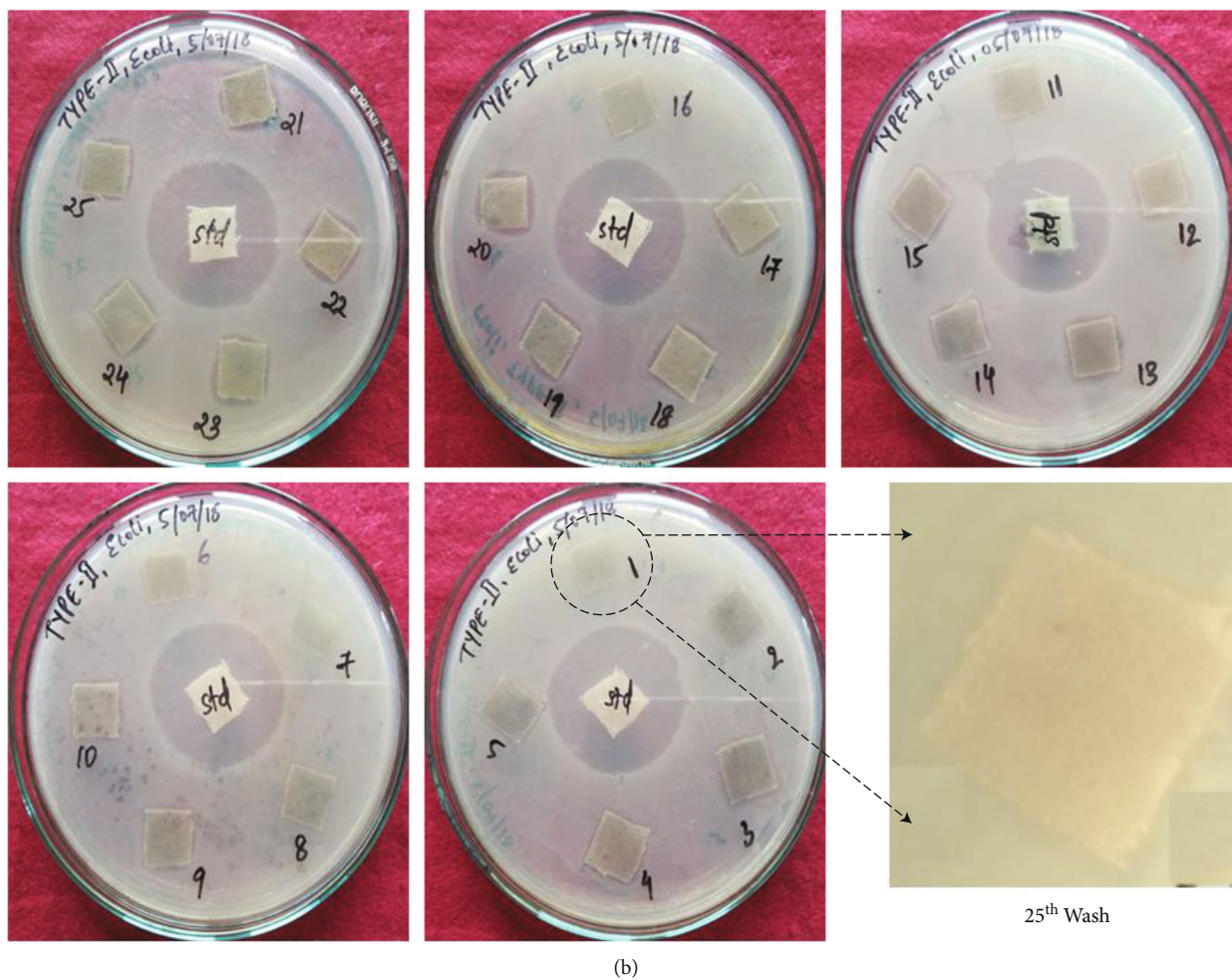
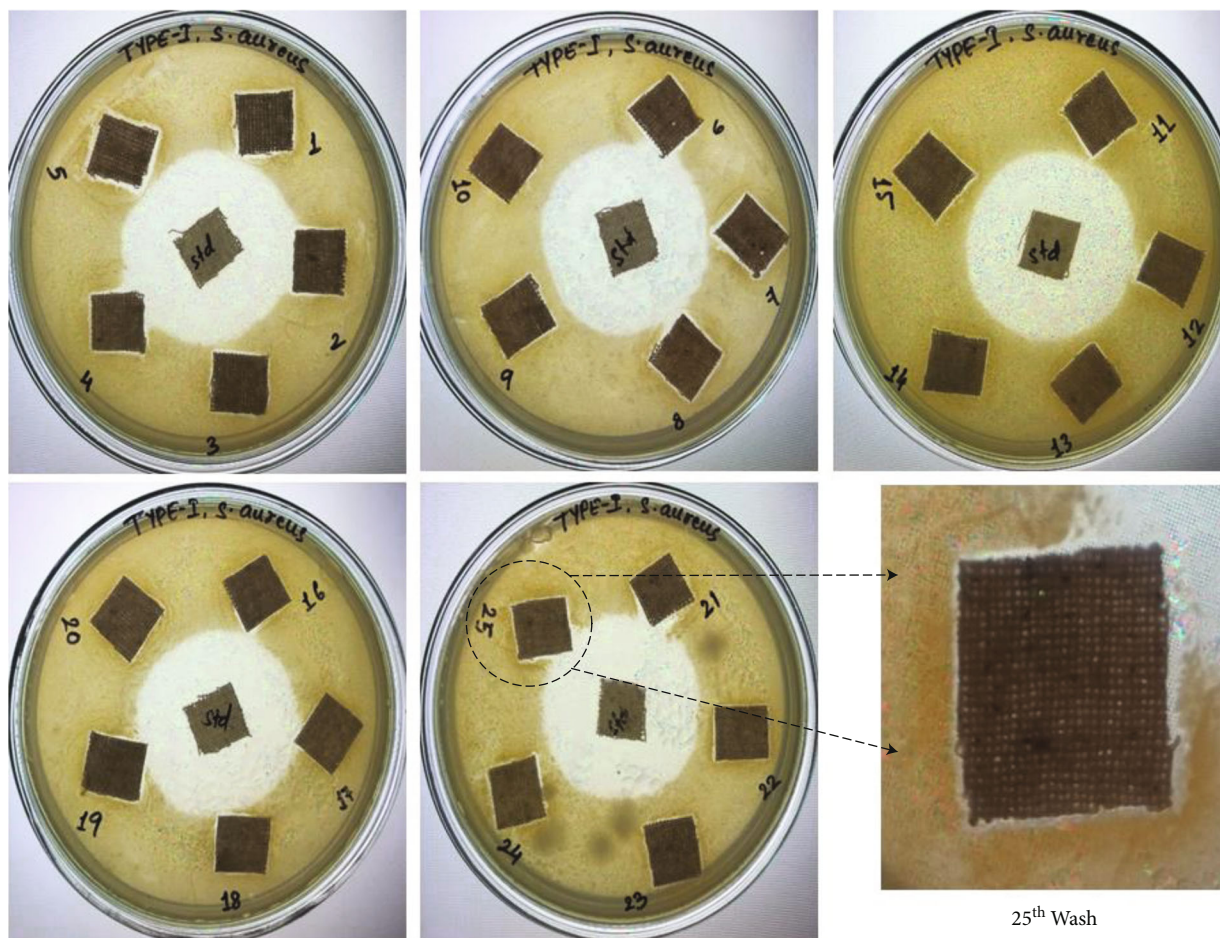


FIGURE 4: Antibacterial activity of AgNPs against *E. coli* species after 25 washes (a) mild detergent and (b) strong detergent.



(a)

FIGURE 5: Continued.

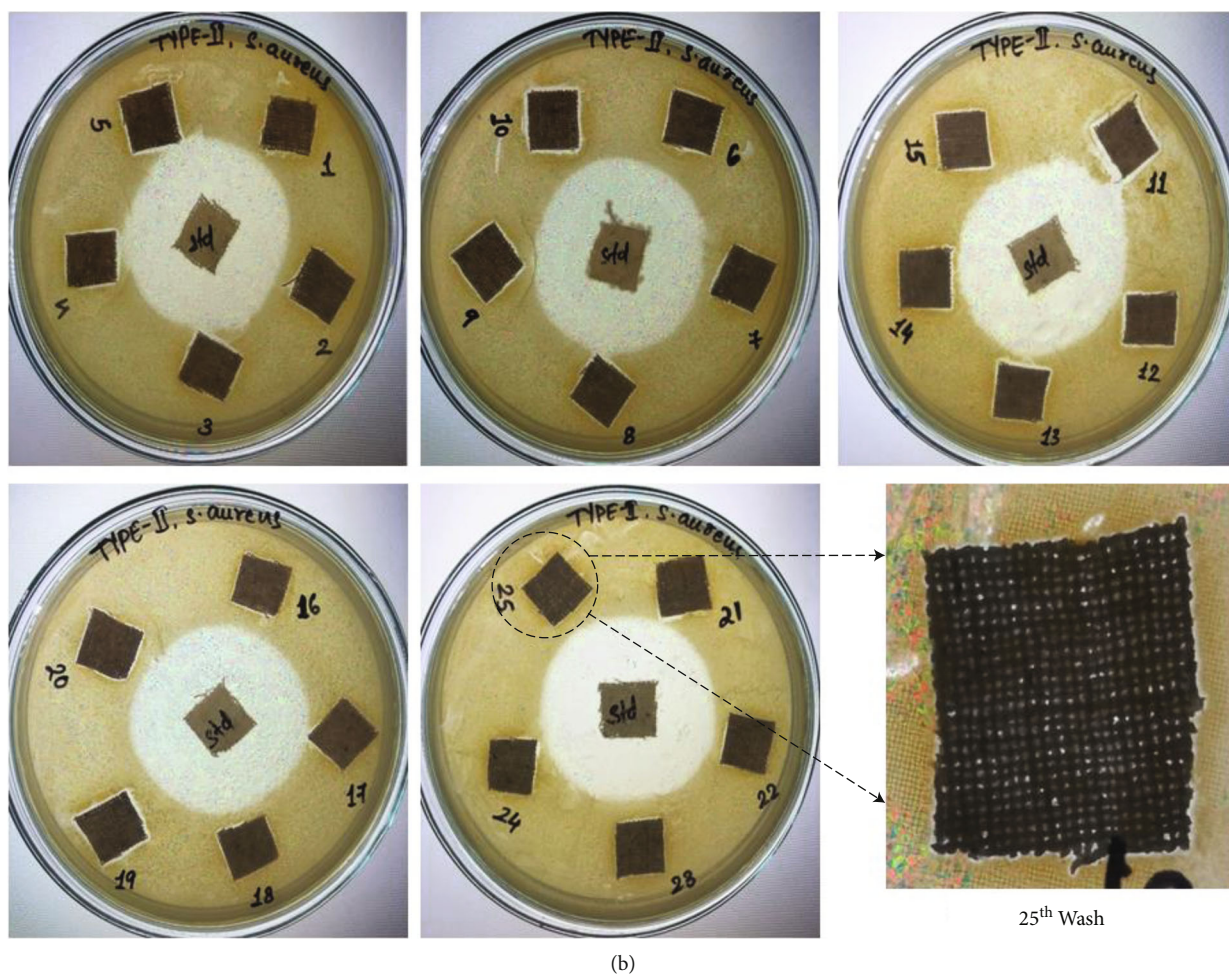
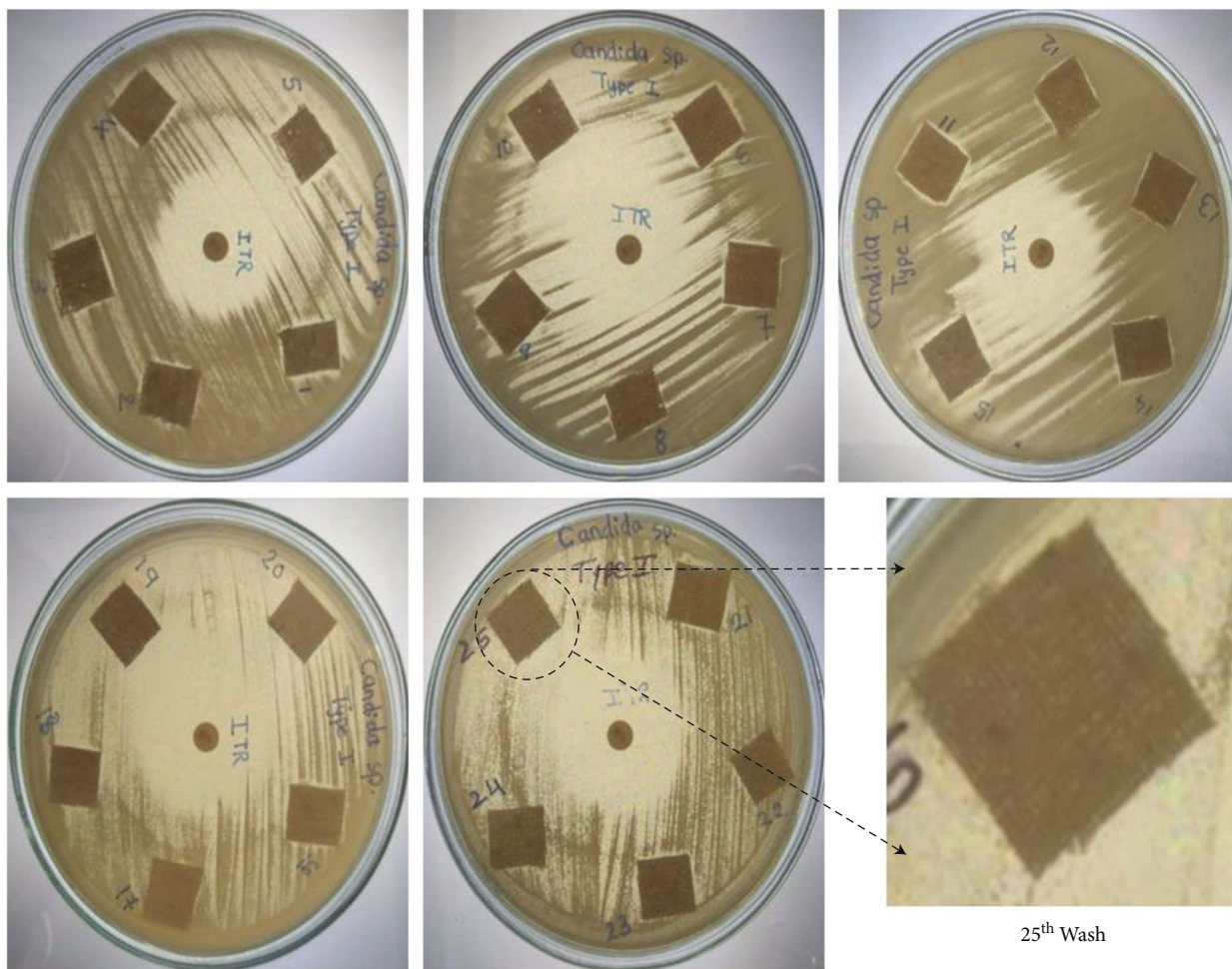


FIGURE 5: Antibacterial activity of AgNPs against *S. aureus* species after 25 washes (a) mild detergent and (b) strong detergent.



(a)

FIGURE 6: Continued.

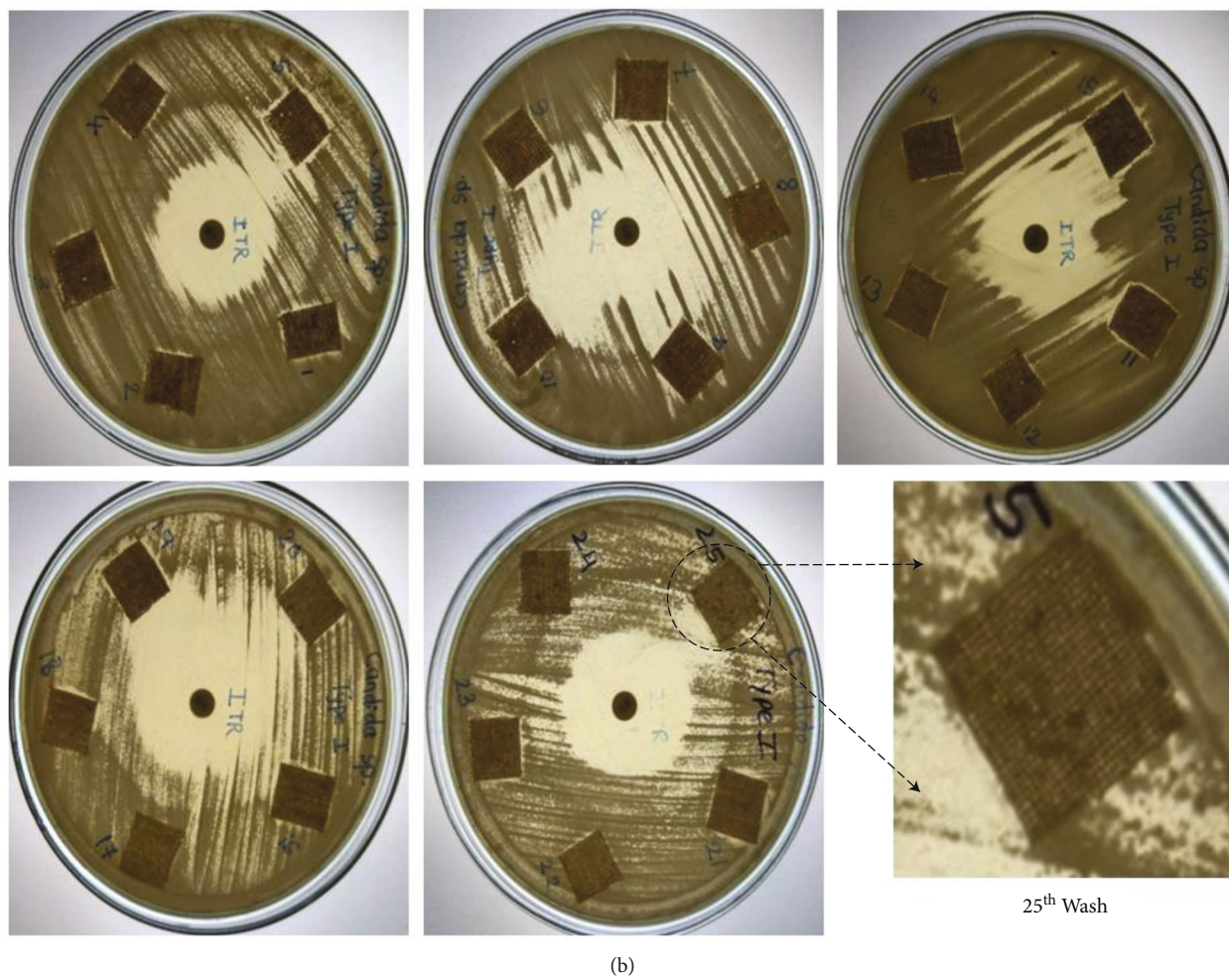
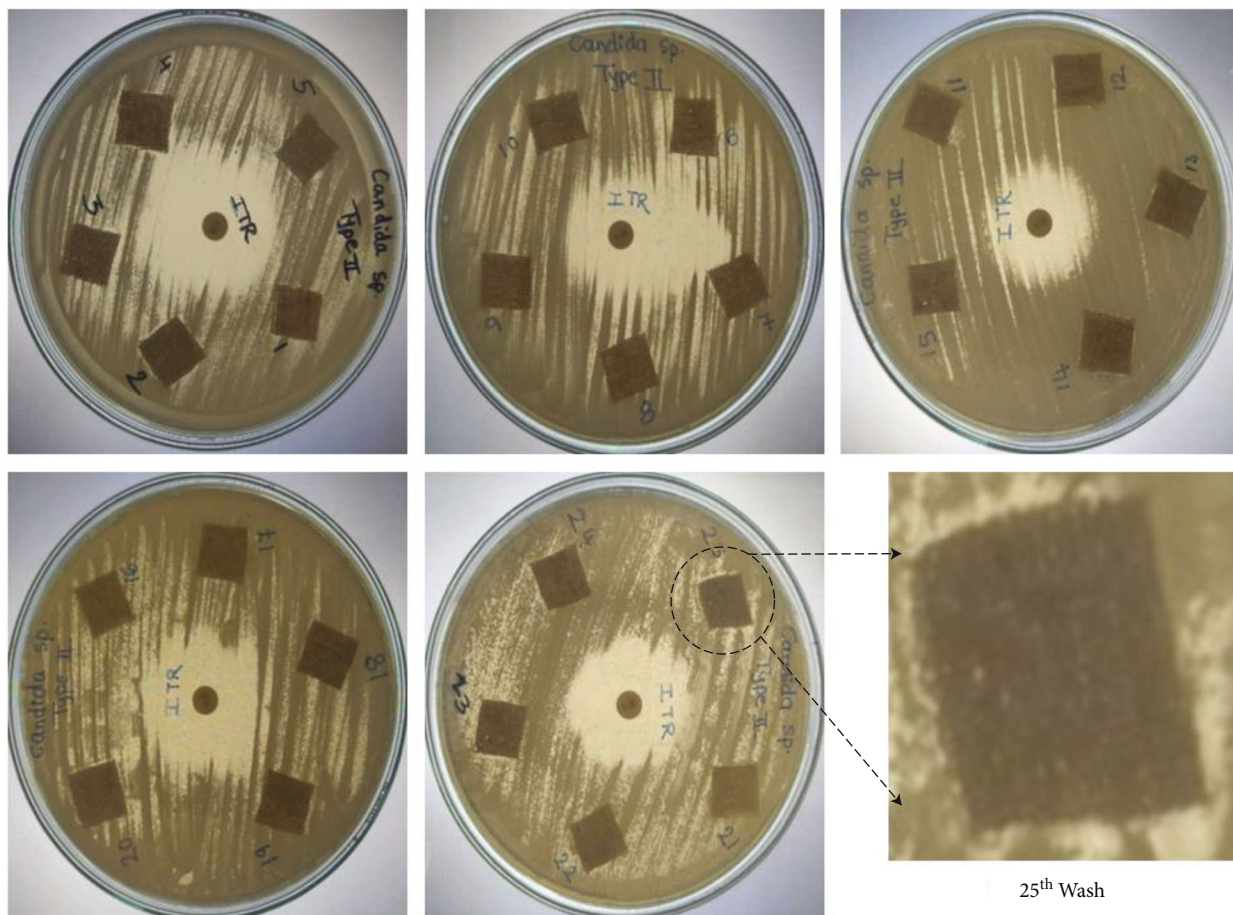


FIGURE 6: Antifungal activity of AgNPs against *C. albicans* after 25 washes of mild detergent (a) 48 h and (b) 72 h.



(a)

FIGURE 7: Continued.

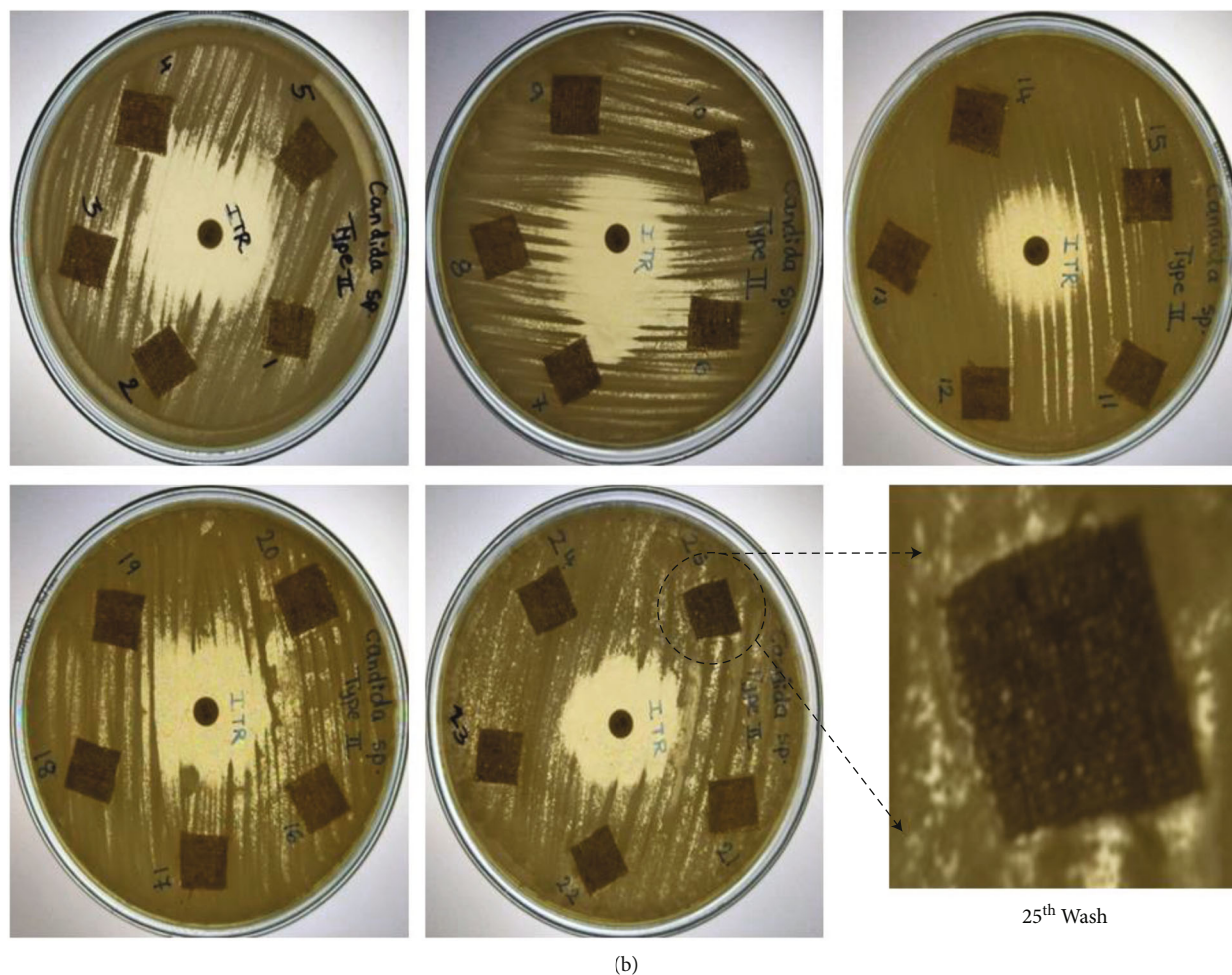


FIGURE 7: Antifungal activity of AgNPs against *C. albicans* after 25 washes of strong detergent (a) 48 h and (b) 72 h.

4. Conclusion

The biological synthesis of AgNPs from *Azadirachta indica* leaf extract was successful. AgNPs produced a characteristic peak at in the range of 400–500 nm due to its SPR seen in UV-Vis spectrophotometer. The TEM and SEM analyses showed that the AgNPs produced were spherical and in the range of 20 nm–100 nm with a capping material around it. The FTIR spectra showed a significant peak of amide I bonds which confirms the presence of capping ligand which are the proteins available in neem leaf extract around the synthesized nanoparticles. AgNPs showed antibacterial activity against both gram-positive (*S. aureus*) bacteria and gram-negative (*E. coli*) and also antifungal activity against *C. albicans*. Thus, we can conclude that the cotton cloth with impregnated AgNPs has numerous medical applications where infections can easily occur like smart-bandages, bed sheets in hospitals, lab coats, and sanitary napkins.

Data Availability

All relevant data are included within the article.

Conflicts of Interest

All authors declare that there is no conflict of interest.

Acknowledgments

The authors would like to acknowledge the Researchers Supporting Project number (RSP-2021/238), King Saud University, Riyadh, Saudi Arabia.

References

- [1] S. Hasan, "A review on nanoparticles: their synthesis and types," *Research Journal of Recent Sciences*, vol. 2277, p. 2502, 2015.
- [2] A. Roy, "Plant derived silver nanoparticles and their therapeutic applications," *Current Pharmaceutical Biotechnology*, vol. 22, no. 14, pp. 1834–1847, 2021.
- [3] A. Roy, A. Sharma, S. Yadav, L. T. Jule, and R. Krishnaraj, "Nanomaterials for remediation of environmental pollutants," *Bioinorganic Chemistry and Applications*, vol. 2021, Article ID 1764647, 16 pages, 2021.

- [4] H. M. Ahmed, A. Roy, M. Wahab et al., "Applications of nanomaterials in agrifood and pharmaceutical industry," *Journal of Nanomaterials*, vol. 2021, Article ID 1472096, 10 pages, 2021.
- [5] F. Della Sala, G. Longobardo, A. Fabozzi, M. di Gennaro, and A. Borzacchiello, "Hyaluronic acid-based wound dressing with antimicrobial properties for wound healing application," *Applied Sciences*, vol. 12, no. 6, p. 3091, 2022.
- [6] N. Swilam and K. A. Nematallah, "Polyphenols profile of pomegranate leaves and their role in green synthesis of silver nanoparticles," *Scientific Reports*, vol. 10, no. 1, pp. 1–11, 2020.
- [7] A. A. Abdellatif, N. S. Tolba, O. Al Rugaie, F. A. Alhumaydhi, and A. M. Mousa, "Green synthesis of silver nanoparticles for enhancing wound healing activity in rats," *Saudi Pharmaceutical Journal*, 2022.
- [8] E. Kim, J. H. Lee, J. K. Kim et al., "Case study on risk evaluation of silver nanoparticle exposure from antibacterial sprays containing silver nanoparticles," *Journal of Nanomaterials*, vol. 2015, Article ID 346586, 8 pages, 2015.
- [9] M. A. Barkat, S. Beg, M. Naim, F. H. Pottou, S. P. Singh, and F. J. Ahmad, "Current progress in synthesis, characterization and applications of silver nanoparticles: precepts and prospects," *Recent Patents on Anti-Infective Drug Discovery*, vol. 13, no. 1, pp. 53–69, 2018.
- [10] J. Natsuki, T. Natsuki, and Y. Hashimoto, "A review of silver nanoparticles: synthesis methods, properties and applications," *International Journal of Materials Science and Applications*, vol. 4, no. 5, pp. 325–332, 2015.
- [11] S. Iravani, H. Korbekandi, S. V. Mirmohammadi, and B. Zolfaghari, "Synthesis of silver nanoparticles: chemical, physical and biological methods," *Research in pharmaceutical sciences*, vol. 9, no. 6, p. 385, 2014.
- [12] M. Khan, M. R. Shaik, S. F. Adil et al., "Plant extracts as green reductants for the synthesis of silver nanoparticles: lessons from chemical synthesis," *Dalton Transactions*, vol. 47, no. 35, pp. 11988–12010, 2018.
- [13] A. Tilwari and R. Saxena, "Biobased nano materials (plant-based for green materials) synthesis, properties and their application in biomedical science," in *Advanced Nanocarbon Materials*, pp. 109–126, CRC Press, 2022.
- [14] M. O. S. Lobregas and D. H. Camacho, "Green synthesis of copper-based nanoparticles using microbes," in *Copper Nanostructures: Next-Generation of Agrochemicals for Sustainable Agroecosystems*, Elsevier, 2022.
- [15] M. A. Huq, M. Ashrafudoulla, M. M. Rahman, S. R. Balusamy, and S. Akter, "Green synthesis and potential antibacterial applications of bioactive silver nanoparticles: a review," *Polymers*, vol. 14, no. 4, p. 742, 2022.
- [16] P. Saha and B. S. Kim, "Plant extract and agricultural waste-mediated synthesis of silver nanoparticles and their biochemical activities," in *Green Synthesis of Silver Nanomaterials*, Elsevier, 2022.
- [17] S. Sudheer, R. G. Bai, K. Muthoosamy, R. Tuvikene, V. K. Gupta, and S. Manickam, "Biosustainable production of nanoparticles via mycogenesis for biotechnological applications: a critical review," *Environmental Research*, vol. 204, no. Part A, article 111963, 2022.
- [18] S. Ahmed, A. M. Saifullah, B. L. Swami, and S. Ikram, "Green synthesis of silver nanoparticles using *Azadirachta indica* aqueous leaf extract," *Journal of radiation research and applied sciences*, vol. 9, no. 1, pp. 1–7, 2016.
- [19] S. Priyadarshini, S. Sulava, R. Bhol, and S. Jena, "Green synthesis of silver nanoparticles using *Azadirachta indica* and *Ocimum sanctum* leaf extract," *Current Science*, vol. 117, no. 8, pp. 1300–1307, 2019.
- [20] S. K. Srivastava, B. Agrawal, A. Kumar, and A. Pandey, "Phytochemicals of *Azadirachta indica* source of active medicinal constituent used for cure of various diseases: a review," *Journal of Scientific Research*, vol. 64, no. 1, pp. 285–290, 2020.
- [21] K. Girish and B. S. Shankara, "Neem—a green treasure," *Electronic Journal of Biology*, vol. 4, no. 3, pp. 102–111, 2008.
- [22] J. R. Morones, J. L. Elechiguerra, A. Camacho et al., "The bactericidal effect of silver nanoparticles," *Nanotechnology*, vol. 16, no. 10, pp. 2346–2353, 2005.
- [23] N. K. Sajesh Kumar, P. J. Vazhacharickal, J. J. Mathew, and J. Joy, "Synthesis of silver nanoparticles from neem leaf (*Azadirachta indica*) extract and its antibacterial activity," *CIB Tech Journal of Biotechnology*, vol. 4, no. 2, pp. 20–31, 2015.
- [24] S. Amaliyah, A. Sabarudin, M. Masruri, and S. B. Sumitro, "Characterization and antibacterial application of biosynthesized silver nanoparticles using Piper retrofractum Vahl fruit extract as bioreductor," *Journal of Applied Pharmaceutical Science*, vol. 12, no. 3, pp. 103–114, 2022.
- [25] V. Alt, T. Bechert, P. Steinrücke et al., "An in vitro assessment of the antibacterial properties and cytotoxicity of nanoparticulate silver bone cement," *Biomaterials*, vol. 25, no. 18, pp. 4383–4391, 2004.
- [26] A. Nasrollahi, K. H. Pourshamsian, and P. Mansourkiaee, "Antifungal activity of silver nanoparticles on some of fungi," *International Journal Of Nano Dimension (Ijnd)*, vol. 1, no. 3, pp. 233–239, 2011.

Research Article

Synthesis and Experimental Investigations of Tribological and Corrosion Performance of AZ61 Magnesium Alloy Hybrid Composites

R. Venkatesh,¹ C. Ramesh Kannan,² S. Manivannan,³ M. Vivekanandan,⁴ J. Phani Krishna,⁵ Amine Mezni,⁶ Saiful Islam,⁷ and S. Rajkumar⁸ 

¹Department of Mechanical Engineering, Saveetha School of Engineering, SIMATS, Chennai, 602105 Tamil Nadu, India

²Department of Mechanical Engineering, Dr. Navalar Nedunchezhiyan College of Engineering Tholudur, 606303, India

³Center for Material Science, Department of Mechanical Engineering, Karpagam Academy of Higher Education Coimbatore, 642021, India

⁴Department of Mechanical Engineering, National Engineering College, Kovilpatti, 628503 Tamil Nadu, India

⁵Design Engineering, Powder Handling Solutions, RIECO Industries Ltd., Pune 411005, India

⁶Department of Chemistry, College of Science, Taif University, P.O. Box 11099, Taif 21944, Saudi Arabia

⁷Civil Engineering Department, College of Engineering, King Khalid University, Abha 61413, Saudi Arabia

⁸Department of Mechanical Engineering, Faculty of Manufacturing, Institute of Technology, Hawassa University, Hawassa, Ethiopia

Correspondence should be addressed to S. Rajkumar; rajkumar@hu.edu.et

Received 1 March 2022; Revised 12 April 2022; Accepted 15 April 2022; Published 2 May 2022

Academic Editor: Hiwa M. Ahmed

Copyright © 2022 R. Venkatesh et al. This is an open access article distributed under the Creative Commons Attribution License, which permits unrestricted use, distribution, and reproduction in any medium, provided the original work is properly cited.

Magnesium alloy is the light weight material compared to aluminium alloy, and it possesses high strength; these alloys are used to manufacturing of vehicle parts. Magnesium alloy has extreme mechanical and thermal properties, and it is applied to aerospace applications. This study planned to improve the tribological and corrosion resistance of AZ61 magnesium alloy with reinforcement of boron carbide (B_4C) and zirconium dioxide (ZrO_2). Magnesium alloy hybrid composites are fabricated through stir casting process. Tribological and corrosion performance are analyzed through Taguchi L27 Orthogonal Array. In the tribological analysis, four parameters are involved such as % of reinforcement (4%, 8%, and 12%), disc speed (1 m/s, 2 m/s, and 3 m/s), normal load (30 N, 40 N, and 50 N), and sliding distance (1300 m, 1500 m, and 1700 m). Similarly, in salt spray corrosion analysis, four parameters are influenced used such as % of reinforcement (4%, 8%, and 12%), pH (7, 8, and 9), temperature (30°C, 35°C, and 40°C), and hanging time (30 hrs, 40 hrs, and 50 hrs). From this analysis, percentage of reinforcement is highly influenced in wear test, and in corrosion test, temperature is extremely influenced.

1. Introduction

Normally, the composite materials are offered excellent mechanical properties and thermal properties. In composite preparation, the matrix material and reinforced particle selections are highly toughest one due to obtain of the desired properties [1]. Naturally, the pure magnesium is the light weight material compared to aluminum; it has 33% lighter in similar manner 75% lighter than steel material

[2]. Magnesium possesses low density, and particular properties are lifting the consuming level of magnesium. For recent trends, the magnesium and its alloys are used in the high end applications. Magnesium is having some good quality characters, namely, excellent manufacturability, easy to fusion, and higher machinability [3–5]. All these points are considered to selection of materials with omitting of aluminium and such other materials. In machinability point of view, the magnesium has 50% higher than aluminium and

possesses more energy [6–8]. In automobile sectors, magnesium is one of the substitute materials for aluminium for making of steering shaft, pistons, and brake components [9]. In major consideration in the engine design, the magnesium reduces the weight of the engine compared to cast iron [10–12]. It is a suitable one for replacing of cast iron engine and improving the vehicle mileage as well as reducing the fuel consumption. In the magnesium material, the wear occurrence takes place in moderate range but addition of reinforced particles is influenced to reduce the wear rate of the magnesium [13–15]. Hybrid composites generally possess high wear resistance as well as corrosion resistance even influencing of high performance parameters [16]. Taguchi optimization is one of the statistical tools to improve the mechanical properties, increasing the corrosion resistance, reduced the wear rate by the way of parameter optimization [17–20]. The main objective of this experimental work is focusing on to prepare the magnesium hybrid composites with influencing of boron carbide and zirconium oxide-reinforced particles. Further study of wear and corrosion rate of the fabricated composites is conducted through Taguchi tool.

2. Materials and Methods

In this experimental investigation, 2 kg of AZ61 magnesium alloy is purchased from the Andavan Arul Alloys, Chennai. Reinforced particles of boron carbide and zirconium dioxide are procured from Ashoka Marketing Agencies, Chennai, by each 500 g. Stir casting methodology is considered for this investigation to make a high strength magnesium alloy hybrid composites [21]. Bottom pouring stir casting equipment is used for this experimental work. Agitation process is controlled by electric motor in the stir casting process.

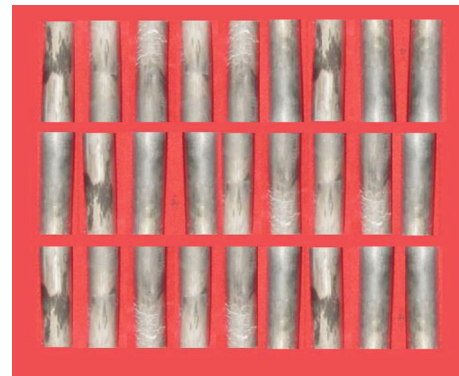
3. Experimental Work

Stir casting process is one of the economical ways to produce the hybrid composites within a short period. Initially, the reinforced particles are preheated in the crucible; different weight percentages (4%, 8%, and 12%) of boron carbide and zirconium oxide are preheated at 450°C for 5 hours in the crucible [22]. The preheating process remove the impurities present in the reinforced particles. Pure magnesium alloy is heated by applying of 800°C in the bottom pouring furnace; further, the preheated reinforce particles are mixed to the pure magnesium alloy. Mixing of preheated reinforced particles and the pure magnesium alloy are mixed well by using stirring action, the stirring process is controlled by electric controller in the motor [23]. Stirring speed is maintained as 400 rpm with 1 hour. After stirring action, the molten material is pouring into the die and allowed to cool; further, the cooled material is separated from the die. The required dimensions of wear and corrosion samples are sliced out from the casted magnesium hybrid composites.

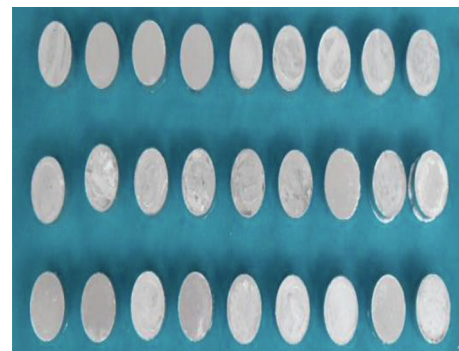
3.1. Wear Test. Wear analysis is conducted through DUCOM model dry sliding wear test apparatus as shown in Figure 1. Specimens are prepared as per the ASTM G99



FIGURE 1: Dry sliding wear test apparatus.



(a)



(b)

FIGURE 2: (a) Image of wear test specimens. (b) Image of salt spray test specimens.

standard under the dimensions of 12 mm diameter and 30 mm length. Initially, the disc and specimens are cleaned well by using, and then, each sample is weighted initially with the help of digital balance [24]. EN 32 steel disc with 65 HRC is used for conducting of dry sliding wear test; different process parameters are involved to conduct the wear test such as % of reinforcement, disc speed, normal load, and sliding distance.

TABLE 1: Wear test process parameters and their levels.

S. no.	Parameters	Level 1	Level 2	Level 3
1	% of reinforcement	4	8	12
2	Disc speed (m/s)	1	2	3
3	Normal load (N)	20	30	40
4	Sliding distance (m)	1300	1500	1700

TABLE 2: Response table for means (wear rate).

Exp. runs	% of reinforcement	Disc speed (m/s)	Normal load (N)	Sliding distance (m)	Wear rate (mm ³ /m)
1	4	1	20	1300	0.0038
2	4	1	20	1300	0.046
3	4	1	20	1300	0.0034
4	4	2	30	1500	0.0341
5	4	2	30	1500	0.0117
6	4	2	30	1500	0.034
7	4	3	40	1700	0.0062
8	4	3	40	1700	0.027
9	4	3	40	1700	0.0071
10	8	1	30	1700	0.0023
11	8	1	30	1700	0.051
12	8	1	30	1700	0.0086
13	8	2	40	1300	0.0073
14	8	2	40	1300	0.0128
15	8	2	40	1300	0.0148
16	8	3	20	1500	0.0039
17	8	3	20	1500	0.0048
18	8	3	20	1500	0.0156
19	12	1	40	1500	0.0028
20	12	1	40	1500	0.0126
21	12	1	40	1500	0.0018
22	12	2	20	1700	0.0107
23	12	2	20	1700	0.0061
24	12	2	20	1700	0.0037
25	12	3	30	1300	0.0027
26	12	3	30	1300	0.0147
27	12	3	30	1300	0.0025

The sample is placed vertically against to rotating disc; time taken to conduct wear test per sample is 20 min. Finally, after conducting the wear test, the samples are weighted to calculate the mass loss. Figure 2(a) illustrates the 27 numbers of wear test specimens.

3.2. Salt Spray Test. Salt spray test is one of the faster methods to analyze the corrosion resistance of the materials. In this work, initially, the samples are prepared as per the ASM standard ax (ASTM B117) with the dimensions of 30 mm diameter and 10 mm thickness. Samples are cleaned well and weighted; the initial weights are noted carefully

for evaluating the difference of mass loss and also find the corrosion rate. Figure 2(b) shows the salt spray test specimens; initially, the specimens are loaded in the salt spray chamber such as all the specimens are hung in the chamber [25]. The salt spray model is CARELAB with the dimensions of 650 mm × 450 mm × 4010 mm. After loading the samples, the chamber cabin door is closed; using an atomizer, the 5% of NaCl solution is continually sprayed on the specimen's surfaces [26]. The salt spray is achieved by using of pump circulation with constant flow rate. After reaching the specified time period, the specimens are taken out from the chamber and cleaned well with using of running water;

TABLE 3: Response table for signal to noise ratios (wear rate); smaller is better.

Level	% of reinforcement	Disc speed (m/s)	Normal load (N)	Sliding distance (m)
1	0.019267	0.014726	0.010683	0.012052
2	0.013246	0.015028	0.018009	0.013282
3	0.006473	0.009233	0.010294	0.013652
Delta	0.012794	0.005795	0.007715	0.001601
Rank	1	3	2	4

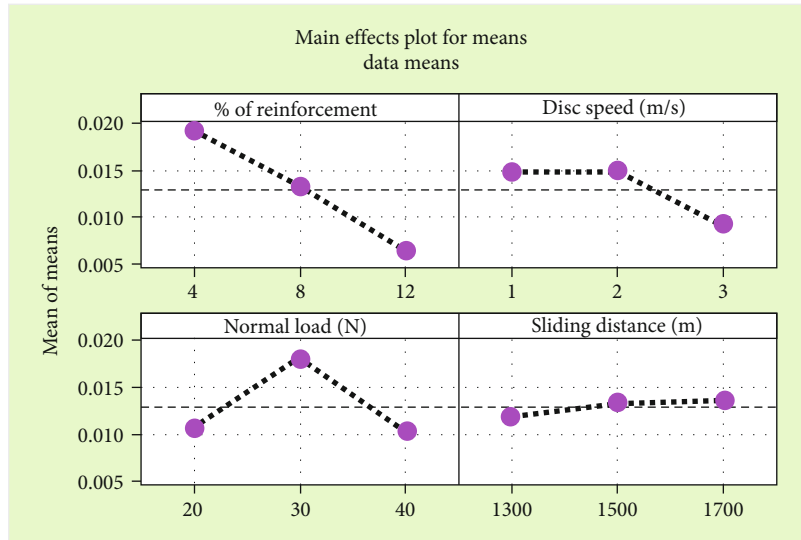


FIGURE 3: Main effects plot for mean (wear rate).

further, the specimens are dried. All specimens are weighed and calculate the difference of mass loss [27].

Table 1 presented the wear test parameters and their levels; in wear test, four parameters such as % of reinforcement, disc speed, normal load, and sliding distance were selected. All four parameters have three levels ton satisfying L27 OA. The wear rate is obtained with

$$\text{Wearrate (WI)} = \frac{W1 - W2}{\text{Time} \times \text{Density}}. \quad (1)$$

4. Results and Discussion

4.1. Wear Analysis. Influencing of four parameters and three levels was extremely influenced to estimate the wear rate of specimens. Table 2 presented the wear input parameters and the response of wear rate. From this wear test analysis, the minimum wear rate was recorded as $0.0018 \text{ mm}^3/\text{m}$. The minimum wear rates attained by the influence of parameters were 12% of reinforcement, 1 m/s of disc speed, 40 N of normal load, and 1500 m of sliding distance. On the contrary, the maximum wear rate was occurred as $0.051 \text{ mm}^3/\text{m}$ by influencing of 8% of reinforcement, 1 m/s of disc speed, 30 N of normal load, and 1700 m of sliding distance.

Table 2 and Table 3 presented the response tables of wear rate; these tables presented the higher influence parameter in priority order. Higher priority was illustrated by the delta and rank order; the percentage of reinforcement was higher priority in the wear test. Normal load was the second priority, disc speed was the third priority, and sliding distance was fourth priority. Optimal parameters of the wear rate was found as 12% of reinforcement, 3 m/s of disc speed, 40 N of normal load, and 1500 m of sliding distance.

Figures 3 and 4 represented the main effects plot for means and S/N ratios of the wear rate; increasing of reinforcement percentage decreases the wear rate. Maximum reinforcement 12% offered minimum wear rate; further increasing of disc speed also reduces the wear rate. Maximum level 3 m/s of disc speed offered minimum wear rate. Influencing of normal load such as 20 N to 30 N wear rates was increased; further, 30 N to 40 N of normal load, the wear rate was decreased. Finally, the 40 N of normal load recorded minimum wear rate. Consideration of sliding distance, 1500 m of sliding distance offered minimum wear rate; further increasing of 1500 m and 1700 m of sliding distance, the wear rate was increased. Figure 5 highlights the residual plot for the wear rate.

Normal probability plot represents that all the points were lying on the mean line; it tell about the selected

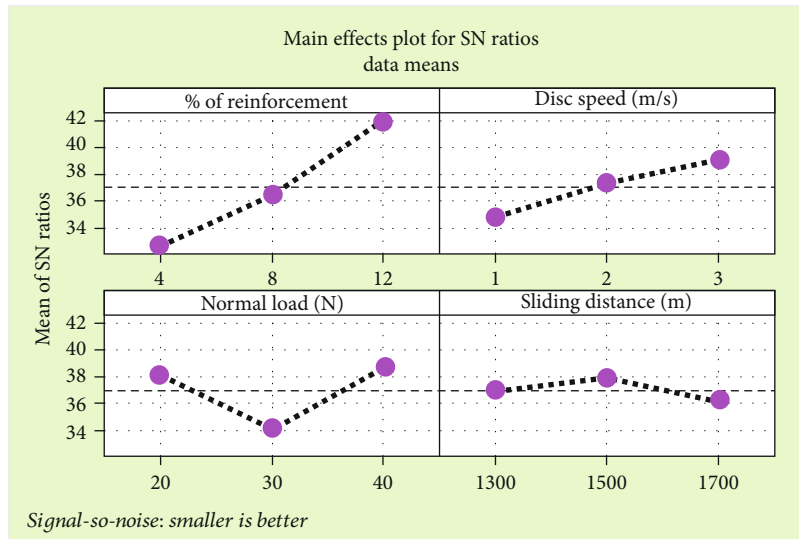


FIGURE 4: Main effects plot for S/N ratios (wear rate).

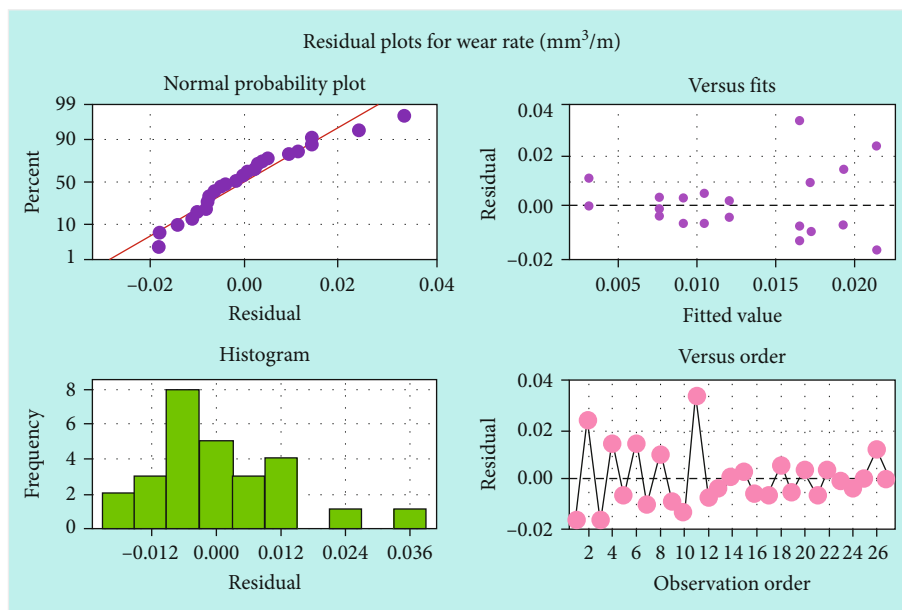


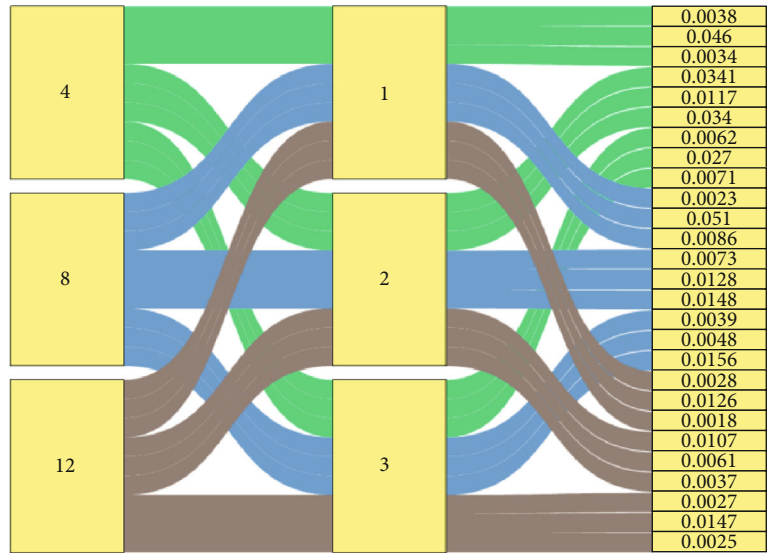
FIGURE 5: Residual plots for wear rate.

parameters, and the levels are good one. In versus fits plot, all the points were distributed uniformly, and within the limits, similar trends were observed in the versus order plot. All these points demonstrate that chosen model is appropriate one. In histogram plot, all the rectangles were skewed in normal position. Figure 6 demonstrates the parallel set plot for wear rate; Figure 6(a) shows the correlation between % of reinforcement and disc speed. From this parameter connection, the minimum wear rate was recorded by 12% of reinforcement and 1 m/s of disc speed.

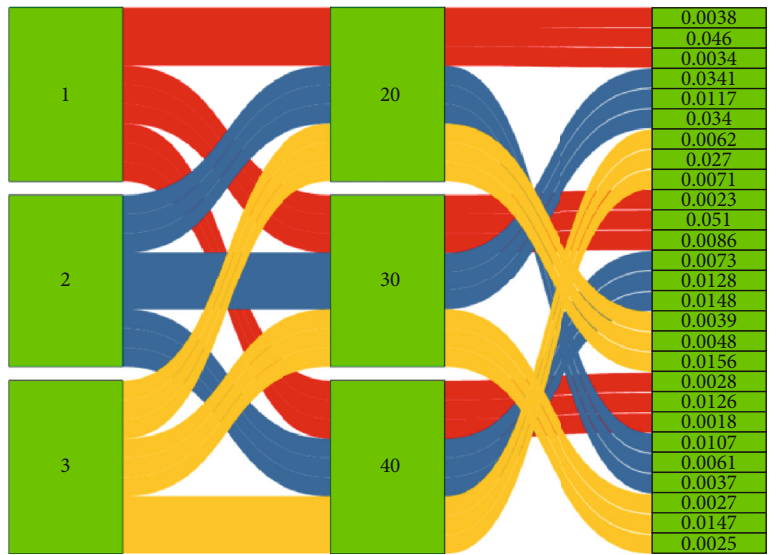
Figure 6(b) illustrates the relations between disc speed and normal load. In this analysis, 1 m/s of disc speed and

40 N of normal load produced minimum wear rate. Figure 6(c) presents the connection between normal load and sliding distance. Minimum wear rate was registered by 40 N of normal load and 1500 m sliding distance. Figure 6(d) shows the minimum wear rate by 20 N of normal load and 12% of reinforcement.

4.2. Corrosion Analysis. Table 4 illustrates the corrosion input parameters and the response of corrosion rate. From this corrosion test analysis, the minimum corrosion rate was registered as 0.112 mm/year. The minimum corrosion rates obtained by the influence of parameters were 8% of

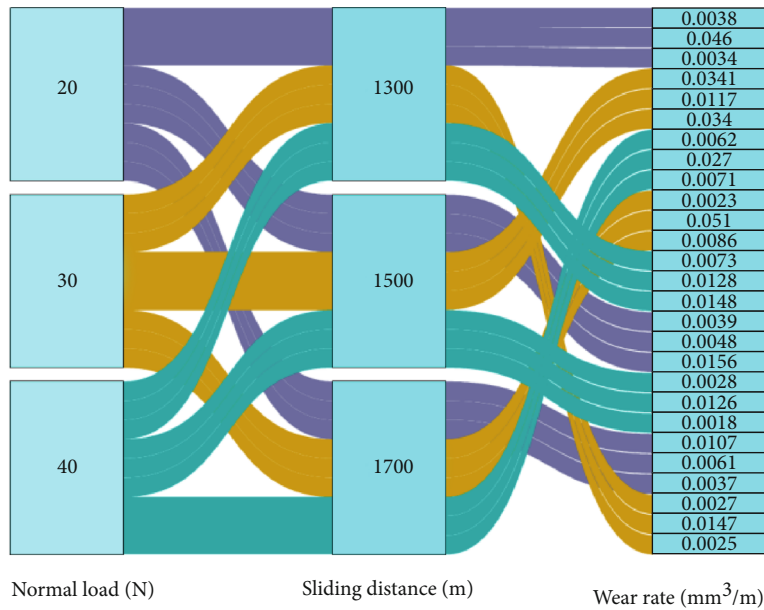


% of reinforcement Disc speed (m/s) Wear rate (mm³/m)
(a)

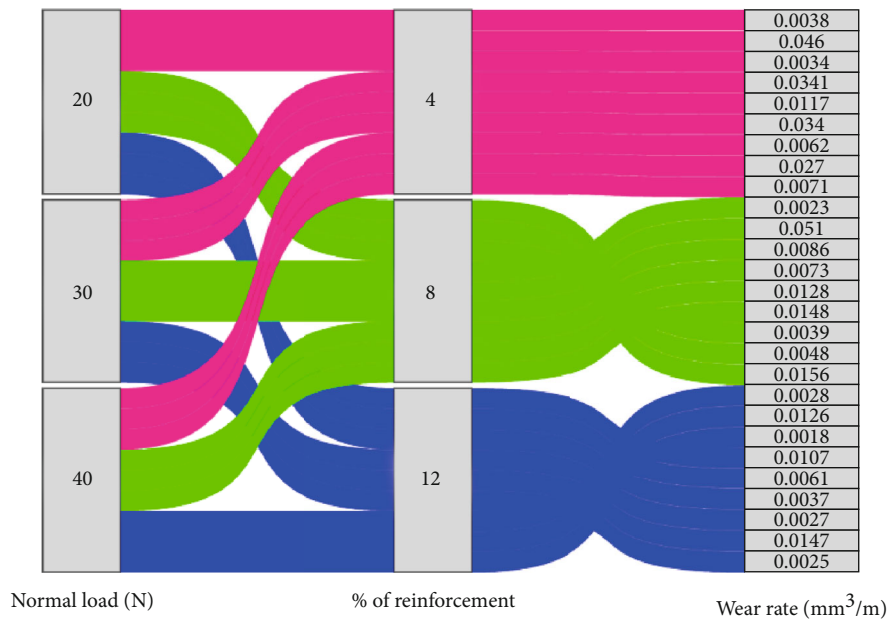


Disc speed (m/s) Normal load (N) Wear rate (mm³/m)
(b)

FIGURE 6: Continued.



(c)



(d)

FIGURE 6: Parallel set plot: (a) % of reinforcement vs. disc speed; (b) disc speed vs. normal load; (c) normal load vs. sliding distance; (d) normal load vs. % of reinforcement.

reinforcement, 7 pH value, 35°C of temperature, and 50 hrs of hanging time.

Table 5 and Table 6 presented the response tables of corrosion rate; these tables illustrated the higher influence parameter in priority order. Based on the delta and rank values, the higher priority was decided; from this analysis, chamber temperature was a higher priority in the corrosion test. Further, the parameters were followed by pH value, hanging time, and percentage of reinforcement. Optimal parameters of the corrosion rate was recorded as 8% of reinforcement, 8 pH value, 35°C of temperature, and 50 hrs of hanging time.

Figures 7 and 8 illustrated the main effects plot for means and S/N ratios of the corrosion rate; increasing of reinforcement percentage decreases the corrosion rate. Minimum corrosion rate was obtained by 8% of reinforcement; similarly, increasing of pH value the corrosion rate was decreased. Minimum corrosion rate was recorded by influencing of 8 pH value. Increasing of temperature from 30°C to 35°C decreases the corrosion rate, 35°C of temperature offered minimum corrosion rate. Higher hanging hours such as 50 hours recorded minimum corrosion rate.

Figure 9 presented the residual plots for corrosion rate; this figure comprises the four plots in a single plot. From

TABLE 4: Summary of corrosion test process parameters and corrosion rate.

Exp. runs	% of reinforcement	pH	Temperature (°C)	Hanging time (hrs)	Corrosion rate $\times 10^{-3}$ (mm/year)
1	4	7	30	30	0.135
2	4	7	30	30	0.178
3	4	7	30	30	0.142
4	4	8	35	40	0.131
5	4	8	35	40	0.118
6	4	8	35	40	0.127
7	4	9	40	50	0.153
8	4	9	40	50	0.149
9	4	9	40	50	0.176
10	8	7	35	50	0.112
11	8	7	35	50	0.119
12	8	7	35	50	0.125
13	8	8	40	30	0.134
14	8	8	40	30	0.142
15	8	8	40	30	0.155
16	8	9	30	40	0.193
17	8	9	30	40	0.143
18	8	9	30	40	0.161
19	12	7	40	40	0.152
20	12	7	40	40	0.149
21	12	7	40	40	0.172
22	12	8	30	50	0.134
23	12	8	30	50	0.121
24	12	8	30	50	0.182
25	12	9	35	30	0.139
26	12	9	35	30	0.127
27	12	9	35	30	0.116

TABLE 5: Response table for means (corrosion rate).

Level	% of reinforcement	pH	Temperature (°C)	Hanging time (hrs)
1	0.1454	0.1427	0.1543	0.1409
2	0.1427	0.1382	0.1238	0.1496
3	0.1436	0.1508	0.1536	0.1412
Delta	0.0028	0.0126	0.0306	0.0087
Rank	4	2	1	3

TABLE 6: Response table for signal to noise ratios (corrosion rate); smaller is better.

Level	% of reinforcement	pH	Temperature (°C)	Hanging time (hrs)
1	16.76	16.95	16.15	17.01
2	16.96	17.15	18.14	16.54
3	16.83	16.45	16.26	17.01
Delta	0.20	0.70	1.98	0.47
Rank	4	2	1	3

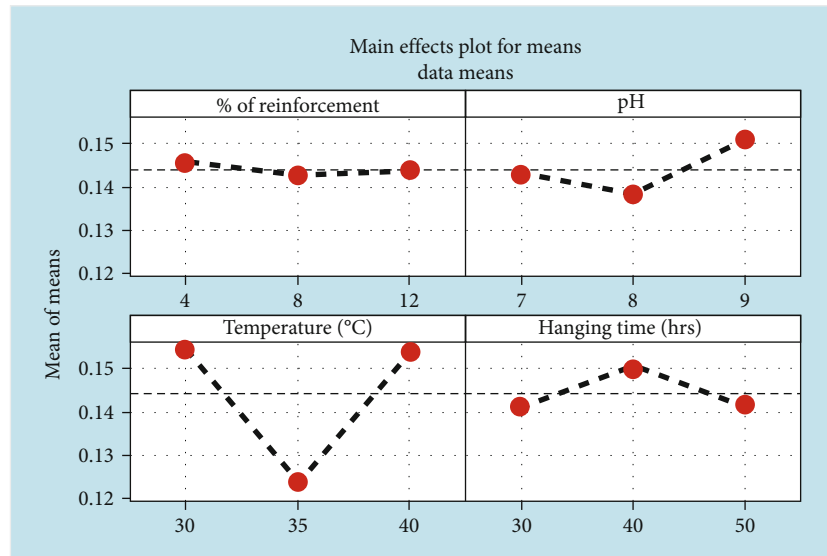


FIGURE 7: Main effects plot for means (corrosion rate).

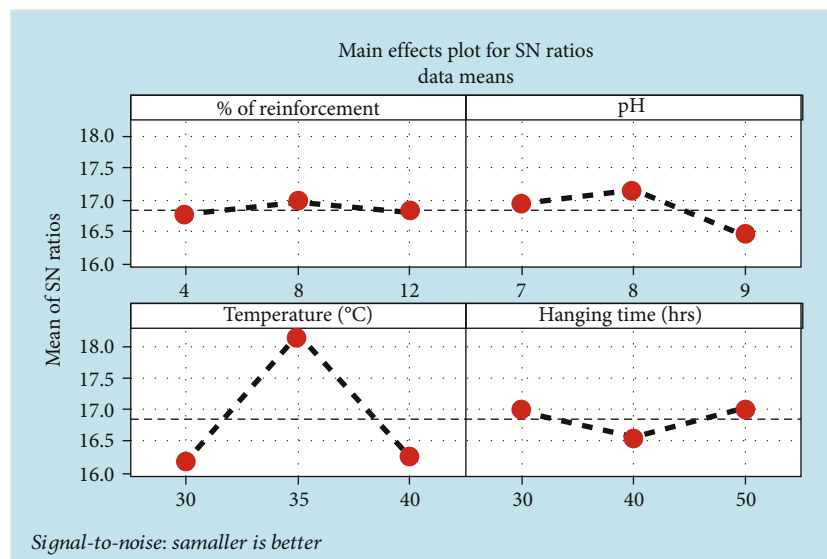


FIGURE 8: Main effects plot for S/N ratios (corrosion rate).

all the four plots, the data points were distributed uniformly and within the limits; hence, the selected parameters and model were suitable one. In the normal probability plot, all the data points touch the mean line; it was denoted that the model was accurate one.

Figure 10 illustrates the contour plot for corrosion rate; Figure 10(a) represents the correlation between % of reinforcement and pH value. In both of these parameters' correlation, the minimum corrosion rate was recorded by 8% of reinforcement and 8 pH value. Figure 10(b) presented the pH value and temperature relations; for that, these parameters offered a minimum corrosion rate by 8 pH value and 35°C of temperature. Figure 10(c) presented the correlation between temperature and hanging time; both were offered

a minimum corrosion rate such as 35°C of temperature and 50 hours of hanging time. Figure 10(c) demonstrates the connection between hanging time and % of reinforcement; 50 hours of hanging and 8% of reinforcement offered minimum corrosion rate.

Normally, the magnesium alloy material was light weight material; adding of reinforcement particles improves the wear properties. In stir casting process, the reinforced particles, namely, boron carbide (B_4C) and zirconium dioxide (ZrO_2), were highly melted and blended into the magnesium alloy. The uniform blending increases the mechanical properties of the magnesium composites; the enhanced strength reduces the wear rate of the composite and also reduces the corrosion. The hybrid reinforced particles make superior

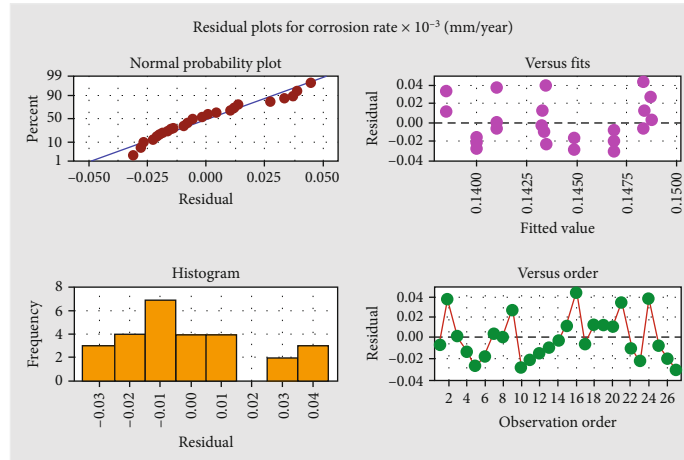


FIGURE 9: Residual plots for corrosion rate.

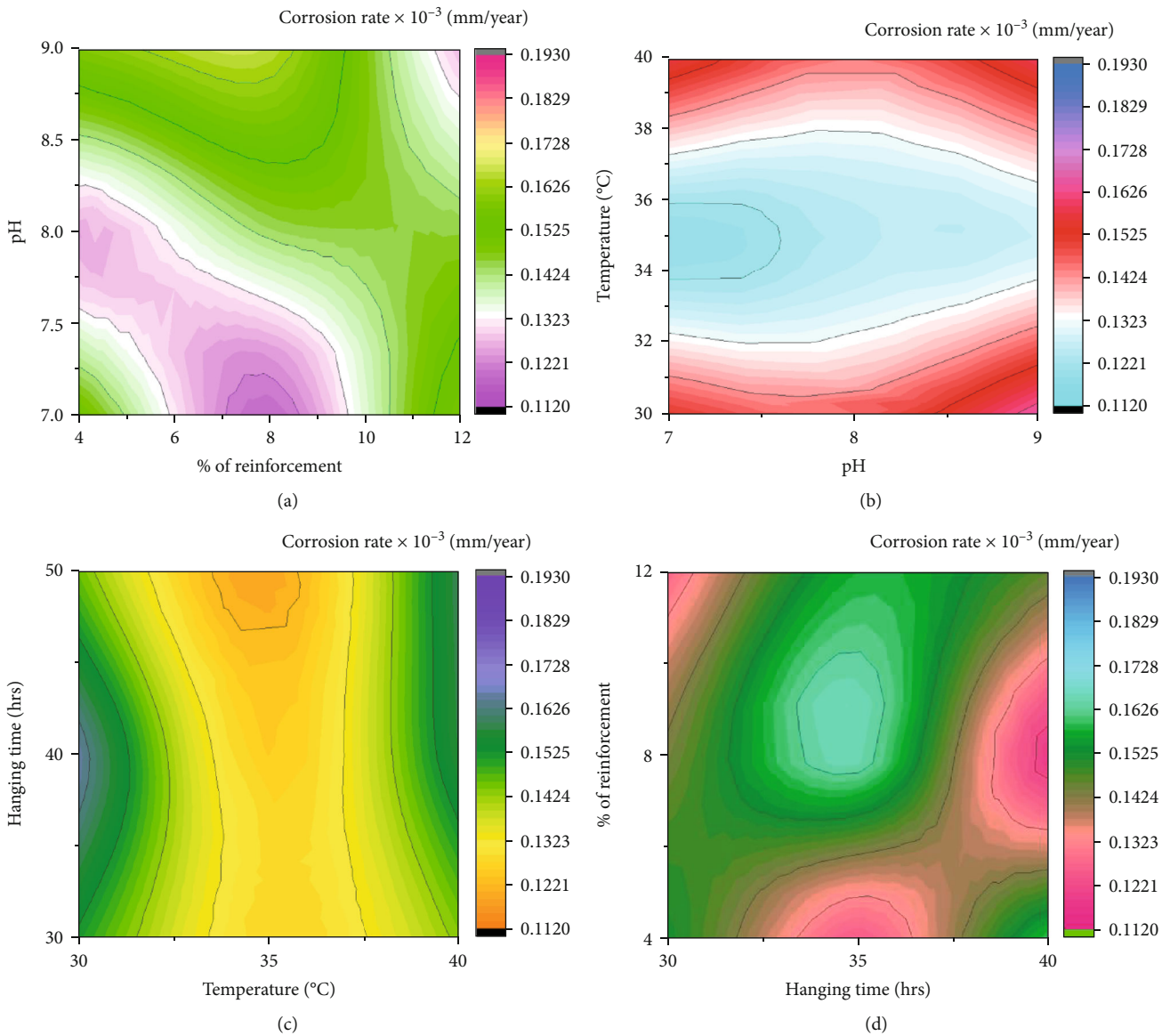


FIGURE 10: Contour plot: (a) % of reinforcement vs. pH value; (b) pH value vs. temperature; (c) temperature vs. hanging time; (d) hanging time vs. % of reinforcement.

strength and offered excellent corrosion resistant to the composite material; it was evidently showed in the numerical analysis.

5. Conclusion

In this experimental investigation, magnesium alloy hybrid composites were prepared through stir casting process with reinforcement of boron carbide and zirconium oxide. Using of Taguchi analysis, the optimal parameters of the wear and corrosion test were evaluated successfully; finally, the minimum wear rate and corrosion rate were obtained, and the results were described as follows:

- (i) From the wear test analysis, the minimum wear rate was recorded as $0.0018 \text{ mm}^3/\text{m}$ due to homogeneous mixture of the reinforced particles into the magnesium alloy composites. Higher percentage of reinforced particles improved the wear properties. In contrary, the lower percentage of reinforced particles is not influenced in the wear behavior of the composites; hence, the maximum wear rate was obtained in the wear test as $0.051 \text{ mm}^3/\text{m}$. Optimal of the wear rate was recorded as 12% of reinforcement, 3 m/s of disc speed, 40 N of normal load, and 1500 m of sliding distance
- (ii) In the salt spray corrosion test analysis, minimum corrosion rate was recorded as $0.112 \text{ mm}/\text{year}$ owing to uniform distribution of reinforced particles into the magnesium alloy composites. From the corrosion rate analysis, the optimal parameters were registered as 12% of reinforcement, 3 m/s of disc speed, 40 N of normal load, and 1500 m of sliding distance. Percentage of reinforcement was highly influenced in the wear analysis, and the chamber temperature was extremely influenced in the salt spray corrosion analysis.

Data Availability

The data used to support the findings of this study are included in the article. Should further data or information be required, these are available from the corresponding author upon request.

Conflicts of Interest

The authors declare that there are no conflicts of interest regarding the publication of this paper.

Acknowledgments

The authors appreciate the technical assistance to complete this experimental work from the Department of Mechanical Engineering, Faculty of Manufacturing, Institute of Technology, Hawassa University, Ethiopia, and also Taif University Researchers Supporting Project number TURSP-2020/28, Taif University, Taif, Saudi Arabia. It was performed as a part of the Employment Hawassa University, Ethiopia.


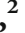






References

- [1] J. Zhu, J. Qi, Q. Guan, L. Ma, and R. Joyce, "Tribological behaviour of self-lubricating Mg matrix composites reinforced with silicon carbide and tungsten disulfide," *Tribology International*, vol. 146, article 106253, 2020.
- [2] W. Yu, D. Chen, L. Tian, H. Zhao, and X. Wang, "Self-lubricate and anisotropic wear behavior of AZ91D magnesium alloy reinforced with ternary Ti_2AlC MAX phases," *Journal of Materials Science and Technology*, vol. 35, no. 3, pp. 275–284, 2019.
- [3] S. K. Chourasiya, G. Gautam, and D. Singh, "Mechanical and tribological behavior of warm rolled Al-6Si-3graphite self-lubricating composite synthesized by spray forming process," *Silicon*, vol. 12, no. 4, pp. 831–842, 2020.
- [4] R. A. Prasad, K. P. Vamsi, and R. N. Rao, "Tribological behaviour of Al6061–2SiC-xGr hybrid metal matrix nanocomposites fabricated through ultrasonically assisted stir casting technique," *Silicon*, vol. 11, no. 6, pp. 2853–2871, 2019.
- [5] A. Moharami, "High-temperature tribological properties of friction stir processed Al-30Mg2Si composite," *Mater at High Temp*, vol. 37, no. 5, pp. 351–356, 2020.
- [6] A. Maamari, K. Iqbal, and D. Nuruzzaman, "Wear and mechanical characterization of Mg-Gr self-lubricating composite fabricated by mechanical alloying," *Journal of Magnesium and Alloys*, vol. 7, no. 2, pp. 283–290, 2019.
- [7] A. Kumar and A. Kumar, "Mechanical and dry sliding wear behavior of B_4C and rice husk ash reinforced Al 7075 alloy hybrid composite for armors application by using Taguchi techniques," *Materials Today: Proceedings*, vol. 27, pp. 2617–2625, 2020.
- [8] T. Singh, P. Patnaik, G. Fekete, R. Chauhan, and B. Gangil, "Application of hybrid analytical hierarchy process and complex proportional assessment approach for optimal design of brake friction materials," *Polymer Composites*, vol. 40, no. 4, pp. 1602–1608, 2019.
- [9] M. Kumar, "Mechanical and sliding wear performance of AA356-Al 2O_3 /SiC/graphite alloy composite materials: parametric and ranking optimization using Taguchi DOE and hybrid AHP-GRA method," *Silicon*, vol. 13, no. 8, pp. 2461–2477, 2021.
- [10] A. Kumar and V. Kukshal, "Assessment of mechanical and sliding wear performance of Ni particulate filled Al7075 aluminium alloy composite," *Materials Today: Proceedings*, vol. 44, pp. 4349–4356, 2020.
- [11] A. Lotfy, A. V. Pozdniakov, V. S. Zolotarevskiy, M. T. Abou El-khair, A. Daoud, and A. G. Mochugovskiy, "Novel preparation of Al-5%Cu / BN and Si_3N_4 composites with analyzing microstructure, thermal and mechanical properties," *Materials Characterization*, vol. 136, pp. 144–151, 2018.
- [12] Y. Pazhouhanfar and B. Eghbali, "Microstructural characterization and mechanical properties of TiB_2 reinforced Al6061 matrix composites produced using stir casting process," *Materials Science and Engineering A*, vol. 710, pp. 172–180, 2018.
- [13] P. S. Reddy, R. Kesavan, and B. V. Ramnath, "Investigation of mechanical properties of aluminium 6061-silicon carbide, boron carbide metal matrix composite," *Silicon*, vol. 10, no. 2, pp. 495–502, 2018.
- [14] D. Bandhu, A. Thakur, R. Purohit, R. K. Verma, and K. Abhishek, "Characterization & evaluation of Al7075 MMCs reinforced with ceramic particulates and influence of age hardening on their tensile behavior," *Journal of Mechanical Science and Technology*, vol. 32, no. 7, pp. 3123–3128, 2018.

- [15] P. K. Yadav and G. Dixit, "Erosive-corrosive wear of aluminium-silicon matrix (AA336) and SiCp/TiB2p ceramic composites," *SILICON*, vol. 11, no. 3, pp. 1649–1660, 2019.
- [16] J. David Raja Selvam, I. Dinaharan, R. S. Rai, and P. M. Mashinini, "Dry sliding wear behaviour of in-situ fabricated TiC particulate reinforced AA6061 aluminium alloy," *Tribol-Mater Surfaces Interfaces*, vol. 13, no. 1, pp. 1–11, 2019.
- [17] A. Bhowmik, D. Dey, and A. Biswas, "Comparative study of microstructure, physical and mechanical characterization of SiC/TiB2 reinforced Aluminium matrix composite," *Silicon*, vol. 13, no. 6, pp. 2003–2010, 2020.
- [18] V. Erturun, S. Cetin, and O. Sahin, "Investigation of microstructure of aluminum based composite material obtained by mechanical alloying," *Metals and Materials International*, vol. 27, no. 6, pp. 1662–1670, 2021.
- [19] R. Singh, M. Shadab, A. Dash, and R. N. Rai, "Characterization of dry sliding wear mechanisms of AA5083/B4C metal matrix composite," *Journal of the Brazilian Society of Mechanical Sciences and Engineering*, vol. 41, no. 2, 2019.
- [20] R. Ambigai and S. Prabhu, "Fuzzy logic algorithm based optimization of the tribological behavior of Al-Gr-Si₃N₄ hybrid composite," *Measurement*, vol. 146, pp. 736–748, 2019.
- [21] A. Bhowmik, D. Chakraborty, D. Dey, and A. Biswas, "Investigation on wear behaviour of Al7075-SiC metal matrix composites prepared by stir casting," *Materials Today: Proceedings*, vol. 26, no. 2, pp. 2992–2995, 2020.
- [22] T. Sathish, V. Mohanavel, K. Ansari et al., "Synthesis and characterization of mechanical properties and wire cut EDM process parameters analysis in AZ61 magnesium alloy+ B4C+ SiC," *Materials*, vol. 14, no. 13, p. 3689, 2021.
- [23] T. Satyanarayana, P. S. Rao, and M. G. Krishna, "Influence of wear parameters on friction performance of A356 aluminum - graphite/ granite particles reinforced metal matrix hybrid composites," *Heliyon*, vol. 5, no. 6, article e01770, 2019.
- [24] N. Ramadoss, K. Pazhanivel, and G. Anbuhezhiyan, "Synthesis of B₄C and BN reinforced Al7075 hybrid composites using stir casting method," *Journal of Materials Research and Technology*, vol. 9, no. 3, pp. 6297–6304, 2020.
- [25] T. Sathish and N. Sabarirajan, "Nano-alumina reinforcement on AA 8079 acquired from waste aluminium food containers for altering microhardness and wear resistance," *Journal of Materials Research and Technology*, vol. 14, pp. 1494–1503, 2021.
- [26] Y. Otani and S. Sasaki, "Effects of the addition of silicon to 7075 aluminum alloy on microstructure, mechanical properties, and selective laser melting processability," *Materials Science and Engineering A*, vol. 777, article 139079, 2020.
- [27] Y. Liu, A. Laurino, T. Hashimoto et al., "Corrosion behaviour of mechanically polished AA7075-T6 aluminium alloy," *Surface and Interface Analysis: An International Journal devoted to the development and application of techniques for the analysis of surfaces, interfaces and thin films*, vol. 42, no. 4, pp. 185–188, 2010.

Review Article

Fabrication, Characteristics, and Therapeutic Applications of Carbon-Based Nanodots

Zoya Zaidi ¹, Niladri Maiti ², Mohammad Irfan Ali ³, Gunjan Sharma ⁴,
Sarmad Moin ⁴, Harihara Padhy ^{5,6}, G. L. Balaji ^{1,6},
and Venkatesa Prabhu Sundramurthy ^{7,8}

¹*Synthetic Organic Chemistry Research Lab, Department of Chemistry, Thanthai Hans Roever College, Perambalur, 621212 Tamil Nadu, India*

²*Department of Pharmacology, Medical School, Akfa University, Tashkent, Uzbekistan*

³*Faculty of Life Sciences, Mandsaur University, Mandsaur 458001, India*

⁴*School of Applied Sciences, Suresh Gyan Vihar University, Jaipur, 302017 Rajasthan, India*

⁵*Department of Chemistry, GITAM Institute of Science, Visakhapatnam, Andhra Pradesh 530045, India*

⁶*School of Advanced Sciences and Languages, VIT Bhopal University, Kotri Kalan, 466114 MP, India*

⁷*Centre of Excellence for Bioprocess and Biotechnology, Addis Ababa Science and Technology University, Addis Ababa, Ethiopia*

⁸*Department of Chemical Engineering, College of Biological and Chemical Engineering, Addis Ababa Science and Technology University, Addis Ababa, Ethiopia*

Correspondence should be addressed to Venkatesa Prabhu Sundramurthy; venkatesa.prabhu@aastu.edu.et

Received 30 January 2022; Accepted 18 March 2022; Published 30 April 2022

Academic Editor: Arpita Roy

Copyright © 2022 Zoya Zaidi et al. This is an open access article distributed under the Creative Commons Attribution License, which permits unrestricted use, distribution, and reproduction in any medium, provided the original work is properly cited.

Carbon nanodots are a recently discovered sort of carbon nanoparticles, demonstrating excellent fluorescence and physical-chemical properties that make them appealing for diagnostics and chemotherapeutics, including biosensing, bioimaging, and nanocarriers for drug delivery ground-breaking therapeutic agents in photothermal and photodynamic therapy. This critical review strongly focuses on the varied sorts of processes involved in the synthesis of carbon nanodots alongside the benefits and shortcomings. Furthermore, the multiple applications of carbon nanodots are established and used to develop potential theranostic nanoarchitectures. This review paper analyses with a discussion focusing on the discovery, synthesis processes, and diverse biomedical applications.

1. Introduction

Carbon quantum dots (CQDs), also known as carbon nanodots, are a class of carbon nanoparticles. Carbon nanodots were discovered by Xu et al. [1] accidentally while attempting to purify single-walled carbon nanotubes (SWCNT). Carbon nanodots are less than 10 nm in size, and since their discovery, extensive research has been conducted on their unique properties, such as fluorescence, making it an exceptional discovery [2].

The process of synthesis of carbon nanodots, its analytical applications in oxygen reduction, plant cell imaging, and

more have been studied throughout the years. The fluorescent properties of carbon nanodots make them essential for studying several chemical and biological processes, as previously mentioned [3]. Reviewing the existing literature and the research conducted on this particular domain would enable researchers to focus on the gaps in the literature and evaluate further research carried out in this context.

2. Carbon Nanodot Discovery and Structure

Xu et al. [1] had been engaged in purifying single-walled carbon nanotubes when they accidentally discovered these

particles. Synthetic methods have been implemented in their extraction and discovery. In this context, it needs to be stated that the carbon nanodots exhibit various structures responsible for the demonstration of multiple properties of the particles [4]. According to Roy et al. [5], the carbon nanodots are usually quasispherical or spherical shaped, generally from 4 nm to 8 nm in diameter, produced from natural soot, with lattice spacing almost equal to graphite. Additionally, carbon dots developed from natural ingredients such as glycerine and coffee exhibited crystalline and monodisperse structures [3, 6]. The presence of particular functional groups on the carbon dots can be determined through XPS analysis or FTIR spectroscopy. Additionally, carbon dots have been noted to be more stable as compared to nanodots of metals such as Ag and Au [7].

3. Synthesis Processes of Carbon Nanodots

Carbon nanodots can be broadly classified into two categories for the purpose of synthesis, namely, top-down approaches and bottom-up approaches.

3.1. Top-Down Approaches. Arc-discharge method: this method provides approximately 1.6% quantum yield (QY) of carbon nanodots from the crude material oxidizing process. The oxidation was carried out by using HNO_3 (3.3N); then, the oxidized crude carbon nanodots were extracted with alkaline solution (pH 8.4), and purification was done by conducting gel electrophoresis. This particular process was used by Roy et al. [5] during the discovery of carbon nanodots and is considered cost-effective. However, adequate growth conditions are necessary for this method to ensure success (Figure 1) [8]. An electrical discharge around two graphite electrodes bathed in octane was used to make luminous carbon nanodots in a single-step method [9]. The arc-discharge method was also used by Andhika et al. [10] in the toluene environment for the production of carbon nanoparticles. Direct current arc-discharge plasma was used to make SnO_2 /carbon nanotube nanonests (SnO_2 /CNT NNs) composites in one step [11].

Electrochemical method: the QY of the nanodots produced through this method is usually around 2.8%–2%. The size of the carbon nanodots can be maintained by keeping 20–180 mA cm^2 as the range of the current density [12]. Therefore, caution is to be exercised for maintaining a particular size of carbon dots. The easy single-step electrochemical production of CQDs with diameters ranging from 1.2 to 3.8 nm was synthesized that shows size-dependent photoluminescence (pl) and outstanding upconversion luminescence capabilities [13].

Laser ablation: the use of Nd:YAG laser at a frequency of 10 Hz and 1064 nm may yield carbon dots from graphite powder. According to Hsu and Chang [14], the use of citric acid is also noted to enhance hydrophilic properties in CQDs. This is supported by Zhu et al. [15], where soy milk is used to synthesize carbon dots. Nguyen et al. [16] reported the synthesis of ultrasmall CQDs by double-pulse femtosecond laser ablation. CQDs, also prepared by a pulsed laser ablation method with no posttreatments, have been devel-

oped by Yang et al. [17]. Laser pyrolysis of two typical volatile chemical precursors, toluene and pyridine, yielded monodisperse carbon nanodots with controllable pl [18].

3.2. Bottom-Up Approaches. Hydrothermal and aqueous-based methods: several methods established for the synthesis of carbon nanodots can be attributed to various natural substances. For instance, this method implements ground coffee or green tea, as carbon nanodots can be synthesized from organic compounds [12]. Aslan and Eskalen used a single-step hydrothermal approach to make water-soluble carbon nanodots from tangerine juice [19]. Under blue light illumination, fluorescent nitrogen-doped CQDs generated using a single-pot hydrothermal process using multiple isomers, displaying exceptionally intense fluorescence [20], while Chen et al. [21] synthesized spherical CQDs ranging 3–7 nm from the plant material and agriculture waste.

Microwave-assisted methods: synthesis of carbon nanodots has also been found to be effective using PEG₂₀₀ saccharides, such as sucrose, by developing an aqueous transparent solution of the same to extract carbon nanodots. There are three prime examples of modified carbon nanodots synthesized with the help of microwave-assisted method, namely, N, S-carbon nanodots (N,S-doped carbon quantum dots, N, S-CND), N-carbon nanodots-1 (N-CNDs-1), and N-carbon nanodots-2 (N-CNDs-2). N-CNDs-1 and N-CNDs-2 are strongly agglomerated and highly hydrophilic, respectively. Thiol and carboxylic groups are present on N, S-CND [22]. These particles are useful in studying lung and pulmonary diseases in humans.

Carbon nanodots with 30 nm dimensions synthesized by an efficient route by using coffee grounds to the precursor followed the microwave-assisted hydrothermal method where the 10 g spent coffee grounds were soaked in dilute H_2SO_4 solution (50 mL of 0.01 g/mL) heating in the microwave for two hours. The precursor was oxidized in HNO_3 (10%, 20 mL), then sonicated for 0.5 h at 45°C, and then kept on magnetic stirring for 0.5 h at 90°C. The reaction mixture was then cooled down then diluted by cold water to obtain light-yellow carbon nanodot powder [6].

Thermal routes: carbon soot has been primarily considered as the fundamental substance for the production of carbon nanodots. Treatment with an oxidant, namely, HNO_3 and H_2O_2 /AcOH, results in the formation of carbon nanodots [23]. However, the QY values are quite low, ranging between 0.8% and 1.9%.

The stages primarily carried out to synthesize carbon nanodots are dehydration, polymerization, carbonisation, and finally, passivation, as depicted in Figure 2. The use of various compounds has been noted in the synthesis of C-dots. For instance, APTMS or (3-Aminopropyl) trimethoxysilane and glycine, along with other substances like urea, sucrose, and alanine, have been a crucial precursor for the synthesis of carbon nanodots [24]. As formerly stated, there are broadly two major processes involved in synthesizing carbon dots: the bottom-up approach and the top-down approach. As previously discussed, the significant advantages of using carbon dots include low toxicity, the property of being chemically inert, outstanding biocompatibility,

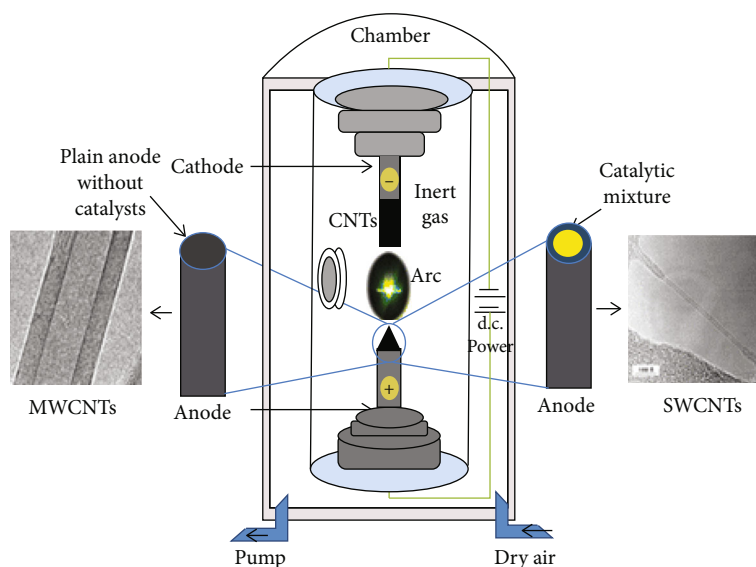


FIGURE 1: Arc discharge apparatus for the synthesis of CNT or carbon dots (reproduced from Das et al. 2016).

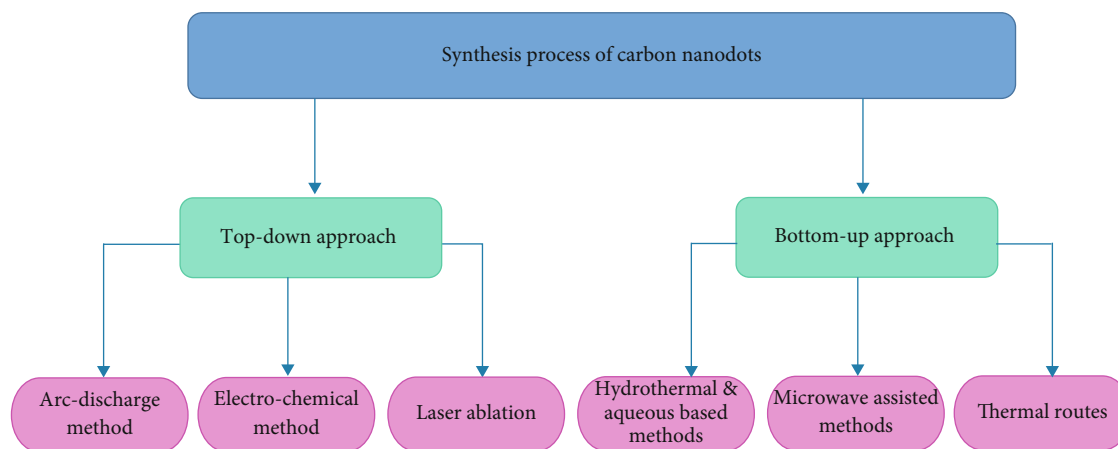


FIGURE 2: Synthesis process of carbon nanodots.

good water solubility, and multiphoton excitation, as well as excellent pl properties. Additionally, the physicochemical, electronic, optical, and electrochemical properties of carbon nanodots have been noted to be unique features and environment-friendly. Electrochemical properties were used to observe the energy gap of the carbon nanodots and Hückel level calculations of the highest occupied molecular orbital (HOMO) and lowest unoccupied molecular orbital (LUMO).

There are certain limitations identified for each of the approaches. For instance, it has been evident that synthesis steps are monotonous and occur at extremely high temperatures, utilizing toxic or harmful substances such as alkali or acids [25]. Hence, it becomes evident that Karfa et al. [25] contradict the existing idea or concept that C-dot synthesis is inexpensive. Apart from the statement that carbon dot synthesis has high costs, Karfa et al. [25] state that special equipment and nonpolar organic solvents are used in the process.

4. Properties of Carbon Nanodots

Modification is a process that is integrated into the overall mechanism of the formation of carbon nanodots. As noted previously, though carbon nanodots have a profound impact in biosensing or bioimaging, carbon dots face extreme competition in terms of their applications [26]. In this context, it must be noted that a high QY must be achieved to compete with other similar compounds effectively. Though there have been instances for producing carbon nanodots with a quantum yield of ~80%, most of the carbon nanodots synthesized through various methods have exhibited QY, less than 10%. To improve the quantum yield for the synthesized nanodots, surface passivation and other doping methods are implemented for modifying the same. Figure 3 illustrated the water-soluble carbon nanodot of the size range 20 to 50 nm [26].

Another significant property illustrated by the carbon nanodots is the reduced levels of cytotoxicity compared to

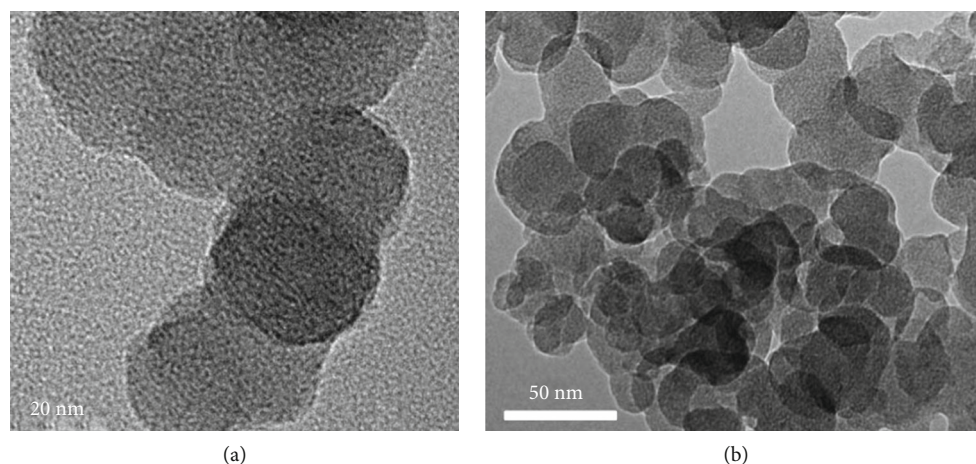


FIGURE 3: (a, b) TEM images of carbon nanodots (reproduced from Tripathi et al. 2017).

other carbon nanoparticles. The enhanced stability, biocompatibility, and hydrophilicity have been considered to contribute to the lower levels of cytotoxicity in carbon nanodots. Carbon nanodots continue to draw attention in biomedical applications, though their therapeutic efficacy becomes conceded due to rapid clearance from the human body. However, rapid clearance of carbon nanodots is advantageous in terms of cytocompatibility, but it is a significant restraint for their prolonged utilization as imaging and therapeutic agents, and this clearance depends on the surface charge on carbon nanodots [27–29]. Goryacheva et al. [30] state that they are cheap to produce and demonstrate bright light emissions, demonstrating the potential to completely replace the inorganic quantum dots for their applications in photocatalysis, solar cells, and more. Other physicochemical properties include absorption, variant morphology, surface properties, pl, and stability as a compound.

The property of pl of carbon nanodots has been used for several applications in biosensing and bioimaging [31]. According to Nguyen et al. [32], certain surface functional groups in carbon nanodots are responsible for the exhibition of this particular property. C-dots were utilized as agents for multicolor labelling to detect bacteria *Staphylococcus aureus* and *Escherichia coli* [19]. Hence, the pl property is increased as the conditions mentioned above serve as an excitation energy trap [33]. The impact of an extreme environment containing hydrogen peroxide, a potent oxidizing agent, has been tested, where the Zn-CDs manifested steady fluorescence and high stability against highly oxidizing H_2O_2 [33].

In addition, Himaja et al. [34] mention that synthesizing highly fluorescent carbon nanodots from kitchen waste is a thriving green process. Furthermore, the color of light emissions has been noted to be primarily yellow. Contradictory evidence illustrates that the carbon nanodots produced exhibited green and blue color emissions when synthesized with the help of controllable flame reactors, which are essentially fuel-rich [35]. Laser ablation has been regarded as a potentially effective procedure for synthesizing carbon nanodots, mainly when produced in ionic fluids [36]. Furthermore, it has been evident with the help of bioimaging that

agglomeration behavior is strongly demonstrated by the particles, N-CND-1 or N, S-CND. Agglomeration property could be due to successful construction and doping with nitrogen/sulfur and nitrogen. Positively charged N-CNDs-1, bearing amide groups at the surface, displayed a highly amorphous profile [37].

In order to further illustrate the impact of exposure to the modified carbon nanodots, a 3D human lung had been exposed to these particles over a period of 24 hours. With the help of the pseudo-air-liquid interface, by maintaining a concentration of $100 \mu\text{g/mL}$, alveolar epithelial cells, primarily the A549 cell line as well as the two primary immune cells, namely, dendritic cells and macrophages, were exposed to the carbon nanodots [37]. Utilizing the property of pl, researchers were able to identify that after 1 hour, approximately 80% of the N, S-CND and N-carbon dots-1 were left on the apical surface of the lungs [22]. It has been previously mentioned that the properties of the surface functional groups play a critical role in studying the overall behavior exhibited by carbon nanodots. In this case, amide groups and amino acids have been noted to be present on the surface of the nanodots, which enhanced the uptake properties of the N-carbon dots, as compared to the ones, which bore carboxylic acid groups, as the surface functional groups [22].

5. Applications of Carbon Nanodots

5.1. Imaging Applications. To date, many specific and novel methods have been discovered to identify bacterial species for instant and precise microorganism detection. CQDs have been innovative for imaging numerous microorganisms [38]. The carbon dots had tunable pl that empowered the identification of *Escherichia coli* through multicolor imaging after three hours of incubation with the carbon dots and the imaging-based attachment of the carbon dots to the surface of the bacterial cell [39]. Yu et al. [40] synthesized N-doped carbon dots by creating a combination of curcumin and polyethyleneimine hydrothermally. The synthesized carbon dots were kept incubated for three hours that have been utilized for the multicolor imaging of *Staphylococcus aureus* and *E. coli* [41].

Furthermore, the tested carbon dots no longer display antibacterial activity against the tested bacteria, permitting the identification and labelling of live bacteria. Baig and Chen [33] produced carbon dots from the white portion of the egg that was suitable for multicolor pl identification of *S. aureus* and *E. coli*, despite the fact that these carbon dots were fabricated at a much higher QY i.e., 45%, and used for identification and labeling bacteria upon 10 minutes of incubation, allowing them to be viable and lower quantity of carbon dots used for faster labeling of microorganisms. In another study, N, S-codoped carbon dots have been produced using a microwave irradiated method and a combination of thiourea and tris-acetate-ethylenediamine. The QY of the produced carbon dots was higher, making them feasible for multicolor labelling of microorganisms. Multicolor labelling demonstrates against four microorganism species, including *E. coli*, *Pseudomonas aeruginosa*, *S. aureus*, and *Klebsiella pneumoniae*. The bacterial species can efficiently be identified as endocytosis of the carbon dots has to be observed, except pneumonia bacteria which have no longer exhibited fluorescence after incubation. The equal conditions due to the catabolic pathway expresses for fragrant compounds could devastate the carbon dots [33]. Wang et al. [42] utilized a urea, sodium citrate, and thiourea to produce carbon dots with a QY of 37% that emitted blue fluorescence and, therefore, enable the utilization of labelling of *Xanthomonas axonopodis* with incubation of three hours which exhibits blue fluorescence under UV light; here, microorganism was found alive, and no distraction in shape and morphology observed [42].

Aside from microorganism cells, the potential of carbon dots for imaging purposes has conjointly been explored in other cells. Applications of carbon dots are overemphasized and exploited for imaging of cells of mammals. Most of the manufactured carbon dots accomplish the needs for a composite that could be used as an imaging agent. They showed a stable fluorescent signal and did not show adverse effects on cells' physiology [43]. Many reports on imaging revolve around cell imaging that is incredibly giant and not prudent or sensible to include all individual findings. Several properties of manufactured carbon dots created from citrus sinensis, apple seeds, and citrus limon, were observed when they were utilised to label A549, MDA-MB-231, HeLa, and HEK-293 cells for imaging purposes. Carbon dots are also synthesized from human fingernails that exhibit various pl properties [44].

The carbon dots produced with oil of vitriol from microwave irradiation exhibit an associated degree emission at 380 nm, whereas those produced from pyrolysis showed a dual emission at 450 nm and 380. Besides the different pl features, these carbon dots produce the 42.8% QY with microwave treatment and 81.4% QY from pyrolysis that efficiently utilizes four different cell lines [45]. Furthermore, carbon dots produced from pyrolysis after forty-eight hours of incubation will promote HEK-293 cell proliferation by up to 18 hrs. These findings were thus vital that could be utilized for additional advanced clinical applications [41].

Du et al. [46] synthesized carbon dots from the hydrothermal treatment of glycine and glucose that effectively

label MTEC1 and Sh-y5y cells in which the carbon dots localized within the membrane and protoplasm, while the nucleus pl was not strong. Pal et al. [47] produced polyethyleneimine carbon dots from the hydrothermal method of polyethyleneimine and curcumin used for microorganism labelling. These carbon dots were also utilized for labelling of NIH 3T3, A549, and HCT-15 cells and exhibited multicolored pl. Though differences in the pl intensity were recorded in all tested cells. Cancer cells HCT-15 and A549 showed high pl as compared to fibroblasts NIH3T3 cells due to the higher rate and uptake by cancer cells [48]. Carbon dots formed by irradiated microwave method by using a mixture of acid and ethylenediamine exhibited excitation-dependent red pl that was helpful for labelling of animal tissue cells, retinal, lens, and CHO cells to exhibit multicolored pl [49].

Furthermore, the red pl was significantly helpful as cells became ready to emit pl once excited at 635 nm. This way, the fluorescence was reduced, resulting in the quantitative ratio of signal to background which was amplified. Carbon dots produced by the irradiated microwave method by using aspirin-hydrazine were used to imaging HeLa, RAW246.7, KB, and BMSC cells. Notably, the carbon dots will enter the cell organelle and label it with the cytoplasmic space [50].

In another study, carbon dots made from histidine and cotton were ready to enter the organelle of AD-293 cells used to label organelle of A193 cells, respectively [51]. In this regard, it needs to be mentioned that there are several widespread applications of carbon nanodots, and most of the applications can be attributed to its property of pl.

Bioimaging is one of the significant applications of carbon dots, which can be attributed to its fluorescent property. Carbon dots have been noted to emit lights of varying wavelengths in their excited state. Kim et al. [52] mention that dual-color emitting carbon dots have been used in gaining optogenetic control of ion channels and multicolor bioimaging. According to Mishra et al. [53], targeted drug delivery is another option being considered for medical purposes of carbon nanodots. Despite the potential applications of carbon nanodots in advanced medicine, Atchudan et al. [54] mention that carbon dots can be synthesized conveniently from *Malus floribunda*, commonly known as Japanese crab or purple chokeberry, illustrating and supporting the former views of driving carbon dots from natural sources [5].

5.2. Biosensing Applications. The detection of various biological and chemical compounds can be performed with the help of carbon nanodots. In addition, Bui and Park [55] further mention the use of carbon nanodots in the screening of cholesterol as a part of biosensing. It has been formerly discussed that the detection of carbon nanodots in the human lung has been measured owing to their fluorescence property [56]. The biosensor mentioned above comprises primarily of haemoglobin complex and C-dot components, respectively.

Another critical application of carbon dots in biosensing is the detection of gene mutation [57]. Additionally, Yu et al. [58] mention that *Saccharomyces* or yeast may aid in the

production of carbon nanodots, which has been noted to be effective in detecting vitamin B₁₂ and pH. Hong et al. [59] further illustrate that multimodal carbon dots act as effective biosensors. Moreover, it has been stated that the use of carbon dots may influence and even enhance the provision of therapeutic functionalities and trigger the development of theranostic materials (Figure 4) [59].

5.3. Antibacterial Potential. Carbon nanodot's bactericidal potential is due to oxidative stress persuaded by reactive oxygen species produced by carbon nanodots that act as a signalling particle inside the cells in response to the pathogen. Oxidative stress progresses when the reactive oxygen species production surpasses the usual defense of antioxidant in bacterium that induces oxidative injury to biomolecules such as nucleotides, lipids, and proteins resulting in damage to the cell wall and bacterial death. Heteroatoms present in functionalized carbon dots improve the production of reactive oxygen species due to free-electron integration in carbon dots [60–63]. The life of reactive oxygen species is usually short that depends upon the type of reactive oxygen species. For instance, hydrogen peroxide has an elongated life of about 1 ms compared to other reactive oxygen species, while other types of reactive oxygen species have a short life that measures in microsecond range [64]. As a consequence, reactive oxygen species can diffuse over very short distances to several 100 nm allowing diffusion around the lipid bilayer, which is required for the generation of reactive oxygen species in the close locality of its target to show effective bactericidal potential. Nitrogen atoms in carbon dots produce groups, which are positively charged results in augmenting the electrostatic interaction to cell surface, which are negatively charged resulting in reactive oxygen species production which leads to target pathogens and exhibits antibacterial effects [62].

Positively charged carbon dots are synthesized from spermidine or quaternary ammonium salts. These carbon dots firmly adhere to proteins, porins, and peptidoglycan of the bacterial cell wall resulting in inhibition of cell wall synthesis of Gram-positive and Gram-negative bacteria, indicating their enhanced antibacterial activity [65–67]. Carbon dots entered into the bacteria interior result in oxidative damage to biomolecules, including DNA content which leads to damaging the cell wall [61].

Additionally, synergistic utilization of carbon dots with antibiotics or photosensitizers shows better efficacy; for instance, photoactivated carbon dots combined with photosensitizers like toluidine blue and methylene blue achieve higher reactive oxygen species generation than photosensitizers or carbon dots alone under the illumination of visible light, thus resulting in enhanced killing of bacteria [68, 69].

Carbon is usually nontoxic and showed no apparent side effects and toxicity in treating infected wounds in rats and pneumonia in tested mice [70, 71]. A biosafety evaluation of photoluminescent carbon dots produced by nitric acid oxidation found no acute toxicity, genotoxicity, or abnormalities or lesions in the organs of mice [72]. No cytotoxicity of cadmium-selenide quantum dots was observed, which was improved by a coating of polyethylene glycol [73].

5.4. Cancer Diagnosis. The higher sensitivity, including spatial and temporal resolution of fluorescence imaging, makes carbon dots the most auspicious agent in cell sensing, targeting, and imaging [74]. For instance, Song et al. [75] produced carbon dots coupled with folic acid to distinguish folate receptor-positive from folate receptor-negative cells that were utilized to identify and label and analyse HeLa and NIH-3T3 cells. Lee et al. [75] synthesized carbon dots coupled with maleimide-terminated TTA1 aptamer expressed highly in C6 rat glioma cell line and HeLa cell line and not expressed in normal healthy CHO Chinese hamster ovary cell line cells. The incubation of the carbon dots conjugated with maleimide-terminated TTA1 aptamer exhibits a strong fluorescence and selectively along with cancer cells and is only very less absorbed in normal cells. Zhang et al. [76] synthesized carbon dots coupled with folic acid that were able to selectively recognise cancer cells in a combination of PC12 and HepG2 by showing a bright green luminescence after incubation of 2 hours. In another study, Li et al. [74] revealed a new tumor therapy that depends on autophagy by combining the folic acid and biocompatible N-doped carbon dots that possess a broad range of high ability of targeted including 26 kinds of tumor cell and distress the metabolism which results in autophagy. Bhunia et al. [77] synthesized functionalized fluorescent carbon dots with folate or TAT peptide and incubated them with folate receptor-positive cancerous cells and folate receptor-negative normal cells that enhanced cell labelling and uptake.

5.5. Cancer Therapy. Photodynamic therapy is of utmost promising and noninvasive cancer therapeutic approaches with fewer side effects that could be utilized unaided or in amalgamation with ionizing radiation, surgery, and chemotherapy and can be utilized to abolish cancerous cells, which are undetected [78]. Photodynamic therapy employed photosensitizing drugs as these are inactive pharmacologically till a specific wavelength of light irradiates that generates reactive oxygen species resulting in induced cell death and necrosis [78–81]. For instance, photosensitizing drugs such as porphyrin and phthalocyanine and their derivatives have potential in cancer imaging and therapeutic approved for medical applications [82, 83]. Their utilization is limited due to cutaneous photosensitivity enhancement, water solubility reduction, low photostability, and selectivity [84]. For this cause, many other approaches have been examined. For instance, Huang et al. [85] revealed an innovative theranostic method that depends on chlorin e6-conjugated carbon dots which exhibit good solubility, stability, low cytotoxicity, enhanced photosensitizer fluorescence detection, good biocompatibility, and outstanding photodynamic efficacy as compared to utilization of Ce6 alone. Furthermore, in another study, in vitro or in vivo utilization of a carbon dot-chlorin e6-hyaluronate coupled, which is transdermal, was successfully utilized for the photodynamic therapy in skin cancer that showed significant photodynamic outcomes on cancer cells as compared to Cdot-Ce6 and Ce6 alone [86]. Li et al. [87] synthesized porphyrin-containing carbon dots

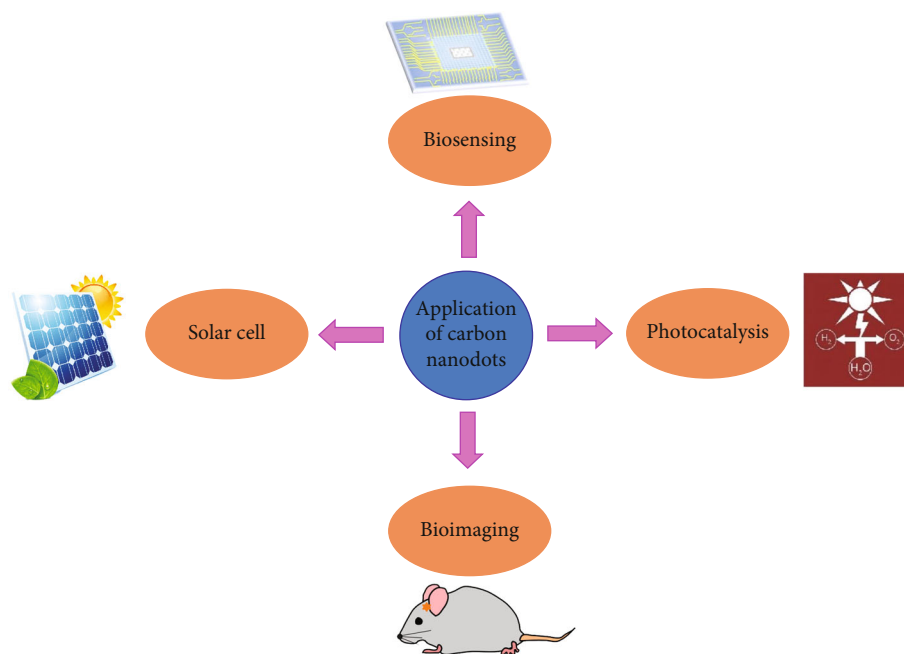


FIGURE 4: Applications of carbon nanodots.

utilized in the effective photodynamic therapy in hepatoma treatment and showed good photostability, cellular uptake, biocompatibility, and potent cytotoxicity which leads to suppress the tumor.

Recently, carbon dots have also been utilized as photosensitizing chemicals as they possess substantial temperature variations upon irradiation. Sun et al. [88] revealed red emissive carbon dots and utilized them quickly and efficiently that convert laser energy into heat resulting in reduction of the viability of MCF-7 cells. Geng et al. [89] synthesized near-infrared absorbing nitrogen and oxygen codoped carbon dots that generate high efficiency under laser irradiation results in attaining 100% of ablation of tumor tissue without any harm or side effects. Zheng et al. [90] produced near-infrared fluorescent hydrophobic cyanine dye and polyethylene glycol-doped carbon dots that exhibit superior uptake and accumulation in tumors with high photothermal conversion efficiency. Ge et al. [91] synthesized carbon dots using polythiophene benzoic acid that shows photodynamic and photothermal effects under laser irradiation of 635 nm. Lan et al. [92] synthesized S, Se-codoped carbon dots by utilizing polythiophene and diphenyl diselenide that utilized new multifunctional phototheranostic reagents. Wang et al. [23] synthesized near-infrared-emissive boron and nitrogen-doped carbon dots to induce higher penetration into tissue that exhibits a photothermal therapeutic effect and kills cancer cells entirely to suppress tumor growth in vivo.

5.6. Other Applications

5.6.1. Solar Cells. Margraf et al. [93] mention that carbon nanodots can be actively used in mesoscopic solar cells as sensitizers, since these particles are environment-friendly and relatively inexpensive. Furthermore, Chatzimitakos

and Stalikas [94] state that carbon nanodots can be easily produced or generated from the most common natural resources, making their availability abundant and production cost cheaper. This can be further substantiated by Marinovic et al. [95], who mention that carbon nanodots have been noted to have the highest recorded solar PCE or solar power conversion efficiency, attributing to approximately 0.36%. L-arginine carbon dots had been used for this purpose as sensitizers. On the contrary, the use of lobster shells in hydrothermal carbonisation resulted in the generation of PCE of 0.22%. Loading CQDs into perovskite precursor solution results in a superior hybrid $\text{Cs}_{0.15}\text{FA}_{0.85}\text{PbI}_3$ thin film. The productivity of the associated ITO/PTAA/ $\text{Cs}_{0.15}\text{FA}_{0.85}\text{PbI}_3$ /PC₆₁BM/BCP/Ag inverted planar perovskite solar cells increased from 17.36 percent to 20.06 percent [96]. Wang et al. [97] reported that to enhance the productivity of the associated perovskite solar cells, CQDs were added to the CsPbI_2Br photoactive layer. Upon incorporating CQNDs in an ideal amount, it is discovered that the trap density may be significantly reduced and crystallinity can be improved. Riaz and Park [98] used freeze-dried urea and CQD precursors to make nitrogen-rich CQDs that were implanted in CN nanotubes. The CN nanotubes that had been synthesized were utilized as efficient light harvesters.

5.6.2. Photocatalysis. Liu et al. [99] have stated that carbon nanodots act as efficient catalysts for oxidation as well as reduction reactions. Furthermore, the surface modifications have been found to play a critical role in the same. On the other hand, it has been mentioned previously that Margraf et al. [93] mention the use of carbon dots in mesoscopic solar cells, mostly carried out with the bottom-up microwave approach, deploying resources such as urea, citric acid, and formic acid. However, despite expecting PCE of 0.24%, it

has been evident from research and experimentation that the PCE deteriorates, and the lower performance rates can be attributed to photovoltage decay [93].

Other key applications of carbon nanodots include the detection of luminescence or fluorescence of hydrazine hydrate and such compounds [100]. Furthermore, Sai et al. [101] mention that carbon nanodots may effectively utilize UV light by acting as light conversion material. In this regard, it needs to be mentioned that the fundamental advantages or benefits of using carbon nanodots are the environment-friendly nature and the easy generation process from various natural sources, making it relatively inexpensive compared to other types of carbon nanoparticles [102, 103]. In addition to that, it has been established that carbon dots are quite effective in biosensing as they are relatively sensitive and efficient, rapid, and selective in their mode of action [104, 105].

Graphene quantum dots have the potential to be utilized as surfactants in miniemulsion polymerization for various vinyl monomers, which were employed for hybrid nanocomposite synthesis [106]. The Ag/CQDs microspheres displayed excellent catalytic activity [107]. Carbon dot-stabilized Pickering emulsions were effectively used to load hydrophobic and hydrophilic pharmaceuticals into poly-lactide-co-glycolide (PLGA) drug delivery systems [108]. Carboxylated graphene quantum dots were used as effective surfactants in miniemulsion polymerization employed of novel hybrid nanocomposite synthesis [109].

The coaxial electrosprayed nanoparticles and carbon dot composites showed a fluorescence “on-off” behavior due to the volume phase transition of the poly(*N*-isopropylacrylamide) shell. These composite in Pickering emulsions exhibits the motions of coaxial electrosprayed NPs in response to changes in temperature [110]. Fluorescent carbon nanodots derived from mandarin peel can be used to detect micromolar amounts of hydrazine hydrate solution with exceptional sensitivity [100].

6. Conclusion

Carbon dots have shown a promising future, especially in biomedical applications that exhibit alternatives to traditional quantum dots based on heavy metal. This review stated various methods of synthesizing carbon dots and their recent applications as diagnosis and therapy. Primarily, we studied physical and chemical properties, including optical and stability, then biological properties including cytotoxicity, internalization at the cellular level, biocompatibility, and distribution that could be exploited in various biomedical applications such as antibacterial, diagnosis, and therapy bioimaging including in vitro and in vivo studies on functionalized carbon dots that show impressive results in reference to their cytotoxicity, photostability, biocompatibility, and anticancer effects. All these applications represent that carbon dots could be a promising method for biomedical applications, cancer diagnosis, and cancer therapy and have potential medical uses in the near future.

Data Availability

The authors can also make data available on request through a data access committee, institutional review board, or the authors themselves. In this case, they can contact the corresponding author to request the data.

Conflicts of Interest

The authors declare that they have no conflicts of interest.

Supplementary Materials

Graphical Abstract. (*Supplementary Materials*)

References

- [1] X. Xu, R. Ray, Y. Gu et al., “Electrophoretic analysis and purification of fluorescent single-walled carbon nanotube fragments,” *Journal of the American Chemical Society*, vol. 126, no. 40, pp. 12736–12737, 2004.
- [2] Z. Wang, Y. Qu, X. Gao, C. Mu, J. Bai, and Q. Pu, “Facile preparation of oligo(ethylene glycol)-capped fluorescent carbon dots from glutamic acid for plant cell imaging,” *Materials Letters*, vol. 129, pp. 122–125, 2014.
- [3] C. W. Lai, Y. H. Hsiao, Y. K. Peng, and P. T. Chou, “Facile synthesis of highly emissive carbon dots from pyrolysis of glycerol; gram scale production of carbon dots/mSiO₂ for cell imaging and drug release,” *Journal of Materials Chemistry*, vol. 22, no. 29, pp. 14403–14409, 2012.
- [4] D. Kukreja, J. Mathew, R. Lakshmipathy, and N. C. Sarada, “Synthesis of fluorescent carbon dots from mango peels,” *International Journal of ChemTech Research*, vol. 8, no. 5, pp. 61–64, 2015.
- [5] P. Roy, P. C. Chen, A. P. Periasamy, Y. N. Chen, and H. T. Chang, “Photoluminescent carbon nanodots: synthesis, physicochemical properties and analytical applications,” *Materials Today*, vol. 18, no. 8, pp. 447–458, 2015.
- [6] H. Xu, L. Xie, and M. Hakkarainen, “Coffee-ground-derived quantum dots for aqueous processable nanoporous graphene membranes,” *ACS Sustainable Chemistry & Engineering*, vol. 5, no. 6, pp. 5360–5367, 2017.
- [7] A. Sciortino, A. Cannizzo, and F. Messina, “Carbon nanodots: a review—from the current understanding of the fundamental photophysics to the full control of the optical response,” *C—Journal of Carbon Research*, vol. 4, no. 4, p. 67, 2018.
- [8] R. Das, Z. Shahnava, M. Ali, M. M. Islam, and S. B. Abd Hamid, “Can we optimize arc discharge and laser ablation for well-controlled carbon nanotube synthesis?,” *Nanoscale Research Letters*, vol. 11, no. 1, pp. 1–23, 2016.
- [9] A. Nevar, N. Tarasenko, M. Nedelko, and N. Tarasenko, “Carbon nanodots with tunable luminescence properties synthesized by electrical discharge in octane,” *Carbon Letters*, vol. 31, no. 1, pp. 39–46, 2021.
- [10] I. F. Andhika, T. E. Saraswati, and S. Hastuti, “The structural characteristics of carbon nanoparticles produced by arc discharge in toluene without added catalyst or gases,” *Evergreen Joint Journal of Novel Carbon Resource Sciences & Green Asia Strategy*, vol. 7, no. 3, pp. 417–428, 2020.
- [11] D. Zhang, Y. Tang, C. Zhang, Q. Dong, W. Song, and Y. He, “One-step synthesis of SnO₂/carbon nanotube nanonests

- composites by direct current arc-discharge plasma and its application in lithium-ion batteries,” *Nanomaterials*, vol. 11, no. 11, p. 3138, 2021.
- [12] P. C. Hsu, Z. Y. Shih, C. H. Lee, and H. T. Chang, “Synthesis and analytical applications of photoluminescent carbon nanodots,” *Green Chemistry*, vol. 14, no. 4, pp. 917–920, 2012.
- [13] H. Li, X. He, Z. Kang et al., “Water-soluble fluorescent carbon quantum dots and photocatalyst design,” *Angewandte Chemie International Edition*, vol. 49, no. 26, pp. 4430–4434, 2010.
- [14] P. C. Hsu and H. T. Chang, “Synthesis of high-quality carbon nanodots from hydrophilic compounds: role of functional groups,” *Chemical Communications*, vol. 48, no. 33, pp. 3984–3986, 2012.
- [15] C. Zhu, J. Zhai, and S. Dong, “Bifunctional fluorescent carbon nanodots: green synthesis via soy milk and application as metal-free electrocatalysts for oxygen reduction,” *Chemical Communications*, vol. 48, no. 75, pp. 9367–9369, 2012.
- [16] V. Nguyen, N. Zhao, L. Yan, P. Zhong, and P. H. Le, “Double-pulse femtosecond laser ablation for synthesis of ultrasmall carbon nanodots,” *Materials Research Express*, vol. 7, no. 1, article 015606, 2020.
- [17] M. J. Yang, J. X. Shi, Y. Yin, and C. G. Shi, “Preparation of carbon nanodots with ultraviolet emission by pulsed laser ablation,” *Physica status solidi (b)*, vol. 258, no. 10, article 2100110, 2021.
- [18] N. Mas, J. L. Hueso, G. Martinez et al., “Laser-driven direct synthesis of carbon nanodots and application as sensitizers for visible-light photocatalysis,” *Carbon*, vol. 156, pp. 453–462, 2020.
- [19] M. Aslan and H. Eskalen, “A study of carbon nanodots (carbon quantum dots) synthesized from tangerine juice using one-step hydrothermal method,” *Fullerenes, Nanotubes, and Carbon Nanostructures*, vol. 29, no. 12, pp. 1026–1033, 2021.
- [20] P. C. Yang, Y. X. Ting, S. Gu, Y. A. Gandomi, and C. T. Hsieh, “Fluorescent nitrogen-doped carbon nanodots synthesized through a hydrothermal method with different isomers,” *Journal of the Taiwan Institute of Chemical Engineers*, vol. 123, pp. 302–309, 2021.
- [21] Y. Y. Chen, W. P. Jiang, H. L. Chen et al., “Cytotoxicity and cell imaging of six types of carbon nanodots prepared through carbonization and hydrothermal processing of natural plant materials,” *RSC Advances*, vol. 11, no. 27, pp. 16661–16674, 2021.
- [22] E. Durantie, H. Barosova, B. Drasler et al., “Carbon nanodots: opportunities and limitations to study their biodistribution at the human lung epithelial tissue barrier,” *Biointerphases*, vol. 13, no. 6, p. 06D404, 2018.
- [23] H. Wang, Q. Mu, K. Wang et al., “Nitrogen and boron dual-doped graphene quantum dots for near-infrared second window imaging and photothermal therapy,” *Applied Materials Today*, vol. 14, pp. 108–117, 2019.
- [24] A. Roy, S. Kim, P. Paoprasert, S. Park, and I. in, “Preparation of biocompatible and antibacterial carbon quantum dots derived from resorcinol and formaldehyde spheres,” *RSC Advances*, vol. 5, no. 40, pp. 31677–31682, 2015.
- [25] P. Karfa, S. De, K. C. Majhi, R. Madhuri, and P. K. Sharma, *Functionalization of carbon nanostructures*, Academic Press, 2019.
- [26] K. M. Tripathi, T. S. Tran, T. T. Tung, D. Losic, and T. Kim, “Water soluble fluorescent carbon nanodots from biosource for cells imaging,” *Journal of Nanomaterials*, vol. 2017, 10 pages, 2017.
- [27] J. Yan, S. Hou, Y. Yu et al., “The effect of surface charge on the cytotoxicity and uptake of carbon quantum dots in human umbilical cord derived mesenchymal stem cells,” *Colloids and Surfaces. B, Biointerfaces*, vol. 1, no. 171, pp. 241–249, 2018.
- [28] L. N. Ramana, L. N. Dinh, and V. Agarwal, “Influence of surface charge of graphene quantum dots on their uptake and clearance in melanoma cells,” *Nanoscale Advances*, vol. 3, no. 12, pp. 3513–3521, 2021.
- [29] L. Dong, W. Li, L. Yu, L. Sun, Y. Chen, and G. Hong, “Ultra-small Ag₂Te quantum dots with rapid clearance for amplified computed tomography imaging and augmented photonic tumor hyperthermia,” *ACS Applied Materials & Interfaces*, vol. 12, no. 38, pp. 42558–42566, 2020.
- [30] I. Y. Goryacheva, A. V. Sapelkin, and G. B. Sukhorukov, “Carbon nanodots: mechanisms of photoluminescence and principles of application,” *TrAC Trends in Analytical Chemistry*, vol. 90, pp. 27–37, 2017.
- [31] S. C. Ray, A. Saha, N. R. Jana, and R. Sarkar, “Fluorescent carbon nanoparticles: synthesis, characterization, and bioimaging application,” *The Journal of Physical Chemistry C*, vol. 113, no. 43, pp. 18546–18551, 2009.
- [32] V. Nguyen, J. Si, L. Yan, and X. Hou, “Direct demonstration of photoluminescence originated from surface functional groups in carbon nanodots,” *Carbon*, vol. 108, pp. 268–273, 2016.
- [33] M. M. F. Baig and Y. C. Chen, “Bright carbon dots as fluorescence sensing agents for bacteria and curcumin,” *Journal of Colloid and Interface Science*, vol. 501, no. 501, pp. 341–349, 2017.
- [34] A. L. Himaja, P. S. Karthik, B. Sreedhar, and S. P. Singh, “Synthesis of carbon dots from kitchen waste: conversion of waste to value added product,” *Journal of Fluorescence*, vol. 24, no. 6, pp. 1767–1773, 2014.
- [35] C. Russo, B. Apicella, and A. Ciajolo, “Blue and green luminescent carbon nanodots from controllable fuel-rich flame reactors,” *Scientific Reports*, vol. 9, no. 1, pp. 1–8, 2019.
- [36] H. P. Castro, V. S. Souza, J. D. Scholten et al., “Synthesis and characterisation of fluorescent carbon nanodots produced in ionic liquids by laser ablation,” *European Journal*, vol. 22, no. 1, pp. 138–143, 2016.
- [37] C. Wang, Z. Xu, and C. Zhang, “Polyethyleneimine-functionalized fluorescent carbon dots: water stability, pH sensing, and cellular imaging,” *ChemNanoMat*, vol. 1, no. 2, pp. 122–127, 2015.
- [38] X. Su, Y. Xu, Y. Che, X. Liao, and Y. Jiang, “A type of novel fluorescent magnetic carbon quantum dots for cells imaging and detection,” *Journal of Biomedical Materials Research*, vol. 103, no. 12, pp. 3956–3964, 2015.
- [39] N. Puvvada, B. Kumar, S. Konar, H. Kalita, M. Mandal, and A. P. Mahanty, “Synthesis of biocompatible multicolor luminescent carbon dots for bioimaging applications,” *Science and Technology of Advanced Materials*, vol. 13, no. 4, article 045008, 2012.
- [40] T. Yu, H. Wang, C. Guo, Y. Zhai, J. Yang, and J. Yuan, “A rapid microwave synthesis of green-emissive carbon dots

- with solid-state fluorescence and pH-sensitive properties,” *Royal Society Open Science*, vol. 5, no. 7, article 180245, 2018.
- [41] M. Zhang, C. Chi, P. Yuan, Y. Su, M. Shao, and N. Zhou, “A hydrothermal route to multicolor luminescent carbon dots from adenosine disodium triphosphate for bioimaging,” *Materials Science and Engineering:C*, vol. 76, pp. 1146–1153, 2017.
- [42] J. Wang, X. Liu, G. Milcovich et al., “Co-reductive fabrication of carbon nanodots with high quantum yield for bioimaging of bacteria,” *Beilstein Journal of Nanotechnology*, vol. 9, no. 1, pp. 137–145, 2018.
- [43] M. Hassan, V. Gomes, A. Dehghani, and S. Ardekani, “Engineering carbon quantum dots for photomediated theranostics,” *Nano Research*, vol. 11, no. 1, pp. 1–41, 2018.
- [44] W. Niu, Y. Li, R. Zhu, D. Shan, Y. Fan, and X. Zhang, “Ethylenediamine-assisted hydrothermal synthesis of nitrogen-doped carbon quantum dots as fluorescent probes for sensitive biosensing and bioimaging,” *Sensors and Actuators B: Chemical*, vol. 218, pp. 229–236, 2015.
- [45] G. He, M. Xu, S. Mengjun et al., “Rapid solid-phase microwave synthesis of highly photoluminescent nitrogen-doped carbon dots for Fe^{3+} detection and cellular bioimaging,” *Nanotechnology*, vol. 27, no. 39, article 395706, 2016.
- [46] F. Du, J. Li, Y. Hua et al., “Multicolor nitrogen-doped carbon dots for live cell imaging,” *Journal of Biomedical Nanotechnology*, vol. 11, no. 5, pp. 780–788, 2015.
- [47] T. Pal, S. Mohiyuddin, and G. Packirisamy, “Facile and green synthesis of multicolor fluorescence carbon dots from curcumin: in vitro and in vivo bioimaging and other applications,” *ACS Omega*, vol. 3, no. 1, pp. 831–843, 2018.
- [48] W. Zou, Y. Ji, X. Wang et al., “Insecticide as a precursor to prepare highly bright carbon dots for patterns printing and bioimaging: a new pathway for making poison profitable,” *Chemical Engineering Journal*, vol. 294, pp. 323–332, 2016.
- [49] H. Sadhanala and K. Nanda, “Boron-doped carbon nanoparticles: size-independent color tunability from red to blue and bioimaging applications,” *Carbon*, vol. 96, pp. 166–173, 2016.
- [50] X. Xu, K. Zhang, L. Zhao et al., “Aspirin-based carbon dots, a good biocompatibility of material applied for bioimaging and anti-inflammation,” *ACS applied materials & interfaces*, vol. 8, no. 48, pp. 32706–32716, 2016.
- [51] A. Kasouni, T. Chatzimitakos, and C. Stalikas, “Bioimaging applications of carbon nanodots: a review,” *C*, vol. 5, no. 2, p. 19, 2019.
- [52] H. Kim, Y. Park, S. Beack et al., “Dual-color-emitting carbon nanodots for multicolor bioimaging and optogenetic control of ion channels,” *Advanced Science*, vol. 4, no. 11, p. 1700325, 2017.
- [53] V. Mishra, A. Patil, S. Thakur, and P. Kesharwani, “Carbon dots: emerging theranostic nanoarchitectures,” *Drug Discovery Today*, vol. 23, no. 6, pp. 1219–1232, 2018.
- [54] R. Atchudan, T. N. J. I. Edison, S. Perumal, N. Muthuchamy, and Y. R. Lee, “Eco-friendly synthesis of tunable fluorescent carbon nanodots from *Malus floribunda* for sensors and multicolor bioimaging,” *Journal of Photochemistry and Photobiology A: Chemistry*, vol. 390, article 112336, 2020.
- [55] T. T. Bui and S. Y. Park, “A carbon dot–hemoglobin complex-based biosensor for cholesterol detection,” *Green Chemistry*, vol. 18, no. 15, pp. 4245–4253, 2016.
- [56] Y. Wu, H. Wu, C. Kuan et al., “Multi-functionalized carbon dots as theranostic nanoagent for gene delivery in lung cancer therapy,” *Scientific Reports*, vol. 6, no. 1, p. 21170, 2016.
- [57] T. García-Mendiola, I. Bravo, J. M. López-Moreno et al., “Carbon nanodots based biosensors for gene mutation detection,” *Sensors and Actuators B: Chemical*, vol. 256, pp. 226–233, 2018.
- [58] Y. Yu, C. Li, C. Chen et al., “Saccharomyces-derived carbon dots for biosensing pH and vitamin B 12,” *Talanta*, vol. 195, pp. 117–126, 2019.
- [59] J. Hong, M. Kim, and C. Cha, “Multimodal carbon dots as biosensors,” in *Theranostic Bionanomaterials*, pp. 377–400, Elsevier, 2019.
- [60] P. Sharma, A. B. Jha, R. S. Dubey, and M. Pessarakli, “Reactive oxygen species, oxidative damage, and antioxidative defense mechanism in plants under stressful conditions,” *Journal of Botany*, vol. 2012, 26 pages, 2012.
- [61] W. Bing, H. Sun, Z. Yan, J. Ren, and X. Qu, “Programmed bacteria death induced by carbon dots with different surface charge,” *Small*, vol. 12, no. 34, pp. 4713–4718, 2016.
- [62] N. A. Travlou, D. A. Giannakoudakis, M. Algarra, A. M. Labella, E. Rodríguez-Castellón, and T. J. Bandoz, “S- and N-doped carbon quantum dots: surface chemistry dependent antibacterial activity,” *Carbon*, vol. 135, pp. 104–111, 2018.
- [63] Y. Li, W. Zhang, J. Niu, and Y. Chen, “Mechanism of photo-generated reactive oxygen species and correlation with the antibacterial properties of engineered metal-oxide nanoparticles,” *ACS Nano*, vol. 6, pp. 5164–5173, 2021.
- [64] F.-J. Schmitt, G. Renger, T. Friedrich et al., “Reactive oxygen species: re-evaluation of generation, monitoring and role in stress-signaling in phototrophic organisms,” *Biochimica et Biophysica Acta*, vol. 1837, no. 6, pp. 835–848, 2014.
- [65] Y. J. Li, S. G. Harroun, Y. C. Su et al., “Synthesis of self-assembled spermidine-carbon quantum dots effective against multidrug-resistant bacteria,” *Advanced Healthcare Materials*, vol. 5, no. 19, pp. 2545–2554, 2016.
- [66] H. J. Jian, R. S. Wu, T. Y. Lin et al., “Super-cationic carbon quantum dots synthesized from spermidine as an eye drop formulation for topical treatment of bacterial keratitis,” *ACS Nano*, vol. 11, no. 7, pp. 6703–6716, 2017.
- [67] Z. Song, H. Wang, Y. Wu, J. Gu, S. Li, and H. Han, “Fabrication of bis-quaternary ammonium salt as an efficient bactericidal weapon against *Escherichia coli* and *Staphylococcus aureus*,” *ACS Omega*, vol. 3, no. 10, pp. 14517–14525, 2018.
- [68] X. Dong, A. E. Bond, N. Pan et al., “Synergistic photoactivated antimicrobial effects of carbon dots combined with dye photosensitizers,” *International Journal of Nanomedicine*, vol. Volume 13, pp. 8025–8035, 2018.
- [69] K. Kholikov, S. Ilhom, M. Sajjad et al., “Improved singlet oxygen generation and antimicrobial activity of sulphur-doped graphene quantum dots coupled with methylene blue for photodynamic therapy applications,” *Photodiagnosis and Photodynamic Therapy*, vol. 24, pp. 7–14, 2018.
- [70] C. Zhao, X. Wang, L. Yu et al., *Quaternized carbon quantum dots with broad-spectrum antibacterial activity for treatment of wounds infected with mixed bacteria*, Research Square, 2020.
- [71] C. Zhao, L. Wu, X. Wang et al., “Quaternary ammonium carbon quantum dots as an antimicrobial agent against gram-positive bacteria for the treatment of MRSA-infected pneumonia in mice,” *Carbon*, vol. 163, pp. 70–84, 2020.

- [72] K. Wang, Z. Gao, G. Gao et al., "Systematic safety evaluation on photoluminescent carbon dots," *Nanoscale Research Letters*, vol. 8, no. 1, p. 122, 2013.
- [73] D. Painuly, A. Bhatt, and V. K. Krishnan, "Mercaptoethanol capped CdSe quantum dots and CdSe/ZnS core/shell: synthesis, characterization and cytotoxicity evaluation," *Journal of Biomedical Nanotechnology*, vol. 9, no. 2, pp. 257–266, 2013.
- [74] J. Li, S. Yang, Y. Deng et al., "Emancipating target-functionalized carbon dots from autophagy vesicles for a novel visualized tumor therapy," *Advanced Functional Materials*, vol. 28, no. 30, p. 1800881, 2018.
- [75] Y. Song, W. Shi, W. Chen, X. Li, and H. Ma, "Fluorescent carbon nanodots conjugated with folic acid for distinguishing folate-receptor-positive cancer cells from normal cells," *Journal of Materials Chemistry*, vol. 22, no. 25, p. 12568, 2012.
- [76] J. L. Zhang, X. W. Zhao, M. Xian, C. Dong, and S. M. Shuang, "Folic acid-conjugated green luminescent carbon dots as a nanoprobe for identifying folate receptor-positive cancer cells," *Talanta*, vol. 183, p. 47, 2018.
- [77] S. K. Bhunia, A. Saha, A. R. Maity, S. C. Ray, and N. R. Jana, "Carbon nanoparticle-based fluorescent bioimaging probes," *Scientific Reports*, vol. 3, no. 1, p. 1473, 2013.
- [78] M. Kurupparachchi, H. Savoie, A. Lowry, C. Alonso, and R. W. Boyle, "Polyacrylamide nanoparticles as a delivery system in photodynamic therapy," *Molecular Pharmaceutics*, vol. 8, pp. 920–931, 2011.
- [79] M. Korbelik, "PDT-associated host response and its role in the therapy outcome," *Lasers in Surgery and Medicine*, vol. 38, no. 5, pp. 500–508, 2006.
- [80] C. A. Robertson, E. D. Hawkins, and H. Abrahamse, "Photodynamic therapy (PDT): a short review on cellular mechanisms and cancer research applications for PDT," *Journal of Photochemistry and Photobiology B: Biology*, vol. 96, no. 1, pp. 1–8, 2009.
- [81] H. Thomsen, N. Marino, S. Conoci, S. Sortino, and M. B. Ericson, "Confined photo-release of nitric oxide with simultaneous two-photon fluorescence tracking in a cellular system," *Scientific Reports*, vol. 8, no. 1, p. 9753, 2018.
- [82] K. Berg, P. K. Selbo, A. Weyergang et al., "Porphyrin-related photosensitizers for cancer imaging and therapeutic applications," *Journal of Microscopy*, vol. 218, no. 2, pp. 133–147, 2005.
- [83] I. Di Bari, A. Fraix, R. Picciotto et al., "Supramolecular activation of the photodynamic properties of porphyrinoid photosensitizers by calix [4] arene nanoassemblies," *RSC Advances*, vol. 6, no. 107, p. 105573–105577, 2016.
- [84] C. M. Moore, D. Pendse, and M. Emberton, "Photodynamic therapy for prostate cancer—a review of current status and future promise," *Nature Clinical Practice. Urology*, vol. 6, no. 1, pp. 18–30, 2009.
- [85] P. Huang, J. Lin, X. Wang et al., "Light-triggered theranostics based on photosensitizer-conjugated carbon dots for simultaneous enhanced-fluorescence imaging and photodynamic therapy," *Advanced Materials*, vol. 24, no. 37, pp. 5104–5110, 2012.
- [86] S. Beack, W. H. Kong, H. S. Jung et al., "Photodynamic therapy of melanoma skin cancer using carbon dot - chlorin e6 - hyaluronate conjugate," *Acta Biomaterialia*, vol. 26, pp. 295–305, 2015.
- [87] Y. Li, X. Zheng, X. Zhang et al., "Porphyrin-based carbon dots for photodynamic therapy of hepatoma," *Advanced Healthcare Materials*, vol. 6, no. 1, p. 1600924, 2017.
- [88] S. Sun, L. Zhang, K. Jiang, A. Wu, and H. Lin, "Toward high-efficient red emissive carbon dots: facile preparation, unique properties, and applications as multifunctional theranostic agents," *Chemistry of Materials*, vol. 28, no. 23, pp. 8659–8668, 2016.
- [89] B. Geng, D. Yang, D. Pan et al., "NIR-responsive carbon dots for efficient photothermal cancer therapy at low power densities," *Carbon*, vol. 134, pp. 153–162, 2018.
- [90] M. Zheng, Y. Li, S. Liu, W. Wang, Z. Xie, and X. Jing, "One-pot to synthesize multifunctional carbon dots for near infrared fluorescence imaging and photothermal cancer therapy," *ACS Applied Materials & Interfaces*, vol. 8, no. 36, pp. 23533–23541, 2016.
- [91] J. Ge, Q. Jia, W. Liu et al., "Carbon dots with intrinsic theranostic properties for bioimaging, red-light-triggered photodynamic/photothermal simultaneous therapy in vitro and in vivo," *Advanced Healthcare Materials*, vol. 5, no. 6, pp. 665–675, 2016.
- [92] M. Lan, S. Zhao, Z. Zhang et al., "Two-photon-excited near-infrared emissive carbon dots as multifunctional agents for fluorescence imaging and photothermal therapy," *Nano Research*, vol. 10, no. 9, pp. 3113–3123, 2017.
- [93] J. T. Margraf, F. Lodermeier, V. Strauß et al., "Using carbon nanodots as inexpensive and environmentally friendly sensitizers in mesoscopic solar cells," *Nanoscale Horizons*, vol. 1, no. 3, pp. 220–226, 2016.
- [94] T. G. Chatzimitakos and C. D. Stalikas, "Carbon nanodots from natural (re) sources: a new perspective on analytical chemistry," in *Handbook of Nanomaterials in Analytical Chemistry*, pp. 3–28, Elsevier, 2020.
- [95] A. Marinovic, L. S. Kiat, S. Dunn, M. M. Titirici, and J. Briscoe, "Carbon-nanodot solar cells from renewable precursors," *ChemSusChem*, vol. 10, no. 5, pp. 1004–1013, 2017.
- [96] Y. Gao, W. Xu, F. He et al., "Carbon nanodots enhanced performance of Cs_{0.15}FA_{0.85}PbI₃ perovskite solar cells," *Nano Research*, vol. 14, no. 7, pp. 2294–2300, 2021.
- [97] Y. Wang, C. Xie, X. Yao et al., "Improved comprehensive performance of CsPbI₂Br perovskite solar cells by modifying the photoactive layers with carbon nanodots," *Journal of Materials*, vol. 8, no. 2, pp. 358–365, 2021.
- [98] S. Riaz and S. J. Park, "Carbon quantum dots-embedded graphitic carbon nitride nanotubes for enhancing the power conversion efficiency of sensitized solar cells," *Materials Today Chemistry*, vol. 24, article 100763, 2022.
- [99] J. Liu, S. Zhao, C. Li et al., "Carbon nanodot surface modifications initiate highly efficient, stable catalysts for both oxygen evolution and reduction reactions," *Advanced Energy Materials*, vol. 6, no. 9, p. 1502039, 2016.
- [100] P. Suvarnapaet, W. Pinyo, S. Pechprasarn, and N. Albutt, "Fluorescence detection of hydrazine hydrate using carbon nanodots synthesized from mandarin rind," in *Applied Mechanics and Materials*, vol. 891, pp. 71–77, Trans Tech Publications Ltd., 2019.
- [101] L. Sai, S. Liu, X. Qian, Y. Yu, and X. Xu, "Nontoxic fluorescent carbon nanodot serving as a light conversion material in plant for UV light utilization," *Colloids and Surfaces B: Biointerfaces*, vol. 169, pp. 422–428, 2018.

- [102] Y. Wang and A. Hu, "Carbon quantum dots: synthesis, properties and applications," *Journal of Materials Chemistry C*, vol. 2, no. 34, pp. 6921–6939, 2014.
- [103] H. Huang, Y. Liu, and Z. Kang, "Carbon nanodot composites: fabrication, properties, and environmental and energy applications," *Novel Carbon Materials and Composites: Synthesis, Properties and Applications*, pp. 223–273, 2019.
- [104] F. Wang, Z. Xie, H. Zhang, C. Liu, and Y. Zhang, "Highly luminescent organosilane-functionalized carbon dots," *Advanced Functional Materials*, vol. 21, no. 6, pp. 1027–1031, 2011.
- [105] H. Huang, C. Li, S. Zhu et al., "Histidine-derived nontoxic nitrogen-doped carbon dots for sensing and bioimaging applications," *Langmuir*, vol. 30, no. 45, pp. 13542–13548, 2014.
- [106] L. N. Dinh, L. N. Ramana, R. P. Kuchel, V. Agarwal, and P. B. Zetterlund, "Miniemulsion polymerization using carboxylated graphene quantum dots as surfactants: effects of monomer and initiator type," *Polymer Chemistry*, vol. 11, no. 36, pp. 5790–5799, 2020.
- [107] X. Zhai, J. Gao, X. Wang et al., "Inverse Pickering emulsions stabilized by carbon quantum dots: influencing factors and their application as templates," *Chemical Engineering Journal*, vol. 345, pp. 209–220, 2018.
- [108] T. Zhou, Z. Huang, F. Wan, and Y. Sun, "Carbon quantum dots-stabilized Pickering emulsion to prepare NIR light-responsive PLGA drug delivery system," *Materials Today Communications*, vol. 23, article 100951, 2020.
- [109] L. N. Dinh, L. N. Ramana, V. Agarwal, and P. B. Zetterlund, "Miniemulsion polymerization of styrene using carboxylated graphene quantum dots as surfactant," *Polymer Chemistry*, vol. 11, no. 18, pp. 3217–3224, 2020.
- [110] J. Chen, C. Zhu, Z. Yang, P. Wang, Y. Yue, and T. Kitaoka, "Thermally tunable Pickering emulsions stabilized by carbon-dot-incorporated core-shell nanospheres with fluorescence "on-off" behavior," *Langmuir*, vol. 34, no. 1, pp. 273–283, 2018.

Research Article

Investigation of TiO₂ Nanoparticles Using Leaf Extracts of *Lippia adoensis* (Kusaayee) for Antibacterial Activity

Lamessa Gudata ¹, Abel Saka ¹, Jule Leta Tesfaye ^{1,2}, R. Shanmugam ³,
L. Priyanka Dwarampudi,⁴ N. Nagaprasad ⁵, B. Stalin ⁶, and Ramaswamy Krishnaraj ^{2,7}

¹Department of Physics, College of Natural and Computational Science, Dambi Dollo University, Ethiopia

²Centre for Excellence-Indigenous Knowledge, Innovative Technology Transfer and Entrepreneurship,
Dambi Dollo University, Ethiopia

³TIFAC CORE HD, Department of Pharmacognosy, JSS Academy of Higher Education and Research, JSS College of Pharmacy Ooty,
Tamilnadu, India

⁴Department of Pharmacognosy, JSS Academy of Higher Education and Research, JSS College of Pharmacy Ooty, Tamilnadu, India

⁵Department of Mechanical Engineering, ULTRA College of Engineering and Technology, Madurai, 625 104 Tamilnadu, India

⁶Department of Mechanical Engineering, Anna University, Regional Campus Madurai, Madurai, 625 019 Tamilnadu, India

⁷Department of Mechanical Engineering, College of Engineering and Technology, Dambi Dollo University, Ethiopia

Correspondence should be addressed to Lamessa Gudata; lamessagudata21@gmail.com
and Ramaswamy Krishnaraj; prof.dr.krishnaraj@dadu.edu.et

Received 8 November 2021; Revised 17 December 2021; Accepted 7 April 2022; Published 30 April 2022

Academic Editor: Arpita Roy

Copyright © 2022 Lamessa Gudata et al. This is an open access article distributed under the Creative Commons Attribution License, which permits unrestricted use, distribution, and reproduction in any medium, provided the original work is properly cited.

Titanium dioxide (TiO₂) nanoparticles with the application of pharmaceutical shrub extract are a hopeful unconventional to the old chemical technique. The investigation is intended to synthesis TiO₂ NPs in biological approach from homegrown plant Kusaayee *Lippia adoensis* leaf extraction which is widespread therapeutic plant and sophisticated in home parks of Ethiopia, in Oromia region in Dambi Dollo town. The bioprepared TiO₂ nanoparticles written off as by using X-ray diffraction (XRD), scanning electron microscopy (SEM), and infrared visible spectrum (UV-Vis) as well as photoluminescence (PL). In addition, this investigation is assessed the antibacterial activities of the prepared TiO₂ nanoparticles in illogicality of medical plus standard anxieties *Escherichia coli*, *Klebsiellae pneumonia*, *Staphylococcus aureus*, and *Enterococcus faecalis* through the disc dispersal technique. Furthermore of this work, TiO₂ nanoparticles prepared using *Lippia adoensis* leaf extraction revealed hopeful result in contradiction of in cooperation Gram-positive (G+) and Gram-Negative (G-) bacterial anxieties by means of extreme reserve area of 14 nm and 12 nm, respectively, using uncalcinated system of the prepared TiO₂ nanoparticles.

1. Introduction

Nanotechnologies have been getting in consideration in the development of today's technology because there is a large surface to volume compared to their masses which balances a peculiar nature of ratio that paradigms themselves as more appropriate contestants in application concerned with performances. The new behavior of nanoparticles is broadly organized for different applications in medicals, cosmetics, biomedical device, ecofriendly remediation, optoelectronics, photo catalysis, energy sources, agroindustry, automobiles, packing, and information technology (IT) [1].

Amongst the existing huge amount of particle metallic oxides, nanoparticles deliberated to more hopeful with their different characteristics, in the deposition process of nanoparticles, using poisonous chemicals for discount and as covering agents indications to numerous side-effects and poisonousness. As a consequence, the deposition of metal-oxide nanoparticles via plant leaf extractions has reputation. The biological method is ecofriendly and contains developed rejoinder rate associated with conservative chemicals. Shrub extracts involve numerous active biomolecules that assist in the decrease and permanence of nanoparticles [2]. Titanium dioxide (TiO₂) is ahead attention by investigators in the

latest past due to its exclusive characteristics and plentiful uses [3]. Grounded on the preceding literature reports, titanium dioxide nanoparticles have equipped from different plant extracts such as *Azadirachta indica* [4], *Passiflora caerulea* [5], aloe vera [6], *Vitex trifolia* [7] *Trifolium pretense* [8], *Bauhinia tomentosa* [9], *Cinnamomum verum* [10], *Camellia sinensis* [11], *Artocarpus gomezianus* [12], *Duranta erecta* [13], and *Moringa oleifera* [14, 15], and their antimicrobial happenings were stated.

In current work, *Lippia adoensis* (Kusaayee) leaf extracts deliberated for the preparation of nanoparticles is the head to ever report on the shrub being operated for green deposition of nanoparticles. *Lippia* classes are widespread therapeutic plant to Ethiopia, Oromia region, in Dambi Dollo Town. The leaves of *Lippia adoensis* are used in Ethiopia conventional medicine for treatment of numerous skin illnesses containing eczema as well as superficial fungus infection [16]. Moreover, the antibacterial activity outline of *Lippia adoensis* in contradiction of bacterial anxieties was studied, and the end outcome shows that Gram-positive (G+) bacteria (*Staphylococcus aureus*) were revealed to be more vulnerable than Gram-negative (G-) bacteria (*E. coli*, salmonella, typhi, and *P. aeruginosa*) [17]. Consequently, this work intended to see the sights the use of *Lippia adoensis* leaf extraction as a covering and dropping agent for photosynthesis of titanium nanoparticles uses in addition to its numerous cultural applications and estimate the antibacterial activities of the equipped TiO_2 NPs in contradiction of pathogenic organisms using the agar disc diffusion technique. Likewise, this work gives an initiation for supplementary investigations on numerous of Ethiopian's homegrown floras for nanomaterial production used in numerous applications.

2. Resources and Methodologies

Assemblage in addition grounding of shrub substantial, calm new leaves of *Lippia adoensis* "Kusaayee" was systematically washed by deionized water to eliminate powders' constituent part and dehydrated kept in sun to eradicate the remaining wetness. Dehydrated leaves were grinded into gunpowder and filtered by using 140 micrometer (μm) size filters. An aqueous extracts of samples organized by sweltering 10 grams of well grinded leaves within 150 milliliters of deionized water at 90°C for 120 min while moving using a magnetized stirrer at 900 rpm. The extraction was then air-conditioned at room temperature (37°C) and clarified using Whatman No. 1 filter paper and stored in refrigerator adjusted temperature of 5°C for further applications [18]. Figure 1 depicts the (*Lippia adoensis*) Kusaayee plant originally taken from Dambi Dollo Town, Kellem Wollega, Oromia region, Ethiopia.

2.1. Synthesization of Titanium Dioxide Nanoparticles from Leaf of *Lippia adoensis* (Kusaayee). Biosynthesis of titanium oxide TiO_2 nanoparticles. 1:1 (50 milliliter *Lippia adoensis* extracts and 50 milliliters of 0.2 Molar titanium isopropoxide), 6:4 (60 milliliter *Lippia adoensis* leaf extraction and 40 milliliters of 0.2 molar titanium acetate), and 18:2 (70 milliliters *Lippia adoensis* leaf extract and 10 milliliters of 0.2 molarity titanium isopropoxide) ratios were added with 60 milliliters, 50 milliliters, and 20 milliliters of 0.3 molar NaOH, corre-



FIGURE 1: (*Lippia adoensis*) Kusaayee plant originally taken from Dambi Dollo Town, Kellem Wollega, Oromia region, Ethiopia.

spondingly. Green synthesis procedures of titanium oxide (TiO_2) nanoparticle deposition from leaf extract are shown in Figure 2.

Ongoing four of mixtures were then stirred constantly for 1 hr using magnetic stirrer at 600 rpm that bring about in yellow color precipitous establishment. Then, the solution filtered by glass filter and pounded frequently in doubled distilled water shadowed in ethanol in order to eliminate the layers and oven dehydrated at 200°C for 90 minutes. The gained dried light yellow colored powders were pounded by mortar and pestle. Finally, after leading thermal constancy of the bioprepared nanoparticles, the pounded yellow powders were heated at 500°C for 2 hr and fine crushed prepared for further analysis [19].

Crystal-like structure and average crystal magnitude of the synthesized TiO_2 nanoparticles were analyzed using an X-ray diffractometer (XRD, 700, Shimadzu Co.) well-appointed with a Cu goal for producing a CuK_α radiation with $\lambda = 1.54056 \text{ \AA}$. X-ray diffraction spectra were recognized from 10° to 80° with 2θ using CuK_α radiation organized at 40 kV and 30 mA. The crystal sizes of the prepared samples are calculated by Scherrer's equation

$$D = \frac{0.94\lambda}{\beta \cos \theta}, \quad (1)$$

where D is the crystallite size (nm), $K = 0.9$ is the Scherrer constant, $\lambda = 0.15406 \text{ nm}$ is the wave length of the X-ray sources, $\beta = \text{FWHM}$ is the radians, and $\theta = \text{peak position}$ is the radians.

In order to examine superficial morphology with configuration, bioprepared TiO_2 nanoparticles were analyzed by field emanation scanning electron microscopy (SEM). Moreover, to characterization the shape, particle size (D), and crystallinity at quickening voltage 200 kV, the fascination spectral of bioprepared TiO_2 nanoparticles were documented by using UV-V is spectroscopy prepared with diffusive reflectance affection for precipitate samples in between a wave length scan of 200 and 800 nanometer. The optical characteristics of bioprepared TiO_2 nanoparticles were also analyzed using photoluminescence spectrophotometer.

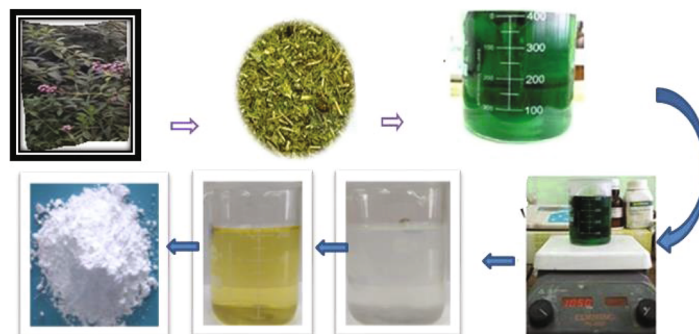


FIGURE 2: Green synthesis procedures of titanium oxide (TiO_2) nanoparticle deposition from leaf extract.

3. Outcomes and Discussions

Figure 3 indicates the characteristics of X-ray diffraction configuration of TiO_2 nanoparticles prepared using titanium isopropoxide and *Lippia adoensis* leaf extraction using titanium isopropoxide and *Lippia adoensis* (Kusaayee) leaf extraction of different concentration varied as 10 ml, 15 ml, 20 ml, and 25 ml. The construction of bioprepared TiO_2 nanoparticles was also definite in X-ray diffraction extents. The deflection peaks performed at 2θ which is agreed with the beforehand reported [20, 21]. All the diffraction peaks were appropriately allocated, and their appearance peaks for pure TiO_2 were perceived in the X-ray diffraction configurations checking the realization of TiO_2 nanoparticles prepared by using *Lippia adoensis* (Kusaayee) leaf extraction titanium dioxide. Then, X-ray diffraction analysis revealed all the deflection peaks fitting with hexagonal wurtzite structures of titanium dioxide nanoparticles [22, 23].

The average crystalline size of the bioprepared TiO_2 nanoparticles was calculated from the three important peaks using Debye Scherer's formula, as discussed in Table 1. The observed average crystalline size of bioprepared TiO_2 nanoparticles has declined when the concentration of the *Lippia adoensis* (Kusaayee) leaf extraction TiO_2 nanoparticles increased. This is because of the larger amount of the *Lippia adoensis* (Kusaayee) leaf extraction TiO_2 nanoparticles used during the deposition procedures shows effectively covering and constancy the equipped nanoparticles and delayed from combination. Table 1 explains that the average crystalline size of TiO_2 nanoparticles prepared at 25 ml and 20 ml is less than that of 10 ml and 15 ml. This may be because of the high concentrations of biomolecules from *Lippia adoensis* (Kusaayee) leaf extract TiO_2 nanoparticles that endure in the nanoparticles that could extremely steady the nanoparticles by covering and delays more crystal development. The crystal size was calculated from using XRD data, and the average crystal size was 46.63 nm.

As the constraints volume increases, the particle size decreases from 92.59 to 15.9. These results are explained in Table 1 below.

3.1. Scanning Electron Microscopy. Surface morphology of prepared nanoparticle was analyzed by scanning electron microscope (SEM) characterization. Superficial morphology of prepared TiO_2 nanoparticles was explained by using scanning electron microscope (SEM), and results are reputed as

Figure 4. Figure 4(a) shows the scanning electron microscope (SEM) micrograph of TiO_2 nanoparticles deposited at concentration 10 ml capacity of reactants. An observed image shows hexagonal wurtzite in which the particles are occurred to be dense composed in small pieces of particle growth, because of the existence of lower concentration that stabilizes the nanoparticles [24]. In another ways, as the concentration of precursor increased, the phases observed were increasingly in grain.

Figures 4(a) and 4(b) show predominantly spherical in shaped even through nanoparticle shape structures were observed. The scanning electron microscopy image of nanoparticles prepared from at higher concentration (d) 25 ml, in which the amount of precursor concentration is much greater than the amount of the other samples looks like nanorod and shaving shapes in accumulated forms. This accumulation may be occurred because of polarization as well as electrostatic attraction of titanium dioxide nanoparticles [22]. As the concentration of the solution increases, the particle size increases; this result is agreed with X-ray diffraction analysis result; again, this revealed that they theoretically and experimentally agreed with the previously reported [23].

3.2. Optical Behavior Analysis. The optical behavior of prepared nanoparticles from *Lippia adoensis* (Kusaayee) leaf extraction was analyzed by using both UV-Vis and photoluminescence spectrum. UV-Vis spectrum of titanium dioxide nanoparticles prepared from *Lippia adoensis* (Kusaayee) leaf extracts of varied in titanium isopropoxide concentration is depicted in Figure 5.

3.3. Photoluminescence Spectral Analysis. The existence of different concentrations of precursors in *Lippia adoensis* (Kusaayee) reduces titanium ions in the mixtures to titanium dioxide. Leaf extraction acts as sinking agents but also comforting agents as glowing. These results were established by using ultra violet visible spectral characterization in the variety of 200 to 750 nanometers. The continuum at 300 nanometers is specifically identical to TiO_2 nanoparticles. The absorbance peak is gained between 200 and 800 nanometers of wavelength [24]. Graph (a) shows more peak captivation in the green to lower concentrations of precursor solution. The graph in (d) shows the smaller absorption peak. In sample (b), three absorption peaks were observed. Sophisticated fascination peak specifies that sample (a) was

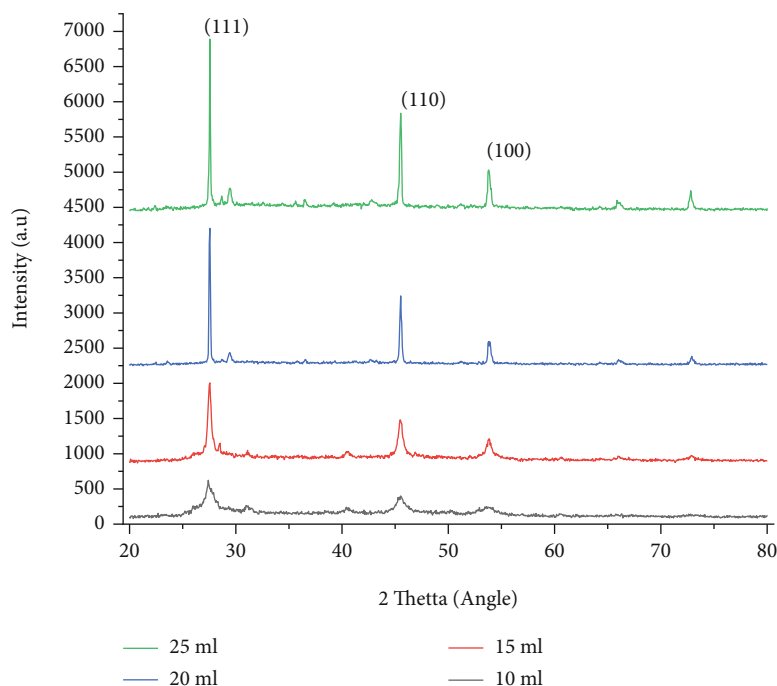


FIGURE 3: XRD patterns of titanium dioxide nanoparticles prepared using titanium isopropoxide and *Lippia adoensis* (Kusaayee) leaf extracts of different concentration (a) 10 ml, (b) 15 ml, (c) 20 ml, and 25 ml.

TABLE 1: Crystal parameters obtained from XRD data.

Sample	Concentration (ml)	2 theta (degree)	FWHM (radian)	D (nm)
1	10	27.56302	0.08834	92.59424
2	15	45.50703	0.18653	46.18404
3	20	53.83391	0.27959	31.86635
4	25	74.17485	0.00636	15.9

initially taken for consideration, and the other three show the increment in peaks as concentration increased. Sample (a) shows more absorbance; because of lower meditation, the sample was considered for supplementary analysis. To explain optical behaviors of prepared TiO_2 nanoparticles, photoluminescence was applied. Wavelength ranges 300 nm-700 nanometers at different concentration, shown in Figure 6.

Photoluminescence (PL) spectral emissions of the prepared were appeared. Maximum PL hardness is mostly because of self surrounded exciton recombination, prepared particle size known as defect centers. Photoluminescence intensity declines instantaneously with precursor concentration. In contrast, the photoluminescence strength for wavelengths of greater concentrations has greater wavelength. The prepared nanoparticles at 25 ml and 20 ml have smaller wave length than nanoparticles deposited at 10 ml and 15 ml. The recognized anatase and rutile patterns are mainly accountable for this action. The anatase pattern of TiO_2 nanoparticle is given to the minor group spectrum perceived from wavelength of 600 nanometer, Figure 4, while the peaks 500-550 nanometers are recognized to the rutile pattern of TiO_2 nanoparticles; this result is agreed with

the previously reported. The maximum peak gained shows that the prepared nanoparticles at higher concentration have good quality [25–27].

3.4. The Application of TiO_2 Nanoparticles for Antibacterial Activities. The antibacterial activities of TiO_2 nanoparticles on Gram-positive (G+) (*Staphylococcus aureus* and *Enterococci faecali*) and Gram-Negative (G-) (*Escherichia coli* and *Klebsiella pneumonia*) bacteria were examined by disc diffusion technique according to steps previously stated [28]. A bacteriological anxiety was developed aerobically in nutrient soup for 20 hr at room temperature so that the characteristics of bacterial interruptions were attained to 2.35×10^8 CFU/ml by contrasting with the 0.6 Mc-Farland standards. Bacterial agar media were preserved on nutrient Muller Hinton agar at room temperature, the antibiotics vancomycin and car penicillin were applied on positive control, and dimethyl sulfoxide in credit was used as the negativity control [29]. The antibacterial activity of TiO_2 nanoparticles in (a) *Escherichia coli*, (b) *Klebsiella pneumonia*, (c) *Staphylococcus aureus*, and (d) *Enterococci faecalis* at various concentrations is illustrated in Figure 7.

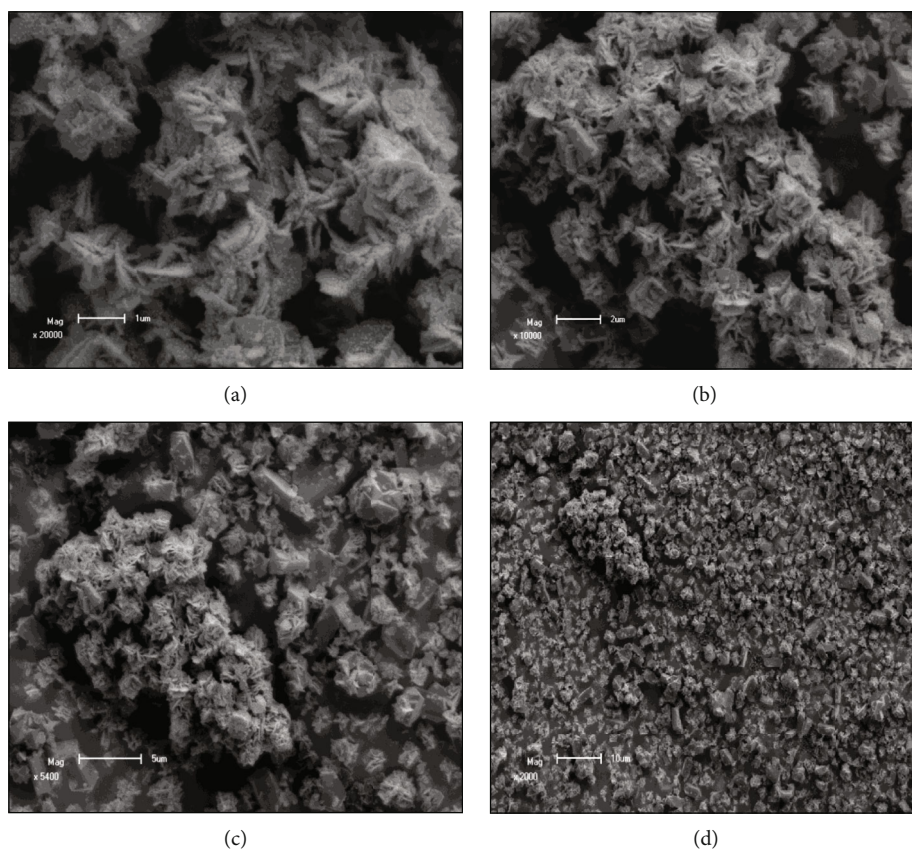


FIGURE 4: Scanning electron microscope (SEM) micrographs of titanium dioxide nanoparticles prepared with *Lippia adoensis* (Kusaayee) leaf extracts of different titanium isopropoxide concentrations as (a) 10 ml, (b) 15 ml, (c) 20 ml, and (d) 25 ml.

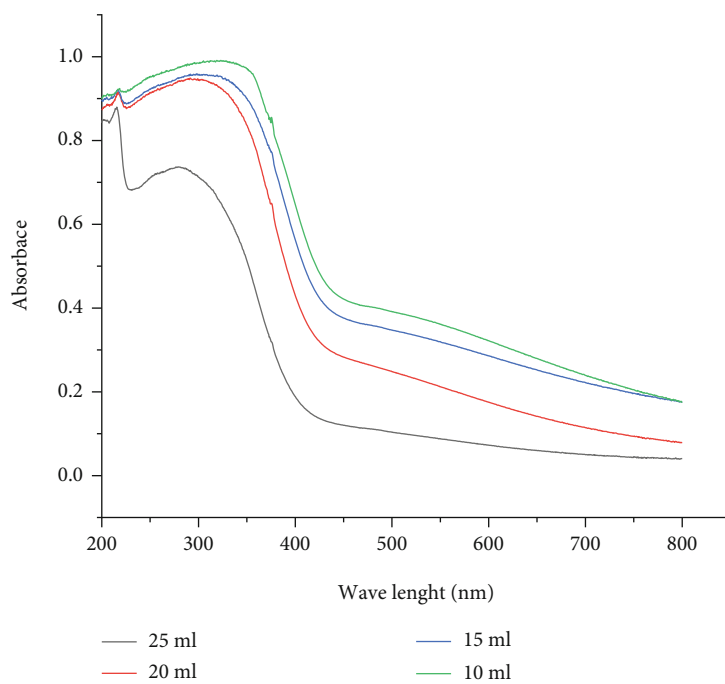


FIGURE 5: UV-Vis spectrum of titanium dioxide nanoparticles prepared from *Lippia adoensis* (Kusaayee) leaf extracts of varied in titanium isopropoxide concentration as (a) 10 ml, (b) 15 ml, (c) 20 ml, and (d) 25 ml.

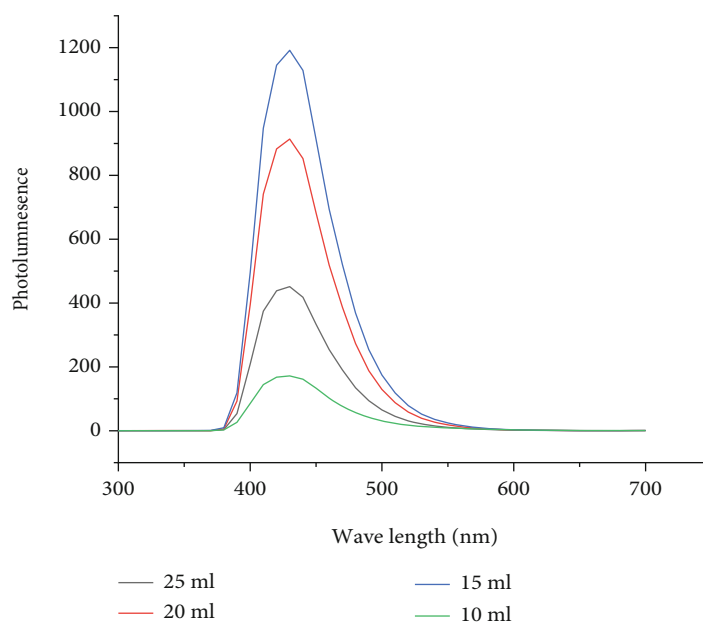


FIGURE 6: Photoluminescence (PL) spectrum of titanium dioxide nanoparticles prepared from *Lippia adoensis* (Kusaayee) leaf extracts of different isopropoxide concentrations (a) 10 ml, (b) 15 ml, (c) 20 ml, and (d) 25 ml.

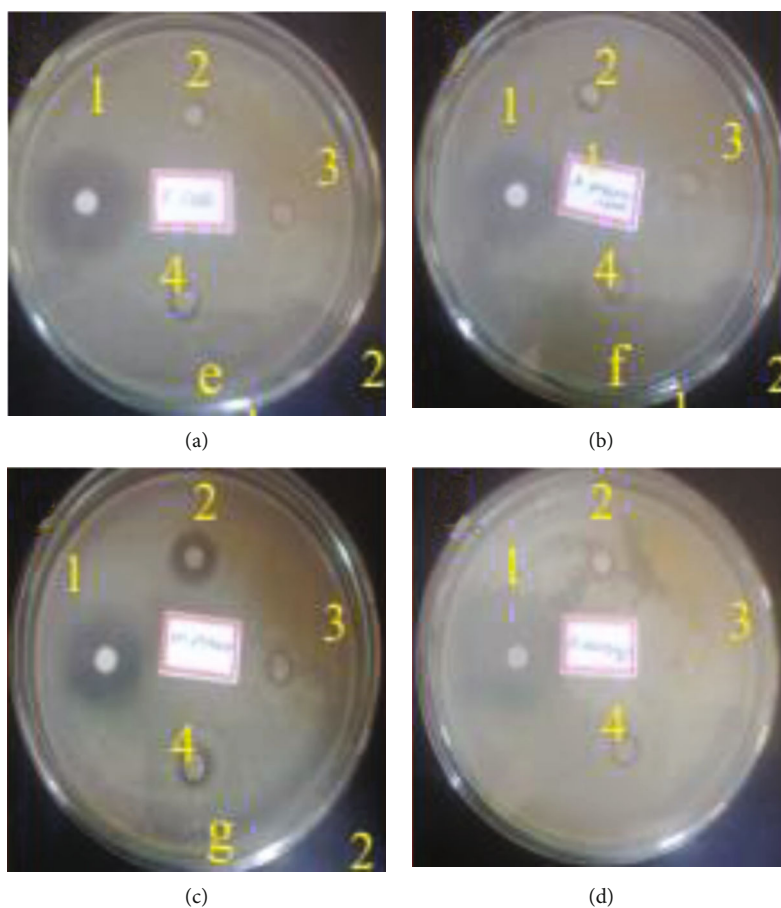


FIGURE 7: The antibacterial activity of TiO_2 nanoparticles in (a) *Escherichia coli*, (b) *Klebsiella pneumonia*, (c) *Staphylococcus aureus*, and (d) *Enterococcus faecalis* at various concentrations.

The dishes were rotated upside down as well as hatched at room temperature for 20 hr in incubator. The dish was stunned moderately to permit similar intercourse of bacteria cells and culture. 80 milliliter dish that housed 2 discs and titanium dioxide nanoparticles lacking unnecessary overlying of areas was used. Bacterial culture disc was separated into three segments: antibiotic disc, TiO₂ nanoparticles prepared, and both antibiotic disc and TiO₂ nanoparticles. Then, 150 mg of TiO₂ nanoparticles was melted in 200 μL of (DMSO) flush to get 2:8 and 2:16 watering factors. From each influences, 200 μL of each concentration soaked with disc (8 diameter disc) remained kept on a dish and incubated at room temperature for 20 hr. Antibacterial events were then calculated with computing diameter (mm) of inhibition area everywhere of the disc in contradiction of trial bacteria with a caliper.

4. Conclusion

The study TiO₂ of nanoparticles was effectively prepared from using leaf extracts of *Lippia adoensis* (Kusaayee) taken from Oromia region, Western Wollega, Kellem, Dambi Dollo town, Ethiopia. The application nanoparticles from leaf extracts of *Lippia adoensis* (Kusaayee) are a hopeful substitute to the conservative chemical technique. The bioprepared TiO₂ nanoparticles considered using X ray diffraction (XRD), scanning electron microscopy (SEM), ultraviolet visible spectrum (UV-Vis), and photoluminescence (PL). Additionally, this study considered the antibacterial activities of the prepared TiO₂ nanoparticles with contradiction of scientific as well as customary anxieties of *Escherichia coli*, *Klebsiella pneumoniae*, *Staphylococcus aureus*, and *Enterococcus faecalis* by the disc diffusion technique. Finally TiO₂ nanoparticles prepared using *Lippia adoensis* (Kusaayee) leaf extraction showed hopeful result in contradiction of Gram-positive (G+) and Gram-negative (G-) bacterial strains with an extreme inhibition area of 14 mm and 12 mm, correspondingly using constant amount of prepared TiO₂ nanoparticles.

Data Availability

The data used to support the findings of this study are included within the article.

Disclosure

This study was performed as a part of the employment of the authors.

Conflicts of Interest

The authors declare that there are no conflicts of interest.

References

- [1] S. Faisal, H. Jan, S. A. Shah et al., "Green synthesis of Zinc oxide (ZnO) Nanoparticles using aqueous fruit extracts of *Myristica fragrans*: their characterizations and biological and environmental applications," *ACS Omega*, vol. 6, no. 14, pp. 9709–9722, 2021.
- [2] A. Jayachandran, T. R. Aswathy, and A. S. Nair, "Green synthesis and characterization of zinc oxide nanoparticles using *Cayratia pedata* leaf extract," *Biochemistry and Biophysics Reports*, vol. 26, p. 100995, 2021.
- [3] R. A. Gonçalves, R. P. Toledo, N. Joshi, and O. M. Berengue, "Green synthesis and applications of ZnO and TiO₂ nanostructures," *Molecules*, vol. 26, no. 8, p. 2236, 2021.
- [4] M. C. Patino-Portela, P. A. Arciniegas-Grijalba, L. P. Mosquera-Sanchez et al., "Effect of method of synthesis on antifungal ability of ZnO Nano particles: chemical route vs green route," *Advances in nano research*, vol. 10, no. 2, pp. 191–210, 2021.
- [5] S. Awan, K. Shahzadi, S. Javad, A. Tariq, A. Ahmad, and S. Ilyas, "A preliminary study of influence of zinc oxide nanoparticles on growth parameters of *Brassica oleracea* var *italica*," *Journal of the Saudi Society of Agricultural Sciences*, vol. 20, no. 1, pp. 18–24, 2021.
- [6] M. S. E. D. Salem, A. Y. Mahfouz, and R. M. Fathy, "The antibacterial and antihemolytic activities assessment of zinc oxide nanoparticles synthesized using plant extracts and gamma irradiation against the uro-pathogenic multidrug resistant *Proteus vulgaris*," *Biometals*, vol. 34, no. 1, pp. 175–196, 2021.
- [7] R. Hamouda and M. Elshamy, *Using Bioprepared Titanium Oxide Nano Particles to Alleviate the Toxicity on Banana Parasitic-Nematode*, 2021.
- [8] M. Raafat, A. S. El-Sayed, and M. T. El-Sayed, "Biosynthesis and anti-mycotoxigenic activity of *Zingiber officinale* roscoederived metal nanoparticles," *Molecules*, vol. 26, no. 8, p. 2290, 2021.
- [9] A. Naseer, A. Ali, S. Ali et al., "Biogenic and eco-benign synthesis of platinum Nano particles (Pt NPs) using plants aqueous extracts and biological derivatives: environmental, biological and catalytic applications," *Journal of Materials Research and Technology*, vol. 9, no. 4, pp. 9093–9107, 2021.
- [10] M. Asemani and N. Anarjan, "Green synthesis of copper oxide nanoparticles using *Juglans regia* leaf extract and assessment of their physico-chemical and biological properties," *Green Processing and Synthesis*, vol. 8, no. 1, pp. 557–567, 2019.
- [11] S. Ahmad, S. Munir, N. Zeb et al., "Green nanotechnology: a review on green synthesis of silver nanoparticles — an ecofriendly approach," *International Journal of Nanomedicine*, vol. Volume 14, pp. 5087–5107, 2019.
- [12] R. Abbasian and H. Jafarizadeh-Malmiri, "Green approach in gold, silver and selenium nanoparticles using coffee bean extract," *Open Agriculture*, vol. 5, no. 1, pp. 761–767, 2020.
- [13] S. Sarli, M. R. Kalani, and A. Moradi, "A potent and safer anticancer and antibacterial *Taxus*-Based green Synthesized silver Nanoparticle," *International Journal of Nanomedicine*, vol. Volume 15, pp. 3791–3801, 2020.
- [14] M. S. Jameel, A. A. Aziz, and M. A. Dheyab, "Green synthesis: proposed mechanism and factors influencing the synthesis of platinum nanoparticles," *Green processing and synthesis*, vol. 9, no. 1, pp. 386–398, 2020.
- [15] H. Aslam, *Synthesis and Evaluation of ZnO Nano Particles of *Trigonella Foenum* for their Biological Activities*, Doctoral Dissertation, Capital University, 2020.
- [16] A. Banerjee, A. Sarkar, K. Acharya, and N. Chakraborty, "Nanotechnology: an Emerging Hope in Crop Improvement," *Letters in Applied NanoBioScience*, vol. 10, no. 4, pp. 2784–2803, 2021.

- [17] M. Batool, A. Shafeeq, B. Haider, and N. M. Ahmad, "TiO₂ nanoparticle filler-based mixed-matrix PES/CA Nanofiltration membranes for enhanced desalination," *Membranes*, vol. 11, no. 6, p. 433, 2021.
- [18] Y. S. Khoo, W. J. Lau, Y. Y. Liang, M. Karaman, M. Gürsoy, and A. F. Ismail, "Eco-friendly surface modification approach to develop thin film nanocomposite membrane with improved desalination and antifouling properties," *Journal of Advanced Research*, vol. 36, pp. 39–49, 2022.
- [19] B. Shrestha, M. Ezazi, and G. Kwon, "Engineered Nanoparticles with decoupled photocatalysis and wettability for membrane-based desalination and separation of oil-saline water mixtures," *Nanomaterials*, vol. 11, no. 6, p. 1397, 2021.
- [20] G. Ma, Z. Almansoori, B. Khorshidi, and M. Sadrzadeh, "Development of antifouling thin film nanocomposite polyamide membrane using ITO nano particles," *Journal of Material Sciences & Engineering*, vol. 10, no. 5, 2021.
- [21] A. Ghaffar, S. Kiran, M. A. Rafique et al., "Citrus paradisi fruit peel extract mediated green synthesis of copper nanoparticles for remediation of disperse yellow 125 dye," *Desalination and Water Treatment*, vol. 212, pp. 368–375, 2021.
- [22] O. N. Borisova, I. G. Doronkina, and V. M. Feoktistova, "Resource-saving nanotechnologies in waste water treatment," *Nanotechnologies in Construction*, vol. 13, no. 2, pp. 124–130, 2021.
- [23] D. A. Tatarinov, S. R. Sokolnikova, and N. A. Myslitskaya, "Applying of chitosan-TiO₂ nanocomposites for photocatalytic degradation of anthracene and pyrene," *Journal of Biomedical Photonics & Engineering*, vol. 7, no. 1, article 010301, 2021.
- [24] A. M. El Shafey, M. K. Abdel-Latif, and H. M. Abd El-Salam, "The facile synthesis of poly(acrylate/acrylamide) titanium dioxide nanocomposite for groundwater ammonia removal," *Desalination and Water Treatment*, vol. 212, pp. 61–70, 2021.
- [25] A. Juliani, S. Rahmawati, and M. Yoneda, "Heavy metal characteristics of wastewater from batik industry in Yogyakarta area, Indonesia," *International journal*, vol. 20, no. 80, pp. 59–67, 2021.
- [26] E. Wibowo, M. Rokhmat, D. Y. Rahman, R. Murniati, and M. Abdullah, "Batik wastewater treatment using TiO₂ nanoparticles coated on the surface of plastic sheet," *Procedia engineering*, vol. 170, pp. 78–83, 2017.
- [27] B. M. P. Pereira and B. P. Backx, "Nanotechnology in Water Treatment: An Optimistic Perspective for the Near Future," *Journal of Nanotechnology and Nanomaterials*, vol. 2, no. 1, 2021.
- [28] A. Saka, J. L. Tesfaye, L. Gudata et al., "Synthesis, characterization, and antibacterial activity of ZnO nanoparticles from fresh leaf extracts of Apocynaceae, *Carissa spinarum* L. (Hagamsa)," *Journal of Nanomaterials*, vol. 2022, 6 pages, 2022.
- [29] D. Chandra Lekha, R. Shanmugam, K. Madhuri et al., "Review on silver nanoparticle synthesis method, antibacterial activity, drug delivery vehicles, and toxicity pathways: recent advances and future aspects," *Journal of Nanomaterials*, vol. 2021, 11 pages, 2021.

Review Article

Bioinspired Advances in Nanomaterials for Sustainable Agriculture

S. Malini ¹, **Kalyan Raj**,¹ **S. Madhumathy**,² **Khalid Mohamed El-Hady**,³ **Saiful Islam**,⁴ and **Mycal Dutta** ⁵

¹Department of Chemistry, B.M.S. College of Engineering, Bangalore, India

²Department of Chemistry, Government College for Women, Kolar, India

³Civil Engineering Department, King Khalid University, Saudi Arabia

⁴Civil Engineering Department, College of Engineering, King Khalid University, Abha, 61421 Asir, Saudi Arabia

⁵Department of Pharmacy, BGC Trust University Bangladesh, Chittagong 4381, Bangladesh

Correspondence should be addressed to S. Malini; malinis.chem@bmsce.ac.in and Mycal Dutta; mycal@bgctub.ac.bd

Received 30 March 2022; Accepted 11 April 2022; Published 29 April 2022

Academic Editor: Hiwa M. Ahmed

Copyright © 2022 S. Malini et al. This is an open access article distributed under the Creative Commons Attribution License, which permits unrestricted use, distribution, and reproduction in any medium, provided the original work is properly cited.

Rising demand for food production and an intensified usage of hazardous substances on the farmland are the driving force behind the emergence of green nanotechnology. Eco-friendly nanomaterials synthesised using plant sources and microorganisms are expected to catalyse a revolution in the agricultural sector by introducing nano-enabled smart sensors for metals along with organic toxins, supplying micronutrients; balancing the plant hormones, soil quality, and moisture content; stimulating plant growth; and minimising the usage of toxic chemicals by nanofertilizers and nanopesticides. As no single nanocompound has proved to be completely sustainable, this review discusses a wide variety of sustainable routes to implement nanomaterials to increase productivity, protect, and monitor crops through innovative nano-aided agricultural practices. Nevertheless, as the progress of research and commercialization in this area is still marginal, an understanding of complex dynamic behaviour, careful evaluation with targeted delivery of these compounds in the environment, and strong governmental regulatory norms are necessary to realize the effectiveness of green nanotechnology for sustainable agriculture. This article outlines some major advancements in recent years related to the implementation of eco-friendly nanomaterials in the agricultural sector. A systematic and comprehensive approach to adopting green nanotechnology would certainly promote a sustainable movement resulting in a beneficial economic and ecological impact.

1. Introduction

The most prevalent problem associated with the agricultural sector worldwide is the management of available natural resources in a sustainable manner. Despite numerous drastic technological innovations and huge capital investments which have successfully increased food production, the prevailing farming practices have a profound negative impact on ecological systems creating an imbalance in the natural cycle. Some of the ills such as depletion of soil productivity [1], soil salinization [2], soil moisture [3], soil organic matter [4], reduction of genetic diversity [5], creation of pesticide-resistant pathogens [6], and seeping of pesticides and fertilizers into groundwater [7] are increasingly being observed

as barriers to sustainability. Many countries have attempted to increase the gross value of production through shifting towards perennial crops and expansion of usage of land. In view of these factors, a set of technologies acting as an engine of growth is becoming crucial to face the food production challenge without harming the environment.

“Green nanotechnology” often refers to the synthesis of nanomaterials by reducing or eliminating the use of harmful chemicals and harsh reaction conditions. The utilization of plants and microorganisms to generate nanomaterials has gained popularity owing to their genetic diversity and variety of plant constituents such as phenols and alkaloids that help metal ions to be reduced to the nanodimension through a concerted step. The shift of agricultural science towards the

use of nanomaterials has revolutionized food production [8] through eco-friendly means of managing natural resources and has opened up new avenues in agriculture. Often referred to as “green nano agro science,” this area of study has a great potential to implement the strong foundations of green chemistry and engineering into real practice of agriculture in an eco-friendly, simplified, cost-effective, scalable, and biocompatible route. This article focuses on some notable trends, such as the use of microorganisms and plant extracts in the development of green nanomaterials, which are globally renowned applications for pesticides. Herbicides, improving soil quality, soil moisture content, and detection of toxic metals and organic moieties for sustainable agricultural production systems, possess the competency of escalating the agro-output that has continued to be an unprecedented challenge for years.

2. Microbial Synthesis

Synthesis and application of biological nanomaterial, using microorganisms, offer a highly scalable, biocompatible route. Originating from biological sources, these eco-friendly microfactories offer a wide variety of bioremediative applications. Several approaches are available for microbial biosynthetic engineering among which bacterial synthesis, fungi, and yeast-assisted routes are the prominent ones as represented in Figure 1. Additionally, microorganisms have an edge over plant sources for nanosynthesis, as nanomaterials prepared using plant extract have a tendency to become polydispersed [9] caused by phytochemicals whose proportions vary with seasons. The shape, surface characteristics, bioavailability, homogeneity of size, and quality of NPs produced by microorganisms may, however, differ considerably from those generated by other methods.

2.1. Bacteria. Bacterial synthesis of nanoparticles has become highly popular due to the ability of bacterial cells to multiply vigorously under various pH, temperatures, and high concentrations of metals. The protein in the bacterial cell membrane functions as either ATPase or as chemo-osmotic or proton antitransporters facilitating the extracellular or intracellular production of nanoparticles. The benefits of probiotic microorganisms have been realized through the negative electrokinetic potential enabling the attraction of cations that often serve as the initial point of the biosynthesis process [10]. The mechanistic understanding of the process has led to many valuable metal nanoparticles such as colloidal silver nanoparticles using *Lactobacillus* [11, 12], gold nanoparticles using *Lactobacillus kimchicus* DCY51T [13, 14], and cadmium sulfide with the aid of poly(hydroxybutyrate) [15]. The environmental compatibility shown by these bacterial strains has shown a great promise and has inspired numerous researchers worldwide to explore other microorganisms for increasing crop production.

2.2. Fungi. The major distinction among bacteria and fungi is that fungi consist of larger proportions of proteins, which enable higher productivity of nanoparticles. Additionally, the use of fungi allows large-scale synthesis and well-defined mor-

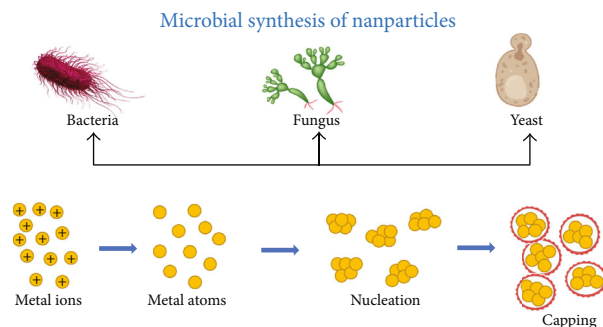


FIGURE 1: Microbial bioproduction approaches to green nanomaterials.

phology, because of the intracellular enzymes that trigger both intracellular and extracellular synthesis. Intracellular synthesis starts with the adhering of heavy metals to the fungal cell wall using proteins that act as enzymes that produce electrostatic interactions that are responsible for the movement of electrons leading to the reduction of metal ions. Recent developments in this regard include fungi that act as reducing and capping agents in the synthesis of gold [16], silver [17], and SnO_2/Pd [18] nanoparticles.

2.3. Yeast. Largely explored recently, these unicellular microorganisms with a wide variety of 1500 species assist the synthesis of nanoparticles with innumerable advantages. Despite the limitation of severe pathogenicity towards humans, fungal species are used to produce nanomaterials on a large scale using different incubating conditions, such as precursor resolutions and response time. The extracellular biosynthesis of AgNPsK and AgNPsU [19] with the aid of yeast strains of *Pichia kudriavzevii*HA-NY2 and *Saccharomyces uvarum*HA-NY3, quantum dots of CdSe using tryptone-enriched media [20], and nano-AgCl [21] using commercial yeast extract are some of the classic examples. A nanomaterial with high stability can be achieved through an optimization of the inherited, genetic, and enzymatic properties of the chosen yeast and its cell growth.

3. Phytosynthesis

Plant mediation for synthesis is often termed “phytocatalysis” and is applied worldwide to the synthesis of nanomaterials. Vegetal constituents such as polyphenolic compounds, nitrogen-containing alkaloids, water-soluble diversified tannic acids, iridoids, highly nutritious secoiridoids, benzopyrone derivatives called coumarins, and isoprenoids together form a complex catalytic system exerting its action through chemical reduction or electrochemical reduction processes to produce nanomaterials. Nano-Ag particles [22] generated using extract of leaves from *Alstonia macrophylla* were found to be highly effective in transforming 4-nitrophenol to 4-aminophenol and p-nitroaniline to p-phenylenediamine. Bello et al. [23] also reported a similar reduction in 4-nitrophenol [23].

Although researched rarely, the gold nanoparticles find usefulness in catalysing the reduction of 4-nitrophenol

TABLE 1: Examples of plant-based nanoparticles, morphology, and applications.

Prepared nanometal	Extracted from plant	Size	Shape	Application	Ref
Silver	<i>Alstonia macrophylla</i>	70 nm	Spherical	Reduction of 4-nitrophenol and p-nitroaniline	[22]
Silver	<i>Guiera senegalensis</i>	50 nm	Spherical		[23]
Gold	<i>Artemisia dracunculus</i>	91 nm	Hexagonal and triangular	Reduce 4-nitrophenol	[24]
Palladium	Chitosan-tannin	6.01 nm	Spherical	Degradation of Congo red	[25]
Iron	<i>Lagerstroemia speciosa</i>	50–100 nm	Spherical	Degradation of methylene blue	[26]
Copper	<i>Plantago asiatica</i>	7–35 nm	Spherical	Cyanation of aldehydes	[27]
Ag/Au	<i>Silybum marianum</i>	40 nm	Spherical	Reduction of 4-nitrophenol	[28]
Ag/Fe	Palm date fruit extract	5–40 nm	Disks	Degradation of bromothymol blue	[29]

[24]. A comparatively widely used Pd nano [25] and popularly studied Fe nano [26] produced through plant extract used to degrade environmentally harmful dyes prove the unparalleled catalytic activity of plant extracts. The use of transition metals has been endorsed with Cu nanoparticles produced by the extract of *Plantago asiatica* [27] in a short time of 30–60 min. These particles within the range of 7–35 nm successfully completed cyanation of aldehydes with over 85% yield. Besides these metals, bimetallic nanoparticles have also been described such as Ag/Au [28] nanoparticles produced using seed extract from *Silybum marianum* which plays the role of a reducing and stabilizing agent. Ag/FeNP disks [29] with dimensions 5–40 nm were produced by palm date fruit extract which could degrade bromothymol blue dye via a Ag/FeNP/H₂O₂ catalytic system.

Numerous mono- and bimetallic nanoparticles are studied and reported with a focus on synthetic methodologies, characterisation, and novel applications, among which a few are listed in Table 1.

4. Why Green Nanotechnology for Agriculture?

With the increasing dependency on insecticides and pesticides and the concurrent awareness of exposure to these chemicals at small levels impacting the environment, there is a burning need for agrotechnology to shift towards greener technological systems to be implemented on farms. Implementation of nanotechnology in agriculture after rendering remarkable contributions is now a proven solution to move towards sustainability. However, many processes involved in the synthesis of nanosynthesis and application involve high temperatures [30], pressures [31], acidification [32], and toxic metals [33].

Hence, the last two decades have witnessed a tremendous change over in the approach to nanosynthesis from traditional methods to plant-based protocols due to many advantages such as sustainable pathway, diversified plant metabolites, advanced extraction and separation strategies, development of exhaustive phytoconstituent database, and instrumental aid extended by high-performance liquid chromatography-mass spectrometry, high-performance liquid chromatography-nuclear magnetic resonance, high-performance liquid chromatography-mass spectrometry,

and centrifugal partition chromatography. Highly efficient extraction methods such as chemogenomics, metabolomics, coupled with ultrasound, enzymes, hydrodistillation, and supercritical fluid extraction have led to the preparation of customized extracts that were not feasible with traditional methods [34]. On the other hand, nanotechnology can be used in conjunction with these advancements to successfully achieve a sustainable agricultural system, and a large emphasis is therefore laid on plant-based nanotechnology formulations which have a great potential to solve major problems of farming.

5. Agro Applications of Bio-Based Nanomaterials

A group of agricultural practices, often referred to as farming, represents an open system with an easy exchange of energy and matter. With abundant public funding and considerable momentum, the agricultural sector has been considered an umbrella for nation development for decades. However, with the fast development of technology, the intervention of agrochemical agents and the lack of control over the input of toxic chemicals have become unavoidable.

With the advent and development of nanomaterials, precision farming has gained high popularity and is viewed as a remedial measure to many problems in farming. Combating insecticide resistance, soil moisture balancing, nanoparticle-mediated gene or DNA transfer in plants, food processing, increasing shelf life, treating agricultural waste, reducing spraying of pesticides, plant breeding, and food packing are some of the areas where nanomaterials are expected to play a vital role. The possibility of generating these nanomaterials by a greener route has added an impetus to transforming farming practices. When these agents are produced using eco-friendly and green methods, they would help the agricultural community avoid harmful chemicals and thereby help evolve a healthy environment.

5.1. Fertilizers. The primary function of fertilizers is to maintain a balance in the mineral content to raise the yield. The excessive use of these mineral fertilizers may cause serious problems for soil fertility. Nanofertilizer formulations synthesised by green methods are found to supply a balanced

supply of essential minerals with minimum intervention and also impart pest protection efficiency. Various categories of nanomaterials widely used to design fertilizers, as depicted in Figure 2, are recently reviewed by Guo et al. [35] with a comprehensive evaluation of their importance and limitation in agricultural practices.

Among the various important metals, zinc is one of the main micronutrients widely studied as leaching of Zn is posing a serious threat to crop yield since the past two decades. ZnO nanoparticles [36] at three different concentrations of 40, 80, and 120 ppm on wheat farms in the harvest stage have benefited the height of the plant and the weight of the seed, which was much higher than that obtained using traditional chemical zinc in the form of zinc nitrate. Alternatively, such physiological and morphological changes can also be affected by copper oxide loaded onto chitosan/alginate nanoparticles [37]. This leads to a spherically shaped 300 nm shell which encapsulates CuO and slowly releases Cu which is very essential for seedling growth. The polymeric-like shell has good adhesive properties and hence forms a protective layer against the loss of nutrients, preventing premature degradation. The germination evaluation results on *Fortunella margarita Swingle* seeds showed a clear synergic effect on epigeal and hypogeal parts. The Zn and Cu [38] nanoparticles in combination effectively influenced the morphological parameters that intensely affected the biochemical traits of the basil plant and exerted antioxidant activity. The nanoparticles of Zn and Cu which originated from the basil extract are said to be formed by reducing agents such as vitamin C, sucrose, flavonoids, or oxalic acid. The study promotes the quantity and quality of basil with the dual benefit of reducing fertilizer consumption and toxicity.

While plants are constantly challenged by fluctuating environmental metal ion concentrations and researchers worldwide are striving to strike upon the right proportion of the N-P-K ratio, the quantities of some major metals such as Ca, Mg, and S are highly crucial. A promising strategy for optimal nutrient management has recently been reported through K- and N-doped amorphous calcium phosphate [39]. Nitrogen incorporated through urea and nitrate by modulating reaction conditions facilitates a slow release owing to the two different chemical forms. The chemical state of the metal plays a vital role as it decides the absorption kinetics that determines the ease with which the roots absorb it. Therefore, a suitable platform that can supply the metal in an appropriate oxidation state becomes highly important. The nano-sized surface layers of zeolites have the property of slowly releasing metals which are used to deliver Fe^{3+} ions through the zeolite/ Fe_2O_3 nanocomposite [40], which has potential for commercialization. A slow consistent release of Fe nanoparticles was confirmed, though the specific efficiency towards various crops needs to be determined.

5.2. Nanopesticides. The use of nanopesticides synthesised by a green route is a well-recognised area. Pesticides in the nano form are becoming a prominent part of agriculture due to their ability to solve many problems pertaining to pesticide toxicity. Nanopesticides can contain either the effective ingredient in nanosize or the ingredient being doped with

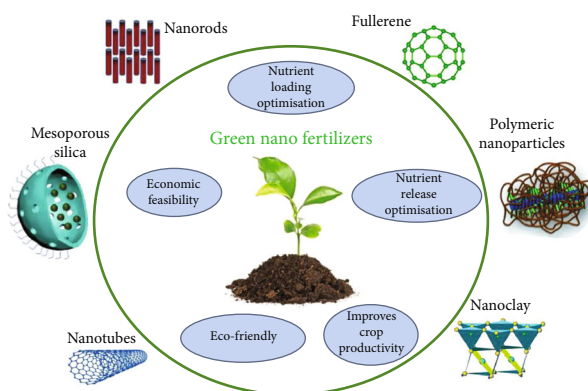


FIGURE 2: Different types of nanostructured materials in practical agricultural practice.

the nanomaterial, which improves the dispersibility, biological compatibility, performance, shelf life, functionality, and agricultural cost of pesticides and hence is considered to be a better alternative to the traditional pesticides. Nisha Raj et al. [41] have recently reviewed and elaborated on the various aspects of nanoagrochemicals such as nanoencapsulation, methodologies involved in the synthesis, enhancement of productivity in agriculture, influence on horticulture, and contribution to crop conservation. One of the promising applications of this technology is the regulated and controlled release of pesticide chemicals which greatly reduce waste pollution.

Graphene oxide is intelligently used as a nanocarrier for revolutionizing the application of pyrethroid pesticide [42] against spider mite which is a phytophagous mite pest. The newly designed GO-pesticide nanocomposite is found to exhibit a good loading capacity and has an excellent release behaviour both indoor and field. A uniform dispersion and effective adsorption on the cuticle of spider mites and bean plant leaves demonstrate its efficiency and prospects for practical applications.

Similar satisfactory results are also observed against microbial pests *Acidovorax oryzae* along with *Rhizoctonia solani* [43] for enhanced rice production by chitosan-magnesium nanocomposite and a simple chitosan nanocomposite against *Spodoptera litura* [44] in the larval phase. The former nanocomposition, a native *Bacillus* sp. strain RNT3, was utilized to prepare spherically shaped nanocomposite in the range 29 to 60 nm which could destroy the cellular organelles of the pathogen. Such biologically synthesised nanocomposites not only contribute significantly to pest management but also can serve as a platform for degradation and removal of pests after the intended use. An example of this kind of phenomenon is reported on degrading acephate pesticide using MCM-41/ Co_3O_4 nanocomposite [45] prepared from rice husk silica gel and peach leaves. The composite generates intermediates that are susceptible to visible light and highly sensitive to photocatalytic activity. Apart from these, synthesis of silver nanocomposites [46] using the extracts of bioactive red seaweeds has proved to possess nanopesticidal potential. Synthesis involves reduction of Ag^+ to Ag^0 using red seaweeds G.

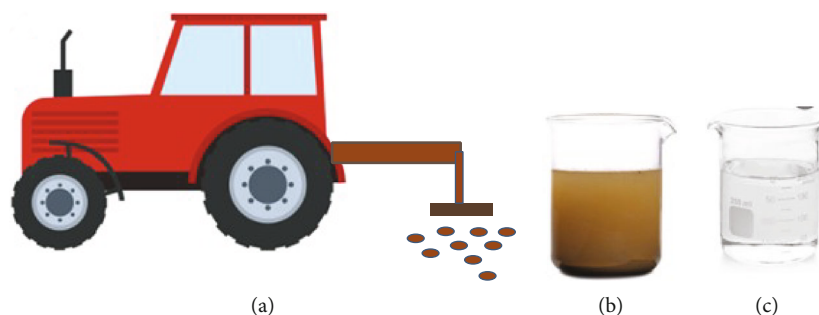


FIGURE 3: (a) Model diagram of magnetic collection of nanoparticles from soil; pH-responsively controlled-release pesticide suspension [48].

corticata, *G. edulis*, *H. musciformis*, and *S. hypnoides* indicated by a clear change in color across 410 nm and 430 nm. One of the prominent contributions to the green nanopesticides is the synthesis of ZrO nanoparticles against twig blight disease caused by the most deadly fungal pathogen of the past decade *Pestalotiopsis versicolor* [47] in bayberry plant. Optimal activity of the nanooxide at $20 \mu\text{g mL}^{-1}$ was observed in inhibiting twig blight on the leaf of these plants. A remarkable innovation in this area is the development of pesticide-loaded magnetic nanocarriers such as high porosity diatomite/ Fe_3O_4 and subsequent coating with chitosan, which enables pH-responsive regulated release pesticide [48] that can be collected by application of an external magnetic field as indicated in Figure 3. This technique offers a high collection ratio without harming the soil quality whose efficiency can be measured by a magnetometer. These pesticide release systems attempt to reinforce the efficacy, impact, and sustainability of nanotechnology as a substitute for toxic chemicals in agriculture.

5.3. Soil Quality and Water Retention. The depletion of soil fertility on farmlands across the world is an issue that must be addressed with serious attention to meet the needs of the growing world population and social changes. In this regard, nanotechnology, through its unique material properties, has the potential to improve soil quality or mitigate nutrient imbalance by providing or carrying macro- and micronutrients. The large surface area, high adsorption capacity, and porous surface enable them to be controlled by release and act as efficient vehicles by encapsulation to carry the nutrients.

One of the serious concerns is the cadmium uptake by plants triggered by the large content of Cd^{2+} salts. Several cases have been reported in which the large specific surface area of nanomaterials helps in determining the uptake of cadmium [49]. The effect exerted on the nutritional quality includes absorption where Cd (II) is converted into an exchangeable form that can be assimilated by the seedlings or by a chemical transformation that increases the tolerance to cadmium ions by a regulated metabolic pathway. A study through an electrokinetic model [50] reveals Cd migration that shows a high Cd^{2+} adsorption efficiency up to 434.78 mg/g beyond pH 4. In addition, other metals such as bivalent lead and copper [51] along with monovalent potassium and sodium showed an active response. Such nanoremediation is also observed to reduce soil toxicity towards

other metal pollutants [52] using graphene oxide validated by the Spanish official methodology, and few similar examples are listed in Table 2.

The techniques discussed so far can also be extended to soils contaminated with more than one metal ion. Hybrid bionanocomposites incorporating filamentous fungi [61] have been popularly used recently in the immobilization of Cd and Pb with *Aspergillus niger* found to be more efficient than *Penicillium chrysogenum*. Both heavy metals were found to be independently one to four times that of nanohydroxyapatites.

Moreover, the uptake of metals is closely related to moisture in the soil [62], and hence, the moisture content is considered to be a crucial parameter in most irrigational regimes [63]. The integration of nanomaterials into conventional agricultural practices can improve water-absorbing and retention properties. A huge stride in this direction is the development of low-cost superabsorbent nanocomposite that can be used to encapsulate conventional fertilizers [64] so that slow release is ensured as recommended by the Committee for European Normalization. A consistent release under varying pH and different concentrations of saline solutions proves its agricultural applications and water retention capability. A similar functionality is exhibited by xanthan gum-cl-poly (acrylic acid)/AgNPs hydrogel nanocomposite [65]. The embedded nanosilver particles which are characterised by several analytical techniques enable the composite towards water retention over sixty days. Also, it is observed that the composite releases KCl in a kinetically controlled manner with $5.458 \times 10^{-6} \text{ m}^2/\text{h}$ and $1.453 \times 10^{-7} \text{ m}^2/\text{h}$ being the initial and final rate of diffusion coefficient, respectively. These biopolymer-based hydrogel composites have a dual advantage of soil conditioning and biodegradability. The novel application of this technology is reflected in the development of carboxymethylcellulose along with hydroxyethylcellulose bridged with citric acid [66] and galactomannan fenugreek cross-linked by borax [67] where the water retention time can be extended up to 2 to 11.5 days at a temperature of 20°C with 60% humidity. The soil mixed with the galactomannan-borax fenugreek galactomannan-borax (FGB) increased the swelling index of sandy soil which is an indication of the increase in the water retention time as shown in Figure 4.

Despite the excellent efficiency exhibited by these water holding materials, unification with clay composites and

TABLE 2: Examples of soil remediation using nano-based material.

Nanomaterial	Dosage of nanomaterial	Contaminant in soil	Ref
Polyvinylpyrrolidone stabilized nano-zero-valent iron	0.01 g	Trichloroethylene	[53]
Nano-Fe/Cu	10 g per layer	Nitrate ions	[54]
Multiwalled carbon nanotubes	1, 2.5, 5 wt%	Cr(VI)	[55]
Modified carbon black nanoparticle	1% <i>w/w</i>	Petroleum	[56]
Single-walled carbon nanotubes	0.058, 0.145, 0.29 wt%	DDT	[57]
Goethite nanospheres	0.5, 2, 5, 10 wt%	As	[58]
Nano-Fe ₃ O ₄ @C-COOH	0.6, 1.3, 2.0, 2.6, 3.3, 4.0 wt%	Pb	[59]
Magnetite nanoparticles	1% <i>w/w</i>	As	[60]

machine installations would intensify water retention through adoption of green nanomaterials.

5.4. Nanosensors. Biological entities have eased the understanding of nanoparticle-biomolecule interactions by inducing positive responses in soils and plants. As conventional sensors adopt tissue-destructive techniques and pose limitations on precise measurements, most sensing systems pertaining to agriculture now resort to green nanosensors that can efficiently translate chemical reactions into quantified voltages. Often, these nanosensors apart from holding sensitive signalling molecules on their surface also possess antimicrobial [68, 69] and antifungal [70] action.

Various novel receptors are designed to detect traces of heavy elements such as Hg²⁺, Pb²⁺, and Cr⁶⁺ that recirculate in the food chain causing degenerative toxicity. Chitosan, a naturally available polycationic linear long-duration polysaccharide originating from chitin, is interestingly widely used in the area of nanosensors. The first-ever chitosan capped gold nanoparticles act as a Hg (II) sensor [71] when tested on agricultural soil which works on plug and play mode and is found to be compliant with the “gold standard.” Similarly, ryegrass, which aids the one-step synthesis of carbon dots [72], was found to be useful for chelating heavy metals. Regarding chitosan-based nanocomposites, its association with the surface plasmon resonance phenomenon makes it popular in building a detector for glyphosate [73] and is considered a prominent herbicide highly polar and water-soluble. Chitosan is composited with zinc oxide or graphene oxide and coated onto the Au chip using the spin coating technique as represented in Figure 5.

The sensor is widely used as a thin film probe for the on-field detection of glyphosate in natural soil and waters. The technique used resembles another sensor for glyphosate made of a chitosan composite [74] with reduced graphene oxide and carbon nanotubes with a double wall along with Fe₃O₄ with an octahedral configuration. The composite is screen printed on gold electrodes forming an electroactive surface area 1.7 times larger than the bare electrode. The method analysed for river water samples utilised for agriculture holds a great promise as an efficient sensing platform.

The report has inspired another chitosan composite with carbon nanofiber with nanocopper as the supporting matrix used to fabricate an electrochemical sensor for car-

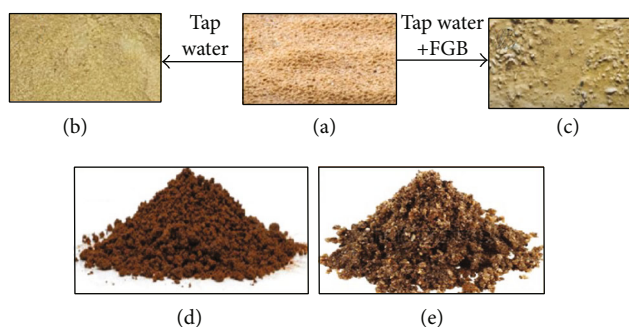


FIGURE 4: (a) Saturation of sandy soil with tap water; (b) sandy soil; (c) saturation of sandy soil with tap water along with fenugreek galactomannan-borax hydrogel; (d) untreated sandy soil with low porosity; (e) fenugreek galactomannan-borax hydrogel-treated sandy soil with enhanced porosity [67].

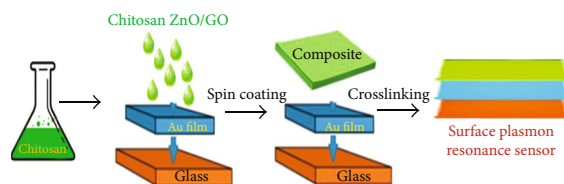


FIGURE 5: Scheme for the fabrication of surface plasmon resonance sensor.

bendazim [75], which is of great environmental interest. The biocompatible chitosan functionalized platform of Cu-containing carbon nanofiber has a high degree of selectivity, a low detection limit, and a wide range of sensitivity 0.8–277.0 μM . The detection process is validated using real soil-washed water samples from farmlands using linear sweep voltammetry.

Several natural polymeric compounds are being explored as a nanocompound sensing platform because they are biodegradable and readily eliminated. Lignin, which is a widely found phenolic polymer, is used to stabilize silver nanoparticles which possess colorimetric sensing properties [76], with respect to arsenic, iron, and lead in nanomolar concentrations. A solution of 100 to 10 mM showed a red shift, and a solution of 1 μM to 1 nM showed a blue shift due to metal reduction by nanosilver particles. Colorimetric

TABLE 3: Comparison of analytical methods of green nano-based sensors in agriculture.

Nanomaterial in sensor	Sensing methodology	Sensing target	Limit of detection	Ref
Thiol-gold	Colorimetric	<i>Listeria monocytogenes</i>	0.015 and 0.013 ng mL ⁻¹	[79]
Fluorescent-SiO ₂	Fluorescence	<i>Brucella</i> spp	50 μL	[80]
Bis-aniline-cross-linked Au	Surface plasmon resonance	Neomycin	2.00 ± 0.21 pM	[81]
Hyperbranched polyethyleneimine scaffolds-AgNPs	Fluorescence quenching	Nitrite	100 nM	[82]
FDH-single-walled carbon nanotube paste electrode	Electrochemical detection	D-Fructose	1 μM	[83]
DLS-superparamagnetic beads-AuNPs	Dynamic light scattering	Aflatoxin	37.7 ng L ⁻¹	[84]
AuNPs	Immunodipstick	Vitamin B12	1 mg mL ⁻¹	[85]
MIP/sol-gel/MWNTs-CS/GCE	Electrochemical detection	Quinoxaline-2-carboxylic acid	4.4 × 10 ⁻⁷ mol L ⁻¹	[86]
OVA-hapten conjugate and AuNPs	Lateral flow immunoassay	Sulfathiazole	15 ng g ⁻¹	[87]
XOD/CHIT/Fe-NPs@Au/PGE	Electrochemical detection	Xanthine	0.1 μM	[88]

detection is extended to detect a broad-spectrum pesticide (O,O-diethyl-O- α -oximinophenyl cyanophosphorothioate) [77]. The contribution of this sensor is remarkable as the pesticide is popularly sold under the name “Phoxim” whose residues are posing a threat to human health. The authors used *Lycii Fructus*, a berry fruit, as a precursor to synthesise the carbon dots functionalized with amino, hydroxyl, and carboxyl groups that can hold silver nanoparticles. The nanosilver particles synthesised indicate the presence of pesticides by aggregation, which displays a color change from yellow to red. The silver particles for colorimetric aggregation properties are used not only to detect pesticides but also for pharmaceutical antibiotics used in treating infections. An excellent successful exploration is to incorporate silver nanoparticles conjugated to green synthesised gentamicin [78]. The gentamicin sensor is a significant step in the prevention of gentamicin-resistant bacteriocoenosis as it shows high sensitivity in the range of 1–100 μM, along with detection and quantification in the range of 0.29 μM and 1 μM.

These new sensors, which are adding to the list of existing systems as listed in Table 3, require no sophisticated instruments and mark the beginning of a new age with naturally derived, environmentally friendly green nanomonitoring systems.

5.5. Limitations and Future Challenges. Although nanotechnology holds many promises in agricultural technology, these compounds, being extremely small and highly soluble and possessing high reactivity because of their large surface area, may also have long-term effects leading to combined toxicity. Additionally, these compounds may trigger altered gene expression leading to nanogenetic manipulation with a severe change in color, growth, reduced pollen, and yield. Treating the root tips of *Allium cepa* with nanooxides is reported to cause cellular deformation through chromosomal aberration. Among simple oxides such as Al₂O₃, TiO₂, and ZnO, abnormal anaphase accompanied by sticky metaphase was exhibited by TiO₂ [89] in the concentration range 0.1, 10, and 100 mg/L. The severity of aberration is found to be maximum for TiO₂ and fairly lower in the case of Al₂O₃ and ZnO.

A similar comparative study between CuO-NPs and Al₂O₃-NPs of 18 nm along with 21 nm, respectively, is exploring the extent of the internalization and translocation in tomato plants [90]. The binding studies with TmDNA by fluorescence quenching revealed a higher activity of CuO nanoparticles compared to Al₂O₃ nanoparticles.

There is also a possibility of these nanocompounds entering the food chain. Some studies such as on soyabean [91] where chemical damage is caused, rice suspension cells [92] treated with multiwalled carbon nanotubes initiating a self-defence response, and magnetic nanoparticles causing brown spots on leaves of maize plantlets [93] due to genetic deformation [94] also predict the interaction of nanocompounds with plants leading to an imbalance in the uptake of nutrients. The study of in vitro oxidative damage caused by Ni nanoparticles, which triggers an antioxidant response, affecting the growth of *Lycium barbarum L* [95], has been shown to be highly damaging compared to its bulk counterpart NiSO₄.

These studies highlight the need for a deeper understanding of the vascular system of the plant with guided administration to the targeted sites. The site-specific nanotransfer potential could help to optimize the physiological and biochemical usage of these compounds to maintain a balance in plant hormones and nucleic acids in the localized areas of plant tissues. The effect of nanoparticles on biological pathways and the associated mechanistic factors hence deserve a risk assessment procedure at the genomic or biochemical level.

6. Conclusions

The application of nanotechnology at the global level has made many agricultural procedures faster, cheaper, and more accurate. Green nanotechnology with its eco-friendly means of generating functionalized nanoparticles has a great potential to dispense pesticides and fertilizers in a controlled manner, thereby avoiding collateral damage. This area of research has many novel solutions to offer in the area of plant growth of development and could also permit rapid advances in agricultural reproductive science. However,

effective commercialization of green nanotechnology still requires a thorough understanding of these moieties with biotic or abiotic components and the possibility of bioaccumulation. The problems associated with safety issues, public perception, scalability, and regulating processing costs are the recognised future challenges in bringing green nanotechnology from R&D laboratories to industrial production. It is high time for the governments and nongovernmental organisations across the world to come together to form common regulations and norms to strictly monitor the commercialization and bulk usage of green nanocompounds in the agricultural sector.

Data Availability

All relevant data are included within the article.

Conflicts of Interest

All authors declare that there is no conflict of interest.

Acknowledgments

The authors gratefully acknowledge the Deanship of Scientific Research, King Khalid University (KKU), Abha-61421, Asir, Kingdom of Saudi Arabia, for funding this research work under grant number R.G.P1/183/41.

References

- [1] O. R. Ernst, A. R. Kemanian, S. R. Mazzilli, M. Cadenazzi, and S. Dogliotti, "Depressed attainable wheat yields under continuous annual no-till agriculture suggest declining soil productivity," *Field Crops Research*, vol. 186, pp. 107–116, 2016.
- [2] J. Cuevas, I. N. Daliakopoulos, F. del Moral, J. J. Hueso, and I. K. Tsanis, "A review of soil-improving cropping systems for soil salinization," *Agronomy*, vol. 9, no. 6, p. 295, 2019.
- [3] J. Joo, S. Jeong, C. Zheng, C.-E. Park, H. Park, and H. Kim, "Emergence of significant soil moisture depletion in the near future," *Environmental Research Letters*, vol. 15, no. 12, article 124048, 2020.
- [4] R. Lal, "Soil organic matter content and crop yield," *Journal of Soil and Water Conservation*, vol. 75, no. 2, pp. 27A–32A, 2020.
- [5] Y. G. Carvalho, L. C. Vitorino, U. J. de Souza, and L. A. Bessa, "Recent trends in research on the genetic diversity of plants: implications for conservation," *Diversity*, vol. 11, no. 4, p. 62, 2019.
- [6] Y. Lurwanu, Y.-P. Wang, E.-J. Wu et al., "Increasing temperature elevates the variation and spatial differentiation of pesticide tolerance in a plant pathogen," *Evolutionary Applications*, vol. 14, no. 5, pp. 1274–1285, 2021.
- [7] X.-S. He, Y.-L. Zhang, Z.-H. Liu et al., "Interaction and coexistence characteristics of dissolved organic matter with toxic metals and pesticides in shallow groundwater," *Environmental Pollution*, vol. 258, p. 113736, 2020.
- [8] A. F. Hamad, J.-H. Han, B.-C. Kim, and I. A. Rather, "The intertwine of nanotechnology with the food industry," *Saudi journal of biological sciences*, vol. 25, no. 1, pp. 27–30, 2018.
- [9] R. Ahmad, S. Srivastava, S. Ghosh, and S. K. Khare, "Phytochemical delivery through nanocarriers: a review," *Colloids and Surfaces, B: Biointerfaces*, vol. 197, article 111389, 2021.
- [10] K. Khosravi-Darani, A. da Cruz, M. Mozafari, Z. Abdi, and N. Ahmadi, "Biosynthesis of metal nanoparticles by probiotic bacteria," *Letters in Applied NanoBioScience*, vol. 8, no. 3, pp. 619–626, 2019.
- [11] D. SÁSKOVÁ, J. POŘÍZKA, P. KULICH, A. ŠPANOVÁ, P. DIVIŠ, and B. RITTICH, "Silver nanoparticles production with probiotic bacteria," *Materials Science Forum*, vol. 851, pp. 32–36, 2016.
- [12] S. B. Nadhe, R. Singh, S. A. Wadhvani, and B. A. Chopade, "Acinetobacter sp. mediated synthesis of AgNPs, its optimization, characterization and synergistic antifungal activity against *C. albicans*," *Journal of Applied Microbiology*, vol. 127, no. 2, pp. 445–458, 2019.
- [13] J. Markus, R. Mathiyalagan, Y.-J. Kim et al., "Intracellular synthesis of gold nanoparticles with antioxidant activity by probiotic *Lactobacillus kimchicus*_ DCY51^T isolated from Korean kimchi," *Enzyme and Microbial Technology*, vol. 95, pp. 85–93, 2016.
- [14] J. Li, Q. Li, X. Ma et al., "Biosynthesis of gold nanoparticles by the extreme bacterium *Deinococcus radiodurans* and an evaluation of their antibacterial properties," *International Journal of Nanomedicine*, vol. Volume 11, pp. 5931–5944, 2016.
- [15] S. Riaz, Z. A. Raza, and M. I. Majeed, "Preparation of cadmium sulfide nanoparticles and mediation thereof across poly (hydroxybutyrate) nanocomposite," *Polymer Bulletin*, vol. 77, no. 2, pp. 775–791, 2020.
- [16] M. N. Owaid, S. S. S. Al-Saeedi, and I. A. Abed, "Biosynthesis of gold nanoparticles using yellow oyster mushroom *Pleurotus cornucopiae*_ var. *_citrinopileatus_*," *Environmental nanotechnology, monitoring & management*, vol. 8, pp. 157–162, 2017.
- [17] S. Tyagi, P. K. Tyagi, D. Gola, N. Chauhan, and R. K. Bharti, "Extracellular synthesis of silver nanoparticles using entomopathogenic fungus: characterization and antibacterial potential," *SN Applied Sciences*, vol. 1, no. 12, p. 1545, 2019.
- [18] L. Shokrzadeh, P. Mohammadi, M. R. Mahmoudian, W. J. Basirun, and M. Bahreini, "L-Glycine-assisted synthesis of SnO₂/Pd nanoparticles and their application in detection of biodeteriorating fungi," *Materials Chemistry and Physics*, vol. 240, article 122172, 2020.
- [19] H. A. Ammar, A. A. Abd, E. Aty, and S. A. El Awdan, "Extracellular myco-synthesis of nano-silver using the fermentable yeasts *Pichia kudriavzevii*HA-NY2 and *Saccharomyces uvarum*HA-NY3, and their effective biomedical applications," *Bio-process and Biosystems Engineering*, vol. 44, no. 4, pp. 841–854, 2021.
- [20] V. P. Sur, M. Kominkova, Z. Buchtova, K. Dolezelikova, O. Zitka, and A. Moullick, "CdSe QD biosynthesis in yeast using tryptone-enriched media and their conjugation with a peptide hecate for bacterial detection and killing," *Nanomaterials*, vol. 9, no. 10, p. 1463, 2019.
- [21] A. Sivaraj, V. Kumar, R. Sunder, K. Parthasarathy, and G. Kasivelu, "Commercial yeast extracts mediated green synthesis of silver chloride nanoparticles and their antimycobacterial activity," *Journal of Cluster Science*, vol. 31, no. 1, pp. 287–291, 2020.
- [22] H. P. Borase, C. D. Patil, R. B. Salunkhe, R. K. Suryawanshi, B. K. Salunke, and S. V. Patil, "Catalytic and synergistic antibacterial potential of green synthesized silver nanoparticles:








- their ecotoxicological evaluation on *Poecillia reticulata*,” *Biotechnology and Applied Biochemistry*, vol. 61, no. 4, pp. 385–394, 2014.
- [23] B. A. Bello, S. A. Khan, J. A. Khan, F. Q. Syed, Y. Anwar, and S. B. Khan, “Antiproliferation and antibacterial effect of bio-synthesized AgNPs from leaves extract of *Guiera senegalensis* and its catalytic reduction on some persistent organic pollutants,” *Journal of Photochemistry and Photobiology. B*, vol. 175, pp. 99–108, 2017.
- [24] S. Waclawek, Z. Gončuková, K. Adach, M. Fijałkowski, and M. Černík, “Green synthesis of gold nanoparticles using *Artemisia dracunculus* extract: control of the shape and size by varying synthesis conditions,” *Environmental Science and Pollution Research International*, vol. 25, no. 24, pp. 24210–24219, 2018.
- [25] I. U. H. Bhat, M. N. K. Anwar, and J. N. Appaturi, “Polymer based palladium nanocatalyst for the degradation of nitrate and Congo red,” *Journal of Polymers and the Environment*, vol. 27, no. 7, pp. 1475–1487, 2019.
- [26] V. J. Garole, B. C. Choudhary, S. R. Tetgure, D. J. Garole, and A. U. Borse, “Detoxification of toxic dyes using biosynthesized iron nanoparticles by photo-Fenton processes,” *International journal of Environmental Science and Technology*, vol. 15, no. 8, pp. 1649–1656, 2018.
- [27] M. Nasrollahzadeh, S. S. Momeni, and S. M. Sajadi, “Green synthesis of copper nanoparticles using *Plantago asiatica* leaf extract and their application for the cyanation of aldehydes using $K_4Fe(CN)_6$,” *Journal of Colloid and Interface Science*, vol. 506, pp. 471–477, 2017.
- [28] R. Gopalakrishnan, B. Loganathan, and K. Raghu, “Green synthesis of Au-Ag bimetallic nanocomposites using *Silybum marianum* seed extract and their application as a catalyst,” *RSC Advances*, vol. 5, no. 40, pp. 31691–31699, 2015.
- [29] A. Al-Asfar, Z. Zaheer, and E. S. Aazam, “Eco-friendly green synthesis of bimetallic nanoparticles: antioxidant, antimicrobial and photocatalytic degradation of bromothymol blue,” *Journal of Photochemistry and Photobiology. B*, vol. 185, pp. 143–152, 2018.
- [30] T. Sugai, H. Yoshida, T. Shimada, T. Okazaki, H. Shinohara, and S. Bandow, “New synthesis of high-quality double-walled carbon nanotubes by high-temperature pulsed arc discharge,” *Nano Letters*, vol. 3, no. 6, pp. 769–773, 2003.
- [31] M. Santoro, F. A. Gorelli, R. Bini, J. Haines, and A. van der Lee, “High-pressure synthesis of a polyethylene/zeolite nanocomposite material,” *Nature Communications*, vol. 4, no. 1, 2013.
- [32] X. W. Lou and H. C. Zeng, “Hydrothermal synthesis of α - MoO_3 nanorods via acidification of ammonium heptamolybdate tetrahydrate,” *Chemistry of Materials*, vol. 14, no. 11, pp. 4781–4789, 2002.
- [33] N. A. Khan, I. J. Kang, H. Y. Seok, and S. H. Jhung, “Facile synthesis of nano-sized metal-organic frameworks, chromium-benzenedicarboxylate, MIL-101,” *Chemical Engineering Journal*, vol. 166, no. 3, pp. 1152–1157, 2011.
- [34] S. S. Takla, E. Shawky, H. M. Hammada, and F. A. Darwish, “Green techniques in comparison to conventional ones in the extraction of *Amaryllidaceae* alkaloids: best solvents selection and parameters optimization,” *Journal of Chromatography. A*, vol. 1567, pp. 99–110, 2018.
- [35] H. Guo, J. C. White, Z. Wang, and B. Xing, “Nano-enabled fertilizers to control the release and use efficiency of nutrients,” *Current Opinion in Environmental Science & Health*, vol. 6, pp. 77–83, 2018.
- [36] P. Sheoran, S. Grewal, S. Kumari, and S. Goel, “Enhancement of growth and yield, leaching reduction in *Triticum aestivum* using biogenic synthesized zinc oxide nanofertilizer,” *Biocatalysis and Agricultural Biotechnology*, vol. 32, article 101938, 2021.
- [37] M. Leonardi, G. M. Caruso, S. C. Carroccio et al., “Smart nanocomposites of chitosan/alginate nanoparticles loaded with copper oxide as alternative nanofertilizers,” *Environmental Science: Nano*, vol. 8, no. 1, pp. 174–187, 2021.
- [38] A. Abbasifar, F. Shahrabadi, and B. V. Kaji, “Effects of green synthesized zinc and copper nano-fertilizers on the morphological and biochemical attributes of basil plant,” *Journal of Plant Nutrition*, vol. 43, no. 8, pp. 1104–1118, 2020.
- [39] G. B. Ramírez-Rodríguez, G. Dal Sasso, F. J. Carmona et al., “Engineering biomimetic calcium phosphate nanoparticles: a green synthesis of slow-release multinutrient (NPK) nanofertilizers,” *ACS Applied Bio Materials*, vol. 3, no. 3, pp. 1344–1353, 2020.
- [40] H. Jahangirian, R. Rafiee-Moghaddam, N. Jahangirian et al., “< p>Green synthesis of zeolite/Fe₂O₃ nanocomposites: toxicity & cell proliferation assays and application as a smart iron nanofertilizer</p>,” *International Journal of Nanomedicine*, vol. Volume 15, pp. 1005–1020, 2020.
- [41] S. Nisha Raj, E. S. Anooj, K. Rajendran, and S. Vallinayagam, “A comprehensive review on regulatory invention of nano pesticides in agricultural nano formulation and food system,” *Journal of Molecular Structure*, vol. 1239, article 130517, 2021.
- [42] X. Gao, F. Shi, F. Peng et al., “Formulation of nanopesticide with graphene oxide as the nanocarrier of pyrethroid pesticide and its application in spider mite control,” *RSC Advances*, vol. 11, no. 57, pp. 36089–36097, 2021.
- [43] T. Ahmed, M. Noman, J. Luo et al., “Bioengineered chitosan-magnesium nanocomposite: a novel agricultural antimicrobial agent against *Acidovorax oryzae* and *Rhizoctonia solani* for sustainable rice production,” *International Journal of Biological Macromolecules*, vol. 168, pp. 834–845, 2021.
- [44] S. K. Namasivayam, R. A. Bharani, and K. Karunamoorthy, “Insecticidal fungal metabolites fabricated chitosan nanocomposite (IM-CNC) preparation for the enhanced larvicidal activity - an effective strategy for green pesticide against economic important insect pests,” *International Journal of Biological Macromolecules*, vol. 120, no. Part A, pp. 921–944, 2018.
- [45] M. R. AbuKhadra, A. S. Mohamed, A. M. El-Sherbeeney, and M. A. Elmeligy, “Enhanced photocatalytic degradation of acephate pesticide over MCM-41/ Co_3O_4 nanocomposite synthesized from rice husk silica gel and peach leaves,” *Journal of Hazardous Materials*, vol. 389, article 122129, 2020.
- [46] T. A. Roseline, M. Murugan, M. P. Sudhakar, and K. Arunkumar, “Nanopesticidal potential of silver nanocomposites synthesized from the aqueous extracts of red seaweeds,” *Environmental Technology and Innovation*, vol. 13, pp. 82–93, 2019.
- [47] T. Ahmed, H. Ren, M. Noman et al., “Green synthesis and characterization of zirconium oxide nanoparticles by using a native *Enterobacter* sp. and its antifungal activity against bayberry twig blight disease pathogen *Pestalotiopsis versicolor*,” *NanoImpact*, vol. 21, article ???, 2021.
- [48] Y. Xiang, G. Zhang, Y. Chi, D. Cai, and Z. Wu, “Fabrication of a controllable nanopesticide system with magnetic

- collectability,” *Chemical Engineering Journal*, vol. 328, pp. 320–330, 2017.
- [49] M. Gao, X. Yalei, X. Chang, Y. Dong, and Z. Song, “Effects of foliar application of graphene oxide on cadmium uptake by lettuce,” *Journal of Hazardous Materials*, vol. 398, article 122859, 2020.
- [50] J. C. Xu, Q. Ma, C. Chen, Q. T. Wu, and X. X. Long, “Cadmium adsorption behavior of porous and reduced graphene oxide and its potential for promoting cadmium migration during soil electrokinetic remediation,” *Chemosphere*, vol. 259, article 127441, 2020.
- [51] X. Zhang, X. Zhenlan, W. Mansha et al., “Potential environmental risks of nanopesticides: application of Cu(OH)₂ nanopesticides to soil mitigates the degradation of neonicotinoid thiacloprid,” *Environment International*, vol. 129, pp. 42–50, 2019.
- [52] D. Baragaño, R. Forján, L. Welte, and J. L. Gallego, “Nanoremediation of As and metals polluted soils by means of graphene oxide nanoparticles,” *Scientific Reports*, vol. 10, no. 1, p. 1896, 2020.
- [53] H. Tian, Y. Liang, D. Yang, and Y. Sun, “Characteristics of PVP-stabilised NZVI and application to dechlorination of soil-sorbed TCE with ionic surfactant,” *Chemosphere*, vol. 239, article 124807, 2020.
- [54] T. Shubair, O. Eljamal, A. M. E. Khalil, and N. Matsunaga, “Multilayer system of nanoscale zero valent iron and nano-Fe/Cu particles for nitrate removal in porous media,” *Separation and Purification Technology*, vol. 193, pp. 242–254, 2018.
- [55] Y. Zhang, J. Yang, L. Zhong, and L. Liu, “Effect of multi-wall carbon nanotubes on Cr (VI) reduction by citric acid: implications for their use in soil remediation,” *Environmental Science and Pollution Research*, vol. 25, no. 24, pp. 23791–23798, 2018.
- [56] J. Cheng, Z. Sun, Y. Yu, X. Li, and T. Li, “Effects of modified carbon black nanoparticles on plant-microbe remediation of petroleum and heavy metal co-contaminated soils,” *International Journal of Phytoremediation*, vol. 21, no. 7, pp. 634–642, 2019.
- [57] J. Zhang, J.-L. Gong, G.-M. Zeng, H.-C. Yang, and P. Zhang, “Carbon nanotube amendment for treating dichlorodiphenyltrichloroethane and hexachlorocyclohexane remaining in Dong-ting Lake sediment – an implication for in-situ remediation,” *Science of The Total Environment*, vol. 579, pp. 283–291, 2017.
- [58] D. Baragaño, J. Alonso, J. R. Gallego, M. C. Lobo, and M. Gil-Díaz, “Zero valent iron and goethite nanoparticles as new promising remediation techniques for As-polluted soils,” *Chemosphere*, vol. 238, article 124624, 2020.
- [59] C. Ma, F. Y. Liu, M. B. Wei, J. H. Zhao, and H. Z. Zhang, “Synthesis of novel core-shell magnetic Fe₃O₄@C nanoparticles with carboxyl function for use as an immobilisation agent to remediate lead-contaminated soils,” *Polish Journal of Environmental Studies*, vol. 29, no. 3, pp. 2273–2283, 2020.
- [60] D. Baragaño, J. Alonso, J. R. Gallego, M. C. Lobo, and M. Gil-Díaz, “Magnetite nanoparticles for the remediation of soils contaminated with As and PAHs,” *Chemical Engineering Journal*, vol. 399, article 125809, 2020.
- [61] Z. Yang, L. Liang, W. Yang et al., “Simultaneous immobilization of cadmium and lead in contaminated soils by hybrid bio-nanocomposites of fungal hyphae and nano-hydroxyapatites,” *Environmental Science and Pollution Research*, vol. 25, no. 12, pp. 11970–11980, 2018.
- [62] A. Stafford, P. Jeyakumar, M. Hedley, and C. Anderson, “Influence of soil moisture status on soil cadmium phytoavailability and accumulation in plantain (*Plantago lanceolata*),” *Soil systems*, vol. 2, no. 1, p. 9, 2018.
- [63] Z. Zhang, X. Wu, C. Tu et al., “Relationships between soil properties and the accumulation of heavy metals in different *Brassica campestris* L. growth stages in a Karst mountainous area,” *Ecotoxicology and Environmental Safety*, vol. 206, article 111150, 2020.
- [64] A. Olad, H. Zebhi, D. Salari, A. Mirmohseni, and A. R. Tabar, “Slow-release NPK fertilizer encapsulated by carboxymethyl cellulose-based nanocomposite with the function of water retention in soil,” *Materials Science and Engineering: C*, vol. 90, pp. 333–340, 2018.
- [65] J. Singh and A. S. Dhaliwal, “Water retention and controlled release of KCl by using microwave-assisted green synthesis of xanthan gum-cl-poly (acrylic acid)/AgNPs hydrogel nanocomposite,” *Polymer Bulletin*, vol. 77, no. 9, pp. 4867–4893, 2020.
- [66] S. Durpekova, A. Di Martino, M. Dusankova, P. Drohsler, and V. Sedlarik, “Biopolymer hydrogel based on acid whey and cellulose derivatives for enhancement water retention capacity of soil and slow release of fertilizers,” *Polymers*, vol. 13, no. 19, p. 3274, 2021.
- [67] C. Liu, F. Lei, P. Li, J. Jiang, and K. Wang, “Borax crosslinked fenugreek galactomannan hydrogel as potential water-retaining agent in agriculture,” *Carbohydrate Polymers*, vol. 236, article 116100, 2020.
- [68] A. Rautela, J. Rani, and M. Debnath, “Green synthesis of silver nanoparticles from *Tectona grandis* seeds extract: characterization and mechanism of antimicrobial action on different microorganisms,” *Journal of Analytical Science and Technology*, vol. 10, no. 1, p. 5, 2019.
- [69] S. Khodadadi, N. Mahdinezhad, B. Fazeli-Nasab, M. J. Heidari, B. Fakheri, and A. Miri, “Investigating the possibility of green synthesis of silver nanoparticles using *Vaccinium arctostaphylos* extract and evaluating its antibacterial properties,” *Ecology and Biotechnological Applications of Biofilms*, vol. 2021, pp. 1–13, 2021.
- [70] E. K. Elumalai, T. N. Prasad, K. Venkata, P. C. Nagajyothi, and E. David, “Green synthesis of silver nanoparticle using *Euphorbia hirta* L and their antifungal activities,” *Archives of Applied Science Research*, vol. 2, pp. 76–81, 2010.
- [71] K. Sadani, P. Nag, and S. Mukherji, “LSPR based optical fiber sensor with chitosan capped gold nanoparticles on BSA for trace detection of Hg (II) in water, soil and food samples,” *Biosensors & Bioelectronics*, vol. 134, pp. 90–96, 2019.
- [72] A. Afonso Jr., F. T. Aquino, G. M. Dalmônico, M. V. Nascimento, E. Wrasse, and K. M. de Aguiar, “Green synthesis of carbon nanodots from agro-industrial residues,” *Carbon Letters*, vol. 91, 2022.
- [73] M. H. Do, B. Dubreuil, J. Peydecastaing et al., “Chitosan-based nanocomposites for glyphosate detection using surface plasmon resonance sensor,” *Sensors*, vol. 20, no. 20, p. 5942, 2020.
- [74] C. T. Thanh, N. H. Binh, P. N. D. Duoc et al., “Electrochemical sensor based on reduced graphene oxide/double-walled carbon nanotubes/octahedral Fe₃O₄/chitosan composite for glyphosate detection,” *Bulletin of Environmental Contamination and Toxicology*, vol. 106, no. 6, pp. 1017–1023, 2021.
- [75] P. Sundaresan, F. Chun-Chieh, S.-H. Liu, and R.-S. Juang, “Facile synthesis of chitosan-carbon nanofiber composite supported copper nanoparticles for electrochemical sensing of

- carbendazim,” *Colloids and Surfaces A: Physicochemical and Engineering Aspects*, vol. 625, article 126934, 2021.
- [76] K. R. Aadil, N. Pandey, S. I. Mussatto, and H. Jha, “Green synthesis of silver nanoparticles using acacia lignin, their cytotoxicity, catalytic, metal ion sensing capability and antibacterial activity,” *Journal of Environmental Chemical Engineering*, vol. 7, no. 5, article 103296, 2019.
- [77] M. Zheng, C. Wang, Y. Wang et al., “Green synthesis of carbon dots functionalized silver nanoparticles for the colorimetric detection of phoxim,” *Talanta*, vol. 185, pp. 309–315, 2018.
- [78] N. Ul Ain, Z. Aslam, M. Yousuf et al., “Green synthesis of methyl gallate conjugated silver nanoparticles: a colorimetric probe for gentamicin,” *New Journal of Chemistry*, vol. 43, no. 4, pp. 1972–1979, 2019.
- [79] Z. Y. Fu, X. M. Zhou, and D. Xing, “Rapid colorimetric sensing of food pathogenic bacteria using biomodification-free gold nanoparticle,” *Sensors and Actuators B: Chemical*, vol. 182, pp. 633–641, 2013.
- [80] S. S. Vyas, S. V. Jadhav, S. B. Majee, J. S. Shastri, and V. B. Patravale, “Development of immunochromatographic strip test using fluorescent, micellar silica nanosensors for rapid detection of *B. abortus* antibodies in milk samples,” *Biosensors & Bioelectronics*, vol. 70, pp. 254–260, 2015.
- [81] M. Frasconi, R. Tel-Vered, M. Riskin, and I. Willner, “Surface plasmon resonance analysis of antibiotics using imprinted boronic acid-functionalized Au nanoparticle composites,” *Analytical Chemistry*, vol. 82, no. 6, pp. 2512–2519, 2010.
- [82] C. Chen, Z. Q. Yuan, H. T. Chang, F. N. Lu, Z. H. Li, and C. Lu, “Silver nanoclusters as fluorescent nanosensors for selective and sensitive nitrite detection,” *Analytical Methods*, vol. 8, no. 12, pp. 2628–2633, 2016.
- [83] R. Antiochia, G. Vinci, and L. Gorton, “Rapid and direct determination of fructose in food: a new osmium-polymer mediated biosensor,” *Food Chemistry*, vol. 140, no. 4, pp. 742–747, 2013.
- [84] Z. Zhang, M. Lin, S. Zhang, and B. Vardhanabhuti, “Detection of aflatoxin M1 in milk by dynamic light scattering coupled with superparamagnetic beads and gold nanoprobe,” *Journal of Agricultural and Food Chemistry*, vol. 61, no. 19, pp. 4520–4525, 2013.
- [85] L. S. Selvakumar, K. V. Ragavan, K. S. Abhijith, and M. S. Thakur, “Immunodipstick based gold nanosensor for vitamin B12 in fruit and energy drinks,” *Analytical Methods*, vol. 5, no. 7, article 1806, 2013.
- [86] Y. K. Yang, G. Z. Fang, G. Y. Liu et al., “Electrochemical sensor based on molecularly imprinted polymer film via sol-gel technology and multi-walled carbon nanotubes-chitosan functional layer for sensitive determination of quinoxaline-2-carboxylic acid,” *Biosensors & Bioelectronics*, vol. 47, pp. 475–481, 2013.
- [87] I. Guillén, J. A. Gabaldón, E. Núñez-Delicado, R. Puchades, A. Maquieira, and S. Morais, “Detection of sulphathiazole in honey samples using a lateral flow immunoassay,” *Food Chemistry*, vol. 129, no. 2, pp. 624–629, 2011.
- [88] R. Devi, S. Yadav, R. Nehra, S. Yadav, and C. S. Pundir, “Electrochemical biosensor based on gold coated iron nanoparticles/chitosan composite bound xanthine oxidase for detection of xanthine in fish meat,” *Journal of Food Engineering*, vol. 115, no. 2, pp. 207–214, 2013.
- [89] P. Debnath, A. Mondal, K. Sen, D. Mishra, and N. K. Mondal, “Genotoxicity study of nano Al₂O₃, TiO₂ and ZnO along with UV-B exposure: An *Allium cepa* root tip assay,” *Science of The Total Environment*, vol. 713, article 136592, 2020.
- [90] B. Ahmed, M. S. Khan, and J. Musarrat, “Toxicity assessment of metal oxide nano-pollutants on tomato (*Solanum lycopersicon*): a study on growth dynamics and plant cell death,” *Environmental Pollution*, vol. 240, pp. 802–816, 2018.
- [91] J. H. Priester, Y. Ge, R. E. Mielke et al., “Soybean susceptibility to manufactured nanomaterials with evidence for food quality and soil fertility interruption,” *ACS*, vol. 7, pp. 2451–2456, 2013.
- [92] X.-M. Tan and B. Fugetsu, “Multi-walled carbon nanotubes interact with cultured rice cells: evidence of a self-defense response,” *Journal of Biomedical Nanotechnology*, vol. 3, no. 3, pp. 285–288, 2007.
- [93] M. Racuciu and D. Creanga, “Biocompatible magnetic fluid nanoparticles internalized in vegetal tissues,” *Romanian Journal of Physics*, vol. 54, pp. 115–124, 2009.
- [94] T. M. Klein, L. Kornstein, J. C. Sanford, and M. E. Fromm, “Genetic transformation of maize cells by particle bombardment,” *Plant Physiology*, vol. 91, no. 1, pp. 440–444, 1989.
- [95] M. Pinto, C. Soares, A. S. Pinto, and F. Fidalgo, “Phytotoxic effects of bulk and nano-sized Ni on *Lycium barbarum* L. grown *in vitro* - oxidative damage and antioxidant response,” *Chemosphere*, vol. 218, pp. 507–516, 2019.

Research Article

Exclusion of Chromium(VI) Ion in Grueling Activated Carbon Fabricated from *Manilkara zapota* Tree Wood by Adsorption: Optimization by Response Surface Methodology

S. Sujatha ¹, R. Sivarethinamohan ², A. Oorkalan ¹, V. Senthilkumar ³,
B. Anuradha ⁴, B. Veluchamy,⁵ P. Prabhu ⁶, Magda H. Abdellattif ⁷,
and Abdulmohsen Khalaf Dhahi Alsukaibi⁸

¹Department of Civil Engineering, K.Ramakrishnan College of Technology, Tiruchirapalli, Tamilnadu, India

²CHRIST (Deemed to be University), Bangalore Karnataka, India

³Department of Civil Engineering, M.Kumarasamy College of Engineering, Karur, India

⁴Department of Civil Engineering, Chennai Institute of Technology, Chennai, India

⁵Department of Mechanical Engineering, K.Ramakrishnan College of Engineering, Trichy, India

⁶Department of Mechanical Engineering, College of Engineering and Technology, Mettu University, Ethiopia

⁷Department of Chemistry, College of Science, Taif University, P.O. Box 11099, Taif 21944, Saudi Arabia

⁸Department of Chemistry, College of Sciences, University of Hail, Hail-2440, Saudi Arabia

Correspondence should be addressed to P. Prabhu; drprabhu@meu.edu.et

Received 20 January 2022; Accepted 1 April 2022; Published 23 April 2022

Academic Editor: Hiwa M. Ahmed

Copyright © 2022 S. Sujatha et al. This is an open access article distributed under the Creative Commons Attribution License, which permits unrestricted use, distribution, and reproduction in any medium, provided the original work is properly cited.

The current paper makes obvious the elimination of chromium(VI) ion, from wastewater via adsorption technique with activated carbon generated from *Manilkara zapota* tree (MZTWAC). Preliminarily MZTWAC has undergone characterization studies which uncovered the suitability of MZTWAC to expel chromium(VI) from aqueous solution. Batch adsorption experimentation was premeditated with the competence of central composite design (CCD) and it was executed. Response surface methodology (RSM) was the key optimization software to appraise the adsorptive chattels of MZTWAC engaged in removing chromium(VI) ion in aqueous solution which explored the interactions flanked between four expounding variables explicitly initial concentration of chromium(VI) ion, pH of the solution, MZTWAC dose and time of exposure, and contact time. The response variable that was concentrated in the study was adsorption capacity. It was deduced a polynomial in quadratic equation was documented amid the adsorption capacity and variables influencing the adsorption with $R^2 = 0.9792$ which was projected as the best suit for the adsorption process. ANOVA that is expanded as analysis of variance judged the connotation of adsorption process variables. 0.2 g of MZTWAC dosage has removed 87.629% chromium(VI) from aqueous solution. The enhancement of adsorption process reclined on the attainment of maximum adsorption capacity which further depends on the optimization of variables under consideration. This criterion was accomplished by the desirability function optimizing the process variables.

1. Introduction

Rapid increase in population and modern innovative technology and its progression guide environment towards the polluted scenario reported during the history of the last few decades [1]. Natural resources are extensively used and exploited nowadays abruptly deteriorating the atmo-

sphere and thereby the lives on the earth in turn. The metals like chromium, copper, lead, and arsenic are naturally occurring objects whose usage increases randomly in many industrial operations. These metals are universally accepted as heavy metals which hold a 5g/cm^3 specific density more than that of water. Though these metals are inherent to the functioning of the physiological

activities for the humans, its addition more than that required adversely distresses the surroundings and livelihood of the organisms [2]. Ejection of effluents domestically and industrially has provoked in superior altitudes of heavy metal attentiveness in resources of water [3]. Amid different metal ions, chromium(VI) is the most frequently used and present in the surroundings and very perilous to the ecosystem. Exposure to chromium(VI) and health hazards go hand in hand with each other. Health issues like abdominal cancer [4, 5] and skin problems are inferred due to exposure towards chromium(VI) [6, 7]. The chromium(VI) concentration necessity is to be below 0.1 mg/L [8, 9] which is prescribed according to USEPA (U.S. Environment Protection Agency) Bureau of Indian Standards (BIS) that is highlighted in El-Bestawy et al. in the year 2013 and by Sharma in the year 2009. Environmental pollution is indebted to chromium mainly manifested in many industries that manufacture leather products, manufacturing electronic devices, and industries that engage in operations making inherent use of metals [10, 11]. Every researcher is inquisitive in their research to exclude the toxic metal from wastewater by customary treatment practices such as precipitation of chemicals [12, 13], coagulation, ion exchange [14], adsorption [15, 16], solvent extraction [17], foam flotation, and electrodialysis [18]. Conversely, adsorption process is the proficient, cost-effective, and green technique distinctively in removing heavy metal ions from wastewater. Many adsorbents were utilized so far in extracting chromium from the polluted water. One among them is groundnut shell powder reported in the year 2019 by Jonas et al. Commercial activated carbon is in usage worldwide for the deletion of heavy metals from the effluent expelled from industries. Since the expenditure of its use is in elevated side, researchers are striving to uncover economical sources for preparing the adsorbents. As a consequence, the main extent of the current paper is meant at uncovering a novel adsorbent. *Manilkara zapota* tree [19] which is commonly known as sapodilla, a fruit-producing tree which is profusely grown in Indian nation, may possibly be employed as an alternating adsorbent. Existing study gave attention to synthesis of derivative, an activated carbon from *Manilkara zapota* tree wood treated with citric acid [19] to treat chromium(VI) ion-polluted water batch adsorption mode. Wood pieces of *Manilkara zapota* tree wood [19, 20] were gathered. Optimum conditions for process variables, for instance, initial concentration of chromium(VI), pH, contact time of the experiment, and MZTWAC (adsorbent) dosage, were tested through a rotatable central composite design under response surface methodology with support of software version 7, namely, Design Expert.

2. Materials and Methods

Activated carbon was prepared from *Manilkara zapota* tree wood. The process remained encrypted in the authors' original article [20]. To get to know the presence of functional groups that favour chromium(VI) ion adsorption and to have an idea on the surface morphology, Fourier transform

infrared spectroscopy (FTIR) and scanning electron microscopy (SEM) analysis were performed.

2.1. Experimentation. Optimize the process variables of the least experiments by employing the response surface methodology (RSM) technique. The main intent here is in the direction of upgrading the response on which the chosen process variables have much impact. It too computes the association amid the chosen inputs and the response. A set of advanced design of experiment (DoE) techniques is said to be a response surface design that helps to understand better and to optimize the response. The design procedure [21] for RSM follows four stages as listed below.

- (i) Experimental design for satisfactory and trustworthy extent of the response by central composite design
- (ii) Emergence of the second-order mathematical response model by means of the best fit
- (iii) Establishing the optimal solution for investigational variables producing a maximum response
- (iv) Two- and three-dimensional (3D) charts are used to represent the collaborative impacts of process factors

The requisite experimental figures are reliant on the elected design in central composite design [22, 23]. CCD gives ample facts and figures as a multilevel factorial which entails considerably littler experiments more than a complete factorial that are satisfactory to pronounce the majority of steady-state course responses. The factors (variables) investigated were initial concentration, pH, MZTWAC (adsorbent), and interaction time, with adsorption capacity as response. The objective of this current study is to see how the factors interact, and a four-factor second-order polynomial equation was employed in the determination of those statistics. Batch adsorption process is affianced in adsorbing chromium(VI) ion from wastewater. As a result, the process design is more solidified. Table 1 lists the variables and investigational values utilized in the rotatable CCD.

As a result, the design of the process has become more defined. In a summary, the variables and experimental settings utilized in the rotatable central composite design are listed in Table 1 (CCD).

2.2. Batch Adsorption Studies. To build up a 1000 mg/L concentration of chromium(VI) stock solution, dissolve 2.89 g of $K_2Cr_2O_7$ in 1 L of distilled water [24, 25]. Dilution with distilled water is used to create any remaining solutions. Batch adsorption mode experiments were carried out for the specified time duration at a constant rpm using a shaker (manufactured by Remi). Batch adsorption investigations were conducted with chains of conical flasks containing 100 mL chromium(VI) solution. At ambient conditions, the reaction of concentration, pH, adsorbent dosage, and contact time were investigated, culminating in filtration using Whatman filter paper no. 41 [16], and filtrate was stacked to determine the equilibrium concentration of chromium(VI) with the support of a UV/Vis spectrophotometer.

TABLE 1: Chosen process variables.

Variable	Unit	Low value	High value
Initial chromium(IV) ion concentration (<i>A</i>)	mg/L	40	60
pH (<i>B</i>)	Not applicable	4	6
Adsorbent dose (<i>C</i>)	g	0.2	0.4
Contact time (<i>D</i>)	min	60	80

The proportion of chromium(VI) removed was calculated using the equation below [26].

$$\% \text{removal of chromium(VI) ion by adsorption} = \frac{(C_0 - C_t)}{C_0} \times 100, \quad (1)$$

where C_0 denotes the initial chromium(VI) content in mg/L and C_t denotes the chromium(VI) equilibrium concentration in milligrams per litre. The following equation [23, 27] was utilized to compute adsorption capacity of the adsorbent:

$$q_e = \frac{(C_0 - C_t)W}{V}, \quad (2)$$

where q_e represents the quantity of chromium(VI) adsorbed in mg/g, V denotes the solution volume represents in L, and W denotes the adsorbent weight in grams.

3. Results and Discussion

3.1. Properties of MZTWAC. The SEM exhibited in Figure 1 MZTWAC reveals the availability of irregular and porous surface that facilitates the adsorption process to take place [20]. From Figure 2 [19], it is visible that MZTWAC possessed broad peaks, -OH stretching from hydroxyl to phenolic groups [28–30], C-H stretching of aliphatic acids, C-O stretching of alcohols [28, 29], and C-O stretching of carboxylic acid [7] and alcohols.

3.2. Experimental Design and Model Development

3.2.1. Mathematical Model Development and Design of Experiments. The mathematical-statistical quadratic model was assessed by analysis of variance (ANOVA). Critical parameters taken into account have been experimented for their optimized values in adsorption which were figured using the models that may fit and the same were validated. The current experimental work hired fourteen experiment *A*, *B*, *C*, *D*, *AB*, *AC*, *AD*, *BC*, *BD*, *CD*, A^2 , B^2 , C^2 , and D^2 , where *A* is the beginning concentration, *B* is the pH, *C* is the adsorbent dosage, and *D* is the contact period. At this point, the Design Expert has a variety of modeling options for fitting the response, including linear, two-factor interaction (2FI), quadratic, and cubic polynomials, and the evaluation was done to confirm the best model fit based on the R^2 value obtained from sequential model sum of squares. Table 2 is in charge of compiling a model evaluation summary. The programme selected the optimal model for the research project. When compared to other models, the

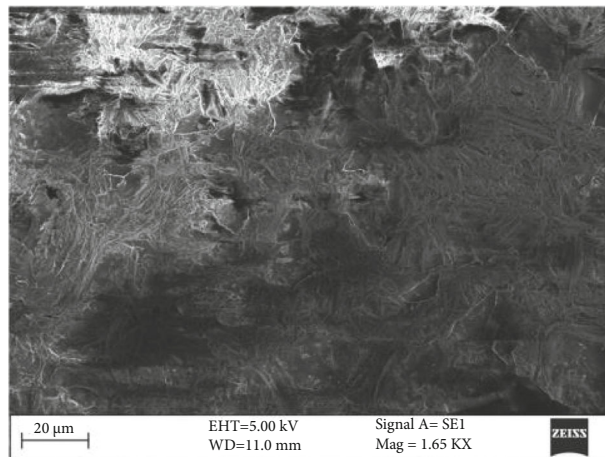


FIGURE 1: SEM image of MZTWAC (source: [19]).

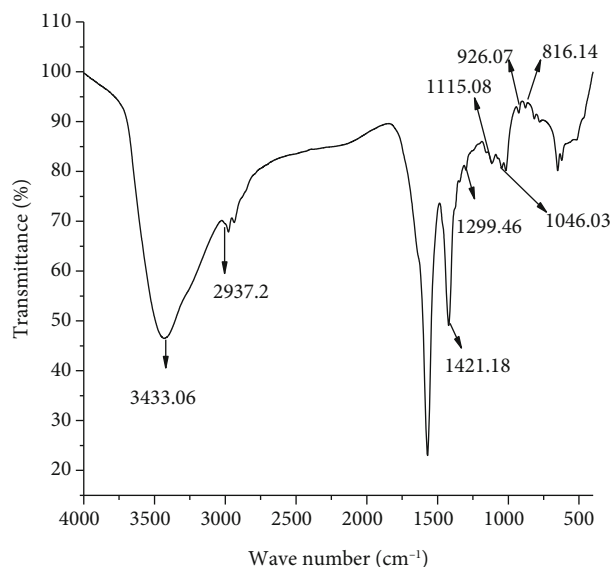


FIGURE 2: FTIR range of MZTWAC (source: [19]).

quadratic model was suggested, while the cubic model was aliased; thus, it must not be used.

3.3. Validation of Quadratic Model. Multiple regression analysis was applied to figure out the coefficients of quadratic model that was intended to fit the results. The noteworthy connotation of autonomous process parameters was studied with 29 batch experiments. From Table 3, the model's F value of 1292.46 entailed that the model is

TABLE 2: Summary data for various models.

Source	Std. dev.	R^2	Adj. R_2	Pred. R^2	PRESS	Results
Linear	2.69	0.836784	0.805696	0.732741	248.4826	
2FI	3.01	0.853407	0.755678	0.574057	396.0193	
Quadratic	0.26	0.999211	0.998206	0.991994	7.44358	Suggested
Cubic	0.16	0.999856	0.999281			Aliased

TABLE 3: ANOVA table.

Source	SS	df	MS	F value	p value Prob > F	Inference
Model	928.97	12	77.41	1292.46	<0.0001	Significant
A	104.38	1	104.38	1742.61	<0.0001	
B	4.39	1	4.39	73.35	<0.0001	
C	392.60	1	392.60	6554.58	<0.0001	
D	6.48	1	6.48	108.23	<0.0001	
AB	1.25	1	1.25	20.87	0.0005	
AC	8.87	1	8.87	148.05	<0.0001	
AD	3.12	1	3.12	52.01	<0.0001	
BD	1.71	1	1.71	28.51	0.0001	
CD	1.27	1	1.27	21.19	0.0005	
A^2	0.36	1	0.36	6.08	0.0284	
B^2	1.02	1	1.02	17.11	0.0012	
C^2	126.41	1	126.41	2110.47	<0.0001	
Residual	0.78	13	0.06			
Lack of fit	0.64	8	0.08	3.0	0.1197	Not significant
Pure error	0.13	5	0.03			
Cor. total	929.75	25				

significant. There is only 0.01% chance that an F value is large, and this could occur due to noise. Values of “Prob > F ” less than 0.0500 indicate the model terms are significant. Here, A , B , C , D , AB , AC , AD , BD , CD , A^2 , B^2 , and C^2 are significant model terms. The rest of the source term values, which are larger than 0.1000 signpost, are not noteworthy and are deliberated as eliminating terms. The “lack-of-fit F value” entails the lack of fit is not significant.

In addition, the ANOVA in Table 4 is supplemented by a variety of indications provided by the Design Expert. Low experimental variance is shown by the standard deviation of 0.247295. The 0.9955 “Pred. R^2 ” and the 0.9984 “Adj. R^2 ” have an excellent correlation, with a difference of less than 0.2. The tolerable precision of 163.9238 indicates that the signal is viable. The signal-to-noise ratio is measured by “Adeq. precision,” and a number greater than 4 is preferable. In summary, the R^2 statistics are excellent since they are near to 1, implying that the regression model offers a substantial connection amid the observed and anticipated values. As a result, this model may be utilized to traverse the design.

The second-order polynomial equation is derived based on RSM results. Equation (3) shows how a particular com-

ponent and the interaction between the four independent process parameters impacted the adsorption process [22].

Adsorption Capacity $Y =$

$$\begin{aligned}
 &12.200 \\
 &+2.895 \quad *A \\
 &-0.598 \quad *B \\
 &-5.219 \quad *C \\
 &+0.630 \quad *D \\
 &0.241 \quad *A * B \\
 &-0.752 \quad *A * C \\
 &+0.621 \quad *A * D \\
 &-0.490 \quad *B * D \\
 &-0.417 \quad *C * D \\
 &+0.282 \quad *A^2 \\
 &-0.199 \quad *B^2 \\
 &+2.709 \quad *C^2.
 \end{aligned}
 \tag{3}$$

TABLE 4: Post-ANOVA statistics.

Std. dev.	0.247295	R^2	0.99919668
Mean	14.91756	Adj. R^2	0.99845516
C.V. %	1.657743	Pred. R^2	0.99554983
PRESS	4.40417	Adeq. precision	163.923897

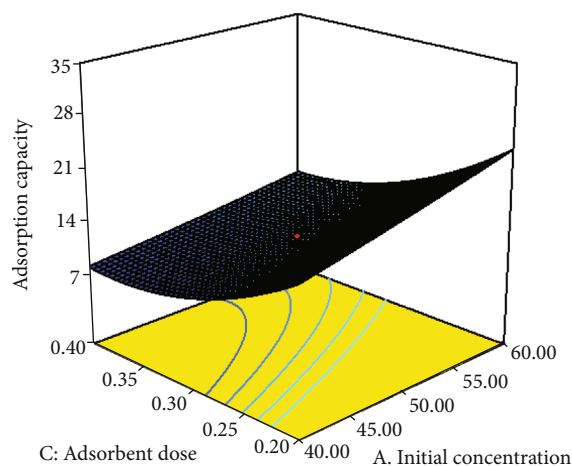


FIGURE 3: Upshot of interface connecting pH and the initial concentration of chromium(VI).

Equation (3), when used with coded variables, may predict the response for different degrees of each element. Obviously, the process variables' higher levels are entered as +1, and the variables' low degrees are coded as -1. When looking at the factor coefficients, the coded condition is expedient for detecting overall influence of variables. Negative and positive coefficients show how considerable metal particles are ejected in a negative or positive way. An optimistic consequence of a factor indicates that response improves as the factor level increases, whereas a negative effect indicates that the reaction does not improve as the factor level increases. As the circumstances show, starting concentration and contact duration have a beneficial impact on chromium(VI) retention, but pH and adsorbent percentage have a negative impact. As a result, as IC increased, so did adsorption ability. In any instance, when the pH and adsorbent fraction increased, the adsorption rate lessened. The relapse equation is graphically shown in the 3D response surface plots shown below (Figures 3–5). The adsorption limit widened as the underlying fixation was amplified from 40 mg/L to 60 mg/L and the pH declined from 6 to 4, as shown in Figure 6. The addition of the adsorption limit was suggested by the high initial fixing of initial concentration and the low pH values. The adsorption limit grew in lockstep with the experiment, even if not as dramatically (Figure 4). Similarly, a large adsorbent dosage did not support the adsorbent's adsorption limit, as shown in Figure 4. Low pH and long contact duration, as seen in Figure 5, resulted in a remarkable adsorption limit for the MZTWAC.

3.4. Capability of Model. Analytic plots, with predicted versus definite and normal probability plot that has studentized

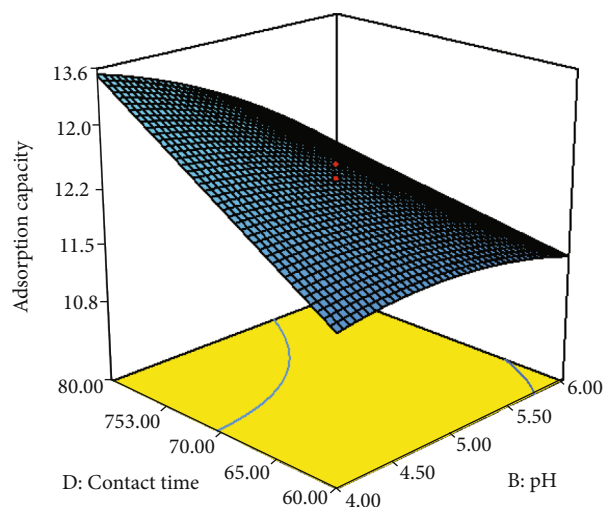


FIGURE 4: Upshot of interface connecting MZTWAC (adsorbent dose) and the initial concentration of chromium(VI).

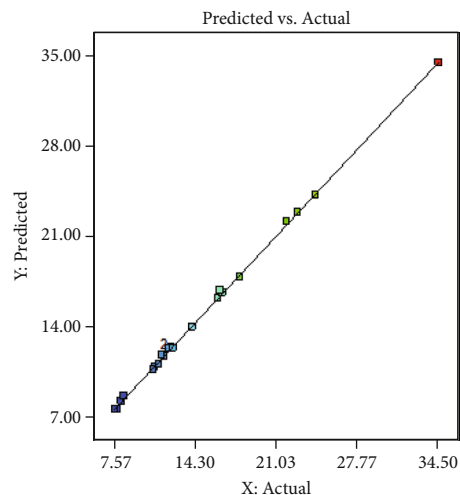


FIGURE 5: Upshot of interface connecting pH and the contact time.

residuals, are used to assess the adequacy of the numerical model and to analyse the relapsing model's sufficiency. Figure 6 depicts the association amid the actual and projected adsorption limits. The graph demonstrates proclivities in straight relapse fit, and the model effectively describes the trial run under consideration. Furthermore, it establishes a strong link between the data gathered through testing and the predictions made by the regression model meant for the chromium adsorption process (VI).

The normal probability plot (Figure 7) is also regarded as the most appropriate graphical method for verifying and

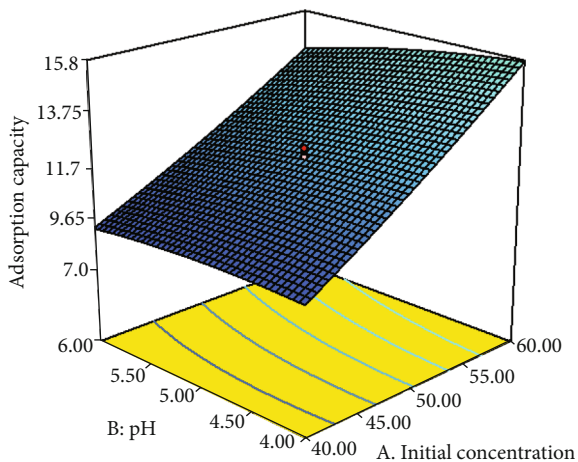


FIGURE 6: Interface connecting the actual and anticipated figures of adsorption capacity.

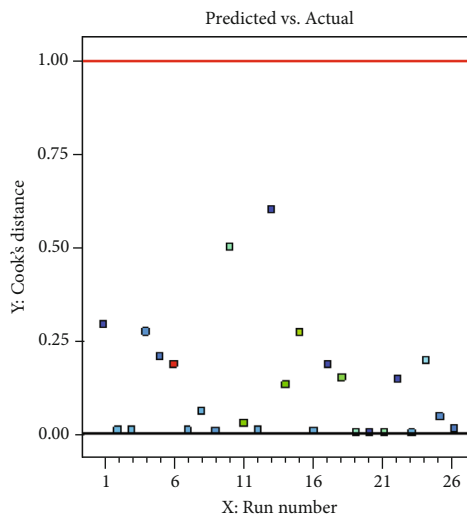


FIGURE 9: Cook's distance.

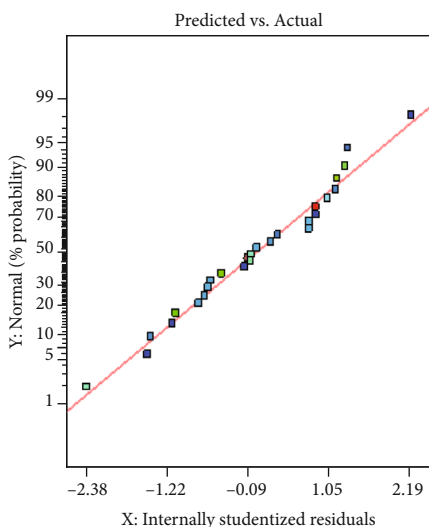


FIGURE 7: Normal probability design.

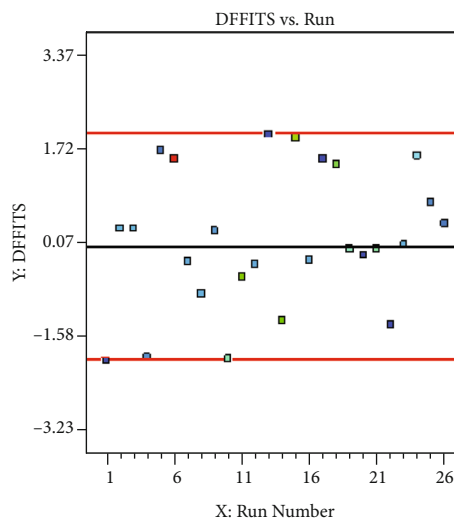


FIGURE 10: DEFFITS vs. run number.

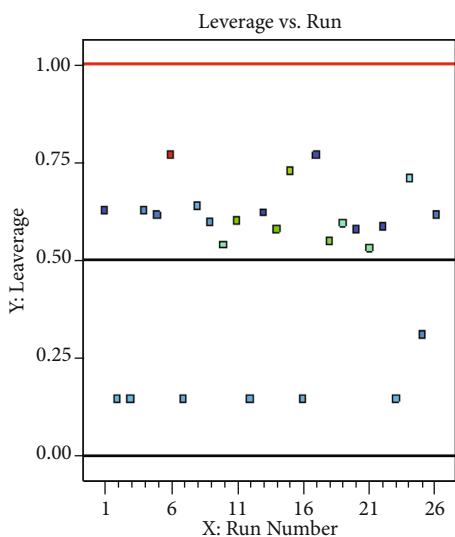


FIGURE 8: Leverage vs. run.

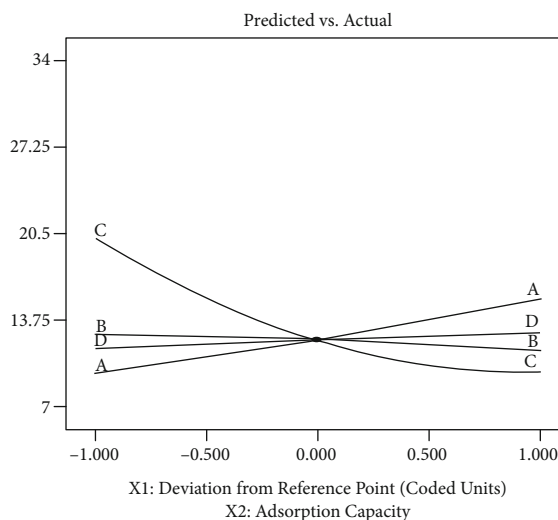


FIGURE 11: Perturbation plot.

TABLE 5: Numerical optimization report showing optimized predicted adsorption capacity and calculated %removal of chromium(VI).

Adsorbent	Adsorbate	Initial concentration (mg/L)	Process variables		Contact time (min)	Predicted adsorption capacity (mg/g)	Desirability value	%removal (calculated)
			pH	Adsorbent dose (g)				
MZTWAC	Chromium(VI)	59.98	4.08	0.2	80	26.279	0.694	87.629

evaluating normality of the residual. The aforementioned depicts residual behaviour that tracks a normal distribution and is straight, i.e., dispersal of residuals in a regular manner with minimal divergences. It is discovered that the model is suitable meant for the evacuation of chromium(VI) during the adsorption method when MZTWAC is used.

3.5. Influence Plots. The model's residuals are roughly parallel to the straight line. Although they appear to follow a normal probability distribution, the residuals explicit minimal deviation from normalcy. To examine the impact of outliers, it is never needed that the mistakes be genuinely regularly distributed in general terms. In this examination, Design Expert is used to create several graphical representations of the residuals. Estimates of the leverage (influence), Cook's distance, and DFFITS plots are requested to examine the regression model's exactness to discover the statistical features of the experimental model. Figure 8 shows that the influence statistics were all in the range of 0 to 1 [31]. There is no information which emphasizes that there is an unreasonably negative impact on the model fit because the effects of all run values in the current evaluation are less than 1. Figure 8 shows that the influence values were all within the range of 0 to 1 [31]. There are no information foci that have an unreasonably negative impact on the model fit because the effects of all run values in the current evaluation are less than 1.

Additionally, Cook's distance (Figure 9) estimates the impact of erasing a certain observation and is used to govern the outlier in the data (data). It must fall between the ranges of +1 and -1. Apart from DFFITS plots, Figure 10 assesses the influence of observed values on its projected value, and its run is in the centre of the typical farthest that reaches +2 to -2.

3.6. Outcome of Independent Variables. Tsai and Wu [32] used a case-weight perturbation plan in 1992 to get an elective nearby impact indicator that considers the Jacobian perturbation consequences. However, in this study, a perturbation diagram (Figure 11) was plotted to consider the relationship between four independent factors, pH, adsorbent dose, contact time, and initial concentration, in the adsorption procedure aimed at the removal of chromium(VI), as well as their contrasting impact on the response.

The response acquired by operation Design Expert is assessed by altering only one variable while keeping the other components constant. Although the starting concentration (A) line goes upward on the opposite side, the perilous slant down of adsorbent dosage (C) and pH (B) reveals that adsorption capacity is subtle to adsorbent dose

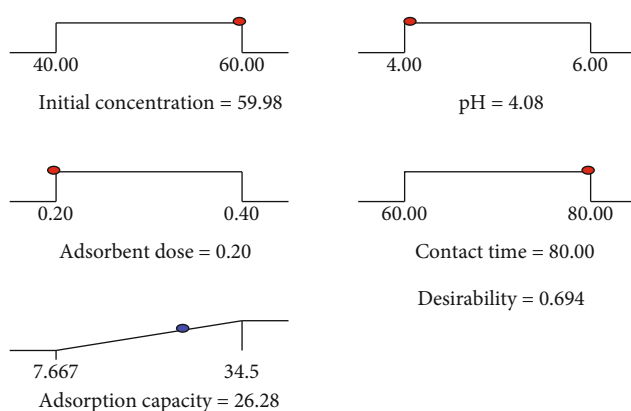


FIGURE 12: RAMP plot for adsorption of chromium(VI) by MZTWAC.

(C) followed by pH (B) for expulsion. It shows that adsorption capability for removing chromium(VI) increases with increasing chromium(VI) concentration (A), but declines with growing adsorbent dosage (C) and pH (B).

Initially concentration (A) and adsorbent dosage (C) were additionally profound to the adsorption process than changing pH (B) and contact duration, according to the perturbation plot (D). Nevertheless, the perturbation plot reveals that pH, adsorbent dosage, contact duration, and beginning concentration all have a significant influence on adsorption capacity in the chromium(VI) expulsion proficiency.

3.7. Optimization of the Process Variable. Exploratory data is used to ensure the most accurate estimates of variables for chromium(VI) expulsion by MZTWAC from the model. The optimization of multiple response models is done using the desirability function. It is filled out as target work and used to create a custom mix of process parameters ahead of time. For each element and reaction, Design Expert provides five alternative objectives: maximize, reduce, target, in range, and set to a precise number. In this current study, the desired target for adsorption capacity was set to 1 maximum and "in the range" for four independent variables such as starting concentration, pH, contact duration, and adsorbent dosage.

The analysis of desirability predicted that the desirability for the response function selected is furnished in detail in Table 5. The RAMP plot (Figure 12) depicts that 26.279 mg/g is an optimized response while the independent variables are 59.98 mg/L (initial concentration), 4.08 (pH), 0.2 g (adsorbent dosage), and 80 minutes at maximum desirability.

4. Concluding Remarks

The high match was established among the experimental value and predicted value of the adsorption capacity in the optimization procedure of chromium(VI) adsorption by MZTWAC which recommended that the model chosen was an excellent fit. Auxiliary inference was that the optimized outcome acknowledged from the plots of RAMP that the activated carbon fabricated from *Manilkara zapota* tree is the best choice in removing chromium(VI) ion from aqueous solution and it is economically worthy too. The inclusion of central composite design in the experimental study reduced the experimentation work, and the optimum results were arrived for the chosen process parameters. The response surface methodology conferred a clear picture between the process parameter interactions through the three-dimensional images. Many adsorbents such as aluminum–lanthanum mixed oxyhydroxide (ALMOH), chitosan/aluminum–lanthanum mixed oxyhydroxide (CSALMOH), ionic solid impregnated phosphate chitosan, and PAN–CNT/TiO₂–NH₂ have been involved in the removal of chromium ion with the adsorption capacity of 49.8, 78.9, 266.67, and 714.27 mg/g, respectively. The more water pollution, the more there is a want of a new adsorbent to treat polluted water to make safe water either to be disposed of or be reused. In this context, MZTWAC is best suited which costs low and is efficient as well.

Data Availability

The data used to support the findings of this study are included within the article. Should further data or information be required, these are available from the corresponding author upon request.

Disclosure

The study was performed as a part of the employment of Mettu University, Ethiopia.

Conflicts of Interest

The authors declare that there are no conflicts of interest regarding the publication of this paper.

Acknowledgments

The authors appreciate the technical assistance to complete this experimental work from the Department of Mechanical Engineering, K. Ramakrishnan College of Technology, Trichy, Tamil Nadu, India. The authors thank the technical assistance to complete this experimental work. This research was funded by University Researchers, supporting project number TURSP2020/91, Taif University, Taif, Saudi Arabia.

References

- [1] I. M. Goklany, "Have increases in population, affluence and technology worsened human and environment well-being?," *The Electronic Journal of Sustainable Development*, vol. 1, no. 3, pp. 3–28, 2009.
- [2] L. Jarup, "Hazards of heavy metal contamination," *British Medical Bulletin*, vol. 68, no. 1, pp. 167–182, 2003.
- [3] R. Vinodhini and M. Narayanan, "Bioaccumulation of heavy metals in organs of fresh water fish *Cyprinus carpio* (common carp)," *International Journal of Environmental Science and Technology*, vol. 5, no. 2, pp. 179–182, 2008.
- [4] J. J. Beaumont, R. M. Sedman, S. D. Reynolds et al., "Cancer mortality in a Chinese population exposed to hexavalent chromium in drinking water," *Epidemiology*, vol. 19, no. 1, pp. 12–23, 2008.
- [5] A. B. Duwiejuah, S. J. Cobbina, and N. Bakobie, "Review of eco-friendly biochar used in the removal of trace metals on aqueous phases," *International Journal of Environmental Bioremediation & Biodegradation*, vol. 5, no. 2, pp. 27–40, 2017.
- [6] M. Wiemann, K. Schirmacher, and D. Busselberg, "Interference of lead with the calcium release activated calcium flux of osteoblast-like cells," *Calcified Tissue International*, vol. 65, no. 6, pp. 479–485, 1999.
- [7] M. N. Younis, M. S. Saeed, S. Khan, M. U. Furqan, R. U. Khan, and M. Saleem, "Production and characterization of biodiesel from waste and vegetable oils," *Journal of Quality and Technology Management*, vol. 5, no. 1, pp. 111–121, 2009.
- [8] E. El-Bestawy, M. A. Rass, and M. A. Abdel-Kawi, "Removal of chromium(VI) and oil hydrocarbon from oil refining-contaminated wastewater using *Pseudomonas* spp.," *Journal of Natural Science Research*, vol. 3, no. 11, pp. 112–124, 2013.
- [9] S. Khaoya and U. Pancharoen, "Removal of lead (II) from battery industry wastewater by HFSLM," *International Journal of Chemical Engineering and Applications*, vol. 3, no. 2, pp. 98–103, 2012.
- [10] S. T. Mughal, T. Shafique, and T. Aftab, "Treatment of electro plating effluent," *Journal of the Chemical Society of Pakistan*, vol. 30, no. 1, pp. 29–32, 2008.
- [11] S. R. Tariq, M. H. Shah, N. Shaheen, A. Khaliq, S. Manzoor, and M. Jaffar, "Multivariate analysis of trace metal levels in tannery effluents in relation to soil and water: a case study from Peshawar, Pakistan," *Journal of Environmental Management*, vol. 79, no. 1, pp. 20–29, 2006.
- [12] L. Agwarambo, N. Magee, S. Nunez, and K. Mitt, "Biosorption and chemical precipitation of Lead using biomaterials, molecular sieves, and chlorides, carbonates, and sulfates of Na & Ca," *Journal of Environmental Protection*, vol. 4, no. 11, pp. 1251–1257, 2013.
- [13] M. S. Oncel, A. Muhcu, E. Demirbas, and M. Kobya, "A comparative study of chemical precipitation and electrocoagulation for treatment of coal acid drainage wastewater," *Journal of Environmental Chemical Engineering*, vol. 1, no. 4, pp. 989–995, 2013.
- [14] R. W. Peters, Y. Ku, and D. Bhattacharyya, "Evaluation of recent treatment techniques for removal of heavy metals from industrial wastewaters," *Separation of Heavy Metals, AIChE Symposium Series*, vol. 81, no. 243, pp. 165–203, 1985.
- [15] M. Danish, R. Hashim, M. Rafatullah, O. Sulaiman, and A. Ahmad, "Adsorption of Pb(II) ions from aqueous solutions by date bead carbon activated with ZnCl₂," *Clean-Soil, Air, Water*, vol. 39, no. 4, pp. 392–399, 2011.
- [16] S. Sujatha, G. Venkatesan, and R. Sivarethinamohan, "Principal determinants of toxicity reduction by de-oiled soya using multivariate statistics: principal component analysis and multiple linear regression analysis," *Applied Ecology and Environmental Research*, vol. 15, no. 3, pp. 1717–1737, 2017.

- [17] J. Konczyk, C. Kozłowski, and W. Włakowiak, "Lead (II) removal from aqueous solutions by solvent extraction with tetra carboxylresorcin (4) arene," *Physicochemical Problems in Mineral processing*, vol. 49, no. 1, pp. 213–222, 2013.
- [18] R. K. Jadhao, "Application of electro-dialysis (ED) to remove divalent metals ions from waste water," *International Journal of Chemical Sciences and Applications*, vol. 4, no. 1, pp. 68–72, 2013.
- [19] S. Sujatha, G. Venkatesan, and R. Sivarethinamohan, "Optimization of lead removal in exhausting *Manilkara zapota* based activated carbon: application of response surface methodology," *Environmental Technology*, vol. 41, no. 19, pp. 2478–2493, 2019.
- [20] S. Sujatha and R. Sivarethinamohan, "Investigation of detoxification nature of activated carbons developed from *Manilkara zapota* and de oiled soya," *Materials today Proceeding*, vol. 21, no. 1, pp. 663–668, 2019.
- [21] J. Kwak, "Application of Taguchi and response surface methodologies for geometric error in surface grinding process," *International Journal of Machine Tools & Manufacture*, vol. 45, no. 3, pp. 327–334, 2005.
- [22] A. R. Khatee, M. Fathinia, S. Aber, and M. Zarei, "Optimization of photocatalytic treatment of dye solution on supported TiO₂ nanoparticles by central composite design: intermediates identification," *Journal of Hazardous Materials*, vol. 181, no. 1–3, pp. 886–897, 2010.
- [23] B. Sadhukhan, N. K. Mondal, and S. Chattoraj, "Optimisation using central composite design (CCD) and the desirability function for sorption of methylene blue from aqueous solution onto *Lemna major*," *Karbala International Journal of Modern Science*, vol. 2, no. 3, pp. 145–155, 2016.
- [24] N. Khatoon, A. H. Khan, V. Pathak, N. Agnihotri, and M. Rehman, "Removal of hexavalent chromium from synthetic waste water using nano zero valent iron (NZVI) as adsorbent," *International Journal of Innovative Research in Science, Engineering and Technology*, vol. 2, no. 1, pp. 6140–6149, 2013.
- [25] S. A. Wanees, A. M. M. Ahmed, M. S. Adam, and M. A. Mohamed, "Adsorption studies on the removal of hexavalent chromium contaminated wastewater using activated carbon and bentonite," *Chemistry Journal*, vol. 2, no. 3, pp. 95–105, 2012.
- [26] A. M. El-Wakil, W. M. A. El-Maaty, and F. S. Award, "Removal chromium(VI) from aqueous solution on activated carbon and modified activated carbon prepared from dried water hyacinth plant," *Journal Analytical & Bioanalytical*, vol. 5, no. 2, pp. 1–14, 2014.
- [27] M. A. Ackacha and L. A. Elsharif, "Adsorption removal of lead ions by acacia *Tortilis* leaves: equilibrium, kinetics and thermodynamics," *International Journal of Environmental Science and Development*, vol. 3, no. 6, pp. 584–589, 2012.
- [28] S. F. S. Draman, N. Mohd, N. H. I. Wahab, N. S. Zulkfli, and N. F. A. A. Bakar, "Adsorption of lead(II) ions in aqueous solution using selected agro-waste," *ARPJ Journal of Engineering and Applied Sciences*, vol. 10, no. 1, pp. 297–300, 2015.
- [29] C. Suresh, Y. Harinath, R. B. Naik, and K. Seshaiiah, "Removal of Pb (II) from aqueous solution by citric acid modified manilkara: equilibrium and kinetic studies," *Journal of Chemical and Pharmaceutical Research*, vol. 7, no. 4, pp. 1161–1174, 2015.
- [30] T. Wang, W. Zhang, and X. Lu, "Preparation and Cu (II) adsorption characteristics of carboxymethyl cross-linked sewage sludge," *Polish Journal of Environmental Studies*, vol. 25, no. 2, pp. 805–811, 2016.
- [31] B. Das, "Response surface modeling of copper (II) adsorption from aqueous solution onto neem (*Azadirachta indica*) bark powder: central composite design approach," *Journal of Material Environmental Science*, vol. 8, no. 7, pp. 2442–2454, 2017.
- [32] Z. Al-Qodah and R. Shawabkha, "Production and characterization of granular activated carbon from activated sludge," *Brazilian Journal of Chemical Engineering*, vol. 26, no. 1, pp. 127–136, 2009.

Research Article

Biogenic Synthesis of Magnetite Nanoparticles Using Leaf Extract of *Thymus schimperi* and Their Application for Monocomponent Removal of Chromium and Mercury Ions from Aqueous Solution

Sintayehu Tamenne Geneti,¹ Gemechis Asfaw Mekonnen,¹ H. C. Ananda Murthy ¹,
Endale Tsegaye Mohammed,² C. R. Ravikumar,³ Bedasa Abdisa Gonfa ¹,
and Fedlu Kedir Sabir ¹

¹Department of Applied Chemistry, School of Applied Natural Science, Adama Science and Technology University, P.O. Box 1888, Adama, Ethiopia

²Department of Chemistry, College of Natural Science, Hawassa University, P.O. Box 05, Hawassa, Ethiopia

³Research Center, Department of Science, East West Institute of Technology, VTU, Bengaluru 560091, India

Correspondence should be addressed to Bedasa Abdisa Gonfa; bedassa.abdissa@astu.edu.et
and Fedlu Kedir Sabir; fedluked130@gmail.com

Received 11 October 2021; Revised 2 March 2022; Accepted 2 April 2022; Published 15 April 2022

Academic Editor: Dong Kee Yi

Copyright © 2022 Sintayehu Tamenne Geneti et al. This is an open access article distributed under the Creative Commons Attribution License, which permits unrestricted use, distribution, and reproduction in any medium, provided the original work is properly cited.

Currently, plant templated synthesis of magnetite iron oxide nanoparticles (Fe_3O_4 NPs) was emerged for multifunctional purposes. In this study, the leaf extract of the plant *Thymus schimperi* was utilized to synthesize Fe_3O_4 NPs. The synthesized NPs were characterized by using technical tools such as X-ray diffraction (XRD) spectroscopy, Fourier transform infrared (FT-IR) spectroscopy, scanning electron microscopy-energy dispersive X-ray (SEM-EDX) analysis, and ultraviolet-visible (UV-Vis) spectroscopy, and thermal analysis (TGA-DTA). The XRD result corroborated the presence of desired phase formation having pure cubic face centered phase structure with average crystallite particle size ranging from 20 nm to 30 nm. SEM micrographs confirmed microstructural homogeneities and remarkably different morphology of Fe_3O_4 NPs. Mercury (II) and chromium (VI) removal efficiencies of Fe_3O_4 NPs were found to be 90% and 86% from aqueous solution at initial concentration of 20 mg/L, respectively. Various factors which affect the metal ion removal efficiency such as metal ion initial concentrations, pH, contact time, and adsorbent dosage were also studied. The optimum pH and contact time for chromium ion adsorption were pH 5 and 60 min and that of mercury were observed to be pH 7 and 90 min, respectively. The Langmuir isotherm was best fitted for sorption of Hg(II) ion, and the Freundlich isotherm was best fitted with sorption of Cr(VI) ion onto the surface of Fe_3O_4 NPs. The mechanism of adsorption of both Hg(II) and Cr(VI) ions was obeyed pseudo 2nd order kinetics. The recorded percent removal efficiencies revealed that these Fe_3O_4 NPs synthesized through leaf extract of the plant called *Thymus schimperi* have demonstrated excellent potentiality in the remediation of heavy metal ions. The synthesized Fe_3O_4 NPs were regenerated (reused) for adsorptive removal of Hg(II) and Cr(VI) for five consecutive cycles without significant loss of removal efficiency. Fe_3O_4 NPs were reused with only 4.17% loss of removal efficiency against Hg(II) and only 3% loss of removal efficiency against Cr(VI) metal ions.

1. Introduction

Pollution of water bodies due to some toxic heavy metal ions is increasing day by day because of increased environmental population and industrialization. Due to their hazardousness, non-biodegradability, and their long-time tenacity in nature, removal of these heavy metals from water bodies is very important [1]. Different types of techniques currently used in the removal of heavy metals from wastewater are ion exchange flotation, membrane separation, adsorption, precipitation, biosorption, and electrochemical treatment processes [2–5]. In current days, most widely employed approach for the removal of heavy metal ions from water is adsorption process. Various types of adsorbent materials have got application in the removal of heavy metals, including activated carbon [2], silica gel supported materials [6], nanocellulose materials [7, 8], and metal oxides [9]. Among these mentioned adsorbent materials, magnetite nanomaterials (Fe_3O_4) NPs have distinguished themselves by their unique properties, such as larger surface area to volume ratio, magnetic nature, diminished consumption of chemicals, and has no contribution for secondary pollutants [9]. For the removal of heavy metal ions from contaminated water, magnetic separation has been combined with adsorption so as to enhance the decontamination process [10].

The interest in Fe_3O_4 NPs for heavy metal ions remediation has been increasing due to their enhanced reactivity as a result of very high surface area to volume ratio [11]. Fe_3O_4 NPs have gained special attention in water purification to remove cationic pollutants like heavy metals and dyes which could be attributed to their high separation efficiency, superior magnetic properties, simple manipulation process, placid operation conditions, and easy functionalization methods [12–14].

Synthesis of metal and metal oxide nanoparticles (NPs) using the extracts from different parts (mostly leaf) of the plant is the most effective, economical, and eco-friendly method. Plant extract mediated synthesis has recently gained significance due to its simplicity. The processes adopted for synthesizing metallic and metal oxide NPs by the application of plant extracts were explored to be easily scalable and more economical compared to the other methods which depend completely on the microbes and whole plants [15].

The two prominent toxic and carcinogenic metal ions, Hg(II) and Cr(VI), are normally found in various wastewaters from many industries including plating, mining, battery, and tanneries. Their accumulation in living organisms resulted in varieties of disorders and diseases [16]. Reports have shown that the concentration of Cr(VI) and Hg(II) ions in wastewater in Africa is above the WHO's permissible limit [17, 18]. Concentration of Cr(VI) in industrial wastewater is estimated in the range of 0.1 to 200 mg/L and recommended safe limit of Cr(VI) in drinking water is 0.05 mg/L [18, 19], and permissible concentration of Hg(II) in wastewater is 0.05 mg/L [18, 19] and that of recommended safe limit in drinking water is 0.001 mg/L [20, 21].

The recent surveys conducted by the U. S. Environment Protection Agency (EPA) on national water quality indicated that more than one-third of the lakes and about half

of the rivers across the nation are getting polluted by the noxious discharges such as Hg(II) and chromium (VI) from industrial facilities [22].

Since mercury (II) and chromium (VI) pollution has been a significant challenge in the world; the researchers in the area are striving a lot to alleviate this problem. Towards this contribution, the present work was aimed to synthesize Fe_3O_4 NPs using leaf extract of the plant *Thymus schimperi*, and apply it for the remediation of Hg(II) and Cr(VI) ions from wastewater.

The plant *Thymus schimperi*, is a grass-like indigenous plant (Figure 1s in supplementary section) in Ethiopia and commonly known by its local name as “*Tosign*” [23], is used as reducing agent and capping agent in synthesis of Fe_3O_4 NPs in this work.

In this study, *Thymus schimperi* leaf extract templated synthesis of Fe_3O_4 NPs was done by one reaction pot. The synthesized Fe_3O_4 NPs used as adsorbent materials for removal of Hg(II) and Cr(VI) ions from wastewater. The optimization of parameters such as pH, contact time and initial concentration of aqueous solutions, and adsorbent doses was performed against a set of batch adsorption of Hg(II) and Cr(VI) ions from wastewater. The kinetics of adsorption and isotherm models was evaluated to propose mechanism of adsorption.

2. Experimental Methods

2.1. Chemicals and Reagents. The chemicals (analytical grade) and reagents used in this work were ferric chloride hexahydrate ($\text{FeCl}_3 \cdot 6\text{H}_2\text{O}$, Blulux Ltd, India), ferrous chloride tetrahydrate ($\text{FeCl}_2 \cdot 4\text{H}_2\text{O}$, Atico, India), potassium dichromate ($\text{K}_2\text{Cr}_2\text{O}_7$, Blulux Ltd, India), mercury (II) chloride (HgCl_2 , Blulux Ltd, India), sodium hydroxide (NaOH), ethanol (99.9%), HCl, H_2SO_4 , KMnO_4 , diphenylcarbazide (DPC) (Ranchem Industry and Trading, India), and distilled water.

2.2. Collection of Plant Leaves. Fresh, matured, and disease-free leaves of the plant, *Thymus schimperi*, were collected from Chilalo Mountain, East Arsi Zone, Oromia, Ethiopia, after conducting prior field surveys. The collected leaves of *Thymus schimperi* were used to make the aqueous extracts.

2.3. Preparation of *Thymus schimperi* Leaf Extract. The plant leaves were washed by using domestic water and then rinsed with distilled water many times. The wet leaves were allowed to air dry under shade at room temperature. The dried plant leaves were then stored for further use.

A 10 gm of powder of the plant leaves was boiled with 200 mL of distilled water under stirring at 80°C for about one hour until the color of the aqueous solution changes to light brown. The aqueous extract of the sample was cooled and filtered first with ordinary filter paper and then using Whatman filter paper. Then, the filtrate was stored in a refrigerator at 4°C for further experiments [24–26]. Figure 1 shows the flow chart of extraction of active compounds from powders of leaves of *Thymus schimperi* in distilled water.

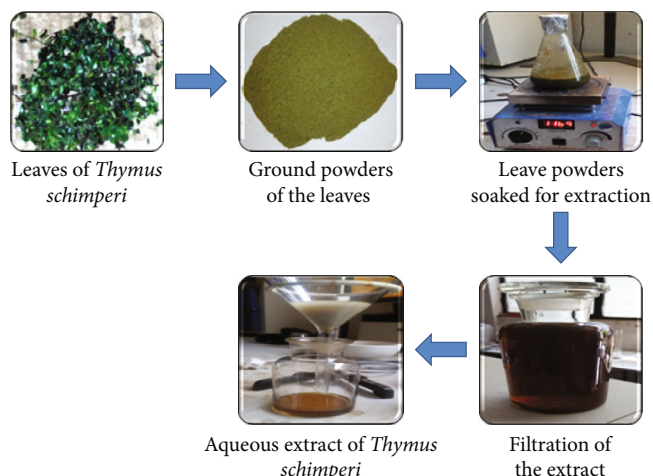


FIGURE 1: Flow chart of the extraction of active compounds from the powders of leaves of *Thymus schimperi* in distilled water.

2.4. Preparation of Precursor Salt Solution. Ferric chloride ($\text{FeCl}_3 \cdot 6\text{H}_2\text{O}$) and ferrous chloride ($\text{FeCl}_2 \cdot 4\text{H}_2\text{O}$) salt solutions were used in the synthesis of Fe_3O_4 NPs [27] using aqueous extract of *Thymus schimperi*. Ferric/ferrous salt precursor solutions were prepared by mixing and dissolving 13.6 gm of $\text{FeCl}_3 \cdot 6\text{H}_2\text{O}$ and 5 gm of $\text{FeCl}_2 \cdot 4\text{H}_2\text{O}$ salts in 500 mL of distilled water in 1000 mL volumetric flask. The mixture was stirred at room temperature for about 15 minutes and then stored for further use. Then, three different samples were prepared by taking different volume ratios of precursor salts solution with *Thymus schimperi* leaf extract.

2.5. Biogenic Synthesis of Fe_3O_4 NPs. In a typical experiment, the extract was added to ferric/ferrous chloride precursor solution in three different volume ratios. 50 mL of the extract was added to 100 mL of the precursor solution with 2 M NaOH for NPs (S12) preparation in one 250 mL conical flask, and then the solution mixture was labelled as (1:2). The second solution mixture (S11) was prepared by the addition of 100 mL of the extract to 100 mL of the precursor solution (1:1) with 2 M NaOH for NPs (S11) preparation in the second 250 mL conical flask. In the same way, the third solution mixture (S21) was prepared by adding 100 mL of the extract to 50 mL of the precursor solution (2:1) with 2 M NaOH. All the solutions were stirred continuously at 60°C for 1 hour to get a black precipitate (Figure 2). The precipitates were filtered using Whatman filter paper No 1 and washed repeatedly using distilled water and ethanol to remove impurities. Finally, the precipitate was dried in an oven at 60°C for 1 hour and ground to get fine powder. The black powder obtained was later calcined at 700°C for 1 hour [28].

2.6. Characterization Techniques. Thermal analysis was conducted using DTA-TGA instrument (DTG-60H, Shimadzu Co., South Korea) in order to decide the calcination temperature and to study thermal stability of the synthesized Fe_3O_4 NPs. A small amount of the powder was taken and the crys-

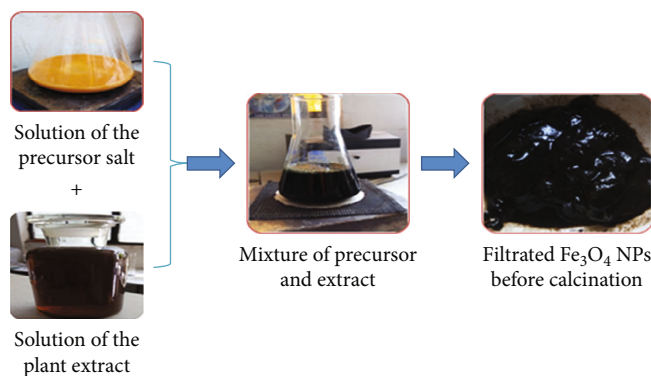


FIGURE 2: The schematic diagram of synthetic procedure for Fe_3O_4 NPs.

tal structure of the Fe_3O_4 NPs was studied by using XRD-7000 X-Ray diffractometer, Shimadzu Co., Japan.

The FT-IR spectra of the synthesized Fe_3O_4 NPs were recorded using the instrument, Perkin Elmer65, PerkinElmer, Inc., Waltham, USA [29]. SEM-EDX (Carl Zeiss Model: Neon-40, FESEM/FIB, SMT, AG, Germany) analysis was also conducted to know the external morphology and chemical composition of the sample [30]. UV-Vis-diffuse reflectance spectrophotometer (Elico SL-150) was employed to measure the band gap energy of Fe_3O_4 NPs using Tauc equation (1), [31].

$$(\alpha h\nu)^{1/n} = A(h\nu - E_g), \quad (1)$$

where

α = absorption coefficient constant

$h\nu$ = photon energy

E_g = energy gap

$n = 1/2$ for allowed direct transition (Fe_3O_4 NPs)

$n = 2$ for allowed indirect transition

2.7. Preparation of Chromium (VI) and Mercury (II) Solutions. The stock solution of Cr(VI) was prepared by dissolving 2.826 g of $\text{K}_2\text{Cr}_2\text{O}_7$ in 1 L of distilled water. Similarly, 1.354 g of HgCl_2 was taken in 1 L of distilled water to get stock solution of Hg(II). The stock solutions were further subjected to dilution to obtain the desired concentration of standard solutions for absorbance measurement. 1, 5-diphenylcarbazide was used for spectrophotometric determination of Cr(VI). Potassium permanganate (KMnO_4) solution was prepared for color development of the mercury ion solution after adsorption. Full color development for these two solutions was formed and after 10 min, 4 mL of these solutions was used in an absorbance measurement cell (cuvette) and the concentrations were measured spectroscopically at 540 nm for chromium solution [32] and at 253.7 nm for mercury solution in UV spectrophotometer [33, 34].

2.8. Batch Adsorption Study. Batch adsorption studies were conducted to evaluate the efficiency of Fe_3O_4 NPs for the remediation of chromium (VI) and mercury (II) ions from the aqueous solutions. All the measurements were

performed in triplicates and the average values were reported. All the studies were executed at a temperature of 25°C (± 0.5). The required pH of the solution was obtained by adding appropriate amounts of a mixture that contains solutions of 0.1 M NaOH and 0.1 M HCl. A calculated amount of the adsorbent was added to the sample with continuous agitation to attain adsorption equilibrium. The extent of removal of chromium and mercury ions was investigated separately by changing adsorption dose (100 mg, 300 mg, 500 mg, and 700 mg), contact time (30 min, 60 min, 90 min, and 120 min), initial concentration (20 mg/L, 40 mg/L, 60 mg/L, and 80 mg/L), and pH of the solution (3, 5, 7, 9, and 11). After adsorption, the separation of the adsorbent was achieved by filtration and the initial and final metal concentrations were deduced. The equilibrium adsorption capacity (Q_e) was calculated according to equation (2)

$$Q_e = \left(\frac{C_o - C_e}{M} \right) V, \quad (2)$$

where

Q_e = equilibrium adsorption capacity (mg/g)

C_o = initial liquid phase solute concentration (mg/L)

C_e = equilibrium liquid phase solute concentration (mg/L)

V = liquid phase volume (L)

M = amount of adsorbent (g)

In the same way, the present removal efficiency (%) of Fe₃O₄ NPs for chromium (VII) and mercury (II) heavy metals was deduced using the equation (3)

$$\text{Removal efficiency (\%)} = \frac{C_o - C_e}{C_o} \times 100, \quad (3)$$

where C_o and C_e are the initial and equilibrium concentration after treatment with adsorbent. Optimum period of time to achieve maximum percent removal was determined.

2.9. Sorption Kinetics and Isotherm Studies

2.9.1. Sorption Kinetics Studies. The kinetics parameters associated with the adsorption process were determined for contact time varying between 1 and 120 min by monitoring the removal percentage for the Cr(VI) and Hg(II) ions.

2.9.2. Pseudo-First-Order Model. Pseudo-first-order rate model based on adsorption capacity of adsorbent is generally expressed as:

$$\log (Q_e - Q_t) = \log Q_e - k_1 t, \quad (4)$$

where Q_e and Q_t are the amounts (mg/g) of Cr(VI) and Hg(II) adsorbed at equilibrium and at time given (t), respectively.

Plot of $\log (Q_e - Q_t)$ versus t gives a straight line for the 1st order adsorption kinetics through which rate constant k_1 is determined (Figure 2s in supplementary section).

2.9.3. Pseudo-Second-Order Model. The following equation describes the pseudo-second-order model in the linear form,

$$\frac{t}{q_t} = \frac{1}{k_2 q_e^2} + \frac{1}{q_e} t, \quad (5)$$

where

k_2 = adsorption rate constant (g/mg-min)

k_2 and q_e are found from the intercept and slope of t/q_t versus t linear plot such that $q_e = 1/\text{slope}$ and $k_2 = \text{slope}^2/\text{intercept}$

2.9.4. Sorption Isotherm Studies. The interaction between the solute particles and the adsorbent is provided by the adsorption isotherm. The Langmuir and Freundlich models are usually applied to explore equilibrium adsorption isotherms.

2.9.5. Langmuir Isotherm. The Langmuir isotherm (assumes monolayer adsorption) is represented by,

$$\frac{C_e}{q_e} = \frac{K_L C_e}{Q_o} + \frac{1}{Q_o}, \quad (6)$$

where q_e (mg/g) and C_e (mg/L) are the amount of adsorbed chromium or mercury per unit mass of sorbent and unadsorbed chromium or mercury concentration in solution at equilibrium, respectively. Q_o is the maximum adsorption at monolayer (mg g^{-1}) on the surface bound at high C_e , and K_L is a constant related to the affinity of the binding sites (L/mg).

The Langmuir constants Q_o and K_L were determined from the intercept and slope of the linear plot of (C_e/q_e) against the equilibrium concentration (C_e).

2.9.6. Freundlich Isotherm. Freundlich isotherm (an empirical equation) is usually employed to describe heterogeneous systems.

The Freundlich equation is expressed as:

$$q_e = K_f C_e^{1/n} \quad (7)$$

where K_f and n are Freundlich constants with K_f ($\text{mg/g (L/mg)}^{1/n}$) is the adsorption capacity of the sorbent and n giving an indication of how favorable the adsorption process. The magnitude of the exponent, $1/n$, gives an indication of the favorability of adsorption. Values of $n > 1$ represent favorable adsorption condition.

To determine the constants K_f and n , the linear form of the equation may be used to produce a graph of $\ln (q_e)$ against $\ln (C_e)$.

$$\ln q_e = \ln K_f + \left(\frac{1}{n} \right) \ln C_e. \quad (8)$$

Values of K_f and n are calculated from the intercept and slope of the plot (Figure 3s in supplementary section), respectively. If $n = 1$, then the partition between the two phases is independent of the concentration. If value of $1/n$

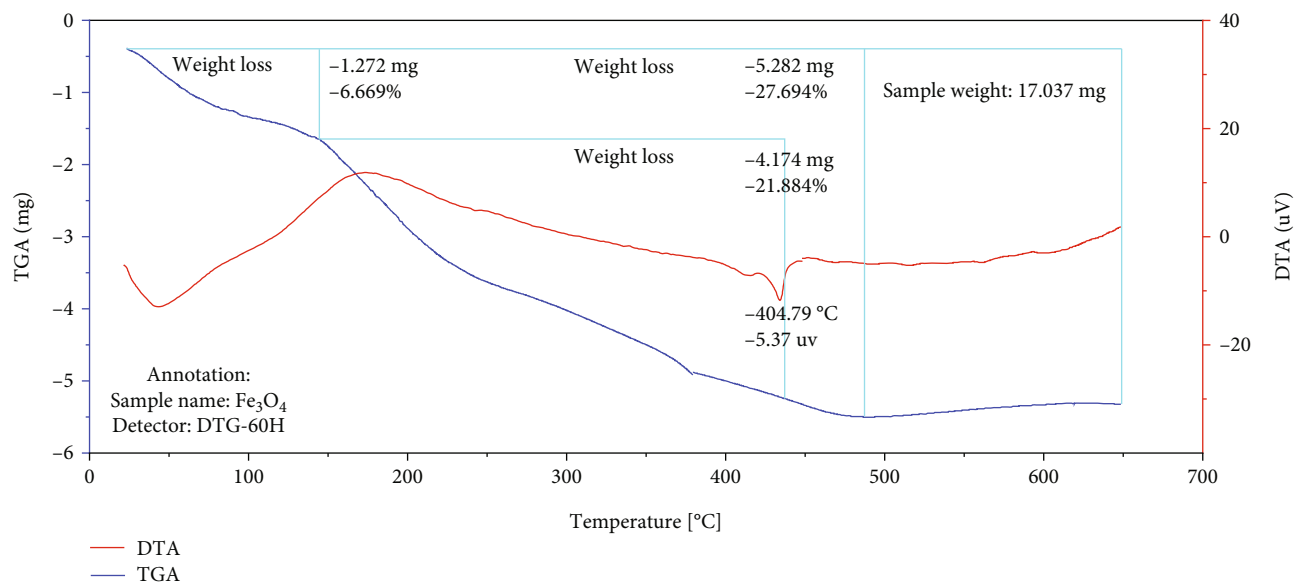


FIGURE 3: The TGA-DTA plots of uncalcined Fe_3O_4 NPs.

is below one, it indicates a normal adsorption. On the other hand, $1/n$ being above one indicates cooperative adsorption [20, 35].

3. Results and Discussion

3.1. TGA-DTA Analysis. The thermal analysis of the synthesized Fe_3O_4 NPs was conducted using TGA-DTA instrument. Figure 3 depicts TGA-DTA curves for the uncalcined sample of Fe_3O_4 NPs, two peaks in DTA curve (one endothermic peak at 160°C and one exothermic peak at 400°C), indicating two-step decomposition and weight removal of initial sample. The endothermic peak observed between 80 and 200°C can be attributed to the loss of water and low molecular weight phytochemicals of *Thymus schimperi* adhered to the NPs, the exothermic peak of DTA curve at 404.29°C ; and 49.57% weight loss between 350°C and 450°C in TGA curve is possibly due to vaporization of carbonized residues present over the surface of the biogenic Fe_3O_4 NPs. As it can be observed in Figure 3, after temperature of 450°C , TGA curve became almost constant. The temperature beyond which the weight loss is constant is used as the calcination temperature of the synthesized Fe_3O_4 nanoparticles [36]. The temperature above which the weight loss of sample remained constant is taken as a calcination temperature. Calcination was performed at 450°C to remove unwanted remnants of the plant extract, and improve the purity of iron oxide NPs.

3.2. XRD Analysis. Figures 4(a)–4(c) depicts the XRD patterns of Fe_3O_4 NPs. As indicated in Figure 4, the XRD peaks of Fe_3O_4 NPs were observed at 2θ values, $30.15, 31.58, 35.49, 43.12, 45.26, 53.73, 57.11, 62.65^\circ$ for S12; $30.06, 31.67, 35.42, 43.06, 45.38, 53.37, 56.42, 62.55^\circ$ for S11; and at $30.06, 31.56, 35.41, 43.15, 45.25, 53.38, 56.83, 62.56^\circ$ for S21. All the diffraction peaks observed are in compliance with the standard pattern for JCPDS Card No. 79-0417 for Fe_3O_4 NPs [37]. The

Miller indices, (220), (200), (311), (400), (220), (422), (511) and (440), observed for Fe_3O_4 NPs correspond to cubic spinel structure [38].

The average crystallite sizes of Fe_3O_4 NPs calculated using Debye-Scherrer equation [37] are 20.26 nm, 29.12 nm, and 26.88 nm for S12, S11, and S21 samples, respectively.

The diffraction pattern of Fe_3O_4 NPs presented in Figure 4 (S11) was studied and the sharp intense peak obtained at 2θ values of $30.06, 31.67, 35.42, 43.06, 45.38, 53.37, 56.42, 62.55^\circ$ corresponds to the lattice plane (220), (200), (311), (400), (220), (422), (511), and (440), respectively. All the diffraction peaks were well indexed to the hexagonal phase and crystallographic planes proving the structure of Fe_3O_4 NPs synthesized to be cubic structure [38].

3.3. FT-IR Analysis. FT-IR spectrum of the calcined green synthesized Fe_3O_4 NPs, as depicted in Figure 5(a), presents the strong absorption bands at $3440, 1622, 1425, 875,$ and 570 cm^{-1} while Figure 5(b) shows the absorption bands of uncalcined Fe_3O_4 NPs which were observed at $3420, 2959, 1623, 1456, 1377, 1064,$ and 600 cm^{-1} .

In the spectrum of the calcined Fe_3O_4 NPs, the wide absorption around 3440 cm^{-1} is caused by the presence of an O-H stretching vibrations from the absorbed water present over the surface of the NPs. The absorption peaks at 1622 cm^{-1} were attributed to the N-H bending of amide compound. 1425 cm^{-1} corresponded to the $-\text{CH}_2$ bending vibrations of the compound. Significant new peak was found at 875 cm^{-1} which corresponds to C-H bending. The presence of band at 570 cm^{-1} corroborates Fe-O stretching of Fe_3O_4 nanoparticles, as reported earlier [39].

Figure 5(b) depicts the FT-IR spectrum of uncalcined Fe_3O_4 NPs. The presence of strong and broad absorption band at 3420 cm^{-1} is caused by the presence of an O-H stretching vibrations of phytochemicals such as *Thymol* and *Carvacrol* [40] and was also due to absorbed water by

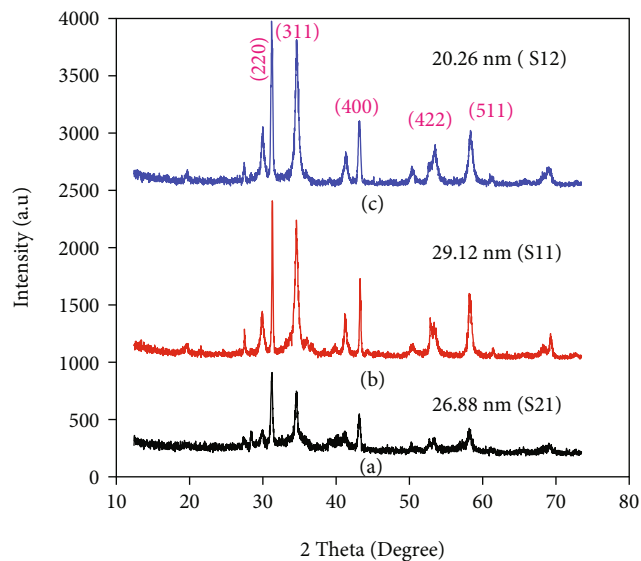


FIGURE 4: XRD pattern of synthesized Fe_3O_4 NPs in three different ratios of plant extract to precursor salt (a) S21 (2:1), (b) S11 (1:1), and (c) S12 (1:2).

the sample. The presence of bands at 2959 cm^{-1} and 1456 cm^{-1} can be attributed to the $-\text{CH}_2$ stretching vibrations of the functional group [29]. The absorption band at 1623 cm^{-1} corresponds to the N-H bending vibrations of the compound and 1377 cm^{-1} to bending functional group of the O-H. The bands at 1051 cm^{-1} revealed the vibration of C-N bond and 600 cm^{-1} indicates C-O stretching band corresponding to the C-O- SO_3 group [41]. FT-IR absorption bands at 2340 cm^{-1} correspond to physisorbed CO_2 to surface of Fe_3O_4 NPs from the atmosphere [42].

3.4. SEM-EDX Analysis. The SEM images of Fe_3O_4 NPs have different morphology as shown in Figures 6(a)–6 (d). The morphology of uncalcined Fe_3O_4 NPs as indicated in Figure 6(a) is not clearly identified. The SEM images of calcined Fe_3O_4 NPs in Figures 6(b)–6 (d) indicate the agglomeration of particles that increases with the concentration of iron salts precursor. The morphology of Fe_3O_4 NPs synthesized from mixture of hydrated ferric and ferrous chloride in different mixing ratio of precursor salt to the plant extract such as 2:1, 1:1, and 1:2 has agglomerated cubic spinel structure.

The scanning electron microscope results confirmed that the grain sizes of the NPs were strongly dependent on mixing ratio of iron salts and leaf extract under the same reaction conditions. The SEM images clearly showed microstructural features and diverse morphologies for Fe_3O_4 nanopowder.

The chemical composition of Fe_3O_4 NPs synthesized in different mixing ratios of precursor salt to the plant extract such as 2:1, 1:1, and 1:2 samples was elucidated by energy-dispersive X-Ray spectroscopy (EDX) (Figure 7). Figure 7(a) reveals the elemental composition of uncalcined Fe_3O_4 NPs, and Figures 7(b)–7(d) depicted EDX spectra of Fe_3O_4 NPs synthesized in 1:1, 1:2, and 2:1 ratios, respec-

tively. The EDX spectral intensity in Figure 7 revealed that iron atom has high proportion than oxygen.

The EDX analysis of all the Fe_3O_4 NPs is shown in Figures 7(a)–7(d). It is evident from EDX spectrum of all the samples in which Fe and O are found in the respective spectrum. In addition to that, interestingly it is observed that there was foreign material present in the spectrum. It could be due to the impurity of the samples.

3.5. UV-Vis Analysis. From the data of UV-Vis reflectance spectra of uncalcined and calcined samples of Fe_3O_4 NPs, bandgaps were calculated from Tauc plots shown in Figure 8. Accordingly, the bandgap value of uncalcined Fe_3O_4 NPs was found to be 2.25 eV, and bandgap values of Fe_3O_4 NPs prepared in different salt to the plant extract volume ratios of 1:2, 1:1, and 2:1 were calculated to be 2.35, 2.02, and 2.1 eV which are in agreement with previously reported results [43].

3.6. Adsorption Batch Studies

3.6.1. Optimizer Design of Different Parameters. Since the adsorption efficiency of the sample S11 was higher than the other samples, all the parameter optimizer designs were done on this best sample of Fe_3O_4 NPs for remediation of Cr(VI) and Hg(II). The optimizer design processes of variables were done to get maximum % removal of chromium and mercury. At initial concentration of 20 mg/L, maximum removal of 85% chromium and 95% of mercury was achieved with the Fe_3O_4 NPs by keeping other parameters constant (pH=5, adsorbent dosage=300 mg, contact time = 90 min) (Figure 9(a)). At pH 5, 85% of chromium and at pH 7, 85% of mercury removal was achieved (at $C_0 = 20\text{ mg/L}$, contact time=90 min, and adsorbent dosage = 300 mg). 85% of chromium and 90% of mercury were removed at adsorbent dosage of 700 mg (at $C_0 = 20\text{ mg/L}$, contact time=90 min, and pH=5). Removal efficiency for chromium at 60 min was found to be 86% and at 90 min for mercury was found to be 90% by keeping other parameters constant (pH=5, $C_0 = 20\text{ mg/L}$, and adsorbent dosage = 300 mg).

3.6.2. Factors Affecting the Adsorption. It was reported in the past studies that various factors possibly affect the adsorption capacity of nano-adsorbents during the adsorption process. Efficiency of any adsorbent is significantly affected by the physicochemical characteristics of the solutions such as pH value, initial concentration, contact time, and adsorbent dosage. Higher adsorption capacities can be obtained by optimizing the above parameters [44].

(1) (1) *Effect of Initial Concentration.* The initial solution concentration serves to be the driving force to overcome the mass transfer resistance of metal across the solvent and solid phases [45].

The effect of initial concentrations on adsorption of chromium and mercury ions was investigated from 20 mg/L to 80 mg/L, by keeping all the other parameters constant (at pH=5, contact time=90 min, and adsorbent dosage =

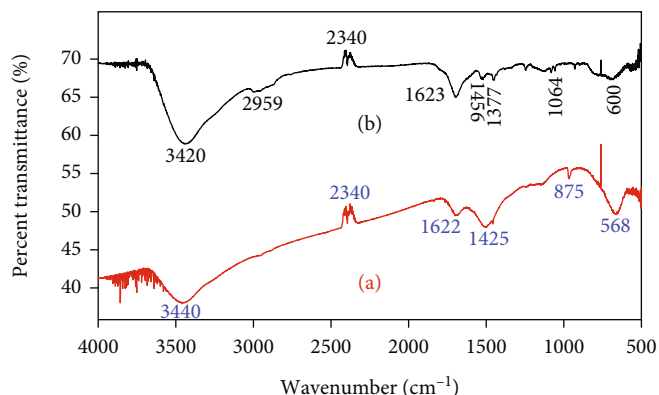


FIGURE 5: FT-IR spectrum of (a) calcined and (b) uncalcined Fe_3O_4 NPs.

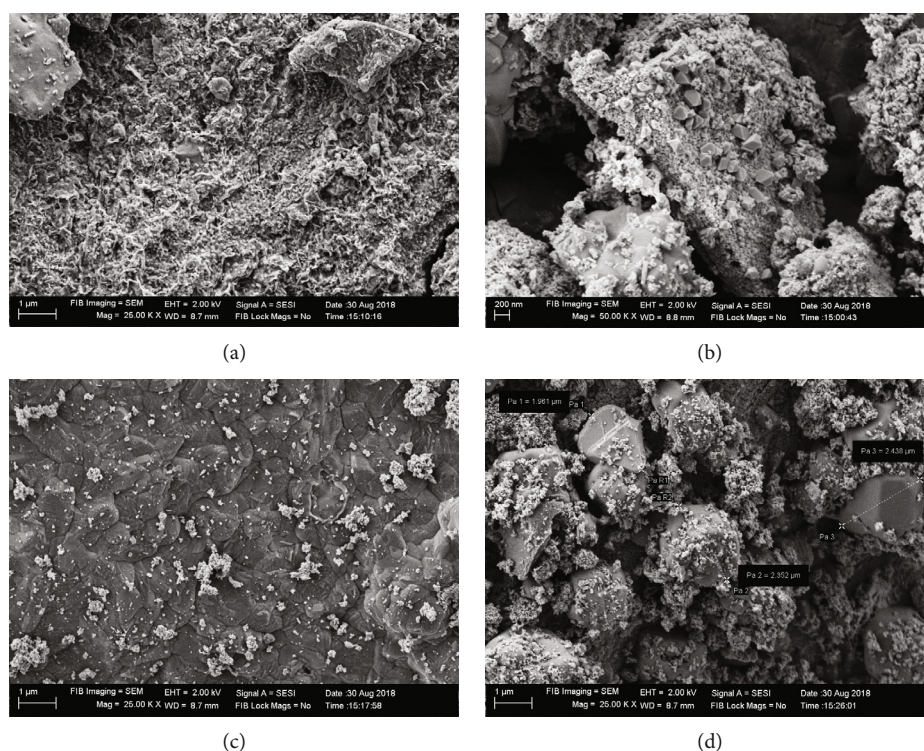


FIGURE 6: SEM images of Fe_3O_4 NPs: (a) for uncalcined in (1:1), (b) for calcined S11 in (1:1), (c) for calcined S12 in (1:2), and (d) for calcined S21 in (2:1).

300 mg). The equilibrium curve (Figure 9(a)) revealed that the overall percentage of removal of Cr(VI) and Hg(II) from the solution was found to decrease with an increase in the initial of concentration Cr(VI) and Hg(II). This could be justified by the fact that, with the increase in the concentration of Cr(VI) or Hg(II) in solution with a fixed amount of adsorbent, binding capacity of adsorbent is believed to approach to the saturation point resulting in decrease in both Cr(VI) and Hg(II) removal. At higher Cr(VI) and Hg(II) concentration; the number of active sites on adsorbent surface is not enough to accommodate both chromium and mercury ions; however, at low concentration, the ratio of surface active sites to total concentration of Cr(VI) and Hg(II) was high and therefore the two metal ions were found to interact

effectively with the active sites on adsorbent surface sufficiently [46].

(2) (2) *Effect of Adsorbent Dosage*. Figure 9(b) presents a fact that the percentage removal of Cr(VII) and Hg(II) ions was found to increase with an increase in the amount of adsorbent dosage. This observation clearly indicates that the number of available adsorption sites influences removal efficiency. Metal ion adsorption efficiency by adsorbent was found to increase with the increase in adsorbent dose.

(3) (3) *Effect of Contact Time*. The adsorption experiments were conducted for various contact times with the fixed values for the other factors, sorbent dose, pH, and initial

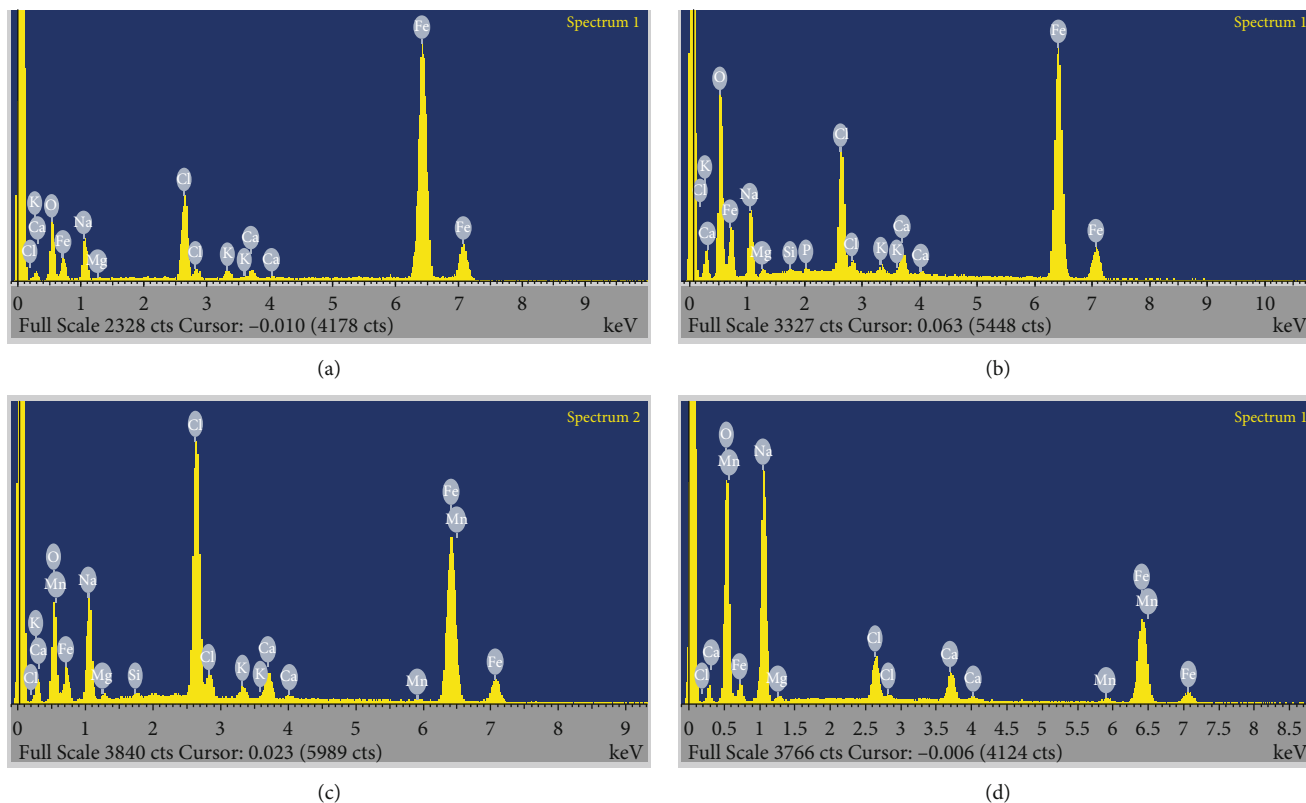


FIGURE 7: EDX spectra of Fe_3O_4 NPs: (a) for uncalcined sample S11 in (1 : 1), (b) for calcined sample S11 in (1 : 1), (c) for calcined sample S12 in (1 : 2), and (d) for calcined S21 in (2 : 1).

concentration. These results are depicted in Figure 9(c). It reveals that the removal efficiency of chromium and mercury by the adsorbent was found to increase in the beginning but later continues to increase at a relatively slower rate with contact time until equilibrium is reached. Generally, the rate of removal of adsorbate appears to be rapid initially, but after saturation of removal efficiency at optimum contact time, the trend of percent removal efficiency for both metal ions slightly declines with time. As shown in Figure 9(c), the optimum equilibration time (contact time) for adsorption of Cr(VI) ion was 60 min and for that of Hg(II) ion was 90 min at percent removal efficiency for 86% and 90%, respectively.

(4) (4) *Effect of pH on Adsorption.* The pH of the solution affects both the degree of dissociation of functional groups from the adsorbent surface and the solubility of the metal ions. The various species of Hg(II) and Cr(VI) are greatly dependent on the pH of the solution [47], and pH values from 3 to 11 were selected for the experimentation. The obtained results (Figure 9(d)) showed that the removal of metal ions was strongly influenced by the pH of the solution. The removal efficiency of adsorbent Fe_3O_4 NPs was increased from pH 3 to 5 for chromium ion and 3 to 7 for mercury ion. Fe_3O_4 NPs exhibited the highest percent removal of chromium (VI) at pH value of 5 and of mercury at pH value of 7, respectively. At low pH conditions ($\text{pH} < 5$), the active surface sites of Fe_3O_4 NPs adsorbent were proton-

ated [48], lowering the adsorption of heavy metal ions (chromium ions and mercury ions) as there is competition between H^+ ions and metal ions. Metal ion removal of Fe_3O_4 NPs remains significantly high beyond optimum values of pH (at $\text{pH} > 7$), as there was electrostatic interaction between metal ions and negatively charged surface of the adsorbent, and also because of hydrolysis of metal ions at higher pH [49].

Percent removal efficiency (%R) and adsorption capacities (q) of Fe_3O_4 NPs for removal of Hg(II) and Cr(VI) ions in wastewater against pH and contact time are summarized in Table 1. As shown in Table 1, both %R and adsorption capacity values were increased with increasing the contact time up to maximum removal efficiency of 90% and maximum adsorption capacity (qm) of 60 mg/g at contact time of 90 minute for Hg(II) and in the same way, %R and adsorption capacity were increased up to maximum removal efficiency of 86% and maximum adsorption capacity of 57.37 mg/g with increase in contact time up to 90 minute for Cr(II), respectively. Increasing the contact time beyond 90 minute for both Hg(II) and Cr(VI) results in decreasing removal efficiency and adsorption capacity. As depicted in Table 1, percent removal efficiency (%R) and adsorption capacity of Fe_3O_4 NPs for removal of Hg(II) and Cr(VI) ions in wastewater against pH show maximum %R value (85%) and g (56.66 mg/g) for Hg(II) (at $\text{pH} = 7$), and maximum percent removal value (85%) and maximum adsorption

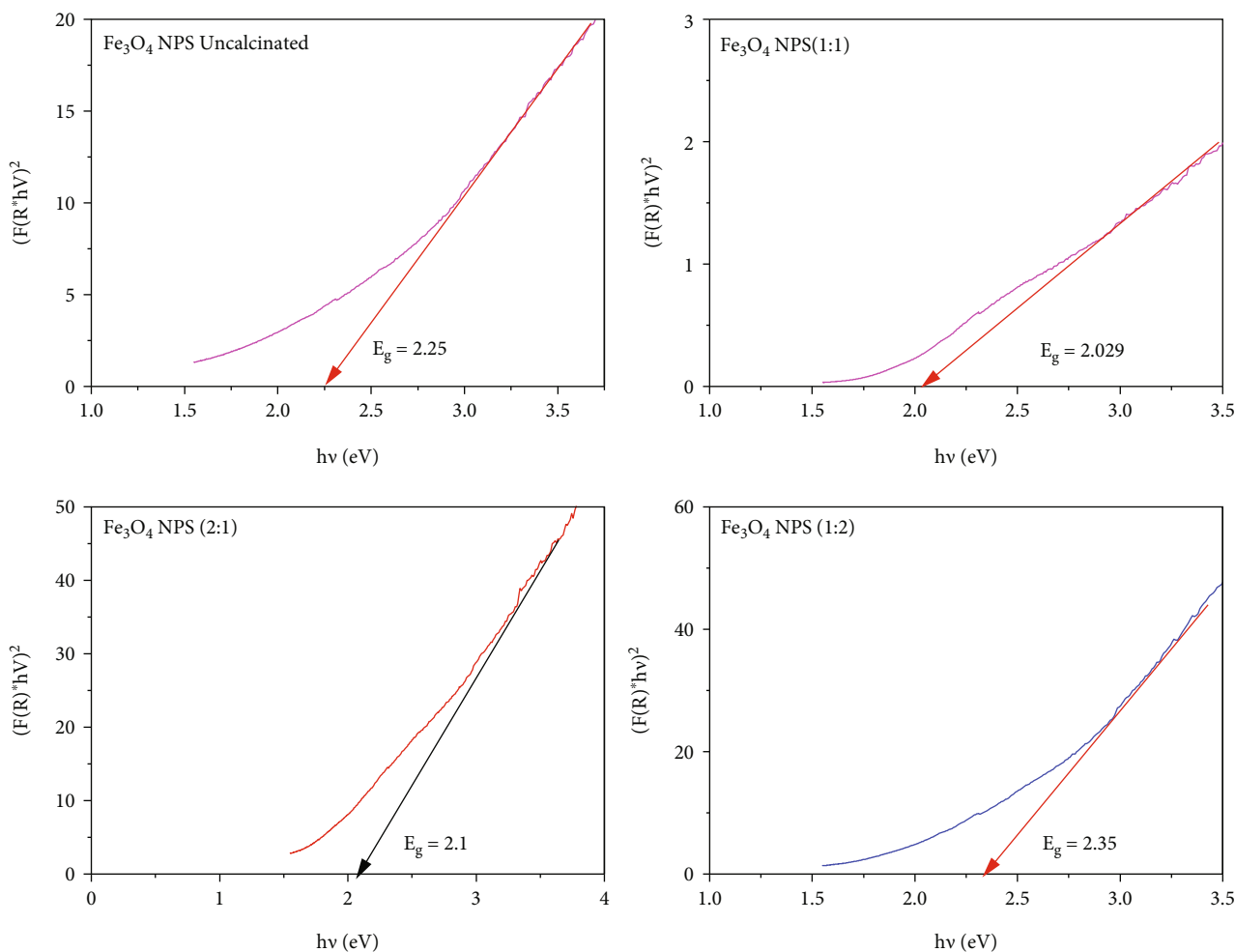


FIGURE 8: Tauc plots and the bandgaps of uncalcined and calcined samples of (S11), (S12), and (S21) Fe_3O_4 NPs.

capacity (56.66 mg/g) for Hg(II) (at pH=5), respectively. Based on the data of Figure 9(a), at lower initial concentration (20 mg/L), maximum percent removal efficiency of 95% for Hg(II) and 86% for Cr(VI) were observed. Correspondingly, maximum adsorption capacity of Fe_3O_4 NPs was extracted from the same figure to be 63.33 mg for Hg(II) and 56.61 mg/g for Cr(VI).

3.7. Sorption Kinetics Studies. The kinetics of sorption of Cr(VI) and Hg(II) on the surface of Fe_3O_4 NPs was investigated against pseudo-first-order and pseudo-second-order models (Figure 2s in supplementary section and Table 2). From the values of R^2 , the data of adsorption of Cr(VI) and Hg(II) was found to fit well with pseudo-second-order models (Table 2).

The degree of goodness of linear fit in kinetic models can be judged from the value of rate constants and R^2 . Table 2 presents the kinetic rate constants of pseudo-first-order and pseudo-second-order models. The pseudo-second-order kinetics present the high correlation coefficients than pseudo-first-order for both Hg(II) and Cr(VI) adsorptions, and the experimental q_e values obtained are closer to those calculated for the pseudo-second-order kinetic model.

3.8. Sorption Isotherm Studies. To evaluate the mechanism of uptake of Hg(II) and Cr(VI) ions in wastewater on to the surface of Fe_3O_4 NPs, the Langmuir and Freundlich adsorption isotherm models were employed to analyze the adsorption data (Figure 3s in supplementary section).

K_f and n are parameters characteristic of the sorbent-sorbate system, which were determined by data fitting and whereas linear regression was determined from the fits of the kinetic and isotherm models [50].

Table 3 summarizes the Langmuir and Freundlich isotherm models for both Cr(VI) and Hg(II) adsorption. The values of isotherm parameters, $1/n=0.483$ (at $n=2.07$), indicating that the sorption of Cr(VI) unto the magnetic adsorbent was favorable with R^2 value of 0.9814.

From the data of Table 3, the values of isotherm parameters, $1/n=0.294$ (at $n=3.40$), indicating that the sorption of Hg(II) unto the magnetic adsorbent of Fe_3O_4 NPs was favorable with R^2 value of 0.967. Based on information obtained from value of $R^2=0.90$ for Cr(VI) sorption and from value of $R^2=0.9741$ for Hg(II) using the Langmuir isotherm model, sorption of Hg(II) best fits with the Langmuir isotherm than Cr(VI). In the same way, the sorption of Cr(VI) best fits with the Freundlich isotherm than Hg(II) does.

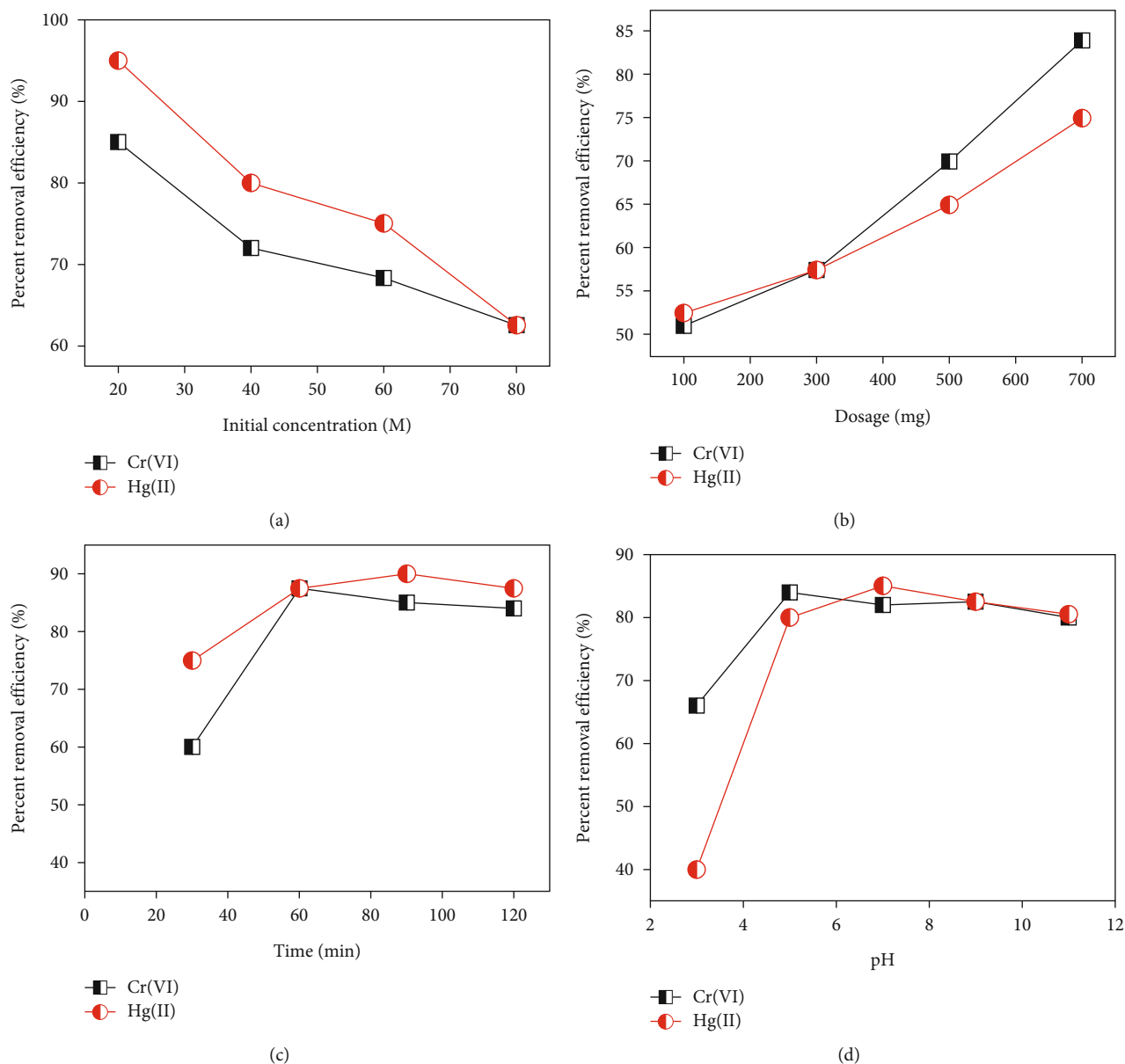


FIGURE 9: Influence of initial concentration of Cr(VII) and Hg(II) (a). Dosage of adsorbent (b), contact time (c), and pH (d) of the solution medium on the percent removal efficiency of Fe₃O₄ NPs on heavy metals (Cr(VII), and Hg(II)).

TABLE 1: Summary of parameters such as pH and contact time on percent removal efficiency and adsorption capacity of Fe₃O₄ NPs in removing Hg(II) and Cr(VI) ions from wastewater.

pH	Hg(II)		Cr(VI)		Contact time (min)	Hg(II)		Cr(VI)	
	%R	q (mg/g)	%R	q (mg/g)		%R	q (mg/g)	%R	q (mg/g)
3	40	26.66	66	44.00	30	75	50.00	60	40.00
5	80	53.33	85	56.66	60	87.5	58.33	86	57.33
7	85	56.66	82	54.66	90	90	60.00	85	56.66
9	82.5	55.00	82.5	55.00	120	87.5	58.33	84	56.66
11	80	53.33	82	55.00					

Table 3 shows a summary of the Langmuir and Freundlich isotherm model constants and correlation coefficients for the adsorption of chromium and mercury [51].

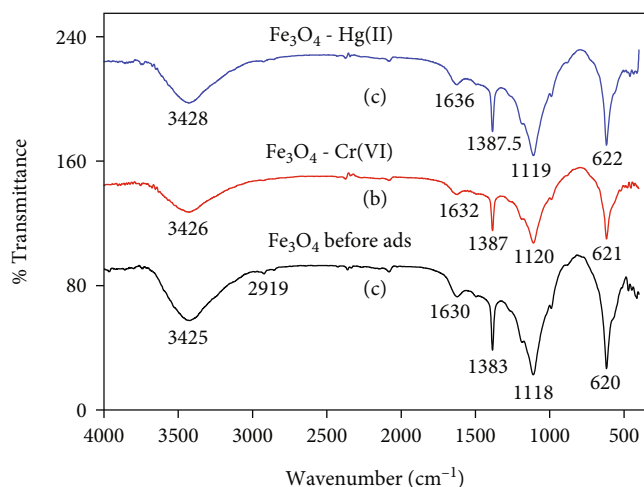
3.9. FT-IR Analysis before and after Adsorption of Hg(II) and Cr(VI). FT-IR spectral of synthesized Fe₃O₄ NPs (adsorbent) before and after adsorption (loading) of Cr(VI) and Hg(II)

TABLE 2: The adsorption kinetic model rate constants for adsorption of chromium and mercury.

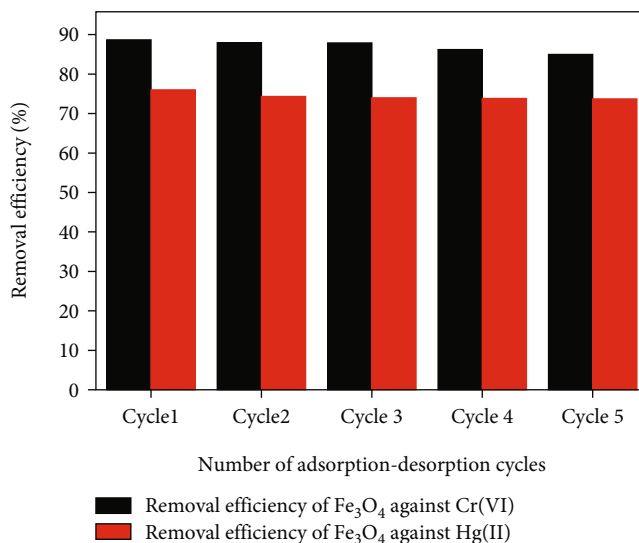
Metal ions	Pseudo 1 st order kinetic model			Pseudo 2 nd order kinetic model		
	q_e	K_1	R^2	q_e	K_2	R^2
Cr(VI)	2.11	-7.00E ⁻⁴	0.2391	1.36	0.057	0.9750
Hg(II)	1.95	-5.33E-4	0.32	1.33	0.142	0.9944

TABLE 3: Langmuir and Freundlich isotherm model constants and correlation coefficients for adsorption of chromium and mercury.

Isotherms	R^2	Cr(VI)		Hg(II)	
		R^2	Estimated isotherm parameters	R^2	Estimated isotherm parameter
Langmuir	0.90	0.9741	Q_o (mg/g)=0.951 K_L (L/mg)=0.078	0.9741	Q_o (mg/g) = 2.631 K_L (L/mg) = 0.287
Freundlich	0.9814	0.967	K_f =1.614 n =2.07	0.967	K_f =3.16 n =3.40

FIGURE 10: FT-IR spectra of green synthesized Fe_3O_4 Nanostructures (a) before and (b) after adsorption of Cr(VI) and (c) Hg(II), respectively.

heavy metal ions was recorded and shown in Figure 10. The FT-IR spectra of Fe_3O_4 NPs after adsorption of Cr(VI) and Hg(II) metal ions have shown various functional groups, and slight peak shifts. In Figure 10, the peaks at 3425, 1630, 1383, and 1118 cm^{-1} shifted towards the peak at 3426, 1632, 1387, and 1120 cm^{-1} , respectively, for Cr(VI) ion adsorption, and shifted to the peaks at 3428, 1636, 1387.5, and 1119 cm^{-1} for Hg(II) ion adsorptions. Small peak at 2959 has been disappeared and the hydroxyl peak at around 1630 cm^{-1} shifted to 1632 cm^{-1} and to 1636 cm^{-1} after adsorption of Cr(VI) and Hg(II) ions, respectively. The peak intensity reduction and peak shift has been also shown after adsorption of Hg(II) onto Fe_3O_4 nanostructures [52].

FIGURE 11: Regeneration study of synthesized Fe_3O_4 nanoparticle for adsorptive removal of Hg(II) and Cr(VI) meta-ions in wastewater.

The peak at around 1118 cm^{-1} attributed to ($-\text{C}-\text{O}$) bond stretching in thymol and carvacrol phytochemicals extracted from *Thymus schimperi*; and the peak due to the hydroxyl group at 1632 cm^{-1} has decreased after adsorption of Cr(VI) (Figure 10(b)), and at 1636 after adsorption of Hg(II) (Figure 10(c)). The intense peaks at around 1118 cm^{-1} (due to C-O functional group of the plant extracts) and at around 1405 cm^{-1} (due to carboxylic functional groups) have been decreased after adsorption of Cr(VI) (Figure 10(b)) and Hg(II) (Figure 10(c)). These changes in the absorption peaks indicated that the active sites on the surface of Fe_3O_4 nanostructures contained hydroxyl, ketonic, and carboxylic functional groups, which formed new chemical bonds with Hg(II) and Cr(VI) ions [53]. The presence of intense band between 650 and 550 cm^{-1} is due to Fe-O bond vibration in Fe_3O_4 NPs [39]. This further confirms the mechanism of adsorption evaluated using adsorption kinetic and isotherm models.

3.10. Regeneration Study. For a cost-effective magnetite nano-adsorbent, Fe_3O_4 NPs, it was essential to study the reusability or recyclability in repeated use for removal of Hg(II) and Cr(VI) ions from wastewater. Magnetic iron oxide (Fe_3O_4) NPs have been applied in adsorptive removal of metallic ions from contaminated water and recovered back for repeated use [54, 55].

For example, Rivera et al. studied Cr(VI) ion removal using 2 g/L of the magnetic magnetite NP [56].

The regenerations study for adsorption-desorption of Hg(II) ions using synthesized Fe_3O_4 NPs in wastewater was done at optimum initial concentration of 20 mg/L , contact time of 60 minutes, and with 30 mg of Fe_3O_4 NPs in 100 ml volumetric flask. The same procedures were followed for adsorption-desorption of Cr(VI) against Fe_3O_4 NPs at the optimum pH of 5 and contact time of 90 minutes. In the process of loading and elution of Hg(II) and Cr(VI) ions

TABLE 4: Maximum sorption efficiencies (%R) and sorption capacities (q_m) of magnetite iron oxide nanoparticles and related adsorption parameters for removal of Cr(VI) and Hg(II) ions from wastewater.

S.no	Adsorbate	Adsorbent material	Maximum adsorption capacity (q_m , mg/g)	Removal efficiency (%R)	pH of solution	Temperature (°C)	Adsorption kinetics	Adsorption isotherm	References
1	Hg(II)	Fe ₃ O ₄ NPs	NA	87	5.5	25	PSO	Freundlich	[59]
2	Hg(II)	Fe ₃ O ₄ NPs	NA	43.74	6	25	PSO	Langmuir	[59]
3	Cr(VI)	Fe ₃ O ₄ NPs	105.26	82	5.2	25	PSO	Langmuir	[61]
4	Cr(VI)	Fe ₃ O ₄ NPs	NA	72.45		25	PSO	Freundlich	[62]
5	Cr(VI)	Fe ₃ O ₄ NPs	NA	98.95	2	25	PSO	Langmuir	[63]
6	Cr(VI)	Fe ₃ O ₄ NPs	26.5	NA	2	25	PSO	Freundlich	[64]
7	Cr(VI)	Fe ₃ O ₄ NPs	15	NA	1	25	PFO	Langmuir	[52]
8	Hg(II)	Schiff base decorated PAMAM dendrimer/Fe ₃ O ₄ composites	605.78	NA	6	25	PSO	Langmuir	[13]
9	Hg(II)	Sulfur-functionalized PAMAM dendrimer/Fe ₃ O ₄ composites	160.47	NA	6	25	PSO	Langmuir	[14]
10	Cr(VI)	Fe ₃ O ₄ NPs	8.67	NA	4	25	PSO	Langmuir	[65]
11	Hg(II)	Fe ₃ O ₄ NPs	63.33	95	7	27	PSO	Langmuir	This study
	Cr(VI)	Fe ₃ O ₄ NPs	56.61	86	5	27	PSO	Freundlich	

N.B: PFO = pseudo first order; PSO = pseudo second order; PAMAM = polyamidoamine; NA = not available.

to and from Fe₃O₄ NPs, the elution operations were carried out by shaking the Hg(II) adsorbed and Cr(VI) adsorbed Fe₃O₄ NPs with 0.50 M HCl in 100 ml volumetric flask separately. The regeneration of the nanoparticles was done for multiple adsorption-desorption cycles. The recycled Fe₃O₄ NP were tested against removal of Hg(II) and Cr(VI) metal ions for 1st, 2nd, 3rd, 4th, and 5th cycles, respectively (Figure 4s and Figure 5s in supplementary section). The data of the regeneration study of Fe₃O₄ NP against Hg(II) and Cr(VI) metal ions for the 1st five cycles are shown in Figure 11.

The regeneration cycles of the magnetic nanomaterials showed a slight decrease (about 4.17% for Cr(VI) and 3% for Hg(II) ions) in the removal efficiency between the 1st cycle and 5th cycle, indicating that the nanomaterial was reused for up to 5 cycles sequentially without significant reduction in removal efficiency of Fe₃O₄ NPs against Hg(II) and Cr(VI) metal ions. This finding is in line with previous reports in regeneration study for magnetite and magnetite-based nanostructures [3, 56–58] for the similar heavy metal ions.

Maximum removal efficiency (%R), maximum adsorption capacity (q_m), optimum pH, working temperature of solution medium, kinetics, and adsorption isotherms for sorption of Hg(II) and Cr(VI) onto synthesized Fe₃O₄ NPs are collected in Table 4. The comparative data for removal efficiency (%R), maximum adsorption capacity (q_m), and other adsorption conditions of Fe₃O₄ nanoparticles and Fe₃O₄-based nanocomposites for Hg(II) and Cr(VI) sorption are summarized in Table 4. The percent removal efficiency (%R) of synthesized Fe₃O₄ NPs in this study for adsorption of Hg(II) is in agreement with reported value

by Zaki et al. [59], and is higher than other reported values by [60, 61]; and % R for adsorption of Cr(VI) in this study is higher than reported value by [62] whereas it is lower than the reported value by [63]. Obtained maximum adsorption capacity (q_m) for Cr(VI) (56.61 mg/g) and Hg(II) (63.33 mg/g) is in between the maximum value from by Y. Zhou et al., L. Luan et al., and H. Kumar et al. and other related minimum q_m values reported in [64, 65].

Schiff-based functionalized polyamidoamine (PAMAM) dendrimer composites of Fe₃O₄ NPs and sulfur-functionalized PAMAM dendrimer/Fe₃O₄ nanocomposite materials were studied to decontaminate aqueous Hg(II) by Y. Zhou et al. [65], and by L. Luan et al. [14] and the maximum adsorption capacity of 605.78 mg/g and 160.47 mg/g, respectively, was achieved. In other related reports, magnetite Fe₃O₄ NPs were used to remove Cr(VI) ion from wastewater at initial concentration of adsorbate of 2 g/d m³ and at pH = 4, and with maximum adsorption capacity of 8.67 mg/g was achieved [65].

From the data of adsorption kinetics, adsorption isotherms, and FT-IR analysis before and after adsorption of the heavy metal ions onto Fe₃O₄ NPs, the uptake of Hg(II) and Cr(VI) ion by the magnetite iron oxide NPs is dominated by the chemical interaction between adsorbent (Fe₃O₄ NPs) and adsorbate (Hg(II) and Cr(VI)).

4. Conclusion

The XRD study revealed that the phase structure of Fe₃O₄ NPs were cubic face centered with average crystallite size between 20 and 30 nm. The SEM micrographs depicted the

agglomerated grain size of synthesized Fe_3O_4 NPs. The maximum percent removal efficiency of the adsorbent material (Fe_3O_4 NPs) for adsorption of chromium (VI) was 86% (at initial concentration of 20 mg/L, contact time of 90 min, and adsorbent dose of 300 mg) and for mercury (II) 90% (at initial concentration of 20 mg/L, and contact time of 90 min) from aqueous polluted water. At pH=7, the percent removal efficiency of Fe_3O_4 NPs to adsorb Hg(II) was 90% (at constant time of 90 min, initial concentration of 20 mg/L, and adsorbent dose of 300 mg); at pH =5, the percent removal efficiency of Fe_3O_4 NPs to adsorb Cr(VI) ion was 86% (at constant time of 60 min, initial concentration of 20 mg/L, and adsorbent dose of 300 mg). The mechanism of both Hg(II) and Cr(VI) metal ion adsorptions was best fitted with pseudo-second-order kinetics, and Cr(VI) ion sorption follows the Freundlich adsorption isotherm model whereas Hg(II) ion sorption fitted with the Langmuir isotherm model. The regenerability study of the adsorbent material (Fe_3O_4 NPs) performed for five consecutive cycles shows only slight decrease in removal efficiency (4.17% for Cr(VI) and 3% for Hg(II)) between the 1st and the 5th adsorption-desorption cycle.

Data Availability

The data of FT-IR spectra, XRD Analysis, SEM-EDX, TGA-DTA, and kinetic study used to support the findings of this study are included within the article; and also can be released from the corresponding author upon request to the Hindawi (Journal of Nanomaterials).

Conflicts of Interest

There are no potentially available conflicts of interest, authorship, and/or publication of this article.

Acknowledgments

I (F. K. Sabir) and S. T. Geneti (my student who used this work as his M.Sc. Thesis) greatly acknowledged Adama Science and Technology University (ASTU) for providing financial support through ASTU's 12th cycle research grant successfully. The authors extend their thanks to the Department of Applied Chemistry and Department of Materials Science and Engineering at ASTU for providing facilities such as TGA-DTA analyzer and XRD setup. Department of Chemistry at Addis Ababa University was also thanked by the authors for allowing FT-IR characterization. The authors also acknowledged East West Institute of Technology (India) for SEM-EDX and UV-Visible reflectance analysis.

Supplementary Materials

Supplementary section has included five figure data (Figure 1s–Figure 5s). The photograph of the plant used in synthesis of Fe_3O_4 NPs (*Thymus schimperi*) is given by Figure 1s. The plots of pseudo-first and pseudo-second-order kinetic models for adsorption of Hg(II) and Cr(VI) metal ions onto

Fe_3O_4 NPs are shown by Figure 2s. The plots of the Freundlich and Langmuir adsorption isotherm models are shown in Figure 3s. The basic data for regeneration study is given by Figures 4s and 5s. The UV-Vis absorbance spectra of Cr(VI) and Hg(II) metal ions for five sequential cycles of adsorption–desorption phenomena were depicted by Figure 4s and Figure 5s, respectively. (*Supplementary Materials*)

References

- [1] K. Parajuli, A. K. Sah, and H. Paudyal, "Green synthesis of magnetite nanoparticles using aqueous leaves extracts of *Azadirachta indica* and its application for the removal of As(V) from water," *Green and Sustainable Chemistry*, vol. 10, no. 4, pp. 117–132, 2020.
- [2] H. T. Ha, N. T. Huong, L. L. Dan, N. D. Tung, V. B. Trung, and T. D. Minh, "Removal of heavy metal ion using polymer-functionalized activated carbon: aspects of environmental economic and chemistry education," *Journal of Analytical Methods in Chemistry*, vol. 2020, 13 pages, 2020.
- [3] R. Kumar, P. Rauwel, and E. Rauwel, "Nano-adsorbents for the removal of heavy metals from contaminated water: current scenario and future directions," *PRO*, vol. 9, no. 8, pp. 1379–1408, 2021.
- [4] B. E. Igiri, S. I. R. Okoduwa, G. O. Idoko, E. P. Akabuogu, A. O. Adeyi, and I. K. Ejiogu, "Toxicity and bioremediation of heavy metals contaminated ecosystem from tannery wastewater: a review," *Journal of Toxicology*, vol. 2018, 16 pages, 2018.
- [5] T.-K. Tran, H.-J. Leu, K.-F. Chiu, and C.-Y. Lin, "Electrochemical treatment of heavy metal-containing wastewater with the removal of COD and heavy metal ions," *Journal of the Chinese Chemical Society*, vol. 64, no. 5, pp. 493–502, 2017.
- [6] Z. Chen, B. Tang, Y. Niu et al., "Synthesis of silica supported thiosemicarbazide for Cu(II) and Zn(II) adsorption from ethanol: a comparison with aqueous solution," *Fuel*, vol. 286, pp. 119287–119295, 2021.
- [7] H. T. Kara, S. T. Anshebo, and F. K. Sabir, "Preparation and characterization of functionalized cellulose nanomaterials (CNMs) for Pb(II) ions removal from wastewater," *Journal of Chemistry*, vol. 2021, 18 pages, 2021.
- [8] H. T. Kara, S. T. Anshebo, F. K. Sabir, and G. A. Workineh, "Removal of methylene blue dye from wastewater using peroxidized modified nanocellulose," *International Journal of Chemical Engineering*, vol. 2021, 6 pages, 2021.
- [9] Z. Cheng, A. L. K. Tan, Y. Tao, D. Shan, K. E. Ting, and X. J. Yin, "Synthesis and characterization of iron oxide nanoparticles and applications in the removal of heavy metals from industrial wastewater," *International Journal of Photoenergy*, vol. 2012, 5 pages, 2012.
- [10] A. M. Gutierrez, T. D. Dziubla, and J. Z. Hilt, "Recent advances on iron oxide magnetic nanoparticles as sorbents of organic pollutants in water and wastewater treatment," *Reviews on Environmental Health*, vol. 32, no. 1-2, pp. 111–117, 2017.
- [11] M. Gui, V. Smuleac, L. E. Ormsbee, D. L. Sedlak, and D. Bhattacharyya, "Iron oxide nanoparticle synthesis in aqueous and membrane systems for oxidative degradation of trichloroethylene from water," *Journal of Nanoparticle Research*, vol. 14, no. 5, pp. 861–877, 2012.
- [12] G. Yirga, H. C. A. Murthy, and E. Bekele, "Synthesis and characterization of humic acid-coated Fe_3O_4 nanoparticles for

- methylene blue adsorption activity,” *Advanced Materials Letters*, vol. 10, no. 10, pp. 715–723, 2019.
- [13] Y. Zhou, L. Luan, B. Tang et al., “Fabrication of Schiff base decorated PAMAM dendrimer/magnetic Fe_3O_4 for selective removal of aqueous $\text{Hg}(\text{II})$,” *Chemical Engineering Journal*, vol. 398, article 125651, 2020.
- [14] L. Luan, B. Tang, Y. Liu et al., “Selective capture of $\text{Hg}(\text{II})$ and $\text{Ag}(\text{I})$ from water by sulfur-functionalized polyamidoamine dendrimer/magnetic Fe_3O_4 hybrid materials,” *Separation and Purification Technology*, vol. 257, article 117902, 2021.
- [15] K. Mittal, Y. Chisti, and U. C. Banerjee, “Synthesis of metallic nanoparticles using plant extracts,” *Biotechnology Advances*, vol. 31, no. 2, pp. 346–356, 2013.
- [16] W. S. W. Ngah and M. A. K. M. Hanafiah, “Removal of heavy metal ions from wastewater by chemically modified plant wastes as adsorbents: review,” *Biotechnology*, vol. 99, pp. 3935–3948, 2008.
- [17] T. B. Asfaw, T. M. Tadesse, and A. M. Ewnetie, “Determination of total chromium and chromium species in Kombolcha tannery wastewater, surrounding soil, and lettuce plant samples, South Wollo, Ethiopia,” *Advances in Chemistry*, vol. 2017, 7 pages, 2017.
- [18] G. K. Kinuthia, V. Ngure, D. Beti, R. Lugalia, A. Wangila, and L. Kamau, “Levels of heavy metals in wastewater and soil samples from open drainage channels in Nairobi, Kenya: community health implication,” *Scientific Reports*, vol. 10, no. 1, pp. 8434–8844, 2020.
- [19] H. Khademi, M. Gabarron, A. Abbaspour, S. Martinez-Martinez, A. Faz, and J. A. Acosta, “Environmental impact assessment of industrial activities on heavy metals distribution in street dust and soil,” *Chemosphere*, vol. 217, pp. 695–705, 2019.
- [20] H. T. Kara, S. T. Anshebo, and F. K. Sabir, “A novel modified cellulose nanomaterials (CNMs) for remediation of chromium (VI) ions from wastewater,” *Materials Research Express*, vol. 7, no. 11, article 115008, 2020.
- [21] WHO (2003), *Chromium in drinking-water. Background document for preparation of WHO Guidelines for drinking-water quality*, World Health Organization (WHO/SDE/WSH/03.04/4), Geneva, 4th edition, 2017.
- [22] J. Mateo-Sagasta, S. M. Zadehand, H. Turrall, and IWMI & FAO, *Water pollution from agriculture: a global review*, 2017.
- [23] A. Nigist, H. J. Storesund, L. Skattebol, F. Tonnesen, and A. J. Aasen, “Volatile oil constituents of two Thymus species from Ethiopia,” *International Journal of Science*, vol. 15, no. 2, pp. 123–125, 2000.
- [24] M. Sravanthi, D. MuniKumar, M. Ravichandra, G. Vasu, and K. P. J. Hemalatha, “Green synthesis and characterization of iron oxide nanoparticles using Wrightia tinctoria leaf extract and their antibacterial studies,” *International Journal of Current Research Academic Review*, vol. 4, no. 8, pp. 30–44, 2016.
- [25] E. T. Bekele, E. A. Zereffa, N. S. Gultom, D.-H. Kuo, B. A. Gonfa, and F. K. Sabir, “Biotemplated synthesis of titanium oxide nanoparticles in the presence of root extract of Kniphofia schemperi and its application for dye sensitized solar cells,” *International Journal of Photoenergy*, vol. 2021, 12 pages, 2021.
- [26] E. T. Bekele, B. A. Gonfa, O. A. Zelekew, H. H. Belay, and F. K. Sabir, “Synthesis of titanium oxide nanoparticles using root extract of Kniphofia foliosa as a template, characterization, and its application on drug resistance bacteria,” *Journal of Nanomaterials*, vol. 2020, 10 pages, 2020.
- [27] N. Ajinkya, X. Yu, P. Kaithal, H. Luo, P. Somani, and S. Ramakrishna, “Magnetic iron oxide nanoparticle (IONP) synthesis to applications: present and future,” *Materials*, vol. 13, no. 20, p. 4644, 2020.
- [28] M. A. J. Kouhbanani, N. Beheshtkho, A. M. Amani et al., “Green synthesis of iron oxide nanoparticles using Artemisia vulgaris leaf extract and their application as a heterogeneous Fenton-like catalyst for the degradation of methyl orange,” *Materials Research Express*, vol. 5, no. 11, article 115013, 2018.
- [29] A. M. Awwad and N. M. Salem, “A Green and facile approach for synthesis of magnetite nanoparticles,” *Journal of Nanoscience and Nanotechnology*, vol. 2, no. 6, pp. 208–213, 2012.
- [30] Z. Chen, T. Wang, X. Jin, M. Megharaj, and R. Naidu, “Multi-functional kaolinite-supported nanoscale zero-valent iron used for the adsorption and degradation of crystal violet in aqueous solution,” *Journal of Colloid and Interface Science*, vol. 398, pp. 59–66, 2013.
- [31] N. Basavegowda, K. B. S. Magar, K. Mishra, and Y. R. Lee, “Green fabrication of ferromagnetic Fe_3O_4 nanoparticles and their novel catalytic applications for the synthesis of biologically interesting benzoxazinone and benzthioxazinone derivatives,” *Journal of Chemistry*, vol. 38, pp. 5415–5420, 2014.
- [32] K. S. Padmavathy, G. Madhu, and P. V. Haseena, “A study on effects of pH, adsorbent dosage, time, initial concentration and adsorption isotherm study for the removal of hexavalent chromium (Cr (VI)) from wastewater by magnetite nanoparticles,” *International Conference Engineering, Science and Technology*, vol. 24, pp. 585–594, 2016.
- [33] A. Mohd, R. Sumbul, A. Masood, and P. Arulazhagan, “Adsorption of $\text{Hg}(\text{II})$ from Aqueous Solution Using Adulsa (Justicia adhatoda) Leaves Powder: Kinetic and Equilibrium Studies,” *Journal of Chemistry*, vol. 2013, 11 pages, 2013.
- [34] K. K. Onchoke and S. A. Sasu, “Determination of hexavalent chromium (Cr(VI)) concentrations via ion chromatography and UV-Vis spectrophotometry in samples collected from Nacogdoches Wastewater Treatment Plant, East Texas (USA),” *Advances in Environmental Chemistry*, vol. 2016, 10 pages, 2016.
- [35] H. M. F. Freundlich, “Über die adsorption in Lösungen,” *Journal of Physical Chemistry*, vol. 57U, no. 1, pp. 385–470, 1907.
- [36] M. Herlekar and S. Barve, “Calcination and microwave assisted biological synthesis of iron oxide nanoparticles,” *International Research Journal of Environmental Science*, vol. 4, pp. 28–36, 2015.
- [37] H. E. Ghandoor, H. M. Zidan, M. H. K. Mostafa, and M. I. M. Ismail, “Synthesis and some physical properties of magnetite (Fe_3O_4) nanoparticles,” *International Journal of Electrochemical Science*, vol. 7, pp. 1–12, 2012.
- [38] N. Sanpo, C. C. Berndt, C. Wen, and J. Wang, “Transition metal-substituted cobalt ferrite nanoparticles for biomedical applications,” *Acta Biomaterialia*, vol. 9, no. 3, pp. 5830–5837, 2013.
- [39] M. Gotic, T. Jurkin, and S. Music, “Iron (III) precursor to magnetite and vice versa,” *Materials Research Bulletin*, vol. 44, no. 10, pp. 2014–2021, 2009.
- [40] T. Abera, E. Debebe, R. Ashebir et al., “Phytochemical constituents, safety and efficacy study of Thymus schimperii and Thymus serrulatus,” *Journal of Clinical and Experimental Pharmacology*, vol. 9, no. 5, pp. 1–7, 2019.

- [41] F. B. G. Camara, L. A. Costa, G. P. Fidelis et al., "Heterofucans from the brown seaweed *Canistrocarpus cervicornis* with anti-coagulant and antioxidant activities," *Marine Drugs*, vol. 9, no. 1, pp. 124–138, 2011.
- [42] C. Yang and C. Wöll, "IR spectroscopy applied to metal oxide surfaces: adsorbate vibrations and beyond," *Advances in Physics: X*, vol. 2, no. 2, pp. 373–408, 2017.
- [43] L. Guo, Q. Huang, X. Li, and S. Yang, "Iron oxide nanoparticles synthesis and applications in surface enhanced raman scattering and electrocatalysis," *Physical Chemistry*, vol. 3, pp. 1661–1665, 2001.
- [44] M. Hua, S. Zhang, B. Pan, W. Zhang, L. Lv, and Q. Zhang, "Heavy metal removal from water/wastewater by nanosized metal oxides: A review," *Journal of Hazardous Materials*, vol. 211–212, pp. 317–331, 2012.
- [45] H. I. Adegoke, F. AmooAdekola, O. S. Fatoki, and B. J. Kimba, "Adsorption of Cr(VI) on synthetic hematite (α -Fe₂O₃) nanoparticles of different morphologies," *Korean Journal of Chemical Engineering*, vol. 31, no. 1, pp. 142–154, 2014.
- [46] A. Y. Orbak and I. Orbak, "Effective Factor Analysis for Chromium(VI) Removal from Aqueous Solutions and Its Application to Tunçbilek Lignite Using Design of Experiments," *Journal of Chemistry*, vol. 2019, 10 pages, 2019.
- [47] R. Ansari and N. K. Fahim, "Application of polypyrrole coated on wood sawdust for removal of Cr(VI) ion from aqueous solutions," *Reactive and Functional Polymers*, vol. 67, no. 4, pp. 367–374, 2007.
- [48] B. N. Pham, J.-K. Kang, C.-G. Lee, and S.-J. Park, "Removal of heavy metals (Cd²⁺, Cu²⁺, Ni²⁺, Pb²⁺) from aqueous solution using *Hizikia fusiformis* as an algae-based bioadsorbent," *Applied Sciences*, vol. 11, no. 18, pp. 8604–8616, 2021.
- [49] A. A. Naef Qasem, R. H. Mohammed, and D. U. Lawal, "Removal of heavy metal ions from wastewater: a comprehensive and critical review," *Nature Partner Journals Clean Water*, vol. 4, no. 1, pp. 1–15, 2021.
- [50] B. Abebe, H. C. A. Murthy, and A. Enyew, "Summary on adsorption and photocatalysis for pollutant remediation: mini review," *Journal of Encapsulation and Adsorption Sciences*, vol. 8, no. 4, pp. 225–255, 2018.
- [51] K. S. Somit, H. C. Ananda, and S. V. Murthy, "Adsorption of mercury from aqueous solution using gum acacia-silica Composite: kinetics, Isotherms and thermodynamics studies," *Advanced Materials Letters*, vol. 7, no. 8, pp. 673–678, 2016.
- [52] P. M. Thabede, N. D. Shooto, T. Xaba, and E. B. Naidoo, "Magnetite functionalized *Nigella sativa* seeds for the uptake of chromium(VI) and lead(II) ions from synthetic wastewater," *Adsorption Science & Technology*, vol. 2021, pp. 1–15, 2021.
- [53] W. Zhang, Y. An, S. Li et al., "Enhanced heavy metal removal from an aqueous environment using an eco-friendly and sustainable adsorbent," *Scientific Reports*, vol. 10, no. 1, p. 16453, 2020.
- [54] A. N. Baghani, A. H. Mahvi, M. Gholami, N. Rastkari, and M. Delikhoon, "One-Pot synthesis, characterization and adsorption studies of amine-functionalized magnetite nanoparticles for removal of Cr (VI) and Ni (II) ions from aqueous solution: kinetic, isotherm and thermodynamic studies," *Journal of Environmental Health Science & Engineering*, vol. 14, p. 11, 2016.
- [55] F. Tsegaye, A. M. Tadesse, E. Teju, and M. Aschalew, *Bulletin of the Chemical Society of Ethiopia*, vol. 34, no. 1, pp. 105–121, 2020.
- [56] F. L. Rivera, F. J. Palomares, P. Herrasti, and E. Mazario, "Improvement in heavy metal removal from wastewater using an external magnetic inductor," *Nanomaterials*, vol. 9, no. 11, p. 1508, 2019, [CrossRef].
- [57] Y. Bagbi, A. Sarswat, D. Mohan, A. Pandey, and P. R. Solanki, "SciENTific REPOrTS, Lead and chromium adsorption from water using L-cysteine functionalized magnetite (Fe₃O₄)," *Nano*, vol. 7, no. 1, article 7672.
- [58] S. Tao, C. Wang, W. Ma, S. Wu, and C. Meng, "Designed multifunctionalized magnetic mesoporous microsphere for sequential sorption of organic and inorganic pollutants," *Microporous and Mesoporous Materials*, vol. 147, no. 1, pp. 295–301, 2012.
- [59] M. Zaki, A. Maulana, F. Tirtayani, P. N. Alam, and H. Husin, "Mercury removal in wastewater by iron oxide nanoparticles," *Journal of Physics: Conference Series*, vol. 687, article 012050, 2016.
- [60] H. Parham, B. Zargar, and R. Shiralipour, "Fast and efficient removal of mercury from water samples using magnetic iron oxide nanoparticles modified with 2-mercaptobenzothiazole," *Journal of Hazardous Materials*, vol. 205–206, pp. 94–100, 2012.
- [61] H. Kumar, S. K. Sinha, V. V. Goud, and S. Das, "Removal of Cr(VI) by magnetic iron oxide nanoparticles synthesized from extracellular polymeric substances of chromium resistant acid-tolerant bacterium *Lysinibacillus sphaericus* RTA-01," *Journal of Environmental Health Science and Engineering*, vol. 17, no. 2, pp. 1001–1016, 2019.
- [62] M. Agarwal, P. Dey, S. Upadhayaya, and R. Dohare, "Adsorption efficiency of magnetite nanoparticles for chromium(VI) removal from water," *Journal of the Indian Chemical Society*, vol. 93, pp. 199–209, 2016.
- [63] N. Saber, M. Duaa, and M. Najj, "Statistical analysis of the removal of Chromium(VI) by Iron Oxide Nanoparticle (Fe₃O₄)," *Journal of Engineering*, vol. 24, 2018.
- [64] S. Liang, S. Shi, H. Zhang et al., "One-pot solvothermal synthesis of magnetic biochar from waste biomass: Formation mechanism and efficient adsorption of Cr(VI) in an aqueous solution," *Science of the Total Environment*, vol. 695, article 133886, 2019.
- [65] J. Zhang, S. Lin, M. Han, S. Qing, L. Xia, and Z. Hui, "Adsorption properties of magnetic magnetite nanoparticle for coexistent Cr(VI) and Cu(II) in mixed solution," *Watermark*, vol. 12, no. 2, p. 446, 2020.

Review Article

Renewable Polysaccharide and Biomedical Application of Nanomaterials

Rahul Kanaoujiya ¹, Shruti Kumari Saroj,¹ Shekhar Srivastava,¹
and Manoj Kumar Chaudhary ²

¹*Synthetic Inorganic and Metallo-Organic Research Laboratory, Department of Chemistry, University of Allahabad, Prayagraj, India*

²*Central Department of Physics, Tribhuvan University, Kathmandu, Nepal*

Correspondence should be addressed to Rahul Kanaoujiya; rahul.k@allduniv.ac.in
and Manoj Kumar Chaudhary; manoj.chaudhary@ac.tu.edu.np

Received 15 February 2022; Revised 27 March 2022; Accepted 31 March 2022; Published 15 April 2022

Academic Editor: H C Ananda Murthy

Copyright © 2022 Rahul Kanaoujiya et al. This is an open access article distributed under the Creative Commons Attribution License, which permits unrestricted use, distribution, and reproduction in any medium, provided the original work is properly cited.

Nanotechnology being undoubtedly an uncut gem over the past few years has been in sighting as a new form of branch with its vigorous discoveries which have led to its divergent evolution giving emergence not only in the pathway of knowledge but also developing technological techniques. The constituting nanoparticles and its versatile properties with dynamic structures have made a major breakthrough in the past few years for its role in biotechnology arising nanobiotechnology, antipollution, renewable polymers, and its biomedical applications. Nanostructure composites forming nanomaterials on the basis of its working are pectin, cellulose, lignin, hyaluronic acid, bacterial cellulose, Arabic gum, and bacterial biosurfactants. In the recent years, it is seen that nanocomposites are giving promising results in medical technology incorporating with useful metal nanoparticles such as silver nanoparticles (AgNPs), gold nanoparticles (AuNPs), diamond nanoparticles, zinc oxide (ZnO), and titanium oxide (TiO). Some useful biomedical applications are in anticancerous, sunscreen, antiageing, and antitumorous. They have shown to be nontoxic at a certain level. Nanoparticle composites have proven with right amount of doping, and experienced techniques have given excellent results. Nanofibers of biodegradable poly(L-lactide) (PLLA)/poly(lactide-co-glycolide) (PLGA) compounds are used in drug delivery, folate redox-responsive chitosan nanoparticles (FTC-NPs) also as anticancer drug delivery, and mesoporous silica nanoparticles-silver nanoparticles as a tissue growth in vivo processes. The study of a biosynthetic pathway of therapeutic drugs is still much needed. Waste management of renewable nanopolymers are an ultimate goal so that there are less haphazard elements towards the environment.

1. Introduction

As we approach to the recent times of our study with biological environment, we observe that not only it provides us with basic necessities but also classifying itself into producing different forms of nanocomposites with splendid attributes and serving many purposes. These nanocomposites aligned in the formation of polymers giving a spectrum of scope. The fact that withholds with the nanocomposite's polymers is its unique way of matrix formation constituting molecules (e.g., carbohydrates, colloids, and amino acids). The importance of these colloids is not only subjected with

the formation of it but also in regard with sustainability. Renewable polymers are the polymers composed of natural product or the tendency of it converted into simpler polymers that are unpolluting to the biological ecosystem, ceaseless resource of energy contributing a promising shelf life. The polymers from renewable resources [1] include polysaccharides, lignin, triglycerides, chitosan, and amino acids. Some other renewable resources of nanocomposites materials including fibroin of spider, silkworm's fibroin [2], and nacre mother layer [3] of mollusks have an emerging contribution towards renewable polymers; thus, these polymers owing to its sustainability possessing compact matrix

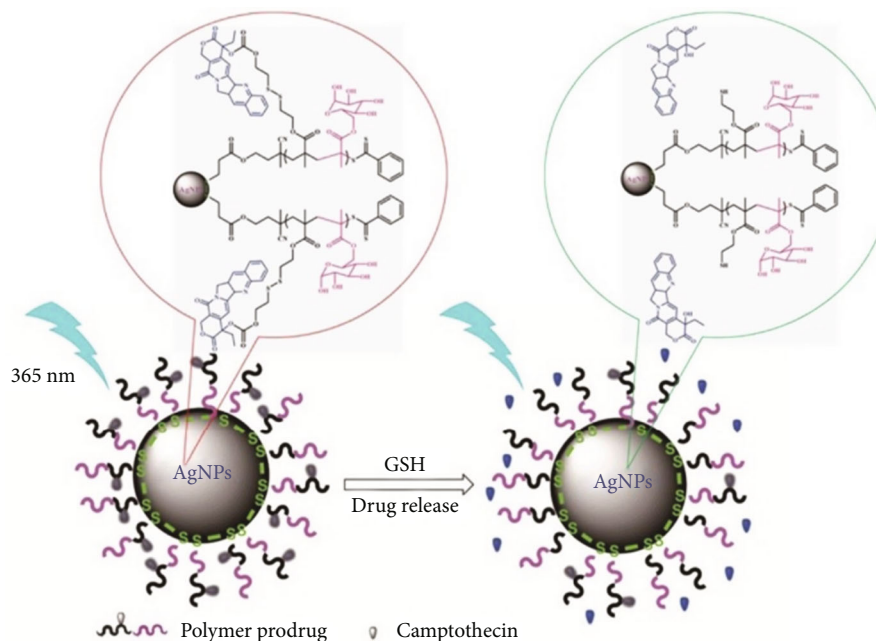


FIGURE 1: Representation of fluorescence “off” and “on” with the release of CPT from redox-responsive P(MACPTS-coMAGP) @AgNPs nanoparticles. Reproduced from [73]. Chinese Chemical Letters (Elsevier).

structure are established with other nanocomposite polymers; the following physical attributes such as interfacial tensile, layering of matrix, bonding energy, resistance under pressure, elasticity, and fabrication are considered. In terms of chemical versatility of nanostructure composites of the renewable polymers, we see the 1D, 2D, and 3D [4] forms and wavelength of electrons and photons [5], mitigating damages at nanoscale level, stability, redox properties [6], optical activity, and crystallinity [7]. On analyzing the physical and chemical versatility of the following nanocomposite particles with technology and advanced resources, this can be crafted by engineers and aid in the rapid production of quality in the polymers. The metallic catalyzed nanoparticle has its own different functions with respect to its contributing strategic properties. Some metallic catalyzed nanoparticles are titanium (II) oxide (TiO) [8], zinc oxides (ZnO), silica, iron oxides (Fe₂O₃), silver nanoparticles (AgNPs) [9], gold nanoparticles (AuNPs) [10], diamond nanoparticles [11], and noble nanostructured particles [12]. Zinc oxide (ZnO) and titanium oxide (TiO) are known to be manufactured worldwide with a contribution of 10,000 tons annually. Zinc oxide (ZnO) and titanium oxide (TiO) own a photocatalytic attribute of cosmetics in sunscreen. Silver nanoparticles (AgNPs) display the ability to cease microbes making it a prerequisite quality for packaging (Figure 1). Gold nanoparticle (AuNPs) and its nanoscale reduce ageing and help as an elixir of anti-inflammatory with blood circulation. Iron oxide (Fe₂O₃) [13] nanoparticles are showcased as an acceptable food colorant, and lastly, diamond nanoparticles with antioxidizing and nontoxic levels with other nanocomposites enact as shielding agent against UV and oxidation. During last year, major power cuts were observed all claiming to the shortages of fossil resources (coals, crude oils, etc.)

and hikes in oil prices and commodity goods. Increasing unlimited demand of consumption goods and other vital resources is leading to scarcity of resources which are set to be depleted in some years about time. There is a need to combat with such crisis; thus, the vigorous conversion of biomass materials into chemical materials has led to an increasing demand in companies. This major breakthrough from the past few years has not limited with an idea of consumption, but with abroad spectrum in urge of biorefineries with less wastage, materials are being mandated but execution is slow. During the esterification of glycerol with fatty acids from plant oils of triglycerides [14] containing other modification that led to increasing chances of new nanostructured materials as shown in (Figure 2), this promising nanostructure from such plant-based oils is manifested in proving with different possibilities of matrices and functions. They are not exclusively in narrow fundamental consumption but a breakthrough of other applications too.

We see that the polysaccharide are subdivided into three nanomolecular structure in order to give the desired result that was accomplished by interaction of two opposite charge form, i.e., anionic and cationic polymer (Figure 2); to form a polyelectrolyte complex, the amphiphilic polysaccharide orients themselves to accomplish emulsions, and the addition of crosslinkers unites into ionotropic gelation per its activating function. Some drawbacks reported are seen that all renewable polymers are not guaranteed biodegradable polymers even despite having biological nanocomposites. Secondly, there is not much improvisation with the transportation to the target receptors or a pathway that has been developed to transport the nanostructured polymers. In this article, we will not be discussing much of microstructured particles.

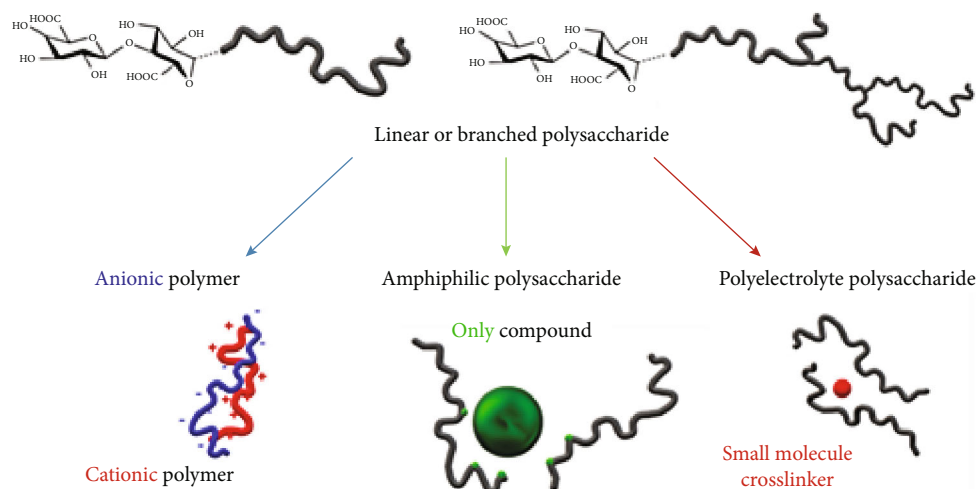


FIGURE 2: Diagrammatic representation of formation of polysaccharide-based nanostructures. Reproduced from [15]. Copyright2020, Molecules (MDPI).

2. Historical Review of Nanostructure Polymeric Material

Humans have previously utilized the natural concrete nanofibers more than 4500 years a long time ago. Based with the synthetic chemical process, the ancient Egyptians also used nanomaterials besides than 4000 years ago [16]. The synthesized approximately ≈ 5 nm diameter PbS nanoparticles were used in hair dye [17]. In the 3rd century, Egyptians used sintered mixture nanometer-sized glass and also in quartz; the “Egyptian blue” was the first synthetic pigment first used and prepared by the Egyptians [18]. Egyptian blue constitutes a mixture of $\text{CaCuSi}_4\text{O}_{10}$ and SiO_2 , i.e., mixture of glass and quartz. On the basis of archaeological explorations, the Egyptian blue used for decorative purposes has been observed in the ancient period in the region of Mesopotamia, Egypt, and Greece. In the scientific arena, Michael Faraday scientifically first described nanoparticle preparation and also initiated the history of nanomaterials in the year 1857. He also give out that the optical features of gold colloids, i.e., Au, are differing compared to their bulk. In the year 1908, Mie explored that the metal colloids have a specific color, the reason behind their quantum size effects. SiO_2 nanoparticles were manufactured as derivative to carbon black for rubber strengthening in the year 1940s. Nowadays, manufactured nanomaterials can significantly enhance the features of bulk materials inside their conductivity, lightness, durability, and strength, and they can give a very useful features such as antifreezing, antibacterial, self-healing, and self-cleaning. In the medieval period, it was found that the red- and yellow-colored stained glass was produced by Au and Ag nanoparticles approximately [19]. In the 9th century, Mesopotamians started using ceramics for metallic luster ornament [20]. In the 19th century, a famous Satsuma glass in Japan was produced. The adsorption properties of Cu nanoparticles are improved by brightening Satsuma glass with ruby color [21]. In the 5000 BC, clay was frequently used to bleach wools and cyprus in cloth [22]. Samsung introduced an antibacterial technology based on

Ag nanoparticle they used in air purifiers, vacuum cleaners, washing machines, refrigerators, and air conditioners, studied in the year 2003 [23]. Nanoparticles are considerably used in the production such as transparent layers used for heated fillers in tires to enhance adhesion on the road and improve the stiffness and window panes [24]. Mercedes-Benz studies a series of production for both type of metallic and nonmetallic paint finishes studies in the year 2003. TiO_2 nanoparticles are used in dye sensitization ability and in solar cells. In the year 2012, Summer represents the first major commercial use of dye-sensitized solar cells [25]. A series of product approximately 1814 nanotechnology-based consumer products are commercially accessible in over 21 countries.

3. Nanostructured Natural Renewable Polymers

3.1. Polysaccharide. Polysaccharide is one of the most versatile and foremost compounds in the biological nature. Polysaccharide is in an abundant quantity and cosmopolitan. Polysaccharide is one of the emerging nanocomposite polymers and highly in demand than the synthetic polymers. Their versatility is in terms of medical, industrial, economic, cosmetic, and recreational activities; thus, with this trait, they are harmonically aligned with the biological systematic resulting in a biodegradable resource. These nanostructured polymers are not only a good biodegradable resource but also in developing an eco-friendly performance. On studying the structural figure of the polysaccharide compounds, we see interlinking functional groups that have a capacity of forming noncovalent bonds with living and nonliving tissues with its carboxyl, hydroxyl, and amino groups. This compact raw structure of polysaccharides is being essentially involved in the production of pure chemical substances for, e.g., polyaddition of bioethanol for ethylene glycol. When other polysaccharides come into contact with hydrophobic and hydrophilic parts, the insertion of polar groups towards the hydrophobic part can result in a glucose backbone arrangement, which may boost the amphiphilic character of the

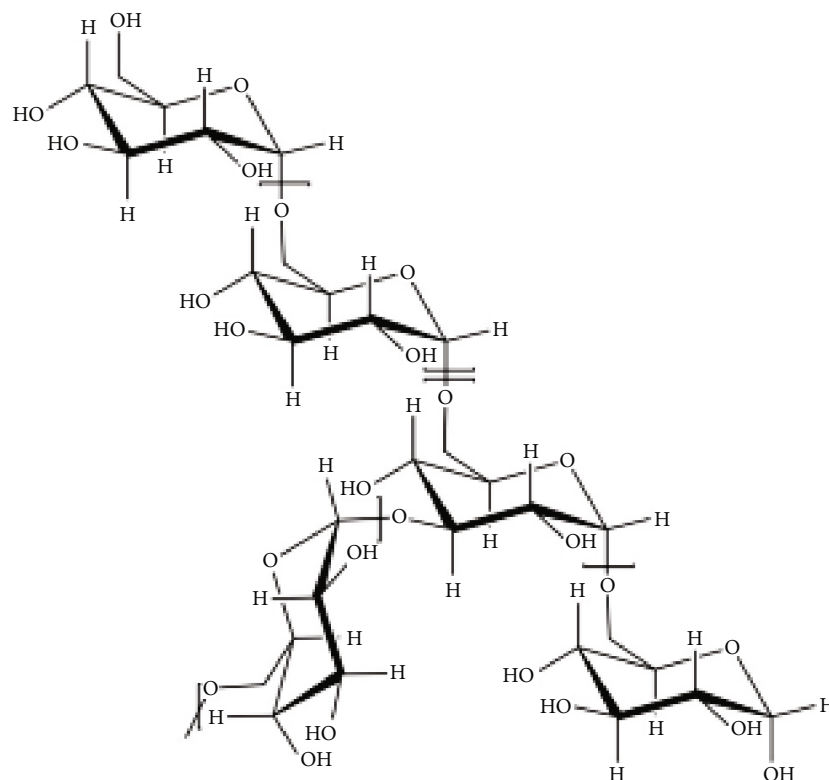


FIGURE 3: Schematic representation of dextran as an example of a branched polysaccharide. Reproduced from [33]. Copyright 2014, Frontiers in Chemistry.

polysaccharide [26]. With the introduction of a polar group through esterification in the polysaccharide nanocomposites, it has expressed the hydroxyl groups [27]. With this process, it has led to the improvement of polysaccharides with the modular structure of cellulose and its derivatives [28, 29] as in cellulose ethers (methylcellulose, carboxymethyl cellulose, and hydroxypropyl cellulose) [30]. They have been a promising nanocomposite for the industrial, medical, cosmetic (shampoos and toothpastes), and lastly edibles (gelato manufacturing).

3.2. Lignin. Lignin nanocomposites are considered being in a profound aggregate in nature. In recent years, lignin, the second most prevalent biopolymer after cellulose, has attracted a lot of attention. Every year, it is predicted that around 21011 tons of lignocellulosic biomass wastes are generated worldwide, making lignin a readily available renewable phenolic component. It has the potential to assist the shift from a fossil-based to a biobased economy by supplanting synthetic chemicals now generated from fossil resources because it is already produced in side streams of pulp and biorefineries. Because only around 40% of the lignin generated in pulping processes is required to meet the processes' internal energy requirement, there is the potential to greatly increase the quantity of lignin (Figure 3) used for material purposes, while still maximizing the efficiency of all biomass components should be expanding in terms of sustainability. Plants are a major component for lignin about 15-30% of its biomass apart from cellulose. So not only it is a considerable material for the paper and cardboard industry but it also

provides a poor solvation rate with respect to aqueous solution; this is because of its lignin composition matrix. Dextran (Figure 3) was originally derived from wine. Lignin has a highly branched polyphenolic polyether comprising of three structural monomers of 4 hydroxyl phenyl guanylyl and syringyl (Figure 3) derivatives chained with the aromatic and aliphatic ether with hyper branches (Figure 3) [31, 32].

Lignin nanocomposites (Figure 3) are considered being in a profound aggregate in nature. Plants are a major component for lignin about 15-30% of its biomass apart from cellulose. So not only it is a considerable material for the paper and cardboard industry but it also provides a poor solvation rate with respect to aqueous solution; this is because of its lignin composition matrix. Lignin (Figure 3) has a highly branched polyphenolic polyether comprising of three structural monomers of 4 hydroxyl phenyl guanylyl and syringyl derivatives chained with the aromatic and aliphatic ether with hyper branches. It is an asymmetric matrix with 2% of lignosulphonate seen in promoters of adhering in material allowing industrial manufacturers in making of bricks, ceramics, fodder pods for livestock, pavement materials, and most importantly circulation of oil-seizing platforms. Since lignin is an asymmetric compound, it was found that with phenolic and aliphatic compounds on further characterization using carbon nanotubes (2,4 toluene diisocyanate), TDI tailed with polymer of propylene glycol functions as chemical sensors.

Further, the hydroxyl groups of lignin films were altered with poly(N-iso-propyl acrylamide) on using this technique

of atom transfer radical polymerization (ATRP) in a bathed environment resulting in ion-sensing nanofibers [34]. In order of carrying hydrophilic substances in lignin nanostructured containers, it was observed with the creation of a hollow nanocapsules by forming a boundary with polyaddition of lignin with TDI in reverse processing in minute emulsion and carrying with dissolving the lignin derivative in an organic solvent and water giving rise to a biodegradable lignin nanocontainer which are able to transport hydrophilic compound.

3.3. Pectin. This is the first most studied and investigated polysaccharide. It is found mainly in the cell wall and middle lamellae of some herbaceous plants such as the peels of citrus fruits like lemon, kumquats, peels of apple pomace, sunflower depurating, and stems of broccoli, thus producing white to light brown-colored powder. Pectin is a heteropolysaccharide constructed polymer of galacturonic acid and rhamnose as its spine with connecting links with arabinose, fucose, galactose, and xylose. This is a structural heteropolysaccharide having a main component composed of α -D galacturonic acid and other sugar acids like D-galactose and L arabinose residues [35]. The contributing characteristics of nanoparticle size of pectin have degree of esterification, methoxylation, and pH levels; it can be detected in the diverse range of ~50 nm-850 nm. Pectin can be studied on the basis of size, shape, and biocompatibility ensuing in three reasonable classifications based on methoxylation of pectin as high methoxylated pectin (HMP), low methoxylated pectin (LMP), and amidated methoxy pectin (AMP). High methoxylated pectin (HMP) having a degree of esterification smaller than 50% and low methoxylated pectin (LMP) having a degree of esterification greater than 50%. When HMP is deesterified using ammonium ions, low methoxylated amidated pectin (AMP) is formed having a DE greater than 25%. Due to its strong mucoadhesiveness, gelling capability, and solubility in many pectin, nanoparticles (NPs) are used in wound healing and oral medication administration natural settings. As a counter to metallic nanoparticles, Birch and Schiffman produced self-assembled polyelectrolyte complex nanoparticles comprised of chitosan and pectin for the treatment of persistent wounds caused by different lifestyle conditions. Antibacterial, anti-inflammatory, and preferred stability in pH ranges of 3.5 to 6.0 are provided by bioadhesive and biodegradable polymeric nanoparticles such as chitosan and pectin NPs, implying significant future potential in wound healing.

It is considered to be a natural diet for human beings but still insignificant with its nutritional amount. Isolated pectin is found to have 30% of polysaccharide in them. Pectin uniquely characterized with a thick gel like appearances is mainly used in confectionaries such as jams, gelato, preservative, and conserves on adding to concentrated solution. Since pectin's resource comes mainly from citrus, their nanostructures are packed with vitamin C which is one most crucial effective in the cosmetic industry. Heavy metal toxicity, which can be caused by exposure to lead, mercury, arsenic, and other elements, has also been treated with pectin. Some individuals feel that modified citrus pectin (MCP)

might aid in the excretion of harmful chemicals from the body. However, there is a scarcity of neutral research to back up such conclusions. Furthermore, due to pectin's strong mucoadhesive nature, all three citrus pectin specimens showed similarities in their description investigations, and we believe they are excellent carriers for oral administration of hydrophobic drugs in regulated dose forms. We aim to conduct comprehensive drug delivery research in the near future using the created and well-characterized pectin nanoparticles. Pectin is indigestible to humans in its native condition. The nanostructure composite of pectin is isolated from the technique of nanoemulsions that can prepare an aqueous gel of sodium caseinate forming a multifunctional complex electrolyte loaded with curcumin extract [36]; its unique compact nanocomposite matrix has been a favorable model for shampoos and lotions.

3.4. Arabic Gum. Arabic gum comes from the *Acacia senegal* and *Acacia seyal* trees that are found in the desert regions. The Acacia tree is most commonly grown in water scarce region and hot climate of African region. The productive extraction of the nanopolymer gum resin is dependent with the season, harvest time, life span of the tree, and most importantly with the quality condition of the tree. The origin of Arabic gum has been found to be one of the ancient times dating back to 2650 BC as due to their viscous nature, they were considered to be utilized in mummification of dead bodies and prime source to protect food from decay. The Arabic gum (Figure 4) nanobiopolymers consist of a cocktail of carbohydrates (mainly D galactose and L arabinose unit) (Figure 4) [37] and proteins (arabinogalactan protein complex (AGP), arabinogalactan, and glycoprotein) (Figure 4) [38]. The dual nature of Arabic gum both being hydrophilic and hydrophobic has made it suitable for easily altering food tastes with shielding and long-lasting amalgamative in food quality products. Other source of Arabic gum such as xanthan, gaur, and locust bean is being explored [39].

Likewise, the adsorbents' exceptional regeneration and recovery of the adsorbed species indicated that it may be used for water filtration. The nanocomposite's superparamagnetic nature, thermal stability, large surface area, and porous structure made it a one-of-a-kind material for wastewater treatment applications. Arabic gum possesses several biological characteristics as an antioxidant in lipid metabolism and in the treatment of a variety of disorders, including diseases of the kidneys, the heart, and the gastrointestinal tract. Arabic gum is used in confectionery, bakery, dairy, and beverage and as a preservative in the food sector. A microencapsulating agent is a substance that may be used to encapsulate. It is used as a stabilizer in dairy products. Because Arabic gum contains a variety of amino acids, it boosts antioxidant capability. Lysine, tyrosine, and histidine are typically considered acid residues as biomolecules that act as antioxidants.

The biological features include antioxidant qualities, an influence of Arabic gum on renal function, blood glucose concentration, intestinal absorption, Arabic gum breakdown in the gut, lipid metabolism, tooth mineralization, and hepatic macrophages, among others. Because Arabic gum

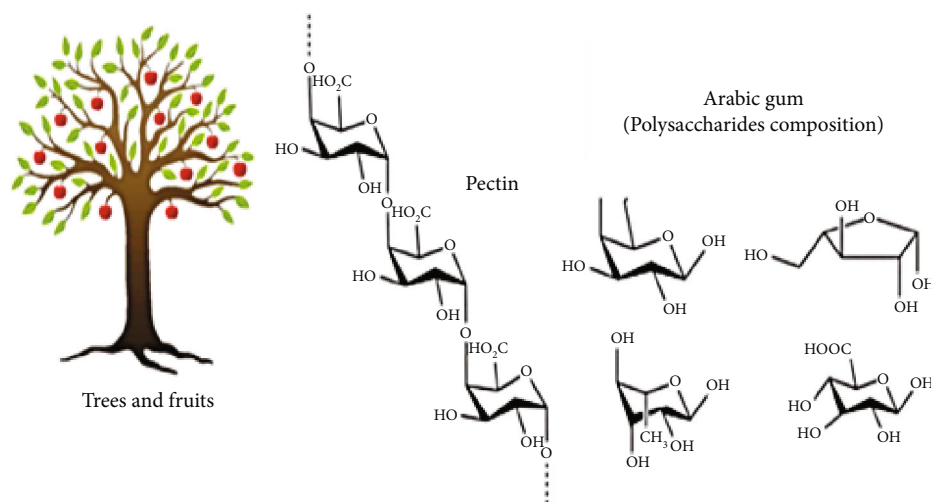


FIGURE 4: Schematic representation of chemical structure of Arabic gum. Reproduced from [15]. Copyright2020, Molecules (MDPI).

contains a variety of amino acids, it boosts antioxidant capability. Arabic gum affects renal function via lowering blood pressure and reducing concentration levels of creatinine and urea nitrogen in diabetic nephropathy patients. Arabic gum leads an effect on fasting blood glucose levels, and glycosylated hemoglobin levels were both considerably lower: HbA_{1c} as well as a considerable drop in blood pressure and HbA_{1c} as well as a considerable decrease in blood uric acid and total protein levels. The transport of water and electrolytes from the intestinal lumen to the bloodstream is facilitated by Arabic gum. Intestinal bacteria may convert Arabic gum to propionate, a short-chain fatty acid. Arabic gum is rich in fiber that aids in weight loss and fat deposition. Arabic gum is employed as a medication carrier in the pharmaceutical sector since it is nontoxic.

It is thought to be a biologically innocuous chemical. Arabic gum possesses several biological characteristics as an antioxidant in lipid metabolism and in the treatment of a variety of disorders, including diseases of the kidneys, the heart, and the gastrointestinal tract.

3.5. Starch. This nanopolymer composite mainly is a store house of energy for plants. The nanocomposites matrix structure comprise of linear poly(1,4- α -D-glucopyranose) with branches of (1,6- α -D-glucopyranose) (amylopectin) (Figure 5) [40]. Starch is a heteropolysaccharide made up of two types of macromolecules: linear amylose (which makes up around 10–30% of the granule) and branching amylopectin (which makes up the remaining 70–90% of the granule). Amylose (Figure 5) is a linear polysaccharide chain made up of d-glucose units joined by a (1,4)-glycosidic bond with a polymer degree varying from 300 to 10,000. Amylopectin (Figure 5) is a high-molecular-weight polymer having an amylose spine that is connected together with -(1,6) glycosidic linkages. The nanostructured composites of starch are mainly obtained by conditioning the granules using ultrasonication which has been one of the utmost factors for substituting with the fat or oil in edible oils. As emulsion stabilizers, fat replacers, flexible films, carriers of bioactive compounds, drug delivery, and adsorbents in sew-

age treatment or wastewater treatment, starch-based nanocomposites have a wide range of applications in food and agriculture, packaging, biomedical, and environmental remediation. Starch nanoparticles have an active surface area of more than 300 nm and are typically less than 300 nm in size. Starch nanoparticles, starch nanospheres, starch micelles, starch vesicles, starch nanogels, and starch nanofibers are examples of starch-based nanoparticles. Because of its renewability, biodegradability, availability, eco-friendliness, cheap cost, nontoxicity, high adsorptive capabilities, amenability to numerous chemical changes, and cohesive film-forming abilities, starch has received much interest. Through the functional (hydroxyl) groups on the starch structure, starch molecules can bond with heavy metal ions or pollutants. Secondly, starch with a high amylopectin concentration exhibits strong swelling capabilities, which are crucial in sorption applications. Carbohydrates have been utilized as reducing, stabilizing, and/or complexing agents in the majority of reported studies. Due to the interactions between the individual constituents, starch-based hybrid materials show a range of capabilities and/or novel properties, most of which are associated with synergetic effects, and have been observed in environmental remediation applications. Several starch-based composites have been found to have a strong adsorption ability for heavy metals and dyes removal. Since starch comes from a polysaccharide derivative, thus it is one of the governing factors for its versatility. However, starch in its pure or natural form has disadvantages such as poor processability, high brittleness, retrogradability, high viscosity, low adsorption capacity, and increased hydrophilicity or high water absorption capacity, which restricts its numerous environmental uses. Starch is transformed physically (hydrothermal processing (i.e. gelatinization)) or chemically (etherification, esterification, crosslinking, grafting, oxidation, and enzymatic hydrolysis) or a combination of these two processes to overcome this challenge and generate water-insoluble polymers. Polysaccharides include several reactive hydroxyl groups that can be used for direct esterification, etherification, and other chemical changes. This replacement has brought with the manageable industrial wastes. These materials offer a realistic

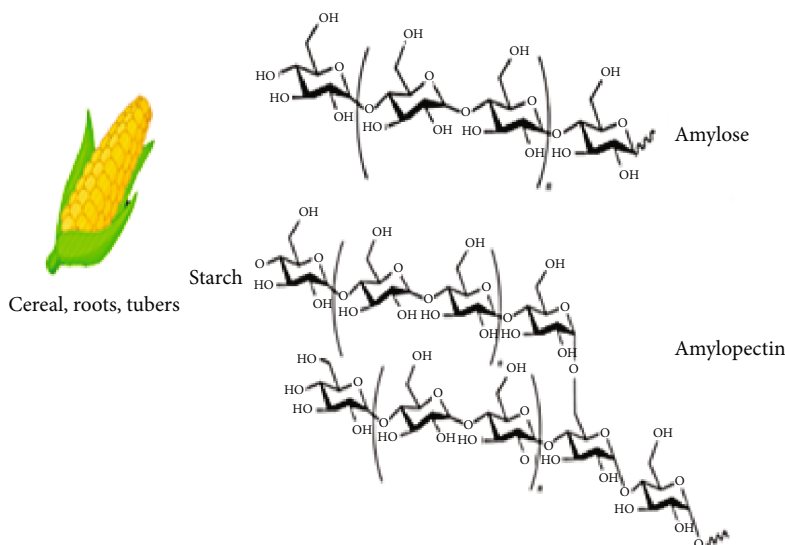


FIGURE 5: Schematic representation of chemical structure Amylose & Amylopectin. Reproduced from [15]. Copyright 2020, Molecules (MDPI).

and cost-effective alternative to petroleum-based counterparts in the fight against pollution. To eliminate different harmful impurities such as heavy metals, organic contaminants, and dye wastewater, starches are combined with metal NPs, metal oxide NPs, zero-valent metals, CNTs, and other polymers as reducing, stabilizing, and/or complexing agents. In African countries, starch meals are one of their food resources in order to combat with hunger, but still, this polysaccharide nanocomposite derivative is in the need of advancement due to their lesser number of calories provided as compared to other food resources.

3.6. Bacterial Cellulose. Bacterial cellulose is one of the natural biopolymers. It withholds a unique structure of nanofiber which are three-dimensional reticulated network matrix. In 1883, Brown discovered in *Acetobacter xylinum* and *Gluconacetobacter xylinus* aerobic conditions thriving in glucose as carbon source. Bacterial cellulose can also be extracted from *Agrobacterium* and *Sarcinia ventriculi*. Because of its nanofibrillar matrix, bacterial cellulose is very biodegradable and has excellent physicochemical qualities. Because of the high level of natural purity, this substance demonstrates negligible toxicity in practically all applications, allowing this dressing to be used directly. However, fungi, seaweed, and some bacterial species may produce cellulose, most notably the non-pathogenic, strictly aerobic, Gram-negative bacterium *Komagateibacter* sp. (previously *Acetobacter* and *Gluconacetobacter*), with *Komagateibacter xylinus* being the best researched species (*K. xylinus*). Bacterial cellulose has features that are consistent in integrating macromolecular and surface properties, which are important for clinical field both in vivo and in vitro. Bacterial cellulose has since been proven to be a promising new biomaterial for biomedical use. As a result, the objective of this review is to summarize and evaluate the most recent advancements and uses of bacterial cellulose in a biomedical environment, including the bioengineered material and bacterial cellulose.

Bacterial cellulose is at the forefront of regenerative medicine, since it improves cellular adhesion, stimulates cell proliferation, migration, and eventual differentiation, and therefore speeds wound healing. Biomedical devices built of bacterial cellulose have several advantages, including minimal toxicity and the capacity to keep wounds wet. The bacteria begin the manufacture of cellulose by passively collecting glucose from the environment, which is subsequently isomerized from glucose-6-phosphate to glucose-1-phosphate. The uridine diphosphate glucose, UDP-glucose, is formed when this isomer interacts with uridine-5-triphosphate (UTP). This UTP-glucose is subsequently converted into linear 1,4 glucan chains by cellulose synthase A, which is triggered by cyclic-di-GMP. The cellulose chains are subsequently expelled by the bacteria through holes in the cell wall. If the bacteria run out of glucose, it will switch to the fructose pathway, which uses the same biochemical pathways as the glucose pathway. A particular operon termed bacterial cellulose synthesis ABCD (bcsABCD) that was discovered in *K. xylinus* in 1999 modulates the metabolic pathways. The first gene in the bcsABCD operon, bcsA, is responsible for encoding cellulose synthase, the enzyme's catalytic component. The second gene, bcsB, is responsible for the creation of a regulatory component located on cellulose synthase that binds to c-di-GMP, which is very important since this contact promotes the formation of cellulose. The activities of bcsC and bcsD remain unknown; however, it is thought that bcsC plays a role in the formation of holes in the cell membrane, and the proteins encoded by these genes are comparable to pore-forming proteins. *K. xylinus* may grow in shallow containers with semidefined growth media in a static incubator at 30°C for 7 to 14 days, after which a thick pellicle of cellulose develops at the liquid surface contact and is readily collected. Although this is the most common technique of manufacturing BC, it has some drawbacks, including cultivation time and expense. Furthermore, since the organisms are exposed to different growth

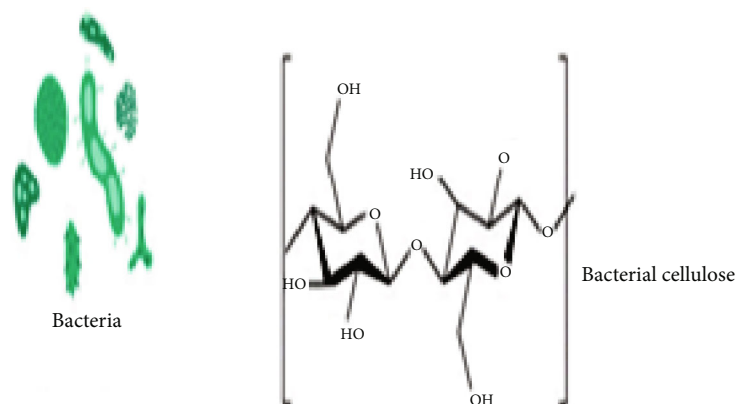


FIGURE 6: Schematic representation of chemical structure of Bacterial Cellulose. Reproduced from [15]. Copyright 2020, Molecules (MDPI).

environments, such as some being exposed to oxygen while others are exposed to anaerobic conditions, and because of changes in carbon supply gradients, cellulose synthesis might be unequal. Bacterial cellulose has been in much use over plant cellulose due to it being in much greater quantity than plant cellulose. It shows much profit with the terms of cost-effective manufacturing, free from impurities, and much wider scope than plant cellulose. The structural property of bacterial cellulose aids in understanding the potential uses and drawbacks of the composition in order to configure the magnitude and way of production. Cellulose is made up of linear homopolysaccharides connected by 1,4-glycosidic connections (Figure 6) and conjugated by β -D-glucose units (Figure 6). This is due to the unique 3D structure of bacterial cellulose, which accounts for its better physical qualities as compared to vegetal cellulose. Bacterial cellulose fibrils, for example, form extensive aggregate networks with an average diameter of 1.5 nm, resulting in significantly increased surface area, flexibility, elasticity, and tensile strength.

Following the successful production of cellulose exopolysaccharides, the linear chains of cellulose are organized into 10–15 polymer chains, resulting in nanofibers that are then sequentially structured to produce microfibrils that are 100 times smaller than their vegetal counterparts. Microfibril bundles are formed by bundling the microfibrils together (Figure 6). Microfibril bundles are formed by bundling the microfibrils together. The microfibril bundles are grouped together to produce cellulose ribbons that are 3–4 nm thick and 70–80 nm broad. These ribbons then randomly intertwine to produce a thick matrix of cellulose fibers, which is formed by strong inter- and intrachemical interaction, principally hydrogen bonding, that happens between consecutive sheets of cellulose. This high amount of hydrogen bonding also permits cavities to develop inside the cellulose, which has an ionic charge that allows elements like silver ions to be implanted into the material. This characteristic of cellulose will enable manipulations such as loading the cellulose with antibacterial compounds having an ionic charge aiming at organisms causing harm. Bacterial cellulose has shown flexibility with lipophilic molecules used in ice cream production and gum as a lipid substitute, production in coconut milk fermentation, and amalgamating constancy with an increase in manufacturing.

The unique structure of nanofiber encompasses hydroxyl groups and crystalline structure with hydrogen bonds for improved hydrophilicity and possible hydrophobicity owing to its nanocrystal's matrix [41]. It is seen that these nanocrystals can interact with lipophilic molecules even without a hydrophobic group.

3.7. Bacterial Biosurfactants. These are commonly known as microbial surfactants; they are known to produce microorganisms which are said to be in dual nature towards aqueous medium being hydrophilic and hydrophobic. Some commonly known microbes are yeast, bacteria, and fungi. Bacterial biosurfactants comprises of glycolipid, lipopeptides, lipoproteins, fatty acids, polysaccharides, and phospholipids [42]. The structural composition of a biosurfactant is a polar hydrophobic tail with a polar head group linked with a carbon chain group. Agricultural production is negatively impacted by changing climatic circumstances such as increasing temperatures, unpredictable rainfall, and biotic and abiotic stress factors. Agronomists, researchers, and the scientific community are also concerned about the emergence of new pests, pathogens, or plant diseases. Indeed, for pathogen control or plant disease management, a bigger population in both industrialized and developing nations relies on chemical pesticides or agrochemicals. Yet, the prolonged and unrepresentative use of agrochemicals results in hazardous chemical residues in food, poor nutritional quality, and the rise of pesticide-resistant diseases. Agrochemical deposition also has an unfavorable impact on the texture, nutritional quality, and natural microflora of the soil, as well as causing environmental issues by damaging soil and water habitats. In the last two decades, however, microorganisms and their products have been widely used to improve agricultural productivity and crop output, as well as to reduce harmful and dangerous environmental pollutants. Microbes are also preferred in numerous industries for sustainable development and production due to their diverse nature, simple production methods, cost-effectiveness, and minimal or no hazardous influence on the surrounding environment.

Biosurfactants are one of the most recently discovered microbially generated biomolecules, and they are widely used as raw materials in the agriculture, waste management, and pharmaceutical sectors for lubrication, wetting, and

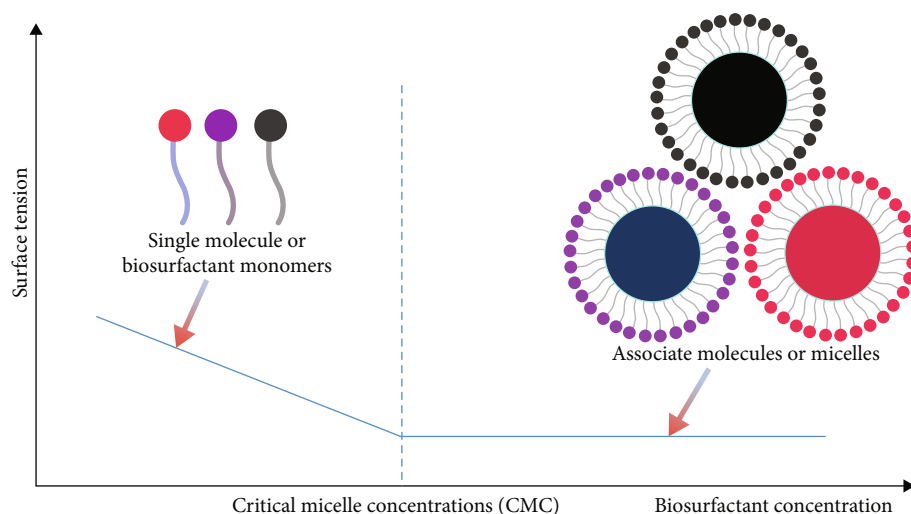


FIGURE 7: Critical micelle formation (CMC) and combination of micelles with other biosurfactant monomers. Reproduced from [43]. Copyright 2021, Antioxidants (MDPI).

other activities. We observe that when these biosurfactants aggregate, i.e., monomers (Figure 7), with each other, they form a compact associate molecules or micelles (Figure 7) at a particular temperature enough to activate and produce the desired results.

The quality and quantity of biosurfactants, on the other hand, are dependent on a number of elements, including the kind of microbe, medium additives, substrate nature, and many internal and external conditions during microbial culture development. The fundamental procedure in the synthesis of biosurfactants is the selection of microbial strains. Therefore, during the exponential or stationary phases of development, when nutritional levels are restricted, biosurfactant production occurs either intracellularly or extracellularly in the microbial strain. The composition of biosurfactants (Figure 7) is also influenced by the source and separation tactics of microorganisms; for example, a strain isolated from a polluted location is regarded a good candidate for contaminant degradation. The idea behind this is that the isolated bacterium may employ the contamination as a food source. Biosurfactants (Figure 7) also play a physiologic factor in improving the bioavailability of hydrophobic molecules involved in cellular activation and development processes, as well as facilitating the absorption of carbon sources found in the soil. Indeed, the physiological aspect of biosurfactant generation in a polluted site is unknown, although it is thought to improve nutrient absorption from hydrophobic substrates, biofilm development, and cellular motility by lowering surface tension at the phase boundary. During the study of biosurfactant molecules, quick and reliable methods for the isolation and screening of microbial strains, as well as subsequent assessment of their involvement in emulsification, lowering interfacial, or surface tension, are key aspects. Bushnell and Hass discovered biosurfactants generated by the microorganisms *Corynebacterium simplex* and *Pseudomonas aeruginosa* in early 1941. Microbial growth depends on the presence of carbon (C) and nitrogen (N) sources in the medium. In both

laboratory and large-scale industrial fermenters, the type, quantity, and ratio of carbon and nitrogen in the medium have a direct impact on microbial growth and biosurfactant synthesis. Most research employed glucose, sucrose, and glycerol as carbon and yeast extract, respectively, and NaNO_3 , urea, and soya broth as a nitrogen source in the medium. For example, for optimal biosurfactant formation, an abundance of carbon sources and nitrogen limitation are desired. For *Pseudomonas* species, for example, a C/N ratio of 20 has been determined to be the most beneficial. The most favorable use has been in the detergents, emulsifiers, wetting, and foaming agents and also to promote solubilization of hydrophobic substances [44].

3.8. Hyaluronic Acid. Hyaluronic acid (HA) (Figure 8) also known as hyaluronan is a linear, negatively charged comprising of repeated structure of β -1,4 D glucuronic acid and β -1,3-N-acetyl-D-glucosamine disaccharide units as shown in Figure 8. Hyaluronic acid has been found to be a cornerstone to beauty industry due its immense hydrophilicity trait.

The nanostructured polyelectrolyte complex was modified with polycation chitosan and then used as an enveloping agent towards menthol and eugenol to provide slow growth of microbes. There is more work to be needed in the upcoming days.

4. Biomedical Application

In the industrial arena, nanostructured polymeric materials can be used to improve a wide range of biological applications including wound healing devices, pharmacological patches, glues, and drug carriers. Application of vegetable oil-based polymeric materials can increase the biodegradation of the material. Various biomedical application essential materials range from soft to hard. In human metabolism, both endogenous compounds such as glycerol and sebacic acid in two monomers are found.

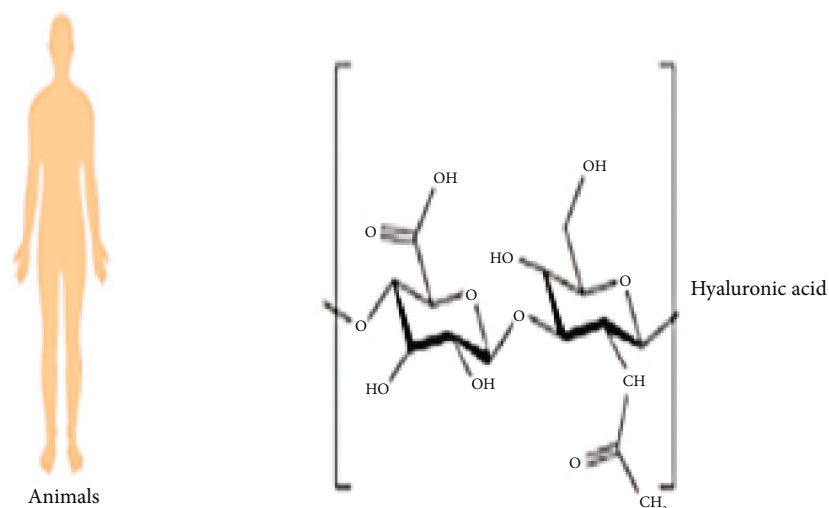


FIGURE 8: Schematic representation of chemical structure of hyaluronic acid. Reproduced from [15]. Copyright 2020, Molecules (MDPI).

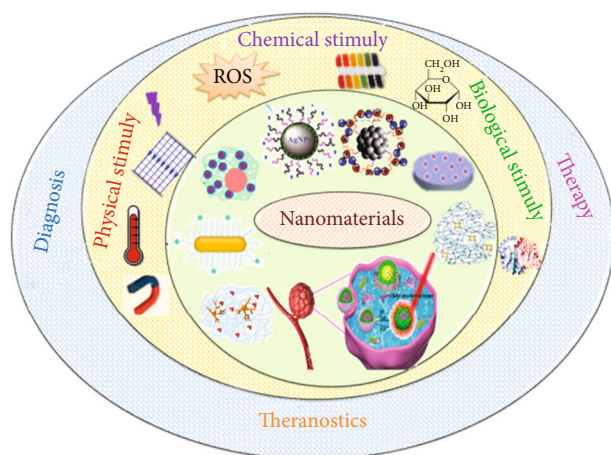


FIGURE 9: Biomedical applications of smart nanomaterials as a function of their nanostructure. Reproduced from [51]. Copyright 2021, Nanomaterials, MDPI.

Cis platinum and paclitaxel exhibit localized antitumor agent delivery [45–48]. Similarly, polymers were utilized for controlled release of peptide drugs and protein [49]. Treatment of osteomyelitis is used in the delivery of gentamicin sulphate and used in delivery of local anesthetics [50]. On the other hand, the harder materials such as polyurethane polymeric soya bean oil polystyrene membranes system are mainly based on the sunflower oils and soya bean. They were exploring for tissue engineering showing encouraging proliferation and cell adherence (Figure 9). Various examples of physioresponsive nanomaterials and their biomedical applications are reported in Table 1. Several examples of chemical-responsive nanomaterials and their biomedical applications are discussed in Table 2. Several examples of biological-responsive nanomaterials and their biomedical applications are discussed in Table 3. Various research papers such as dual and multiresponsive nanomaterials and their biomedical applications are reported in Table 4.

For monitoring the release of anticancer drugs, a drug carrier system based on the redox-responsive P[(2-((camptothecin)-oxy)ethyl) disulfanyl)ethylmethacrylate]-co-(2-(D-galactose)methylmethacrylate)] (P(MACPTS-co-MAGP)) and AgNPs has been developed. The anticancer medication camptothecin (CPT) is bound to the surface of AgNPs through a redox-sensitive disulfide bond on the side chain of P(MACPTS-coMAGP) (Figure 1). Reversible addition-fragmentation chain transfer (RAFT) polymerization of monomers of 2-(D-galactose) methylmethacrylate (MAGP) and 2-(2-((camptothecin)-oxy)ethyl)disulfanyl) ethylmethacrylate (MACPTS) coupling with CPT yielded P(MACPTS-coMAGP). MAGP units with a D-galactose structure have a high biocompatibility and are commonly employed in medicine. Disulfide bonds, a well-known redox-responsive structure, have long been used in drug delivery systems to stimulate drug release. Additionally, disulfide bonds have a strong interaction with metal nanoparticles, allowing them to easily bind to their surfaces. As a result, the distance between CPT and AgNPs is near enough to meet the requirements. The NSET effect causes CPT fluorescence to be suppressed (“off”). When a reducing agent, such as glutathione, is present (GSH), because of this, the CPT molecule is released from the hybrid nanoparticles. The disulfide link is cleaved, allowing the disulfide bond to be recovered: CPT fluorescence (“on” state). As a result, the stimulus-responsive system anticancer medicine delivery and monitoring are both possible with a complicated system. CPT is released when the fluorescence “turn-on” signal of CPT is activated (as seen in Figure 1).

5. Conclusion and Future Prospects

The promising era of science and technology has led to the fact that some trustworthy natural nanostructured polymers are in the aim of being biodegradable and sustaining in nature. Natural nanostructured derivative polymers have proven its capacity of overtaking the synthetic polymers. There has been environmentally favored unsheathing

TABLE 1: Various examples of physioresponsive nanomaterials and their biomedical applications.

Sr. no.	Nanomaterials	Application	References
1.	3D collagen hydrogel	Directed neuronal regeneration	[52]
2.	Fe ₃ O ₄ /MePEG-PLA nanocapsules	MRI	[53]
3.	Ruthenium-containing block copolymer poly-Ru nanoparticles	In vivo photodynamic therapy and photochemotherapy	[54]
4.	Poly(ethylene glycol) PEG	Switchable fluorescent probes	[55]
5.	Fe ₃ O ₄ /polyaniline Fe ₃ O ₄ /PANI	Fe ₃ O ₄ /polyaniline Fe ₃ O ₄ /PANI	[56]
6.	Polyaniline/gold nanocomposite PANI/AuNCs	Immunosensor detection of chronic kidney disease	[57]
7.	Poly(catechol)/graphene Oxide/graphene sheet suspension/AuNP/pol/gr/GCEs	DNA biosensor/electrochemical biosensors/lymphoblastic leukemia	[58]
8.	Gold nanoparticles	Drug delivery, photothermal platform, and skin wound healing	[59]
9.	Nanofibers of biodegradable poly(L-lactide) (PLLA)/poly(lactide-co-glycolide) (PLGA)	Drug delivery	[60]
10.	PMASH magnetic nanocapsules	Tumor therapy	[61]
11.	Polyaniline, poly(3,4-ethylenedioxythiophene) PANIP, and PEDOT	Neural prostheses	[62]

TABLE 2: Various examples of chemical-responsive nanomaterials and their biomedical applications.

Sr. no.	Nanomaterials	Application	References
1.	Octasulfonate-modified zinc (II) phthalocyanine (ZnPcS ₈) and layered double hydroxide (LDH)	Theranostics	[63]
2.	P(MACPTS-co-MAGP)@AgNPs nanoparticles/P(MACPTS-co-MAGP)@AgNPs	Drug release	[64]
3.	Folate redox-responsive chitosan nanoparticles FTC-NPs	Anticancer drug delivery	[65]
4.	Hyaluronic acid-functionalized nanoparticles/(HACSLA-NPs)	Breast cancer therapy	[66]
5.	PEGylated redox-responsive nanoscale COFs (denoted F68@SS-COFs)	Cancer therapy	[67]
6.	Hybrid nanotransistor	Receptor-mediated endocytosis in tumor cells	[68]
7.	Melanin-like nanoparticles	Photoacoustic imaging of tumors	[69]
8.	PEG-Ag NPs	Antibacterial, wound healing	[70]
9.	Poly(ethylene glycol)	Prodrug for breast cancer cells	[71]
10.	AgNPs hybrid nanoparticles	Drug delivery	[72]

TABLE 3: Various examples of biological-responsive nanomaterials and their biomedical applications.

Sr. no.	Nanomaterial	Application	References
1.	(CMCS-PBA-LV) NPs/liposomal nanoparticles	Oral administration of insulin	[74]
2.	ATP-ag nanoparticles/chitosan-based multifunctional nanocarriers	Participate in signal transduction and protein activity	[75]
3.	Silver nanoparticles	Therapeutic delivery	[76]
4.	Mesoporous silica nanoparticles-silver nanoparticles	Tissue growth in vivo process	[77]
5.	Hyaluronic acid- (HA-) coated calcium carbonate NP	Oral insulin delivery	[78]
6.	Chitosan/poly(gamma-glutamic acid) nanoparticles	Oral insulin delivery	[79]
7.	Boronic acid-derived polymers	Drug delivery	[80]
8.	ATP-Ag nanoparticles	Participate in signal transduction and protein activity	[81]

techniques, and emulsifying polysaccharides have proven to be cost reliable in terms of isolation of a nanopolymer matrix from biopolymers. Nanostructured natural polymers

have expressed in synthesizing different biopolymers to some useful chemical structures. Since polysaccharide are available in bulk, it is seen that there is maximum

TABLE 4: Examples of dual and multiresponsive nanomaterials and their biomedical applications.

Sr. no.	Nanomaterial	Application	References
1.	(LAE-co-PGDE-co-Lys) core-crosslinked nanocarrier	Anticancer drug delivery	[82]
2.	Nanogels based on alginate and cystamine	Anticancer drug delivery	[83]
3.	Poly(ethylene glycol) nanoparticles PLL-ICG	Photothermal and photodynamic therapy	[84]
4.	Histidine-4 polyamidoamine dendrimer Nanocarrier	Anticancer drug delivery	[85]
5.	Poly(NIPAM) nanogel @ Fe ₃ O ₄ NPs	Anticancer drug delivery	[86]
6.	Silica-coated mesoporous carbon nanocomposite (MCN@Si)	Chemophotothermal therapy of tumor	[87]
7.	Magnetic nanoparticles MFNPs	Targeting, drug delivery, and MR	[88]
8.	2-hydroxyethylmethacrylate (HEMA)/ <i>N,N'</i> -bis(acryloyl)cystamine (BACy)/poly(<i>N</i> -isopropylacrylamide) (PNIPAM)/methacrylic acid (MAA)	Drug delivery	[89]
9.	Poly(ethylene oxide, 2-(diethylamino)ethyl methacrylate	Drug release	[90]
10.	Six-arm star-shaped amphiphilic copolymer with poly(caprolactone)-bpoly(acrylic acid)-b-poly(poly(ethylene glycol) methyl ether methacrylate)	Anticancer drug delivery	[15]

productivity and chemical composition of material from it. However, the setback is all given. In conclusion, all three citrus pectin samples depicted similarity in their characterization studies, and because of the high mucoadhesive nature of pectin, we believe them to be suitable carriers for oral delivery of hydrophobic drug in controlled dosage forms. We plan to conduct a detailed drug delivery studies in the near future based on the developed and well-characterized pectin nanoparticles. The dissolving rate of lignin and also pectin has proven to be challenging. As a result, there is less nutritional content and a less agitated digestive system, which can lead to major health problems if consumed on a regular basis without medical supervision. Modified citrus pectin (MCP), a modified kind of pectin, on the other hand, has properties that make it digestible. Pectin might be useful in cancer therapy. MCP seemed to slow prostate cancer development. Pectin needs advancement in terms of biodegradability in order to sustain the biological environment. Before any judgments concerning MCP's potential as an anticancer drug can be reached, larger, better-designed research are required. In environmental remediation, starch-based materials offer a more cost-effective and environmentally benign alternative to petroleum-based polymers. Though starch is an organic nanomaterial with several features such as renewability, biodegradability, abundance, eco-friendliness, cheap cost, nontoxic, weak barrier, and mechanical qualities, raw starch has poor processability, high brittleness, and high hydrophilicity. As a result, physical and/or chemical processes such as gelatinization, etherification, esterification, crosslinking, grafting, oxidation, and enzymatic hydrolysis are used to modify starch, while the physical qualities of gum Arabic are affected by tree age and processing circumstances. Moisture, total ash, volatile matter, and other quality characteristics have been developed internal power. Because Arabic gum contains a variety of amino acids, it boosts antioxidant capability. Arabic gum is employed as a medication carrier in the pharmaceutical sector since it is nontoxic. It is thought to be a biologically

innocuous chemical. Starch-based materials contain a wide range of functions and/or unique characteristics, which are mostly linked to synergetic effects and have been documented in environmental remediation applications. Various natural starch sources, green nanomaterial production, recyclability, and the toxicity effect of nanowaste should all be explored in future studies. For commercial use, ongoing research of biodegradable starch-based hybrids and nanomaterials emphasizing on new functional materials, processing technology, and cost reduction is required. Bacterial cellulose has been recognized as a highly adaptable material for producing medically relevant materials such as wound dressings, composites, dental grafts, and gels, all of which have unique properties that are well matched to their functions. Furthermore, bacterial cellulose biomaterials have been studied for use in a variety of biomedical applications, including the production of wound dressings for mild to severe wounds. These investigations are ongoing. Bacterial biosurfactants have a long history of helpful compatibility in terms of physical, chemical, and biological applications, making them an excellent choice for multifunctional nanopolymer composites. Bacteria are global; thus, studying these nanocomposites is easier. Biosurfactant chemicals require extensive investigation in order to develop new antibacterial, antioxidant, and antiproliferative agents. This is not only economical, but it also protects the body from the substance's hazardous effects. Biosurfactant-based cancer therapy and drug delivery, on the other hand, require further investigation for the treatment of chronic disorders. Despite advancements in technology and raw materials, biosurfactants' high manufacturing costs and low yield continue to be a challenge to overcome. Furthermore, none of these alternatives has yet to adequately address all of the issues that have arisen. The maximum propagation of natural nanostructured biopolymers with the new rising technology is still not being able to quantify its amount with the rapid on-going demands which is also challenging. When looking at the quality of the nanostructured biopolymer, the quantity

trait becomes underestimated which is also proven to be one of the major setbacks. There is still research and still opportunities of more research to be conducted. The future of nanomaterials is very bright, and it beckons all the areas of modern science.

Data Availability

No data were used to support this study.

Conflicts of Interest

The authors declare that the research was conducted in the absence of any commercial or financial relationships that could be construed as a potential conflict of interest.

Acknowledgments

We express our sincere gratitude to the Head and Dean, Department of Chemistry, Central University of Allahabad, Prayagraj, for providing laboratory facility. The authors are very thankful to the Under Grant Commission, New Delhi, for the economic support in the form of CRET Fellowship.

References

- [1] A. Gandini and T. M. Lacerda, "From monomers to polymers from renewable resources: recent advances," *Progress in Polymer Science*, vol. 48, pp. 1–39, 2015.
- [2] F. Luzi, D. Puglia, and L. Torre, "Natural fiber biodegradable composites and nanocomposites: a biomedical application," in *Biomass, Biopolymer-Based Materials, and Bioenergy*, pp. 179–201, Woodhead Publishing, 2019.
- [3] F. J. Martin-Martinez, K. Jin, D. López Barreiro, and M. J. Buehler, "The rise of hierarchical nanostructured materials from renewable sources: learning from nature," *ACS Nano*, vol. 12, no. 8, pp. 7425–7433, 2018.
- [4] M. Wysokowski, I. Petrenko, A. Stelling, D. Stawski, T. Jesionowski, and H. Ehrlich, "Poriferan chitin as a versatile template for extreme biomimetics," *Polymers*, vol. 7, no. 2, pp. 235–265, 2015.
- [5] N. Corrigan, J. Yeow, P. Judzewitsch, J. Xu, and C. Boyer, "Seeing the light: advancing materials chemistry through photopolymerization," *Angewandte Chemie*, vol. 131, no. 16, pp. 5224–5243, 2019.
- [6] U. A. Banin, N. Waiskopf, L. Hammarström et al., "Nanotechnology for catalysis and solar energy conversion," *Nanotechnology*, vol. 32, no. 4, article 042003, 2020.
- [7] Y. Wang, A. Vogel, M. Sachs et al., "Current understanding and challenges of solar-driven hydrogen generation using polymeric photocatalysts," *Nature Energy*, vol. 4, no. 9, pp. 746–760, 2019.
- [8] P. A. DeSario, J. J. Pietron, T. H. Brintlinger et al., "Oxidation-stable plasmonic copper nanoparticles in photocatalytic TiO₂ nanoarchitectures," *Nanoscale*, vol. 9, no. 32, pp. 11720–11729, 2017.
- [9] T. Naseem and T. Durrani, "The role of some important metal oxide nanoparticles for wastewater and antibacterial applications: a review," *Environmental Chemistry and Ecotoxicology*, vol. 3, pp. 59–75, 2021.
- [10] S. Wu, T. Wang, and X. Hangxun, "Regulating heterogeneous catalysis of gold nanoparticles with polymer mechanochemistry," *ACS Macro Letters*, vol. 9, no. 9, pp. 1192–1197, 2020.
- [11] S. Navalón, A. Dhakshinamoorthy, M. Álvaro, and H. García, "Diamond nanoparticles in heterogeneous catalysis," *Chemistry of Materials*, vol. 32, no. 10, pp. 4116–4143, 2020.
- [12] J. Prakash, J. C. Pivin, and H. C. Swart, "Noble metal nanoparticles embedding into polymeric materials: from fundamentals to applications," *Advances in Colloid and Interface Science*, vol. 226, no. Part B, pp. 187–202, 2015.
- [13] D. Roper, K. R. Berry, J. R. Dunklin et al., "Effects of geometry and composition of soft polymer films embedded with nanoparticles on rates for optothermal heat dissipation," *Nanoscale*, vol. 10, no. 24, pp. 11531–11543, 2018.
- [14] S. Goyal, N. B. Hernández, and E. W. Cochran, "An update on the future prospects of glycerol polymers," *Polymer International*, vol. 70, no. 7, pp. 911–917, 2021.
- [15] A. Massironi, A. Morelli, D. Puppi, and F. Chiellini, "Renewable polysaccharides micro/nanostructures for food and cosmetic applications," *Molecules*, vol. 25, no. 21, p. 4886, 2020.
- [16] T. A. Debele, S. L. Mekuria, and H.-C. Tsai, "Polysaccharide based nanogels in the drug delivery system: application as the carrier of pharmaceutical agents," *Materials Science and Engineering*, vol. 68, pp. 964–981, 2016.
- [17] F. J. Heiligtag and M. Niederberger, "The fascinating world of nanoparticle research," *Materials Today*, vol. 16, no. 7–8, pp. 262–271, 2013.
- [18] D. A. Scott, "A review of ancient Egyptian pigments and cosmetics," *Studies in Conservation*, vol. 61, no. 4, pp. 185–202, 2016.
- [19] S. Bayda, M. Adeel, T. Tuccinardi, M. Cordani, and F. Rizzolio, "The history of nanoscience and nanotechnology: from chemical–physical applications to nanomedicine," *Molecules*, vol. 25, no. 1, p. 112, 2020.
- [20] P. Sciau, L. Noé, and P. Colomban, "Metal nanoparticles in contemporary potters' master pieces: Lustre and red "Pigeon blood" potteries as models to understand the ancient pottery," *Ceramics International*, vol. 42, no. 14, pp. 15349–15357, 2016.
- [21] J. Jeevanandam, A. Barhoum, Y. S. Chan, A. Dufresne, and M. K. Danquah, "Review on nanoparticles and nanostructured materials: history, sources, toxicity and regulations," *Beilstein Journal of Nanotechnology*, vol. 9, no. 1, pp. 1050–1074, 2018.
- [22] D. Schaming and H. Remita, "Nanotechnology: from the ancient time to nowadays," *Foundations of Chemistry*, vol. 17, no. 3, pp. 187–205, 2015.
- [23] A. Ravindran, P. Chandran, and S. Sudheer Khan, "Biofunctionalized silver nanoparticles: advances and prospects," *Colloids and Surfaces B: Biointerfaces*, vol. 105, pp. 342–352, 2013.
- [24] J. Mathew, J. Joy, and S. C. George, "Potential applications of nanotechnology in transportation: a review," *Journal of King Saud University-Science*, vol. 31, no. 4, pp. 586–594, 2019.
- [25] R. Vittal and K.-C. Ho, "Zinc oxide based dye-sensitized solar cells: a review," *Renewable and Sustainable Energy Reviews*, vol. 70, pp. 920–935, 2017.
- [26] S. De, A. M. Balu, J. C. van der Waal, and R. Luque, "Biomass-derived porous carbon materials: synthesis and catalytic applications," *ChemCatChem*, vol. 7, no. 11, pp. 1608–1629, 2015.
- [27] R. Wu, K. Liu, J. Ren et al., "Cellulose nanocrystals extracted from grape pomace with deep eutectic solvents and application for self-healing nanocomposite hydrogels," *Macromolecular Materials and Engineering*, vol. 305, no. 3, article 1900673, 2020.

- [28] C. Hervé, A. Rogowski, A. W. Blake, S. E. Marcus, H. J. Gilbert, and J. P. Knox, "Carbohydrate-binding modules promote the enzymatic deconstruction of intact plant cell walls by targeting and proximity effects," *Proceedings of the National Academy of Sciences*, vol. 107, no. 34, pp. 15293–15298, 2010.
- [29] S. A. A. Mohamed, M. El-Sakhawy, and M. A.-M. El-Sakhawy, "Polysaccharides, Protein and Lipid -Based Natural Edible Films in Food Packaging: A Review," *Carbohydrate Polymers*, vol. 238, article 116178, 2020.
- [30] H. C. Arca, L. I. Mosquera-Giraldo, V. Bi, D. Xu, L. S. Taylor, and K. J. Edgar, "Pharmaceutical applications of cellulose ethers and cellulose ether esters," *Biomacromolecules*, vol. 19, no. 7, pp. 2351–2376, 2018.
- [31] N. K. Mandlekar, *Integration of wood waste to develop multi-functional fully biobased textile structure*, Soochow University, China, 2019.
- [32] S. Beisl, A. Miltner, and A. Friedl, "Lignin from micro- to nanosize: production methods," *International Journal of Molecular Sciences*, vol. 18, no. 6, p. 1244, 2017.
- [33] F. R. Wurm and C. K. Weiss, "Nanoparticles from renewable polymers," *Frontiers in Chemistry*, vol. 2, p. 49, 2014.
- [34] F. Rol, M. N. Belgacem, A. Gandini, and J. Bras, "Recent advances in surface-modified cellulose nanofibrils," *Progress in Polymer Science*, vol. 88, pp. 241–264, 2019.
- [35] D. O. Bokov, R. I. Sharipova, O. G. Potanina et al., "Polysaccharides of crude herbal drugs as a group of biologically active compounds in the field of modern pharmacognosy: physico-chemical properties, classification, pharmacopoeial analysis," *Proteins*, vol. 2, pp. 4–6, 2020.
- [36] S. Zhang, G. I. N. Waterhouse, F. Xu et al., "Recent advances in utilization of pectins in biomedical applications: a review focusing on molecular structure-directing health-promoting properties," *Critical Reviews in Food Science and Nutrition*, vol. 61, pp. 1–34, 2021.
- [37] S. M. Avramescu, C. Butean, C. V. Popa, A. Ortan, I. Moraru, and G. Temocico, "Edible and functionalized films/coatings—Performances and perspectives," *Coatings*, vol. 10, no. 7, p. 687, 2020.
- [38] L. Han, B. Hu, R. Ma et al., "Effect of arabinogalactan protein complex content on emulsification performance of gum arabic," *Carbohydrate Polymers*, vol. 224, p. 115170, 2019.
- [39] S. Ahmad, M. Ahmad, K. Manzoor, R. Purwar, and S. Ikram, "A review on latest innovations in natural gums based hydrogels: preparations & applications," *International Journal of Biological Macromolecules*, vol. 136, pp. 870–890, 2019.
- [40] F. Fahma, Sugiarto, T. C. Sunarti, S. M. Indriyani, and N. Lidayana, "Thermoplastic cassava starch-PVA composite films with cellulose nanofibers from oil palm empty fruit bunches as reinforcement agent," *International Journal of Polymer Science*, vol. 2017, 5 pages, 2017.
- [41] H. Kargarzadeh, M. Mariano, D. Gopakumar et al., "Advances in cellulose nanomaterials," *Cellulose*, vol. 25, no. 4, pp. 2151–2189, 2018.
- [42] J. D. Desai and I. M. Banat, "Microbial production of surfactants and their commercial potential," *Microbiology and Molecular Biology Reviews*, vol. 61, no. 1, pp. 47–64, 1997.
- [43] A. Kumar, S. K. Singh, C. Kant et al., "Microbial biosurfactant: a new frontier for sustainable agriculture and pharmaceutical industries," *Antioxidants*, vol. 10, no. 9, p. 1472, 2021.
- [44] K. G. O. Bezerra, R. D. Rufino, J. M. Luna, and L. A. Sarubbo, "Saponins and microbial biosurfactants: potential raw materials for the formulation of cosmetics," *Biotechnology Progress*, vol. 34, no. 6, pp. 1482–1493, 2018.
- [45] S. Doppalapudi, A. Jain, A. J. Domb, and W. Khan, "Biodegradable polymers for targeted delivery of anti-cancer drugs," *Expert Opinion on Drug Delivery*, vol. 13, no. 6, pp. 891–909, 2016.
- [46] M. A. Farooq, M. Aquib, A. Farooq et al., "Recent progress in nanotechnology-based novel drug delivery systems in designing of cisplatin for cancer therapy: an overview," *Artificial cells, nanomedicine, and biotechnology*, vol. 47, no. 1, pp. 1674–1692, 2019.
- [47] W. Zhang, C. Li, C. Shen et al., "Prodrug-based nano-drug delivery system for co-encapsulate paclitaxel and carboplatin for lung cancer treatment," *Drug Delivery*, vol. 23, no. 7, pp. 2575–2580, 2016.
- [48] Z. Zhang, M. Lin, and S.-S. Feng, "Paclitaxel drug delivery systems," *Expert Opinion on Drug Delivery*, vol. 10, no. 3, pp. 325–340, 2013.
- [49] Q. Cheng and Y. Liu, "Multifunctional platinum-based nanoparticles for biomedical applications," *Wiley Interdisciplinary Reviews: Nanomedicine and Nanobiotechnology*, vol. 9, no. 2, article e1410, 2017.
- [50] M. Lucke, B. Wildemann, S. Sadoni et al., "Systemic versus local application of gentamicin in prophylaxis of implant-related osteomyelitis in a rat model," *Bone*, vol. 36, no. 5, pp. 770–778, 2005.
- [51] M. Aflori, "Smart nanomaterials for biomedical applications—a review," *Nanomaterials*, vol. 11, no. 2, p. 396, 2021.
- [52] M. Antman-Passig and O. Shefi, "Remote magnetic orientation of 3D collagen hydrogels for directed neuronal regeneration," *Nano Letters*, vol. 16, no. 4, pp. 2567–2573, 2016.
- [53] B. Xu, H. Dou, K. Tao et al., "'Two-in-one' fabrication of Fe₃O₄/MePEG-PLA composite nanocapsules as a potential ultrasonic/MRI dual contrast agent," *Langmuir*, vol. 27, no. 19, pp. 12134–12142, 2011.
- [54] W. Sun, S. Li, B. Häupler et al., "An amphiphilic ruthenium polymetallo-drug for combined photodynamic therapy and photochemotherapy in vivo," *Advanced Materials*, vol. 29, no. 6, article 1603702, 2017.
- [55] R. Klajn, "Spiropyran-based dynamic materials," *Chemical Society Reviews*, vol. 43, no. 1, pp. 148–184, 2014.
- [56] M. K. Hossain, H. Minami, S. M. Hoque et al., "Mesoporous electromagnetic composite particles: electric current responsive release of biologically active molecules and antibacterial properties," *Colloids and Surfaces B: Biointerfaces*, vol. 181, pp. 85–93, 2019.
- [57] M. O. Shaikh, B. Srikanth, P.-Y. Zhu, and C.-H. Chuang, "Impedimetric immunosensor utilizing polyaniline/gold nanocomposite-modified screen-printed electrodes for early detection of chronic kidney disease," *Sensors*, vol. 19, no. 18, p. 3990, 2019.
- [58] M. Mazloum-Ardakani, B. Barazesh, A. Khoshroo, M. Moshtaghiun, and M. H. Sheikhha, "A new composite consisting of electrosynthesized conducting polymers, graphene sheets and biosynthesized gold nanoparticles for biosensing acute lymphoblastic leukemia," *Bioelectrochemistry*, vol. 121, pp. 38–45, 2018.
- [59] M. G. Arafa, R. F. El-Kased, and M. M. Elmazar, "Thermoresponsive gels containing gold nanoparticles as smart antibacterial and wound healing agents," *Scientific Reports*, vol. 8, no. 1, article 13674, 2018.

- [60] M. R. Abidian, D.-H. Kim, and D. C. Martin, "Conducting-polymer nanotubes for controlled drug release," *Advanced Materials*, vol. 18, no. 4, pp. 405–409, 2006.
- [61] C.-S. Chiang, Y.-S. Shen, J.-J. Liu, W.-C. Shyu, and S.-Y. Chen, "Synergistic combination of multistage magnetic guidance and optimized ligand density in targeting a nanoplatform for enhanced cancer therapy," *Advanced Healthcare Materials*, vol. 5, no. 16, pp. 2131–2141, 2016.
- [62] J. Liu, Y. S. Kim, C. E. Richardson et al., "Genetically targeted chemical assembly of functional materials in living cells, tissues, and animals," *Science*, vol. 367, no. 6484, pp. 1372–1376, 2020.
- [63] X. Li, B.-Y. Zheng, M.-R. Ke, Y. Zhang, J.-D. Huang, and J. Yoon, "A tumor-pH-responsive supramolecular photosensitizer for activatable photodynamic therapy with MinimalIn VivoSkin phototoxicity," *Theranostics*, vol. 7, no. 10, pp. 2746–2756, 2017.
- [64] R. Singh et al., "Synthesis of three-dimensional reduced-graphene oxide from graphene oxide," *Journal of Nanomaterials*, Article ID 8731429, pp. 1–8, 2022.
- [65] E. Mazzotta, S. de Benedittis, A. Qualtieri, and R. Muzzalupo, "Actively targeted and redox responsive delivery of anticancer drug by chitosan nanoparticles," *Pharmaceutics*, vol. 12, no. 1, p. 26, 2020.
- [66] S. Rezaei, S. Kashanian, Y. Bahrami, L. J. Cruz, and M. Motiei, "Redox-sensitive and hyaluronic acid-functionalized nanoparticles for improving breast cancer treatment by cytoplasmic 17α -methyltestosterone delivery," *Molecules*, vol. 25, no. 5, p. 1181, 2020.
- [67] S. Liu, J. Yang, R. Guo, L. Deng, A. Dong, and J. Zhang, "Facile fabrication of redox-responsive covalent organic framework nanocarriers for efficiently loading and delivering doxorubicin," *Macromolecular Rapid Communications*, vol. 41, no. 4, article 1900570, 2020.
- [68] Y. Wang, C. Wang, Y. Li et al., "Digitization of endocytic pH by hybrid ultra-pH-sensitive nanoprobe at single-organelle resolution," *Advanced Materials*, vol. 29, no. 1, article 1603794, 2017.
- [69] U. Sivasankaran and K. G. Kumar, "A cost effective strategy for dual channel optical sensing of adrenaline based on 'in situ' formation of copper nanoparticles," *Spectrochimica Acta Part A: Molecular and Biomolecular Spectroscopy*, vol. 223, article 117292, 2019.
- [70] K.-Y. Ju, J. Kang, J. Pyo, J. Lim, J. H. Chang, and J.-K. Lee, "pH-induced aggregated melanin nanoparticles for photoacoustic signal amplification," *Nanoscale*, vol. 8, no. 30, pp. 14448–14456, 2016.
- [71] X. Xie, T. C. Sun, J. Xue et al., "Ag nanoparticles cluster with pH-triggered reassembly in targeting antimicrobial applications," *Advanced Functional Materials*, vol. 30, no. 17, article 2000511, 2020.
- [72] N. B. Mutlu-Agardan, C. Sarisozen, and V. P. Torchilin, "Cytotoxicity of novel redox sensitive PEG2000-S-S-PTX micelles against drug-resistant ovarian and breast cancer cells," *Pharmaceutical Research*, vol. 37, no. 3, pp. 1–8, 2020.
- [73] L. Qiu, L. Zhao, C. Xing, and Y. Zhan, "Redox-responsive polymer prodrug/AgNPs hybrid nanoparticles for drug delivery," *Chinese Chemical Letters*, vol. 29, no. 2, pp. 301–304, 2018.
- [74] S. Mollazadeh, M. Mackiewicz, and M. Yazdimamaghani, "Recent advances in the redox-responsive drug delivery nano-platforms: a chemical structure and physical property perspective," *Materials Science and Engineering: C*, vol. 118, article 111536, 2021.
- [75] L. Li, G. Jiang, W. Yu et al., "Preparation of chitosan-based multifunctional nanocarriers overcoming multiple barriers for oral delivery of insulin," *Materials Science and Engineering: C*, vol. 70, Part 1, pp. 278–286, 2017.
- [76] L. P. Datta, A. Chatterjee, K. Acharya, P. de, and M. Das, "Enzyme responsive nucleotide functionalized silver nanoparticles with effective antimicrobial and anticancer activity," *New Journal of Chemistry*, vol. 41, no. 4, pp. 1538–1548, 2017.
- [77] S. T. Gunawan, K. Kempe, T. Bonnard et al., "Multifunctional thrombin-activatable polymer capsules for specific targeting to activated platelets," *Advanced Materials*, vol. 27, no. 35, pp. 5153–5157, 2015.
- [78] D. Liu, G. Jiang, W. Yu et al., "Oral delivery of insulin using CaCO_3 -based composite nanocarriers with hyaluronic acid coatings," *Materials Letters*, vol. 188, pp. 263–266, 2017.
- [79] K. Sonaje, Y.-J. Chen, H.-L. Chen et al., "Enteric-coated capsules filled with freeze-dried chitosan/poly(γ -glutamic acid) nanoparticles for oral insulin delivery," *Biomaterials*, vol. 31, no. 12, pp. 3384–3394, 2010.
- [80] W. Tang and C. Cheng, "Hydrogel-based colloidal photonic crystal devices for glucose sensing," *Polymers*, vol. 12, no. 3, p. 625, 2020.
- [81] R. Biba, P. P. Štefanić, P. Cvjetko, M. Tkalec, and B. Balen, "Silver nanoparticles phytotoxicity mechanisms," in *Silver Nanomaterials for Agri-Food Applications*, pp. 317–356, Elsevier, 2021.
- [82] Q. Hu, Y. Wang, L. Xu, D. Chen, and L. Cheng, "Transferrin conjugated pH- and redox-responsive Poly(Amidoamine) dendrimer conjugate as an efficient drug delivery carrier for cancer Therapy," *International journal of nanomedicine*, vol. 15, pp. 2751–2764, 2020.
- [83] X. Xu, X. Wang, W. Luo et al., "Triple cell-responsive nanogels for delivery of drug into cancer cells," *Colloids and Surfaces B: Biointerfaces*, vol. 163, pp. 362–368, 2018.
- [84] P. Zhang, Z. Gao, J. Cui, and J. Hao, "Dual-stimuli-responsive polypeptide nanoparticles for photothermal and photodynamic therapy," *ACS Applied Bio Materials*, vol. 3, no. 1, pp. 561–569, 2020.
- [85] Y. Shi, S. Shan, C. Li et al., "Application of the tumor site recognizable and dual-responsive nanoparticles for combinational treatment of the drug-resistant colorectal cancer," *Pharmaceutical Research*, vol. 37, no. 4, pp. 1–14, 2020.
- [86] Y. Huang, Z. Tang, S. Peng et al., "pH/redox/UV irradiation multi-stimuli responsive nanogels from star copolymer micelles and Fe^{3+} complexation for "on-demand" anticancer drug delivery," *Reactive and Functional Polymers*, vol. 149, article 104532, 2020.
- [87] H. Lu, Q. Zhao, X. Wang et al., "Multi-stimuli responsive mesoporous silica-coated carbon nanoparticles for chemophotothermal therapy of tumor," *Colloids and Surfaces B: Biointerfaces*, vol. 190, article 110941, 2020.
- [88] D. Bhattacharya, B. Behera, S. K. Sahu, R. Ananthkrishnan, T. K. Maiti, and P. Pramanik, "Design of dual stimuli responsive polymer modified magnetic nanoparticles for targeted anti-cancer drug delivery and enhanced MR imaging," *New Journal of Chemistry*, vol. 40, no. 1, pp. 545–557, 2016.

- [89] B. Yu, N. Song, H. Hu, G. Chen, Y. Shen, and H. Cong, "A degradable triple temperature-, pH-, and redox-responsive drug system for cancer chemotherapy," *Journal of Biomedical Materials Research Part A*, vol. 106, no. 12, pp. 3203–3210, 2018.
- [90] W. Chen and D. Jianzhong, "Ultrasound and pH dually responsive polymer vesicles for anticancer drug delivery," *Scientific Reports*, vol. 3, no. 1, pp. 1–9, 2013.

Research Article

Evaluation of Anticancer Potential of Biogenic Copper Oxide Nanoparticles (CuO NPs) against Breast Cancer

Torki A. Zughaihi ^{1,2} Ahmed A. Mirza ² Mohd Suhail ^{1,2} Nasimudeen R. Jabir ³
Syed Kashif Zaidi ⁴ Samina Wasi ⁵ Ayat Zawawi ² and Shams Tabrez ^{1,2}

¹King Fahd Medical Research Center, King Abdulaziz University, Jeddah, Saudi Arabia

²Department of Medical Laboratory Sciences, Faculty of Applied Medical Sciences, King Abdulaziz University, Jeddah, Saudi Arabia

³Department of Biochemistry, Centre for Research and Development, PRIST University, Vallam, Thanjavur, Tamil Nadu, India

⁴Center of Excellence in Genomic Medicine Research (CEGMR), King Abdulaziz University, Jeddah, Saudi Arabia

⁵Department of Biochemistry, College of Medicine, University of Dammam, Dammam, Saudi Arabia

Correspondence should be addressed to Shams Tabrez; shamstabrez1@gmail.com

Received 1 March 2022; Accepted 28 March 2022; Published 11 April 2022

Academic Editor: Arpita Roy

Copyright © 2022 Torki A. Zughaihi et al. This is an open access article distributed under the Creative Commons Attribution License, which permits unrestricted use, distribution, and reproduction in any medium, provided the original work is properly cited.

The present study evaluated the anticancer potential of copper oxide nanoparticles (CuO NPs) synthesized from pumpkin seed extract in human breast cancer cell line (MDA-MB-231) using a battery of tests such as MTT [3-(4,5-dimethylthiazol-2-yl)-2,5-diphenyltetrazolium bromide] assay, morphological alteration, reactive oxygen species (ROS) generation, and changes in mitochondrial membrane potential (MMP). The biogenic CuO NPs showed a dose-dependent decline in cell viability with 50% inhibitory concentration (IC₅₀) at 20 µg/ml. Treatment with an IC₅₀ dose of CuO NPs resulted in considerable morphology changes, such as shrinkage, detachment, membrane blebbing, and deformed shape in MDA-MB-231 cells. We also observed a significant dose-dependent increase in ROS production and MMP modulation due to CuO NP treatment. Overall, CuO NPs showed significant anticancer potential in the breast cancer cell line. However, further validation of our data is required in *ex vivo* and *in vivo* models before this nanoformulation could be exploited for the treatment/management of human breast cancer.

1. Introduction

Cancers are considered one of the foremost reasons of mortality, where 1.9 million new cases and around 609,360 cancer deaths are expected in the United States by the end of 2022 [1]. Breast cancer (BC) is the most common cancer in women globally and the primary cause of cancer-related deaths in women, with the second-highest incidence rate (11.6%) among all cancers, necessitating the development of effective therapies [2, 3]. Currently, available chemotherapeutics for BC are costly, have frightening side effects, and could also lead to resistant cells [4–6]. Traditional therapies can reduce aggressive BC to moderately invasive BC; however, most invasive kinds have no effective treatment till now. Therefore, the urgent need is to find an effective, bio-

compatible, and cost-effective therapeutic agent for BC especially invasive one, that has few or no adverse effects [7].

In this regard, cancer nanomedicine has taken a significant stride in the last few decades and improved the therapeutic index of cancer drugs [8, 9]. Nanotechnology has extensive application in biomedical sciences, particularly cancer therapeutics [10]. The advantages of nanomaterials are their large surface area and small particle size, making them excellent for synthesizing pharmaceutical formulations [11–13]. Metal oxide nanoparticles have recently come up as a promising research area due to their vast range of applications [9, 14]. Copper oxide nanoparticles (CuO NPs) have been widely studied nanoformulation owing to their intriguing physical, biochemical, and pharmacological features [9, 15]. Cu-based products have been permitted for human

use by the United States Environmental Protection Agency (USEPA) since February 2008 [7]. These nanoparticles are widely explored because they are essential trace element and have significant roles in metabolism and physiological processes [16, 17]. Different tumor cells, such as lung adenocarcinoma (A549), leukemia monocytic cells (THP-1), and colon cancer (HCT-116), have exhibited substantial toxicity to these nanoparticles [7, 9, 18].

Plant seeds are considered a significant source of biogenic nanoparticles production [19–21]. Among plants, pumpkin is a popular vegetable found in many foods such as bonbons, comestibles, and rice cakes and has shown several benefits [22]. The diverse bioactive compounds such as carotenoids, polysaccharides, para-aminobenzoic acid, fixed oil, sterol, protein, and peptides in pumpkins make them suitable against various cancer [23, 24]. Previous studies have shown the significant anticancer potential of pumpkins against gastric, breast, lung, colon, and prostate cancer [25, 26]. Biogenic nanoparticles have gained considerable attention lately because of their low-cost, eco-friendly nature, reliability, and relative safety [27, 28].

In our earlier study, we successfully synthesized and characterized biogenic CuO NPs from pumpkins seed extract using a green, environmental friendly, and nontoxic approach [9]. The biosynthesized CuO NPs showed significant anticancer against HCT-116 cell lines. The current study is a continuation of our previous work, and it aims to analyze the anticancer potential of CuO NPs in breast cancer cell lines (MDA-MB-231) in order to compare its efficacy. Based on the findings, we intend to expand our research to the most responsive cancer model.

2. Materials and Methods

All the chemicals utilized in this investigation were acquired commercially from companies like Merck, Sigma, and others. Streptomycin, penicillin, phosphate-buffered saline (PBS), 3-(4,5 dimethylthiazol-2-yl)-2,5-diphenyl tetrazolium bromide (MTT), 2',7'-diacetyl dichlorofluorescein (DCFH), trypsin-EDTA, acridine orange, and ethidium bromide were obtained from the companies mentioned above. All the other chemicals were purchased locally and were of analytical grade.

2.1. Synthesis and Characterization of CuO NPs. In our previous study, we described the synthesis and characterization of CuO NPs from pumpkin seeds extract in detail [9]. Briefly, the pumpkin seed extract was prepared and subsequently added in 3 mM of $\text{Cu}(\text{OAc})_2$ solution with continuous stirring. The addition of NaOH to the extract solution resulted in the formation of CuO NPs. CuO NPs were characterized using a variety of analytical techniques, including UV-vis absorption spectroscopy, Fourier transform infrared spectrum analysis (FTIR), X-ray diffraction (XRD), energy dispersive X-ray analysis (EDX), scanning electron microscopy (SEM), and transform electron microscopy (TEM). These techniques confirmed the biogenic synthesis of CuO NPs in the 20 nm range.

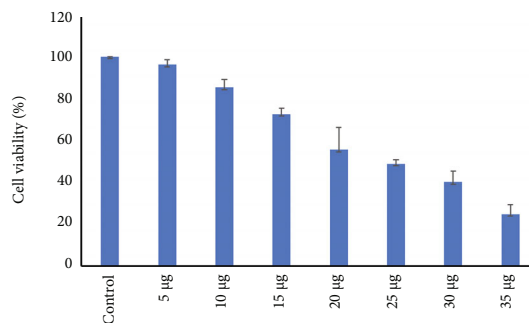


FIGURE 1: A dose-dependent decrease in MDA-MB-231 cell viability.

2.2. Cell Culture Maintenance. The National Centre for Cell Sciences (NCCS) in Pune, India, provided the MDA-MB-231 breast cancer cell line. The cell line was grown in DMEM media supplemented with 10% FBS, penicillin (100 U/ml), and streptomycin (100 µg/ml) at 37°C in 5% CO_2 incubator.

2.3. Cytotoxicity (MTT) Assay. To measure cytotoxicity, MDA-MB-231 cells were treated with different doses of CuO NPs (5–35 µg/ml) in 96-well plate for 24 hours. After treatment, each well was added with 10 µl of MTT, followed by 2 hours of incubation at 37°C. The purple precipitated formazan was dissolved by adding 100 µl of DMSO, and the absorbance was measured at 540 nm using a multiwell plate reader [9]. The cytotoxicity of CuO NPs was calculated by comparing the percentage of treated cells to control cells.

Inhibitory of cell proliferation (%) = $(\text{Mean absorbance of the control} - \text{Mean absorbance of the sample}) / (\text{Mean absorbance of the control}) \times 100$.

The sample CuO NP dose-responsive curve was used to calculate the 50% inhibitory concentration (IC50).

2.4. Induction of Apoptosis Using Acridine Orange/Ethidium Bromide (AO/EB) Dual Staining Technique. Microscopic fluorescence assessment of apoptotic induction was performed using the approach described by Baskic et al. [29]. Before being examined under a fluorescence microscope, the treated cells were rinsed in cold PBS and stained with AO/EB (1:1 ratio; 100 µg/ml) for 5 minutes. The number of cells undergoing apoptosis was computed as a fraction of the total number of cells (40× magnification).

2.5. Measurement of Reactive Oxygen Species (ROS). Intracellular ROS generation was detected using the dichlorodihydro-fluorescein diacetate (DCFH-DA) [30]. After washing the treated cells with PBS, it was exposed with 25 µM DCFH-DA for 30 minutes at 37°C as we reported previously [27]. The fluorescence was measured every 5 minutes for up to 30 minutes using a spectrofluorometer (excitation 485 nm and emission 535 nm) (Shimadzu, Columbia, USA). A mean slope/min was used to calculate the increase in ROS production, which was then normalized to the unexposed control cells.

2.6. Measurement of Mitochondrial Membrane Potential (MMP). The established approach by Bhosle et al. [31] was

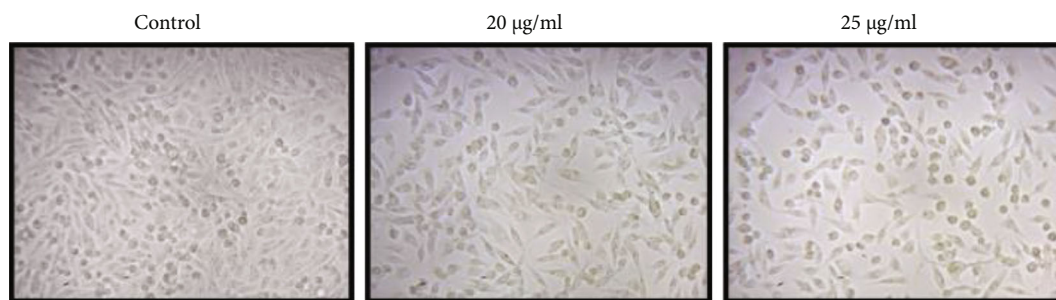


FIGURE 2: Morphological changes in control and treated MDA-MB-231 cells.

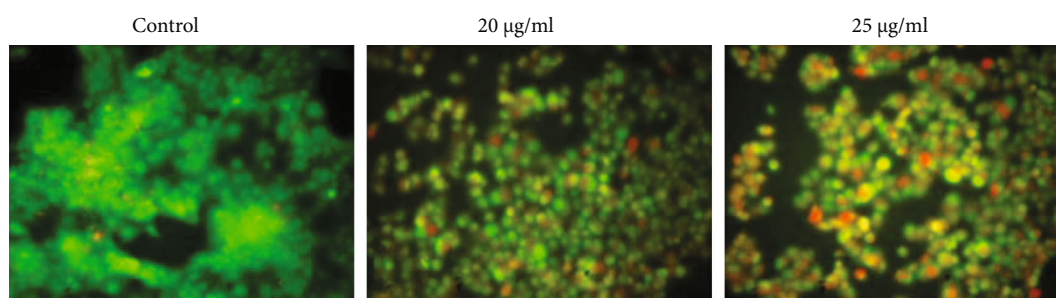


FIGURE 3: Effect of CuO NPs on the apoptotic incidence in MDA-MB-231 cells.

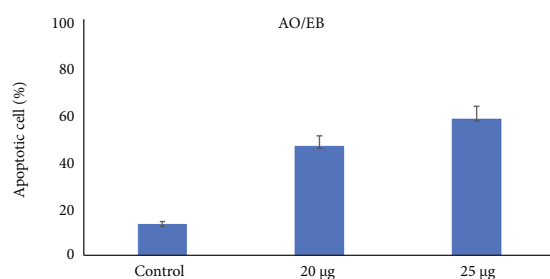


FIGURE 4: The percentage of apoptotic cells after AO/EB staining.

used to measure the modulation in mitochondrial membrane potential. The Rh-123 dye was used to stain the treated cells and was incubated for 15 minutes. The cells were fixed after being washed twice with PBS, and the fluorescence intensity was measured at 535 nm.

3. Results and Discussion

3.1. Cytotoxicity Assay and Morphological Alterations. A concentration-dependent rise in cytotoxicity was recorded in the MDA-MB-231 cell line in response to the treatment of CuO NPs. The IC₅₀ concentration was found to be 20 µg/ml. The cell viability percentage was reduced to 24% at the highest tested dose, i.e., 35 µg/ml (Figure 1). The cytotoxicity of CuO NPs synthesized from various biological sources has previously been reported in several cancers cell lines, such as HepG2, Amj 13, MCF-7, MDA-MB-231, A549, and HCT-116 [9, 32–36]. The characteristics of NPs, such as nanoparticle size, surface charge, and functional groups determine the therapeutic potential of NPs [11]. A recent study highlighted the better pharmaceutical and bio-

medical capacity of CuO NPs with smaller NP sizes [37]. The advantage of our synthesized CuO NPs is the lower particle size (20 nm) compared to earlier reported ones [37]. The smaller size of CuO NPs could result in extensive tissue distribution, deeper penetration inside specific tissues, better cellular uptake, and increased toxic effects to the cancer cells [37–39]. Earlier studies also reported higher IC₅₀ of CuO NPs in human breast cancer cell lines compared with our biogenic CuO NPs, i.e., 20 µg/ml indicating its better efficacy [34, 35]. The smaller size and varied surface characteristics of CuO NPs could explain the lower IC₅₀ value of our nanoformulation.

In addition, CuO NP treatment caused morphological changes in MDA-MB-231 cells, such as shrinkage, detachment, membrane blebbing, and distorted shape. On the other hand, control cells showed typical intact cell morphology (Figure 2).

3.2. Induction of Apoptosis in Response of CuO NP Treatment. Living cells showed green fluorescence and had normal nuclear appearance. However, a significant induction of apoptosis was observed at 20 µg/ml CuO NP concentration. Figure 3 depicts a fragmented nucleus showing yellow fluorescence with condensed chromatin, indicating early apoptotic cells. However, the orange fluorescence with chromatin condensation or fragmentation (uniformly red/orange-stained cell nuclei) indicate late apoptotic cells. In addition, we also quantitatively measured the percentage of apoptotic cells, which showed 57% apoptotic cells at 25 µg/ml of CuO NP treatment (Figure 4).

Apoptosis is considered a significant anticancer mechanism that involves the activation of a sequence of molecular events culminating into cell death with cellular,

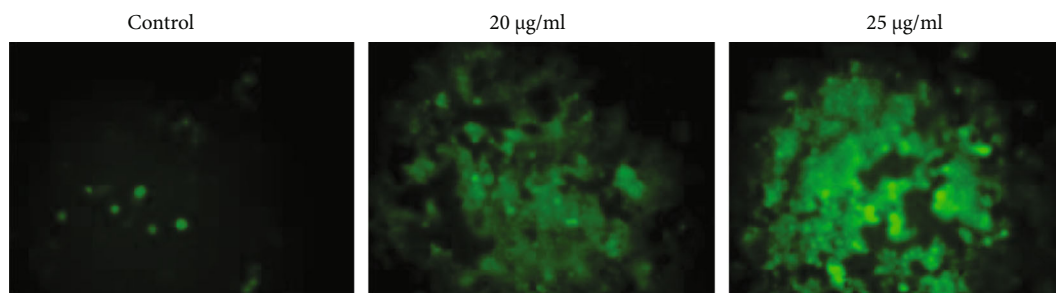


FIGURE 5: Fluorescence microscopic images of MDA-MB-231 cells treated with CuO NPs.

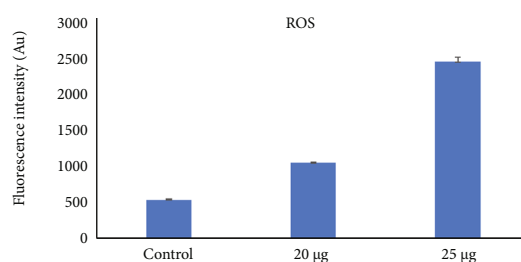


FIGURE 6: The quantitative estimation of ROS generation in MDA-MB-231 cells treated with CuO NPs.

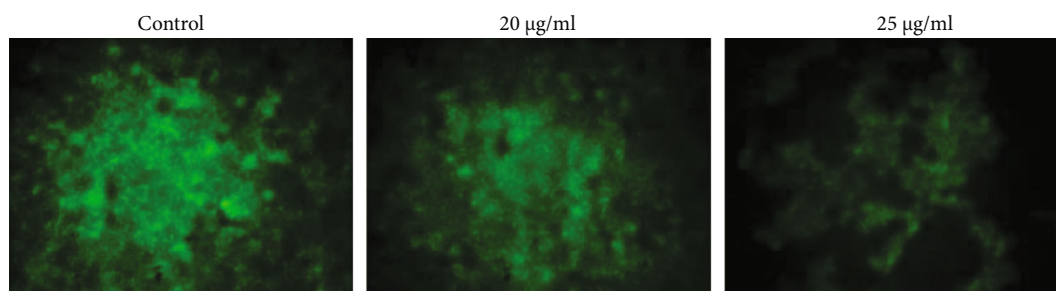


FIGURE 7: Fluorescence microscope images of breast cancer cells treated with CuO NPs.

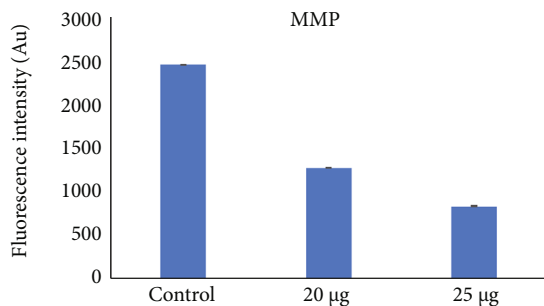


FIGURE 8: Modulation in MMP quantified by fluorescence intensity (Au) in breast cancer cells treated with CuO NPs.

morphological, and biochemical changes [40]. It is well-known that excessive generation of ROS/RNS, oxidative stress, and cancer cell Sub G1 arrest is connected to DNA damage and apoptosis/necrosis [41, 42]. Our results agree with earlier studies that observed induction of apoptosis as a result of green synthesized nanoparticles [40, 43]. Of late, endoplasmic reticulum stress-mediated induction of apopto-

sis has also been reported in response to CuO NP treatment in Wistar rats [44]. Other apoptosis-promoting pathways have also been identified in response to green synthesized copper nanoparticles in Hep-2 and MCF-7 cells, that include upregulation of tumor suppressor genes (p53, Bax, caspase-3, and caspase-9) and downregulation of oncogenes (Ras and Myc) [45, 46].

3.3. Effect of CuO NPs on the Intracellular ROS Generation in MDA-MB-231 Cells. Control cells (dull green fluorescence) and CuO NP treated cells showed bright DCF stained green fluorescence indicating production of ROS (Figure 5). The ROS generation was also quantified by estimating fluorescence intensity (Au) in breast cancer cells (Figure 6), showing increased formation of ROS in a dose-dependent manner. Our findings support previous research that identified enhanced ROS generation as the key cytotoxic mechanism of green synthesized CuO NPs [41, 47]. In addition, our study also demonstrated comparatively higher ROS production at lesser dose of CuO NP. Increased generation of ROS is important for cell apoptosis regulation [35].

3.4. Effects of CuO NPs on the Mitochondrial Membrane Potential (MMP) in MDA-MB-231 Cells. We observed a gradual decrease in green fluorescence with an increasing concentration of CuO NPs, indicating a dose-dependent decline in MMP. The fluorescent image at 40× magnification shows rhodamine accumulation in control cells and its absence in treated cells (Figure 7). Modulation in MMP was also quantified by estimating fluorescence intensity (Au) in MDA-MB-231 cells indicating a notable change in MMP in response to CuO NP treatment (Figure 8). Green synthesized CuO NPs from black bean extract have also affected the mitochondrial structure and modulated membrane potential in Hela cells [36]. Induction of apoptosis increased formation of ROS/NO, loss of MMP, etc. has been suggested as possible mechanisms of action of green synthesized NPs in the scientific literature [43, 48, 49]. Our biogenic synthesized NPs are also adopting the same mechanism of action for their anticancer effects.

4. Conclusion

The current study exploited an environmentally safe and biogenic approach for synthesizing CuO NPs from pumpkin seed extract. Our findings suggest a robust anticancer potential of CuO NPs, indicating induction of apoptosis, increased formation of ROS, and loss of MMP as possible mechanism of action. We advocate validating our *in vitro* results in *ex vivo* and *in vivo* models, given the considerable benefits of these NPs. Adequate replication of our findings could lead to the utilization of these biosynthesized CuO NPs in pharmacological, clinical, and biotechnological domains. Understanding the specific mechanism of action of these NPs could also provide a better insight into their application in different fields.

Data Availability

Data will be available upon genuine request to corresponding author.

Conflicts of Interest

The authors declare that there is no conflict of interest regarding the publication of this article.

Authors' Contributions

ST and AAM conceived, guidance, funding, and made first/final draft. MS, MK, and TAZ performed biological experiments. NRJ and SW did the statistical analysis, presented the results in a scientific manner, and also made the article's first draft.

Acknowledgments

This project was funded by the Deanship of Scientific Research (DSR) at King Abdulaziz University Jeddah under grant number KEP-1-141-40. The authors, therefore, acknowledge with thanks DSR for technical and financial support.

References

- [1] R. L. Siegel, K. D. Miller, H. E. Fuchs, and A. Jemal, "Cancer statistics, 2022," *CA: a Cancer Journal for Clinicians*, vol. 72, no. 1, pp. 7–33, 2022.
- [2] S. Jahan, M. E. Karim, and E. H. Chowdhury, "Nanoparticles targeting receptors on breast cancer for efficient delivery of chemotherapeutics," *Biomedicine*, vol. 9, no. 2, p. 114, 2021.
- [3] E. Amjad, S. Asnaashari, B. Sokouti, and S. Dastmalchi, "Systems biology comprehensive analysis on breast cancer for identification of key gene modules and genes associated with TNM-based clinical stages," *Scientific Reports*, vol. 10, no. 1, article 10816, 2020.
- [4] B. Mansoori, A. Mohammadi, S. Davudian, S. Shirjang, and B. Baradaran, "The different mechanisms of cancer drug resistance: a brief review," *Advanced Pharmaceutical Bulletin*, vol. 7, no. 3, pp. 339–348, 2017.
- [5] Q.-Y. Zhang, F.-X. Wang, K.-K. Jia, and L.-D. Kong, "Natural product interventions for chemotherapy and radiotherapy-induced side effects," *Frontiers in Pharmacology*, vol. 9, p. 1253, 2018.
- [6] N. B. Leighl, S. Nirmalakumar, D. A. Ezeife, and B. Gyawali, *An arm and a leg: the rising cost of cancer drugs and impact on access*, no. 41, 2021 American Society of Clinical Oncology Educational Book, 2021.
- [7] M. Azizi, H. Ghourchian, F. Yazdian, F. Dashtestani, and H. Alizadeh Zeinabad, "Cytotoxic effect of albumin coated copper nanoparticle on human breast cancer cells of MDA-MB 231," *PLOS ONE*, vol. 12, no. 11, article e0188639, 2017.
- [8] N. R. Jabir, K. Anwar, C. K. Firoz, M. Oves, M. A. Kamal, and S. Tabrez, "An overview on the current status of cancer nanomedicines," *Current Medical Research and Opinion*, vol. 34, no. 5, pp. 911–921, 2018.
- [9] S. Tabrez, A. Khan, A. Mirza et al., "Biosynthesis of copper oxide nanoparticles and its therapeutic efficacy against colon cancer," *Nanotechnology Reviews*, vol. 11, no. 1, pp. 1322–1331, 2022.
- [10] A. Roy, "Plant derived silver nanoparticles and their therapeutic applications," *Current Pharmaceutical Biotechnology*, vol. 22, no. 14, pp. 1834–1847, 2021.
- [11] I. Khan, K. Saeed, and I. Khan, "Nanoparticles: properties, applications and toxicities," *Arabian Journal of Chemistry*, vol. 12, no. 7, pp. 908–931, 2019.
- [12] C. Pandit, A. Roy, S. Ghotekar et al., "Biological agents for synthesis of nanoparticles and their applications," *Journal of King Saud University - Science*, vol. 34, no. 3, article 101869, 2022.
- [13] A. Roy, A. Elzaki, V. Tirth et al., "Biological synthesis of nanocatalysts and their applications," *Catalysts*, vol. 11, no. 12, p. 1494, 2021.
- [14] M. R. Shait Mohammed, V. Ahmad, A. Ahmad et al., "Prospective of nanoscale metal organic frameworks [NMOFs] for cancer therapy," *Seminars in Cancer Biology*, vol. 69, pp. 129–139, 2021.
- [15] M. B. Gawande, A. Goswami, F.-X. Felpin et al., "Cu and Cu-based nanoparticles: synthesis and applications in catalysis," *Chemical Reviews*, vol. 116, no. 6, pp. 3722–3811, 2016.
- [16] P. Nagore, S. Ghotekar, K. Mane, A. Ghoti, M. Bilal, and A. Roy, "Structural properties and antimicrobial activities of *Polyalthia longifolia* leaf extract-mediated CuO nanoparticles," *BioNanoScience*, vol. 11, no. 2, pp. 579–589, 2021.

- [17] S. Raina, A. Roy, and N. Bharadvaja, "Degradation of dyes using biologically synthesized silver and copper nanoparticles," *Environmental Nanotechnology, Monitoring & Management*, vol. 13, article 100278, 2020.
- [18] S. Lanone, F. Rogerieux, J. Geys et al., "Comparative toxicity of 24 manufactured nanoparticles in human alveolar epithelial and macrophage cell lines," *Particle and Fibre Toxicology*, vol. 6, no. 1, p. 14, 2009.
- [19] A. T. Khalil, J. Iqbal, A. Shah et al., "The bio-nano interface as an emerging trend in assembling multi-functional metal nanoparticles," *Nano*, vol. 7, pp. 1–24, 2021.
- [20] M. Khan, A. U. Khan, I. S. Moon et al., "Synthesis of biogenic silver nanoparticles from the seed coat waste of pistachio (*Pistacia vera*) and their effect on the growth of eggplant," *Nanotechnology Reviews*, vol. 10, no. 1, pp. 1789–1800, 2021.
- [21] A. Naseer, A. Ali, S. Ali et al., "Biogenic and eco-benign synthesis of platinum nanoparticles (Pt NPs) using plants aqueous extracts and biological derivatives: environmental, biological and catalytic applications," *Journal of Materials Research and Technology*, vol. 9, no. 4, pp. 9093–9107, 2020.
- [22] M. Y. Kim, E. J. Kim, Y.-N. Kim, C. Choi, and B.-H. Lee, "Comparison of the chemical compositions and nutritive values of various pumpkin (*Cucurbitaceae*) species and parts," *Nutrition Research and Practice*, vol. 6, no. 1, pp. 21–27, 2012.
- [23] A. H. Dar, S. A. Sofi, and S. Rafiq, "Pumpkin the functional and therapeutic ingredient: a review," *International Journal of Food Sciences and Nutrition*, vol. 2, no. 6, pp. 165–170, 2017.
- [24] S. Moccia, M. Russo, M. Durante, M. S. Lenucci, G. Mita, and G. L. Russo, "A carotenoid-enriched extract from pumpkin delays cell proliferation in a human chronic lymphocytic leukemia cell line through the modulation of autophagic flux," *Current Research in Biotechnology*, vol. 2, pp. 74–82, 2020.
- [25] T. Nomikos, K. Gioti, M. Tsoukala, and R. Tenta, "Pumpkin seed extracts inhibit proliferation and induce autophagy in PC-3 androgen insensitive prostate cancer cells," *Journal of Medicinal Food*, vol. 24, no. 10, pp. 1076–1082, 2021.
- [26] J. M. Dotto and J. S. Chacha, "The potential of pumpkin seeds as a functional food ingredient: a review," *Scientific African*, vol. 10, article e00575, 2020.
- [27] M. S. Khan, A. Alomari, S. Tabrez et al., "Anticancer potential of biogenic silver nanoparticles: a mechanistic study," *Pharmaceutics*, vol. 13, no. 5, p. 707, 2021.
- [28] M. Oves, M. Aslam, M. A. Rauf et al., "Antimicrobial and anticancer activities of silver nanoparticles synthesized from the root hair extract of *Phoenix dactylifera*," *Materials for Biological Applications*, vol. 89, pp. 429–443, 2018.
- [29] D. Baskić, S. Popović, P. Ristić, and N. N. Arsenijević, "Analysis of cycloheximide-induced apoptosis in human leukocytes: fluorescence microscopy using annexin V/propidium iodide versus acridin orange/ethidium bromide," *Cell Biology International*, vol. 30, no. 11, pp. 924–932, 2006.
- [30] A. Aranda, L. Sequedo, L. Tolosa et al., "Dichloro-dihydro-fluorescein diacetate (DCFH-DA) assay: a quantitative method for oxidative stress assessment of nanoparticle-treated cells," *Toxicology In Vitro: an international journal published in association with BIBRA*, vol. 27, no. 2, pp. 954–963, 2013.
- [31] S. M. Bhosle, N. G. Huilgol, and K. P. Mishra, "Enhancement of radiation-induced oxidative stress and cytotoxicity in tumor cells by ellagic acid," *Clinica Chimica Acta; International Journal of Clinical Chemistry*, vol. 359, no. 1-2, pp. 89–100, 2005.
- [32] M. A. Siddiqui, H. A. Alhadlaq, J. Ahmad, A. A. Al-Khedhairi, J. Musarrat, and M. Ahamed, "Copper oxide nanoparticles induced mitochondria mediated apoptosis in human hepatocarcinoma cells," *PLOS ONE*, vol. 8, no. 8, article e69534, 2013.
- [33] R. Sankar, R. Maheswari, S. Karthik, K. S. Shivashangari, and V. Ravikumar, "Anticancer activity of *Ficus religiosa* engineered copper oxide nanoparticles," *Materials Science and Engineering: C*, vol. 44, pp. 234–239, 2014.
- [34] P. Yugandhar, T. Vasavi, P. Uma Maheswari Devi, and N. Savithramma, "Bioinspired green synthesis of copper oxide nanoparticles from *Syzygium alternifolium* (Wt.) Walp: characterization and evaluation of its synergistic antimicrobial and anticancer activity," *Applied Nanoscience*, vol. 7, no. 7, pp. 417–427, 2017.
- [35] E. Nagaraj, K. Karuppanan, P. Shanmugam, and S. Venugopal, "Exploration of bio-synthesized copper oxide nanoparticles using *Pterolobium hexapetalum* leaf extract by photocatalytic activity and biological evaluations," *Journal of Cluster Science*, vol. 30, no. 4, pp. 1157–1168, 2019.
- [36] P. C. Nagajyothi, P. Muthuraman, T. V. M. Sreekanth, D. H. Kim, and J. Shim, "Green synthesis: *in-vitro* anticancer activity of copper oxide nanoparticles against human cervical carcinoma cells," *Arabian Journal of Chemistry*, vol. 10, no. 2, pp. 215–225, 2017.
- [37] A. Abbasi, K. Ghorban, F. Nojoomi, and M. Dadmanesh, "Smaller copper oxide nanoparticles have more biological effects versus breast cancer and nosocomial infections bacteria," *Asian Pacific journal of cancer prevention: APJCP*, vol. 22, no. 3, pp. 893–902, 2021.
- [38] S. A. Akintelu, A. S. Folorunso, F. A. Folorunso, and A. K. Oye-bamiji, "Green synthesis of copper oxide nanoparticles for biomedical application and environmental remediation," *Heliyon*, vol. 6, no. 7, article e04508, 2020.
- [39] A. Wongrakpanich, I. A. Mudunkotuwa, S. M. Geary et al., "Size-dependent cytotoxicity of copper oxide nanoparticles in lung epithelial cells," *Environmental Science. Nano*, vol. 3, no. 2, pp. 365–374, 2016.
- [40] P. Taherzadeh-Soureshjani and M. Chehelgerdi, "Algae-mediated route to cuprous oxide (Cu₂O) nanoparticle: differential expression profile of MALAT1 and GAS5 lncRNAs and cytotoxic effect in human breast cancer," *Cancer Nanotechnology*, vol. 11, no. 1, p. 11, 2020.
- [41] E. S. Al-Sheddi, N. N. Farshori, M. M. Al-Oqail et al., "Anticancer potential of green synthesized silver nanoparticles using extract of *Nepeta deflersiana* against human cervical cancer cells (HeLa)," *Bioinorganic Chemistry and Applications*, vol. 2018, Article ID 9390784, 12 pages, 2018.
- [42] Y.-H. Hsin, C.-F. Chen, S. Huang, T.-S. Shih, P.-S. Lai, and P. J. Chueh, "The apoptotic effect of nanosilver is mediated by a ROS- and JNK-dependent mechanism involving the mitochondrial pathway in NIH3T3 cells," *Toxicology Letters*, vol. 179, no. 3, pp. 130–139, 2008.
- [43] D. Letchumanan, S. P. M. Sok, S. Ibrahim, N. H. Nagoor, and N. M. Arshad, "Plant-based biosynthesis of copper/copper oxide nanoparticles: an update on their applications in biomedicine, mechanisms, and toxicity," *Biomolecules*, vol. 11, no. 4, p. 564, 2021.
- [44] H. Liu, W. Lai, X. Liu et al., "Exposure to copper oxide nanoparticles triggers oxidative stress and endoplasmic reticulum (ER)-stress induced toxicology and apoptosis in male rat liver and BRL-3A cell," *Journal of Hazardous Materials*, vol. 401, article 123349, 2021.

- [45] N. N. Farshori, M. A. Siddiqui, M. M. Al-Oqail et al., "Copper oxide nanoparticles exhibit cell death through oxidative stress responses in human airway epithelial cells: a mechanistic study," *Biological Trace Element Research*, 2022.
- [46] S. S. Biresaw and P. Taneja, "Copper nanoparticles green synthesis and characterization as anticancer potential in breast cancer cells (MCF7) derived from *Prunus nepalensis* phytochemicals," *Materials Today: Proceedings*, vol. 49, no. 8, pp. 3501–3509, 2022.
- [47] S. R. Alizadeh and M. A. Ebrahimzadeh, "O-glycoside quercetin derivatives: biological activities, mechanisms of action, and structure-activity relationship for drug design, a review," *Phytotherapy Research*, vol. 36, no. 2, pp. 778–807, 2022.
- [48] A. Dey, S. Manna, S. Chattopadhyay et al., "Azadirachta indica leaves mediated green synthesized copper oxide nanoparticles induce apoptosis through activation of TNF- α and caspases signaling pathway against cancer cells," *Journal of Saudi Chemical Society*, vol. 23, no. 2, pp. 222–238, 2019.
- [49] A. Khursheed, S. Quaiser, A. Bilal et al., "Bio-functionalized CuO nanoparticles induced apoptotic activities in human breast carcinoma cells and toxicity against *Aspergillus flavus*: an *in vitro* approach," *Process biochemistry*, vol. 91, pp. 387–397, 2020.

Review Article

Role of *Moringa oleifera* on Green Synthesis of Metal/Metal Oxide Nanomaterials

Vikram Jadhav^{1,2}, Arun Bhagare¹, Ismat H. Ali³, Akshay Dhayagude¹,
Dnyaneshwar Lokhande⁴, Jayraj Aher², Mohammed Jameel⁵, and Mycal Dutta⁶

¹Department of Chemistry, M.V.P. Samaj's K.K. Wagh Arts, Science, and Commerce College, Pimpalgaon (B.), Nashik-422 209, Maharashtra, India

²Post Graduate Department of Chemistry, K.R.T. Arts, B.H. Commerce, and A.M. Science College, Nashik-422002, Maharashtra, India

³Department of Chemistry, College of Science, King Khalid University, P.O. Box 9004, Abha 61413, Saudi Arabia

⁴Department of Chemistry, M.V.P. Samaj's K.P.G. Arts, Science, And Commerce College, Igatpuri, Nashik-422 403, Maharashtra, India

⁵Department of Civil Engineering, College of Engineering, King Khalid University, Abha, Saudi Arabia

⁶Department of Pharmacy, BGC Trust University Bangladesh, Chittagong 4381, Bangladesh

Correspondence should be addressed to Vikram Jadhav; mevikramjadhav@gmail.com and Mycal Dutta; mycal@bgctub.ac.bd

Received 11 March 2022; Accepted 21 March 2022; Published 7 April 2022

Academic Editor: Arpita Roy

Copyright © 2022 Vikram Jadhav et al. This is an open access article distributed under the Creative Commons Attribution License, which permits unrestricted use, distribution, and reproduction in any medium, provided the original work is properly cited.

Being an environmentally benign method biosynthesis of nanomaterial paying much more attention to researchers, it has many advantages over other routes, such as one pot, facile synthesis, and cost-effective; synthesized material can have good affinity due to surface modification and hence became a most attractive candidate for medicinal and biological applications. Moreover, biosynthesis creates a bridge of interdisciplinary research. Biosynthesis can be done by using bacteria, microbes, plant extracts, etc. In this study, we focus on the synthesis of some metal and metal oxide nanomaterials (M/MO NMs) by using an extract of parts from the *Moringa oleifera* plant. It is a natural source that can serve as a capping, stabilizing, and reducing/oxidizing agent due to the presence of some of the phytochemical parameters. Moreover, it is a rich source of antioxidants, including quercetin and chlorogenic acids, such as flavonoids, phenolics, astragalins, anthocyanins, cinnamates, and carotenoids, as well as a good source of carotene, iron, potassium, calcium, terpenes, quinines, saponins, alkaloids, proteins, tannins, and vitamin. These components produce smaller particles and give a compelling impact on the activities of M/MO NMs nanoparticles. Here, we discuss nanoparticles such as FeO, CuO, ZnO, NiO, MgO, Ag, and Au.

1. Introduction

Nanotechnology is the most rapidly developing discipline in advanced material science research ([1] [2][3]. It will play a crucial role in several essential technologies due to advancements in organizing nanoscale structures into specified unique structures [4][5]) based on particular features such as size and distribution morphology ([6]; [7]). It is becoming more popular in the domestic and commercial fields [8]), including chemical science [9], physical science, biomedical sciences, drug delivery ([10] [11], photocatalysis, and opto-

electronic devices [12]. [13]. For example, nanoscale Ge and Si quantum dots (>10 nm) could be produced in a controlled manner for innovative optoelectronic device applications such as electroluminescent devices [14] and ZnO-based nanomedicine for biomedical applications [15]. Nanoparticles are fascinating because of their unique surface area, which causes physical and chemical changes in their parameters compared to the original materials of the chemical compounds [16]; [17]). At the nanoscale, controlling the size and shape can thus be used to create and manufacture materials that give a variety of applications, including

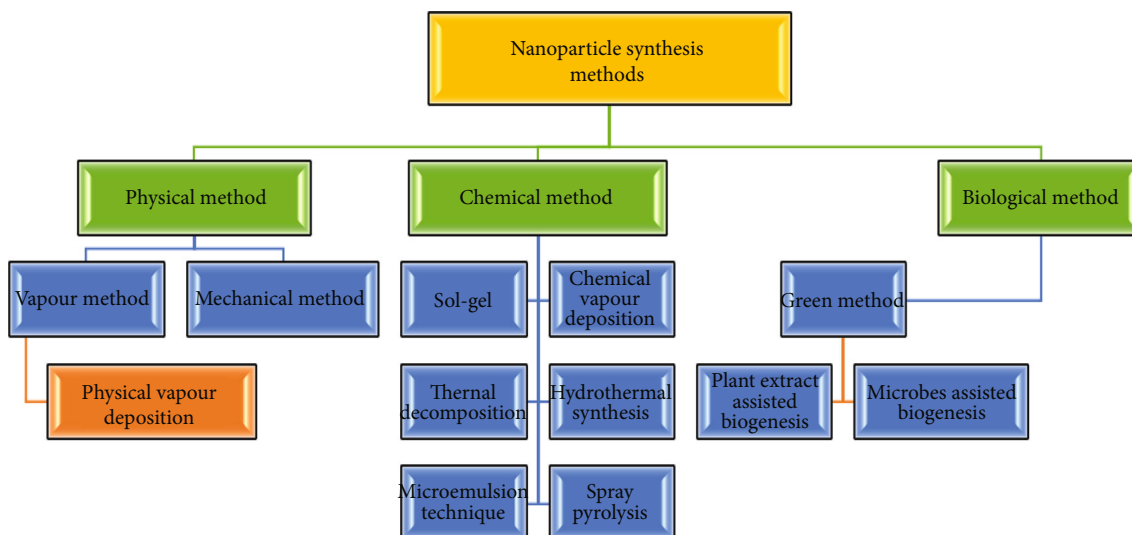


FIGURE 1: Overview of different types of nanoparticle synthesis methods.

antimicrobial activities [18, 19], anticancer activities [20–22], antidiabetic activities [23], biosensing [24], catalysis [25], medication delivery, tumour hyperthermia, and agriculture sector [26] which are just a few of the applications for these particles [27]. Various techniques and methods have been documented for synthesizing M/MO NPs (Figure 1) like hydrothermal, sol-gel, chemical vapour deposition, gas-phase technique, microwave-assisted, microemulsion, electrochemical method, laser irradiation, and solvothermal method [28, 29]. The overview of some of the nanoparticles synthesis methods is shown in Figure 1.

Chemical and physical method approaches are not as practical as biosynthesis processes. Due to the stabilizing and reducing agent nature, the biosynthetic technique involves the utilization of harmless materials, more cost-effective and environmentally friendly, as shown in Figure 2, such as a biocompatible and benign extract from a plant [30]. Plant-mediated nanoparticles are simple to make, easily available, inexpensive, and readily scaled up. The presence of metabolites and phytochemicals in plant leaf extracts such as terpenoids, alkaloids, flavonoids, proteins, peptides, and tannins increased the biosynthetic manufacturing of nanoparticles [31, 32]. The extract's inherent components determine the nanoparticles' various shapes, sizes, and morphologies. The use of plant parts extracts in nanoparticle synthesis is commonly referred to as a green synthesis method approach [33]. The idea of nanoparticles may be linked to the mechanism of nanoparticle production in plants. Plant-mediated nanoparticles are being investigated as a possible next-generation disinfectant, with uses in clinical care, consumer items, and other industrial settings [34]. The antibacterial, antifungal, anticancer, anti-HIV, antidiabetic, high catalytic, and photochemical activity nanoparticles have also gotten much attention [35, 36].

Several research groups have shown considerable interest in its unique qualities and discovered excellent uses in various fields. Researchers have devised several synthetic approaches for nanoparticle manufacturing, revealing a sig-



FIGURE 2: Advantages of green synthesis method.

nificant advantage to ecosystems and biodiversity via clean, harmless, and ecologically friendly processes, including bacteria, fungus, and plants [37]. However, several nanoparticle compositions have exhibited toxicity at the nanodimensions [38, 39]. Nanomaterials and green chemistry are collaborating to develop ecologically, or ecofriendly benign M/MO nanoparticles are utilizing plants, microbes, and other natural resources to solve toxicity problems [40].

Parts of *Moringa oleifera* plants have been reported to various phytochemical parameters [41]; it is a good source of antioxidants, including quercetin and chlorogenic acids, such as flavonoids, phenolics, astragalins, anthocyanins, cinnamates, and carotenoids, as well as a rich source of carotene, Fe, K, Ca, terpenes, quinines, saponins, alkaloids, proteins, tannins, and vitamin C [42, 43]. As shown in Figure 3, the advantages of *Moringa oleifera*, thus improving

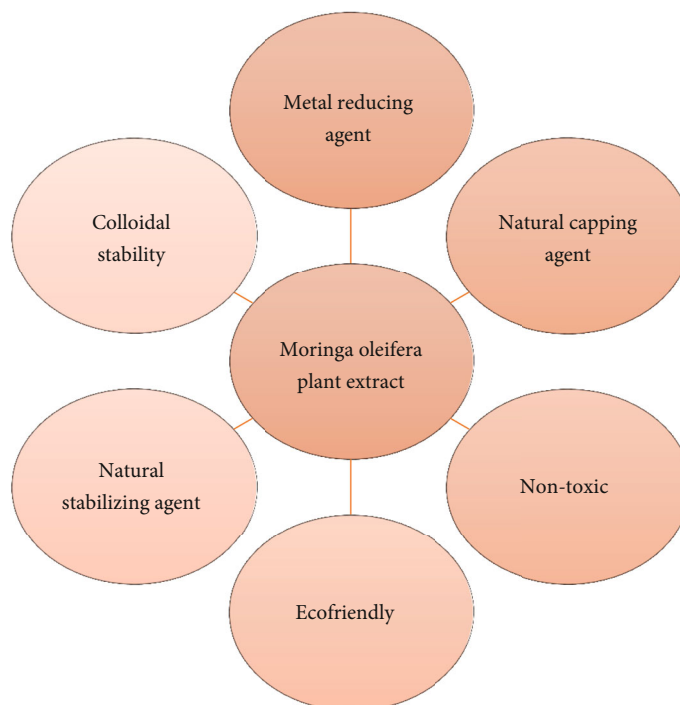


FIGURE 3: Advantages of Moringa oleifera plant leaf extract.

the shelf life of fat-containing foods, act as a good metal-reducing, capping, and stabilizing agent [44–46]. The recent work of this review is Moringa oleifera plant leaf extracts utilized for the biosynthesis of FeO, NiO, MgO, CuO, ZnO, Ag, and Au nanoparticles since it has been acting as an environmentally ecofriendly process. Researchers and scientists have been drawn to this path to synthesize M/MO NPs using Moringa oleifera leaf extract because of the readily available, safe use, and rich sources of diverse metabolites.

2. Biosynthesis of Metal Nanoparticles

The Moringa oleifera plant synthesized M/MO NPs in many processes (Figure 4). The method consists of three steps: primary treatment, biosynthesis, and characterization of nanomaterials. Moringa oleifera plant extract was utilized as a reducing/oxidizing, capping, and stabilizing agent in producing the M/MO NPs. According to the literature survey, some of the M/MO NPs, their synthesis, and comparative study have been discussed in Table 1.

2.1. Iron Oxide (FeO) NPs. Aisida et al. [47], in their research worked, synthesized a green and environmentally friendly approach for nanoparticles in which using an aqueous extract of the Moringa oleifera plant serves as a reductant and capping agent. MO leaf powder extract and FeCl₃ solution were used to synthesize dark-brown-capped MO-FeO NPs. UV-Vis spectroscopy confirmed the noticeable color change from orange to dark brown (Figure 5), leading to FeO NPs. The rod-like morphologies of NPs were shown by SEM and TEM, with a 15 nm average particle size. In terms of antimicrobial activity, biosynthesized FeO NPs inhibited growth more effectively than chemical FeO NPs

against antimicrobial. Additionally, smaller particles have a greater surface area and bioactivity, making them excellent antimicrobial agents against harmful microorganisms.

Tovar et al. [48] almost have similar work as previous authors. Using the MO leaf extract and (Iron (III) chloride hexahydrate) for the synthesis of FeO NPs, in this process, the Moringa oleifera acted as a capping agent. The germination rate and development of corn seeds were studied using synthesized FeO NPs loaded with N, P, and K. Moringa, and chitosan had a favourable influence on corn plant speed germination parameters, with no adverse effects on seed germination.

MO FeO NP possesses structural and superparamagnetic properties and suitable particle sizes for biomedical applications [47] performed two parts in which the Moringa oleifera (MO) leaves were dried at room temperature (RT) and sunlight (SL). MO acted as a capping agent; both solutions were gradually reduced from brown to dark black by adding FeCl₃·6H₂O solution. The FeO NPs obtained were characterized and the size of RT FeO and SL FeO NPs measured by SEM was 16 to 18 nm and 18 to 20 nm, respectively. XRD analysis showed a BCC lattice structure for RT, while SL exhibited a quasicrystalline structure.

2.2. Copper Oxide (CuO) NPs. The researchers [54] used MO leaf extract as a capping agent and copper acetate solution to synthesize nanocrystalline CuO powder (fine dark black). A simple green chemistry strategy made CuO NPs from Moringa oleifera leaf extract, and XRD, FE-SEM, EDX, FT-IR, UV-DRS, and PL were used to characterize. CuO NPs show good antifungal activity [56] used Moringa oleifera (MO) leaf extract for the synthesis of CuO microspheres. The color of the solution changed from bluish to dark green during

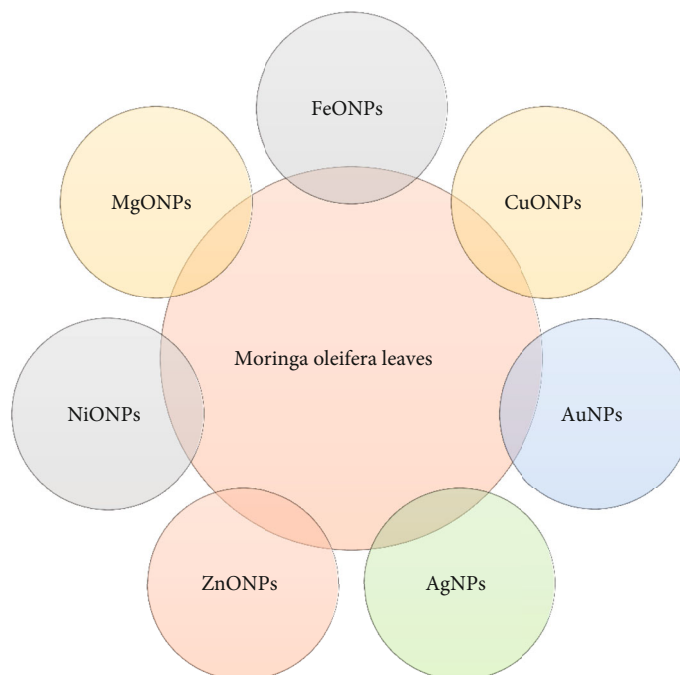


FIGURE 4: Green synthesis of M/MO NPs using MO leaves.

stirring, indicating that the biological components included in the MO leaf extract converted $\text{Cu}(\text{NO}_3)_2 \cdot 3\text{H}_2\text{O}$ to Cu^{2+} ions. The formation of monoclinic crystal-structured CuO was revealed by the XRD pattern, which confirms the conversion of $\text{Cu}(\text{NO}_3)_2 \cdot 3\text{H}_2\text{O}$ to Cu^{2+} ions by phytochemicals contained in the MO leaf extract. As seen by SEM micrographs, it shows the cluster-like morphologies that mimic hierarchical CuO microspheres. In the FTIR spectrum, the asymmetric stretching deformation vibration bands correspond to Cu–O bonds, which imparted monoclinic unit crystal formation, and the synthesized NPs show better antibacterial activity.

2.3. Zinc Oxide (ZnO) NPs. Elumalai et al. [62] employed a straightforward and environmentally safe chemical route to synthesize zinc oxide nanoparticles (ZnO NPs) from Moringa oleifera leaf extract. UV–Vis, XRD, FESEM, EDX, FT–IR, and PL evaluated the ZnO NPs. The hexagonal wurtzite structure of NPs was found by the XRD investigation. The functional groups act as a stabilizing agent in the leaf extract for the ZnO NPs confirmed by FT–IR. The size (16–20 nm) and morphology (spherical and agglomerated) were characterized by FE-SEM. The typical absorption peak of Zn NPs was seen in UV–Vis absorption. Antimicrobial activity studies confirmed the presence of a maximum inhibition zone [64] biosynthesized NiO NP and ZnO NP using extracts of Moringa Oleifera leaves as an efficient chelating and oxidant/reductant of $[\text{Ni}(\text{H}_2\text{O})_6](\text{NO}_3)_2$ and $\text{Zn}(\text{NO}_3)_2 \cdot 6\text{H}_2\text{O}$. XRD, Attenuated Total Reflection-FTIR, UV-Vis-NIR, and PL methods explore the NiO NP and ZnO NP structural and optical characteristics of these two semiconductors created in the same process. Pure cubic NiO-NPs and pure wurtzite ZnO-NPs with average crystallite sizes of

17.80 nm and 10.81 nm, respectively, were formed, according to the structural study. The diffuse reflectance investigation revealed that their band gaps were 4.28 eV and 3.35 eV, respectively.

2.4. Nickel Oxide (NiO) NPs. Ezhilarasi et al. [66] synthesized the nickel oxide nanoparticles (NiO-NPs) using the green method. It shows cytotoxicity and antibacterial activity. In this process, the color changed from dark brown to reddish ink, and after applying temperature, a light-yellow powder of NiO NPs was produced. The NiO NMs were single crystalline with a face-centred cubic phase and two strong PL at 305.46 nm and 410 nm. XRD and FTIR verified the formation of a pure NiO phase (average size 9.69 nm). HR-TEM confirmed the creation of nano and microstructures (agglomerated spherical shape). With different doses of NiO NPs generated from Moringa oleifera plant extract, the in vitro cytotoxicity and antibacterial activity were tested.

2.5. Magnesium Oxide (MgO) NPs. Fatiqin et al. [68] green synthesized magnesium oxide nanoparticles (MgO NPs) were achieved in this work by combining Moringa oleifera leaf extracts with a magnesium chloride solution. The produced MgO NPs vary from 20 to 50 nm (spherical shape). The absorption of MgO nanoparticles in the UV-Vis spectrum is at 280 nm. The inhibition zones showed the antibacterial activity of MgO NPs against *S. aureus* and *E. coli*. [69] used an aqueous extract of Moringa oleifera (MO) leaves as a green agent to produce nanosize MgO (MgO NPs) from MgCl_2 solution. UV-Vis absorption was used to validate the formation of MgO NPs in this synthesis. XRD investigation validated the spherical crystal structure of MgO NPs. Using SEM, TEM, and particle size analyzer (PSA) data,

TABLE 1: Summary of parameters and conditions for biosynthesized nanoparticles from *Moringa oleifera* plant.

NPs	Precursor	MO extract conc. (g/ml)	Reaction Temp./ Time	Size (nm)/Morphology	Photocatalytic/biological activity	References
FeO	0.5 M FeCl ₃	10 g, capping agent	100°C, 24 hrs	15.01 ± 6.03 nm rod like	Antibacterial test	Aisida, S. O. et al. [47]
FeO	1.60g of FeCl ₃ ·6H ₂ O	2 g, reducing agent	250°C, 15 hrs	66 ± 20 nm agglomeration	—	[48]
FeO	0.5 M FeCl ₃	10 g/100ml, reductant	100°C, 24 hrs	76 ± 2.0 nonuniform rod like	Photocatalytic and antibacterial activity	[49]
FeO	0.15 M FeCl ₃ ·6H ₂ O	30g	60°C	26.2 nm, irregular spherical	—	Aisida, S. O. et al. [50]
FeO	0.01 M FeCl ₃	20 gm reductant	500°C, 5 hrs	Below 5 nm (quantum dots)	—	[51]
FeO	0.1 M (Fe(NO ₃)) ₃ ·9H ₂ O	60g/lit, Reductant	50°C	Less than 100nm, spherical agglomerated	—	[52]
FeO	0.5 M FeCl ₂ ·7H ₂ O	Reducing power	—	45 nm irregular shape	Antioxidant and antibacterial activities	[53]
CuO	0.01 M Cu(CH ₃ COO) ₂ ·H ₂ O	5 gm	400°C, 1 hr	35-95 nm, quasispherical shape	Antifungal activity	[54]
CuO	CuSO ₄ ·5H ₂ O	60g, natural reducing agent	50°C	Lower to 100 nm aggregation	—	[55]
CuO	1 gm Cu(NO ₃) ₂ ·3H ₂ O	5 gm, reducing and stabilizing agent	200°C for 1 h	Average size 45.30nm, cluster-like	Bactericidal activity	[56]
CuO	2 g/20 ml copper acetate tetrahydrate	20 gm/100 ml, reducing and capping agent	400°C for 2 h	Average size 12 nm aggregates	Antioxidant and anticancer activity	[57]
CuO	3gm/10 ml copper (II) nitrate	3 gm biocapping agent	100°C, 1 h	12 and 18 nm spherical	Antimicrobial activity	[58]
ZnO	1 mM Zn(NO ₃) ₂ ·6H ₂ O	5 gm reducing agent	60°C 20 min	—	—	Manokari, M., and Shekhawat, M. S. [59].
ZnO	(Zn(NO ₃) ₂ ·6H ₂ O)	30 gm, reducing agent	500°C, 1 hr	16 to 31.9 nm spherical shape	Electrochemical activity	[60]
ZnO	2.1 g zinc acetate	5 g, stabilizing and accelerating agents	350°C, 5 hrs	52 nm, spherical	Photocatalytic and antibacterial activity	[61]
ZnO	2 g, (Zn (NO ₃) ₂ ·6H ₂ O)	20 gm, stabilizing agent	400°C for 2 hrs	16– 20 nm spherical and agglomerated particles	Antimicrobial activity	[62]
ZnO	1.5 g Zn(NO ₃) ₂ ·6H ₂ O	5 g (flowers, seeds, and leaves) chelating agent	500°C, 2 hrs	(13.2, 13.9, and 10.8 nm)	Photocatalytic activity	[63]
NiO	3 g/100 ml nickel nitrate hexahydrate	9 gm/300 ml, chelating reduction/oxidizing agent	500°C, 2 hrs	Average size 17.80nm	—	[64]
NiO	1.82 g/100 ml, nickel nitrate	2 gm/200 ml, reducing agent and capping agent	500°C, 3 min	Average size 12 nm, spherical shape	Photocatalytic and antimicrobial activity	[65]
NiO	0.1 mM Ni (NO ₃) ₂	20 g/100 ml acts as a fuel	400°C, 9 hrs	9.69 nm agglomerated spherical shape	Cytotoxicity and antibacterial activity	[66]
MgO	1 mM MgCl ₂ ·6H ₂ O	4 gm biocapping and bio-reducing agent	600°C	60-100 nm spherical shape	Antioxidant and antibacterial activities	[67]
MgO	1 mM MgCl ₂ ·6H ₂ O	4 gm reducing agent	600°C for 5 hrs	20-50 nm spherical shape	Antibacterial activity	[68]

TABLE 1: Continued.

NPs	Precursor	MO extract conc. (g/ml)	Reaction Temp./ Time	Size (nm)/Morphology	Photocatalytic/biological activity	References
MgO	1 mM MgCl ₂ ·6H ₂ O	4 g green agent	600°C for 5 hrs	40–70 nm spherical shape	Antioxidant, antibacterial, and antifungal	[69]
MgO	MgCl ₂ ·6H ₂ O	4gm/100 ml reducing agent and stabilizing agent	600°C for 5 hrs	40 to 100 nm cubic shape	—	[70]
Ag	1 mM AgNO ₃	20 gm reducing agent	—	46 nm spherical shape	—	[71]
Ag	1 mM AgNO ₃	10 g reducing agent	—	9–11 nm agglomerated	Antimicrobial activity	[72]
Ag	1 mM AgNO ₃	20 g reducing agent	—	8 nm monodispersed spherical shape	Antimicrobial activity	[73]
Ag	1 mM AgNO ₃	5 g (stem barks) reducing agent	60°C	40 nm spherical shape	Anticancer activity	[74]
Ag	1 mM AgNO ₃	10 g reducing agent	60–80°C, 20 min	57 nm spherical shape	Antimicrobial activity	[75]
Ag	0.001 M, 0.01 M, and 0.1 M AgNO ₃	3, 5, and 7 g reducing agent	—	15–25 nm disperse and semispherical shapes	Antibacterial activity	[76]
Ag	1 mM AgNO ₃	Reducing agent	37°C for 24 hours	Uniform-sized	Antibacterial activity	[77]
Au	1 mM (HAuCl ₄) ₃ H ₂ O, ACS reagent	20 g capping agent and reducing agent	—	100 nm triangular, hexagonal, and spherical	Catalytic activity and anticancer	[78]
Au	0.0254 mmol/L HAuCl ₄ ·3H ₂ O	43.6 mg/ml reducing and stabilizing agent	30°C, 10 min	20–60 nm spherical shape	—	[79]
Au	1 mM HAuCl ₄ ·3H ₂ O	20 g bioreduction	—	15.2 nm spherical, oval, and hexagonal shape	Antioxidant, antidiabetic, and anticancer activities	[80]
Au	1 mM HAuCl ₄	5 gm reducing and capping agent	—	96 nm	Anticancer activity	[81]
Au	1 mM HAuCl ₄ ·3H ₂ O	5 g bioreduction	—	10–20 nm spherically shaped	Anticancer activity	[82]



FIGURE 5: Biosynthesis of FeO nanorods.

the particle size of the synthesized MgO NPs was determined to be between 40 and 70 nm. The NPs showed excellent antibacterial and antifungal activity.

2.6. Silver (Ag) NPs. Moodley et al. [72] described silver nanoparticles (AgNPs) synthesized from *Moringa oleifera* leaf extracts and studied their antibacterial activities. UV-Vis spectrum analysis was used to establish the synthesis of AgNPs by reducing Ag^+ (AgNO_3). A UV-Vis spectrometer was used to scan NP solutions and the control from 190 to 900 nm. Surface plasmon resonance at 450 nm and 440 nm verified the production of silver nanoparticles in both fresh and freeze-dried leaf samples. According to FTIR spectroscopic technique, flavonoids, terpenoids, and polysaccharides predominate and are useful for the reduction as well as capping agents during the synthesis of Ag NPs. According to the X-ray diffraction examination, shows 9 and 11 nm NPs size. The antimicrobial activity of Ag NPs was shown in both bacterial and fungal strains.

Vasanth et al. [74], in their work, synthesized colloidal silver nanoparticles (AgNPs) from *Moringa oleifera* (MO) stem bark extract. Morphology was studied using electron and atomic force microscopic imaging (40 nm, and pentagon-shaped). Human cervical cancer cells (HeLa) were used to analyze the effects of produced AgNPs, and cell morphology was assessed using 4,6-diamidino-2-phenylindole (DAPI) staining. The effectiveness of AgNPs was investigated using fluorescence-activated cell sorting (FACS), and it was discovered that they trigger death in HeLa cells via generating reactive oxygen species (ROS).

2.7. Gold (Au) NPs. Anand et al. [78] used 1 M chloroauric acid with *Moringa oleifera* (MO) aqueous flower extract for the AuNP synthesis. The UV-Vis spectrophotometer (200–800 nm) was used to describe the formation of the colloidal solution of Au NP. TEM was analyzed to particle size (100 nm) that was triangular, hexagonal, and irregular spherical. Primary analytical tests analyzed AuNP and functional group interaction in floral extract and FTIR, and the ¹H-NMR technique was used to investigate capping agents. Catalytic reduction of nitrophenol and nitroaniline using Au NP, which were analyzed by UV-Vis, revealed a fast decrease in some minutes, suggesting industrial effluent degradation. Furthermore, AuNPs might have anticancer activities. [79] worked on an ecofriendly method to synthesize

gold nanoparticles (AuNPs) by reducing chloroauric acid with *Moringa oleifera* leaf extract which acts as a reducing agent. The chloroauric acid solution was reduced and transformed to AuNPs in the size range of 20–60 nm (spherical shape) using leaf extract. The MO plant extract contains several phytochemicals that function as reducers and stabilizers. These are environmentally acceptable synthesizing stabilized gold nanoparticles suitable for various biological applications.

3. Conclusion

This review summarised that *Moringa oleifera* plant leaves have active compounds that serve as capping, reducing, and stabilizing agents and produce biosynthesized M/MO NPs. Several approaches were gathered, and it was found that *Moringa oleifera* plant leaves can readily biosynthesize numerous types of M/MO nanoparticles. Biosynthesized ZnO and AgNPs outperform chemically produced NPs in terms of antibacterial characteristics. However, not all articles discuss the size of NPs resulting from the concentration of *Moringa oleifera* plant leaf extract or temperature changes. In general, the size of the nanoparticles was determined by manipulating the concentration of *Moringa oleifera* leaf extract and the temperature during biosynthesis.

Data Availability

All relevant data are included within the article.

Conflicts of Interest

All authors declare that there is no conflict of interest.

Acknowledgments

The authors extend their appreciation to the Deanship of Scientific Research at King Khalid University for funding this work through research group program under the grant number R.G.P.1/105/42

References

- [1] P. S. Weiss, "Where are the products of nanotechnology?," *Acc Nano*, vol. 9, no. 4, pp. 3397–3398, 2015.


- [2] S. Raina, A. Roy, and N. Bharadvaja, "Degradation of dyes using biologically synthesized silver and copper nanoparticles," *Environmental Nanotechnology, Monitoring & Management*, vol. 13, article 100278, 2020.
- [3] A. Roy, A. Elzaki, V. Tirth et al., "Biological synthesis of nanocatalysts and their applications," *Catalysts*, vol. 11, no. 12, article 1494, 2021.
- [4] L. Pereira, F. Mehboob, A. J. Stams, M. M. Mota, H. H. Rijnaarts, and M. M. Alves, "Metallic nanoparticles: microbial synthesis and unique properties for biotechnological applications, bioavailability and biotransformation," *Critical Reviews in Biotechnology*, vol. 35, no. 1, pp. 114–128, 2015.
- [5] C. Pandit, A. Roy, S. Ghotekar et al., "Biological agents for synthesis of nanoparticles and their applications," *Journal of King Saud University-Science*, vol. 34, no. 3, article 101869, 2022.
- [6] I. Khan, K. Saeed, and I. Khan, "Nanoparticles: properties, applications and toxicities," *Arabian Journal of Chemistry*, vol. 12, no. 7, pp. 908–931, 2019.
- [7] A. Roy and N. Bharadvaja, "Silver nanoparticle synthesis from *Plumbago zeylanica* and its dye degradation activity," *Bioinspired, Biomimetic and Nanobiomaterials*, vol. 8, no. 2, pp. 130–140, 2019.
- [8] R. Anselmann, "Nanoparticles and nanolayers in commercial applications," *Journal of Nanoparticle Research*, vol. 3, no. 4, pp. 329–336, 2001.
- [9] M. Guix, C. C. Mayorga-Martinez, and A. Merkoçi, "Nano/micromotors in (bio) chemical science applications," *Chemical Reviews*, vol. 114, no. 12, pp. 6285–6322, 2014.
- [10] P. Srinoi, Y. T. Chen, V. Vittur, M. D. Marquez, and T. R. Lee, "Bimetallic nanoparticles: enhanced magnetic and optical properties for emerging biological applications," *Applied Sciences*, vol. 8, no. 7, article 1106, 2018.
- [11] A. Roy, H. A. Murthy, H. M. Ahmed, M. N. Islam, and R. Prasad, "Phyto-genic synthesis of metal/metal oxide nanoparticles for degradation of dyes," 2021.
- [12] K. Tanabe, "Optical radiation efficiencies of metal nanoparticles for optoelectronic applications," *Materials Letters*, vol. 61, no. 23–24, pp. 4573–4575, 2007.
- [13] A. Barhoum and A. S. H. Makhlof, *Emerging Applications of Nanoparticles and Architecture Nanostructures*, Elsevier, Amsterdam, The Netherlands, 2018.
- [14] L. Spindlberger, S. Prucnal, J. Aberl, and M. Brehm, "Thermal Stability of Defect-Enhanced Ge on Si Quantum Dot Luminescence upon Millisecond Flash Lamp Annealing," *Physica Status Solidi*, vol. 216, no. 17, article 1900307, 2019.
- [15] J. Wang, J. S. Lee, D. Kim, and L. Zhu, "Exploration of zinc oxide nanoparticles as a multitarget and multifunctional anticancer nanomedicine," *ACS Applied Materials & Interfaces*, vol. 9, no. 46, pp. 39971–39984, 2017.
- [16] A. Roy, A. Sharma, S. Yadav, L. T. Jule, and R. Krishnaraj, "Nanomaterials for remediation of environmental pollutants," *Bioinorganic Chemistry and Applications*, vol. 2021, 16 pages, 2021.
- [17] A. Roy, "Plant derived silver nanoparticles and their therapeutic applications," *Current Pharmaceutical Biotechnology*, vol. 22, no. 14, pp. 1834–1847, 2021.
- [18] S. Mittal and A. Roy, "Fungus and plant-mediated synthesis of metallic nanoparticles and their application in degradation of dyes," in *Photocatalytic degradation of dyes*, pp. 287–308, Elsevier, Netherlands, 2021.
- [19] I. Ocsoy, M. L. Paret, M. A. Ocsoy et al., "Nanotechnology in plant disease management: DNA-directed silver nanoparticles on graphene oxide as an antibacterial against *Xanthomonas perforans*," *ACS Nano*, vol. 7, no. 10, pp. 8972–8980, 2013.
- [20] R. Geetha, T. Ashokkumar, S. Tamilselvan, K. Govindaraju, M. Sadiq, and G. Singaravelu, "Green synthesis of gold nanoparticles and their anticancer activity," *Cancer Nanotechnology*, vol. 4, no. 4–5, pp. 91–98, 2013.
- [21] P. Nagore, S. Ghotekar, K. Mane, A. Ghoti, M. Bilal, and A. Roy, "Structural properties and antimicrobial activities of *Polyalthia longifolia* leaf extract-mediated CuO nanoparticles," *BioNanoScience*, vol. 11, no. 2, pp. 579–589, 2021.
- [22] Y. Zhu and L. Liao, "Applications of nanoparticles for anticancer drug delivery: a review," *Journal of Nanoscience and Nanotechnology*, vol. 15, no. 7, pp. 4753–4773, 2015.
- [23] D. Ashwini and G. Mahalingam, "Green synthesized metal nanoparticles, characterization and its antidiabetic activities—a review," *Research Journal of Pharmacy and Technology*, vol. 13, no. 1, pp. 468–474, 2020.
- [24] J. M. George, A. Antony, and B. Mathew, "Metal oxide nanoparticles in electrochemical sensing and biosensing: a review," *Microchimica Acta*, vol. 185, no. 7, pp. 1–26, 2018.
- [25] D. Astruc, "Introduction: nanoparticles in catalysis," *Chemical Reviews*, vol. 120, no. 2, pp. 461–463, 2020.
- [26] H. M. Ahmed, A. Roy, M. Wahab et al., "Applications of nanomaterials in agrifood and pharmaceutical industry," *Journal of Nanomaterials*, vol. 2021, 10 pages, 2021.
- [27] R. Bazak, M. Hourri, S. El Achy, S. Kamel, and T. Refaat, "Cancer active targeting by nanoparticles: a comprehensive review of literature," *Journal of Cancer Research and Clinical Oncology*, vol. 141, no. 5, pp. 769–784, 2015.
- [28] M. Aliofkhaezrai, Ed., *Handbook of nanoparticles*, Springer International Publishing, Switzerland, 2016.
- [29] D. L. Fedlheim and C. A. Foss, *Metal nanoparticles: synthesis, characterization, and applications*, CRC press, 2001.
- [30] A. K. Shukla and S. Iravani, *Green synthesis, characterization and applications of nanoparticles*, Elsevier, Netherlands, 2018.
- [31] Z. Li, H. Jiang, C. Xu, and L. Gu, "A review: using nanoparticles to enhance absorption and bioavailability of phenolic phytochemicals," *Food Hydrocolloids*, vol. 43, pp. 153–164, 2015.
- [32] R. Prasad, *Plant Nanobionics: Volume 2, Approaches in Nanoparticles, Biosynthesis, and Toxicity*, Springer Nature, Switzerland, 2019.
- [33] S. Iravani, "Green synthesis of metal nanoparticles using plants," *Green Chemistry*, vol. 13, no. 10, pp. 2638–2650, 2011.
- [34] M. Shahrashoub and S. Bakhtiari, "The efficiency of activated carbon/magnetite nanoparticles composites in copper removal: industrial waste recovery, green synthesis, characterization, and adsorption-desorption studies," *Microporous and Mesoporous Materials*, vol. 311, article 110692, 2021.
- [35] I. Hussain, N. B. Singh, A. Singh, H. Singh, and S. C. Singh, "Green synthesis of nanoparticles and its potential application," *Biotechnology Letters*, vol. 38, no. 4, pp. 545–560, 2016.
- [36] T. Mazhar, V. Shrivastava, and R. S. Tomar, "Green synthesis of bimetallic nanoparticles and its applications: a review," *Journal of Pharmaceutical Sciences and Research*, vol. 9, no. 2, article 102, 2017.
- [37] H. Nadaroglu, A. A. Gungor, and İ. N. C. E. Selvi, "Synthesis of nanoparticles by green synthesis method," *International Journal of Innovative Research and Reviews*, vol. 1, no. 1, pp. 6–9, 2017.

- [38] J. Jeevanandam, A. Barhoum, Y. S. Chan, A. Dufresne, and M. K. Danquah, "Review on nanoparticles and nanostructured materials: history, sources, toxicity and regulations," *Beilstein Journal of Nanotechnology*, vol. 9, no. 1, pp. 1050–1074, 2018.
- [39] N. B. Turan, H. S. Erkan, G. O. Engin, and M. S. Bilgili, "Nanoparticles in the aquatic environment: usage, properties, transformation and toxicity—a review," *Process Safety and Environmental Protection*, vol. 130, pp. 238–249, 2019.
- [40] A. Rana, K. Yadav, and S. Jagadevan, "A comprehensive review on green synthesis of nature-inspired metal nanoparticles: mechanism, application and toxicity," *Journal of Cleaner Production*, vol. 272, article 122880, 2020.
- [41] N. Bhalla, N. Ingle, S. V. Patri, and D. Haranath, "Phytochemical analysis of Moringa oleifera leaves extracts by GC-MS and free radical scavenging potency for industrial applications," *Saudi Journal of Biological Sciences*, vol. 28, no. 12, pp. 6915–6928, 2021.
- [42] K. Belay and M. J. C. M. R. Sisay, "Phytochemical constituents and physicochemical properties of medicinal plant (Moringa Oleifera) around bule hora," *Chemistry and Materials Research*, vol. 6, no. 7, pp. 61–72, 2014.
- [43] L. Gopalakrishnan, K. Doriya, and D. S. Kumar, "Moringa oleifera : a review on nutritive importance and its medicinal application," *Food Science and Human Wellness*, vol. 5, no. 2, pp. 49–56, 2016.
- [44] S. O. Aisida, E. Ugwoke, A. Uwais et al., "Incubation period induced biogenic synthesis of PEG enhanced Moringa oleifera silver nanocapsules and its antibacterial activity," *Journal of Polymer Research*, vol. 26, no. 9, pp. 1–11, 2019.
- [45] C. Tiloke, K. Anand, R. M. Gengan, and A. A. Chuturgoon, "Moringa oleifera_ and their phytonanoparticles: potential antiproliferative agents against cancer," *Biomedicine & Pharmacotherapy*, vol. 108, pp. 457–466, 2018.
- [46] W. G. Shousha, W. M. Aboulthana, A. H. Salama, M. H. Saleh, and E. A. Essawy, "Evaluation of the biological activity of Moringa oleifera leaves extract after incorporating silver nanoparticles, in vitro study," *Bulletin of the National Research Centre*, vol. 43, no. 1, pp. 1–13, 2019.
- [47] S. O. Aisida, N. Madubuonu, M. H. Alnasir et al., "Biogenic synthesis of iron oxide nanorods using Moringa oleifera leaf extract for antibacterial applications," *Applied Nanoscience*, vol. 10, no. 1, pp. 305–315, 2020.
- [48] G. I. Tovar, S. Briceño, J. Suarez, S. Flores, and G. González, "Biogenic synthesis of iron oxide nanoparticles using Moringa oleifera_ and chitosan and its evaluation on corn germination," *Environmental Nanotechnology, Monitoring & Management*, vol. 14, article 100350, 2020.
- [49] N. Madubuonu, S. O. Aisida, A. Ali et al., "Biosynthesis of iron oxide nanoparticles via a composite of Psidium guajava-Moringa oleifera_ and their antibacterial and photocatalytic study," *Journal of Photochemistry and Photobiology B: Biology*, vol. 199, article 111601, 2019.
- [50] S. O. Aisida, K. Ugwu, P. A. Akpa et al., "Synthesis and characterization of iron oxide nanoparticles capped with Moringa Oleifera: the mechanisms of formation effects on the optical, structural, magnetic and morphological properties," *Materials Today: Proceedings*, vol. 36, pp. 214–218, 2021.
- [51] G. D. Reddy, M. Noorjahan, K. G. Mangatayaru, and M. Krishnakanth, "Microwave assisted phytosynthesis and characterization of magnetic iron oxide quantum dots using Moringa oleifera," *Material Science Research India*, vol. 15, no. 2, pp. 145–150, 2018.
- [52] C. Silveira, Q. L. Shimabuku, M. Fernandes Silva, and R. Bergamasco, "Iron-oxide nanoparticles by the green synthesis method using Moringa oleifera leaf extract for fluoride removal," *Environmental Technology*, vol. 39, no. 22, pp. 2926–2936, 2018.
- [53] G. B. Jegadeesan, K. Srimathi, N. S. Srinivas, S. Manishkanna, and D. Vignesh, "Green synthesis of iron oxide nanoparticles using Terminalia bellirica_ and Moringa oleifera_ fruit and leaf extracts: antioxidant, antibacterial and thermoacoustic properties," *Biocatalysis and Agricultural Biotechnology*, vol. 21, article 101354, 2019.
- [54] K. Pagar, S. Ghotekar, T. Pagar et al., "Antifungal activity of biosynthesized CuO nanoparticles using leaves extract of Moringa oleifera and their structural characterizations," *Asian Journal of Nanosciences and Materials*, vol. 3, no. 1, pp. 15–23, 2020.
- [55] C. R. Galan, M. F. Silva, D. Mantovani, R. Bergamasco, and M. F. Vieira, "Green synthesis of copper oxide nanoparticles impregnated on activated carbon using Moringa oleifera leaves extract for the removal of nitrates from water," *The Canadian Journal of Chemical Engineering*, vol. 96, no. 11, pp. 2378–2386, 2018.
- [56] G. Kalaiyan, S. Suresh, K. M. Prabu et al., "Bactericidal activity of Moringa oleifera_ leaf extract assisted green synthesis of hierarchical copper oxide microspheres against pathogenic bacterial strains," *Journal of Environmental Chemical Engineering*, vol. 9, no. 1, article 104847, 2021.
- [57] D. Rehana, D. Mahendiran, R. S. Kumar, and A. K. Rahiman, "Evaluation of antioxidant and anticancer activity of copper oxide nanoparticles synthesized using medicinally important plant extracts," *Biomedicine & Pharmacotherapy*, vol. 89, pp. 1067–1077, 2017.
- [58] G. T. Anand, S. J. Sundaram, K. Kanimozhi, R. Nithiyavathi, and K. Kaviyarasu, "Microwave assisted green synthesis of CuO nanoparticles for environmental applications," *Materials Today: Proceedings*, vol. 36, pp. 427–434, 2021.
- [59] M. Manokari and M. S. Shekhawat, "Zinc oxide nanoparticles synthesis from Moringa oleifera lam. Extracts and their characterization," *World Scientific News*, vol. 55, pp. 252–262, 2016.
- [60] N. Matinise, X. G. Fuku, K. Kaviyarasu, N. Mayedwa, and M. J. A. S. S. Maaza, "ZnO nanoparticles via Moringa_oleifera_ green synthesis: physical properties & mechanism of formation," *Applied Surface Science*, vol. 406, pp. 339–347, 2017.
- [61] S. Pal, S. Mondal, J. Maity, and R. Mukherjee, "Synthesis and characterization of ZnO nanoparticles using Moringa oleifera leaf extract: investigation of photocatalytic and antibacterial activity," *International Journal of Nanoscience and Nanotechnology*, vol. 14, no. 2, pp. 111–119, 2018.
- [62] K. Elumalai, S. Velmurugan, S. Ravi, V. Kathiravan, and S. Ashokkumar, "RETRACTED: green synthesis of zinc oxide nanoparticles using Moringa oleifera leaf extract and evaluation of its antimicrobial activity," vol. 143, pp. 158–164, 2015.
- [63] I. Ngom, B. D. Ngom, J. Sackey, and S. Khamlich, "Biosynthesis of zinc oxide nanoparticles using extracts of Moringa Oleifera: structural & optical properties," *Materials Today: Proceedings*, vol. 36, pp. 526–533, 2021.
- [64] I. Ngom, N. M. Ndiaye, A. Fall, M. Bakayoko, B. D. Ngom, and M. Maaza, "On the use of Moringa Oleifera leaves extract for the biosynthesis of NiO and ZnO nanoparticles," *MRS Advances*, vol. 5, no. 21–22, pp. 1145–1155, 2020.

- [65] K. C. Suresh and A. Balamurugan, "Evaluation of structural, optical, and morphological properties of nickel oxide nanoparticles for multi-functional applications," *Inorganic and Nano-Metal Chemistry*, vol. 51, no. 2, pp. 296–301, 2021.
- [66] A. A. Ezhilarasi, J. J. Vijaya, K. Kaviyarasu, M. Maaza, A. Ayeshamariam, and L. J. Kennedy, "Green synthesis of NiO nanoparticles using *Moringa oleifera* extract and their biomedical applications: cytotoxicity effect of nanoparticles against HT-29 cancer cells," *Journal of Photochemistry and Photobiology B: Biology*, vol. 164, pp. 352–360, 2016.
- [67] H. Amrulloh, A. Fatiqin, W. Simanjuntak, H. Afriyani, and A. Annissa, "Bioactivities of nano-scale magnesium oxide prepared using aqueous extract of *Moringa oleifera* leaves as green agent," *Natural Science*, vol. 12, no. 1, 2021.
- [68] A. Fatiqin, H. Amrulloh, and W. Simanjuntak, "Green synthesis of MgO nanoparticles using *Moringa oleifera* leaf aqueous extract for antibacterial activity," *Bulletin of the Chemical Society of Ethiopia*, vol. 35, no. 1, pp. 161–170, 2021.
- [69] H. Amrulloh, A. Fatiqin, W. Simanjuntak, H. Afriyani, and A. Annissa, "Bioactivities of nanoscale magnesium oxide prepared using aqueous extract of *Moringa Oleifera* leaves as green agent," *Advances in Natural Sciences: Nanoscience and Nanotechnology*, vol. 12, no. 1, article 015006, 2021.
- [70] A. Fatiqin, H. Amrulloh, W. Simanjuntak et al., "Characteristics of nano-size MgO prepared using aqueous extract of different parts of *Moringa oleifera* plant as green synthesis agents," *AIP Conference Proceedings*, vol. 2331, no. 1, article 040001, 2021.
- [71] R. Sathyavathi, M. Krishna, and D. N. Rao, "Biosynthesis of silver nanoparticles using *Moringa oleifera* leaf extract and its application to optical limiting," *Journal of Nanoscience and Nanotechnology*, vol. 11, no. 3, pp. 2031–2035, 2011.
- [72] J. S. Moodley, S. B. N. Krishna, K. Pillay, and P. Govender, "Green synthesis of silver nanoparticles from *Moringa oleifera* leaf extracts and its antimicrobial potential," *Advances in Natural Sciences: Nanoscience and Nanotechnology*, vol. 9, no. 1, article 015011, 2018.
- [73] M. R. Bindhu, M. Umadevi, G. A. Esmail, N. A. Al-Dhabi, and M. V. Arasu, "Green synthesis and characterization of silver nanoparticles from *Moringa oleifera* flower and assessment of antimicrobial and sensing properties," *Journal of Photochemistry and Photobiology B: Biology*, vol. 205, article 111836, 2020.
- [74] K. Vasanth, K. Ilango, R. MohanKumar, A. Agrawal, and G. P. Dubey, "Anticancer activity of *Moringa oleifera* mediated silver nanoparticles on human cervical carcinoma cells by apoptosis induction," *Colloids and Surfaces B: Biointerfaces*, vol. 117, pp. 354–359, 2014.
- [75] T. N. V. K. V. Prasad and E. Elumalai, "Biofabrication of Ag nanoparticles using *Moringa oleifera* leaf extract and their antimicrobial activity," *Asian Pacific Journal of Tropical Biomedicine*, vol. 1, no. 6, pp. 439–442, 2011.
- [76] H. M. Ibrahim, S. Zaghoul, M. Hashem, and A. El-Shafei, "A green approach to improve the antibacterial properties of cellulose based fabrics using *Moringa oleifera* extract in presence of silver nanoparticles," *Cellulose*, vol. 28, no. 1, pp. 549–564, 2021.
- [77] A. Islam, C. Mandal, and A. Habib, "Antibacterial potential of synthesized silver nanoparticles from leaf extract of *Moringa oleifera*," *JABET*, vol. 4, no. 1, p. 67, 2021.
- [78] K. Anand, R. M. Gengan, A. Phulukdaree, and A. Chuturgoon, "Agroforestry waste *Moringa oleifera* petals mediated green synthesis of gold nanoparticles and their anti-cancer and catalytic activity," *Journal of Industrial and Engineering Chemistry*, vol. 21, pp. 1105–1111, 2015.
- [79] A. Chakraborty, D. K. Das, M. Sinha, S. Dey, and S. Bhattacharjee, "*Moringa oleifera* Leaf extract mediated green synthesis of stabilized gold nanoparticles," *Journal of Bionanoscience*, vol. 7, no. 4, pp. 415–419, 2013.
- [80] M. S. Kiran, C. R. Kumar, U. R. Shwetha, H. S. Onkarappa, V. S. Betageri, and M. S. Latha, "Green synthesis and characterization of gold nanoparticles from *Moringa oleifera* leaves and assessment of antioxidant, antidiabetic and anticancer properties," *Chemical Data Collections*, vol. 33, article 100714, 2021.
- [81] S. Gupta, H. Hemlata, and K. Tejavath, "Synthesis, characterization and comparative anticancer potential of phytosynthesized mono and bimetallic nanoparticles using *Moringa oleifera* aqueous leaf extract," *Beilstein Arch*, vol. 1, article 95, 2020.
- [82] C. Tiloke, A. Phulukdaree, K. Anand, R. M. Gengan, and A. A. Chuturgoon, "*Moringa oleifera* gold nanoparticles modulate oncogenes, tumor suppressor genes, and caspase-9 splice variants in a549 cells," *Journal of Cellular Biochemistry*, vol. 117, no. 10, pp. 2302–2314, 2016.

Research Article

Mechanical and Durability Characteristics of TiO_2 and Al_2O_3 Nanoparticles with Sisal Fibers

R. Rajkumar,¹ R. Nirmala,² and V. Vivekananthan ³

¹Department of Civil Engineering, Sri Sivasubramaniya Nadar College of Engineering, Chennai, India

²Department of Civil Engineering, Sathyabama Institute of Science and Technology, Chennai, India

³Department of Construction Technology and Management, Mettu University, Mettu, Ethiopia

Correspondence should be addressed to V. Vivekananthan; vvivekurfriend@gmail.com

Received 27 January 2022; Revised 25 February 2022; Accepted 11 March 2022; Published 4 April 2022

Academic Editor: Arpita Roy

Copyright © 2022 R. Rajkumar et al. This is an open access article distributed under the Creative Commons Attribution License, which permits unrestricted use, distribution, and reproduction in any medium, provided the original work is properly cited.

The use of nanoparticles in concrete increases the material's strength and durability, making it useful in the building sector. Nanomaterials can lower the amount of cement in a building since cement releases carbon dioxide, which contributes to global warming. The mechanical response of concrete is studied in this study by replacing cement with various dosages of nanotitanium dioxide and nanoalumina. Nanotechnology has attracted a lot of attention in recent years because of its potential uses for particles. Cementitious materials at the nano/atomic level are the primary focus of current research. The mechanical characteristics of cementitious materials have been significantly improved by introducing nanotitanium dioxide and nanoalumina into cement. Nanotitanium dioxide and nanoalumina have been added to concrete in this study to examine its sorptivity and water absorption properties. To lower the carbon footprint of concrete, nanotitanium dioxide and nanoalumina can be used in place of cement.

1. Introduction

Due to the growing demand for the construction sector in the recent times, it has become a necessity to find alternatives for building materials for various reasons. One being, over exploitation of non renewable resources. Second being, the existing rapid usage of the resources is polluting the environment, which creates a great impact on the human and animal ecosystem [1, 2]. Thus, there has been various researches in modifying the conventional matrix by adding additives to make it more efficient and effective in terms of performance [3–5]. Cement has been one of the very important aspect in the construction sector, which is also very widely used. Reports are shown that, by using a ton of the conventional Ordinary Portland Cement (OPC), the same amount of the carbon dioxide gas is effused in the atmosphere. This ultimately increases the carbon footprint in the environment [6]. And also, it has been reported that the construction sector is responsible for about 7-8% of the carbon dioxide emission worldwide [7]. Thus, all these situations have aggravated the process of using various additives

or modifying the conventional concrete to make it greener and more economical.

The durability and efficiency of the cementitious particles depend upon calcium silicate hydrate (C-S-H) particles present in the cement [8]. The characteristics of these particles are due to the fact that their size is about few nanometers, which gives them the properties like binding, etc. Thus, nanoparticles are widely researched sector as additives to the concrete, which enhances the efficiency and performance of the same [9, 10]. As compared to the conventional concrete particles, nanoparticles are higher when properties like reactivity and specific area are considered. Thus, the nanoparticles which are smaller size, the chemical reaction in the cement is more enhanced [11]. Nanotechnology involves particles which are less than or equal to nanometers (0.1 nm to 100 nm). Researches have shown that the particles which are smaller can react easily and effectively than the same particles which are bigger in size. The nanoscale of the particles can be achieved by, namely, two approaches, one being the top-down approach and second the bottom down approach. Both the approaches have their own advantages and

disadvantages to them. In the top-down approach, the larger particles are made to size down, which may or may not give finer particles. It is also observed that the size distribution is higher in terms of top-down approach. Whereas in the bottom-up approach, the smaller-sized atomic particles are made to size up via self-assembly, which creates difficulty in scaling [12, 13]. There are various methods used in various approaches. For example, in the bottom-up approach, methods like nanolithography, high pressure torsion, accumulative roll bonding, etc. are used. In the top-down approach, methods like spray conversion processing and chemical vapor deposition are used [14]. But either of the methods demands various heavy machinery and toxic chemicals, which take up higher manual labor and energy, which is not environmentally friendly [15]. But, usage of phytochemicals and enzymes present in the plants for the production of the nanoparticles is a greener option, which is environment friendly and economically viable [16].

Concrete as a building material has its demand in the infrastructure sector for a long time. Owing to its attributes such as its versatility, mechanical properties, and availability, concrete has been used at about 20 billion tones as per the per capita consumption globally [17]. Moreover, due to the dynamic nature of the concrete, it is possible for various interventions that can be done to increase the efficiency and performance of the building material. These interventions are required to be environment friendly and economically viable [29,30].

Nanotechnology has been most researched sector for the infrastructure industry to be integrated to increase the efficacy of the same [27,28,34]. Researches have been done by using nanoparticles of Al_2O_3 , SiO_2 , and ZnO as additives for the concrete, and it has been observed that it led to improvement in the packaging [18–20]. The high reactive property of the nanoparticles leads to good efficiency in the pozzolanic reaction. Zinc oxide (ZnO) is a semiconductor which found its way to the solar cells, photocatalysts, chemical sensors, etc. [21]. It has been observed that usage of the ZnO nanoparticles in the cement alters and improves the kinetics of the hydration process in its initial stage. Studies conducted by Olmo et al. suggested that by using cement paste consisting of 15% of ZnO , the setting time increased, observing that the presence of ZnO led to reduction of the compressive strength of the mixture [20]. Arefi and Rezaei-Zarchi observed that by using 5% of ZnO in the mixture, the initial stages were more enhanced and improved [22]. It is seen that by using ultramicro ZnO nanoparticles, it produces filler effect and also reduces the production of the CH particles by using the OH^- ions. Moreover, by using ZnO nanoparticles, it slows the process of hydration reaction, and thus, density of the overall structure is improved, and it is more densely packed [20, 23].

Titanium oxide (TiO_2) nanoparticles have also been studied to be used as additives for the concrete. Li et al. observed that by using the TiO_2 nanoparticles with the concrete, the fatigue performance is increased significantly [24]. When the attribute of abrasion resistance is taken into consideration, it has been seen by Li et al. that the abrasion resistance is directly proportional to the amount of the

nanoparticles added. It has been observed that as the number of nanoparticles used increases, the extent of the abrasion resistance is also increased [25].

Muzenski et al. [30] found that adding a small amount of Al_2O_3 nanofibers (0.25 percent by cement weight) increased the strength properties of cement-based composites by about 30%. Yang et al. [31] evaluated the chloride-binding ability of cement specimens after adding a range of nano- Al_2O_3 concentrations (0.5–5%). The chloride-binding ability of cement increased by 37.2 percent when nano- Al_2O_3 particles were added at a concentration of 5%, and the researchers concluded that adding the right amount of nanoalumina can enhance the chloride-binding ability of cement. It has also been found that even a 3% incorporation of nanoalumina to mortar can densify the microstructure [32].

This paper is aimed at researching about the usage of alumina and TiO_2 as additives in the concrete mixture.

1.1. Mix Proportions. Various replacements of alumina and TiO_2 nanoparticles were incorporated in concrete as a partial replacement of cement. Sisal fibers were incorporated in concrete at a constant percentage of 2% as a partial replacement of cement. The usage of nanomaterials beyond 5% minimizes the strength properties of cement; the incorporation of nanoparticles was fixed as 3% and 4%. Table 1 depicts the mix proportions of nanoparticles and sisal fibers incorporated concrete specimens.

2. Result and Discussions

2.1. Experimental Procedure. Indian standard IS: 516-1959 [24] specifies procedures for examining hardened concrete properties and fresh concrete mix properties. Concrete workability is determined by conducting a slump cone test. In order to determine the hardened concrete properties, split tensile strength and flexural and compressive strength are measured at 7, 28, and 90 days, respectively, after curing in water. A variety of specimen sizes is considered for all tests. An experimental specimen with a size of 150 mm cube sides will undergo compressive strength testing, and another 1-meter long cylindrical specimen with a size of 150 mm and a height of 300 mm will undergo split tensile strength testing.

Specimens measuring 100 mm*100 mm*500 mm are used for flexural strength testing. In addition to these tests, the longevity of the concrete is also evaluated. A series of endurance tests is being conducted to test hardened concrete quality to study how it holds up after the hydration process and chemical exposure. These tests include water absorption and sorptivity. In accordance with ASTM C1585-thirteen, a 150 mm dice specimen is tested for sorptivity in order to examine the capillary upward thrust in concrete specimens due to its porous nature. A microwave oven is used to achieve consistent weight after 28 days of wet curing prior to appearance of this check. Furthermore, the concrete aspects are applied with oil to prevent water penetration besides for the lowest surface and are stored in water for 30 min.

The surface of the water bath is dried with an absorbent cloth after 30 minutes and then weighed. Concrete is also

TABLE 1: Mix proportions of concrete specimens.

Mix ID	Cement (kg/m ³)	Fine aggregate (kg/m ³)	Coarse aggregate (kg/m ³)	Water content (kg/m ³)	TiO ₂ nanoparticles (kg/m ³)	Al ₂ O ₃ nanoparticles (kg/m ³)	Sisal fibers (kg/m ³)
CC	435	672	1179	172	0	0	0
CC-1	413.25	672	1179	172	13.05	0	8.7
CC-2	408.9	672	1179	172	17.4	0	8.7
CC-3	413.25	672	1179	172	0	13.05	8.7
CC-4	408.9	672	1179	172	0	17.4	8.7
CC-5	400.2	672	1179	172	13.05	13.05	8.7
CC-6	391.5	672	1179	172	17.4	17.4	8.7

subjected to a water absorption test to determine its ability to absorb water or other liquids. A 150 mm cube sample after 28 days of curing is stored in a microwave oven until it reaches a constant dry weight before water. The absorption test begins. We weigh the samples every 12 hours until they reach a stable absorbed weight by keeping the cubes in a water bath. By comparing the wet and dry weight of the sample, we can determine the rate of water uptake.

2.2. Slump Cone Test. The slump cone test, which is based on the Indian Standard IS: 516-1959 [24], assesses the quality of new concrete.

The workability of all mixtures is determined by a slump cone test. Figure 1 illustrates the slump value based on various mix proportions. We can observe from the test results that a larger proportion of nanoparticles correspond to a higher slump value, indicating a high-quality and practical concrete. Slump was considerably enhanced when sisal fiber, and nanoparticles were added to mixed concrete.

Slump cone results can be viewed as a graphical representation. Slump values gradually grow until CC-6 and conclude that increase in nanoparticles percentage increases the slump value of concrete. Maximum slump values at 4% TiO₂ and 4% Al₂O₃, with taking any sisal fibers into consideration. Figure 1 depicts the graphical fluctuation of slump values with and without nanomaterials. Fibrous aggregate performs better than nonfibrous aggregate in concrete mixes. Concrete becomes more workable as the fiber content and nanoparticles rise. The graphical variant illustrates and supports these findings.

2.3. Compressive Strength. Using a compression testing machine, cube specimens of 150 mm*150 mm*150 mm size are used to measure the compressive strength of concrete. As per the Indian Standard, 250 square specimens were added together to test compressive strength. Tests are conducted after 7, 28, and 90 days of curing. The data shows a significant increase in compressive strength as nanomaterial percentage increases as shown in Figure 2. When 4% Al₂O₃ is replaced in CC-4 composition of concrete, maximum strength is obtained. Concrete reinforced with fibrous hybrid nanomaterials exhibits similar enhanced strength. Conventional concrete seen a decline in strength. A nanomaterial (TiO₂ and Al₂O₃) effectively increases the strength of the material up to a certain percentage. These two examples

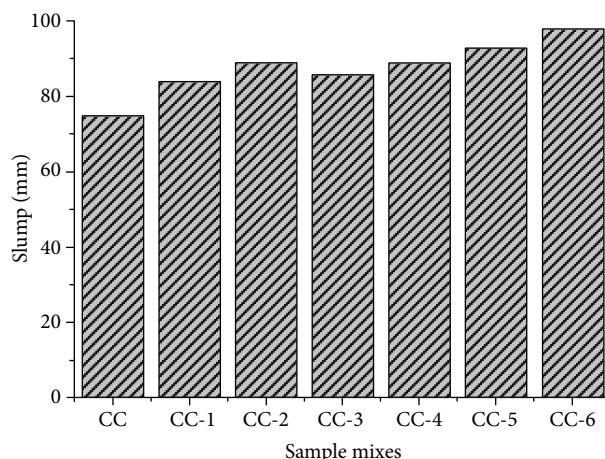


FIGURE 1: Slump values of concrete specimens.

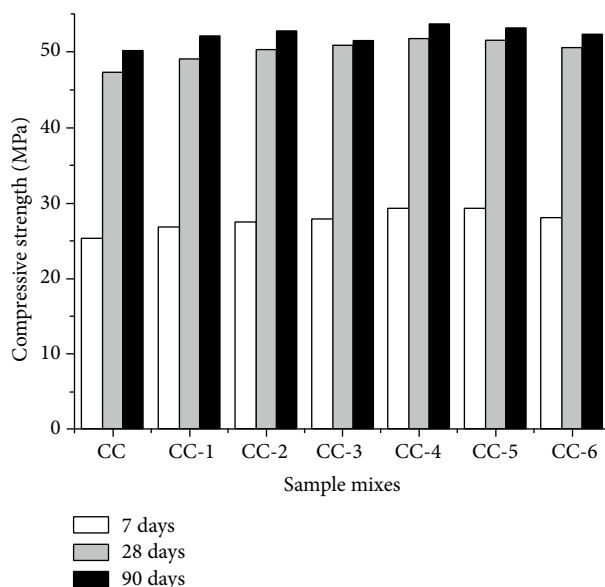


FIGURE 2: Compressive strength of concrete specimens.

compare a variety of mixes to the reference mix of concrete and show the strength variations between them. These nanomaterials have been tested separately and have proven to be as strong as standard concrete when combined by replacing cement with 4%TiO₂ and 4% Al₂O₃ along with sisal fibers. Our experimental study, however, took into account

different percentages of nanomaterials compared to those that were tested with sisal fibers. Its economic and environmental benefits make it a positive development. A maximum strength of 54.41 MPa can also be achieved.

2.4. Split Tensile Strength. Compression testing equipment is used to measure the split tensile strength of concrete using a cylindrical specimen with a length of 300 mm and a diameter of 150 mm.

The tensile strength of cylindrical samples is evaluated according to the Indian Standard. The test is performed after 7, 28, and 90 days of wet curing. The average strength of cylindrical specimens was tested, and the findings are shown in Figure 3. We can see a rise in split tensile strength as the proportion of nanomaterials increases in the data. At all ages, the maximum strength is attained in concrete with a CC-4 composition including 4% Al_2O_3 and sisal fibers.

The rise of nanomaterials over the optimal proportion has resulted in a decrease in strength. The inclusion of nanoparticles (TiO_2 and Al_2O_3) enhances the strength of a segment of the material until it reaches a point where it begins to deteriorate. Figure 3 shows the strength differences between various mixtures when compared to a standard concrete mix. According to the graphical fluctuation of test findings, nanomaterials enhance the strength of CC-4 and CC-5 before decreasing somewhat. This reduction in strength is due to a higher proportion of nanomaterial substitution.

CC-4 has a higher strength, reaching 4.94 MPa and 5.11 MPa after 28 and 90 days of curing, respectively. When compared to conventional concrete, CC-4's performance improves due to the addition of sisal fibers to the concrete mix.

2.5. Flexural Strength. To evaluate the flexural strength of concrete, a compression machine is utilized to test a specimen of 100 mm*100 mm*500 mm. Figure 4 shows that an increase in nanomaterials enhances flexural strength. The greatest strength is attained when 4% Al_2O_3 and sisal fibers are substituted in the CC-4 concrete mix. Sisal fibers and nanomaterial incorporated concrete shows improvement in strength due to microstructure densification. The use of nanomaterials has exceeded the optimal replacement percentage, resulting in a loss of strength. In addition to nanomaterials (TiO_2 and Al_2O_3), the strength rises for a short period of time before declining. Figure 4 demonstrates the differences in strength of concrete with and without sisal fibers and nanoparticles. We explored expanding the study to include durability testing after seeing these differences in strength test results.

2.6. Water Absorption. Water is absorbed less by nanoparticles as the percentage of nanomaterials rises, according to the results of the experiments. The same tendency may be seen when sisal fiber is included. Water absorption is limited in CC-4 and CC-5 compared to other concrete specimens, indicating that gaps or pores have been minimized, resulting in a more compact concrete. The highest resistance to water absorption is obtained when sisal fibers were coupled with 4% Al_2O_3 . Because of its firm texture, concrete acquires strength and resistance to absorption as it ages. Similar

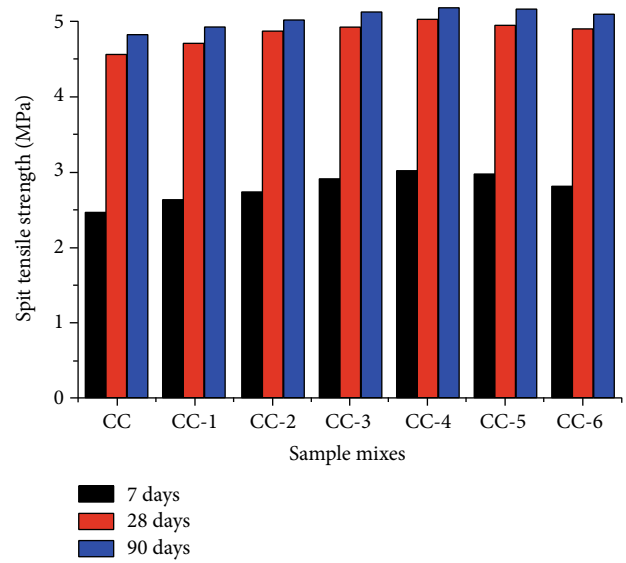


FIGURE 3: Split tensile strength of concrete specimens.

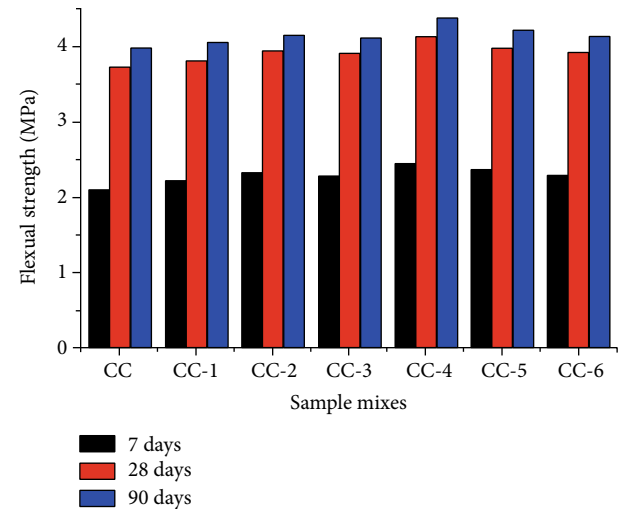


FIGURE 4: Flexural strength of concrete specimens.

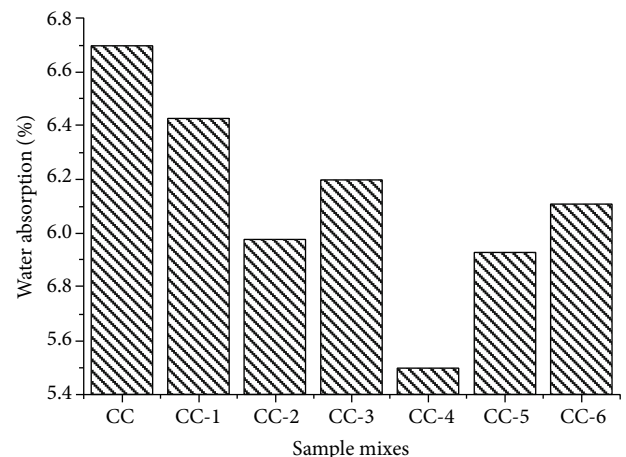


FIGURE 5: Water absorption % of concrete specimens.

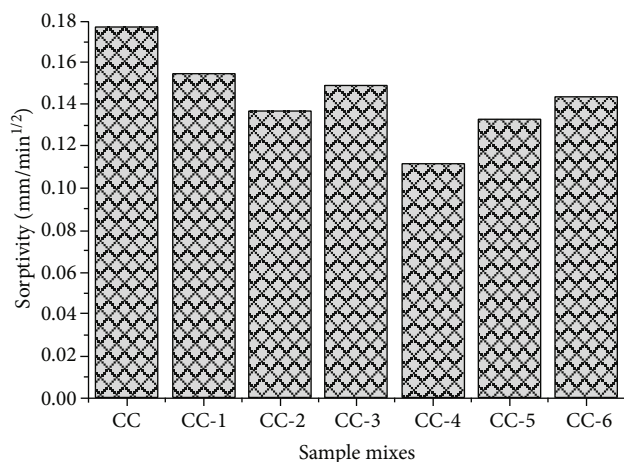


FIGURE 6: Sorptivity of concrete specimens.

resistance characteristics are obtained when sorptivity tests are performed on CC-4 and CC-5.

CC-4, which is composed of 4% Al_2O_3 and sisal fibers, exhibits the least movement rate in concrete. The graphical interpretation clearly illustrates these variations. Figures 5 and 6 demonstrate the variation in water absorption and sorptivity, respectively, according to the mix and fiber content.

3. Conclusion

The combined influence of alumina oxide, titanium dioxide, and sisal fibers in concrete on fresh, durability, and mechanical qualities is the primary subject of this investigation. Based on the results of the experiment, the following conclusions are formed.

In concrete, nanoparticles such as alumina and titanium dioxide (TiO_2) have increased workability. Slump tests show that the workability of concrete improves up to Mix-4 (4 percent Al_2O_3 and 2.5% sisal fibers), which is the highest mix. The incorporation of fibers into concrete also increased its workability, compared to mixes that did not contain fibers. Using Al_2O_3 , TiO_2 , and fiber decreases internal friction between the various components. As a result, just a slight increase in the fresh concrete qualities can be observed.

In terms of mechanical qualities such as the compressive, split tensile, and flexural strength of concrete, an increase in the use of Al_2O_3 and TiO_2 is noted. CC-4 (4 percent Al_2O_3 and sisal fibers) shows an enhancement in the mechanical characteristics of concrete up to that point. To put it another way, the use of TiO_2 and Al_2O_3 in place of cement resulted in a stronger link between the concrete's components. Mechanical qualities of concrete begin to decline after an increase in Al_2O_3 and TiO_2 is observed. Additionally, mixes with fibers (0.6 percent of the cement weight) had higher strengths than mixes without fibers. An improved C-S-H gel formation may result from the addition of nanomaterial fibers to concrete, which makes the concrete denser. According to the findings of mechanical property tests, the optimal use of TiO_2 and Al_2O_3 is found to be 4% and 4% with fibers.

Concrete made with nanoparticles (Al_2O_3 and TiO_2) and fibers shows better resistance to degradation in terms of quality when exposed to diverse environmental conditions. Using nanoparticles and fibers in concrete reduces the material's susceptibility to chemical assault and water absorption, according to research. Concrete made with Al_2O_3 and tin oxides is more resistant to chemical assault because of the replacement of cement with these materials.

Data Availability

The data used to support the findings of this study are included within the article.

Conflicts of Interest

The authors declare that they have no conflicts of interest.





References

- [1] C. Meyer, "The greening of the concrete industry," *Cement and Concrete Composites*, vol. 31, no. 8, pp. 601–605, 2009.
- [2] R. Siddique, "Utilization of industrial by-products in concrete," *Procedia Engineering*, vol. 95, pp. 335–347, 2014.
- [3] K. M. Liew, A. O. Sojobi, and L. W. Zhang, "Green concrete: prospects and challenges," *Construction and Building Materials*, vol. 156, pp. 1063–1095, 2017.
- [4] M. S. Meddah, "Recycled aggregates in concrete production: engineering properties and environmental impact," *MATEC Web Conference*, vol. 101, p. 05021, 2017.
- [5] V. W. Y. Tam, M. Soomro, and A. C. J. Evangelista, "A review of recycled aggregate in concrete applications (2000–2017)," *Construction and Building Materials*, vol. 172, pp. 272–292, 2018.
- [6] M. S. Meddah, M. A. Ismail, S. El-Gamal, and H. Fitriani, "Performances evaluation of binary concrete designed with silica fume and metakaolin," *Construction and Building Materials*, vol. 166, no. 30, pp. 400–412, 2018.
- [7] M. S. Meddah, "Durability performance and engineering properties of shale and volcanic ashes concretes," *Construction and Building Materials*, vol. 79, pp. 73–82, 2015.
- [8] Y. Reches, "Nanoparticles as concrete additives: review and perspectives," *Construction and Building Materials*, vol. 175, pp. 483–495, 2018.
- [9] V. Vishwakarma and D. Ramachandran, "Green concrete mix using solid waste and nanoparticles as alternatives - a review," *Construction and Building Materials*, vol. 162, pp. 96–103, 2018.
- [10] D. Kong, S. Huang, D. Corr, Y. Yang, and S. P. Shah, "Whether do nano-particles act as nucleation sites for C-S-H gel growth during cement hydration," *Cement and Concrete Composites*, vol. 87, pp. 98–109, 2018.
- [11] J. Zhang, L. Qin, and Z. Li, "Hydration monitoring of cement-based materials with resistivity and ultrasonic methods," *Materials and Structures*, vol. 42, no. 1, pp. 15–24, 2009.
- [12] R. Yu, P. Spiesz, and H. J. H. Brouwers, "Effect of nano-silica on the hydration and microstructure development of ultra-high performance concrete (UHPC) with a low binder amount," *Construction and Building Materials*, vol. 65, pp. 140–150, 2014.

- [13] P. Iqbal, J. A. Preece, and P. M. Mendes, "Nanotechnology: the top-down and bottom-up approaches," *Supramolecular Chemistry*, 2012.
- [14] B. S. Murty, P. Shankar, B. Raj, B. B. Rath, and J. Murday, *Textbook of nanoscience and nanotechnology*, Springer Science & Business Media, 2013.
- [15] H. Agarwal, S. Venkat Kumar, and S. Rajeshkumar, "A review on green synthesis of zinc oxide nanoparticles - an eco-friendly approach," *Resource-Efficient Technologies*, vol. 3, no. 4, pp. 406–413, 2017.
- [16] R. Garg, R. Garg, M. Bansal, and Y. Aggarwal, "Experimental study on strength and microstructure of mortar in presence of micro and nano-silica," *Materials Today: Proceedings*, vol. 43, pp. 769–777, 2021.
- [17] P. Siler, I. Kolarova, J. Bednarek et al., "The effect of zinc, water to binder ratio and silica fume on the hydration and mechanical properties of Portland cement mixtures," in *IOP Conference Series: Materials Science and Engineering*, vol. 583, article 012008, 2019.
- [18] K. Loh, C. C. Gaylarde, and M. A. Shirakawa, "Photocatalytic activity of ZnO and TiO₂ 'nanoparticles' for use in cement mixes," *Construction and Building Materials*, vol. 167, pp. 853–859, 2018.
- [19] E. Mohseni, B. M. Miyandehi, J. Yang, and M. A. Yazdi, "Single and combined effects of nano-SiO₂, nano- Al₂O₃ and nano-TiO₂ on the mechanical, rheological and durability properties of self-compacting mortar containing fly ash," *Construction and Building Materials*, vol. 84, pp. 331–340, 2015.
- [20] I. Fernández Olmo, E. Chacon, and A. Irabien, "Influence of lead, zinc, iron (III) and chromium (III) oxides on the setting time and strength development of Portland cement," *Cement and Concrete Research*, vol. 31, no. 8, pp. 1213–1219, 2001.
- [21] A. M. Rashad, "Effects of ZnO₂, ZrO₂, Cu₂O₃, CuO, CaCO₃, SF, FA, cement and geothermal silica waste nanoparticles on properties of cementitious materials - a short guide for civil engineer," *Construction and Building Materials*, vol. 48, pp. 1120–1133, 2013.
- [22] M. R. Arefi and S. Rezaei-Zarchi, "Synthesis of zinc oxide nanoparticles and their effect on the compressive strength and setting time of self-compacted concrete paste as cementitious composites," *International Journal of Molecular Sciences*, vol. 13, no. 4, pp. 4340–4350, 2012.
- [23] T. Nochaiya, Y. Sekine, S. Choopun, and A. Chaipanich, "Microstructure, characterizations, functionality and compressive strength of cement-based materials using zinc oxide nanoparticles as an additive," *Journal of Alloys and Compounds*, vol. 630, pp. 1–10, 2015.
- [24] H. Li, M. H. Zhang, and J. P. Ou, "Flexural fatigue performance of concrete containing nano-particles for pavement," *International Journal of Fatigue*, vol. 29, no. 7, pp. 1292–1301, 2007.
- [25] H. Li, M. H. Zhang, and J. P. Ou, "Abrasion resistance of concrete containing nano-particles for pavement," *Wear Journal*, vol. 260, no. 11-12, pp. 1262–1266, 2006.
- [26] L. S. I. Reddy, M. M. Vijayalakshmi, and T. R. Praveenkumar, "Thermal conductivity and strength properties of nanosilica and GGBS incorporated concrete specimens," *Silicon*, vol. 14, no. 1, pp. 145–151, 2022.
- [27] P. T. R. Manigandan, S. A. M. Al-Mohaimed, K. Brindhadevi, and A. Pugazhendhi, "Characterization of polyurethane coating on high performance concrete reinforced with chemically treated Ananas erectifolius fiber," *Progress in Organic Coatings*, vol. 150, article 105977, 2021.
- [28] M. S. C. Rao, M. M. Vijayalakshmi, and T. R. Praveenkumar, "Behaviour of green concrete (blended concrete) using agro-industrial waste as partial replacement of cement along with nanoparticles," *Applied Nanoscience*, 2021.
- [29] K. Chiranjeevi, M. M. Vijayalakshmi, and T. R. Praveenkumar, "Investigation of fly ash and rice husk ash-based geopolymer concrete using nano particles," *Applied Nanoscience*, 2021.
- [30] S. Muzenski, I. Flores-Vivian, and K. Sobolev, "Ultra-high strength cement-based composites designed with aluminum oxide nano- fibers," *Construction and Building Materials*, vol. 220, pp. 177–186, 2019.
- [31] Z. Yang, Y. Gao, S. Mu, H. Chang, W. Sun, and J. Jiang, "Improving the chloride binding capacity of cement paste by adding nano- Al₂O₃," *Construction and Building Materials*, vol. 195, pp. 415–422, 2019.
- [32] K. P. Bautista-Gutierrez, A. L. Herrera-May, J. M. Santamaría-López, A. Honorato-Moreno, and S. A. Zamora-Castro, "Recent progress in nanomaterials for modern concrete infrastructure: advantages and challenges," *Materials (Basel)*, vol. 12, pp. 1–40, 2019.

Research Article

Green Synthesis of Gold and Silver Nanoparticles Using *Opuntia dillenii* Aqueous Extracts: Characterization and Their Antimicrobial Assessment

Anees Ahmed,¹ Abdur Rauf ,¹ Hassan A. Hemeg,² Muhammad Nasimullah Qureshi,¹ Rohit Sharma ,³ Abdullah S. M. Aljohani,⁴ Fahad A. Alhumaydhi ,⁵ Ibrahim Khan,¹ Amir Alam,¹ and Md. Mominur Rahman ⁶

¹Department of Chemistry, University of Swabi, Anbar, Swabi, KPK, Pakistan

²Department of Medical Laboratory Technology, College of Applied Medical Sciences, Taibah University, P.O. Box 344, Al-Medinah Al-Monawara 41411, Saudi Arabia

³Department of Rasa Shastra and Bhaishajya Kalpana, Faculty of Ayurveda, Institute of Medical Sciences, Banaras Hindu University, Varanasi, 221005 Uttar Pradesh, India

⁴Department of Veterinary Medicine, College of Agriculture and Veterinary Medicine, Qassim University, Buraydah, Saudi Arabia

⁵Department of Medical Laboratories, College of Applied Medical Sciences, Qassim University, Buraydah, Saudi Arabia

⁶Department of Pharmacy, Faculty of Allied Health Sciences, Daffodil International University, Dhaka 1207, Bangladesh

Correspondence should be addressed to Abdur Rauf; abdurrauf@uoswabi.edu.pk, Rohit Sharma; rohisharma@bhu.ac.in, and Md. Mominur Rahman; mominur.ph@gmail.com

Received 30 January 2022; Accepted 16 March 2022; Published 26 March 2022

Academic Editor: Arpita Roy

Copyright © 2022 Anees Ahmed et al. This is an open access article distributed under the Creative Commons Attribution License, which permits unrestricted use, distribution, and reproduction in any medium, provided the original work is properly cited.

In the present study, gold (Au) and silver (Ag) nanoparticles (NPs) were synthesized from aqueous extracts of *Opuntia dillenii*, characterized by various advanced techniques and investigated for antibacterial and antifungal potential. Phytochemical screening of *O. dillenii* showed the presence of alkaloids, betacyanin, saponins, tannins, flavonoids, and phlobatannins. The characterizations of the synthesized metal NPs were performed such as UV-visible spectrophotometer, FTIR (Fourier transform infrared) spectrophotometer, SEM (scanning electron microscopy) and EDX (energy-dispersive X-ray). Through the application of such advance techniques, the UV-visible spectrophotometer showed the bands of absorbance for AgNPs and AuNPs at 420 nm and 525 nm range, respectively. The FTIR spectra for both and AgNPs also appeared in the range of 4000-400 cm^{-1} . SEM was performed for the textural and morphological characteristics of the NPs such as shape, size distribution, and surface structure. Elemental analysis was recorded for the synthesis of Au and AgNPs, which confirmed its purity. The *O. dillenii* extract and their synthesized Au and AgNPs showed a clear zone of inhibition against the *E. coli*, *S. aureus*, *K. pneumoniae*, and *P. aeruginosa* bacteria and *T. viride*, *C. albicans*, *C. krusei*, and *A. niger* fungal species.

1. Introduction

The past decades have witnessed rising importance of nanotechnology in medicine and healthcare [1–3]. Keeping this in view, the green synthesis methods which are having abilities of producing the environment friendly nanoparticles NPs are being adapted by the various field experts [4]. Therefore, the importance is being given to such technologies which are not only environment

friendly but also have the wide range of the nutrients. The NPs are crystallographic with high surface area and they are very small sized structures having high reactivity [5]. So, the use of green technology is now becoming more popular than ever before.

The crops at subtropical areas are difficult to grow because of the lack of water and salinity in soil. The natural beauty of the subtropical areas may be enhanced by using the species of the *Opuntia* which may be grown in the

subtropical areas. *Opuntia* is a genus which is medically important as well and it is required to be explored in term of the medical characteristics. *Opuntia* specie was first grown in America as there are many subtropical areas in America where this *Opuntia* specie may be easily grown. It is mostly found in dry and scarce water condition as it is a xerophytic plant. Specific species including *O. dillenii* belongs to the cactus family and is commonly called as prickly pear plant, with 1500 known species across the globe [6]. Hence, the scholars emphasized on cultivation of the *O. dillenii* in the tropical and subtropical areas for the purpose of animal feeding and medical implications [7]. In the zones of South Africa, Egypt, and South America, its fruit is also used for feeding the animals [8]. Similar types of the researches related to the *O. dillenii* proved that it may be used in the production of the nectar, sweeteners, jellies, jams and beverages of various types [9, 10]. *O. dillenii* is also grown in the sandy areas of Egypt as it has high drought resistance quality is widely used source of animal food and also act as air resistance during the storm [11]. *O. dillenii* has been used as a folk medicine to treat health disorders in several countries. This botanical is also used to prepare several cosmetic products like creams, lotions, and shampoos. In food industry it is being used to prepare as wines, jams [12]. Researchers have proved that many phytochemicals are present in different parts of cactus plant. *O. dillenii* have the potential against diverse environmental conditions [13]. The alcoholic extract of *O. dillenii* has antibacterial, anti-inflammatory, hypoglycemic activities. It has been used as anti-diabetic agent for the treatment of diabetes due to its hypoglycemic property [14]. The scientists are researching on the phytochemical as well as other pharmacological actions of this botanical in order to explore the use of this plant for prevention, management and treatment of many dreadful diseases [8]. Different plants were utilized for the synthesis of NPs including *Aloe vera* [15], *Cicer arietinum* [16], *Cymbopogon citratus* [3], and *Argemone mexicana* [17].

Plant crude extracts and their phytoconstituents with proven biocidal properties in therapeutic medicine are extremely important. In more recent years, various surveys have been conducted in various countries to demonstrate this efficacy. The secondary metabolites produced by the plants are thought to be responsible for the plants' antibacterial properties. As a result, these plants are commonly employed for therapeutic purposes. The antimicrobial ability of plant bioactive substances has been proven through phytochemical screening that vascular plants could be a source of unique antimicrobial properties [18]. Phytochemicals are preferable to manufactured biomolecules because they have no or low toxicity in humans [19]. This feature makes them ideal candidates for drug manufacture and development [20]. The discovery of novel antifungal medicines relies heavily on phytochemicals without endangering human health [21]. The present study is aimed at developing gold (Au) and silver (AgNPs) from the aqueous extract of *O. dillenii* and at exploring their antimicrobial potential.

2. Material and Methods

2.1. Collection of Plant. *O. dillenii* plant was collected from various regions of district Nowshera, Khyber Pakhtunkhwa, Pakistan. The plant was identified by professional taxonomist Dr. Muhammad Ilyas in the Department of Botany University of Swabi, Pakistan. The voucher specimen UOS-Bot-SP NO-101 was deposited in herbarium of Department of Botany University of Swabi, Pakistan. The plant material was dried under shade and grinded and crushed by grinder machine. The powder was soaked in organic solvent methanol for a week and then filtered. The filtrate was concentrated in rotatory evaporator. The crude methanolic extract was suspended in water and successively partitioned with *n*-hexane and chloroform, ethyl acetate and methanol.

2.2. Extract Preparation. The fine powder (1 kg) of the plant material was divided into three parts 550 gm, 350 gm, and 100 gm. About 550 gm of plant material were dipped in methanol, 350 gm in distilled water and 100 gm in *n*-hexane. The plant material was kept for one week in order to obtain crude extract. The obtain extract will be concentrated in rotatory evaporator to obtain crude *n*-hexane, methanolic and aqueous extract. Three different fractions were prepared in three different solvents to check the presence of most of the active ingredients, the active ingredients involved in capping and biological activities. As in *n*-hexane only nonpolar ingredients were determined and they are not involved in the capping during nanoparticle synthesis. The methanolic fraction will be applied next time for the synthesis of Ag and AuNPs, and biological activities. The plant material was stored in refrigerator for further NP synthesis.

2.3. Phytochemical Analysis. Phytochemical screening was performed to identify bioactive secondary metabolites. The glycosides, alkaloids, tannins, saponins, flavonoids, anthraquinones, betacyanins, phlobatannins, anthocyanins, emodins, steroids, carbohydrates, and terpenoids were screened using the specific tests.

2.4. Synthesis of NPs. 1 mM solution of silver salt (AgNO_3) and gold salt [HAuCl_4] were prepared for the synthesis of Ag and AuNPs by using plant crude extract at different ratio 1:1, 1:2, 1:3, 1:4, and 1:5. Then, the solution was placed on stirrer with constant stirring at room temperature for 5 hours. After that, characterization of NPs was carried out.

2.5. Pharmacological Activities. The crude extract and synthesized NPs were evaluated for antibacterial and antifungal activities.

2.6. Chemical Used. The analytical grade chemicals were used in the synthesis of Au/AgNPs. AgNO_3 was purchased from Sigma-Aldrich, and HAuCl_4 , methanol, and deionized water were purchased from Merck.

2.7. Biosynthesis of AgNPs Using the Aqueous Extract of *O. dillenii*. 100 ml of the already prepared extract was taken. 1 mM solution of AgNO_3 was prepared using distilled water. Different fractions of the preparations were prepared using Ag and extract solution in different ratios such as 1:1, 2:1,

3:1, 4:1, 5:1, 6:1, 7:1, and 8:1, respectively. The fraction was prepared in vials and kept on stirring for 24 hours. The change in color of the reaction mixture in each vial indicates the formation of NPs. The solutions were evaluated using a UV-visible spectrophotometer for the confirmation of AgNPs synthesis. The result of the UV-visible spectrophotometer revealed that the optimized ratio for AgNPs was 7:1.

2.8. Biosynthesis of AuNPs from the Aqueous Extract of *O. dilleni*. 1 mM HAuCl₄ was prepared using deionized water. Different ratio of Au salt solution and plant extract were taken such as 1:1, 3:1, 5:1, 6:1, 7:1, 8:1, and 9:1 in vials and kept for stirring for a period of 4 hours. The absorption spectrums were recorded for each fraction using a UV-visible spectrophotometer. The 8:1 was observed to be the optimized ratio of gold and extract for the preparation of AuNPs. Effects of other factors such as pH effect, NaCl effect, different salt effect, kinetic study, and temperature were also examined. The characterization of AuNPs was done using FTIR, SEM, EDX instruments.

2.9. Characterization of AgNPs and AuNPs

2.9.1. UV-Visible Spectroscopy. Initially the NPs were characterized by UV-visible spectrophotometer in the wavelength ranging from 200 to 800 nm. The spectroscopic analysis for both silver and gold NPs were carried out by using freshly prepared fractions at 37-38°C and by using optical path 1 cm length of quartz cuvettes using spectrometer (300 Plus Optima Japan). The AgNPs solution gave an absorption maximum at 420-450 nm while that of AuNPs was 520-530 nm.

2.9.2. Scanning Electron Microscopy (SEM). The size and morphological surface of NPs were determined using JEM 2100, Jeol CRL Scanning Electron Microscope (University of Peshawar, Pakistan).

The size and shape of the AgNPs and AuNPs were determined using SEM images. By using an electron microscope, a layer of AuNPs thin sediment was placed under vacuum pressure of 5-8 Torr.

2.9.3. Fourier Transform Infrared (FTIR) Spectroscopy Analysis. The functional group involved in the formation of Au and AgNPs was evaluated using Shimadzu FTIR - 8400-S (AWKUM) Fourier transform spectrometer. The samples were prepared using the powdered sample. The powdered samples were placed in NaCl cells and were placed in pellet cells of KBr. The bands detected on the computer showed the results. The range of 4000-400 cm⁻¹ was used.

2.9.4. Energy-Dispersive X-Ray (EDX) Spectroscopy Analysis. Au and AgNPs geometry and morphology were also determined. Using a Bruker X-flash in energy dispersive X-ray spectroscopy the colloids of Au and AgNPs were prepared determined. For EDX and imaging 15 keV energy of the electron beam was maintained.

2.9.5. Antibacterial Activity. The MIC and MBC which are commonly known as minimum inhibitory concentration

and Minimum bactericidal concentration, respectively, of AgNPs and AuNPs were also determined in the microbial activity.

The bacteria *S. aureus* and *E. coli* were used in the microbial assay. Micro dilutions of the NPs were prepared. The bacterial culture was prepared using nutrient agar and incubated for 24 hours at a temperature of 37°C. NPs dilutions were also employed at a specific area to evaluate the MIC of NPs.

The NPs containing Petri dishes were also incubated at the temperature of 37°C and for 24 hours. MBC or minimum bactericidal concentration evaluation of AuNPs and AgNPs was also determined. The lowest dose or dilutions of Au/AgNPs were used to test the area of inhibition. The process was repeated twice to get accurate results.

2.10. Antifungal Activity. The micro dilution plate assay method was used to determine fungicidal activity. The fungus species of *Candida albicans* was used in the assay. 20 mM buffer solution of sodium phosphate was mixed with 20 µl of both Au and AgNPs dilution 5, 2.5, 1.25 mg/ml in water. The sample was incubated at a temperature of 37°C for 2 hours.

The NP visibility loss was calculated using the following formula:

$$\left[1 - \left(\frac{\text{colony-forming unit in the presence of NPs}}{\text{CFUs with no particles}} \right) \right] \times 100. \quad (1)$$

2.11. Stability of NPs. The stability of Au and AgNPs were checked against varying pH, different concentration of NaCl, same concentration of different salt and heat effect. After each treatment UV-visible spectra were recorded.

2.12. Kinetic Study of Synthesis of NPs. For the time-dependent synthesis of Au and AgNPs, samples were drawn from reaction mixture at regular interval of time and UV-visible spectra were recorded.

2.13. Phytochemical Analysis. The qualitative screening for the assessment of phytochemical components like flavonoids, terpenoids, alkaloids, carbohydrate and steroids, in the methanol, *n*-hexane, and distilled water extracts of the plant was carried out.

3. Results and Discussion

3.1. Phytochemical Screening. The qualitative screening for the assessment of phytochemical components like flavonoids, polyphenols, terpenoids, alkaloids, carbohydrates, and steroids in the methanol in each extract was performed by using the following reagents (Table 1).

The results of qualitative screening for the assessment of bioactive secondary metabolites such as flavonoids, polyphenols, terpenoids, alkaloids, carbohydrates, and steroids in the methanol, *n*-hexane, and distilled water extracts of the title plant are given in Table 2. The methanol plant extracts of *O. dilleni* showed presence of steroids, coumarins,

TABLE 1: List of reagents used for identification of secondary metabolites in extracts.

Phytochemicals	Method	Results for the presence of an ingredient
Alkaloids	0.5 g plant extract+2% H ₂ SO ₄ +Dragendorff reagent	Orange red ppt
Tannins	Filtered extract+drops of ferric chloride	Dark green color
Glycosides	Extract+HCl+NaOH+Fehling reagent	Appearance red ppt
Saponins	Extract+H ₂ O (boiled)	Frothing occur
Anthraquinones	0.5 g extract+10% HCl (boil) and then add chloroform+10% ammonia and heat	Appearance rose pink color
Flavonoids	0.2 g extract+NaOH+HCl	The yellowish color disappears on adding HCl
Steroids	0.3 g extract+acetic acid (heat)+H ₂ SO ₄	Color change to green
Terpenoids	0.2 g extract+2 ml chloroform+3 ml H ₂ SO ₄	Reddish brown color
Emodin	0.5 g extract+2 ml NH ₄ OH+3 ml benzene	Appearance of red color
Anthocyanin and betacyanin	0.2 g extract+2NaOH (heat)	Appearance of bluish green color

TABLE 2: Phytochemical evaluation of methanol, *n*-hexane, and distilled water plant extracts of *O. dillenii*.

Constituents	<i>Opuntia dillenii</i> plant extract		
	Methanol	<i>n</i> -Hexane	Distilled water
Steroids	+	-	-
Terpenoids	+	+	+
Glycosides	-	-	-
Flavonoids	+	-	+
Saponins	+	-	+
Carbohydrates	-	-	-
Tannins	+	-	-
Coumarins	+	-	-
Betacyanin	+	-	-
Anthraquinones	-	-	-
Anthocyanin	-	-	-
Emodins	-	-	-
Phlobatannins	-	-	-

“+” shows the presence and “-” shows the absence of the compound.

betacyanin, terpenoids, tannins, flavonoids while the *n*-hexane plant extract confirms the presence of saponins, terpenoids, flavonoids, and coumarin and the distilled water plant extracts of *O. dillenii* revealed saponins, terpenoids, flavonoids presence and the absence of carbohydrate, glycosides, anthraquinones, anthocyanin, emodins, and phlobatannins.

3.2. Characterization of Au and AgNPs

3.2.1. UV-Visible Spectroscopy. UV-visible spectroscopy is the technique which is considered as the colorimetry extension, it works on the principle of the absorption of light from the test sample, by using various components that are similar to the colorimeter but spectroscopy has the advantage of improved accuracy in a wide range of wavelengths between 190 and 700 nm [22].

This wavelength range was used because the absorption by the Au and Ag is usually observed in this range. In this

work, we used a 300 Plus Optima Japan Spectrophotometer, with quartz cells and 1 ml deionized water as a blank. The formation of the NPs was confirmed by the formation of color visually. Scanning the absorption using wavelength ranges of 200 and 800 nm was used to confirm the formation of the Au and AgNPs. Spectra show the band wavelength of the Au and AgNPs obtained using the plant extract. The difference in the bands and the wavelengths indicate the different sizes and the shapes of the Au and AgNPs obtained (Figure 1).

The prominent UV-visible spectrum was observed at the wavelength of 543 nm and 445 nm which confirmed the synthesis of Ag and AuNPs, respectively (Figure 1). The UV-visible absorption spectrum of the aqueous extract *O. dillenii* has not shown any significant bands. But after the extract of *O. dillenii* with the silver nitrate colorless and chloroauric acid yellow colored solution the color of the solutions were changed to characteristic ruby-red color and reddish-brown showing the convenient excitation due to the surface Plasmon resonance phenomenon, that indicates the silver and gold NPs formation [23]. This research also observed the synthesis of Au and AgNPs within 15 to 20 minutes in the case of silver and 10 to 15 minutes in the case of the synthesis of gold NPs, respectively.

3.2.2. Scanning Electron Microscopy (SEM). The analysis of the size and shape of the Au and AgNPs was determined using SEM. For this purpose, SEM images and photographs of SEM using JEM 2100, Jeol CRL, Scanning Electron Microscope. By using an electron microscope, a layer of Au and AgNPs thin sediment was placed under vacuum pressure of 5-8 Torr.

The results of the SEM analysis revealed the shape of the NPs were roughly spherical-shaped NPs and in some areas stacked together. The characterization results of the Au and AgNPs by SEM analysis also confirm the method developed was suitable and effective to obtain the silver and AuNPs of different sizes and in diverse shapes (Figure 2). The size distribution of the NPs ranges from 45 nm to 77 nm approximately and was uniformly distributed.

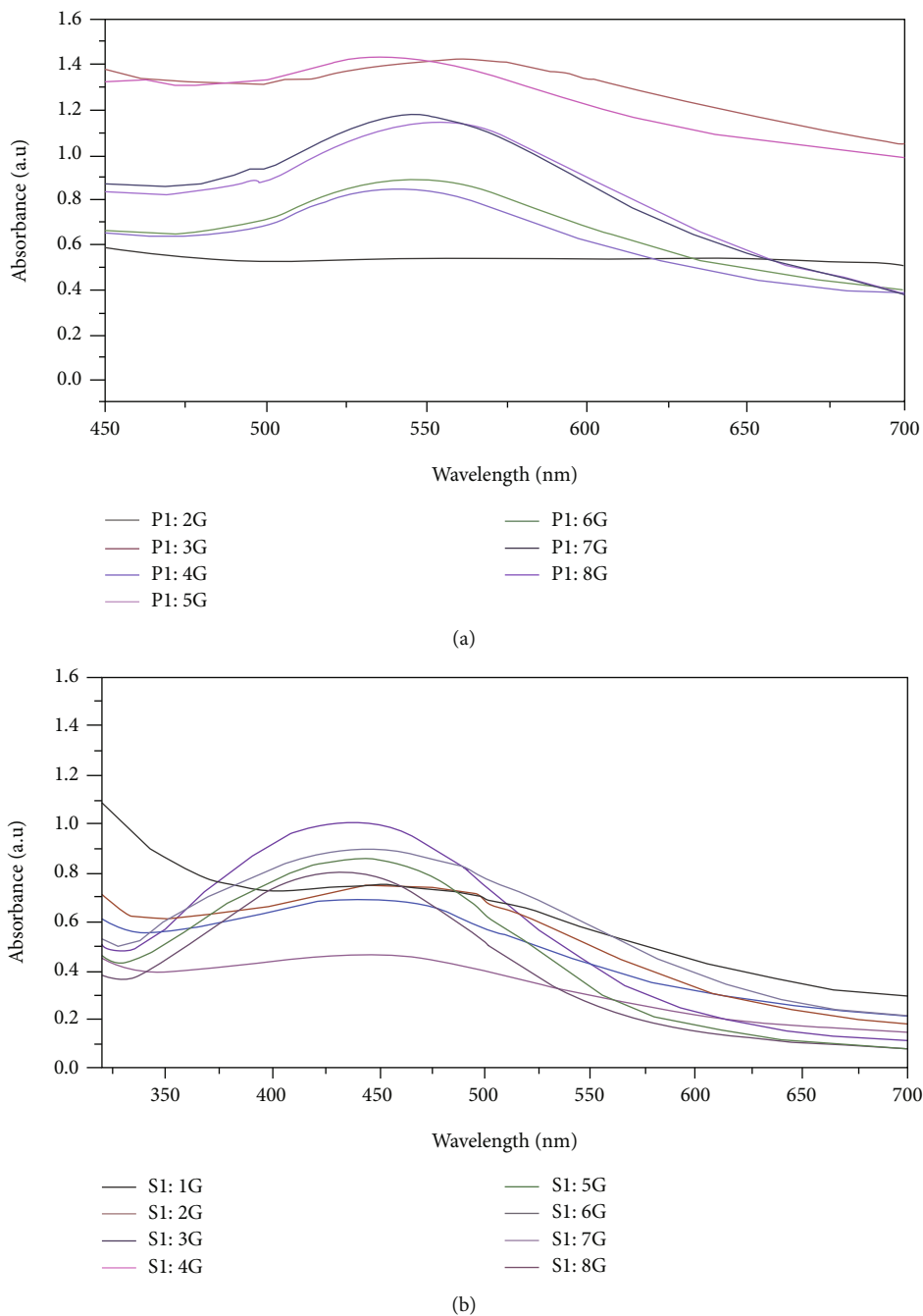


FIGURE 1: UV-visible spectrum of the synthesized AuNPs (a) and AgNPs (b).

3.2.3. Fourier Transform Infrared (FTIR) Spectral Analysis.

The detection of functional groups present on Au and AgNPs was evaluated using Shimadzu FTIR - 8400-S (AWKUM) Fourier transform spectrometer. The range of $4000\text{--}400\text{ cm}^{-1}$ was used. The spectrum obtained by the analysis of the Au and AgNPs are given in Figure 3. The spectrum of FTIR of the extract containing *O. dilleni* obtained by employing the colloidal solution of silver and gold NPs envisages the different molecular arrangements of various functional groups present as shown in Figures 3, respectively. When different obtained transmission bands were

compared, in the colloidal solutions, it resulted in the increased/suppressed bands that were because of the consequence of metallic NPs which were bound to the bioorganic molecules. The shifted bands were the characteristics of C=O and O-H modes of stretching which occur because of the free carboxylic acid, hydroxyl

group, respectively. Another shift in the band could be due to the vibrations of the C-OH group of the primary alcohol present in the extract solutions. FTIR spectra obtained provide clear evidence of the presence of various functional groups in the extract of *O. dilleni* which can also

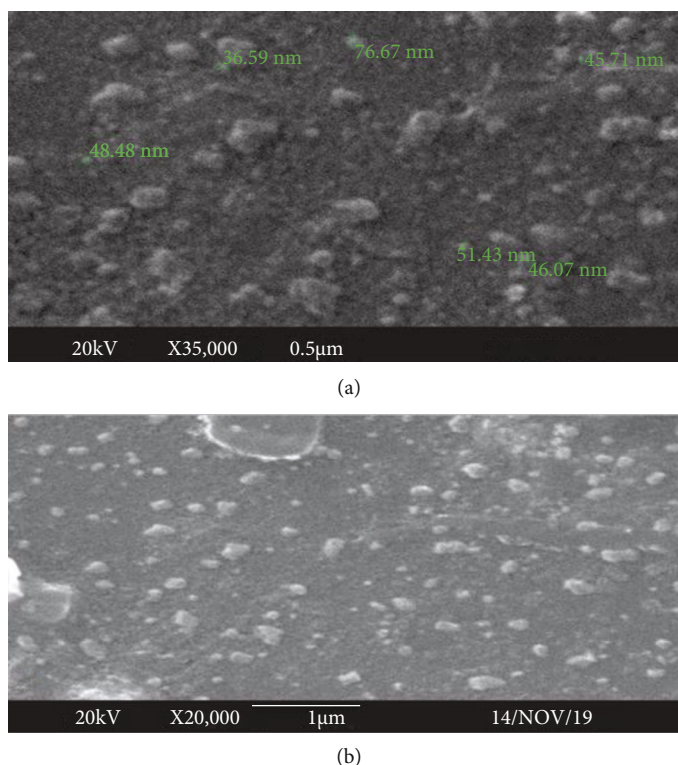


FIGURE 2: SEM analysis of AgNPs (a) and AuNPs (b).

act as the capping or reducing agents of the Au and AgNPs. Correspondingly the results of these studies were observed compared to the study in which a similar phenomenon was observed to evaluate the biological molecules acting as the capping and reduction agents for Au and AgNPs [24].

3.2.4. Energy-Dispersive X-Ray (EDX) Spectroscopy Analysis. Au and AgNPs geometry and morphology were also determined. Using a Bruker X-flash in energy dispersive X-ray spectroscopy the colloids of Au and AgNPs were prepared. For EDX and imaging 15 keV energy of the electron beam was maintained. The obtained spectra are given in Figure 4.

The synthesized Au and AgNPs were further characterized qualitatively as well as quantitatively using EDX analysis, which revealed the highest signal proportion of Au and Ag in the solutions as shown in Figure 4.

The results of the EDX analysis confirmed the major metal in the precipitate were Au and Ag, respectively. The results obtained were consistent with the outcome of the EDX analysis. The identification of Cl in the spectrum was due to the ions of salt in the sample. The energy bands for a strong signal of Au were in the range of 2 to 2.5 keV, 9.5 to 10 keV, and 10 to 11 keV and for Ag, it was observed in the range of 2.9 to 3.8 keV which were similar to the observations and evaluations of the study of Au and AgNPs [25, 26].

The EDX analysis of these NPs also shows the presence of other elements in the precipitate mainly carbon, aluminum, sulfur. Oxygen was also identified in the spectrum of the precipitate, which is assumed to be associated with the

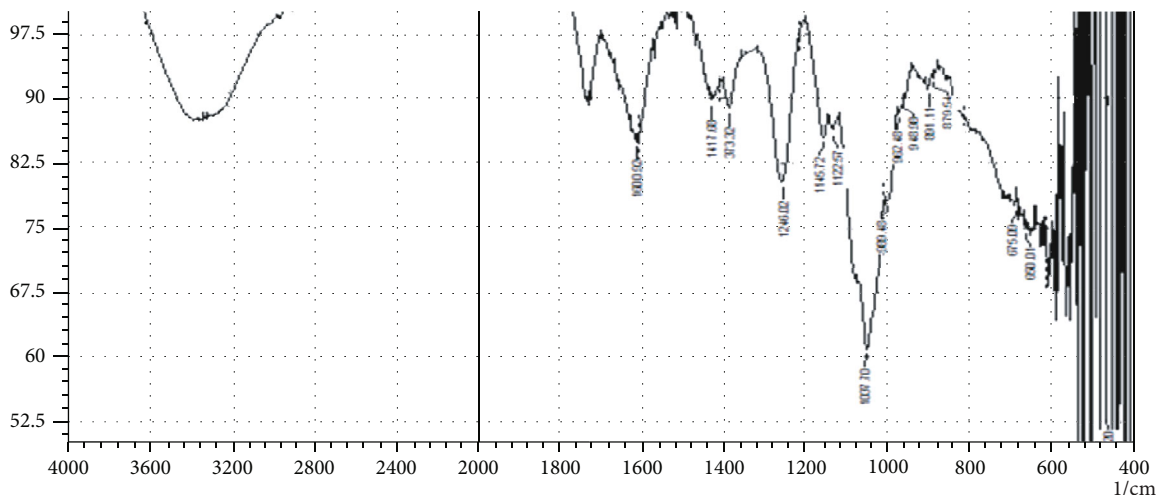
metals as the oxides or hydroxide of metals. For the presence of grid composition, Si showed the band. Minor carbon bands were also observed that may be due to the biomolecules which were bound to the NPs surface.

The bands of C and O along with the bands of metal signals suggested the Au and AgNPs may be capped due to the presence of phytochemicals of the plant extract by the atoms of an oxygen atom or may be related due to the existence of consequent oxides of metals which were identified in sample precipitate [25].

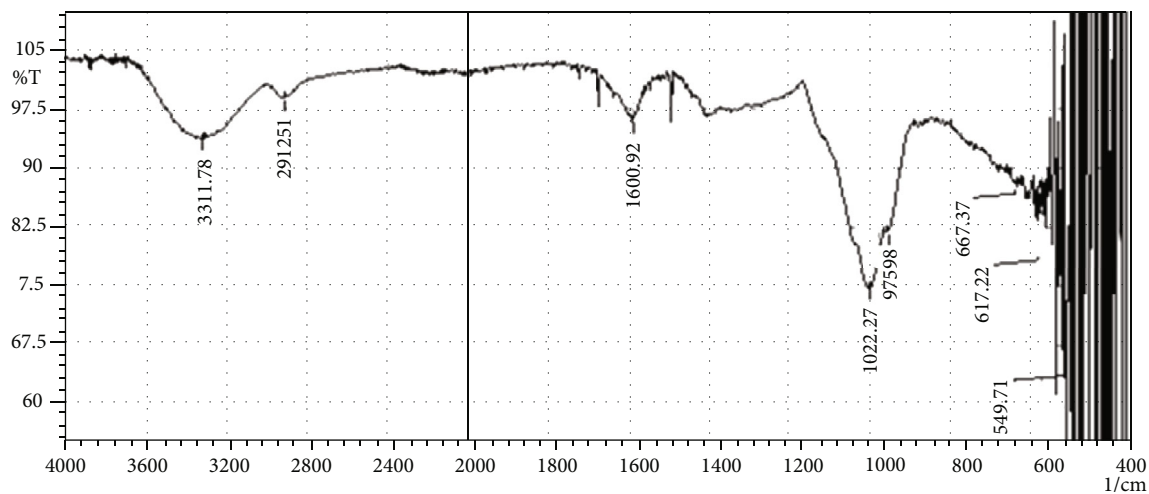
3.3. Antibacterial Activity. The MIC and MBC which are commonly known as minimum inhibitory concentration and Minimum bactericidal concentration, respectively, of Au and AgNPs were also determined in the microbial assay using *S. aureus*, *E. coli*, *P. aeruginosa*, *S. typhi*, and *B. subtilis*. These results are obtained by comparing with standard.

The antibacterial activity of the extract of *O. dilleni* was in range of 11 to 14 mm against selected bacterial strains *S. typhi*, *B. subtilis*, *S. aureus*, *P. aeruginosa*, and *E. coli* while for AgNPs, the zone of inhibition was 11 to 16 mm and for AuNPs, it was 11 to 17 mm. The Au and AgNPs exhibited good antibacterial property against various strains of bacteria as shown in Table 3.

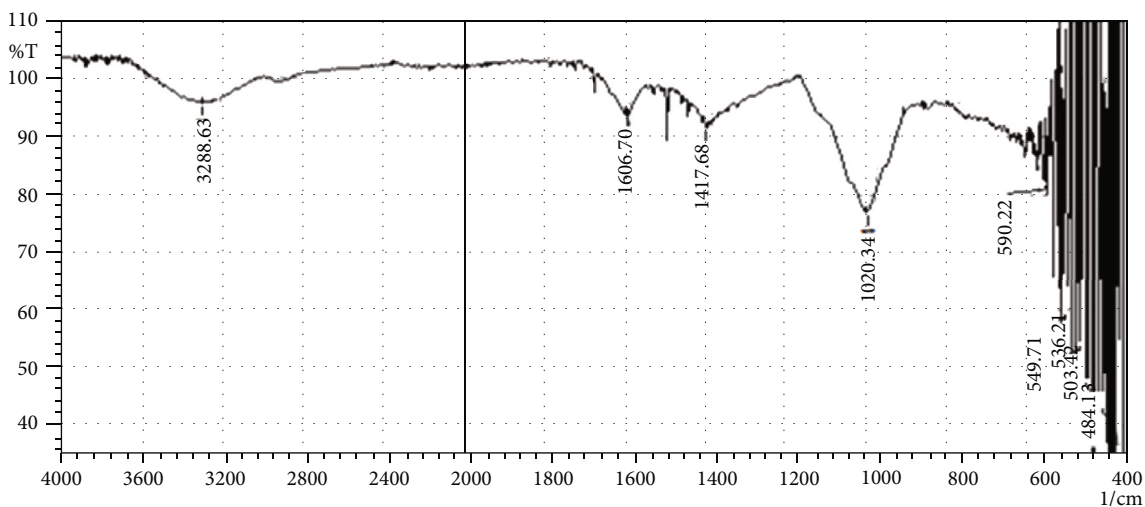
3.4. Antifungal Activity. The microdilution plate assay method was used to determine fungicidal activity. The fungus species of *C. albicans*, *A. niger*, and *P. notatum* were used in the assay. In this assay of spot plating, the antifungal activity of the *O. dilleni* extract, and its synthesized Au



(a)

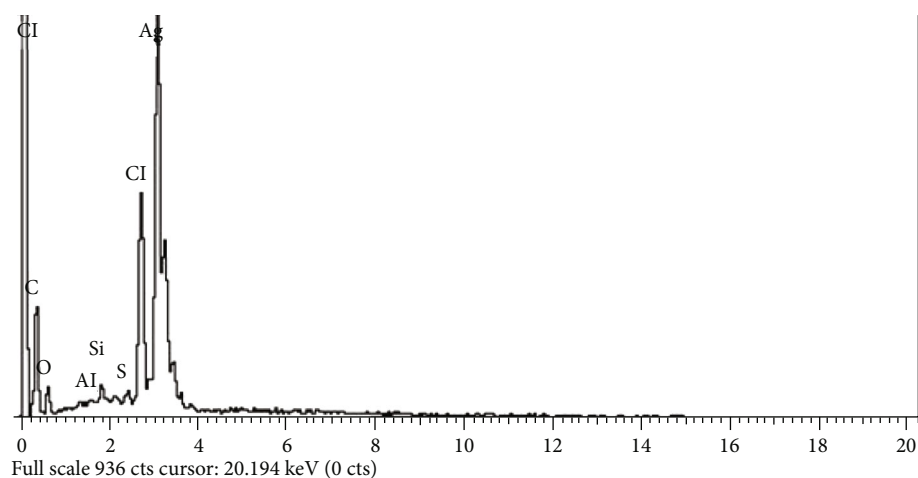


(b)

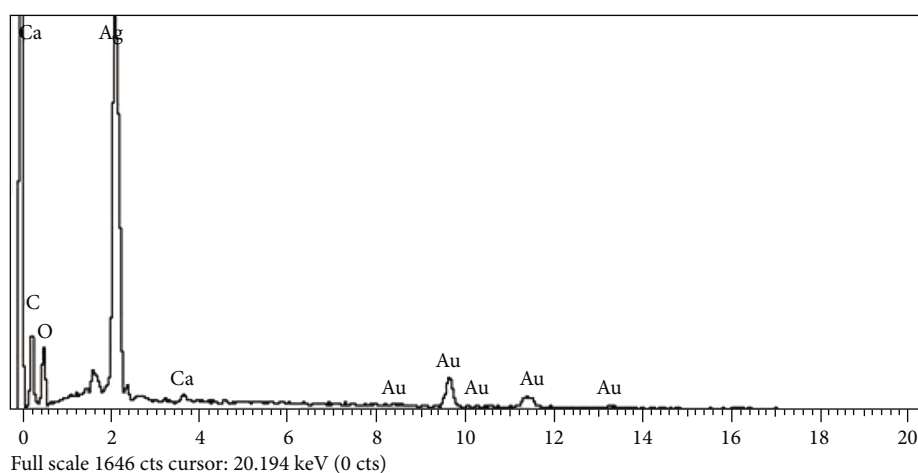


(c)

FIGURE 3: FTIR spectra of (a) extract, (b) AuNPs, and (c) AgNPs.



(a)



(b)

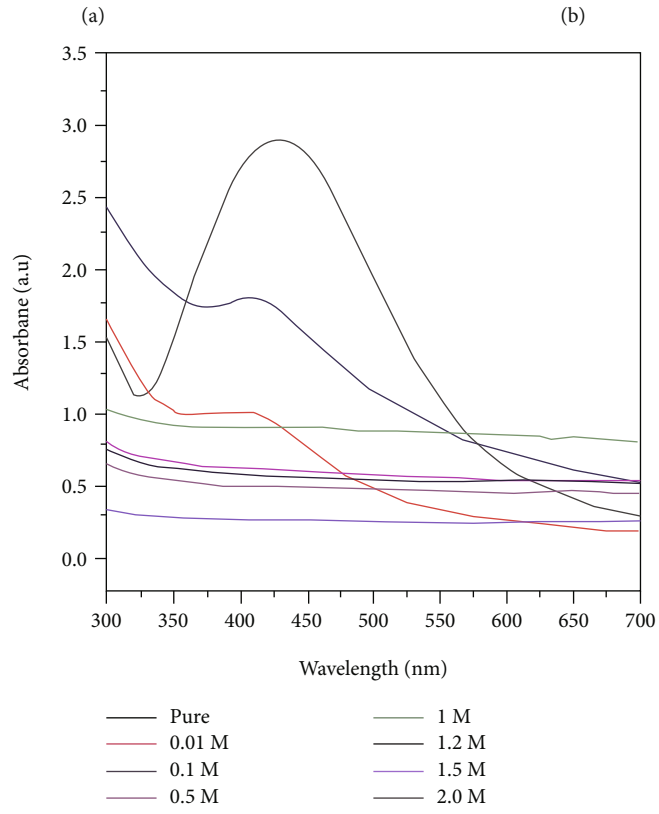
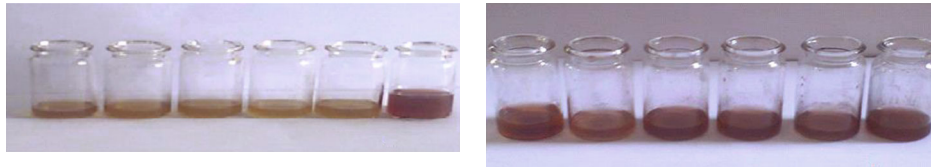
FIGURE 4: EDX spectrum of AgNPs (a) and AuNPs (b).

TABLE 3: Antibacterial activity of extract, AgNPs, and AuNPs of *O. dilleni*.

S. no	Samples	<i>Bacillus subtilis</i>	<i>Staphylococcus aureus</i>	<i>Escherichia coli</i>	<i>Pseudomonas aeruginosa</i>	<i>Salmonella typhi</i>
1	Plant extract of <i>O. dilleni</i>	14.24 ± 1.67	13.32 ± 1.54	11.09 ± 1.11	12.65 ± 1.23	14.34 ± 1.08
2	AgNPs of <i>O. dilleni</i>	16.11 ± 1.65	15.43 ± 1.43	11.23 ± 1.20	12.12 ± 1.98	15.43 ± 1.00
3	AuNPs of <i>O. dilleni</i>	16.34 ± 1.98	17.20 ± 1.43	13.21 ± 1.65	13.54 ± 1.88	13.33 ± 1.23
4	Amoxicillin (standard)	23.65 ± 1.54	26.98 ± 1.32	25.77 ± 1.43	29.09 ± 1.98	29.66 ± 1.43

TABLE 4: Comparative antifungal activity of the aqueous extract, AgNPs, AuNPs, and standard antifungal drugs.

S. no	Samples	<i>Candida albicans</i>	<i>Aspergillus niger</i> Zone of inhibition (mm)	<i>Penicillium notatum</i>
1	Extract of <i>O. dilleni</i>	12.76 ± 1.23	11.76 ± 1.65	13.23 ± 1.54
2	AuNPs of <i>O. dilleni</i>	22.03 ± 1.00	19.98 ± 1.43	21.65 ± 1.09
3	AgNPs of <i>O. dilleni</i>	24.23 ± 1.29	21.54 ± 1.09	27.76 ± 1.65
4	Miconazole (standard drug)	100.00 ± 0.02	100.00 ± 0.08	100.00 ± 0.04



(c)

FIGURE 5: Continued.

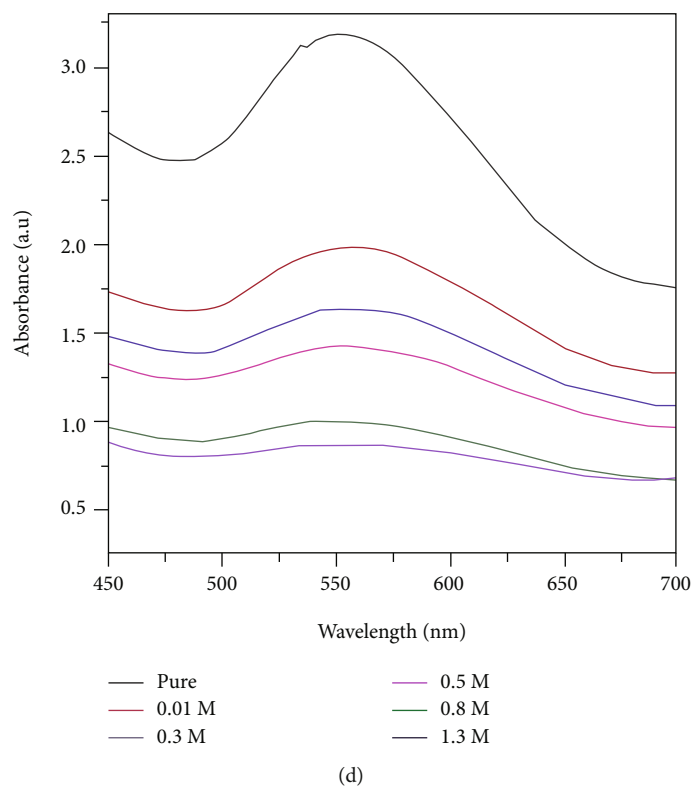


FIGURE 5: Visual effect of NaCl on of AgNPs (a) and AuNPs (b). UV-visible data of NaCl effect on AgNPs (c) and AuNPs (d) of *O. dillenii*.

and AgNPs was tested in a growing medium. This assay ascertained whether the division and the growth are prerequisites for Au and AgNP antifungal activity. The results of the antifungal activity are given in Table 4.

These results of the antifungal assay confirmed that extract of *O. dillenii* contain only mild antifungal activity while the Au and AgNPs possess some antifungal activity. The antifungal activity exhibited by extract of *O. dillenii* against different fungal strains ranged between 11 and 13 mm. The antifungal activity 13 mm was found against *P. notatum*, followed by *C. albicans* (12 mm) > *A. niger* (11 mm). The antifungal activity of AuNPs of *O. dillenii* against different fungal strains ranged between 19 and 22 mm. The antifungal activity 22 mm was noted against *C. albicans* followed by *P. notatum* (21 mm) > *A. niger* (19 mm). Likewise, the antifungal activity of AgNPs of *O. dillenii* against different fungal strains ranged between 21 and 27 mm. The antifungal activity 27 mm was found against *P. notatum* followed by *C. albicans* (24 mm) > *A. niger* (21 mm) as shown in Table 4.

3.5. Stability Factors

3.5.1. Effect of NaCl on Ag and AuNPs. Effect of different concentrations of the NaCl was performed on the solutions of Au and AgNPs using pure, 0.01, 0.1, 0.5, 1, 1.2, 1.5, and 2 M solution of NaCl for AgNPs and 0.1, 0.3, 0.5, 0.8, 1.3 and 1.5 M NaCl solution for evaluating stability on AuNPs. The solutions were made by dissolving the required amount

of NaCl in specific volume of distilled water. 0.5 ml of all the prepared molar solution was added in 2 ml of Au and AgNP solution and was shaken well, and the effect of different NaCl concentrations on the NPs was evaluated using a UV-visible spectrophotometer and spectrum was drawn based on the absorbance values on different wavelengths ranging from 200 to 800 nm as shown in Figure 5.

The Au and AgNP solution contains Au and Ag atoms, respectively, along with negatively charged chloride ions which allow the Au and Ag atoms to be dispersed in the solution. The NPs then starts forming agglomerate and change the solution color because the NPs absorb wavelength e.g., green, orange, red, and yellow excluding shorter wavelengths of purple and blue. Then, the color of the colloids changes to bluish by absorbing shorter wavelengths: green and blue and green instead of red and orange and red. By increasing the concentration of NaCl, the solution became colorless because of the no suspended particles in the solution they started forming precipitates and aggregates at the bottom therefore no absorbance of light occurred by the solution.

3.5.2. Effects of Different Salts on Au and AgNPs. The effects of the different ionic strengths on the size of both Au and AgNPs were also evaluated. The investigation of the NPs in different salts range of ionic strength is also necessary for assessment of the NPs behavior in the different salt environment since the relevant environmental conditions may vary according to different salts and their ionic strength.

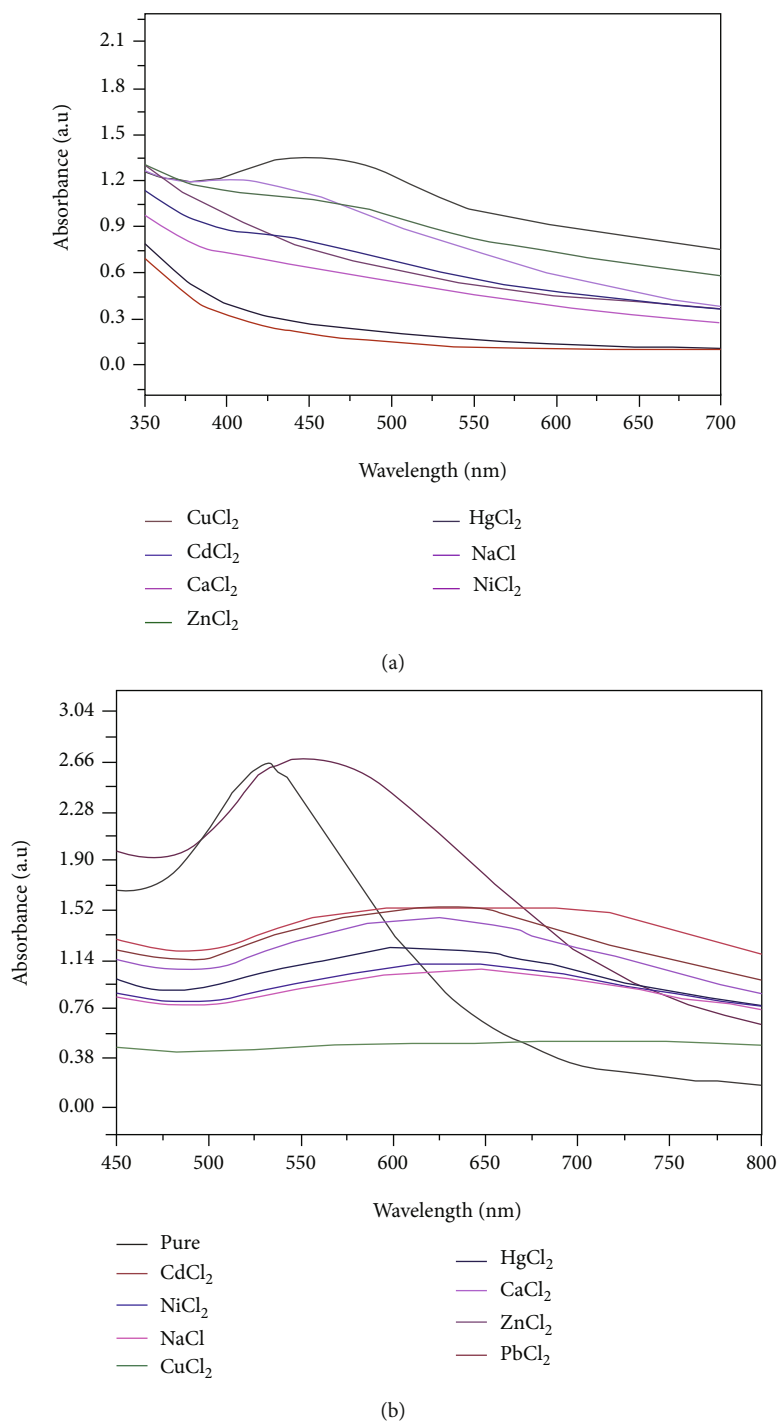


FIGURE 6: UV-visible spectra for effect of different salts on AgNPs (a) and AuNPs (b).

The salts used in the evaluation of the effects on Au and AgNPs were NiCl₂, CuCl₂, HgCl₂, CaCl₂, ZnCl₂, and PbCl₂.

The difference in the particle sizes as a function of the ionic strength is shown in Figure 6. As revealed from the spectrum steep gradient it is manifested that the AuNPs are highly susceptible to high salts strength as compared to the AgNPs. As the size of NPs increase it lead to formation of the aggregates in the media. The steepness in the spec-

trum shows the particle aggregation caused by ionic strength. The research by NPs evaluated and compared the effects of different electrolytes and concluded that salts with the divalent cations have a great influence on NPs aggregation in comparison to the salts with monovalent cations. The chloride ions also enhanced the NPs aggregation [27]. Likewise, Badawy also analyzed AgNPs and the consequence of different monovalent and divalent cations [28]. The Au

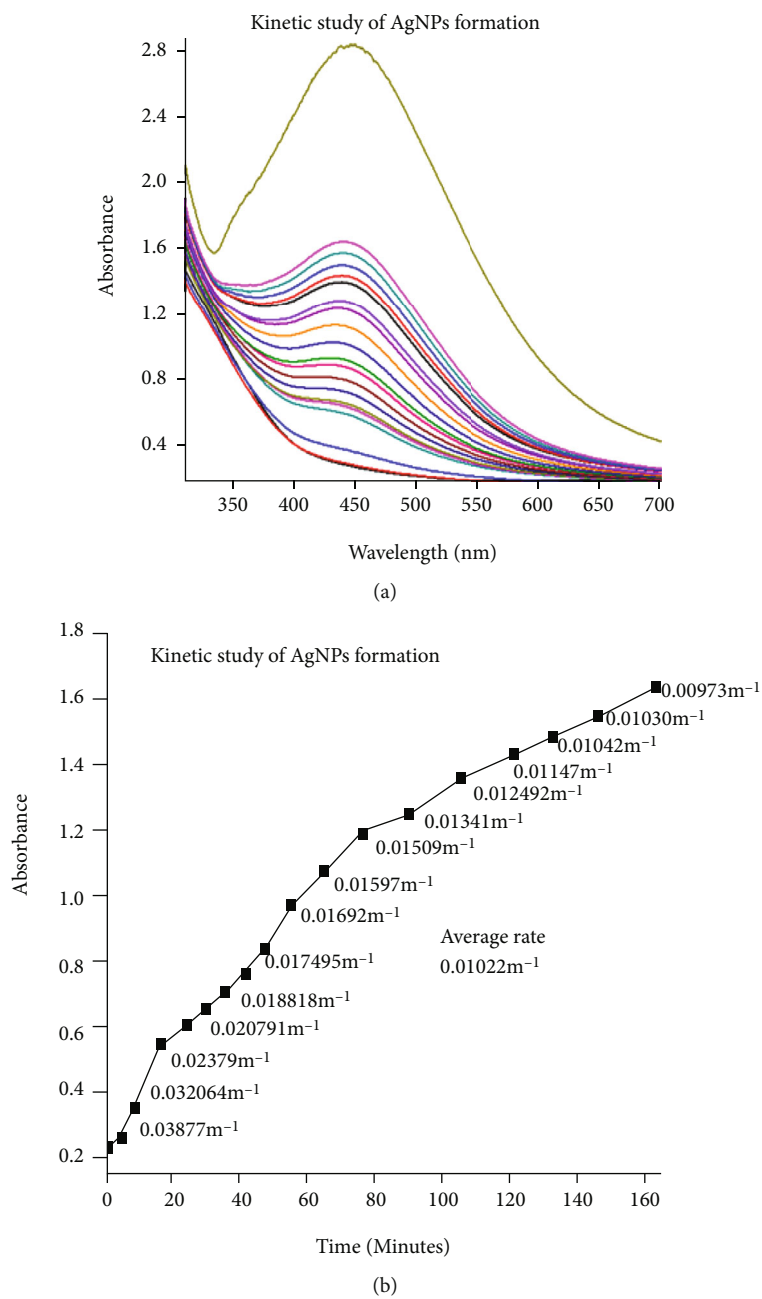


FIGURE 7: Continued.

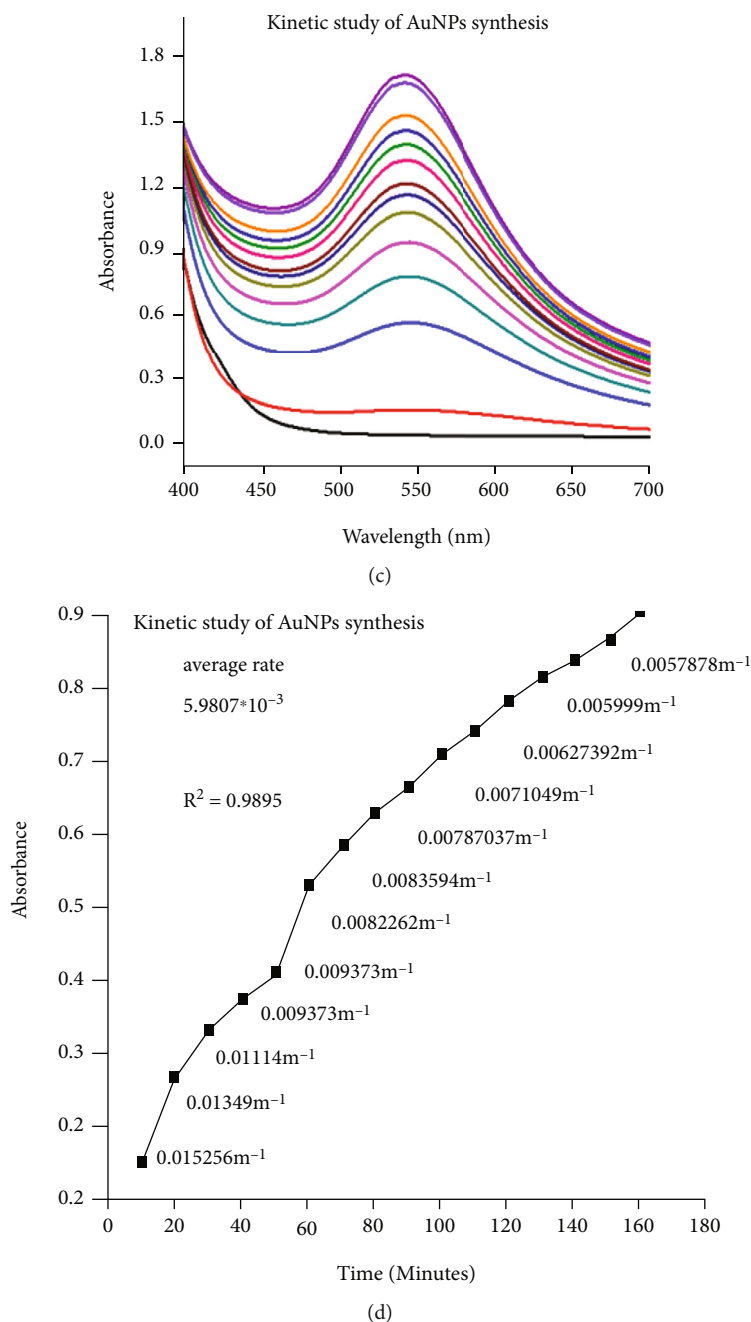


FIGURE 7: UV-visible data of kinetic study of AgNPs (a). Rate of reaction for the synthesis of AgNPs (b). UV-visible data of kinetic study of AuNPs (c). Rate of reaction for the synthesis of AuNPs (d).

and AgNPs, at a higher strength of ionic salts, have aggregated and Ca^{2+} cations presence have resulted in the enhancement of the apparent aggregation. The aggregation of the NPs has revealed that NPs were efficiently destabilized by divalent electrolytes [29].

3.5.3. Kinetic Studies of Au and AgNPs. The kinetic study of Au and AgNPs showed that with the passage of time the number and uniformity of NPs increases. When the absorbance was plotted against time, it gave almost a straight line,

from which the rate of reaction was calculated (Figure 7). After specific intervals of time revealed that the production and the uniformity of the NPs increase with the increases in time, the slope bands in the spectrum showed the maximum production of the NPs in the solution.

3.5.4. Effects of Heat on Ag and AuNPs. The effect of the temperature on the NPs is considered as the major factor which can affect the synthesis of Au and AgNPs. This analysis was conducted on different temperatures visually

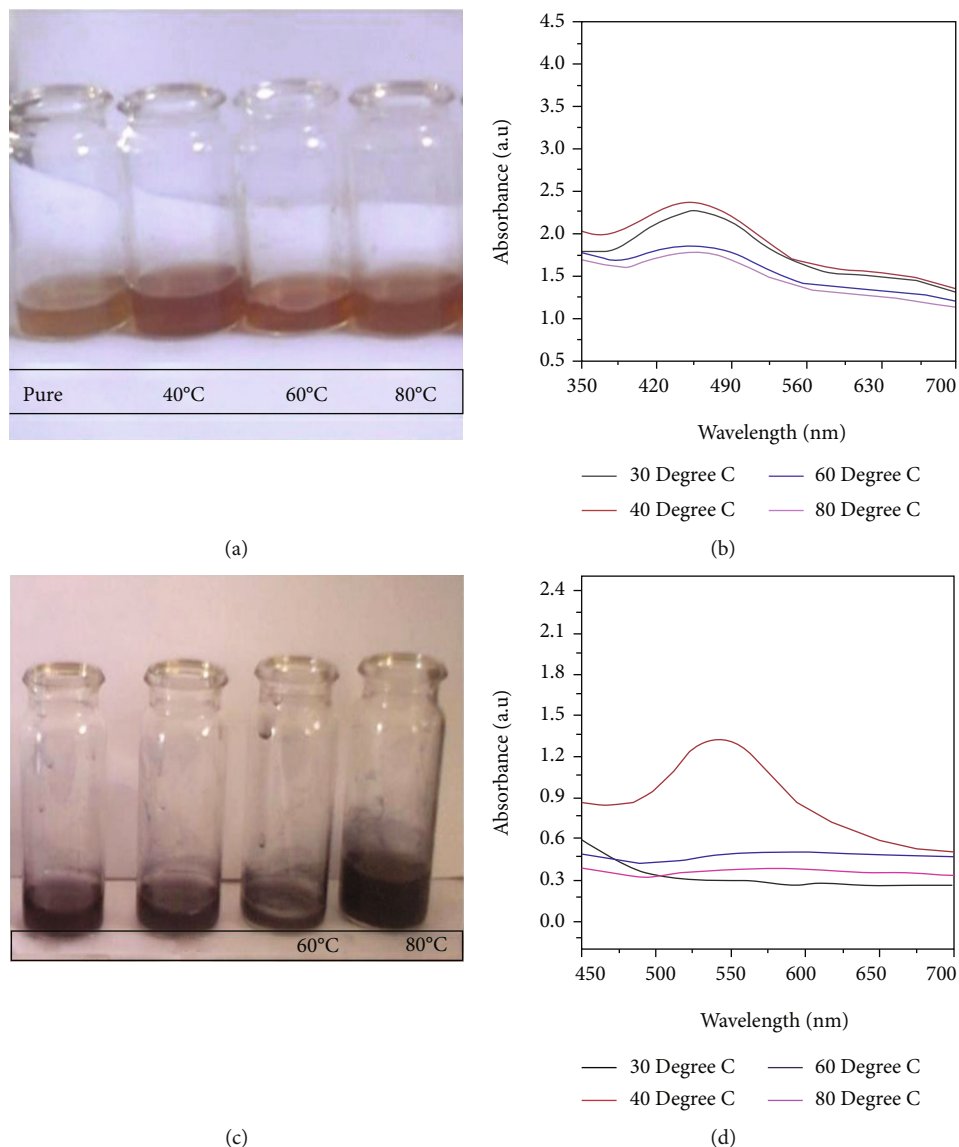


FIGURE 8: Visual effect of heat on AgNPs (a) and AuNPs (c) and UV-visible data of heat effect on AgNPs (b) and AuNPs (d).

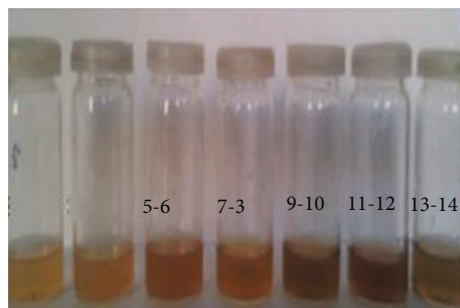
shown in Figure 8 and was confirmed by analysis by the UV-visible spectra at three different temperatures 40°C, 60°C, and 80°C.

It can be observed clearly from the spectra of UV-visible spectrophotometer that synthesis of Ag and AuNPs increases with temperature but after certain temperature, it became destabilized which caused the NPs to clump together and agglomerated. It also caused the broadening of peak which indicate the big NPs that settled down. in the formation of Au and AgNPs with an increase in the temperature [30].

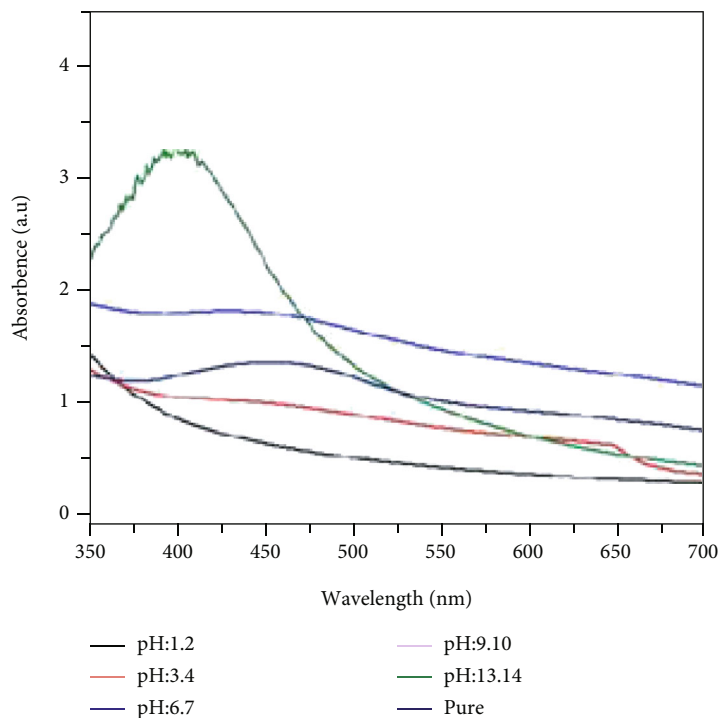
3.5.5. Effects of pH on Au and AgNPs. The effect on the Au and AgNPs was also studied due to the change in the pH was studied in different conditions including the pH ranges from 1 to 14. The pH was adjusted by dropwise addition of HCl and NaOH. Figure 9 shows the visual

analysis of pH on NPs, and the effect of changes in pH on UV-Vis spectra of Au and AgNPs synthesized is shown in Figure 9.

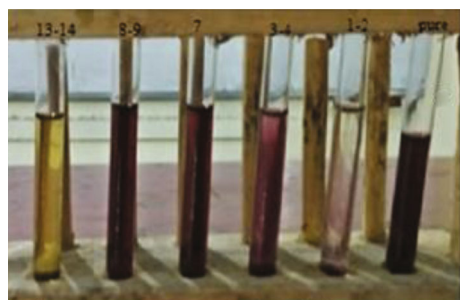
The effect of pH on stability of NPs can be observed by change in the color of NPs solution [31]. At low pH ranges small the broadening of the bands was formed which indicates the formation of large-sized NPs. In the extract mediated synthesis of NPs alkaline pH shows the narrowing of the band at 400 nm with maximum sharp band production. The formation of the sharp band indicates the formation of the spherical shape of NPs [32]. Several studies reported that pH plays a vital role in the determination of the size and shape control synthesis process of NPs. This research indicates that alkaline pH 6-7 is more suitable for the synthesis of Ag and 8-9 for AuNPs. It was reported that AuNPs at pH 10 showed maximum stability using the extract of *M. charantia* [33].



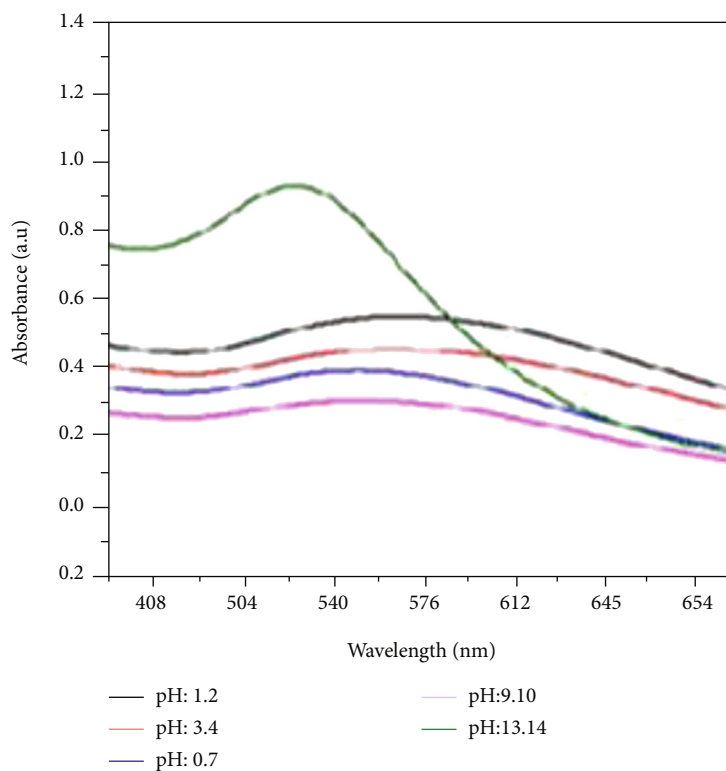
(a)



(b)



(c)



(d)

FIGURE 9: Visual effect of pH on AgNPs (a) and AuNPs (c) and UV-visible data of pH effect on AgNPs (b) and AuNPs (d).

4. Conclusions

The Au and AgNPs were characterized using UV, FTIR, SEM, and EDX spectra and showed the rapid biosynthesis

of NPs using *O. dillenii*. An increase in the awareness of utilizing green chemistry and adopting the green route for the production of metallic nanoparticles leads to the development of efficient and ecofriendly techniques. The advantages

of the synthesis of Au and AgNPs by the use of plant extracts are being most economical, cost-effective, and energy-efficient and provide an efficient application towards the communities, protecting environment and health leading towards the lessening in the production of hazardous wastes and development of safe products. Green-synthesized Au and AgNPs have various significant nanotechnology aspects with matchless applications.

Data Availability

The data produced in this finding has been included in the main text of this paper.

Conflicts of Interest

The authors declare no potential conflict of interest.

References

- [1] A. K. Khan, R. Rashid, G. Murtaza, and A. J. T. R. Zahra, "Gold nanoparticles: synthesis and applications in drug delivery," *Tropical Journal of Pharmaceutical Research*, vol. 13, no. 7, pp. 1169–1177, 2014.
- [2] R. Sharma and P. K. Prajapati, "Nanotechnology in medicine: leads from Ayurveda," *Journal of Pharmacy & Bioallied Sciences*, vol. 8, no. 1, pp. 80–81, 2016.
- [3] R. Sharma and P. K. Prajapati, "Liquid media's in Bhavana Samskara: a pharmaceutico-therapeutic prospect," *The Journal of Phytopharmacology*, vol. 4, pp. 49–57, 2015.
- [4] D. MubarakAli, N. Thajuddin, K. Jeganathan, and M. Gunasekaran, "Plant extract mediated synthesis of silver and gold nanoparticles and its antibacterial activity against clinically isolated pathogens," *Colloids and Surfaces B: Biointerfaces*, vol. 85, no. 2, pp. 360–365, 2011.
- [5] G. Barbera, P. I. Barbera, and E. Pimienta Barrios, "History, economic and agro-ecological importance," in *Agro-ecology cultivation and uses of cactus pear*, FAO, Roma, 1995.
- [6] Z. Bouzoubaâ, Y. Essoukrati, S. Tahrouch, A. Hatimi, S. Gharby, and H. Harhar, "Phytochemical study of prickly pear from southern Morocco," *Journal of the Saudi Society of Agricultural Sciences*, vol. 15, no. 2, pp. 155–161, 2016.
- [7] W. Brand-Williams, M. E. Cuvelier, and C. L. Berset, "Use of a free radical method to evaluate antioxidant activity," *LWT-Food Science and Technology*, vol. 28, no. 1, pp. 25–30, 1995.
- [8] M.-N. Cha, H.-I. Jun, W.-J. Lee, M.-J. Kim, M.-K. Kim, and Y.-S. Kim, "Chemical composition and antioxidant activity of Korean cactus (*Opuntia humifusa*) fruit," *Food Science and Biotechnology*, vol. 22, no. 2, pp. 523–529, 2013.
- [9] A. Schröfel, G. Kratošová, I. Šafařík, M. Šafaříková, I. Raška, and L. M. Shor, "Applications of biosynthesized metallic nanoparticles - a review," *Acta Biomaterialia*, vol. 10, no. 10, pp. 4023–4042, 2014.
- [10] R. A. Chavez-Santoscoy, J. A. Gutierrez-Urbe, and S. O. Serna-Saldívar, "Phenolic composition, antioxidant capacity and in vitro cancer cell cytotoxicity of nine prickly pear (*Opuntia* spp.) juices," *Plant Foods for Human Nutrition*, vol. 64, no. 2, pp. 146–152, 2009.
- [11] R. K. Das, P. Sharma, P. Nahar, and U. Bora, "Synthesis of gold nanoparticles using aqueous extract of *Calotropis procera* latex," *Materials Letters*, vol. 65, no. 4, pp. 610–613, 2011.
- [12] Z. Ghazi, M. Ramdani, M. Tahri et al., "Chemical composition and antioxidant activity of seeds oils and fruit juice of *Opuntia ficus indica* and *Opuntia dillenii* from Morocco," *Journal of Materials and Environmental Science*, vol. 6, no. 8, pp. 2338–2345, 2015.
- [13] E. M. D. Medina, E. M. Rodríguez Rodríguez, and C. Díaz Romero, "Chemical characterization of *Opuntia dillenii* and *Opuntia ficus indica* fruits," *Food Chemistry*, vol. 103, no. 1, pp. 38–45, 2007.
- [14] P. Elia, R. Zach, S. Hazan, S. Kolusheva, Z.'e. Porat, and Y. Zeiri, "Green synthesis of gold nanoparticles using plant extracts as reducing agents," *International Journal of Nanomedicine*, vol. 9, pp. 4007–4021, 2014.
- [15] T. Muralikrishna, M. Pattanayak, and P. L. Nayak, "Green synthesis of gold nanoparticles using (aloe vera) aqueous extract," *World Journal of Nano Science & Technology*, vol. 3, no. 2, pp. 45–51, 2014.
- [16] A. B. Singh, M. M. Sharma, and A. M. Batra, "Synthesis of gold nanoparticles using chick pea leaf extract using green chemistry," *Journal of Optoelectronics and Biomedical Materials*, vol. 5, no. 2, pp. 27–32, 2013.
- [17] S. Varun, S. Sellappa, M. RafiqKhan, and S. Vijayakumar, "Green synthesis of gold nanoparticles using Argemone mexicana L. leaf extract and its characterization," *International Journal of Pharmaceutical Sciences Review and Research*, vol. 32, pp. 42–44, 2015.
- [18] A. J. Afolayan, "Extracts from the shoots of *Arctotis arctoides* inhibit the growth of bacteria and fungi," *Pharmaceutical Biology*, vol. 41, no. 1, pp. 22–25, 2003.
- [19] F. E. Koehn and G. T. Carter, "The evolving role of natural products in drug discovery," *Nature Reviews Drug Discovery*, vol. 4, no. 3, pp. 206–220, 2005.
- [20] M. J. Balunas and A. Douglas Kinghorn, "Drug discovery from medicinal plants," *Life Sciences*, vol. 78, no. 5, pp. 431–441, 2005.
- [21] C. Canals, A. F. Remacha, M. P. Sarda, J. M. Piazuelo, M. Teresa Royo, and M. Angeles Romero, "Clinical utility of the new Sysmex XE 2100 parameter-reticulocyte hemoglobin equivalent-in the diagnosis of anemia," *Haematologica*, vol. 90, no. 8, pp. 1133–1134, 2005.
- [22] W. Haiss, N. T. K. Thanh, J. Aveyard, and D. G. Fernig, "Determination of size and concentration of gold nanoparticles from UV-Vis spectra," *Analytical Chemistry*, vol. 79, no. 11, pp. 4215–4221, 2007.
- [23] P. Mulvaney, "Surface plasmon spectroscopy of nanosized metal particles," *Langmuir*, vol. 12, no. 3, pp. 788–800, 1996.
- [24] Z. L. Wang, "Transmission electron microscopy of shape-controlled nanocrystals and their assemblies," *The Journal of Physical Chemistry B*, vol. 104, no. 6, pp. 1153–1175, 2000.
- [25] P. Balashanmugam, P. Durai, M. D. Balakumaran, and P. T. Kalaichelvan, "Phytosynthesized gold nanoparticles from *C. roxburghii* DC. leaf and their toxic effects on normal and cancer cell lines," *Journal of Photochemistry and Photobiology B: Biology*, vol. 165, pp. 163–173, 2016.
- [26] Y. Huang, Y. Fang, L. Chen, L. Ang, and L. Zhang, "One-step synthesis of size-tunable gold nanoparticles immobilized on chitin nanofibrils via green pathway and their potential applications," *Chemical Engineering Journal*, vol. 315, pp. 573–582, 2017.
- [27] M. Baalousha, Y. Nur, I. Römer, M. Tejamaya, and J. R. Lead, "Effect of monovalent and divalent cations, anions and fulvic

- acid on aggregation of citrate-coated silver nanoparticles,” *Science of the Total Environment*, vol. 454-455, pp. 119–131, 2013.
- [28] A. M. Badawy, T. P. Luxton, R. G. Silva, K. G. Scheckel, M. T. Suidan, and T. M. Tolaymat, “Impact of environmental conditions (pH, ionic strength, and electrolyte type) on the surface charge and aggregation of silver nanoparticles suspensions,” *Environmental Science & Technology*, vol. 44, no. 4, pp. 1260–1266, 2010.
- [29] K. A. Huynh and K. L. Chen, “Aggregation kinetics of citrate and polyvinylpyrrolidone coated silver nanoparticles in monovalent and divalent electrolyte solutions,” *Environmental Science & Technology*, vol. 45, no. 13, pp. 5564–5571, 2011.
- [30] S. E.-D. Hassan, A. Fouda, E. Saied et al., “Rhizopus oryzae-mediated green synthesis of magnesium oxide nanoparticles (MgO-NPs): a promising tool for antimicrobial, mosquitocidal action, and tanning effluent treatment,” *Journal of Fungi*, vol. 7, no. 5, p. 372, 2021.
- [31] M. Sathishkumar, K. Sneha, and Y. S. Yun, “Immobilization of silver nanoparticles synthesized using *Curcuma longa* tuber powder and extract on cotton cloth for bactericidal activity,” *Bioresource Technology*, vol. 101, no. 20, pp. 7958–7965, 2010.
- [32] M. M. Kumari, J. Jacob, and D. Philip, “Green synthesis and applications of Au-Ag bimetallic nanoparticles,” *Spectrochimica Acta Part A: Molecular and Biomolecular Spectroscopy*, vol. 137, pp. 185–192, 2015.
- [33] S. Pandey, G. Oza, A. Mewada, and M. Sharon, “Green synthesis of highly stable gold nanoparticles using *Momordica charantia* as nano fabricator,” *Archives of Applied Science Research*, vol. 4, no. 2, pp. 1135–1141, 2012.

Research Article

Experimental Analysis of Heat Transfer by Using Nanofluid and Impact of Thermophysical Properties

L. Karikalan,¹ S. Baskar ,² N. Poyyamozhi ,³ and Kassu Negash ⁴

¹Department of Automobile Engineering, Vels Institute of Science, Technology & Advanced Studies (VISTAS) Chennai, Tamilnadu, India

²Department of Automobile Engineering, Vels Institute of Science, Technology & Advanced Studies (VISTAS) Chennai, Tamilnadu, India

³Department of Mechanical Engineering, Panimalar Engineering College, Chennai, Tamilnadu, India

⁴Department of Mechanical Engineering, Faculty of Manufacturing, Institute of Technology, Hawassa University, Hawassa, Ethiopia

Correspondence should be addressed to S. Baskar; baskar133.se@velsuniv.ac.in

Received 7 January 2022; Revised 8 February 2022; Accepted 10 February 2022; Published 16 March 2022

Academic Editor: H C Ananda Murthy

Copyright © 2022 L. Karikalan et al. This is an open access article distributed under the Creative Commons Attribution License, which permits unrestricted use, distribution, and reproduction in any medium, provided the original work is properly cited.

The scope of the project is to analyse the heat transfer behaviours by using shell and tube heat exchangers and measurements of various thermophysical properties of carbon nanotube nanofluid. The nanofluid is created using different volume fractions at different operation temperatures. The research focuses on theoretical and experimental research on CNT nanofluids, with the goal of improving thermophysical parameters such as thermal conductivity, specific heat, and viscosity. The thermophysical characteristics of CNTs were investigated using this theoretical method. Various tests were carried out to investigate the thermophysical qualities, and they were found to have an impact. The improved characteristics of carbon nanotubes (CNTs) have the potential to save energy and reduce CO₂, NO₂, and SO₂ emissions in industrial settings. Improving heat exchange performance in the thermal sector would result in a high heat-to-power conversion efficiency. Nanofluids can considerably enhance critical heat flux (CHF) in heat transfer systems.

1. Introduction

The majority of scientists think that facilitating contamination and worldwide climate change, primarily as a result of excessive carbon dioxide emissions, poses a threat to the environment. Because manufacturing is one of the most power-intensive sectors, a change toward increased energy-efficiency in manufacturing, particularly in manufacturing, is essential. Using thermal systems to reduce energy consumption and emissions is a new issue. Many approaches for improving heat transfer have been implemented over the last decade [1–3]. This can be accomplished by reducing the thickness of the thermal limit. At the heat transfer wall, there will be a velocity gradient, interrupting fluid flow and raising velocity from laminar to turbulent flows, thus raising the heated wall's extended surface and modifying the surface and fluid thermophysical characteristics [4].

In the process sector, heat transfer procedures are quite frequent to transmit a large quantity of thermal energy from one fluid to another for various purposes. Water is the most popular heat transfer fluid (HTF) owing to its more specific heat, ease of use, and affordability. Traditional heat transfer fluids, such as water, include minor thermal conductivity, the most important thermophysical attribute, resulting in reduced efficiency of heat transfer [5]. The adding of nanoparticles extremely thermal conductive materials, particularly at the nanoscale, produces nanofluid (NF), which has emerged as an effective HTF over the past two decades and has been studied in an extensive variety of applications [6, 7].

The heat transfer quality of traditional effective fluid is a concern. The production of well-organized and compacted thermal systems, particularly heat exchangers, is a major challenge. They are commonly used in the thermal industry. Nanofluids are now well recognised as demanding resources

by virtue of their potential applications in heat exchangers, convective systems, energy, solar collectors, and electronic devices [8, 9]. Due to their prospective applications, they have also become a global study focus. Nanofluid consumes superior thermal conductivity than the base fluid, which increases dramatically as the concentration of nanomaterials increases. These advantages are also influenced by the type of nanoparticles [10]. Fluids that are commonly used with carbon-based nanomaterials are also of great interest due to their unique properties and excellent thermal characteristics intrinsically.

The various strategies were designed to improve the nanofluid heat transfer coefficient with the goal of creating a compact system that was low in cost and efficient in energy use. Since Mukesh Kumar et al. [11–13], the use of suspensions rather than traditional heat transfer liquids has been recommended because solids have higher thermal conductivities than liquids. Although using suspensions to contain microparticles will pose significant challenges, such as particle corrosion of transport equipment, high pumping power constraints, and sedimentation, Mondragon et al. describe a suspension containing nanoparticles in the fluid as a suspension containing nanoparticles in the fluid. In addition, when compared to typical suspension, fluid conveyance has negligible corrosion effects and requires little pumping power [14]. Furthermore, it is referred to as nanofluid since it has a high heat conductivity when compared to base fluid and conventional suspension [15]. The nanofluid contains a minor amount of metals, such as Cu, as well as nonmetals, such as Al_2O_3 , SiC, and CuO nanoparticles. Pay special attention to the CNT's unusual arrangement and exceptional thermal characteristics [16–18].

Nanofluid has been extensively employed as excellent performances in heat transfer fluid with variety of application due to its greater performance compared to base fluid [19–21]. Heat transfer during various heat exchanger like shell and tube heat exchanger, solar collectors, heat pipe, for energy storage, and many other applications is among the most common uses for NF [22–25]. Because of their superior thermophysical qualities, nanofluid has a significant possible use in favour of recovering waste heat and increasing the energy effectiveness of many operations [26–28].

2. Treatment of Nanofluid

2.1. Purification. The treatment of the nanofluid is shown in Figure 1, for understanding easily. The creation of the nanofluid can be done in two ways, with the two-step process being more convenient and being employed by many researchers. The nanotube comes in a wide variety of lengths, flaws, and twists. As a result, the main concern is how to separate them as garbage stain and sanitise the tube. Various postenlargement therapies have evolved to clean the tube and remove flaws. In an ultrasonicator, the materials can be treated to release the tubes from the particles that have bound them all together.

2.2. Stability. The nanofluid is said to be stable when the concentration of scattered nanoparticles remains constant

throughout time. The pictures of the nanofluid test tube should be taken every day to determine the sedimentation rate (stability test) are shown in Table 1.

Although nanotubes show perfect uniqueness, the samples are taken under unusual settings, such as when they are exposed to air or water, confirming that they are distinct. As a result, impurities like O_2 clinging to the nanotubes made them extremely vulnerable. The lubricated nanotube stain is repeatedly distributed in ethanol, where it may be preserved without causing damage to the tubes. It is worth noting that the nanotubes are stable, preserving their structure even when contaminated.

2.3. Effect of Sonication Time. The carbon nanotube nanofluid is affected by ultrasonication in two ways. Though the optimum time had reached more ultrasonication outcomes than before, which was more than the break rate of nanotubes and reduced the aspect ratio of carbon nanotubes, ultrasonication aids in the formation of superior dispersions under the ideal processing time. With a 140 W and 20 kHz ultrasonicator, the most favourable ultrasonication time was up to 35 minutes at 1 wt percent MWCNT. The nanofluid viscosity is increased by sonication time until it reaches its maximum value, after which it declines. The declustering of the carbon nanotube bundle was linked to the early ascent, which led to the production of enhanced dispersal. Due to the increased breakage rate of carbon nanotubes, the latter reduces viscosity, resulting in a shorter nanotube and poor dispersion of carbon nanotubes. With a 35-minute ultrasonication time, the maximum thermal conductivity enhancement is observed, but this decreases with additional sonication.

3. Experimental Setup

The experimental apparatus is schematically depicted in Figure 2, which includes an experiment section, water loop, nanofluid loop, and data monitoring system.

The test unit is 2 m length and a tube in tube heat exchanger with a counter flow arrangement in which the nanofluid flows from beginning to end of the inside copper tube with inside diameter of 10 mm and water flow is taken by the shell side with outside diameter of 25 mm. The experiment part remains separated to five equal length sections, and the whole unit is wrapped in insulating material. On the inner side of a wooden box packed with the help of glass wool, the insulated test part is placed. To display the bulk temperatures of nanofluid, RTDs remain directly placed where the fluid flows at the entrance and outflow of each section. The following approach is used to calculate the convective heat transfer coefficients of nanofluids flowing inside the tube using the measured data. Using the nanofluid inlet as reference, the length of each segment is calculated.

4. Measurement of Thermophysical Properties

4.1. Density Measurement. The addition of solid nanoparticles, which have a higher density, results in NF having a higher density than BF. The density is determined using

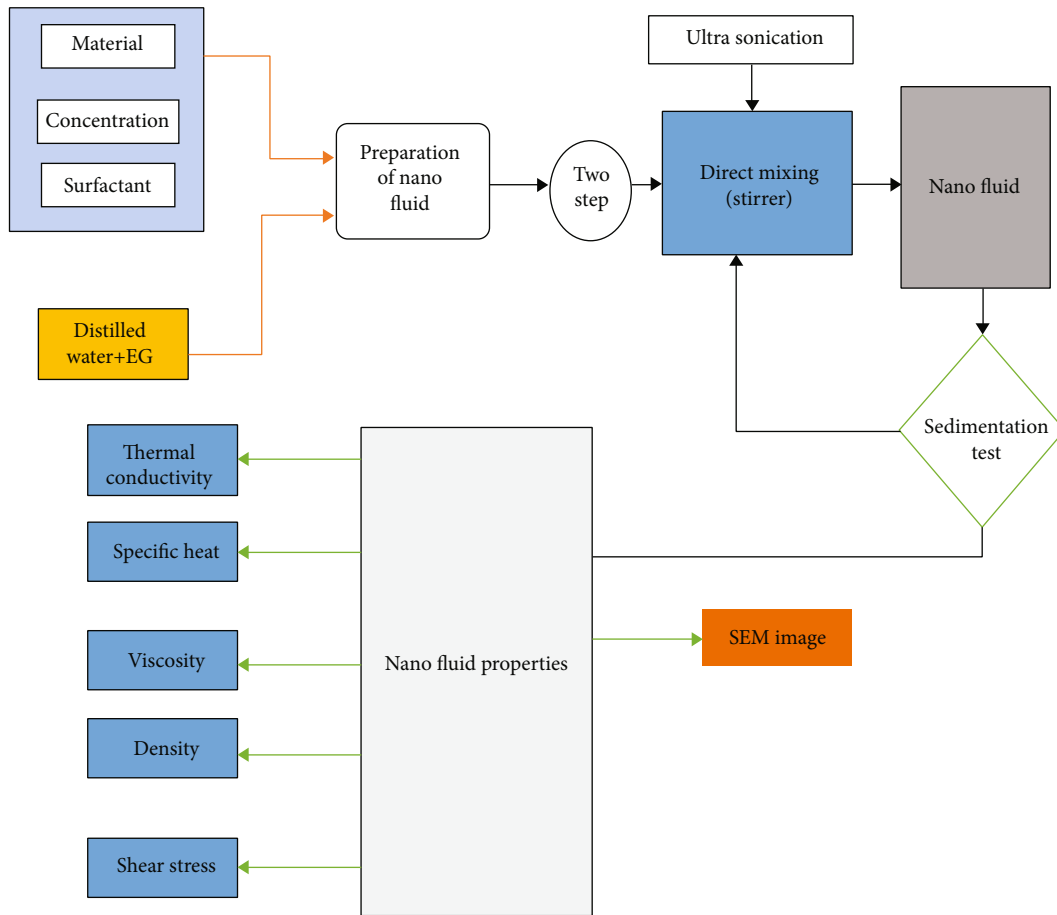


FIGURE 1: Treatment of nanofluid.

the volumetric flask method, in which a known amount of nanofluid is placed in a conventional volumetric flask of a given volume and the mass of the flask containing nanofluid is measured using a highly valuable electronic balance (M_2). Using the same electronic balance, the empty flask mass (M_1) is measured first. The difference between M_2 and M_1 yields the precise nanofluid mass for a given volume. As a result, the density of nanofluid is determined utilising

$$\rho_{nf} = (M_2 - M_1)/V_{fl}, \quad (1)$$

where,

- ρ_{nf} : Density of the nanofluid,
- M_2 : Flask mask with nanofluid,
- M_1 : Mass of empty flask,
- V_{fl} : Volume of the flask.

The density measurements arrangement is exposed in the Figure 3.

The empty flask was initially kept in the electronic balance machine without water to set the zero reading in the electronic balance machine. The nanofluid concentrations are then put into the flask and kept in an electronic balance machine, where the values are recorded. This is useful for determining density measurements for varied

nanofluid concentrations. The electronic balance machine's specifications are as follows: BL 220H, 220 g capacity, 0.001 g readability, and digital model. The Pak and Cho correlations were used to compare the density values. The Pak and Cho correlations are calculated as follows:

$$\rho = \Phi\rho_p + (1 - \Phi)\rho_f, \quad (2)$$

where,

- ρ : Density of the nanofluid,
- Φ : Fraction of volume,
- ρ_f : Base fluid density,
- ρ_p : Nanoparticle density.

4.2. Specific Heat. The heat transfer rate is very much influenced by the specific heat; hence, the situation requires analysis of the consequence of CNT in the base fluid. The specific heat capacity remains essentially the quantity of an energy needed to increase the temperature of unit mass substance by 1° Celsius, represented in metric units as J/g.K. The heating or cooling ability of the fluid per unit raises or decreases the temperature determined by the specific heat capacity of the nanofluid as a characteristic of heat transfer fluid, in which just the creation of the fluid flow rate and the specific heat capacity in J/K, by means of superior heat

TABLE 1: Stability test.

Illustrate	Description	Time in Hrs	Remarks
	Water +0.15 volume % of CNT	1	CNT is settled
	Water with 0.20% Cetyl pyridinium chloride +0.15 volume % of CNT	2.15	CNT is settled
	Water with 0.20% Cetyl dimethyl benzyl-ammonia chloride +0.15 volume % of CNT	2.30	CNT is settled
	Water with 0.20% benzyl trimethyl ammonia chloride +0.15 volume % of CNT	6	CNT is settled
	Water with 0.20% SDBS+0.15 volume % of CNT	24	CNT is not settled

capability with superior heat transfer fluid. As a result, as specific heat capacity increases, heat capacity decreases, necessitating low HTF flows for given heating or cooling jobs, lowering pumping power requirements.

A differential scanning calorimeter with a nitrogen chilling facility is used to test the nanofluid specific heat. A known mass of nanofluid is placed in a pan, and the solution is heated and cooled at a rate of 50 degrees Celsius per

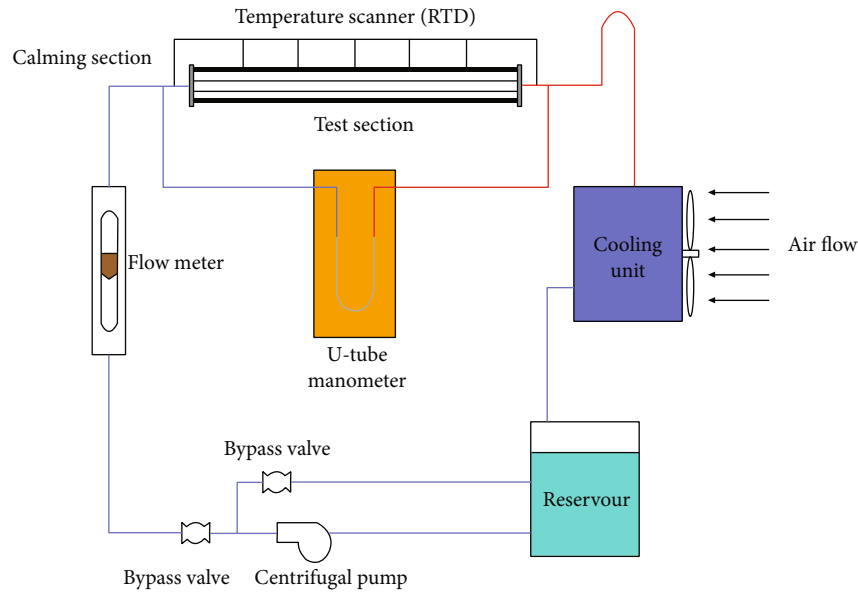


FIGURE 2: Experimental Setup.



FIGURE 3: Flask with 0.15 vol %.

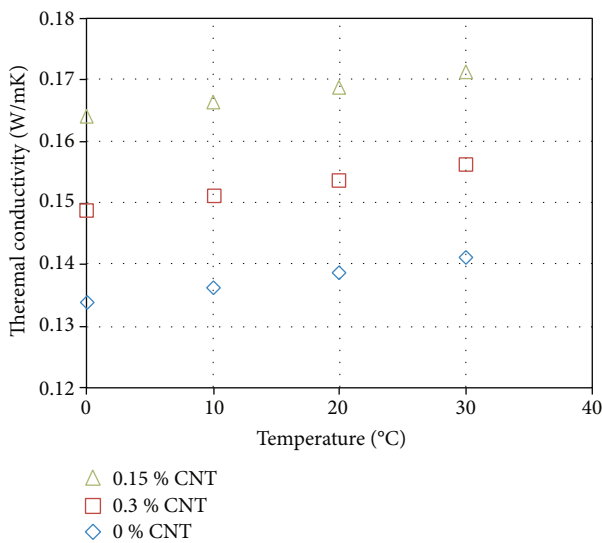


FIGURE 4: Temperature versus specific heat.

minute. $C_p = Q/(mn_f\Delta T)$ is the formula for finding nano-fluid specific heat established on results of the heating rate and heat flow.

The results show in Figure 4, as how the specific heat of nanofluids varies with temperature. It should be noted that the specific heat of a nanofluid is proportional to its temperature. Incorporating carbon nanotubes (CNTs) into water increases the specific heat of a nanofluid. It is due to an increase in nonconsistent intermolecular forces between the CNT and the fluid, which require more energy to rise in temperature than water.

4.3. Thermal Conductivity. The most essential property of NF is its increased thermal conductivity, with high thermal conductive NPs added specifically to boost BF's thermal conductivity. Thermodynamic conductivity is an important feature in heat transfer applications. To determine the effective thermal conductivity of propanol-based CNT, a variety of correlations are available in the open literature. The system is set up in this paper, and it is utilised to determine the effective thermal conductivities of nanofluids. It was chosen because the majority of experimental results correlate well with projected values using this model, which takes into account both liquid and CNT form and size.

The variant of thermal conductivities of nanofluid at different temperatures is depicted in Figure 5. The outcome shows that nanofluid thermal conductivities increase with the addition of carbon nanotube in the water. The framework displays that the thermal conductivity of nanofluid is the function of the different temperature.

4.4. Viscosity. In heat transfer application, the pumping power is a vital aspect by the way it depends on the viscosity of HTF. Viscosity is simply the fluid's resistance to flow as a result of interlayer or fluid or surface contact. Alike to the density, viscosities have dual negative effect on the pressure

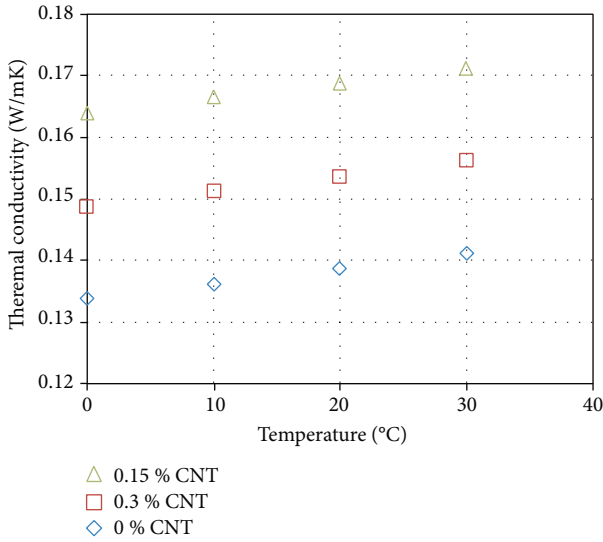


FIGURE 5: Temperature versus thermal conductivity.

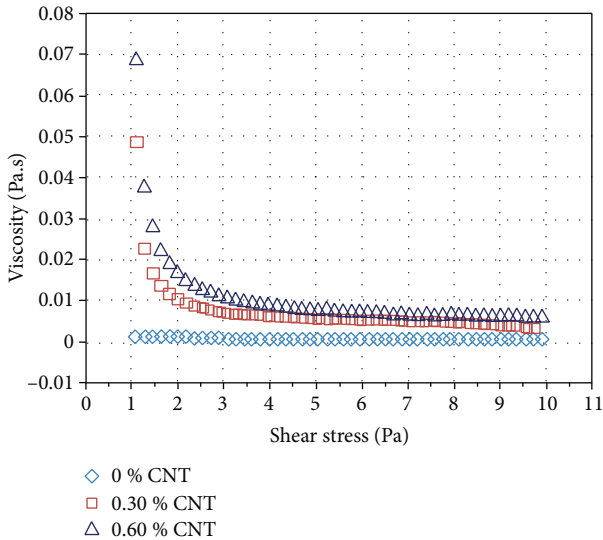


FIGURE 6: Viscosity versus shear stress.

drop and the amount of pumping power needed. Because of nanoparticles/surface collision and previous interlayer resistances and interfacial forces, the occurrence of nanoparticle in water, i.e., creating nanofluid, increases friction at fluid/surface contact. As a result, the NF's viscosity is increased in comparison to the BF as a result of these interfacial resistances. To take use of the nanofluid's good effects, it is necessary to compute the increased pumping power caused by the addition of carbon nanotubes to the water-based base fluid. It is required to determine the viscosity of the nanofluid at different temperatures.

Experimentally, the viscosity of CNT nanofluid was estimated at various concentrations of 0.15 and 0.3 at 25°C. Figure 6 depicts the relationship between nanofluid viscosities and shear stresses. It is clearly seen that nanofluid viscosity drops as shear stress increases from 0 to 3 N m⁻²,

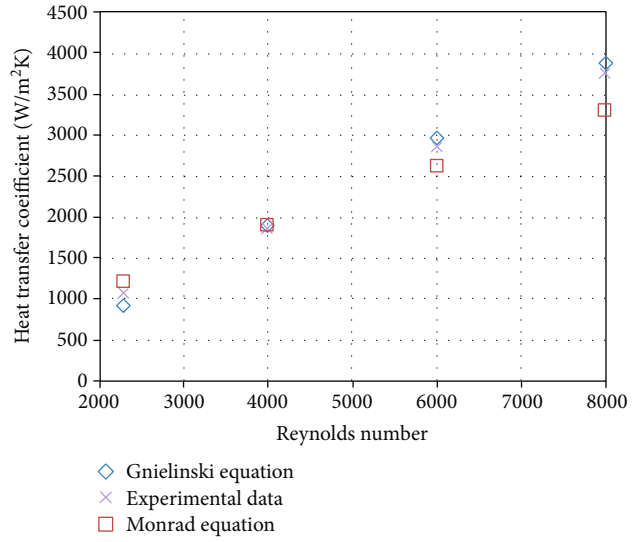


FIGURE 7: Comparison of measured HTC for water and those calculated from the Gnielinski equation and Monrad equation.

indicating that the nanofluid performs non-Newtonian at low shear stress.

4.5. Comparison of Measured HTC for Water and Those Calculated from the Gnielinski Equation and Monrad Equation. Figure 7 compares the measured HTC of the base fluid flow from end to end tube to that of predicated values using the Gnielinski equation and Monrad equation at various flow conditions ($Re > 2200$). The water flows from end to end of the tube at 10°C, and in the annulus fluid it is at 25°C. It is understood from the graph that the investigational values match those obtained from the correlations. Having established confidence, the experiment is conducted with base fluid and a heat transfer fluid on tube side and water on annular side.

5. Conclusion

Nanofluid has recently been developed as a high-efficiency heat transfer fluid with excellent thermophysical characteristics. To progress the thermophysical property of commonly used fluid, a variety of nanostructures, specifically nanoparticles, have been introduced. In this work, the effective thermophysical properties of the carbon nanotube have been discussed and subsequent conclusion has been attained. The thermal performance of system can be considerably enhanced by adding of CNT in base fluid (water). The following conclusion is drawn from the results of the thermal conductivity, viscosity, and shear stress of CNT nanofluid: the viscosity of nanofluid increases as the concentration of the nanofluid increases, and the nanofluid is appropriate when the operating temperature is greater than 45°C with superior concentration. As the temperature rises, the thermal conductivity of the nanofluid increases. Carbon nanotubes have an advantage in the nanofluid because they conserve energy, reduce emissions, and improve convective heat transfer and efficiency.

Nomenclature

Φ : Concentration (%)
 k : Thermal conductivity ($\text{W m}^{-1} \text{K}^{-1}$)
 h : Convective heat coefficient ($\text{W m}^{-2} \text{K}$)
 C_p : Specific heat ($\text{J kg}^{-1} \text{K}^{-1}$)
 ρ : Density (kg m^{-3})
 Re : Reynolds number
 T : Temperature ($^{\circ}\text{C}$)
 m : Mass flow rate (kg s^{-1})
 ΔT : Change in temperature

Special characters

CNT: Carbon nanotube
 CHF: Critical heat flux
 HTF: Heat transfer fluid
 BF: Base fluid
 NF: Nanofluid
 MWCNT: Multiwalled carbon nanotube
 RTD: Resistance temperature detector

Subscripts

n_f : Nanofluid
 b_f : Base fluid
 n_p : Nanoparticle

Data Availability

The data used to support the findings of this study are included in the article. Should further data or information be required, these are available from the corresponding author upon request.

Disclosure

It was performed as a part of the Employment Hawassa University, Ethiopia.

Conflicts of Interest

The authors declare that there are no conflicts of interest regarding the publication of this paper.

Acknowledgments

The authors appreciate the technical assistance to complete this experimental work from the Department of Automobile Engineering, Vels Institute of Science, Technology & Advanced Studies, Chennai, Tamil Nadu, India. The authors thank for the technical assistance to complete this experimental work.



References

- [1] M. Sheikholeslami, M. Jafaryar, M. Hedayat et al., "Heat transfer and turbulent simulation of nanomaterial due to compound turbulator including irreversibility analysis," *International Journal of Heat and Mass Transfer*, vol. 137, pp. 1290–1300, 2019.
- [2] M. Jafaryar, M. Sheikholeslami, Z. Li, and R. Moradi, "Nano-fluid turbulent flow in a pipe under the effect of twisted tape with alternate axis," *Journal of Thermal Analysis and Calorimetry*, vol. 135, no. 1, pp. 305–323, 2018.
- [3] J. Kumaraswamy, V. Kumar, and G. Purushotham, "Evaluation of the microstructure and thermal properties of (ASTM A 494 M grade) nickel alloy hybrid metal matrix composites processed by sand mold casting," *International Journal of Ambient Energy*, vol. 42, pp. 1–22, 2021.
- [4] M. Chandrasekar and P. M. Kumar, "Experimental investigation on heat transfer and pressure drop in double helically coiled tube heat exchanger with MWCNT/water nanofluid," *Journal of Applied Fluid Mechanics*, vol. 11, no. SI, 2018.
- [5] P. C. Mukesh Kumar and M. Muruganandam, "Stability analysis of heat transfer MWCNT with different base fluids," *Journal of Applied Fluid Mechanics*, vol. 10, pp. 51–59, 2017.
- [6] M. Muruganandam and P. C. Mukesh Kumar, "Experimental analysis of four stroke diesel engine by using carbon nano tubes based nanofluids as a coolant," *Journal of Applied Fluid Mechanics*, vol. 10, pp. 1–5, 2017.
- [7] C. M. K. Periyasamy and C. Manickam, "Experimental studies on stability of multi walled carbon nanotube with different oil based nanofluids," *Thermal Science - International Scientific Journal- Online First*, vol. 24, no. 1 Part B, pp. 533–539, 2020.
- [8] J. Kumaraswamy, V. Kumar, and G. Purushotham, "Thermal analysis of nickel alloy/Al₂O₃/TiO₂ hybrid metal matrix composite in automotive engine exhaust valve using FEA method," *Journal of Thermal Engineering*, vol. 7, no. 3, pp. 415–428, 2021.
- [9] V. Vijayan, S. Saravanan, A. Godwin Antony, M. Loganathan, and S. Baskar, "Heat transfer enhancement in mini compact heat exchanger by using alumina nanofluid," *International Journal of Mechanical Engineering and Technology (IJMET)*, vol. 10, no. 1, pp. 564–570, 2019.
- [10] V. Kumaresan and R. Velraj, "Experimental investigation of the thermophysical properties of water – ethylene glycol mixture based CNT nanofluids," *Thermochemical Acta*, vol. 545, pp. 180–186, 2012.
- [11] P. C. Mukesh Kumar, J. Kumar, S. Sendhilnathan, R. Tamilarasan, and S. Suresh, "Heat transfer and pressure drop analysis of Al₂O₃nanofluid as coolant in-shell and helically coiled tube heat exchanger," *Bulgarian Chemical Communications*, vol. 46, no. 4, pp. 743–749, 2014.
- [12] K. Jayappa, V. Kumar, and G. G. Purushotham, "Effect of reinforcements on mechanical properties of nickel alloy hybrid metal matrix composites processed by sand mold technique," *Applied Science and Engineering Progress*, vol. 14, no. 1, pp. 44–51, 2020.
- [13] V. Kumaresan, S. M. A. Khader, S. Karthikeyan, and R. Velraj, "Convective heat transfer characteristics of CNT nanofluids in a tubular heat exchanger of various lengths for energy efficient cooling/heating system," *International Journal of Heat and Mass Transfer*, vol. 60, pp. 413–421, 2013.
- [14] R. Mondragon, C. Segarra, J. C. Jarque, J. E. Julia, L. Hernandez, and R. Martinez-Cuenca, "Characterization of Physical Properties of Nanofluids for Heat Transfer Application," *IOP Journal of Physics: Conference Series*, vol. 395, article 012017, 2012.
- [15] P. Estelle, S. Halefadl, and T. Mare, "Thermophysical Properties and Heat Transfer Performance of Carbon Nanotubes Water-Based Nanofluids," *Journal of Thermal Analysis and Calorimetry*, vol. 127, no. 3, pp. 2075–2081, 2017.

- [16] K. Elsaid, M. A. Abdelkareem, H. M. Maghrabie et al., "Thermophysical properties of graphene-based nanofluids," *International Journal of Thermofluids*, vol. 10, article 100073, 2021.
- [17] N. K. Gupta, S. Mishra, A. K. Tiwari, and S. K. Ghosh, "A review of thermophysical properties of nanofluids," *Materials Today: Proceedings*, vol. 18, pp. 968–978, 2019.
- [18] V. Ding, V. Alias, D. Wen, and R. A. Williams, "Heat transfer of aqueous suspensions of carbon nanotubes (CNT nanofluids)," *International Journal of Heat and Mass Transfer*, vol. 49, no. 1–2, p. 240, 2006.
- [19] S. Z. Heris, S. G. Etemad, and M. N. Esfahany, "Experimental investigation of oxide nanofluids laminar flow convective heat transfer," *International Communications in Heat and Mass Transfer*, vol. 33, no. 4, pp. 529–535, 2006.
- [20] Y. Jin, H. Chen, Y. Ding, and D. Cang, "Heat transfer and flow behaviour of aqueous suspensions of TiO_2 nanoparticles (nanofluids) flowing upward through a vertical pipe," *International Journal of Heat and Mass Transfer*, vol. 50, no. 11–12, pp. 2272–2281, 2007.
- [21] C. H. Li and G. P. Peterson, "Experimental investigation of temperature and volume fraction variations on the effective thermal conductivity of nanoparticle suspensions (nanofluids)," *Journal of Applied Physics*, vol. 99, no. 8, article 084314, 2006.
- [22] C. T. Nguyen, G. Ro, C. Gauthier, and N. Galanis, "Heat transfer enhancement using Al_2O_3 -water nanofluid for an electronic liquid cooling system," *Applied Thermal Engineering*, vol. 27, no. 8–9, pp. 1501–1506, 2007.
- [23] B. C. Pak and Y. I. Cho, "Hydrodynamic and heat transfer study of dispersed fluids with submicron metallic oxide particles," *Experimental Heat Transfer: An International Journal*, vol. 11, no. 2, pp. 151–170, 1998.
- [24] L. Syam Sundar, M. T. Naik, K. V. Sharma et al., "Experimental investigation of forced convection heat transfer and friction factor in a tube with Fe_3O_4 magnetic nanofluid," *Experimental Thermal and Fluid Science*, vol. 37, pp. 65–71, 2012.
- [25] C. Y. Tsai, H. T. Chien, P. P. Ding, B. Chan, and T. Y. Luh, "Effect of structural character of gold nanoparticles in nanofluid on heat pipe thermal performance," *Materials Letters*, vol. 58, no. 9, pp. 1461–1465, 2004.
- [26] W. Duangthongsuk and S. Wongwises, "Heat transfer enhancement and pressure drop characteristics of TiO_2 -water nanofluid in a double-tube counter flow heat exchanger," *International Journal of Heat and Mass Transfer*, vol. 52, no. 7–8, pp. 2059–2067, 2009.
- [27] D. Wen and Y. Ding, "Experimental investigation into convective heat transfer of nanofluids at the entrance region under laminar flow conditions," *International Journal of Heat and Mass Transfer*, vol. 47, no. 24, pp. 5181–5188, 2004.
- [28] Y. Yang, Z. G. Zhang, E. A. Grulke, W. B. Anderson, and G. Wu, "Heat transfer properties of nanoparticle-in-fluid dispersions (nanofluids) in laminar flow," *International Journal of Heat and Mass Transfer*, vol. 48, no. 6, pp. 1107–1116, 2005.

Research Article

Synthesis and Applications of Green Synthesized TiO₂ Nanoparticles for Photocatalytic Dye Degradation and Antibacterial Activity

Annin K. Shimi ¹, **Hiwa M. Ahmed** ^{2,3}, **Muhammad Wahab**⁴, **Snehlata Katheria**⁵, **Saikh Mohammad Wabaidur**⁶, **Gaber E. Eldesoky**^{6,7}, **Md Ataul Islam**⁷, and **Kantilal Pitamber Rane**⁸

¹Department of Physics, Manonmaniam Sundaranar University, Tirunelveli, Tamilnadu-627012, India

²Sulaimani Polytechnic University, Slemani, 46001 Kurdistan Region, Iraq

³Department of Horticulture, University of Raparin, Ranya, Kurdistan Region, Iraq

⁴Food Science and Quality Control Department, College of Agricultural Engineering Science, University of Sulaimani, Slemani, Kurdistan Region, Iraq

⁵Department of Chemistry, University of Lucknow, Lucknow-226007, Uttar Pradesh, India

⁶Department of Chemistry, College of Science, King Saud University, Riyadh-11451, Saudi Arabia

⁷Division of Pharmacy and Optometry, School of Health Sciences, Faculty of Biology, Medicine and Health, University of Manchester, Manchester, UK

⁸Electronics and Communication Engineering Department, KL University, Hyderabad, India

Correspondence should be addressed to Hiwa M. Ahmed; hiwa2009@yahoo.com

Received 2 January 2022; Revised 27 January 2022; Accepted 14 February 2022; Published 2 March 2022

Academic Editor: Wenhui Zeng

Copyright © 2022 Annin K. Shimi et al. This is an open access article distributed under the Creative Commons Attribution License, which permits unrestricted use, distribution, and reproduction in any medium, provided the original work is properly cited.

Metal oxide photocatalyst is one of the promising photocatalysts in the water remediation process. The present work is aimed at synthesizing the green production of TiO₂ (G-TiO₂) nanoparticles from mulberry plant extract. Plant phytochemicals serve a different role to produce the nanophase particles. The bioreductant is safer and noxious free compound for synthesizing the G-TiO₂ nanoparticles. The synthesized G-TiO₂ nanoparticles in anatase phase and their crystallite size of 24 nm were characterized from X-ray diffraction analysis. The Ti-O bonding and plant derivatives and their reduction were confined from FTIR analysis. The wide bandgap of G-TiO₂ nanoparticles (3.16 eV) and their optical characterization were captured from UV-DRS analysis. The spherical surface morphology and their Ti and O elemental configurations were characterized from FESEM with EDX technique. The photocatalytic dye degradation was examined against methylene blue dye, and their pseudo-first-order kinetics were evaluated. The cyclic experiments declared their catalytic potential. The bacterial resistance of G-TiO₂ nanoparticles was examined against gram-positive and gram-negative bacteria. Hence, the catalytic potential and bacterial stability of G-TiO₂ nanoparticles are the powerful candidate for water remediation and biomedical applications.

1. Introduction

The phrase “nanotechnology” refers to the design, manufacture, and application of functional structures with at least one characteristic dimension measured in nanometers [1]. Catalysis, optical, electric, and magnetic characteristics, diagnostics, biological probes, and display devices are all

areas where metal oxide nanoparticles have a lot of potentials [2]. Due to their simple production and eco-loving nature, there is no need of high-cost equipment setup. Recently, green production of nanomaterials was the focus of the researchers [3, 4]. Metallic nanoparticles are synthesized in two ways: top-down and bottom-up, via chemical, physical, and biological methods. The bottom-up technique

follows the combining of atoms to generate bulk nanoparticles, while the top-down method follows the method of transforming bulk materials to nanoparticles [5]. They have also been used as chemical reaction catalysts, biosensors, antioxidants, and DNA delivery. The peculiar properties of nanoparticles, such as their stability, catalytic activity, biocompatibility, high conductivity, and strong surface area-to-volume ratio, could be due to these diverse activities. Instead of the toxic materials used in chemical and physical synthesis, the green synthesis of nanomaterials utilizing plants/plant component extracts had played a vital role in the field of nanotechnology out of all the approaches enumerated. The green synthesis of NPs can be accomplished by using the metabolites of bacteria, fungi, yeast, algae, actinomycetes, and plants as reducing and capping agents. Green synthesis of nanoparticles has gotten more publicity, because of its low cost, simplicity, scalability, eco-friendliness, and the wide range of metabolites secreted by plants. Plant products such as leaves, bark, roots, stems, peels, and other biological resources are accessible in nature and could be used for the green production of nontoxic nanoparticles. Traditional Indian medical systems rely heavily on medicinal herbs. The importance of medicinal plants as a possible source of bioactive chemicals has been recognized in pharmacological investigations [6]. Medicinal plants have been discovered to be effective in the treatment of a variety of health issues over time. *Morus alba* Linnaeus is one of those species in the Moraceae family. The majority of the species are endemic to Asia, for which the environment is warm. It is used as traditional medicine and modern drug preparation, mainly constitutes diet for the silkworm [7, 8]. Phytochemicals are compounds found in medicinal plants, leaves, vegetables, and roots that act as a defense mechanism and provide protection against a variety of ailments. Primary and secondary compounds are referred to as phytochemicals. Primary ingredients include chlorophyll, proteins, and simple carbohydrates, whereas secondary chemicals include terpenoids, alkaloids, and phenolic chemicals. Many health concerns, such as cancer, heart disease, diabetes, and high blood pressure, are being pushed for the prevention and treatment of phytochemicals [9–12]. *Morus* plant has shown strong antifungal activities. *M. alba* has garnered great attention for its antioxidative and antidiabetic effects [13]. *M. alba* has antioxidant, antibacterial, antiviral, and anti-inflammatory properties [14, 15]. The mulberry extract using nanoparticles exhibited the enhanced bacterial activity [16–21]. The present work reports the green production of TiO_2 (G- TiO_2) nanoparticles and their bacterial activity and catalytic dye degradation activity.

2. Materials and Methods

2.1. Materials. Titanium tetra isopropoxide-Analytical Reagent (TTIP-AR) solution was purchased from Sigma Aldrich, India. The methylene blue dye was purchased from HiMedia, India. The fresh mulberry leaves were collected from Kanyakumari market, Tamilnadu, India. The procured materials were used without further modifications

to synthesize the nanoparticles, and the solvent is double distilled water.

2.2. Preparation of Mulberry Plant Extract. The collected fresh mulberry leaves (10 g) were washed with running water. The purified leaves were combined with 100 mL double distilled water. The combined compounds were heated by using magnetic stirrer at 100°C for 10 minutes, and the remaining impurities were removed by using Whatman No. 1 filter paper (HiMedia, Mumbai). The collected solutions were stored for refrigerator at 4°C for further analysis.

2.3. Nano Production of G- TiO_2 Nanoparticles. One molar concentration of TTIP solution was mixed with 10 mL mulberry plant extract to synthesize the G- TiO_2 nanoparticles. The combined solution was stirred by using magnetic stirrer at 80°C temperature and 800 rpm. The milk white precipitate was formed in 30 minutes, and the colour formations were evident of the nanophase materials. The white participate solutions were centrifuged at 15000 rpm for 10 minutes, and the same process was repeated for three times. The centrifuged samples were filtered by Whatman No. 1 filter paper. The collected samples were heated at 100°C for 1 hour. The dried samples were stored in desiccator for further characterizations.

2.4. Characterization of G- TiO_2 Nanoparticles. The crystalline structure and sizes were captured from X-ray diffractometer (PANalytical XPert-Cu $K\alpha$ radiation) worked in 30 KV and 40 mA. The plant compounds and their functional groups and metal bonding were derived from FTIR (Perkin Elmer) spectroscopy. The optical information was determined from UV-DRS (Shimadzu-2700) analysis. The surface shape and their exiting elements were characterized from FESEM with EDX (Carl Zeiss) analysis.

2.5. Antibacterial Activity. The synthesized G- TiO_2 nanoparticle bacterial activities were evaluated by using gram-positive *Staphylococcus aureus* (ATCC 6538) and gram-negative *Escherichia coli* (ATCC 8739) over the well diffusion method. The nutrient broth was inoculated by bacterial culture (10^6 CFU/mL), and inoculated suspensions were incubated for 24 hours. The incubated suspensions were swabbed over the Mueller-Hinton-mediated petri plates. The gel puncture was used to make the well about 5 mm on agar-mediated petri plates, and the same concentrations (20 $\mu\text{g}/\text{ml}$) were put it over the well. The loaded petri plates were incubated for overnight at 37°C. Finally, the incubated samples exhibited the zones around the well. The bacterial inactivity was measured by zone of inhibitions in the range of millimeter scale. The bacterial inactivity of G- TiO_2 nanoparticles was compared with the same concentration of mulberry plant extract and antibiotic drug (gentamycin-SD195 Gentamicin, 120 micrograms).

2.6. Photocatalytic Activity. The photocatalytic activity of synthesized G- TiO_2 nanoparticles was evaluated by methylene blue dye under UV light irradiation (wavelength = 300 nm). 10 ppm dye solution was used in the catalytic activity. The 100 mL MB dye solution was mixed with 10 mg

nanocatalyst of G-TiO₂ nanoparticles. The combined catalyst solution was stirred under dark condition by using magnetic stirrer. The dark conditions help to achieve the adsorption-desorption equilibrium position. The combined solutions were kept in a UV chamber and light irradiated for 120 minutes. For the periodic intervals (30 minutes), the irradiated solution was taken out for 5 mL to measure the degradation efficiency. The collected dye solutions were centrifuged at 10000 rpm for 5 minutes to eliminate the unwanted elements and nanocatalyst. The centrifuged samples were measured for UV-Visible spectroscopy. The same working procedure was followed by reusability analysis. The dye degradation efficacy was characterized from below mentioned equation as follows:

$$\text{Photocatalytic dye degradation (\%)} = \frac{(C_0 - C_t)}{C_0} \times 100, \quad (1)$$

where the initial dye concentration is C₀ (without UV light irradiation) and the concentration of the dye at different UV light irradiation time is C_t. The free radicals and holes are measured from the quenching experiment. The p-benzoquinone (BQ) was used to determine the superoxide ion activity, isopropyl alcohol (IPA) was used to find the hydroxyl activity, and triethanolamine (TEOA) was used to analyze the hole activity in the catalytic activity. These compounds restrict the free radicals, holes, and superoxides, and their concentration is 1 mmol/L.

3. Results and Discussion

3.1. XRD Analysis. The phase, purity, and structural average crystallite size values of amalgamated G-TiO₂ nanoparticles were observed by the XRD pattern exhibited in Figure 1. The X-ray diffraction peaks examined at 25.38°, 37.97°, 48.14°, 54.40°, 55.20°, 62.71°, 68.51°, 71.71°, and 75.30° correspond to Miller index (hkl) value of (101), (004), (200), (105), (211), (118), (116), (220), and (315), respectively. The collected outcomes were verified utilizing JCPDS Card No. 78-2486 (Joint Committee on Powder Diffraction Standards) [22]. The photocatalytic activity is improved by the crystallinity of the nanoparticles, as evidenced by a strong peak. The regular crystalline size of the particle was evaluated utilizing Debye Scherrer's equation is given by $D = 0.89\lambda/\beta \cos \theta$ [23]. To evaluate the crystalline size, the (101) plane was selected. The as-prepared TiO₂ nanoparticles elicited utilizing mulberry solution had an average crystalline size of approximately 22 nm, which was measured by repeating the experiment 3 times with standard deviation (SD) value ± 0.024 . The surface area [23] of the catalyst is $7.33 (\times 10^5 \text{ g/cm}^2)$. As an outcome, it is determined that TiO₂ nanoparticles possess a tremendous surface area and dye molecules on their surface, which might be responsible for occurring in better photocatalytic performance.

3.2. FTIR Analysis. Figure 2 shows the FTIR spectra of G-TiO₂ nanoparticles synthesized from mulberry plant extract green chemical-reduction method. The strong absorption peak at 1633 cm^{-1} and 3428 cm^{-1} is responsible for the OH

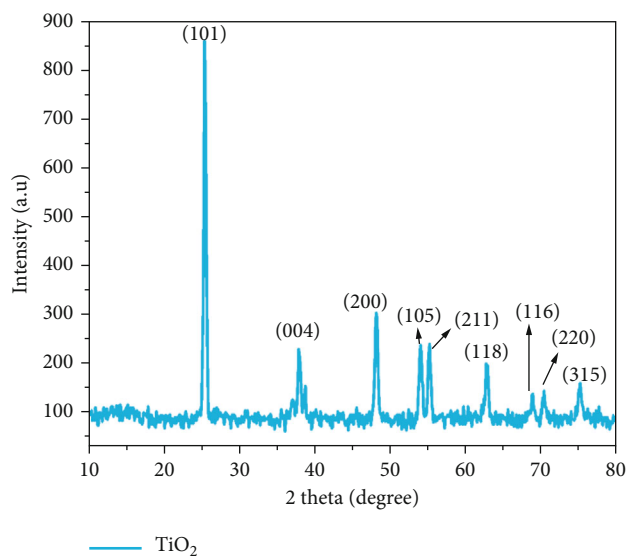


FIGURE 1: XRD diffraction pattern of synthesized G-TiO₂ nanoparticles.

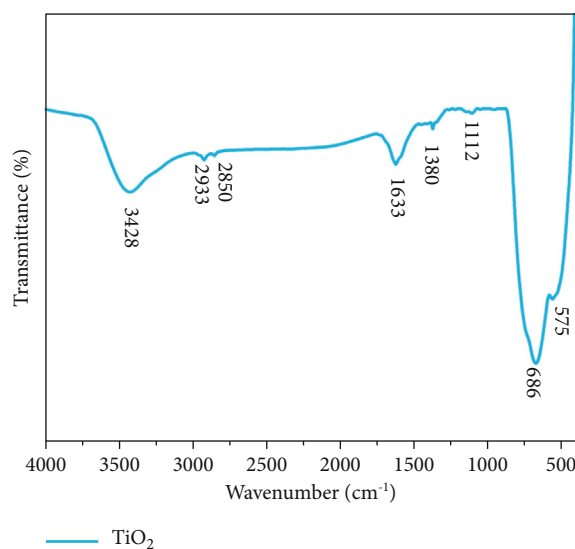


FIGURE 2: FTIR spectrum of synthesized G-TiO₂ nanoparticles.

groups [24]. The peaks which are 2933 cm^{-1} and 2850 cm^{-1} attribute the C-H stretching which confirmed the organic compound reduction from the surface [25]. The peak at 1380 cm^{-1} represents the plant biocompounds and their C-C bond stretching and C-O bond stretching from the plant extract [26]. The metal-oxygen peak at 686 cm^{-1} represents O-Ti-O bonding in cationic anatase phase [27]. The plant extract and metallic peaks responsible for band assignment were derived from FTIR analysis. The phenolic compounds from the plant extract serve a bioreductant to synthesis G-TiO₂ nanoparticles.

3.3. UV-DRS Analysis. The green production of G-TiO₂ nanoparticle optical endurance was measured from UV-DRS analysis. The optical absorption edge is located at

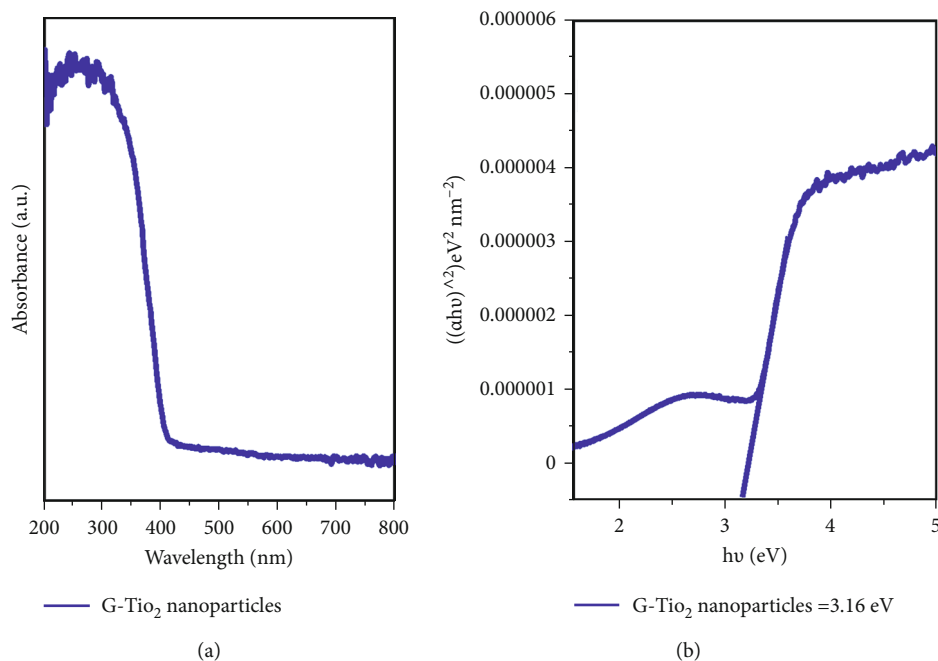


FIGURE 3: (a) UV-DRS absorption and (b) bandgap energy spectrum of synthesized G-TiO₂ nanoparticles.

around 398 nm (Figure 3(a)) which acknowledges the transition of electrons from valence band to conduction band (O-2p to Ti-3d) [28]. The high valency Ti-3d orbitals were suppressed by 2-p orbitals from oxide compounds. The photoexcited electrons and electrons are recombined each other. The excited electrons were restricted by oxide compounds, and their recombination was suppressed. The charge transformation decreased the recombination activity and extended their life time [29]. These activities increase the light absorption activity. The optical bandgap energy was detected from the Kubelka-Munk equation. The obtained bandgap values are displayed in Figure 3(b). The wide bandgap of G-TiO₂ nanoparticles restricts the charge carriers and promotes the carrier production. The separated charge carriers promote the extension of e-h pair activity. The wide bandgap is one of the key factors for better photocatalytic activity. The suppressed charge carriers increased the reactive oxygen species and hydroxyl radical formations [30]. These productions promote the reduction of pollution from environment through the photocatalysis and bacterial degradation activity.

3.4. FESEM with EDX Analysis. Figure 4 displays the FESEM images and EDX values of G-TiO₂ nanoparticles. The size, shape, and elemental compositions were captured from FESEM analysis. The FESEM images of G-TiO₂ nanoparticles showed a spherical shape and conjoint spherical shapes with the size of 24 nm. The spherical shape is one of the largest surface area shapes than another nanostructure [31]. The conjoint spherical shapes are attained from the plant extract on the surface G-TiO₂ nanoparticles. The excessive amount of plant extracts was reassured from FTIR spectroscopy. The title materials were identified from EDX analysis shown in Figures 4(c) and 4(d). The EDX spectrum derived the Ti

and O peaks with respect to the energy levels. The Ti has major peaks than O. The atomic and weight percentage of G-TiO₂ nanoparticles represent the Ti and O. The O presence is very important for radical formation. The formed radicals are broadly applicable in biological and water remediation process.

3.5. Antibacterial Activity. Figure 5 represents the antibacterial activity of G-TiO₂ nanoparticles. The bacterial inactivity was measured by zone of inhibitions which is displayed in Figure 5. The antibacterial activity of G-TiO₂ nanoparticles against gram-positive (*S. aureus*) and gram-negative (*E. coli*) bacterial strains was compared with antibiotic drug gentamycin and mulberry plant extract. The G-TiO₂ nanoparticles own the high valency Ti³⁺ and dissolved oxygen compounds which can restrict the cell production. The dissolved oxygen provokes the free radical generation and superoxide formation [32–34]. These actions can disconnect the electron transfer to the cell system. The disconnected electron supply miscommunicates the cell production which can lead a cell demise. The gram-positive bacterial strain is more sensitive than gram-negative bacteria due to their weak cell wall membrane.

3.6. Photocatalytic Activity. A significant quantity of trash is created throughout numerous dyeing and finishing operations. Humans, microbes, and aquatic species are all poisoned by dye-containing discharge pollutants. When these colours are released into rivers or lakes, they create unsightly pollution, physiologically increasing eutrophication, toxicity, and disruption in aquatic life. Traditional water treatments are not completely degrading the dyes because such colours are chemically stable [35–37].

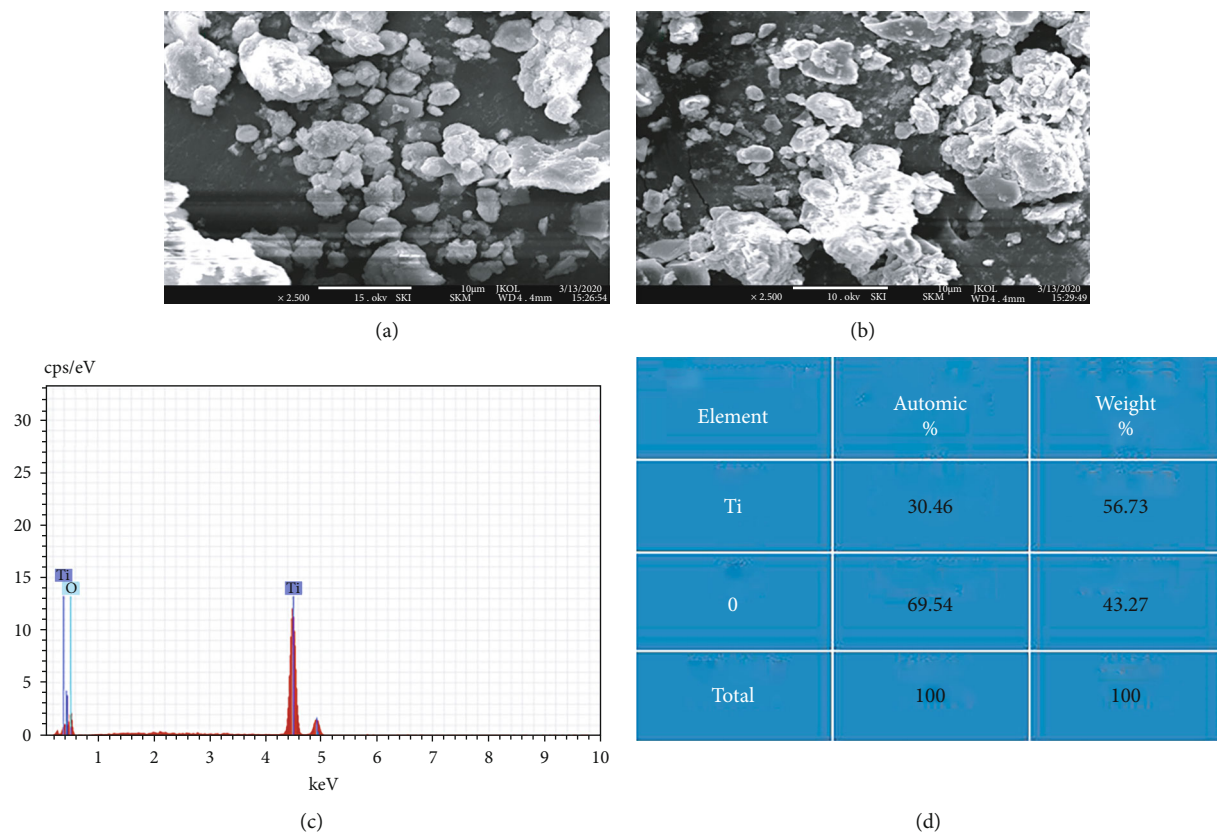


FIGURE 4: (a, b) FESEM images, (c) EDX spectra, and (d) EDX table of the G-TiO₂ nanoparticles.

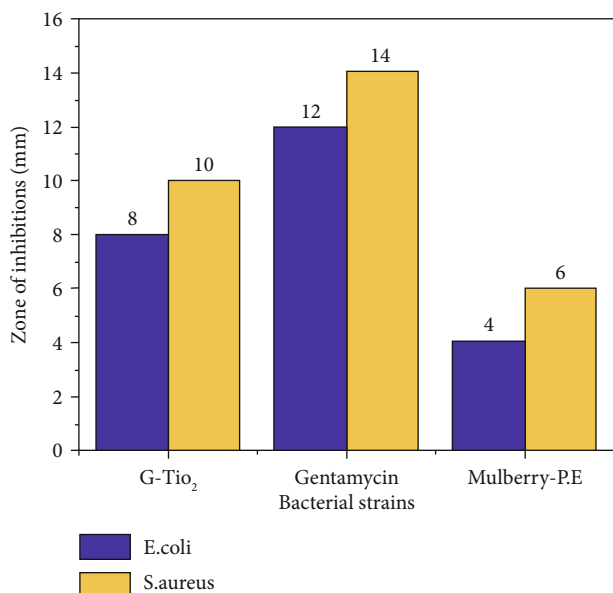


FIGURE 5: Antibacterial activity of synthesized G-TiO₂ nanoparticles.

The UV light-irradiated MB dye degradation spectrum is shown in Figure 6. The dye degradation without catalyst is shown in Figure 6(a). The degradation is 6% which is very lower degradation efficiency. The catalytic degradation efficiency was found to be very high from 0 min to 30 min and reached to a maximum of 96% at 120 min due to the

presence of G-TiO₂ nanoparticles (Figure 6(b)). It might be due to the huge surface area of the materials [25–29]. The C/C₀ spectrum and pseudo-first-order kinetics spectrum show the catalytic activity of G-TiO₂ nanoparticles in Figures 6(b)–6(d). For improved oxidative breakdown of colours in wastewater, a UV radiation combination has been applied. UV reactions degrade the chromophoric structure of such dyes, resulting in complete decolourization. The superoxides have more power than the holes and hydroxyl ions which is displayed in Figure 6(e). The O₂^{•-} molecules strongly degrade the MB dye molecules and holes and hydroxyl radical are associated part in the catalytic reaction of G-TiO₂ nanoparticles. The G-TiO₂ nanoparticles exhibit excellent catalytic activity due to their adsorbed O₂^{•-} which induced the catalytic stability. The recycle study inferred the catalytic stability and endurance of the G-TiO₂ nanoparticles (Figure 6(f)). When exposed to ultraviolet light, a photon of energy $h\nu$ is emitted; the photon of energy $h\nu$ greater than the band gap stimulates the electron (e⁻) from the valence band to the conduction band and leaves a hole (h⁺) on the valence band, resulting in the production of an electron-hole pair [35–39]. The OH* radical is formed when photogenerated holes on the valence band react with dyes or water attached to the surface. On the photocatalytic dye degradation process, such OH* free radicals are referred to as active species. At the adsorbed molecule, the electron on the conduction band interacts with oxygen to form the anionic superoxide radical O₂^{•-}. The anion O₂^{•-} does not contribute to the oxidation process any longer, but instead react

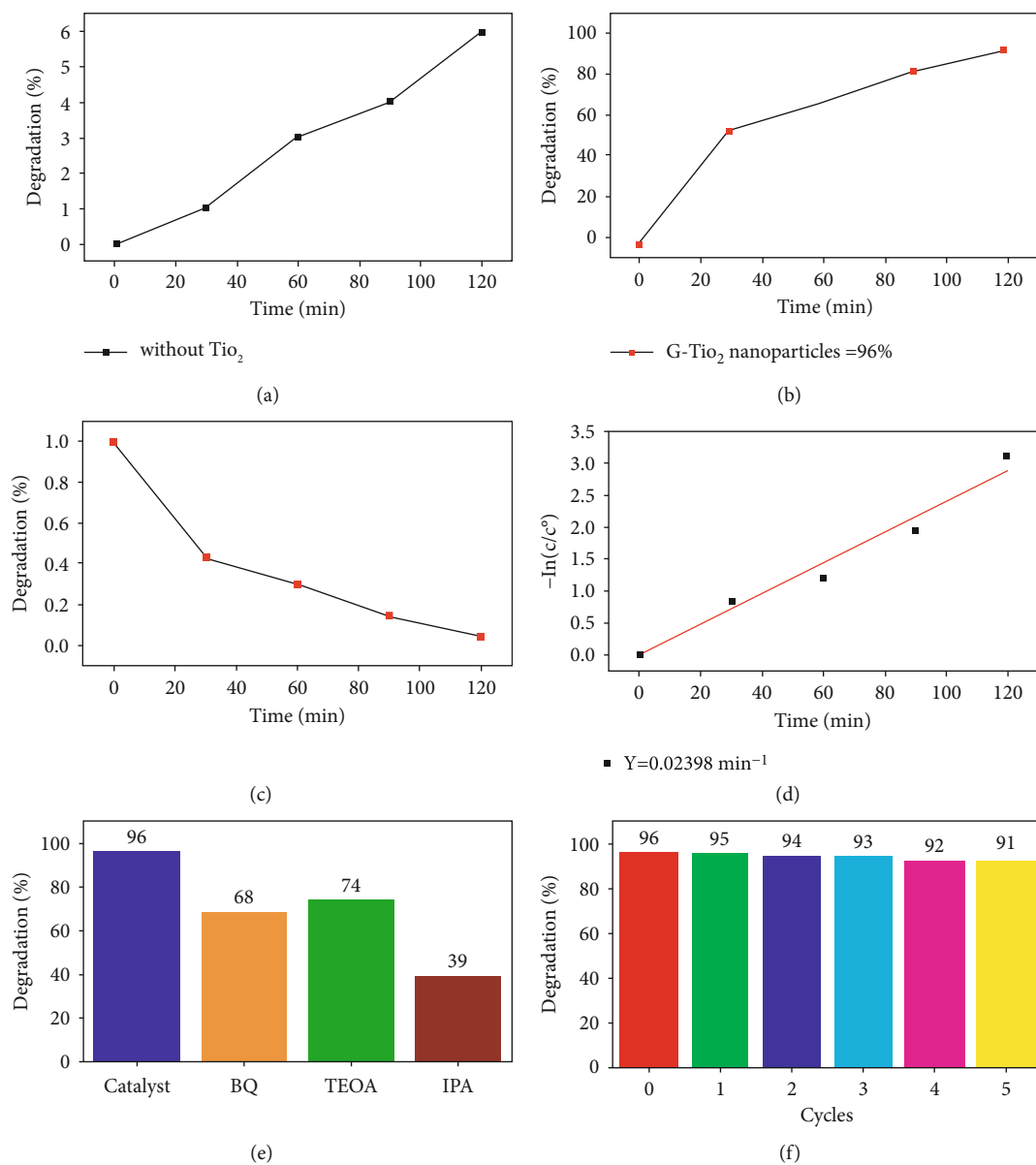


FIGURE 6: (a) Without catalyst dye degradation study, (b) degradation efficiency, (c) C/C_0 absorption rate, (d) photocatalytic degradation kinetics, (e) quenching experiment, and (f) recycle study of the synthesized G-TiO₂ nanoparticles.

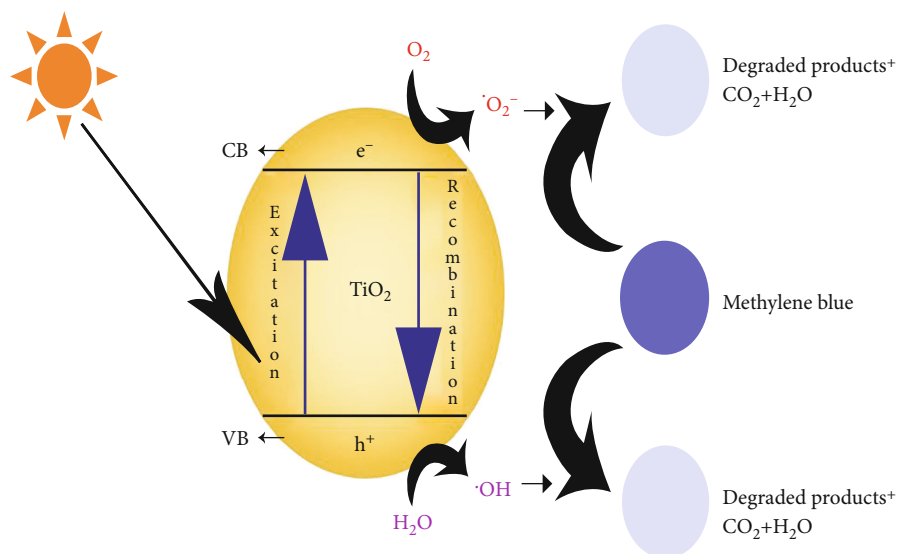


FIGURE 7: Photocatalysis mechanism for G-TiO₂ nanoparticles.

with H⁺ to produce H₂O₂. More trapped electrons are released, resulting in the formation of OH* free radicals. As a result, increasing the creation of electron-hole pairs maximizes the active organism's size and degradation performance [40–44]. The detailed mechanism is shown in Figure 7. The detailed mechanism was derived from the quenching analysis. The photocatalyst stability is displayed in Figure 6(f). According to the results of the current experiment, the performance of samples developed for degrading MB indicates that they can be effective photocatalyst and have an efficient reaction on the degradation of environmental contaminants.

4. Conclusion

The present work effectively synthesized the G-TiO₂ nanoparticles by using mulberry plant extract. The wide bandgap and anatase phase of nanoparticles confirmed the G-TiO₂ nanoparticles. The methylene blue degradation under ultraviolet illumination in 120 minutes exhibited the 96% degradation. The pseudo-first-order kinetics (0.02398 min⁻¹) revealed the catalytic performance of the G-TiO₂ nanoparticles. The reusability of the G-TiO₂ nanoparticles showed the catalytic stability in 5 cycles. The bacterial activity of G-TiO₂ nanoparticles revealed the enriched bacterial sensitiveness against the *S. aureus* bacterial strain. The green nanoproduction is ecological friendly production method, and chemical-free secondary products are released in the outlet. Based on the attained findings, the synthesized G-TiO₂ nanoparticles are suitable for photocatalytic application and microbial resistance-oriented devices.

Data Availability

All research data used to assist the findings of this work are included within the manuscript.

Conflicts of Interest

The authors have no conflict of interests.

Acknowledgments

Authors are grateful to the Researchers Supporting Project No. (RSP-2021/161), King Saud University, Riyadh, Saudi Arabia.

References

- [1] A. Jalill, D. H. Raghad, R. S. Nuaman, and A. N. Abd, "Biological synthesis of titanium dioxide nanoparticles by *Curcuma longa* plant extract and study its biological properties," *World Scientific News*, vol. 49, no. 2, pp. 204–222, 2016.
- [2] R. Subbaiya, R. S. Lavanya, K. Selvapriya, and M. M. Selvam, "Green synthesis of silver nanoparticles from *Phyllanthus amarus* and their antibacterial and antioxidant properties," *International Journal of Current Microbiology and Applied Sciences*, vol. 3, no. 1, pp. 600–606, 2014.
- [3] N. I. Rasli, H. Basri, and Z. Harun, "Zinc oxide from aloe vera extract: two-level factorial screening of biosynthesis parameters," *Heliyon*, vol. 6, no. 1, 2020.
- [4] G. Tailor, B. L. Yadav, J. Chaudhary, M. Joshi, and C. Suvalka, "Green synthesis of silver nanoparticles using *Ocimum canum* and their anti-bacterial activity," *Biochemistry and Biophysics Reports*, vol. 24, 2020.
- [5] M. S. Chavali and M. P. Nikolova, "Metal oxide nanoparticles and their applications in nanotechnology," *SN applied sciences*, vol. 1, no. 6, pp. 1–30, 2019.
- [6] K. Mallikarjuna, S. V. P. Vattikuti, R. Manne et al., "Sonochemical synthesis of silver quantum dots immobilized on exfoliated graphitic carbon nitride nanostructures using ginseng extract for photocatalytic hydrogen evolution, dye degradation, and antimicrobial studies," *Nanomaterials*, vol. 11, no. 11, 2021.
- [7] M. S. Butt, A. Nazir, M. T. Sultan, and K. Schroën, "*Morus alba* L. nature's functional tonic," *Trends in Food Science & Technology*, vol. 19, no. 10, pp. 505–512, 2008.

- [8] C. C. Chen, L. K. Liu, J. D. Hsu, H. P. Huang, M. Y. Yang, and C. J. Wang, "Mulberry extract inhibits the development of atherosclerosis in cholesterol-fed rabbits," *Food Chemistry*, vol. 91, no. 4, pp. 601–607, 2005.
- [9] H. M. Ahmed, A. Roy, M. Wahab et al., "Applications of nanomaterials in agri food and pharmaceutical industry," *Journal of Nanomaterials*, vol. 2021, Article ID 1472096, 10 pages, 2021.
- [10] H. M. Ahmed, S. Nabavi, and S. Behzad, "Herbal drugs and natural products in the light of nanotechnology and nanomedicine for developing drug formulations," *Mini Reviews in Medicinal Chemistry*, vol. 21, no. 3, pp. 302–313, 2021.
- [11] A. Roy, H. C. Ananda Murthy, H. M. Ahmed, M. N. Islam, and R. Prasad, "Phytogenic synthesis of metal/metal oxide nanoparticles for degradation of dyes," *Journal of Renewable Materials*, vol. 2021, 2021.
- [12] R. Verma, A. Rawat, S. A. Ganie et al., "In vitro antibacterial activity of Cichorium intybus against some pathogenic bacteria," *British Journal of Pharmaceutical Research*, vol. 3, no. 4, p. 767, 2013.
- [13] S. Ahmad, R. Sharma, S. Mahajan, and A. Gupta, "Antibacterial activity of Celtis australis by invitro study," *International Journal of Pharmacy and Pharmaceutical Sciences*, vol. 4, 2012.
- [14] K. O. Chung, B. Y. Kim, M. H. Lee et al., "In-vitro and in-vivo anti-inflammatory effect of oxyresveratrol from Morus alba L.," *Journal of Pharmacy and Pharmacology*, vol. 55, no. 12, pp. 1695–1700, 2003.
- [15] H. A. El-Beshbishy, A. N. B. Singab, J. Sinkkonen, and K. Pihlaja, "Hypolipidemic and antioxidant effects of Morus alba L. (Egyptian mulberry) root bark fractions supplementation in cholesterol-fed rats," *Life Sciences*, vol. 78, no. 23, pp. 2724–2733, 2006.
- [16] S. P. R. Mallem, M. Koduru, K. Chandrasekhar et al., "Potato chip-like 0D interconnected ZnCo2O4 nanoparticles for high-performance supercapacitors," *Crystals*, vol. 11, no. 5, p. 469, 2021.
- [17] S. Some, B. Sarkar, K. Biswas et al., "Bio-molecule functionalized rapid one-pot green synthesis of silver nanoparticles and their efficacy toward the multidrug resistant (MDR) gut bacteria of silkworms (Bombyx mori)," *RSC Advances*, vol. 10, no. 38, pp. 22742–22757, 2020.
- [18] L. N. Liem and D. Nguyen, "Microwave assisted green synthesis of silver nanoparticles using mulberry leaves extract and silver nitrate solution," *Technologies*, vol. 7, no. 1, p. 7, 2019.
- [19] J. Singh, N. Singh, A. Rathi, D. Kukkar, and M. Rawat, "Facile approach to synthesize and characterization of silver nanoparticles by using mulberry leaves extract in aqueous medium and its application in antimicrobial activity," *Journal of Nanostructures Spring*, vol. 7, no. 2, pp. 134–140, 2017.
- [20] A. M. Awwad and N. M. Salem, "Green synthesis of silver nanoparticles by Mulberry leaves extract," *Nanoscience and Nanotechnology*, vol. 2, no. 4, pp. 125–128, 2012.
- [21] L. Xu, W. Li, Q. Shi et al., "Synthesis of mulberry leaf extract mediated gold nanoparticles and their ameliorative effect on Aluminium intoxicated and diabetic retinopathy in rats during perinatal life," *Journal of Photochemistry and Photobiology B: Biology*, vol. 196, 2019.
- [22] G. Ma, X. Chai, G. Hou, F. Zhao, and Q. Meng, "Phytochemistry, bioactivities and future prospects of mulberry leaves: a review," *Food Chemistry*, vol. 372, 2022.
- [23] B. Liu, H. Zhao, X. Li, Z. Yang, D. Zhang, and Z. Liu, "Effect of pore structure on the thermophysical and frictional properties of high-density graphite," *Microporous and Mesoporous Materials*, vol. 330, 2022.
- [24] R. Rajendhiran, V. Deivasigamani, J. Palanisamy, S. Masan, and S. Pitchaiya, "Terminalia catappa and carissa carandas assisted synthesis of TiO₂ nanoparticles - A green synthesis approach," *Materials Today: Proceedings*, vol. 45, pp. 2232–2238, 2021.
- [25] Y. Cao, P. Wang, J. Fan, and H. Yu, "Covalently functionalized graphene by thiourea for enhancing H₂-evolution performance of TiO₂ photocatalyst," *Ceramics International*, vol. 47, no. 1, pp. 654–661, 2021.
- [26] Z. Zhang, Y. M. K. Bader, J. Yang, and L. A. Lucia, "Simultaneously improved chitin gel formation and thermal stability promoted by TiO₂," *Journal of Molecular Liquids*, vol. 328, 2021.
- [27] J. George, C. C. Gopalakrishnan, P. K. Manikuttan, K. Mukesh, and S. Sreenish, "Preparation of multi-purpose TiO₂ pigment with improved properties for coating applications," *Powder Technology*, vol. 377, pp. 269–273, 2021.
- [28] E. M. Hussein, W. M. Desoky, M. F. Hanafy, and O. W. Guirguis, "Effect of TiO₂ nanoparticles on the structural configurations and thermal, mechanical, and optical properties of chitosan/TiO₂ nanoparticle composites," *Journal of Physics and Chemistry of Solids*, vol. 152, 2021.
- [29] G. Li, Y. Sun, Q. Zhang, Z. Gao, W. Sun, and X. Zhou, "Ag quantum dots modified hierarchically porous and defective TiO₂ nanoparticles for improved photocatalytic CO₂ reduction," *Chemical Engineering Journal*, vol. 410, 2021.
- [30] H. Khalid, H. Iqbal, R. Zeeshan et al., "Silk fibroin/collagen 3D scaffolds loaded with TiO₂ nanoparticles for skin tissue regeneration," *Polymer Bulletin*, vol. 78, no. 12, pp. 7199–7218, 2021.
- [31] Y. Sun, G. Li, Y. Gong, Z. Sun, H. Yao, and X. Zhou, "Ag and TiO₂ nanoparticles co-modified defective zeolite TS-1 for improved photocatalytic CO₂ reduction," *Journal of Hazardous Materials*, vol. 403, 2021.
- [32] R. Aswini, S. Murugesan, and K. Kannan, "Bio-engineered TiO₂ nanoparticles using Ledebouria revoluta extract: larvicidal, histopathological, antibacterial and anticancer activity," *International Journal of Environmental Analytical Chemistry*, vol. 101, no. 15, pp. 2926–2936, 2021.
- [33] K. S. Khashan, G. M. Sulaiman, F. A. Abdulameer et al., "Antibacterial activity of TiO₂ nanoparticles prepared by one-step laser ablation in liquid," *Applied Sciences*, vol. 11, no. 10, p. 4623, 2021.
- [34] R. Kaur, A. Kaur, R. Kaur et al., "Cu-BTC metal organic framework (MOF) derived Cu-doped TiO₂ nanoparticles and their use as visible light active photocatalyst for the decomposition of ofloxacin (OFX) antibiotic and antibacterial activity," *Advanced Powder Technology*, vol. 32, no. 5, pp. 1350–1361, 2021.
- [35] O. Ouerghi, M. H. Geesi, E. O. Ibnouf et al., "Sol-gel synthesized rutile TiO₂ nanoparticles loaded with cardamom essential oil: enhanced antibacterial activity," *Journal of Drug Delivery Science and Technology*, vol. 64, 2021.
- [36] J. Singh, S. Juneja, R. K. Soni, and J. Bhattacharya, "Sunlight mediated enhanced photocatalytic activity of TiO₂ nanoparticles functionalized CuO-Cu₂O nanorods for removal of methylene blue and oxytetracycline hydrochloride," *Journal of Colloid and Interface Science*, vol. 590, pp. 60–71, 2021.
- [37] S. Sagadevan, J. A. Lett, G. K. Weldegebrail et al., "Enhanced gas sensing and photocatalytic activity of reduced graphene

- oxide loaded TiO₂ nanoparticles,” *Chemical Physics Letters*, vol. 780, 2021.
- [38] K. N. Pandiyaraj, D. Vasu, R. Ghobeira et al., “Dye wastewater degradation by the synergetic effect of an atmospheric pressure plasma treatment and the photocatalytic activity of plasma-functionalized Cu–TiO₂ nanoparticles,” *Journal of Hazardous Materials*, vol. 405, 2021.
- [39] O. Kose, M. Tomatis, F. Turci et al., “Short preirradiation of TiO₂ nanoparticles increases cytotoxicity on human lung coculture system,” *Chemical Research in Toxicology*, vol. 34, no. 3, pp. 733–742, 2021.
- [40] N. R. Reddy, U. Bharagav, M. M. Kumari et al., “Inclusion of low cost activated carbon for improving hydrogen production performance of TiO₂ nanoparticles under natural solar light irradiation,” *Ceramics International*, vol. 47, no. 7, pp. 10216–10225, 2021.
- [41] A. C. Chu, R. S. Sahu, T. H. Chou, and Y. H. Shih, “Magnetic Fe₃O₄@TiO₂ nanocomposites to degrade bisphenol A, one emerging contaminant, under visible and long wavelength UV light irradiation,” *Journal of Environmental Chemical Engineering*, vol. 9, no. 4, 2021.
- [42] L. Goñi-Ciaurriz, M. Senosiain-Nicolay, and I. Vélaz, “Aging studies on food packaging films containing β-cyclodextrin-grafted TiO₂ nanoparticles,” *International Journal of Molecular Sciences*, vol. 22, no. 5, p. 2257, 2021.
- [43] N. Bono, F. Ponti, C. Punta, and G. Candiani, “Effect of UV irradiation and TiO₂-photocatalysis on airborne bacteria and viruses: an overview,” *Materials*, vol. 14, no. 5, p. 1075, 2021.
- [44] U. Mahanta, M. Khandelwal, and A. S. Deshpande, “TiO₂@SiO₂ nanoparticles for methylene blue removal and photocatalytic degradation under natural sunlight and low-power UV light,” *Applied Surface Science*, vol. 576, 2022.

Research Article

Probe Sonicated Synthesis of Bismuth Oxide (Bi_2O_3): Photocatalytic Application and Electrochemical Sensing of Ascorbic Acid and Lead

K. B. Kusuma ¹, M. Manju ², C. R. Ravikumar ¹, V. G. Dileepkumar ³,
A. Naveen Kumar ¹, Mysore Sridhar Santosh ^{3,4}, H. C. Ananda Murthy ⁵
and K. Gurushantha ⁶

¹Research Center, Department of Science, East West Institute of Technology, V.T.U., -91, Bangalore, India

²Department of Chemistry, Sri Krishna Institute of Technology, VTU, -90, Bangalore, India

³Coal to Hydrogen Energy for Sustainable Solutions (CHESS), CSIR-Central Institute of Mining & Fuel Research (CIMFR), Digwadih Campus, PO: FRI, Dhanbad - 828 108, Jharkhand, India

⁴Academy of Scientific and Innovative Research (AcSIR), Ghaziabad - 201002, Uttar Pradesh, India

⁵Department of Applied Chemistry, School of Applied Natural Science, Adama Science and Technology University, PO Box 1888, Adama, Ethiopia

⁶Department of Chemistry, M S Ramaiah Institute of Technology, MSR Nagar, Bengaluru-560054, India

Correspondence should be addressed to H. C. Ananda Murthy; anandkps350@gmail.com

Received 9 October 2021; Accepted 17 January 2022; Published 12 February 2022

Academic Editor: Gaurav Sharma

Copyright © 2022 K. B. Kusuma et al. This is an open access article distributed under the Creative Commons Attribution License, which permits unrestricted use, distribution, and reproduction in any medium, provided the original work is properly cited.

A simple and low-cost and highly calibrated probe sonication method was used to prepare bismuth oxide nanoparticles (Bi_2O_3 NPs). The formation of a well-crystalline sample at the end of the product has been further calcined at 600°C for 2 hrs. The powder X-ray diffraction (PXRD) patterns of the NPs substantiated the monoclinic structure (space group $\text{P}2_1/\text{c}$), and the average crystallite size was found to be 60 nm, which was also confirmed by transmission electron microscopic (TEM) studies. Scanning electron microscopic (SEM) images depicted highly porous Bi_2O_3 NPs with little agglomeration. Utilizing diffused reflectance spectra (DRS) data, the energy bandgap (E_g) value of 3.3 eV was deduced for Bi_2O_3 NPs, and their semiconductor behavior has been confirmed. Two dyes, methylene blue (MB) and acid green (AG) were utilized for degradation studies using Bi_2O_3 NPs under UV light irradiation (from 0 to 120 min). The photocatalytic degradation was found to be maximum for MB (93.45%) and AR (97.80%) dyes. Cyclic voltammetric (CV) and sensor studies using the electrochemical impedance spectroscopy (EIS) were performed. The specific capacitance value of 25.5 Fg^{-1} was deduced from the cyclic voltammograms of the Bi_2O_3 electrode in 0.1 N HCl with a scan rate of 10 to 50 mV/s. From the obtained EIS data, the Bi_2O_3 electrode showed pseudocapacitive characteristics. The prepared electrodes also exhibited high sensitivity towards the detection of ascorbic acid and lead. Hence, sonochemically synthesized Bi_2O_3 NPs are possibly hopeful for excellent photocatalytic and electrochemical sensing of biomolecules.

1. Introduction

With the rapid escalation of industrial activities by mankind, environmental remediation of pollutants has become an issue of global concern. Many industries such as textile, food processing, pharmaceuticals, tannery, papermaking, and electro-

plating are the source of dyes in the water bodies leading to the contamination of water [1, 2]. A significant amount of industrial waste is being released into the environment as the chemical industry grows, and this waste has a high likelihood of causing adverse reactions in human beings, such as immunological dysfunction and reproductive system abnormalities,

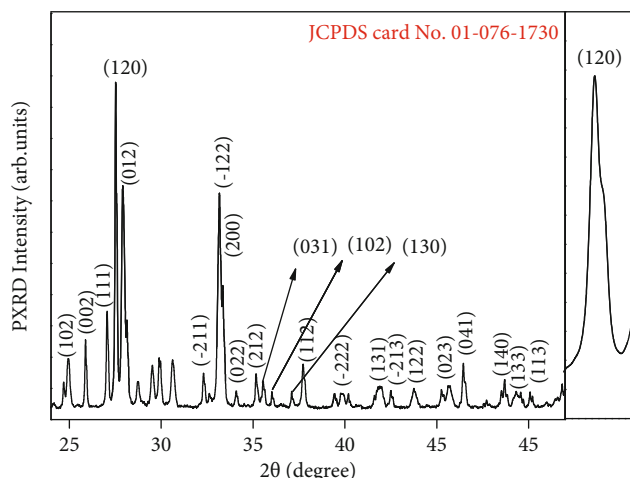


FIGURE 1: PXRD patterns of Bi_2O_3 NPs.

TABLE 1: FWHM values, d -spacing, and Miller indices for Bi_2O_3 .

Miller indices (hkl)	2θ (degree)	FWHM (degree)	d -spacing (nm)	Crystal size (nm)
102	24.9	0.17	0.43	55.78
002	25.8	0.20	0.37	52.00
120	27.5	0.13	0.33	65.78
012	27.9	0.15	0.39	53.13
-122	33.1	0.19	0.40	63.11
212	35.2	0.14	0.32	59.21
112	37.6	0.16	0.35	60.14
041	46.4	0.21	0.42	61.21

Average crystallite size = 58.79 nm.

as well as neurological and behavioral abnormalities. Because the therapy or cure for many diseases, such as diabetes, is still in the early stages of development, it is critical to control the living conditions associated with the disease. The monitoring of heavy metals such as lead and monitoring of the drug ascorbic acid is necessary to induce the welfare of humans as well as water bodies. As a result, the development of novel sensors for the detection of substances at trace quantities has emerged as a highly essential area of research. Electrochemical detection methods have a number of advantages over other conventional procedures. Electrochemical sensors are one of the fields that are growing at the fastest rate. Amperometric sensors use the voltage difference between a reference and an electrode to cause the oxidation or reduction of an electroactive species in a reaction [3–6]. A large number of nanometal oxides have been applied to degrade many pollutant dyes for many decades [7].

There are numerous transition metal oxides such as ZnO , Mn_2O_3 , Fe_3O_4 , TiO_2 , and Fe_2O_3 , which have been applied to degrade the plenty of dye molecules [8–11]. Each of these metal oxides exhibits good degradation efficiency, but still face serious drawbacks such as fast electron-hole recombination, agglomeration, and inefficient band gap values. Thus, to find an alternative metal oxide for the effective photocatalytic degradation, Bi_2O_3 has been chosen in this work due to its environmental friendly applications in

solid oxide fuel cells, gas sensors, photocatalyst, energy, and medicine [12–14]. It is well known that bismuth oxide has six polymorphic forms, denoted by α - Bi_2O_3 (monoclinic), β - Bi_2O_3 (tetragonal), δ - Bi_2O_3 (face-centered cubic), γ - Bi_2O_3 (body-centered cubic), φ - Bi_2O_3 (orthorhombic), and Bi_2O_3 (triclinic), respectively [15, 16]. Among them, α - and δ -phases are stable both at low temperatures as well as at higher temperatures, respectively, but the others remain in a metastable phase at high temperatures. Bi_2O_3 has a lot of peculiar physical and chemical properties, such as a wide energy gap change (from 2 to 3.96 eV), high metal oxide ion conductivity properties (1.0 s/cm), high refractive index, dielectric permittivity, addition to that, and excellent photo conductivities and photoluminescence properties [17, 18].

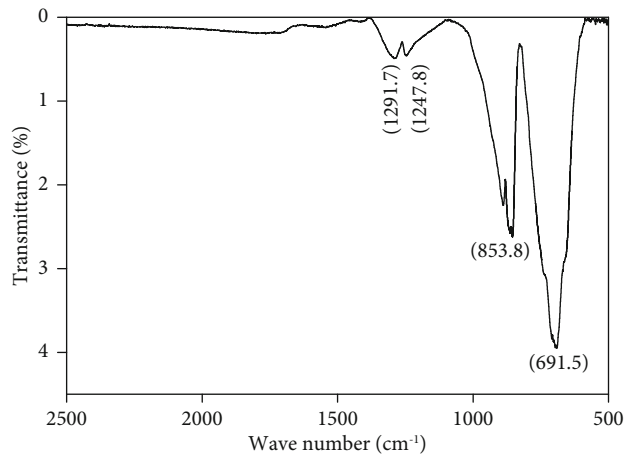
Modified nanoelectrodes have been utilized for the determination of paracetamol in pharmaceutical preparations including electrodeposition attachment of metal nanoparticles such as Au, Ru, and Cu. In addition, fullerene and carbon nanotube-based electrodes also showed high sensitivity with a low detection limit [19, 20]. Generally, the modification of the electrode is needed for a sensitive and selective determination of overdose levels of paracetamol in whole blood or urine samples [21–23]. Bismuth oxide NP modified carbon electrode has been employed for the determination of heavy metal ions present in drinking water, mineral water, and urine samples [24, 25]. The fabrication of chemically modified nanoelectrode (CMNE) has been widely used to improve the sensitivity and selectivity of amino acids, vitamins, drugs, DNA, and many more [26–28].

Many researchers have reported different methods for the synthesis of NPs, such as thermal decomposition using organic solvents which create hampers. The combustion method is one of the fast methods for the synthesis of NPs, but in the combustion method, it is difficult to control the agglomeration of the NPs. The other method for the fast and better yield is the coprecipitation method where there will be no control over the size distribution of the NPs. The probe-sonication method was proven to be the best due to its accuracy and capacity to form nanosized small particles. The synthesis of NPs by the application of ultrasonic waves exhibited various advantages like fast rate of reaction, high purity, and narrow distribution of particle sizes [29]. Several authors have reported the synthesis of many NPs through the sonochemical method.

In the present work, we aimed to synthesize Bi_2O_3 NPs by using the probe sonication method. This method is usually applied for the preparation of nanometal oxides. This method usually differs from other traditional procedures. In recent times, this method has also been applied to prepare binary metal oxides. Probe sonicationally synthesized powdered Bi_2O_3 nanomaterials using $\text{Bi}(\text{NO}_3)_3 \cdot 5\text{H}_2\text{O}$ offer many advantages like a good degree of crystallinity, well-established morphology, and high purity. After the calcination, the obtained pure powders of Bi_2O_3 NPs were characterized by the techniques like PXRD, FTIR, SEM, and TEM. To the best of our knowledge, no one has reported the improvement of electrocatalytic oxidation of paracetamol using nanoparticle bismuth oxide modified by graphite

TABLE 2: Estimated structural parameters of Bi₂O₃ NPs prepared from probe sonication method.

Plane for Bi ₂ O ₃	$\beta \times 10^{-3}$	D (nm)	d (nm)	$V \times 10^{-30} \text{ m}^3$	$n \times 10^{-21}$	$Dx \times 10^4$ (kgm ⁻³)	$\delta \times 10^{15}$ (kgm ⁻³) ⁻²	$\epsilon \times 10^{-3}$	E (GPa)	$\sigma \times 10^8$ (Pa)	SF
(120)	0.13	65.78	0.33	20.0	6.47	8.63	22.32	8.650	119.2	3.41	0.35

FIGURE 2: FT-IR spectrum of Bi₂O₃ NPs.

carbon electrode. The characterization of a known amount of Bi₂O₃ NPs that could catalyse the oxidation process of paracetamol in an acidic medium was investigated.

2. Experimental

2.1. Synthesis of Bismuth Oxide Nanoparticles (Bi₂O₃ NPs). The synthesis of Bi₂O₃ NPs by probe sonication method from the precursors, bismuth nitrate pentahydrate (Bi(NO₃)₃·5H₂O), and sodium hydroxide (NaOH) taken in the ratio of 1:2 was carried out with the support of ultrasound radiation. All the chemicals were used as received in analytical reagent (AR) grade. 1.0 M solution of bismuth nitrate pentahydrate (4.85 g) was added to a mixture of 5 mL of concentrated nitric acid (HNO₃) and 45 mL of deionized water with continuous stirring. Then, 0.5 M solution of sodium hydroxide (1 g) was added dropwise to the above precursor solution under stirring. This solution was bombarded with high-intensity ultrasound radiation at 40°C for 1 hr by using a microprocessor unit controlled ultrasonic probe of 13 mm diameter made up of high-grade titanium alloy (model PRO-550, 20 kHz, 500 W), operated at 20% amplitude, 20 kHz frequency with 100 W theoretical power dissipation [30]. On completion of the reaction process, a light yellow precipitate was formed. Then, the solution was centrifuged and the obtained precipitate was washed with distilled water and ethanol to remove excess NaOH. The precipitate was dried in a hot air oven at 100°C for 1 hr and calcined at 600°C for 2 hrs to get greenish coloured Bi₂O₃ NPs.

2.2. Instrumentation. The structural analysis, functional group analysis, morphological studies, and optical analysis were carried out using, X-ray diffractometer (Shimadzu) (CuK α -1.541 Å) with a scan rate of 20 per minute, Perkin

Elmer FTIR (Spectrum-1000) spectrometer in the range of 4000-400 cm⁻¹, JEOL transmission electron microscopy (TEM) (JEM-2100 (accelerating voltage up to 200 kV, LaB6 filament)), and Shimadzu UV-Vis spectrophotometer model 2600 in the range of 200-800 nm, respectively. The cyclic voltammetric and impedance measurements were executed on an electrochemical analyzer CHI608E potentiostat and in a tri-electrode system.

2.3. Preparation of an Electrode from Carbon Paste. The working electrode was made by blending Bi₂O₃ NPs with graphite powder (conducting carbon) and silicon oil (binder) in the weight ratio of 15:70:15 and made into a consistent slurry by physically grinding [31, 32]. Finely grounded material was filled into a teflon cavity tube (home-made) and confirming a fitted packing and the packed carbon paste surface was then smoothed.

3. Results and Discussion

3.1. Powder X-Ray Diffraction Studies. Figure 1 reveals the PXRD patterns of Bi₂O₃ NPs synthesized by the probe sonication method and calcined at 600°C for 2 hrs. The diffraction peaks appeared at 2 θ values of 24.9°, 25.8°, 27.4°, 27.9°, 33.1°, 35.2°, 37.6°, and 46.4° are correlated to (102), (002), (120), (012), (-122), (212), (112), and (041) planes which are very well indexed to monoclinic structure and in compliance with JCPDS card no. 01-076-1730 with phase group P2₁/c [33]. The lattice parameters were found to be; $a = 5.8499 \text{ \AA}$, $b = 8.1698 \text{ \AA}$, and $c = 7.5123 \text{ \AA}$ and $\alpha = 90^\circ$, $\beta = 112.988^\circ$, and $\gamma = 90^\circ$. From Debye-Scherrer's formula (equation (1)), the crystallite size of Bi₂O₃ NPs was deduced to be in the range between 55 and 60 nm (Table 1).

$$D = \frac{k\lambda}{\beta \cos \theta}, \quad (1)$$

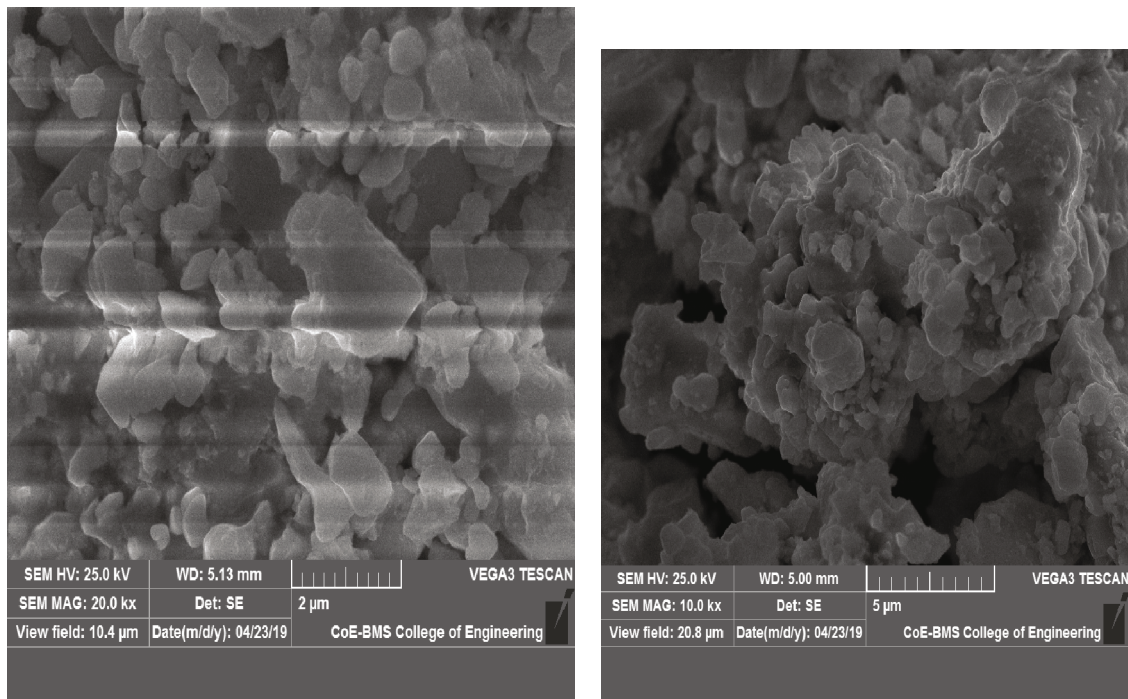
where β is full width at half maximum (FWHM) of the diffraction peak, λ is wavelength of X-ray (1.5418 Å), θ is Bragg's angle, and k is Scherrer's constant (0.88-0.92); the average value of 0.9 was used for the calculation.

The d -spacing can be deduced using the following equation

$$\frac{1}{d^2} = \frac{1}{\sin^2 \beta} \left[\frac{h^2}{a^2} + \frac{k^2 \sin^2 \beta}{b^2} + \frac{l^2}{c^2} - \frac{2hl \cos \beta}{ac} \right], \quad (2)$$

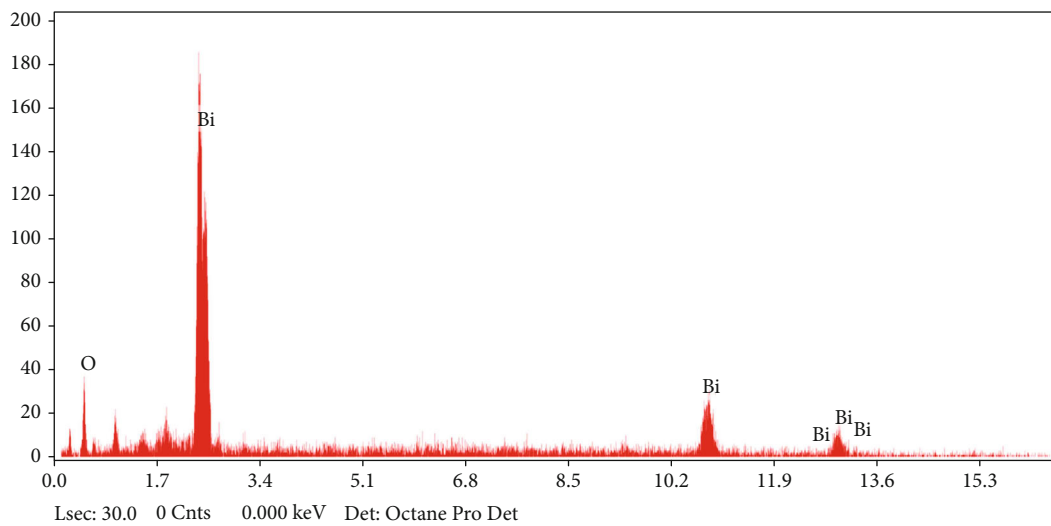
where a , b , and c are lattice parameters, (hkl) is Miller indices, and d_{hkl} is interplanar spacing for (hkl) .

FWHM values, crystallite sizes, d -spacing values, and Miller indices for Bi₂O₃ NPs obtained from the probe sonication method have been tabulated in Table 1.



(a)

(b)



(c)

FIGURE 3: (a) and (b) SEM images. (c) EDAX of Bi_2O_3 NPs.

TABLE 3: Compositional data obtained from EDAX.

Element	Weight %	Atomic %
O K	15.09	69.89
Bi L	84.91	30.11

Various other crystal parameters such as unit cell volume (V), the number of unit cells (n), X-ray density (Dx), dislocation density (δ), microstrain (ϵ), stress (σ), and stacking fault were determined using PXRD data (Table 2) and following relationships [14, 21, 34]:

$$V = a^3, \quad (3)$$

$$N = \frac{4}{3\pi(D/2V)}, \quad (4)$$

$$Dx = \frac{16M}{Na^3}, \quad (5)$$

$$\delta = \frac{1}{D^2}, \quad (6)$$

$$\epsilon = \frac{\beta \cos \theta}{4}, \quad (7)$$

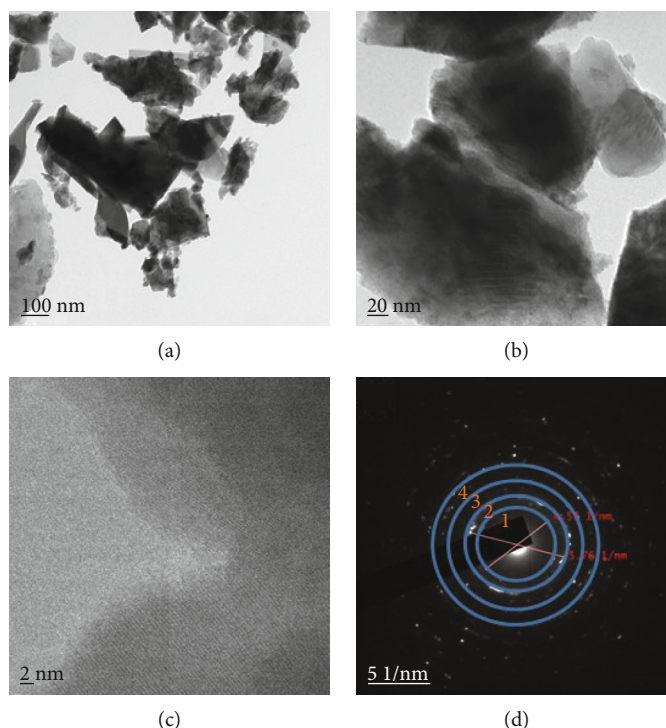


FIGURE 4: (a) and (b) TEM images, (c) SAED pattern, and (d) HR-TEM of Bi_2O_3 NPs.

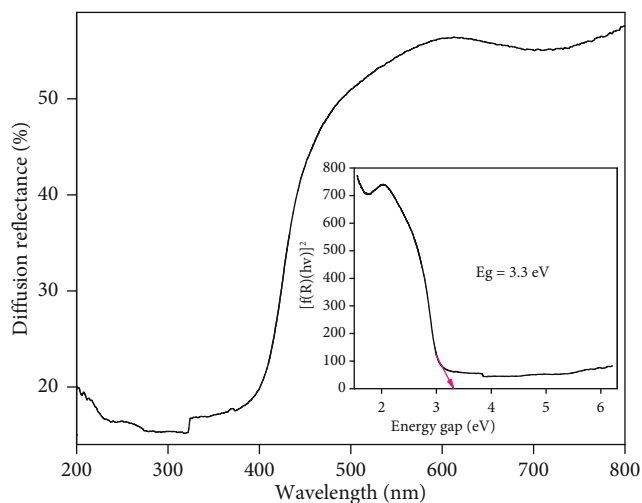


FIGURE 5: DRS and energy bandgap spectra patterns of Bi_2O_3 NPs.

$$\sigma_{\text{stress}} = \epsilon E, \quad (8)$$

$$S.F = \frac{2\pi^2}{45\sqrt{3} \tan \theta}, \quad (9)$$

where M is molecular mass, N is Avogadro's number (6.0223×10^{23} particles mol^{-1}), and E is elastic constant of the material.

3.2. Fourier-Transform Infrared Spectroscopy. The Fourier transform infrared (FTIR) spectrum of Bi_2O_3 NPs was recorded in the wavenumber range of $400\text{--}4000\text{ cm}^{-1}$ at room temperature using KBr pellets Figure 2. The appear-

ance of two peaks at 691.5 cm^{-1} and 853.8 cm^{-1} corresponds to the metal-oxygen (Bi-O) vibration [35]. After calcination of Bi_2O_3 NPs at 500°C , many peaks were assumed to have disappeared because of the evaporation of most of the solvent molecules and decomposition of the organic ingredient. The additional peaks, at about 1291 cm^{-1} and 1247 cm^{-1} , can be attributed to $\text{Bi}^{3+}\text{--O}^{2-}$ stretching.

3.3. SEM Analysis. SEM micrographs of Bi_2O_3 NPs as shown in Figures 3(a) and 3(b) approve the formation of highly porous and agglomerated nanoparticles with an irregular morphology which is possibly due to the escape of a large amount of gases during the probe sonication process [36, 37]. These NPs were found to possess active surface sites and thus they can be suitably employed for applications in electrochemical and supercapacitor devices. The EDX spectrum of Bi_2O_3 NPs is presented in Figure 3(c). The spectrum confirmed the presence of only Bi and O elements (Table 3) in Bi_2O_3 NPs confirming the purity of the NPs.

3.4. TEM Analysis. The surface morphology of the synthesized Bi_2O_3 nanostructures was investigated using high-resolution transmission electron microscopy (HRTEM), and the morphology is depicted in Figure 4. Figures 4(a) and 4(b) show that the morphology has been slightly agglomerated, but SEM and TEM images show that the prepared Bi_2O_3 has a sheet shape morphology, which is consistent with previous findings [38]. It is possible that the sheet shape morphology is caused by the nature of the laminar structure. Clear fringes can be seen in Figure 4(d) with an interplanar distance of 4.57 nm , which corresponds to the plane of (120), and an interplanar distance of 5.76 nm

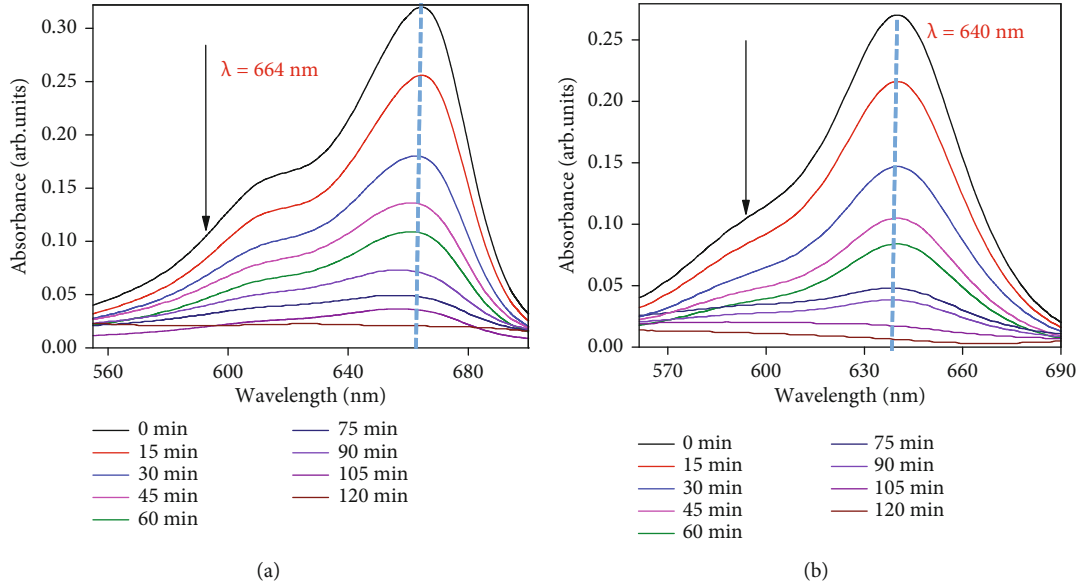


FIGURE 6: (a) and (b) Absorption spectra of MB and AR dyes decomposition for Bi_2O_3 NPs.

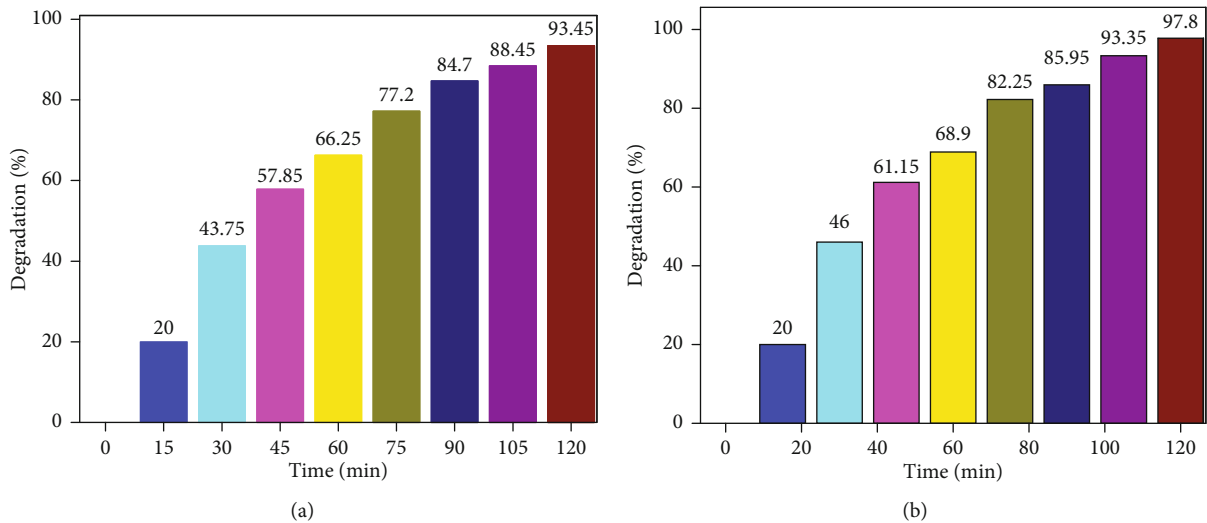


FIGURE 7: (a) and (b) Plot of C/C_0 for the decolorization of MB and AR under UV light illumination.

TABLE 4: Rate constants and kinetic studies of Bi_2O_3 for methylene blue (MB) decolorization under UV light irradiation.

20 ppm MB + 60 mg Bi_2O_3 + UV light					
t	c	c/c_0	$\text{Log } c/c_0$	$-\text{log } c/c_0$	%D
0	20	1	0	0	0
15	16	0.8	-0.09691	0.09691	20
30	11.25	0.5625	-0.24988	0.249877	43.75
45	8.43	0.4215	-0.3752	0.375202	57.85
60	6.75	0.3375	-0.47173	0.471726	66.25
75	4.56	0.228	-0.64207	0.642065	77.2
90	3.06	0.153	-0.81531	0.815309	84.7
105	2.31	0.1155	-0.93742	0.937418	88.45
120	1.31	0.0655	-1.18376	1.183759	93.45

Rate = $0.018758 \text{ min}^{-1}$.

(Figure 4(c)), which corresponds to the plane of (-122). The other planes, which are denoted by the numbers 3 and 4 in the SAED pattern of prepared Bi_2O_3 , correspond to the planes of (112) and (041). The planes observed in the SAED pattern are in excellent agreement with the planes observed in the XRD pattern.

3.5. Diffuse Reflectance Spectroscopy (DRS) Analysis. The value of E_g for Bi_2O_3 NPs was evaluated by using the UV-vis reflectance spectroscopy is given in Figure 5 [39]. The synthesized NPs exhibited a representative reflectance with a strong transition in the UV region corresponding to the band-gap transition of the Bi_2O_3 semiconductor. The Kubelka-Munk function $F(R)$ provides the diffused reflectance as a function of absorption coefficient and can be utilized for examining the powders as given by the following equation:

TABLE 5: List of dyes.

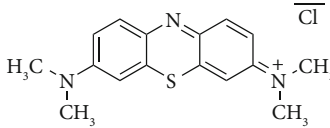
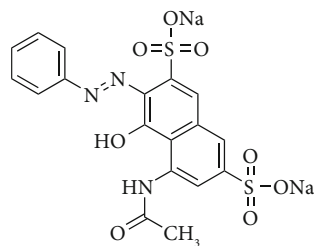
Name of dye	Type of dye	Class of dye	Structure	Mol.wt (g/mol)
Methylene blue	Basic dye	Thiazine		319.9
Acid red	Acid dye	Azo dye		400.38

TABLE 6: Rate constants and kinetic studies of Bi₂O₃ for acid red (AR) decolorization under UV light irradiation.

<i>t</i>	20 ppm AR + 60 mg Bi ₂ O ₃ + UV light				
	<i>c</i>	<i>c/c₀</i>	Log <i>c/c₀</i>	-log <i>c/c₀</i>	% <i>D</i>
0	20	1	0	0	0
15	16	0.8	-0.09691	0.09691	20
30	10.8	0.54	-0.26761	0.267606	46
45	7.77	0.3885	-0.41061	0.410609	61.15
60	6.22	0.311	-0.50724	0.50724	68.9
75	3.55	0.1775	-0.7508	0.750802	82.25
90	2.81	0.1405	-0.85232	0.852324	85.95
105	1.33	0.0665	-1.17718	1.177178	93.35
120	0.44	0.022	-1.65758	1.657577	97.8

Rate = 0.020392 min⁻¹.

$$F(R) = \frac{(1 - R)^2}{2R}, \quad (10)$$

where *R* is reflectance and *F*(*R*) is Kubelka-Munk functions.

The inset of Figure 5 shows the direct bandgap energy was estimated by plotting $[f(R)(h\nu)]^2$ vs. energy gap (eV). The optical energy gap was calculated using the Tauc relation [40], as given by the following equation.

$$(\alpha h\nu) = A (h\nu - E_g)^n, \quad (11)$$

where *hν*; photon energy, *α*; absorption coefficient ($\alpha = 4\pi k/\lambda$); (*k*; absorption index or absorbance, *λ*; the wavelength in nanometer), *E_g*; energy band gap, *A*; constant, *n* = 1/2 for the allowed direct bandgap. The exponent “*n*” depends on the type of transition, and it may have values 1/2, 2, 3/2, and 3 corresponding to the allowed direct, allowed indirect, forbidden direct, and forbidden indirect transitions, respectively [41, 42]. The optical energy gap thus calculated for the synthesized Bi₂O₃ NPs is 3.3 eV and is shown in the inset of Figure 5. This resulted in the genera-

tion of higher electron-hole pairs for better photocatalytic efficiency.

3.6. Photocatalytic Studies. Spherical glass reactor with 176.6 cm² surface areas and mercury vapor lamps UV light source with 125 W medium pressures were used to carry out photocatalytic experiments. The emission wavelength with the highest emission at 370 nm (UVA) in the range of 350–400 nm was utilized, and no filters were used to exclude the light of different wavelengths. In open-air conditions, at a distance of 23 cm, the light was directly irradiated onto the reaction mixture. Double distilled water was used to perform all the experiments. The experiment was conducted using 60 mg of photocatalyst sample Bi₂O₃ was dissolved in 250 mL of 20 ppm concentrated dye solution. Throughout the experiment, the solution was stirred continuously by using a magnetic stirrer. At definite time intervals, 5 mL of the reaction mixture was collected from the dye solution, and the catalyst particles were removed using an external magnet [43, 44].

Photocatalytic activity (PCA) of the Bi₂O₃ NPs was assessed by photodegradation of methylene blue (MB), a cationic dye with maximum absorption at 664 nm, and acid red (AR), an anionic dye with maximum absorption at 640 nm as shown in Figures 6(a) and 6(b). Initially, the PCA experiments were carried out in the dark condition to see the photocatalytic activity for (MB) and (AG) dye using the synthesized catalysts. The dyes did not undergo any degradation, and hence, no change was observed [45, 46].

As presented in Figures 7(a) and 7(b) after 120 min of UV light irradiation, the photodegradation rate of MB dye (Tables 4 and 5) was found to be 93.45%, but, in the same environment, the photodegradation rate of AR dye (Tables 6 and 5) was recorded to be 97.8%. This clearly indicates that AR dye is more susceptible to decolorization than MB when exposed to UV light for 120 min. The obtained results are superior compared to the earlier published work where the dye degradation efficiencies were found to be 95.02% for Fast Red acid dye [47] and 92.3 for methylene blue dye [48]. The percentage of degradation was calculated from the following equation,

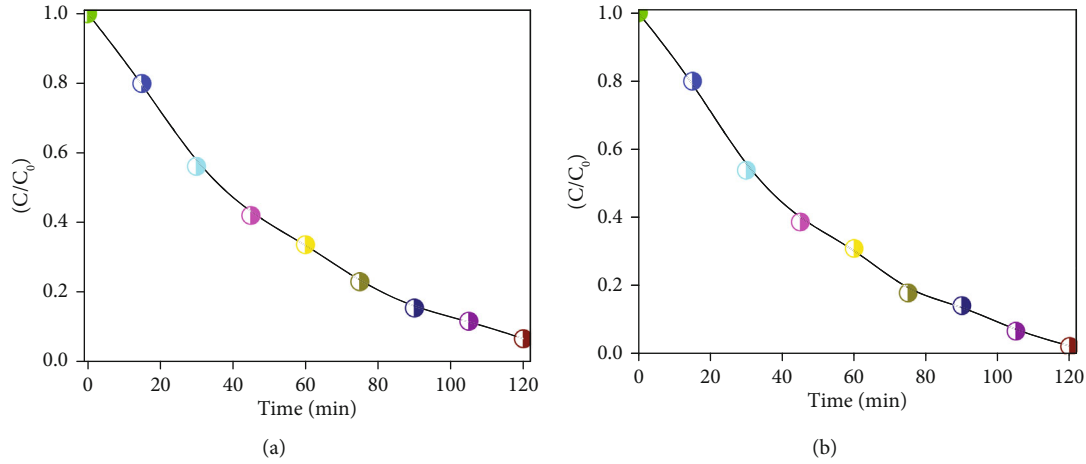


FIGURE 8: (a) and (b) Percentage decomposition of MB and AR dyes over Bi_2O_3 NPs.

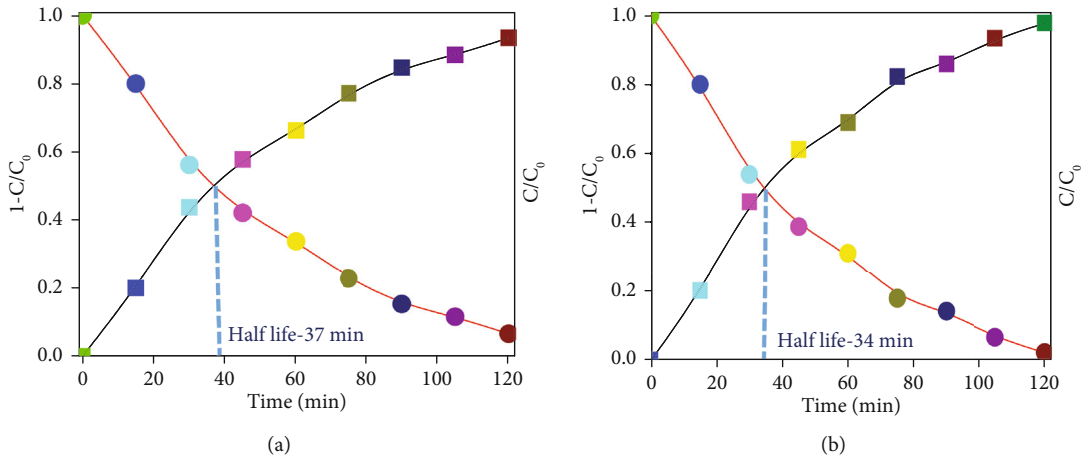


FIGURE 9: (a) and (b) Time span of MB and AR dyes over Bi_2O_3 NPs.

$$\%D = \frac{C_0 - C}{C_0} \times 100, \quad (12)$$

where $\%D$ is photo-decolorization efficiency, C_0 and C are initial concentrations of the dye solutions and the residual concentration of the dye in solution after decolorization in equilibrium, respectively.

Langmuir-Hinshelwood kinetic model was utilized to discuss photocatalytic degradation Kinetics of MB and AR by Bi_2O_3 NPs as shown in Figures 8(a) and 8(b), using the following equation.

$$\log \frac{C}{C_0} = -Kt, \quad (13)$$

where C_0 is concentration of MB and AG dyes initially, C is concentration at time t , k is rate of first-order kinetics (min^{-1}), and t is time in seconds.

The slope of $(\log C/C_0)$ vs. time (t) gives the rate constant K . The rate constant values for Bi_2O_3 NPs are $0.018758 \text{ min}^{-1}$ (MB) and $0.020392 \text{ min}^{-1}$ (AG). First-order kinetics was confirmed from the values calculated from the direct relationship between $\log C/C_0$ and k .

In Figures 9(a) and 9(b), the degradation half-life was evaluated in which 50% dye degradation was observed in a time span of 37 min for (MB) and 34 min (AG). The results indicated that bismuth oxide is prominent material for the degradation of textile dye pollutants and is also useful for the removal of secondary pollutants. A novel bismuth oxide-based thin film as a photocatalyst recorded 98% degradation under UV light irradiation for 8 hours while obtaining a 73.47% COD (chemical oxygen) reduction. The photocatalytic degradation managed to degrade the smaller organic molecules that were formed during the initial stages of degradation, leaving behind the less decomposable by-products [49].

3.7. Mechanism of Photocatalytic Degradation. As the solution containing photocatalyst (Bi_2O_3 NPs) is irradiated by visible (Vis) radiation, electrons in the valence band (VB) of the catalyst get transferred to the conduction band (CB) by creating a hole in VB (Figure 10) [46]. These holes and electrons interact with H_2O and O_2 to yield $\text{OH}\cdot$ and $\text{O}_2\cdot^-$, respectively, and then the hydroxyl radicals interact with dye molecules to degrade to smaller molecules [50, 51]. The main steps involved in the reaction process of photocatalytic degradation under visible light irradiation are as follows:

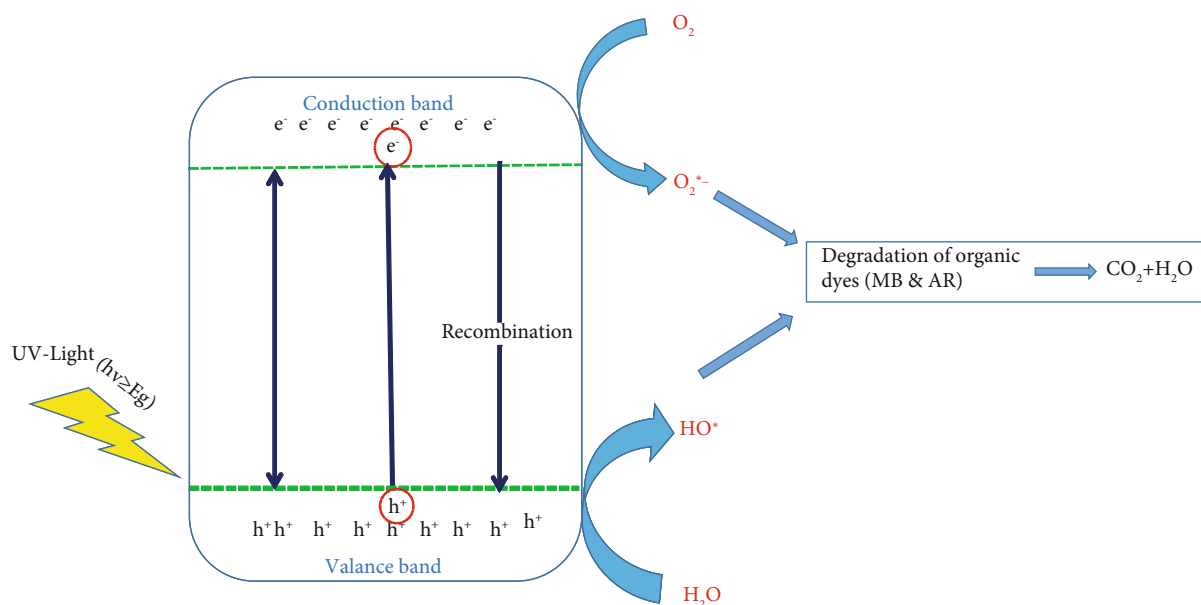


FIGURE 10: The mechanism of MB and AR dyes decomposition for Bi₂O₃ NPs.

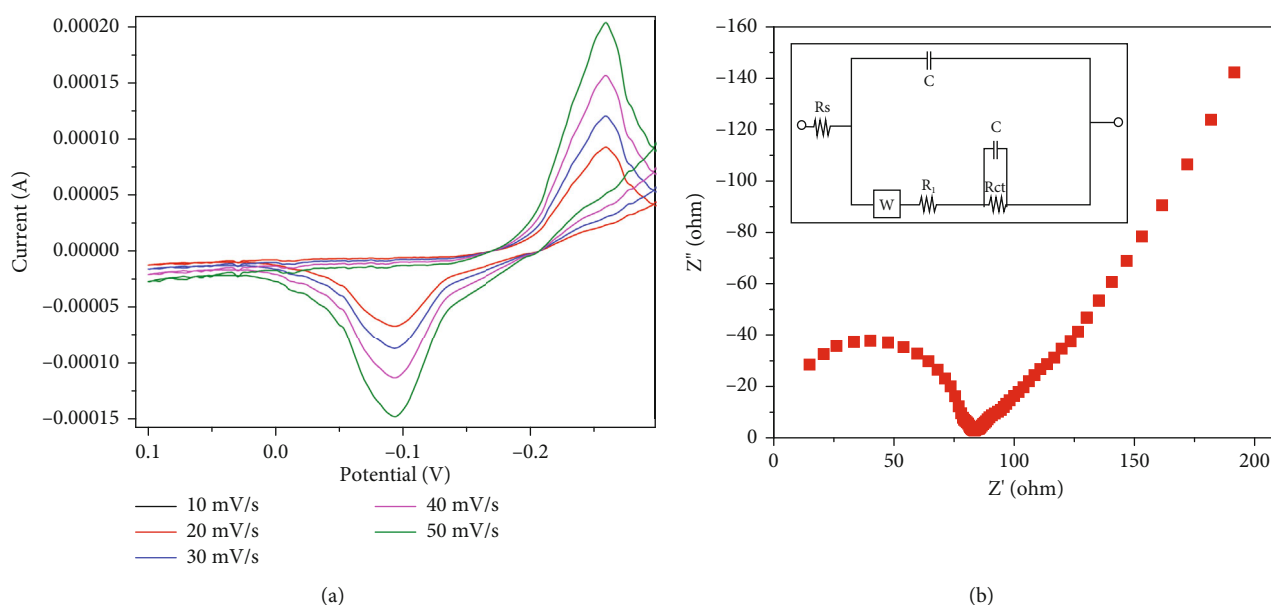
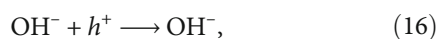
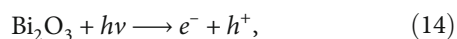


FIGURE 11: (a) Cyclic voltammogram of Bi₂O₃ NPs with different scanning rates. (b) EIS spectra with equivalent circuit of Bi₂O₃ NPs.



It contributed towards the practicality of the synthesized Bi₂O₃ NPs as they could be applied in the degradation of other organic pollutants.

3.8. Cyclic Voltammetric Studies. In order to characterize the synthesized Bi₂O₃ NPs based sensor, a variety of electrochemical measurements were performed in 0.1 M HCl

using lead and ascorbic acid, including cyclic voltammetry (CV) and electrochemical impedance spectroscopy (EIS) (Figure 11). For the cyclic voltammetry studies of the synthesized Bi₂O₃, a standard three-electrode system in 0.1 M HCl was used. Using a scan rate ranging from 10 mV/s to 50 mV/s, this process was carried out in the absence of lead and/or ascorbic acid. It has been determined that the reduction and oxidation peaks observed at potentials of -0.25 V and -0.09 V, respectively, when the potential range was varied from -0.3 to +0.1, were caused by variations in the potential range from -0.3 to +0.1. With the help of cyclic voltammograms, the specific capacitance of the electrode (Fg⁻¹) could be calculated using the following equation,

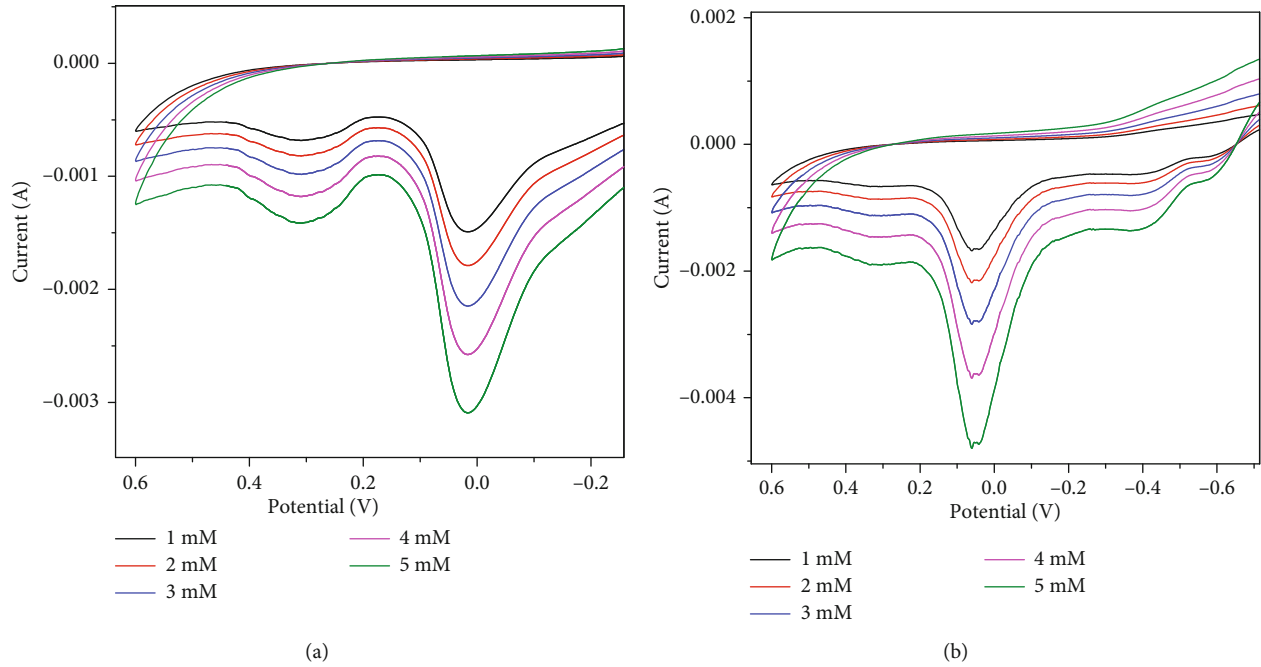


FIGURE 12: Cyclic voltammogram of Bi_2O_3 NPs. Detection of (a) ascorbic acid and (b) lead concentration range 1–5 mM.

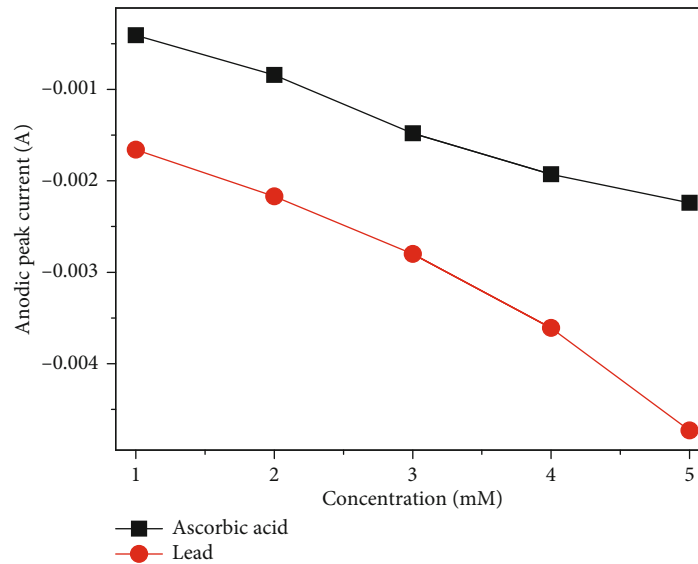


FIGURE 13: Anodic peak current vs. concentration plot using linear sweep voltammetry (LSV).

$$C_{sp} = \frac{S}{2mk\Delta V}. \quad (18)$$

The area under the CV curve can be represented by S , as given in equation (18), where the mass of the material was represented by m , voltage window was represented by ΔV , and scan rate was given by k . The specific capacitance values were calculated using equation (18) and were found to be 86.6, 55.7, 36.1, 29.8, and 25.5 Fg^{-1} , respectively, for scan rates of 10, 20, 30, 40, and 50 mV in 0.1 M HCl. It can be seen from the specific capacitance values that as the scan rate increases, the specific capacitance values decrease. This can be attributed to the fact

that the ions in the electrolyte will have sufficient time to penetrate into the electrode material at a lower scan rate, whereas at a higher scan rate, the ions will simply collect on the electrode material's outer surface [52]. This results in a decrease in the values of specific capacitance as a result of an increase in scan rate as well [53].

The Nyquist plot (Figure 11(b)) can be used to determine the electronic conductivity or charge transfer capacity of the prepared electrode. This plot also provides information on the capacitance behavior of the electrode. It is possible to divide the Nyquist plot into two main regions: the first denotes the high-frequency region, which provides information about the charge transfer process at the interface of

electrode and/or electrolyte, which is typically seen as a semicircle [54, 55]. The other region represents the low-frequency region, which denotes the capacitance of the electrode and which was given the shape of a straight line in order to represent it accurately. The charge transfer resistance R_{ct} was calculated from the diameter of the semicircle in the Nyquist plot [56]. When the EIS technique was used, it was possible to obtain the equivalent circuit of the system which was given in Figure 11(b) inset.

The sensing capability of the synthesized nanomaterial (Bi_2O_3) for ascorbic acid and lead was investigated using a modified carbon paste electrode, and the obtained results were presented in Figure 12. We experimented with different concentrations of ascorbic acid/lead from 1 to 5 mM in order to better understand the sensing ability of synthesized Bi_2O_3 . According to the results, in the absence of ascorbic acid and lead, the oxidation and reduction peaks were at -0.09 V and -0.2 V , respectively, whereas in the presence of ascorbic acid and lead, the oxidation and reduction peaks shifted to the more positive side of the potential curve [57]. After the addition of ascorbic acid, the oxidation peak at -0.09 V shifts to 0.019 V , and an additional oxidation peak appears at 0.03 V , whereas when the lead is added, the oxidation peak at -0.09 V shifts to 0.05 V . After the addition of ascorbic acid/lead, there is a complete disappearance of the reduction peak in the voltammogram (Figure 12). We can infer from the data that the synthesized material Bi_2O_3 can function as a good sensing material for ascorbic acid and lead, which is supported by the significant variation in the oxidation and reduction peak positions of the material. Figure 13 shows the concentration of ascorbic acid and lead vs. anodic peak current plot obtained by LSV, which also shows an increase in anodic peak current with increasing concentration of ascorbic acid and lead.

4. Conclusions

To summarize, in this research, we have used a well-known probe sonication approach for the synthesis of Bi_2O_3 nanoparticles that is low in cost and highly calibrated. The produced nanoparticles were submitted to a number of different characterization procedures in order to gain a better understanding of their crystal structure, as well as their morphological and optical characteristics. It was discovered from the optical properties of the Bi_2O_3 nanoparticles have a bandgap of 3.3 eV , which makes them excellent for the degradation of dyes when exposed to ultraviolet radiation. The SEM, TEM, and HRTEM analyses revealed that the nanoparticles are highly porous materials with a small agglomeration. MB and AR dyes were both subjected to degradation under ultraviolet (UV) radiation in the presence of the catalyst, and it was observed that the degradation of MB and AR dyes was 93.45% and 97.80% , respectively, and that the results were quite impressive. In the electrochemical investigations, it was discovered that the produced nanomaterial has the ability to detect several heavy metals as well as the ascorbic acid medication. The specific capacitance of the sample was calculated to be 25.5 Fg^{-1} in 0.1 N HCl , according to the results of

the experiment. Hence, Bi_2O_3 nanoparticles can be used as bifunctional materials for degradation and for sensing applications.

Data Availability

The [Excel] data used to support the findings of this study are available from the corresponding author upon request.

Conflicts of Interest

The authors declare that they have no conflicts of interest.

References

- [1] H. M. Zaid, "Synthesis of bismuth oxide nano powders via electrolysis method and study the effect of change voltage on the size for it," *Australian Journal of Basic and Applied Sciences*, vol. 11, pp. 97–101, 2017.
- [2] N. Cornei, N. Tancet, F. Abraham, and O. Mentré, "Synthesis and characterization of bismuth oxide nanoparticles via sol-gel method inorganic chemistry," *Journal of Inorganic Chemistry*, vol. 3, 165 pages, 2006.
- [3] A. Kumar, A. Rana, C. Guo et al., "Acceleration of photo-reduction and oxidation capabilities of $\text{Bi}_4\text{O}_5\text{I}_2$ / alginate by metallic Ag: wide spectral removal of nitrate and azithromycin," *Chemical Engineering Journal*, vol. 423, article 130173, 2021.
- [4] A. Kumar, G. Sharma, A. Kumari et al., "Construction of dual Z-scheme $\text{g-C}_3\text{N}_4/\text{Bi}_4\text{Ti}_3\text{O}_{12}/\text{Bi}_4\text{O}_5\text{I}_2$ heterojunction for visible and solar powered coupled photocatalytic antibiotic degradation and hydrogen production: boosting via Γ/I_3^- and $\text{Bi}^{3+}/\text{Bi}^{5+}$ redox mediators," *Applied Catalysis B: Environmental*, vol. 284, article 119808, 2021.
- [5] P. Dhiman, A. Kumar, M. Shekh et al., "Robust magnetic $\text{ZnO-Fe}_2\text{O}_3$ Z-scheme heterojunctions with in-built metal-redox for high performance photo- degradation of sulfamethoxazole and electrochemical dopamine detection," *Environmental Research*, vol. 197, article 111074, 2021.
- [6] A. Bouziani, J. Park, and A. Ozturk, "Effects of fluorination and thermal shock on the photocatalytic activity of Bi_2O_3 nanopowders," *Colloids and Surfaces A: Physicochemical and Engineering Aspects*, vol. 626, article 127049, 2021.
- [7] A. P. Kumar, D. Bilehal, T. Desalegn et al., "Studies on synthesis and characterization of $\text{Fe}_3\text{O}_4@\text{SiO}_2@\text{Ru}$ hybrid magnetic composites for reusable photocatalytic application," *Adsorption Science & Technology*, vol. 2022, Article ID 3970287, 18 pages, 2022.
- [8] B. Abebe and H. C. Ananda Murthy, "Synthesis and characterization of Ti-Fe oxide nanomaterials for lead removal," *Journal of Nanomaterials*, vol. 2018, Article ID 9651039, 10 pages, 2018.
- [9] B. Abebe, E. A. Zereffa, and H. C. A. Murthy, "Synthesis of poly(vinyl alcohol)-aided $\text{ZnO}/\text{Mn}_2\text{O}_3$ nanocomposites for acid orange-8 dye degradation: mechanism and antibacterial activity," *ACS Omega*, vol. 6, no. 1, pp. 954–964, 2021.
- [10] B. Abebe, H. C. A. Murthy, E. A. Zereffa, and Y. Qiang, "Synthesis and characterization of PVA-assisted metal oxide nanomaterials: surface area, porosity, and electrochemical property improvement," *Journal of Nanomaterials*, vol. 2020, Article ID 6532835, 14 pages, 2020.

- [11] B. Abebe, C. R. Ravikumar, E. A. Zereffa, A. Naveen Kumar, and H. C. A. Murthy, "Photocatalytic and superior ascorbic acid sensor activities of PVA/Zn-Fe-Mn ternary oxide nanocomposite," *Inorganic Chemistry Communications*, vol. 123, article 108343, 2021.
- [12] G. Viruthagiri, P. Kannan, and V. K. Indhumathi, "Photocatalytic activity of α -phase bismuth oxide nanoparticles under visible light," *International Journal of Advanced Science and Research*, vol. 2, pp. 1–7, 2017.
- [13] B. Abebe, E. A. Zereffa, H. C. A. Murthy, and C. R. Ravikumar, "A novel poly (vinyl alcohol)-aided ZnO/Fe₂O₃ nanocomposite as an ascorbic acid sensor," *Journal of Materials Science: Materials in Electronics*, vol. 32, no. 6, pp. 7778–7790, 2021.
- [14] M. R. A. Kumar, B. Abebe, H. P. Nagaswarupa, H. C. A. Murthy, C. R. Ravikumar, and F. K. Sabir, "Enhanced photocatalytic and electrochemical performance of TiO₂-Fe₂O₃ nanocomposite: its applications in dye decolorization and as supercapacitors," *Scientific Reports*, vol. 10, no. 1, p. 1249, 2020.
- [15] M. Ahmed, A. Dief, and W. S. Mohamed, " α -Bi₂O₃ nanorods: synthesis, characterization and UV-photocatalytic activity," *Materials Research Express*, vol. 4, pp. 35–39, 2017.
- [16] L. Liu, J. Jiang, S. Jin, Z. Xiabc, and M. Tangc, "Hydrothermal synthesis of β -bismuth oxide nanowires from particles," *Cryso-EngComm*, vol. 13, pp. 25–29, 2011.
- [17] Z. Hamid, "Synthesis of bismuth oxide nano powders via electrolysis method and study the effect of change voltage on the size for it," *Australian journal of basic and applied sciences*, vol. 7, pp. 97–101, 2017.
- [18] T. R. Das, S. Patra, R. Madhuri, and K. P. Sharma, "Bismuth oxide decorated graphene oxide nanocomposites synthesized via sonochemical assisted hydrothermal method for adsorption of cationic organic dyes," *Journal of colloid and interface science*, vol. 509, pp. 82–93, 2018.
- [19] M. M. Patil, V. V. Deshpande, S. R. Dhage, and V. Ravi, "Synthesis of bismuth oxide nanoparticles at 100 °C," *Materials letters*, vol. 59, no. 19–20, pp. 2523–2525, 2005.
- [20] D. Sánchez-Martínez, I. Juárez-Ramírez, L. M. Torres-Martínez, and I. de León-Abarte, "Photocatalytic properties of Bi₂O₃ powders obtained by an ultrasound-assisted precipitation method," *Ceramics International*, vol. 42, no. 1, pp. 2013–2020, 2016.
- [21] Y. Astuti, A. Fauziyah, S. Nurhayati et al., "Synthesis of α -bismuth oxide using solution combustion method and its photocatalytic properties," *IOP Conference Series: Materials Science and Engineering*, vol. 107, article 012006, 2016.
- [22] N. M. Sammes, G. A. Tompsett, H. Näfe, and F. Aldinger, "Bismuth based oxide electrolytes— structure and ionic conductivity," *Journal of the European Ceramic Society*, vol. 19, no. 10, pp. 1801–1826, 1999.
- [23] Y. Dimitriev, M. Y. Krupchanska Ivanova, and A. Staneva, "Sol-gel synthesis of material in the system Bi₂O₃-SiO₂," *Journal of the University of Chemical Technology and Metallurgy*, vol. 45, pp. 39–42, 2010.
- [24] J. Y. Xia, M. T. Tang, C. H. Cui, S. M. Jin, and Y. M. Chen, "Preparation of α - Bi₂O₃ from powders through low temperature oxidation," *Transactions of Nonferrous Metals Society of China*, vol. 22, pp. 2289–2294, 2012.
- [25] H. Kim, J. Kim, W. Kim, and W. Choi, "Enhanced photocatalytic and photoelectrochemical activity in the ternary hybrid of CdS/TiO₂/WO₃through the cascaded electron transfer," *The Journal of Physical Chemistry C*, vol. 115, no. 19, pp. 9797–9805, 2011.
- [26] N. Cornei, N. Tancet, F. Abraham, and O. Mentré, "Synthesis and characterization of bismuth oxide nanoparticles via sol-gel method," *Inorganic Chemistry*, vol. 3, pp. 162–165, 2006.
- [27] N. Jiang and E. D. Wachsman, "Structural stability and conductivity of phase-stabilized cubic bismuth oxides," *Journal of the American Ceramic Society*, vol. 82, no. 11, pp. 3057–3064, 1999.
- [28] M. Zidan, "Electrochemical oxidation of paracetamol mediated by nanoparticles bismuth oxide modified glassy carbon electrode," *International Journal of Electrochemical Science*, vol. 6, pp. 279–288, 2011.
- [29] M. Mallahi, A. Shokuhfar, M. R. Vaezi, A. Esmaeilirad, and V. Mazinani, "Synthesis and characterization of bismuth oxide nanoparticles via sol-gel method," *Journal of Engineering Research (AJER)*, vol. 3, pp. 162–165, 2014.
- [30] M. A. S. Amulya, H. P. Nagaswarupa, M. R. A. Kumar, C. R. Ravikumar, and K. B. Kusuma, "Sonochemical synthesis of MnFe₂O₄ nanoparticles and their electrochemical and photocatalytic properties," *Journal of Physics and Chemistry of Solids*, vol. 148, article 109661, 2021.
- [31] M. W. Alam, V. G. Dileep Kumar, C. R. Ravikumar, S. C. Prashantha, H. C. Ananda Murthy, and M. R. Anil Kumar, "Chromium (III) doped polycrystalline MgAl₂O₄ nanoparticles for photocatalytic and supercapacitor applications," *Journal of Physics and Chemistry of Solids*, vol. 161, p. 110491, 2022.
- [32] C. R. Ravi Kumar, M. S. Santosh, H. P. Nagaswarupa, S. C. Prashantha, S. Yallappa, and M. R. Anil Kumar, "Synthesis and characterization of β -Ni(OH)₂ embedded with MgO and ZnO nanoparticles as nanohybrids for energy storage devices," *Materials Research Express*, vol. 4, no. 6, article 065503, 2017.
- [33] A. Yamuna, P. Sundaresan, and S. M. Chen, "Sonochemical preparation of bismuth oxide nanotiles decorated exfoliated graphite for the electrochemical detection of imipramine," *Ultrasonics sonochemistry*, vol. 64, article 105014, 2020.
- [34] M. G. Naseri, E. B. Saion, H. A. Ahangar, and A. H. Shaari, "Fabrication, characterization, and magnetic properties of copper ferrite nanoparticles prepared by a simple, thermal-treatment method," *Materials Research Bulletin*, vol. 48, no. 4, pp. 1439–1446, 2013.
- [35] T. Saison, N. Chemin, C. Chaneac et al., "Bi₂O₃, BiVO₄, and Bi₂WO₆: impact of surface properties on photocatalytic activity under visible light," *The Journal of Physical Chemistry C*, vol. 115, no. 13, pp. 5657–5666, 2011.
- [36] S. Nandi and S. K. Das, "An electrochemical study on bismuth oxide (Bi₂O₃) as an electrode material for rechargeable aqueous aluminum-ion battery," *Solid State Ionics*, vol. 347, article 115228, 2020.
- [37] J. Feng, L. Q. Guo, X. D. Xu, S. Y. Qi, and M. L. Zhang, "Hydrothermal synthesis and characterization of Mn_{1-x}Zn_xFe₂O₄ nanoparticles," *Physica B: Condensed Matter*, vol. 394, no. 1, pp. 100–103, 2007.
- [38] T. Liu, Y. Zhao, L. Gao, and J. Ni, "Engineering Bi₂O₃-Bi₂S₃ heterostructure for superior lithium storage," *Scientific Reports*, vol. 5, no. 1, pp. 1–5, 2015.
- [39] P. Kubelka and F. M. Aussig, "Ein Beitrag zur optik der farbanstriche," *Zeitschrift fur technische Physik*, vol. 12, pp. 593–601, 1931.

- [40] M. Stucchi, C. L. Bianchi, C. Argiris et al., "Ultrasound assisted synthesis of Ag-decorated TiO₂ active in visible light," *Ultrasonics Sonochemistry*, vol. 40, no. Part A, pp. 282–288, 2018.
- [41] Y.-C. Chu, G.-J. Lee, C.-Y. Chen et al., "Preparation of bismuth oxide photocatalyst and its application in white-light LEDs," *Journal of Nanomaterials*, vol. 2013, Article ID 596324, 7 pages, 2013.
- [42] K. Rana, P. Thakur, P. Sharma, M. Tomar, V. Gupta, and A. Thakur, "Improved structural and magnetic properties of cobalt nanoferrites: influence of sintering temperature," *Ceramics International*, vol. 41, no. 3, pp. 4492–4497, 2015.
- [43] Q. R. Deng, X. H. Xia, M. L. Guo, Y. Gao, and G. Shao, "Mn-doped TiO₂ nanopowders with remarkable visible light photocatalytic activity," *Materials Letters*, vol. 65, no. 13, pp. 2051–2054, 2011.
- [44] M. R. A. Kumar, C. R. Ravikumar, H. P. Nagaswarupa et al., "Evaluation of bi-functional applications of ZnO nanoparticles prepared by green and chemical methods," *Journal of Environmental Chemical Engineering*, vol. 7, no. 6, article 103468, 2019.
- [45] M. Chireh and M. Naseri, "Effect of calcination temperature on the physical properties of LiFe₅O₈ nanostructures," *Advanced Powder Technology*, vol. 30, no. 5, pp. 952–960, 2019.
- [46] M. R. A. Kumar, H. P. Nagaswarupa, C. R. Ravikumar, S. C. Prashantha, H. Nagabhushana, and A. S. Bhatt, "Green engineered nano MgO and ZnO doped with Sm³⁺: synthesis and a comparison study on their characterization, PC activity and electrochemical properties," *Journal of Physics and Chemistry of Solids*, vol. 127, pp. 127–139, 2019.
- [47] Y. Kambalagere, M. Madhusudana, and K. M. Mahadevan, "Decolourization of fast red acid dye using photoactive Bi₂O₃ nanoparticle under solar irradiation," in *Proceedings of the International Conference on Future Environment Pollution and Prevention (ICFEPP)*, pp. 11–16, Beijing, China, 2019.
- [48] N. Nurmalasari, Y. Yulizar, and D. O. Apriandanu, "Bi₂O₃ nanoparticles: synthesis, characterizations, and photocatalytic activity," in , Article ID 0120363rd *International Symposium on Current Progress in Functional Materials*, vol. 763, Depok, Indonesia, 2020.
- [49] L. Zhang, W. Wang, J. Yang et al., "Sonochemical synthesis of nanocrystallite Bi₂O₃ as a visible-light-driven photocatalyst," *Applied Catalysis A: General*, vol. 308, pp. 105–110, 2006.
- [50] A. Tadesse, M. Hagos, N. Belachew, H. C. Ananda Murthy, and K. Basavaiah, "Enhanced photocatalytic degradation of Rhodamine B, antibacterial and antioxidant activities of green synthesised ZnO/N doped carbon quantum dot nanocomposites," *New Journal of Chemistry*, vol. 45, no. 46, pp. 21852–21862, 2021.
- [51] Y. Yao, F. Lu, Y. Zhu et al., "Magnetic core-shell CuFe₂O₄@C₃N₄ hybrids for visible light photocatalysis of orange II," *J. Hazard.Mater.*, vol. 297, pp. 224–233, 2015.
- [52] B. Shruthi, B. J. Madhu, V. B. Raju et al., "Synthesis, spectroscopic analysis and electrochemical performance of modified β -nickel hydroxide electrode with CuO," *Journal of Science: Advanced Materials and Devices*, vol. 2, no. 1, pp. 93–98, 2017.
- [53] K. B. Kusuma, M. Manju, C. R. Ravikumar et al., "Photocatalytic and electrochemical sensor for direct detection of paracetamol comprising γ -aluminium oxide nanoparticles synthesized via sonochemical route," *Sensors International*, vol. 1, article 100039, 2020.
- [54] C. Pratapkumar, S. C. Prashantha, H. Nagabhushana et al., "White light emitting magnesium aluminate nanophosphor: near ultra violet excited photoluminescence, photometric characteristics and its UV photocatalytic activity," *Journal of Alloys and Compounds*, vol. 728, pp. 1124–1138, 2017.
- [55] Y. Wu, S. Liu, H. Wang, X. Wang, X. Zhang, and G. Jin, "A novel solvothermal synthesis of Mn₃O₄/graphene composites for supercapacitors," *Electrochimica Acta*, vol. 90, pp. 210–218, 2013.
- [56] A. S. Manjunatha, N. S. Pavithra, M. Shivanna, G. Nagaraju, and C. R. Ravikumar, "Synthesis of Citrus Limon mediated SnO₂-WO₃ nanocomposite: applications to photocatalytic activity and electrochemical sensor," *Journal of Environmental Chemical Engineering*, vol. 8, no. 6, article 104500, 2020.
- [57] C. R. Ravi kumar, P. Kotteeswaran, V. B. Raju et al., "Influence of zinc additive and pH on the electrochemical activities of β -nickel hydroxide materials and its applications in secondary batteries," *Journal of Energy Storage*, vol. 9, pp. 12–24, 2017.

Research Article

Effect of Nanoaluminium Nitride Ceramic Particles on Microstructure, Mechanical Wear, and Machining Behavior of Al-Si-Mg Alloy Matrix Composites Produced by Bottom Pouring Type Stir Casting Route

M. Meignanamoorthy,¹ V. Mohanavel ,² P. Velmurugan ,² M. Ravichandran ,¹ Wadi B. Alonazi ,³ S. Sivakumar,⁴ and Atkilt Mulu Gebrekidan ⁵

¹Department of Mechanical Engineering, K. Ramakrishnan College of Engineering, Tiruchirappalli, 621112 Tamil Nadu, India

²Centre for Materials Engineering and Regenerative Medicine, Bharath Institute of Higher Education and Research, Selaiyur, Chennai, 600073 Tamil Nadu, India

³Health Administration Department, College of Business Administration, King Saud University, PO Box 71115, Riyadh 11587, Saudi Arabia

⁴Department of Bioenvironmental Energy, College of Natural Resource and Life Science, Pusan National University, Miryang 50463, Republic of Korea

⁵Department of Mechanical Engineering, Faculty of Mechanical Engineering, Arba Minch Institute of Technology (AMIT), Arba Minch University, Ethiopia

Correspondence should be addressed to Atkilt Mulu Gebrekidan; atkilt.mulu@amu.edu.et

Received 16 November 2021; Revised 22 December 2021; Accepted 24 December 2021; Published 3 February 2022

Academic Editor: Arpita Roy

Copyright © 2022 M. Meignanamoorthy et al. This is an open access article distributed under the Creative Commons Attribution License, which permits unrestricted use, distribution, and reproduction in any medium, provided the original work is properly cited.

Aluminium alloy strengthened with the ceramic particle is widely utilized for numerous engineering usages owing to its less weight, and superior mechanical and tribological behavior. The purpose of this research is to manufacture AA6063-Nano AlN composites via stir casting (SC) process and to examine the mechanical, tribological, electrical, and thermal and CNC drilling behavior. Nano AlN was mixed with AA6063 at 4, 8, and 12 wt.%. The occurrence and dispersal of Nano AlN particles in AA6063 matrix were inspected via Scanning Electron Microscope (SEM). The density and porosity were explored. The mechanical studies on microhardness, tensile strength and yield strength, flexural strength, and compressive strength have been done. SEM fractographic examination was made on the tensile fracture samples. The thermal conductivity, electrical resistivity and electrical conductivity, and salt spray corrosion analysis were made on the produced composites. The tribological behavior of the composites was studied using numerous parameters, reinforcement wt.%, load (L), sliding velocity (SV), and sliding distance (SD). The worn surface examination was done via SEM. The CNC drilling behavior was done at different parameter speed (S), feed (F), and depth of cut (DOC). Experiments were carried out according to the L9 orthogonal array (OA). Optimal process parameter to attain higher material removal rate (MRR) and least surface roughness (SR) was identified via Grey Relational Analysis (GRA). ANOVA outcomes revealed that feed rate is the foremost noteworthy parameter (45.89%) influencing MRR and SR.

1. Introduction

Nowadays, metal matrix composites (MMC) reinforced with ceramics have progressed as noteworthy focuses despite

their progressive usages equivalent to the traditional alloys. Because of their excellent properties, MMCs are largely utilized for different applications than traditional alloys [1]. MMCs can be finely strengthened with another material to

enhance their properties. In MMCs, the alloy or metal is a matrix phase and the reinforcement could be ceramic or organic. Generally, metal is an important one for numerous engineering applications; however, many attempts have been put forth to improve its properties via utilizing appropriate reinforcements [2, 3]. MMCs strengthened with particulates are majorly utilized in various engineering fields' aircraft and structural parts because of their higher strength, good toughness, better wear and corrosion opposition, etc. [4]. Currently, aluminium matrix composites (AMCs) are a majorly utilized material in various engineering fields. Aluminium is a lightweight metal, but it possesses poor mechanical properties. Furthermore, to improve the mechanical property of aluminium, it is reinforced with different kinds of ceramics. Hence, the desired properties can be attained [5]. Numerous engineering components need good strength, hardness, and wear and corrosion resistance materials with less weight. Despite this intention, aluminium is mixed with harder ceramic particles via a liquid metallurgy process to manufacture AMCs [6]. AMCs have aluminium or alloy as a matrix; nowadays, the usage of these AMCs has been enhanced in industry because of their superior properties. Because of these merits, aluminium alloy is combined with different reinforcements to obtain explicit properties [7]. Amid the numerous ceramics, AlN has been accredited as a superior one because it exhibits better mechanical, wear, corrosion, and thermal properties [8]. Due to better wettability and higher stability tendency of AlN with aluminium, it is attracted much more than other ceramics; additionally, AlN has good hardness and elastic modulus [9]. Several fabrication routes are available to prepare MMC hot pressing, PM, and stir casting. Amongst the different processes, stir casting (SC) has been identified as a major operative one despite its easiness, litheness, large capacity, fabrication capability, and economical [10]. SC process confirms the fine dispersal of reinforcements with the aid of a stirrer. The strength of interfacial closeness amid reinforcement and alloys depends on wettability, because it is a noteworthy factor, which results in extreme enhancement of tribological and mechanical properties [11]. Chellapilla et al. [12] developed TiC strengthened AA6063 composites via in situ process and stated that inclusion of TiC with AA6063 enhances the composite properties. David Joseph et al. [12] produced MoS₂ reinforced AA6063 composites via PM route and concluded that the addition of MoS₂ to AA6063 enhances the material property. Saravanan et al. [13] synthesized TiC reinforced AA6063 matrix composites via the SC method, and the outcomes displayed that particle-reinforced AMCs increase the mechanical properties extremely. Mohanavel et al. [14] examined the AlN strengthened AA7075 composite mechanical behavior prepared via SC process and described that the increment of AlN reinforcement with matrix increases the properties significantly. Ashok Kumar et al. [15] explored the tribological behavior of AlN strengthened AA6061 composite and the results showed that a raise in AlN particles rises the wear opposition. Zhao et al. [16] manufactured AA6061-AlN composites by SC process and studied the mechanical behavior, and the outcomes explored

that the inclusion of reinforcement particles improves the properties. Mahesh Kumar et al. [17] analyzed the mechanical properties of AA7079-AlN composites prepared via SC route and stated that an increase in AlN wt.% enhances the properties of the composites. Fale et al. [18] explored the tensile, compressive, and wear behavior of Al-AlN composites prepared via ex situ process and stated that inclusions of AlN particles enhance the compressive and tensile strength and increase the wear resistance. Shalaby and Churyumov [19] fabricated AlN strengthened with A359 composites and the outcomes displayed that a rise in AlN wt.% improves the mechanical properties. Radhika and Raghu [20] explored the hardness, tensile strength, and abrasion wear behavior of Al-AlN composites and reported that dramatic improvement in properties was achieved due to the addition of AlN particles. Radhika and Raghu [21] studied the tensile strength; hardness and wear behavior of AlN strengthened LM13 composite and indicated that the inclusion of AlN particles enhances the properties of the composites significantly. Basavarajappa et al. [22] studied the drilling characteristics of AA2219-15SiC-3Gr composites prepared via SC route and burr height, thrust force, and surface roughness that were analyzed. Rajmohan and Palanikumar [23] explored the CNC drilling characteristics of Al356-SiC composites and concluded that the feed rate is a major significant parameter to affect the thrust force, burr height, tool wear, and surface roughness. Rajmohan et al. [24] investigated the CNC drilling parameters of Al356-SiC-mica composites, and the results revealed that the feed rate and addition of reinforcement wt.% were the major noteworthy parameters. Elango and Annamalai [25] examined the CNC machining characteristics of Al-SiC-Gr composites, and the results showed that cutting speed is the major influencing parameter to attain least surface roughness. Yahya Altunpak et al. [26] explored the drilling characteristics of aluminium composites, and the outcomes showed that the feed rate is the most substantial one to attain the least surface roughness.

Till now, various examinations have been conducted to study the mechanical, tribological, and CNC drilling behavior of AMC-based composites, but very little work has been done by utilizing Nano AlN particles as reinforcement. Therefore, this work made an effort to manufacture AA6063-Nano AlN composites via the SC process and studied the behavior of the prepared composites.

2. Materials and Methods

AA6063 chemical compositions are Si:0.2-0.6, Fe:0.35, Cu:0.1, Mn:0.1, Mg:0.45-0.9, Zn:0.1, Ti:0.1, Cr:0.1, and Al:Balance. AA6063 was preferred as matrix and Nano AlN (4, 8, and 12 wt.%) as reinforcement. The desired amount of AA6063 and Nano AlN was measured via electronic weighing equipment. AA6063 was liquefied at 750°C temperature [27]. Nano AlN particle was preheated at 400°C before being added into the liquefied metal [14]. The least amount of magnesium was added to raise the wettability [28]. Stirring was conducted at 400 rpm for 15 min [17]. Finally, the molten metal was transferred into a mould of

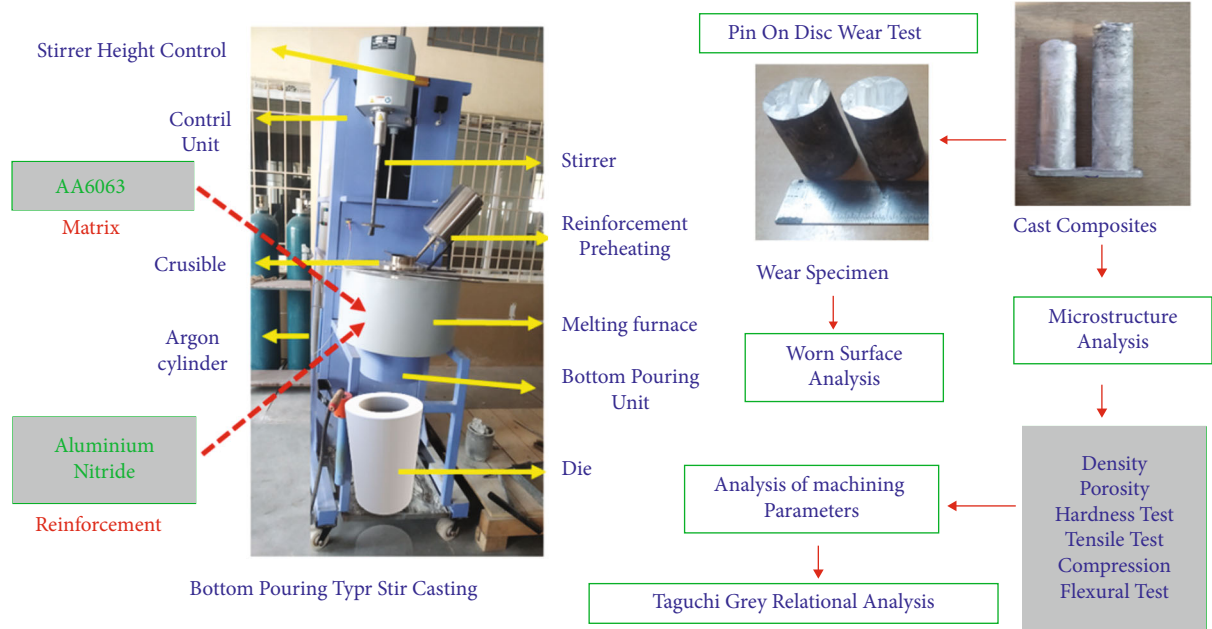


FIGURE 1: Experimental details of the present work.

the requisite dimensions. Microstructure exploration was made via SEM on the manufactured samples. By utilizing Archimedes' principle, the density was calculated and porosity was also measured. The prepared samples' hardness was determined as per ASTM E92 using a Vickers hardness machine [29]. According to ASTM E8–04 standard, a tensile test was done using computerized universal testing equipment [29]. As per ASTM E9-89a, a compression test was done utilizing computerized universal testing equipment [30]. The flexural strength was conducted according to ASTM standard C1161 via three-point bending equipment [13]. The thermal conductivity analysis was done at room temperature via a thermal diffusivity analyzer. Electrical conductivity examination was done via the four-point probe technique. According to ASTM B, the 117 standard salt spray corrosion test was conducted utilizing a salt spray chamber in 5% NaCl for 72 hours. Later, the specimens are washed with water and air-dried up before measuring weight loss. The tribological behavior of the prepared composites was analyzed concerning ASTM G99 via a pin-on-on-a-disc instrument (Ducom Instruments Pvt Ltd). The parameters for tribological experimentation are (1) speed of 300 rpm, (2) time of 1000 s, and (3) sliding velocity 0.5–2.0 m/s at an interval of 0.5. The CNC drilling process was done using Siemens CNC lathe (MTAB) to analyze the MRR and SR. The MRR was found by determining the weight of samples previously and later machining, and SR was measured using the surface roughness tester TR110. Overall, the experimental scheme is given in Figure 1.

3. Results and Discussion

3.1. SEM Examination of Composites. Figures 2(a)–2(d) show the SEM images of AA6063-4wt.%Nano AlN, AA6063-8wt.%Nano AlN, and AA6063-12wt.%Nano AlN

composites. Figures 2(b)–2(d) display the occurrence and even dispersal of Nano AlN particles in the AA6063 matrix. From the SEM images (Figures 2(b)–2(d)), while increasing the wt.% from 4 to 12, more amount of particle dispersal can be seen in Figure 2(d); it indicates that fine dispersal was attained in the composites. Furthermore, no voids, cracks, pores, and clustering of particles are witnessed in any of the composites. The composites possess good bonding amid matrix and particle; this is owing to the matrix boundary that becomes hardened initially; then, Nano AlN reinforcement left out via solid/liquid boundary which leads Nano AlN particles becomes separated at the interdendrite zone [17].

3.2. Density and Porosity Analysis. Figure 3 displays the density and porosity examination of AA6063-Nano AlN composites. From Figure 3, it is clear that experimental density is lesser than the theoretical density when increasing the reinforcement from 0 to 12 wt.%. The increment in theoretical density is due to the hard tendency of Nano AlN particles and additionally excellent bonding occurred amid the matrix and reinforcement. It is witnessed from the SEM images (Figures 2(b)–2(d)). Furthermore, the density of Nano AlN is higher than that of AA6063, this might be one of the reasons for density enhancement. While increasing the wt.% of Nano AlN from 4 to 12, the porosity of the composites reduced gradually; this is because no pores, voids, and cracks were found in any of the composites; it is clear from the SEM images (Figures 2(a)–2(d)).

Due to the selection of suitable stir casting process parameters, uniform dispersal of reinforcement and matrix was occurred.

3.3. Influence of Nano AlN on Microhardness. The influence of Nano AlN wt.% on microhardness was studied, and

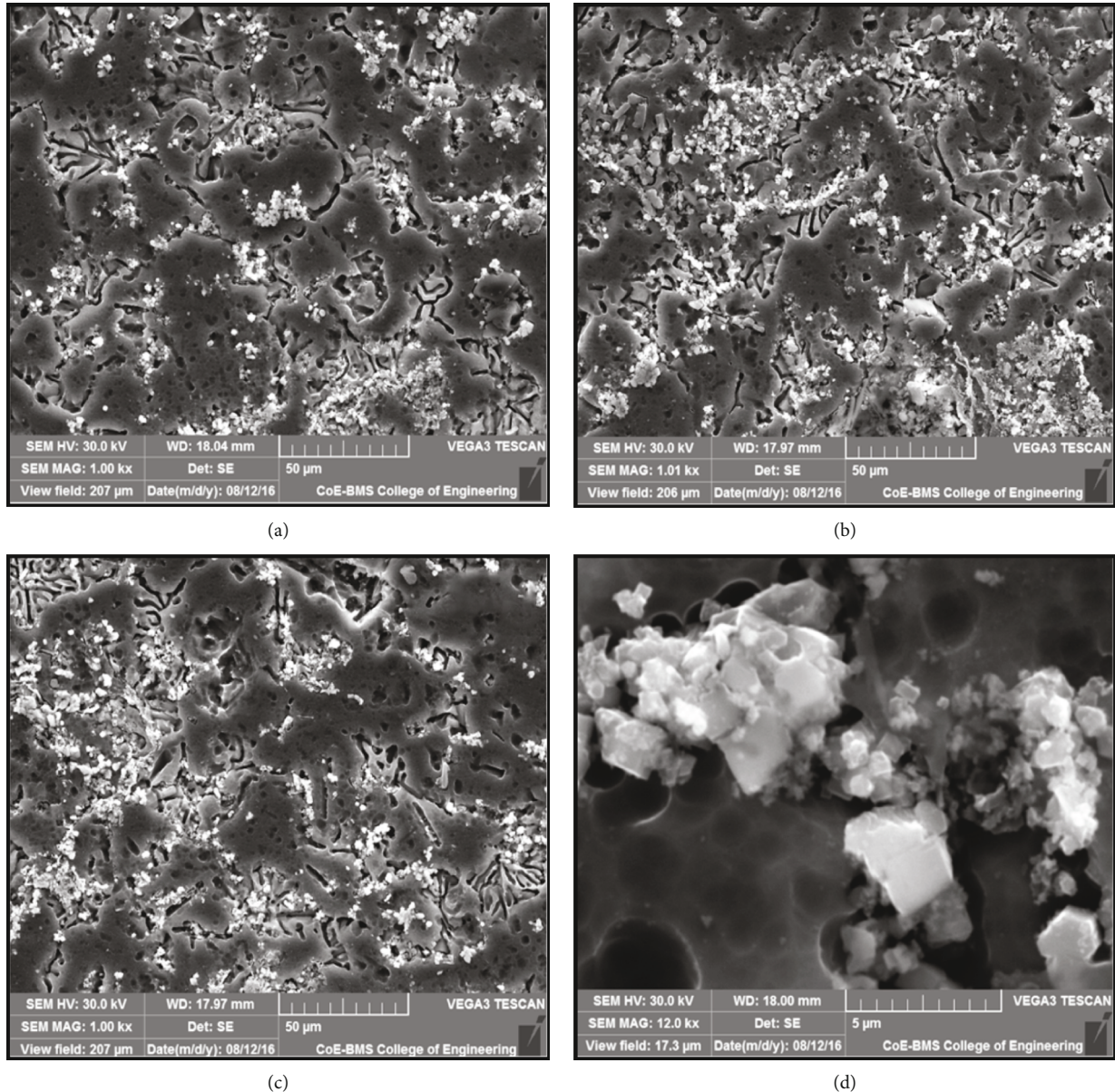


FIGURE 2: (a–d) SEM images of AA6063-4wt.%Nano AlN, AA6063-8wt.%Nano AlN, and AA6063-12wt.%Nano AlN.

Figure 4 shows the AA6063-Nano AlN composites microhardness. The microhardness of AA6063-Nano AlN composites was enhanced when increasing the Nano AlN wt.% from 4 to 12. This is owing to the high hardness of Nano AlN particles than the AA6063 matrix and proper bonding amid the matrix and reinforcement; it is witnessed by SEM images (Figures 2(b)–2(d)). Despite grain enhancement, the particle strengthening and load-bearing ability of hard reinforcement particle to matrix hardness of the composites improved. The surface area was improved due to inclusion of Nano AlN reinforcement into AA6063 matrix; additionally, the grain size of the matrix was reduced. However, more amount of reinforcement in the matrix hints to improved dislocation density all through the solidification owing to the thermal absurdity amid the matrix and reinforcement [17]. The least hardness attained was 64 HV for the

AA6063 matrix, and the higher hardness attained was 92 HV for the composites AA6063-12 wt%. Nano AlN. The 30.43% of improvement in hardness was achieved when 12 wt% of Nano AlN were added to AA6063 matrix.

3.4. Influence of Nano AlN on Tensile and Yield Strength.

The effect of Nano AlN wt.% on the tensile and yield strength of AA6063 matrix composites is shown in Figure 5. It is witnessed that AA6063 matrices possess the least tensile and yield strength than that of AA6063-Nano AlN composites. From Figure 5, it is clear that increasing the Nano AlN wt.% from 4 to 12, a gradual enhancement in tensile and yield strength was attained. The various reasons for the enhancement in tensile strength are the grain refinement obtainable via Nano AlN; Nano AlN particles act as obstacles to the motion of displacements which results

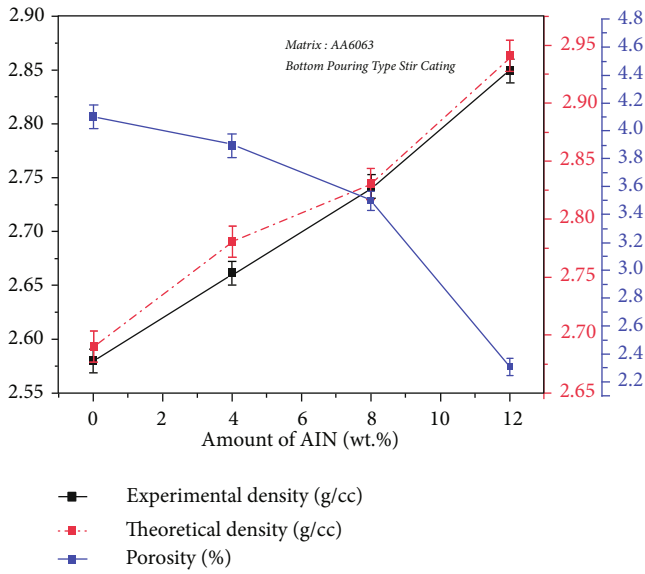


FIGURE 3: Experimental and theoretical densities and porosity of AA6063-Nano AlN composites.

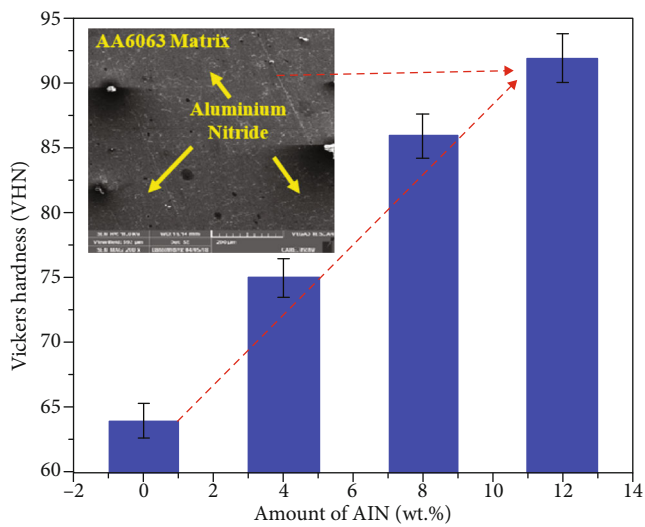


FIGURE 4: Microhardness of AA6063-Nano AlN composites and inset shows the SEM image of the composite sample with uniform distribution of Nano AlN particles.

in enhanced tensile strength [14]. Even the dispersal of Nano AlN takes the conversion of smeared load from matrix to Nano AlN particles; moreover, coefficient of thermal development amid matrix reinforcement originates an enormous amount of dislocation density about the surface of reinforcement particles, and the one major reason is dispersal strengthening mechanism [8]. The lowest ultimate tensile strength attained was 13.51 MPa for AA6063 matrix, and the extreme ultimate tensile strength obtained was 297.21 MPa for the AA6063-12wt.%Nano AlN composites. The 54.4% of enhancement in ultimate tensile strength was attained when 12 wt.% of Nano AlN were added to AA6063 matrix.

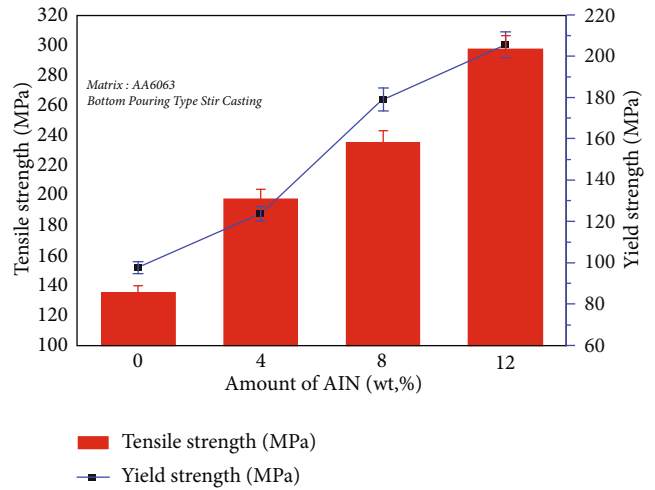


FIGURE 5: Tensile and yield strength of AA6063-Nano AlN composites.

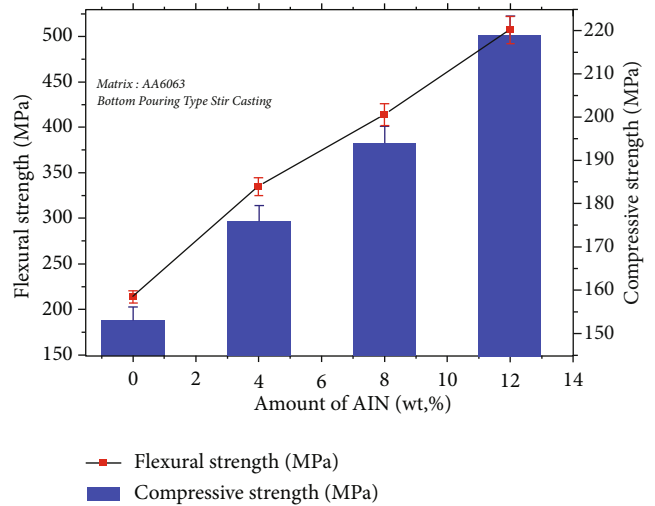


FIGURE 6: Compressive and flexural strength of AA6063-Nano AlN composites.

Figure 5 displays yield strength (YS) of AA6063-Nano AlN composite. Figure 5 surely displays that AA6063 matrix exhibits the least yield strength after the addition of Nano AlN particle to AA6063 matrix increase in YS of the produced composites acquired. The occurrence of Nano AlN particles in matrix frontrunners due to diminished matrix grain size. Reference to Hall-Petch correlation yield strength is in reverse relational with grain size. Likewise, yield strength of the AA6063-Nano AlN composites rises [14]. The least yield strength 97.59 MPa was attained for AA6063 matrix, and the maximum yield strength 205.60 was attained for the AA6063-12wt.%Nano AlN composites.

3.5. Influence of Nano AlN on Compressive Strength. The influence of Nano AlN wt.% on the compressive strength of AA6063 matrix composites is shown in Figure 6. It is observed that AA6063 matrix exhibits minimum

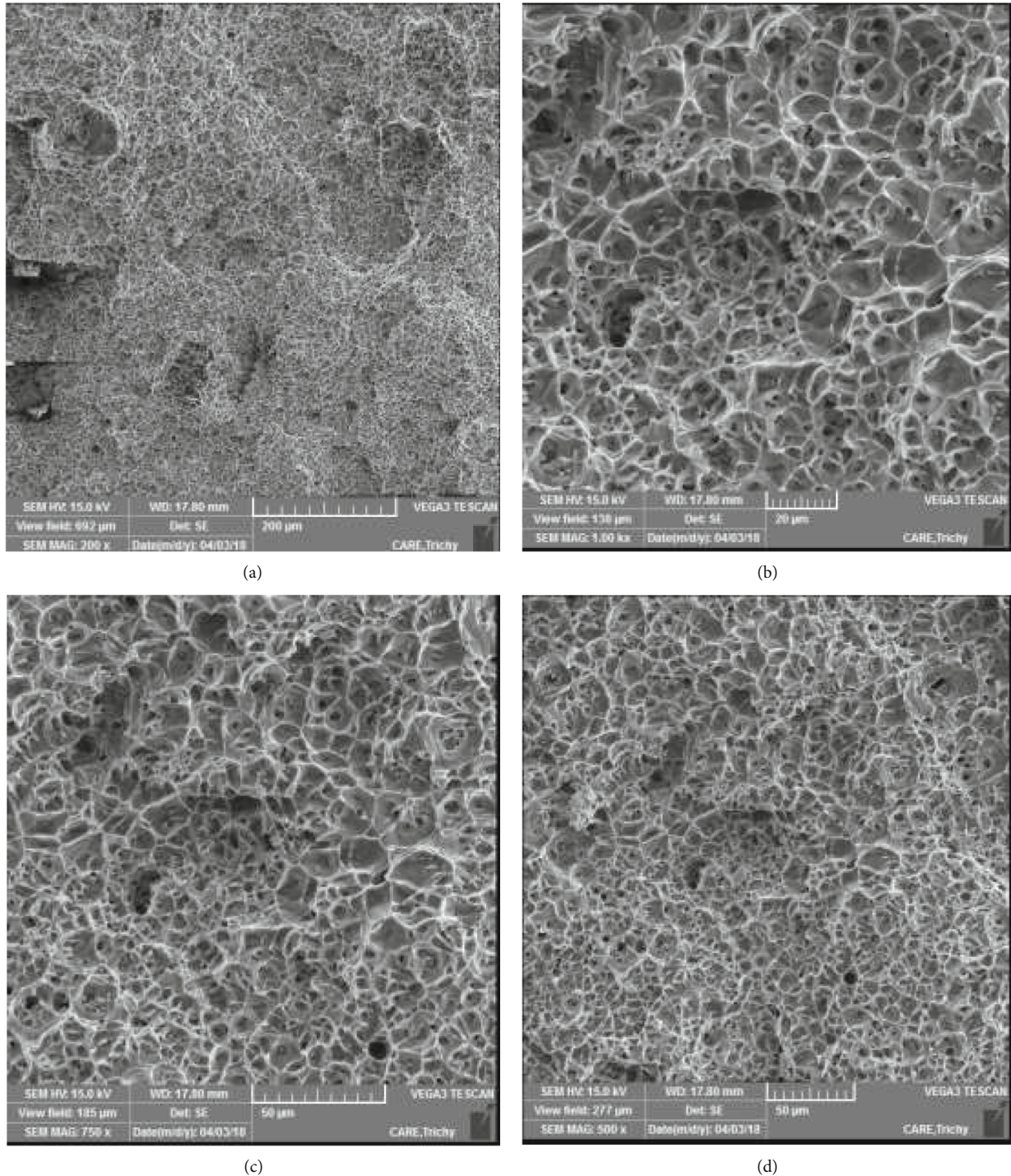


FIGURE 7: Tensile fracture surface of AA6063, AA6063-4 wt.%Nano AlN, AA6063-8 wt.%Nano AlN, and AA6063-12 wt.%Nano AlN composites.

compressive strength than that of AA6063-Nano AlN composites. From Figure 6, it can be understood that a raise in Nano AlN wt.% from 4 to 12 an enhancement in compressive strength was obtained. The existence of Nano AlN particles in matrix performs as a hindrance to the movement of dislocation pointer with an additional enhancement in compression strength. The enhanced dislocation instigated via

CTE divergence is one of the reasons for the increment in compression strength. The major important reason for compressive strength enhancement is the fine and even scattering of Nano AlN particles in matrix [31]. The lowest compressive strength achieved was 153 MPa for AA6063 matrix, and the extreme compressive strength attained was 219 MPa for the composites AA6063-12wt.%Nano AlN.

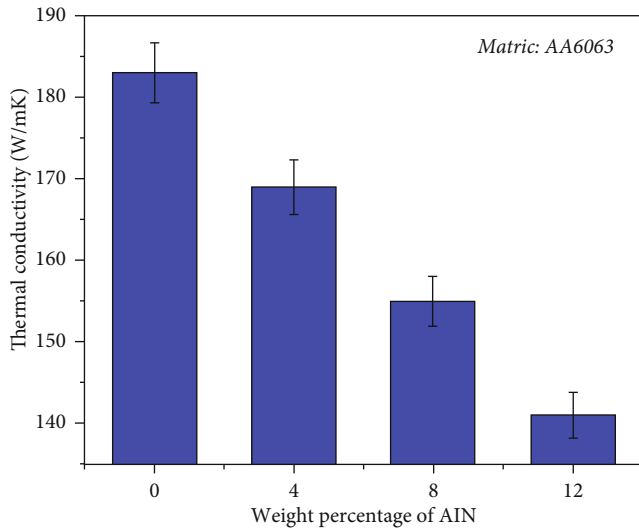


FIGURE 8: Thermal conductivity of AA6063-Nano AlN composites.

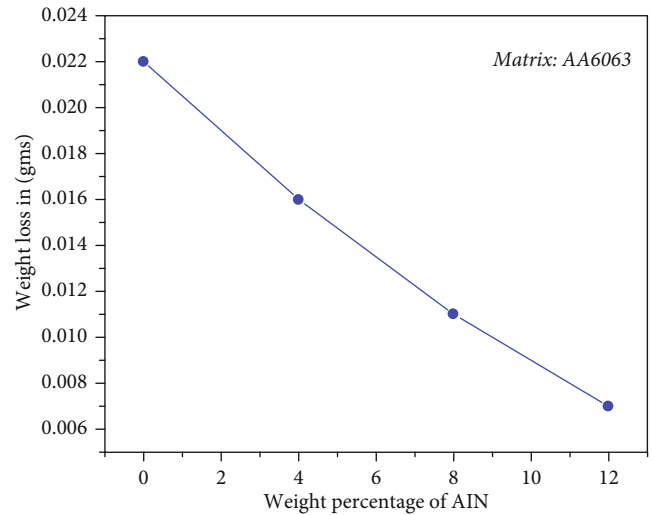


FIGURE 10: Effect of Nano AlN on wear properties.

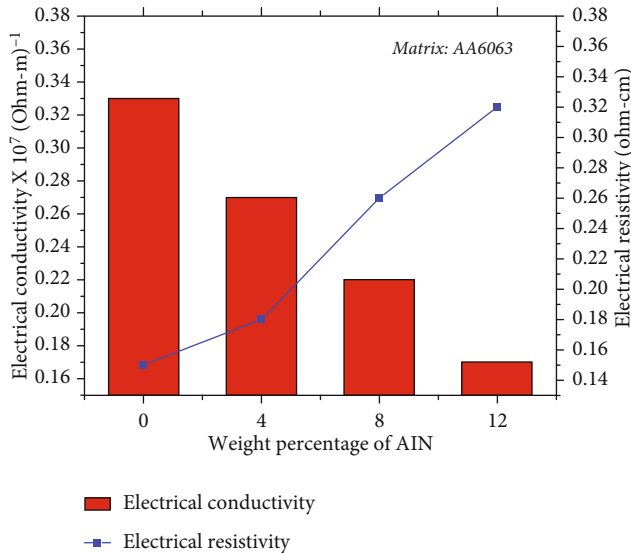


FIGURE 9: Thermal conductivity of AA6063-Nano AlN composites.

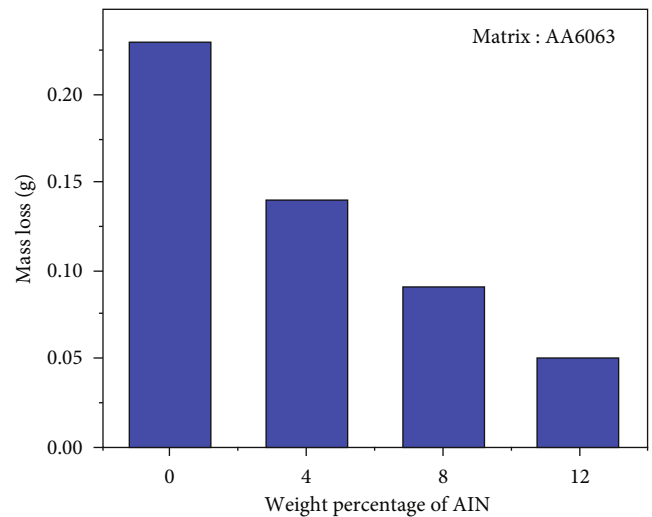


FIGURE 11: Salt spray corrosion of AA6063-Nano AlN composites.

Therefore, it can be clearly implicit that 12 wt.%Nano AlN composites possess superior strength than that of the unreinforced alloy.

The influence of Nano AlN wt.% on the flexural strength of AA6063 matrix composites was shown in Figure 6. It is detected that AA6063 matrix exhibits the least flexural strength than that of AA6063-Nano AlN composites. From Figure 6, it is clear that the increment in Nano AlN wt.% from 4 to 12 results in increased flexural strength. This may be ascribed to an enhanced dislocation density triggered via thermal coefficient growth conflict amid the matrix and reinforcement, which results in the improvement of the flexural strength [32]. Besides, the boundary amid matrix and Nano AlN reinforcement transports the load from the matrix to reinforcement particle outstandingly.

3.6. SEM Examination of Tensile Fractures. Figures 7(a)–7(d) show tensile fracture of AA6063 and AA6063-Nano AlN composites. Figure 7(a) clearly shows the large dimples, this dimple formation is despite of the ductile nature of the AA6063 matrix, and Figure 7(a) specifies that uniformly dispersed voids display a ductile nature. From Figures 7(b)–7(d), it might be implicit that the void sizes of the produced AA6063-Nano AlN composites are smaller when compared to the matrix alloy (Figure 7(a)). The fractured surface represents a moderately flat presence, which shows macroscopically breakable fractures and microscopically malleable fractures. A smaller void formation occurred when the Nano AlN particles reinforced with AA6063 matrix, which developed the grain size and ductility decreased. Furthermore, it is witnessed that Nano AlN particles left over the whole in

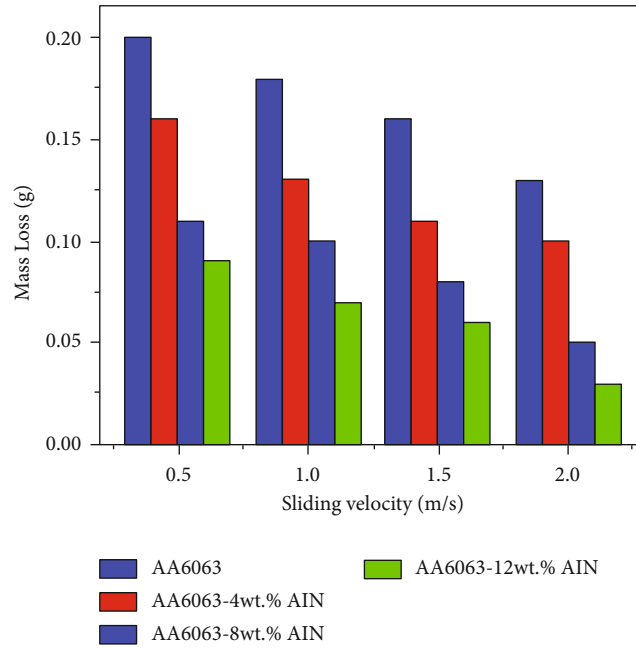


FIGURE 12: Plot between sliding velocity and mass loss.

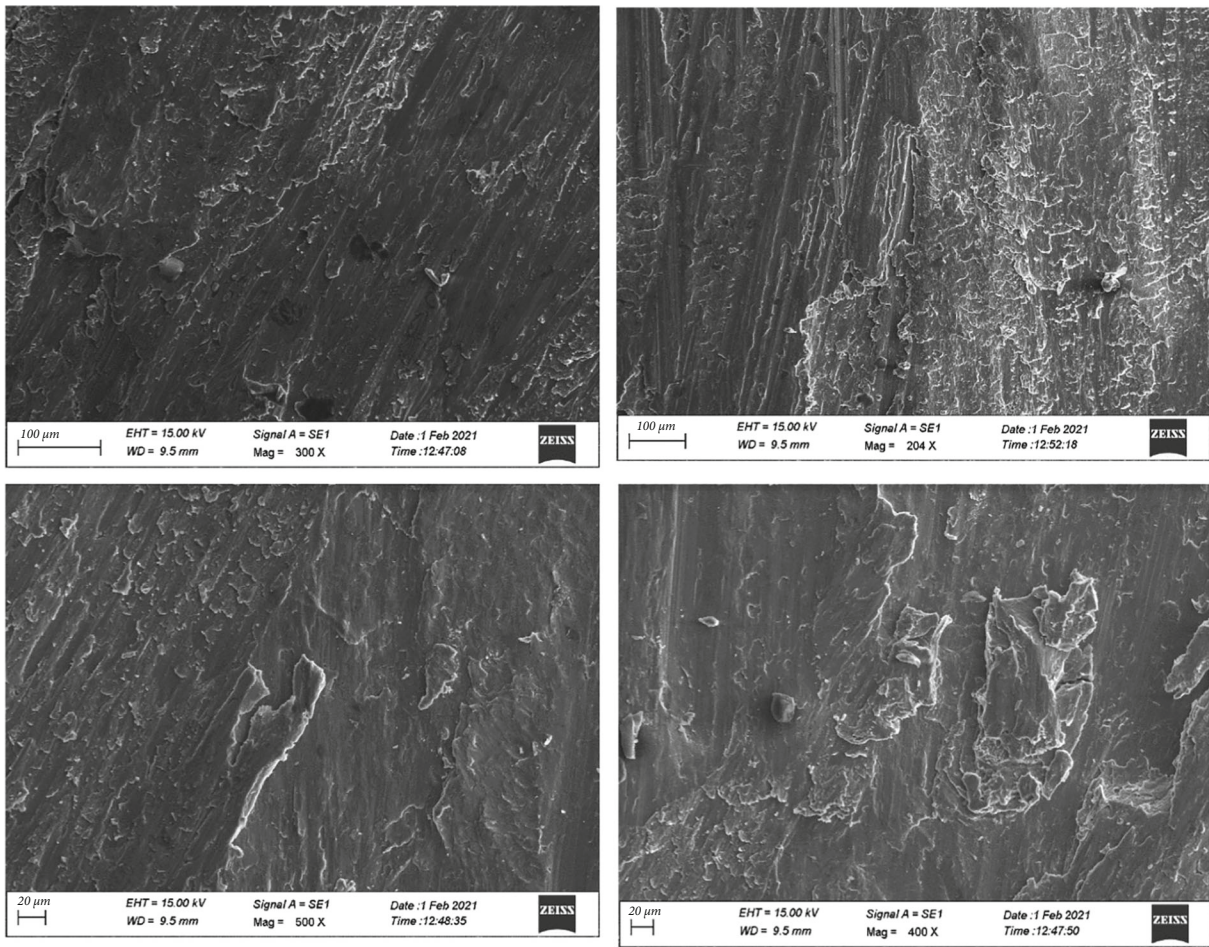


FIGURE 13: Worn surface analysis of AA6063, AA6063-4wt.%Nano AlN, AA6063-8wt.%Nano AlN, and AA6063-12wt.%Nano AlN composites.

TABLE 1: Input parameters and output results.

Ex. No	CS (rpm)	FR (mm/rev)	DOC (mm)	MRR (g/min)	SR (μm)
1	1000	0.05	0.2	0.073	1.88
2	1000	0.15	0.3	0.097	1.68
3	1000	0.25	0.4	0.118	1.75
4	2000	0.05	0.3	0.081	2.02
5	2000	0.15	0.4	0.104	2.25
6	2000	0.25	0.2	0.124	2.09
7	3000	0.05	0.4	0.09	2.17
8	3000	0.15	0.2	0.112	1.59
9	3000	0.25	0.3	0.147	1.80

some locations on the fracture surface, which provides confirmation for the occurrence of enhanced bonding amid AA6063 matrix and reinforced Nano AlN particles.

3.7. Thermal Conductivity. The influence of Nano AlN particles on the thermal conductivity of AA6063 matrix is shown in Figure 8. The addition of Nano AlN to AA6063 reduces the thermal conductivity. The AA6063-Nano AlN composite thermal conductivity reduces while adding wt.% from 4 to 12. The thermal conductivity of the composites is commonly pretentious by weight percentage and kind of reinforcement, density, or porosities, and fabrication routes utilized are vital factors, which affect the thermal conductivity values. However, in this investigation, it is clear that the thermal conductivity of AA6063 matrix is higher than Nano AlN particle, and this is the major cause for the decline in the composite thermal conductivity. Therefore, the inclusion of Nano AlN with AA6063 furthermore declines the composite thermal conductivity. From the investigations, it is clear that 12 wt.%Nano AlN reinforced AA6063 composites possess less thermal conductivity when compared with other composites. The major cause might be interference of oxide particles could improve the mechanical properties. However, it reduces the thermal conductivity. The obtained outcomes are finely matched with the earlier results of different researchers [33, 34].

3.8. Electrical Conductivity. The effect of Nano AlN particles on the electrical resistivity and conductivity of AA6063 matrix is shown in Figure 9. It is clearly visible from Figure 9 that addition of Nano AlN to AA6063 improves the electrical resistivity. The major reason for the enhancement in electrical resistivity is grain size reduction. Simultaneously, the addition of Nano AlN to AA6063 decreases the electrical conductivity. The reason for the decline in electrical conductivity is despite of the oxidative nature of Nano AlN particles in addition to that Nano AlN particles possess less electrical conductive nature.

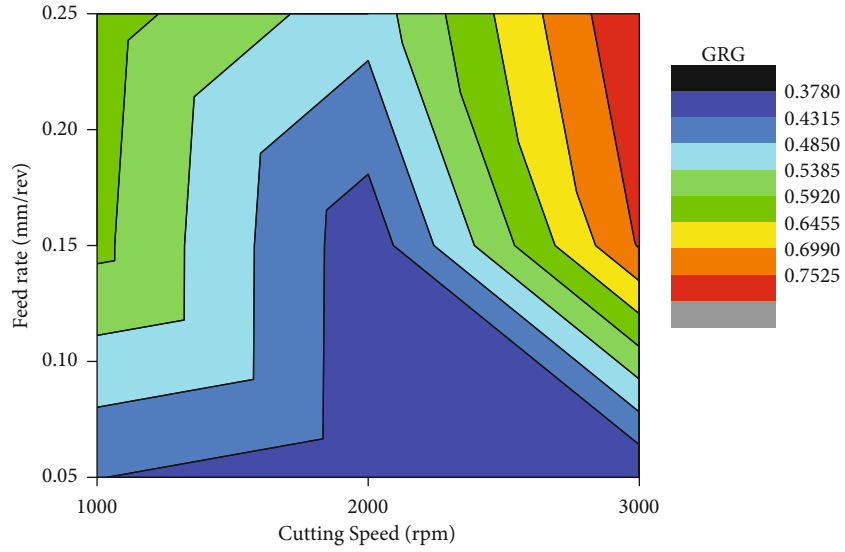
3.9. Salt Spray Corrosion Analysis. The effect of Nano AlN particles on the corrosion behavior of AA6063 matrix is shown in Figure 10. It is indeed noticeable from Figure 11 that inclusion of Nano AlN with AA6063 improves the corrosion resistivity of the composites. This is because of the

mechanical and hard nature of the Nano AlN particles. In addition to that, even distribution of Nano AlN particles in AA6063 matrix is also one of the reasons for the improved corrosion resistance which is clear from SEM analysis (Figures 2(a)–2(d)). While increasing the reinforcement weight percentage from 4 to 12, oxide layers formed over the AA6063 matrix surface reduced the weight loss. The oxide film guards the basic surface from extra corrosion outbreak [35]. Because of the above-mentioned reasons, the weight loss of AA6063-12wt.%Nano AlN composite is less when compared to other composites.

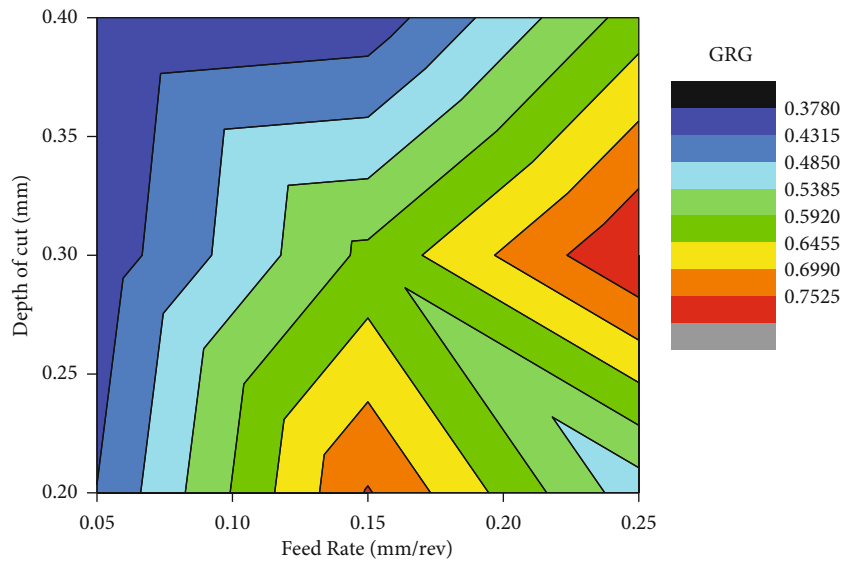
3.10. Tribological Analysis. Figures 10 and 12 display the influence of Nano AlN particles on the tribological behavior of the prepared composites. Figure 10 displays the wt.% of Nano AlN vs. mass loss amid wear analysis. AA6063 matrices attained higher mass loss, and 12 wt.% reinforced Nano AlN composites attain the least mass loss. It can be clearly witnessed that hard Nano AlN particles strengthened with AA6063 matrix lead to noteworthy enhancement in mass loss. It could be understood from the Archard equation that materials wear opposition is straightly linked to hardness [36]. From the obtained results, it is clear that the higher mass loss was attained for AA6063-12 wt.%Nano AlN composites and this is because of the effect of Nano AlN particle. The other major cause for the decline in mass loss while the wt.% range is despite of the greater hardness of Nano AlN particles. With reference to the rule of mixtures, a raise in hard reinforcement particles results in better wear opposition.

Figure 12 displays the graph for SV and mass loss of AA6063-Nano AlN composites. It is clear from the graph (Figure 9) that the decline in mass loss was obtained while increasing the SV from 0.5 to 1.5 m/s. Increment in mass loss for AA6063 was attained while increasing the SV up to 2 m/s. The cause for the enhancement in mass loss at a SV of 2 m/s might be owing to the maximum temperature expansion at maximum SV. However, the maximum temperature expansion reduces the stress and strain rate amid sliding [36].

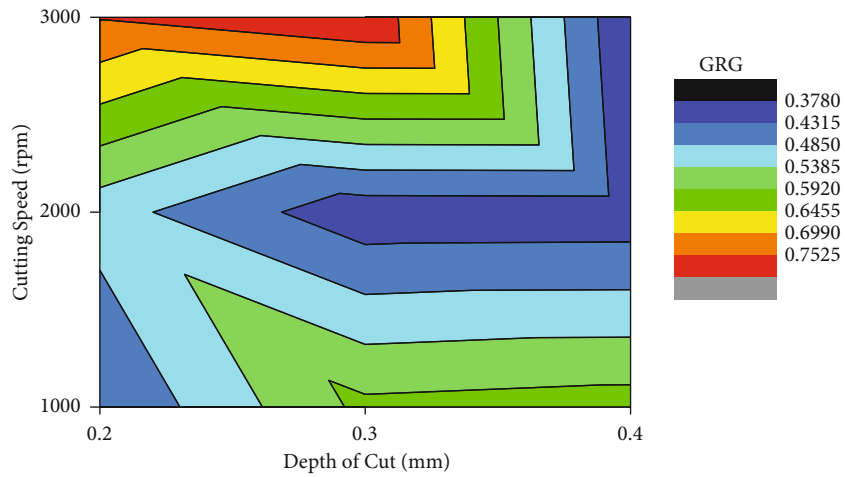
3.11. Worn Surface Examination. Figures 13(a)–13(d) show the worn surface examination of AA6063-Nano AlN composites. The SEM analysis of AA6063-Nano AlN composites displays some craters, grooves, pullouts, and plastic



(a)



(b)



(c)

FIGURE 14: (a) Contour plot for MRR and SR CS vs FR. (b) Contour plot for MRR and SR FR vs. CS. (c) Contour plot for MRR and SR DOC vs. CS.

TABLE 2: Normalized S/N ratio and deviation sequence.

Ex. No	Normalized S/N ratio		Deviation sequence	
	MRR	SR	MRR	SR
1	0	0.560606	1	0.439394
2	0.324324	0.863636	0.675676	0.136364
3	0.608108	0.757576	0.391892	0.242424
4	0.108108	0.348485	0.891892	0.651515
5	0.418919	0	0.581081	1
6	0.689189	0.242424	0.310811	0.757576
7	0.22973	0.121212	0.77027	0.878788
8	0.527027	1	0.472973	0
9	1	0.681818	0	0.318182

deformation. The Nano AlN particles occurred in the crater display few fragmented particles, and from the surface dragged out particles was found. The outcome specifies the abrasive wear mechanism, which is an outcome of Nano AlN particles wide-open over the worn surface and loose fragments amid surfaces. The inclusion of Nano AlN particles repels the delamination process (Figures 13(a)–13(c)). The raise in Nano AlN wt.% from 4 to 12 enhances the wear resistance. It is witnessed that AA6063 matrix and 4 wt.% reinforced Nano AlN composites exposed to extreme plastic deformation compared to 12 wt.% reinforced Nano AlN.

3.12. Drilling Behavior of AA6063-Nano AlN Composites. MRR and SR analysis was done to predict the optimal parameters to acquire higher MRR and SR for manufactured samples through GRA. Tests were conducted with reference to L9 OA. The results are displayed in Table 1.

3.13. Effect of Process Parameter on MRR and SR. Figures 14(a)–14(c) display the contour plot for MRR and SR (a) CS vs. FR, (b) FR vs. DOC, and (c) DOC vs CS. It is perceived that higher MRR and least SR were obtained while improving the feed rate. From Figures 14(a)–14(c), it can be understood that FR 0.25 mm/rev is the major influencing parameter than that of CS and DOC. The MRR and SR is in the order of 3000 > 2000 > 1000 feed rate mm/rev.

3.14. Grey Relational Analysis (GRA). A GRA is a newer technique for estimate, establishing relational examination, and in choice making in various fields of fabrication industries [37]. To acquire higher MRR and SR for drilling of AA6063-Nano AlN composites, appropriate process parameters should be chosen for that GRA is the most suitable optimization process. Table 2 displays the normalized S/N ratio and deviation sequence for MRR and SR. Table 3 shows the GRC, GRG with rank for 9 trials. From Table 3, it is clear that the 9th trial is the optimal one to attain higher MRR and SR. From Table 4, it is seen that 0.2407 is the boundary of max-min regard (Figure 15). From Table 4, it is clear that FR is the substantial parameter tracked by CS and DOC. The series of influencing parameters is in the order as numbered FR (0.2407), CS (0.2130), and DOC (0.3182).

TABLE 3: Evaluated GRC and GRG rank.

Ex. No	GRC		GRG	Rank
	MRR	SR		
1	0.333333	0.532258	0.432796	6
2	0.425287	0.785714	0.605501	4
3	0.560606	0.673469	0.617038	3
4	0.359223	0.434211	0.396717	8
5	0.4625	0.333333	0.397917	7
6	0.616667	0.39759	0.507129	5
7	0.393617	0.362637	0.378127	9
8	0.513889	1	0.756944	2
9	1	0.611111	0.805556	1

TABLE 4: Response table for means.

Level	CS (rpm)	FR (mm/rev)	DOC (mm)
1	0.5518	0.4025	0.5656
2	0.4339	0.5868	0.6026
3	0.6469	0.6432	0.4644
Delta	0.2130	0.2407	0.1382
Rank	2	1	3

3.15. Analysis of Variance. The outcomes of the process parameters inducing several lead features are inspected through ANOVA. To predict the major extensive parameters, ANOVA for GRG is shown in Table 5. It is clearly witnessed from Table 5 that FR is a noteworthy parameter (subsidizing 45.89%). The FR possesses major influence multienactment characteristics for AA6063-Nano AlN composites lagged behind by CS (32.96%) and DOC (14.83%).

4. Conclusions

- (i) AA6063-Nano AlN composite was efficaciously manufactured via SC process
- (ii) The effects of Nano AlN particles on AA6063 matrix on the microstructure and properties were analyzed
- (iii) SEM analysis shows the existence and even dispersal of Nano AlN particles in AA6063 matrix
- (iv) The inclusion of Nano AlN particles with AA6063 enhances the density and reduces the porosity
- (v) The 12 wt.% addition of Nano AlN particles into AA6063 matrix improves the complete mechanical behavior of the composites
- (vi) The tensile fracture analysis was done on the AA6063-Nano AlN composites using SEM
- (vii) The thermal conductivity examination was carried out and stated that the inclusion of Nano AlN particles into AA6063 matrix reduces the thermal conductivity



FIGURE 15: Main effects plot for SN ratios.

TABLE 5: ANOVA table.

Source	DF	Seq SS	Adj SS	Adj MS	F	P	Contribution (%)
CS (rpm)	2	0.068284	0.068284	0.034142	5.23	0.161	32.96%
FR (mm/rev)	2	0.095065	0.095065	0.047533	7.27	0.121	45.89%
DOC (mm)	2	0.030728	0.030728	0.015364	2.35	0.298	14.83%
Error	2	0.013068	0.013068	0.006534			
Total	8	0.207146					

$S = 0.0808336$; $R\text{-Sq} = 93.69\%$; $R\text{-Sq}(\text{adj}) = 74.77\%$.

- (viii) The electrical resistivity and electrical conductivity analysis was conducted and found that an increase in Nano AlN particles with AA6063 matrix enhances the electrical resistivity and declines the thermal conductivity
- (ix) Tribological behaviors of AA6063-Nano AlN composites were analyzed and concluded that the inclusion of Nano AlN particles with AA6063 reduces the mass loss
- (x) The worn surface analysis was done on the AA6063-Nano AlN composites via SEM to predict the wear mechanism
- (xi) The CNC drilling behavior of AA6063-Nano AlN composites was studied via GRA and the optimal parameters to acquire higher MRR, and the least SR was determined as FR 0.25 mm/rev, CS 3000 rpm, and DOC 0.3 mm
- (xii) To determine the influencing parameters on the responses FR, CS, and DOC, ANOVA was utilized

Data Availability

The data used to support the findings of this study are included in the article.

Conflicts of Interest

The authors declare that there is no conflict of interest regarding the publication of this paper.

Acknowledgments

The authors thank the Bharath Institute of Higher Education and Research and K. Ramakrishnan College of Engineering for providing facilities support to complete this research work. The authors also thank the AMIT, Arbaminch University, Ethiopia, and Pusan National University, South Korea, for providing help during the research and preparation of the manuscript. This project was supported by Researchers Supporting Project number (RSP-2021/332), King Saud University, Riyadh, Saudi Arabia.

References

- [1] S. Chand, P. Chandrasekhar, S. Roy, and S. Singh, "Influence of dispersoid content on compressibility, sinterability and mechanical behaviour of B4C/BN reinforced Al6061 metal matrix hybrid composites fabricated via mechanical alloying," *Metals and Materials International*, vol. 27, no. 11, pp. 4841–4853, 2021.
- [2] N. Singh, R. M. Belokar, and R. S. Walia, "A critical review on advanced reinforcements and base materials on hybrid metal matrix composites," *Silicon*, pp. 1–24, 2020.

- [3] A. Mahato and S. Mondal, "Fabrication and microstructure of micro and nano silicon carbide reinforced copper metal matrix composites/nanocomposites," *Silicon*, vol. 13, pp. 1097–1105, 2021.
- [4] S. I. Gad, M. A. Attia, M. A. Hassan, and A. G. El-Shafei, "Predictive computational model for damage behavior of metal-matrix composites emphasizing the effect of particle size and volume fraction," *Materials*, vol. 14, no. 9, p. 2143, 2021.
- [5] B. Hekner, J. Myalski, P. Wrześniowski, and T. Maciąg, "Al matrix composites reinforced by Ti and C dedicated to work at elevated temperature," *Materials*, vol. 14, no. 11, p. 3114, 2021.
- [6] B. Gobalakrishnan, C. Rajaravi, G. Udhayakumar, and P. R. Lakshminarayanan, "Effect of ceramic particulate addition on aluminium based ex-situ and in-situ formed metal matrix composites," *Metals and Materials International*, vol. 27, no. 9, pp. 3695–3708, 2021.
- [7] A. Kareem, J. A. Qudeiri, A. Abdudeen, T. Ahammed, and A. Ziout, "A review on AA 6061 metal matrix composites produced by stir casting," *Materials*, vol. 14, no. 1, p. 175, 2021.
- [8] V. Mohanavel, "Synthesis and evaluation on mechanical properties of LM4/AlN alloy based composites," *Energy Sources, Part A: Recovery, Utilization, and Environmental Effects*, vol. 2019, article 1647313, 8 pages, 2019.
- [9] H. Yu, H. Chen, R. Ma, and G. Min, "Fabrication of AlN-TiC/Al composites by gas injection processing," *Rare Metals*, vol. 25, no. 6, pp. 659–664, 2006.
- [10] K. Sanesh, S. S. Sunder, and N. Radhika, "Effect of reinforcement content on the adhesive wear behavior of Cu₁₀Sn₅Ni/Si₃N₄ composites produced by stir casting," *Metallurgy and Materials*, vol. 24, no. 9, pp. 1052–1060, 2017.
- [11] R. Nithesh, N. Radhika, and S. Shiam Sunder, "Mechanical properties and adhesive scuffing wear behaviour of stir cast Cu-Sn-Ni/Si₃N₄ composites," *Journal of Tribology*, vol. 139, no. 6, 2017.
- [12] J. S. D. Joseph, B. Kumaragurubaran, and S. Sathish, "Effect of MoS₂ on the wear behavior of aluminium (AlMg0.5Si) composite," *Silicon*, vol. 12, no. 6, pp. 1481–1489, 2020.
- [13] S. Saravanan, P. Senthilkumar, M. Ravichandran, and V. Anandakrishnan, "Mechanical, electrical, and corrosion behavior of AA6063/TiC composites synthesized via stir casting route," *Journal of Materials Research*, vol. 32, no. 3, pp. 606–614, 2017.
- [14] V. Mohanavel and M. Ravichandran, "Experimental investigation on mechanical properties of AA7075-AlN composites," *Materials Testing*, vol. 61, no. 6, pp. 554–558, 2019.
- [15] B. A. KUMAR, N. MURUGAN, and I. DINAHARAN, "Dry sliding wear behavior of stir cast AA6061-T6/AlN_p composite," *Transactions of Nonferrous Metals Society of China*, vol. 24, no. 9, pp. 2785–2795, 2014.
- [16] M. Zhao, G. Wu, D. Zhu, L. Jiang, and Z. Dou, "Effects of thermal cycling on mechanical properties of AlNp/Al composite," *Material Letters*, vol. 58, no. 12-13, pp. 1899–1902, 2004.
- [17] V. M. Kumar and C. V. Venkatesh, "Evaluation of microstructure, physical and mechanical properties of Al 7079 – AlN metal matrix composites," *Materials Research Express*, vol. 6, no. 12, article 126503, 2019.
- [18] S. Fale, A. Likhite, and J. Bhatt, "Compressive, tensile and wear behavior of ex situ Al/AlN metal matrix nanocomposites," *Journal of Composite Materials*, vol. 49, no. 16, pp. 1917–1928, 2015.
- [19] E. A. M. Shalaby and A. Y. Churyumov, "Development and characterization of A359/AlN composites for automotive applications," *Journal of Alloys and Compounds*, vol. 727, pp. 540–548, 2017.
- [20] N. Radhika and R. Raghu, "Abrasive wear behavior of monolithic alloy, homogeneous and functionally graded aluminum (LM25/AlN and LM25/SiO₂) composites," *Particulate Science and Technology An International Journal*, vol. 37, no. 1, pp. 10–20, 2019.
- [21] N. Radhika and R. Raghu, "Investigation on mechanical properties and analysis of dry sliding wear behavior of Al LM13/AlN metal matrix composite based on Taguchi's technique," *Journal of Tribology*, vol. 139, no. 4, article 041602, 2017.
- [22] S. Basavarajappa, G. Chandramohan, J. P. Davim et al., "Drilling of hybrid aluminium matrix composites," *International Journal of Advanced Manufacturing Technology*, vol. 35, no. 11-12, pp. 1244–1250, 2008.
- [23] T. Rajmohan and K. Palanikumar, "Modeling and analysis of performances in drilling hybrid metal matrix composites using D-optimal design," *International Journal of Advanced Manufacturing Technology*, vol. 64, no. 9-12, pp. 1249–1261, 2013.
- [24] T. Rajmohan, K. Palanikumar, and M. Kathirvel, "Optimization of machining parameters in drilling hybrid aluminium metal matrix composites," *Transactions of the Nonferrous Metals Society of China*, vol. 22, article 12861297, 2012.
- [25] M. Elango and K. Annamalai, "High speed machining and optimisation of Al/SiC/Gr hybrid metal matrix composites using ANOVA and grey relational analysis," *Australian Journal of Mechanical Engineering*, vol. 2020, article 1761587, 12 pages, 2020.
- [26] Y. Altunpak, M. Ay, and S. Aslan, "Drilling of a hybrid Al/SiC/Gr metal matrix composites," *International Journal of Advanced Manufacturing Technology*, vol. 60, no. 5-8, pp. 513–517, 2012.
- [27] K. K. Alaneme and M. O. Bodunrin, "Mechanical behaviour of alumina reinforced aa6063 metal matrix composites developed by two-step – stir-casting process, acta technica corviniensis bulletin of engineering," *Acta Technica Corviniensis-bulletin of engineering*, vol. 6, no. 3, p. 105, 2013.
- [28] T. Anandaraj, P. P. Sethusundaram, M. Meignanamoorthy, and M. Ravichandran, "Investigations on properties and tribological behavior of AlMg4.5Mn0.7(AA5083)-MoO₃ composites prepared by stir casting method," *Surface Topography: Metrology and Properties*, vol. 9, no. 2, article 025011, 2021.
- [29] R. Jojith and N. Radhika, "Mechanical and tribological properties of LM13/TiO₂/MoS₂ hybrid metal matrix composite synthesized by stir casting," *Particulate Science and Technology*, vol. 37, no. 5, pp. 570–582, 2019.
- [30] G. K. Meenashisundaram, S. Seetharaman, and M. Gupta, "Enhancing overall tensile and compressive response of pure Mg using nano- TiB₂ particulates," *Materials characterization*, vol. 94, pp. 178–188, 2014.
- [31] B. Kuldeep, K. P. Ravikumar, S. Pradeep, and K. R. Gopi, "Effect of boron nitride and zirconium dioxide on mechanical behavior of Al7075 metal matrix hybrid composite," *Materials Research Express*, vol. 6, no. 3, article 036509, 2019.
- [32] E. Nas and H. Gokkaya, "Mechanical and physical properties of hybrid reinforced (Al/B4C/Ni(K)Gr) composite materials

- produced by hot pressing,” *Materials Testing*, vol. 57, no. 6, pp. 524–530, 2016.
- [33] P. Zhang, J. Jie, Y. Gao et al., “Preparation and properties of TiB₂ particles reinforced Cu-Cr matrix composite,” *Materials Science and Engineering A*, vol. 642, pp. 398–405, 2015.
- [34] B. Stalin, G. T. Sudha, and M. Ravichandran, “Investigations on characterization and properties of Al-MoO₃ composites synthesized using powder metallurgy technique,” *Silicon*, vol. 10, no. 6, pp. 2663–2670, 2018.
- [35] G. S. Pradeep Kumar and R. Keshavamurthy, “Corrosion behaviour of TiB₂ reinforced aluminium based in situ metal matrix composites,” *Perspectives in Science*, vol. 8, pp. 172–175, 2016.
- [36] S. Arivukkarasan, V. Dhanalakshmi, B. Stalin, and M. Ravichandran, “Mechanical and tribological behaviour of tungsten carbide reinforced aluminum LM4 matrix composites,” *Particulate Science and Technology*, vol. 36, no. 8, pp. 967–973, 2018.
- [37] S. Singh, I. Singh, and A. Dvivedi, “Multi objective optimization in drilling of Al6063/10% SiC metal matrix composite based on grey relational analysis,” *Journal of Engineering Manufacture.*, vol. 227, no. 12, pp. 1767–1776, 2013.

Research Article

Effect of Sodium Selenosulfate Concentration on Microstructural, Morphological, and Luminescence Characteristics of Cadmium Selenide Nanoparticles

Saka Abel ¹, Jule Leta Tesfaye,^{1,2} R. Shanmugam,³ L. Priyanka Dwarampudi,⁴ N. Nagaprasad ⁵, Lamessa Gudata,¹ and Ramaswamy Krishnaraj ^{2,6}

¹Department of Physics, College of Natural and Computational Science, Dambi Dollo University, Ethiopia

²Centre for Excellence-Indigenous Knowledge, Innovative Technology Transfer and Entrepreneurship, Dambi Dollo University, Ethiopia

³TIFAC CORE HD, Department of Pharmacognosy, JSS Academy of Higher Education and Research, JSS College of Pharmacy Ooty, Tamil Nadu, India

⁴Department of Pharmacognosy, JSS Academy of Higher Education and Research, JSS College of Pharmacy Ooty, Tamil Nadu, India

⁵Department of Mechanical Engineering, ULTRA College of Engineering and Technology, Madurai, 625104 Tamil Nadu, India

⁶Department of Mechanical Engineering, College of Engineering and Technology, Dambi Dollo University, Ethiopia

Correspondence should be addressed to Saka Abel; latijejesus@gmail.com and Ramaswamy Krishnaraj; prof.dr.krishnaraj@dadu.edu.et

Received 19 October 2021; Revised 22 December 2021; Accepted 28 December 2021; Published 17 January 2022

Academic Editor: Arpita Roy

Copyright © 2022 Saka Abel et al. This is an open access article distributed under the Creative Commons Attribution License, which permits unrestricted use, distribution, and reproduction in any medium, provided the original work is properly cited.

CBD-deposited cadmium selenide nanoparticles in acidic medium production at pH value of bath solution was stayed constant at 6.5 using EDTA as complexing agents; sodium selenosulfite acts as a source of Se^{2-} ion and cadmium acetate as source of Cd^{2+} ion. The nanoparticles of binary compound CdSe were also grown at different concentrations of sodium selenosulfite, and the influence of this parameter on the behaviours of the nanoparticles was studied. The as-synthesized cadmium selenide nanoparticles are investigated by scanning electron microscopy (SEM), X-ray diffraction (XRD), and PL absorption spectroscopy. Cadmium-selenide nanoparticles were produced using various concentrations as 10, 15, and 20 milliliters on a microscopic glass plate by chemical technique at a growth temperature of 90 degree Celsius. Microstructural constraints realized from the X-ray diffraction pattern decrease in grain size with an increase of concentration (8.25 nm–0.01 nm). It witnessed that the synthesized nanoparticle has a cubic crystal structure with favoured direction towards the (111) Miller indices' plane. The oriented peak was investigated from the planes (311) and (111). From patterns of PL emissions, it was detected that in increasing concentration of sodium selenosulfate intensity, the nanoparticles with small crystal size could represent maximum luminescence intensity associated with the larger crystal size. This is due to the fact that the amount of ions on the nanoparticle surface rapidly increases as the crystal size of the nanoparticles reduces. Additionally, the transporter recombination ratio was increased as the size of the transporter reduces resulting in an increase in the overlap between the electron and hole wave functions. SEM inspection of produced nanoparticles reveals that the surface is free of cracks and that the grains are spherically formed. The surface is coated with granules of consistent size and shape. There are no fractures or holes visible inside the thin films under examination.

1. Introduction

The usage of nanostructure instruments for optoelectronic tools, containing light-emitting diodes, laser-diodes, photo-

detectors, and photovoltaic panels, has newly concerned significant attention because of their distinctive geometry. Nanostructures in narrow length could be effortlessly assimilated into numerous technological platforms, giving new

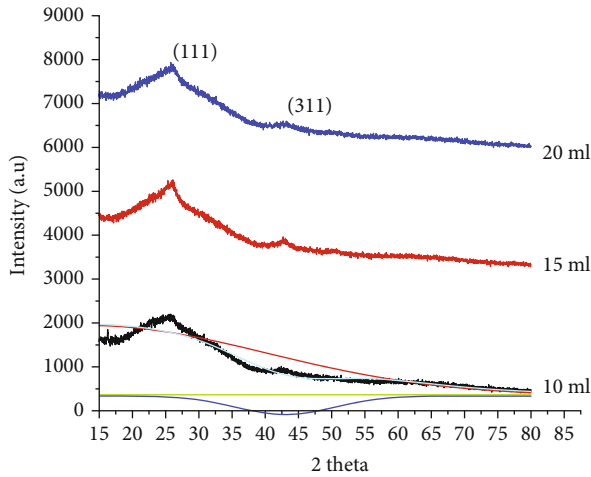


FIGURE 1: The patterns for CdSe nanoparticles generated with varying concentrations.

TABLE 1: Parameters obtained from XRD results.

Concentration (ml)	2 theta (degree)	FWHM (radians)	D (nm)
10	53	107807	8.25
15	15	54626.62	0.18
20	14	-7862.93	0.01

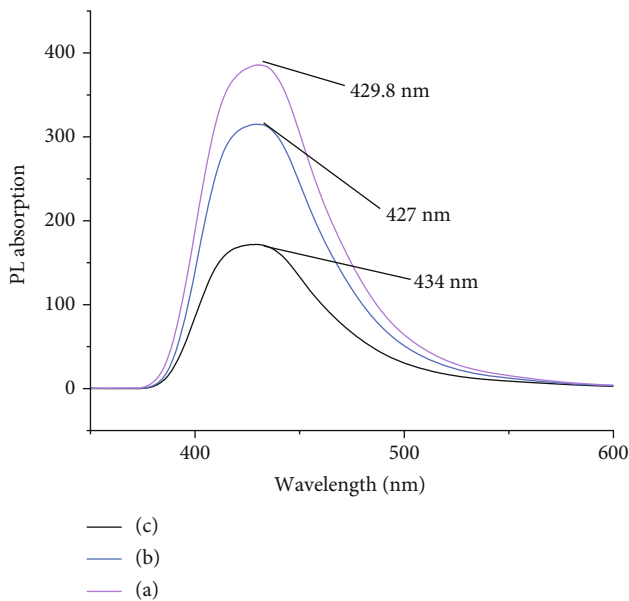


FIGURE 2: Photoluminescence emission spectrum of cadmium selenide nanoparticles for different concentrations of sodium selenosulfate as (a) 10 ml, (b) 15 ml, and (3) 20 ml.

physiological and chemical behaviours for maximum enactment of optoelectronic devices. The misuse of new nanostructures, as well as their optical and electrical characteristics, is important for their developing applied instrumental applications [1]. In recent years, CdSe nanoparticles have been very interesting in the study community

with their maximum demands regarding their application in optical electronics. CdSe was a largely used semiconductor compound because of its direct bandgap (1.74 eV) at a normal temperature radius of 5.6 nm from Bohr's theory [2, 3]. The size of cadmium selenide increased the volume ratio; so, it can be found vastly in different fields from light-emitting diode to photovoltaic cells. A lot of journalists are demanding to study different properties of CdSe, which is a kind of (II-VI) semiconductors in cost-effective ways [4]. CBD is a somewhat inexpensive method for the deposition of nanomaterials as it does not need extremely cultured materials. Cadmium selenide nanostructures have been produced by numerous scientists by using different methods such as microwave deposition, sputtering, precipitation, sonochemical, and solvothermal [4, 5]. In order to prepare for nanostructure temperatures of deposition, annealing and the volume ratio of source solution have a vital role in the behaviours of the samples to be produced [6]. The crystal size of the nanoparticle is once more solely relying on the nucleation hotness/coldness and the other listed factors. The previous ways of synthesizing CdSe nanoparticles cause pollution of the environment and can lead to greenhouse effect and drought except for chemical bath deposition techniques which are sometimes known as green synthesis.

It is a very difficult maximum quality production of CdSe nanoparticles by using basic chemical atmospheric infusion unless the problems of CdSe synthesis are overcome [7]. The influence of hydroxide is reduced when CdSe nanoparticles are prepared in an acidic medium. For most metal ions widely used in CBD, it is fair to conclude that no hydroxide is available under such conditions and also that deposition occurs through ion-by-ion processes [8]. The aim of this research was to look at CdSe nanoparticles grown under various concentrations for optoelectronic applications. Having this in consideration, we have deposited cadmium selenide nanoparticles with various concentrations of sodium selenosulfite via chemical bath deposition techniques.

During this work, we have a tendency to gift the result of bimetallic precursor concentration on morphological, structural, and optical properties of CdSe nanoparticles deposited from chemical containing Cd acetate, hydroxyl acid ammonia, and metallic element selenosulfite, at a temperature of 90°C and a pH of 6.5. To make our investigation effective, cadmium-acetate is often primarily used because of the supply of Cd ions in reaction with hydroxyl acid as a complexing agent for the deposition of Cd selenide films at a concentration of selenosulfite 10, 15, and 20 ml.

2. Experimental Details

2.1. Cleaning Materials. Cleaning laboratory instruments are a serious side that can give to nanoparticle observance. The microscopic glass plate, bath beaker, small beakers for measurements, and spoons were purified in weak acid over a day and successively put in ethanol for 40 min, at that moment; ultrasonically washed with deionized water; and got dehydrated underneath ambient temperatures before being used for the synthesis [9, 10].

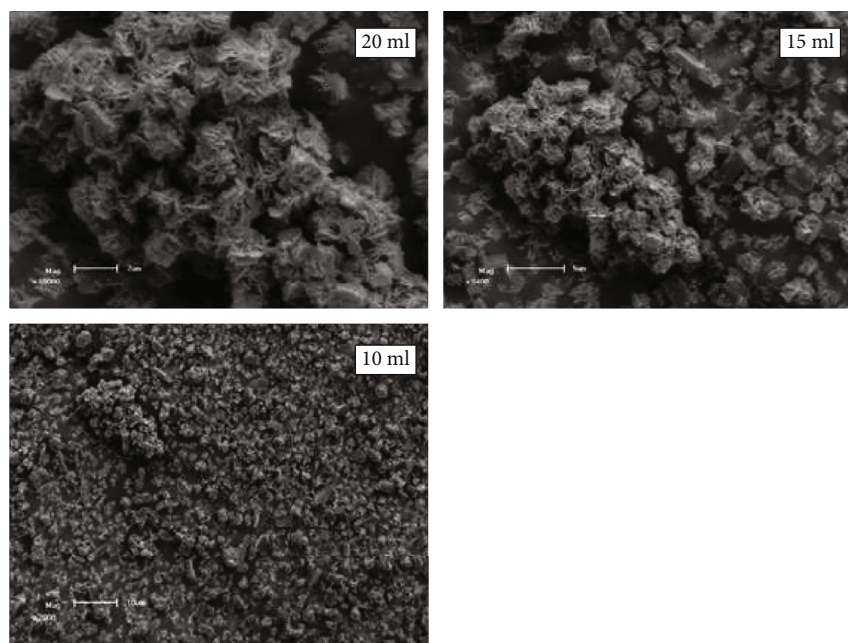


FIGURE 3: The scanning electron microscope images of cadmium selenide nanoparticles synthesized fewer than three different concentrations of sodium selenosulfite.

2.2. Sample Preparation (Cadmium Selenide Nanoparticles).

In synthesization of cadmium selenide films, water bath was arranged by adding 20-milliliter (0.4) molarity of cadmium-acetate [$\text{Cd}(\text{CH}_3\text{COO})_2 \cdot 2\text{H}_2\text{O}$] deeds as cadmium ion bases; 10 ml (0.5 M) ethylenediamine (EDTA) acts as a complex agent, in a 150 ml beaker. To this, adding different one molarity of sodium selenosulfate (Na_2SeSO_3) was used for a source of selenide ion (Se-2) at ordinary temperature. The total volume was kept to be 70 milliliters by filling with distilled water. The pH value of the mixture solution was accustomed to be around 6.5 by using some drop-lets of sulfuric acid (H_2SO_4), and the bath temperature adjusted to 313 Kelvin. Glass beaker was then set aside in a water bath. Then, a magnetic stirrer revolves at a continuous rate per second (rps). Likewise, the systems adjusted three times, keeping all parameter values the same and varying the volume of concentration of sodium selenosulfite as 10, 15, and 20 milliliters; this is to be done for the first time for 120 minutes without troubling. Finally, cadmium selenide nanofluids were deposited. After 120 min bath beaker was taken from the heater, by using a syringe, the bath solution was fetched gently, and nanofluid left on the bottom side of the beaker was transferred on a pure glass plate and dried in the warm air; finally, CdSe nanoparticles were kept in the oven for characterization.

3. Results and Discussion

The characterization of samples is an integrated process with nanoparticle deposition. Various methods were used for the characterization of the nanoparticles. The samples of CdSe nanoparticles were structurally characterized by using a Bruker D8 X-ray diffractometer functioning at 45 kV and 40 mA

with Cu $K\alpha$ monochromatic radiation ($\lambda = 0.15406$ nm) in the Bragg-Brentano geometry [11].

Figure 1 shows the patterns for CdSe nanoparticles generated with varying concentrations of nonmetallic precursor values and deposited for 120 minutes; X-ray diffraction patterns were observed. Figure 1 demonstrates the XRD spectra of the CdSe nanoparticles deposited at different concentration values. Because of this, it can be concluded that the XRD phase of the CdSe nanoparticles as generated by the chemical bath deposition approach is polycrystalline in nature. According to the samples, the observed d -values and the corresponding noticeable peak that were obtained are in the best accord with the data [12]. This revealed that the synthesized nanoparticle has a cubic crystal structure with a favoured orientation towards the (111) Miller indices' plane. The oriented peak was investigated from the planes (311) and (111) for the 20 ml of sodium selenosulfate concentration; other little intensity peak was performed at $2\theta = 14$ degrees. The angle of the diffraction peak in relation to the (400) plane is in good agreement with the permissible limit that was previously mentioned. Thus, it was determined that the CdSe nanoparticles generated from a 20 ml concentration exhibited good crystallite formation. In the diffraction phase, there have been no peaks associated with contaminants that could be detected. Raising the volume ratio of sodium selenosulfate did not alter the cubic structure of the produced cadmium selenide nanoparticles. Furthermore, the XRD results are in agreement with reported data [13].

The crystalline size (D) was calculated from XRD data and calculated by using the Scherrer formula, given by

$$D = \frac{0.9\lambda}{\beta \cos\theta}, \quad (1)$$

where λ is the wavelength and β is denoted for FWHM in radian θ position angle of diffraction. Some parameters obtained from XRD are summarized in Table 1.

The photoluminescence properties of the prepared nanoparticles are shown in Figure 2. From the patterns of photoluminescence emissions, it was detected that increasing concentration of sodium selenosulfate intensity of photoluminescence emission peaks was confirmed because of the wide area to volume ratio for the small-size crystals. Therefore, the nanoparticles having small crystal sizes can reflect the maximal luminescence intensity associated with the larger-crystal-size nanoparticles [12, 14]. This is due to the fact that the amount of ions on the nanoparticle surface rapidly increases as the crystal size of the nanoparticles reduces. Moreover, the transporter recombination ratio as high as the size of the transporter reduces due to the increase in the overlap between the electron and hole wave functions [12]. The external topography of deposited CdSe nanoparticles was characterized using a scanning electron microscope (SEM) since it substitutes an enormously authoritative attractiveness on the outcome of cell. SEM is a favourable and very important method to investigate and evaluate the surface morphology of nanoparticles. The SEM micrograph of cadmium selenide is depicted in Figure 3. This demonstrates that there are no fissures on the surface and that the grains are spherically formed. The surface was covered with granules of consistent size and shape. There have been no fractures or holes visible inside the thin films under examination. So as to supplementarily show the aspect and crystalline segment of the nanoparticle, image became taken and is represented in Figure 3. The obtained photograph of synthesized nanoparticles is composed of globular crystallites of approximately 60 nm. The grains were cumulative in formed clusters, and this agreed with previous report [15].

4. Conclusion

CdSe nanoparticles were deposited for the first time via low-cost chemical bath methods in the acidic bath at a pH value of 6.5. The influence of sodium selenosulfate concentrations on microstructural, surface morphology, and optical properties of prepared nanoparticles was studied. The XRD analyses revealed that the cubic structure could be found in all of the grown samples. With the rising of the concentration of nonmetallic precursors, the crystal size declined. The difference in the optical behaviour of cadmium selenide nanoparticles was caused by the quantum size effect, which could have occurred as a result of the concentration of selenide ions in the ion source. The scanning electron microscope micrographs revealed that surface morphology of nanoparticles was composed of nearly cubic formed grains via changed sizes. There were blue variations in the photoluminescence spectrum caused by the crystal size, and these shifts were noticeable. All of these findings supported studying the concentration of precursor deliveries for the production of high-quality cadmium selenide nanoparticles by chemical bath approach for the applications of nanotechnology.

Data Availability

The data used to support the findings of this study are included within the article.

Disclosure

This study was performed as a part of the employment of the authors.

Conflicts of Interest

The authors declare that there are no conflicts of interest.








References

- [1] K. Amreen and S. Goel, "Review—Miniaturized and microfluidic devices for automated nanoparticle synthesis," *ECS Journal of Solid State Science and Technology*, vol. 10, no. 1, article 017002, 2021.
- [2] H. N. Rosly, K. S. Rahman, S. F. Abdullah et al., "The role of deposition temperature in the photovoltaic properties of RF-sputtered CdSe thin films," *Crystals*, vol. 11, no. 1, p. 73, 2021.
- [3] V. Singh, Priyanka, P. V. More, E. Hemmer, Y. K. Mishra, and P. K. Khanna, "Magic-sized CdSe nanoclusters: a review on synthesis, properties and white light potential," *Materials Advances*, vol. 2, no. 4, pp. 1204–1228, 2021.
- [4] S. Pokhriyal and S. Biswas, "Inducing ferromagnetism in surface stabilised intrinsic CdSe nanoparticles by a simple process," *Materials Science and Technology*, vol. 36, no. 13, pp. 1503–1506, 2020.
- [5] P. Maldonado-Altamirano, L. A. Martínez-Ara, M. . . A. Hernandez-Perez, J. R. Aguilar-Hernández, M. López-López, and J. Santoyo-Salazar, "Laser wavelength-dependent size of CdSe nanoparticles synthesized by laser fragmentation in liquid medium," *Optical Materials*, vol. 111, article 110637, 2021.
- [6] M. M. Abdullah, M. Faisal, J. Ahmed, F. A. Harraz, M. Jalalah, and S. A. Alsareii, "Sensitive detection of aqueous methanol by electrochemical route using mesoporous α -Fe₂O₃ Doped CdSe nanostructures modified glassy carbon electrode," *Journal of the Electrochemical Society*, vol. 168, no. 5, article 057525, 2021.
- [7] S. Abel, J. Leta Tesfaye, R. Kiran et al., "Studying the effect of metallic precursor concentration on the structural, optical, and morphological properties of zinc sulfide thin films in photovoltaic cell applications," *Advances in Materials Science and Engineering*, vol. 2021, Article ID 7443664, 6 pages, 2021.
- [8] N. Arif and C. S. Fun, "Impact on development of ZnS nanoparticles thin film deposited by chemical bath deposition and spin coating," *International Journal of Advanced Engineering and Nano Technology*, vol. 4, no. 5, pp. 1–4, 2021.
- [9] N. I. M. Fauzi, Y. W. Fen, N. A. S. Omar et al., "Nanostructured chitosan/maghemite composites thin film for potential optical detection of mercury ion by surface plasmon resonance investigation," *Polymers*, vol. 12, no. 7, p. 1497, 2020.
- [10] T. Debele and F. Gashaw, "Effect of temperature on morphological, structural and optical properties of cadmium selenide (CdSe) thin films deposited by chemical bath deposition method," *Advances in Life Science and Technology*, vol. 67, pp. 12–16, 2018.
- [11] V. S. Raut, C. D. Lokhande, and V. V. Killedar, "Studies on effect of pH on structural, optical and morphological

- properties of chemisynthesized CdSe grains,” *International Journal of Engineering*, vol. 10, no. 1, p. 2017, 2017.
- [12] K. C. Handique and P. K. Kalita, “Effects of cadmium ion concentration on the optical and photo-response properties of CdSe/PVP nanocomposites for white light sensing application,” *Applied Physics A*, vol. 126, no. 9, 2020.
- [13] A. G. Habte, F. G. Hone, and F. B. Dejene, “The influence of malonic acid on the structural, morphological and optical properties of CdSe thin films prepared by chemical bath deposition method,” *Inorganic Chemistry Communications*, vol. 103, pp. 107–112, 2019.
- [14] I. R. Agool, H. M. Mohammed, and S. M. A. Al Hussan, “Synthesis, characterization and optoelectronic properties of solar cells device for vacuum thermally evaporated pure and gallium doped CdSe nanoparticles,” *Earth and Environmental Science*, vol. 790, article 012086, 2021.
- [15] D. N. Ahilfi, A. S. Alkabbi, K. A. Mohammed, and K. M. Ziadan, “Fabrication and characterization of polyaniline/CdSe device for applications in nano structured solar cells,” *Materials Science and Engineering*, vol. 928, article 072069, 2020.

Research Article

Synthesis of Silver and Gold Nanoparticles: Chemical and Green Synthesis Method and Its Toxicity Evaluation against Pathogenic Bacteria Using the ToxTrak Test

Pankaj Kumar Tyagi ¹, Cristina Quispe,² Jesús Herrera-Bravo ^{3,4}, Shruti Tyagi ⁵,
D. Barbhai Mrunal ⁶, Manoj Kumar ⁶, Anas S. Dabool,⁷ Saad Alghamdi ⁸,
Gaber El-Saber Batiha,⁹ Javad Sharifi-Rad ¹⁰ and Seema Ramniwas¹¹

¹Department of Biotechnology, Noida Institute of Engineering and Technology, Greater Noida, Affiliated to APJ Abdul Kalam Technical University Lucknow, UP, India

²Facultad de Ciencias de la Salud, Universidad Arturo Prat, Avda Arturo Prat 2120, Iquique 1110939, Chile

³Departamento de Ciencias Básicas, Facultad de Ciencias, Universidad Santo Tomas, Chile

⁴Center of Molecular Biology and Pharmacogenetics, Scientific and Technological Bioresource Nucleus, Universidad de La Frontera, Temuco 4811230, Chile

⁵Young Scientist of UPSCST Scheme, Department of Biotechnology, Noida Institute of Engineering and Technology, greater Noida, India

⁶Chemical and Biochemical Processing Division, ICAR-Central Institute for Research on Cotton Technology, Mumbai 400019, India

⁷Department of Public Health, Health Sciences College at Al-Leith, Umm Al-Qura University, Makkah, Saudi Arabia

⁸Laboratory Medicine Department, Faculty of Applied Medical Sciences, Umm Al-Qura University, Makkah 21955, Saudi Arabia

⁹Department of Pharmacology and Therapeutics, Faculty of Veterinary Medicine, Damanhour University, Damanhour, Egypt

¹⁰Facultad de Medicina, Universidad del Azuay, Cuenca, Ecuador

¹¹University Center for Research and Development Chandigarh University Gharuan Mohali Punjab, India

Correspondence should be addressed to Shruti Tyagi; stgenetics@gmail.com and Javad Sharifi-Rad; javad.sharifirad@gmail.com

Received 11 October 2021; Accepted 30 November 2021; Published 30 December 2021

Academic Editor: H C Ananda Murthy

Copyright © 2021 Pankaj Kumar Tyagi et al. This is an open access article distributed under the Creative Commons Attribution License, which permits unrestricted use, distribution, and reproduction in any medium, provided the original work is properly cited.

In the current investigation, silver/gold nanoparticles (NPs) were synthesized using two methods: chemical and biological, and then characterized colloidal solutions of both NPs using UV-Vis, transmission electron microscopy (TEM) and zeta potential analyzers, X-ray powder diffraction (XRD), and energy dispersive X-ray (EDX) as well as the ToxTrak test for *in vitro* toxicity and antibacterial activity against Gram-positive bacteria (*B. subtilis*) and Gram-negative bacteria (*E. coli*). The plasmon peak of chemical synthesized silver NPs (CH-AgNPs) and gold NPs (CH-AuNPs) was observed at 414 and 530 nm, respectively, while the sharp plasmon peak of biological synthesized silver NPs (Bio-AgNPs) and gold NPs (Bio-AuNPs) was observed at 410 and 525 nm. Under transmission electron microscopy (TEM), the average sizes of CH-AgNPs and CH-AuNPs were 50.56 and 25.98 nm, respectively. Bio-AgNPs and Bio-AuNPs, on the other hand, had average sizes of 25.25 and 16.65 nm, respectively. The stability of NPs was also investigated using the zeta potential. The crystalline structure of AgNPs was confirmed through XRD, and EDX results confirm the element compositions. In the ToxTrak test, the toxic effect value/percentage inhibition (TEV/PI) was calculated. The results showed that CH-AgNPs have the highest TEV/PI value (85.45% for *B. subtilis* and 83.77% for *E. coli*) when compared to Bio-AgNPs (55.75% for *B. subtilis* and 54.42% for *E. coli*). CH-AuNPs, on the other hand, were 33.51% toxic to *B. subtilis* and 36.85% toxic to *E. coli*, compared to Bio-AuNPs, which were 23.36% toxic to *B. subtilis* and 24.46% toxic to *E. coli*. The antibacterial activity of Ag/Au NPs was tested and monitored; zone of inhibition (mm in diameter) against *B. subtilis* and *E. coli*, with the following pattern emerging: CH-AgNPs (24.80) had the highest antibacterial activity followed by Bio-AgNPs (22.80) < CH-AuNPs (10.60) < Bio-AuNPs (09.00), whereas the control sample (tetracycline antibiotic) revealed a 25.08 mm, zone of inhabitation. Overall, Bio-AgNPs and Bio-AuNPs are the most effective

pathogen-killing materials with the lowest toxicity. Our suggestion is that such materials instead of chemical synthesized NPs can be used to coat antibiotic drugs and could be a game-changer for the pharmaceutical industry in terms of effectively controlling the pathogenic bacteria.

1. Introduction

Silver, gold, and titanium dioxide nanoparticles have long been used for its antibacterial properties. The famous historian Herodotus first wrote about the use of silver to keep water fresh in the 5th century BC, and Hippocrates was using silver for treating wounds and ulcers [1]. The prevalence of silver nanoparticles has increased significantly, but it is still unclear what antimicrobial properties with toxicity estimation make it attractive and attentive. Nowadays, biological substances such as plants, bacteria, yeast, actinomycetes, and viruses are commonly employed in the green synthesis of silver nanoparticles [2–4]. Nanosilver has been widely used to paints, dye degradation and clothing [5–8], children toys, cosmetics and medicinal products [2, 9], food storage and handling containers [10], bacterial contaminations [11–13], and other applications [14]. The interest in nanomaterial stems from their nanoscale properties that differ from their properties in bulk. For example, bulk gold has an unmistakable yellow hue. Gold nanoparticles, on the other hand, change in colour depending on their size; small NPs are red, medium NPs are purple, and giant NPs are blue, and the differences are not purely visual. In contrast to their bulk counterparts, the gold NPs are good catalysts, have a decreased melting temperature, are reactive in nature with magnetic properties, and change from metal to a semiconductor [15]. Toxicity is also impacted by size [16]. A harmless material in bulk can become toxic at the nanoscale. Another aspect of nanomaterial toxicity is their sensitivity to synthesis method, seemingly minor changes, batch-to-batch, can have drastic impacts of the resulting NP. These changes include size and shape changes, coatings, and charges [17, 18]. In an *in vitro* comparative study of silicon dioxide (SiO₂) and TiO₂, SiO₂ NPs exhibited significant proinflammatory activity for human monocyte, while TiO₂ had less activity [19]. Some studies were conducted in rat liver cells to assess nanosilver as an *in vitro* toxicity assay, and the results showed that low levels of silver NP exposure resulted in oxidative stress and impaired mitochondrial function [20]. Nowadays, green synthesis of NPs by using plant extracts is popularizing due to more safety features. The phenolic compounds and other secondary metabolites present in the plant extracts improve the specific bioactivity (for example, improvement in antimicrobial activity) of synthesized NPs. Gram's positive and negative aspects *B. subtilis* and *E. coli*, both facultative anaerobic and rod-shaped bacteria, are commonly found in the human lower intestine and account for 0.1% of gut flora [13, 21]. These gut microbes known as probiotics and enhance immunity of the body and allowing the organism to tolerate extreme environmental conditions. The authors of the current study employed chemical and biological methods to synthesis silver and gold nanoparticles, which were then tested for toxicity and antibacterial activity against pathogenic bacteria including *B. subtilis* and *E. coli*.

2. Materials and Methods

2.1. Sample Preparation. Tetrachloroauric acid, silver nitrate, trisodium citrates, nutrient agar, and resazurin dye of AR grade were used and obtained from Sigma and Merck for chemical synthesis of Ag/Au NPs. Fresh plant leaves of *Hibiscus Rosa sinensis* (gurhal) were collected from the Institute campus for biological synthesis of Ag/Au NPs. For the study of toxicity and antibacterial activities, *B. subtilis* (Gram-positive) and *E. coli* (Gram-negative) cultures were collected from the microbiology laboratory of this Institute.

2.2. Extraction Preparation. To obtain the extract, the plant leaves were thoroughly washed three times with double distilled water and 10 g leaves were ground. The 10 mL extract was combined with 90 mL deionized water and boiled for 15 minutes at 90°C. The extracts were centrifuged for 10 minutes at 10000 rpm.

2.3. Chemical Synthesis of Silver/Gold Nanoparticles. 38 mM trisodium citrate dehydrate (Na₃C₆H₅O₇·2H₂O) and 0.75 mM silver nitrate used for synthesis CH-AgNPs. 50 mL AgNO₃ mixed with 10 mL trisodium citrate into dropwise method and heated up to 90°C and CH-AgNPs obtained with chemical degradation and gradually by the erosion and the transparent light color turned to brownish black indicating the presence of AgNPs. On the other hand, the chemical synthesis of AuNPs, the 1% trisodium citrate dehydrate solution, and 1.0 mM HAuCl₄ were used for CH-AuNPs. Continuous rolling boiled with magnetic stir bar 20 mL of chloroauric acid mixed with 1% trisodium citrate dihydrate solution of 2 mL. In this process, trisodium citrate reduces the gold solution and solution turned light reddish violet in color. The light reddish violet color indicates the formation of AuNPs.

2.4. Biological Synthesis of Silver/Gold Nanoparticles. 95 mL plant leaf extract (supernatant) in conical flasks and added 5 mL of 0.75 mM AgNO₃ aqueous solution as a precursor for obtaining Bio-AgNPs. This solution was incubated in incubator shaking at 30°C of 150 rpm up to 72 h. Under incubation time, the extract of this solution act as a reducing and stabilizing agent and silver ions may be changes into colloidal silver solution. During this process the changes in color pale yellow to blackish brown indicates the synthesis of Bio-AgNPs. The same process applied for synthesis of gold NPs. 95 mL plant leaf extract (supernatant) in conical flasks and added 5 mL of an aqueous solution of tetrachloroauric acid solution as a precursor for obtaining Bio-AuNPs. The 100 mL solution was incubated in incubator shaking of 150 rpm at 30°C for 72 h. In this process, change in color pale yellow to purple reddish indicates the synthesis of Bio-AuNPs.

2.5. Characterization Techniques of Ag/AuNPs. The CH-Ag/AuNPs and Bio-Ag/AuNPs in the form of colloidal solutions were primary characterized with visible spectrophotometry, transmission electron microscopy (TEM), XRD, and zeta potential analyzers were also carried out. TEM was used to examine the size and morphology of the NPs. An accelerating voltage of 200 kV was used in the microscope. After diluting the silver samples (1:10) in distilled water, an aliquot (20 L) was applied to a carbon-coated grid. The solution was then left for 1 minute before being blotted with filter paper to remove any excess from the grid. Before imaging, the grids were placed in the grid box for two hours to dry. The zeta potential is a physical property determined by the net surface charge of NPs. A Coulomb explosion occurs between the charges of these particles when they repel each other in a solution, resulting in no tendency for the particles to agglomerate. When the zeta potential values ranged from higher than +30 mV to lower than -30 mV, the criteria for NP stability were measured [22]. The laser zeta meter was used to measure surface zeta potentials, and using NaCl as a suspending electrolyte solution, liquid samples of NPs (5 mL) were diluted with double distilled water (50 mL) (2×10^{-2} M NaCl). After that, the pH was adjusted to the desired level. For 30 minutes, the samples were shaken. The zeta potential of the metallic particles was measured, and the equilibrium pH was recorded after shaking. The surface potential of NPs was determined using a zeta potential. An average of three separate measurements was reported in each case. When the zeta potential values ranged from higher than +30 mV to lower than -30 mV, the criteria for NPs stability were measured [23]. The crystalline structure of AgNPs was confirmed through XRD analysis and EDX results confirm the element compositions.

2.6. Toxicity of Metal Nanoparticles through ToxTrak Test. Toxicity of CH-Ag/AuNPs and Bio-Ag/AuNPs was assessed using the ToxTrak test, and the toxic effect value/percentage inhibition (TEV/PI) was calculated after a minor modification to the previously published protocol [24]. 10 culture tubes of broth for 48 hours, each containing 25 g/mL solutions of *B. subtilis* and *E. coli* cultures, divided into two groups: k_1 for *B. subtilis* and k_2 for *E. coli*. The first test tube of the k_1 group was designated as a control sample for determining the toxicity of Ag/Au NPs against *B. subtilis*. The second and third culture tubes were labelled as chemically synthesized NPs, and 1 mL of CH-AgNPs and CH-AuNPs were added to each culture tube. The Bio-AgNPs and Bio-AuNPs were added to the 4th and 5th culture tubes, which were labelled as biologically synthesized NPs. The 6th culture tube of the k_2 group was designated as a control sample for determining the toxicity of Ag/Au NPs against *E. coli*. Chemically synthesized NPs were added to the 7th and 8th culture tubes, respectively, with 1 mL of CH-AgNPs and CH-AuNPs. The ninth and tenth culture tubes were labelled as biologically synthesized NPs, and 1 mL of Bio-AgNPs and Bio-AuNPs, respectively, was added to them. In both groups (k_1 and k_2), 40 μ L resazurin dye was added to each culture tube, and the tubes were incubated for 0 to 4 h [25]. The absorption was measured in all culture tubes of the k_1 and

k_2 groups immediately after adding the dye, from 0 to 4 h after 1 h intervals.

2.6.1. In Vitro Toxic Effect Value (TEV) Evaluation. The ToxTrak test was used to assess the toxicity of chemical and biologically synthesized Ag/AuNPs [24, 26]. At 603 nm wavelength, we calculated the percentage inhibition (PI/TEV) of *B. subtilis* (k_1) and *E. coli* (k_2) in this test [13, 24]. The final result of the PI reaction is known as the toxic effect value (TEV), and the PI is written as follows:

$$\left[\text{PI} = - \left(\frac{\Delta A_{\text{sample}}}{\Delta A_{\text{control}}} \right) \times 100 \right], \quad (1)$$

where ΔA = Initial absorbance value – final absorbance value in this equation.

The differences (decrease) in absorbance for the control samples and chemical and biologically synthesized Ag and AuNPs were used to calculate the PI/TEV value in percentage [27].

2.6.2. Methods for Calculating Absorbance Differences (Decreases)

- (i) $\Delta A_{\text{control}}$ is used to present the control sample, and the control value is -2.7151 (k_1) and -2.6915 (k_2)
- (ii) CH-AgNPs resembling with $\Delta A_{\text{CH-AgNPs}}$ and absorbance values of -0.3952 (k_1) and -0.4368 (k_2)
- (iii) CH-AuNPs interacting with $\Delta A_{\text{CH-AuNPs}}$ and absorbance values of -1.8072 (k_1) and -1.3396 (k_2)
- (iv) Bio-AgNPs resembling with $\Delta A_{\text{Bio-AgNPs}}$ and absorbance values of -1.2026 (k_1) and -1.2269 (k_2)
- (v) Bio-AuNPs representing with $\Delta A_{\text{Bio-AuNPs}}$ and absorbance values of -2.0829 (k_1) and -2.0330 (k_2)

2.7. Antibacterial Potential of Ag/AuNPs. The antibacterial potential of CH-Ag/AuNPs and Bio-Ag/AuNPs was determined using the standard disc diffusion method against *B. subtilis* and *E. coli* [28]. The bacterial pathogens were taken from the microbiology lab of this Institute and kept on nutrient agar media. The colloidal solution of Ag/AuNPs synthesized by chemical and biological methods was prepared prior to use by dissolving Ag/AuNPs in 5% dimethyl sulfoxide (DMSO, 1000 g/mL) and sonicating the samples at 30°C for 15 minutes. The assay was performed using filter paper discs containing 50 g of Ag/AuNPs per disc. Tetracycline, a common antibiotic, was used as a positive control at 5 g/disk, while 5% DMSO was used as a negative control. For the assay, overnight grown cultures of tested bacteria were diluted to 1×10^{-7} colony-forming unit. After 24 h of incubation at 37°C, the diameter of zones of inhibition was measured to determine the antibacterial activity of the Ag/AuNPs.

2.8. Statistical Analysis. The data in this paper was analyzed using Statistica, release 7.0 StatSoft an advanced analytics software system.

3. Results

Silver/gold nanoparticles (NPs) were generated employing two ways in this study: chemical and biological. The chemical process of Ag/AuNPs can begin with AgNO_3 and AuCl_4 , respectively, and be followed by the use of trisodium citrate dehydrate as a capping and chelating agent, which plays a critical role in chemical degradation and the production of Ag and Au ions. On the other hand, the presence of phytochemicals in the plant extract as capping agents initiates the biological process (green synthesis) of Ag/AuNPs, the leaf extract also plays a significant role as a reducing agent after being exposed to only the precursors of AgNO_3 and AuCl_4 without using any intermediate chemicals. After being exposed to AgNO_3 and AuCl_4 with the trisodium citrate dehydrate, the amount of Ag and Au ions obtained with chemical degradation and gradually by the erosion the transparent color turned to brownish black, indicating the presence of CH-AgNPs (Figure 1(b)), and light reddish violet color in CH-AuNPs (Figure 2(b)). In the biological method of Ag/AuNPs, the amount of Ag and Au ions in the leaf extract is reduced via phytochemicals present in the plant extract after being exposed to precursor AgNO_3 and AuCl_4 and the pale-yellow color of plant extract changed to blackish brown, indicating the Bio-AgNPs (Figure 3(b)) and purple reddish color in Bio-AuNPs (Figure 4(b)), respectively. The surface plasmon resonance phenomenon in Ag/AuNPs NPs [29, 30] as a result of the excitation of free electrons in NPs (K. [31]) causes this color change. Similar results have been reported in previous studies [32–36], indicating that the reaction between extracts and AgNO_3 is complete. After 24 h, there were no more color changes, indicating that the reduction process was complete. This is consistent with previous research [37], which showed that *Hibiscus Rosa sinensis* leaf extract was used to synthesize Ag/Au NPs in just 24 h. In aqueous medium, surface plasmon vibrations cause AgNPs to appear yellowish brown [38]. Similar color shifts have been observed in previous studies [34, 39].

3.1. UV-Vis Spectroscopy. In the UV-Vis spectra of CH-AgNPs and CH-AuNPs, the plasmon peak was found at 414 nm with absorption of 0.77 and 530 nm with absorption of 1.20, respectively (Figures 1(a) and 2(a)). The surface plasmon peak in Bio-AgNPs and Bio-AuNPs was observed at 410 nm with absorption of 3.52 and at 525 nm with an absorption of 0.98, respectively (Figures 3(a) and 4(a)). In CH-AgNP, the broadening of the peak indicated that the particles are polydispersed. The formation of polydispersed large NPs due to slow reduction rates was indicated by broadening of the peak [40–44].

3.2. TEM Analysis of Nanoparticles. The morphology, particle shape, size, and distribution profile of Ag/AuNPs was revealed by TEM images. Figure 5(a) depicts CH-AgNPs in cuboidal, hexagonal, and spherical shapes, with spherical shapes being the most common and average sizes of 50.56 nm at 100 nm scale and 200 kV accelerating voltage analysis. CH-AuNPs, on the other hand, had an average size of 25.98 nm at 100 nm scale with 200 kV accelerating voltage

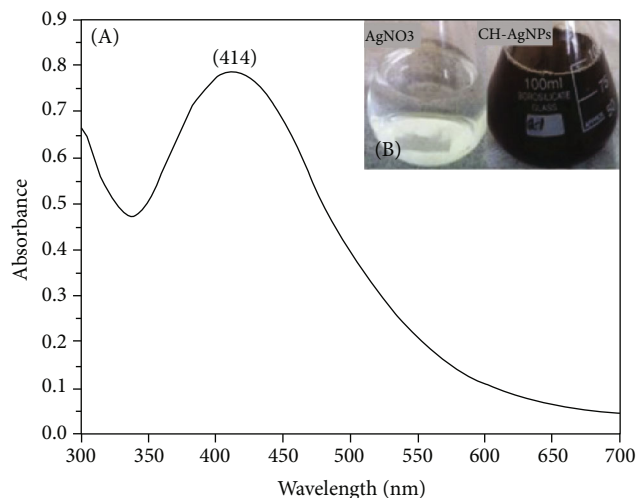


FIGURE 1: (a) UV-Vis absorption spectrum (A) of CH-AgNPs produced by AgNO_3 solution reduction. (b) Beakers showing chemical degradation and erosion, with the transparent light color gradually turning brownish black (B), indicating the presence of silver nanoparticles.

analysis and appeared to have a spherical morphology (Figure 5(b)). When sodium citrate was used as the reducing agent, spherical and ellipsoidal AgNPs with sizes ranging from 20 to 60 nm were obtained [45]. On the other hand, Bio-AgNPs and Bio-AuNPs with cubic, hexagonal, and spherical shapes with average sizes of 25.25 and 16.65 nm were obtained, respectively (Figure 6(a) and 6(b)). Biological synthesized AuNPs with size ranges of 15 to 55 nm with pseudospherical, triangular, and hexagonal [46–50]. All observed NPs are uniformly distributed in various sizes without significant agglomeration.

3.3. Zeta Potential Analysis. Surface zeta potentials were measured using a zeta analyzer in order to study the stability of NPs, which is critical for many applications. The pH of liquid NP samples (5 mL) was adjusted to the required value by diluting them with double distilled water (50 mL). For 30 minutes, the samples were shaken. The zeta potential of the metallic particles was measured after shaking. The surface potential of NPs was determined using a zeta potential. The CH-AgNPs and CH-AuNPs solutions had zeta potentials of -29.18 mV and -18.30 mV, respectively, with a single peak indicating the presence of repulsion among the synthesized NPs (Figures 7(a) and 7(b)). Meanwhile, the zeta potential of the Bio-AgNPs and Bio-AuNPs solutions was -23.19 mV and -23.90 mV, respectively (Figures 8(a) and 8(b)). When all of the particles in a suspension have a large negative or positive zeta potential, they repel one another and have no tendency to clump together. There will be no force to keep the particles from colliding and flocculating if their zeta potential values are low (S. [51]). The zeta potential of chemical and biosynthesized Ag/AuNPs was found to be negative, indicating that they repel each other and increasing the formulation's stability.

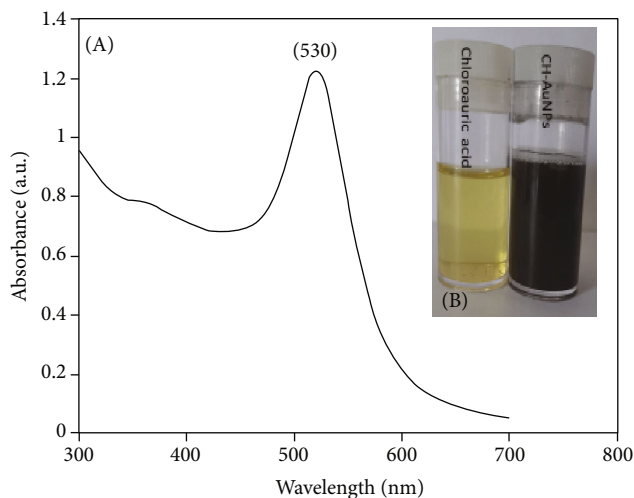


FIGURE 2: (a) UV-Vis absorption spectrum of CH-AuNPs by reduction of HAuCl₄ solution (A). (b) Vials showing that the gold solution is reduced by trisodium citrate and the solution turn light reddish violet in colour (B), indicating the formation of Au nanoparticles.

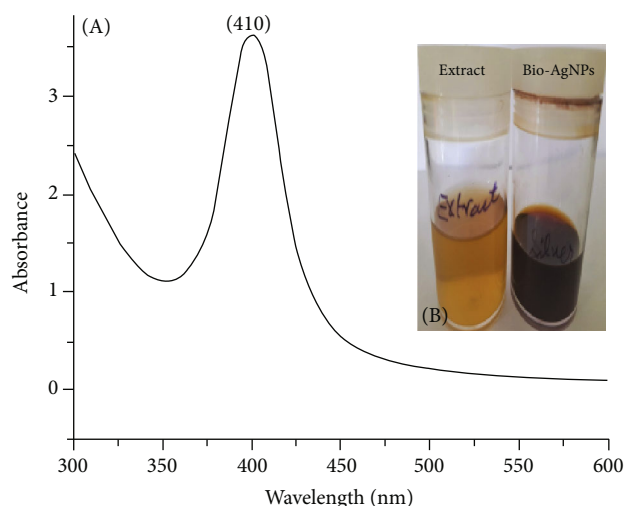


FIGURE 3: (a) UV-Vis absorption spectrum of Bio-AgNPs with the aqueous extract of *Hibiscus Rosa sinensis* (gurhal). (b) Vials showing colour changes (B), from pale yellow to blackish brown, indicating Bio-AgNP synthesis.

3.4. XRD Analysis. The powder XRD of silver nanoparticles reveals their crystalline nature. The crystalline structure of silver nanoparticles in powder form was investigated using XRD, and the results are consistent with previous research that revealed plausible silver metal peaks in Figure 9(a) [52–54]. At 40°, 49°, 66°, 77°, and 83°, AgNPs display Bragg diffraction 2θ peaks, which correspond to 111, 200, 220, 311, and 222, respectively.

3.5. EDX Analysis. The elemental composition of AgNPs was shown in Figure 9(b). EDX investigation of silver nanoparticles at 3 keV detects the presence (10.01%), P (0.65%), S (0.45%), and Cl (0.46%). The studied sample also included

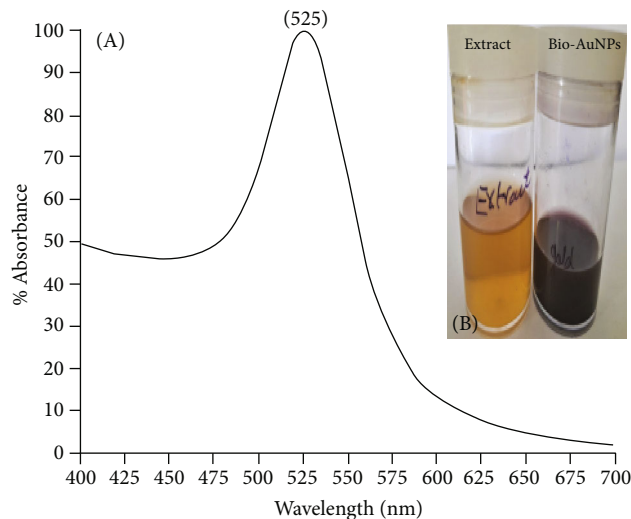


FIGURE 4: (a) UV-Vis absorption spectrum of Bio-AuNPs with the aqueous extract of *Hibiscus Rosa sinensis* (gurhal). (b) Vials with colour changes ((B) pale yellow to purple reddish) indicate Bio-AuNP synthesis.

the highest peak of C (88.43%). The Ag elemental peaks were identified at 1.00 and 3.00 keV.

3.6. Antibacterial Activity. Antibacterial activity was measured in zone of inhibition (mm in diameter), and the CH-AgNPs had high antibacterial activity of 24.80 ± 1.50 and 23.98 ± 0.89 , whereas the CH-AuNPs had moderate antibacterial activity of 10.60 ± 0.82 and 12.80 ± 0.90 against *B. subtilis* (Figure 10(a)) and *E. coli* (Figure 10(b)), respectively. Bio-AgNPs, on the other hand, had also excellent antibacterial activity 22.80 ± 1.80 and 23.40 ± 1.20 , whereas Bio-AuNPs had poor antibacterial activity 09.60 ± 1.91 and 10.70 ± 1.22 against *B. subtilis* (Figure 10(a)) and *E. coli* (Figure 10(b)), respectively. Similar results were also reported for photosynthesized silver and gold NPs [42, 49, 55–57]. Tetracycline, a positive control and standard antibiotics, at $5 \mu\text{g}/\text{disk}$, has good inhibitory activity 18.45 ± 1.67 and 18.09 ± 0.50 against *B. subtilis* and *E. coli* pathogens (Table 1). Our findings suggest that Bio-Ag/Au NPs have good antibacterial activity with low toxicity and could be a good antibiotic replacement. Despite the fact that NPs are widely used as antimicrobials, their mechanism is still unknown. Interference with cell wall synthesis, inhibition of protein synthesis, interference with nucleic acid synthesis, and inhibition of a metabolic pathway are all possible antimicrobial mechanisms [58, 59]. Nanomaterials can increase cell membrane permeability, interfere with DNA replication, denature bacterial proteins, and release silver ions within the bacterial cell [60].

3.7. Calculation of Toxic Effect Value (TEV) in Percentage. By plugging absorbance values into equation-X (see Section 2.6.1.), TEV of chemical synthesized NPs was calculated in both the k_1 and k_2 groups.

CH-AgNPs of k_1 : $PI = [1 - (-0.3952/-2.7151)] \times 100 = PI = 85.45\%$, (TEV = 85.45),

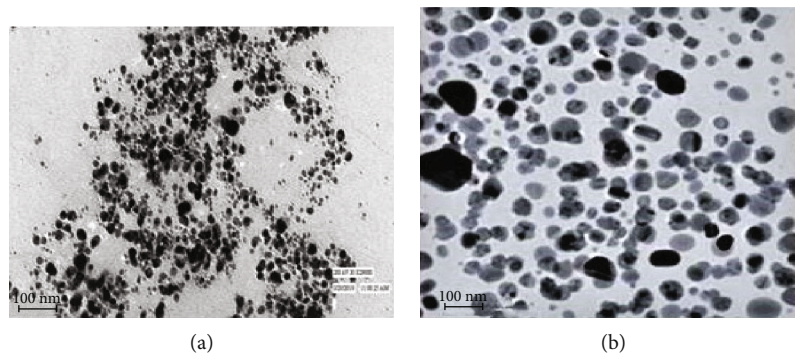


FIGURE 5: TEM monograph of chemical synthesized nanoparticles (a) CH-AgNPs and (b) CH-AuNPs.

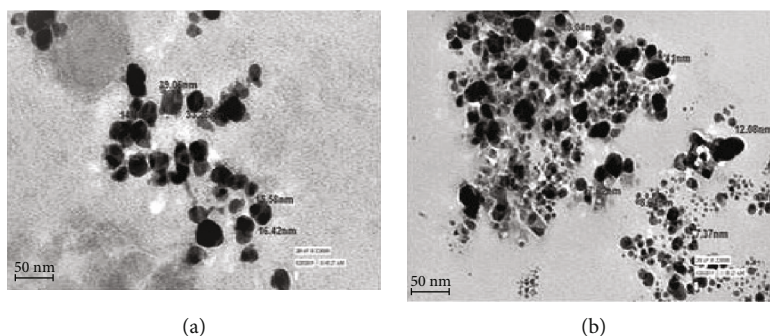


FIGURE 6: TEM monograph of biological synthesized nanoparticles: (a) Bio-AgNPs and (B) Bio-AuNPs.

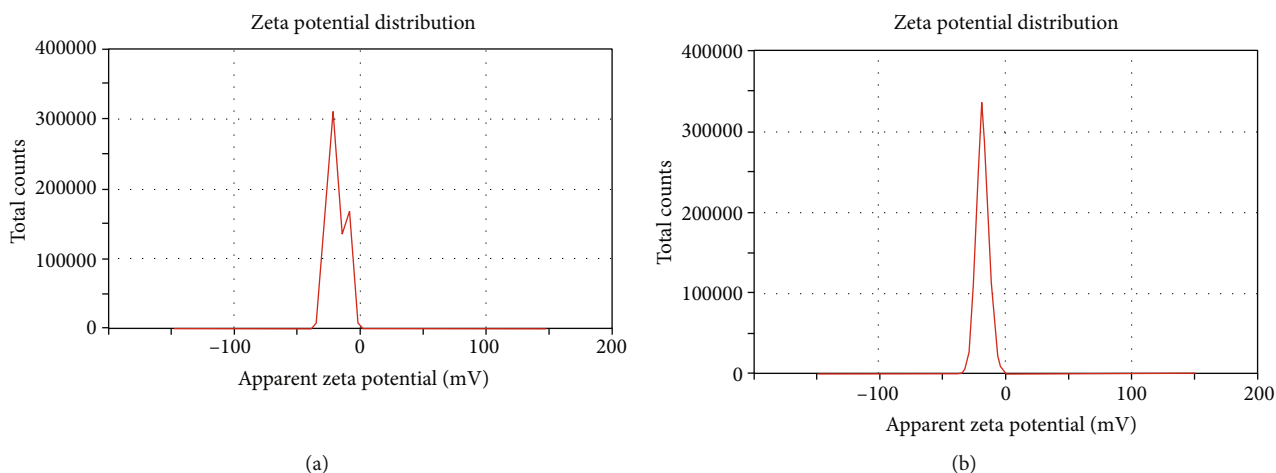


FIGURE 7: Zeta potential distribution pattern: (a) CH-AgNPs (-29.18 mV) and (b) CH-AuNPs (-18.30 mV).

CH-AgNPs of k_2 : $PI = [1 - (-0.4368/-2.6915)] \times 100 = PI = 83.77\%$, (TEV = 83.77),

CH-AuNPs of k_1 : $PI = [1 - (-1.8072/-2.7151)] \times 100 = PI = 33.51\%$, (TEV = 33.51),

CH-AuNPs of k_2 : $PI = [1 - (-1.3396/-2.6915)] \times 100 = PI = 36.85\%$, (TEV = 36.85).

The data on toxicity clearly shows that CH-AgNPs are more toxic than CH-AuNPs.

By plugging absorbance values into equation-X (see Section 2.6.1.), TEV of biologically synthesized NPs were calculated in both the k_1 and k_2 groups.

Bio-AgNPs of k_1 : $PI = [1 - (-1.2026/-2.7151)] \times 100 = PI = 55.75\%$, (TEV = 55.75),

Bio-AgNPs of k_2 : $PI = [1 - (-1.2269/-2.6915)] \times 100 = PI = 54.42\%$, (TEV = 54.42),

Bio-AuNPs of k_1 : $PI = [1 - (-2.0829/-2.7151)] \times 100 = PI = 23.36\%$, (TEV = 23.36),

Bio-AuNPs of k_2 : $PI = [1 - (-2.0330/-2.6915)] \times 100 = PI = 24.46\%$, (TEV = 24.46).

CH-AgNPs had the highest TEV, with 85.45% and 83.77%, compared to Bio-AgNPs, which had 55.75% and 54.42% for both the k_1 and k_2 groups, respectively. In the

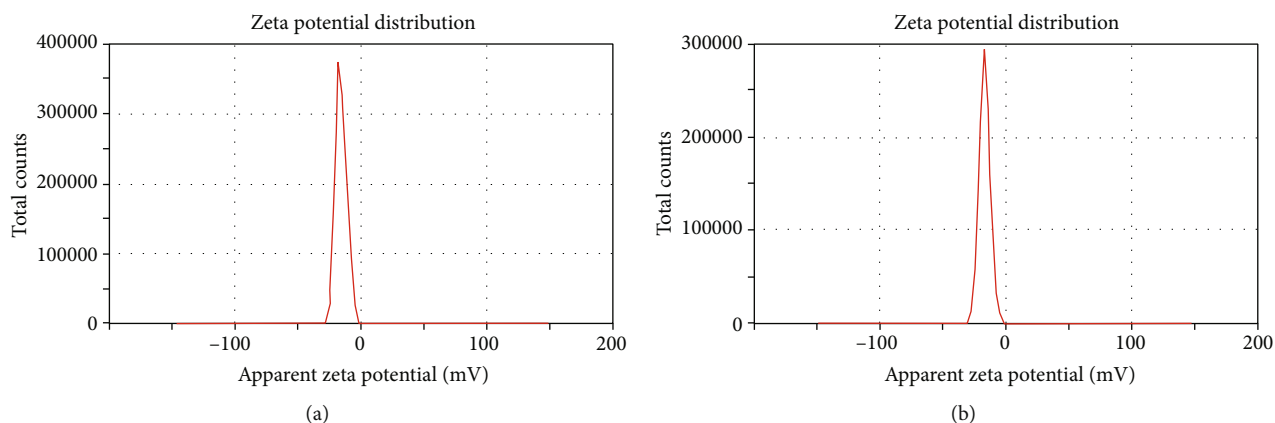


FIGURE 8: Zeta potential distribution pattern: (a) Bio-AgNPs (-23.19 mV) and (b) Bio-AuNPs (-23.90 mV).

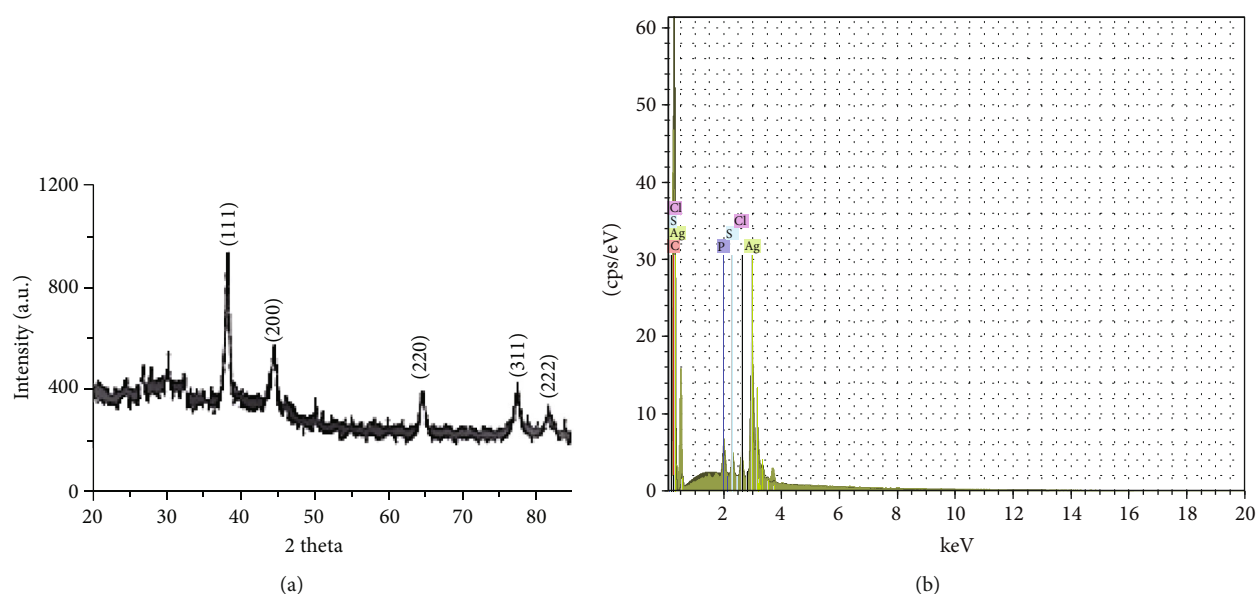


FIGURE 9: XRD spectrum of synthesized AgNPs (a). EDX spectrum of synthesized AgNPs (b).

k_1 and k_2 groups, CH-AuNPs have 33.51 and 36.85%, whereas Bio-AuNPs have 23.36% and 24.46%, respectively. A nonsignificant difference in TEV of CH-Ag/AuNP (Figure 11(a)) and Bio-Ag/AuNP (Figure 11(b)) solutions was found in both the k_1 and k_2 groups. The following is the pattern of the TEV of CH-Ag/AuNPs and Bio-Ag/AuNPs in decreasing order.

CH-AgNPs for the k_1 group > CH-AgNPs for k_2 group > Bio-AgNPs for k_1 group > Bio-AgNPs for k_2 group > CH-AuNPs for k_2 group > CH-AuNPs for k_1 group > Bio-AuNPs for k_2 group > Bio-AgNPs for k_1 group. When comparing silver NPs to gold NPs, as well as chemical vs biological methods, biologically synthesized (Ag and Au) NPs have lower toxicity than chemically synthesized (Ag and Au) NPs Figures 11(a) and 11(b). On the other hand, the chemical vs. biological method, AgNPs vs. AuNPs, and bacterial species k_1 vs. k_2 group, finding results were depicted in Figures 12(a) and 12(b). When comparing AgNPs vs. AuNPs in both bacterial species k_1 and k_2 , a significant TEV difference was observed in the chemical vs.

biological method. The process of whole organisms' uptake and accumulating NPs was less well understood. However, it is clear how whole organisms will react to NPs in their bodies, but how can a possibility of translocation within the body be left to fat droplets [61, 62]. NPs can enter cells by diffusing into the cell membrane via adhesion and endocytosis, according to some studies [63–65]. In higher organisms, such as marine invertebrates, where silver bioaccumulation is relatively quick compared to other trace metals, endocytosis appears to explain silver NP toxicity. Silver can be taken up by transporters in the ionic form because its properties are most similar to sodium and copper ions [66, 67]. The mechanism by which the gut community (gut microbiota) induces its effect is not through translocation, but rather dysbiosis. This process occurs naturally as a result of aging. Aerobic bacteria dominate the gut at birth and are altered in the first weeks to form an anaerobic dominated environment. By adolescences, the gut has the highest proportion of Bifidobacteria and Clostridia that it ever will and will then begin to stabilize throughout adulthood. In

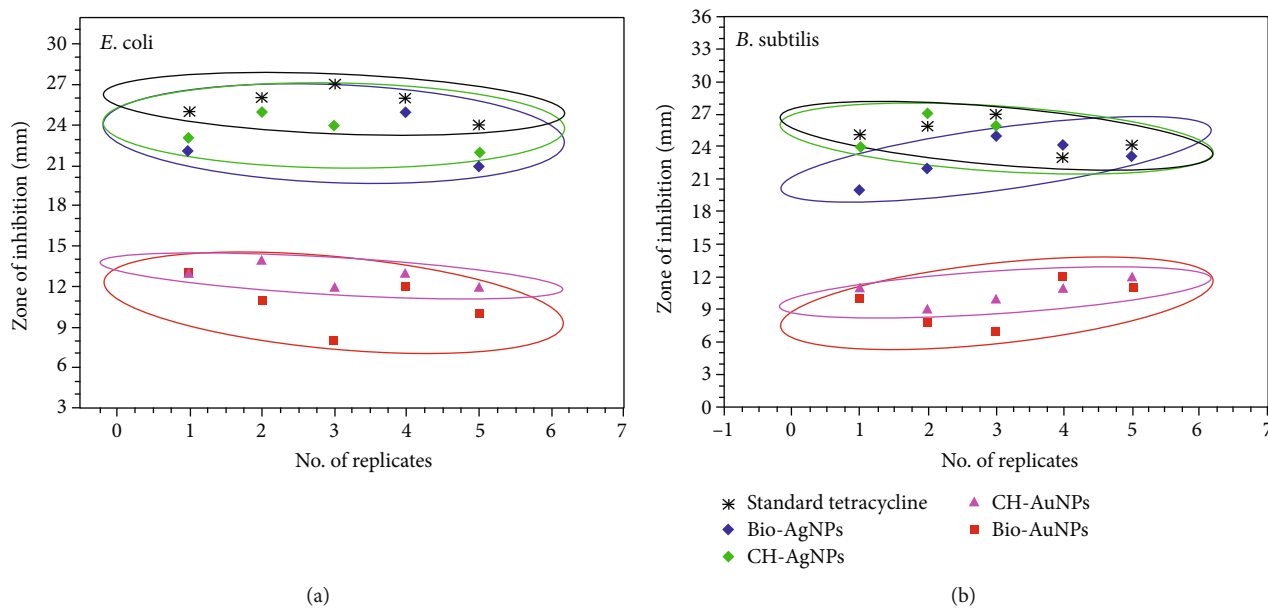


FIGURE 10: A comparison of antibacterial potential between zone of inhibition (mm) and no. of replicates of CH-Ag/AuNPs, Bio-Ag/AuNPs, and a standard control tetracycline antibiotic against (a) *B. subtilis* and (b) *E. coli*.

TABLE 1: Antibacterial activity of CH-Ag/AuNPs and Bio-Ag/AuNPs against *B. subtilis* and *E. coli*.

S.no.	Name of the organism	Zone of inhibition (mm in diameter)					
		CH-AgNPs	CH-AuNPs	Bio-AgNPs	Bio-AuNPs	HLE-hibiscus (Aq.)	PC-1
1	<i>B. subtilis</i>	24.80 ± 1.50	10.60 ± 0.82	22.80 ± 1.80	09.00 ± 1.96	$8.90.50 \pm 1.50$	25.00 ± 0.19
2	<i>E. coli</i>	24.00 ± 1.32	12.80 ± 0.96	23.40 ± 1.20	10.80 ± 1.25	07.40 ± 1.20	25.90 ± 0.48

CH-AgNPs: chemical synthesized silver nanoparticles; CH-AuNPs: chemical synthesized gold nanoparticles; Bio-AgNPs: biological synthesized silver nanoparticles; Bio-AuNPs: biological synthesized gold nanoparticles; HLE: hibiscus leaf extract (aqueous); PC-(1): positive control (tetracycline).

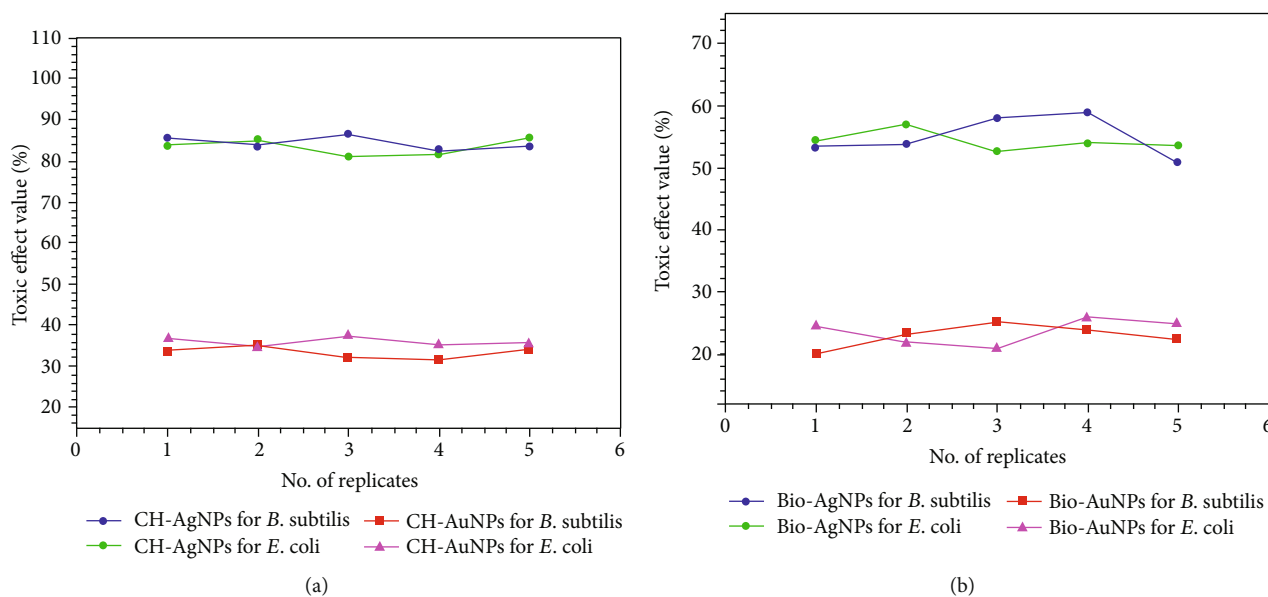


FIGURE 11: A comparison of toxic effect values (TEV) using the ToxTrak test as an *in vitro*. (a) CH-Ag/AuNPs vs. both bacterial species *B. subtilis* and *E. coli*. (b) Bio-Ag/AuNPs vs. both bacterial species *B. subtilis* and *E. coli*.

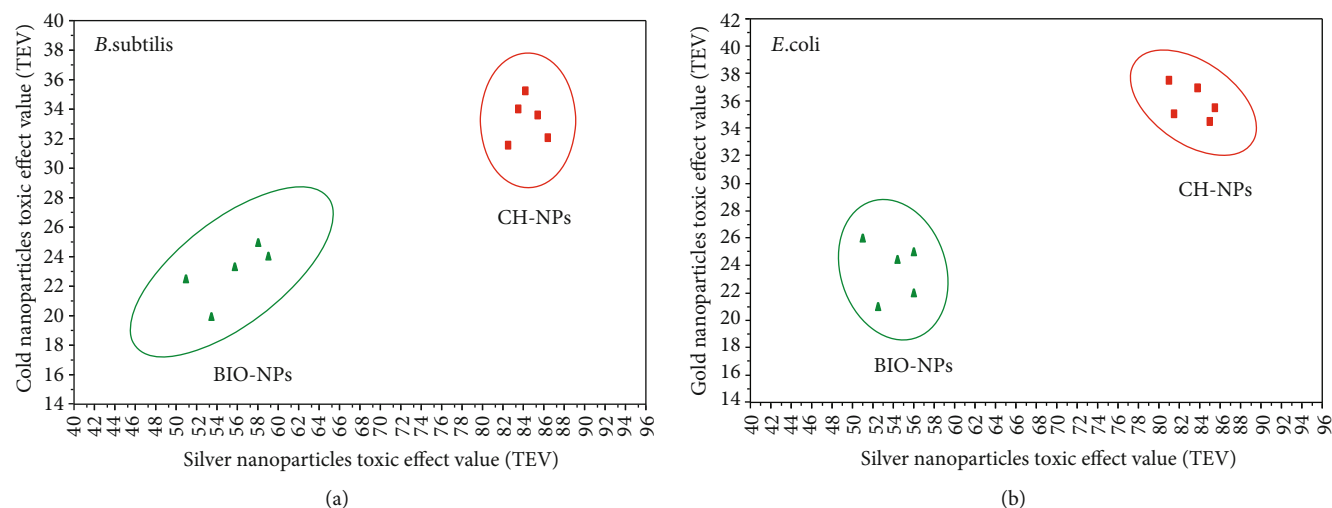


FIGURE 12: A comparison of silver and gold nanoparticles toxicity synthesized from chemical (CH-NPs) and biological (Bio-NPs) methods: (a) *B. subtilis* and (b) *B. coli*.

old age, the gut community shows a decrease in Bifidobacteria (genus) and Bacteroidetes (phylum), an increase in Firmicutes (phylum), and overall shows an increase in the number of facultative anaerobes. The percentage inhibition of *in vitro* toxicity of chemical and biological synthesized Ag/Au NPs was investigated in this study, and it was discovered that biological synthesized both Ag/AuNPs are less toxic, more friendly and biocompatible to human gut microbial community probiotics as compared to chemical synthesized Ag/AuNPs. Our findings corroborate previous research, which found that CH-AgNPs are more toxic than Bio-AgNPs from different plant species and algae [68–71]. Our findings suggest that, in comparison to chemically synthesized Ag/AuNPs, biologically synthesized Ag/AuNPs may be a good alternative for coating antibiotic drugs for pharma industries. The upper coatings of nanoparticles on the drugs may be more effective for killing pathogenic bacteria and safe for humans because biologically synthesized Ag/AuNPs are very less toxic and also less harmful to probiotics present in the human gut in the form of probiotic bacteria.

4. Conclusion

In this work, silver and gold nanoparticles were synthesized using two methods: chemical and biological. The nanoparticles were characterized by UV-Vis spectroscopy, TEM, XRD, EDX, and zeta potential analyzers. The ToxTrak test was applied as *in vitro* to measure the toxicity of synthesized nanoparticles as well as antibacterial activity against Gram-positive (*B. subtilis*) and Gram-negative (*E. coli*) bacteria after satisfactory characterization. The ToxTrak results show that CH-AgNPs are more hazardous than Bio-AgNPs, having a higher TEV/PI value. Similar patterns were seen with CH-AuNPs, which had somewhat higher TEV than Bio-AuNPs. When Ag/Au NPs were examined for antibacterial activity, the following pattern emerged: CH-AgNPs < Bio-AgNPs < CH-AuNPs < Bio-AuNPs, whereas the control sample (tetracycline antibiotic) revealed a highest zone of

inhabitation. Overall, Bio-AgNPs and Bio-AuNPs are the most effective pathogen-killing materials with the lowest toxicity. Our findings show that biologically synthesized Ag/AuNPs might be a suitable alternative to chemically synthesized Ag/AuNPs for coating antimicrobial medicines in the pharmaceutical industry. Because biologically synthesized Ag/AuNPs are less toxic and also less destructive to probiotics present in the human gut in the form of probiotic bacteria, the upper coatings of nanoparticles on the drugs may be more effective for destroying pathogenic bacteria and safe for humans.

Data Availability

The data used to support the findings of this study are available from the corresponding author upon request.

Conflicts of Interest

The authors declare that they have no conflicts of interest.

Acknowledgments

The author ST gratefully acknowledges Council of Science and Technology, U.P. (CST, Uttar Pradesh) (Grant no.: CST/8276 (Young Scientist Scheme)) for funds. The authors also acknowledge the constant support from the Director of this Institute.

References

- [1] J. W. Alexander, "History of the medical use of silver," *Surgical Infections*, vol. 10, no. 3, pp. 289–292, 2009.
- [2] T. Desalegn, C. R. Ravikumar, and H. C. A. Murthy, "Ecofriendly synthesis of silver nanostructures using medicinal plant *Vernonia amygdalina* Del. leaf extract for multifunctional applications," *Applied Nanoscience*, vol. 11, no. 2, pp. 535–551, 2021.

- [3] S. Ghotekar, S. Pansambal, S. P. Pawar, T. Pagar, R. Oza, and S. Bangale, "Biological activities of biogenically synthesized fluorescent silver nanoparticles using *Acanthospermum hispidum* leaves extract," *SN Applied Sciences*, vol. 1, no. 11, pp. 1–12, 2019.
- [4] S. Ghotekar, A. Savale, and S. Pansambal, "Phytofabrication of fluorescent silver nanoparticles from *Leucaena leucocephala* L. leaves and their biological activities," *Journal of Water and Environmental Nanotechnology*, vol. 3, no. 2, pp. 95–105, 2018.
- [5] D. Gola, A. kriti, N. Bhatt et al., "Silver nanoparticles for enhanced dye degradation," *Current Research in Green and Sustainable Chemistry*, vol. 4, article 100132, 2021.
- [6] D. Gola, P. K. Tyagi, A. Arya et al., "Antimicrobial and dye degradation application of fungi-assisted silver nanoparticles and utilization of fungal retentate biomass for dye removal," *Water Environment Research*, vol. 93, no. 11, pp. 2727–2739, 2021.
- [7] A. Kaushik, D. Gola, J. Raghav et al., "Synthesis of silver nanoparticles using egg white: dye degradation and antimicrobial potential," *Biointerface Research in Applied Chemistry*, vol. 12, no. 2, pp. 2361–2372, 2022.
- [8] S. Raina, A. Roy, and N. Bharadvaja, "Degradation of dyes using biologically synthesized silver and copper nanoparticles," *Environmental Nanotechnology, Monitoring & Management*, vol. 13, article 100278, 2020.
- [9] S. Gajbhiye and S. Sakharwade, "Silver nanoparticles in cosmetics," *Journal of Cosmetics, Dermatological Sciences and Applications*, vol. 6, no. 1, pp. 48–53, 2016.
- [10] A. Kumar, A. Choudhary, H. Kaur, S. Mehta, and A. Husen, "Metal-based nanoparticles, sensors, and their multifaceted application in food packaging," *Journal of Nanobiotechnology*, vol. 19, no. 1, pp. 1–25, 2021.
- [11] Q. Chaudhry, M. Scotter, J. Blackburn et al., "Applications and implications of nanotechnologies for the food sector," *Food Additives & Contaminants: Part A*, vol. 25, no. 3, pp. 241–258, 2008.
- [12] G. Schmid and B. Corain, "Nanoparticulated gold: syntheses, structures, electronics, and reactivities," *European Journal of Inorganic Chemistry*, vol. 2003, no. 17, pp. 3081–3098, 2003.
- [13] P. K. Tyagi, S. Tyagi, C. Verma, and A. Rajpal, "Estimation of toxic effects of chemically and biologically synthesized silver nanoparticles on human gut microflora containing *Bacillus subtilis*," *Journal of Toxicology and Environmental Health Sciences*, vol. 5, no. 9, pp. 172–177, 2013.
- [14] S. Ghotekar, K. Pagar, S. Pansambal, H. C. A. Murthy, and R. Oza, "Biosynthesis of silver sulfide nanoparticle and its applications," in *Handbook of Greener Synthesis of Nanomaterials and Compounds*, pp. 191–200, Elsevier, 2021.
- [15] P. K. Tyagi, V. Sarsar, and A. Ahuja, "Synthesis of metal nanoparticles : a biological prospective for analysis," *International Journal of Pharmaceutical Innovations*, vol. 2, no. 4, pp. 48–60, 2012.
- [16] R. Posgai, C. B. Cipolla-McCulloch, K. R. Murphy, S. M. Hussain, J. J. Rowe, and M. G. Nielsen, "Differential toxicity of silver and titanium dioxide nanoparticles on *Drosophila melanogaster* development, reproductive effort, and viability: Size, coatings and antioxidants matter," *Chemosphere*, vol. 85, no. 1, pp. 34–42, 2011.
- [17] S. M. Hussain, K. L. Hess, J. M. Gearhart, K. T. Geiss, and J. J. Schlager, "In vitro toxicity of nanoparticles in BRL 3A rat liver cells," *Toxicology In Vitro*, vol. 19, no. 7, pp. 975–983, 2005.
- [18] S. W. P. Wijnhoven, W. J. G. M. Peijnenburg, C. A. Herberts et al., "Nano-silver - a review of available data and knowledge gaps in human and environmental risk assessment," *Nanotoxicology*, vol. 3, no. 2, pp. 109–138, 2009.
- [19] C. M. Lappas, "The immunomodulatory effects of titanium dioxide and silver nanoparticles," *Food and Chemical Toxicology*, vol. 85, pp. 78–83, 2015.
- [20] L. M. Rossbach, D. H. Oughton, E. Maremonti, C. Coutris, and D. A. Brede, "In vivo assessment of silver nanoparticle induced reactive oxygen species reveals tissue specific effects on cellular redox status in the nematode *Caenorhabditis elegans*," *Science of the Total Environment*, vol. 721, article 137665, 2020.
- [21] P. B. Eckburg, E. M. Bik, C. N. Bernstein et al., "Diversity of the human intestinal microbial flora," *Science*, vol. 308, no. 5728, pp. 1635–1638, 2005.
- [22] M. F. Meléndrez, G. Cárdenas, and J. Arbiol, "Synthesis and characterization of gallium colloidal nanoparticles," *Journal of Colloid and Interface Science*, vol. 346, no. 2, pp. 279–287, 2010.
- [23] R. Bywalez, H. Karacuban, H. Nienhaus, C. Schulz, and H. Wiggers, "Stabilization of mid-sized silicon nanoparticles by functionalization with acrylic acid," *Nanoscale Research Letters*, vol. 7, no. 1, pp. 1–7, 2012.
- [24] P. K. Tyagi, M. Mishra, N. Khan, S. Tyagi, and S. Sirohi, "Toxicological study of silver nanoparticles on gut microbial community probiotic," *Environmental Nanotechnology, Monitoring & Management*, vol. 5, pp. 36–43, 2016.
- [25] S. Anoopkumar-Dukie, J. B. Carey, T. Conere, E. O'Sullivan, F. N. van Pelt, and A. Allshire, "Resazurin assay of radiation response in cultured cells," *British Journal of Radiology*, vol. 78, no. 934, pp. 945–947, 2005.
- [26] E. Liwarska-Bizukojc, R. Ślęzak, and M. Klink, "Study on wastewater toxicity using ToxTrak™ method," *Environmental Science and Pollution Research*, vol. 23, no. 9, pp. 9105–9113, 2016.
- [27] P. Tyagi, S. Tyagi, and S. Singh, "Estimation of silver nanoparticles toxicity on human gut micro flora," *International Journal of Development Research*, vol. 3, no. 9, pp. 027–030, 2013.
- [28] W. R. Diao, Q. P. Hu, S. S. Feng, W. Q. Li, and J. G. Xu, "Chemical composition and antibacterial activity of the essential oil from green huajiao (*Zanthoxylum schinifolium*) against selected foodborne pathogens," *Journal of Agricultural and Food Chemistry*, vol. 61, no. 25, pp. 6044–6049, 2013.
- [29] F. K. Alsammarraie, W. Wang, P. Zhou, A. Mustapha, and M. Lin, "Green synthesis of silver nanoparticles using turmeric extracts and investigation of their antibacterial activities," *Colloids and Surfaces B: Biointerfaces*, vol. 171, pp. 398–405, 2018.
- [30] J. M. Awda, "Biosynthesis of silver nanoparticles using mints leaf extract and evaluation of their antimicrobial activity," *Biochemical and Cellular Archives*, vol. 19, no. 2, pp. 2903–2908, 2019.
- [31] K. Roy, S. Biswas, and P. C. Banerjee, "Green synthesis of silver nanoparticles by using grape (*Vitis vinifera*) fruit extract: characterization of the particles and study of antibacterial activity," *Research Journal of Pharmaceutical, Biological and Chemical Sciences*, vol. 4, no. 1, pp. 1271–1278, 2013.
- [32] A. Lalitha, R. Subbaiya, and P. Ponmurugan, "Green synthesis of silver nanoparticles from leaf extract *Azhadirachta indica* and to study its anti-bacterial and antioxidant property original research article green synthesis of silver nanoparticles from leaf extract *Azhadirachta indica* and to study its,"

- International Journal of Current Microbiology and Applied Sciences*, vol. 2, pp. 228–235, 2015.
- [33] N. Namratha and P. Monica, “Synthesis of silver nanoparticles using *Azadirachta indica* (Neem) extract and usage in water purification,” *Asian Journal of Pharmacy and Technology*, vol. 3, no. 4, pp. 170–174, 2013.
- [34] D. Philip and C. Unni, “Extracellular biosynthesis of gold and silver nanoparticles using Krishna tulsi (*Ocimum sanctum*) leaf,” *Physica E: Low-dimensional Systems and Nanostructures*, vol. 43, no. 7, pp. 1318–1322, 2011.
- [35] V. K. Shukla, S. Pandey, and A. C. Pandey, “Green synthesis of silver nanoparticles using neem leaf (*Azadirachta indica*) extract,” *AIP Conference Proceedings*, vol. 1276, pp. 43–49, 2010.
- [36] R. Singh, C. Hano, G. Nath, and B. Sharma, “Green biosynthesis of silver nanoparticles using leaf extract of *Carissa carandas* l. and their antioxidant and antimicrobial activity against human pathogenic bacteria,” *Biomolecules*, vol. 11, no. 2, p. 299, 2021.
- [37] D. Cruz, P. L. Falé, A. Mourato, P. D. Vaz, M. Luisa Serralheiro, and A. R. L. Lino, “Preparation and physico-chemical characterization of Ag nanoparticles biosynthesized by *Lippia citriodora* (Lemon Verbena),” *Colloids and Surfaces B: Biointerfaces*, vol. 81, no. 1, pp. 67–73, 2010.
- [38] T. Y. Suman, S. R. Radhika Rajasree, A. Kanchana, and S. B. Elizabeth, “Biosynthesis, characterization and cytotoxic effect of plant mediated silver nanoparticles using *Morinda citrifolia* root extract,” *Colloids and Surfaces B: Biointerfaces*, vol. 106, pp. 74–78, 2013.
- [39] R. Vijayan, S. Joseph, and B. Mathew, “Anticancer, antimicrobial, antioxidant, and catalytic activities of green-synthesized silver and gold nanoparticles using *Bauhinia purpurea* leaf extract,” *Bioprocess and Biosystems Engineering*, vol. 42, no. 2, pp. 305–319, 2019.
- [40] I. Fatimah, “Green synthesis of silver nanoparticles using extract of *Parkia speciosa* Hassk_ pods assisted by microwave irradiation,” *Journal of Advanced Research*, vol. 7, no. 6, pp. 961–969, 2016.
- [41] P. S. F. Musere, A. Rahman, V. Uahengo et al., “Biosynthesis of silver nanoparticles using pearl millet (*Pennisetum glaucum*) husk to remove algae in the water and catalytic oxidation of benzyl alcohol,” *Journal of Cleaner Production*, vol. 312, article 127581, 2021.
- [42] K. Nahar, M. Hafezur Rahaman, G. Arifuzzaman Khan, M. Khairul Islam, and S. Md Al-Reza, “Green synthesis of silver nanoparticles from *Citrus sinensis* peel extract and its antibacterial potential,” *Asian Journal of Green Chemistry*, vol. 5, no. 1, pp. 135–150, 2021.
- [43] D. S. Priya, S. Sankaravadivu, S. Sudha, and H. K. S. Christy, “Synthesis and characterisation of silver nanoparticles using *phallusia nigra*,” *Annals of the Romanian Society for Cell Biology*, vol. 25, no. 4, 2021.
- [44] G. Singhal, R. Bhavesh, K. Kasariya, A. R. Sharma, and R. P. Singh, “Biosynthesis of silver nanoparticles using *Ocimum sanctum* (Tulsi) leaf extract and screening its antimicrobial activity,” *Journal of Nanoparticle Research*, vol. 13, no. 7, pp. 2981–2988, 2011.
- [45] D. P. Ramírez Aguirre, E. Flores Loyola, N. M. De la Fuente Salcido, L. Rodríguez Sifuentes, A. Ramírez Moreno, and J. E. Marszalek, “Comparative antibacterial potential of silver nanoparticles prepared via chemical and biological synthesis,” *Arabian Journal of Chemistry*, vol. 13, no. 12, pp. 8662–8670, 2020.
- [46] M. A. Elbahnasawy, A. M. Shehabeldine, A. M. Khattab, B. H. Amin, and A. H. Hashem, “Green biosynthesis of silver nanoparticles using novel endophytic *Rothia endophytica*: Characterization and anticandidal activity,” *Journal of Drug Delivery Science and Technology*, vol. 62, article 102401, 2021.
- [47] B. Fan, J. Wan, J. Zhai, X. Chen, and S. H. Thang, “Triggered degradable colloidal particles with ordered inverse bicontinuous cubic and hexagonal mesophases,” *ACS Nano*, vol. 15, no. 3, pp. 4688–4698, 2021.
- [48] R. Mariychuk, R. Smolková, V. Bartošová et al., “The regularities of the *Mentha piperita* L. extract mediated synthesis of gold nanoparticles with a response in the infrared range,” *Applied Nanoscience*, pp. 1–13, 2021.
- [49] Z. Qiusheng and M. Jun, “Reactive oxygen species and morphine addiction,” in *Reactive Oxygen Species in Biology and Human Health*, pp. 501–512, CRC Press, 2017.
- [50] S. Tyagi, A. Kumar, and P. K. Tyagi, “Comparative analysis of metal nanoparticles synthesized from *Hibiscus ROSA SINESIS* and their antibacterial activity estimation against nine pathogenic bacteria,” *Asian Journal of Pharmaceutical and Clinical Research*, vol. 10, no. 5, pp. 323–329, 2017.
- [51] S. Roy, T. Mukherjee, S. Chakraborty, and T. K. Das, “Biosynthesis, characterisation & antifungal activity of silver nanoparticles synthesized by the fungus *Aspergillus foetidus* MTCC8876,” *Digest Journal of Nanomaterials and Biostructures*, vol. 8, no. 1, pp. 197–205, 2012.
- [52] P. Kanniah, P. Chelliah, J. R. Thangapandi, G. Gnanadhas, V. Mahendran, and M. Robert, “Green synthesis of antibacterial and cytotoxic silver nanoparticles by *Piper nigrum* seed extract and development of antibacterial silver based chitosan nanocomposite,” *International Journal of Biological Macromolecules*, vol. 189, pp. 18–33, 2021.
- [53] M. Narayanan, S. Divya, D. Natarajan et al., “Green synthesis of silver nanoparticles from aqueous extract of *Ctenolepis garcini* L. and assess their possible biological applications,” *Process Biochemistry*, vol. 107, pp. 91–99, 2021.
- [54] N. V. Reddy, H. Li, T. Hou, M. S. Bethu, Z. Ren, and Z. Zhang, “Phytosynthesis of silver nanoparticles using *perilla frutescens* leaf extract: characterization and evaluation of antibacterial, antioxidant, and anticancer activities,” *International Journal of Nanomedicine*, vol. 16, pp. 15–29, 2021.
- [55] S. A. Akintelu, B. Yao, and A. S. Folorunso, “Green synthesis, characterization, and antibacterial investigation of synthesized gold nanoparticles (AuNPs) from *Garcinia kola* pulp extract,” *Plasmonics*, vol. 16, no. 1, pp. 157–165, 2021.
- [56] P. K. Tyagi, R. Mishra, F. Khan, D. Gupta, and D. Gola, “Antifungal effects of silver nanoparticles against various plant pathogenic fungi and its safety evaluation on *Drosophila melanogaster*,” *Biointerface Research in Applied Chemistry*, vol. 10, no. 6, pp. 6587–6596, 2020.
- [57] S. Tyagi, P. K. Tyagi, D. Gola, N. Chauhan, and R. K. Bharti, “Extracellular synthesis of silver nanoparticles using entomopathogenic fungus: characterization and antibacterial potential,” *SN Applied Sciences*, vol. 1, no. 12, pp. 1–9, 2019.
- [58] A. Herman and A. P. Herman, “Nanoparticles as antimicrobial agents: their toxicity and mechanisms of action,” *Journal of Nanoscience and Nanotechnology*, vol. 14, no. 1, pp. 946–957, 2014.

- [59] P. K. Tyagi, P. Upadhyay, P. Kaul, S. Chaudhary, and E. Mansi Mishra, "Detection of routes of interaction between silver nanoparticles and bacterial cell membrane," *International Journal of Basic and Applied Biology*, vol. 3, no. 2, pp. 111–114, 2016.
- [60] M. Guzman, J. Dille, and S. Godet, "Synthesis and antibacterial activity of silver nanoparticles against gram-positive and gram-negative bacteria," *Nanomedicine: Nanotechnology, Biology, and Medicine*, vol. 8, no. 1, pp. 37–45, 2012.
- [61] S. J. Klaine, P. J. J. Alvarez, G. E. Batley et al., "Nanomaterials in the environment: Behavior, fate, bioavailability, and effects," *Environmental Toxicology and Chemistry*, vol. 27, no. 9, pp. 1825–1851, 2008.
- [62] J. R. Lead, G. E. Batley, P. J. J. Alvarez et al., "Nanomaterials in the environment: behavior, fate, bioavailability, and effects—an updated review," *Environmental Toxicology and Chemistry*, vol. 37, no. 8, pp. 2029–2063, 2018.
- [63] F. Oroojalian, M. Beygi, B. Baradaran, A. Mokhtarzadeh, and M. A. Shahbazi, "Immune cell Membrane-Coated biomimetic nanoparticles for targeted cancer therapy," *Small*, vol. 17, no. 12, article 2006484, 2021.
- [64] V. Sheth, L. Wang, R. Bhattacharya, P. Mukherjee, and S. Wilhelm, "Strategies for delivering nanoparticles across tumor blood vessels," *Advanced Functional Materials*, vol. 31, no. 8, article 2007363, 2021.
- [65] M. Sousa de Almeida, E. Susnik, B. Drasler, P. Taladriz-Blanco, A. Petri-Fink, and B. Rothen-Rutishauser, "Understanding nanoparticle endocytosis to improve targeting strategies in nanomedicine," *Chemical Society Reviews*, vol. 50, no. 9, pp. 5397–5434, 2021.
- [66] W. J. Do Nascimento, R. Landers, M. Gurgel Carlos da Silva, and M. G. A. Vieira, "Equilibrium and desorption studies of the competitive binary biosorption of silver(I) and copper(II) ions on brown algae waste," *Journal of Environmental Chemical Engineering*, vol. 9, no. 1, article 104840, 2021.
- [67] B. Keskin, B. Zeytuncu-Gökoğlu, and I. Koyuncu, "Polymer inclusion membrane applications for transport of metal ions: a critical review," *Chemosphere*, vol. 279, article 130604, 2021.
- [68] F. Liaqat, U. Hanif, S. Bahadur et al., "Comparative evaluation of the toxicological effect of silver salt (AgNO₃) and silver nanoparticles on *Cyprinus carpio* synthesized by chemicals and marine algae using scanning electron microscopy," *Microscopy Research and Technique*, vol. 84, no. 7, pp. 1531–1541, 2021.
- [69] N. Saha and S. Dutta Gupta, "Low-dose toxicity of biogenic silver nanoparticles fabricated by *Swertia chirata* on root tips and flower buds of *Allium cepa*," *Journal of Hazardous Materials*, vol. 330, pp. 18–28, 2017.
- [70] S. S. Salem and A. Fouda, "Green synthesis of metallic nanoparticles and their prospective biotechnological applications: an overview," *Biological Trace Element Research*, vol. 199, no. 1, pp. 344–370, 2021.
- [71] A. Yaqub, N. Malkani, A. Shabbir et al., "Novel biosynthesis of copper nanoparticles using *Zingiber* and *Allium* sp. with synergic effect of doxycycline for anticancer and bactericidal activity," *Current Microbiology*, vol. 77, no. 9, pp. 2287–2299, 2020.

Research Article

Anti-inflammatory and Antimicrobial Potential of *Cissus quadrangularis*-Assisted Copper Oxide Nanoparticles

S. Rajeshkumar ¹, Soumya Menon,² Venkat Kumar S,² M. Ponnaniakamideen,³ Daoud Ali,⁴ and Kalirajan Arunachalam ⁵

¹Nanobiomedicine Lab, Department of Pharmacology, Saveetha Dental College and Hospitals, SIMATS, 600077, Chennai, India

²Department of Biotechnology, School of Biosciences and Technology, VIT, Vellore 632014, India

³Department of Pharmacology and Toxicology, University of Mississippi Medical Centre, Jackson, Mississippi, USA

⁴Department of Zoology, College of Science, King Saud University, PO Box 2455, Riyadh 11451, Saudi Arabia

⁵Department of Science and Mathematics, School of Science, Engineering and Technology, Mulungushi University, Kabwe 80415, Zambia

Correspondence should be addressed to S. Rajeshkumar; ssrajeshkumar@hotmail.com

Received 7 October 2021; Accepted 30 November 2021; Published 27 December 2021

Academic Editor: Arpita Roy

Copyright © 2021 S. Rajeshkumar et al. This is an open access article distributed under the Creative Commons Attribution License, which permits unrestricted use, distribution, and reproduction in any medium, provided the original work is properly cited.

Recently, nontoxic origin-mediated synthesis of copper oxide nanoparticles acquires further recognition because of the key role of bioapplications. The plant *Cissus quadrangularis* is one most prominent herbs used in the treatment of diabetes, asthma, tissue regeneration, etc. In this study, we tested the process of copper oxide nanoparticle synthesis and their role in many functions from *Cissus quadrangularis*. The synthesis of copper oxide nanoparticles uses plant extract and characterization by X-ray diffraction, thermogravimetric analysis (TGA), Fourier-transform infrared spectroscopy (FT-IR), atomic force microscope (AFM), and scanning electron microscope (SEM). The synthesized nanoparticles were analyzed for their biomedical applications such as antibacterial, antifungal, antioxidant, antidiabetic, and anti-inflammatory activity and antiproteinase action. The results show that the *C. quadrangularis* plant-mediated nanoparticles may be used in many biomedical applications related to arthritis, diabetes, and the production of various antimicrobial products in the future.

1. Introduction

The biosynthesis of nanoparticles is the collaboration of both fields of biotechnology and nanotechnology which involves biomaterials commonly used for the synthesis due to various advantages, but most importantly is due to its environment friendly nature [1]. The importance of green nanotechnology has become a latest trend among the researchers lately, as it does not require any utilization of hazardous chemical or reagents; these reducing or stabilizing agents are nontoxic, biocompatible to the environment as well as for any biomedical applications. These agents include microorganisms, parts of plants, enzymes, or green chemicals like chitosan [2], curcumin [3], and chitin [4]. Copper nanoparticles are slightly toxic in nature. To curb in toxicity

sulfidation of CuNP can be performed to form copper oxide nanoparticles [5]. Copper sulfide is an interesting area of research because of its ability to mould into various morphologies; it is a member of transition metal chalcogenides, and behaves like a p-type semiconductor where copper vacancies act as acceptor sites like digenite ($\text{Cu}_{1.8}\text{S}$), sulphur rich covellite (CuS), copper rich chalcocite (Cu_2S), anilite ($\text{Cu}_{1.75}\text{S}$), or djurleite ($\text{Cu}_{1.95}\text{S}$). The ability to form nonstoichiometric phases is because of the variable valence states of copper which has a formula of Cu_xS_y [6, 7]. Various methods have been employed for the synthesis of these nanoparticles like laser induction [8], pulse laser ablation [9], solvothermal [10], phase-controlled synthesis [11], sonochemical [12], or electrobiosynthesis [13]. The major setback of these mentioned methods is the requirement of



FIGURE 1: Synthesis of copper oxide nanoparticles using plant extract.

complicated or expensive equipment and external usage of stabilization agents along with reducing agents. This can result in irregular impact in our surroundings; therefore, the utilization of phytochemicals from plants can be better alternative to this issue, which can act as both reducing and capping agent [14].

The antimicrobial evaluation is important to be considered as it has become a major threat to human via contaminated water or food. The demand for disinfectants has increased tremendously, then protection against food contamination which can be done by packaging, or the development of antibiotics that can be used against pathogenic agents or new formulation against multidrug-resistant (MDR) pathogens [15]. Oxidative stress is caused due to high generation of ROS, which may lead to chronic inflammation; therefore, production of anti-inflammatory agents that can act as antioxidant agents which reduces the oxidative stress caused is also mandatory now [16].

This paper suggests the exploitation of copper oxide nanoparticles using fresh leaves of *Cissus quadrangularis* through various biomedical applications like antimicrobial, antioxidant, and anti-inflammatory or analyzing the anti-proteinase activity.

2. Materials and Methods

For the synthesis of nanoparticles, the fresh leaves of *Cissus quadrangularis* were collected from Vellore district. The doubled-distilled water was used for the entire experiments. All the reaction was completed with glassware washed and rinsed by distilled water and dried in hot air oven [17]. The filtration was done by Whatman No.1 filter papers.

2.1. Plant Details. *Cissus quadrangularis* in South Indian treebine is a climbing, foetid shrub. The outermost layer of the stem is blackish to reddish; division of stem is densely pubescent, swollen at node (hold one or more leaves), and 4 petals are present [18]. It acts as a drug for local tissue injury that is better remedy and relief from wound problems and swelling issues.

Herbal plants have medicinally important components in their various kinds of parts like stem and leaves [19]. The synthesis of nanoparticles by plants depends upon the nature of plant that is their phytochemical compounds, specific adaptation, and medicinal values. In this study, we report the eco-friendly and cost-effective green synthesis of

TABLE 1: Phytochemicals screening of the plant extract *Cissus quadrangularis*.

S/No.	Phytochemicals	Results
1	Carbohydrates	Reddish colour
2	Tannins	Greenish blue
3	Flavonoids	Yellow
4	Alkaloids	Greenish
5	Anthraquinone	Pink
6	Anthacyanaside	Negative
7	Steroids	Red colour layer
8	Terpenoids	Negative
9	Saponins	Foam layer

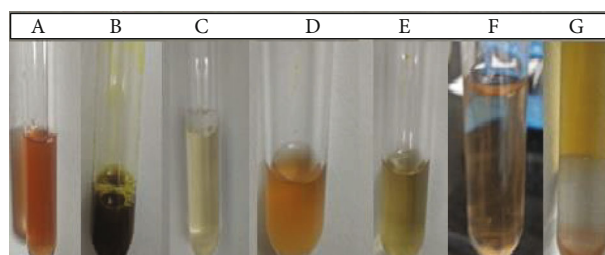


FIGURE 2: Phytochemical screening of plant extract *Cissus quadrangularis*.

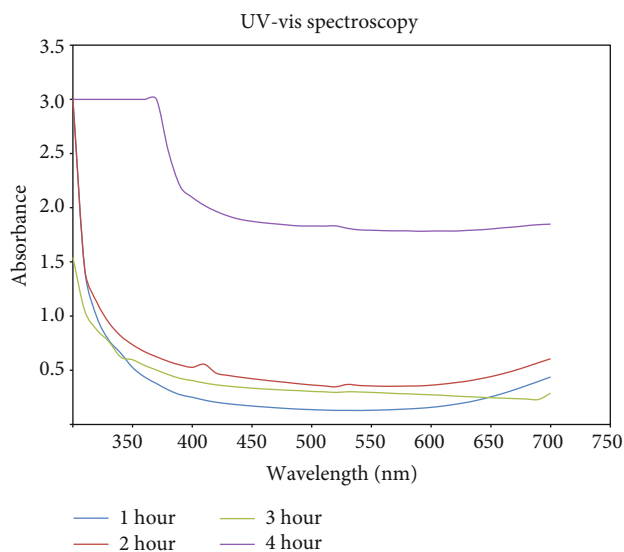


FIGURE 3: *C. quadrangularis*-mediated synthesis of copper oxide nanoparticles.

copper oxide nanoparticle using leaf extract of *Cissus quadrangularis*.

Botanical name: *Cissus quadrangularis*
Family: VITACEAE (grape family)

2.2. Preparation of Plant Extract. The fresh *Cissus quadrangularis* leaves were collected and thoroughly washed several times using normal water. Then, it was allowed to dry

TABLE 2: Particle sizes of nanoparticles by Debye-Scherrer equation.

Samples	2 theta	Crystalline size	Particles size
<i>C. quadrangularis</i> -mediated synthesis of CuO NPs	32.61	0.192	43 nm

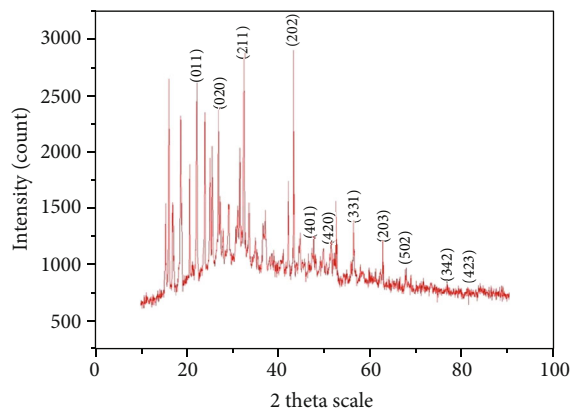
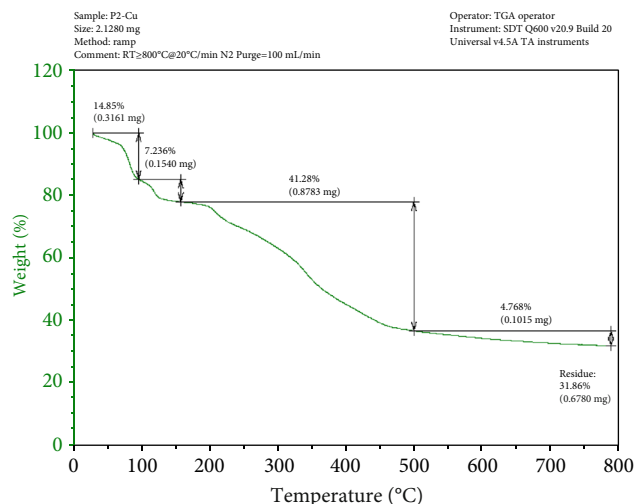
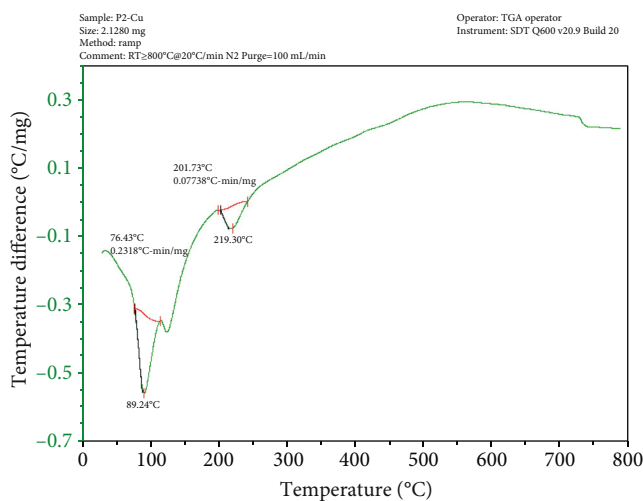
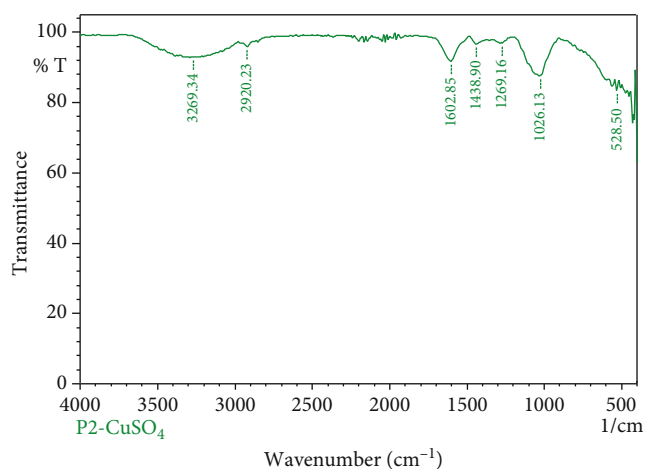


FIGURE 4: XRD patterns of plant-mediated synthesis of copper oxide nanoparticles.

FIGURE 6: TGA curve of copper oxide nanoparticles by *Cissus quadrangularis*.FIGURE 5: Data curve of copper oxide nanoparticles by *Cissus quadrangularis*.FIGURE 7: *Cissus quadrangularis*-mediated synthesis of copper oxide nanoparticles.

sunshades. The dried leaves were grained as fine powder [17]. This plant powder was used for the further process of synthesis of nanomaterials.

2.3. Phytochemical Screening of Plant Extract. Medicinal plants are the richest biosource of drugs of traditional system, pharmaceuticals, nutraceuticals and food source, and chemical synthetic drugs. Extraction is the separation of medicinal active parts and tissues of plants with using of solvents by standard procedure [17]. The plant extracts and methanolic, ethanolic solvents were assessed for the phytochemical screening of carbohydrates, tannis saponins, flavonoid, alkaloids, anthraquinone, anthocyanide, steroids, and terpenoids by using standard methods.

2.4. Synthesis of Plant-Mediated Nanoparticles. The fine dried powder of *Cissus quadrangularis* extract were used for the synthesis. 1g of plant powder was dissolved in 100 mL of double-distilled water and kept for boiled in oven 2 minutes. This mixture was filtered by Whatman filter paper. The 20 mL of filtered solution was mixed with 80 mL of distilled water [20]. Then, 10 mM of copper sulphate was added to this mixture and kept in shaker for 24 hours. After incubation, the solution was centrifuged for 10 minutes at 10000 rpm. Then, the pellet was collected and dried by hot air oven as shown in Figure 1 [17].

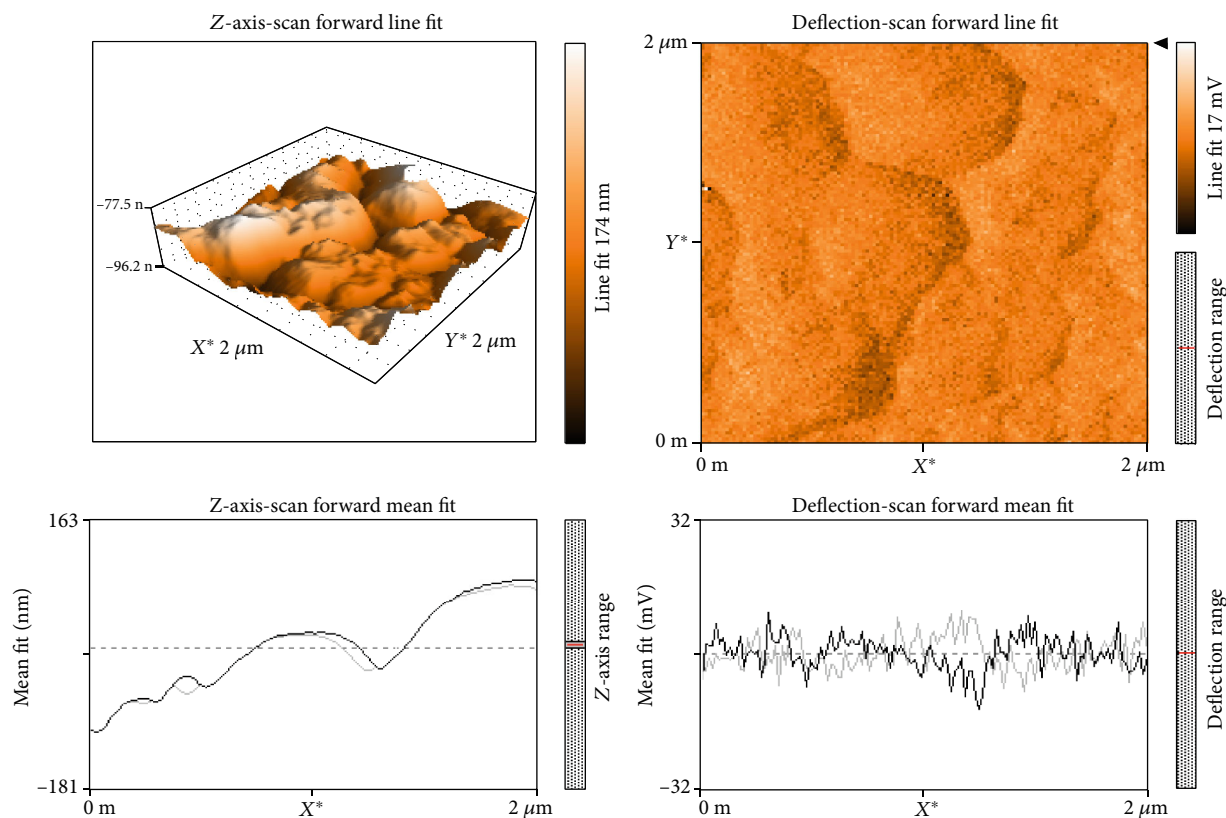


FIGURE 8: AFM data for *C. quadrangularis*-mediated copper oxide NPs.

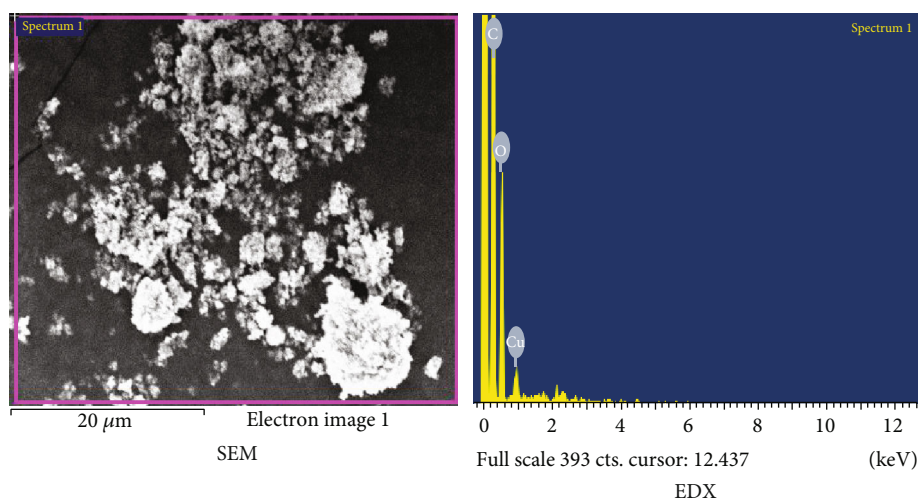


FIGURE 9: SEM and EDAX data for *C. quadrangularis*-mediated copper oxide NPs.

2.5. Characterization. Characterization is essential to determine the average size, shape, and features of the synthesised nanoparticles. These bioactive nanomaterials are analysed by UV-Vis spectrophotometer, X-ray diffraction (Bruker–D8 advance, Germany model), thermogravimetric analysis (SDT Q600 V20.9 build 20), Fourier-transform infrared spectroscopy (FT-IR), atomic force microscope (AFM), and scanning electron microscope (SEM) [21].

TABLE 3: Antibacterial activity against plant-mediated synthesis CuO NPs.

Clinical isolates	Ab	Ab+NP	NP
<i>Staphylococcus aureus</i>	16	21	11
<i>Streptococcus</i> sp.	15	18	26
<i>Serratia marscesnes</i>	8	10	20
<i>Escherichia coli</i>	25	26	R

2.6. Applications

2.6.1. Antibacterial-Enhanced Method. Antimicrobial activity of copper oxide-mediated synthesis of nanoparticle acts against pathogenic bacterial strains (*Staphylococcus aureus*, *Streptococcus*, *E. coli*, and *Serratia marcescens* [17]). To determine the zone of inhibition was observed using MHA agar [22]. Muller Hinton agar was prepared and sterilized at 120 lbs for 45 minutes. Media were poured on the respective plates; after solidification, the disc was placed and kept for incubation at 37°C for 24 hours. After incubation, the zone of inhibition was measured [23].

2.6.2. Antifungal Activity. Antifungal activity of biosynthesised copper oxide nanoparticle was determined against four fungal strains (*Candida albicans*, *Aspergillus niger*, *Aspergillus flavus*, *Aspergillus aculeatus*). This action was done by disc diffusion method using potato dextrose agar [24]. Pour the sterilized media on the plates allowed to solidification. The disc was placed on the plates and kept for incubation at 25°C for 48 hours after treated with UV radiation [25].

2.6.3. Antioxidant Activity. Antioxidant activity was performed by DPPH (1,1-diphenyl-2-picrylhydrazyl) assay to CuO nanoparticle [26]. Antioxidants play a major role in health protecting factor; it is reducing the chronic disorders [27]. This method gives the antioxidants possible potential of *quadangularis*-mediated synthesis of NPs. Free radical scavenging activity of different concentration (50 µg/mL, 100 µg/mL, 150 µg/mL, and 200 µg/mL) of nanoparticles by 0.01 Mm of DPPH (39.432 g/mol) were prepared dissolved in ethanol [27]. The prepared DPPH solution was incubated for 30 minutes at dark place. Then, solution (2 mL) was added to the different concentration NPs, and 2 mL of ethanol was added and incubated for 30 minutes. The reference standard (positive control) compound being used was ascorbic acid, the absorbance measured at 517 nm [28].

2.6.4. Antidiabetic Activity. Diabetes mellitus is a chronic disorder which leads to severe tissue damage and vascular damage due to insulin sufficient. The herbal products are playing major role in drug development [29]. Here, the *Cissus quadrangularis*-mediated synthesis of NPs was used to determine the efficiency against diabetes characterized by alpha amylase activity. To take the different concentrations of NPS (50 µg/mL, 100 µg/mL, 150 µg/mL, and 200 µg/mL), add the 500 µL of phosphate buffer containing alpha amylase (0.5 mg/mL) solution. The mixture was incubated for 10 minutes at RT. Then, 500 µL of 1% starch-containing phosphate buffer solution was incubated for 10 minutes. Then, add the 1 mL of DNSA (containing 0.5 g of dinitro salicylic acid, 15 g of sodium potassium tartrate diluted in 50 mL of distilled water). It was kept for 5 minutes in water bath [29]. The reaction mixtures make up into 5 mL of distilled water, and optical density was observed at 540 nm.

2.6.5. Anti-inflammatory Activity. Inflammation in biological response from damage cells (local tissue injury) is a difficult response that prevent the tissue damage and invasion of microbes through the small cuts, scratch, and abrasions [30].

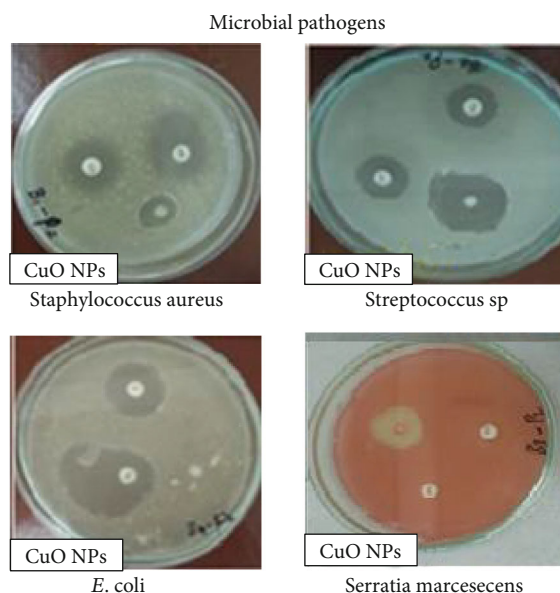
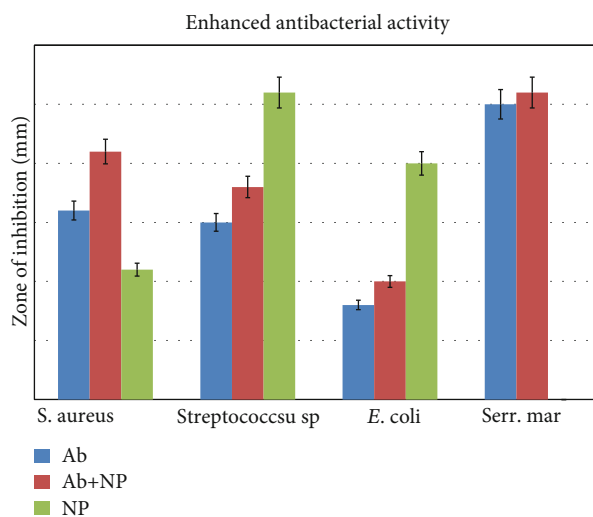


FIGURE 10: Antibacterial activity of copper oxide nanoparticles against *Staphylococcus aureus*, *Streptococcus*, *E. coli*, and *Serratia marcescens*.

TABLE 4: Antifungal activity against plant-mediated synthesis copper oxide NPs.

Clinical isolates	Ab	Ab+NP	NP
<i>Candia albicans</i>	7	22	17
<i>Aspergillus niger</i>	7	16	R
<i>Aspergillus flavus</i>	7	8	R
<i>Aspergillus aculeatus</i>	11	14	R

The membrane stabilization assay was performed by O positive blood. 10 mL of blood were collected with equal volume of Alsever solution (1 g of dextrose, 0.8 g of sodium citrate, 0.025 g citric acid, and 0.21 g sodium chloride in 50 mL) centrifuged at 3000 rpm, then the cells were separated and washed with isosaline (0.9 g of NaCl in 100 mL of distilled

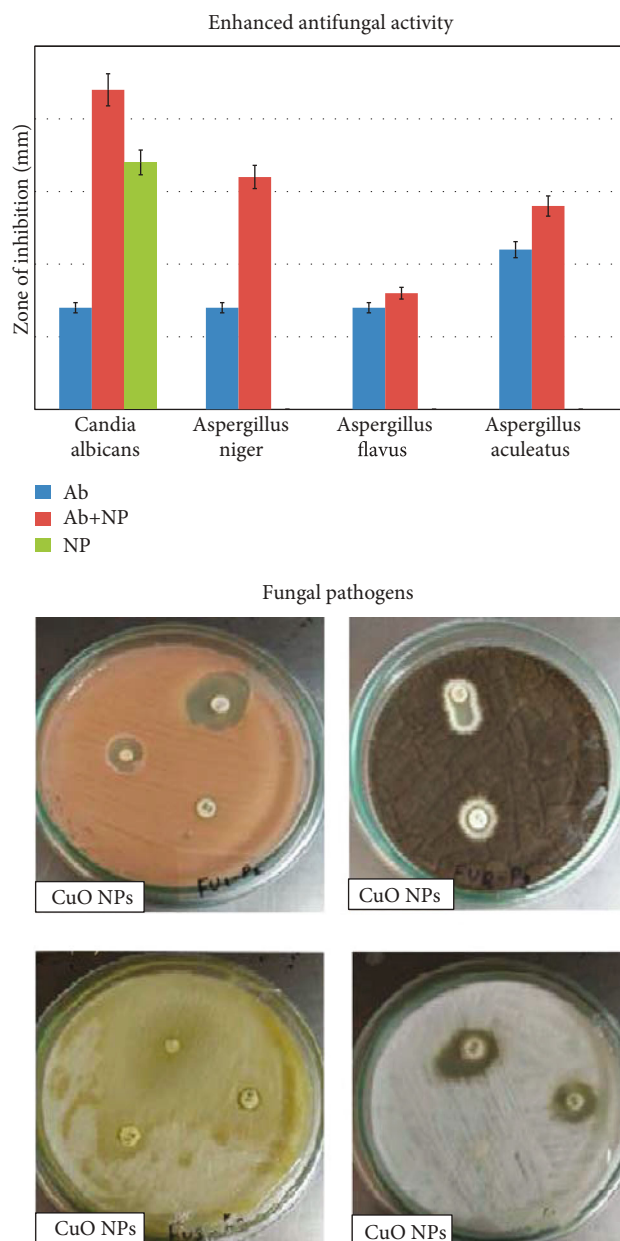


FIGURE 11: Antifungal activity of copper oxide nanoparticles.

water). Then, the different concentrations of NPs were mixed with HRBC (0.5 mL), phosphate buffer (0.5 mL), and 2 mL of hyphosaline (0.4 g NaCl in 100 mL). The mixture of solution was incubated at 37°C for 30 minutes and centrifuged at 3000 rpm. Then, the absorbance of haemoglobin content was estimated at 560 nm [31].

2.6.6. Antiproteinase Action. The herbal-mediated synthesis of nanoparticle was studied for anti-inflammatory activity by antiproteinase action. The reaction mixture contains 0.06 mg of trypsin, 1 mL of test Mm tris Hcl buffer, and different concentration (50 µg/mL, 100 µg/mL, 150 µg/mL, and 200 µg/mL) of nanoparticle. These mixtures of solution were incubated at 37°C for 5 minutes [30]. After incubation 1 mL of 8% (W/V) casein was added and incubated for 20

TABLE 5: *C. quadrangularis*-mediated synthesis of CuNo4 NPs.

Concentration	Standard	Control	NPs	Scavenging activity	IC 50
50 µg/mL	0.084	0.934	0.245	73.76874	
100 µg/mL	0.095	0.934	0.856	8.351178	264.69
150 µg/mL	0.102	0.934	0.867	7.173448	
200 µg/mL	0.108	0.934	0.871	6.745182	

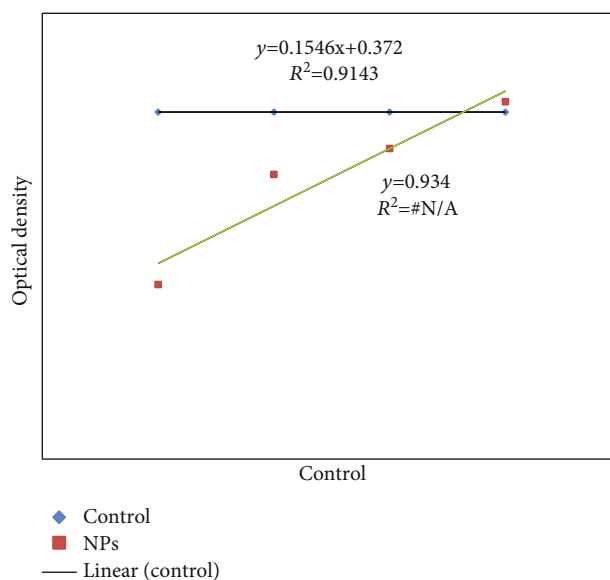


FIGURE 12: Antioxidant activity of copper oxide NPs.

minutes. The 2 mL of perchloric acid was added. The cloudy suspension were centrifuged, and the absorbance of nanoparticles were taken at 210 nm [32].

2.7. Statistical Analysis. All the data are represented as mean ± SD. The standard one-way ANOVA was used for standardization with p value < 0.05 which is considered as statistically significant.

3. Results and Discussion

3.1. Phytochemical Screening. The collected plant material was analysed by the phytochemical screening to check the presence of amino acid like carbohydrates and other compounds. Table 1 and Figure 2 shows the positive and negative result of the plant extract.

3.2. Characterization

3.2.1. UV-Visible Spectrophotometer. The characterization of nanoparticles begins with the UV-Visible absorbance, which depends upon the principle of SPR (surface plasmon resonance), where the conducting electrons get excited, and the absorbance is measured. The absorbance of nanomaterials observed ranges between the 300 and 700 nm. In this case, the copper ions reduced to nanoparticulate forms using the extract of *Cissus quadrangularis*. The reaction time taken was 4 h with maximum absorbance of 340 nm as shown in Figure 3 [22].

TABLE 6: *C. quadrangularis*-mediated synthesis of copper oxide NPs.

Concentration	I	II	III	MEAN	STD DEV	STD ERR	Final
50 $\mu\text{g/mL}$	1.286	1.334	1.378	1.33	0.046014	0.03	11.07 \pm 0.21
100 $\mu\text{g/mL}$	2.055	2.145	2.223	2.14	0.084071	0.05	11.07 \pm 0.22
150 $\mu\text{g/mL}$	2.257	1.278	1.345	1.63	0.546912	0.32	11.07 \pm 0.23
200 $\mu\text{g/mL}$	3.157	3.234	3.279	3.22	0.061695	0.04	11.07 \pm 0.24

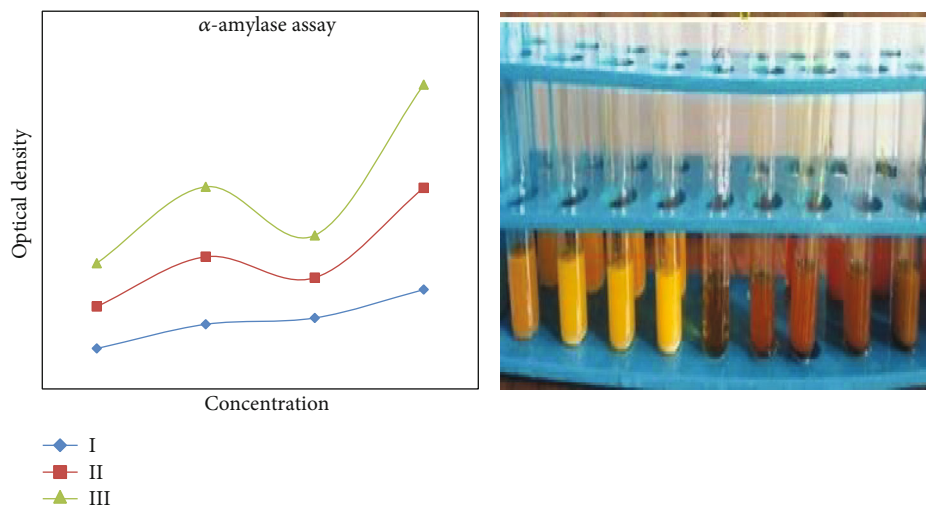


FIGURE 13: Antidiabetic activity of copper oxide NPs.

3.2.2. *X-Ray Diffraction Analysis*. The size of the nanoparticles was calculated according to these peak values and crystalline size [33]. The synthesised herbal and fungal nanoparticles by copper sulfide size were found by the Debye-Scherrer equation from the 2θ values and crystalline size from Table 2 and Figure 4.

$$D = k\lambda/B \cos \theta \quad (\text{Particle Size} = (0.9 \times \lambda)/(d \cos \theta))$$

$$K = 0.9(\text{constant}); \lambda = 1.54060(\text{constant}); 2\theta = 29.72;$$

$$\theta = 12.86; B = 0.187 = 0.9 \times 1.5406 \times 10^{-10}/0.187 \\ \times \cos 12.86 \times 0.01744$$

$$D = 42\text{nm} \quad B = \text{Full width half maximum (radian)} \quad (1)$$

3.2.3. *TGA Analysis*. From this result, to evaluate the loss of weight and peak of the temperature was observed [34, 35]. To find the weather, the nanoparticles increase or decrease their weight by TGA. The analysis of room temperature was observed from 800°C. The differential thermal analysis shows the (CuO-plant) 2.2060 mg ranges for synthesised materials. The thermal gravimetric analysis gave the weight loss of material at a particular temperature as shown in Figures 5 and 6.

3.2.4. *Fourier-Transform Infrared Spectroscopy*. The functional groups of *Cissus quadrangularis* plant-mediated synthesis of copper oxide nanoparticles is 3269.34 cm^{-1} N-H stretch band due to presence of amine group. This primary amine produces two N-H absorptions, 2920.23 cm^{-1} belongs

TABLE 7: *C. quadrangularis*-mediated synthesis of copper oxide NPs.

Concentration	Standard	NPs
50 $\mu\text{g/mL}$	1.22	0.649
100 $\mu\text{g/mL}$	2.403	0.198
150 $\mu\text{g/mL}$	2.311	0.248
200 $\mu\text{g/mL}$	2.363	0.246

to alkene group (C-H bond), and 1602.85 cm^{-1} and 1438.90 cm^{-1} have an aromatic compounds (C=C bond). From this analysis, it is suggested that antioxidant enzymes with amines, ethyl Ester, aromatic compounds, alkenes, and acetic acids might be absorbed on biosynthesized copper oxide nanoparticle as shown in Figure 7.

3.2.5. *Atomic Force Microscope*. Figure 8 shows the AFM images and express their surface size such as for scanned area range of *C. quadrangularis*-mediated synthesis of copper oxide NPs 70 to 100 nm. From this surface analysis, the particle size display the clusters of even line of profile [36].

3.2.6. *Scanning Electron Microscope*. It was observed 90 nm copper oxide nanoparticles synthesized using *Cissus quadrangularis*. The plant extracts exhibit different shapes of nanoparticles confirmed using SEM [37]. The presence of copper nanoparticle was confirmed by the EDX analysis, whereas the peaks gave the amount of particles in sample as shown in Figure 9.

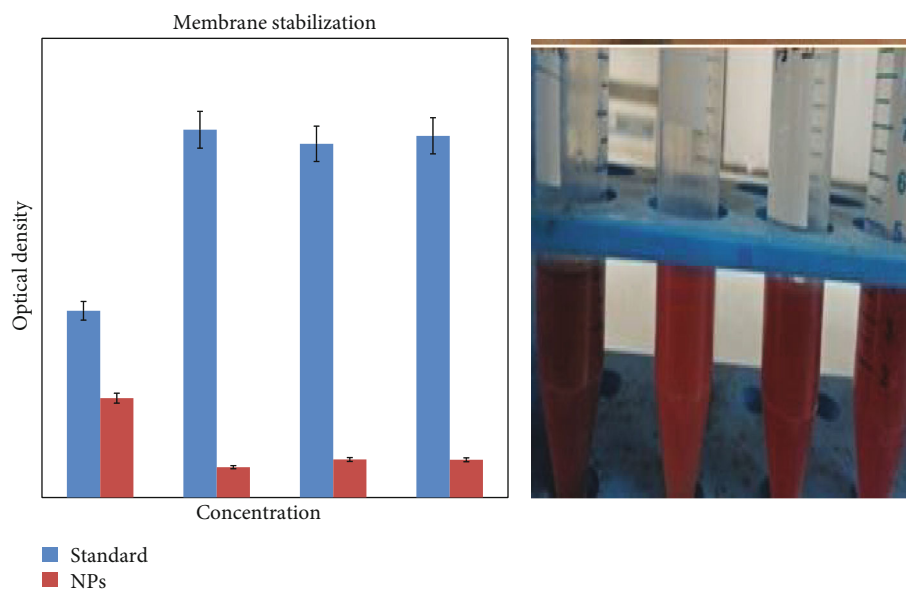


FIGURE 14: Anti-inflammatory activity of copper oxide NPs.

TABLE 8: *C. quadrangularis*-mediated synthesis of copper oxide nanoparticles.

Concentration	I	II	III	MEAN	Std. dev	Std. err	Final
50 $\mu\text{g/mL}$	1.426	1.467	1.521	1.47	0.047648	0.03	11.07 \pm 0.21
100 $\mu\text{g/mL}$	1.836	1.895	1.921	1.88	0.043555	0.03	11.07 \pm 0.22
150 $\mu\text{g/mL}$	2.422	1.491	1.567	1.83	0.516972	0.30	11.07 \pm 0.23
200 $\mu\text{g/mL}$	3.191	3.245	3.456	3.30	0.140037	0.08	11.07 \pm 0.24

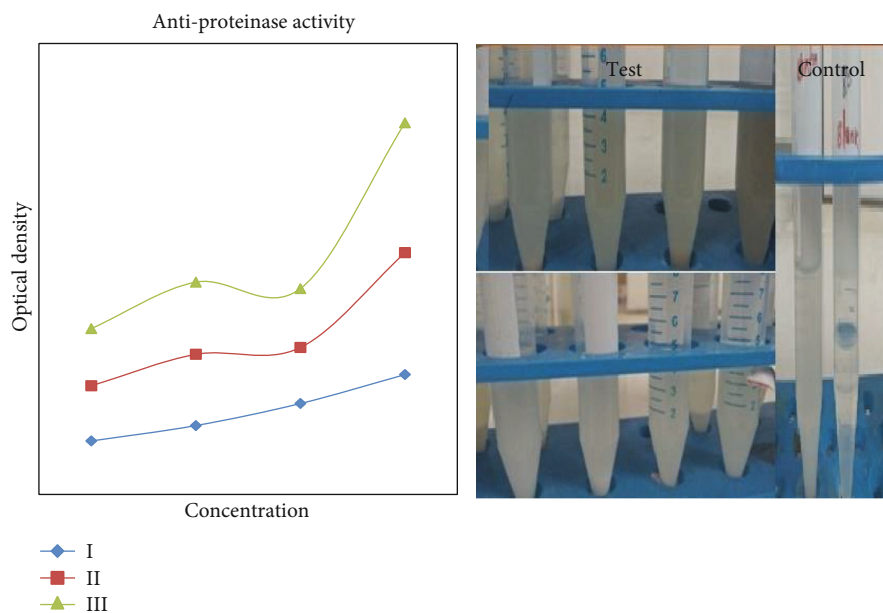


FIGURE 15: Antiproteinase activity of copper oxide NPs.

3.2.7. Antibacterial Activity. The antibacterial activity of the copper oxide nanoparticle was observed by the antibacterial-enhanced method using control as streptomycin. Different formulations which involve the different mode of preparation

or surface-decorated biomolecules of antimicrobial agents are produced which is cost effective, safe, and can also be treated against many MDR cultures [38]. The antibacterial activity was evaluated against *Staphylococcus aureus*, *Streptococcus*,

E. coli, and *Serratia marcescens*. The zone of inhibition measured between the three different modes such as in each space contains the antibiotic disc, antibiotic disc with nanoparticles, and nanoparticles. From the result, the nanoparticle copper oxide (26 nm) has a high effect against *E. coli*, the form of antibiotics with NPs as shown in Table 3 and Figure 10. The need to develop novel antibacterial agents has become an important task amongst researchers as a problem of resistance against bacterial cultures is being generated. The mechanism behind its antibacterial potential is explained by the interaction of the nanoparticles with outer surface of the cell membrane of the cultures, which eventually leads to disruption of the integrity of the membrane by producing pits in them, and increase of permeability causes a release of lipopolysaccharide molecules or other protein materials, and this results in cell death [39, 40].

3.2.8. Antifungal Activity. The antifungal activity of copper oxide NP against *Candida albicans*, *Aspergillus niger*, *Aspergillus flavus*, and *Aspergillus aculeatus* was executed; the result has a good antifungal agent. The green synthesised copper oxide nanoparticle acts as better antifungal agent compared to earlier report and commercially available standards as shown in Table 4 and Figure 11.

3.2.9. Antioxidant Activity. Antioxidant activity of copper oxide NP was determined by DPPH assay through the free radical scavenging activity. The ascorbic was used as a standard and methanol act as a negative control. From the calibration curve, the IC 50 values denoted the inhibition of concentration in scavenge 50% of the DPPH free radical activity as shown in Table 5 and Figure 12.

$$\text{Scavenging activity} = A_0 - A_1/A_0 \times 100$$

$$A_0 = \text{Absorbance of the control}$$

$$A_1 = \text{absorbance of the test sample} \quad (2)$$

$$Y = 0.153x + 0.362 \quad (mx + c)$$

$$\text{IC 50} = 50 - 0.362/0.153$$

$$Y = 324.42$$

3.2.10. Antidiabetic Activity. Alpha amylase activity of copper oxide NP was assessed by the DNSA method. The triplicate values of amylase assay confirm the information in the measurement process which gave the mean of average the 3 values and standard deviation for exact variation in the samples of nanoparticles as shown in Table 6 and Figure 13.

3.2.11. Anti-inflammatory Activity. The anti-inflammatory activity of copper oxide NPs shows the values about the inhibition of the concentration. Stabilization of membrane will produce the various disorder related to the inflammation due to release of lysosomal enzymes (as shown in Table 7 and Figure 14).

3.2.12. Antiproteinase Action. Antiproteinase action is one of the assessments of anti-inflammatory activity. It played an important role in the tissue damage during the inflammation

action. This analysis is done by triplicate, and the results were calculated through the mean and standard deviation to find the variables between the samples as shown in Table 8 and Figure 15.

4. Conclusion

The nanoparticle screening confirms the presence of phytochemicals such as carbohydrates, saponins, tannins, flavonoid, alkaloids, and steroids. Characterization of NPs gave the structures and size for XRD evaluated by the Debye-Scherrer formula, and for FTIR, the presence of functional group distinguishes by value of peaks. For microbial studies, the result of antibacterial and antifungal activities was observed by the zone of inhibition. Other potentials of copper oxide nanoparticles were also evaluated like antioxidant, antidiabetic, and anti-inflammatory activity and antiproteinase action. Therefore, the mechanism behind its action is yet to be researched, but these nanoparticles can also be an agent which fills the criteria of eco-friendly, nontoxic, and easy production in larger scale.

Data Availability

The data used to support the findings of this study are included within the article.

Conflicts of Interest

The authors declare that there is no conflict of interest.

Authors' Contributions

SR designed the research; and SR and SM carried out research; and SM, SV, MP, DA, and KA wrote and corrected the manuscript.

Acknowledgments

The authors would like to acknowledge Saveetha Dental College and Hospital, SIMATS, and the work was funded by Researchers Supporting Project number (RSP-2021/165), King Saud University, Riyadh, Saudi Arabia.

References

- [1] A. I. El-Batal, N. E. Al-Hazmi, F. M. Mosallam, and G. S. El-Sayyad, "Biogenic synthesis of copper nanoparticles by natural polysaccharides and *Pleurotus ostreatus* fermented fenugreek using gamma rays with antioxidant and antimicrobial potential towards some wound pathogens," *Microbial Pathogenesis*, vol. 118, pp. 159–169, 2018.
- [2] N. Ali, Awais, T. Kamal et al., "Chitosan-coated cotton cloth supported copper nanoparticles for toxic dye reduction," *International Journal of Biological Macromolecules*, vol. 111, pp. 832–838, 2018.
- [3] M. Kumari, L. Ray, M. P. Purohit et al., "Curcumin loading potentiates the chemotherapeutic efficacy of selenium nanoparticles in HCT116 cells and Ehrlich's ascites carcinoma bearing mice," *European Journal of Pharmaceutics and Biopharmaceutics*, vol. 117, pp. 346–362, 2017.

- [4] K. T. Smitha, A. Anitha, T. Furuike, H. Tamura, S. V. Nair, and R. Jayakumar, "In vitro evaluation of paclitaxel loaded amorphous chitin nanoparticles for colon cancer drug delivery," *Colloids Surfaces B Biointerfaces*, vol. 104, pp. 245–253, 2013.
- [5] S. Roy, J. W. Rhim, and L. Jaiswal, "Bioactive agar-based functional composite film incorporated with copper sulfide nanoparticles," *Food Hydrocolloids*, vol. 93, pp. 156–166, 2019.
- [6] X. Huang, C. Xu, Y. Li, H. Cheng, X. Wang, and R. Sun, "Quaternized chitosan-stabilized copper sulfide nanoparticles for cancer therapy," *Materials Science and Engineering: C*, vol. 96, pp. 129–137, 2019.
- [7] S. Yadav, K. Shrivastava, and P. K. Bajpai, "Role of precursors in controlling the size, shape and morphology in the synthesis of copper sulfide nanoparticles and their application for fluorescence detection," *Journal of Alloys and Compounds*, vol. 772, pp. 579–592, 2019.
- [8] A. Sharma, A. Yadav, S. K. Sharma, and R. K. Sharma, "Laser induced morphology change in copper sulphide nanoparticles," *Colloids and Surfaces A: Physicochemical and Engineering Aspects*, vol. 565, pp. 172–179, 2019.
- [9] S. Shaji, V. Vinayakumar, B. Krishnan et al., "Copper antimony sulfide nanoparticles by pulsed laser ablation in liquid and their thin film for photovoltaic application," *Applied Surface Science*, vol. 476, pp. 94–106, 2019.
- [10] K. Saravanan, S. Selladurai, S. Ananthakumar, and R. Suriakarthick, "Solvothermal synthesis of copper cadmium sulphide (CuCdS₂) nanoparticles and its structural, optical and morphological properties," *Materials Science in Semiconductor Processing*, vol. 93, pp. 345–356, 2019.
- [11] M. Akhtar, Y. Alghamdi, J. Akhtar, Z. Aslam, N. Revaprasadu, and M. A. Malik, "Phase controlled synthesis of copper sulfide nanoparticles by colloidal and non-colloidal methods," *Materials Chemistry and Physics*, vol. 180, pp. 404–412, 2016.
- [12] A. Singh, R. Manivannan, and S. Noyel Victoria, "Simple one-pot sonochemical synthesis of copper sulphide nanoparticles for solar cell applications," *Arabian Journal of Chemistry*, vol. 8, pp. 1–9, 2019.
- [13] M. R. Hosseini, M. Schaffie, M. Pazouki, A. Schippers, and M. Ranjbar, "A novel electrically enhanced biosynthesis of copper sulfide nanoparticles," *Materials Science in Semiconductor Processing*, vol. 16, pp. 250–255, 2013.
- [14] K. Dobrovolný, P. Ulbrich, M. Švecová et al., "Copper nanoparticles in glycerol-polyvinyl alcohol matrix: in situ preparation, stabilisation and antimicrobial activity," *Journal of Alloys and Compounds*, vol. 697, pp. 147–155, 2017.
- [15] T. Kruk, K. Szczepanowicz, J. Stefańska, R. P. Socha, and P. Warszyński, "Synthesis and antimicrobial activity of monodisperse copper nanoparticles," *Colloids Surfaces B Biointerfaces*, vol. 128, pp. 17–22, 2015.
- [16] L. R. Ferguson, N. Karunasinghe, S. Zhu, and A. H. Wang, "Selenium and its' role in the maintenance of genomic stability," *Mutation Research/Fundamental and Molecular Mechanisms of Mutagenesis*, vol. 733, no. 1-2, pp. 100–110, 2012.
- [17] G. Caroling, M. N. Priyadarshini, E. Vinodhini, A. M. Ranjitham, and P. Shanthy, "Biosynthesis of copper nanoparticles using aqueous guava extract-characterisation and study of antibacterial effects," *International Journal of Pharmacy and Biological Science*, vol. 5, no. 2, pp. 25–43, 2015.
- [18] A. Y. Ghidan, T. M. Al-Antary, and A. M. Awwad, "Green synthesis of copper oxide nanoparticles using *Punica granatum* peels extract: Effect on green peach Aphid," *Environmental Nanotechnology, Monitoring & Management*, vol. 6, pp. 95–98, 2016.
- [19] I. Gnanasundaram and K. Balakrishnan, "Synthesis and evaluation of anti-inflammatory activity of silver nanoparticles from *Cissus vitiginea* leaf extract," *Journal of Nanoscience and Technology*, vol. 3, pp. 266–269, 2017.
- [20] C. Khurana, P. Sharma, O. P. Pandey, and B. Chudasama, "Synergistic effect of metal nanoparticles on the antimicrobial activities of antibiotics against biorecycling microbes," *Journal of Materials Science and Technology*, vol. 32, pp. 524–532, 2016.
- [21] B. H. Patel, M. Z. Channiwal, S. B. Chaudhari, and A. A. Mandot, "Biosynthesis of copper nanoparticles; its characterization and efficacy against human pathogenic bacterium," *Journal of Environmental Chemical Engineering*, vol. 4, pp. 2163–2169, 2016.
- [22] S. S. Shankar, A. Ahmad, R. Pasricha, and M. Sastry, "Bioreduction of chloroaurate ions by geranium leaves and its endophytic fungus yields gold nanoparticles of different shapes," *Journal of Materials Chemistry*, vol. 13, p. 1822, 2003.
- [23] F. Ijaz, S. Shahid, S. A. Khan, W. Ahmad, and S. Zaman, "Green synthesis of copper oxide nanoparticles using abutilon indicum leaf extract: antimicrobial, antioxidant and photocatalytic dye degradation activities," *Tropical Journal of Pharmaceutical Research*, vol. 16, pp. 743–753, 2017.
- [24] F. Elahian, S. Reisi, A. Shahidi, and S. A. Mirzaei, "High-throughput bioaccumulation, biotransformation, and production of silver and selenium nanoparticles using genetically engineered *Pichia pastoris*," *Nanomedicine: Nanotechnology, Biology and Medicine*, vol. 13, no. 3, pp. 853–861, 2017.
- [25] N. Vigneshwaran, A. A. Kathe, P. V. Varadarajan, R. P. Nachane, and R. H. Balasubramanya, "Biomimetics of silver nanoparticles by white rot fungus, *Phaenerochaete chrysosporium*," *Colloids and Surfaces B: Biointerfaces*, vol. 53, no. 1, pp. 55–59, 2006.
- [26] A. Nasser Singab, F. S. Youssef, and M. L. Ashour, "Medicinal plants with potential antidiabetic activity and their assessment," *Medicinal & Aromatic Plants*, vol. 3, no. 1, pp. 1–12, 2014.
- [27] L. R. Jaidev and G. Narasimha, "Fungal mediated biosynthesis of silver nanoparticles, characterization and antimicrobial activity," *Colloids Surfaces B Biointerfaces*, vol. 81, pp. 430–433, 2010.
- [28] H. Y. El-kassas, M. Abd, and E. Okbah, "Phytotoxic effects of seaweed mediated copper nanoparticles against the harmful alga: *Lyngbya majuscula*," *Journal, Genetic Engineering & Biotechnology*, vol. 15, pp. 41–48, 2017.
- [29] P. A. Akah, S. U. Uzodinma, and C. E. Okolo, "Antidiabetic activity of aqueous and methanol extract and fractions of *Gongronema latifolium* (Asclepidaceae) leaves in alloxan diabetic rats," *Journal of Applied Pharmaceutical Science*, vol. 1, pp. 99–102, 2011.
- [30] G. Leelaprakash, S. M. Dass, and B. Road, "Invitro anti-inflammatory activity of methanol extract of *enicostemma axillare*," *International Journal of Drug Development and Research*, vol. 3, pp. 189–196, 2011.
- [31] N. S. Mahabal and B. B. Kaliwal, "In vitro anti-inflammatory activity of L-asparaginase from soil rhizosphere fungus *Aspergillus tamarii*," *Current Trends in Biomedical Engineering & Biosciences*, vol. 4, no. 5, 2017.
- [32] J. Y. Kim, S. C. Park, I. Hwang et al., "Protease inhibitors from plants with antimicrobial activity," *International Journal of Molecular Sciences*, vol. 10, pp. 2860–2872, 2009.

- [33] J. Suárez-Cerda, H. Espinoza-Gómez, G. Alonso-Núñez, I. A. Rivero, Y. Gochi-Ponce, and L. Z. Flores-López, "A green synthesis of copper nanoparticles using native cyclodextrins as stabilizing agents," *Journal of Saudi Chemical Society*, vol. 21, pp. 341–348, 2017.
- [34] K. G. Rao, C. H. Ashok, K. V. Rao, C. S. Chakra, and P. Tambur, "Green synthesis of TiO₂ nanoparticles using aloe vera extract," *International Journal of Advanced Research (IJAR)*, vol. 2, pp. 28–34, 2016.
- [35] R. Dobrucka, "Synthesis of titanium dioxide nanoparticles using *Echinacea purpurea* herba," *Iranian Journal of Pharmaceutical Research: IJPR*, vol. 16, pp. 753–759, 2017.
- [36] P. Ananthi and S. M. J. Kala, "Plant extract mediated synthesis and characterization of copper nanoparticles and their pharmacological activities," *International Journal of Advanced Research (IJAR)*, vol. 6, pp. 13455–13465, 2017.
- [37] N. Soni and S. Prakash, "Efficacy of fungus mediated silver and gold nanoparticles against *Aedes aegypti* larvae," *Parasitology Research*, vol. 110, pp. 175–184, 2012.
- [38] H. Harikrishnan, A. Naif Abdullah, K. Ponmurugan, and R. Shyam Kumar, "Microbial synthesis of selenium nanocomposite using *Saccharomyces cerevisiae* and its antimicrobial activity against pathogens causing nosocomial," *Chalcogenide Letters*, vol. 9, pp. 509–515, 2012.
- [39] P. Jamdagni, P. Khatri, and J. S. Rana, "Green synthesis of zinc oxide nanoparticles using flower extract of *Nyctanthes arbor-tristis* and their antifungal activity," *Journal of King Saud University-Science*, vol. 30, no. 2, pp. 168–175, 2016.
- [40] A. Tovar-Corona, M. A. Lobo-Sánchez, J. L. Herrera-Perez, R. Zanella, J. I. Rodríguez-Mora, and O. Vázquez-Cuchillo, "Green synthesis of copper (0) nanoparticles with cyanidine-O-3-glucoside and its strong antimicrobial activity," *Materials Letters*, vol. 211, pp. 266–269, 2018.